Proceedings of the Seventh U.S.-Japan Workshop on Earthquake Resistant Design of Lifeline Facilities and Countermeasures Against Soil Liquefaction

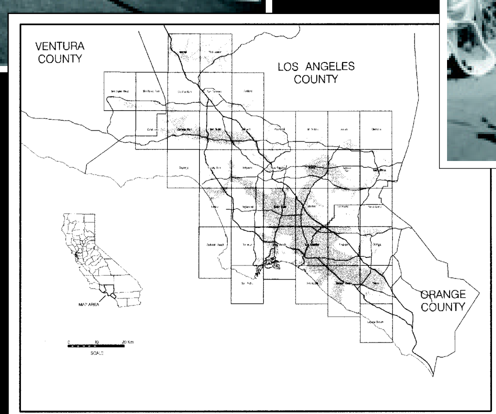

Edited by

Thomas D. O'Rourke
School of Civil and
Environmental Engineering
Cornell University
Ithaca, NY 14853-3501

Jean-Pierre Bardet
Department of Civil/
Environmental Engineering
University of Southern California
Los Angeles, California 90089-2531

Masanori Hamada
Department of Civil Engineering
Waseda University
3-4-1 Okubo Shinjuku-ku
Tokyo 169 Japan

MCEER
MULTIDISCIPLINARY CENTER FOR EARTHQUAKE ENGINEERING RESEARCH
A National Center of Excellence in Advanced Technology Applications

ISSN 1520-295X

Technical Report MCEER-99-0019
November 19, 1999

This workshop was held August 15-17, 1999 at the Sheraton Hotel and Towers, Seattle, Washington, and was supported by the National Science Foundation under Contract Number CMS 97-01471.

NOTICE

Cover Photo/Illustration Credits

Left photograph of subsidence of street surface over the collapsed Daikai Station following the Hanshin-Awaji, Japan earthquake, provided by T.D. O'Rourke. *Center illustration* from "Seismic Zonation for Liquefaction in California," by Mark J. DeLisle and Charels R. Real, pp. 217 in this volume. *Right photograph* of road failure following the Chi-Chi, Taiwan earthquake, provided by T.D. O'Rourke.

MULTIDISCIPLINARY CENTER FOR EARTHQUAKE ENGINEERING RESEARCH

A National Center of Excellence in Advanced Technology Applications

---

Proceedings of the Seventh U.S.-Japan Workshop on Earthquake Resistant Design of Lifeline Facilities and Countermeasures Against Soil Liquefaction

Held at the
Sheraton Hotel and Towers
Seattle, Washington
August 15-17, 1999

Edited by
Thomas D. O'Rourke[1], Jean-Pierre Bardet[2] and Masanori Hamada[3]

Publication Date: November 19, 1999

Technical Report MCEER-99-0019

Task Number 99-6002

NSF Master Contract Number CMS 97-01471

1 Thomas R. Briggs Professor of Engineering, School of Civil and Environmental Engineering, Cornell University
2 Professor, Department of Civil/Environmental Engineering, University of Southern California
3 Professor, Department of Civil Engineering, Waseda University

MULTIDISCIPLINARY CENTER FOR EARTHQUAKE ENGINEERING RESEARCH
University at Buffalo, State University of New York
Red Jacket Quadrangle, Buffalo, NY 14261

Preface

When the Seventh US-Japan Workshop was held in Seattle, WA, a devastating earthquake occurred in western Turkey, near Izmit, an industrial city of about 1 million people, approximately 90 km southeast of Istanbul. The 7.4 magnitude earthquake resulted in tens of thousands of deaths and serious injuries, destroyed thousands of buildings, incapacitated water delivery and electric power systems, caused a catastrophic fire at an oil refinery, and led to the failure of sea walls with serious flooding of waterfront developments. Participants of the workshop were among the first to be dispatched in US and Japanese reconnaissance teams to the earthquake-stricken area. The earthquake in Turkey is a sobering reminder of the importance of the workshop topics and the need to transfer lessons learned from earthquake experience into engineering practice.

The Seventh US-Japan Workshop was a forum for Japanese and US colleagues to share their ideas about earthquake damage to lifelines and explore advanced technologies for characterizing liquefaction, stabilizing hazardous sites, and improving post earthquake response and recovery. It is our hope that research results presented in these proceedings will be applied in engineering decisions, and that the workshop will act as a catalyst in promoting the transfer of technology from theory to practice.

J.P. Bardet
Professor, University of Southern California

M. Hamada
Professor, Waseda University

T.D. O'Rourke
Professor, Cornell University

US-Japan Cooperative Research Program and Workshops

The US-Japan Research Program on Earthquake Resistant Design of Lifeline Facilities and Countermeasures Against Soil Liquefaction focuses on the earthquake performance of lifelines, with emphasis on liquefaction-induced large ground deformations. Large ground deformations are the principal cause of subsurface structural damage during earthquakes. Currently, there is a growing recognition in the civil and earthquake engineering communities of the importance of large ground deformations. Our understanding of the mechanisms of large ground deformations and their effects on lifeline facilities, and our ability to predict the magnitude and distribution of ground displacements have improved substantially in recent years to provide a rational framework for siting, design, and protective measures. Both Japanese and US researchers have been working on this topic, and it was recognized that considerable benefits will result from their cooperative efforts to collect case history data and recommend the most appropriate analytical methods and design procedures.

The program was initiated formally in November, 1988 with the signing of a Memorandum of Understanding between the Japanese and US sides. The document was signed at a ceremony during a workshop in Tokyo, Japan by K. Kubo, Professor Emeritus of Tokyo University, and M. Shinozuka, currently the Champion Professor of Civil Engineering at the University of Southern California. Professor Kubo signed on behalf of the Association for the Development of Earthquake Prediction (ADEP), the Japanese sponsoring agency. Professor Shinozuka signed on behalf of Robert L. Ketter, then Director of the National Center for Earthquake Engineering Research (NCEER), the US sponsoring agency.

The research program has concentrated on case histories of earthquake-induced ground deformations and their effects on lifeline facilities. In addition to the publication of the case history volumes, the products of the cooperative research include US-Japan workshops and associated publications of the proceedings covering case history data, analytical modeling, experimental studies and recommendations for improved practices.

The US-Japan Workshop program is a major instrument for collaboration and cooperative exchange. To date, there have been seven workshops. The first was held in Tokyo and Niigata, Japan on November 16-19, 1988. The proceedings of this workshop were published by the Association for the Development of Earthquake Prediction, and are available from the Multidisciplinary Center for Earthquake Engineering and Research (MCEER). The second, third, fourth, fifth, and sixth workshops were held in Buffalo and Ithaca, NY, on September 26-29, 1989, San Francisco, CA on December 17-19, 1990, Honolulu, HI on May 27-29, 1992, Snowbird, UT on September 29-30 and October 1, 1994, and Waseda University, Tokyo, Japan on June 11-13, 1996, respectively. The proceedings of these workshops were published by MCEER. The seventh workshop was held at Seattle, WA on August 15-17, 1999. This volume contains the proceedings of the seventh workshop.

Cooperative research between Japanese and US earthquake engineers has resulted in significant new findings about liquefaction and its effects on lifeline facilities, assessment of liquefaction potential, modeling of liquefaction-induced large ground displacements, performance of lifeline facilities and foundations, dynamic response of underground structures, and countermeasures and earthquake resistant design against liquefaction.

It is hoped that the spirit of cooperation fostered by these workshops and research program will contribute to a strong and enduring relationship among US and Japanese engineers. It is believed that the research accomplishments of this collaborative activity will encourage additional joint projects and lead to improved understanding and mastery in the field of earthquake engineering.

T.D. O'Rourke
Professor, Cornell University

M. Hamada
Professor, Waseda University

J.P. Bardet
Professor, University of Southern California

Acknowledgments

The workshop co-chairs acknowledge and thank the Japanese Ministry of Education, Science, Sports, and Culture and the National Science Foundation (NSF), both of which have supported the workshop through the US-Japan Cooperative Research in Urban Earthquake Disaster Mitigation Program. In particular, the US co-chairs thank Drs. C. Astill and C. Liu of NSF for their encouragement and support. The co-chairs also acknowledge both the Multidisciplinary Center for Earthquake Engineering Research (MCEER) for its support with the conference organization and facilities as well as the publication of the proceedings, and the California Department of Transportation (Caltrans) for its support of the workshop organization and travel of the US participants. The co-chairs thank George Lee and Andrea Dargush, Director and Assistant Director of MCEER, respectively, for their assistance. The co-chairs also thank James Roberts, Director of Caltrans, Engineering Service Center, for his support and encouragement. Special thanks are extended to Siang-Huat Goh for his assistance in editing and organizing the proceedings.

M. Hamada
Professor, Waseda University

J.P. Bardet
Professor, University of Southern California

T.D. O'Rourke
Professor, Cornell University

Contents

I. Liquefaction and Ground Deformation

SASW Testing to Delineate Potentially Liquefiable Zones and Evaluate Remediation Measures
By R. Andrus and K. Stokoe, II 3

Judgement Method of Liquefaction Potential Using Acceleration Response Spectra
By S. Sawada and K. Toki 21

Evaluation of CPT Liquefaction Analysis Methods Against Inclinometer Data from Moss Landing
By R. Kulasingam, R. W. Boulanger, and I. M. Idriss 35

Site Amplification Ratios Estimated from Geomorphological Land Classification and JMA Strong Motion Records
By F. Yamazaki, K. Wakamatsu, K. Shabestari, and J-I. Onishi 55

CPT- and SPT-Based Probabilistic Assessment of Liquefaction Potential
By S. Toprak, T. L. Holzer, M. J. Bennett, and J. C. Tinsley, III 69

Conditions Underlying the Lateral Displacement of Sloped Ground During the 1964 Niigata and 1983 Nihonkai-Chubu Earthquakes
By K. Wakamatsu and M. Hamada 87

Revised MLR Equations for Predicting Lateral Spread Displacement
By T. L. Youd, C. M. Hansen, and S. F. Bartlett 99

Permanent Ground Deformation Due to Northridge Earthquake in the Vicinity of Van Norman Complex
By Y. Sano, T. D. O'Rourke, and M. Hamada 115

Fluid Dynamics Based Prediction of Liquefaction Induced Lateral Spreading Load
By R. Uzuoka, A. Yashima, and T. Kawakami 131

Experimental Study of Mitigation of Liquefied Ground Flow by Using Gravel Drain System
By M. Miyajima, M. Yoshida, and M. Kitaura 145

Large-Scale Modeling of Liquefaction-Induced Ground Deformation Part I: A Four-Parameter MLR Model
By J. P. Bardet, N. Mace, T. Tobita, and J. Hu 155

Large-Scale Modeling of Liquefaction-Induced Ground Deformation Part II: MLR Model Applications and Probabilistic Model
By J. P. Bardet, T. Tobita, N. Mace, and J. Hu 175

Similitude Law for Liquefied-Ground Flow
By M. Hamada 191

Seismic Zonation for Liquefaction in California
By M. J. DeLisle and C. R. Real 207

Verification of the Similitude Law for Flow of Liquefied Ground
By S. Hadush, A. Yashima, and R. Uzuoka 221

Limit State Model for Soil-Pile Interaction During Lateral Spread
By S. H. Goh and T. D. O'Rourke 237

Seismic Site Response and Liquefaction-Induced Shear Deformation
By Z. Yang, E. Parra, and A. Elgamal 261

Application of 3-D Distinct Element Method to Liquefaction
By K. Meguro and *T. Katayama* 271

Characteristics of Ground Motions at a Liquefiable Site
By J. Yang and T. Sato 279

De-Liquefaction Shock Waves
By B. L. Kutter and D. W. Wilson 295

A Simplified Practical Method for Evaluating Liquefaction-Induced Flow
By S. Yasuda, N. Yoshida, H. Kiku, and K. Adachi 311

Numerical Evaluation of Liquefaction Induced Ground Oscillation and Lurch
By G. R. Martin and P. Qiu 321

Time Dependent Ground Motion Amplification Due to Liquefaction on Man-made Island
By Y. Furumoto, E. Oka, M. Sugito, A. Yashima, and Y. Fukagawa 345

II. Lifelines and Earthquake Effects

Quantifying Earthquake and Geologic Hazards for the Portland, Oregon Water System Vulnerability Assessment
By D. Ballantyne, C. Scawthorn, and A. Vessely 363

The 1995 Kobe Earthquake and the New JWWA Seismic Design Guideline for Waterworks Facilities
By M. Matsushita 377

Estimation of Post Earthquake Water System Serviceability
By M. J. O'Rourke 391

Development of New Aseismic Joints for Casing Pipes of Underground Transmission Lines
By E. Miura, T. Tanaka, Y. Oda, and N. Ito 405

Case Study of the Granada Trunk Line During Two Near-Field Earthquakes
By C. A. Davis 415

Success in Lifeline Seismic Mitigation Programs
By L. V. Lund 431

Effects of Material Property on Inelastic Shell Buckling Strength of Line Pipe
By N. Suzuki, A. Katoh, E. Matsuyama, and M. Yoshikawa 441

Large Deformation Behavior of Low-Angle Pipeline Elbows
By K. Yoshizaki, M. Hamada, and T. D. O'Rourke 453

Summary of the Earthquake Resistant Design Standards for Railway Structures
By A. Nishimura 467

Visual Interpretation of Site Dynamic Response
By M. Zeghal, C. Oskay, M. K. Sharp, and R. Dobry 483

Formulation of Level 2 Earthquake Motions for Civil Engineering Structures
By T. Ohmachi 497

III. Waterfront Structures, Pile Foundations, and Buildings

Reliability and Redundancy of Engineering Systems by Information Entropy
By M. Hoshiya, K. Yamamoto, and H. Ohno 509

New Remedial Technique for Bridge Foundations Against Lateral Flow due to Liquefaction
By S. Mori and M. Terazawa 517

Centrifuge Modeling of Lateral Spreading Behind a Caisson Type Quay Wall During an Earthquake
By C-J. Lee, R. Dobry, T. Abdoun, and B-R. Wu 533

Residual Displacement of Gravity Quaywalls - Parameter Study Through Effective Stress Analysis
By S. Iai, K. Ichii, H. Sato, and H. Liu 549

Analysis on Liquefaction-Induced Subsidence of Shallow Foundation
By Y. Kobayashi, I. Towhata, and A. Acacio 565

Seismic Response Analysis of Pile Foundations at Liquefiable Sites
By W. D. L. Finn, T. Thavaraj, D. W. Wilson, R. W. Boulanger, and B. L. Kutter 579

Displacement Field of Granular Backfill Due to Earthquake Induced Quaywall Movement
By H. Akagi, K. Komiya, and H. Saitoh 587

Centrifuge Modeling of Effect of Superstructure Stiffness on Pile Bending Moments Due to Lateral Spreading
By R. Ramos, T. Abdoun, and R. Dobry 599

Applied Element Method: A New Efficient Tool for Design of Structure Considering its Failure Behavior
By K. Meguro and H. Tagel-Din 609

Appendix

Working Group Session Reports 627

Workshop Agenda 635

Workshop Participants 637

Liquefaction and Ground Deformation

SASW Testing to Delineate Potentially Liquefiable Zones and Evaluate Remediation Measures
By R. Andrus and K. Stokoe, II

Judgement Method of Liquefaction Potential Using Acceleration Response Spectra
By S. Sawada and K. Toki

Evaluation of CPT Liquefaction Analysis Methods Against Inclinometer Data from Moss Landing
By R. Kulasingam, R. W. Boulanger, and I. M. Idriss

Site Amplification Ratios Estimated from Geomorphological Land Classification and JMA Strong Motion Records
By F. Yamazaki, K. Wakamatsu, K. Shabestari, and J-I. Onishi

CPT- and SPT-Based Probabilistic Assessment of Liquefaction Potential
By S. Toprak, T. L. Holzer, M. J. Bennett, and J. C. Tinsley, III

Conditions Underlying the Lateral Displacement of Sloped Ground During the 1964 Niigata and 1983 Nihonkai-Chubu Earthquakes
By K. Wakamatsu and M. Hamada

Revised MLR Equations for Predicting Lateral Spread Displacement
By T. L. Youd, C. M. Hansen, and S. F. Bartlett

Permanent Ground Deformation Due to Northridge Earthquake in the Vicinity of Van Norman Complex
By Y. Sano, T. D. O'Rourke, and M. Hamada

Fluid Dynamics Based Prediction of Liquefaction Induced Lateral Spreading Load
By R. Uzuoka, A. Yashima, and T. Kawakami

Experimental Study of Mitigation of Liquefied Ground Flow by Using Gravel Drain System
By M. Miyajima, M. Yoshida, and M. Kitaura

Large-Scale Modeling of Liquefaction-Induced Ground Deformation Part I: A Four-Parameter MLR Model
By J. P. Bardet, N. Mace, T. Tobita, and J. Hu

Large-Scale Modeling of Liquefaction-Induced Ground Deformation Part II: MLR Model Applications and Probabilistic Model
By J. P. Bardet, T. Tobita, N. Mace, and J. Hu

Similitude Law for Liquefied-Ground Flow
By M. Hamada

Seismic Zonation for Liquefaction in California
By M. J. DeLisle and C. R. Real

Verification of the Similitude Law for Flow of Liquefied Ground
By S. Hadush, A. Yashima, and R. Uzuoka

Limit State Model for Soil-Pile Interaction During Lateral Spread
By S. H. Goh and T. D. O'Rourke

Seismic Site Response and Liquefaction-Induced Shear Deformation
By Z. Yang, E. Parra, and A. Elgamal

Application of 3-D Distinct Element Method to Liquefaction
By K. Meguro and *T. Katayama*

Characteristics of Ground Motions at a Liquefiable Site
By J. Yang and T. Sato

De-Liquefaction Shock Waves
By B. L. Kutter and D. W. Wilson

A Simplified Practical Method for Evaluating Liquefaction-Induced Flow
By S. Yasuda, N. Yoshida, H. Kiku, and K. Adachi

Numerical Evaluation of Liquefaction Induced Ground Oscillation & Lurch
By G. R. Martin and P. Qiu

Time Dependent Ground Motion Amplification Due to Liquefaction on Man-made Island
By Y. Furumoto, F. Oka, M. Sugito, A. Yashima, and Y. Fukagawa

SASW Testing to Delineate Potentially Liquefiable Zones and Evaluate Remediation Measures

Ronald D. Andrus[1] and Kenneth H. Stokoe, II[2]

Abstract

Shear wave velocity measurements represent one way to evaluate the liquefaction resistance of soil. Spectral-Analysis-of-Surface-Waves (SASW) testing is an emerging seismic technique which can be used to measure shear wave velocity (V_S) profiles in all types of soil. Since the SASW technique is noninvasive, it is especially useful for testing hard-to-sample materials such as potentially liquefiable deposits containing large amounts of gravel and/or cobbles. Furthermore, the noninvasive nature of the technique makes it a cost-effective means of developing two- and three-dimensional (2-D and 3-D) profiles of V_S, both before and after remediation measures have been performed. The simplified procedure for evaluating the liquefaction resistance of granular soil based on V_S measurements is briefly discussed. One example is presented showing the use of SASW testing to develop a 2-D V_S profile along the south-eastern perimeter of Treasure Island, California. The area profiled was about 240 m long and 20 m deep. The profile covers zones of unimproved and improved sandy fill. The improved sandy fill had been remediated by densification to a depth of about 12 m using a vibrating probe. The improved zone was correctly delineated in the 2-D profile. Based on shear wave velocities, the improved zone was correctly predicted to not liquefy during the 1989 Loma Prieta earthquake (M_W = 7) while the unimproved zone was correctly predicted to exhibit marginal liquefaction during the same earthquake.

[1] Assistant Professor, Clemson University, Clemson, South Carolina 29634
[Formerly, Research Civil Engineer, National Institute of Standards and Technology, Gaithersburg, MD 20899-8611]

[2] Cockrell Family Regents Chair No. 9, University of Texas at Austin, Austin, TX 78712

Introduction

Liquefaction of loose deposits of granular soil is a major cause of damage in many earthquakes. Delineation of soft soil layers and prediction of their liquefaction resistance are key inputs in the engineering design of new and retrofitted structures. This information is also essential for reliable estimation of economic losses during future earthquakes. When projects extend for great distances, such as lifelines, cost-effective evaluations for extensive areas are required. Screening techniques based on geology, hydrology, and soil conditions show promise for identifying areas requiring more rigorous analyses. However, even these areas requiring further analyses can be quite large.

One promising technique for spatially evaluating the liquefaction susceptibility of granular soils is the Spectral-Analysis-of-Surface-Waves (SASW) technique. This technique can also be employed to evaluate soil conditions after remediation. The SASW technique is an in situ seismic method for determining small-strain shear wave velocity, V_S, profiles of soil deposits and pavement systems (Stokoe and Nazarian, 1985; Stokoe et al., 1988a; Nazarian and Stokoe 1989; Gucunski and Woods, 1991; Stokoe et al., 1994). SASW testing does not require boreholes, and is well suited for profiling large areas with the objective of developing two- and three-dimensional V_S images of the subsurface. The use of V_S as an index of liquefaction potential is discussed below. Also, a case history is presented where unimproved and improved (remediated) sandy fills were profiled by SASW testing and their liquefaction resistances were evaluated using the V_S profiles. It should be noted that the bulk of the material presented herein has been excerpted from one paper, Andrus et al., 1998a, and two NIST reports, Andrus et al., 1998b and Andrus et al., 1999.

Liquefaction Resistance Based On V_S

Small-strain shear wave velocity measurements provide a promising alternative, or supplement, to penetration-based approaches such as the Standard Penetration Test (SPT) and Cone Penetration Test (CPT) approaches originally developed by Seed and Idriss (1971) and Robertson and Campanella (1985), respectively. The use of V_S as an index of liquefaction resistance is soundly based, since both V_S and liquefaction resistance are similarly influenced by many of the same factors (e.g., void ratio, state of stress, stress history, and geologic age). Furthermore, the strong theoretical basis underlying stress wave propagation offers the opportunity for additional advances in the approach.

During the past two decades, a number of simplified procedures for evaluating liquefaction resistance based on V_S have been proposed (Dobry et al., 1981; Dobry et al., 1982; Seed et al., 1983; Bierschwale and Stokoe, 1984; de Alba et al., 1984; Hynes, 1988; Stokoe et al., 1988b; Tokimatsu and Uchida, 1990; Tokimatsu et al., 1991; Robertson et al., 1992; Kayen et al., 1992; Andrus, 1994; Lodge, 1994; Rashidian, 1995; Kayabali, 1996; Rollins et al., 1998;

Andrus and Stokoe, 1997; and Andrus, et al., 1999). Several of these procedures follow the general format of the Seed-Idriss simplified procedure, with V_S corrected to a reference overburden stress and correlated with the cyclic stress ratio. However, nearly all of the simplified V_S procedures have been developed with limited or no field performance data.

Outlined below is the assessment procedure based on V_S that was originally proposed by Andrus and Stokoe (1997) and subsequently updated by Andrus, et al. (1999). The updated procedure uses an expanded database consisting of field performance data from 26 earthquakes and in situ V_S measurements at over 70 sites. Much of the new data are from the 1995 Hyogoken-Nanbu (Kobe), Japan earthquake.

Evaluation Procedure

Three parameters are required to evaluate the liquefaction resistance of soil. These parameters are: 1. the level of cyclic loading of the soil, expressed as a cyclic stress ratio; 2. the stiffness of the soil, expressed as an overburden-stress-corrected shear wave velocity; and 3. the boundary separating liquefaction and non-liquefaction occurrences, expressed as a cyclic resistance ratio. Each parameter is discussed below.

Cyclic stress ratio (CSR) - The cyclic stress ratio, τ_{av}/σ'_v, at a particular depth in a level soil deposit can be expressed as (Seed and Idriss, 1971):

$$\frac{\tau_{av}}{\sigma'_v} = 0.65 \left(\frac{a_{max}}{g}\right)\left(\frac{\sigma_v}{\sigma'_v}\right) r_d \qquad (1)$$

where τ_{av} is the average equivalent uniform cyclic shear stress caused by the earthquake and is assumed to be 0.65 of the maximum induced stress, a_{max} is the peak horizontal ground surface acceleration, g is the acceleration of gravity, σ'_v is the initial effective vertical (overburden) stress at the depth in question, σ_v is the total vertical (overburden) stress at the same depth, and r_d is a shear stress reduction coefficient to adjust for flexibility of the soil profile.

Stress-corrected shear wave velocity- (V_{S1}) - Following the traditional procedures for correcting SPT blow count to account for overburden stress, one can correct V_S to a reference overburden stress by (Sykora, 1987; Robertson et al., 1992):

$$V_{S1} = V_S \left(\frac{P_a}{\sigma'_v}\right)^{0.25} \qquad (2)$$

where V_{S1} is the overburden-stress-corrected shear wave velocity, P_a is a reference stress of 100 kPa or about atmospheric pressure, and σ'_v is the initial effective overburden stress in kPa. In using Eq. 2, it is implicitly assumed that the initial effective horizontal stress, σ'_h, is a constant factor of the effective vertical stress. The factor, generally referred to as K'_o, is assumed to be approximately 0.5 at sites where liquefaction has occurred. Also, in applying Eq. 2, it is implicitly assumed that V_S is measured with both the directions of particle motion and wave propagation polarized along principal stress directions and one of these directions is vertical (Stokoe et al., 1985).

Cyclic resistance ratio (CRR)- The value of the cyclic stress ratio, CSR, separating liquefaction and non-liquefaction occurrences for a given V_{S1} (or corrected blow count in the SPT procedure) is called the cyclic resistance ratio, CRR. Andrus and Stokoe (1997) proposed the following relationship between cyclic resistance ratio, *CRR*, and V_{S1}:

$$\mathrm{CRR} = \left\{ a\left(\frac{V_{S1}}{100}\right)^2 + b\left(\frac{1}{V_{S1}^* - V_{S1}} - \frac{1}{V_{S1}^*}\right)\right\}\mathrm{MSF} \quad (3)$$

where V_{S1}^* is the limiting upper value of V_{S1} for liquefaction occurrence, a and b are curve fitting parameters, and MSF is the magnitude scaling factor. The first term of Eq. 3 is based on a modified relationship between V_{S1} and *CSR* for constant average cyclic shear strain suggested by R. Dobry (personal communication to R. D. Andrus, 1996). The second term is a hyperbola with a small value at low values of V_{S1}, and a very large value as V_{S1} approaches V_{S1}^*.

The magnitude scaling factor, which accounts for the effect of earthquake magnitude on the CRR, can be expressed by:

$$\mathrm{MSF} = \left(\frac{M_w}{7.5}\right)^n \quad (4)$$

where n is an exponent. The lower bound for the range of magnitude scaling factors recommended by the 1996 National Center for Earthquake Engineering Research (NCEER) Workshop on Evaluation of Liquefaction Resistance of Soils (Youd et al., 1997) is defined by Eq. 4 with n = -2.56 (Idriss, personal communication to T. L. Youd, 1995). More recently, Idriss (1999) proposed revised magnitude scaling factors that can be reasonably approximated by Eq. 4 with n = -1.75. The difference in the two proposed MSF relationships is not significant for earthquake with magnitudes of about 7 to 7.5, the range of the majority of the liquefaction case histories.

Liquefaction Evaluation Charts

The case history data for magnitude 5.9 to 8.3 earthquakes adjusted using Eq. 4 with n = -2.56 are presented in Fig. 1. Also presented in the figure are the proposed *CRR*-V_{S1} curves. The curves are defined by Eq. 3 with a = 0.022, b = 2.8, and V_{S1}^* = 200 m/s for a fines content (FC) ≥ 35 %, V_{S1}^* = 208 m/s for FC = 20 % and V_{S1}^* = 215 m/s for FC ≤ 5 %. The case history data, and *CRR*-V_{S1} curves, are limited to relatively level ground sites with average depths less than 10 m, uncemented soils of Holocene age, ground water table depths between 0.5 m and 6 m, and V_S measurements performed below the water table.

Of the 90 liquefaction case histories shown in Fig. 1, only two incorrectly lie in the no-liquefaction region. The two liquefaction cases that lie in the no-liquefaction region are for sites at Treasure Island, California. These sites are located along the perimeter of the island where liquefaction was marginal during the 1989 Loma Prieta earthquake ($M_W = 7.0$).

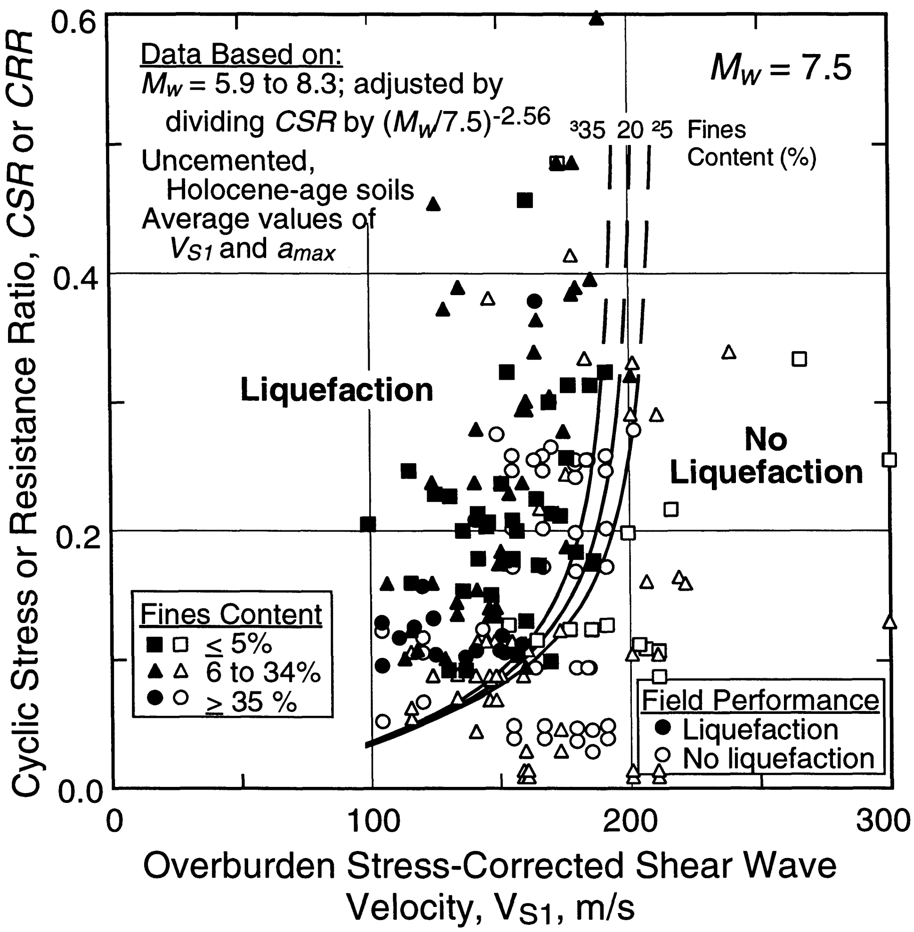

Figure 1 **Curves Proposed by Andrus et al. (1999) for Calculation of *CRR* from V_S Measurements Along with Case History Data Based on Lower Bound Values of MSF for the Range Recommended by the 1996 NCEER Workshop (Youd et al., 1997) and Average r_d Values Developed by Seed and Idriss (1971)**

To illustrate the effect of using different magnitude scaling factors on the case history data, the data have been recalculated using the MSF proposed by Idriss (1999). The recalculated case history data are presented in Fig. 2. Also shown in Fig. 2 are the same three liquefaction resistance curves from Fig. 1. Many of the case history data in Fig. 2 plot at higher CSR values than in Fig. 1 since the earthquake magnitude is ≤ 7.5 for most of the data. The upward shifting in the liquefaction data points near the curves at CRR of about 0.08 is less than 0.01. This difference is not significant and is within the accuracy of the plotted case history data.

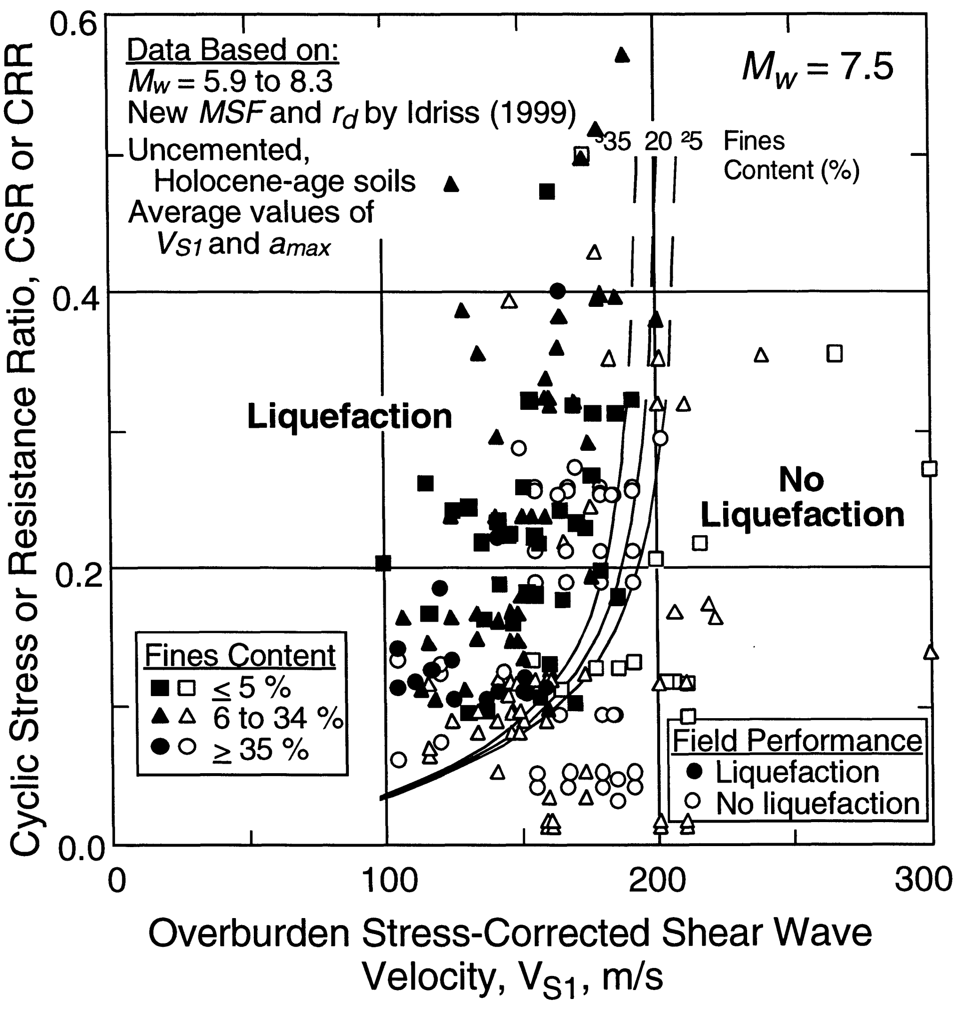

Figure 2 **Curves Recommended for Calculation of *CRR* from Shear Wave Velocity Measurements Along with Case History Data Based on Revised Values of MSF and r_d Proposed by Idriss (1999)**

The three CRR- V_{S1} curves shown in Figs. 1 and 2 exhibit V_{S1} values of 195 m/s and 210 m/s at CRR near 0.6 for FC $\geq$ 35 % and FC $\leq$ 5 %, respectively. These V_{S1} values are considered equivalent to corrected blow counts, $(N_1)_{60}$, of 21 for FC $\geq$ 35 % and 30 for FC $\leq$ 5 % commonly assumed in the SPT-based procedure as the limiting upper values for cyclic liquefaction occurrence in the respective soils.

Factor of Safety

A common way to quantify the potential or hazard for liquefaction is in terms of a factor of safety. The factor of safety, FS, against liquefaction for a material characterized by V_{S1} can be defined by:

$$FS = \frac{CRR}{CSR} \tag{5}$$

Liquefaction is predicted to occur when FS $\leq$ 1. Liquefaction is predicted not to occur when FS > 1. (In those cases where $V_{S1} > V_{S1}^*$, the FS is undefined meaning no liquefaction is predicted for any magnitude earthquake.) The acceptable value of FS will depend on several factors, including the acceptable level of risk for the project, the extent and accuracy of seismic measurements, the availability of other site information, and the conservatism in determining the design earthquake magnitude and the expected value of a_{max}.

Case Study

SASW tests were conducted along the south-eastern perimeter of Treasure Island (TI), California. Testing was performed across an area of remediated (densified) sand, called the Improved Soil Area (ISA) herein. This area is located on the south-eastern corner of the island, as shown in Fig. 3. This island is man-made and was formed by hydraulic filling behind a perimeter rock dike in 1936-37. The perimeter dike served to contain the hydraulic fill, and was raised in sections over the previously placed fill.

In 1991, TI was selected as a national geotechnical experimentation site. Much of the work to date centers around a ground response experiment (de Alba and Faris, 1996). Six accelerometers and eight piezometers are operating at various elevations near the fire station (see Fig. 3). Inclinometer casings are in place at the fire station and at two sites along the perimeter of TI, including the Improved Soil Area.

Improved Soil Area

The location of the Improved Soil Area and the locations where SASW tests were performed are shown in Fig. 4. The general perimeter of TI is essentially level and the area where SASW testing was conducted is capped by a 127 mm-thick layer of asphaltic pavement.

The upper 12 m of soil is sand fill that was initially deposited in a loose to medium dense state during hydraulic filling. Grain-size distribution curves for six samples taken from the fill are shown in Fig. 5. Samples above a depth of 6 m contain as much as 17% fines (silt and clay). Below 6 m, samples contain 1% to 4% fines. The fill is underlain by native materials, including 3 m of silty clayey sand followed by 27 m of soft to stiff clay with interbedded sand layers. Additional details about the profile are presented in Andrus et al. (1998b). At the time of SASW testing, the water surface in the bay was about 2 m below the ground surface.

Because of concern for the seismic instability of the waterfront slope, the fill beneath the approach to Pier 1 was densified to a depth of 12 m by a vibrating probe technique in 1985. The area penetrated by the large metal-tube probe was 23 m wide and 97 m long, as shown by the shaded area in Fig. 4. From construction drawings by Foundation Constructors Inc., initial tests were conducted at the northwest corner of the improved area to determine the optimal probe spacing. Subsequent production probes were performed to produce a final 1.90-m or 2.24-m probe spacing in a triangular grid pattern. Gravelly material was inserted through holes in the wall of the probe and vibrated into the ground. Gradation curves 4-6 shown in Fig. 5 are for samples taken from the improved zone.

Earthquake Performance

Following the 1989 Loma Prieta earthquake (M_W = 7.0), no signs of ground disturbance were observed in the improved area, while sinkholes, sand boils and cracks were seen in the adjacent unimproved areas (Geomatrix, 1990; Mitchell and Wentz, 1991).

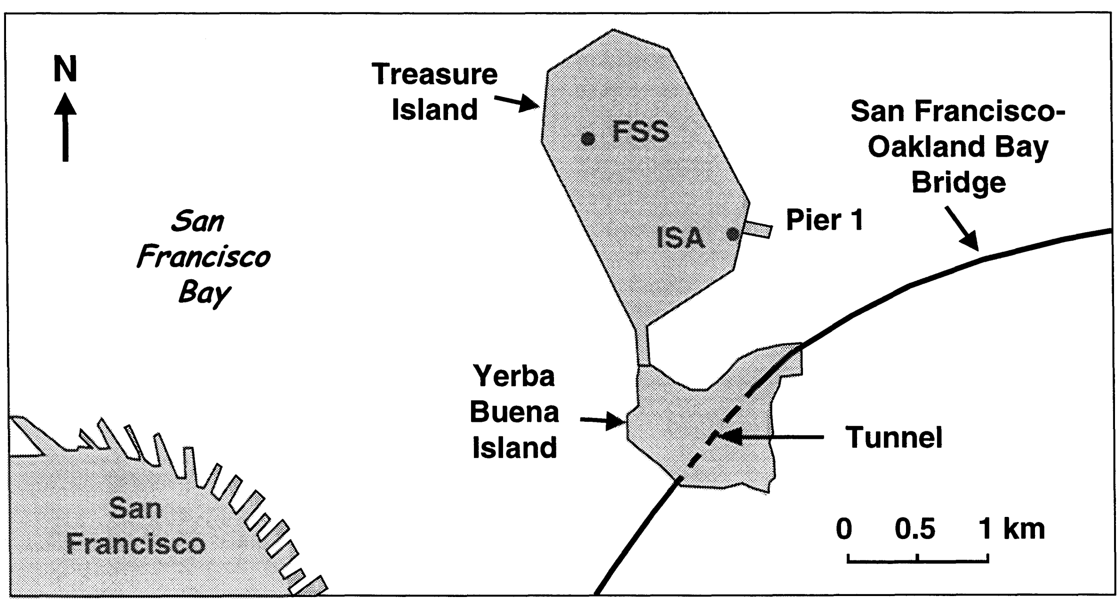

Figure 3 San Francisco Bay Showing Locations of the Improved Soil Area (ISA) and Fire Station Site (FSS) at Treasure Island

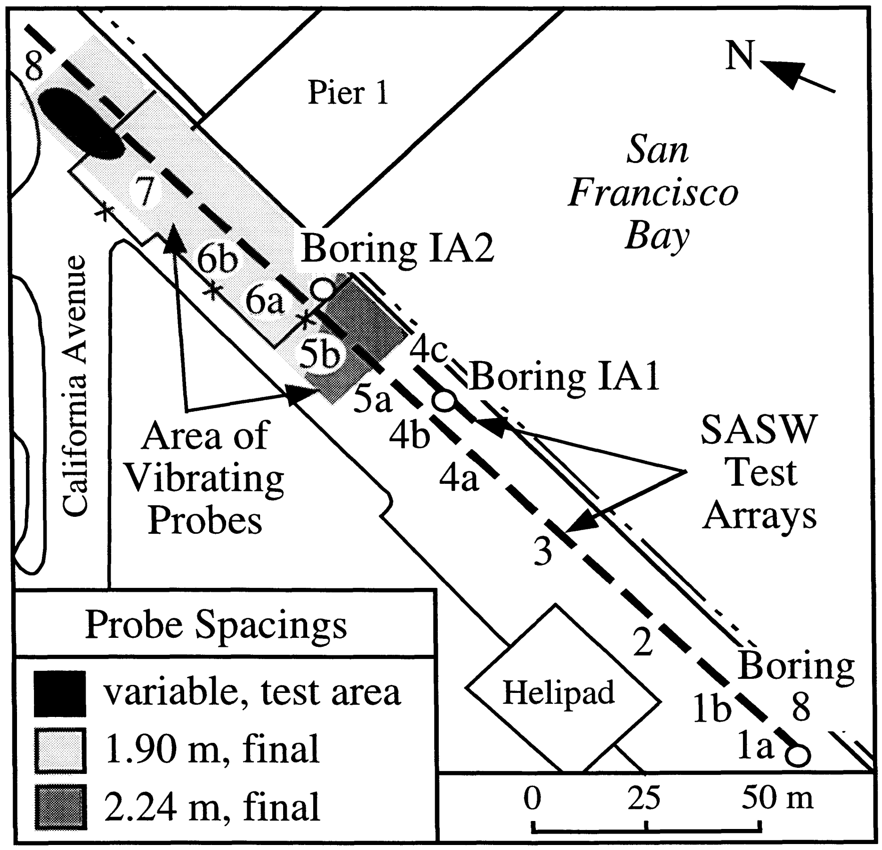

Figure 4 **Line Along which SASW Testing was Performed and Locations of Improved Soil Area and Surrounding Structures**

SASW Test Results

SASW testing was performed at eight primary array locations and several secondary array locations as shown in Fig. 4. Field tests were performed by placing two receivers on the ground surface a distance D apart, as illustrated in Fig. 6. A truck-mounted seismic vibrator (or vibroseis) weighing 180 kN was used as the source for spacings over 8 m. For shorter spacings, hand-held hammers and dropped weights were used. Generally, a total of five or six receiver spacings ranging from 1.5 m to 30 m was employed at each primary array location. Testing and data analyses are described in detail in Andrus et al. (1998b). All work followed the SASW procedures discussed by Stokoe et al. (1994).

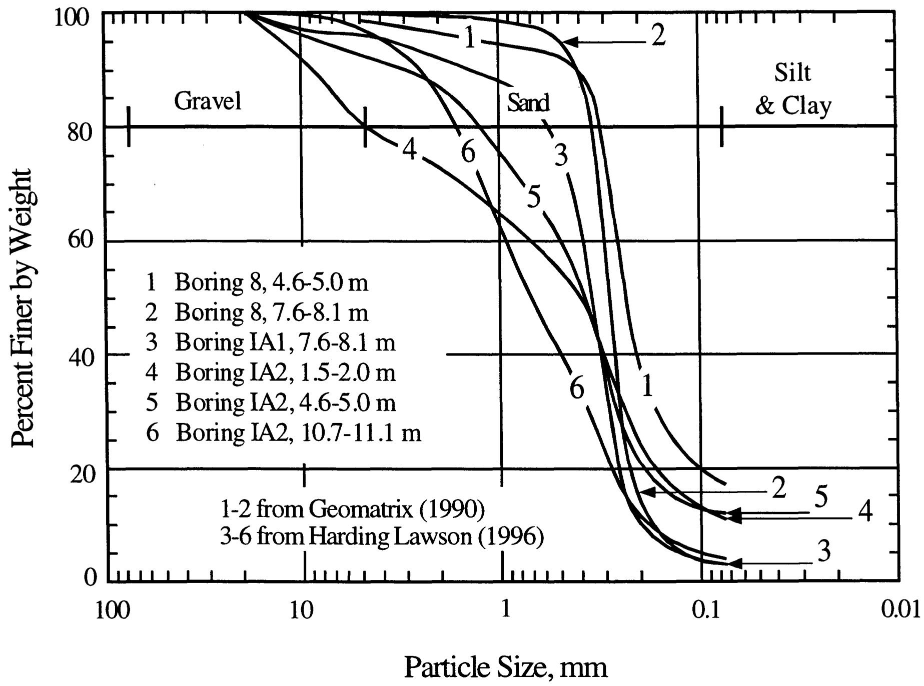

Figure 5 Grain-Size Distribution Curves of Six Split-Barrel Samples Taken from the Sand Fill

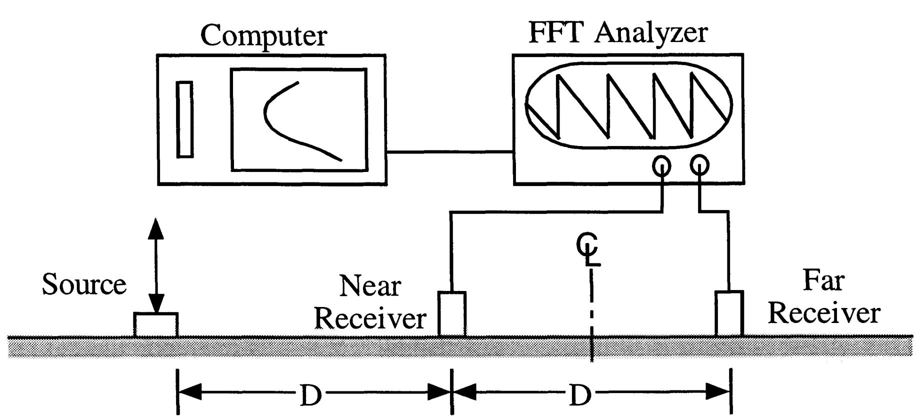

Figure 6 General SASW Test Configuration

Shear wave velocity profiles were determined from each SASW test location shown in Fig. 4. In terms of general trends, values of V_S for the improved area are about 94 m/s higher than values of V_S for the unimproved area at a depth of 1 m (226 m/s versus 132 m/s). At a depth of 13 m, the difference between V_S -values is about 7 m/s (193 m/s versus 186 m/s). A depth of 13 m agrees well the reported depth of densification of 12 m. Between the depths of 2 m and 13 m, average V_S -values for the undensified and densified fill are 167 m/s and 192 m/s, respectively.

A 2-D V_S profile of the unimproved and improved areas is shown in Fig. 7. Several test setups near the southern end of the improved area permit good resolution of the boundary separating densified and undensified sands. At the northern end of the improved area, however, the number of test setups was limited, and the agreement between the velocity profiles and the lateral limit of vibrating probes is rather poor. Nevertheless, the zone of densified sand is clearly identified in the 2-D profile.

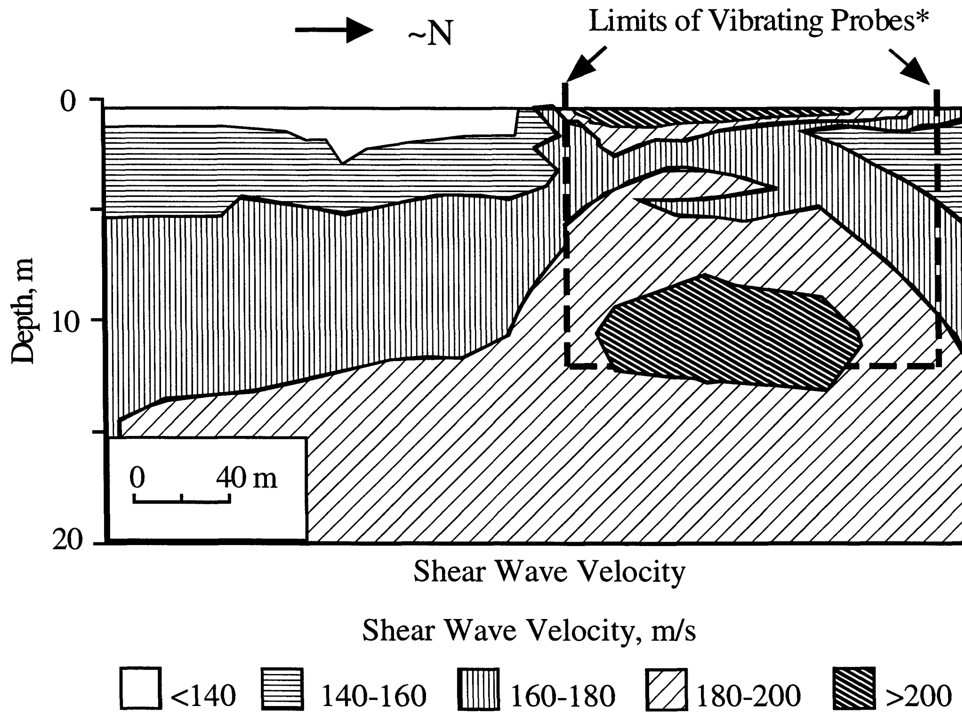

*Lateral limits of the zone remediated with the vibrating probe. Lateral limits are based on construction drawings. Depth limit is 12 m.

Figure 7 Two-Dimensional Shear Wave Velocity Profile

Liquefaction Assessment

The liquefaction assessment procedure described earlier was used to evaluate two locations in the 2-D profile shown in Fig. 7. One location is representative of the unimproved area and the second location is representative of the improved area. The earthquake is the 1989 Loma Prieta (M_w = 7.0) which was estimated to have generated an average value for the peak horizontal ground surface acceleration (a_{max}) of 0.14g at the site (Andrus et al., 1998b interpretation of the measurements presented by Brady and Shakal, 1994). Vertical stresses were estimated using total unit weights of 17.3-18.9 kN/m^3 and 19.5-21.2 kN/m^3 for soils above and below the water table, respectively.

The liquefaction evaluations of the unimproved and improved sites are shown in Figs. 8 and 9, respectively. Values of V_S, V_{S1}, CSR and CRR are shown in Figs. 8a and 8d for the unimproved site and Figs. 9a and 9d for unimproved site. Values of CSR are based on a_{max} equal to 0.14 g. A value of MSF of 1.19 was used to calculate the CRR values. This MSF value represents of the lower bound value recommended by the 1996 NCEER Workshop (Youd et al., 1997).

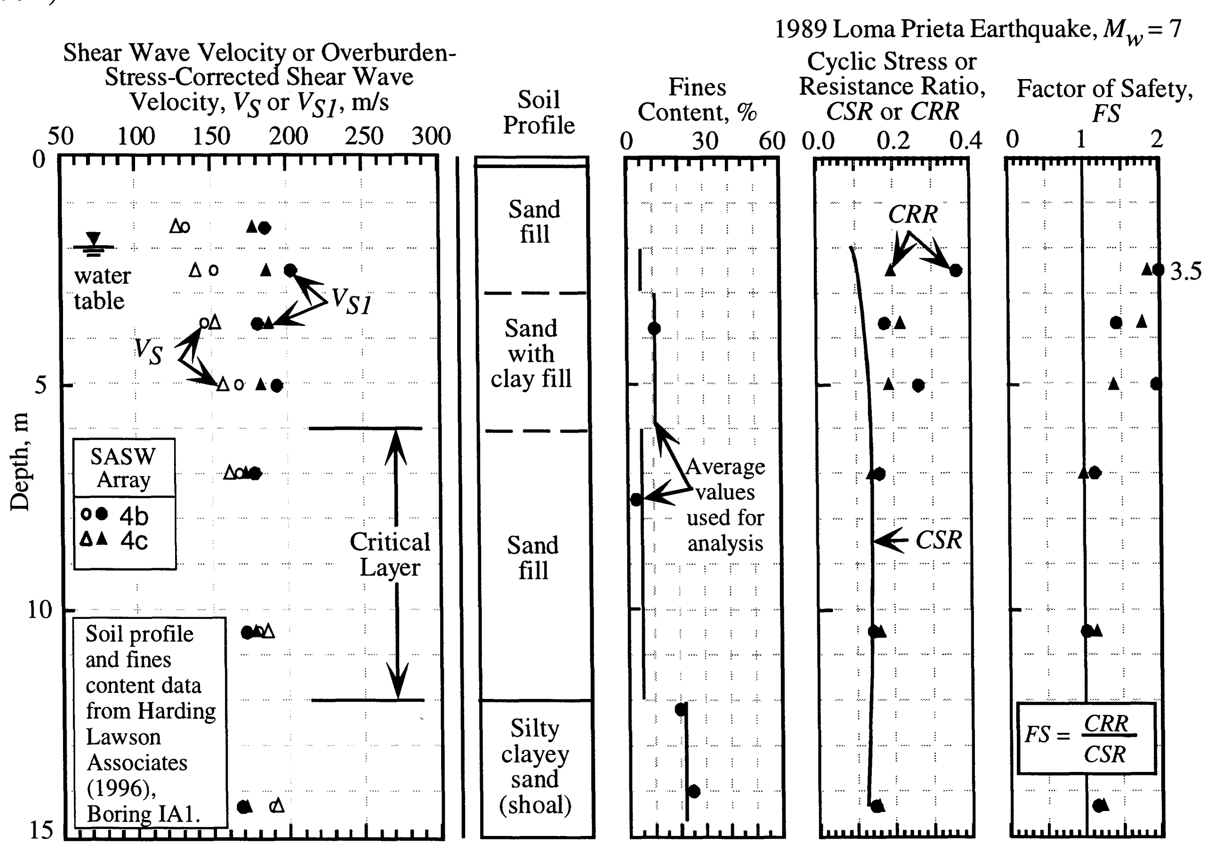

Figure 8 Application of the Recommended Procedure to the Treasure Island Approach to Pier Site, SASW Test Arrays 4b and 4c (see Fig. 4) in the Unimproved Area (Depth of 1.5 m to 14.3 m)

Values of FS are shown in Figs. 8e and 9e for the unimproved and improved sites, respectively. Based on the unimproved site, the critical layer is between depths of 6 m and 12 m, where the sand has about 5% fines and the calculated FS values are in the range of 1.0 to 1.1 . These FS values are considered to represent a site is marginally liquefiable. This assessment agrees with the earthquake performance observed in the area of the unimproved fill. This area is located close to the perimeter of the island and sloping ground likely contributed to the significant liquefaction effects observed there. In addition, the maximum lateral ground displacement was only about 80 mm. Thus, a prediction of marginal liquefaction for the unimproved area is considered correct.

At the improved site, the FS values associated with this layer exceed 2.0. Therefore, liquefaction is not predicted. This assessment of no liquefaction agrees with the observed field performance.

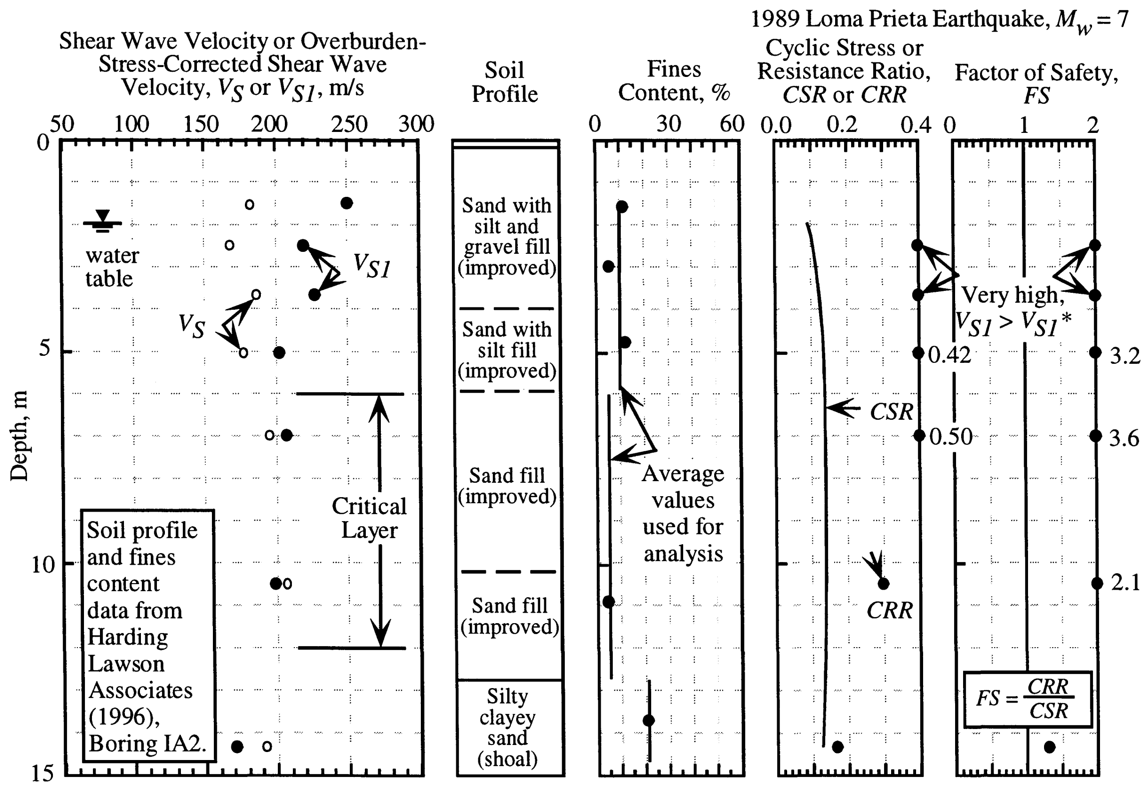

Figure 9 Application of the Recommended Procedure to the Treasure Island Approach to Pier Site, SASW Test Array 6 (see Fig. 4) in the Improved Area (Depth of 1.5 m to 14.3 m)

Summary and Conclusions

A procedure is briefly outlined for evaluating the liquefaction resistance of soil with V_S measurements. The proposed procedure follows the general format of the Seed-Idriss (1971) simplified procedure using the SPT. The simplified V_S procedure has been validated with case history data involving soils ranging from fine sand to sandy gravel with cobbles. Caution should be exercised, however, when applying this procedure to sites where conditions are different from the database. As discussed by Andrus et al. (1998b), additional well-documented case histories with all types of soil that have and have not liquefied during earthquakes are needed to further validate the procedure, particularly for denser soils (V_{S1} > 200 m/s) shaken by stronger ground motions (a_{max} > 0.4 g).

A case study is presented in which multiple SASW tests were conducted across an area containing a zone of improved (densified) sandy fill. The sandy fill was originally placed hydraulically. A portion of the fill was subsequently densified with a vibrating probe. The zone of densified sand was correctly delineated in the 2-D V_S profile, with velocities in the improved area about 25 m/s greater than those in the unimproved area. The simplified V_S procedure for liquefaction assessment was applied to representative profiles in the unimproved and improved areas. The procedure correctly predicted no liquefaction for the improved area and marginal liquefaction for the unimproved area during the 1989 Loma Prieta earthquake. This case study illustrates the usefulness of in situ V_S measurements for predicting liquefaction resistance, and demonstrates the potential of the SASW test for delineating sandy layers that have been remediated by densification.

Acknowledgements

Much of the work presented in this paper was funded by the National Institute of Standards and Technology (NIST). The authors gratefully acknowledge the support and encouragement of Riley Chung, formerly with NIST, and Nicholas Carino at NIST. Special thanks to Richard Faris, Naval Facilities Engrg. Command, for scheduling the SASW tests at TI and supplying site data. The help of Brent Rosenblad and Prof. James Bay with field work and Prof. Sung-Ho Joh with initial data reduction is also greatly appreciated.

References

Andrus, R.D., Stokoe, K. H., II, and Chung, R. M. (1999). "Draft Guidelines for Evaluating Liquefaction Resistance Using Shear Wave Velocity Measurements and Simplified Procedures," *NISTIR 6277*, National Institute of Standard and Technology, Gaithersburg, MD, 121 p.

Andrus, R.D., Stokoe, K.H., II, Bay, J.A. and Chung, R.M. (1998a). "Delineation of Densified Sand at Treasure Island by SASW Testing," *Proceedings,* First International Conference on Site Characterization, P.K. Robertson and P.W. Mayne, editors, Atlanta, GA, April 19-22, pp.459-464.

Andrus, R.D, Stokoe, K.H., II, Chung, R.M. and Bay, J.A. (1998b). "Liquefaction Evaluation of Densified Sand at Approach to Pier 1 on Treasure Island, California, Using SASW Method," *NISTIR 6230*, National Institute of Standards and Technology, Gaithersburg, MD.

Andrus, R.D. and Stokoe, K.H., II (1997). "Liquefaction Resistance Based on Shear Wave Velocity," NCEER Workshop on Evaluation of Liquefaction Resistance of Soils, *Technical Report NCEER-97-0022*, T. L. Youd and I. M. Idriss, Eds., held 4-5 Jan. 1996, Nat. Ctr. for Earthquake Engrg. Res., Buffalo, NY, pp. 89-128.

Andrus, R.D. (1994). "In Situ Characterization of Gravelly Soils That Liquefied in the 1983 Borah Peak Earthquake," *Ph.D. Dissertation*, Univ. of Texas at Austin, 533 p.

Bierschwale, J.G. and Stokoe, K.H., II (1984). "Analytical Evaluation of Liquefaction Potential of Sands Subjected to the 1981 Westmorland Earthquake," *Geotech. Engrg. Rep. GR-84-15*, Univ. of Texas at Austin, 231 p.

Brady, A.G., and Shakal, A. F. (1994). "Strong-Motion Recordings," *The Loma Prieta, Calif., Earthquake of Oct. 17, 1989--Strong Ground Motion*, U.S. Geological Survey Professional Paper 1551-A, R. D. Borcherdt, Ed., U.S. Gov. Printing Office, Washington, D.C., pp. A9-A38.

de Alba, P. and Faris, J. R. (1996). "Workshop on Future Research Deep Instrumentation Array, Treasure Island NGES, July 27, 1996: Report to the Workshop Current State of Site Characterization and Instrumentation," Univ. of New Hampshire at Durham, 45 p.

de Alba, P., Baldwin, K., Janoo , V., Roe, G., and Celikkol, (1984). "Elastic-Wave Velocities and Liquefaction Potential," *Geotechnical Testing Journal*, Vol. 7 No. 2, ASTM, PA, pp. 77-87.

Dobry, R., Ladd, R.S., Yokel, F.Y., Chung, R.M. and Powell, D. (1982). "Prediction of Pore Water Pressure Buildup and Liquefaction of Sands During Earthquakes by the Cyclic Strain Method," *NBS Building Science Series 138*, National Bureau of Standards, Gaithersburg, MD, 152 p.

Dobry, R., Stokoe, K.H., II, Ladd, R.S., and Youd, T.L. (1981). "Liquefaction Susceptibility from S-Wave Velocity," *Proceedings,* In Situ Tests to Evaluate Liquefaction Susceptibility, ASCE Nat. Convention, held 27 Oct., St. Louis, MO.

Geomatrix Consultants. (1990). "Evaluation of Interior Area Performance," Naval Station Treasure Island, San Francisco, CA, Vol. 1-5.

Gucunski, N. and Woods, R.D. (1991). "Instrumentation for SASW Testing," *Recent Advances in Instrumentation, Data Acquisition and Testing in Soil Dynamics, Geotechnical Special Publication No. 29*, ASCE, New York, NY, pp. 1-16.

Harding Lawson Associates. (1996). "Geotechnical Engineering Services National Geotechnical Experimentation Site Soil Boring and Sampling Phase II, NS Treasure Island, California," report prepared for U.S. Navy, Naval Facilities Engineering Command, Western Division, San Bruno, CA, December.

Hynes, M. E. (1988). "Pore Pressure Generation Characteristics of Gravel Under Undrainded Cyclic Loading," *Ph.D. Dissertation*, Univ. of California, Berkeley.

Idriss, I.M. (1999). Presentation Notes, Transportation Research Board Workshop on Recent Advances in Liquefaction Evaluations, 1999 TRB Meeting, Washington, D.C.

Kayabali, K. (1996). "Soil Liquefaction Evaluation Using Shear Wave Velocity," *Engrg. Geology*, Elsevier Publisher, New York, NY, Vol. 44, No. 4, pp. 121-127.

Kayen, R. E., Mitchell, J. K., Seed, R. B., Lodge, A., Nishio, S., and Coutinho, R. (1992). "Evaluation of SPT-, CPT-, and Shear Wave-Based Methods for Liquefaction Potential Assessment Using Loma Prieta Data," *Proceedings,* Fourth Japan-U.S. Workshop on Earthquake Resistant Design of Lifeline Facilities and Countermeasures for Soil Liquefaction, Technical Rep. NCEER-92-0019, M. Hamada and T. D. O'Rourke, Eds., held 27-29 May, Honolulu, Hawaii, Nat. Ctr. for Earthquake Engrg. Res., Buffalo, NY, Vol. 1, pp. 177-204.

Lodge, A. L. (1994). "Shear Wave Velocity Measurements for Subsurface Characterization," *Ph.D. Dissertation*, University of California at Berkeley.

Mitchell, J.K. and Wentz, F.J., Jr. (1991). "Performance of Improved Ground During the Loma Prieta Earthquake," *Rep. No. UCB/EERC-91/12*, University of California, Berkley.

Nazarian, S. and Stokoe, K.H., II. (1989). "Nondestructive Evaluation of Pavements by Surface Wave Method," *American Society for Testing and Materials, ASTM STP 1026*, pp. 119-137.

Rashidian, M. (1995). "Undrained Shearing Behavior of Gravelly Sands and its Relation with Shear Wave Velocity," *M.S. Thesis*, Geotech. Engrg. Lab., Dept. of Civil Engrg., Univ. of Tokyo, Japan, 343 p.

Robertson, P.K., Woeller, D.J., and Finn, W.D. L. (1992). "Seismic Cone Penetration Test for Evaluating Liquefaction Potential Under Cyclic Loading," *Canadian Geotech. Journal*, Vol. 29, pp. 686-695.

Robertson, P.K. and Campanella, R.G. (1985). "Liquefaction Potential of Sands Using the Cone Penetration Test," *Journal of the Geotechnical Engineering Division*, ASCE, March 1985, 22(3), pp. 298-307.

Rollins, K.M., Diehl, N.B., and Weaver, T.J. (1998). "Implications of V_S-BPT $(N_1)_{60}$ Correlations for Liquefaction Assessment in Gravels," *Geotech. Earthquake Engrg. and Soil Dyn. III*, Geotech. Special Pub. No. 75, P. Dakoulas, M. Yegian, and B. Holtz, Eds., ASCE, Vol. I, pp. 506-517.

Seed, H. B., Idriss, I. M., and Arango, I. (1983). "Evaluation of Liquefaction Potential Using Field Performance Data," *Journal of Geotech. Engrg.*, ASCE, Vol. 109, No. 3, pp. 458-482.

Seed, H. B. and Idriss, I. M. (1971). "Simplified Procedure for Evaluating Soil Liquefaction Potential," *Journal of the Soil Mechanics and Foundations Div.*, ASCE, Vol. 97, SM9, pp. 1249-1273.

Stokoe, K.H., II, Wright, S.G., Bay, J.A. and Roesset, J.M. (1994). "Characterization of Geotechnical Sites by SASW Method," Geophysical Characterization of Sites, *Technical Committee 10 for XIII ICMFE*, A.A. Balkema Publishers/Rotterdam, Netherlands, pp. 785-816.

Stokoe, K. H., II, Nazarian, S., Rix, G.J., Sanchez-Salinero, I., Sheu, J.C. and Mok Y.J. (1988a). "In Situ Testing of Hard-to Sample Soils by Surface Wave Method," Earthquake Engineering and Soil Dynamics II, *Geotechnical Special Publication No. 20*, J.L. Von Thun, editor, ASCE, pp. 264-278.

Stokoe, K.H., II, Roesset, J.M., Bierschwale, J.G and Aouad, M. (1988b). "Liquefaction Potential of Sands from Shear Wave Velocity," *Proceedings*, 9th World Conference on Earthquake Engineering, Vol. III, Tokyo, Japan, Nissei Kogyo Col., Ltd., pp. 213-218.

Stokoe, K.H., II, Lee, S.H.H. and Knox, D.P. (1985). Shear Moduli Measurements Under True Triaxial Stress," *Proceedings*, Advances in the Art of Testing Soils Under Cyclic Conditions, Geotechnical Engineering Division, ASCE, October, pp. 166-185.

Stokoe, K.H., II and Nazarian, S. (1985). "Use of Rayleigh Waves in Liquefaction Studies," *Proceedings*, Measurements and Use of Shear Wave Velocity for Evaluating Dynamic Soil Properties, Denver, CO, R.D. Woods, editor, ASCE, New York, NY, pp. 1-17.

Sykora, D.W. (1987). "Creation of a Data Base of Seismic Shear Wave Velocities for Correlation Analysis," Geotechnical Laboratory Miscellaneous Paper GL-87-26, U.S. Army Engineer Waterways Experiment Station, Vicksburg, MS.

Tokimatsu, K. and Uchida, A. (1990). "Correlation Between Liquefaction Resistance and Shear Wave Velocity," *Soils and Foundations*, Japanese Society of Soil Mechanics and Foundation Engrg., Vol. 30, No. 2, pp. 33-42.

Tokimatsu, K., Kuwayama, S., and Tamura, S. (1991). "Liquefaction Potential Evaluation Based on Rayleigh Wave Investigation and Its Comparison with Field Behavior," *Proceedings,* Second Int. Conf. on Recent Advances in Geotech. Earthquake Engrg. and Soil Dyn., March 11-15, St. Louis, MO, Univ. of Missouri at Rolla, Vol. I, pp. 357-364.

Youd, T.L., Idriss, I.M., Andrus, R.D., Arango, I., Castro, G., Christian, J.T., Dobry, R., Finn, W. D.L., Harder, L.F., Jr., Hynes, M.E., Ishihara, K., Koester, J.P., Liao, S.S.C., Marcuson, W.F., III, Martin, G. R., Mitchell, J.K., Moriwaki, Y., Power, M.S., Robertson, P.K., Seed, R.B., and Stokoe, K.H., II (1997). "Summary Report," *NCEER* Workshop on Evaluation of Liquefaction Resistance of Soils, Technical Rep. NCEER-97-0022, T. L. Youd and I. M. Idriss, Eds., January 4-5, Nat. Ctr. for Earthquake Engrg. Res., Buffalo, NY, pp. 1-40.

Judgement Method of Liquefaction Potential using Acceleration Response Spectra

Sumio SAWADA
Disaster Prevention Research Institute, Kyoto University, Uji, Japan
(California Institute of Technology, Pasadena, CA, USA (until January 2000))

Kenzo TOKI
Graduate School of Civil Engineering, Kyoto University, Kyoto, Japan

ABSTRACT

We propose a new judgement method of liquefaction potential based on the theory of Seismic Deformation Method using the acceleration response spectrum defined on ground surface. Firstly we propose a new method to determine ground displacement by acceleration response spectra defined on ground surface. The proposed method makes possible to design the underground structures and overground structures from the same design spectra and to include the seismic and ground environment in the design spectra of under ground structures. Secondly, the new method is proposed to judge liquefaction potential using the ground displacement estimated by the previous method. The judgement method can consider the predominant period of surface layer of the ground and duration of the earthquake input motion.

The summary of the proposed method is written by an equation, as follows;

$$F_L = \frac{R_{20}\sigma'_V(z)}{C_A \cdot 2h\left(\dfrac{T_S}{2\pi}\right)^2 S_A(T_S)\sin\left(\dfrac{\pi}{2z_{N-1}}z\right) \Big/ -\sum_{l=1}^{N-1}\left[\dfrac{2z_{N-1}}{\pi}\dfrac{1}{G_l}\left\{\cos\left(\dfrac{\pi}{2z_{N-1}}z_l\right)-\cos\left(\dfrac{\pi}{2z_{N-1}}z_{l-1}\right)\right\}\right]},$$

where,

- F_L: factor of liquefaction potential,
- z : depth from ground surface,
- C_A: parameter for correcting the amplification factor of the site,
- S_A, h : acceleration response spectrum on ground surface with damping factor h,
- T_S: natural period of the surface layer,
- N: number of layers including the seismic base layer,
- G_i and z_i : shear modulus and lower boundary depth of the layer i, respectively,
- $\sigma'_v(z)$: effective vertical stress,
- R_{20} : liquefaction resistance when the number of cycles of input motion is 20.

The acceleration spectrum and soil profile including shear modulus, unit weights, liquefaction resistances are only necessary to judge the liquefaction potential. If F_L is less than 1.0 it is judged that liquefaction will occur.

INTRODUCTION

Judgement of Liquefaction Potential

In order to judge whether liquefaction will occur or not, based on the results of laboratory test, it is necessary to estimate the distribution of ground stress with depth during earthquakes. Seed and Idriss (1971) proposed the following equation to estimate the distribution.

$$\tau_{cyc}(z) = C_E \frac{a_{\max}}{g} \sigma_v(z) r_d(z) \qquad (1)$$

where, $\tau_{cyc}(z)$ is the stress distribution which should be compared with the shear strength against liquefaction, α_{max} the peak acceleration on ground surface, $\sigma_v(z)$ total vertical stress, $r_d(z)$ the correction function of stress distribution with depth. The factor C_E considers the non-stationary effects of input motion and the relationship between shear strength of liquefaction and number of cycles applied. They showed C_E=0.65 as an example.

This method is widely used in various seismic design codes of structures. In the case of "Earthquake Resistant Design of Bridges (ERDB)" code (Japan Road Association 1990), the judgement of liquefaction potential is done from the factor of liquefaction potential, F_L, obtained by Eq.(2).

$$F_L = R/L \qquad (2)$$

where, R is the liquefaction resistance which consider the characteristics of soil, duration of input motion, effects of multi-directional input and the difference of confining condition between in laboratory test and in the field. If F_L is less than 1.0 it is judged that liquefaction will occur. The parameter L in Eq.(2) is the ratio of shear stress and the effective vertical stress, $\sigma'_v(z)$, as follows;

$$L = \tau(z)/\sigma'_v(z). \qquad (3)$$

Note that $\tau(z)$ in Eq.(3) is the same with $\tau_{cyc}(z)$ in Eq.(1) when the factor C_E is eliminated because the factor is considered in the liquefaction resistance R, as follows;

$$R = R_{20} / C_E \qquad (4)$$

where, R_{20} is the liquefaction resistance when 20 cycles of input motion is applied. The following relationship is used for the correction function in Eq.(1).

$$r_d(z) = 1 - 0.015z, \qquad (5)$$

Note that Eq.(5) has no relationship between the soil profile and the factor C_E in Eq.(4) is not defined by detail characteristics of input motions. In addition, α_{max} is mostly defined without relation to the soil conditions at the site.

Acceleration Response Spectrum

Acceleration response spectrum is widely used in earthquake resistant design of the most types of structures such as bridges, buildings, and so on. In ERDB the design response spectra

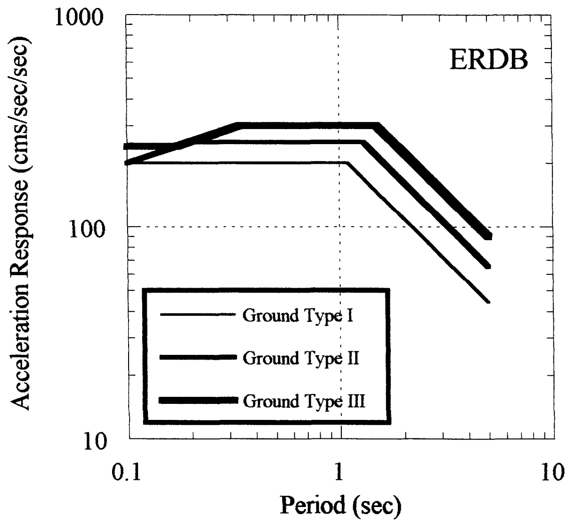

Figure 1 Design acceleration response spectrum defined in "Earthquake Resistant Design of Bridges" of Japan.

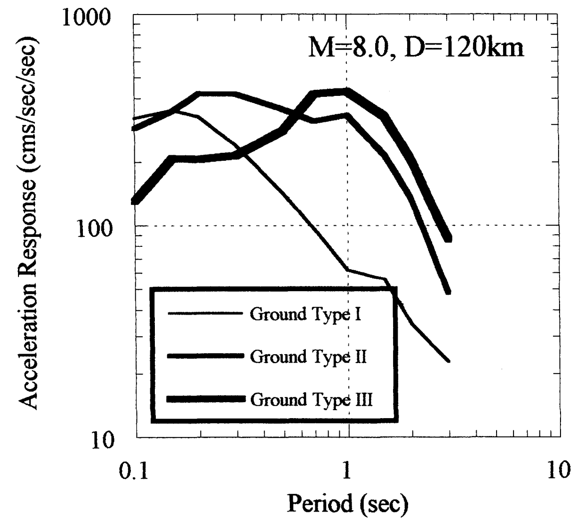

Figure 2 Average acceleration spectrum with earthquake magnitude of 8.0 and epicentral distance of 120 km

are defined on ground surface for fixed damping factor of 0.05, as shown in Figure 1. Note that the design spectra have no clear relationship with α_{max} used for the judgement of liquefaction potential. The ground condition is classified into 3 groups by soil types and the design spectra are defined for each ground type. Type I stands for the outcropped bedrock with 0.1 to 0.2 seconds of natural period of surface layer, type II is hard soil deposit with 0.2 to 0.6 seconds of natural period of surface layer, and type III is soft alluvium for which the natural period of surface layer is over 0.6 seconds.

Many attenuation equations have been proposed to define the average acceleration spectrum for given earthquake magnitude and epicentral distance. ERDB shows one of the attenuation equations, which is obtained by regression analysis on 394 components of strong motion records. Figure 2 shows an example of the average acceleration spectrum in the case of earthquake magnitude of 8.0 and epicentral distance of 120 km.

Seismic Deformation Method for Designing Underground Structure

Seismic Deformation Method (SDM) is applied to seismic design of underground structures, such as pipeline and submerged tunnels. This is a design method that the displacement of ground exerts seismic deformation on the structure. The design code for underground parking lot (UPL, Japan Road Association 1992) is the typical code for underground structure in Japan. In the code of UPL, the vertical distribution of horizontal ground displacement in surface layer of which shear wave velocity is less than 300 m/sec is modeled by a quarter of cosine wave shape, as shown in Figure 3. The distribution of maximum displacement of the ground is given by Eq. (6).

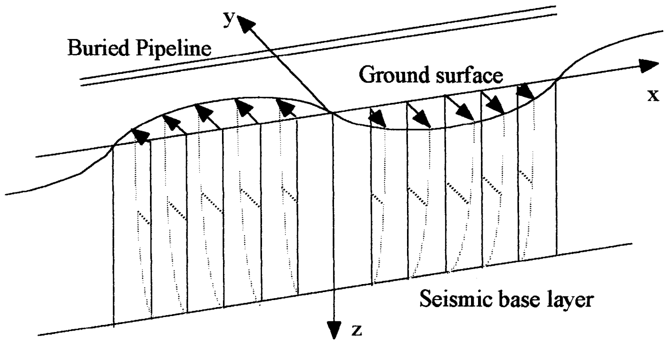

Figure 3 Schematic diagram of distribution of maximum displacement of subsurface ground.

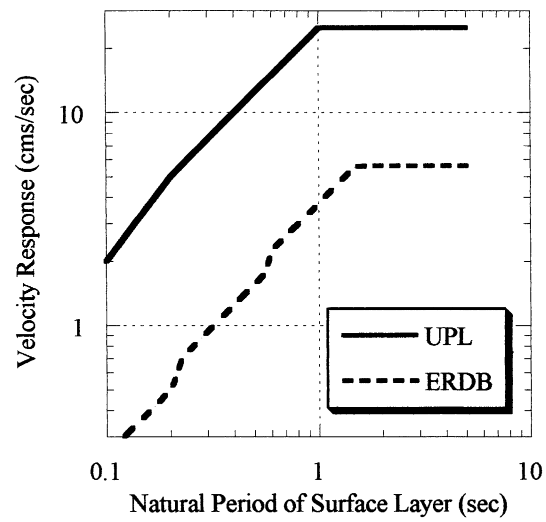

Figure 4 UPL spectrum and the converted ERDB spectrum.

$$u(z) = \frac{2}{\pi^2} S_V T_S \cos\left(\frac{\pi}{2H} z\right) \tag{6}$$

where $u(z)$: maximum displacement amplitude at depth z, z: depth from the surface of the ground, T_S: natural period of surface layer, H: thickness of surface layer, S_V: response velocity spectrum. SDM is a method for estimating distribution of ground stress with depth which may be used for judging liquefaction potential.

In SDM, the seismic design spectrum S_V is defined on the interface between the surface layer and the seismic base layer(V_S > 300m/sec). Figure 4 shows the design spectra of UPL. Note that the abscissa in Figure 3 is the natural period of "Surface Layer". The design spectra for SDM are not the response spectrum calculated from the records observed on the interface between the surface layer and the seismic base ground because the records on the interface are affected by the surface layer at the site. Those are also different from the response spectrum of the records observed on the outcropped seismic base layer because the spectrum must be affected by the surface layer if it exists on the seismic base layer. For these reasons, it is difficult to understand the meaning of the design spectrum for SDM. Thus, spectrum for SDM has the following drawbacks;

1) The physical meanings of the design spectra are ambiguous so that there is no way to obtain the spectrum applicable to different site conditions and seismic environments.
2) Seismic design force is not specified for such structure that extends continuously above the ground surface from underground.
3) Seismic ground motion is not defined for structures laying in the ground deeper than the seismic base layer.

Objectives

If the seismic design spectrum is defined on the ground surface and can be easily modified for the judgement process of liquefaction potential and the design process of overground and underground structures, it is much easy to understand and to use the spectrum in seismic design (Sawada et al., 1999). Fortunately we have large accumulation of strong motion records observed on the ground surface, which will provide enough dataset to specify the seismic ground motion on the ground surface.

In this paper, a new judgement method of liquefaction potential is proposed based on the theory of SDM using the acceleration response spectra on ground surface. The liquefaction resistance is not discussed except the effects of duration of input motions. We discuss how the stress distribution should be estimated in the judgement process of liquefaction potential.

A METHOD TO ESTIMATE DISPLACEMENT ON GROUND SURFACE USING ACCELERATION RESPONSE SPECTRUM

Basic Theory

It is necessary to estimate peak displacement on ground surface for calculating the distribution of ground displacement and stress based on the theory of SDM. As the response spectrum shows the peak values of the single degree of freedom (SDOF) systems which are fixed on ground surface, the peak values of the seismic motion on ground surface can be estimated by removing the effects of SDOF responses from the response spectrum.

If a stationary sinusoidal displacement wave $u(\omega)$ with angular frequency ω is applied to SDOF system with natural angular frequency ω_n, the ratio of acceleration response amplitude $S_A(\omega_n)$ to $u(\omega)$ is given by Eq. (7).

$$\frac{S_A(\omega_n)}{u(\omega)} = \omega^2 \frac{(\omega/\omega_n)^2}{\sqrt{\left\{1-(\omega/\omega_n)^2\right\}^2 - 4h^2(\omega/\omega_n)^2}} \tag{7}$$

The maximum response ratio is obtained by letting $\omega = \omega_n$ in Eq. 7, as follows;

$$u(\omega) = \frac{2h}{\omega^2} S_A(\omega) \tag{8}$$

Eq.(8) enables that the peak displacement on ground surface is estimatied from acceleration response spectra.

Comparison with the Values in SDM

In order to show the validity of Eq.(8), we develop a conversion method from the spectrum on ground surface to the spectrum for SDM. In SDM, amplitude of displacement wave at ground surface is given by Eq. (9), which is given by letting $z = 0$ in Eq. (6).

$$u(\omega) = \frac{4}{\pi} \cdot \frac{1}{\omega} S_V(\omega) \tag{9}$$

Although the design spectrum of SDM is explained as the velocity response spectrum on the seismic base layer, it is considered that it simply represents the relationship between the natural period of surface layer and the amplitude of velocity wave on ground surface which is obtained by differential calculus of the displacement wave. the relationship between $S_A(\omega)$ and $S_V(\omega)$ is obtained from Eqs. (8) and (9) as follows;

$$S_V(\omega) = \frac{\pi}{4} \cdot \frac{2h}{\omega} S_A(\omega). \tag{10}$$

Figure 4 also shows the comparison with the spectra for UPL and the converted spectrum from ERDB spectra. The UPL spectrum is about 4 times larger than the converted ERDB spectrum. The difference can be explained by following two reasons.

The difference between envelope value and average value of response spectra of many strong motion record is an explanation. As shown in Figure 5, while the spectrum of ERDB is defined as an average of spectra obtained from many accelerograms, the response values of a record corresponding to the natural period of surface layer often exceeds the value of the ERDB spectrum. There is no problem for overground structure except the case that the natural period of surface layer is equal to that of the structure. On the other hand, the underground structure must be designed for the response value corresponding to the natural period of the surface layer. The ratio of the peak value to the average spectrum must be considered.

The non-stationary property of seismic motion must be another reason. Eq. (8) is inferred under the assumption that the input seismic motion is sinusoidal and stationary. There may be many cases the assumption is not satisfied. Figure 6 shows the response factor $r(n)$ of SDOF

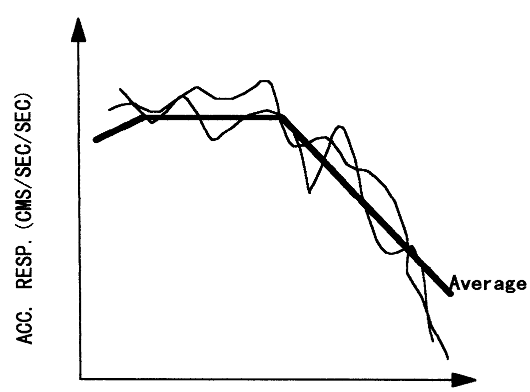

Figure 5 Relationship between the response spectra of strong motion record and averaged response spectrum.

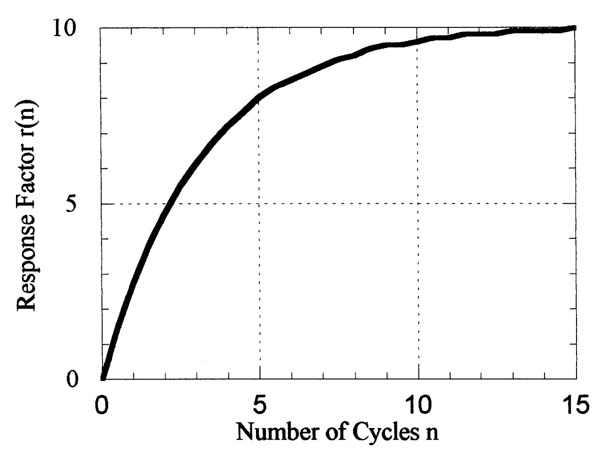

Figure 6 Relationship between input number of cycles and response factor of SDOF system.

system with a damping coefficient of 0.05 excited by input sinusoidal motions with various number of cycles n whose period is the same as the natural period of the SDOF system. Eq. (8) is exactly satisfied when the factor reaches 10.0. The factors are only 2.7 and 4.7 if the numbers of cycles are 1.0 and 2.0, respectively. In the case that the response factor is 5.0, $u(\omega)$ in Eq. (8) must be multiplied by 2. This operation is represented as,

$$u(\omega) = f(n)\frac{2h}{\omega^2}S_A(\omega) \tag{11}$$

where, $f(n)$ is

$$f(n) = r(\infty)/r(n). \tag{12}$$

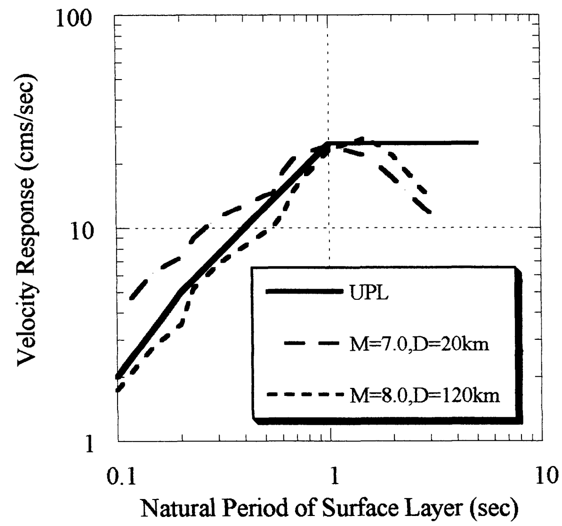

Figure 7 Comparison of SDM spectra with the converted average acceleration spectra.

Proposal of an Estimation Method of Peak Displacement on Ground Surface

Now we introduce the new parameters to Eq. (8) in order to consider the effects mentioned above.

$$u(\omega) = C_N \cdot C_A \frac{2h}{\omega^2} S_A(\omega) \tag{13}$$

where, C_N is the parameter for considering non-stationary properties of seismic motion which represents the effect of $f(n)$, C_A the parameter for correcting the amplification factor of the site. If the product of C_N and C_A is about 4.0, the ERDB spectrum coincides with the UPL spectrum.

The average acceleration spectra, which are calculated by the ERDB attenuation equation for different magnitudes and epicentral distances, are converted to SDM spectra by the proposed method. Figures 7 show the converted average spectra to compare with UPL spectrum. The converted spectra coincide with the design spectrum for SDM.

DISTRIBUTIONS OF GROUND STRESS WITH DEPTH

Stress Distribution in Two Layered Ground

If the ground structure can be modeled by a surface layer and a seismic base layer, the distribution of displacement, $u(z)$, has a quarter of cosine function shape, as shown in Figure 1 and Eq.(6).

$$u(z) = u_{\max} \cos\left(\frac{\pi}{2H} z\right) \tag{14}$$

where u_{max} is the peak displacement on ground surface, z the depth, H the thickness of the surface layer. The distributions of strain and stress in the surface layer are represented by following equations;

$$\gamma(z) = \frac{\pi}{2H} u_{\max} \sin\left(\frac{\pi}{2H} z\right), \tag{15}$$

$$\tau(z) = \tau_{\max} \sin\left(\frac{\pi}{2H} z\right) = \frac{\pi G}{2H} u_{\max} \sin\left(\frac{\pi}{2H} z\right), \tag{16}$$

respectively. Where, G is the shear modulus of the surface layer. In this case, the relationship between peak displacement on ground surface and maximum stress of the ground is represented simply as follows;

$$\tau_{\max} = u_{\max} \Big/ \left(\frac{2H}{\pi} \frac{1}{G}\right). \tag{17}$$

Stress Distribution in Multi-layered Ground

Multi-layered models are used for modeling soil profile in most cases. Here we assume that the distribution of stress in the layers over the seismic base layer can be approximated by a quarter of sine function shape, as follows;

$$\tau(z) = \tau_{\max} \sin\left(\frac{\pi}{2H} z\right). \tag{18}$$

where, τ_{max} is obtained by the following process. The distribution of strain is obtained if the distribution of stress is divided by shear modulus of each layers, G_i.

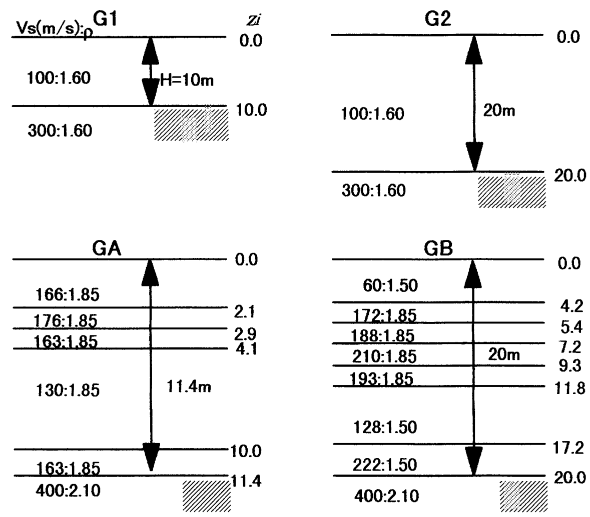

Figure 8 Ground models analysed.

$$\gamma(z) = \frac{\tau_{\max}}{G_i} \sin\left(\frac{\pi}{2H} z\right) \tag{19}$$

Consequently, $u(z)$, the displacement at depth z, is calculated by integrating Eq.(19), as follows;

$$\begin{aligned} u(z) &= u_{\max} + \int_0^Z \gamma(z) dz \\ &= u_{\max} + \sum_{l=1}^{i-1} \left[\frac{2H}{\pi} \frac{\tau_{\max}}{G_l} \left\{ \cos\left(\frac{\pi}{2H} z_l\right) - \cos\left(\frac{\pi}{2H} z_{l-1}\right) \right\} \right] \\ &\qquad + \left[\frac{2H}{\pi} \frac{\tau_{\max}}{G_i} \left\{ \cos\left(\frac{\pi}{2H} z\right) - \cos\left(\frac{\pi}{2H} z_{i-1}\right) \right\} \right] \end{aligned} \tag{20}$$

where, z_i is the depth of lower boundary of layer i. Note that $z_0 = 0$ and $z_{N-1} = H$. Here a boundary condition must be considered. The displacement at the depth on the upper boundary of the seismic base layer, $u(H)$, is zero, as follows;.

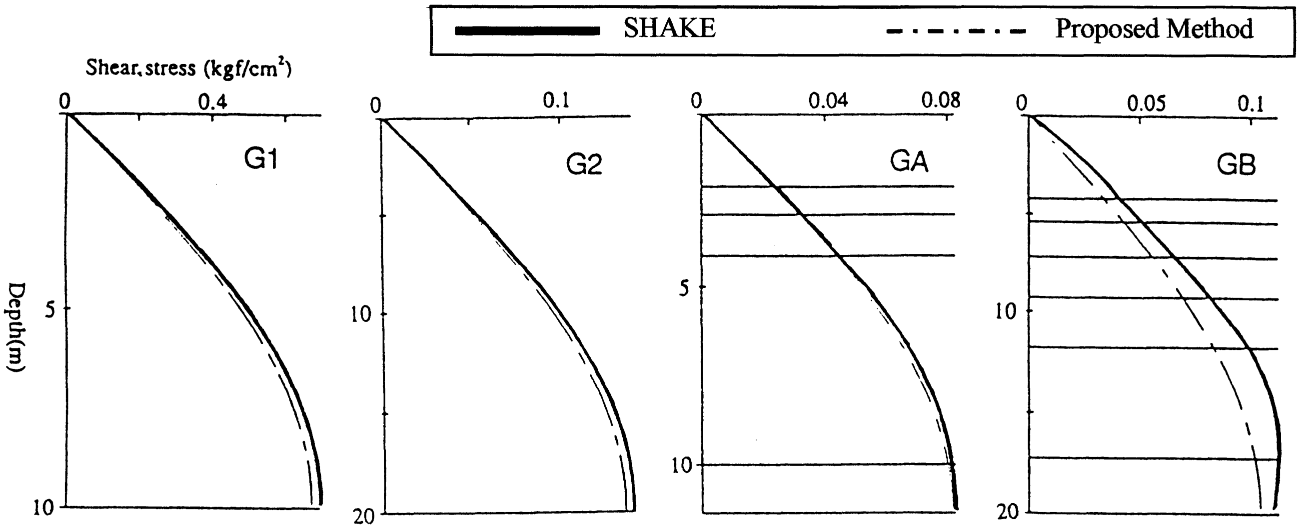

Figure 9 Comparison between the calculated stress distribution by SHAKE and the estimated stress distributions by the proposed method based on stationary input..

$$u(H) = u_{\max} + \sum_{l=1}^{N-1}\left[\frac{2H}{\pi}\frac{\tau_{\max}}{G_l}\left\{\cos\left(\frac{\pi}{2H}z_l\right) - \cos\left(\frac{\pi}{2H}z_{l-1}\right)\right\}\right] = 0 \qquad (21)$$

where, N is the number of layers including the seismic base layer. Finally, the maximum stress, $\tau_{\max}$, is obtained.

$$\tau_{\max} = u_{\max} \Big/ -\sum_{l=1}^{N-1}\left[\frac{2H}{\pi}\frac{1}{G_l}\left\{\cos\left(\frac{\pi}{2H}z_l\right) - \cos\left(\frac{\pi}{2H}z_{l-1}\right)\right\}\right] \qquad (22)$$

In the case of N=2, Eq.(22) gives the same as Eq.(17). Eqs.(18) and (22) make possible to estimate the distribution of stress over the seismic base layer from the peak displacement on ground surface, $u_{\max}$.

Numerical examples

Numerical analyses are conducted to show the precision of the proposed method. Figure 8 shows two ground models used. Model G1 and G2 are two layered models and model GA and GB are based on actual soil profiles. Non-linear behavior of soil is not considered. Input motions are sinusoidal wave which periods are the same as natural periods of the ground models. Firstly the program SHAKE (Schnabel et al. 1972.) is used for calculating ground responses and the distributions of stress in the ground. Secondary the acceleration spectra are obtained from the ground responses. Lastly the distributions of ground stress are estimated by the proposed method from the acceleration spectra and compared with the distributions from SHAKE. Figure 9 shows the result of the comparisons. The distributions of ground stress by the proposed method coincide well with those by SHAKE.

JUDGEMENT OF LIQUEFACTION POTANTIAL CONSIDERING NON-STATIONARY EFFECTS OF INPUT MOTION

Characteristics of Liquefaction Resistance

It is well known that the liquefaction resistance decreases when the number of cycles of input motion increases. Thick lines in Figure 10 shows the typical relationship between the liquefaction resistance and number of cycles applied. The judgement method of liquefaction potential must consider the non-stationary characteristics of input motion. The factor C_E in Eq.(1) or Eq.(4) are the parameter for this purpose.

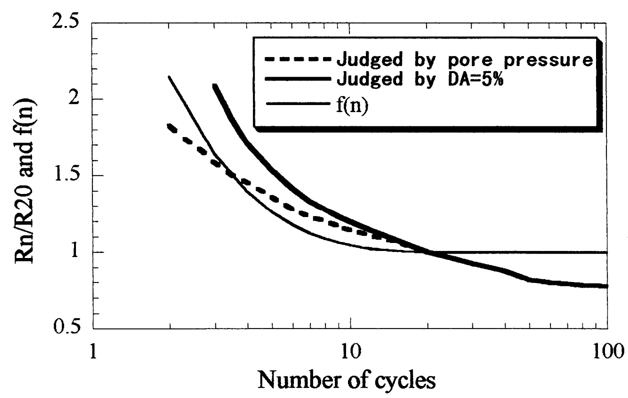

Figure 10 Comparison between liquefaction resistance and response factor.

Characteristics of response of SDOF system

As discussed before, the peak displacement on ground surface estimated from S_A is affected by the duration of input motion, as shown in Eq.(11). Consequently the estimated ground stress is also affected. The ratio of the stress for non-stationary input motion to that for stationary input motion can be represented from Eqs.(11), (18) and (22) as follows;

$$\tau_n / \tau_\infty = f(n) \tag{23}$$

where n is the number of cycles applied. Figure 10 also shows the function $f(n)$ by a thin line to compare with the characteristics of the liquefaction resistance against the number of cycles. It can be recognized that these lines are quite similar.

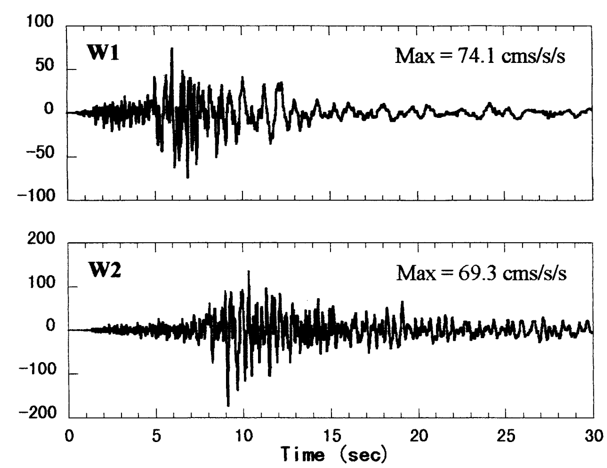

Figure 11 Input ground motions used in the analyses.

Proposal of a New Judgement Method of Liquefaction Potential

A new judgement method of liquefaction potential can be developed using the property mentioned above. In other words, the characteristics of SDOF system in the response spectrum can approximate the characteristics of the liquefaction resistance against the duration of input motion. This approximation is shown as follows;

$$R_n/R_{20} \approx f(n). \tag{24}$$

Consequently following relationship can be obtained from Eqs.(23) and (24).

$$F_L = \frac{R_{20}}{(\tau_\infty/\sigma'_v)} \approx \frac{R_n}{(\tau_n/\sigma'_v)} \tag{25}$$

Eq.(25) shows that F_L value from the liquefaction resistance at the 20 cycle and stress distribution for stationary input motion can judge approximately the occurrence of liquefaction for every input motions.

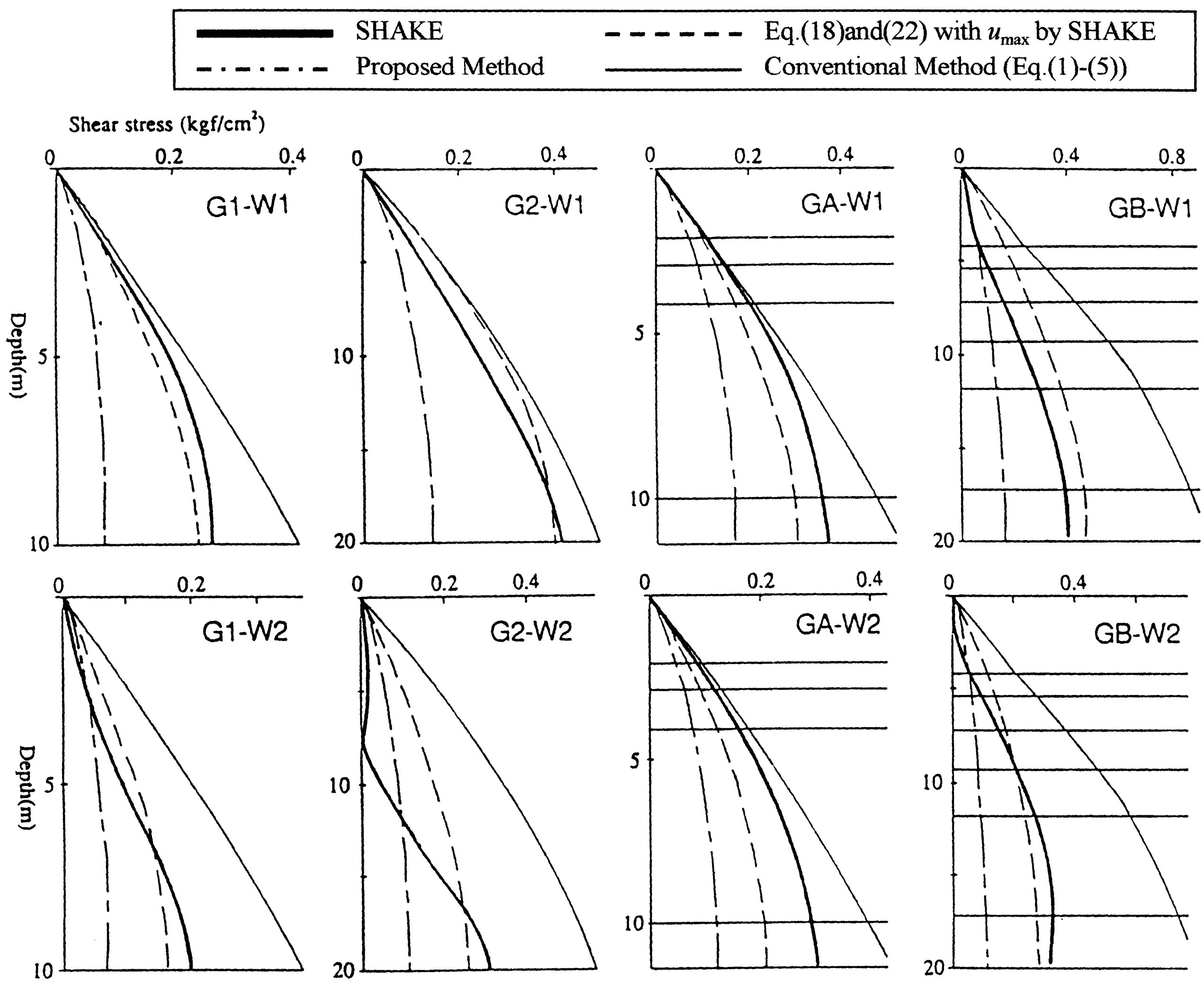

Figure 12 Comparison between the estimated stress distributions by proposed method, the calculated distributions by SHAKE and those of the conventional method based on the seismic records.

Figure 12 shows the example of the estimated ground stress based on the seismic ground motion records which are shown in Figure 11. W1 was recorded during 1980 Izu-hanto-toho-oki earthquake at Shuzenji, W2 during1987 Chibaken-toho-oki earthquake at Chiba experiments station of the University of Tokyo (Association of Earthquake Disaster Prevention, 1992) . The estimated stress distributions by proposed method are compared with the estimated stress by Eqs.(18)and(22) from u_{max} of the results of SHAKE, the conventional method by Eqs.(1)-(5) and the maximum stress distributions obtained by SHAKE in Figure 12. It is shown that the proposed method can consider the non-stationary characteristics of seismic motions which were represented by C_E in Eq.(1), for example. However the proposed method can not consider the effects of higher modes of ground response than the first mode. It should be considered in relation to the effects of high frequency component on the liquefaction resistance. This will be a future research subject.

SUMMARY OF PROPOSED METHOD

We propose a new judgement method of liquefaction potential based on the acceleration response spectrum defined on ground surface. The peak displacement on ground surface, u_{max} , is obtained in terms of the acceleration spectrum on ground surface, $S_A(T)$, as follows;

$$u_{\max} = C_N \cdot C_A \cdot 2h\left(\frac{T_S}{2\pi}\right)^2 S_A(T_S), \tag{26}$$

where,

C_N: parameter for indicating non-stationary properties of seismic motion. In the case of judgement of liquefaction potential, the value must be 1.0.

C_A: parameter for correcting the amplification factor of the site.

h: damping factor of $S_A(T)$.

T_S: natural period of the surface layer.

The vertical distribution of stress in the ground, $\tau(z)$, is estimated by

$$\tau(z) = u_{\max} \sin\left(\frac{\pi}{2z_{N-1}} z\right) \Big/ -\sum_{l=1}^{N-1}\left[\frac{2z_{N-1}}{\pi}\frac{1}{G_l}\left\{\cos\left(\frac{\pi}{2z_{N-1}} z_l\right) - \cos\left(\frac{\pi}{2z_{N-1}} z_{l-1}\right)\right\}\right]. \tag{27}$$

where,

z : depth from ground surface,

N: number of layers including the seismic base layer,

G_i and z_i : shear modulus and lower boundary depth of the layer i, respectively.

The factor of liquefaction potential, F_L, is given as

$$F_L = \frac{R_{20}}{\left(\tau(z)/\sigma'_V(z)\right)}, \tag{28}$$

where,

$\sigma'_v(z)$: effective vertical stress,

R_{20} : liquefaction resistance when the number of cycles of input motion is 20.

If F_L is less than 1.0 it is judged that liquefaction will occur.

CONCLUSION

(1) A new method to estimate the peak ground displacement from the acceleration response spectrum defined on ground surface is proposed. The method makes possible to design underground structures based on acceleration spectrum on ground surface.
(2) The functions for modeling distributions of ground displacement, strain and stress are proposed which can be applied to multi-layered ground.
(3) A new judgement method of liquefaction potential is proposed which is based on the theory of Seismic Deformation Method using the acceleration response spectrum on ground surface. The judgement method can consider the predominant period of surface layer of the ground and duration of the earthquake input motion.
(4) The effects of the higher modes of ground response must be considered for shallow surface layers. It should be a future subject.

REFERENCES

Association of Earthquake Disaster Prevention, 1992. *Strong Motion Array Record Database.*

Japan Road Association, 1990. *Earthquake Resistant Design of Bridges.*

Japan Road Association, 1992. *Design and Execution Standards of Underground Parking Lot* (In Japanese).

Sawada,S., Toki, K. and Takada, S., 1999. Design Spectra for the Seismic Deformation Method Defined on Ground Surface, *Proceedings of the Second International Conference on Earthquake Geotechnical Engineering*, Vol.2, pp.501-506.

Schnabel,P.B., Lysmer,J. and Seed,H.B., 1972. SHAKE, A Computer Program for Earthquake Analysis of Horizontally Layered Sites, *UBC/EERC Report*, No.72/12.

Seed,H.B. and Idriss,I.M., 1971. Simplified Procedure for Evaluating Soil Liquefaction During Cyclic Loading, Journal of the Soil Mechanics and Foundation Division, ASCE, Vol.107, No.SM9, pp.1249-1274.

EVALUATION OF CPT LIQUEFACTION ANALYSIS METHODS AGAINST INCLINOMETER DATA FROM MOSS LANDING

R. Kulasingam[1]
R. W. Boulanger[2]
&
I. M. Idriss[3]

[1]Graduate Student, [2]Associate Professor, and [3]Professor
Department of Civil and Environmental Engineering
University of California
Davis, CA 95616

ABSTRACT

This paper presents an evaluation of CPT-based liquefaction analysis methods against inclinometer data from a laterally spreading shoreline at Moss Landing, and discusses several other key aspects related to the development and application of CPT-based liquefaction analysis methods. Moss Landing suffered extensive liquefaction damage due to the 1989 Loma Prieta earthquake, including the lateral spreading of a shoreline where three slope inclinometers had previously been installed. Analyses are presented for CPT soundings located beside each slope inclinometer (along the shoreline edge of Sandholdt Road) and on the landward side of Sandholdt Road where settlements and displacements appeared to be negligible. This unique set of continuous data on lateral movement variation with depth, obtained from a site which has highly inter-layered sands, silts, and clays, provides a good test of CPT-based liquefaction analysis methods. The analysis results show that the observed surface lateral displacements at these six locations or the lateral displacement profiles at the three inclinometers could not simultaneously be predicted based on analyses of the CPT data. The key limitations in these analysis methods and the complications involved at these particular sites are discussed.

INTRODUCTION

The Cone Penetration Test (CPT) has proven to be an excellent tool for obtaining subsurface information and evaluating cyclic liquefaction. Recent developments in CPT-based liquefaction analysis methods include the compilation of larger case history databases and the proposal of new analysis procedures. Researchers have proposed liquefaction analysis procedures that infer soil characteristics from the CPT tip resistance and friction ratio, and thus circumvent the need for drilling and sampling to directly determine grain size and fines characteristics, unless site specific calibration is judged necessary (e.g., Olsen 1997, Robertson and Wride 1998). CPT analyses have also been combined with various correlations for volumetric and shear strains, and hence used to provide estimates of settlements (e.g., Ishihara 1993) and lateral displacements (e.g., Robertson and Wride 1999).

This paper presents an evaluation of CPT analysis methods against inclinometer data from a laterally spreading shoreline at Moss Landing, and discusses several other key aspects related to the development and application of CPT-based liquefaction evaluation methods. Moss Landing, which is located on Monterey Bay in California, suffered extensive liquefaction damage due to the 1989 Loma Prieta earthquake (e.g., Boulanger et al. 1995 & 1997, Mejia 1998). Three slope inclinometers installed along the shoreline edge prior to the earthquake provided a unique data set of lateral deformation with depth due to the earthquake. These data, obtained from a site which has highly inter-layered sands, silts, and clays, provide a good test of CPT-based liquefaction analysis methods.

DEVELOPMENT OF CPT-BASED LIQUEFACTION CORRELATIONS

Semi-empirical correlations between the cyclic stress ratio required to cause liquefaction (CSR_{liq}) and normalized CPT tip resistance ($q_{c1N} = q_{c1}/p_a$, with p_a = atmospheric pressure) have evolved in recent years as the CPT data-base for field case histories has grown. In developing such correlations, there are two approaches that might reasonably be followed. The most common approach to date has been to reduce the experience from individual sites (or individual CPT soundings) to data points on a plot of CSR_{liq} - q_{c1N} with each data point being associated with the occurrence or nonoccurrence of liquefaction. The alternative approach is to try and represent each site in greater detail and evaluate what form the correlation would have to take to be consistent with the observations at all sites. In either approach, it is extremely important to be consistent in the logic and procedures that are used to both develop the correlation and apply it in engineering practice. The need for formal guidelines to selecting representative penetration resistances for liquefaction sites was noted in NRC (1985), and that need still persists.

Consistent procedures for selecting representative q_{c1N} values from CPT soundings help to reduce potential biases that may be introduced by different individuals. Boulanger et al. (1997) proposed guidelines as follows. First, if the critical depth (where liquefaction is judged to have occurred) is within a thick stratum of similar material the representative tip resistance is taken as an average tip resistance over a moving 0.6-m interval. The interval of 0.6 m was selected because continuous layers of this thickness have been observed to cause significant lateral displacements, and incidentally corresponds to the approximate minimum measurement interval in a Standard Penetration Test. However, if the depth is near an interface between soft and stiff soils, then the tip resistance within 0.15 m of the interface was considered be to affected by the adjacent layer, and thus omitted from the averaging. Second, if the critical interval was between 0.15 and 0.6 m thick, excluding zones influenced by adjacent contacts, then the average value was taken over the full interval thickness. Critical intervals less than 0.15 m thick generally cannot develop a representative q_c, and thus characterization of such intervals requires judgement on a case by case basis.

The minimum value of q_{c1N} obtained as a moving average depends on the thickness of the interval over which it is obtained, as illustrated in Fig. 1 for five CPTs from the Moss Landing area. In the extreme, the minimum q_{c1N} obtained over a moving 1.5-m interval was up to 100% greater than was obtained over a moving 0.1-m interval.

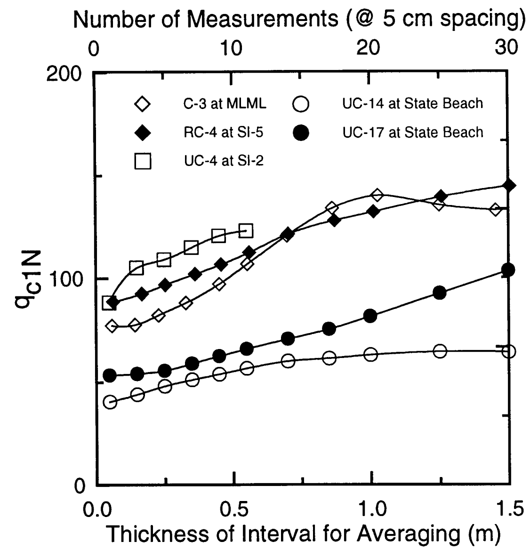

Fig. 1. CPT Tip Resistance Versus Thickness of Interval Used for Averaging (Boulanger et al. 1995, 1997)

Recently Idriss et al. (1997) proposed a new correlation between CSR_{liq} and q_{c1N} based on seven of the key liquefaction and non-liquefaction case histories involving clean sand. The guidelines proposed by Boulanger et al. (1997) were followed for the selection of averaged q_{c1N} values, but a more conservative procedure was adopted for selecting representative combinations between CSR and q_{c1N} as shown in Fig. 2. First, the cyclic stress ratio was plotted versus depth at each site. Second, in case of liquefied sites, the layers at which liquefaction has probably occurred according to investigators were located. Representative tip resistances from the minimum to maximum averaged values within the liquefied layer were selected (e.g., points A and B in Fig. 2). In case of non-liquefied sites, representative tip resistances from the minimum to maximum averaged values for the entire profile were selected. The proposed curve along with the case history data points are shown in Fig. 3. Note that the proposed curve turns sharply upwards at a q_{c1N} of about 175. The curve described by Robertson and Wride's (1998) equation, which is slightly different from Robertson and Campanella's (1985) curve, is also shown on Fig. 3.

The relationship by Idriss et al. (1997) is conservative because it is based on CSR - q_{c1N} points corresponding to maximum critical q_{c1N} values estimated at the range of depth where liquefaction probably occurred according to the site investigations (dictated by points like B rather than points like A in Fig. 2). It should be also noted that if less conservatism is desirable,

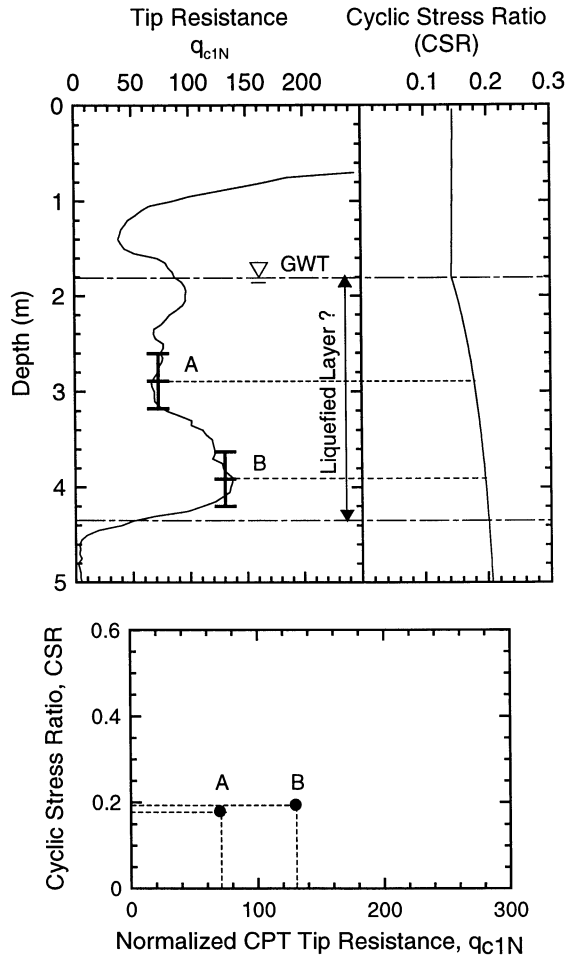

Fig. 2. Selection of Representative Combinations of CSR and q_{c1N} using a 0.6-m Averaging Interval

another curve could be drawn that is dictated by points corresponding to the "average" combination between CSR and q_{c1N} estimated at the range of depth where liquefaction occurred (i.e., a point between A and B in Fig. 2).

Consistent procedures for selecting representative q_{c1N} values from the case history database is important to both the development of a correlation and to its application in practice. In the most general sense, suppose that a correlation was developed using only points like A in Fig. 2. Then in practice, the prediction of liquefaction over a 0.6-m-thick interval (as used to obtain point A) at some site would have to be considered capable of producing displacements comparable to those of similar sites in the case history database. Similarly, if a correlation was developed using only points like B in Fig. 2, then prediction of liquefaction over thicker intervals might be necessary for one to expect displacements to be comparable to similar sites in the case history database. In more general terms, the observed displacements represent an accumulation of strains over the soil profile, and thus there are advantages to pursuing a more general evaluation method where the expected thickness of liquefied soil is related to the observed

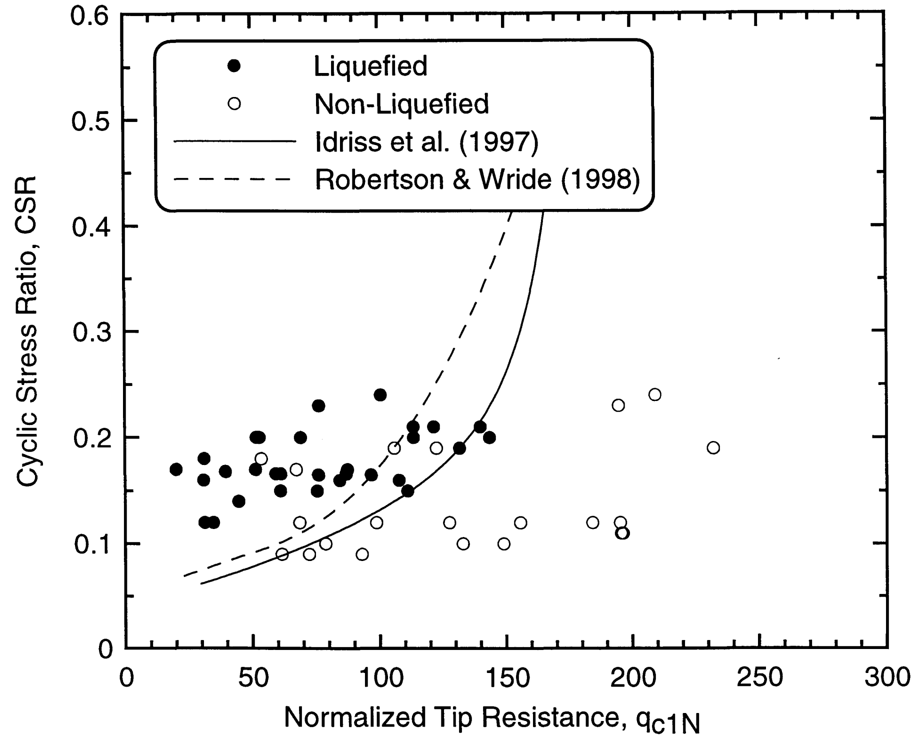

Fig. 3. CSR$_{liq}$ – q_{c1N} Curve Proposed by Idriss et al. (1997) for Clean Sand and M=7.5

displacements. This is further complicated, however, by uncertainties in the mechanisms of liquefaction in heterogeneous deposits (e.g., the role of pore pressure redistribution from looser to denser zones, or the role of void redistribution or water interlayers on lateral spreading). The above discussion emphasizes the need for formal guidelines for selecting representative values of q_{c1N} to avoid inconsistencies between interpretations by different investigators.

There are numerous other factors that must be carefully considered in developing semi-empirical liquefaction methods from case histories, including the limitations of site characterizations, uncertainties in the extent of liquefaction in the subsurface, and uncertainties in the ground motions. The preceding discussion has been limited to only one aspect of this problem, mainly the effect of different investigators' interpretation methods.

LIQUEFACTION AND DEFORMATION ANALYSIS USING CPT DATA

Robertson and Wride (1998) proposed a CPT-based liquefaction analysis method that uses the soil behavior type index I_c (Jefferies and Davies 1993) which is a function of measured CPT tip resistance (q_c) and friction ratio (R_f) only. There are large uncertainties involved in estimating grain characteristics (e.g., fines content or plasticity) from I_c, but Robertson and Wride (1998) suggest that I_c may be a more appropriate parameter for liquefaction analysis because it reflects the combined influences of all grain characteristics. If I_c is less than 2.6 a correction factor K_c which is a function of I_c is calculated. The equivalent clean sand tip resistance is calculated as $q_{c1N\text{-}cs} = K_c\, q_{c1N}$, and this value is used to obtain the CSR_{liq} for $M_w = 7.5$ from their CSR_{liq} - q_{c1N} correlation for clean sand. If I_c is greater than 2.6 the soils are expected to contain sufficient clay that the above procedure is not applied and instead soil sampling and lab testing are recommended for evaluating their cyclic loading behavior. Soils with $I_c > 2.6$ are generally expected to be nonliquefiable unless they are sensitive; a $R_f < 1\%$ with $I_c > 2.6$ was recommended as criteria to identify potentially sensitive soils. These correlations were recommended for low-risk, small-scale projects or for initial screening of medium to high-risk projects. A site-specific correlation was recommended otherwise. The liquefaction analysis is applied to CPT data on a point by point basis to give the continuous variation of the factor of safety against liquefaction with depth. Even though the correlations are based on some kind of average or representative values for the inferred liquefied layers, the point by point continuous interpretation was considered to be conservative in variable deposits where small intervals in the CPT data could indicate possible liquefaction.

Estimating settlements and lateral displacements from CPT data requires estimating potential volumetric and shear strains. Charts for these purposes have been derived from cyclic laboratory tests on mostly clean sands, and thus their applicability to natural soil deposits can only be evaluated through experience. Past case histories have provided some validation of the charts for volumetric strain, while the charts for shear strain have remained of questionable applicability to field conditions. The current study provides an evaluation of such charts in combination with CPT-based liquefaction analyses.

Volumetric strains and maximum shear strains were estimated using the charts proposed by Ishihara and Yoshimine (1992). Maximum strain during earthquake shaking may be different from the residual strain and therefore it strictly should not be used for calculating permanent displacement but rather to provide an indicator of the potential displacements. In the study presented herein, Ishihara and Yoshimine's (1992) chart for maximum shear strains was modified by capping the maximum shear strains based on the limiting shear strains proposed by Seed et al. (1985) – note that maximum shear strains were unbounded for some D_r in the original chart. The modified chart is shown in Fig. 4. Volumetric and shear strains in dry soils were not included in the analyses. In applying these charts to CPT data, it is implicitly assumed that an equivalent clean sand $q_{c1N\text{-}cs}$ can be used to estimate behavior of silty sands and sandy silts. This assumption remains to be substantiated, but is not a serious concern for the sites analyzed herein because the sand layers were relatively clean.

Calculations of shear and volumetric strain using the above-discussed charts depend on the estimated value of relative density (D_r). For the analyses presented herein, two different D_r - q_{c1N} correlations were used to provide a range of results; one proposed by Tatsuoka et al. (1990) and used in Ishihara and Yoshimine (1992), and the other proposed by Kulhawy and Mayne (1990) for medium compressibility sands. For example, these two correlations would indicate D_r values of about 67% and 59%, respectively, for a q_{c1N} value of 100 in clean sand. Again, these correlations are applied to CPT data under the implicit assumption that equivalent clean sand values can be used for estimating the behavior of silty sands or sandy silts.

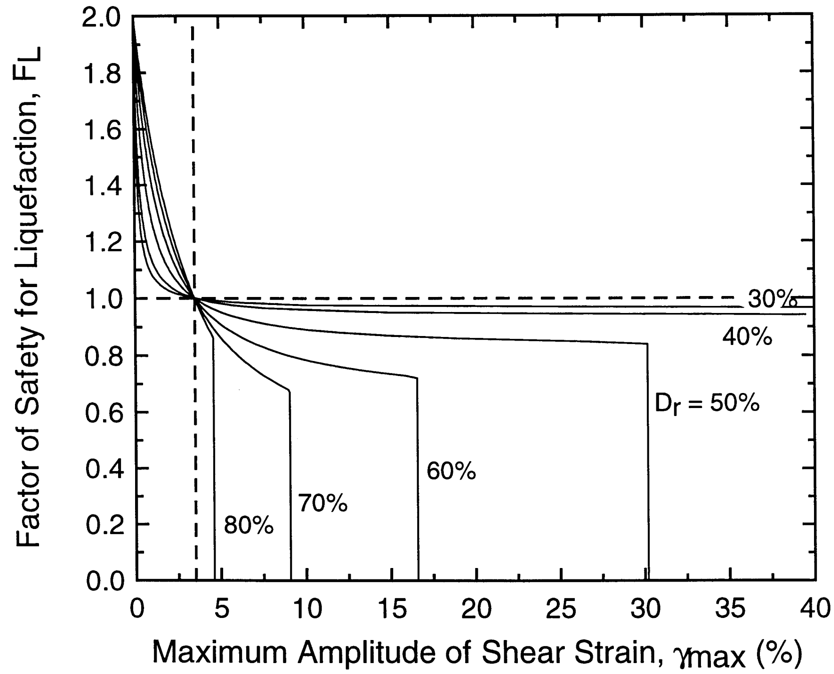

Fig. 4. Ishihara and Yoshimine's (1992) Relationship for Maximum Shear Strain Modified to Include Limiting Shear Strains

Three different versions of a CPT liquefaction analysis method are presented herein, as summarized in Table 1. All three methods calculate the earthquake-induced $CSR_{M=7.5}$ using the Seed and Idriss (1971) simplified procedure with the magnitude scaling factor MSF and stress reduction factor r_d proposed by Idriss (1997), and calculate a $q_{c1N\text{-}cs}$ using the procedures proposed by Robertson and Wride (1998). The three methods use different correlations to estimate values for CSR_{liq} and D_r, and compare automated versus manual interpretations of the soil profile. A correction for sloping ground conditions (K_α) was considered, but was not applied because it would be relatively small for the range of densities encountered, based on the relationships recommended by Harder and Boulanger (1997).

Method A infers soil characteristics from the CPT tip resistance and friction ratio and uses automated point-by-point calculations with no manual interpretation of the profile, such as might be obtained from simple commercial software. A typical set of results obtained using Method A is illustrated in Fig. 5.

Methods B-1 and B-2 include manual interpretation of the soil profile based on borehole and geologic data. Manual interpretation includes adjusting, as judged appropriate, the analysis results at interfaces between different soil types, as well identifying soil types based on laboratory test data. In addition, the CPT data are analyzed using a moving average of CPT data over a 0.6-m thick interval rather than point by point; note that averaging does not extend across interfaces per the procedures proposed by Boulanger et al. (1997). Method B-2 uses more conservative relationships for CSR_{liq} and D_r than were used for Methods A or B-1 (see Table 1).

Table 1. Versions of CPT Liquefaction Analyses

Method	CSR_{liq}-q_{c1} Relationship	D_r-q_{c1} Relationship	Comments
Method A	Robertson & Wride (1998)	Tatsuoka et al. (1990)	Soil characteristics inferred from CPT. Point by point analysis with no manual interpretation.
Method B-1	Robertson & Wride (1998)	Tatsuoka et al. (1990)	Manual interpretation using site-specific borehole and geologic data. Analysis with moving average over 0.6-m interval in defined strata.
Method B-2	Idriss et al. (1997)	Kulhawy & Mayne – med. compressibility sand (1990)	"

APPLICATION TO MOSS LANDING SITE

Moss Landing is located on the Monterey Bay about midway between the cities of Santa Cruz and Monterey in California. Boulanger et al. (1995, 1997) summarized the location and geologic setting details. The Moss Landing area is underlain by Holocene deposits consisting of relatively thick sands offshore and estuarine and fluvial deposits onshore, up to about 60 m deep (Dupre and Tinsley 1980). The Moss landing spit is underlain by littoral soils comprising eolian, fluvial, estuarine and beach deposits of gravel, sand, silt and clay deposited in a shoreline environment within the zone of tidal fluctuations. Fig. 6 shows an aerial photo of the Moss landing area from 1952. Historical shoreline mapping suggests that the shoreline along this portion of Sandholdt Road has varied significantly (Barminski 1993). Furthermore, the shoreline along the Sandholdt Road was modified recently as part of slope modifications and harbor dredging operations (Harding Lawson 1988).

The Loma Prieta earthquake (M_w = 7.0), which occurred on October 17, 1989 caused extensive liquefaction damage in the Moss Landing area (Barminski 1993, Boulanger et al. 1997, Mejia 1998). Extensive ground deformations were observed along Sandholdt Road, with cracks in the asphalt pavement occurring parallel to the waterfront. The zone of significant cracking was generally located between the road centerline and the shoreline edge of the road (Fig. 7). A peak horizontal surface acceleration of about 0.25 g is found to be a reasonable estimate for use in liquefaction analysis due to this earthquake (Boulanger et al. 1997). The water table depth along Sandholdt Road was about 1.8 m.

Three slope inclinometers SI-2, SI-4 and SI-5 installed along the shoreline edge near the Sandholdt Road prior to the earthquake provide a unique set of continuous data of lateral deformation with depth due to the earthquake (Boulanger et al. 1997, Mejia 1998). Inclinometer readings were taken before and after the earthquake (Harding Lawson 1988), and it was also found that the shoreline was not deforming measurably before the earthquake. The subsurface conditions along cross sections perpendicular to the shoreline, at the locations of the 3 slope inclinometers are shown in Boulanger et al. (1997).

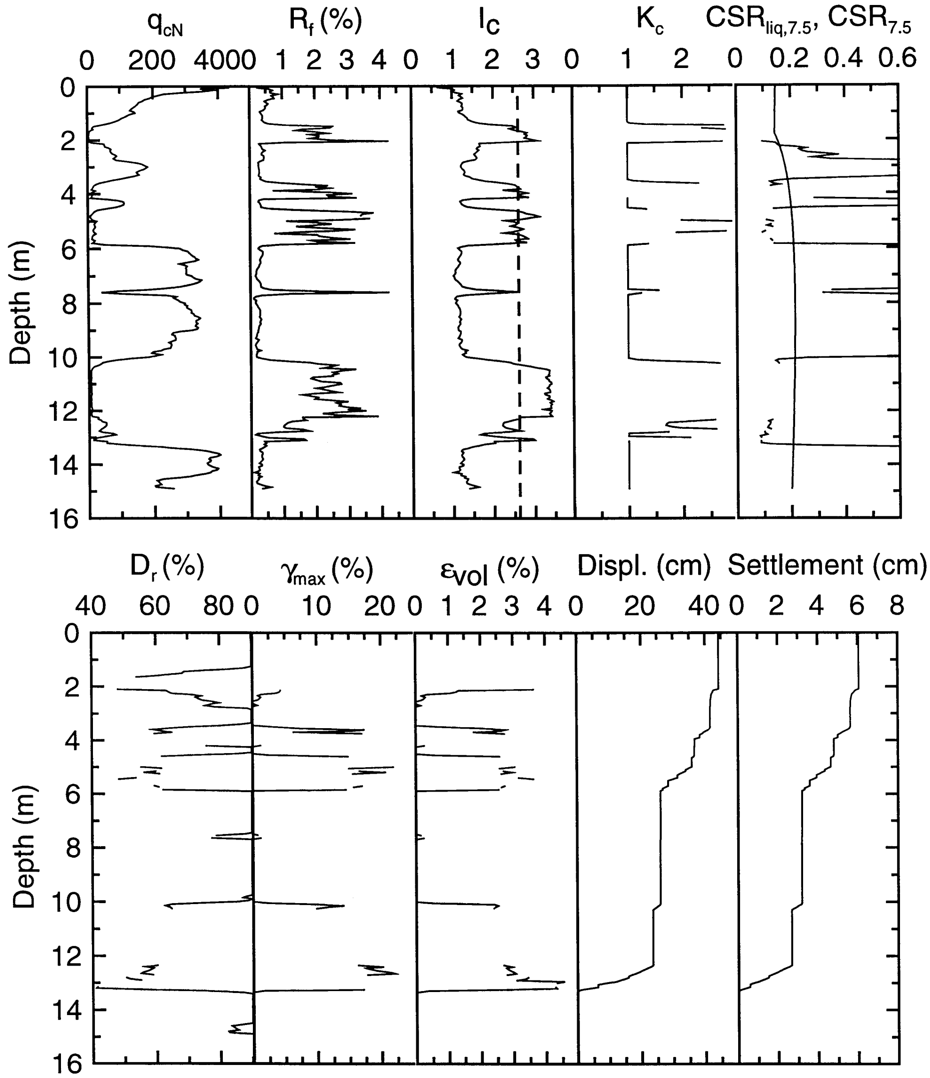

Fig. 5. Example of Results Obtained Using Analysis Method A.

Inclinometer SI-2

Measurements taken from slope inclinometer SI-2 positioned near the shoreline edge of Sandholdt Road (Fig. 8) indicates that the edge of the road displaced laterally about 28 cm towards the water and 10 cm roughly parallel to the shoreline. There was also settlements of 5-8 cm and cracking of the road surface approximately 4.5-6.0 m landward of the slope crest (Fig. 7). There were no cracks or settlements observed on the landward half of the road. The slope inclinometer data are shown in Fig. 8 with the data from the adjacent CPT (1.5 m away). Predictions of lateral deformations obtained by using the three methods described in Table 1 are also shown on Fig. 8.

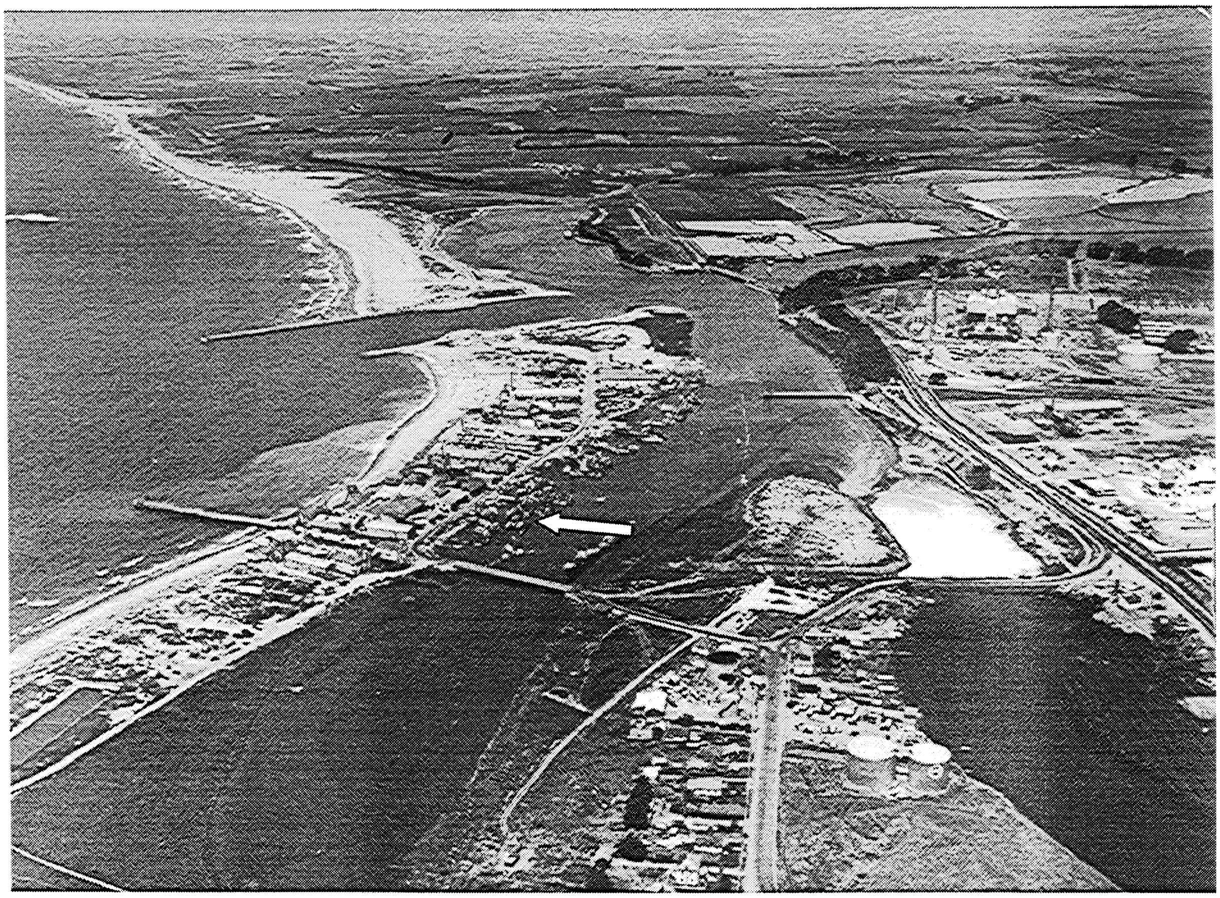

FIG. 6. Aerial Photograph of Moss Landing Harbor in 1952. (Sandholdt Road runs along the south harbor shoreline, with the inclinometers in the area marked by an arrow.)

Method A predicts lateral displacements of 44 cm at the ground surface, significantly higher than the observed displacements (Fig. 8). More importantly, the predicted distribution of shear strains does not agree with the observed distribution. Significant strains were predicted in clayey silt layers or at transitions between layers where none occurred, while negligible strains were predicted in the sand layer between 2.1 and 3.4 m depth where shear strains of about 12% were observed. Robertson and Wride (1999) also analyzed the CPT data at this inclinometer using their procedure with modifications to estimate settlements and lateral displacements. Their analyses are similar to Method A used herein, and predicted a similar surface lateral displacement potential of about 42 cm with similar discrepancies in the distribution of strains versus depth (Boulanger et al. 1999).

Samples from an adjacent boring (3.0 m away) showed that the clayey silt between depths of 3.6 m and 4.2 m had a liquid limit (LL) of 32, a plasticity index (PI) of 7, a USCS classification of ML, and 18% finer than 5 μm. The clayey silt layer just below the zone of lateral deformations had similar characteristics, with the upper portion classified as CL (LL = 46, PI = 21) and the lower portion classified as ML (14% finer than 5 μm). For this range of index properties, the cyclic loading behavior of these clayey silts would best be evaluated by laboratory

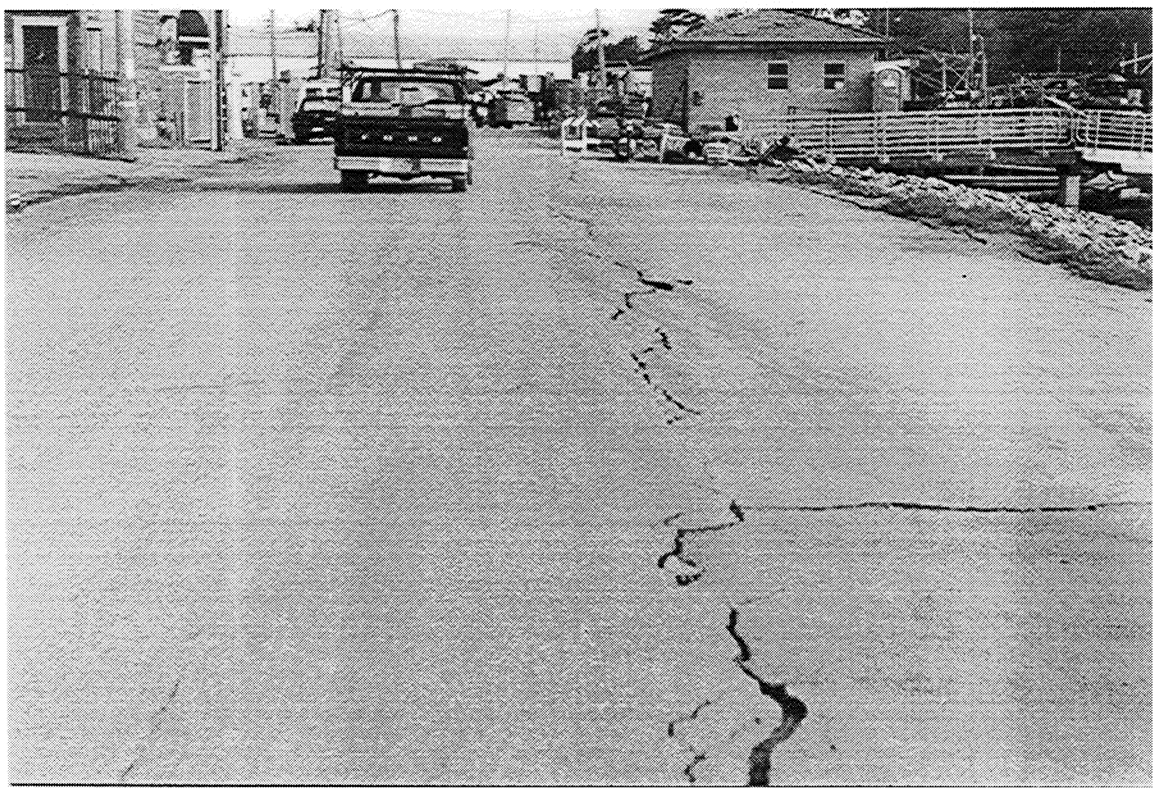

FIG. 7. Looking North along Sandholdt Road Shortly After the Loma Prieta Earthquake (MBARI Pier is shown in the upper-right corner)

testing. A low likelihood of these clayey silts developing high excess pore pressures or undergoing large deformations due to the earthquake shaking experienced at this site is suggested by the fact that the clayey silt at the bottom of the thin sand layer did not have any measurable strains. This would support a hypothesis that the 0.6 m thick clayey silt layer did not significantly strain itself, but rather that the slope inclinometer deformations across the layer were due to lateral loads imposed on the casing by liquefied sands above and below it. Deformations of the casing could have been facilitated by the softening of the clayey silt layer, which would have reduced its ability to restrain the inclinometer casing.

The soft to medium stiff silty clay between depths of about 10 and 13 m was encountered in several borings across this site as described in Boulanger et al. (1997). Laboratory tests indicated liquid limits (LL) of 50-77 and plasticity indices (PI) of 25-43, giving Unified Soil Classifications of CH and MH. The underlying soil layer is stiff to very stiff silty clay (LL = 55-70, PI = 23-34) with dense sand interlayers. The soils within the 12.3-13.3 m depth interval, where Method A predicts liquefaction, can reasonably be expected to consist of similar high-plasticity silty clay with thin sand interlayers. These sand interlayers are too thin to develop fully representative tip resistances, and thus it is overly conservative to use their tip resistances to predict liquefaction resistance. Furthermore, the thin sand interlayers within the 12.3-13.3 m depth interval are well below the adjacent channel bottom and thus would not be expected to contribute substantially to lateral deformations even if they did liquefy. Consequently, the soil

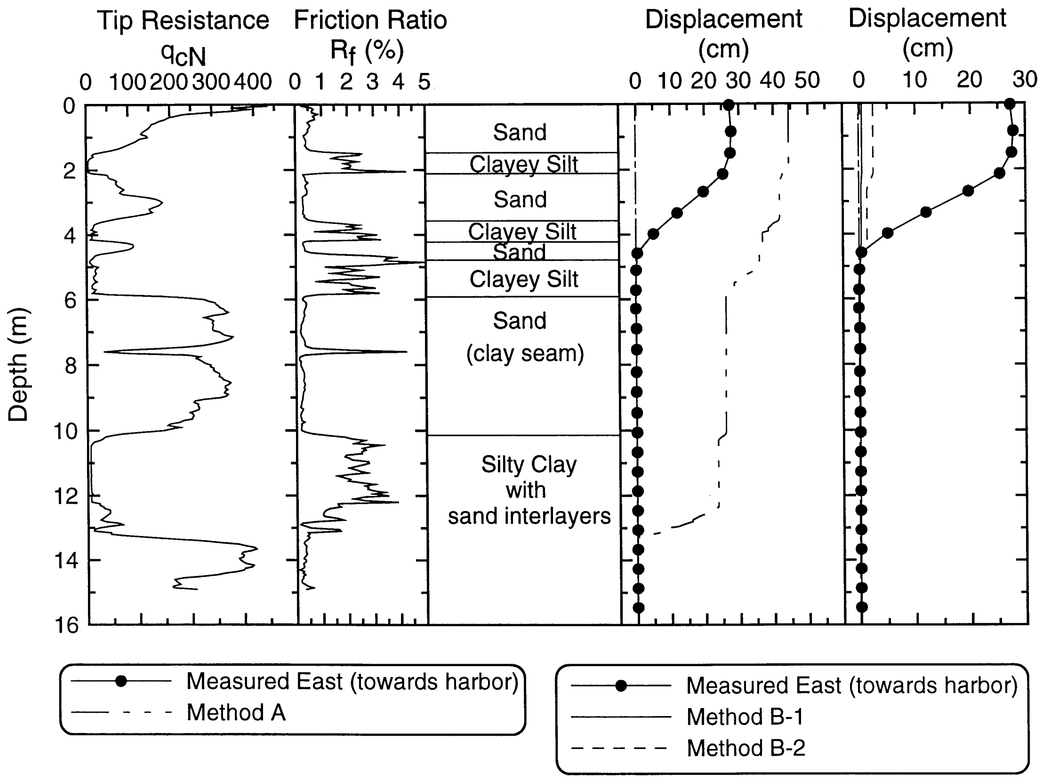

Fig. 8. Liquefaction Analysis of CPT Sounding Adjacent to Slope Inclinometer SI-2

sample data and site stratigraphy provide a justifiable basis to manually modify the results indicated by Method A.

Liquefaction-induced shear strains at slope inclinometer SI-2 appear to be relatively uniform across the sand layer between depths of about 2.1 and 3.6 m despite the q_{cN} varying from about 75 to about 160 (see Fig. 8; $q_{cN} = q_c/p_a$, with p_a = atmospheric pressure). The mean grain size is relatively similar across the full thickness of this sand layer and thus the differences in q_c do not appear to be a grain size effect. Possible explanations for the uniform shear strains include pore pressure redistribution from looser to denser zones or the CPT sounding not being adequately representative of the soil mass that was laterally spreading (i.e., lateral heterogeneity within the lateral spread).

Results for Methods B-1 and B-2 are also shown in Fig. 8 for comparison. For simplicity, these analyses assume that the clayey silt layers and interface (transition) intervals have negligible potential for shear strains. In practice, estimating strains in the clayey silt layers based only on the CPT and SPT data is difficult, with procedures still needing development. The extra deformation due to strains in the fine-grained layers can be evaluated separately in the comparisons of predicted and observed deformations versus depth. Predicted lateral surface displacements are about 0.4 cm and 2 cm for Methods B-1 and B-2, respectively. Settlement predictions are not presented for this CPT sounding because it is at the top of a slope and hence settlements will not be due to one-dimensional strains alone.

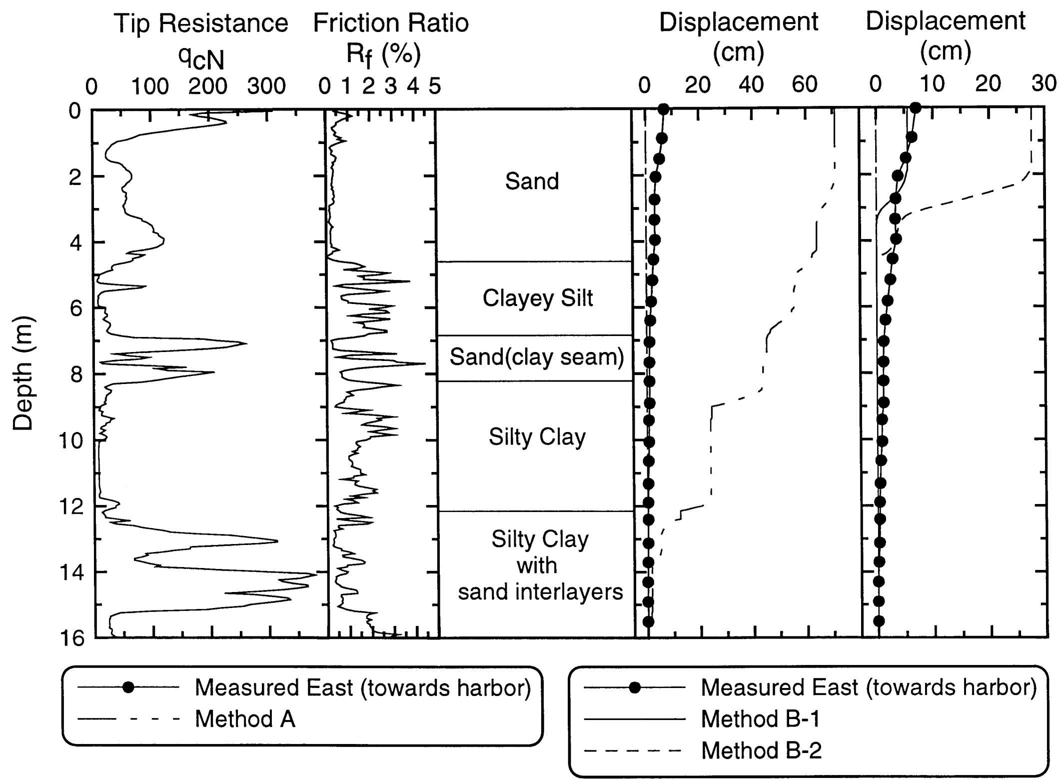

Fig. 9. Liquefaction Analysis of CPT Sounding Adjacent to Slope Inclinometer SI-4

Similar analyses were performed for a CPT sounding across the road (landward side) to slope inclinometer SI-2. Settlement calculations were made for this CPT sounding because it was relatively far from the edge of the slope. Method A again predicts strains at transitions between layers and in clayey silt layers and gives surface lateral displacement and settlement values of 127 cm and 15 cm, respectively. No cracks or settlements were observed near this CPT location, and Methods B-1 and B-2 correctly predict negligible displacement or settlement.

Inclinometer SI-4

Measurements taken from slope inclinometer SI-4 positioned near the shoreline edge of Sandholdt Road (Fig. 9) indicates that the edge of the road displaced laterally about 7 cm towards the water and negligibly along the shoreline direction. Lateral movements were observed above the assumed water table depth of 1.8 m, possibly reflecting saturation due to capillary rise or a higher than expected water table. CPT data from the adjacent sounding was used for predictions as before.

Method A predicted a high surface displacement of about 71 cm (Fig. 9), with most of the predicted displacement occurring in the clayey silt and silty clay layers. The comments previously made for slope inclinometer SI-2 are applicable to this location as well.

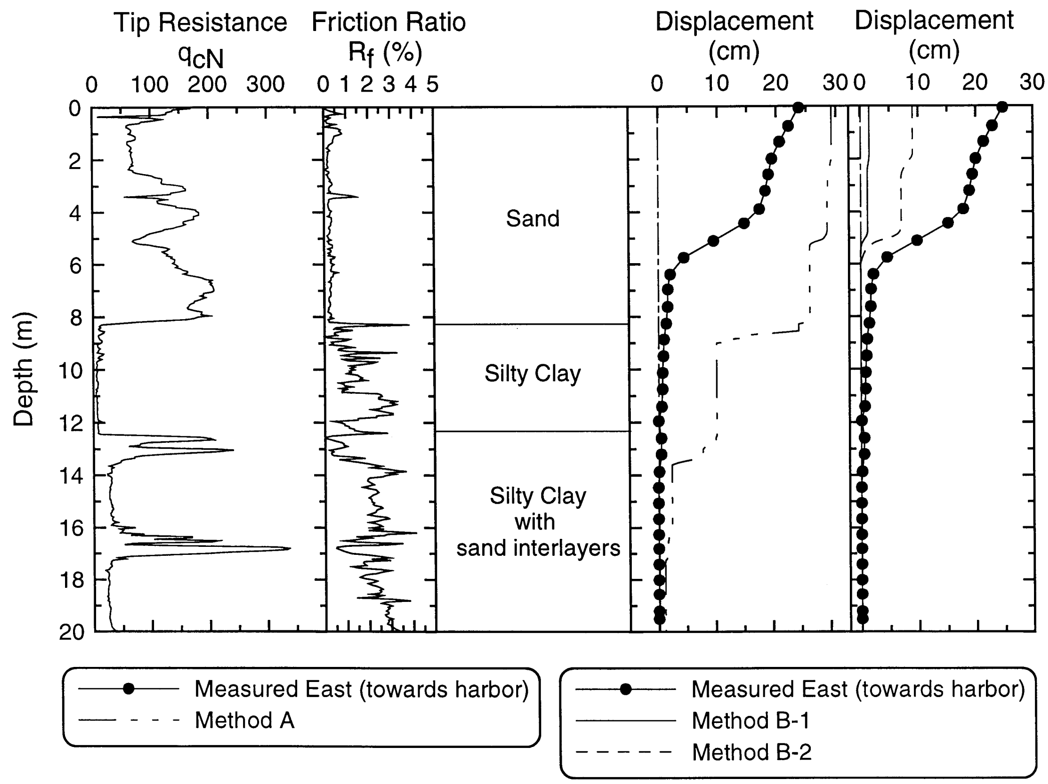

Fig. 10. Liquefaction Analysis of CPT Sounding Adjacent to Slope Inclinometer SI-5

Methods B-1 and B-2 gave better predictions, with Method B-2 over-predicting (28 cm) and Method B-1 only slightly under-predicting (6 cm). As previously discussed, these analyses assume that the clayey silt layers and interface (transition) intervals have negligible potential for shear strains. At this location, however, the inclinometer did show about 3 cm of lateral surface displacement due to shear strains of 0.3-0.7% across the clayey silt and silty clay layers.

Similar analyses were performed for a CPT sounding across the road (landward side) to slope inclinometer SI-4. Method A again predicts strains at transition between layers and in clayey silt layers and gives surface lateral displacement and settlement values of about 217 cm and 23 cm, respectively. No cracks or settlements were observed near this area and again Methods B-1 and B-2 correctly predict negligible displacements at this location.

Inclinometer SI-5

Measurements taken from slope inclinometer SI-5 positioned near the shoreline edge of Sandholdt Road (Fig. 10) indicates that the edge of the road displaced laterally about 25 cm towards the water and negligibly along the shoreline direction. Lateral movements were also observed above the assumed water table depth of 1.8 m. CPT data from an adjacent sounding was used for predictions as before.

Table 2. Measured and Predicted Lateral Displacement Potential along Sandholdt Road

	Lateral Displacement Potential at the Ground Surface (cm)					
	SI-2	Across road from SI-2	SI-4	Across road from SI-4	SI-5	Across road from SI-5
Measured	28	None visible	7	None visible	25	None visible
Method A	44	127	71	217	29	114
Method B-1	0.4	0	6	0	2	0
Method B-2	2	0.6	28	0	9	0
Method B-2, with a_{max}=0.4 g	12	3	40	0	23	0

Method A predicted lateral displacements of the ground surface of about 29 cm (Fig. 10). Even though this is close to the measured value this is again a result of compensating errors; i.e., over-prediction of strains in fine grained layers and at transitions, and under-prediction of strains in the sand. Again, the detailed comments made for slope inclinometer SI-2 are largely applicable to this site. Method B-1 predicts very little strains or displacements, while Method B-2 predicts lateral surface displacements of 9 cm. Methods B-1 and B-2 greatly under-predict the observed lateral surface movement of 25 cm. At this location, about 1 cm of lateral displacement occurred due to strains of 0.3% in the silty clay.

Similar analyses were performed for a CPT sounding across the road (landward side) from slope inclinometer SI-5. Method A again predicts strains at transitions between layers and in clayey silt layers and gives surface lateral displacement and settlement values of about 114 cm and 12 cm, respectively. No cracks or settlements were observed near this area and Methods B-1 and B-2 correctly predict negligible displacements in this case.

Overall Comparison and Parameter Studies

Measured and predicted lateral surface displacements at the three slope inclinometers and across the road from each inclinometer are summarized in Table 2. None of the CPT analysis methods could accurately predict the observed displacements at all six locations or the distribution of deformations with depth at all three inclinometers (Figs. 8, 9 and 10). Consequently, a parameter study evaluated the effect of uncertainties in key analysis parameters, including peak ground acceleration, ground water level, duration, and soil unit weights. For example, analyses by Method B-2 with a peak ground acceleration of 0.40 g gives a reasonable range of surface lateral displacements at the three inclinometers (12 to 40 cm) while correctly predicting small displacements on the landward side of the road (<3 cm), as shown in Table 2. However, regardless of the method used, it was found that when the parameters were adjusted to get a match between the measured and predicted surface displacements for any one location, the prediction for at least one of the other locations was always poor.

The clayey silts encountered by these six CPT soundings could be distinguished from the other soil types using the criteria that I_c be greater than about 2.15 to 2.30. A slightly lower I_c criterion is needed for the landward side of Sandholdt Road than for the shoreline side. A consequence of this is that Method A (which uses $I_c > 2.6$ as the criteria) predicts more extensive strains in the clayey silt layers (and hence larger lateral displacements and settlements) on the landward side of Sandholdt Road than on the shoreline side, as shown in Table 2. In any event, it should be noted that Method A would produce very similar results to Method B-1 if its criteria for identifying "clayey" soils was changed to $I_c > 2.15$ and if it included manual interpretation of transitions between soil layers.

Lateral displacements along Sandholdt Road might well have been estimated by the following simple approximations using the SPT-based liquefaction analysis results completed for this site by Boulanger et al. (1995). Sand layers that are predicted to liquefy along the shoreline occur in thicknesses of 1 to 2.5 m. Shear strains of 5 to 15% might be expected based on the range of penetration resistances (SPT and CPT) and factors of safety against liquefaction only slightly less than unity (based on SPT data). Thus, lateral displacements of 5 cm (5% of 1 m) to 38 cm (15% of 2.5 m) might be expected along the shoreline, with the distribution of deformations being unpredictable due to heterogeneity and other complicating factors. In this sense, the predicted and observed range of displacements would be in good agreement.

SUMMARY AND CONCLUSIONS

Three versions of a CPT-based liquefaction analysis method were evaluated against slope inclinometer data from a laterally spreading shoreline in Moss Landing during the 1989 Loma Prieta earthquake. These three methods (Table 1) used different correlations to estimate values for CSR_{liq} and D_r and compared automated versus manual interpretations of the soil profile. Select aspects related to developing and applying CPT-based liquefaction analysis methods were also discussed. The following observations and conclusions are drawn from these comparisons and related discussions.

- Correlations of cyclic stress ratio versus CPT tip resistance need to be developed and applied with consistent guidelines and procedures, and suggestions towards this goal were presented herein.

- Site-specific correlations between CPT data and soil characteristics should always be required, regardless of the project. The use of $I_c > 2.6$ to identify fine-grained soils as "clayey" is not reliable enough to warrant its use without sampling and laboratory testing. Experience in the same geologic units at adjacent sites is always useful, but not necessarily sufficient. It is the geotechnical engineer's responsibility to ascertain if such experience is sufficient for a given project.

- Method A inferred soil characteristics from the CPT data and used automated point-by-point calculations with no manual interpretation of the profile, such as might be obtained from simple commercial software. This method over-predicted lateral displacements at the ground surface for all 6 locations (at the 3 inclinometers and across the road from each inclinometer).

Large strains were predicted in fine-grained layers and at interfaces where the observed deformations were actually small. Small or negligible strains were predicted in sand layers where the observed deformations were actually greatest.

- Methods B-1 and B-2 (see Table 1 for details) included manual interpretation of the soil profile based on borehole and geologic data. Method B-1 greatly under-predicted lateral displacements for all 3 inclinometers, while Method B-2 greatly under-predicted for 2 inclinometers and over-predicted for 1 inclinometer. Both methods correctly predicted the absence of visible settlements or displacements on the landward side of Sandholdt Road. These methods neglected strains in the fine-grained soils, but this only accounted for a small portion (up to 3 cm) of the underestimation in displacements at the inclinometer locations. Method B-2 used more conservative correlations and was slightly better on average in estimating strains in the sand layers.

- None of the CPT analysis methods could accurately predict the observed displacements at the 6 locations or their distribution with depth at the 3 inclinometers. Regardless of the method used, when the parameters were adjusted to get a match between the measured and predicted surface displacements for one inclinometer, the prediction for at least one of the other inclinometers was always poor. This suggests that the discrepancies are not attributable to a systematic error in any one of the analysis steps or empirical correlations, but rather to some other complicating factors.

- The poor agreement between analyses of individual CPT soundings and observed lateral deformation profiles is likely due to the combined effects of several factors, including:
  - spatial heterogeneity (geologic variability) of the shoreline deposits;
  - pore pressure redistribution, both laterally and vertically;
  - limitations in the supporting correlations (e.g., CSR_{liq} - q_{c1N}, D_r - q_{c1N}, fines corrections, charts for maximum shear strains or volumetric strains, use of equivalent clean sand $q_{c1N\text{-}cs}$ values in estimating strains);
  - effect of the shoreline slope;
  - limitations in the inclinometer readings (e.g., effect of casing stiffness);
  - any restraint imposed on the lateral spread by the piles for the adjacent docks; and
  - uncertainties in the ground motions.

- Complicating factors similar to those listed above often occur in practice, and thus the poor agreement between analyses of individual CPT soundings and observed deformation profiles provides an important example of the current limitations in many of our analysis methods.

- At this time, it appears that Method B-2 produces the most physically reasonable results for these Moss Landing data (i.e., the strains being largest in the sands rather than the clayey silts, and the distinct difference in displacements across Sandholdt Road). However, Method B-2 only predicted a reasonable range of lateral displacements along the shoreline when various input parameters (e.g., peak ground acceleration) were varied to produce more adverse conditions (e.g., greater cyclic loading conditions or smaller cyclic loading resistances).

ACKNOWLEDGMENTS

The field studies presented herein were funded by the U.S. Geological Survey, Department of the Interior, under USGS award number 1434-93-G-2337. The analyses were funded by the National Science Foundation under award CMS-9502530. We have benefited from many lengthy discussions with our colleague Dr. Lelio H. Mejia regarding Moss Landing. The above support and interactions are greatly appreciated.

REFERENCES

Barminski, R. F. Jr. (1993). "Onshore and offshore effects of the 1989 Loma Prieta earthquake in the Moss landing, California area." MS thesis, San Jose State Univ., San Jose, Calif.

Boulanger, R. W., Idriss, I. M., and Mejia, L. H. (1995). "Investigation and evaluation of liquefaction related ground displacements at Moss Landing during the 1989 Loma Prieta earthquake." Report UCD/CGM-95/02, Center for Geotechnical Modeling, University of California, Davis, CA.

Boulanger, R. W., Mejia, L. H., and Idriss, I. M. (1997). "Liquefaction at Moss Landing during Loma Prieta earthquake." J. Geotech. Engrg., ASCE, 123(5), 453 – 467.

Boulanger, R. W., Mejia, L. H., and Idriss, I. M. (1999). Closure to "Liquefaction at Moss Landing during Loma Prieta earthquake." J. Geotech. Engrg., ASCE, 125(1): 92-96.

Dupre, W. R., and Tinsley, J. C. (1980). "Geology and liquefaction potential, northern Monterey and Southern Santa Cruz counties, California." Map MF-1199, 1:62,500, U.S. Geological Survey Miscellaneous Field Studies.

Harder, L. F., and Boulanger, R. W. (1997). "Application of K_σ and K_α correction factors." Proc., NCEER Workshop on Evaluation of Liquefaction Resistance of Soils, T. L. Youd and I. M. Idriss, Eds., NCEER-97-0022, National Center for Earthquake Engrg. Research, SUNY, Buffalo, 167-190.

Harding Lawson Associates (1988). "Geotechnical investigation, dredging and slope improvements, Moss landing south harbor." Report for Moss Landing Harbor District, HLA, Concord, Calif.

Idriss, I. M. (1997). "Evaluation of liquefaction potential and consequences." 3rd Seismic Short Course on Evaluation and Mitigation of Earthquake Induced Liquefaction Hazards, T. D'Orazio, ed., San Francisco State University, San Francisco, Calif.

Idriss, I. M., Sakoumpenta, E., and Boulanger, R. W. (1997). "An examination of CPT-based methods for evaluating liquefaction susceptibility of clean sands." Report UCD/CGM-97/06, Center for Geotechnical Modeling, Dept. of Civil and Envir. Engrg., University of California, Davis, CA.

Ishihara, K., and Yoshimine, M. (1992). "Evaluation of settlements in sand deposits following liquefaction during earthquakes." Soils and Foundations, 32(1), 173 – 188.

Ishihara, K. (1993). "Liquefaction and flow failure during earthquakes." Geotechnique 43(3): 351-415.

Jefferies, M. G., and Davies, M. P. (1993). "Use of CPTu to estimate equivalent SPT N_{60}." ASTM Geotechnical Testing Journal, 16(4): 458 – 467.

Kulhawy, F., and Mayne, P. (1990). *Manual on Estimating Soil Properties for Foundation Design.* EPRI Report EL-6800, August, EPRI, Calif.

Mejia, L. H. (1998). "Liquefaction at Moss Landing." *The Loma Prieta, California, Earthquake of October 17, 1989 – Liquefaction*, Prof. Paper 1551-B, T. L. Holzer, ed., U.S. Geol. Survey, 129-150.

Mitchell, J. K., and Tseng, D. J. (1990). "Assessment of liquefaction potential by cone penetration resistance." Proc., H. Bolton Seed Memorial Symp., J. M. Duncan, ed., Bitech Publishers, 2:335-350.

NRC (1985). *Liquefaction of soils during earthquakes.* National Research Council, National Academy Press, Washington, D.C.

Olsen, R. (1997). "Cyclic liquefaction based on the cone penetrometer test." Proc., NCEER Workshop on Evaluation of Liquefaction Resistance of Soils, T. L. Youd and I. M. Idriss, Eds., NCEER-97-0022, National Center for Earthquake Engrg. Research, SUNY, Buffalo, 225-276.

Robertson, P. K., and Campanella, D. (1985). "Liquefaction potential of sands using the CPT." J. Geotech. Engrg., ASCE, 111(3), 384 - 403.

Robertson, P. K., and Wride, C. E. (1998). "Evaluating cyclic liquefaction potential using the cone penetration test." Can. Geotech. J. 35: 442 – 459.

Robertson, P. K., and Wride, C. E. (1999). Discussion of "Liquefaction at Moss Landing during Loma Prieta earthquake." J. Geotech. Engrg., ASCE, 125(1): 91 – 92.

Seed, H. B., and Idriss, I. M. (1971). "Simplified procedure for evaluating soil liquefaction potential." J. Geotech. Engrg., ASCE, 97(9), 1249 – 1273.

Seed, H. B., Tokimatsu, K., Harder, L. F., and Chung, R. M. (1985). "Influence of SPT procedures in soil liquefaction resistance evaluations." J. Geotech. Engrg., ASCE, 111(12), 861 – 878.

Shibata, T., and Teparaksa, W. (1988). "Evaluation of liquefaction potential of soils using cone penetration tests." Soils and Found., Tokyo, Japan, 28(2), 49 – 60.

Tatsuoka, F., Zhou, S., Sato, T., and Shibuyas, S. (1990). "Evaluation method of liquefaction potential and its application." Rpt. on seismic hazards on the ground in urban areas, Ministry of Education of Japan. (in Japanese).

Site Amplification Ratios Estimated from Geomorphological Land Classification and JMA Strong Motion Records

Fumio Yamazaki[1], Kazue Wakamatsu[1], Khosrow T. Shabestari[1], and Jun-ichi Onishi[2]

[1] *Institute of Industrial Science, The University of Tokyo, 7-22-1 Roppongi Minato-ku, Tokyo, 106-8558, Japan.*
[2] *Central Japan Railway Company (JR Tokai), 1-6-6 Yaesu, Chuo-ku, 103-0028, Japan.*

Abstract

The relationship between the amplification ratio of earthquake ground motion and geologic conditions at Japan Meteorological Agency (JMA) stations nationwide was examined to propose an estimation method of the amplification ratio that is applicable to the entire Japan. The amplification ratios for the instrumental JMA intensity, as well as for the peak ground acceleration and velocity, were obtained from the station coefficients of the attenuation relationships using strong motion records measured at 77 JMA stations over a period of more than 8 years. A combined use of geomorphological land classification and subsurface geology was found to yield the best estimate of the site amplification ratio. This result suggests that the Digital National Land Information of Japan may be conveniently used for the estimation of strong motion distribution over large areas in Japan.

***Key Words*:** Strong Motion records; Site amplification ratio; Attenuation relation; Geomorphological land classification; Digital National Land Information; PGA; PGV.

Introduction

The estimation of strong motion distribution is important in the seismic design and retrofit of structures, damage assessment of urban structures, and analysis of earthquake damage data. In particular, considering the use of estimated strong motion distribution in damage assessment systems [1-3], it is desirable to have a simple method applicable to large areas based on generally available data.

The major factors that affect the strong ground motion are the source characteristics typically represented by the magnitude, the wave propagation path effect represented by the source-to-site distance, and the subsurface soil condition that governs the amplification ratio. A large number of studies have been carried out by various researchers in the world to correlate the site amplification and geological classification using observed seismic records. However, due to the limitation of available strong motion data and corresponding geological data, together with regional differences in geology and geomorphology, a widely applicable relation has not yet been established.

Attenuation relations provide a convenient tool to estimate the strong ground motion using the magnitude, depth, source-to-site distance, and in some cases, soil conditions. The attenuation relations are often used in earthquake damage assessments and seismic hazard analyses. Molas and Yamazaki [4,5] and Shabestari and Yamazaki [6] have recently developed attenuation relationships for the peak ground acceleration (PGA), peak ground velocity (PGV), JMA (the Japan Meteorological Agency) instrumental seismic intensity and response spectra using records from the JMA-87-type accelerometers. In this series of study, the station coefficients, which represent the relative amplification of observation stations in the attenuation relationships, were employed to characterize the site condition.

Several recent studies in Japan on seismic zonation employed the geomorphological and geological information included in the Digital National Land Information (DNLI), which is a digital database for geographic information systems (GIS) and covers entire Japan with a 1 km x 1 km size mesh, as a method to estimate site amplification characteristics [7,8]. It should be noted that the two previous methods described above were developed based on soil and geomorphological data from specific regions in Japan. Although the applicability of these methods to those respective regions has been demonstrated, a further study may be necessary for their applicability to the other parts of Japan. Hence, there is a need for methods that can be applicable to the entire Japan to the estimate strong motion distribution in seismic hazard and damage assessments. At present, the method by Matsuoka and Midorikawa [7] is used in the earthquake damage assessment systems of the National Land Agency and the Fire Defense Agency of Japan.

The instrumental seismic intensity [9], which replaces the conventional seismic intensity scale based on human perception, came into use as the official measure by the JMA from October 1996. Many seismometers, which monitor the instrumental seismic intensity, have been deployed all over Japan [3]. Hence, the JMA instrumental seismic intensity will be used more than other indices in the near future. Thus a research on the amplification ratio of the JMA intensity is necessary.

Under these circumstances, the present study aims to propose an estimation method of the amplification ratios that is applicable to the entire Japan. Comparing the relationship between geomorphological and geological conditions of the JMA stations nationwide and the amplification ratios determined from the attenuation equations based on the JMA strong motion records, the Digital National Land Information is employed to predict the amplification ratios for PGA, PGV and JMA intensity.

Method for estimation of site amplification ratio

Attenuation relationship and station coefficients

Molas and Yamazaki [4,5] used 2,166 sets of two horizontal component records from 387 earthquakes observed from August 1, 1988 to December 31, 1993 by the JMA-87-type accelerometers at 76 JMA stations in Japan and constructed attenuation relationships for PGA and PGV. Adding data observed till March 31, 1996 by the same instruments, Shabestari and Yamazaki [6] developed an attenuation equation for the instrumental JMA intensity (I) and revised the PGA and PGV attenuation equations. The records used in the study are 3,990 sets from 1,020 earthquakes at 77 JMA free field stations (Fig. 1).The following functions were used in the regression analysis.

$$\log_{10} PGA = b^A{}_0 + b^A{}_1 M_J + b^A{}_2 r - \log_{10} r + b^A{}_4 h + c^A{}_i \tag{1}$$

$$\log_{10} PGV = b^V{}_0 + b^V{}_1 M_J + b^V{}_2 r - \log_{10} r + b^V{}_4 h + c^V{}_i \tag{2}$$

$$I = b^I{}_0 + b^I{}_1 M_J + b^I{}_2 r - 1.89 \log_{10} r + b^I{}_4 h + c^I{}_i \tag{3}$$

in which M_J is the JMA magnitude, r is the shortest distance (km) to the fault plane, h is the focal depth (km), b_0, b_1, b_2, and b_4 are coefficients determined by regression, c_i is the station coefficient representing the site effect at site i. The suffixes A, V and I indicate the PGA, PGV, and instrumental JMA intensity, respectively.

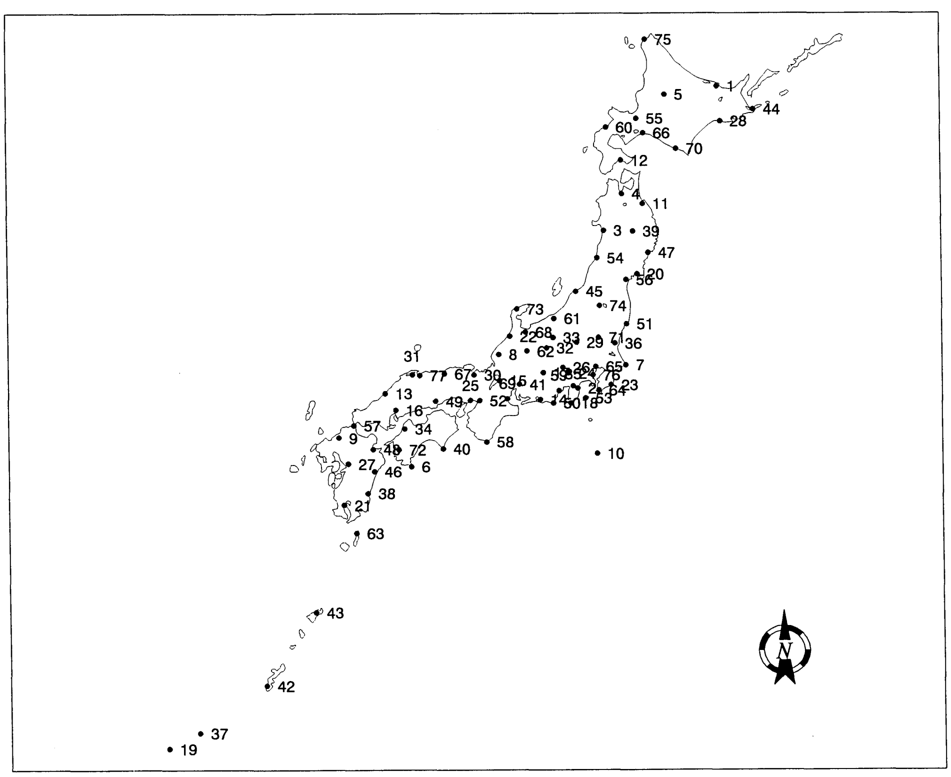

Fig. 1 Location of 77 JMA recording stations of the JMA 87-type-accelerometers

The two-stage regression procedure proposed by Joyner and Boore [10] was employed the regressive analysis, considering the correlation between the magnitude and distance in the data. In this method, a dummy variable was used for each earthquake. The coefficients related to the distance (b_2, b_4) were determined in the first stage, and the coefficients related to the magnitude (b_0, b_1) were determined in the second stage.

Since the station coefficient is different for each station, the same number of dummy variables are also required. Thus, determination of the regression coefficients with the standard two-stage regression method would become difficult due to an excessive number of dummy variables, causing the singularity of the matrix. To solve this problem, a three-stage regression method, named the iterative partial regression was employed [4], and the coefficients were determined.

The station coefficient represents the site effect of the recording station as a supplement of the attenuation equation. The station coefficient may be affected by the geological and geomorphological conditions at the recording site and the conditions of the instrument, e.g. response characteristics of the instrument and its foundation. The mean of the station coefficients for all the recording stations is zero. Stations with positive station coefficients are supposed to have higher amplification ratio than the average site, while stations with negative station coefficients to have lower amplification.

Figure 2 plots these station coefficients with respect to the station number. The station coefficient for PGA and JMA intensity is largest for Kushiro and smallest for Matsushiro. It has been known that large acceleration is always recorded at Kushiro. This analysis proved this fact. Matsushiro is the only site where the instrument is placed in a rock tunnel. This fact explains the reason of the smallest station coefficient at this site. The station coefficients for PGV show similar tendency with those for PGA. The station with the largest coefficient is Sakata, and the smallest coefficient is observed again in Matsushiro.

Conversion of station coefficient to site amplification ratio

If the peak ground acceleration at surface point i and that at the (hypothetical) outcrop beneath point i are represented by PGA_{Si} and PGA_{Bi}, respectively, the amplification ratio ARA_i of PGA at point i is given by

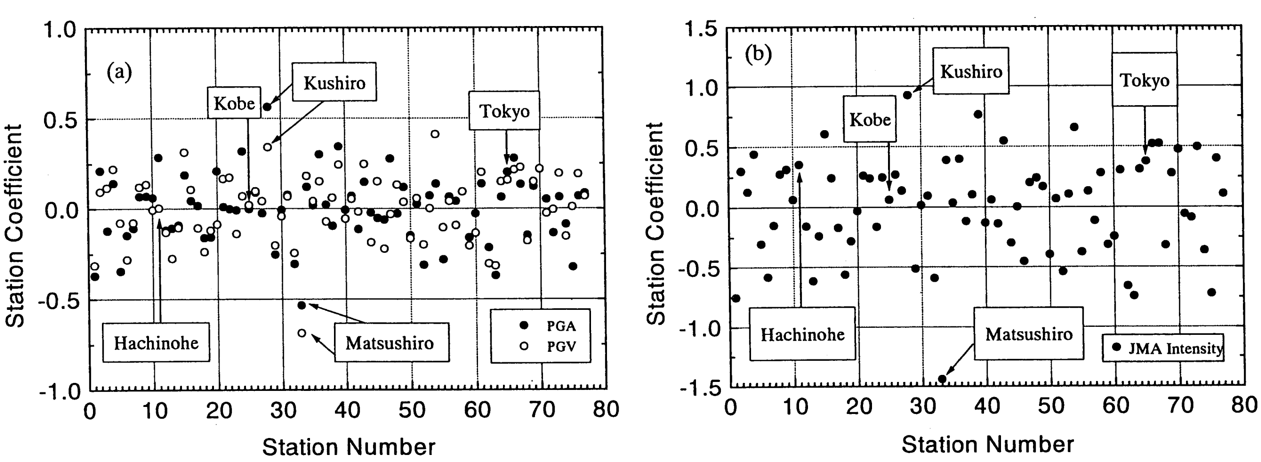

Fig. 2 Station coefficients for (a) peak ground acceleration (PGA) and peak ground velocity (PGV) and (b) JMA intensity for 77 JMA stations

$$ARA_i = PGA_{Si} \,/\, PGA_{Bi} \tag{4}$$

The outcrop in this study is assumed as the surface of a stratum having sufficient rigidity (for example, with V_s of at least 400 m/s). Then the supplement term (station coefficient) of the attenuation relation at the outcrop may have a constant value $C^A{}_0$. From equation (1), PGA_{Bi} at the outcrop is written as

$$\log_{10} PGA_{Bi} = b^A{}_0 + b^A{}_1 M_J + b^A{}_2 r - \log_{10} r + b^A{}_4 h + c^A{}_0 \tag{5}$$

The peak ground acceleration at the ground surface is given by

$$\log_{10} PGA_{Si} = b^A{}_0 + b^A{}_1 M_J + b^A{}_2 r - \log_{10} r + b^A{}_4 h + c^A{}_i \tag{6}$$

The difference between equations (5) and (6) yields

$$\log_{10} (PGA_{Si} \,/\, PGA_{Bi}) = c^A{}_i - c^A{}_0 \tag{7}$$

From equations (4) and (7), we obtain

$$ARA_i = 10^{c^A{}_i - c^A{}_0} \tag{8}$$

Similarly, the amplification ratio of the PGV is determined by

$$ARV_i = 10^{c^V{}_i - c^V{}_0} \tag{9}$$

Performing a similar operation on the amplification ratio of the JMA intensity, we get

$$ARI_i = c^I{}_i - c^I{}_0 \tag{10}$$

From the equations (8), (9) and (10), the amplification ratios for PGA, PGV and JMA intensity can be determined from their station coefficients. For the range of input motion in which soil non-linearity becomes significant, the site amplification ratios, especially for PGA, depends on the amplitude of ground strain. However, the attenuation relationships in this study were developed using the measured records. Since only few records are considered to be in the non-linear range, it would be difficult to introduce this effect to the amplification ratios.

In order to predict strong ground motion at non-recording sites, we must propose a method to estimate the station coefficient for those sites. The most influential factor determining the station coefficient may be the subsurface soil condition. Therefore, we will compare the station coefficients with the geological and topographical conditions of the recording sites hereafter.

Relationship between ground conditions and station coefficients

JMA recording stations and ground conditions

To clarify the relationship between the ground condition and the station coefficient, it is necessary to investigate the geological conditions at the 77 JMA stations. To estimate site condition at the recording stations, which are distributed all over Japan, one feasible way would be the use of geomorphological and geological data compiled in the DNLI. Note that the geomorphological and subsurface geological data in the DNLI were made based on the geomorphological classification maps and subsurface geology maps of the region on a scale of 1/200,000 (1/100,000 scale only for Tokyo and Kanagawa Prefecture). This digital information gives the attributes of geomorphological and subsurface geological pixels, which account for the largest area in each pixel of the standard regional mesh (about 1 km x 1 km), established by the Geographical Survey Institute of Japan. Therefore, although it is effective for the macroscopic determination of the average geomorphological and geological distribution over a large area, the DNLI may lead to an erroneous conclusion in a case obtaining the geomorphological and geological conditions of a specific point, such as a recording station.

Thus, it was decided that other means would be used to determine the land classification of the recording stations. The geomorphological classification, age of deposit, type of the sediment, and subsurface geology were determined using the subsurface geology maps and geomorphological classification maps (published by the Economic Planning Agency and prefectures) from the Fundamental Land Classification Survey of Japan.

Relationship between land classification and station coefficients

The relationships between the land classifications of JMA stations and the station coefficients for PGA, PGV and JMA intensity were investigated. Figure 3 shows the relationship between the geomorphological classification and the station coefficients for PGV, for example. With regard to PGV and JMA intensity, such tendency is observed that the harder the ground corresponding to the geomorphological classification, the smaller the station coefficient becomes. However, there is a great deal of scatter among the station coefficients within the same geomorphological classification. Hence, one can conjecture that the geomorphological classification alone is not the controlling factor of the station coefficient. Possible reasons for this scatter include the followings: 1) the influence from other factors, such as the deep ground structure of the site, may be significant; 2) the recording stations classified as a geomorphologic unit do not present the standard ground condition for the unit; and 3) a large difference in the vertical soil profile may be associated even in the same geomorphological classification. A more detailed classification may be necessary for the geomorphologic units with a large scatter in the station coefficient.

Figure 4 shows the relationship between the geological periods and the station coefficients for PGV. Practically no correlation is seen for any of these indices. Hence, it would be difficult to estimate the station coefficient using only the geological period.

Figure 5 shows the relationship between the subsurface geology and the station coefficients for PGV. In the geologic classification, lava is included under volcaniclastic material since this is a type of volcanic rubble. Loam in Japan, which is a kind of volcanic cohesive soil, is combined with volcanic ash.

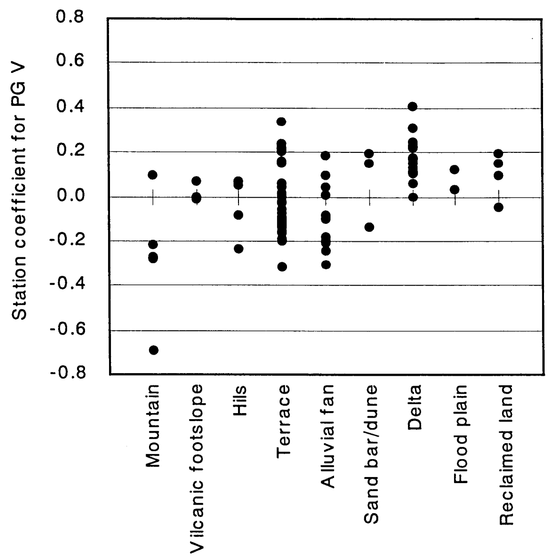

Fig. 3 Station coefficients for PGV with respect to the geomorphological classification at JMA stations

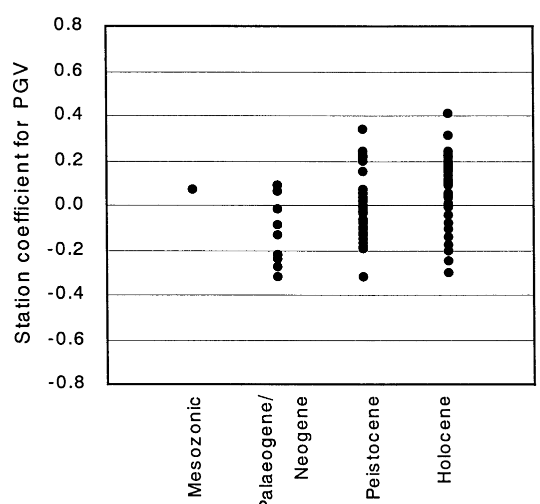

Fig. 4 Station coefficients for PGV with respect to the age of deposit at JMA stations

In the figure, all of the station coefficients exhibit a rising trend in the order of rock, gravelly soil, sandy soil, clayey soil, volcaniclastic material, and volcanic ash (order of smaller particle size); that is, the softer the ground, the larger the amplification ratio becomes.

Table 1 shows the coefficients of correlation between the actual station coefficients and the average values of station coefficients in the same group according to three types of land classification (geomorphological classification, geological period, and subsurface geology). In each of the station coefficients (those for PGA, PGV, and JMA intensity), the correlation coefficient was largest in the classification by subsurface geology, and second largest in that by geomorphology.

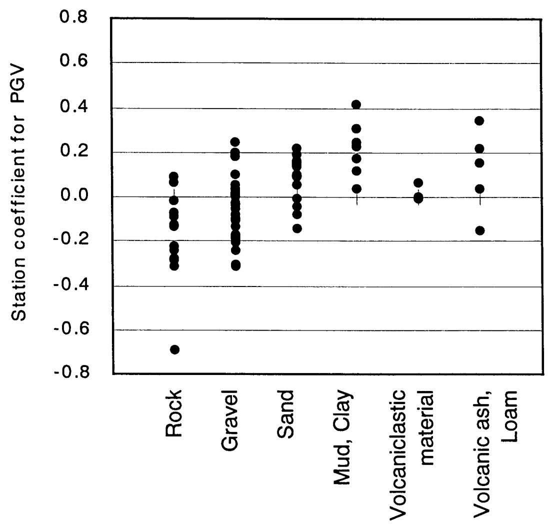

Fig. 5 Station coefficients for with respect to the subsurface geology at JMA stations

Table 1 Correlation coefficient between the mean values of station coefficients in each classification and the station coefficients obtained by Shabestari and Yamazaki [6]

Method of classification	PGA	PGV	JMA intensity
Geomorphology	0.43	0.61	0.57
Age of deposit	0.22	0.36	0.30
Subsurface geology	0.47	0.64	0.61

Relationship between elevation and station coefficients

Matsuoka and Midorikawa [7] and Fukuwa et al. [8] considered the elevation as a factor in the estimation of the site amplification ratio. Hence, we also examined the relationship between elevation and the station coefficient. The relationship was studied for each geomorphological classification, in order to minimize the influence of other factors. As an example, Figure 6 shows the relationship between the elevation and the station coefficient for PGV at the stations classified as terraces. Practically no correlation can be found between them. Categories other than terraces were also studied in the same way, but correlation was again not found. A possible reason for this may be explained as follows.

As stated before, the previous studies [7, 8] were conducted for specific regions of Japan (the Kanto plain and the Nobi plain). If dealing with a single fluvial plain, such as the above regions, the composition of sediment differs upstream to downstream of the river, even with the same geomorphology. In a single alluvial fan, the further downstream you go, the finer the sediment becomes. Matsuoka and Midorikawa [7] considered the effect of change in the characteristics of sediment by elevation. However, this kind of geomorphological principle cannot be applicable for a nationwide study such as the present one, which covers a large number of river basins.

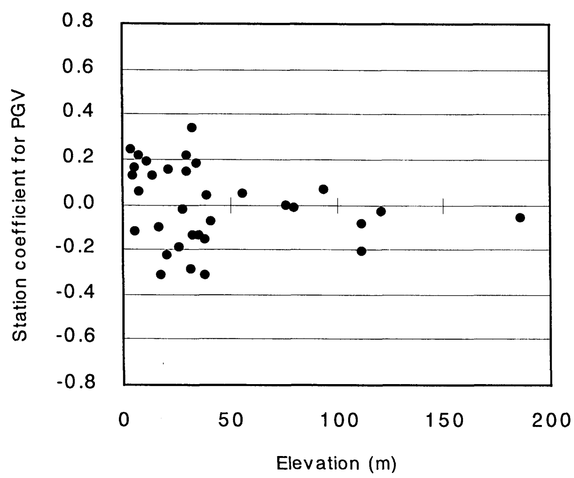

Fig. 6 Station coefficients for PGV with respect to the elevation of JMA stations located on terrace

Relationship between soil type and station coefficients

Classification of ground by soil type has been used in the field of civil engineering. The relationship between the soil type classification [11] shown in Table 2 and the station coefficient was investigated. The soil types of the 77 JMA stations were primarily determined from their geomorphological classification. Boring data were needed to distinguish between soil types 3 and 4. Thus, if boring data revealed that the thickness of the Holocene deposit was equal or more than 25 m, the station was considered to be soil type 4, and if not, it was considered to be soil type 3.

Figure 7 shows the relationship between the soil type and station coefficient for PGV. A large amount of scatter is observed in the station coefficient within the same soil type. However, the average values of the station coefficients increase in the order of type 1 to type 4. That is, the softer the ground, the bigger the seismic response becomes as has already been pointed out in the previous papers [4-6].

Table 2 Classification of soil type in Japanese Highway Bridge Code [11]

Soil type	Geologic definition	Definition by predominant period
Type 1 (rock and hard soil)	Tertiary or older rock (defined as bedrock), of Pleistocene deposit with $H < 10$ m	$T_G < 0.2$ sec
Type 2 (hard soil)	Pleistocene deposit with $H \geq 10$ m or Holocene deposit with < 10 m	$0.2 \leq T_G < 0.4$ sec
Type 3 (medium soil)	Holocene deposit with $H < 25$ m including soft layer with thickness less than 5 m	$0.4 \leq T_G < 0.6$ sec
Type 4 (soft soil)	Other than above, usually soft Holocene deposit or fill	$T_G \geq 0.6$ sec

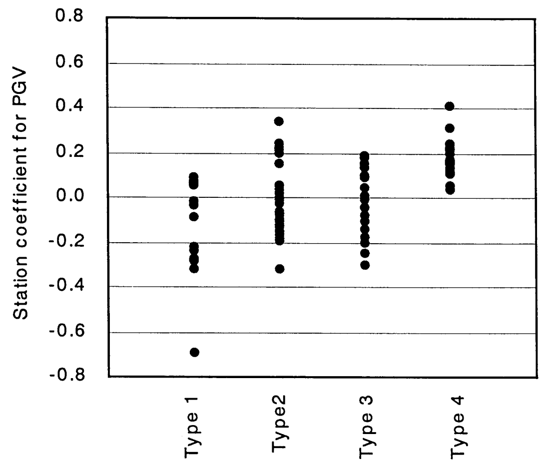

Fig. 7 Station coefficients for PGV with respect to the soil-type classification of JMA sites

Relationship between land classification and site amplification ratio

The relationships between various geological, geomorphological and soil conditions and the station coefficients were investigated above. It was found that a great deal of scatter exists in the relationship if each attribute is considered individually. However, considering the use of amplification ratios to the estimation of seismic motion distribution over a large area, we will develop a method to predict amplification ratios based on land classification. Land classification can be estimated using the Digital National Land Information (DNLI) in Japan, without using information difficult to obtain, such as boring data and predominant periods.

Among the land classifications discussed above, the correlation coefficients for subsurface geology and geomorphological classification were relatively high in Table 1. Therefore, we investigated differences in the station coefficients due to the difference in subsurface geology in the same geomorphological classification.

The subsurface geology of terrace was divided into the groups of rock, sand/gravel, and volcanic ash. The average values of the station coefficients for each group were found to increase in the order of rock, sand/gravel and volcanic ash for the three strong motion indices. Thus, the three-group subdivision was adopted for terrace. The subsurface geology of delta was divided into two groups, sandy soil and clayey soil. The average value of the station coefficients is higher for the clayey soil group than that for the sandy soil group with respect to PGA, PGV, and JMA intensity. Hence, this subdivision for delta was adopted. The geomorphological classifications other than delta and terrace, namely mountain, hill, alluvial fan, sand bank/dune, and reclaimed land, could not be subdivided because the subsurface geology was of the same composition in each classification.

Based on these considerations, the geomorphological classification was used as the major class and then subdivided into groups according to subsurface geology, as shown in Table 3. Note that the geomorphological classification considers the geomorphological origin, topography, material composition, and time of formation, thus resulting in the consideration of age of deposit as well.

Table 3 also shows the average station coefficients in each group, the number of recording stations used to calculate the average values, and the correlation coefficient between the average values and the

Table3 Average station coefficient and amplification ratios for eleven groups in this study

No.	Groups of this study	Number of stations	Average of station coefficient PGA	*PGV*	*JMA intensity*	Amplification ratio PGA	PGV	JMA Intensity
1	Reclaimed land	3	0.009	0.065	0.096	1.31	2.12	0.65
2	Sand bar, sand dune	3	0.038	0.065	0.178	1.40	2.12	0.73
3.	Delta (mud, clay)	8	0.081	0.203	0.389	1.54	2.92	0.94
4	Delta (sand)	8	0.029	0.118	0.216	1.37	2.39	0.77
5	Alluvial fan	11	-0.166	-0.092	-0.286	0.87	1.48	0.27
6	Terrace (volcanic ash)	7	0.205	0.137	0.350	2.05	2.50	0.90
7	Terrace (sand and gravel)	18	-0.005	-0.053	-0.064	1.26	1.62	0.49
8	Terrace (rock)	5	-0.131	-0.134	-0.309	0.95	1.34	0.24
9	Hill	5	0.054	-0.029	-0.069	1.45	1.71	0.48
10	Volcanic foot	3	0.148	0.018	0.134	1.80	1.91	0.69
11	Mountain	3	-0.107	-0.261	-0.554	1.00	1.00	0.00
Correlation coefficient		74	0.602	0.705	0.684			

actual station coefficients. In determining the average station coefficient for each group, three stations (Matsushiro, Ajiro and Wakkanai) were omitted. The instrument of Matsushiro (mountain) is placed in a rock tunnel and that of Ajiro (mountain) is located on talus (colluvial deposit) ground. These conditions significantly differ from those for other stations. Therefore, these station coefficients look singular points in Figs. 2 and 3. Wakkanai station (reclaimed land) is located on a small-scale reclaimed land built adjacent to a mountainous area. This condition was judged to be different from that for ordinary reclaimed lands in Japan, due to the reason that the bedrock lies in a shallow depth.

The correlation coefficient between the average values of the station coefficients in a group and the actual station coefficients is highest for PGV (0.705) and lowest for PGA (0.602). This tendency has also been seen in the other classifications described before.

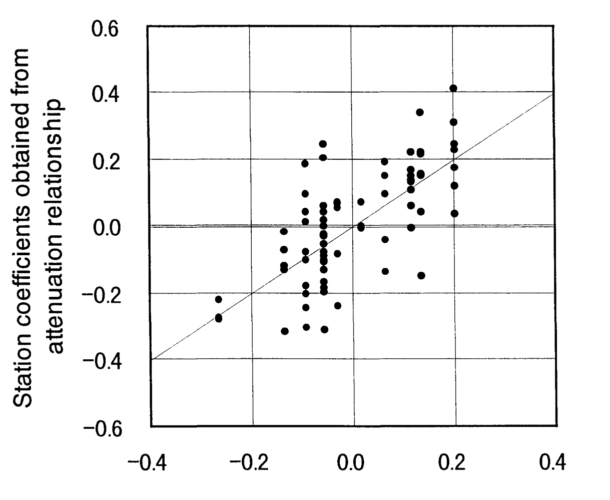

Fig. 8 Mean of the station coefficients based on the classification in this study for PGV compared with the station coefficients obtained from the attenuation relationship proposed by Shabestari and Yamazaki [6]

Table 4 Geomorphological classification and subsurface geology in the Digital National Land Information corresponding to the eleven groups in this study

No.	Groups of this study	Geomorphologic classification in Digital National Land Information	Subsurface geology in Digital National Land Information
1	Reclaimed land	Reclaimed land, Reclaimed land/polder	Sand, Sandy soil
2	Sand bar, sand dune	Natural levee, Natural levee/Sand bar, Lowland between sand dunes, Sand dune	Sand, Sandy soil, Dune sand
3	Delta (mud, clay)	Reclaimed land, Delta, Flood plain	Mud, Muddy soil, Silt, Clay, Peat
4	Delta (sand)	Reclaimed land, Delta, Flood plain	Sand, Sandy soil, Sand and Mud, Alternation of sand and mud
5	Alluvial fan	Alluvial fan, Volcanic fan	Gravel, Gravelly soil, Sand and gravel
6	Terrace (volcanic ash)	Loam terrace, Shirasu terrace, Volcanic sand terrace	Volcanic ash, Loam, Pumice flow deposit, Shirasu,
7	Terrace (sand and gravel)	Sand and gravel terrace	Gravel, Gravelly soil, Sand and gravel
8	Terrace (rock)	Rock terrace, Limestone terrace	Rock
9	Hill	Hill, Volcanic hill	Rock
10	Volcanic foot	Volcanic footslope, Lava flow field, Lava plateau	Volcaniclastic material, Lava, Mud flow deposit
11	Mountain	Mountain, Mountain footslope, Volcano	Rock, Volcanic rock

* Amplification ratio for JMA intensity is defined as the difference between the intensity at ground surface and that at bedrock.

The average values in each of the 11 groups categorized by geomorphology and subsurface geology are proposed as the estimation of the station coefficients. Figure 8 shows the relationship between these values and the actual station coefficients. Even though geomorphology is combined with subsurface geology, considerable variation is still seen in the estimation of station coefficients.

Table 3 also shows the amplification ratios, converted from the average values of station coefficients in the table. The ground surface in the regions geomorphologically classified as mountain is considered to be close to the rock outcrop. Then the conversion is performed so that the amplification ratio of the mountain group is set as 1.0 (for JMA intensity, set as 0.0). Table 4 shows geomorphological and subsurface geological categories in the DNLI corresponding to the eleven groups in this study. Using Table 4 and the DNLI, it is possible to estimate the site amplification ratios throughout Japan by 1 km x 1 km pixel.

Comparison of the results with the previous studies

The amplification ratio for PGV obtained in this study (Table 3) was compared with the results of two previous studies [7, 8]. Both the studies by Matsuoka and Midorikawa [7] and Fukuwa et al. [8] considered the elevation to estimate the site amplification ratio. For the purpose of comparison, elevation values should be assigned for each of the geomorphological and subsurface geological categories used in this study. Using the elevations at the 77 JMA stations, the average elevations for each geomorphological and subsurface geological category were calculated and they were used in the estimation equations [7, 8]. A unified definition of the bedrock was also needed to compare the amplification ratios from the three studies. Matsuoka and Midorikawa's study proposes amplification ratios, taking the hill of the Neogene period or earlier as a reference point. We assumed that this reference point is almost equivalent to our reference ground "mountain" and a direct comparison was made. Since Fukuwa's study considered the

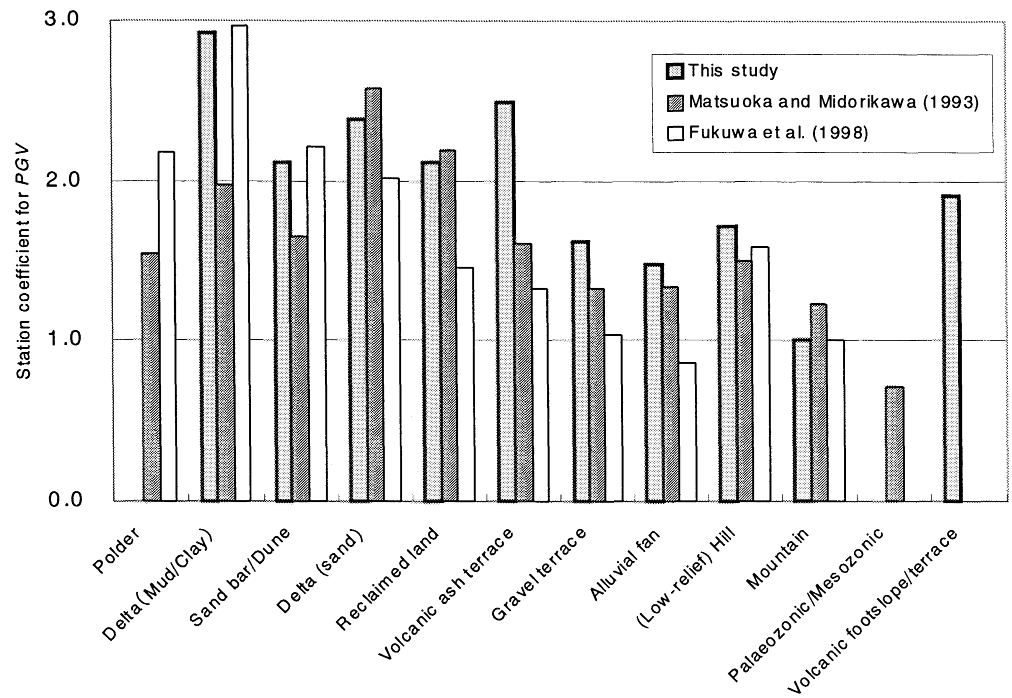

Fig. 9 Comparison of amplification ratios for PGV proposed in this study and two previous studies

bedrock with V_s = 3 km/s as a reference point, the amplification ratios proposed by Fukuwa were divided by 1.45, which is the amplification ratio for mountainous ground in his study.

Figure 9 compares the amplification ratios for PGV by the three studies. All the three estimation methods provide basically the same tendencies in the relative amplification in each geomorphological and geological category. The absolute values of the converted amplification ratios are also similar in spite of the fact that the three studies used completely different seismic records and ground data in deriving the amplification ratios. However, non-trivial differences are still observed for some soil categories. A further study using more comprehensive data set, e.g. from K-NET [12] with 1,000 recording sites nationwide, is suggested.

As stated before, the estimation of amplification ratios of strong motion indices from geomorphology and subsurface geology alone may be associated with considerable variability. Thus, the use of the proposed amplification ratios should be limited for the gross estimation of seismic motion over a large area.

We are currently expanding the proposed relation to response spectra. The period-dependent station coefficients from the spectral attenuation [5] can also be estimated based on geomorphology and subsurface geology. The results of this research will be presented in a separate paper.

Conclusion

A method for estimation of site amplification characteristics in Japan from generally available data was investigated considering its use in earthquake damage assessments for large areas. The station coefficients in the attenuation equations for PGA, PGV and JMA instrumental seismic intensity, based on the strong motion records measured by the JMA-87-type-accelerometers, were compared with land classifications by the Fundamental Land Classification Survey and others. After several trials, the scatter of station coefficients within each soil group was minimized when the 77 JMA stations are divided into 11 soil groups based on their geomorphological classification and subsurface geology.

From the average values of the station coefficients in each group, the site amplification ratios for the strong motion indices were obtained taking a mountainous ground in the geomorphological classification as the reference. Then the amplification ratios for PGA, PGV, and JMA intensity can be estimated by 1 km x 1 km pixels throughout Japan using the geomorphological and subsurface geological data in the Digital National Land Information of Japan. A comparison with two previous studies showed relatively close results for the PGV amplification ratios, irrespective of the differences in the methods and data used.

A further study using more comprehensive strong motion data sets, for example, from K-NET, may improve the accuracy of the proposed relations between the site amplification and land classification.

References

[1] Whitman RV, Anagnos T, Kircher C, Lagorio HJ, Lawson RS, Schneider P. Development of national earthquake loss estimation methodology. Earthquake Spectra, 1997; 13 (4): 643-661

[2] Eguchi R, Goltz JD, Seligson HA, Flores PJ, Blais NC, Heaton TH, Bortugno E. Real-time loss estimation as an emergency response decision support system: the early post-earthquake damage assessment tool (EPEDAT). Earthquake Spectra, 1997; 13 (4): 815-832.

[3] Yamazaki F, Noda S, Meguro K. Developments of early earthquake damage assessment systems in Japan, Structural Safety and Reliability (Proceedings of ICOSSAR'97), 1998: 1573-1580.

[4] Molas GL, Yamazaki F. Attenuation of earthquake ground motion in Japan including deep focus events. BSSA 1995; 85 (5): 1343-1358.

[5] Molas GL, Yamazaki F. Attenuation of response spectra in Japan using new JMA records. Bulletin of Earthquake Resistant Structure Research Center, Institute of Industrial Science, University of Tokyo 1996; 29: 115-128.

[6] Shabestari TK, Yamazaki F. Attenuation relationship of JMA seismic intensity using JMA records. Proceedings of the 10th Japan Earthquake Engineering Symposium. Kobe, 1998: 529-534.

[7] Matsuoka M, Midorikawa S. GIS-based integrated seismic hazard mapping for a large metropolitan area. Proceedings of the 5th International Conference on Seismic Zonation, 1995; (II): 1334-1341.

[8] Fukuwa N, Arakawa M, Nishizaka R. Estimation of site amplification factor using Digital National Land Information, Journal of Structural Engineering 1998; 44(B): 77-84 (in Japanese).

[9] Shabestari KT, Yamazaki F.: A Proposal of new seismic intensity scale compatible with MMI evaluated from seismic records. 11th European Conference on Earthquake Engineering. CD-ROM, 1998.

[10] Joyner WB, Boore DM. Peak horizontal acceleration and velocity from strong-motion records including records from the 1979 Imperial Valley, California, Earthquake. BSSA 1981; 71: 2011-2038.

[11] Japan Road Association. Specifications for Highway Bridges Part V Earthquake Resistant Design. 1980.

[12] Kinoshita S. Kyoshin Net (K-NET). Seismological Research Letters 1998; 69(4): 309-332.

CPT- AND SPT-BASED PROBABILISTIC ASSESSMENT OF LIQUEFACTION POTENTIAL

Selcuk Toprak, Thomas L. Holzer, Michael J. Bennett, and John C. Tinsley, III
U.S. Geological Survey
345 Middlefield Road, MS 977
Menlo Park, CA 94025

ABSTRACT

Following the 1989 Loma Prieta, California, earthquake (M_w = 6.9), the USGS conducted extensive standard penetration tests (SPT) and cone penetration tests (CPT) at 25 natural soil sites in the Monterey and San Francisco Bay regions. Sites with and without evidence of liquefaction were investigated. The data were collected by a single operator using the same equipment which reduces the data uncertainty. In addition, the liquefied layers are well constrained by correlation with sand boils. CPT- and SPT-based probabilistic liquefaction boundary curves were developed using logistic regression analyses. CPT-based probabilistic curves based on these data indicate that the Robertson and Wride (1997) boundary curve corresponds to a 50% probability of liquefaction. The SPT-based probabilistic curves indicate the Youd and Idriss (1997) boundary curve approximately corresponds to a 20% probability for $(N_1)_{60cs}$ less than 10 and 50% for $(N_1)_{60cs}$ greater than 10 blows per foot. Combination of these data with the Noble and Youd (1998) SPT database indicates that the Youd and Idriss (1997) boundary curve corresponds to probabilities of approximately 20, 30, and 40% for $(N_1)_{60cs}$ less than 10, between 10 and 15, and greater than 15 blows per foot, respectively.

INTRODUCTION

Geotechnical field observations of earthquake-induced liquefaction form the primary basis for evaluating liquefaction potential of sandy soils. The most commonly used evaluation method is the "simplified procedure" that was developed by H. Bolton Seed and his colleagues (e.g. Seed and others, 1983). The procedure, which was originally based on standard penetration testing (SPT), has been extended to include cone penetration testing (CPT) (e.g. Robertson and Campanella, 1985). Two challenges to developing and refining the procedure are variability in SPT field techniques and identification of the actual layers that liquefied. The latter aspect is critical to selection of the appropriate penetration resistance for the simplified procedure. Addressing these challenges has become even more important as investigators have attempted to formulate the "simplified procedure" in a probabilistic framework. The variation between SPT techniques is typically accounted for by corrections to a standard method. Identification of the liquefied layer is usually based on the minimum SPT blow count in sand layers in the boring.

In this manuscript, we analyze SPT and CPT data with attributes that reduce uncertainty imposed by both of these problems. Our goal is to present the first CPT-based probabilistic liquefaction potential boundary curves as well as to improve existing SPT-based probabilistic liquefaction potential boundary curves. Logistic regression analyses were used to develop the probabilistic boundary curves. The primary data that we used are the penetration tests that were collected by the U.S. Geological Survey (USGS) following the 1989 Loma Prieta, California, earthquake at primarily alluvial-soil sites with and without liquefaction (Bennett and Tinsley, 1995). The data were collected by a single operator (M.J. Bennett) using constant equipment and procedures. In addition, the liquefied layer could be inferred in many cases from textural analyses of nearby sand boils. Thus, the two major problems in assembling a database, variability in the correction to a standard technique and identification of the liquefied layer, were minimized. Another advantage to these data is that they were collected for a single earthquake and do not require a correction for earthquake magnitude in order to be combined into a coherent data set. The CPT data are particularly useful because the liquefied layer was determined directly by sampling in adjacent SPT borings and there is less ambiguity about which CPT value is appropriate to use.

THE 1989 LOMA PRIETA EARTHQUAKE

The Loma Prieta, California, earthquake occurred on October 17, 1989, at 5:04 p.m. PDT approximately 90 km southeast of San Francisco. The earthquake had a surface-wave magnitude (M_S) of 7.1, a moment magnitude (M_W) of 6.9, and a local magnitude (M_L) of about 6.7 (Spudich, 1996). The fault ruptured bilaterally which limited the source duration to 6 to 15 s. Loma Prieta was the largest earthquake to shake the San Francisco and Monterey Bay areas since the 1906 San Francisco (M_W = 7.8) earthquake.

Liquefaction occurred at approximately 133 sites during the 1989 earthquake (Holzer, 1998). Liquefaction was most extensive in the Monterey Bay area, primarily in alluvial sands beneath the floodplains of the Pajaro and Salinas Rivers (Fig. 1). Damage associated with liquefaction was caused by lateral spreading, dynamic compaction, ground oscillation, and bearing capacity failures. Damage was also widespread in areas underlain by loose, sandy fills along the margins of San Francisco Bay at distances more than 84 km away from the northwest end of the seismic source zone. Total property damage from liquefaction was $99.2 million, about 1.5 per cent of the total earthquake loss (Holzer, 1994).

Loma Prieta generated strong-ground motion at many sites that also had liquefied in 1906 in the San Francisco and Monterey Bay regions. At some of these sites, the 1989 ground motion was sufficient to reliquefy sandy soils, whereas at many sites, 1989 ground motion was insufficient to reliquefy sandy soil. Because many of the fills in San Francisco Bay that liquefied in 1989 had been placed after 1906, they had never been subjected to strong ground motion.

SITE INVESTIGATIONS FOLLOWING THE 1989 LOMA PRIETA EARTHQUAKE

Following the 1989 Loma Prieta earthquake, 25 sites underlain by natural soils were selected for investigation by the USGS with SPT and CPT. Sites with and without evidence of liquefaction were investigated. The decision about what sites to explore was based primarily on air photos taken just after the earthquake and knowledge of liquefaction at particular sites in 1906 (Youd and Hoose, 1978). Surface manifestations of liquefaction such as sand boils, lateral spreading, and ground fissures can be detected on the air photos. Furthermore, prior liquefaction occurrence at a site indicates the existence of liquefiable materials.

Names of the 20 sites used in this study and surface liquefaction features observed at these sites are listed in Table 1. A site was included in this study only if both CPT and SPT tests were available next to each other. Two sites were excluded because data were incomplete; one site was excluded because of the thinness of the sand layer; and two sites were excluded because of high silt content as discussed later in this paper. Abbreviations for the sites, which are used throughout this paper are also given in Table 1. At many of the sites investigated, both sand boils and lateral spreads were observed. During the investigation of sites with evidence of liquefaction, SPT and CPT tests were also performed outside the liquefied zone as much as possible.

The general locations of the sites are shown in Figure 1 and marked as Monterey Bay, Marina District, and Coyote Creek. Detailed location maps for the Monterey Bay and Marina District sites can be found in Bennett and Tinsley (1995) and Bennett (1990), respectively. Descriptions of post-earthquake field observations for all sites are available in Tinsley and others (1998).

Field Testing Procedures

Cone penetration tests were performed using a Hogentogler® cone and conformed to American Society for Testing and Materials (ASTM) standard D3441-79. After soil stratification was determined at each site by using CPT data, SPT's were made in hollow-stem auger borings 1 to 1.5 m away from selected CPT sounding locations. Cone penetration test results were used to determine the depths at which SPT blow counts were measured. The SPT procedures follow the guidelines outlined in ASTM standard D1586-67 with a liner in the sampler. Samples from the SPT's were used to determine fines content and grain-size distribution of soil. The overall efficiency of the hammer-hoist system used is 68%. Field data are described in Bennett and Tinsley (1995).

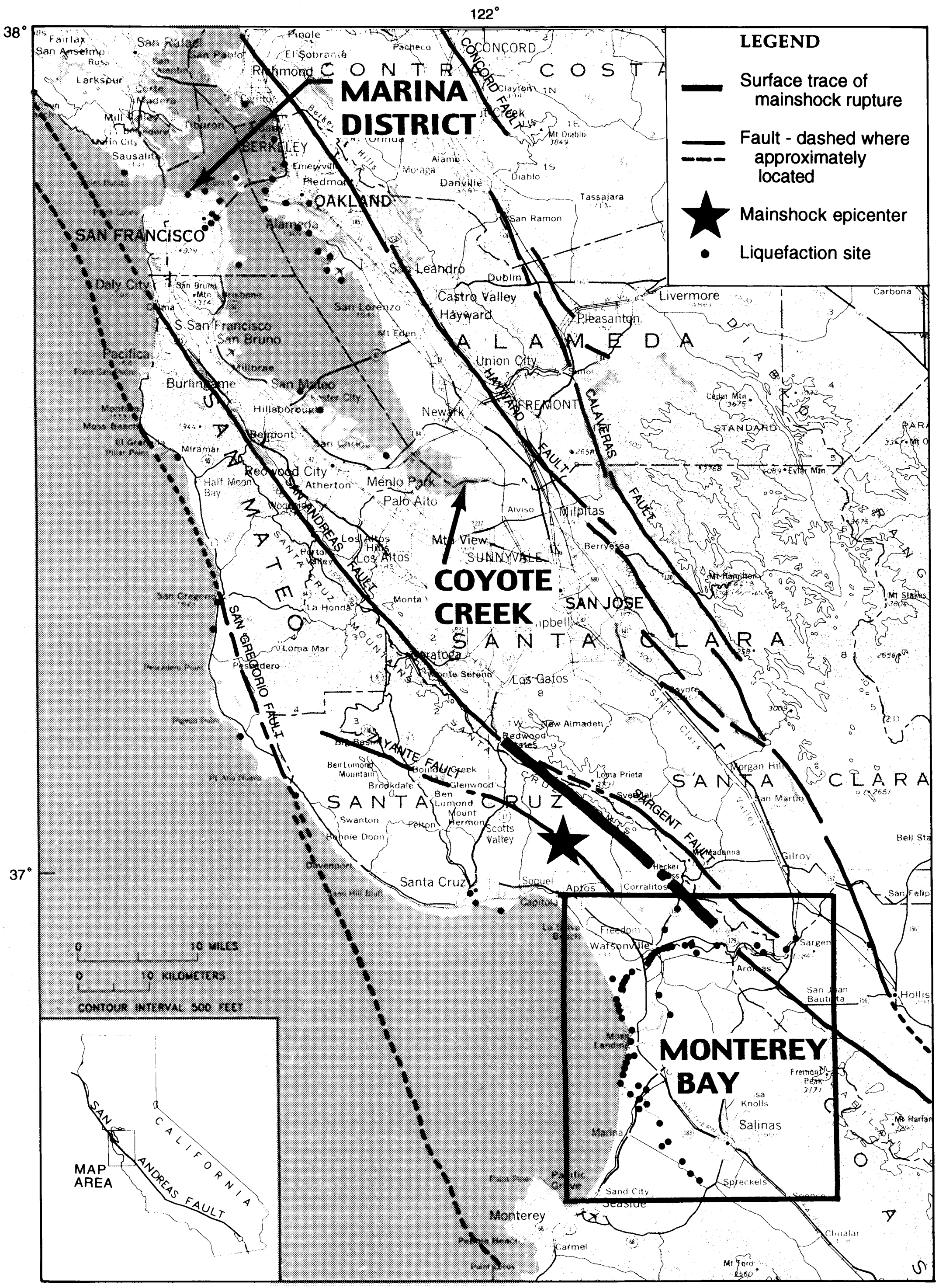

Figure 1. Map of liquefaction in the San Francisco-Monterey Bay region caused by the 1989 Loma Prieta earthquake (From Holzer, 1998)

Table 1. List of the sites investigated after the 1989 Loma Prieta earthquake

Site Name	Abbreviation	Liquefaction Features
Airport	AIR	Sand Boils, Lateral Spread
Clint Miller Farm	CMF	Sand Boils, Lateral Spread
Coyote Creek	CCK	No Evidence of Liquefaction
Farris Farm	FAR	Sand Boils, Lateral Spread
Granite Construction Company	GRA	Sand Boils, Lateral Spread
Jefferson Farm	JEF	Sand Boils, Lateral Spread
Kett	KET	Lateral Spread
Leonardini	LEN	Sand Boils, Lateral Spread
Marina District, SF-Natural Deposits	M	No Evidence of Liquefaction
Marinovich	MRR	Sand Boils, Lateral Spread
Martella	MAR	No Evidence of Liquefaction
McGowan	MCG	No Evidence of Liquefaction
Moss Landing	ML	Sand Boils, Lateral Spread
Pajaro Dunes	PD	Sand Boils, Lateral Spread
Radovich	RAD	Sand Boils, Lateral Spread
Salinas River Bridge	SRB	No Evidence of Liquefaction
Sea Mist	SEA	Sand Boils, Lateral Spread
Silliman	SIL	Sand Boils, Lateral Spread
South Pacific Bridge	SPR	Sand Boils, Lateral Spread
Tanimura	TAN	Lateral Spread

Identification of Liquefied Layer

Following the Loma Prieta earthquake, soil samples from the sand boils at liquefied sites were tested to determine grain-size distributions. The results in terms of sand, silt (< 75 μm), and clay (< 5 μm) fractions and median grain size - d_{50}- are presented in Bennett and Tinsley (1995). These data were compared to data from nearby SPT subsurface samples to determine the liquefied layers. Color of ejecta in sand boils also aided the identification of the liquefied layers. If more than one SPT was conducted in the inferred liquefied layer, the minimum clean sand equivalent SPT blow count, $(N_1)_{60cs}$ within the layer was used in the analyses. SPT blow counts above the ground water table were not used. The correction of SPT blow counts to clean sand equivalent blow counts were made according to Youd and Idriss (1997). In most cases, the minimum $(N_1)_{60cs}$ of the liquefied layer corresponded to the minimum $(N_1)_{60cs}$ in the entire boring. For the few sites where sand boil information was not available, the minimum $(N_1)_{60cs}$ in the entire boring was used to infer the liquefied layer. Sedimentary layers with 15% or more clay were assumed to be nonliquefiable.

The fines content correction described in Youd and Idriss (1997) is constant for soils with fines content greater than 35%. Penetration tests in soils with fines content greater than 50% (silt and sandy silts) in general indicated that soils should have liquefied in 1989 regardless of whether or not liquefaction was observed. To avoid uncertainties associated with the fines content correction, these data were not included in the analyses.

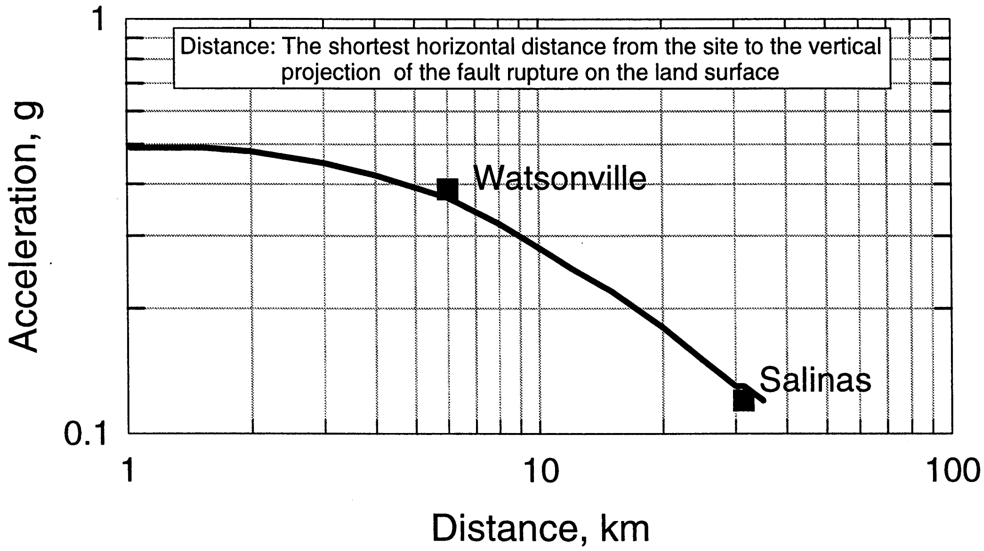

Figure 2. Local attenuation relation for the Loma Prieta earthquake in the Monterey Bay region

Ground-motion Estimation

Peak horizontal acceleration at liquefaction sites in the Monterey Bay area during the Loma Prieta earthquake was estimated by a two-step process. First, strong-motion recordings of the main shock at Watsonville and Salinas in the Pajaro and Salinas River Valleys, respectively, were used to define a local attenuation relation for Loma Prieta earthquake (Fig. 2). Both sites are classified as NEHRP type C sites, which is similar to the liquefaction sites. Our local attenuation curve was computed by minimizing the residuals for Watsonville and Salinas recordings using the functional form proposed by Boore and others (1993). Mean ground motions calculated from Boore and others for $M_w = 6.9$ are significantly higher than the values determined from Figure 2. Although the acceleration at Watsonville was recorded on the ground floor of a four-story building, the recorded acceleration is thought to represent free-field conditions (Holzer and others, 1994). The earthquake was also recorded at strong-motion stations on bedrock in Monterey and on alluvium in Greenfield, approximately 50 km southeast of Salinas. We ignored the Greenfield recording because the Watsonville and Salinas sites approximately bracket our study sites. Monterey was not used because it was a rock site.

The second step in the ground-motion estimation process was to adjust for soil amplification. Site effects were evaluated by deploying portable field instruments to record aftershocks at selected liquefaction sites. The most significant recordings were collected on January 11, 1994, from an M_L 4.2 earthquake that was located 7 km north of Watsonville. Six sites with good regional coverage recorded this aftershock. Recordings were collected along the axes and at the mouths of the Salinas and Pajaro River Valleys and at the Salinas and Watsonville strong motion stations. On the basis of these recordings, we concluded that horizontal peak accelerations near the mouth of the Salinas and Pajaro River Valleys were amplified by a factor of 1.5 relative to those predicted by the attenuation relation shown in Figure 2. The amplification effect appeared to be regional.

Although the liquefaction sites and the Watsonville and Salinas strong motion station sites were both NEHRP soil type C, we were concerned about local variations in site response. The Watsonville and Salinas strong motion recording sites were on older flood-plain deposits and most of the liquefaction occurred in younger flood-plain deposits (see Dupré and Tinsley, 1980). Accordingly, closely spaced portable seismographs were deployed on both units to search for localized variations in site response during aftershocks. Significant differences in ground motion were not detected.

Ground motions at the Marina District and Coyote Creek were inferred from nearby recordings during the 1989 main shock. A recording at Treasure Island was used as the surrogate for the Marina District. Both Treasure Island and the Marina District are underlain by substantial thicknesses of Bay mud and are at comparable distances from the main shock. Coyote Creek was surrounded by several strong motion recordings of the main shock. The horizontal peak accelerations from these recordings were similar. The average value was used in this paper.

LIQUEFACTION ANALYSES

Background

The "simplified procedure" introduced by Seed and Idriss (1971) is used commonly to assess the liquefaction potential of sands. This procedure has been revised and augmented over the past years (e.g. Seed and others, 1983; Youd and Idriss, 1997). The simplified procedure requires calculation or estimation of two variables, namely cyclic stress ratio (CSR) and cyclic resistance ratio (CRR). CSR corresponds to the seismic demand placed on a soil layer whereas CRR corresponds to the capacity of the soil to resist liquefaction. CSR can be calculated by using the following equation (Seed and Idriss, 1971):

$$CSR = (\tau_{av}/\sigma'_{vo}) = 0.65\,(a_{max}/g)(\sigma_{vo}/\sigma'_{vo})r_d \qquad (1)$$

Where a_{max} is the peak horizontal acceleration at ground surface generated by the earthquake, g is the acceleration of gravity, σ_{vo} and σ'_{vo} are total and effective vertical overburden stresses, respectively, and r_d is a stress reduction coefficient.

CSR is determined by using empirical relationships developed from past earthquake data (e.g. Seed and others, 1983; Youd and Idriss, 1997). The empirical relationships, which were originally based on SPT, have been extended to include CPT (e.g. Robertson and Campanella, 1985; Seed and DeAlba, 1986; Robertson and Wride, 1997). A recent summary and update of the simplified procedure are described in Youd and Idriss (1997).

Although the simplified procedure boundary curves estimate the occurrence and nonoccurrence of liquefaction reasonably well, they do not assess probabilistic liquefaction potential for a particular site. Risk analyses or hazard assessment studies require probabilistic liquefaction

Table 2. SPT database from the 1989 Loma Prieta Earthquake ($M_w = 6.9$)[1]

Borehole Location	L	D m	D_{GW} m	σ kPa	σ' kPa	r_d	d_{50} mm	FC %	N	N_1	$(N_1)_{60}$	$(N_1)_{60cs}$	A_{max} g	CSR
AIR-18	1	4.3	2.4	82.4	63.7	0.97	0.21	21	5	6.3	7	11.4	0.26	0.21
AIR-21	1	4.6	2.4	88.2	66.7	0.96	0.47	7	3	3.7	4.1	4.3	0.26	0.21
CMF-3	1	5.8	5.7	109.1	108.1	0.96	0.09	41	6	5.8	6.4	12.7	0.36	0.23
CMF-8	1	6	4.9	113.7	102.9	0.95	0.14	17	9	8.9	11.1	14.7	0.36	0.25
FAR-58	1	7.6	4.8	145.1	117.7	0.94	0.25	5	17	15.8	19.5	19.6	0.36	0.28
FAR-59	1	5.2	4.8	98.1	94.2	0.96	0.14	16	9	9.4	10.3	13.7	0.36	0.24
FAR-61	1	6.5	4.2	124.0	101.5	0.95	0.11	21	9	9.0	11.1	15.9	0.36	0.28
GRA-123	1	7.5	5	143.0	118.5	0.94	0.19	18	8	7.4	9.2	13	0.34	0.25
JEF-121	1	5.8	3.4	111.0	87.4	0.96	0.35	7	3	3.2	3.6	3.7	0.21	0.16
JEF-141	1	3.7	2.1	70.8	55.1	0.97	0.13	26	5	6.8	6.6	11.8	0.21	0.17
JEF-148	1	7.3	3	140.7	98.5	0.94	0.41	5	8	8.1	10	10.1	0.21	0.18
JEF-149	1	5.8	3	111.3	83.8	0.96	0.37	2	5	5.5	6.1	6.1	0.21	0.17
JEF-32	1	2.4	1.8	45.6	39.7	0.98	0.28	4	9	14.4	14.1	14.1	0.21	0.15
KET-74	1	2.7	1.5	51.7	40.0	0.98	0.67	15	14	22.3	21.8	25.3	0.47	0.39
LEN-39	1	4.3	1.9	82.8	59.2	0.97	0.21	11	7	9.2	10.1	11.6	0.22	0.19
LEN-51	1	3.4	1.8	65.2	49.6	0.97	0.09	36	2	2.9	2.8	8.4	0.22	0.18
LEN-53	1	3.4	2.1	65.0	52.2	0.97	0.18	10	6	8.3	8.2	8.9	0.22	0.17
ML-15	1	1.5	1.5	28.2	28.2	0.99	0.08	46	5	9.5	9.3	16.1	0.28	0.18
MRR-65	1	7.6	5.6	144.5	124.9	0.94	0.16	12	13	11.7	14.5	16.5	0.40	0.28
PD-44	1	5.8	3.4	111.0	87.4	0.96	0.24	3	11	11.9	13.1	13.1	0.22	0.17
RAD-99	1	6.4	4.1	122.2	99.6	0.95	0.16	18	8	8.1	10	13.9	0.38	0.29
SEA-31	1	3.4	0.8	66.0	40.5	0.97	0.10	29	5	7.9	7.7	13.5	0.22	0.22
SIL-68	1	6.2	3.5	118.7	92.2	0.95	0.18	15	7	7.4	9.1	12	0.38	0.30
SIL-71	1	6.1	4.9	115.6	103.9	0.95	0.20	9	11	10.9	13.5	14.2	0.38	0.26
SPR-45	1	4.8	4.4	90.6	86.6	0.96	0.17	6	11	11.9	13.2	13.3	0.33	0.22
SPR-48	1	6.4	5.3	121.2	110.4	0.95	0.17	13	7	6.7	8.3	10.5	0.33	0.22
TAN-103	1	5	4.6	94.3	90.4	0.96	0.14	22	7	7.4	8.2	12.9	0.13	0.08
CCK-1	0	9.8	5.5	187.7	145.5	0.91	0.18	7	12	10.0	12.4	12.6	0.17	0.13
CCK-16	0	7.6	2.7	146.8	98.7	0.94	0.12	28	17	17.2	21.3	28.8	0.17	0.16
CCK-17	0	4	3.5	75.6	70.7	0.97	0.10	40	3	3.6	3.5	9.2	0.17	0.12
CCK-23	0	8.2	2.4	158.8	101.9	0.94	0.30	7	8	8.0	9.9	10.1	0.17	0.16
CMF-10	0	7.6	3	146.6	101.4	0.94	0.15	20	12	12.0	14.8	19.6	0.36	0.32
CMF-12	0	8.5	4.6	162.9	124.7	0.93	0.09	47	11	9.9	12.3	19.7	0.36	0.28
LEN-37	0	3.4	2.5	64.6	55.8	0.97	0.11	13	9	12.2	11.9	14.2	0.22	0.16
LEN-52a	0	3.4	2.7	64.5	57.6	0.97	0.16	12	10	13.3	13	14.9	0.22	0.15
M-2	0	7	2.7	132.1	90.4	0.95	0.30	4	9	9.5	11.8	11.8	0.16	0.14
M-6	0	5.8	5.5	102.7	99.7	0.96	0.27	6	28	28.3	31.3	31.3	0.16	0.10
MAR-110	0	3.7	1.8	69.1	51.5	0.97	0.16	13	4	5.6	5.5	7.6	0.13	0.11
MAR-111	0	4.9	1.7	94.7	63.3	0.96	0.21	15	4	5.1	5.6	8.4	0.13	0.12
MCG-136	0	2.7	2.4	51.0	48.1	0.98	0.15	11	6	8.7	8.5	9.9	0.26	0.17
MCG-138	0	3.7	1.8	71.1	52.4	0.97	0.12	29	3	4.2	4.1	9.3	0.26	0.22
ML-14	0	3.7	1.5	71.6	49.9	0.97	0.48	3	22	31.2	30.6	30.6	0.28	0.25
MRR-67	0	6.4	6.2	120.5	118.5	0.95	0.21	15	25	23.0	28.6	32.5	0.40	0.25
PD-43	0	3.7	2.6	70.4	59.7	0.97	0.15	19	19	24.7	24.2	29.4	0.22	0.16
PD-79	0	4.9	1.5	94.8	61.5	0.96	0.39	3	22	28.2	31.3	31.3	0.22	0.21
RAD-98	0	5.5	3.5	105.0	85.4	0.96	0.27	7	14	15.3	16.9	17.2	0.38	0.29
SEA-29	0	7.8	2	151.3	94.4	0.94	0.26	8	32	33.3	41	41.9	0.22	0.21
SRB-116	0	6.4	6.4	120.3	120.3	0.95	0.24	7	7	6.4	8	8.1	0.11	0.07
SRB-117	0	6.4	6.4	120.3	120.3	0.95	0.23	13	7	6.4	8	10.1	0.11	0.07
TAN-105	0	4.9	4.2	92.7	85.8	0.96	0.08	41	6	6.5	7.2	13.7	0.13	0.09

[1] The notations in the column headings are described in Appendix 1.

potential relationships. To meet this need, Liao (1986) and Liao and others (1988) applied logistic regression (logit) analyses to estimate liquefaction probabilities. Logistic regression modeling is appropriate when the outcome variable is binary or dichotomous, such as liquefaction occurrence (yes or no). Applications of this technique to different fields can be found in Hosmer and Lemeshow (1989). Recently, Noble and Youd (1998) and Liao and Lum (1998) presented new probabilistic liquefaction equations for SPT using logistic regression analyses. Probabilistic liquefaction potential relationships have not been developed for CPT.

Details of how to use logistic regression models in evaluating liquefaction probability can be found in Liao (1986) and Liao and others (1988). Several statistics can be used to evaluate the adequacy of such a binary regression model. One such statistic is the modified likelihood ratio index $\bar{\rho}^2$. The statistic $\bar{\rho}^2$ varies theoretically between 0 and 1, with values higher than about 0.4 indicating good fit to the data (Liao and others, 1988).

SPT Correlations

The SPT database that was used in our liquefaction analyses is summarized in Table 2. The data are from the sites listed in Table 1. Figure 3 shows the CSR data in Table 2 plotted with respect to $(N_1)_{60cs}$. The clean sand liquefaction boundary curve shown in the figure was adjusted for earthquake magnitude with the magnitude scaling factors (MSF) developed by I.M. Idriss (Youd and Idriss, 1997). The Youd and Idriss (1997) SPT-based boundary curve distinguishes reasonably well between liquefaction and nonliquefaction sites documented after the Loma Prieta earthquake.

Probabilistic SPT Correlations

Figure 4a shows 50% and 20% liquefaction probability curves superimposed on Figure 3. The regression equation for the curves which was derived from the data in Table 2 is:

$$Q_L = \text{logit}(P_L) = \ln[P_L/(1 - P_L)] = 10.0424 - 0.2215\,(N_1)_{60cs} + 3.9740\,\ln(\text{CSR}) \qquad (2)$$

This equation is similar in form to Liao and others (1988). The term P_L is defined as the probability that liquefaction will occur, 1- P_L is the probability that liquefaction will not occur. The modified likelihood ratio index $\bar{\rho}^2$ for the equation is 0.52.

The probabilistic boundary curves based exclusively on the Loma Prieta database indicates that the simplified base curve is characterized by a probability of liquefaction of approximately 20% for $(N_1)_{60cs}$ below 10 blows per foot. For $(N_1)_{60cs}$ above 10, the simplified base curve is characterized by a probability of approximately 50%.

To expand the SPT database, data from the 1989 Loma Prieta earthquake were supplemented with data collected by the USGS following four other earthquakes. To minimize the effect of MSF, only data from earthquakes with moment magnitudes about 6.9 were included. The supplemental data were collected with the same operator and equipment and followed the same procedures as was used in the postearthquake investigation of the Loma Prieta earthquake. The

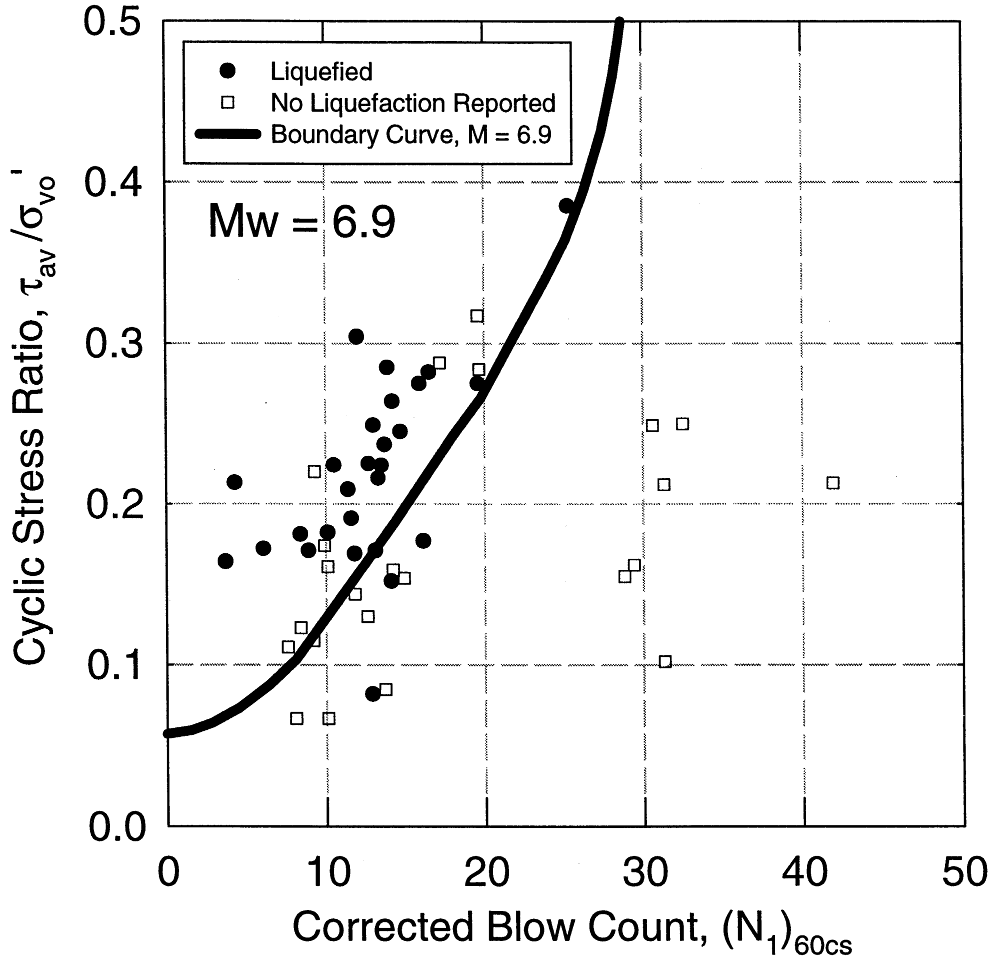

Figure 3. SPT data from the 1989 Loma Prieta earthquake

SPT data for the 1971 San Fernando, 1979 Imperial Valley, 1987 Superstition Hills, and 1994 Northridge earthquakes are listed in Table 3.

The 50% and 20% liquefaction probability curves for the combined database are shown in Figure 4b. This combined database has 79 data points as opposed to 50 data points for the 1989 Loma Prieta earthquake database. In addition to a 60% increase in the number of data points, the new database also includes several data points with CSR between 0.30 and 0.55, which improves the range of CSR in the database. The regression equation for the probabilistic curves is:

$$\text{Logit}(P_L) = \ln[P_L/(1-P_L)] = 12.8759 - 0.2820\,(N_1)_{60cs} + 5.3265\,\ln(\text{CSR}) \qquad (3)$$

The modified likelihood ratio index $\bar{\rho}^2$ for the equation is 0.50 which is similar to the value of the index for equation 2.

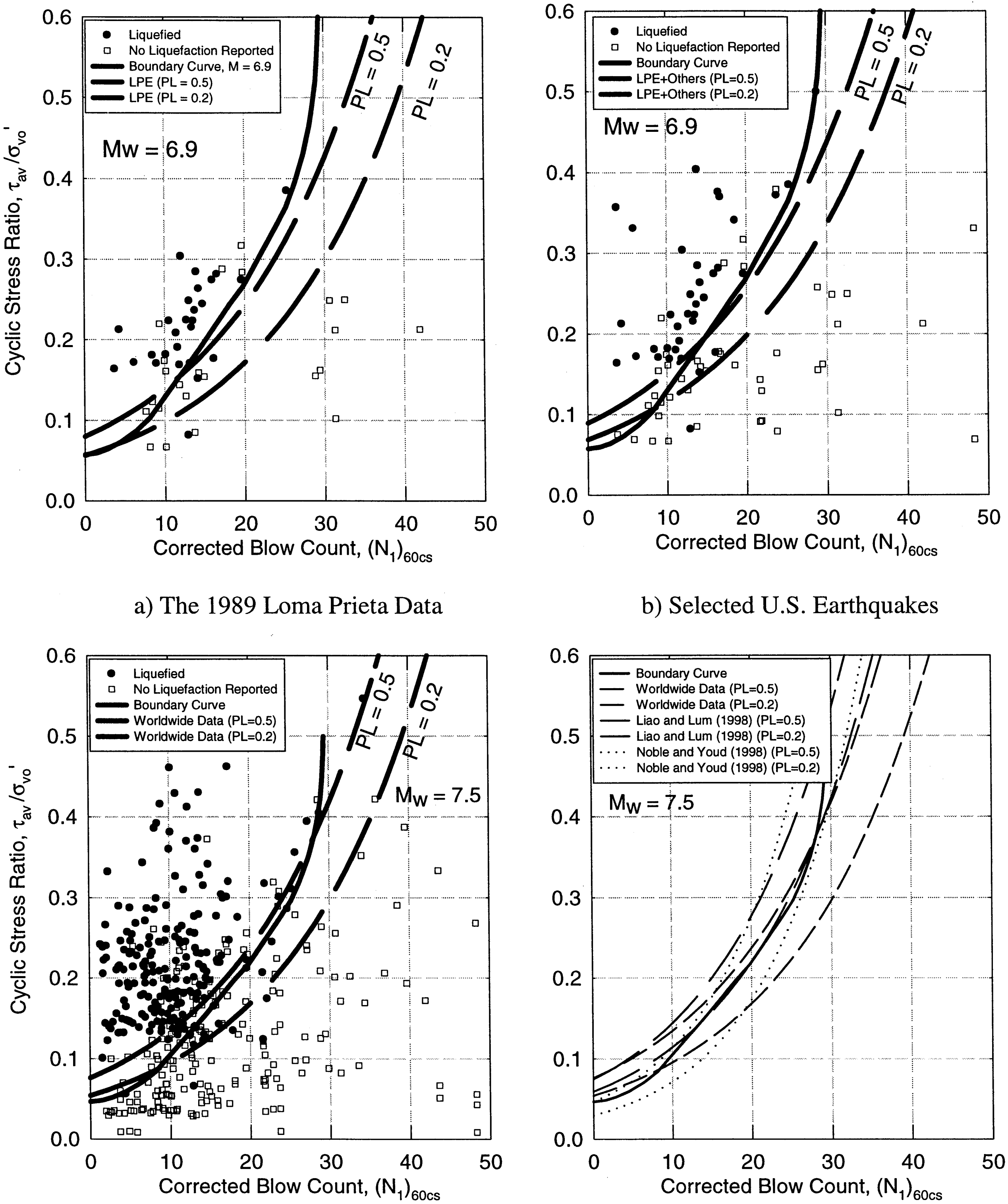

a) The 1989 Loma Prieta Data

b) Selected U.S. Earthquakes

c) Worldwide Database

d) Comparison of Probabilistic Curves

Figure 4. SPT probabilistic curves

Table 3. SPT database from other earthquakes (M_w = 6.5-6.7)

Sounding Location	L	D m	D_{GW} m	σ kPa	σ' kPa	r_d	d_{50} mm	FC %	N	N_1	$(N_1)_{60}$	$(N_1)_{60cs}$	A_{max} g	CSR
The 1994 Northridge (M_w = 6.7)														
Balboa-13	1	9.5	8.2	167.7	155.9	0.92	0.82	13	26	21.1	26.0	28.8	0.84	0.54
Wynne-1	1	6.4	4.7	116.1	99.4	0.95	0.1	43	9	9.09	11.3	18.5	0.51	0.37
Wynne-5a	1	7.6	4.3	140.6	108.2	0.94	0.18	39	8	7.76	9.6	16.5	0.51	0.41
Wynne-7a	1	6.4	3.8	118.0	92.5	0.95	0.1	43	12	12.6	15.5	23.7	0.51	0.40
Wynne-7b	1	6.3	3.8	116.0	91.5	0.95	0.37	30	8	8.4	10.4	16.7	0.51	0.40
The 1987 Superstition Hills (M_w = 6.6)														
Wildlife-2Ng1	1	3.4	1.2	63.4	41.8	0.97	0.1	17	5	7.8	7.6	11.1	0.21	0.20
Heber Road-1	0	2.7	1.8	49.5	40.7	0.98	0.11	13	29	45.8	44.7	48.3	0.1	0.08
Heber Road-4	0	2.7	1.8	49.5	40.7	0.98	0.11	23	1	1.6	1.5	5.8	0.1	0.08
Heber Road-6	0	3.3	1.8	60.9	46.2	0.97	0.12	14	1	1.5	1.4	3.7	0.1	0.08
Heber Road-7	0	4	1.8	74.2	52.6	0.97	0.09	24	13	18.1	17.6	23.7	0.1	0.09
McKim Ranch-TM6-7	0	3.8	1.5	70.7	48.1	0.97	0.11	18	7	10.2	9.9	13.8	0.2	0.19
Radio Tower-R4	0	2.3	2	41.7	38.8	0.98	0.1	18	11	17.8	17.4	21.8	0.15	0.10
River Park-15	0	3.4	1.5	63.1	44.5	0.97	0.16	3	7	10.6	10.3	10.3	0.15	0.14
Vail_V2	0	4	2.7	73.3	60.6	0.97	0.11	13	15	19.4	19.0	21.6	0.21	0.16
Vail-TV2	0	4.9	2.7	90.4	68.8	0.96	0.11	13	5	6.1	6.7	8.9	0.21	0.17
The 1979 Imperial Valley (M_w = 6.5)														
Heber Road-4	1	2.7	1.8	49.5	40.7	0.98	0.11	23	1	1.6	1.5	5.8	0.5	0.39
Heber Road-6	1	3.3	1.8	60.9	46.2	0.97	0.12	14	1	1.5	1.4	3.7	0.5	0.42
McKim Ranch-TM6-7	1	3.8	1.5	70.7	48.1	0.97	0.11	18	7	10.2	9.9	13.8	0.51	0.47
River Park-15	1	3.4	1.5	63.1	44.5	0.97	0.16	3	7	10.6	10.3	10.3	0.22	0.20
Heber Road-1	0	2.7	1.8	49.5	40.7	0.98	0.11	13	29	45.8	44.7	48.3	0.5	0.39
Heber Road-7	0	4	1.8	74.2	52.6	0.97	0.09	24	13	18.1	17.6	23.7	0.5	0.44
Radio Tower-R4	0	2.3	2	41.7	38.8	0.98	0.1	18	11	17.8	17.4	21.8	0.22	0.15
Vail-TV2	0	4.9	2.7	90.4	68.8	0.96	0.11	13	5	6.1	6.7	8.9	0.14	0.12
Vail-V2	0	4	2.7	73.3	60.6	0.97	0.11	13	15	19.4	19.0	21.6	0.14	0.11
The 1971 San Fernando (M_w = 6.6)														
Balboa-13	0	9.5	8.2	167.7	155.9	0.92	0.82	13	26	21.1	26.0	28.8	0.45	0.29
Wynne-1	0	6.4	4.7	116.1	99.4	0.95	0.1	43	9	9.1	11.3	18.5	0.25	0.18
Wynne-5a	0	7.6	4.3	140.6	108.2	0.94	0.18	39	8	7.8	9.6	16.5	0.25	0.20
Wynne-7a	0	6.4	3.8	118.0	92.5	0.95	0.1	43	12	12.6	15.5	23.7	0.25	0.20
Wynne-7b	0	6.3	3.8	116.0	91.5	0.95	0.37	30	8	8.4	10.4	16.7	0.25	0.20

The Youd and Idriss (1997) boundary curve again distinguishes reasonably well between the predicted occurrence and nonoccurrence of liquefaction. The probabilistic curves are slightly higher than the ones shown in Figure 4a. The probabilistic boundary curves indicate that the Youd and Idriss (1997) boundary is characterized by a probability of approximately 20% for $(N_1)_{60cs}$ below 10 blows per foot. For $(N_1)_{60cs}$ above 10, it is characterized by a probability of approximately 50%.

To test the robustness of the USGS database, it was combined with the Noble and Youd (1998) database. To eliminate duplicate records, pre-1989 USGS data that were included in both databases were deleted from the Noble and Youd (1998) database. The total number of data points in the new worldwide liquefaction database is 440. The logistic regression equation obtained from the new worldwide database is:

$$\text{Logit}(P_L) = \ln[P_L/(1-P_L)] = 10.4459 - 0.2295\,(N_1)_{60cs} + 4.0573\,\ln(CSR/MSF) \quad (4)$$

The modified likelihood ratio index $\bar{\rho}^2$ for the equation is 0.98, which is substantially higher than the indicies for equations 2 and 3. To compute this equation, all CSR's were adjusted to M_w= 7.5 using the Idriss MSF. Therefore, Idriss MSF values should be used in the above equation to get probabilistic curves for earthquakes with different magnitudes.

Figure 4c shows 50% and 20% probability curves. Note that the curves in Figure 4c correspond to M_w = 7.5 whereas the ones in Figures 4a and 4b correspond to M_w = 6.9. The probabilistic boundary curves in Figure 4c indicate that the simplified procedure boundary curve is characterized by a probability of approximately 20, 30, and 40% for $(N_1)_{60cs}$ below 10, between 10 and 15, and above 15 blows per foot, respectively.

Figure 4d compares the probabilistic curves from this study with the ones from Liao and Lum (1998) and Noble and Youd (1998). The database used by Liao and Lum (1998) consists of 182 cases which are classified to have fines contents less than or equal to 12%. Liao and others (1988) used 12% fines content as a distinction between clean and silty sands. They developed separate probabilistic equations for clean and silty sands. The Noble and Youd (1998) database included 367 sites with 35% fines or less. The worldwide database used in this study consists of 440 cases, all with less than 50% fines. Only 3% of these data have fines contents between 35 and 50%. Both this study and Noble and Youd (1998) used the fines contents correction described in Youd and Idriss (1997). The comparison shows that Noble and Youd curves give the most conservative results for $(N_1)_{60cs}$ up to 15 blows per foot. The curves from this study are between the Liao and Lum (1998) and Noble and Youd (1998) curves. For $(N_1)_{60cs}$ above 15, however, the curves from this study provide the most conservative results.

Probabilistic CPT Correlations

Table 4 lists the USGS CPT database for the 1989 Loma Prieta earthquake. The CPT values in the table are 0.4-m average values calculated at the SPT depths shown in Table 2. This particular averaging interval was selected because it approximately corresponds to the depth interval at which SPT measurements are taken. Figure 5 shows the data plotted with respect to the CPT-based liquefaction boundary curve proposed by Robertson and Wride (1997). The boundary curve was adjusted for the 1989 Loma Prieta earthquake magnitude using the Idriss MSF.

Figure 5 also includes the 50% and 20% liquefaction probability curves. The logistic regression equation for the probabilistic liquefaction curves is:

$$\text{Logit}(P_L) = \ln[P_L/(1-P_L)] = 11.6896 - 0.0567\,(q_{c1N})_{cs} + 4.0817\,\ln(CSR) \quad (5)$$

Table 4. CPT Database from the 1989 Loma Prieta Earthquake (M_w = 6.9)

Sounding Location	L	D m	D_{GW} m	σ kPa	σ' kPa	d_{50} mm	FC %	q_c kPa	f_s kPa	q_{c1N}	$(q_{c1N})_{cs}$	A_{max} g	CSR
AIR-18	1	4.3	2.4	82.4	63.7	0.209	21	6196	24	77	84	0.26	0.21
AIR-21	1	4.6	2.4	88.2	66.7	0.467	7	6723	29	82	89	0.26	0.21
CMF-3	1	5.8	5.7	109.1	108.1	0.086	41	2398	13	23	47	0.36	0.23
CMF-8	1	6	4.9	113.7	102.9	0.143	17	8362	54	82	95	0.36	0.25
FAR-58	1	7.6	4.8	145.1	117.7	0.250	5	8658	40	79	88	0.36	0.28
FAR-59	1	5.2	4.8	98.1	94.2	0.136	16	2794	24	33	61	0.36	0.24
FAR-61	1	6.5	4.2	124.0	101.5	0.113	21	4222	35	42	67	0.36	0.28
GRA-123	1	7.5	5	143.0	118.5	0.188	18	4586	19	42	57	0.34	0.25
JEF-121	1	5.8	3.4	111.0	87.4	0.347	7	6816	30	72	82	0.21	0.16
JEF-141	1	3.7	2.1	70.8	55.1	0.133	26	1802	15	24	55	0.21	0.17
JEF-148	1	7.3	3	140.7	98.5	0.405	5	7687	29	77	84	0.21	0.18
JEF-149	1	5.8	3	111.3	83.8	0.370	2	4839	24	52	70	0.21	0.17
JEF-32	1	2.4	1.8	45.6	39.7	0.280	4	2226	9	35	51	0.21	0.15
KET-74	1	2.7	1.5	51.7	40.0	0.670	15	4923	59	82	109	0.47	0.39
LEN-39	1	4.3	1.9	82.8	59.2	0.210	11	3670	7	47	55	0.22	0.19
LEN-51	1	3.4	1.8	65.2	49.6	0.088	36	1156	5	16	39	0.22	0.18
LEN-53	1	3.4	2.1	65.0	52.2	0.182	10	3431	7	47	55	0.22	0.17
ML-15	1	1.5	1.5	28.2	28.2	0.080	46	1040	14	19	61	0.28	0.18
MRR-65	1	7.6	5.6	144.5	124.9	0.159	12	6898	53	61	81	0.40	0.28
PD-44	1	5.8	3.4	87.4	111.0	0.235	3	7992	46	85	99	0.22	0.17
RAD-99	1	6.4	4.1	122.2	99.6	0.157	18	4183	52	42	79	0.38	0.29
SEA-31	1	3.4	0.8	66.0	40.5	0.095	29	1160	6	18	42	0.22	0.22
SIL-68	1	6.2	3.5	118.7	92.2	0.175	15	4546	31	47	68	0.38	0.3
SIL-71	1	6.1	4.9	115.6	103.9	0.203	9	5486	34	53	71	0.38	0.26
SPR-45	1	4.8	4.4	90.6	86.6	0.167	6	4862	29	51	69	0.33	0.22
SPR-48	1	6.4	5.3	121.2	110.4	0.168	13	3696	30	35	63	0.33	0.22
TAN-103	1	5	4.6	94.3	90.4	0.142	22	4768	41	50	74	0.13	0.08
CCK-1	0	9.8	5.5	187.7	145.5	0.176	7	8630	131	71	107	0.17	0.13
CCK-16	0	7.6	2.7	146.8	98.7	0.12	28	4601	20	46	61	0.17	0.16
CCK-23	0	8.2	2.4	158.8	101.9	0.300	7	6865	118	68	114	0.17	0.16
CMF-10	0	7.6	3	146.6	101.4	0.152	20	7721	87	92	119	0.36	0.32
LEN-37	0	3.4	2.5	64.6	55.8	0.105	13	3004	11	40	53	0.22	0.16
LEN-52a	0	3.4	2.7	64.5	57.6	0.159	12	5595	30	81	91	0.22	0.15
M-2	0	7	2.7	132.1	90.4	0.298	4	5900	34	62	79	0.16	0.14
M-6	0	5.8	5.5	102.7	99.7	0.268	6	3860	21	38	57	0.16	0.1
MAR-110	0	3.7	1.8	69.1	51.5	0.160	13	3109	20	41	59	0.13	0.11
MAR-111	0	4.9	1.7	94.7	63.3	0.207	15	2662	12	33	51	0.13	0.12
MCG-136	0	2.7	2.4	51.0	48.1	0.148	11	3178	28	58	81	0.26	0.17
MCG-138	0	3.7	1.8	71.1	52.4	0.124	29	1692	13	36	63	0.26	0.22
ML-14	0	3.7	1.5	71.6	49.9	0.479	3	14778	15	207	207	0.28	0.25
MRR-67	0	6.4	6.2	120.5	118.5	0.212	15	14326	98	139	144	0.40	0.25
PD-43	0	3.7	2.6	70.4	59.7	0.15	19	7864	35	101	106	0.22	0.16
PD-79	0	4.9	1.5	94.8	61.5	0.390	3	4966	62	63	101	0.22	0.21
RAD-98	0	5.5	3.5	105.0	85.4	0.273	7	8998	46	97	104	0.38	0.29
SEA-29	0	7.8	2	151.3	94.4	0.262	8	17470	89	180	180	0.22	0.21
SRB-116	0	6.4	6.4	120.3	120.3	0.243	7	4510	130	41	116	0.11	0.07
SRB-117	0	6.4	6.4	120.3	120.3	0.225	13	4510	98	41	100	0.11	0.07
TAN-105	0	4.9	4.2	92.7	85.8	0.076	41	4007	19	43	59	0.13	0.09

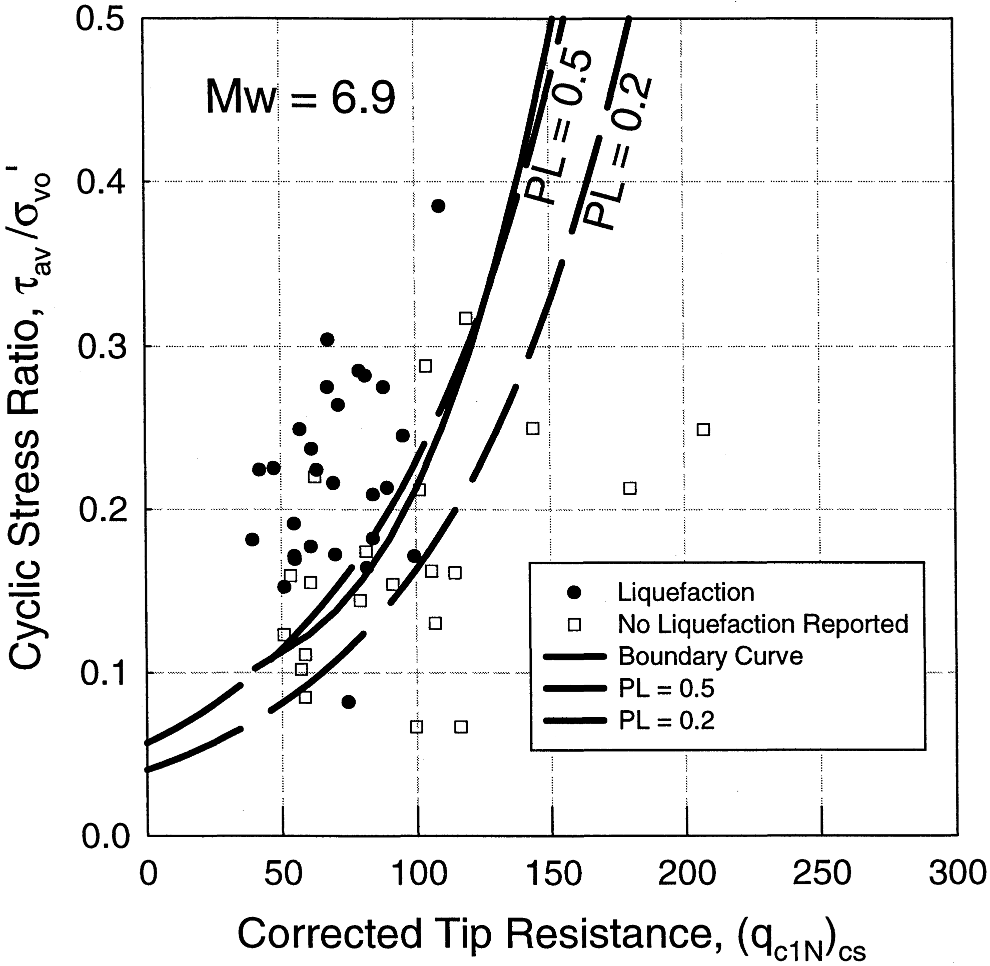

Figure 5. CPT Data from the 1989 Loma Prieta Earthquake

The modified likelihood ratio index, $\bar{\rho}^2$, for the equation is 0.64, which is comparable to the value of the index for SPT logistic equations. The form of this logistic equation is similar to the ones for SPT. For the CPT logistic regression, the clean sand equivalent CPT tip resistance, $(q_{c1N})_{cs}$ and CSR were used. Comparison of the liquefaction probability curves with the simplified base curve in Figure 5 indicates that the simplified base curve is characterized by a probability of approximately 50%.

Boulanger and others (1997) found in their evaluation of liquefaction at Moss Landing during the Loma Prieta earthquake that averaging over different depth intervals resulted in significantly different averaged CPT tip resistances. They recommended a 0.6 m depth interval. To evaluate the sensitivity of the averaging interval on our probabilistic curves, 0.2, 0.4, and 0.6 m averaging intervals were used. The effect of different averaging intervals on the probabilistic curves was not significant.

The application of the CPT-based probabilistic liquefaction curves developed herein to other locations and different earthquakes should be made cautiously until this database is supplemented with data from other earthquakes. However, the comparison of SPT-based liquefaction probability curves obtained from the 1989 Loma Prieta earthquake with the worldwide earthquake databases (see Figures 4a and 4c) suggests the USGS data alone may produce a slightly conservative set of probabilistic boundary curves.

CONCLUSIONS

Logistic regressions of SPT and CPT data from sites with and without liquefaction during the 1989 Loma Prieta earthquake provide insight into the probabilistic significance of the boundary curves of the simplified procedure for evaluating liquefaction potential.

For the SPT data, the probabilistic boundary curves based on the Loma Prieta earthquake indicate that the Youd and Idriss (1997) boundary is characterized by a probability of approximately 20% for $(N_1)_{60cs}$ below 10 blows per foot. For $(N_1)_{60cs}$ above 10, it is characterized by a probability of approximately 50%. Combination of the Loma Prieta earthquake SPT data, USGS data for other U.S. earthquakes (M_W = 6.5-6.7), and the Noble and Youd (1998) worldwide database provided additional perspective on the probabilistic significance of the boundary curves. The combined data indicate that the Youd and Idriss (1997) boundary curve corresponds to a probability of liquefaction of approximately 20, 30, and 40 % for $(N_1)_{60cs}$ less than 10, between 10 and 15, and greater than 15 blows per foot, respectively. For $(N_1)_{60cs} < 15$, the combined data yields probabilistic curves that are less conservative than Noble and Youd (1998) probabilistic curves. For $(N_1)_{60cs} > 15$, the curves are more conservative. The curves from the combined data are consistently more conservative than Liao and Lum (1998).

For the CPT data, the liquefaction probability curves indicate that the simplified boundary curve is characterized by a probability level of approximately 50%. These probability curves were developed by using only the 1989 Loma Prieta earthquake data and the application of the CPT-based probabilistic liquefaction curves developed herein to other locations and different earthquakes should be made cautiously until this database is supplemented with data from other earthquakes. However, comparison of SPT-based liquefaction probability curves obtained for the 1989 Loma Prieta earthquake and the combined worldwide earthquake databases suggests the USGS data may produce a slightly conservative set of probabilistic boundary curves.

ACKNOWLEDGMENTS

This analysis was supported by funding from a USGS CRADA with Pacific Gas and Electric Company. Data were collected with funding from the National Earthquake Hazard Reduction Program. We thank Ray Wilson and Scott Miles for their prompt reviews.

REFERENCES

Bennett, M. J., 1990, Ground deformation and liquefaction of soil in the Marina District, *in* Holzer, T. L., and O'Rourke, T. D., eds., Effects of the Loma Prieta earthquake on the

Marina District, San Francisco, California, Holzer, T.L., and O'Rourke, T.D., eds., U.S. Geological Survey Open-file Report 90-253: Menlo Park, CA, U.S. Geological Survey, p. D-1 to D-36.

Bennett, M. J., and Tinsley, J. C., III, 1995, Geotechnical data from surface and subsurface samples outside of and within liquefaction-related ground failures caused by the October 17, 1989, Loma Prieta earthquake, Santa Cruz and Monterey Counties, California: U.S. Geological Survey Open-file Report 95-663, 357 p.

Boore, D. M., Joyner, W. B., and Fumal, T. E., 1993, Estimation of response spectra and peak accelerations from western North American earthquakes: an interim report: United States Geological Survey Open-file Report 93-509, 72 p.

Boulanger, R. W., Mejia, L. H., and Idriss, I. M., 1997, Liquefaction at Moss Landing during the Loma Prieta earthquake: Journal of Geotechnical and Geoenvironmental Engineering, v. 123, no. 5, p. 453-468.

Dupré, W. R., and Tinsley, J. C., III, 1980, Maps showing geology and liquefaction potential of northern Monterey and southern Santa Cruz Counties, California: U.S. Geological Survey Miscellaneous Field Studies Map MF-1199, scale 1:62,500.

Holzer, T. L., 1994, Loma Prieta damage largely attributed to enhanced ground shaking: EOS, Transactions, American Geophysical Union, v. 75, no. 26, p. 299-301.

Holzer, T. L. (ed.), 1998, The Loma Prieta, California, earthquake of October 17, 1989 - Liquefaction, *in* Holzer, T. L., coord., Strong ground motion and ground failure, U. S. Geological Survey Professional Paper 1551-B, 314 p.

Holzer, T. L., Tinsley, J. C., III, Bennett, M. J., and Mueller, C. S., 1994, Observed and predicted ground deformation -- Miller Farm lateral spread, Watsonville, California, *in* Fifth U.S.-Japan workshop on earthquake resistant design of lifeline facilities and countermeasures against liquefaction, Snowbird, National Center for Earthquake Engineering and Research Technical Report 94-0026, p. 79-99.

Hosmer, D. W., Jr., and Lemeshow, S., 1989, Applied logistic regression: New York, John Wiley & Sons, 307 p.

Liao, S. S. C., 1986, Statistical modeling of earthquake-induced liquefaction [Ph.D. thesis]: Massachusetts Institute of Technology, 470 p.

Liao, S. S. C., and Lum, K. Y., 1998, Statistical analysis and application of the magnitude scaling factor in liquefaction analysis, *in* Geotechnical earthquake engineering and soil dynamics III, Seattle, WA, ASCE Geotechnical Special Publication 75, p. 410-421.

Liao, S. S. C., Veneziano, D., and Whitman, R. V., 1988, Regression models for evaluating liquefaction probability: Journal of Geotechnical Engineering, v. 114, no. 4, p. 389-411.

Noble, S. K., and Youd, T. L., 1998, Probabilistic evaluation of soil liquefaction resistance [Master of Science thesis]: Brigham Young University, 77 p.

Robertson, P.K., and Campanella, R.G., 1985, Liquefaction potential of sands using the CPT: Journal of Geotechnical Engineering, v. 111, no. 3, p. 384-403.

Robertson, P.K., and Wride, C.E., 1997, Cyclic liquefaction and its evaluation based on the SPT and CPT, *in* Youd, T.L., and Idriss, I.M., eds., Evaluation of liquefaction resistance of soils, Salt Lake City, UT, National Center for Earthquake Engineering and Research Technical Report 97-0022, p. 41-87

Seed, H. B., DeAlba, P.A., 1986, Use of SPT and CPT tests for evaluating the liquefaction resistance of sands, *in* Clemence, S.P., ed., ASCE Geotechnical Special Publication No. 6, p. 281-301.

Seed, H. B., Idriss, I. M., and Arango, I., 1983, Evaluation of liquefaction potential using field performance data: Journal of Geotechnical Engineering, v. 109, no. 3, p. 458-482.

Seed, H. B., and Idriss, I.M., 1971, Simplified procedure evaluating soil liquefaction potential: Journal of Soil Mechanics and Foundation Engineering, v. 97, no. 9, p. 1249-1273.

Spudich, P. A. (ed.), 1996, The Loma Prieta, California, earthquake of October 17, 1989 - Main-shock characteristics, *in* Bakun, W. H., and Prescott, W. H., coords., Earthquake occurrence, U. S. Geological Survey Professional Paper 1550-A, 297 p.

Tinsley, J. C., III, Egan, J. A., Kayen, R. E., Bennett, M. J., Kropp, A., and Holzer, T. L., 1998, Appendix: Maps and descriptions of liquefaction and associated effects, *in* Holzer, T. L., coord., The Loma Prieta, California, earthquake of October 17, 1989 - Liquefaction, U. S. Geological Survey Professional Paper 1551-B, p. B287-B314.

Youd, T. L., and Hoose, S. N., 1978, Historic ground failures in northern California triggered by earthquakes: U.S. Geological Survey Professional Paper 993, 177 p.

Youd, T. L., and Idriss, I. M. (eds.), 1997, Proceedings of the NCEER workshop on evaluation of liquefaction resistance of soils, Salt Lake City, UT, National Center for Earthquake Engineering and Research Technical Report 97-0022, 276 p.

APPENDIX I - NOTATION

The following symbols are used in this paper:

L:	Liquefaction occurrence/nonoccurence? 1 = Yes, 0 = No
D:	Depths of liquefaction
D_{GW}:	Depth to the ground water table
σ:	Total overburden pressure
σ':	Effective total overburden pressure
r_d:	Stress reduction factor
d_{50}:	Mean grain size
FC:	Fines Content
N:	Standard penetration resistance
N_1:	Standard penetration resistance corrected for overburden pressure
$(N_1)_{60}$:	Standard penetration resistance corrected for pressure and energy
$(N_1)_{60cs}$:	Standard penetration resistance corrected for pressure, energy and fines content
A_{max}:	Peak horizontal ground acceleration
CSR:	Cyclic stress ratio
q_c:	CPT tip resistance
f_s:	CPT sleeve resistance
q_{c1N}:	Normalized CPT tip resistance corrected for overburden pressure
$(q_{c1N})_{cs}$:	Normalized CPT tip resistance corrected for overburden pressure and fines content

Conditions Underlying the Lateral Displacement of Sloped Ground During the 1964 Niigata and 1983 Nihonkai-Chubu Earthquakes

Kazue WAKAMATSU[1] and Masanori HAMADA[2]

[1]Research Fellow, Institute of Industrial Science, University of Tokyo,
7-22-1 Roppongi, Minato-ku, Tokyo, 106-8558, Japan
[2]Professor, Department of Civil Engineering, Waseda University,
3-4-1 Okubo, Shinjuku-ku, Tokyo, 169-8558, Japan

Abstract

Several equations have been proposed for predicting liquefaction-induced ground displacement. However, because these equations contain parameters such as surface gradients, which are generally difficult to determine, they are often difficult to apply. Therefore, in this study, we sought to develop simple criteria for assessing the potential for occurrence of lateral ground displacement greater than 1 m. We analyzed the ground conditions of regions that suffered liquefaction during the 1964 Niigata and the 1983 Nihonkai-Chubu earthquakes using approximately 150 sets of borehole data. We obtained the following conclusions: (1) ground displacement greater than 1 m correlates strongly with the thickness of the liquefiable layer and the overburden-corrected SPT N-value of the liquefiable layer; (2) ground displacement greater than 1 m is poorly predicted by conventional methods, which are based on the SPT N-value criterion as well as on the thickness relationship between the liquefiable layer and the overlying nonliquefiable layer; and (3) there are some conditions in which severely liquefied sites were not accompanied by significant displacement.

Introduction

Hamada and Wakamatsu[1)] proposed a semi-empirical and semi-theoretical equation for predicting the liquefaction-induced displacement of sloped ground surfaces. Their methodology was based on analyses of field observations of lateral flow in past earthquakes, a similitude law between flow of model grounds and that of actual grounds when liquefied soils are considered to be quasi-plastic fluid, and flow experiments on model grounds. To predict the magnitude of lateral ground displacement using this equation, the following values are needed: the surface gradient along a 100 - 200 m course traversing the studied point, the thickness of the liquefiable layer, and the average value N_1 of the SPT N-value corrected by the effective overburden pressure of the liquefiable layer. The thickness of the liquefiable layer can be estimated by utilizing simplified procedures for evaluating safety factor for liquefaction, F_L, but due to the dense distribution of buildings and other structures in urban areas, it is difficult to measure the surface gradient precisely. Furthermore, no validation studies have been carried out to check whether lateral flow will occur in all sloped areas if an underlying soil layer liquefies.

The purpose of this study is to develop simple criteria for predicting the occurrence of lateral flow accompanied by ground displacement greater than 1 m by analyzing the ground conditions in regions that suffered liquefaction with or without lateral ground displacement during the 1964 Niigata and the 1983 Nihonkai-Chubu earthquakes. We also investigated site conditions in the areas where severe liquefaction occurred but no significant displacement did not occurred.

Thickness of Liquefiable layer at Sites of Past Liquefaction

Figure 1(a) shows the downstream region of the Shinano River in Niigata where liquefaction occurred during the 1964 Niigata earthquake. In that region, ground displacement had already been measured by photogrammetric analysis[2)], and supplementary measurements were taken in this study. The area studied in the present analysis is shown as a hatched area in Fig. 1(a). We excluded zones within 200 m of revetments of the river, as lateral flows in these areas were assumed to have occurred due to the movement of the revetment. The Tsusen River basin located northeast of the region shown in Fig. 1 was also excluded from this study because ground displacement measurements there were less precise (± 99 cm) than in the Shinano River basin (± 72 cm).

Figure 1(b) shows a part of Noshiro City where liquefaction occurred in the 1983 Nihonkai-Chubu earthquake and where the ground displacement had already been measured[2)]. The area studied in the present analysis is again shown as a hatched area.

We collected the existing borehole log data (both pre- and post-earthquake data) for 147 sites (95 sites in the Niigata region and 52 sites in the Noshiro region), and classified the borehole sites into the following five types by referring to maps of ground failures and ground displacement vector diagrams for the Niigata and the Nihonkai-Chubu earthquakes[3) - 5)]: (1) sand boils and lateral ground displacement greater than 1 m were observed; (2) no sand boils were observed, but lateral ground displacement greater than 1 m was observed; (3) sand boils were observed, but lateral ground displacement less than 1 m was observed; (4) sand boils were observed only in the surrounding area and lateral ground displacement less than 1 m was observed; and (5) no sand boils were observed even in the surrounding area, and lateral ground displacement less than 1 m was observed. For all borehole sites, we calculated the factor of safety

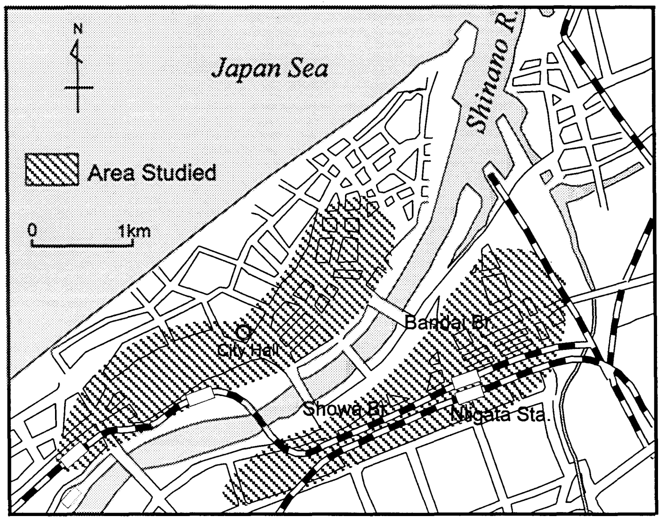

(a) Niigata (1964 Niigata earthquake)

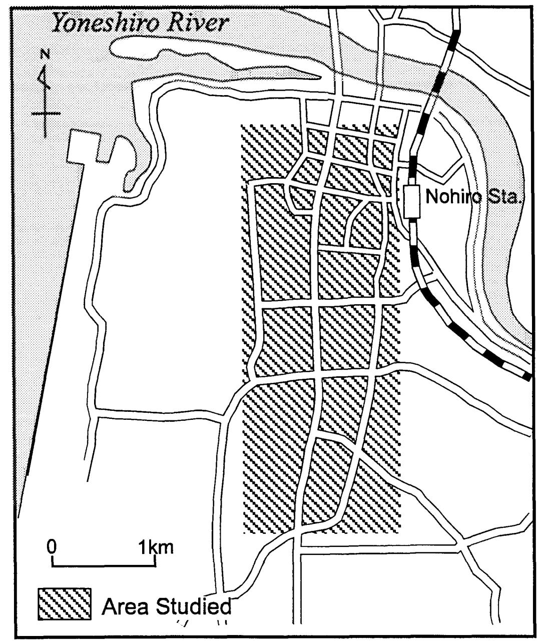

(b) Noshiro (1983 Nihonkai-Chubu earthquake)

Fig. 1 Areas studied

against liquefaction, F_L for four levels of the peak acceleration at the ground surface ranging from 0.17g to 0.3g, utilizing the simplified procedures published in the 1996 Specifications for Japanese Highway Bridges[6]. We used typical constant values of fine content, FC, and mean diameter, D_{50}, for each soil type in Niigata and Noshiro, respectively, for calculating F_L, since the values at most of the sites are unknown. The occurrence of sand boils in both regions can be best explained if we assume that saturated sandy soil layers with $F_L \leq 1$ liquefied when the peak accelerations at the ground surface were 0.2g for Niigata during the Niigata earthquake and 0.25g for Noshiro during the Nihonkai-Chubu earthquake. Therefore, in this study, the sandy soil layers with $F_L \leq 1$ against horizontal peak acceleration of 0.2g and 0.25g for Niigata and Noshiro, respectively, were considered to be the liquefiable layers.

Layer thickness combinations of the liquefiable and nonliquefiable layers in our analysis are plotted in Figs. 2 and 3, classifying them into types 1 - 5 at each borehole site in Niigata and Noshiro. In Niigata (Fig.2), the estimated thickness of the liquefiable layer was large (approx. 10 m) and the thickness of the overlying nonliquefiable layer was generally small (approx. 2 m) at sites where both sand boils and lateral ground displacement greater than 1 m were observed (type 1). For sites with no sand boils but with ground displacement greater than 1 m (type 2), the thickness of the liquefiable layer was as large as that of type 1, but the thickness of the overlying nonliquefiable layer was significantly larger than that of type 1. On the contrary, for types 3 and 4, both without lateral displacement greater than 1 m, the thickness of the liquefiable layer was smaller than for types 1 and 2, and many such sites had multiple liquefiable layers (alternating strata of liquefiable and nonliquefiable layers). However, there was no clear difference in the thickness of the nonliquefiable layer at the surface between type 3 with sand boils and type 4 without sand boils. In type 5 sites with neither sand boils nor ground displacement greater than 1 m, where the surrounding areas also exhibited no obvious signs of liquefaction, it was found that the thickness of the liquefiable layer was less than 2 - 3 m; alternatively, in some areas the liquefiable layer was thicker than 5 m but the overlying nonliquefiable layer was also thick (> 5 m).

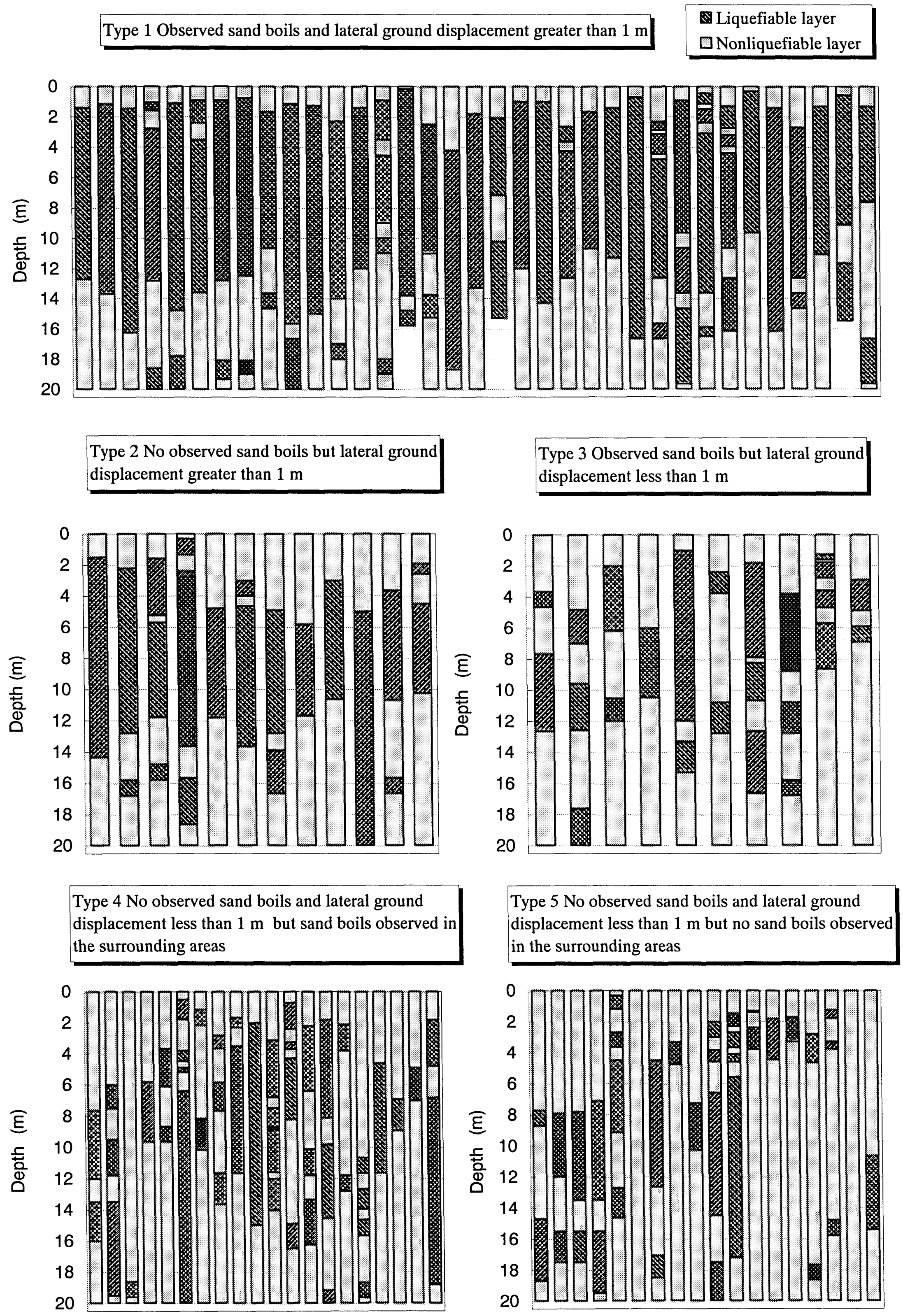

Fig. 2 Estimated Liquefied and Nonliquefied layers in Niigata during the 1964 Niigata Earthquake

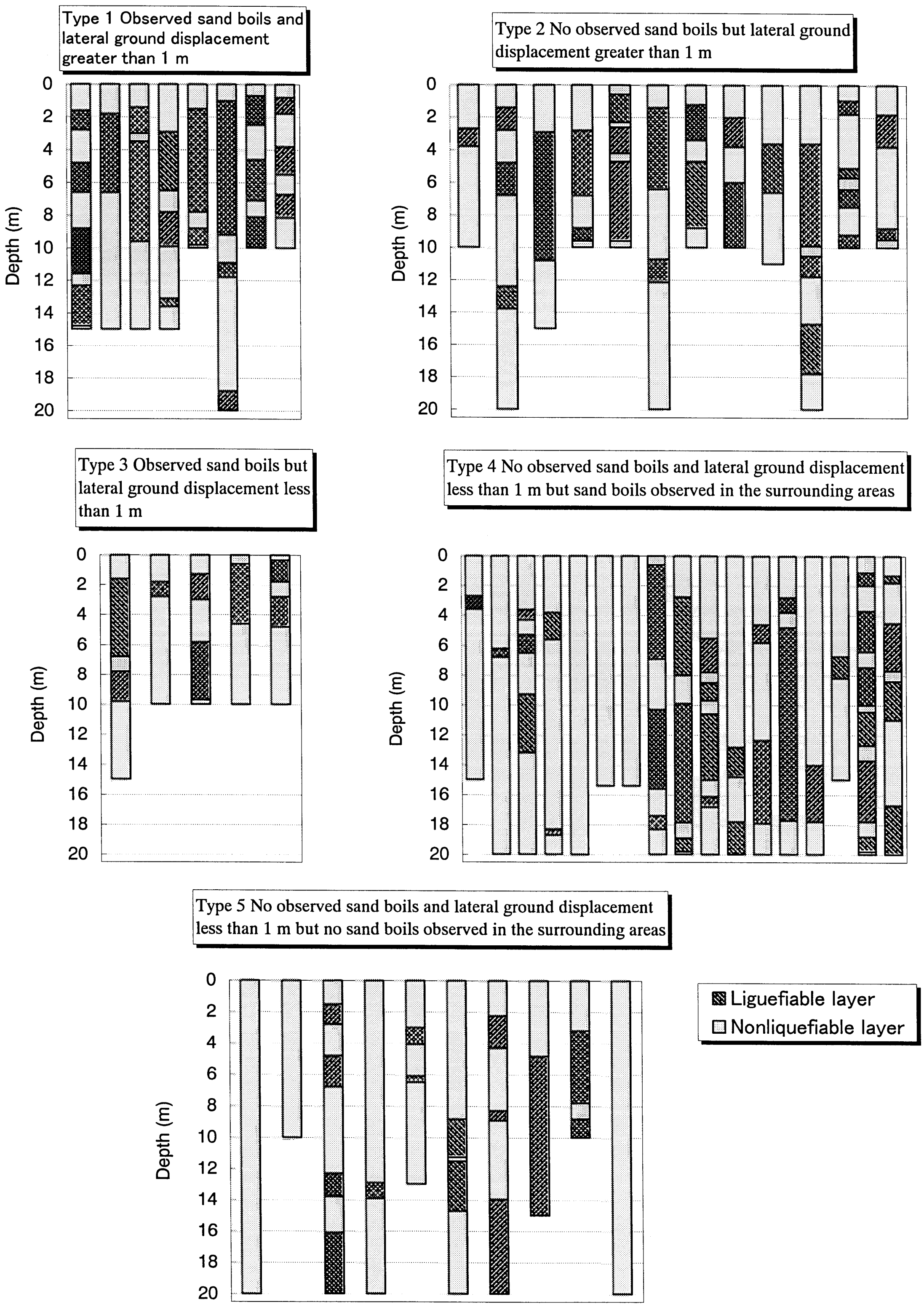

Fig. 3 Estimated Liquefied and Nonliquefied layers in Noshiro during the 1983 Nihonkai-Chubu Earthquake

The ground conditions in Noshiro (Fig.3) were different from those of Niigata, as most of the soil layers underlying sites of types 1 - 5 consisted of alternating strata of liquefiable and nonliquefiable layers. The differences in thickness between the liquefiable and nonliquefiable layers for types 1 and 2 with ground displacement greater than 1m and types 3 - 5 without ground displacement greater than 1m were not as clear as for Niigata.

There were a few points with relatively thick liquefiable layers at type 5 sites where no effects of liquefaction such as sand boils or ground displacement were observed (Figs.2 and 3). This is attributed to the following reasons: (1) in this study, the values of FC and D_{50} used for calculating the F_L, are assumed to be constant for each soil type; (2) the peak accelerations at the ground surface used for calculating the F_L is also assumed to be constant for each region (0.2g for Niigata and 0.25g for Noshiro); and (3) signs of liquefaction such as sand boils were overlooked during the reconnaissance surveys carried out immediately after the earthquakes.

Relationship between SPT N-Value and Effective Overburden Pressure

Figures 4 and 5 show the relationship between SPT N-values and the effective overburden pressure of the sandy soil layers of types 1 - 5 in Niigata and Noshiro. The boundary SPT N-value that differentiates flow and non-flow conditions for sand with a fine content of less than 30%, as derived by Ishihara[7)] based on data from past earthquakes, is also shown in the figures. For Niigata, (Fig.4), the SPT N-values are generally small for types 1 and 2, where ground displacement was greater than 1 m. But the SPT N-values fall on both sides of the relationship proposed by Ishihara, which indicates that ground displacement greater than 1 m is poorly predicted by the SPT N-value criterion. The SPT N-values for types 3 and 4, where ground displacement was less than 1 m, are slightly larger than those for types 1 and 2 and fit the boundary proposed by Ishihara more accurately. The SPT N-values for type 5 were even larger than those for types 3 and 4.

In Noshiro (Fig.5), a similar tendency to that in Niigata (Fig. 4) can be seen, although the difference between the SPT N-values for the five types is not so clear. From Figs. 4 and 5, we may conclude that ground displacement greater than 1 m is poorly predicted by the SPT N-value criterion.

Table 1 shows the range of ground displacement, average thickness of the liquefiable layer, H, average thickness of the overlying nonliquefiable layer, H', average overburden-corrected SPT N-value, N_1 of the liquefiable layer, and average safety factor against liquefaction, F_L, for the above five types. The

Table 1. Range of ground displacement, average thickness of the liquefiable layer, H, average thickness of the surface nonliquefiable layer, H', average overburden-corrected SPT N-value, N_1, $\sqrt{H} / N_1$, and average safety factor against liquefaction, F_L, for 5 types in Niigata

Type of ground failures	Number of borings	Range of ground displacement (m)	H (m)	H' (m)	N_1	$\sqrt{H}/N_1$	F_L
Type 1	35	1.0 - 3.3	12.18	1.40	10.80	0.33	0.72
Type 2	12	1.0 - 2.5	10.10	3.14	9.71	0.33	0.76
Type 3	10	Less than 1 m	6.91	2.96	12.05	0.24	0.77
Type 4	20	Less than 1 m	7.08	4.43	11.78	0.23	0.77
Type 5	16 (2)*	Less than 1 m	7.25	4.01	11.60	0.22	0.80

*Number in parentheses indicates number of boring sites where no liquefiable layer underlies.

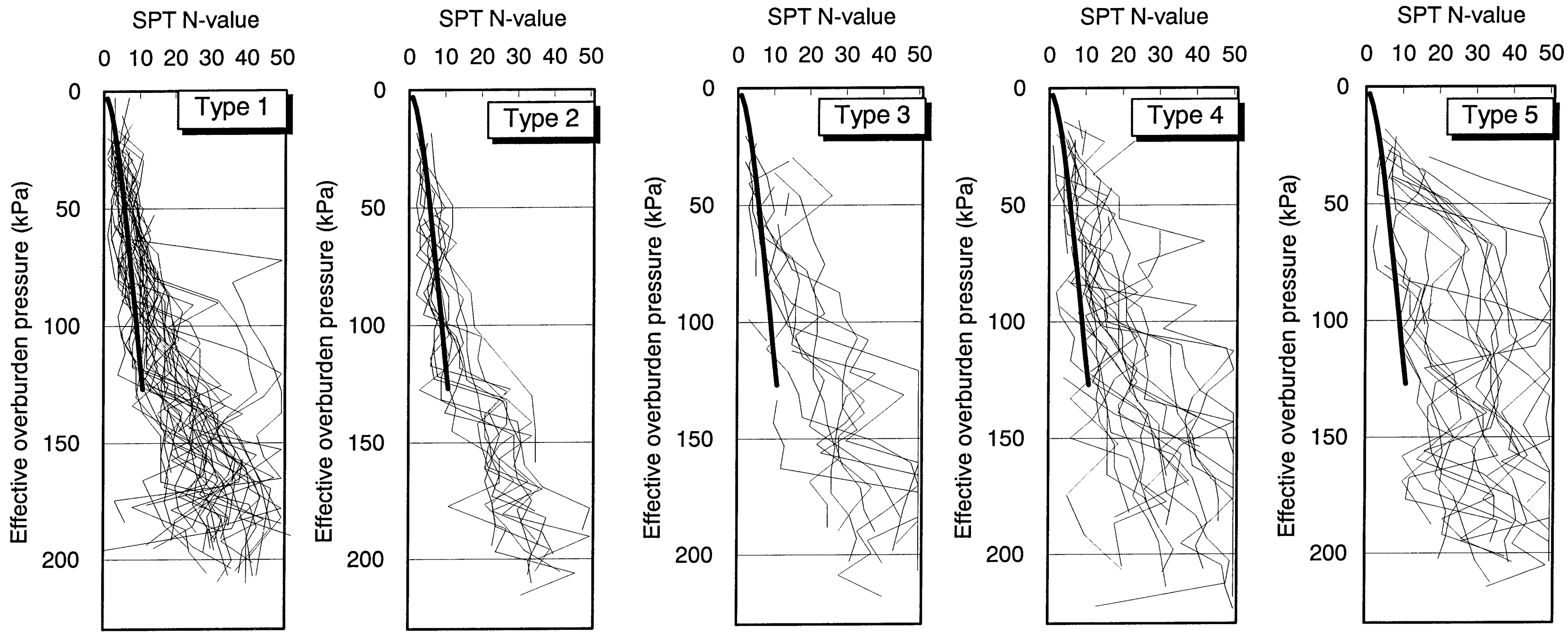

— Boundary in SPT N-value differentiating condition of flow and non-flow for sand with fines content less than 30 % (Ishihara, 1993)

Type 1: Observed sand boils and lateral ground displacement greater than 1 m
Type 2: No observed sand boils but lateral ground displacement greater than 1 m
Type 3: Observed sand boils but lateral ground displacement less than 1 m
Type 4: No observed sand boils and lateral ground displacement less than 1 m but sand boils observed in the surrounding areas
Type 5: No observed sand boils and lateral ground displacement less than 1 m but no sand boils observed in the surrounding areas

Fig. 4 Relationship between SPT N-value and Effective Overburden Pressure for Saturated Sandy Soil in Niigata

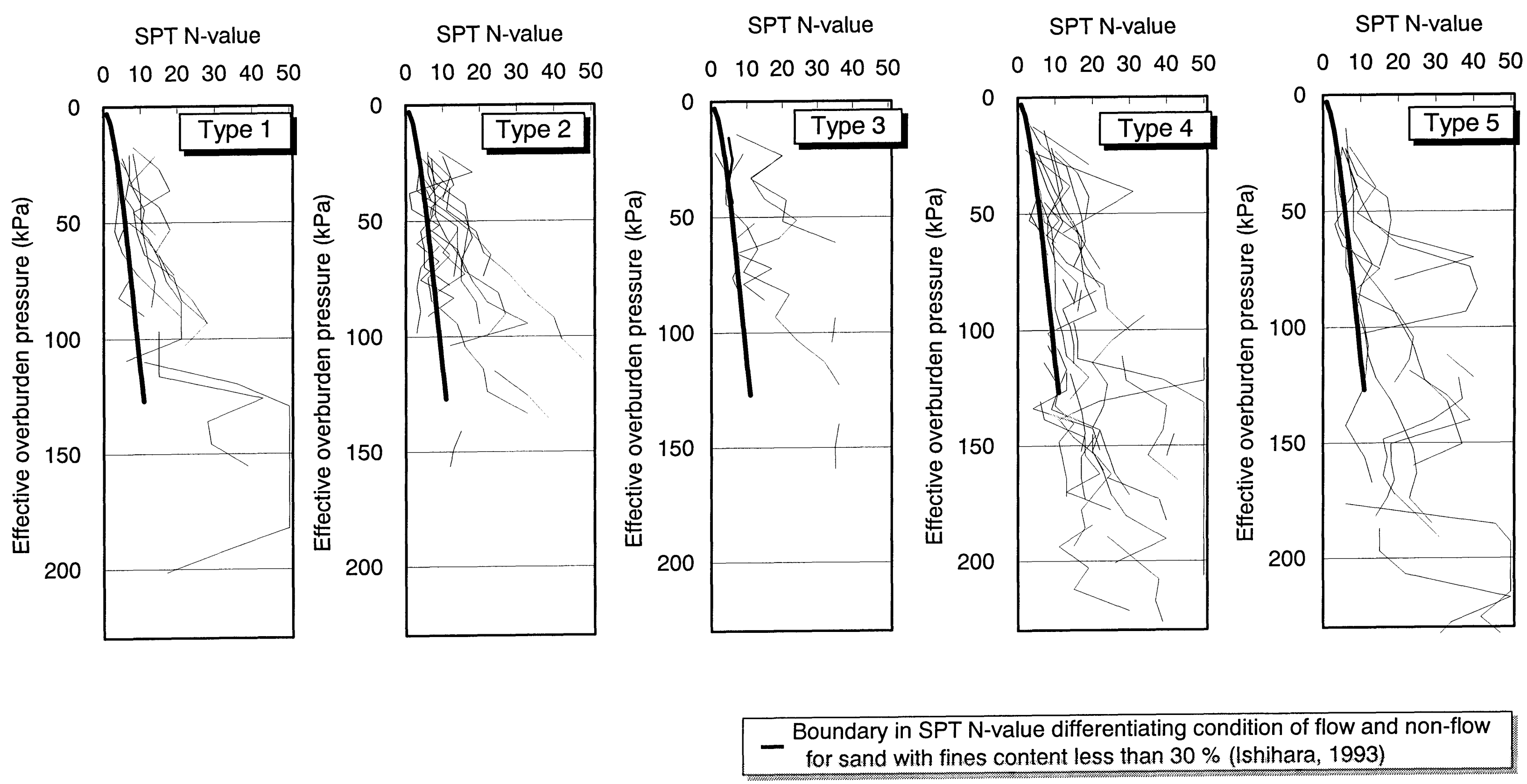

Type 1: Observed sand boils and lateral ground displacement greater than 1 m
Type 2: No observed sand boils but lateral ground displacement greater than 1 m
Type 3: Observed sand boils but lateral ground displacement less than 1 m
Type 4: No observed sand boils and lateral ground displacement less than 1 m but sand boils observed in the surrounding areas
Type 5: No observed sand boils and lateral ground displacement less than 1 m but no sand boils observed in the surrounding areas

Fig. 5 Relationship between SPT N-value and Effective Overburden Pressure for Saturated Sandy Soil in Noshiro

thickness of the liquefiable layer, H, for types 1 and 2, where ground displacement was above 1 m, is significantly greater than that for types 3 - 5, where ground displacement was less than 1 m. Only the thickness of the overlying nonliquefiable layer, H', for type 1, with both sand boils and ground displacement greater than 1 m, is small (1.4 m), as the thicknesses for types 2 - 4 were more than twice as large as those for type 1. There were no significant differences in N_1 and F_L, although N_1 and F_L for types 1 and 2 seemed to be slightly smaller than those for types 3 - 5.

According to a previous study by the authors[1], the lateral displacement of sloped ground surfaces is proportional to the surface gradient and the square root of the thickness of the liquefiable layer H, and is inversely proportional to the average overburden-corrected SPT N-value, N_1. Therefore, we calculated the average value of $\sqrt{H} / N_1$ for types 1 - 5 assuming that the differences due to the surface gradient can be ignored because the estimated ground gradient of the studied region is generally a constant value of 0.5%. The $\sqrt{H} / N_1$values for types 1 and 2 (with ground displacements greater than 1 m) shown in Table 1 were 0.33, while those for types 3 - 5 were 0.22 - 0.24, showing a relatively clear difference.

Thickness Relationship between the Liquefiable Soil and the Overlying Nonliquefiable Soil

Ishihara[8] proposed preliminary empirical criteria to assess the potential for ground-surface failures at liquefied sites. The criteria are based on the relationships between the thickness of the liquefiable layer and the thickness of the overlying nonliquefiable layer. To examine whether Ishihara's criteria can be used to predict ground displacement due to lateral flow, in Fig. 6 we plotted the relationship between the thickness of the liquefiable layer and that of the nonliquefiable layer for the 95 borehole sites shown in Fig. 2. Figures 6(a) and (b) show the results for sites with single and multiple liquefiable layers, respectively. The thickness of the liquefiable layer for sites with multiple layers was considered to be the sum of the thicknesses of all liquefiable layers, and the thickness of the nonliquefiable layer was defined as the thickness of the nonliquefiable layer at the surface only. The plotted thickness in Fig. 6(a) agrees with Ishihara's boundary for a peak acceleration of 0.2 g (also shown in the figure), separating sites with sand boils from sites without sand boils. However, this boundary may not be valid for lateral ground displacement; that is, when there was a single liquefiable layer (Fig. 6(a)), sites with ground displacements greater than 1 m had liquefiable layers thicker than 6 m, and had nonliquefiable layers less than 6 m thick. When multiple liquefiable layers existed (Fig. 6(b)), sites with ground displacements greater than 1 m were limited to sites with liquefiable layers thicker than 6 m and nonliquefiable layers less than approximately 6 m thick. However, many of the sites falling into this category experienced ground displacements of less than 1 m. As shown in Fig.3, an analysis similar to that of Fig. 6 could not be carried out for Noshiro because there was little borehole data for depths reaching 20 m.

Figure 7 shows the relationship between the value $\sqrt{H} / N_1$ and the thickness of the surface nonliquefiable layer. The boundary between ground displacements greater and less than 1 m is found at approx. $\sqrt{H} / N_1 = 0.25$, regardless of the number of liquefiable layers. However, there are still many sites having $\sqrt{H} / N_1$ values greater than 0.25 with ground displacements less than 1 m. These sites meet one or more of the following conditions: (1) the thickness of the nonliquefiable layer is greater than 5 m; (2) the ground surface is level; (3) the elevation of the ground surface is low compared to that in the surrounding regions, so lateral flow stopped at the bottom of the depression; and (4) the site is adjacent to a nonliquefied region, in other words, a thick nonliquefiable layer exists in the direction of the lateral flow of the ground.

Type 1: Observed sand boils and lateral ground displacement greater than 1 m
Type 2: No observed sand boils but lateral ground displacement greater than 1 m
Type 3: Observed sand boils but lateral ground displacement less than 1 m
Type 4: No observed sand boils and lateral ground displacement less than 1 m but sand boils observed in the surrounding areas
Type 5: No observed sand boils and lateral ground displacement less than 1 m but no sand boils observed in the surrounding areas

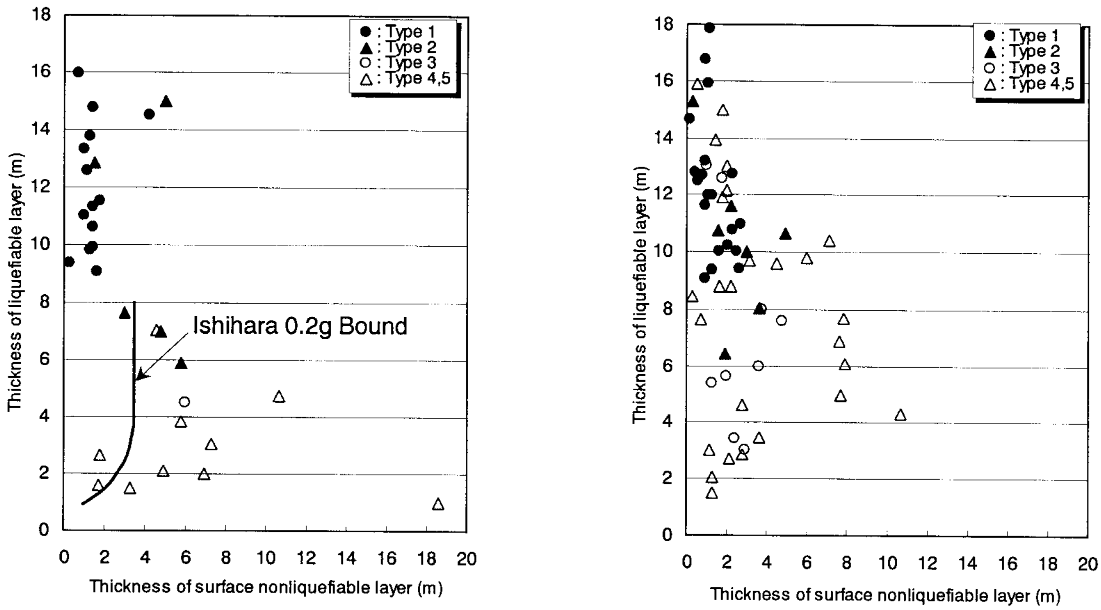

(a) Single liquefiable layer

(b) Multiple liquefiable layer

Fig. 6 Relationships between the thickness of the liquefiable layer and the surface nonliquefiable layer for the sites in Niigata

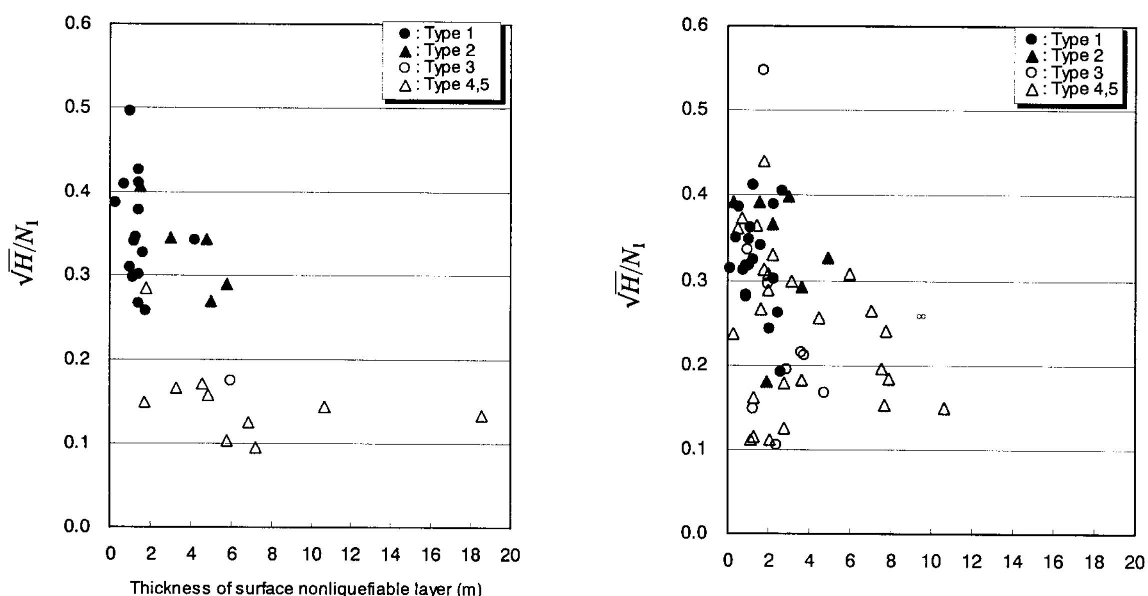

(a) Single liquefiable layer

(b) Multiple liquefiable layer

Fig. 7 Relationship between the value $\sqrt{H} / N_1$ and the thickness of the surface nonliquefiable layer for the sites in Niigata

Other Factors Controlling the Occurrence of Ground Displacement Greater Than 1 m

From previous studies based on analyses of lateral flow[1) 9)], it is known that the lateral displacement of sloped ground surfaces is controlled by the ground surface gradient as well as the thickness of the liquefiable layer and the SPT N-value (relative density) of the liquefiable layer. Out of the 147 sites analyzed in this study, we selected 34 sites with stable ground flow direction (17 in Niigata and 17 in Noshiro). For each borehole site, we established a 100-m-long traverse that extended 50 m from the borehole in both the upstream and downstream directions. We took continuous measurements of the surface profile along this traverse by photogrammetric analysis, and calculated the average surface gradient along the traverse. Although there is one site in Niigata with a surface gradient of 1.7%, most of the sites in Niigata are fairly flat, with a surface gradient of less than 0.5% along the traverse. On the other hand, the surface gradients in Noshiro are widely distributed between 0.1% and 4.3%, and many of the slopes are steeper than those in Niigata. However, because the calculated surface gradient along a traverse sometimes vary drastically depending on factors such as the length and direction of the traverse, we were unable to discuss a quantitative relationship between the occurrence of ground displacement greater than 1 m and the surface gradient.

In addition to the ground conditions previously discussed, the grain size distribution of the liquefiable soil may also affect the amount of ground displacement. However, the liquefiable soils of Niigata and Noshiro examined in the present study consisted mainly of clean, fine to medium sands comprising dune deposits, with a fine content of less than 5%, and so the effect of grain size distribution did not be discussed in the present study.

Conclusions

Using existing borehole data, we analyzed the various ground conditions at sites that experienced ground displacements greater than 1 m and less than 1 m during the 1964 Niigata and the 1983 Nihonkai-Chubu earthquakes. As the results, we obtained the following conclusions: (1) ground displacement greater than 1 m correlates strongly with the thickness of the liquefiable layer and the overburden-corrected SPT N-value of the liquefiable layer; (2) ground displacement greater than 1 m is poorly predicted by conventional methods, which are based on the SPT N-value criterion as well as on the thickness relationship between the liquefiable layer and the overlying nonliquefiable layer; and (3) there are some conditions in which severely liquefied sites were not accompanied by significant displacement.

References

1) Hamada, M. and Wakamatsu, K.: A Study on ground displacement caused by soil liquefaction, *Journal of Geotechnical Engineering, JSCE*, No.596/III-43, pp.189-208, 1998 (in Japanese).
2) Hamada, M. and O'Rourke, T.D. (Eds.): *Case study of liquefaction and lifeline performance during past earthquake, Vol. 1 Japanese case studies*, Technical Report NCEER-92-001, 1992.
3) Depart. of Geology and Mineralogy, Niigata University: *Maps of Ground Failures Caused by Niigata Earthquake*,1964.
4) Geographical Survey Institute, Japan: *Maps Showing Distribution of Damage caused by the Niigata Earthquake and Land Conditions*, 1965.

5) National Land Office, National Land Agency, Japan: *Geomorphological Land Classification Map Showing Locations of Ground Failures during the Nihonkai-Chubu Earthquake*, 1986.
6) Japan Road Association: *Specifications for Highway Bridges Part V Earthquake Resistant Design*. 1996.
7) Ishihara, K.: Liquefaction and flow failure during earthquakes, *Geotechnique* 43, No. 3, pp.349-415, 1993.
8) Ishihara, K.: Stability of natural deposits during earthquake, *Proc., 11th Int, Conf. on Soil Mechanics and Foundation Engineering*, Vol. 1, pp.321-376, 1985.
9) Bartlet, S. and Youd, T.L.: Empirical prediction of liquefaction-induced lateral spread, *Journal of Geotechnical Engineering, ASCE*, pp.316-329, Vol. 121, No.4, 1995.

Revised MLR Equations for Predicting Lateral Spread Displacement

T. Leslie Youd

Professor of Civil Engineering
Brigham Young University
Provo, Utah 84602-4081

Corbett M. Hansen
Geotechnical Engineer
CH2MHill
Salt Lake City, Utah 84107-2177

Steven F. Bartlett
Research Project Manager
Utah Department of Transportation
Salt Lake City, Utah 84114-8410

Abstract

In the early 1990's, Bartlett and Youd (1992; 1995) introduced empirical equations for predicting lateral spread displacement at liquefaction sites. Since that time, those equations have been used in engineering practice. The equations were developed from multilinear regression (MLR) of a large case history data set. Since the MLR equations were developed, several needed modifications have come to our attention. These modifications are addressed herein. (1) Bartlett and Youd, much to their chagrin, miscalculated lateral spread displacements for the 1993 Nihonkai-Chubu, Japan earthquake. This error is corrected in the re-analysis. (2) Several sites where boundary effects significantly interfered with free lateral-spread movement were removed from the data set. (3) Additional case history data were added from four recent earthquakes. (4) Additional sites were added from Port and Rokko Islands, Japan. (5) The functional form of the mean-grain-size term in the MLR equations was modified from ($D50_{15}$) to log ($D50_{15}$). (6) The functional form of the equation was additionally adjusted to the form Log ($D50_{15}$ + 0.1 mm) to prevent predicted displacements from becoming large when small mean grain sizes are entered into the equation. (7) The maximum value of fines content entered into the equation was capped at 55 percent. (8) The form of the equation was changed from Log (R) to Log (R*), where R* is a function of earthquake magnitude. This modification prevents prediction of very large displacements when R becomes small. A new predictive equation is regressed from the enlarged data set and modified form of the MLR equation. The new equation is recommended for application in engineering practice for prediction of lateral spread displacement at liquefiable sites.

Introduction

In the early 1990's, Bartlett and Youd (1992, 1995) introduced empirical equations for predicting lateral spread displacement at liquefaction sites. Since that time, those equations have been used in engineering practice. The equations were developed from multilinear regression (MLR) of a large case history data set. As noted by Bartlett and Youd, the equations are capable of predicting displacements within plus or minus a factor of two for sites with characteristics that are representative of sites in the empirical data base. For sites with characteristics outside the limits of the base, predicted results are much less certain.

Since the MLR equations were developed, several needed modifications have come to our attention. These modifications are addressed herein. (1) Bartlett and Youd, much to their chagrin, miscalculated lateral spread displacements for the 1993 Nihonkai-Chubu, Japan earthquake. The miscalculated displacements were 1.9 times the measured values. This error is corrected in this re-analysis. The erroneously large displacements generally led to over prediction of lateral spread displacement, which is conservative. (2) Bartlett and Youd incorporated data from several sites where boundary effects significantly interfered with free lateral movement of the mobilized ground. To be consistent with a free lateral movement model, eight displacement vectors at localities of restricted movement were removed from the data set. (3) Additional case history data were added from four recent earthquakes--1983 Borah Peak, Idaho, 1989 Loma Prieta, 1994 Northridge, and 1995 Hyogo-Ken Nanbu (Kobe, Japan). (4) Many additional sites were added from Port and Rokko Islands, Japan, although site-specific grain-size data are not available for these sites. We characterized the textural data by average values from a number of reported gradation tests on samples from each island. Because the islands were formed by loose dumping of heterogeneous coarse grained soils, mean grain sizes and fines contents within the fill are highly variable and averaged values may be as valid for the prediction of lateral spread displacement as the more precise local values. (5) The form of the mean-grain-size term in the MLR equations was modified from ($D50_{15}$) to log ($D50_{15}$). This modification greatly improves the performance of the model for coarse grained soils ($D50_{15}$ > 1.0 mm), a limit placed on the equation by Bartlett and Youd. (6) The equation was additionally adjusted to the form Log ($D50_{15}$ + 0.1 mm) to prevent predicted displacements from becoming large when very small mean grain sizes are entered into the equation. (7) The maximum value of fines content entered into the equation was capped at 55 percent. This capping slightly improved performance of the model and provides more conservative estimates of displacement when the equation is extrapolated beyond the suggested 50 percent fines content limit. (8) The form of the equation was changed from Log (R) to Log (R*), where $R^* = Ro + R$ and $Ro = 10^{(0.89\,M - 5.64)}$. This modification prevents prediction of very large displacements when R becomes small, a major shortcoming of the Bartlett and Youd equations.

The following text provides step-by-step summaries of adjustments and analyses made to incorporate the modifications listed above.

Modification of MLR Equation

Modifications to the MLR equations were made in a step-by-step process with a new regression of the data at the end of each step. Comparisons were made with the previous model to assure that regressed results were reasonable and logical. The comparisons were made by examining changes in the coefficients in the MLR equation and in the calculated correlation coefficient, R_c^2. The analysis began with the Bartlett and Youd (1992; 1995) equations and ends at Step 8 with a new MLR model.

Bartlett and Youd Equations

The general form of the Bartlett and Youd (1992) equation is:

$$\begin{aligned} \text{LOG } D_H = {} & b_o + b_{off} + b_1 M + b_2 \text{ LOG } R + b_3 R + b_4 \text{ LOG } W + b_5 \text{ LOG } S \\ & + b_6 \text{ Log } T_{15} + b_7 \text{ LOG } (100 - F_{15}) + b_8 \text{ D50}_{15} \end{aligned} \quad (1)$$

where D_H is the estimated lateral ground displacement, in meters; M is the estimated moment magnitude of the earthquake; R is the horizontal distance from the site to the seismic energy source, in kilometers; T_{15} is the cumulative thickness, in meters, of saturated granular layers with corrected blow counts, $(N_1)_{60}$, less than 15; F_{15} is the average fines content (fraction of sediment sample passing a No. 200 sieve) for granular layers included in T_{15}, in percent; $D50_{15}$ is the average mean grain size in granular layers included in T_{15}, in millimeters; S is the ground slope, in percent; W is the free-face ratio defined as the height (H) of the free face divided by the distance (L) from the base of the free face to the point in question, in percent; and b_o through b_8 are regression coefficients. The coefficient b_o is a general constant for the equation and the coefficient b_{off} is a constant that is added for free face conditions. The regressed coefficients for the Bartlett and Youd equation are listed in Table 1. These coefficients are significant at the 99.9 percent confidence level and the correlation coefficient, R_c^2 for the model is 82.6 percent.

The general quality of the Bartlett and Youd equation is shown in Figures 1 and 2, where measured displacements from the case history data set are plotted against predicted values using Equation 1. Displacements up to 10 m in magnitude are shown in Figure 1 and displacements up to 2 m, which are of greater engineering interest, are plotted in Figure 2. These plots show that the equations are valid for predicting displacements within about a factor of two for sites characteristic of those incorporated in the Bartlett and Youd data set.

Table 1. Coefficients regressed by Bartlett and Youd (1992; 1995) from MLR analysis

Variables	Constants		M	Log R	R	Log W	Log S	Log T_{15}	Log $(100-F_{15})$	$D50_{15}$	Reg Coef
Coefficients	b_o	b_{off}	b_1	b_2	b_3	b_4	b_5	b_6	b_7	b_8	R_c^2
Values	-15.787	-0.579	1.178	-0.927	-0.013	0.657	0.429	0.348	4.527	-0.922	82.6

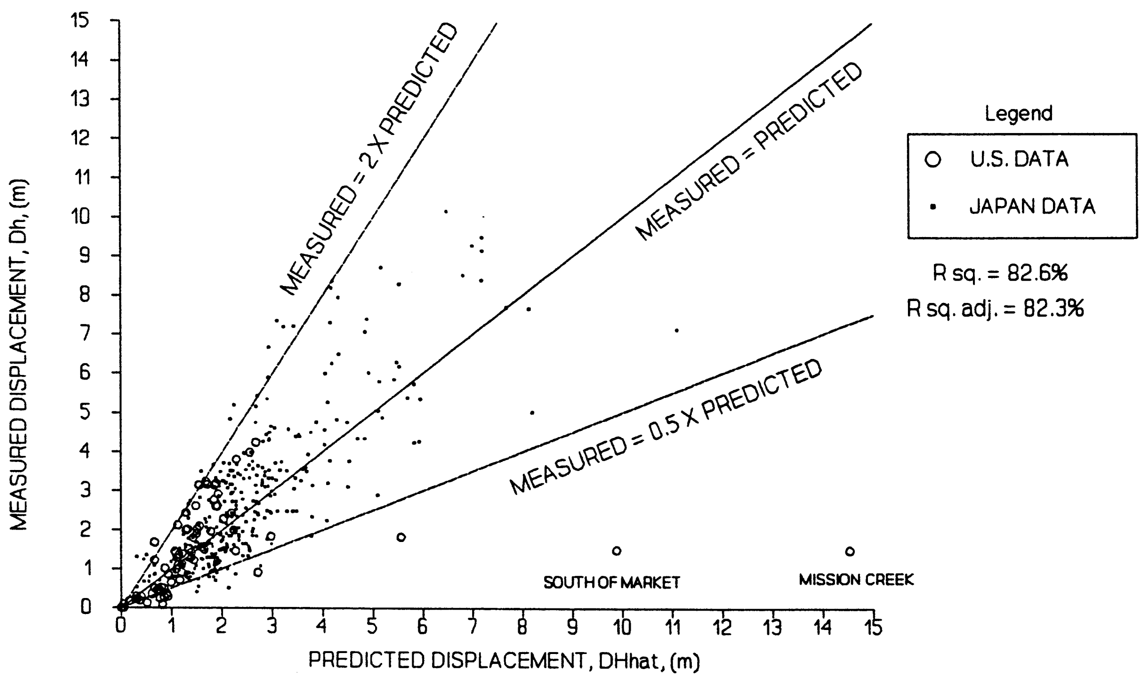

Figure 1. Measured Versus Predicted Displacements for Displacements up to 10 m using the Bartlett and Youd (1992) Model (After Bartlett and Youd, 1992)

Step 1--Correction of Miscalculated Nihonkai-Chubu, Japan Displacements

The first modification to the Bartlett and Youd equations was the correction of miscalculated displacements from the 1998 Nihonkai-Chubu, Japan earthquake. That correction was made by dividing the magnitude of each of the miscalculated displacements by a factor of 1.9. With this correction made, the case history data were re-regressed using the MLR procedure. This regression produced a new set of regression coefficients and a coefficient of correlation as listed in Table 2. All coefficients are significant at the 99.9 percent confidence level and the R^2 for the revised equation is 81.0 percent. This value is slightly lower than the 82.6 percent calculated from the Bartlett and Youd equations, but that small decrease is not very significant.

The percent changes in each coefficient compared to the Bartlett and Youd coefficients are also listed in Table 2. As might be expected, b_5, the coefficient for the slope parameter, S, decreased by a large amount, 35.9 percent. The over-predicted displacements were on sloping ground, where S is the controlling topographic factor in the equation. The erroneously high displacements led to an artificially high b_5 coefficient, which generally caused over-prediction of lateral spread displacement.

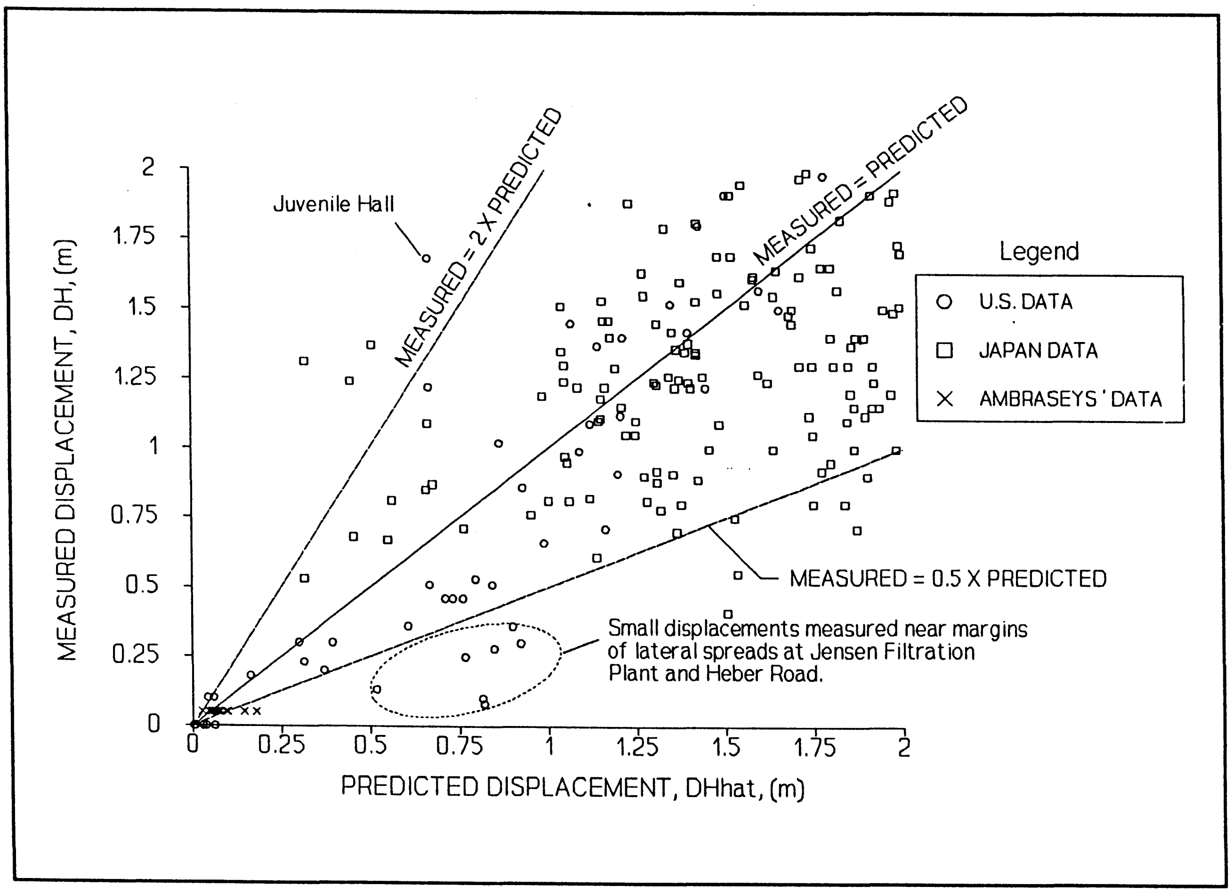

Figure 2. Measured Versus Predicted Displacements for Displacements up to 2 m using the Bartlett and Youd (1992) Model (After Bartlett and Youd, 1992)

Table 2. Coefficients Regressed from Step 1--Correction of Miscalculated Displacements from 1983 Nihonkai-Chubu, Japan Earthquake

Variables	Constants		M	Log R	R	Log W	Log S	Log T_{15}	Log $(100-F_{15})$	$D50_{15}$	Reg Coef
Coefficients	b_o	b_{off}	b_1	b_2	b_3	b_4	b_5	b_6	b_7	b_8	R_c^2
Values	-14.55	-0.483	1.096	-.0873	-0.014	0.634	0.275	.494	4.053	-0.814	81.0
Change from Tab. 1	1.236	0.096	-0.082	0.054	-0.001	-0.023	-0.154	0.146	-0.474	0.108	-1.6
% Change from Tab. 1	7.8%	16.6%	-7.0%	5.8%	-7.7%	-3.5%	-35.9%	42.0%	-10.5%	11.7%	-1.9%

Surprisingly, a larger change, plus 42.0 percent, occurred in b_6, the coefficient for the thickness parameter, T_{15}. This large change apparently occurred because the miscalculated displacements were at sites with relatively thin, 2 m to 3 m thick, T_{15} layers. The erroneously large displacements at sites with relatively thin T_{15} layers apparently caused the Bartlett and Youd regression to undervalue the influence of the thickness of the liquefied layer (approximated by T_{15}). The increase in b_6 is partially counterbalanced by an increase in coefficients b_o and b_{off}. The latter coefficients both increased in value, leading to a larger negative constant in the equation, which leads to smaller predicted displacements.

Step 2--Removal of Sites where Boundary Effects Impeded Displacement

The second adjustment to the MLR equations was the removal of eight displacement vectors where lateral spread displacements were impeded by shear forces along the margins or at the toe of the failure zone. This impedance caused displacements to be over-predicted by factors greater than 3. Two of these sites are marked on Figure 1 as "Mission Creek" and "South of Market. " Both of those lateral spreads occurred during the 1906 San Francisco earthquake. Changes of direction within the Mission Creek zone and buttressing at the toe of the South of Market zone apparently impeded displacement of these failures (Youd and Hoose, 1978). Shear forces along the margins of two lateral spreads impeded free movement at near those margins. Six displacement vectors or sites, noted as "margins of lateral spreads at Jensen Filtration Plant" and "Heber Road" were deleted from the data set. Displacement vectors from the interiors of these spreads, which apparently were not affected by boundary shear, were left in the data set. Coincidentally, all of the eight deleted sites were also relatively near the seismic energy source and some predicted displacements may have been partially overestimated due to the tendency of the Bartlett and Youd equation to over predict displacements near the energy source.

Table 3. Coefficients Regressed from Step 2--Data Removed for Sites Where Boundary Effects Retarded Displacement

Variables	Constants		M	Log R	R	Log W	Log S	Log T_{15}	Log (100-F_{15})	$D50_{15}$	Reg Coef
Coefficients	b_o	b_{off}	b_1	b_2	b_3	b_4	b_5	b_6	b_7	b_8	R_c^2
Values	-14.68	-0.449	1.14	-0.972	-0.013	0.591	0.281	0.507	4.012	-0.867	84.5
Change from Tab. 2	-0.124	0.034	0.044	-0.099	0.001	-0.043	0.006	0.013	-0.041	-0.053	3.5
% Change from Tab. 2	-0.9%	7.0%	4.0%	-11.3%	7.1%	-6.8%	2.2%	2.6%	-1.0%	-6.5%	4.3%
Change from Tab. 1	1.112	0.13	-0.038	-0.045	0	-0.066	-0.148	0.159	-0.515	0.055	1.9
% Change from Tab. 1	7.0%	22.5%	-3.2%	-4.9%	0.0%	-10.0%	-34.5%	45.7%	-11.4%	6.0%	2.3%

After removal of these eight vectors, regression of the data set generated the regression coefficients listed in Table 3. All coefficients are significant at the 99.9 percent confidence level and the R_c^2 increased to 84.5 percent. The only significant changes produced by this regression were decreases of 11.3 percent and 7.1 percent in coefficients b_2 and b_3, respectively. These coefficients modify the distance terms, Log R and R, and the decreases generally cause increased predicted displacement, especially near the energy source.

Step 3--Regression with Sites Added from 1983 Borah Peak, Idaho; 1989 Moss Landing, California; 1995 and Limited Data from Port and Rokko Islands, Japan

Several new sites were added to the data set from earthquakes that occurred after development of the Bartlett and Youd equations in 1992. Four sites were also added from the Whisky Springs lateral spread that occurred during the 1983 Borah Peak, Idaho earthquake. The latter sites were compiled by Bartlett and Youd, but not used because the liquefiable sediments were coarse grained ($D50_{15}$ > 1.0 mm). Two sites were added from a lateral spread at the Monterey Bay Aquarium Research Institute (MBARI), Moss Landing, California. Displacement of that lateral spread occurred during the 1989 Loma Prieta earthquake and movement was precisely measured with the aid of borehole inclinometers. Subsurface data were developed from SPT and grain size analyses on retrieved samples (Boulanger et al., 1997).

Lateral spread occurred pervasively around the margins of Port and Rokko Islands and several other filled areas during the 1995 Hyogo-Ken Nanbu (Kobe) earthquake. Hamada et al. (1995) used areal photographs and photogrammetric techniques to measure displacements in these areas and produced an extensive set of maps of displacement vectors. Lateral spread caused the quay walls around the islands to displace 2 m and 6 m laterally with little apparent resistance to movement of the mobilized ground. Values of free-face ratios, W, for sites within 50 m of the walls, however, were greater than 20 percent, which may have caused flow failure as well as lateral spread. Thus, vectors within 50 m of the sea walls were neglected. Displacement vectors at distanced between 50 m and 300 m from the sea walls were generally between 0.1 m and 2 m in length and directed toward the nearest wall. Beyond 300 m from the walls, displacement vectors were small, randomly oriented, and did not form a consistent pattern. These small chaotic displacements were also neglected in our analyses. Numerous borehole logs with SPT data were reported by Hamada et al. (1995), but grain-size information was not listed on those logs. Many of the logs were near the mapped displacement vectors, allowing calculation of T_{15} at those localities. T_{15} values were rather uniform and ranged from 11 m to 13 m beneath Port Island and 15 m to 17 m beneath Rokko Island. Because of this uniformity, average T_{15} values of 12.5 m for Port Island and 16.0 m for Rokko Island were used to characterize all of the vector sites on the two islands.

Only limited grain size data have been made public from Port and Rokko Islands. Grain size data from soil samples from three boreholes on Port Island and two boreholes on Rokko Island were all that we were able to collect. These data were provided by Kobe City and the Port and Harbors Research Institute. These data show heterogeneous fill beneath the islands with widely varying grain size distributions. Even within a single borehole, fines contents and mean-grain-sizes vary by factors of three or more between adjacent samples. Values of $D50_{15}$ and F_{15} were determined for each borehole by taking the geometric mean of mean-grain-sizes and fines contents, respectively, that were listed within the interval characterized by T_{15}. The geometric mean was used because mean values are less affected by extremes in the data set than average values. The mean values were used to characterize soil properties at sites of measured displacements within a zone about 100 m wide perpendicular to the sea wall and centered on each borehole. Using these procedures, eight sites from Port Island and six sites from Rokko Island were added to the data set.

Table 4. Coefficients Regressed from Step 3--Data Added From Recent Earthquakes

Variables	Constants		M	Log R	R	Log W	Log S	Log T_{15}	Log $(100-F_{15})$	$D50_{15}$	Reg Coef
Coefficients	b_o	b_{off}	b_1	b_2	b_3	b_4	b_5	b_6	b_7	b_8	R_c^2
Values	-12.95	-0.396	1.074	-0.901	-0.016	0.492	0.321	0.479	3.263	-0.167	80.5
Change from Tab. 3	1.724	0.053	-0.066	0.071	-0.003	-0.099	0.040	-0.028	-0.749	0.700	-4.0
% Change from Tab. 3	11.7%	11.8%	-5.8%	7.3%	-23.1%	-16.8%	14.2%	-5.5%	-18.7%	80.7%	-4.7%
Change from Tab. 1	2.836	0.183	-0.104	0.026	-0.003	-0.165	-0.108	0.131	-1.264	0.755	-2.1
% Change from Tab. 1	18.0%	31.6%	-8.8%	2.8%	-23.1%	-25.1%	-25.2%	37.6%	-27.9%	81.9%	-2.5%

A regression analysis of the expanded data set produced the coefficients listed in Table 4. All of these coefficients are significant at the 99.9 percent confidence level. R_c^2, however, decreased to 80.5 percent, largely due to the addition of the coarse grained sites. The addition of several sites with $D50_{15}$ greater than 1 mm, a maximum value allowed for the Bartlett and Youd equation, caused a large change in coefficient b_8, the coefficient for the mean-grain-size term. Substantial changes of 10 to 20 percent also occurred in several other coefficients. As discussed in Step 5, a change of functional form from $D50_{15}$ to log $(D50_{15})$ moderates many of the large changes introduced in this step. Discussion of the influence of large grain sizes is thus delayed to Step 5.

Step 4--Addition of 76 Sites from Port and Rokko Islands

As noted in Step 3, many displacement vectors and borehole logs were reported by Hamada et al. (1995), but do not contain grain-size data. We added 76 vectors (19 from Port Island and 57 from Rokko Island) as sites to the data set to enrich the data set with ground displacements in the 0.25 m to 1.0 m range. Displacements in this important range are not well represented in the Bartlett and Youd data set. We characterized these sites with mean values of all the reported soil property data for each island. The mean fines contents applied are 10 percent and 15 percent for Port and Rokko Islands, respectively, with a $D50_{15}$ of 2.3 mm for both islands. The mean values of T_{15} are 12.5 m and 16 m, respectively. Because of the heterogeneity of the fill, global mean values may be as adequate for modeling soil properties for the prediction of ground displacement as more precise local mean values. Thus, the 76 additional sites were added to the data set. An MLR analysis of the enlarged data set produced the regression coefficients listed in Table 5. All coefficients remain

Table 5. Coefficients Regressed from Step 4--Data Added From Additional Sites on Port and Rokko Islands, Japan

Variables	Constants		M	Log R	R	Log W	Log S	Log T_{15}	Log $(100\text{-}F_{15})$	$D50_{15}$	Reg Coeff
Coefficients	b_o	b_{off}	b_1	b_2	b_3	b_4	b_5	b_6	b_7	b_8	R_c^2
Values	-13.44	-0331	1.177	-0.978	-0.015	0.373	0.361	0.405	3.206	-0.241	76.6
Change from Tab. 4	-0.492	0.065	0.103	-0.077	0.001	-0.119	0.040	-0.074	-0.057	-0.074	-3.9
% Change from Tab. 4	-3.8%	16.4%	9.6%	-8.5%	6.3%	-24.2%	12.5%	-15.4%	-1.7%	-44.3%	-4.8%
Change from Tab. 1	2.344	0.248	-0.001	-0.051	-0.002	-0.284	-0.068	0.057	-1.321	0.681	-6.0
% Change from Tab. 1	14.8%	42.8%	-0.1%	-5.5%	-15.4%	-43.2%	-15.9%	16.4%	-29.2%	73.9%	-7.3%

significant at the 99.9 percent confidence level, although the R_c^2 dropped to 76.6 percent. Discussion of changes to R_c^2 and coefficient values is deferred to Step 5 in which a change of functional form is introduced.

Step 5--Change of Form from $D50_{15}$ to Log $(D50_{15})$

The added case history data from Steps 3 and 4, with their large mean grain sizes, caused apparent degradation of the performance of the MLR model as indicated by the reduced R_c^2. The slightly poorer performance, however, could be removed by a reformulation of the MLR model. The new data extends mean grain sizes ($D50_{15}$) well beyond the 1.0 mm $D50_{15}$ limit recommended by Bartlett and Youd (1992; 1995). To improve the performance, the $D50_{15}$ term in the model was changed to Log $(D50_{15})$. The MLR analysis was repeated on the enlarged data set using the changed form. The resulting regression coefficients and R_c^2 are listed in Table 6. All coefficients in this model are significant at the 99.9 percent confidence level and R_c^2 increased to 83.0 percent, approximately the same value as for the Bartlett and Youd model.

The modified form improved the model, as indicated by R_c^2 and the regression coefficients generally returning to values near those of the Bartlett and Youd model. Coefficients b_o, b_1, b_2, b_3 and b_7 are within 10 percent of the Bartlett and Youd values. The largest change was to b_8, the coefficient for mean-grain-size term, which decreased by 230 percent from the previous model (Table 5), to a value that is only 13.6 percent larger than b_8 in the Bartlett and Youd model. The second largest increase is in b_7, the modifier for the fines content term, which increased by 43.5 percent from Table 5. The increase in b_7 partially offsets the decrease in b_8, a relationship that commonly occurs because fines content generally increases as mean grain size decreases. Coefficient b_{off} decreased and b_4 increased by about the same amount, 34.4 percent and 39.4 percent, respectively, essentially counterbalancing

Table 6. Coefficients Regressed from Step 5--Change of form from $D50_{15}$ to Log ($D50_{15}$)

Variables	Constants		M	Log R	R	Log W	Log S	Log T_{15}	Log ($100-F_{15}$)	$D50_{15}$	Reg Coef
Coefficients	b_o	b_{off}	b_1	b_2	b_3	b_4	b_5	b_6	b_7	b_8	R_c^2
Values	-16.641	-0.445	1.143	-0.920	-0.014	0.520	0.332	0.551	4.602	-0.797	83.0
Change from Tab. 5	-3.171	-0.114	-0.034	0.058	0.001	0.147	-0.029	0.146	1.396	-0.556	6.4
% Change from Tab. 5	-23.6%	-34.4%	-2.9%	5.9%	6.7%	39.4%	-8.0%	36.0%	43.5%	-230.7%	8.4%
Change from Tab. 1	-0.827	0.134	-0.035	0.007	-0.001	-0.137	-0.097	0.203	0.075	0.125	0.4
% Change from Tab. 1	-5.2%	23.1%	-3.0%	0.8%	-7.7%	-20.9%	-22.6%	58.3%	1.7%	13.6%	0.5%

the influence of the free-face coefficients. Coefficient b_6 increased by 36.0 percent, further increasing the influence of the thickness of the liquefied layer.

Step 6--Capping of Fines Content Term ($100-F_{15}$) to Maximum Value of 55 Percent

The final three modifications to the model were made based on engineering judgement to allow application of the model to values beyond the limits of the data base for three commonly used parameters. These modifications allow logical extrapolation of the model to parametric values beyond the limits of the data, without generating large errors due to model limitations.

The first of these modifications, Step 6 in the study, is to cap the value of the fines content parameter at 55 percent. This modification was due to the small number of case histories in the data set with fines contents, F_{15}, greater than 55 percent. If applied, fines content values greater than 55 percent lead to the prediction of very small displacements. To be conservative, the 55 percent cap increases predicted displacements for sediments with fines contents greater than 55 percent. This cap alleviates the problem of small predicted displacements in a region of the data base where the data is insufficient to corroborate the predicted values. The 55 percent cap was determined through analysis of the data base and the relative influence that various caps had on the resulting equations. The 55 percent cap provided the best performance, in terms of R_c^2 and minimal influence of the regression coefficients.

The results of the regression, with a cap of 55 percent on F_{15}, are listed in Table 7. All regression coefficients are significant at the 99.9 percent confidence level, and R_c^2 increased to 83.3 percent. The largest change, as expected, was an increase of 17.2 percent in b_7, the coefficient modifying the ($100 - F_{15}$) term. For an unknown reason, the coefficients for Log R and R, respectively, decreased and increased significantly, but largely counterbalanced each other.

Table 7. Coefficients Regressed from Step 6--Capping of F_{15} at 55 percent

Variables	Constants		M	Log R	R	Log W	Log S	Log T_{15}	Log $(100-F_{15})$	$D50_{15}$	Reg Coef
Coefficients	b_o	b_{off}	b_1	b_2	b_3	b_4	b_5	b_6	b_7	b_8	R_c^2
Values	-17.934	-0.441	1.115	-0.994	-0.012	0.529	0.324	0.575	5.393	-0.822	83.3
Change from Tab. 6	-1.320	0.004	-0.028	-0.074	0.002	0.009	-0.008	0.024	0.791	-0.025	0.3
% Change from Tab. 6	-7.9%	0.9%	-2.4%	-8.0%	14.3%	1.7%	-2.4%	4.4%	17.2%	-3.1%	0.4%
Change from Tab. 1	-2.147	0.138	-0.063	-0.067	0.001	-0.128	-0.105	0.227	0.866	0.100	0.7
% Change from Tab. 1	-13.6%	23.8%	-5.3%	-7.2%	7.7%	-19.5%	-24.5%	65.2%	19.1%	10.8%	0.8%

Step 7--Modification of Log ($D50_{15}$) to Log ($D50_{15}$+0.1 mm)

This modification was applied to ensure that excessively large predictions of displacement do not occur when small values of $D50_{15}$ are entered into the model. The addition of the 0.1 mm had minimal effect on the regressed coefficients as indicated in Table 8. This modification caused decreases of 18.1 percent in b_8 and 8.0 percent in b_7 compared to the previous model. The remaining coefficients did not change by more than about 5 percent and R_c^2 did not change.

Step 8--Change of Functional Form from Log R to Log (R*)

The final modification is to add a magnitude-dependent constant, R_o, to the logarithm-of-distance term in the model. The addition of this constant prevents predicted displacements from becoming excessively large when small values of R are entered into the equation. This model limitation has caused considerable perplexity to users of the Bartlett and Youd procedure for evaluating lateral spread displacements at liquefaction sites near seismic source zones. The constant was added by changing Log R to Log R* in the MLR equation, where:

$$R^*=R+R_o \tag{2}$$

and

$$R_o= 10^{(0.89M-5.64)} \tag{3}$$

Note that R* only replaces R in the term, b_2 Log R. The R in the term b_3 R is the original R rather than R*. The value of R_o was selected to yield predicted displacements at R = 0 km that are consistent with displacements in the compiled case histories and predicted displacements with the Bartlett and Youd equations with application of minimal R-values suggested these investigators (Bartlett and Youd, 1992; 1995). Values of R* were calculated for each site in the data base and entered into the MLR regression. The regression of the modified form of the equation yields the regression coefficients and R_c^2 listed in Table 9. All coefficients are significant at the 99.9 percent confidence level and R_c^2 is 82.5 percent.

Table 8. Coefficients Regressed in Step 7--Change of Form from Log ($D50_{15}$) to Log ($D50_{15}$+0.1 mm)

Variables	Constants		M	Log R	R	Log W	Log S	Log T_{15}	Log ($100-F_{15}$)	$D50_{15}$	Reg Coef
Coefficients	b_o	b_{off}	b_1	b_2	b_3	b_4	b_5	b_6	b_7	b_8	R_c^2
Values	-16.979	-0.437	1.111	-1.007	-0.012	0.531	0.326	0.554	4.964	-0.971	83.3
Change from Tab. 7	0.955	0.004	-0.004	-0.013	0.000	0.002	0.002	-0.021	-0.429	-0.149	0.0
% Change from Tab. 7	5.3%	0.9%	-0.4%	1.3%	0.0%	0.4%	0.6%	-3.7%	-8.0%	-18.1%	0.0%
Change from Tab. 1	-1.192	0.142	-0.067	-0.080	0.001	-0.126	-0.103	0.206	0.437	-0.049	0.7
% Change from Tab. 1	-7.6%	24.5%	-5.7%	-8.6%	7.7%	-19.2%	-24.0%	59.2%	9.7%	-5.3%	0.8%

Table 9. Coefficients Regressed from Step 8--Change of form from Log R to Log R*

Variables	Constants		M	Log R	R	Log W	Log S	Log T_{15}	Log ($100-F_{15}$)	$D50_{15}$	Reg Coef
Coefficients	b_o	b_{off}	b_1	b_2	b_3	b_4	b_5	b_6	b_7	b_8	R_c^2
Values	-17.614	-0.470	1.581	-1.518	-0.011	0.551	0.343	0.547	3.976	-0.923	82.5
Change from Tab. 8	-0.635	-0.033	0.470	-0.511	0.001	0.020	0.017	-0.007	-0.988	0.048	-0.8
% Change from Tab. 8	-3.7%	-7.6%	42.3%	-50.7%	8.3%	3.8%	5.2%	-1.3%	-19.9%	4.9%	-1.0%
Change from Tab. 1	-1.827	0.109	0.403	-0.591	0.002	-0.106	-0.086	0.199	-0.551	-0.001	-0.1
% Change from Tab. 1	-11.6%	18.8%	34.2%	-63.8%	15.4%	-16.1%	-20.0%	57.2%	-12.2%	-0.01%	-0.1%

Recommended MLR Equations

The coefficients listed in Table 9 are the final coefficients developed in our re-analysis and are the coefficients we now recommend for use in engineering practice. The final equations defined for free-face and ground-slope conditions are:

Free face conditions:

$$\text{Log } D_H = -18.084 + 1.581 M - 1.518 \text{ Log } R^* - 0.011 R + 0.551 \text{ Log } W + 0.547 \text{ Log } T_{15} + 3.976 \text{ Log } (100 - F_{15}) - 0.923 \text{ Log } (D50_{15} + 0.1 \text{ mm}) \quad (4a)$$

Ground slope conditions:

$$\text{Log } D_H = -17.614 + 1.581 M - 1.518 \text{ Log } R^* - 0.011 R + 0.343 \text{ Log } S + 0.547 \text{ Log } T_{15} + 3.976 \text{ Log } (100 - F_{15}) - 0.923 \text{ Log } (D50_{15} + 0.1 \text{ mm}) \quad (4b)$$

R^* and R_o are defined by Equations 2 and 3.

The need to change the functional form of the equation from $D50_{15}$ to Log ($D50_{15}$ + 0.1 mm) is illustrated in Figure 3 which shows measured versus predicted displacements for Port and Rokko Islands, Japan. Predicted displacements are plotted from both the Bartlett and Youd equations and Equation 4. This plot clearly shows that the Bartlett and Youd equation severely under-predicts displacements on these islands. The reason for the under-prediction is the large mean grain size ($D50_{15}$ = 2.3 mm) of the liquefiable materials. The change of form to Log ($D50_{15}$ + 0.1 mm) allows prediction of displacements to within a factor of two for mean grain sizes at least as large as 3 mm.

Figure 4 is a plot of measured versus predicted lateral spread displacements for all of the data in the final data set for this study. In this instance, only displacements up to two meters are shown. (This is the range of interest for most engineering applications). Also shown on the plot are the tracked changes in predicted values between the Bartlett and Youd equations and Equation 4 for 22 sites tracked during this study. These tracked changes are shown by the arrows on the plot with the small dot at the head of the arrow plotted from the Bartlett and Youd equation and the symbol at the end of the arrow plotted from Equation 4. Predicted displacements with very little difference between the two methods are marked by an oval surrounding the plotted points. Note that the measured as well as the predicted displacements changed greatly for the three tracked points from the Nihonchai-Chubu earthquake (noted as Noshiro on the plot) due to the correction of miscalculated measured displacements. For most of the 22 tracked points, the difference between displacements was rather minor. For several points, the change was rather large.

Space here does not permit a detailed analysis of the differences and reasons for the differences. One major factor, however, was a significant increase of the importance of T_{15} in the predictive model. That significant increase is largely due to the correction of miscalculated displacements from the Nihonchai-Chubu earthquake. Other factors causing changes in predicted values are the change of form from $D50_{15}$ to Log ($D50_{15}$ + 0.1 mm) which generally increases predicted displacement for coarser grained materials and the change of form from Log R to Log R*. The latter change has considerable impact on predicted near source displacements, many of which increased using Equation 4. Additional analysis is needed to determine the reasons for the latter increases.

Overall, the model in Equation 4 predicts displacement of lateral spreads about equally as well as the Bartlett and Youd equation. This fact is indicated by almost identical R_c^2 values of 82.6 percent for the Bartlett and Youd model and 82.5 percent for Equation 4. Also, the precision with which displacements can be predicted has not been significantly improved. Predicted displacements are still only accurate to a factor of about plus or minus two.

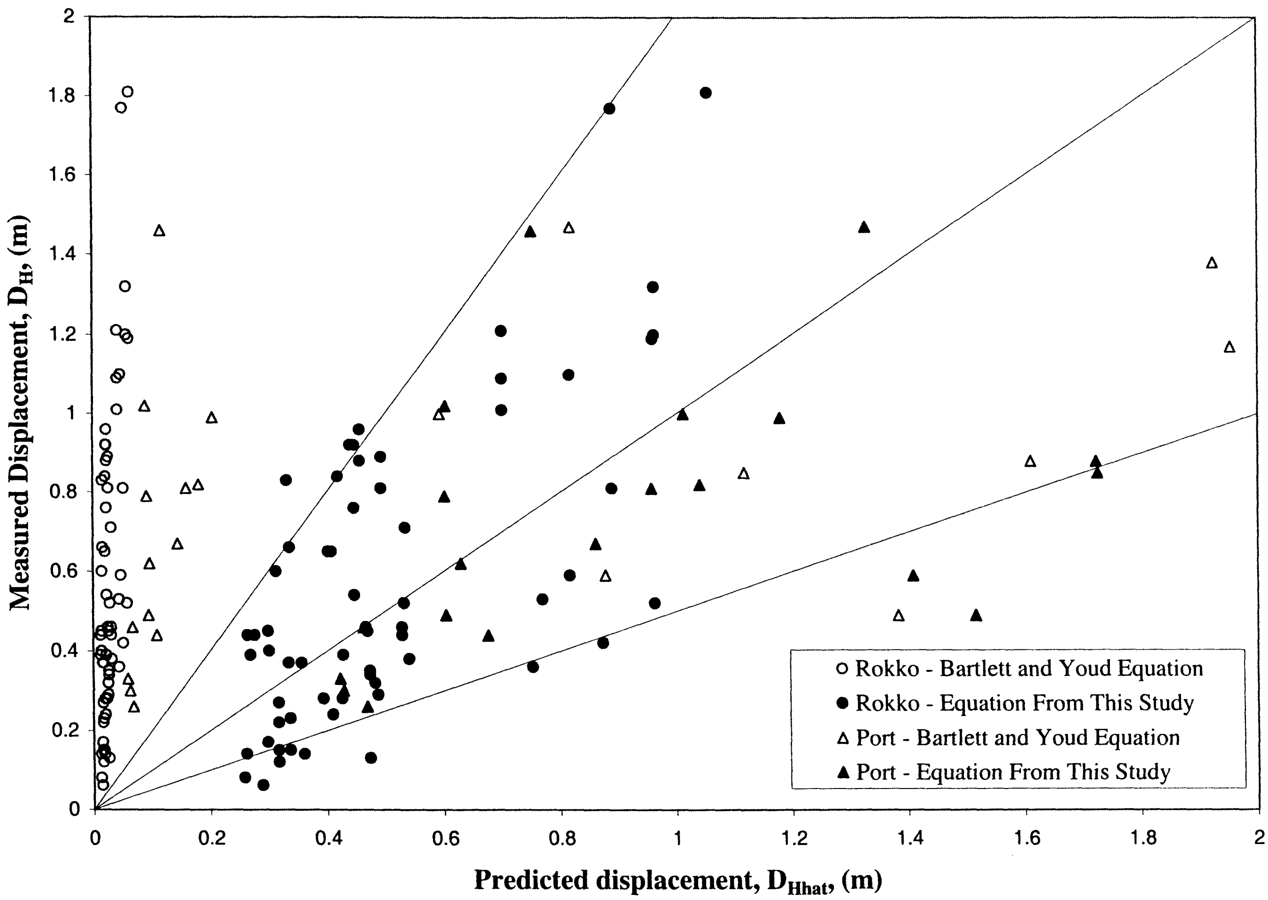

Figure 3. Measured Versus Predicted Displacements for Port and Rokko Islands, Japan Showing That Bartlett and Youd Equations Greatly Underpredict Displacements at Coarse-Grained Sites

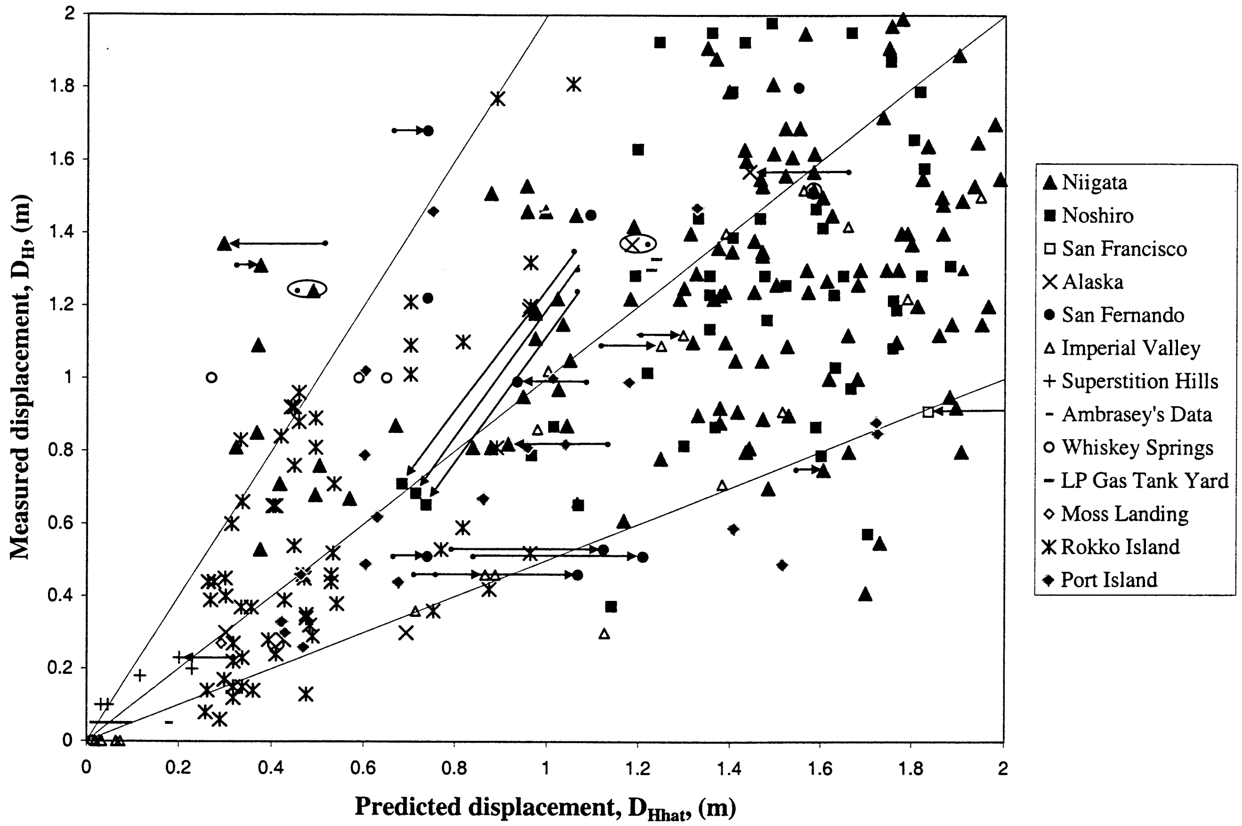

Figure 4. Measured Versus Predicted Displacements using Equation 4 with Comparisons of Values Predicted using the Bartlett and Youd (1992) Model for 22 Tracked Points

Conclusion

A new MLR model for predicting lateral spread displacement is presented in Equation 4. This model corrects errors in the work of Bartlett and Youd (1992; 1995) and incorporates changes to the functional form of the model allowing better applications coarser materials and to sites near seismic energy sources. Additional case histories were added to the data set, adding robustness to new MLR model. We recommend the new model, as formulated in Equation 4, for application in engineering practice.

Acknowledgment

The College of Engineering and Technology, Brigham Young University, provided funding for this project.

References Cited

Bartlett, S.F. and Youd, T.L., 1992, Empirical analysis of horizontal ground displacement generated by liquefaction-induced lateral spread: National Center for Earthquake Engineering Research Technical Report NCEER-92-0021, 114 p.

Bartlett, S.F. and Youd, T.L., 1995, Empirical prediction of liquefaction-induced lateral spread: Journal of Geotechnical Engineering, ASCE, v. 121, No. 4, p. 316-329.

Boulanger, R.W., Idriss, I.M., and Mejia, L.H., 1995, Investigation and Evaluation of Liquefaction Related Ground Displacements at Moss Landing During the 1989 Loma Prieta Earthquake: Center for Geotechnical Modeling, University of California at Davis, Davis, California, Report No. UCD/CGM-95/02.

Hamada, H., Isoyama, R., and Wakamatsu, K., 1995, The Hyogoken-Nambu (Kobe) Earthquake, Liquefaction, Ground Displacement and Soil Condition in Hanshin Area: Monograph, Association for Development of Earthquake Prediction , School of Science and Engineering, Waseda University and Japan Engineering Consultants, Ltd.

Youd, T.L. and Hoose, S.N., 1978, Historic ground failures in northern California triggered by earthquakes: U.S. Geological Survey Prof. Paper 993, 177 p.

PERMANENT GROUND DEFORMATION DUE TO NORTHRIDGE EARTHQUAKE IN THE VICINITY OF VAN NORMAN COMPLEX

Y. Sano[1]
T.D. O'Rourke[2]
and
M. Hamada[3]

[1] Civil Engineer, Konoike Construction Co. Ltd., Osaka, Japan
[2] Professor, Civil and Environmental Engineering, Cornell University, NY
[3] Professor, Department of Civil Engineering, Waseda University, Tokyo, Japan

ABSTRACT

The 1994 Northridge earthquake resulted in strong transient motion and large permanent ground deformation (PGD) and caused extensive damage to the City of Los Angeles water supply system. The Northridge earthquake provides a unique opportunity to evaluate earthquake effects on critical facilities, particularly the relationship among PGD, performance of water supply facilities, and site conditions.

In this paper, results from PGD assessments by means of control point surveys, air photo measurements, and ground failure observations in the vicinity of the Van Norman Complex are presented and discussed. In addition, PGD observed after both the Northridge and 1971 San Fernando earthquakes are compared.

INTRODUCTION

The Northridge earthquake resulted in strong transient motion and significant PGD in the form of tectonic movement and local ground deformation. Tectonic movement, which refers to regional displacements caused by deformation of the earth's crust, were distributed gradually over relatively large distances so that they imposed small to negligible strains on buried lifelines. In contrast, local ground deformation, which refers to displacements of non-tectonic origin associated primarily with liquefaction and landslide activity, generated relatively high levels of strain that, in some instances, caused failures of important lifelines. Investigations in the area near the intersection of Balboa Blvd and Rinaldi St, for example, indicate that local PGD was caused by liquefaction of alluvial sands (Holzer et al., 1996). Lateral movement at this location damaged a gas transmission and two water trunk lines (O'Rourke and Palmer, 1994).

The Northridge earthquake resulted in strong transient motion and PGD in many of the same places affected by the 1971 San Fernando earthquake. A case history of the San Fernando earthquake (O'Rourke et al., 1992) contains maps of PGD, surficial ground failure, and lifeline damage in the vicinity of the Van Norman Complex. The earlier work in connection with this study provides an unique opportunity for comparing PGD and water supply facility performance in response to two near-source earthquakes of similar magnitudes and fault rupture mechanisms at approximately the same locations.

This paper is focused on the assessment of PGD, including tectonic displacements and local ground deformation in the vicinity of the Van Norman Complex. It also compares PGD observed after the Northridge and San Fernando earthquakes.

As shown in Figure 1, the Van Norman Complex is located in the northwestern part of San Fernando Valley about 32 km from downtown Los Angeles. It is also located 12 km southwest and 11 km north of the 1971 San Fernando and the 1994 Northridge earthquakes epicenters, respectively. As shown in Figure 2, the Complex consists of major water supply facilities, including the Los Angeles Dam and Reservoir, Upper and Lower San Fernando Dams, filtration plants, backwash reclamation ponds, debris basins and retaining dams, and several important trunk lines (Davis and Bardet, 1995).

TECTONIC MOVEMENT DUE TO NORTHRIDGE EARTHQUAKE

Although the fault that ruptured during the Northridge earthquake did not break the ground surface, it nevertheless caused permanent displacements, referred to as tectonic movement. The tectonic movement consisted of uplift and lateral deformation of the northwest part of the San Fernando Valley and mountains

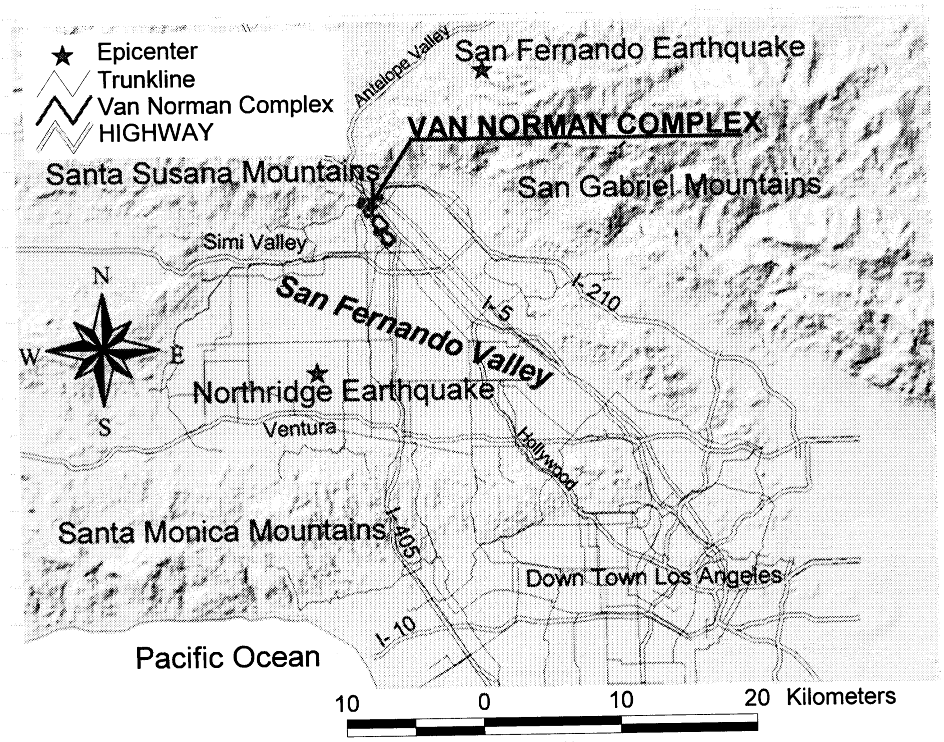

Figure 1 Location of Van Norman Complex

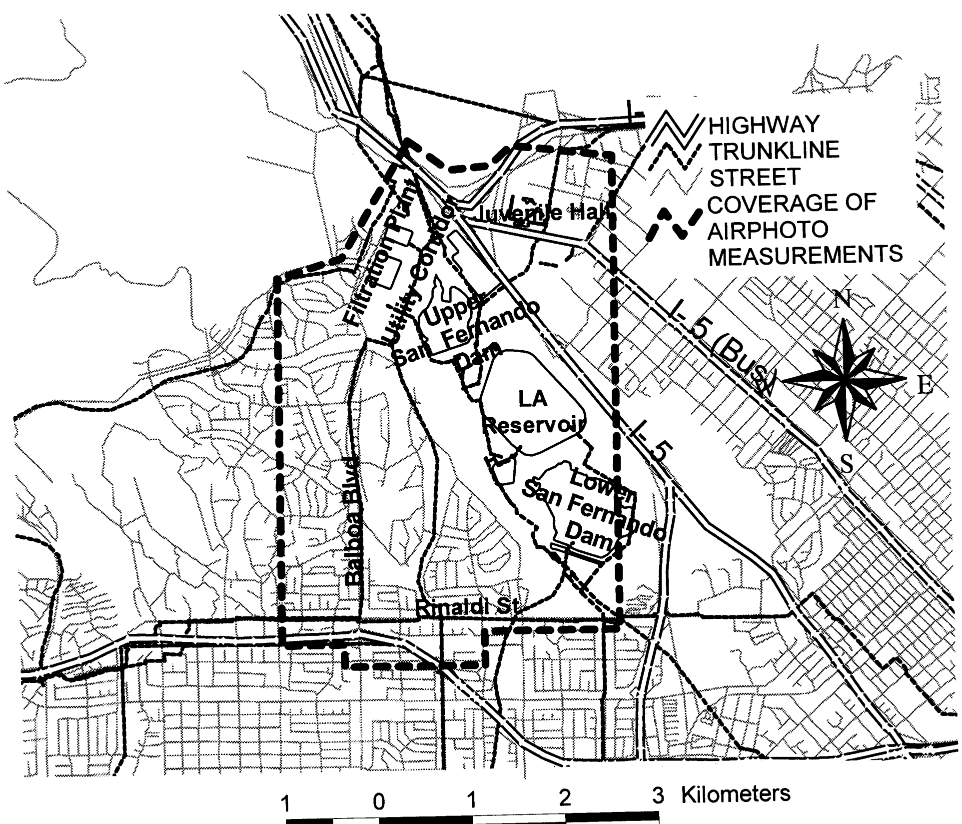

Figure 2 Van Norman Complex and Vicinity

immediately north of the epicentral region. As explained by Sano (1998), tectonic movement around the Complex was determined by evaluating the displacements of control points on bedrock and firm soils before and after the 1994 Northridge earthquake. The magnitudes and directions of tectonic movement were calculated by subtracting the pre-earthquake coordinates from the post-earthquake coordinates.

The survey data were collected from LADWP, Los Angeles Bureau of Engineering (LABE), Metropolitan Water District of Southern California (MWD), and the California Department of Transportation (Caltrans). Before the earthquake LADWP and LABE performed control point surveys by triangulation and transverse ground survey methods, except for a Global Positioning System (GPS) survey of 10 control points by LADWP. Caltrans and MWD performed pre-earthquake surveys using GPS, and all agencies performed post-earthquake surveys with the method. GPS results from LABE were only approximate, and were not used for estimating tectonic movements in this study.

The horizontal control survey data collected by the various agencies had to be converted to a consistent coordinate system. The pre-earthquake triangulation and traverse surveys of the LADWP and LABE were based on the North American Datum of 1927 (NAD27) using the State Plane Coordinate System (SPCS) from the Lambert Conformal Conic Projection for California, Zone VII. All post-earthquake GPS surveys were based on the North American Datum of 1983 (NAD83) for California, Zone V. The local conversion system developed by Davis (1996) was used for converting the coordinates in NAD27 to NAD83.

As shown in Table 1 and Figure 3, the tectonic movements in this area had approximately the same magnitude and direction. The mean value of horizontal tectonic movements is 23.4 cm and the mean direction is N99.3°E (clockwise 99.3° from North, or –9.3° from the East-West azimuth). The standard deviations associated with displacement and direction are less than 2 cm and 4°, respectively. The mean value of upward movements is 23.6 cm and its standard deviation is less than 5 cm. The east-trending movement is the result of south-dipping back thrusting fault movement beneath the northwestern San Fernando Valley. The amount and direction of horizontal and vertical movement in the vicinity of the Van Norman Complex agrees well with the GPS survey results reported by USGS/SCEC (1994).

LOCAL GROUND DISPLACEMENT DUE TO THE NORTHRUDGE EARTHUAKE

Air photo measurements before and after the Northridge earthquake were conducted to determine ground deformation by means of aero-triangulation with simultaneous bundle adjustment (Hasshu Co. Ltd., 1997). Aerial photographs on the scale of 1:24,000, taken on May 10, 1993, were used for the pre-earthquake measurements (2 courses, 6 pieces); aerial photographs on the scale of 1:12,000, taken on January 17 and

Table 1 Tectonic Movement at Control Points*

Point	Horiz. Disp.(m)	Vert. Disp. (m)	Dir (deg)
LAR10	0.234	0.23	-12.0
LAR20	0.227	0.28	-11.6
LAR30	0.228	0.29	-9.3
LAR40	0.237	0.20	-16.3
LAR50	0.251	0.15	-17.8
LAR100	0.258	0.20	-6.6
LAR110	0.267	0.25	-7.9
LAR120	0.233	0.19	-6.8
LAR140	0.248	0.23	-13.2
LAR150	0.239	0.27	-11.8
LAR160	0.234	0.20	-11.5
LAR170	0.246	0.18	-9.8
LAR210	0.237		0.0
LAR220	0.221	0.26	-1.3
LAR230(COB)	0.267	0.22	-10.1
LAR240	0.264	0.22	-9.6
LAR250	0.235	0.21	-5.9
LAR260	0.243	0.20	-8.3
LAR270	0.245	0.20	-9.2
Reservoir	0.211	0.15	-5.7
PAC C2	0.253	0.15	-16.5

Point	Horiz. Disp.(m)	Vert. Disp. (m)	Dir (deg)
PAC E2 ECC1	0.237		-11.2
SYL C11B	0.223		-3.6
SYL A12 RM1A	0.211	0.37	-11.5
North Axis (MWD)	0.218		-6.9
South Axis (MWD)	0.215		-8.8
N. Axis Prod	0.212		-7.6
10+30 Axis	0.219		-5.8
FALLS	0.216		-2.4
4042F	0.237		-10.9
4042G	0.232		-11.2
4042H	0.214		-12.2
4042J	0.215		-14.3
PAC D3B	0.257		-19.3
SYL E10B	0.199		-3.2
SYL E11B	0.245		-4.5
PBM 04-04770		0.22	
PBM 04-05740		0.37	
PBM 04-05761		0.34	
PBM 04-07425		0.31	
Average	0.234	0.236	-9.304
Standard Deviation	0.017	0.051	4.465

*Coordinates, Northing and Easting, are in NAD83. Horizontal displacement is in m and direction of horizontal displacement is in degrees from East-West azimuth. Degrees in the clockwise direction are reported as negative.

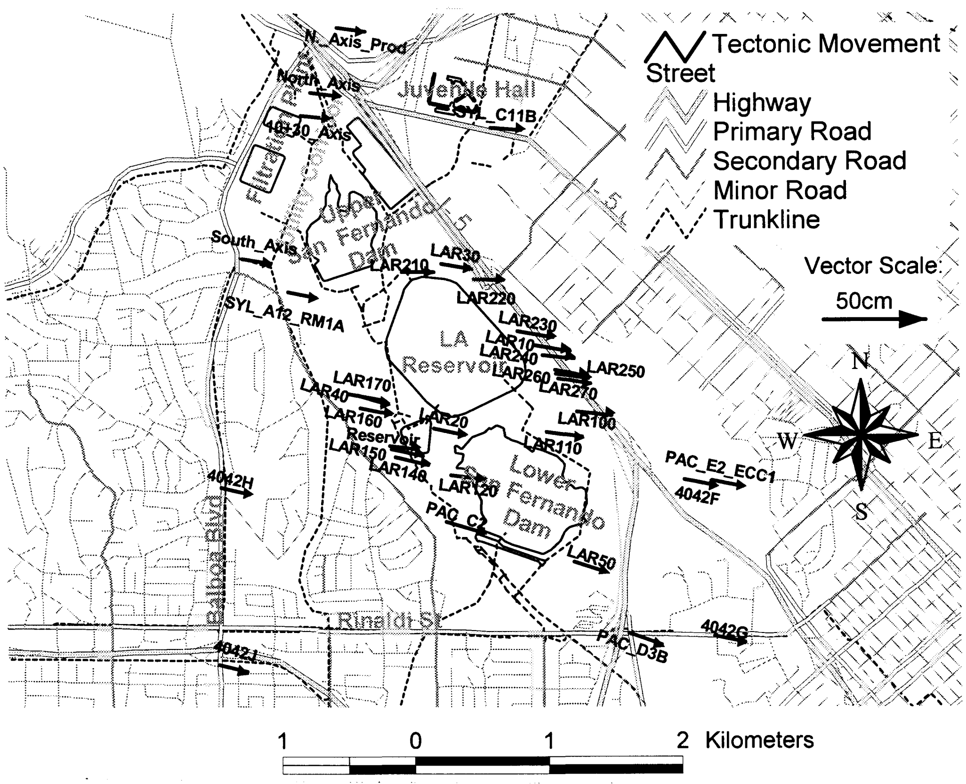

Figure 3 Tectonic Movement in the Vicinity of Van Norman Complex

21, 1994, were used for the post-earthquake measurements (4 courses, 16 pieces). Supplementary photographs at a scale of 1:6,000, taken on February 10, 1994, were used for the southwestern part of the region of interest, including the area around the intersection of Balboa Blvd. and Rinaldi St. (2 courses, 9 pieces). In Figure 2, the area covered by the measurements is shown by the thick broken line. The number of points measured was 1,010, including points around embankments in the Complex. The numbers of pre-earthquake horizontal and vertical, and post-earthquake horizontal and vertical control points that were used to determine measurement accuracy are 9 and 22, and 12 and 16, respectively. Relative accuracy is of greatest interest for horizontal displacement measurements It applies directly to the difference in vector coordinates from which the earthquake-induced movement is assessed. Table 2 shows the absolute accuracy of the coordinates from the measurements and the absolute and relative accuracy of displacement vectors.

Displacements caused by liquefaction and landslide mechanisms were assessed from air photos by means of photogrametric techniques described by Sano (1998). The displacements determined from air photo measurements were compared with the results of optical ground surveys at locations where both were available. For the preponderance of the data, there is favorable comparison between air photo and optical survey measurements, with the differences between these measurements within the relative accuracy of the air photo measurements.

Figures 4, 5, 6 and 7 show PGD from the air photo measurements. The vectors show the directions and magnitudes of PGD. The numbers in italics at the arrowheads show the displacement magnitudes in cm. The numbers at the vector tails are ID numbers, and the numbers in parentheses represent vertical displacements. PGDs at the Lower and Upper San Fernando Dams, utility corridor, and Balboa Blvd are discussed below.

Lower and Upper San Fernando Dams

Figure 4 shows the displacement vectors around the Lower San Fernando Dam calculated from the air photo measurements. The vectors with dotted lines show displacements on the downstream slope, calculated from a series of continuous coordinates. The vectors only show the displacement component perpendicular to the original profile because it is not possible to locate identical points both on the pre- and post-earthquake photographs.

The vectors indicate that the crest displaced slightly upstream, which agrees with the ground survey results (Bardet and Davis, 1996). Larger horizontal displacements were measured near the center of the berm than around the abutments. Air photo measurements show crest settlements of 20-70 cm, with maximum settlement near the center.

Table 2 Accuracy of the Airphoto Measurements

		Accuracy of coordinates	Accuracy of displacement vectors	
			Absolute	Relative
Horiz.	Pre-earthquake	0.299m	0.330m	0.197m
	Post-earthquake	0.140m		
Vert.	Pre-earthquake	0.323m	0.392m	0.326m
	Post-earthquake	0.222m		

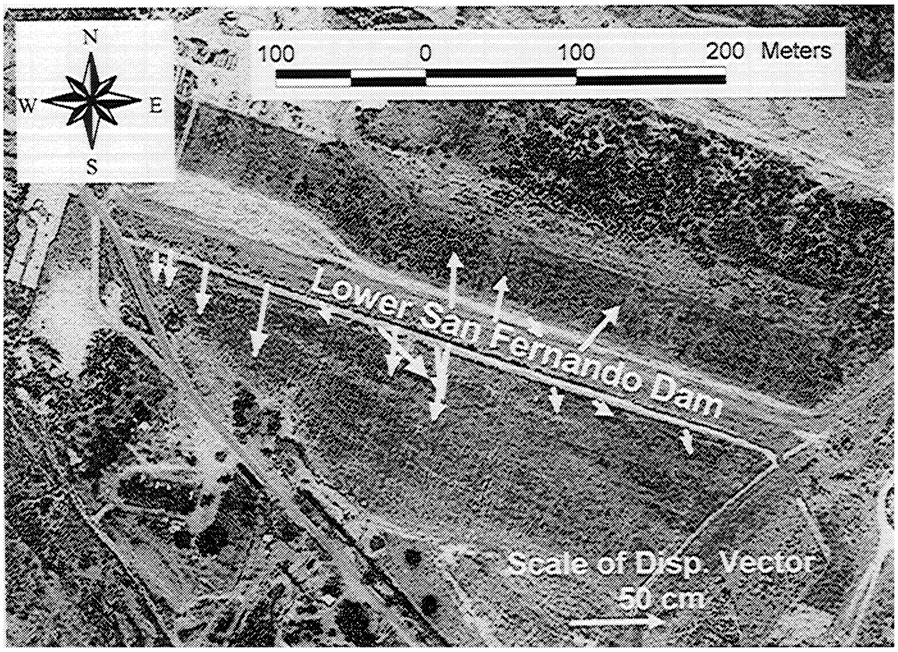

Figure 4 Permanent Ground Deformation Around Lower San Fernando Dam

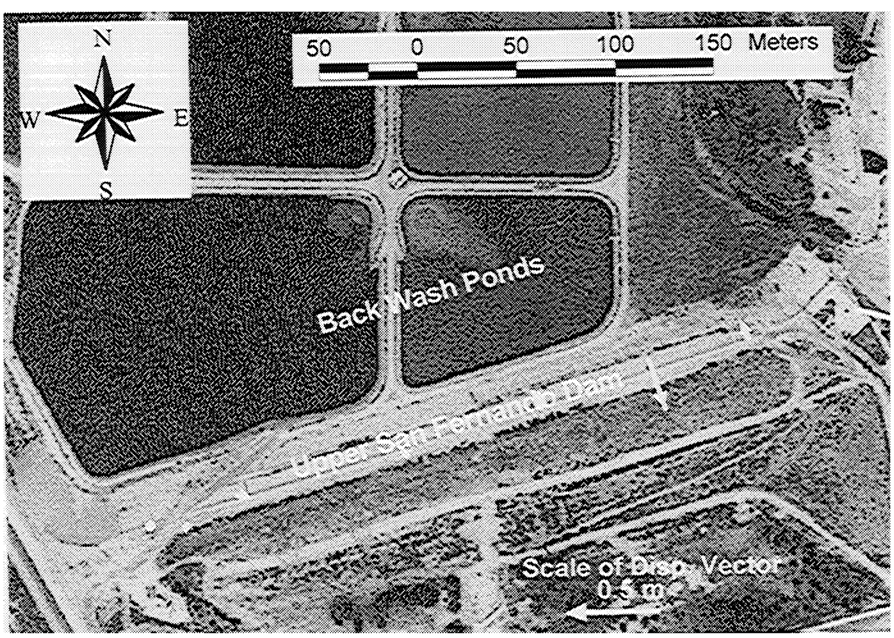

Figure 5 Permanent Ground Deformation Around Upper San Fernando Dam

Figure 5 shows the horizontal and vertical PGD around the Upper San Fernando Dam. The air photo measurements indicate that the crest of the dam displaced downstream as much as 30 cm. The maximum displacement downstream was measured at about 100 m left of center. The displacements on the crest relative to the left abutment are small, which is consistent with the survey records performed by LADWP (Bardet and Davis, 1996).

Utility Corridor

Figure 6 shows the displacement vectors around the utility corridor. The corridor is located near the centerline of embankments east of the Jensen Filtration Plant. The ground around and along the corridor displaced downslope. The air photos indicate that movement varied from 20 cm to 80 cm. The magnitude and direction of relative displacement from air photo measurements agree well with those from the ground survey by LADWP (1996).

The largest displacement vectors are located near prominent ground cracks. For example, the 84-cm displacement vector (ID = 1297) located near the parking lot of the Jensen Plant coincides with the 0.8 to 1.0 m-wide crack shown in Photo 1. The photo was taken during reconnaissance investigations shortly after the earthquake.

Large displacements were measured along the High Speed Channel located near the corridor and the tailrace. The displacement vectors show that the channel was widened by as much as 120-170 cm. This deformation only occurred to the channel itself, while the surrounding ground was not deformed to such a large extent. According to LADWP (1997), widening of the High Speed Channel in this area corresponds with the opening of large longitudinal cracks and separations of gunite overlay from the original liner. It should be noted that a 213-cm drainage pipe was constructed immediately beneath the deformed location along the High Speed Channel.

Balboa Blvd Area

PGD was observed in the area near Balboa Blvd and McLennan Ave from Lorillard St to Rinaldi St. This area slopes toward the south (toward Rinaldi St) at a grade of about 2-3 %. Figure 7 shows lateral and vertical movements in this area from the air photo measurements. Overall, the displacement vectors are oriented towards the south, in the direction of the slope. Compared with the relative displacements along Balboa Blvd evaluated by the ground survey records performed by LABE (1995), the magnitudes and direction from the air photo measurements and ground surveys are in good agreement.

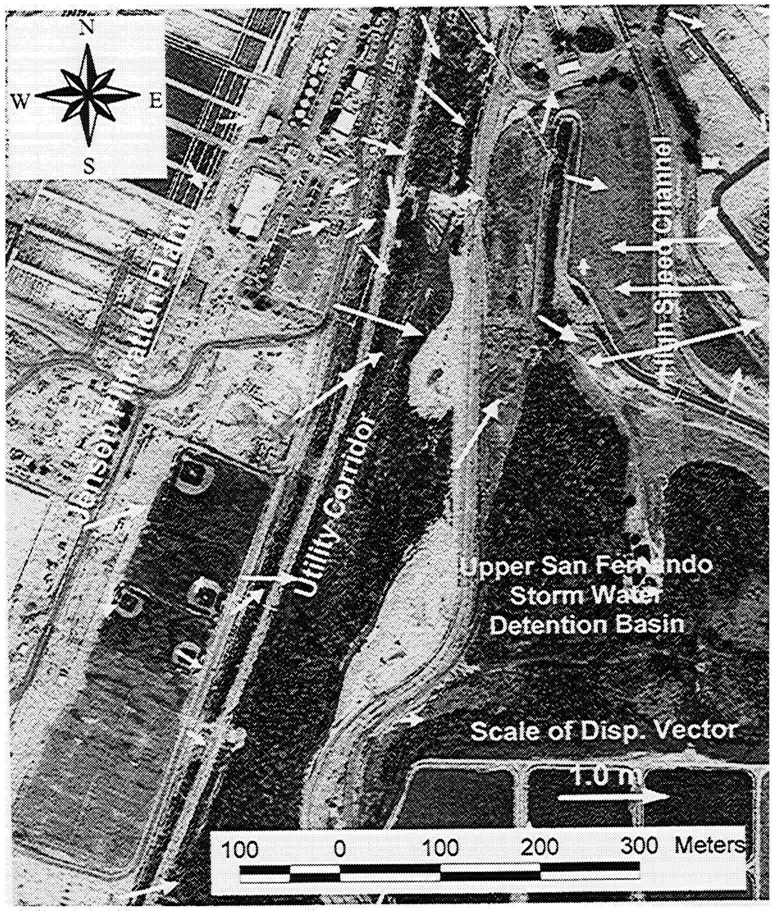

Figure 6 Permanent Ground Deformations Along Utility Corridor

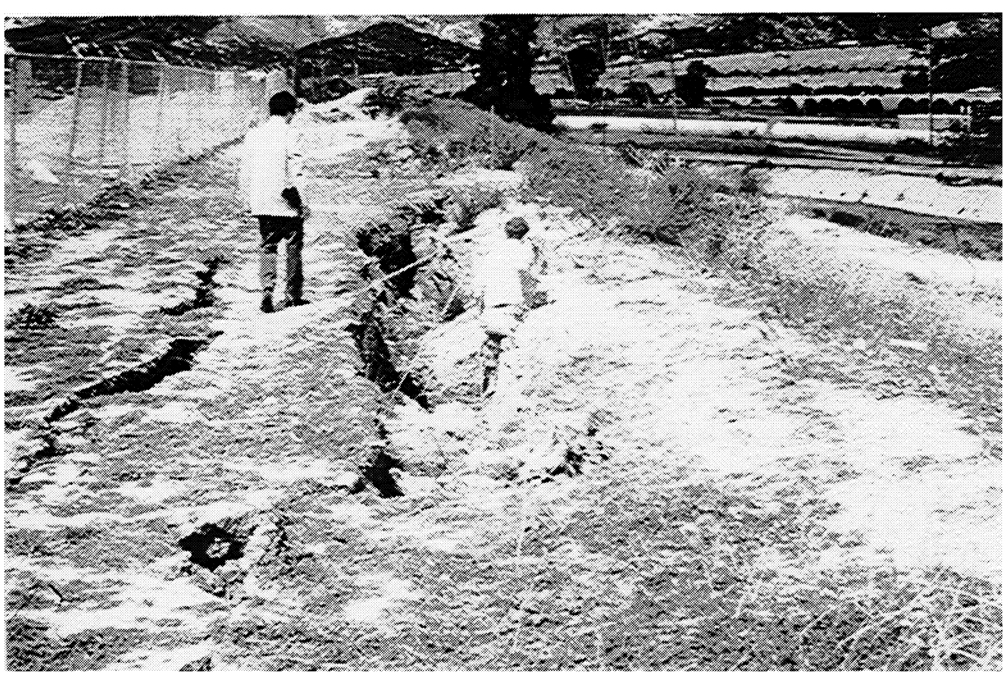

Photo 1 Tension Cracks near the Parking Lot of the Jensen Filtration Plant

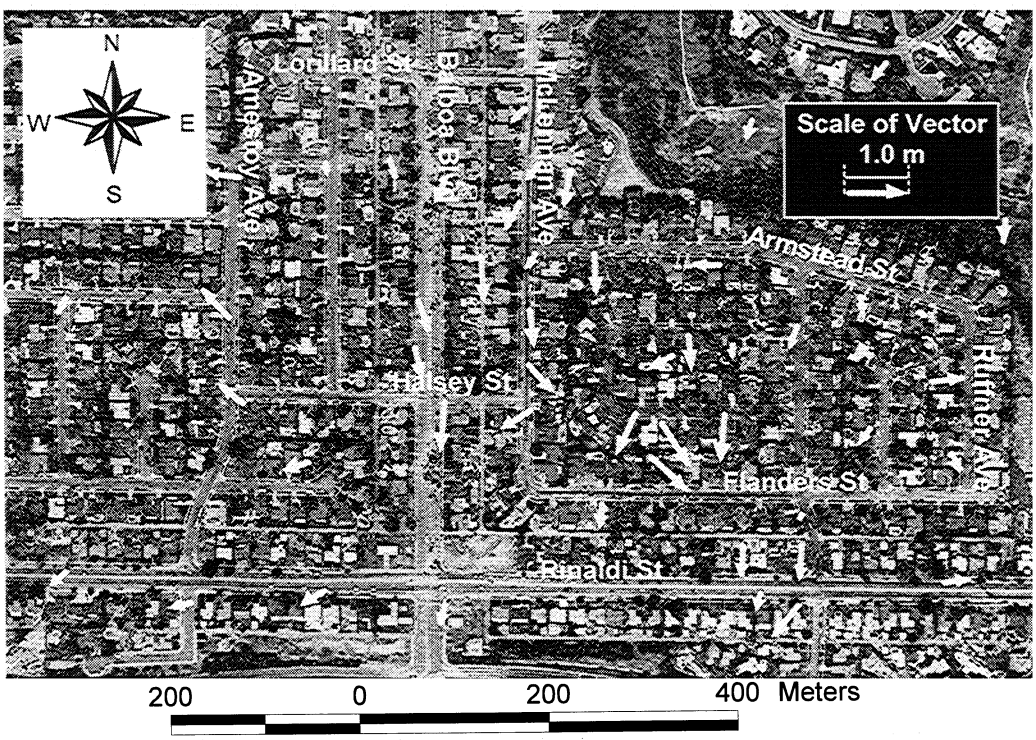

Figure 7 Permanent Ground Deformation Around Balboa Blvd

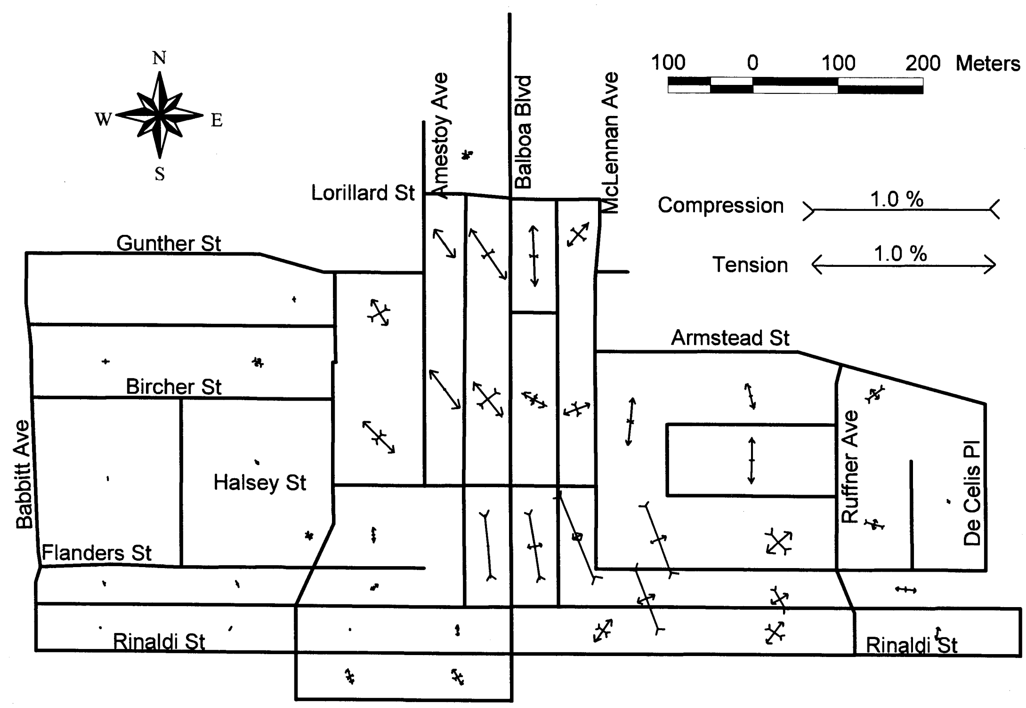

Figure 8 Principal Strains Calculated from Ground Survey

To show the spatial distribution of ground deformation in this area, ground strains were calculated from the survey records. Figure 8 shows the principal strain vectors calculated from the survey record performed by LABE (1995). Tensile strains, as high as 0.04 %, occurred in the area north of Halsey St from Amestoy Ave across Balboa Blvd to Ruffner Ave; compression strains, as high as 0.05 %, were concentrated in the area south of Halsey St from Amestoy Ave across Balboa Blvd to Ruffner Ave.

The spatial distribution of ground strain correlates well with the distribution of ground cracks that were mapped in this area (USGS, 1995). The area of relatively high tensile strain, north of Halsey St, coincides with the area of tension cracks; the area of relatively high compressive strain, south of Halsey St, coincides with the area of compressive cracks.

The soil profile extending 440-500m north of the intersection of Balboa Blvd and Rinaldi St. consists of a silty Holocene sand layer underlain by a Peistocene sand/gravel deposit. According to Holzer et al. (1996), the groundwater table is located within the lower 1-2m of the Holocene sand layer below the zone of observed large ground displacement. A rapid drop of the groundwater table coincides with the zone of compressive ground strain near the intersection of Balboa and Rinaldi, and the water table again falls below the base of the Holocene sands beneath the zone of tensile ground strain approximately 350 m north of the intersection.

COMPARISON OF PGD DUE TO THE NORTHRIDGE AND SAN FERNANDO EARTHQUAKES

The 1971 San Fernando and 1994 Northridge earthquakes were comparable in terms of depth of epicenters, earthquake magnitude, distance from their epicenters to the Van Norman Complex, and peak acceleration measured in the Complex. In 1971, however, much larger PGD and more extensive ground failure occurred, especially around the Lower and Upper San Fernando Dams, the utility corridor, and the San Fernando Valley Juvenile Hall.

According to field investigations by Seed et al. (1975), the crest of the Lower San Fernando Dam in 1971 moved in the upstream direction as much as 5m and the slide mass moved as much as 20 m. Settlement at the crest of the dam was about 12-15 m. In 1994, lateral movement and settlement of the dam were much smaller, as shown in Figure 4. The major differences in the dam are the geometry and soil properties of its reconstructed upstream portion and reductions in the level of the groundwater table. After drainage of the reservoir and reconstruction of the dam, the height of the crest was lowered as much as 10 m, the upstream slope was reconstructed with compacted soil, and the groundwater table was lowered as much as 25 m.

In 1971, the Upper San Fernando Dam also sustained liquefaction-induced PGD. At the centerline, the crest moved downstream about 1.5 m and settled vertically about 0.9 m (Seed et al., 1975). Longitudinal cracks were observed along almost the full length on the upstream slope of the dam. In 1994, lateral movement and settlement were much smaller as shown in Figure 5. Instead of impounding water with a maximum level at El 370 m as it did in 1971, the area upstream of the dam in 1994 was used as a debris basin with backwash pond levels at El 364 m.

The area around the utility corridor lies within an area affected by large liquefaction-induced ground movements during the 1971 San Fernando earthquake. Figure 9 presents selected displacements caused by the San Fernando earthquake from the air photo measurements reported by O'Rourke et al. (1992). They are superimposed on the map of displacement vectors for the Northridge earthquake (Figure 6), which were also obtained from the air photo measurements. As shown in this figure, in 1971 the measured lateral movements along the utility corridor were 2 to 3 m, perpendicular to the corridor axis. In 1994, however, the displacements were significantly smaller (in the range of 20-80 cm), even though the accelerations in this region may have been slightly higher during the Northridge event. LADWP (1996) reported that the groundwater table below the corridor was about 2 m lower, due to the draining of the Upper Van Norman Reservoir.

In the area surrounding the Juvenile Hall, large liquefaction-related PGD occurred in 1971. As reported by O'Rourke et al. (1992), in 1971 maximum lateral movements of 2 to 3 m were in the downslope direction. In 1994, however, displacements were significantly smaller even though this area was subjected to comparable levels of ground shaking in 1971. The diminished level of lateral and vertical movements appear to be related to reductions in the groundwater table of approximately 1-2m brought about by draining the Upper Van Norman Reservoir after 1971.

During the Northridge earthquake, PGD and ground failure recurred approximately in the same areas where liquefaction-induced large PGD occurred in 1971. The Complex experienced significantly larger liquefaction-induced PGD in 1971. The lower groundwater table after drainage of the Upper and Lower Van Norman Lakes appears to be a cause of the smaller PGD during the 1994 Northridge earthquake.

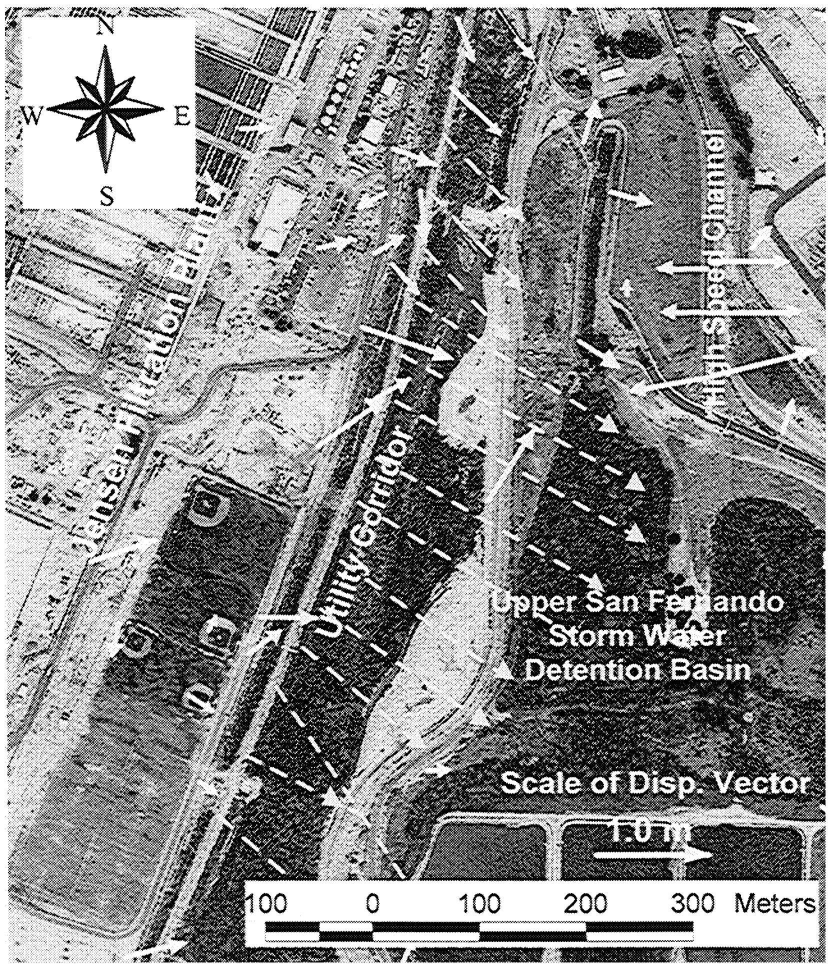

Displacement due to Northridge Earthquake

Displacement due to San Fernando Earthquake

Figure 9 Comparison of Displacements Caused by San Fernando and Northridge Earthquake Along Utility Corridor

SUMMARY

In this paper, results from ground failure observations and PGD assessments by means of control point surveys and air photo measurements in the vicinity of the Van Norman Complex are presented and discussed. In addition, the PGDs observed after both the Northridge and San Fernando are compared.

The results from regional control point surveys show that the tectonic movement in this region consists of approximately 20 cm of east trending horizontal displacement and approximately 20 cm of uplift. The results from airphoto measurements show that, near the intersection of Balboa Blvd and Rinaldi St in Granada Hills, maximum liquefaction-induced lateral spread of about 60-70 cm occurred and caused extensive tensile and compressive ground strains and cracks. The results from air photo measurements indicate that the crests of the Lower and Upper San Fernando Dams settled on the order 20-30 cm, and both the upstream and downstream slopes displaced downslope over 10 cm relative to the crest. Along the utility corridor, east trending large downhill local deformations were measured both from air photos and ground surveys, which is consistent with the large tensile ground crack immediately west of the corridor. The results from air photo measurements indicate downhill displacements of approximately 35 cm around the San Fernando Valley Juvenile Hall.

PGD and ground failure caused by the 1994 Northridge earthquake recurred nearly in the same areas with liquefaction-induced PGD in 1971. In 1994, however, the magnitudes of PGD were smaller even though much of this area was subjected to ground shaking at comparable, and perhaps stronger, levels than in 1971. The drainage of the Upper and Lower Van Norman Lakes after the 1971 earthquake and resulting lower groundwater tables appear to be significant, contributing factors to the smaller PGDs in the Complex after the 1994 Northridge earthquake.

ACKNOWLEDGEMENTS

The research reported in this paper was supported by the Multidisciplinary Center for Earthquake Engineering Research, Buffalo, NY. The authors express their deep gratitude to Mr. C.A. Davis of LADWP for his assistance in obtaining valuable information. Thanks also are extended to Dr. S. Toprak of USGS for his cooperation. The airphoto measurements were conducted by Mr. I. Yasuda of Hasshu Co., Ltd., Tokyo, Japan.

REFERENCES

Bardet, J.P. and C.A. Davis (1996). "Performance of San Fernando Dams during the 1994 Northridge Earthquake," Journal of the Geotechnical Engineering Division, Vol.122, GT.7, ASCE, New York, NY, pp.554-564.

Davis, C.A. (1996). LADWP Water Supply Division, personal communication.

Davis, C.A. and J.P. Bardet (1995). "Seismic Performance of Van Norman Water Lifelines," Lifeline Earthquake Engineering: Proceedings of the Forth US Conference; San Francisco, California, Monograph No.6, ASCE, New York, NY, pp.652-659.

Hasshu Co. Ltd. (1997). The 1994 Northridge Earthquake: the Report of Measurement of Permanent Displacement in San Fernando Valley, Hasshu Co. Ltd., Tokyo, Japan, 41p., 2 maps.

Holzer, T.L., M.J. Bennett, J.C. III Tinsley, D.J. Ponti, and R.V. Sharp (1996). "Causes of Ground Failure in Alluvium during the Northridge, California, Earthquake of January 17, 1994," Proceedings from the Sixth Japan-U.S. Workshop on Earthquake Resistant Design of Lifeline Facilities and Countermeasures Against Soil Liquefaction, M. Hamada and T.D. O'Rourke, Eds., Technical Report NCEER-96-0012, NCEER, Buffalo, NY, pp. 345-360.

Los Angeles Bureau of Engineering (LABE) (1995). Northridge Earthquake Horizontal Movement Study, Survey No. 23988, LABE, Los Angeles, CA.

Los Angeles Department of Water and Power (LADWP) (1996). Geotechnical Report on Earthquake Damage to the Granada Trunk Line at the Van Norman Complex, Water Supply Division, Report No. AX 500, LADWP, Los Angeles, CA.

Los Angeles Department of Water and Power (LADWP) (1997). Response of the High Speed and Bypass Channels to the 1994 Northridge Earthquake and Recommended Repairs, Water Supply Division, Report No. AX 215-47, DSR #68496, LADWP, Los Angeles, CA.

O'Rourke, T.D., B.L. Roth and M. Hamada (1992). "Large Ground Deformations and their Effects on Lifeline Facilities: 1971 San Fernando Earthquake," Case Studies of Liquefaction and Lifeline Performance During Past Earthquakes, Volume 2, United States Case Studies, T.D. O'Rourke and M. Hamada, Eds., Technical Report NCEER-92-0002, NCEER, Buffalo, NY, pp.3-1 – 3-85.

O'Rourke, T.D., and M.C. Palmer (1994). "Earthquake Performance of Gas Transmission Pipelines during the Northridge Earthquake," NCEER Bulletin, Vol. 8, No. 2, NCEER, Buffalo, NY, pp.1-5.

Sano, Y. (1998). "GIS Evaluation of Northridge Earthquake Ground Deformation and Water Supply Damage," M.S. Thesis, Cornell University, Ithaca, NY.

Seed, H.B., K.L. Lee,, I.M. Idriss and F.I. Makdisi (1975). " The Slides in the San Fernando Dams During the Earthquake of February 9, 1971," Journal of the Geotechnical Engineering Division, Vol. 101, GT7, ASCE, New York, NY, pp.651-688.

USGS (1995). "Map of Surface Cracks in the Granada Hills-Mission Hills Area Resulting From the January 17, 1994 Northridge Earthquake," Ground Deformation in Granada Hills and Mission Hills

Resulting from the January 17, 1994, Northridge, California, Earthquake, U.S. Geological Survey Open-File Report 95-62, USGS, Menlo Park, CA.

USGS/SCEC (Scientists of United States Geological Survey and Southern California Earthquake Center) (1994). "The Magnitude 6.7 Northridge, California, Earthquake of January 17, 1994," Science, Vol. 266, American Association for the Advancement of Science

FLUID DYNAMICS BASED PREDICTION OF LIQUEFACTION INDUCED LATERAL SPREADING LOAD

R. Uzuoka[1]
A. Yashima[2]
and
T. Kawakami[3]

1 - Research Engineer, Earthquake Disaster Mitigation Research Center, Hyogo, Japan
2 - Professor, Department of Civil Engineering, Gifu University, Gifu, Japan
3 - Associate Professor, Department of Marine Civil Engineering, Tokai University, Shimizu, Japan

ABSTRACT

This paper presents and verifies a numerical method to predict the lateral spreading of liquefied subsoil based on fluid dynamics. A numerical fluid dynamics code is modified to incorporate the Bingham viscosity with the minimum undrained strength of liquefied subsoil. The numerical method is applied to shaking table tests of a liquefied slope with an underground structure. As the result of simulations, the numerical method is found to reproduce the distribution of the lateral spreading load to the underground wall. The liquefied ground immediately after the lateral spreading was triggered can be modeled as a visco-plastic fluid.

INTRODUCTION

Lateral spreading induced by liquefaction is a phenomenon in which the ground is deformed largely in the lateral direction and leads to flow failure. Many structures were found to be damaged due to liquefaction and some were damaged due to lateral spreading. In the 1995 Hyogoken-Nambu earthquake, structures located along the coastlines and rivers especially suffered serious damage caused by lateral spreading (Hamada et al., 1996). Consequently, lateral spreading due to liquefaction began to be taken into consideration in design codes recently. As a result, a method to predict lateral spreading becomes necessary to make a rational seismic design for structures.

Ideally, an analytical method would be able to predict both permanent deformation and lateral spreading load from the initial state to post-liquefaction. However, under the current state of liquefaction analysis, it is difficult to reproduce the whole behavior of a subsoil during and after liquefaction completely by a single method. The constitutive models have not yet been examined as to whether they are able to describe post-liquefaction behavior in a large strain region. Moreover, it was confirmed that the load acting on the piles corresponded to the fluid load based on the results of the shaking table tests which examined the behavior of piles in lateral spreading ground (Hamada et al., 1992). Hence, an analytical method based on fluid mechanics may be promising to predict lateral spreading loads.

In general, the different analytical methods for post-liquefaction can be put in two categories : a method that treats liquefied ground as a solid, and a method treating liquefied ground as a fluid. However, these methods cannot perfectly describe the lateral spreading behavior. The method which assumes the liquefied soil as a solid has been used to predict the configuration of a permanent deformation. For example, Finn et al. (1991) proposed the finite deformation analysis which used the post-liquefaction stress-strain relation to consider the residual strength. This method can predict permanent deformation, however it cannot describe the flow behavior of liquefied soil during lateral spreading. On the other hand, the method which assumes the liquefied soil as a fluid has been used to predict the magnitude of a permanent deformation. Towhata et al. (1992) proposed a closed form solution of permanent displacement by means of the minimum energy principle. They assumed the liquefied subsoil to be a Bingham fluid, although the sample analyses were done with the zero strength. While these methods were designed to pay a special attention to a permanent deformation of the liquefied subsoil, the prediction of a lateral spreading load acting on the embedded structures has been out of scope.

For the post-liquefaction phenomenon, this paper proposes and verifies a numerical method that is able to predict both the flow process and lateral spreading load. The method models liquefied soil as a Bingham fluid in consideration of the viscous characteristics of the liquefied subsoil. The authors have already applied the proposed method to the shaking table tests without an underground wall. The proposed method was found to reproduce the flow velocity of liquefied ground (Uzuoka et al., 1998). In this study, we present numerical simulations for shaking table tests in which the lateral spreading load on an underground wall in the liquefied ground was measured.

ANALYTICAL METHOD

Modeling of Liquefied Soil

In this study we model the liquefied soil as a Bingham fluid which is one of the visco-plastic models in consideration of the minimum undrained strength. In a pure shear condition, the shear stress-shear strain rate relation of the Bingham model can be modeled by the following equation:

$$\tau = \eta\dot{\gamma} + \tau_{\min} \tag{1}$$

where τ is the shear stress, η is the yield viscosity coefficient, $\dot{\gamma}$ is the shear strain rate and τ_{min} is the minimum undrained strength. Figure 1 shows the shear stress-shear strain rate relation and the behavior of the liquefied soil in this model. This model makes the following assumptions for liquefied soil.

1. Lateral spreading or flow failure does not occur when the driving shear stress due to gravity is smaller than the minimum undrained strength. The liquefied soil behaves as a rigid body and does not deform.
2. Lateral spreading or flow failure occurs when the driving shear stress due to gravity exceeds the minimum undrained strength. The liquefied soil behaves as a fluid with a linear relation to the shear strain rate and deforms considerably.

Bingham models have been used in the deformation analyses for visco-plastic flow behavior like rapid landslides (Hungr, 1995), fresh concrete flow (Tanigawa and Mori, 1989).

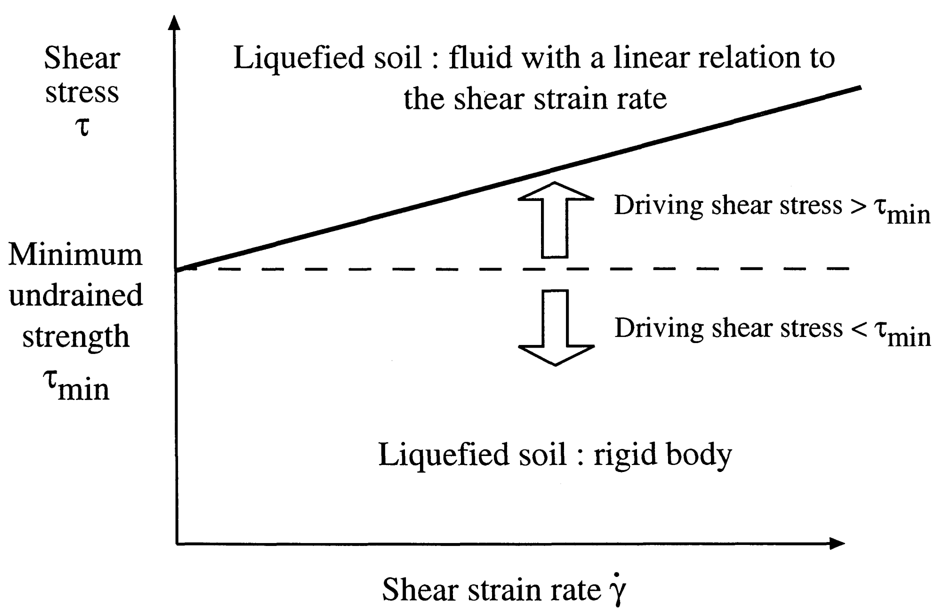

Figure 1. Behavior of liquefied soil by the Bingham model

Experimental data (Hamada et al. 1994, Kawakami et al., 1994) confirmed that the Bingham model is applicable to the behavior of liquefied soil. The experiments investigated the viscosity coefficient of liquefied soil from the viewpoint that the liquefied soil behaves as a fluid. Figure 2 summarizes the relation between the viscosity coefficient and the shear strain rate obtained by three different measurement methods. These results were based on the measurements of the flow displacement in the lateral spreading experiment, the load acting on a sphere moving in the liquefied soil and the viscometer. Enshunada sand was used in the lateral spreading experiments, while Toyoura sand was used in the other measurements. The relative density Dr of the samples ranged from 20% to 60%. As shown in Figure 2, the viscosity coefficient of liquefied soil decreases with increasing shear strain rate and clearly showed nonlinear characteristics. Figure 3 shows the shear stress - shear strain rate relations calculated from the experimental results with a viscometer of soils with different relative densities. The mobilized shear stress was related to the steady-state strength because the sand around the viscometer deformed largely. However, the steady-state at this experiment was different from the steady-state during monotonic loading test. The sand around the viscometer was kept to liquefy during this experiment, therefore this steady-state strength was smaller than common steady-state strength. The mobilized shear stress was related to the minimum undrained strength rather than the steady-state strength. The shear stress had a nonlinear relation with respect to the shear strain rate as shown in Figure 3. These relations have had intercepts which corresponded to the minimum undrained strength on the shear stress axis, and the shear stress slightly increases in a linear manner with respect to the shear strain rate. Therefore, these relations can be described by the Bingham model. The nonlinear characteristics as shown in Figure 2 were considered as the existence of the minimum undrained strength.

The yield viscosity coefficient is one of the parameters of the Bingham model. In the experimental results as shown in Figure 3, if there was no strain rate dependency, the shear stress should be constant, however, the shear stress slightly increased with increasing shear strain rate. The value of the slope which was the yield viscosity coefficient was very small, and was not significantly affected by the relative density of samples, and was of the order of 0.1 - 0.01 Pa•s. This value was a few orders of magnitude larger than the viscosity coefficient of water ($1.002 * 10^{-3}$ Pa•s at 20 °C).

The proposed model needs only two parameters; the yield viscosity coefficient and the minimum undrained strength. This is a great advantage in practical design. Figure 4 illustrates the behavior of the model in flow liquefaction and limited liquefaction (Castro, 1975; Robertson, 1993). This model would let us describe flow liquefaction behavior because strain-hardening behavior was not allowed and the deformation during lateral spreading will stop when the driving shear stress which decreases with the progress of deformation becomes equal to the minimum undrained strength as shown in Figure 4. The model cannot exactly describe limited liquefaction behavior because the model did not take strain-hardening behavior after a quasi-steady state into consideration. In the actual phenomenon, the soil stiffness recovered with the increase in the shear strain, then the soil lead to the steady state. The flow deformation will stop when the driving shear stress is still greater than the minimum undrained strength as shown in Figure 4. Therefore, in the case of limited liquefaction, the model overestimates the deformation and gives the maximum deformation which can be predicted.

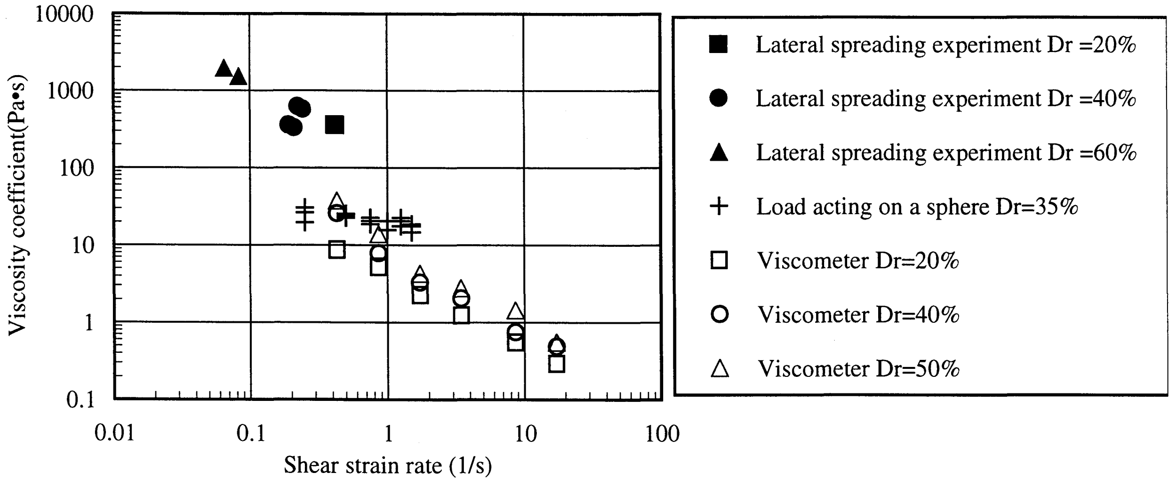

Figure 2. Viscosity coefficient of liquefied soil (Hamada et al., 1994, Kawakami et al., 1994)

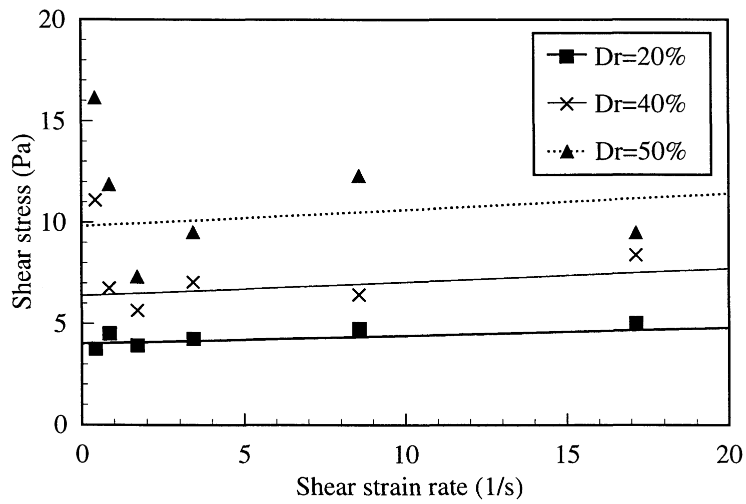

Figure 3. Shear strain rate and shear stress relations of liquefied soil by viscometer (Kawakami et al., 1994)

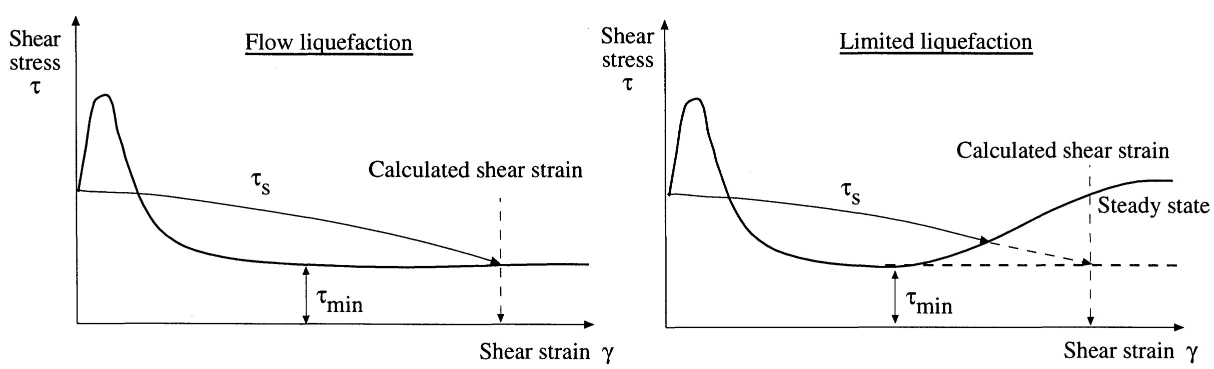

Notes : τ_s : Driving initial shear stress τ_{min} : Minimum undrained strength

Figure 4. Behavior of the model in flow liquefaction and limited liquefaction

Constitutive Equations

Fluid dynamics analysis with the Eulerian description is more advantageous for a large deformation problem during lateral spreading than solid analysis with the Lagrangian description. Navier-Stokes equations in which Newtonian viscosity is incorporated have been widely used in fluid dynamics. We modified an existing non-Newtonian fluid analysis code to treat the Bingham model by introducing the equivalent viscosity. The stress - strain rate relation of Newtonian incompressible fluids can be expressed by the following equation:

$$\sigma_{ij} = -p\delta_{ij} + 2\eta' \dot{e}_{ij} \tag{2}$$

where σ_{ij} is the stress tensor, p is the hydraulic pressure, η' is the equivalent viscosity coefficient and $\dot{e}_{ij}$ is the deviatoric strain rate tensor. In this analysis, we treated the liquefied soil as an incompressible Bingham fluid and expressed the Bingham viscosity by the equivalent Newtonian viscosity. We assumed the equivalent viscosity coefficient as follows:

$$\begin{cases} \eta' = \eta + \dfrac{\tau_{\min}}{2\dot{\gamma}} & if \quad \dot{\gamma} \neq 0 \\ \eta' = \infty & if \quad \dot{\gamma} = 0 \end{cases} \tag{3}$$

$$\tau_{\min} = R_{\min} \cdot p \tag{4}$$

$$\dot{\gamma} = \sqrt{\frac{1}{2} \dot{e}_{ij} \cdot \dot{e}_{ij}} \tag{5}$$

where R_{min} is the minimum undrained strength ratio and $\dot{\gamma}$ is the second invariant of the deviatoric strain rate. When $\dot{\gamma}$ is zero at the start of analysis, the equivalent viscosity coefficient is set to be a large value ($\eta' = 1.0*10^8$ Pa•s). In this unsteady analysis, the equivalent viscosity coefficient is treated as a constant in each calculation step and is updated step by step.

The reason why we used the minimum undrained strength ratio rather than the minimum undrained strength was that we assumed that the minimum undrained strength ratio was independent of the confining pressure. The minimum undrained strength depended on the initial effective confining pressure (e.g. Ishihara, 1993). Therefore, we assumed that the equivalent viscosity coefficient was defined by using the minimum undrained strength ratio which was independent of the confining pressure. However, it should be noted that the minimum undrained strength ratio R_{min} of equation (4) was the ratio of the minimum undrained strength to the total confining pressure. In a fluid analysis, the hydraulic pressure corresponded to the total confining pressure of liquefied soil since the liquefied subsoil was assumed to be one phase material of the fluid.

Field Equations

The field equations can be derived from the theory of fluid dynamics. The general equations consist of the conservation of mass, momentum and energy. The material is considered as incompressible and is not affected by temperature, so the energy equation need not to be considered. For incompressible material, the continuity equation is denoted as:

$$\frac{\partial v_i}{\partial x_i} = 0 \tag{6}$$

where v_i is the velocity vector. The momentum balance equation is

$$\rho \frac{Dv_i}{Dt} = \frac{\partial \sigma_{ij}}{\partial x_j} + \rho g_i \tag{7}$$

where ρ is the mass density, D is the Lagrangian derivative and g_i is the gravity acceleration vector. Substituting the constitutive equation (2) into the momentum balance equation (7) produces the well-known Navier-Stokes equations as follows:

$$\frac{Dv_i}{Dt} = -\frac{1}{\rho}\frac{\partial p}{\partial x_i} + \nu \frac{\partial}{\partial x_j}\left(\frac{\partial v_i}{\partial x_j}\right) + g_i \tag{8}$$

where ν (= η'/ρ) is the kinematic viscosity.

Numerical Scheme

The numerical code utilized SIMPLE (Semi Implicit Method for Pressure Linked Equation) method (Patanker and Spalding, 1972) in order to solve the Navier-Stokes equations. SIMPLE is based on a finite volume method on a staggered grid of the governing equations. The finite volume method discretises the integral form of the governing equations, in contrast to the finite difference method, which is usually applied to discretise the differential form of the governing equation. The integral form is obtained by the weighted residual method .

We must pay attention to free surface treatment in fluid dynamics analysis with Eulerian description in order to predict the surface displacement during lateral spreading. The numerical code used the Volume of Fluid (VOF) method (Hilt and Nichols, 1981) to express a free surface. The VOF method is different from the Marker and Cell (MAC) method (Harlow and Welch, 1965). The MAC method is a typical method for free surface treatment. It employs a set of massless marker particles embedded in the fluid. These markers move with the velocity field. The cell is flagged as full if it contains a marker, or empty if not. For instance, the surface cell contains a marker but the neighboring cell in the atmosphere is empty. The VOF method uses the state function value which is one if the cell is full and zero if the cell is empty, compared to a marker particle in the MAC method. In the VOF method, the free surface is described by the fluid volume balance which satisfies the continuity condition on the free surface, on the other hand, in the MAC method, the free surface is described by the marker movement which satisfies the kinematic condition.

SIMULATION OF LATERAL SPREADING LOAD

Shaking Table Tests with an Underground Wall

The lateral spreading load on an underground wall in the liquefied ground measured by Kawakami (1996) is simulated. In this experiment, after the inclined model ground was liquefied by shaking, measurements of the earth pressure on the underground wall were carried out during lateral spreading. The plane and side views of the soil container with the underground wall model are shown in Figure 5. The underground wall was made of vinyl chloride. According to the measured earth pressure and the stiffness of the underground wall, we calculated the displacement at the top of the wall assuming that the wall acted like a cantilever. As a result, the displacement was about $1.0*10^{-4}$ cm. In the experiments, if the deformation of the underground wall was very small, then it was considered to be rigid. The model ground was prepared in the inclined soil container using the boiling method to set up a homogeneous loose condition. The relative density of the ground was about 50%. The model ground was vibrated in the direction of the shorter side of the soil container in a sinusoidal motion of about 200 gal acceleration. Therefore, the effect of the vibration on the ground movement and the earth pressure could be neglected. The base excitation was continued until the ground surface became horizontal. Measurements of the earth pressure on the underground wall, the ground surface displacement and the excess pore water pressure in the ground were carried out. The location of the earth pressure gauges on both the upstream and downstream sides of the underground wall is shown in Figure 5. The depths of the earth pressure gauges are GL-50 mm, GL-200 mm, and GL-350 mm respectively.

Several kinds of experiments were carried out under varying conditions of ground surface gradient, water table depth and so on. In this paper, we simulate two experimental cases in which the ground surface gradients are 4% and 2% and the water table was at ground surface at the right edge of the soil container as shown in Figure 5. The time histories of the earth pressure on E4, E5 and E6 (at the top, middle and bottom in the central row on the upstream side of the underground wall) are shown in Figure 6 as an example of the experimental results. The ground surface gradient is 4% in this case. The total stress lines in Figure 6 are calculated by the product of the depth and the saturated unit weight of 18.03 kN/m^3. At each depth, the model ground completely liquefied and began to flow about five seconds after the vibrations began. Then, the peak earth pressures were generated in several seconds and decreased gradually. Other experimental results will be described in comparison to the following simulated results.

Analytical Conditions

In this simulations, we used the same parameters for the liquefied soil as the simulation for the shaking table tests without underground wall (Uzuoka et al, 1998) because the conditions of the model ground in both experiments were almost the same. The parameter sets could reproduced the ground flow velocity measured in the experiments. The yield viscosity coefficient η was 1.0 Pa•s and the minimum undrained strength ratio R_{min} was 0.025.

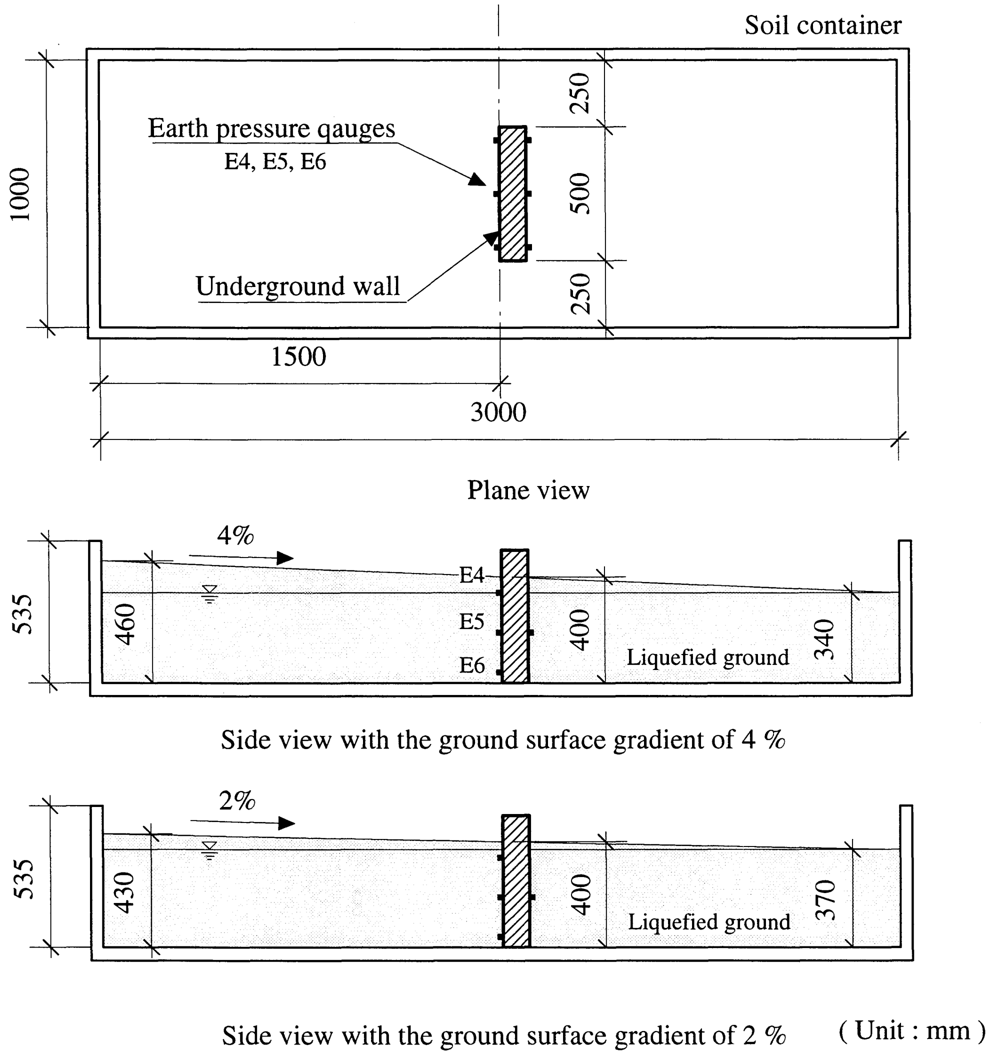

Figure 5. Plane and side views of the soil container with the underground wall model (Kawakami, 1996)

Figure 7 shows a three-dimensional numerical model with a ground surface gradient of 4%. The finite difference grid is 2.5 cm pitch in all directions. The number of cells is 96,000 (= 120*40*20). The number of free degrees for pressures is 96,000, that for velocities is 296,000 (= 121*40*20+120*41*20+120*40*21), and the total degrees of freedom are 392,000. The analytical domain was the whole soil container and the VOF value was allocated in the initial ground area with a gradient of 4%. The underground wall area was outside the calculation area, and the structure was treated as a rigid body in the analysis. The locations of the cells in which the pressures were output roughly corresponded to these of the earth pressure gauges as shown in Figure 5. The boundary conditions of the surfaces at the soil container walls and the underground wall were non-slip boundaries. This analysis targeted the soil behavior after the soil completely liquefied (after about 15 seconds in Figure 6). The simulations were carried out during the 5 seconds after complete liquefaction and did not consider the dissipation of the excess pore water pressure. The calculation time increment was updated in each calculation step to satisfy the stability condition. The stability condition was judged in each cell and each direction by the following equation:

$$\frac{v_i \cdot \Delta t}{\Delta x} \leq 0.1 \tag{9}$$

where Δt is the calculation time increment, Δx is the difference grid pitch. For all cells, the minimum Δt is set to the time increment for next calculation step. The simulations incorporated gravity as the only external force and did not consider the vibration force because its direction was perpendicular to the ground slope. We assumed that the whole ground was completely liquefied neglecting the upper partially saturated area. Therefore, the body force in the ground could be calculated by the saturated unit weight of 18.03 kN/m^3. The initial stress condition was calculated by assuming a large equivalent viscosity coefficient ($\eta' = 1.0 * 10^8$ Pa•s) at the start of computation.

Simulation Results and Discussion

Time history of the lateral spreading load on the underground wall
(for a ground surface gradient of 4%)

Figure 8 shows the simulated time histories of pressure at E4, E5 and E6 in the case where the ground surface gradient is 4%. The pressures at 0 seconds in Figure 8 correspond to initial total stress of the liquefied soil. Therefore, Figure 8 corresponds to the earth pressure histories only in the part which exceeds the total stress line in Figure 6. At each depth, the pressure reaches the peak value about 1.7 seconds after the start of the analysis (about 16.7 seconds in Figure 6). This tendency agrees with the experimental results that the earth pressure reached the peak value at about 18 seconds. Therefore, it is noted that the lateral spreading load will reach its peak value several seconds after the start of lateral spreading.

After the simulated pressure reaches the peak value, it decreases immediately and reaches a constant value after 3.0 seconds when the ground movement stops. However, the experimental pressures did not decrease immediately as shown in Figure 6. After reaching its peak value, the pressure continued to exceed the total stress line for several seconds. This tendency was observed at the upper side of the underground wall especially. According to the observation during the experiment, the soil close to the wall recovered a stiffness earlier than the other parts of the ground surface. The ground surface movement observed by the video recorder almost stopped within 20 seconds in the experiments. Thus, the phase transformation from fluid to solid gradually occurred with the progress of the flow deformation. However, the proposed model could not reproduce the recovery of soil stiffness after liquefaction as mentioned above. We should modify the model by taking a stiffness recovery into consideration, in order to discuss the soil behavior after the pressure reaches the peak value. The difference in the flow duration between the experiments and the simulations should be examined in the future.

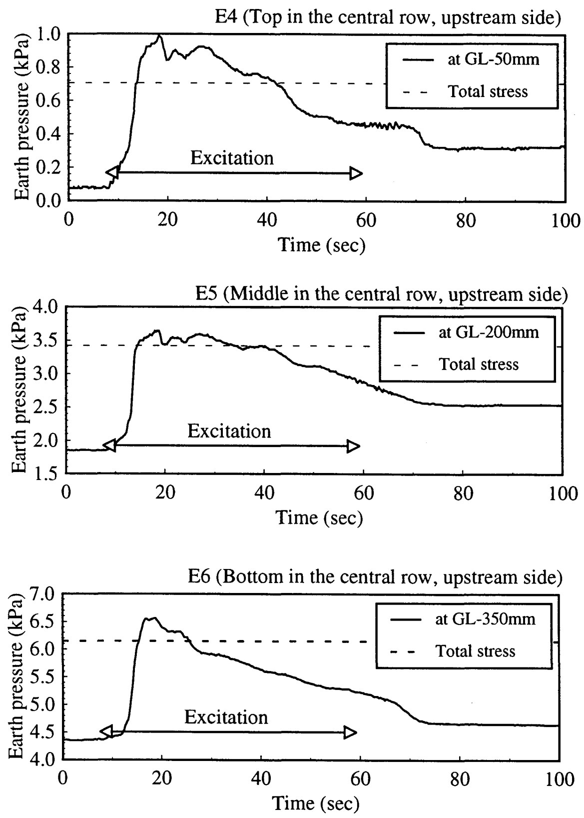

Figure 6. Experimental time histories of the upstream side pressure on the underground wall (Kawakami, 1996)

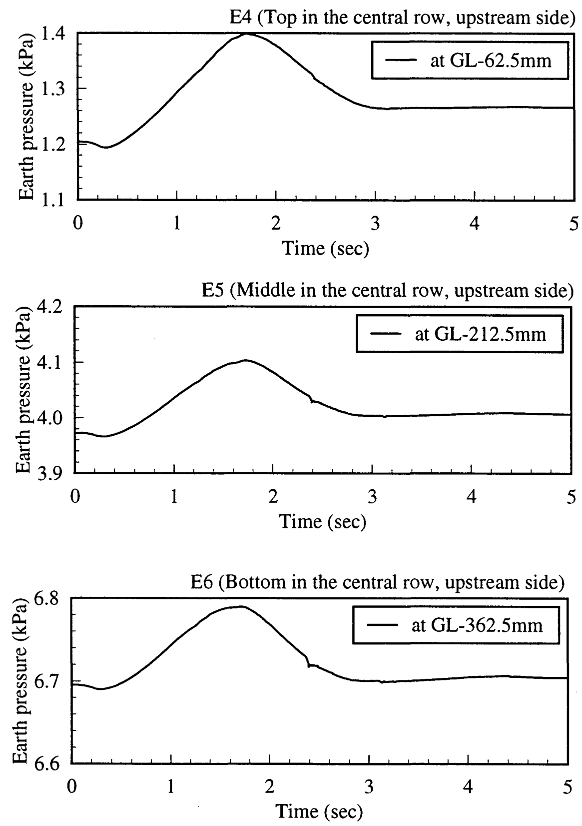

Figure 8. Simulated time histories of the upstream side pressure on the underground wall

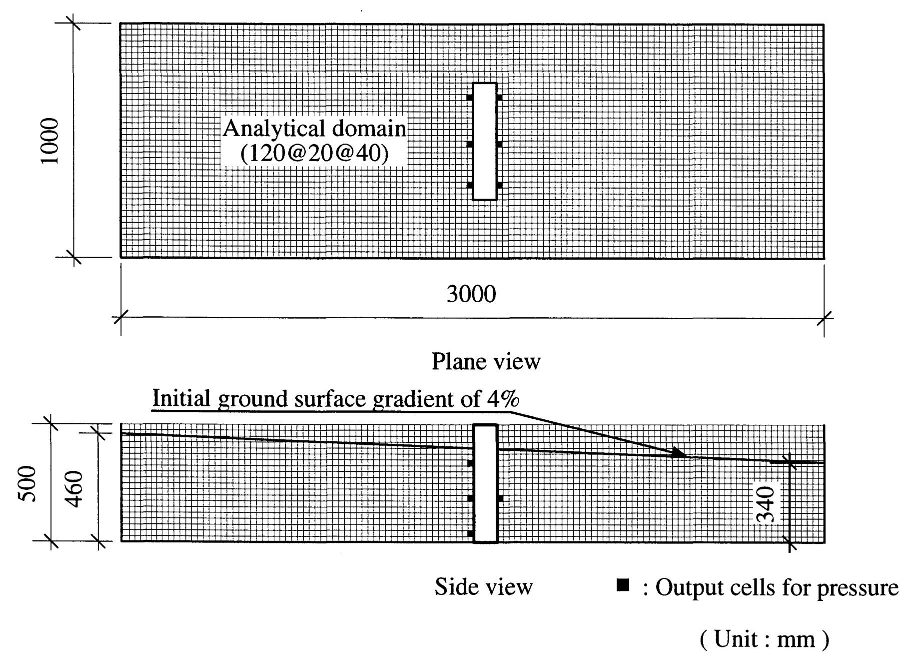

Figure 7. Three-dimensional numerical model with the ground surface gradient of 4%

Flow velocity and ground surface configuration around the underground wall

Figure 9 shows the simulated flow velocity vectors and ground surface configuration around the underground wall. The line contour shows the relative height of the ground surface. The value of 1.00 corresponds to the height of 412.5 mm, and the value of 0.00 corresponds to 387.5 mm. The ground behind the underground wall (up stream side) heaves while the ground in front of the wall (down stream side) sinks. The vectors show the magnitude and direction of the flow velocity. The ground flows through the space between the underground wall and the soil container and the large velocity is generated there.

Distribution of the lateral spreading load in the direction of depth

Figure 10 shows the simulated ratio of the peak pressure to the total stress on the upstream side of the underground wall for a ground surface gradient of 4% and 2% compared to the experimental one. The experimental peak pressure was the mean value of the peak pressure measured in several experimental cases under similar conditions. The simulated peak pressure is the peak value in the cell at the center row of the underground wall. The simulation reproduces the experimental tendencies very well in both cases. It should be noted that the lateral spreading load decreases with the increase in the depth and becomes equal to the total stress at the bottom of the liquefied layer. The lateral spreading load depends on the initial ground surface gradient , i.e., the initial driving shear force.

These results show that the simulations for the lateral spreading load agree with the experimental results very well except for the time history of the lateral spreading load. Both of the experimental and simulated results showed that the lateral spreading load reached the peak value at a few seconds after the ground completely liquefied and began to flow. In addition to these results, the lateral spreading load decreased with the increase in the depth and became equal to the total stress at the bottom of the liquefied layer. Therefore, the liquefied ground can be modeled as a visco-plastic fluid immediately after the lateral spreading was triggered based on these results.

CONCLUSIONS

This paper presented and verified the numerical method based on fluid dynamics to predict lateral spreading due to liquefaction. We used the equivalent viscosity to model the Bingham fluid which has the minimum undrained strength of liquefied soil in the unsteady viscous fluid analysis. We applied the model to lateral spreading experiments with an underground wall. As a result, the simulations for the lateral spreading load agreed with the experimental results very well except for the time history of the lateral spreading load. Therefore, the liquefied ground immediately after the lateral spreading was triggered can be modeled as a visco-plastic fluid.

ACKNOWLEDGMENTS

The authors would like to thank Professor Fusao Oka of Kyoto University for invaluable discussions throughout the research, Professor Kyoji Sassa of the Disaster Prevention Research Institute of

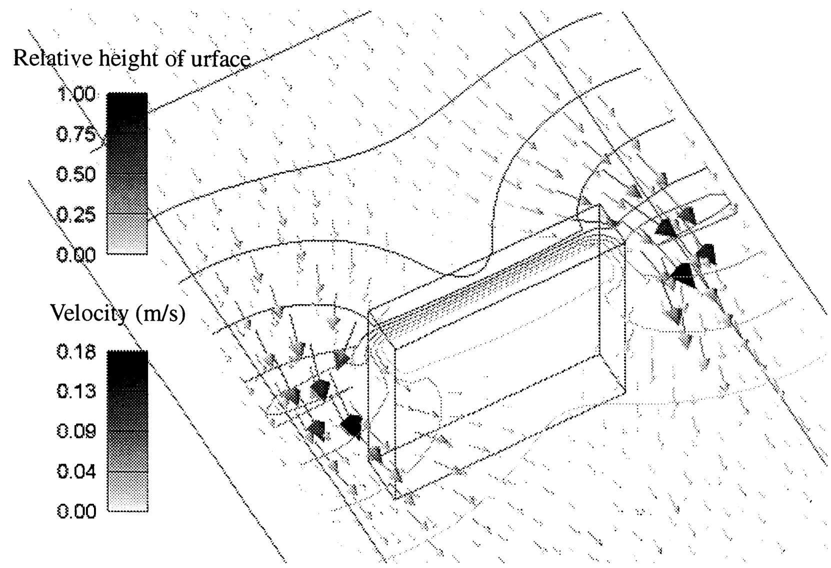

Figure 9. Simulated flow velocity and ground surface around the underground wall

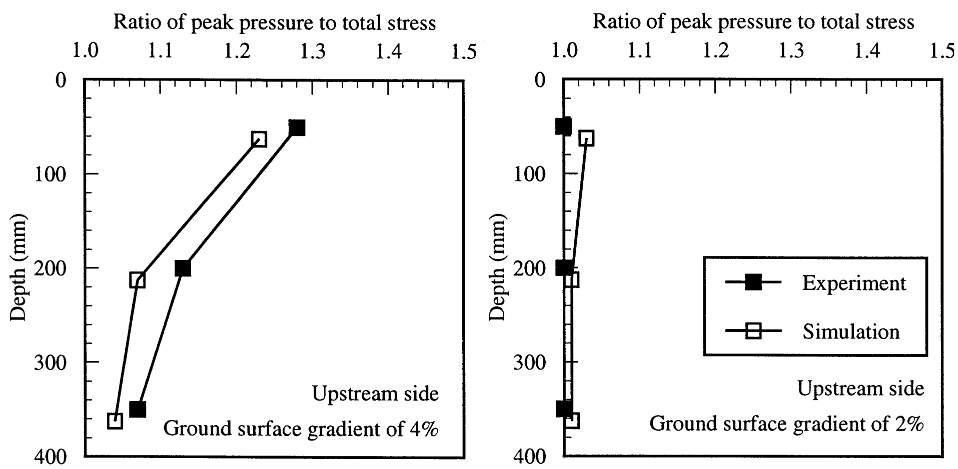

Figure 10. Ratio of the peak pressure to the total stress

Kyoto University for providing the materials on rapid landslides, Professor Hideo Sekiguchi also of the Disaster Prevention Research Institute of Kyoto University for invaluable discussions about the lateral spreading mechanism and Professor Yuichiro Fujita of Gifu University for helpful suggestions about the analysis of fluid dynamics.

REFERENCES

Castro, G., "Liquefaction and cyclic mobility of saturated sands", Journal of the Geotechnical Engineering Division, ASCE, Vol.101, No.GT6, pp.551-569, 1975.

Finn, W. D. L., Yogendrakumar, M., Ledbetter, R. and Yoshida, N., "Analysis of liquefaction induced displacements", Proceedings of 7th International Conference on Computer Methods and Advances

in Geomechanics, pp. 913-921, 1991.
Hamada, M., Ohtomo, K., Sato, H. and Iwatate,T., "Experimental study of effects of liquefaction-induced ground displacement on in-ground structures", Proceedings from the Forth U.S.-Japan Workshop on Earthquake Resistant Design of Lifeline Facilities and Countermeasures Against Soil Liquefaction, Technical Report NCEER-92-0019, pp. 481-492, 1992.
Hamada, M., Sato, H. and Kawakami, T., "A consideration of the mechanism for liquefaction-related large ground displacement", Proceedings from the Fifth U.S.-Japan Workshop on Earthquake Resistant Design of Lifeline Facilities and Countermeasures Against Soil Liquefaction, Technical Report NCEER-94-0026, pp. 217-232, 1994.
Hamada, M., Isoyama R. and Wakamatsu, K., "Liquefaction-induced ground displacement and its related damage to lifeline facilities", Soils and Foundations, Special Issue on Geotechnical Aspects of the January 17 1995 Hyogoken-Nambu Earthquake, pp. 81-97, 1996.
Harlow, H. and Welch, J. E., "Numerical calculation of time-dependent viscous incompressible flow of fluid with free surface", Phys. Fluids, Vol.8, pp.2182-2189, 1965.
Hilt, C. W. and Nichols, B. D., "Volume of fluid method for the dynamics of free boundaries", J. Comp. Phys., Vol.39, pp.201-225, 1981.
Hungr, O., "A model for the runout analysis of rapid flow slides, debris flows and avalanches", Canadian Geotechnical Journal, Vol.32, pp.610-623, 1995.
Ishihara, K., "Liquefaction and flow failure during earthquakes", Geotechnique, Vol.43, No.3, pp.351-415, 1993.
Kawakami, T., Suemasa, N., Hamada, M., Sato, H. and Katada, T., "Experimental study on mechanical properties of liquefied sand", Proceedings from the Fifth U.S.-Japan Workshop on Earthquake Resistant Design of Lifeline Facilities and Countermeasures Against Soil Liquefaction, Technical Report NCEER-94-0026, pp. 285-299, 1994.
Kawakami, T., "Experimental study on coutermeasures against liquefaction-induced latarel ground movement by in-ground wall", Proceedings from the Sixth U.S.-Japan Workshop on Earthquake Resistant Design of Lifeline Facilities and Countermeasures Against Soil Liquefaction, Technical Report NCEER-96-0012, pp.477-486, 1996.
Patanker, S. V. and Spalding, D. B., "A calculation procedure for heat, mass and momentum transfer in three-dimensional parabolic flows", International Journal of Heat Mass Transfer, Vol.15, pp.1787-1806, 1972.
Robertson, P. K., "Design considerations for liquefaction", Proceedings of Thirteenth International Conference on Soil Mechanics and Foundation Engineering, Vol.5, pp. 185-188, 1994.
Tanigawa, Y. and Mori, H., "Analytical study on deformation of fresh concrete", J. Eng. Mec., Proc. of ASCE, Vol.115, No.3, pp.493-508, 1989.
Towhata, I., Sasaki, Y., Tokida, K., Matsumoto, H., Tamari, Y. and Yamada, K., "Prediction of permanent displacement of liquefied ground by means of minimum energy principle", Soils and Foundations, Vol.32, No.3, pp.97-116, 1992.
Uzuoka, R., Yashima. A., Kawakami, T. and Konrad, J.-M., "Fluid dynamics based prediction of liquefaction induced lateral spreading", Computers and Geotechnics, Vol.22, No.3/4, pp.243-282, 1998.

EXPERIMENTAL STUDY OF MITIGATION OF LIQUEFIED GROUND FLOW BY USING GRAVEL DRAIN SYSTEM

by

Masakatsu MIYAJIMA[1), Masaho YOSHIDA[2) and Masaru KITAURA[3)

Abstract

The paper deals with small-scale tests on application of gravel drain system to mitigation of liquefied ground flow. Although the effects of gravel drain system on prevention of liquefaction were verified in the 1993 Kushiro-oki earthquake in Japan, mitigation of ground flow which was induced by liquefaction caused at the adjacent area has not been confirmed yet. Therefore, shaking table tests were conducted with the view of investigating the effects of gravel drain system on mitigation of liquefied ground flow. Test results suggested that liquefied ground flow especially at unimproved upper stream area was reduced by construction of grâvel drain system. The following conclusion may be drawn based on this study. If the gravel drain system is able to prevent liquefaction, liquefied ground flow can be mitigated by the rigidity of the gravel piles and non-liquefied ground around the gravel piles.

1) Associate Professor, Department of Civil Engineering, Kanazawa University, 2-40-20 Kodatsuno, Kanazawa 920-8667 Japan, miyajima@t.kanazawa-u.ac.jp

2) Assistant Professor, Department of Civil Engineering, Fukui National College of Technology, Geshi, Sabae, 916-8507 Japan, masaho@azalea1.ip.fukui-nct.ac.jp

3) Professor, Department of Civil Engineering, Kanazawa University, 2-40-20 Kodatsuno, Kanazawa 920-8667 Japan, kitaura@t.kanazawa-u.ac.jp

INTRODUCTION

Lateral ground flow induced by liquefaction caused severe and extensive damage to underground structures such as lifeline facilities. Several countermeasures against liquefaction have been proposed and for some of them, their effects against liquefaction were verified during the past earthquakes. However, it is not clear that the countermeasures against liquefaction have an effect against the large liquefied ground flow. As a countermeasure against liquefaction, the gravel drain system is installed to increase the permeability of ground with the effect of drainage and, thus, reduce the liquefaction potential. Although the 1993 Kushiro-oki earthquake caused many structural failures induced by liquefaction in Kushiro port, there was little damage at some wharves where the gravel drain system was constructed to mitigate liquefaction[1]. Construction of the gravel drain system produces no greater vibration and noise in comparison with the sand compaction method, which has been one of the most popular countermeasures in Japan.

The present paper aims to clarify whether the gravel drain system is effective as a countermeasure against liquefied ground flow. The shaking table tests in a 1-g field by using a small-scale ground model were conducted to investigate whether construction of gravel piles into a sloping ground decreases the horizontal ground displacements.

TEST APPARATUS AND MATERIALS

The general view of test apparatus is shown in Fig.1. The model ground was made up in a steel sand box, which was set up on the shaking table. The size of the sand box is 1.8m in length, 0.6m in width and 0.8m in height. The lower part of model ground was the non-liquefiable layer with an inclination of 10%. It was made of spread No.5 crushed stones under a wooden board. The upper part was loose liquefiable sand layer, whose relative density was about 35%. The sand used for liquefiable layer was No.5 Soma silica sand. The layer was 40cm in depth and the ground surface was smoothed with an inclination of 10%. The gravel piles were installed in the area bounded by a dotted line shown in Fig.1. This portion is called as an improved area in this paper.

The gravel pile was prepared by the following procedure. First, a casing of vinyl chloride resin pipe covered with a nylon mesh, whose diameter is 55mm, was installed in the sand box. Second, water was filled in the sand box, then sands were poured into the water to make the loose sand layer surrounding the casing pipe. After making of the loose sand layer, the casing was pulled out while tamping the crushed stone down. The physical properties of the sand, crushed stone and model ground are listed in Table 1.

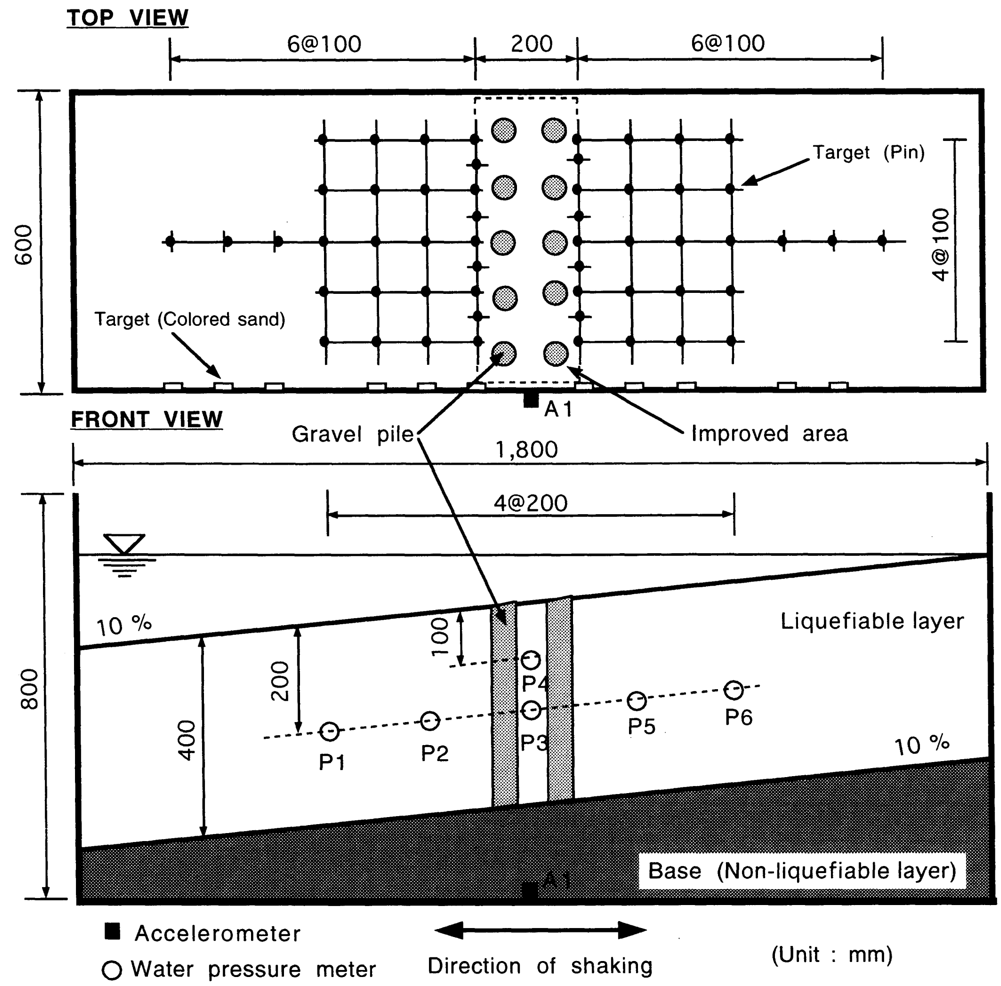

Fig. 1 General view of test apparatus.

Table 1 Physical properties of sand, crushed stone and model ground.

Silica sand (No.5)		
Specific gravity	G_s	2.65
Uniformity coefficient	U_c	1.7
Maximum void ratio	e_{max}	1.02
Minimum void ratio	e_{min}	0.65
Average grain size	D_{50}	0.4 (mm)
Coefficient of permeability	K_s	1.38×10^{-1} (cm/s)
Crushed stone (No.7)		
Specific gravity	G_s	2.67
Maximum grain size	D_{max}	10 (mm)
Coefficient of permeability	K_s	2.9 (cm/s)
Model ground (Liquefiable layer)		
Wet unit weight	γ_{sat}	1.91 (gf/cm^3)
Void ratio	e	0.90
Water content	w	35.9 (%)
Relative density	D_r	35.2 (%)

TEST PROCEDURE AND CONDITIONS

Test names and conditions in each case are summarized in Table 2. The diameter of gravel pile divided by interval between piles that was called as the interval ratio, was used as an index of degree of improvement in case of the line arrangement. The area of gravel pile divided by the area surrounded by the gravel piles which was called as the displacement ratio was used as that in case of the square and triangle arrangements. Two lines of gravel piles formed squares and triangles in square and triangle arrangements, respectively. Piles with no permeability were also used in the case named as GLU-75 shown in Table 2 for a comparative study.

The model ground was vibrated by a sinusoidal wave with 5Hz. The maximum acceleration was 100gal and number of waves was 30. The accelerometer was installed at the bottom of sand box to measure the input acceleration, and pore water pressure meters were buried in the improved and unimproved ground to measure the excess pore water pressure during excitation. After excitation, horizontal and vertical ground displacements were measured. The vertical cross section of model ground was visible through the transparent side wall of sand box at which lines of colored sand was installed.

TEST RESULTS AND DISCUSSION

Figs. 2 and 3 show the horizontal displacement of the ground surface in relation to the distance from the downstream end of sloping ground. Fig. 2 shows the results in case line arrangement and Fig.3 indicates those in case of the triangle and square arrangements. The horizontal displacements in case of no countermeasure were also shown in these figures. It can be seen from these figures that the displacements in case of no countermeasure were greater than 10cm and the great displacement appeared close to the center of model ground. On the other hand, the maximum displacements of ground surface were reduced to 0.5cm to 7.0cm in case of construction of countermeasure. The displacements in the upper stream area of model ground were smaller than those of the downstream area according to Fig. 2. Fig. 4 illustrates the displacements of model ground in vertical cross section in case of GL-110. This figure indicates that the ground surface at the upper stream area close to gravel piles arose. It seems that the gravel piles resisted the ground flow of the upper stream area.

Fig. 5 shows the time histories of excess pore water pressure in the upper and downstream areas of model sloping ground. Since the time histories of excess pore water pressure at same distance upper and downstream from the gravel piles were similar, the degrees of liquefaction also seemed to be similar there. Therefore, it is considered that the difference of ground displacement between upper and downstream areas was not caused by the degree of liquefaction, but caused by the rigidity of the improved surrounding soils of the piles. Since the ground

Table 2 Test names and conditions.

Name	Arrangement	Diameter of pile ϕ(mm)	Interval of pile d (mm)	Number of pile	Interval ratio ϕ/d	Displacement ratio A_g (%)	Permeability
N-1	-	-	-	0	-	-	○
GL-75	Line	55	75	8	0.73	-	○
GLU-75	Line	55	75	8	0.73	-	×
GL-110	Line	55	110	5	0.50	-	○
GL-165	Line	55	165	4	0.33	-	○
GS-110	Square	55	110	10	-	19.6	○
GS-165	Square	55	165	8	-	8.7	○
GT-110	Triangle	55	110	9	-	22.7	○
GT-150	Triangle	55	150	8	-	12.2	○

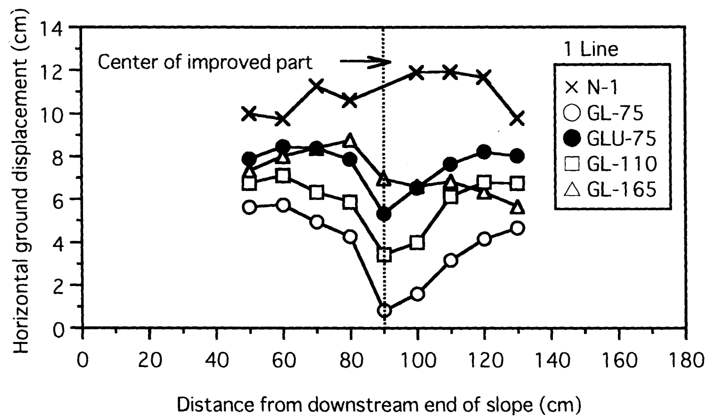

Fig. 2 Horizontal displacement at ground surface in line arrangement.

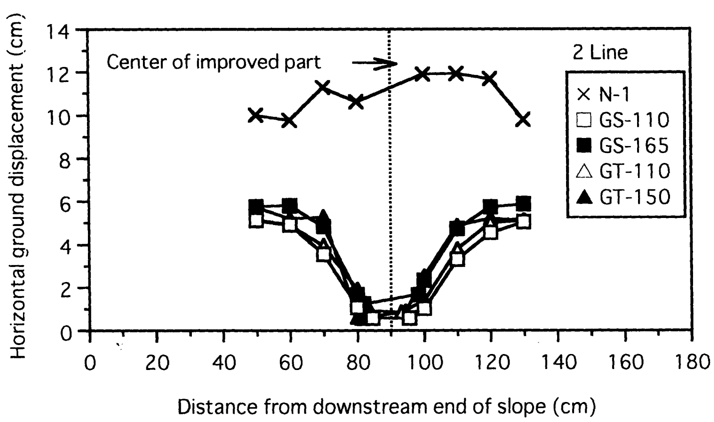

Fig. 3 Horizontal displacement at ground surface in square and triangle arrangements.

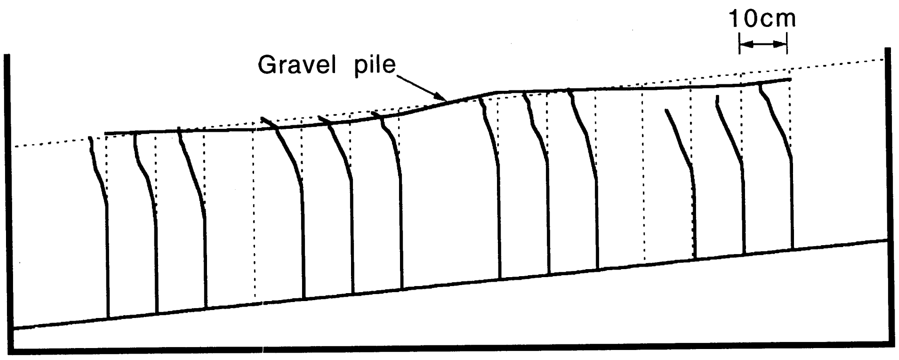

Fig. 4 Displacement of model ground in cross section (GL-110).

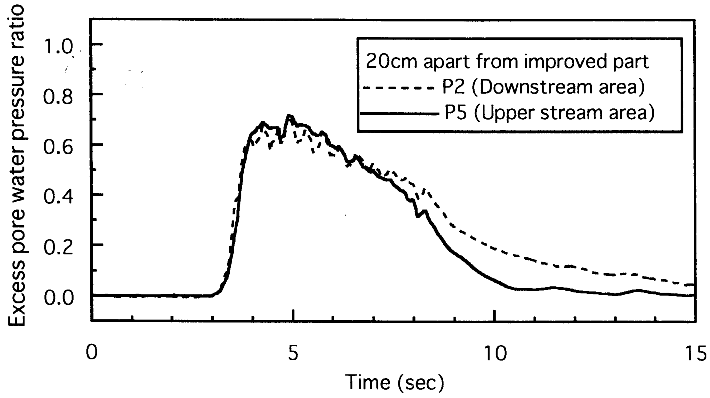

1) 20cm from improved area.

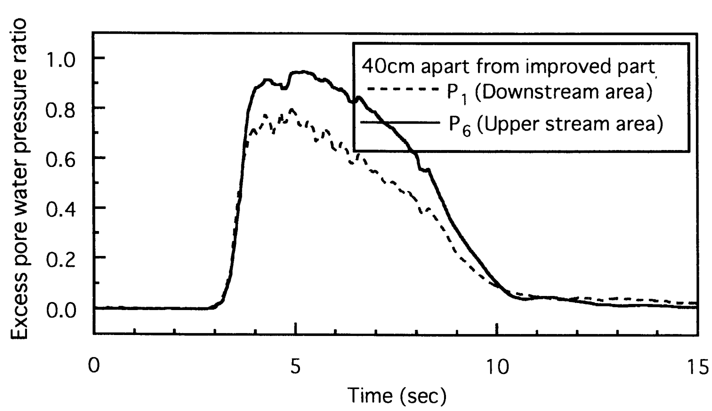

2) 40cm from improved area.

Fig. 5 Time histories of excess pore water pressure ratio (GL-75).

displacements also reduced in case of piles with no permeability (GLU-75 in Fig. 2), the rigidity of piles also seemed to be one of the causes of mitigation of liquefied ground flow. According to Figs. 2 and 3, the ground displacements in cases of the square and triangle arrangements were smaller than those in case of line arrangement. And there was no big difference between upper and downstream area of sloping ground in case of the square and triangle arrangements. It is conceivable that the effects against liquefaction were greater in cases of the square and triangle arrangements than that in the line arrangement.

Fig. 6 indicates the horizontal ground displacement and maximum excess pore water pressure ratio at the improved area in relation to the interval ratio and displacement ratio, respectively. It can be seen from these figures that the maximum excess pore water pressure ratio decreased in increase of the interval ratio and displacement ratio, that is, in decrease of the interval of each pile. The horizontal ground displacement also decreased as same manner. The relationship between the maximum excess pore water pressure ratio at the improved area and horizontal ground displacement is shown in Fig. 7. According to these figures, the horizontal ground displacements decreased in decrease of the maximum excess pore water pressure ratio at the improved area. The displacements of the downstream area seemed to reach a constant value in case of the maximum excess pore water pressure ratio less than 0.5. On the other hand, the displacement of the upper stream area had tendency of decrease even in case of small excess pore water pressure ratio. At the upper stream area, the smaller the excess pore water pressure at the improved area is, the smaller the ground displacement at the upper stream area. It is conceivable that the rigidity of surrounding ground of gravel piles was great when the excess pore water pressure ratio at the improved area was small, therefore, the effect against ground flow became great.

Next, the effect of arrangement of gravel piles on mitigation of the liquefied ground flow was investigated. The results in cases of the line, square and triangle arrangements of same number of gravel piles were compared here. Fig. 8 illustrates the time histories of excess pore water pressure ratio at the same distance upper and downstream from gravel piles. Since there was no big difference in the excess pore water pressure ratio, degree of liquefaction at measuring point in each case was similar. Fig. 9 shows the horizontal ground displacements in relation to the distance from gravel piles. The ground displacements at downstream area were similar in each case because of similar degree of liquefaction. On the other hand, the ground displacements of the line arrangement were smaller than those of the triangle and square arrangements. It can be explained that the degree of liquefaction at the improved area in the line arrangement was smaller than that in the triangle and square arrangements despite of similar degree of liquefaction in unimproved area. Therefore, the rigidity of surrounding ground of gravel piles was one of the causes of mitigation of liquefied ground flow.

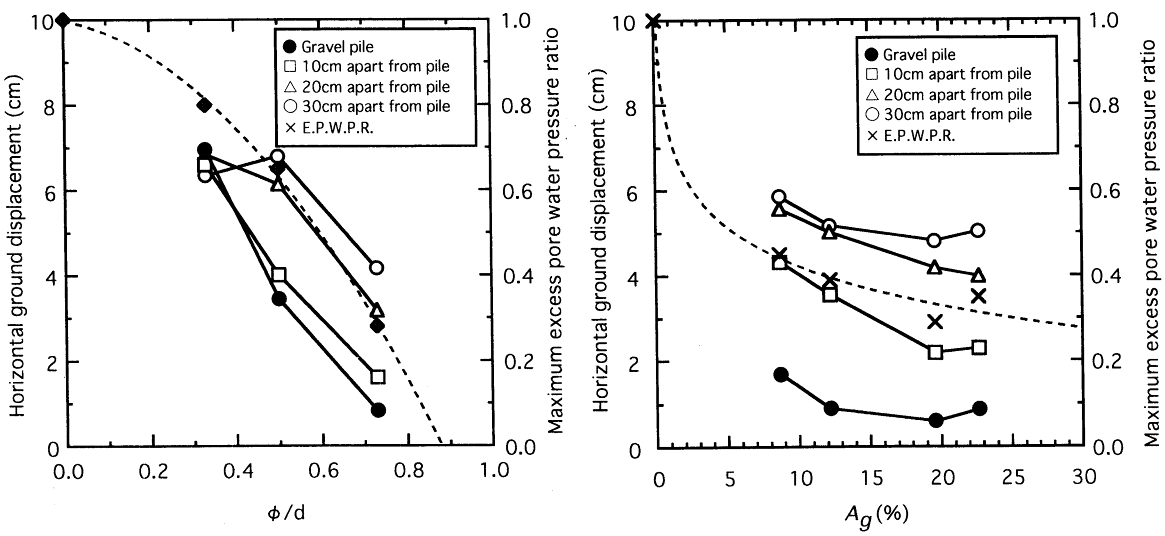

1) One line arrangement.

2) Two line arrangement.

Fig. 6 Relationship between improvement ratio, excess pore water pressure ratio and horizontal ground displacement.

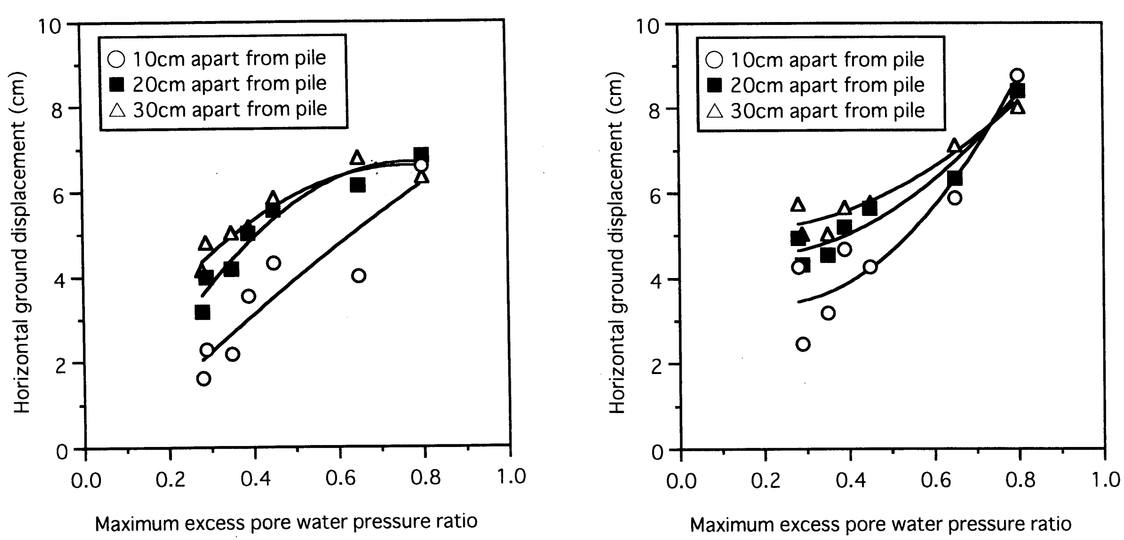

1) Upper stream area.

2) Downstream area.

Fig. 7 Relationship between maximum excess pore water pressure ratio and horizontal ground displacement.

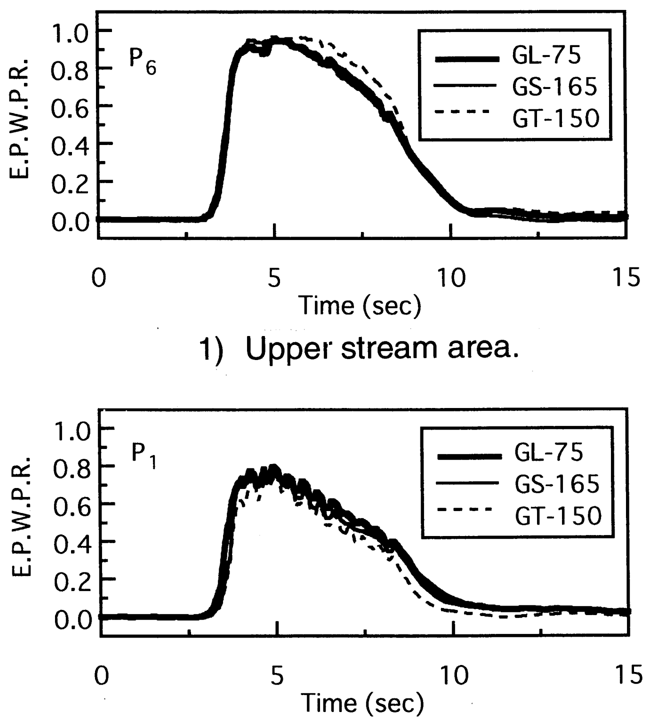

1) Upper stream area.

2) Downstream area.

Fig. 8 Time histories of excess pore water pressure ratio (Number of piles: 8)

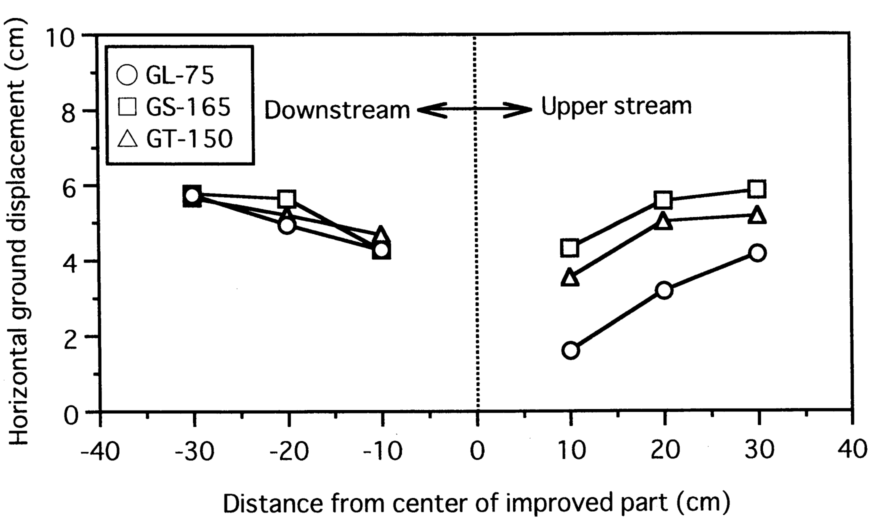

Fig. 9 Relationship between distance from gravel piles and horizontal ground displacement.

CONCLUSIONS

Small-scale tests on gravel drain system as a countermeasure against liquefied ground flow was conducted in the present paper. The following conclusions may be drawn from the present study.

(1) The causes of mitigation of liquefied ground flow were permeability of gravel drain system, rigidity of gravel piles themselves and rigidity of improved surrounding ground of gravel piles. The rigidity of gravel piles and surrounding ground prevent the ground flow at upper stream area of gravel piles.

(2) There was correlation between the horizontal displacement of ground surface and maximum excess pore water pressure ratio in the improved area. The displacements of the downstream area seemed to reach a constant value in case of the maximum excess pore water pressure ratio less than 0.5. On the other hand, the displacement of the upper stream area had tendency of decrease even in case of smaller excess pore water pressure ratio. Therefore, the ground flow at upper stream area could be prevented strongly when the excess pore water pressure in the improved area became small.

ACKNOWLEDGEMENTS

The authors wish to thank Mr. Hiroki Kondoh (graduate student of Kanazawa University) for his cooperation in experiments. A part of expense of this study was defrayed by the Grant-in-Aid for Scientific Research from the Ministry of Education, Science, Sports and Culture of Japan.

REFERENCES

(1) Masaho Yoshida, Masakatsu Miyajima, Masaru Kitaura and Hiroshi Oishi: Effects of Gravel Drain System on Mitigation of Liquefaction-Induced Damage During the 1993 Kushiro-oki Earthquake, Proc. of the 9th Japan Earthquake Engineering Symposium, Vol. 1, pp. 1075-1080, 1994.

LARGE-SCALE MODELING OF LIQUEFACTION-INDUCED GROUND DEFORMATION PART I: A FOUR-PARAMETER MLR MODEL

J.P. Bardet, N. Mace, T. Tobita, and J. Hu
University of Southern California

ABSTRACT

Liquefaction-induced ground deformation is a potential source of major damage to lifelines and structures during earthquakes. This type of permanent ground displacement, which can extend over areas as large as a few square kilometers and have amplitudes ranging from a few centimeters to 5 meters and more, caused substantial damage to lifelines and pile-foundations of buildings and bridge piers along the Kobe shoreline during the 1995 Hyogoken Nanbu, Japan, earthquake. This paper presents a four-parameter Multiple Linear Regression (MLR) model for estimating the amplitude of liquefaction-induced ground displacement. The liquefaction-induced ground deformation model is based on measured displacement data, topographical data, soil borehole information, and earthquake data prior to the 1994 Northridge earthquake and 1995 Hyogoken Nanbu earthquake. The model is proposed for predicting at a regional scale the liquefaction-induced ground deformations for both ground-slope and free-face conditions. The model was calibrated for two data sets including and excluding, respectively, displacements larger than 2 meters. In a companion paper, the MLR model is applied to mapping liquefaction-induced ground deformation over selected regions.

INTRODUCTION

The liquefaction-induced ground deformations resulting from earthquakes have been identified as a potential source of major damage to pipeline networks. These permanent displacements cover areas as large as a few square kilometers and have amplitudes ranging from few centimeters to 5 meters and more. They were numerous during the 1995 Hyogoken-Nanbu earthquake (Hamada et al., 1996a and 1996b) and caused substantial damage to lifelines and pile-foundations of buildings and bridge piers along the Kobe shoreline (Hamada et al, 1996a; Karube and Kimura, 1996; Matsui and Oda, 1996; and Tokimatsu et al., 1996).

This paper reports some results of an ongoing research program, the objective of which is to develop and improve engineering methods for assessing and quantifying liquefaction-induced ground deformations utilizing regional geologic data and detailed borehole data. Ultimately, this research is intended to produce models of liquefaction-induced ground displacement useful for estimating the extent of damage and repair to spatially extended lifeline networks which may be caused by future earthquakes. The paper proposes a model which has a limited number of parameters and is intended for assessing the amplitude of liquefaction-induced ground deformation over large areas and the resulting damage to various types of distributed lifelines systems.

The first and second sections of the paper review the existing databases and models of liquefaction-induced deformation. The third section presents the new liquefaction-induced ground deformation model. In a companion paper, the applicability of the model for mapping liquefaction-induced ground deformation is investigated over selected regions of large extent.

DATABASES OF LIQUEFACTION CASE HISTORIES

Liquefaction-induced lateral spreads

During past earthquakes, large areas of ground were observed to shift laterally due to soil liquefaction. These liquefaction-induced lateral ground deformations have amplitudes ranging from small (1 cm) to very large (>10 m) in the case of flow slides. They can take place for gently sloping ground conditions (0.1% to 6%). Examples of liquefaction-induced ground deformation during the 1994 Northridge earthquake were observed at the Power Plant Tailrace (>1 m) in the Van Norman Complex, and the Lower San Fernando Dam (0.3 m) (Bardet and Davis, 1996). Liquefaction-induced ground deformations are generally observed close to open faces and in gently sloping ground. These deformations are usually driven by a combination of transient and static shear stresses and attributed to the loss of shear strength of underlying saturated soils. During the 1995 Hyogoken-Nanbu earthquake, liquefaction induced lateral ground deformation was one of the major causes of damage to lifelines and pile-foundations of building and bridge piers along the Kobe shoreline (Hamada et al, 1996; Karube and Kimura, 1996; Matsui and Oda, 1996; and Tokimatsu et al., 1996).

The case histories of liquefaction-induced ground deformation during past earthquakes are essential for understanding and characterizing the effects of liquefaction, and for developing physical and empirical models to predict liquefaction damage. A large number of case histories of liquefaction-induced lateral spreads have been compiled in the two volumes edited by Hamada and O'Rourke (1992). Some examples of case histories include those from the 1964 Niigata earthquake; 1971 San Fernando earthquake; 1983 Ninhonkai-Chubu; 1983 Borah peak, Idaho, earthquake (Youd et al., 1985); 1987 Superstition Hills, California, Earthquake (Youd and Holtzer, 1994); 1989 Loma Prieta earthquake, Watsonville (Holtzer et al., 1994); 1993 Hokkaido Nansei-oki Earthquake (Isoyama, 1994); 1994 Northridge earthquake (Holzer et al., 1996; Bardet and Davis, 1996; Davis and Bardet, 1996); and 1995 Hyogoken-Nanbu earthquake (Hamada et al., 1996, Ishihara et al., 1996)

Liquefaction-induced ground deformation database

Bartlett and Youd (1992) assembled one the most comprehensive databases on liquefaction-induced ground deformation, which was recently revised by Bartlett (1998). The main features of the database, which are used in the present modeling, are summarized. The database has 467 entries from seven earthquakes listed in Table 1. The data falls into four main categories:

- Ground displacement amplitude data
- Ground-slope and free-face topographical data
- Seismic data
- Borehole data

Ground displacement amplitude data

Table 1 summarizes the number of data on ground displacement amplitudes per earthquake and site. A site is an area delineating a consistent slide in which the measured displacement vectors can be regrouped. The vectors inside the slide area are included in the database, while the vectors which are isolated or too distant from available geotechnical data, are excluded. The delineation of liquefaction-induced slides from aerial maps is not straightforward in all cases, and requires some engineering judgement. It even becomes more difficult when the displacement vectors are scarce and small.

In the present analysis, the data was divided in two data sets: (A) complete data for all ranges of displacement amplitude; and (B) data limited to displacement amplitudes smaller than 2 meters. The data set B, which excludes the displacement amplitudes in excess of 2 m, was intended to be more relevant to engineering design. Amplitudes in excess of 2 m were arbitrarily considered to be too large for accurate measurement, and to cause excessive ground damage impractical to mitigate. The data was further subdivided into ground-slope and free-face cases. As illustrated in Fig. 3, free faces (FF) are abrupt variations of ground surface elevation, such as quaywalls and embankments. In some instances, the displacement of free faces appears to induce that of the liquefied-induced ground deformation adjacent to it (Hamada and Wakamatsu, 1998). Ground-slope (GS) cases correspond to free-field conditions far away from free faces. Table 2 gives the number of entries in data sets A and B, together with their respective partitions into free-face and ground slope cases. Figure 1 shows the distribution of displacement amplitudes. Most of the data falls in the 4-m range. As shown in Fig. 2, the difference between the databases of Barlett and Youd (1992) and Bartlett (1998) is significant enough to be detectable from the histograms of displacement amplitude. The difference is due to corrections made to the displacement data of the 1983 Nihonkai-Chubu earthquake. As shown in Bardet et al. (1999), this difference leads to MLR models slightly different from that of Bartlett and Youd (1992).

Table 1. Number of sites and displacement vectors in Bartlett and Youd (1992) database.

Earthquake Name	Number of Site	Number of vector
1906 San Francisco Earthquake	4	4
1964 Alaska Earthquake	5	7
1964 Niigata, Japan Earthquake	14	299
1971 San Fernando Earthquake	2	28
1979 Imperial Valley Earthquake	2	32
1983 Nihonkai-Chubu, Japan Earthquake	1	72
1987 Superstition Hills Earthquake	1	6

Table 2. Data sets used in MLR models

Notation	Definition	Number of data points
A	All free-face and ground-slope data (FFGS)	467
	All free-face (FF) data	213
	All ground slope (GS) data	254
B	All data (FFGS) with displacement smaller than 2 m	283
	Free-face (FF) data with displacement smaller than 2 m	118
	Ground slope (GS) data with displacement smaller than 2 m	165

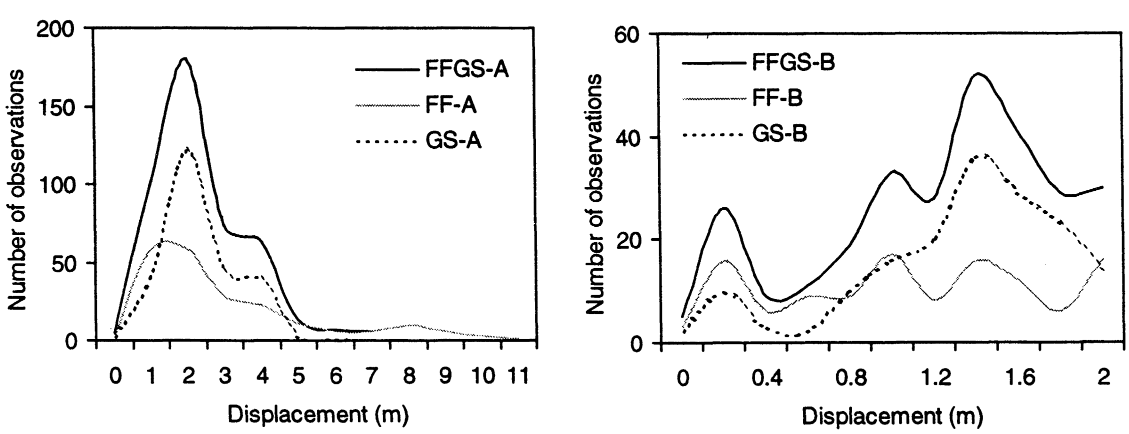

Figure 1. Histograms of displacement-amplitudes for all (FFGS), free-face (FF) and ground slope (GD) data in data sets A and B.

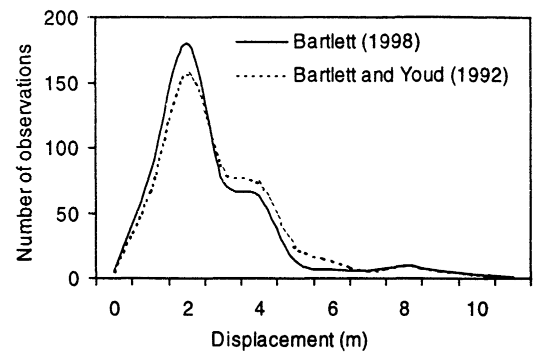

Figure 2. Comparison of histograms of displacement amplitude for database of Bartlett and Youd (1992) and Bartlett (1998) on liquefaction-induced lateral displacement.

Ground slope and free face topographical data

In the present analysis, as in that of Bartlett and Youd (1992), the ground slope and free-face topographical data is used to characterize the effects of static shear loads that drive liquefaction-induced displacements. As shown in Fig. 3, the ground slope S is the inclination of the ground surface at the location of the displacement vector. The free-face data is characterized by the free-face ratio $W = H/L$, where H is the height of the free face (i.e., difference between crest elevation and toe elevation) and L the horizontal distance from the toe of the free face to the displacement vector. Values of S were obtained by measuring ground surface slopes from the elevation contours and control points of topographical maps. The free faces were identified from topographical maps and field observations, and the values of H and L were measured or estimated from topographical maps. Figure 4 shows the distributions of free-face ratio W and ground-slope S for data sets A and B. The values of W in the database are smaller than 55% and those of S smaller than 3%.

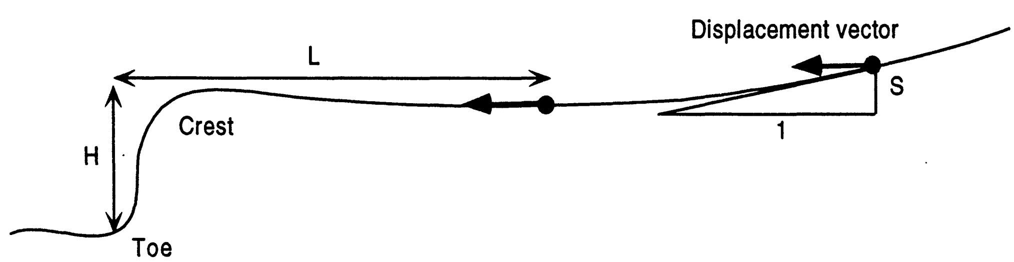

Figure 3. Definition of free-face ratio H/L and ground slope S in Bartlett and Youd (1992) database.

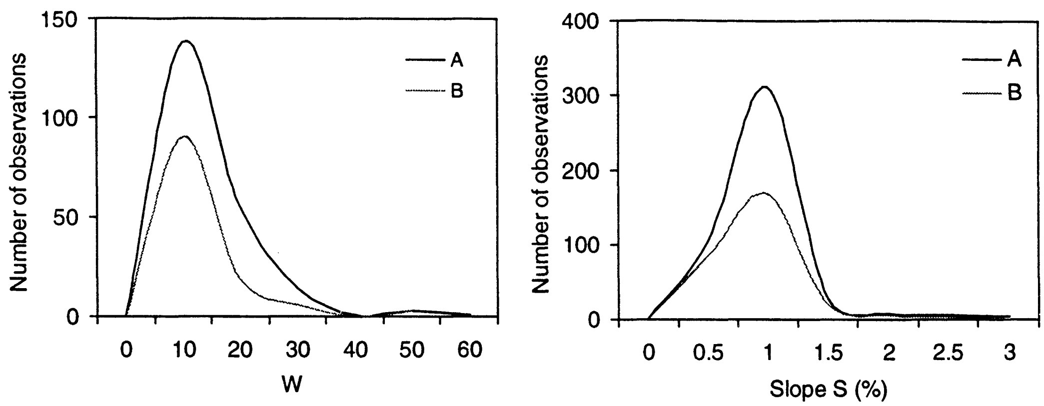

Figure 4. Histograms of (a) free-face ratio *W* and (b) ground slope *S* in data sets A and B.

Seismic data

Table 3 summarizes the seismic parameters of the seven earthquakes in the database. There are minor variations in site specific parameters, i.e., epicentral distance (distance between the epicenter and location at which ground displacements are measured), and peak ground acceleration (PGA). During the earthquakes prior to 1979, the transient ground motion was poorly recorded, mainly because there were very few strong motion instruments deployed before 1979. Figures 5 and 6 shows the histogram of the earthquake magnitude and epicentral distance for ground-slope and free-face cases of data sets A and B. Most liquefaction-induced ground deformations were measured for earthquakes having a magnitude between 7 and 7.8 and at distance less than 30 km for the seismic source.

Table 3. Seismic parameters for earthquakes in Bartlett and Youd (1992) database.

Earthquake Name	Magnitude	PGA (g)	Epicentral distance (km)
1906 San Francisco Earthquake	7.9	0.28-0.26	13-27
1964 Alaska Earthquake	9.2	0.21-0.39	35-100
1964 Niigata, Japan Earthquake	7.5	0.19	21
1971 San Fernando Earthquake	6.4	0.55	1
1979 Imperial Valley Earthquake	6.5-6.6	0.21-0.51	2-6
1983 Nihonkai-Chubu, Japan Earthquake	7.7	0.25	27
1987 Superstition Hills Earthquake	6.6	0.21	23

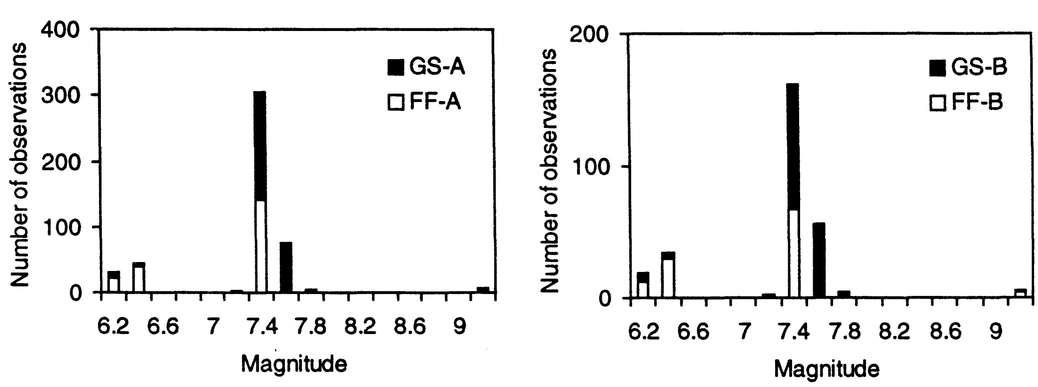

Figure 5. Histograms of earthquake magnitude for ground-slope and free-face cases in data sets A and B.

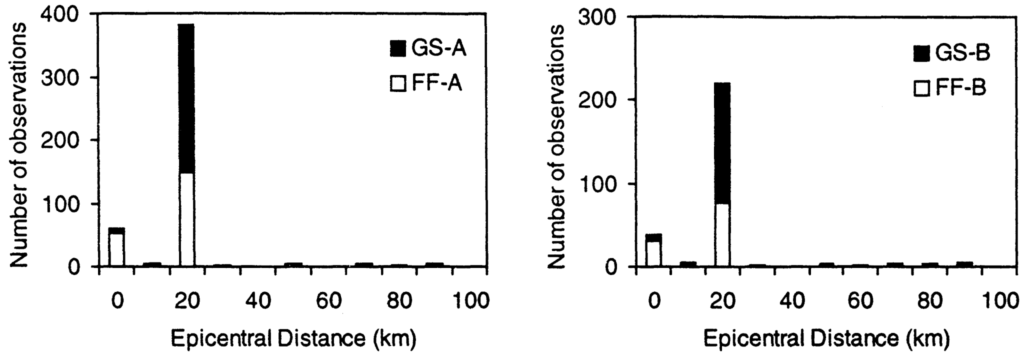

Figure 6. Histograms of epicentral distance for ground-slope and free-face cases in data sets A and B.

As shown in Fig. 7, the data in the database of Bartlett (1998) falls within two boundaries in the R-M plane. Above the upper bound, there is no data available in the database, and any prediction in this region is doomed to uncertain extrapolations. Below the lower bound, which is formed by Ambraseys (1988) data, there has been no observed liquefaction-induced ground deformation.

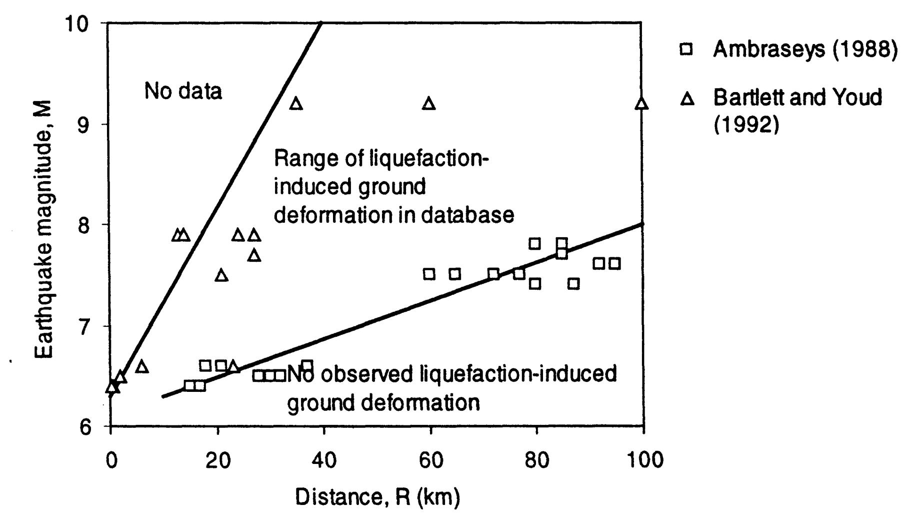

Figure 7. Ranges of available data and no-observed liquefaction-induced ground deformation in the database of Bartlett (1998).

Borehole data

The Bartlett (1998) database contains a total of 239 borehole tests consisting of 224 SPT and 15 CPT soundings. This data is intended to characterize the geometry of soil deposits and soil properties in the vicinity of displacement vectors. In the present analysis, the parameters for characterizing borehole data are selected to be the standard penetration blow count N, and the borehole visual soil classification. The other parameters used by Bartlett and Youd (1992), i.e., the mean grain diameter D_{50} and the fines contents F (percent by weight smaller than 75 µm) are not used in the present analysis. Based on our experience, the data on F and D_{50} is scarce and it is too difficult to obtain a meaningful average over the depth in question. In some instances (e.g., samples lost during SPT sampling), Bartlett and Youd (1992) needed to assume this data in order to complete their analysis. Also, the large variation in the average values of D_{50} and F make interpolation over large areas uncertain. In geotechnical engineering, the blow count N is measured by counting the number of blows required to push a spilt barrel sampler 30 centimeters in the ground. Given borehole preparation, the vertical resolution of the SPT data is therefore at best 50 cm. Bartlett and Youd (1992) refined the SPT resolution and accounted for the change in soil layering as noted in the borehole visual classifications. This refinement is not considered in the present analysis as it becomes also uncertain over large areas. In the case of the 15 CPT boreholes, the blow counts N were correlated from CPT tip resistance using the correlations of Seed and DeAlba (1986).

Soil properties at vector location

The present analysis uses only one soil property T_{15}, the cumulated thickness of saturated cohesionless soils having a blow count $N1_{60}$ smaller than or equal to 15, which is defined as in Bartlett and Youd (1992). Boreholes and displacement vectors usually have different locations, although boreholes are selected for their proximity to the displacement vectors. The average value of T_{15} is first estimated at the borehole location then interpolated to the location of the displacement vectors as suggested by Bartlett and Youd (1992). As shown in Fig. 8, the average value of T_{15} (i.e., $\overline{X}$) located at the displacement vectors is estimated from the average value of T_{15} (i.e., X_i) at the boreholes surrounding the displacement vector through the following weighted average:

$$\overline{X} = \sum_{i=1}^{n} \frac{X_i}{d_i \sum_{j=1}^{n} \left(\frac{1}{d_j} \right)} \tag{1}$$

where n is the number of boreholes used for averaging (the maximum value of n is 4), and d_i is the distance between the i[th] borehole and the displacement vector. Figure 9 shows the distribution of the minimum distance between the locations of displacement vectors and borehole data. In some cases, the minimum distance exceeds 400 m, which raises legitimate questions on the correlation between geotechnical and displacement data. Figure 10 shows the histogram of T_{15} for data sets A and B.

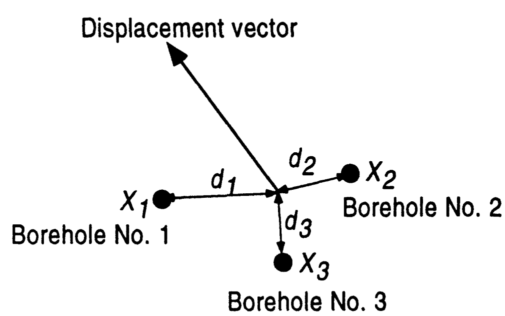

Figure 8. Relation of displacement vectors and boreholes (after Bartlett and Youd, 1992).

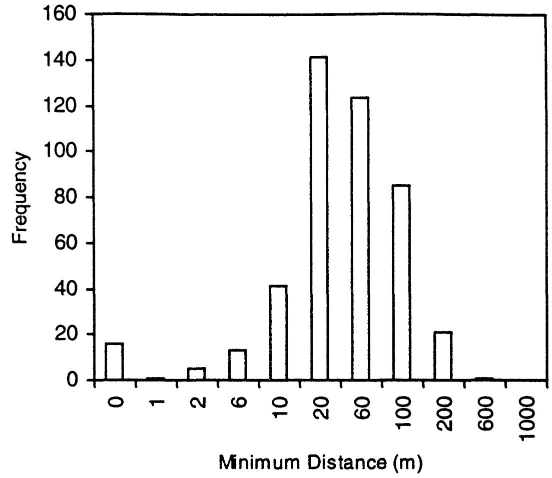

Figure 9. Minimum distance between boreholes and displacement vectors in Bartlett and Youd (1992).

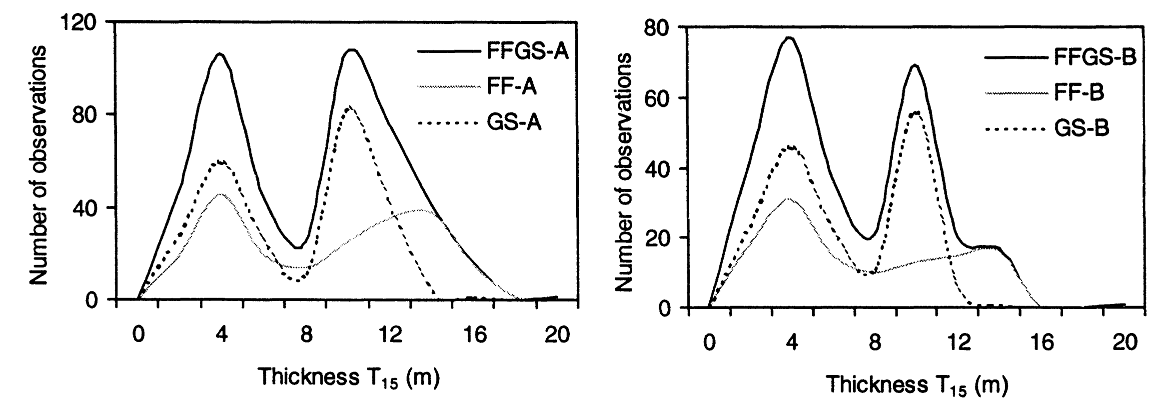

Figure 10. Histograms of thickness T_{15} for free-face, ground slope, and all cases in data sets A and B.

Comparison of Harder (1991) and Bartlett and Youd (1992) databases

Harder (1991) reported a database for case histories of liquefaction occurrence. This database includes case histories for which there was either evidence of liquefaction or no evidence for liquefaction. Such a database is the basis of most liquefaction analysis procedures, as recently described by Youd and Idriss (1998). Other databases of liquefaction occurrence have been developed based on shear wave velocity (Stokoe et al., 1988) and cone penetration test (CPT) data (Robertson and Campanella, 1985). However, these databases are not considered in the present study. Figure 11 compares the entries in the databases of Harder (1991) and Bartlett and Youd (1992). Almost all cases of lateral spreading fall within the boundaries of liquefaction occurrence. The rare exceptions deserve to be studied in detail. In default of detailed information on these particular cases, it is speculated that these lateral deformations were generated by the deformation of nearby liquefied soils.

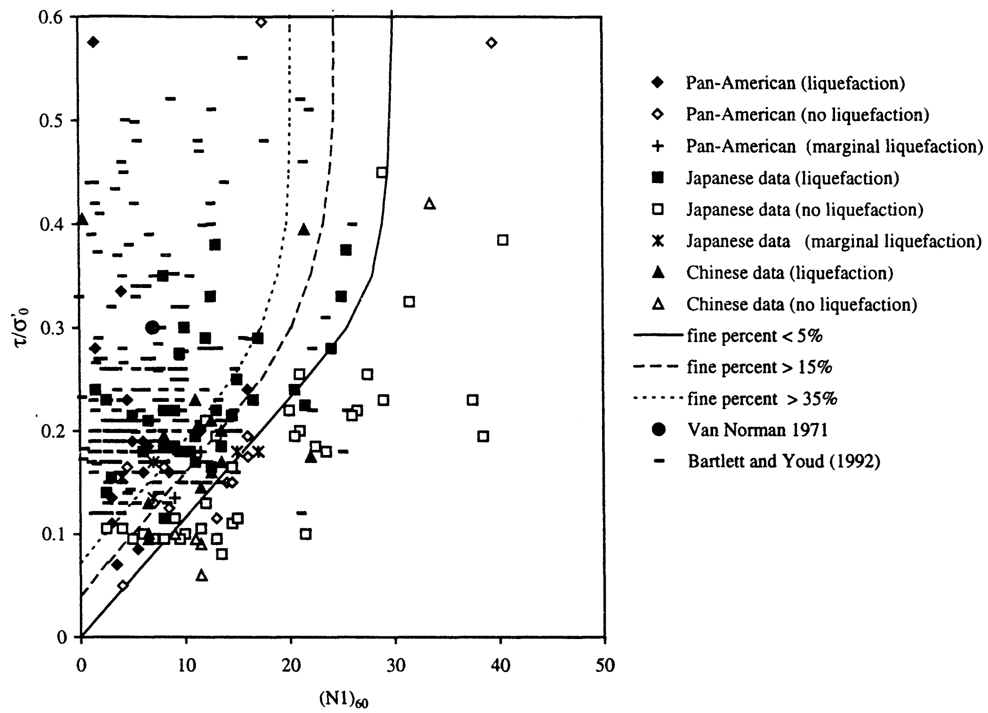

Figure 11. Comparison of databases of Harder (1991) and Bartlett and Youd (1998).

REVIEW OF EMPIRICAL MODELS

Several analytical approaches have been proposed to model liquefaction-induced ground deformation (e.g., Baziar et al., 1992; Byrne, 1991; Jibson, 1994; Towhata et al, 1996, 1997; and Yegian et al, 1991). These analytical models are capable of explaining a few, but not all aspects of liquefaction-induced deformations. Most analytical models require numerous parameters for predicting liquefaction-induced deformation, and are therefore impractical to apply over the large areas covered by lifeline networks. The empirical methods based on case histories of liquefaction-induced deformation are alternate approaches readily applicable for assessing damage to lifeline networks after earthquakes. To our knowledge, there are five models for assessing liquefaction-induced lateral displacements: Youd and Perkins (1987); Hamada (1986); Rauch (1997); Bartlett and Youd (1992); and Youd et al (1999).

The Liquefaction Severity Index (LSI) model (Youd and Perkins, 1987) has similarities to attenuation curves for peak ground acceleration. It relates the amplitude of ground deformations to the distance from seismic energy source and moment magnitude as follows:

$$\log LSI = -3.49 - 1.86 \log R + 0.98\, M_w \quad (2)$$

where *LSI* is the general maximum amplitude of ground failure displacement (inch), *R* is the horizontal distance (km) to seismic energy source, and M_w is the earthquake moment magnitude. Figure 12 compares the measured displacements and those calculated using Eq. 2. The points should fall on the line with a 1:1 slope for a perfect prediction, and on the lines with 1:0.5 and 1:2 slope when the prediction is half or twice the measured value, respectively. As shown in Fig. 12, there is a poor agreement between measured and calculated displacements, which implies that distance *R* and magnitude M_w are not sufficient for predicting liquefaction-induced displacement.

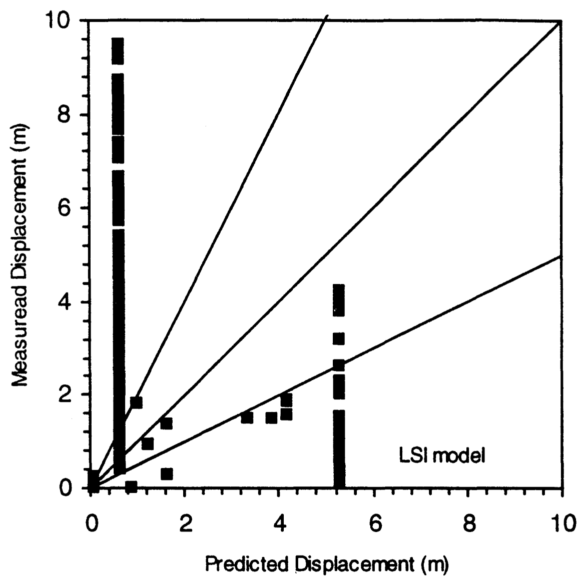

Figure 12. LSI model (Youd and Perkins, 1987): measured versus predicted liquefaction-induced lateral displacement (data points from Bartlett and Youd (1992) database).

Hamada et al. (1986) predict the amplitude of horizontal ground deformation only in terms of slope and thickness of liquefied layer:

$$D = 0.75\, H^{0.5} \theta^{0.33} \tag{3}$$

where D is the horizontal displacement (m), θ is the slope (%) of ground surface or base of liquefied soil, and H is the thickness (m) of liquefied soil. The Hamada model is only based on topographic and geotechnical parameters (i.e., θ and H), and no seismic parameters (e.g., R and M_w).

Rauch (1997) regrouped liquefaction-induced ground deformations within slide areas, instead of considering then as individual displacement vectors, and applied multiple-linear-regression methods to these liquefaction-induced slides. Rauch proposed three different models for the average lateral ground displacement, which are referred to as regional, site and geotechnical. However, Rauch provides no guidance on how to assess the spatial extent of liquefaction-induced slides.

Based on the database described earlier, Bartlett and Youd (1992) proposed the following relation for predicting the amplitude of liquefaction-induced ground deformation:

$$\begin{aligned} Log(D+0.01) &= b_0 + b_{off} + b_1 M + b_2 Log(R) + b_3 R + b_4 Log(W) + b_5 Log(S) \\ &\quad + b_6 Log(T_{15}) + b_7 Log(100 - F_{15}) + b_8 D50_{15} \end{aligned} \tag{4}$$

where D is the horizontal displacement (m); M_w the moment magnitude; R the nearest horizontal distance (km) to seismic energy source or fault rupture; S the slope (%) of ground surface; W the free face ratio (%); T_{15} the thickness (m) of saturated cohesionless soils (excluding depth >20 m and >15% clay content) with $N1_{60}<15$; F_{15} the average fine content (% finer than 75 μm); and $D50_{15}$ the average D_{50} grain size (mm) in T_{15}.

The values of the ten constant coefficients - b_0, b_{off}, and b_1 to b_8 - are given in Table 4. Equation 4 applies to both free-face and ground-slope cases. In the free-face cases, the term *Log(S)* is set equal to zero. In the ground slope cases, the term *Log(W)* is set equal to zero. The coefficient b_{off} only applies to the free-face cases, and is set equal to zero in the ground slope cases. As shown in Fig. 13, most of the model predictions are scattered within the lines with 1:0.5 and 1:2 slope, while they should fall close to the line with a 1:1 slope for a perfect prediction.

Youd et al. (1999) slightly revised Bartlett and Youd (1992) model due to the corrections stemming from the 1983 Nihonkai-Chubu dataset and to account for the liquefaction-induced ground deformation in coarser soils in Kobe, Japan, during the 1995 Hyogoken-Nanbu earthquake. However, this recent model was not available at the time of the present report.

Table 4. Values of MLR coefficients and adjusted R^2 for Bartlett and Youd (1992), and FFGS4 models.

Number of data points		467	213
Coefficients	Bartlett-Youd (1992)	FFGS4-A	FFGS4-B
b_0	-15.787	-6.815	-6.747
boff	-0.579	-0.465	-0.162
b_1	1.178	1.017	1.001
b_2	-0.927	-0.278	-0.289
b_3	-0.013	-0.026	-0.021
b_4	0.657	0.497	0.090
b_5	0.429	0.454	0.203
b_6	0.348	0.558	0.289
b_7	4.527		
b_8	-0.922		
R^2 adjusted	82.60%	64.25%	64.27%

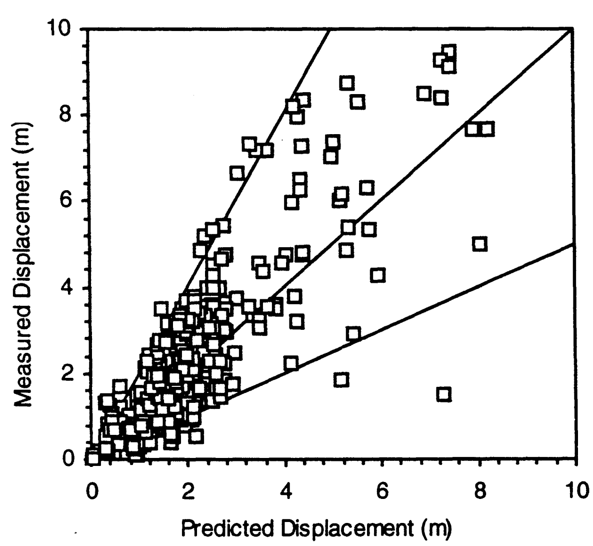

Figure 13. Measured liquefaction-induced ground displacements from the database of Bartlett (1998) versus predicted displacement values by Bartlett and Youd (1992) model.

FOUR-PARAMETER MLR MODEL

Controlling variables

The identification of controlling variables is a critical step in the MLR analysis of liquefaction-induced ground deformation. The controlling parameters in our MLR analysis were identified as a subset of those of Bartlett and Youd (1992) after a careful consideration of other combinations of variables. One of the main criteria for selecting variables was their direct relation to measured data, with as little influence as possible from peripheral analysis. For instance, the thickness T_{15} can be directly obtained from SPT profiles. In contrast, the average depth corresponding to minimum factor of safety Z_{Fsmin}, which is used by Rauch (1997), depends on liquefaction analysis. Given the limitations of the seismic and geotechnical data in the existing database, combinations of variables other than those used by Bartlett and Youd (1992) did not seem promising. However, future studies should reconsider other combinations of variables as other types of entries (e.g., CPT data) are made to the database.

The parameters F_{15} and $D50_{15}$ of Bartlett and Youd (1992) are not used in the present analysis, because they are rather difficult to obtain from borehole data and to determine over large areas. They require taking soil samples from boreholes, performing grain-size analysis in the laboratory, and computing averages within the layers with a SPT blow count smaller than 15. It is obvious that this formidable task is impractical when the areas under investigation become large. The uncertainties of the variables F_{15} and $D50_{15}$ are certainly the largest of any MLR variables in Bartlett and Youd (1992).

For this reason, a four-parameter MLR model with variables - *M, R, W, S,* and T_{15} - is proposed, and calibrated using the data sets A and B. The free-face ratio *W* and ground slope *S* are independent variables and are not used simultaneously. The MLR model was developed to provide a first-order approximation of liquefaction-induced displacement, and to avoid the uncertainties arising from the determination of F_{15} and $D50_{15}$. The MLR model distinguishes free-face and ground-slope cases although this distinction may not always be obvious in all circumstances. It is unclear how far free-face effects can extend from free faces, and how they combine with ground slope effects.

Table 5 shows the range of values for the MLR variables in the data sets A and B, and their corresponding free-face and ground-slope data subsets. The data sets are referred to as *FF, GS* and *FFGS*, which stands for Free-Face, Ground-Slope, and Free-Face & Ground-Slope, respectively. In data set A, the maximum ground-slope displacement (i.e., 5.35 m) is half the maximum free-face displacement. In data set B, both maxima are set equal to 2 m. The range of variables *M, R, W, S,* and T_{15} are almost identical for data sets A and B, and their free-face and ground-slope subsets. Table 5 is useful to define the domain of applicability of the MLR models. It is not recommended to use MLR models for variable values that fall outside the ranges of Table 5.

Table 5. Range of values for MLR variables in data sets A and B, and their free-face and ground-slope subsets.

	Data Set A			Data Set B		
Variables	Complete FFGS-A	Free-Field FF-A	Ground-Slope GS-A	Complete FFGS-B	Free-Field FF-B	Ground-Slope GS-B
D (m)	0 - 10.15	1 - 10.15	0 - 5.35	0 - 1.99	0 -1.98	0 - 1.99
M	6.4 - 9.2	6.4 - 9.2	6.4 - 9.2	6.4 - 9.2	6.4 - 9.2	6.4 - 9.2
R (km)	0.2 - 100	0.5 - 100	0.2 - 100	0.2 - 100	0.5 - 100	0.2 - 100
W	1.64 - 55.68	1.64 - 55.68	-	1.64 - 48.98	1.64 - 48.98	-
S (%)	0.05 - 5.90	-	0.05 - 5.90	0.05 - 2.5	-	0.05 - 2.5
T_{15} *(m)*	0.2 - 19.7	0.2 - 16.7	0.7 - 19.7	0.2 - 19.7	0.2 - 13.6	0.7 - 19.7

The model obtained in the present analysis is referred to as FFGS4, which stands for free-face and ground-slope cases and 4 parameters. It has the following equation:

$$\begin{aligned} Log(D+0.01) &= b_0 + b_{off} + b_1 M + b_2 Log(R) + b_3 R \\ &\quad + b_4 Log(W) + b_5 Log(S) + b_6 Log(T_{15}) \end{aligned} \tag{5}$$

where the variables *M, R, W, S,* and T_{15} are defined below Eq. 4, and the values of the seven coefficients - b_0, b_{off}, and b_1 to b_6 - are given in Table 4. Like Eq. 4, Eq. 5 applies to both free-face and ground-slope cases. The values of variables *M, R, W, S,* and T_{15} should be confined to the observation ranges listed in Table 5. The displacement is considered to be negligible when the values of distance *R* and earthquake magnitude *M* fall below the lower bound of Fig. 7.

The values of the *b*-coefficients were obtained by performing a regression analysis with the program Minitab (1989). The coefficients b_1, b_2, and b_3, which control the magnitude-dependent attenuation of liquefaction-induced displacements with distance, are the same for free-face and ground-slope cases. The attenuation relation for large distance is largely controlled by the additional data points from Ambraseys (1988). The model was calibrated for data sets A and B, therefore producing model FFGS4-A and FFGS4-B. As shown in Table 4, the coefficient values of these two models are similar, and their adjusted R^2 values almost coincide. The R^2 coefficient, which measures the accuracy of the multiple linear regression, is adjusted to account for the difference in the number of data points in data sets A and B. Based on the results of Table 4, it is concluded that models FFGS4-A and -B fit the data sets A and B with similar accuracy, and that they can be used indifferently. Models FFGS4-A and -B simulate liquefaction-induced ground deformation with identical accuracy over all range of measured deformation. Consistent with the MLR approach, the adjusted R^2-values of the four-parameter models are lower than those of the six-parameter models of Bartlett and Youd (1992). Thus, the four-parameter model does not predict measured ground displacement as accurately as the six-parameter models. Figure 14 shows the measured displacements plotted against those predicted by model FFGS4 for data sets A and B. The points are more scattered about the 1:1 line than in Fig. 14, which corresponds to lower values of adjusted R^2 coefficients.

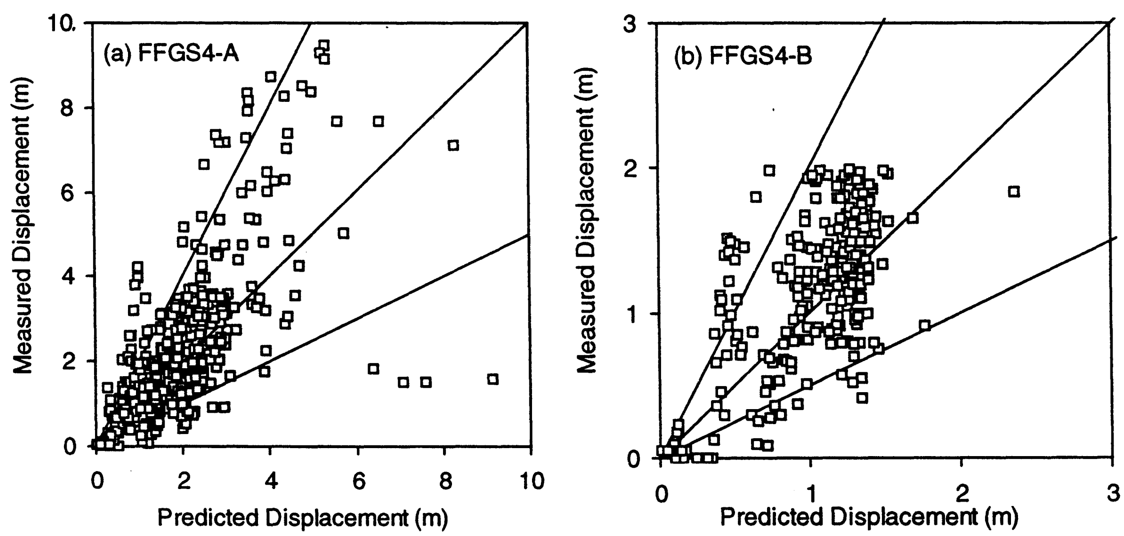

Figure 14. Measured versus predicted displacements for four-parameter model FFGS4 calibrated from (a) data set A, and (b) data set B.

Figures 15 compares the measured displacements in data sets A and B to those predicted by model FFGS4 in a way different from that in Figs. 13 and 14. The observed and predicted values of displacement are plotted as a function of the entry number in the data sets. Overall, this alternate representation indicates that model FFGS4 is capable of modeling the ground displacement over a wide range of displacement amplitude.

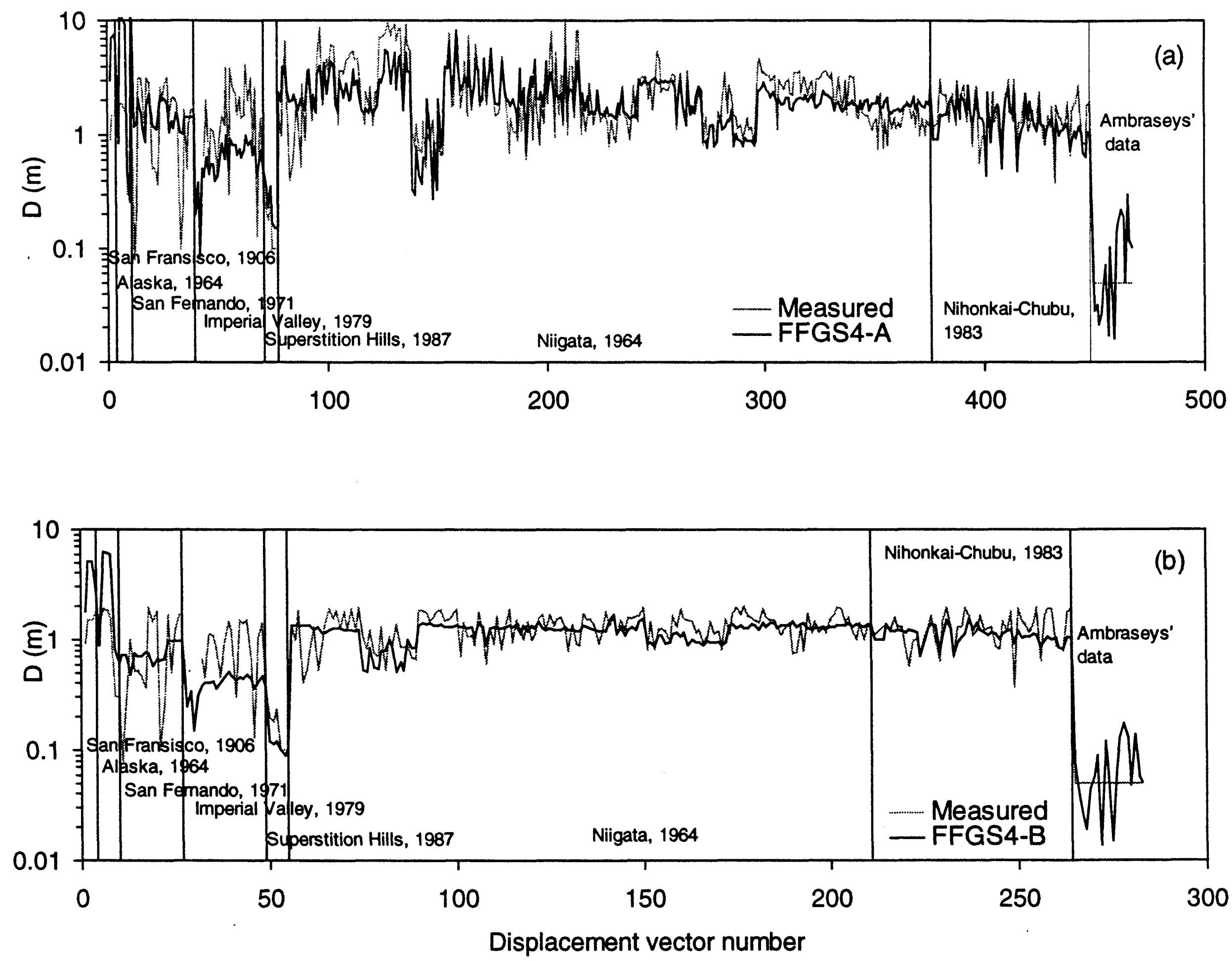

Figure 15. Comparison of amplitudes of liquefaction-induced lateral displacements measured and predicted for data set A by 4-parameter model FFGS4 calibrated from (a) data set A, and (b) data set B.

Figure 16 compares the predictions of FFGS4 and Bartlett and Youd (1992) by plotting the relative error between the measured and predicted displacements. The relative error is defined as follows:

$$\varepsilon = 100\, |D_m - D| / D_m \ (\%) \qquad (7)$$

where D_m is the measured displacement amplitude, and D is the predicted displacement amplitude. As shown in Fig. 16, the six-parameter models are more accurate than the 4-parameter models. Based on the present analysis, some preliminary recommendations can be made regarding the selection of MLR models for predicting liquefaction-induced ground displacement. The choice of a particular model depends on the availability of geotechnical data. When there is information available on the grain-size distribution of soils, Bartlett and Youd (1992) model is recommended. When there is little information on the soil grain-size distribution, model FFGS4 is recommended.

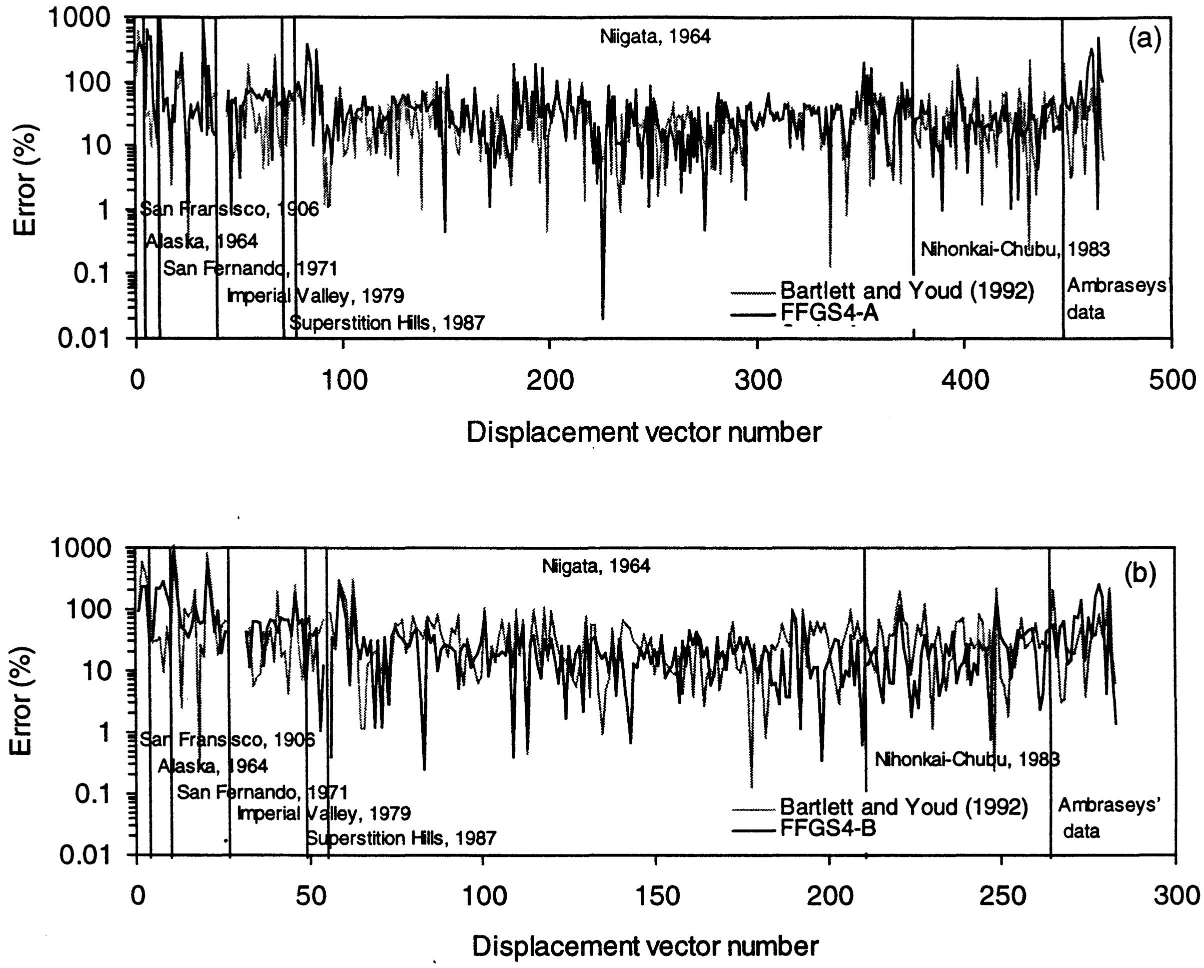

Figure 16. Comparison of relative errors between measured displacement and displacement predicted by the Bartlett and Youd (1992) model and FFGS4 model for (a) data set A and (b) data set B.

DISCUSSION

The MLR model proposed in this study is based on the database of Bartlett (1998), which was constructed from data collected prior to the 1994 Northridge and 1995 Hyogoken Nanbu earthquakes. There is a need to improve and extend the present database on liquefaction-induced lateral spreads by including data sets collected after the 1994 Northridge and the 1995 Hyogoken Nanbu earthquakes. The data should be collected inside and outside the areas where liquefaction-induced displacements were observed to take place. This effort is presently ongoing at the University of Southern California.

CONCLUSION

A four-parameter MLR model has been presented for estimating the amplitude of liquefaction-induced ground displacement. The model applies to ground-slope and free-face conditions, and is calibrated from measured displacements, topographical data, borehole information, and earthquake data prior to the 1994 Northridge and 1995 Hyogoken Nanbu earthquakes. The model has been calibrated from two data sets of all displacement ranges, and displacements smaller than 2 meters, and was found to be identical for these data sets. The model is recommended for assessing liquefaction-induced ground deformation over large areas when only limited geotechnical data is available. In a companion paper, a probabilistic model is also proposed for assessing the confidence interval for predicting ground deformation and the probability of exceeding certain ground deformation levels. The MLR model is preliminary because it is only based on data collected from earthquakes prior to 1994. Ongoing research effort is now focusing on data collection of high-quality case histories of liquefaction-induced ground deformation in the 1994 Northridge and 1995 Hyogoken Nanbu earthquakes. Following the completion of new databases, new generations of models will be proposed.

ACKNOWLEDGEMENTS

The financial support of the Pacific Earthquake Engineering Research center (PEER)-and the Pacific Gas and Electric Company (PG&E) is acknowledged. The financial support of the National Science Foundation is also acknowledged (grant CMS9812521). The authors thank Norm Abrahamson and William Savage of PG&E for their help and advice during the conduct of the research project. The authors thank Prof. L. Youd of Brigham Young University, and Dr. S. Bartlett of the Utah Department of Transportation, for sharing their databases.

REFERENCES

1. **Ambraseys, N. N.,** 1988, "Engineering Seismology," *Earthquake Engineering and Structural Dynamics,* Vol. 17, pp. 1-105.

2. **Bardet, J. P., N. Mace and T. Tobita,** 1999, "Liquefaction-induced ground deformation and failure," *Report to PEER/PG&E, University of Southern California, Civil Engineering Department,* May.

3. **Bardet, J. P, T. Tobita, N. Mace, and J. Hu,** 1999, Large-scale modeling of liquefaction-induced ground deformation. Part II: Mapping applications and probabilistic model," *Technical report MCEER-92-0021,* Multidisciplinary Center for Earthquake Engineering Research, State University of New York, Buffalo.

4. **Bardet, J. P., and C. A. Davis,** 1996, " Engineering Observations on Ground Motion At the Van Norman Complex after the 1994 Northridge Earthquake," *Bulletin of the Seismological Society of America,* Vol. 86, No. 1B, pp. S333-S349.

5. **Bardet, J. P., and C. A. Davis,** 1996, "Performance of San Fernando Dams during the 1994 Northridge Earthquake," *Journal of Geotechnical Engineering,* ASCE, Vol. 122, No. 7, pp. 554-564.

6. **Bartlett, S. F. and T. L. Youd,** 1992, "Empirical analysis of horizontal ground displacement generated by liquefaction-induced lateral spreads," *Technical report NCEER-92-0021,* National Center for Earthquake Engineering Research, State University of New York, Buffalo, pp. 5-14-15.

7. **Bartlett, S. F.,** 1998, Revised liquefaction-induced database, *Private communication.*

8. **Bartlett, S. F. and T. L. Youd,** 1995, "Empirical prediction of Lateral Spread Displacement," *Journal of Geotechnical Engineering,* ASCE, Vol. 121, No. 4, pp. 316-329.

9. **Baziar, M. H., R. Dobry, and A. W. M. Elgamal,** 1992, "Engineering evaluation of permanent ground deformation due to seismically-induced liquefaction," Technical report NCEER-92-0007, *National Center for Earthquake Engineering Research,* State University of New York, Buffalo, 2 Vol.

10. **Byrne, P. M.,** 1991, "A model for predicting liquefaction induced displacement," *Proceedings of the second international conference on recent advances in geotechnical earthquake engineering and soil dynamics*, St. Louis, Missouri, Vol. 2, pp. 1027-1035.

11. **Davis, C., and J. P. Bardet,** 1996, "Performance of two reservoirs during the 1994 Northridge Earthquake," *Journal of Geotechnical Engineering, ASCE,* Vol. 122, No. 8, pp. 613-622.

12. **Hamada, M., and K. Wakamatsu,** 1998, "Liquefaction-induced ground displacement triggered by quaywall movement," *Soils and Foundations, Special Issue Vol. 2, Japanese Geotechnical Society,* pp. 85-96.

13. **Hamada, M., and T. D. O'Rourke**, 1992, "Case histories of liquefaction and lifeline performance during past earthquakes," Technical report NCEER-92-0001, National Center for Earthquake Engineering Research, State University of New York, Buffalo, 2 Vols.

14. **Hamada, M., R. Isoyama. and K. Wakamatsu,** 1996, "Liquefaction-induced ground displacement and its related damage to lifeline facilities," *Soils and Foundations*, Special Issue on Geotechnical Aspects of the January 17 1995 Hyogoken-Nanbu Earthquake, Japanese Geotechnical Society, pp. 81-97.

15. **Hamada, M., R. Isoyama. and K. Wakamatsu,** 1996, "The 1995 Hyogoken-Nanbu (Kobe) Earthquake, Liquefaction, Ground Displacement and Soil Condition in Hanshin Area," *Association for Development of Earthquake Prediction*, The School of Science and Engineering, Waseda University, Japan Engineering Consultants.

16. **Hamada, M., S. Yasuda, R. Isoyama, and K. Emoto,** 1986, "Study on Liquefaction induced permanent ground displacement," *Report for the Association for the Development of Earthquake Prediction.*

17. **Harder, L.,** 1991, "Evaluation of Liquefaction Potential Using the SPT," *Seismic Short Course, Evaluation and Mitigation of Earthquake Induced Liquefaction Hazards*, University of Southern California, Los Angeles, February.

18. **Holzer, T. L., J. C. Tinsley, III, M. J. Bennett, and C. S. Mueller,** 1994, "Observed and predicted ground deformation - Miller Farm lateral spread, Watsonville, California," *Proceedings of the 6th U.S. Japan Workshop on Earthquake Resistant Design of Lifeline Facilities and Countermeasures for Soil Liquefaction*, NCEER, M. Hamada and T. D. O'Rourke, Eds., pp. 79-98.

19. **Holzer, T. L., M. J. Bennett, D. J. Ponti, and J. C. Tinsley, III,** 1998, "Permanent ground deformation in alluvium during the 1994 Northridge, California, earthquake," *USGS Open-file report 98-118,* Menlo Park, CA.

20. **Holzer, T. L., M. J. Bennett, J. C. Tinsley, III, D. J. Ponti, and R. V. Sharp,** 1996, "Causes of ground failure in alluvium during the Northridge," California, earthquake of January 17, 1994," *Proceedings of the 6th U.S. Japan Workshop on Earthquake Resistant Design of Lifeline Facilities and Countermeasures for Soil Liquefaction*, NCEER, M. Hamada and T. D. O'Rourke, Eds., pp. 345-360.

21. **Ishihara, K.,** 1993, "Liquefaction and flow failure during earthquakes," The 33rd Rankine lecture, *Geotechnique*, Vol. 43, No. 3, pp. 351 - 415.

22. **Ishihara, K.,** 1996, *Soil Behavior in Earthquake Geotechnics*, Oxford Science Publications, Clarendon Press, Oxford, UK.

23. **Ishihara, K., K. Yoshida, and M. Kato**, 1997, "Characteristics of lateral Spreading in Liquefied Deposits during the 1995 Hanshin-Awaji Earthquake, *Journal of Earthquake Engineering*, Vol. 1, No. 1, pp. 23-55.

24. **Ishihara, K., S. Yasuda, and H. Nagase**, 1996, "Soil characteristics and ground damage," *Soils and Foundations, Special Issue on Geotechnical Aspects of the January 17 1995 Hyogoken-Nanbu Earthquake*, Japanese Geotechnical Society, pp. 109-118.

25. **Isoyama , R.,** 1994, "Liquefaction-Induced Ground Failures and Displacements Along the Shiribeshi-Toshibetsu River Caused by the 1993 Hokkaido Nansei-oki Earthquake," *Proceedings of the 5th U.S. Japan Workshop on Earthquake Resistant Design of Lifeline Facilities and Countermeasures for Soil Liquefa*ction, NCEER, T. D. O'Rourke and M.. Hamada, Eds., pp. 1-26.

26. **Jibson, R.,** 1994, "Predicting earthquake-induced landslide displacement using Newmark's sliding block analysis," Transportation Research Record 1411, Transportation Research Board, Washington, D.C., pp. 9-17.

27. **Karube, D., and M. Kimura**, 1996, "Damage to Foundation of Railways Structures," Soils and Foundations, *Special Issue on Geotechnical Aspects of the January 17 1995 Hyogoken Nanbu Earthquake*, Japanese Geotechnical Society, pp. 201-210.

28. **Kramer, S. L.,** 1996, *Geotechnical Earthquake Engineering*, Prentice-Hall, Upper Saddle River, NJ, pp. 451-453.

29. **Liao, S. S. C.,** 1986, “Statistical modeling of earthquake-induced liquefaction," *Ph.D. Thesis*, Department of Civil Engineering, Massachusetts Institute of Technology, 470 p.

30. **Matsui, T., and K. Oda,** 1996, "Foundation Damage of Structures," *Soils and Foundations, Special Issue on Geotechnical Aspects of the January 17 1995 Hyogoken Nanbu Earthquake*, Japanese Geotechnical Society, pp. 189-200.

31. **Minitab,** 1989, *Minitab Statistical Software, Release 7*, Minitab Inc., 3081 Enterprise Drive, State College, PA 16801.

32. **O'Rourke, T. D., and P. A. Lane,** 1989, "Liquefaction hazards and their effects on buried pipelines," Technical report NCEER-89-0007, National Center for Earthquake Engineering Research, State University of New York, Buffalo.

33. **Pease, J. W., and T. D. O'Rourke,** 1993, "Liquefaction Hazards in the Mission District and South of Market Stress Areas, San Francisco, California," *U.S. Geological Survey*, External Contract No. 14-08-001-G2128.

34. **Robertson, P. K., and R. G. Campanella,** 1985, "Liquefaction Potential of Sands Using the Cone Penetration Test, " *Journal of Geotechnical Engineering*, ASCE, Vol. 111, No. 3, pp. 298-307.

35. **Rauch, A. F.,** 1997, "EPOLLS: An empirical method for predicting surface displacement due to liquefaction-induced lateral spreading in earthquakes," *PhD thesis*, Virginia Polytechnic Institute, Virginia.

36. **Seed, H. B., and P. De Alba,** 1986, "Use of SPT and CPT Tests for evaluating the liquefaction resistance of sands," *Use of In-Situ Tests in Geotechnical Engineering*, ASCE, Geotechnical Special Publication No. 6, pp. 281-302.

37. **Seed, H. B., and I. M. Idriss,** 1971, "Simplified procedure for evaluating soil liquefaction potential," *Journal of the Soil Mechanics and Foundation Division, ASCE,* Vol. 97, No. 9, pp. 1249-1274.

38. **Stokoe, K. H. II, J. M. Roesset, J. G. Biecherwale, and M. Aoouad,** 1988, "Liquefaction potential of sands from shear wave velocity," *Proceedings of the 9th world conference on earthquake engineering,* Tokyo, Japan, Vol. III, pp. 213-218.

39. **Tokimatsu, K., H. Mizumo, and M. Kakurai**, 1996, "Building Damage Associated with Geotechnical Problems," *Soils and Foundations, Special Issue on Geotechnical Aspects of the January 17 1995 Hyogoken-Nanbu Earthquake*, Japanese Geotechnical Society, pp. 219-234.

40. **Towhata, I., R. P. Orense, and H. Toyota,** 1997, Mathematical principles in prediction of lateral ground displacement induced by seismic liquefaction," *Soils and Foundations.*

41. **Towhata, I., Y. Kogai, K. Amimoto, and H. G. Putra,** 1996, "Theory and model tests on mitigation measures against lateral flow of liquefied ground," *Proceedings of the 6th U.S. Japan Workshop on Earthquake Resistant Design of Lifeline Facilities and Countermeasures for Soil Liquefaction*, NCEER, M. Hamada and T. D. O'Rourke, Eds., pp. 403-419.

42. **Yegian, M. K., E. A. Marciano, and V. G. Gharaman,** 1991, "Earthquake-induced permanent deformation: probabilistic approach," *Journal of Geotechnical Engineering, ASCE,* Vol. 117, No. 1, pp. 35-50.

43. **Youd, T. L., C. M. Hanson, and S. F. Bartlett,** 1999, "Revised MLR equations for predicting lateral spread displacements," *Proceedings of the 7th US-Japan Workshop on Earthquake Resistant Design of Lifeline Facilities and Countermeasures for Soil Liquefaction*, MCEER.

44. **Youd, T. L., and D. M. Perkins,** 1987, "Mapping of Liquefaction Severity Index," *Journal of Geotechnical Engineering Division*, ASCE, No. 11, pp. 1374-1392.

45. **Youd, T. L., and I. M. Idriss,** 1998, *Proceedings of NCEER workshop on evaluation of liquefaction resistance of soils*, National Center for Earthquake Engineering Research, State University of New York, Buffalo.

46. **Youd, T. L., E. L. Harp, D. K. Keefer, and R. C. Wilson,** 1985, "The Borah peak, Idaho earthquake of October 28, 1983 - liquefaction," *Earthquake Spectra,* EERI, Vol. 2, No. 6.

LARGE-SCALE MODELING OF LIQUEFACTION-INDUCED GROUND DEFORMATION PART II: MLR MODEL APPLICATIONS AND PROBABILISTIC MODEL

J.P. Bardet, T. Tobita, N. Mace, and J. Hu

ABSTRACT

Liquefaction-induced ground deformations are potential sources of major damage to lifelines and structures during earthquakes, as demonstrated by the substantial damage caused to lifelines and pile-foundations of buildings and bridge piers along the Kobe shoreline during the 1995 Hyogoken Nanbu, Japan, earthquake. This paper is the continuation of a paper that introduced a four-parameter MLR (Multiple Linear Regression) model for assessing the amplitude of liquefaction-induced ground deformation over large areas. The paper investigates the application of the MLR model for mapping the amplitude of liquefaction-induced ground deformation over selected regions. The paper also introduces a probabilistic model for estimating the probability for the displacements to exceed some threshold amplitude. The probabilistic model, which covers ground-slope and free-face conditions, is based on data measured prior to the 1994 Northridge earthquake and 1995 Hyogoken Nanbu earthquake. The probabilistic model can be used for assessing the confidence interval for predicting liquefaction-induced ground deformation and the probability of exceeding some ground deformation levels over large areas.

INTRODUCTION

In a companion paper (Bardet et al., 1999), a four-parameter MLR (Multiple Linear Regression) model was proposed for assessing the amplitude of liquefaction-induced ground deformations resulting from earthquakes. The amplitudes of liquefaction-induced ground deformation predicted by the MLR model were compared to the observed values as individual data points, without any examination of their spatial distributions over the earthquake-impacted regions. However, during past earthquakes, liquefaction-induced ground deformations were not confined to a few isolated locations but extended over areas as large as a few square kilometers, which caused widespread damage to spatially distributed lifeline networks. There have been very few attempts to map the regional extent of potential hazards related to liquefaction-induced ground deformation (e.g., Martin and Andrews, 1995). These preliminary studies revealed mostly difficulties and uncertainties in using the existing models for permanent ground displacement over large areas. The potential risks to lifeline networks has prompted some utility companies to seek new probabilistic methods for assessing the extent of damage and repair to lifelines after future earthquakes and for implementing retrofit policies for existing lifeline networks. To our knowledge, however, besides the probabilistic model briefly introduced by Bartlett and Youd (1992), no probabilistic approach has been proposed and tested for evaluating the probability of liquefaction-induced ground displacement.

The first section of the present paper investigates the capability of the four-parameter MLR model of Bardet et al. (1999) to predict the spatial distribution of liquefaction-induced displacement vectors in free-face and ground-slope failure cases. The second section presents the probabilistic model for assessing the confidence intervals for liquefaction-induced ground deformation and the probability for liquefaction-induced deformation to exceed some amplitude level.

Mapping of liquefaction-induced ground deformation

Figure 1 shows the surface elevation and the contours of measured displacement amplitudes for the slide referred to by Bartlett and Youd (1992) as G-10 FF′ (Kawagishi-cho) at Niigata, Japan, which resulted from the 1964 Niigata earthquake. The surface elevation is obtained from pre-earthquake elevation data (Hamada, 1999). In this area, there was a liquefaction-induced slide approximately 400 m by 400 m, which was adjacent to the Echigo Railway Bridge and directly beneath the Hakusan Sub-station. Cables attached to a tower at the substation dipped into the river due to movement towards the river (Hamada and O'Rourke, 1992). The measured displacement amplitudes are the largest along the bank of Shinano River (i.e., free face), and decrease with the distance from the free face.

In Fig. 2, the measured displacements are represented as solid vectors corresponding to measurements on the ground surface and feet of bridge footings, but not on buildings. The measured vectors are almost perpendicular to the free face to the south of the Echigo Railway Line. Figure 2 also displays additional measured displacement vectors as dashed lines. These measured displacements were included in the Bartlett and Youd (1992) database as part of a large slide area encompassed with a dashed line in Fig. 2. However, as shown in the aerial photograph of the Hakusan Sub-station (Fig. 3), these vectors appear to have been measured on top of roofs, and may not represent accurately the liquefaction-liquefaction-induced ground deformation.

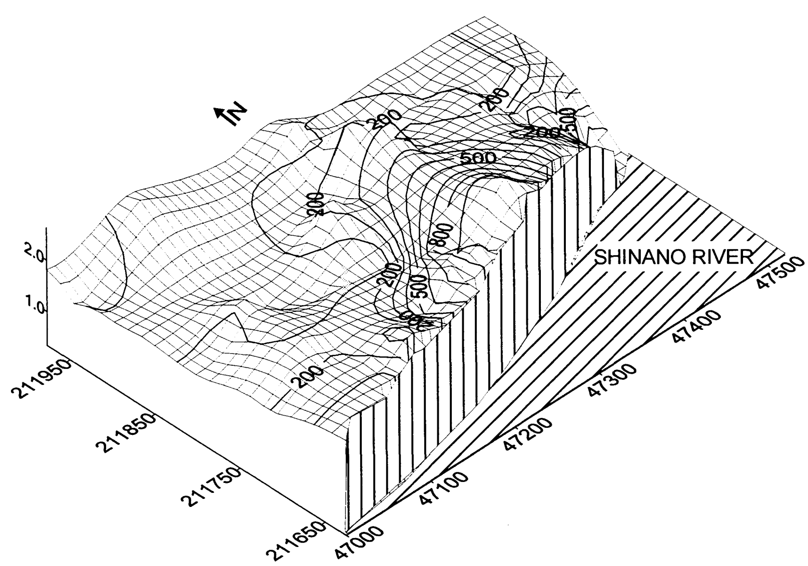

Figure 1. Ground surface elevation and contours of measured amplitude of lateral ground displacement for slide G-10 FF′ (Kawagishi-cho) during 1964 Niigata, Japan, earthquake (data after Hamada, 1999; coordinates are in meters; displacements are in centimeters).

As shown in Fig. 2, the displacement vectors were predicted at the location of measured vectors using the four-parameter MLR model FFGS4A (Bardet et al., 1999). Model FFGS4A was originally developed to predict only the amplitude of liquefaction-induced ground displacement. It requires additional assumptions for predicting the direction of liquefaction-induced lateral displacement. For free-face cases, the horizontal displacements are assumed to be perpendicular to the free face.

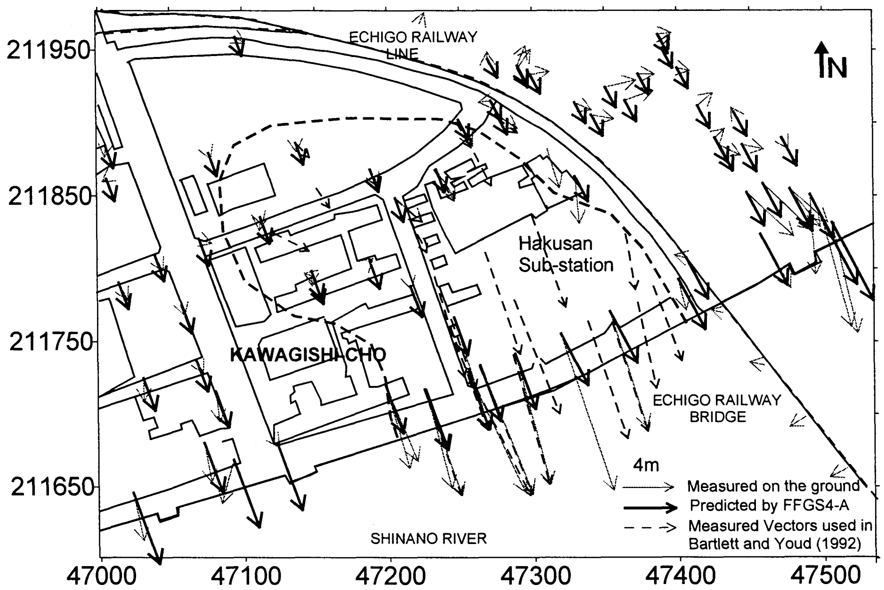

Figure 2. Measured (Bartlett and Youd, 1992; and Hamada, 1999) and predicted liquefaction-induced displacements for slide G-10 FF′ (Kawagishi-cho) at Niigata, Japan, during 1964 Niigata earthquake (coordinates are in meters).

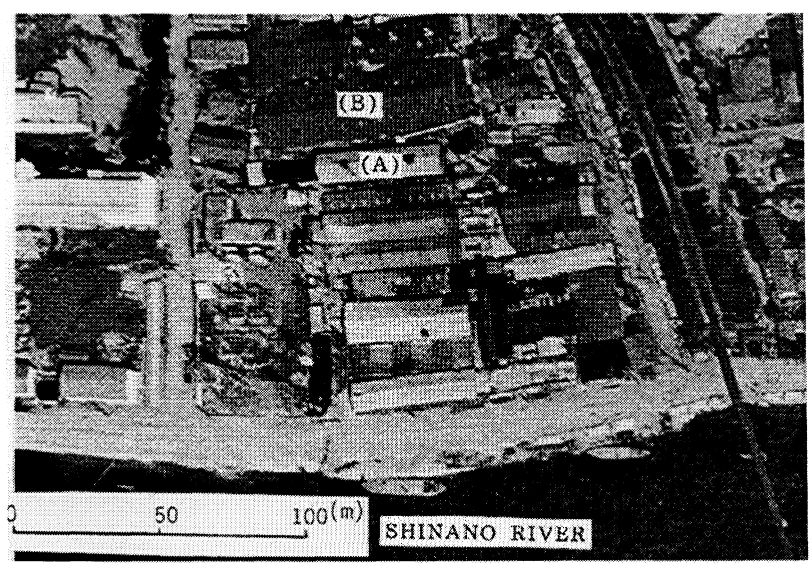

Figure 3. Aerial Photograph of Hakusan Sub-station in slide G10FF′ after the 1964 Niigata Earthquake (after Hamada and O'Rourke, 1992).

Figure 4 shows the observed and predicted displacements, surface map, borehole location, and spatial distribution of the MLR parameters, thickness T_{15} and free-face ratio for the slide G-10 FF′ at Niigata, Japan, during the 1964 Niigata earthquake. The values of T_{15} and free-face ratio W, which are required by model FFGS4-A, were calculated at 50 by 34 grid points evenly spaced at a 10.5-m grid interval. The values of T_{15} at the grid points were generated from the values of T_{15} at the boreholes represented as pins in Fig. 4d using the Kriging method (e.g., Golden Software, 1998). The values of W at the grid points were calculated by determining the minimum distance L between the grid points and the free face along the riverside, which was approximated by two straight segments. The height H of free face was selected equal to 5.2 meter as in the Bartlett and Youd (1992) database. The value of W, which theoretically becomes infinite along the free face, was set equal to the maximum value of 56%, which is the maximum observed value in the database of Bartlett (1998).

As shown in Fig. 4b, the contours indicate that the amplitude of predicted displacements decrease uniformly with the distance from the free face, which translates the significant effects of free-face ratio and the relative small effects of T_{15} spatial variation in model FFGS4A. The model predicts maximum ground deformation in excess of 5 m along the free face. However, the contours in Fig. 4a display a different and more concentrated spatial distribution of observed ground deformation, which may have been caused by the local failure of the embankment along the Shinano river. One may also speculate that displacements would have been more accurately predicted if there were more available data on boreholes and height H of free face along the Shinano river. There are however definite uncertainties in generating spatially the averages from borehole data, which leads generally to overestimating the extent of liquefaction-induced slides. There is a need to collect data outside slide areas for constraining more definitely the spatial extent of liquefaction-induced lateral spreads.

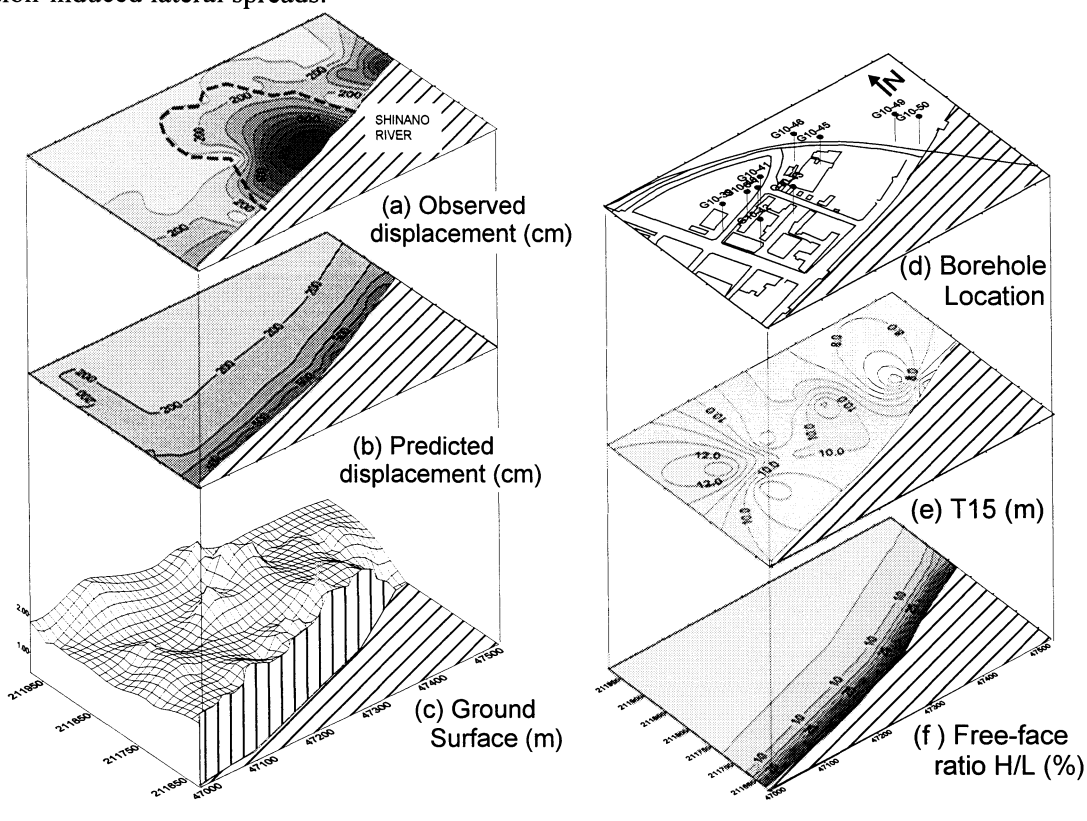

Figure 4. Representation of (a) observed and (b) predicted amplitude of liquefaction-induced lateral ground deformation, (c) ground surface, (d) borehole location, spatial distribution of (e) thickness T_{15}, and (f) free-face ratio for slide G10-FF′ (Kawagishi-cho) in Niigata during the 1964 Niigata, Japan, earthquake (data after Hamada, 1999; coordinates are in meters; displacements are in centimeters).

Figure 5 shows the ground surface elevation and the contours of measured displacement amplitudes for the slide H-10 MM′ (Bandai 5 cho-me) at Niigata, Japan, during the 1964 Niigata earthquake. Slide H-10MM′ occurred in the vicinity of the Hotel Niigata and covered an area of approximately 400 by 200 m.

Catastrophic failure of the hotel piles was documented in Hamada and O'Rourke (1992). The magnitudes and directions of the liquefaction-induced displacement vectors were related to the ground slope. This slide, which took place far away from any free faces, is considered to be a representative example of ground-slope cases.

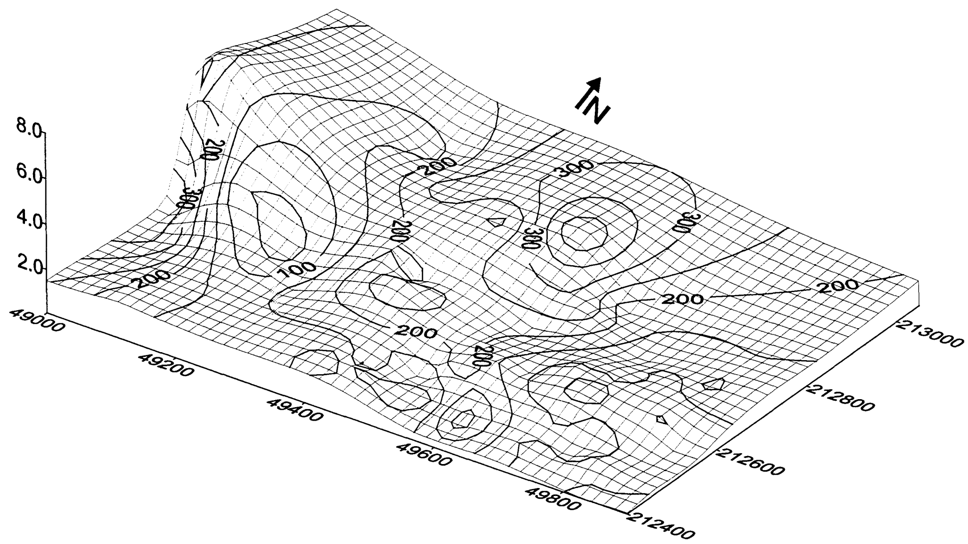

Figure 5. Ground surface elevation and contour of measured amplitude of lateral ground displacement for slide H10-MM′ (Bandai 5 cho-me) during 1964 Niigata, Japan, earthquake (ground elevation and displacement data from Hamada, 1999; coordinates are in meters and displacements are in centimeters).

In Fig. 6, as for Fig. 2, the displacements measured on the ground surface are represented using solid lines, while those measured on buildings and included in Bartlett and Youd (1992) database are drawn with dashed lines. The measured displacements are small compared to those of the free-face case of Fig. 2. The area delineated by a dashed line represents the slide area considered by Bartlett and Youd (1992), which encompasses a junior-high school. The displacement vectors on the ground surface and buildings are often difficult to distinguish when they are plotted on topographical maps. This distinction requires the in-depth examination of the original aerial photographs (Hamada, 1999) which have been used to compute the measured displacement vectors.

As shown in Fig. 6, the liquefaction-induced displacement vectors were predicted over a 900 by 660 m area using model FFGS4A. For this particular ground-slope case, the horizontal displacements are assumed to be collinear to the average slope gradient direction. As shown in Fig. 7c, the area was covered with a 50 x 30 grid, the points of which were evenly spaced at a 18 m and 22 m intervals in the north-south and east-west directions, respectively. The average ground-slope direction was determined through a moving average of the local ground-slope direction over the closest 16 grid points. The values of T_{15} at the grid points were calculated from those at the discrete boreholes represented as numbered pins in Fig. 7d using the same Kriging techniques as in Fig. 4. The displacement vectors were not predicted when the values of T_{15} and ground slope were outside the range of observed values in the database. As shown in Figs. 6 and 7, model FFGS4-A predicts reasonably well the amplitude and spatial distribution of liquefied displacement within the slide area. As in the free-face case of Figs 1 - 4, there are still definite uncertainties in defining the extent of the liquefaction-induced slides, which need to be resolved in future studies.

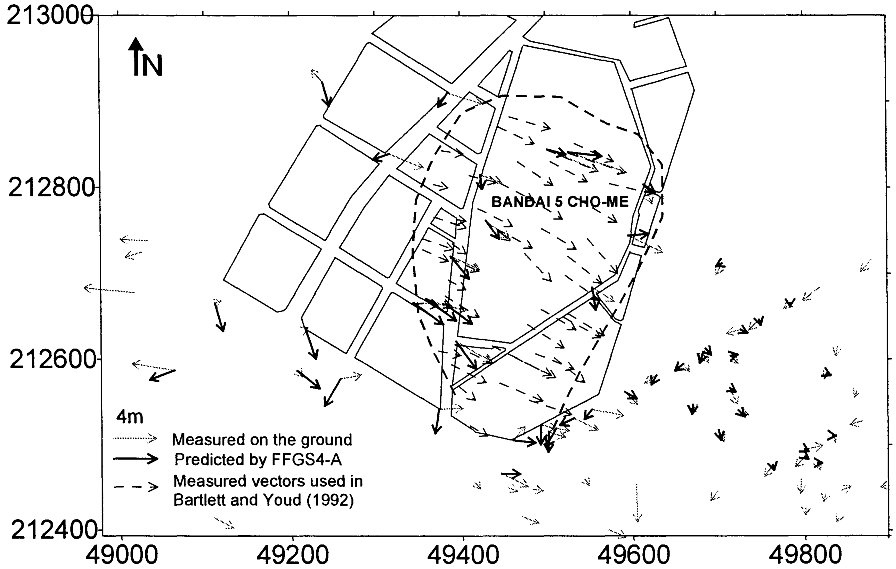

Figure 6. Measured (Bartlett and Youd, 1992; and Hamada, 1999) and predicted liquefaction-induced displacements for slide H-10 MM′ (Bandai 5 cho-me) at Niigata, Japan, during 1964 Niigata earthquake (coordinates are in meters).

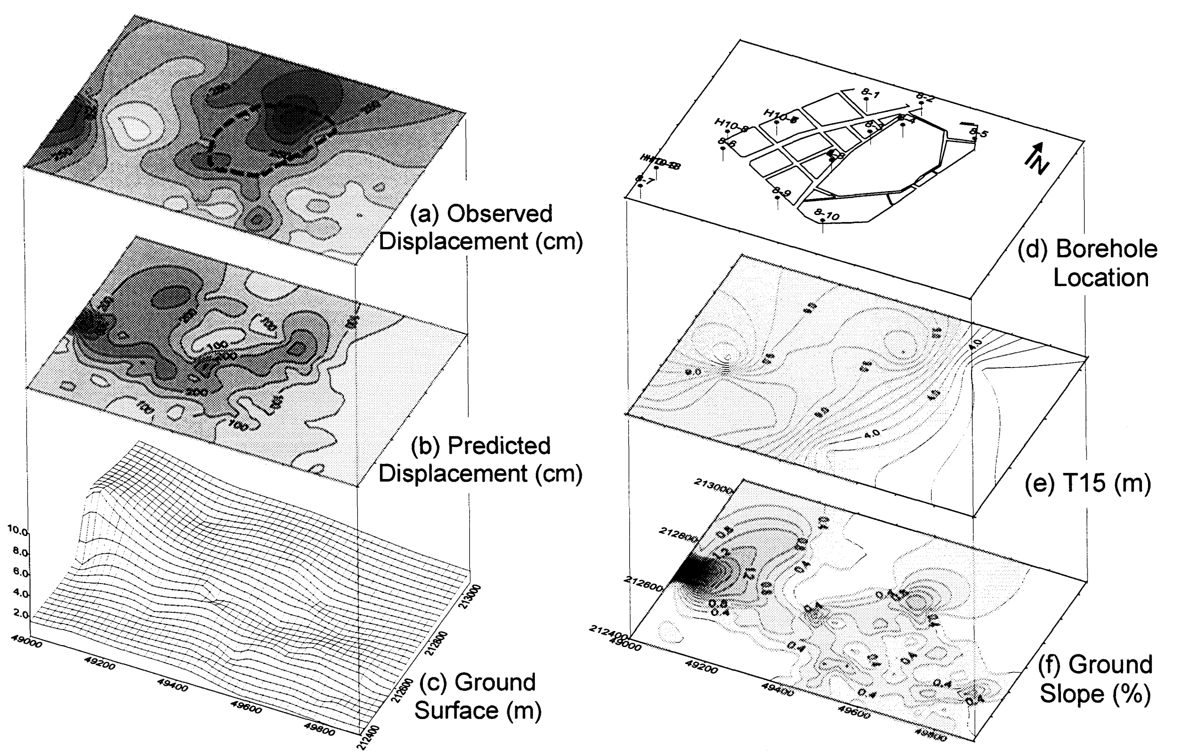

Figure 7. Representation of (a) observed and (b) predicted amplitude of liquefaction-induced lateral ground deformation, (c) ground surface, (d) borehole location, spatial distribution of (e) thickness T_{15}, and (f) average ground slope for slide G10-FF′ (Bandai 5 cho-me) in Niigata during the 1964 Niigata, Japan, earthquake (data from Hamada, 1999; coordinates are in meters; displacements are in centimeters).

PROBABILISTIC MODEL OF LIQUEFACTION-INDUCED GROUND DEFORMATION

The MLR model of Bardet et al. (1999) predicts the mean values of liquefaction-induced ground deformation. Based on the previously developed MLR models, this section determines (1) the confidence limits for liquefaction-induced ground deformation and (2) the probability of exceeding some level of ground deformation. The reader is referred to Draper and Smith (1981) for details on probability analysis.

Mean and variance of ground deformation

The MLR model FFGS4 for liquefaction-induced ground deformation predicts the value of ground deformation $\hat{D}$ in the following generic form:

$$\hat{D} = b_0 + b_1 X_1 + \ldots + b_p X_p \tag{1}$$

where $b_0, \ldots, b_p$ are constant coefficients, $X_1, \ldots, X_p$ are the model variables and p the total number of model variables. The variance of $\hat{D}$ is:

$$V(\hat{D}) = V(b_0 + b_1 X_1 + \ldots + b_p X_p) \tag{2}$$

Eq. 2 can be expanded as follows:

$$\begin{aligned} V(\hat{D}) = {} & V(b_0) + X_1^2 V(b_1) + \ldots + X_p^2 V(b_p) \\ & + 2X_1 \mathrm{covar}(b_0, b_1) + \ldots + 2X_p \mathrm{covar}(b_0, b_p) \\ & + 2X_1 X_2 \mathrm{covar}(b_1, b_2) + \ldots + 2X_{p-1} X_p \mathrm{covar}(b_{p-1}, b_p) \end{aligned} \tag{3}$$

where $\mathrm{V}(b_i)$ is the variance of coefficient b_i, and $\mathrm{covar}(b_i, b_j)$ is the covariance of coefficient b_i and b_j. Equation 3 can be written in a matrix form as follows:

$$V(\hat{D}) = s^2 \mathbf{X}_0^T \mathbf{C} \mathbf{X}_0 \tag{4}$$

s^2 is the residual mean square:

$$s^2 = \frac{1}{n-p-1} \sum_{i=1}^{n} \left(\hat{D}_i - D_i\right)^2 \tag{5}$$

where D_i is the i$^{\text{th}}$ observed value of D, and $\hat{D}_i$ is i$^{\text{th}}$ predicted value corresponding to D_i (i=1 to n).The variance-covariance matrix $s^2\mathbf{C}$ has $p+1$ columns and $p+1$ rows:

$$\mathbf{C} = \left(\mathbf{X}^T \mathbf{X}\right)^{-1} = \begin{pmatrix} c_{00} & c_{01} & \cdots & c_{0p} \\ c_{10} & c_{11} & \cdots & c_{1p} \\ \vdots & & \ddots & \vdots \\ c_{p0} & & & c_{pp} \end{pmatrix} \tag{6}$$

The matrix $\mathbf{X}$ with $p+1$ columns and n rows is defined as:

$$\mathbf{X} = \begin{pmatrix} 1 & X_{1,1} & \cdots & X_{1,p} \\ 1 & X_{2,1} & \cdots & X_{2,p} \\ \vdots & \vdots & \vdots & \vdots \\ 1 & X_{n,1} & \cdots & X_{n,p} \end{pmatrix} \tag{7}$$

where $X_{i,j}$ is the value of the j^{th} variable of the i^{th} observation. In Eq. 4, the vector $\mathbf{X}_0$ represents the values of the model variables for an individual observation. $\mathbf{X}_0$ has the same type of components as a row of $\mathbf{X}$. The vector $\mathbf{X}_0$ and its transpose $\mathbf{X}_0^T$ are:

$$\mathbf{X}_0 = \begin{pmatrix} 1 \\ X_1 \\ X_2 \\ \vdots \\ X_p \end{pmatrix} \quad \text{and } \mathbf{X}_0^T = \begin{pmatrix} 1 & X_1 & X_2 & \cdots & X_p \end{pmatrix} \tag{8}$$

In the case of model FFGS4, the components of $\mathbf{X}_0$ are given in Table 1. The components of matrix **C** and residual mean square s^2 for the MLR model were calculated by using the computer program Minitab (1989). Table 2 and 3 list the values of the components of $\mathbf{X}_0$, matrix **C,** number of observation used in the regression, number of degree of freedom, and s^2 for model FFGS4-A and –B, respectively. Based on the values of **C** and s^2, the confidence limits for ground deformation and probability of exceeding some amplitude threshold can be defined.

Table 1. Components of observation vector $\mathbf{X}_0$.

Component	Variable	Definition
1		
X_1	B_{off}	1 for free face and 0 for ground slope
X_2	M	Earthquake moment magnitude
X_3	R	Closest distance to source (km)
X_4	*Log R*	*Log* of *R*
X_5	*Log W*	Free-face ratio
X_6	*Log S*	Ground slope (%)
X-	*Log* T_{15}	Thickness of saturated cohesionless soils with $(N1)_{60}$<15 (m)

Table 2. Values of coefficients for MLR and probabilistic models FFGS4-A.

Components os X							
1.0	*0 or 1*	*M*	*LOG(R)*	*R*	*LOG(W)*	*LOG(S)*	*LOG(T_{15})*
MLR coefficients							
b_0	b_{off}	b_1	b_2	b_3	b_4	b_5	b_6
-6.815	-0.465	1.017	-0.278	-0.026	0.497	0.454	0.558
Matrix C (symmetric)							
0.0005	0.0001	0.0000	0.0001	0.0000	-0.0004	0.0000	0.0000
	0.0465	-0.0008	-0.0003	0.0001	-0.0399	-0.0113	-0.0051
		0.0006	-0.0023	0.0000	-0.0004	0.0006	-0.0012
			0.0247	-0.0005	0.0061	-0.0027	-0.0056
				0.0000	-0.0002	0.0001	0.0001
					0.0468	0.0000	-0.0002
						0.0443	0.0106
							0.0223

Number of observations (n) = 467

Number of degrees of freedom (p) = 7

Residual mean square (s^2) = 0.084

Table 3. Values of coefficients for MLR and probabilistic models FFGS4-B.

Components os X							
1.0	*0 or 1*	*M*	*LOG(R)*	*R*	*LOG(W)*	*LOG(S)*	*LOG(T_{15})*
MLR coefficients							
b_0	b_{off}	b_1	b_2	b_3	b_4	b_5	b_6
-6.747	-0.162	1.001	-0.289	-0.021	0.090	0.203	0.289
Matrix C (symmetric)							
1.718	0.009	-0.254	0.115	0.002	-0.076	0.012	-0.005
	0.080	-0.003	0.000	0.000	-0.073	-0.030	-0.016
		0.038	-0.021	0.000	0.011	0.000	-0.001
			0.041	0.000	0.003	0.002	-0.002
				0.000	-0.001	0.000	0.000
					0.096	0.006	0.011
						0.084	0.020
							0.035

Number of observations (n) = 283

Number of degrees of freedom (p) = 7

Residual mean square (s^2) = 0.079

Confidence limits

The mean value of q future observations at $\mathbf{X}_0$ is supposed to fall within the following $1-\alpha$ confidence limits D_- and D_+:

$$D_{\pm} = \hat{D} \pm t(n-p-1, 1-\tfrac{1}{2}\alpha)s\sqrt{\frac{1}{q}+\frac{1}{n}+\mathbf{X}_0^T\mathbf{C}\mathbf{X}_0} \tag{9}$$

where $\hat{D}$ is the predicted mean value, t is the t-distribution with n-p-1 degrees of freedom (Fig. 8), α is the significance level, s is the residual mean, and n is the total number of observations used in the regression. When there is only one future observation at $\mathbf{X}_0$, the confidence limits at $\mathbf{X}_0$ are evaluated by setting q equal to 1. When there are more than one future observation at $\mathbf{X}_0$ (i.e., $q > 1$), the confidence interval for the mean value of these q future observations becomes smaller with q. The interval become minimum when there are many future observations at $\mathbf{X}_0$ (i.e., $1/q \rightarrow 0$). When n becomes large (e.g., $n > 500$), the t-

distribution becomes identical to the normal distribution. The probability for the predicted value D at $\mathbf{X}_0$ to be comprised of between D_- and D_+ is equal to $1-\alpha$, i.e.:

$$p(D_- \leq D \leq D_+) = 1 - \alpha \tag{10}$$

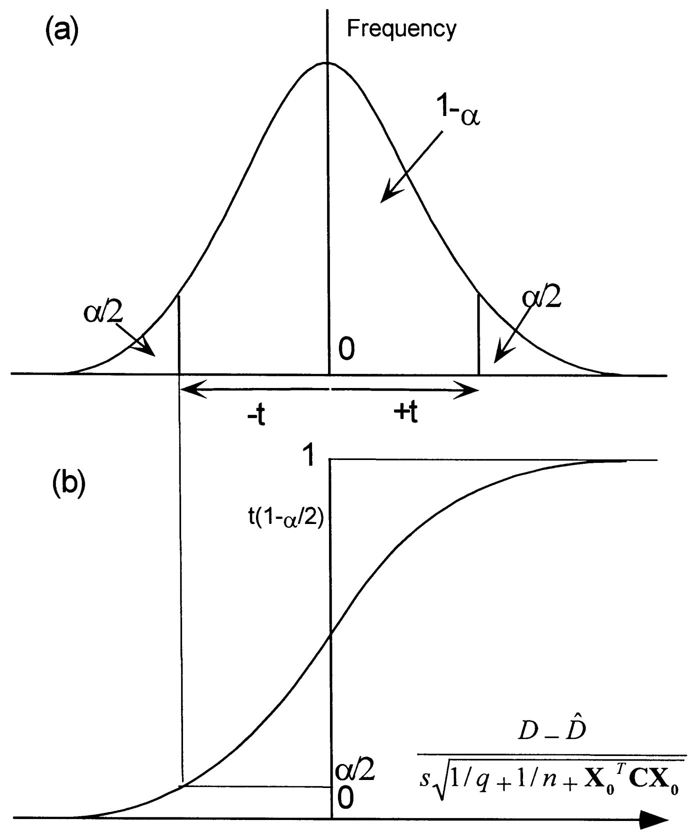

Figure 8. Representation of t-distribution: (a) probability distribution function of t-distribution with two tails, and (b) inverse t-distribution.

Probabilistic model

Based on Eq. 9, the probability $p(D>D^*)$ for the ground deformation D at $\mathbf{X}_0$ to exceed some value D^* is estimated as follows:

$$p(D > D^*) = \beta \tag{11}$$

where β is the area under the t-probability distribution curve as shown in Fig. 9a. Using the inverse t-distribution t^{1} (Fig. 9b), Eq. 11 can be written as follows:

$$
p(D > D^*) = \begin{cases} 1 - t^{-1}\left(n-p-1, \dfrac{\hat{D} - D^*}{s\sqrt{1/q + 1/n + \mathbf{X}_0^T \mathbf{C} \mathbf{X}_0}} \right) & \text{if } D^* < \hat{D} \\ t^{-1}\left(n-p-1, \dfrac{D^* - \hat{D}}{s\sqrt{1/q + 1/n + \mathbf{X}_0^T \mathbf{C} \mathbf{X}_0}} \right) & \text{if } D^* \geq \hat{D} \end{cases} \tag{12}
$$

Equation 12 gives the probability that the value D of liquefaction-induced ground deformation at $\mathbf{X}_0$ exceeds some value D^*. The parameter n refers to the total number of observations used in the regression analysis. The parameter q is the number of future observations at $\mathbf{X}_0$. The probability for the predicted value D to exceed D^* at $\mathbf{X}_0$ is given by setting q equal to 1. The probability corresponding to the mean value of D evaluated from a large number of future observations is given by setting $1/q$ equal to zero.

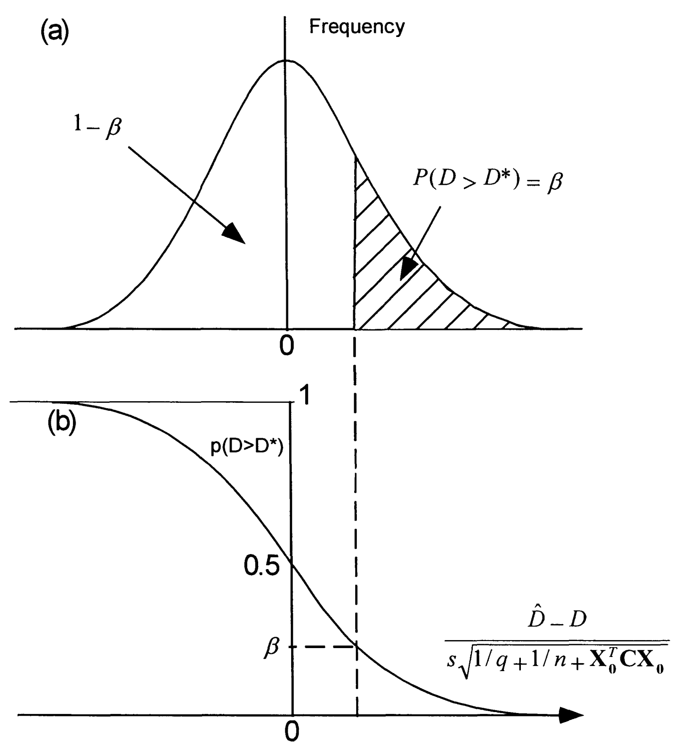

Figure 9. Representation of probabilistic model for exceeding a threshold of deformation: (a) probability distribution function of t-distribution with single tail, and (b) inverse t-distribution $D^* < \hat{D}$.

Confidence intervals for liquefaction-induced ground deformation

Figure 10 shows the confidence limits of liquefaction-induced deformation predicted by model FFGS4-A (q = 1) for all the individual observations in the Bartlett (1998) database. The confidence limits corresponding to 95% confidence are represented by error bars. The numbers along the horizontal axis refer to the numbering system in data set A, which regroups data points by earthquakes. Figure 10 also shows the measured displacement values, and the values of mean displacement predicted by model FFGS4-A as a line centered at the error bars. The confidence intervals enclose most of the measured displacement values. In some cases however, these intervals become large and do not encompass the measured displacement.

Figure 11 shows the confidence limits for model FFGS4-B, which were calibrated from data sets B including only displacements smaller than 2 meters. Overall, the confidence intervals enclose the measured values slightly more accurately than model FFGS4-A.

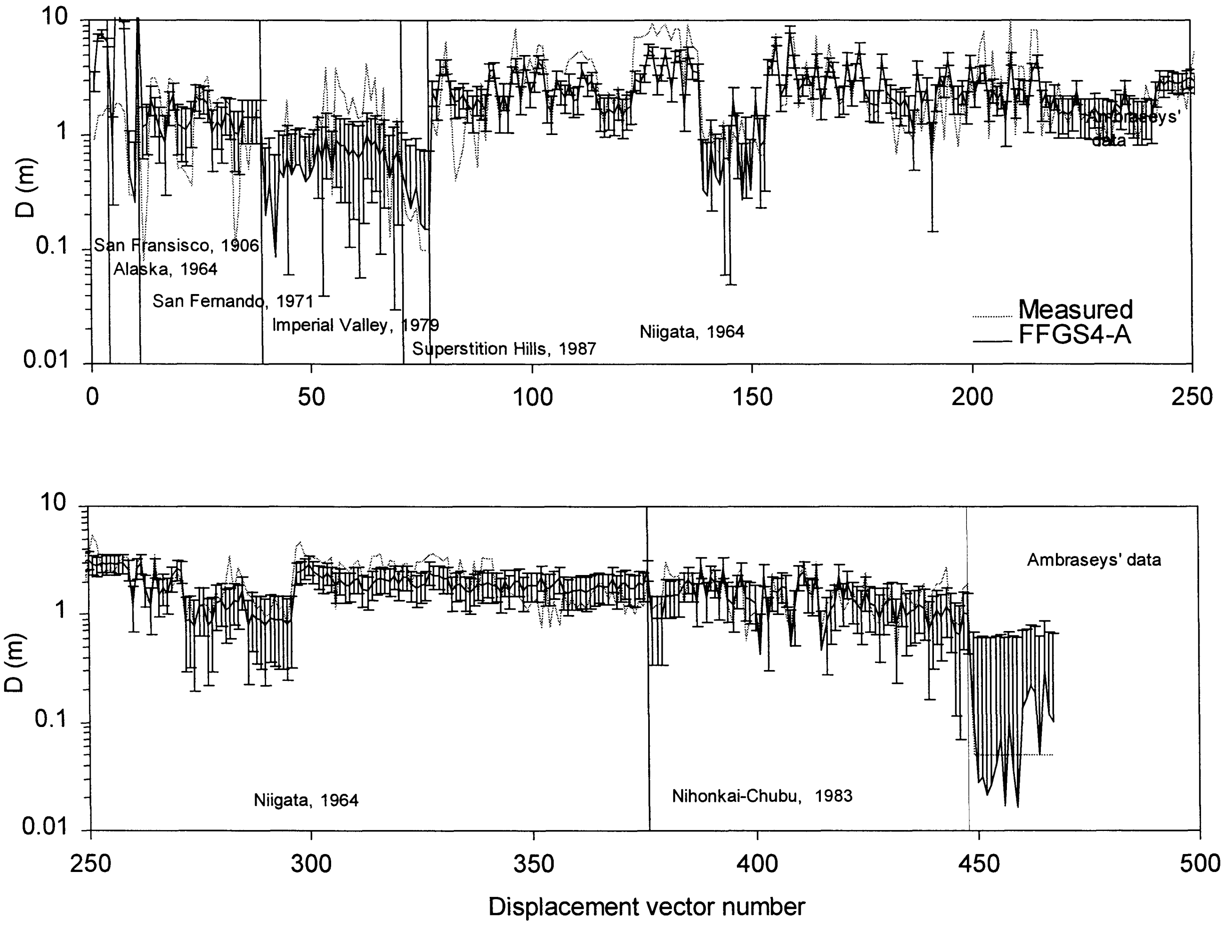

Figure 10. Model FFGS4-A for liquefaction-induced lateral displacement: measured displacement, predicted mean displacement and confidence interval (95% *t*-distribution).

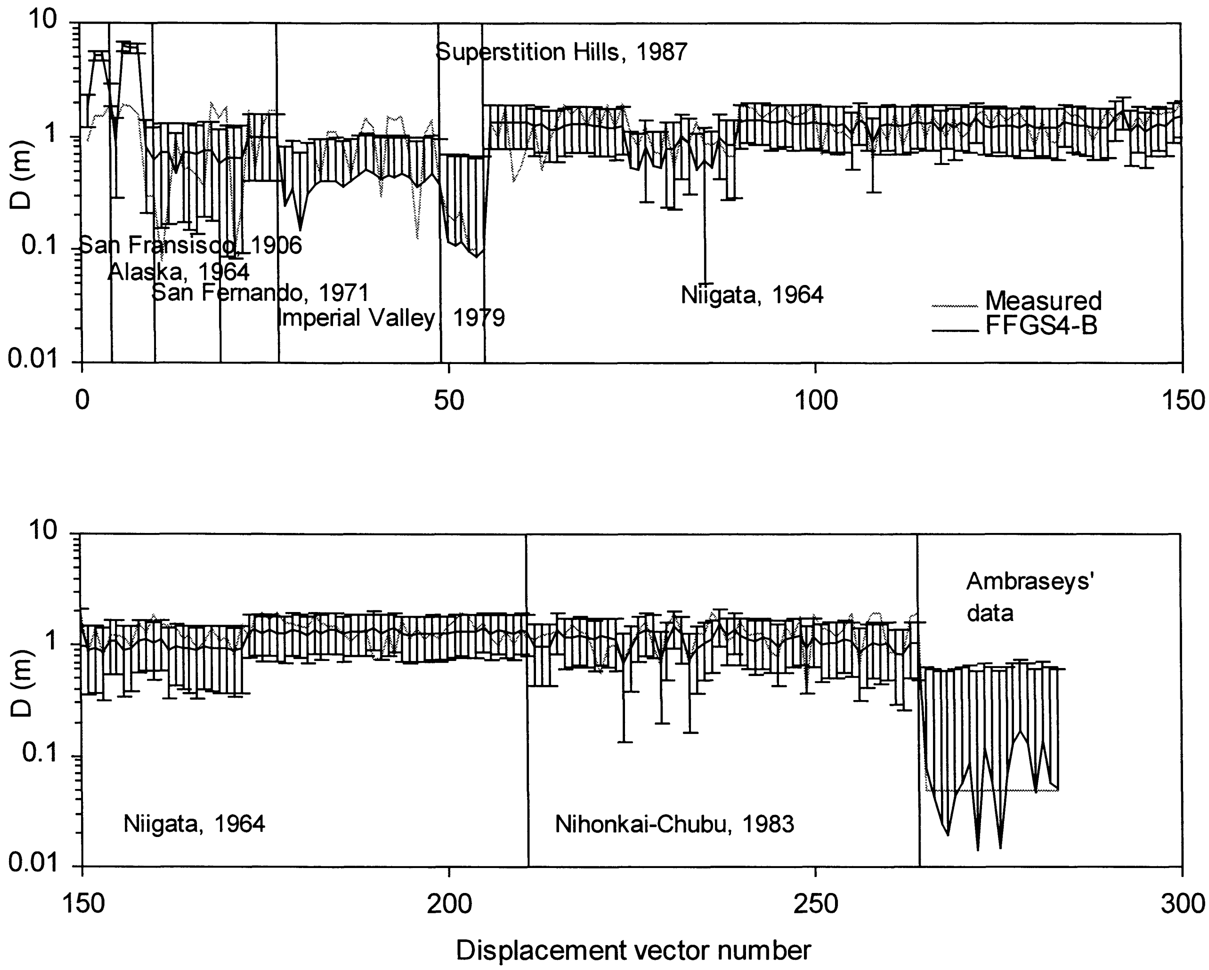

Figure 11. Model FFGS4-B for liquefaction-induced lateral displacement: measured displacement, predicted mean displacement and confidence interval (95% t-distribution).

Probability calculation

Equation 12 defines the probabilistic model for assessing the probability of the liquefaction-induced ground deformation to exceed some threshold value D^*, given some local conditions characterized by the parameter values $\mathbf{X}_0$. The value of q should be set equal to 1 for calculating the probability associated to a single event. Tables 2 and 3 list all the required values for calculating probability including the variance-covariance matrix $s^2\mathbf{C}$, the residual mean square s, and the total number n of observations.

Figure 12 shows an example of the probability map generated using model FFGS4-A over the area of slide G-10 FF′ (Kawagishi-cho) in Niigata, Japan, which would take place for an earthquake having the same magnitude and distance as the 1964 Niigata earthquake. For comparison, Figs. 2 and 4a show the measured displacements in the same area. The probabilities for displacement amplitude to exceed 2 m were evaluated using Eq. 12 at the grid points of Fig. 4, from the values of T_{15} and free-face ratio W previously calculated at these grid points. As shown in Fig. 11, the probability of displacement exceeding 2 m near the free face is

100%. On the West, the probability is slightly higher due to the increase in thickness T_{15} of liquefied layer. The probability contours of Fig. 11 are similar to those of predicted displacement in Fig. 4b.

Figure 13 shows an example of the probability map calculated for ground-slope conditions over the area of slide H-10 MM′ (Bandai 5 Cho-me) in Niigata, Japan, which would occur for an earthquake having parameters identical to those of the 1964 Niigata earthquake. The probabilities for the ground deformation to exceed 2 m were evaluated at the grid points of Fig. 7. For comparison, Figs. 6 and 7a show the measured displacements in the same area. As expected, the 50% probability contours of Fig. 13 correspond to the contours related to a 2 m mean predicted value in Fig. 4b.

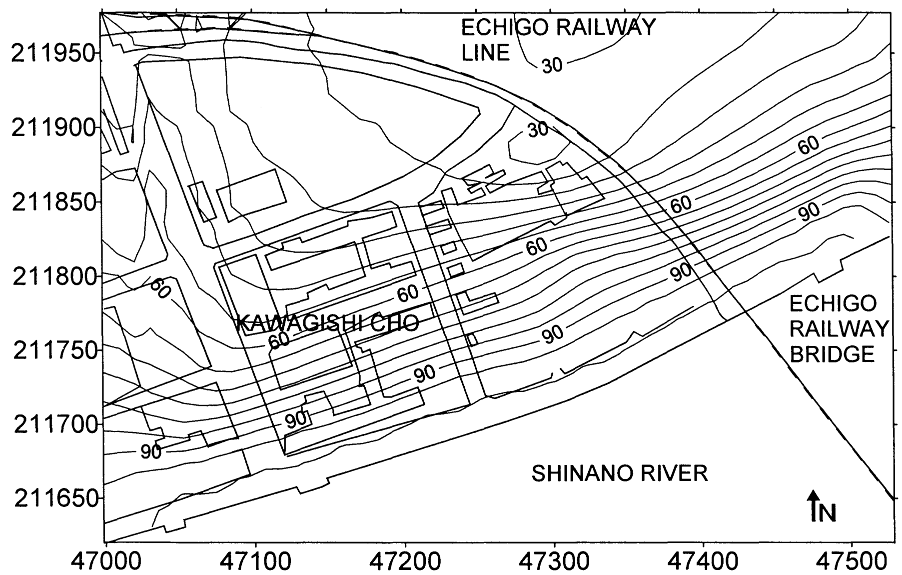

Figure 12. Predicted probability of liquefaction-induced lateral spread larger than 2 m in the area of slide G-10 FF′ (Kawagishi-cho) at Niigata, Japan, corresponding to the 1964 Niigata earthquake.

Discussion

Mapping the probability of liquefaction-induced displacement amplitudes requires the use of spatial interpolation techniques similar to those used for mapping the predicted mean values of displacement. As previously mentioned, there are definite uncertainties in extending the probability maps outside the slide areas, unless sufficient information for the surrounding area is provided.

The probabilistic model in this study is based on the database of Bartlett (1998), which regroups data collected prior to the 1994 Northridge and 1995 Hyogoken Nanbu earthquakes. There is a need to improve and extend the present database on liquefaction-induced lateral spreads by including the data sets from the 1994 Northridge earthquake and 1995 Hyogoken Nanbu earthquake. The data should be collected inside and outside the areas where liquefaction-induced displacements were observed to take place. This effort is presently ongoing at the University of Southern California utilizing GIS (Geographic Information Systems) techniques similar to those used here for representing the spatial extent of liquefaction-induced deformation hazards. Following the completion of the new database on liquefaction-induced ground deformation, new generations of probabilistic models will be proposed.

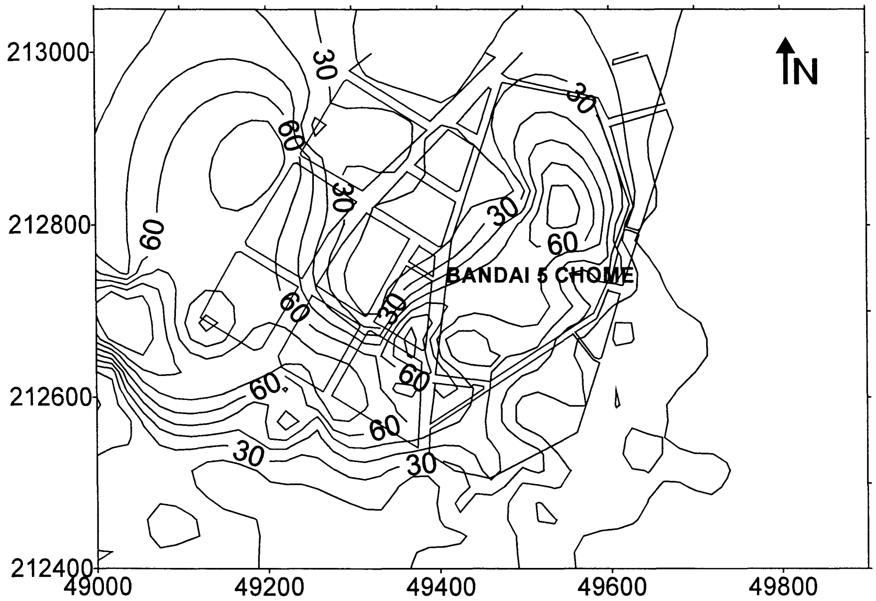

Figure 13. Predicted probability of liquefaction-induced lateral spread larger than 2 m in the area of slide H-10 MM′ (Bandai 5 Cho-me) at Niigata, Japan, corresponding to the 1964 Niigata earthquake.

CONCLUSION

The capabilities of a four-parameter MLR model for assessing the extent of liquefaction-induced ground deformation have been investigated. The model was shown to generate a comprehensive representation of the free-face and ground-slope deformations observed during the 1964 Niigata earthquake. A probabilistic model has been proposed for estimating the probability for liquefaction-induced displacements to exceed some threshold amplitude. The model is intended for assessing the extent of potential damage to spatially distributed lifeline networks resulting from future earthquakes. The model is based on measured data from earthquakes prior to 1994. The model has four parameters, and covers ground-slope and free-face conditions. It was calibrated indifferently from two data sets including all the displacement ranges, and displacements smaller than 2 meters, respectively. The probabilistic model is useful for assessing the confidence interval for predicting ground deformation and the probability of exceeding some ground deformation levels. The probabilistic model is preliminary because it is only based on data collected from earthquakes prior to 1994. Ongoing research is now focusing on assembling case histories of liquefaction-induced ground deformation from the 1994 Northridge and 1995 Hyogoken Nanbu earthquakes.

ACKNOWLEDGEMENTS

The financial support of the Pacific Earthquake Engineering Research center (PEER)-and the Pacific Gas and Electric Company (PG&E) is acknowledged. The financial support of the National Science Foundation (grant CMS9812521) is also acknowledged. The authors thank Norm Abrahamson and William Savage of PG&E for their help and advice during the course of this research project. The authors thank Prof. L. Youd of Brigham Young University, and Dr. S. Bartlett of the Utah Department of Transportation, for sharing their databases. The authors also thank Prof. M. Hamada of Waseda University, Japan, and his colleagues for providing us with reports and digital data.

REFERENCES

1. **Bardet, J. P, N. Mace, T. Tobita, and J. Hu,** 1999, Large-scale modeling of liquefaction-induced ground deformation. Part I: A four-parameter MLR model," *Technical report MCEER-92-0021,* Multidisciplinary Center for Earthquake Engineering Research, State University of New York, Buffalo.

2. **Bartlett, S. F. and T. L. Youd,** 1992, "Empirical analysis of horizontal ground displacement generated by liquefaction-induced lateral spreads," *Technical report NCEER-92-0021,* National Center for Earthquake Engineering Research, State University of New York, Buffalo, pp. 5-14-15.

3. **Bartlett, S. F. and T. L. Youd,** 1995, "Empirical prediction of Lateral Spread Displacement," *Journal of Geotechnical Engineering,* ASCE, Vol. 121, No. 4, pp. 316-329.

4. **Bartlett, S. F.,** 1998, Revised liquefaction-induced database, *Private communication.*

5. **Draper, N. R., and H. Smith**, 1981, *Applied Regression Analysis*, 2nd edition, John Wiley & Sons, New York, p 709.

6. **Golden Software,** 1998, *Surfer for Windows, Version 6*, Golden Software, Inc., Golden, Colorado.

7. **Hamada, M.,** 1999, Digital data of liquefaction-induced lateral spread for the 1964 Niigata Earthquake, *private communication.*

8. **Hamada, M., and T. D. O'Rourke**, 1992, "Case histories of liquefaction and lifeline performance during past earthquakes," Technical report NCEER-92-0001, National Center for Earthquake Engineering Research, State University of New York, Buffalo, 2 Vols.

9. **Martin, G. R., and D. C. Andrews,** 1995, "Map Based Characterization of Liquefaction potential for Southern California," *Task H-8 report, Southern California Earthquake Center*, University of Southern California, December.

10. **Minitab,** 1989, *Minitab Statistical Software, Release 7,* Minitab Inc., 3081 Enterprise Drive, State College, PA 16801.

SIMILITUDE LAW FOR LIQUEFIED-GROUND FLOW

Masanori HAMADA
School of Science and Engineering
Department of Civil Engineering
Waseda University
3-4-1, Ohkubo, Shinjuku-ku, Tokyo, 169-8555, Japan

ABSTRACT

This Paper discusses a similitude law for liquefaction-induced ground flow, which is essential in order to predict displacements of actual grounds from experimental data by flow tests of model grounds. The author has shown that the liquefied soil behaves as a quasi-plastic fluid and that the Reynolds' similitude law holds between the flow of model grounds and that of actual grounds. In the present paper the similitude law is examined by model tests where the thickness of the liquefied soil is varied. Furthermore, horizontal displacements of actual grounds in the case studies were predicted from the experimental results by applying the similitude law, which showed a good coincidence with the displacements observed during the past earthquakes.

Introduction

The liquefaction-induced large ground displacements have caused serious damage to foundation piles and buried pipes of lifeline systems during the past earthquakes such as the 1995 Kobe and the 1994 Northridge earthquakes. Therefore, it is one of urgent research subjects to investigate into the mechanism of large displacements of liquefied ground and behaviors of the underground structures against the ground flow, and to develop rational as well as practical methods for the prediction of ground displacements.

After the 1995 Kobe earthquake in Japan, the effects of the liquefaction-induced ground displacements have been taken partially into the consideration in the development of the earthquake resistant design codes. However, the consideration is not yet sufficient due to lack of information and knowledge about the mechanism of this phenomena.

This paper firstly discusses a similitude law governing the liquefied-ground flow and secondarily applies the law for prediction of displacements of actual grounds from flow tests of model ground.

Examination of Similitude Law of Liquefied-Ground Flow

In order to examine the similitude law which governs the flow of the liquefied-ground a shaking table test of model grounds where the thickness of the liquefied soil varies 15 to 35 cm was carried out. The model ground and the soil box for the test is briefly shown in Figure 1.

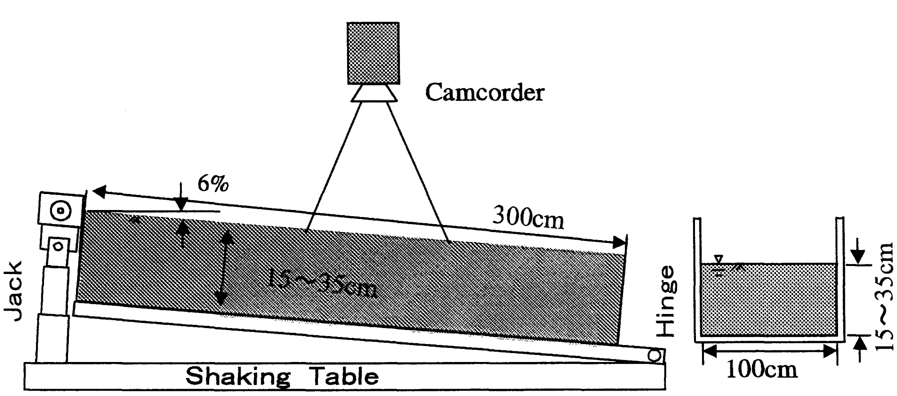

Figure 1 Shaking Table Test of Liquefaction-Induced Ground Flow

The material of the model grounds is beach sand with a mean grain size 0.19 mm and a grain size uniformity 1.9 . The soil box has a length 3 m in the direction of the ground flow and 1 m width. Uniform and saturated model grounds were made by water boiling from the bottom of the soil box and by mixing the soil. After that, the model ground with a relative density 35 ～ 44 % was made through densification by a preliminary shaking of the soil box. Then, the soil box was inclined with a gradient of 6 %. The liquefaction and the ground flow were caused by vibrating the soil box in the horizontal direction perpendicular to the ground flow by a sinusoidal wave with a magnitude of 400 cm / s^2 and a frequency of 5 Hz. The time history of the ground surface displacement is measured by a digital camcorder.

One typical example of the test results is shown in Figure 2. The black square marks show the ground surface displacement while the white circle marks are the ground surface velocity, which calculated from the measured ground displacement. The ground surface velocity reaches a maximum value at point A and decreases towards point B. Then, the ground velocity maintains mostly constant between points B and C, and the ground flow ceases after stop of the vibration of the soil box at point C.

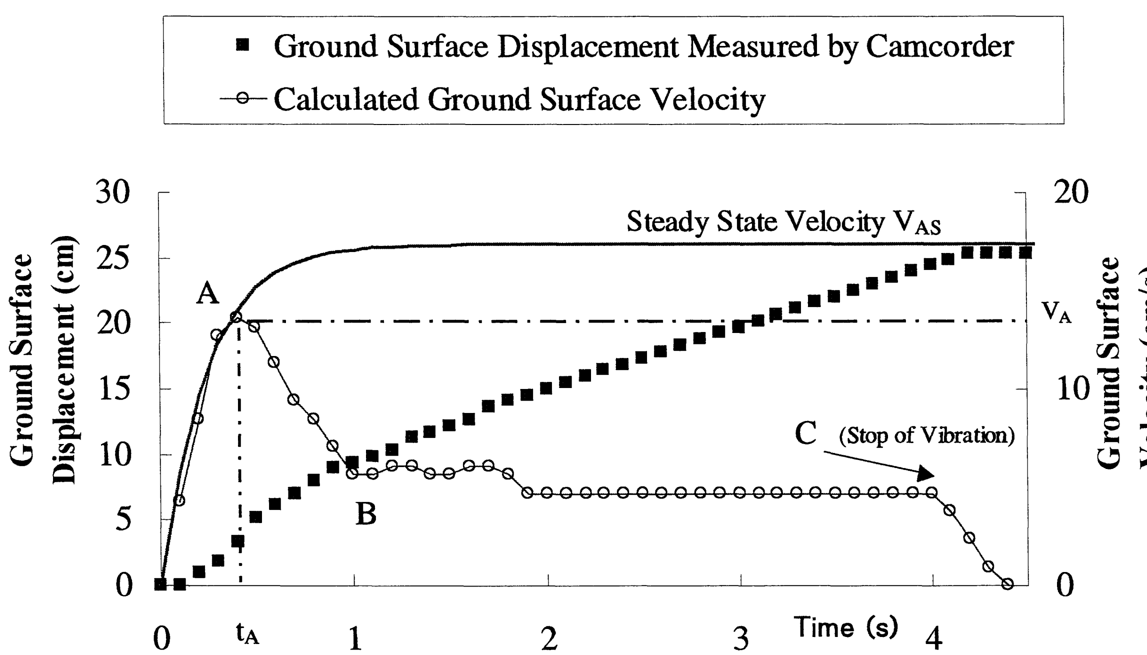

Figure 2 Time Histories of Ground Surface Displacement and Velocity (Model Test)

The decrease of the ground velocity between points A and B can be considered to be resulted from the compaction of the liquefied model ground due to a rapid drainage of the pore water.

Figure 3 shows that the relative density of the model grounds after the test is much higher than that before the test. It can be guessed that the compaction of the model ground was mainly caused between points A and B, since the ground velocity maintained mostly constant between points B and C. This change of the condition of the model ground should be taken into the consideration for the discussions of ground flow characteristics based on the present model test. Therefore, a steady state ground surface velocity, which is calculated according to the following procedure is used for the study on the characteristics of the liquefied-soil flow, hereafter.

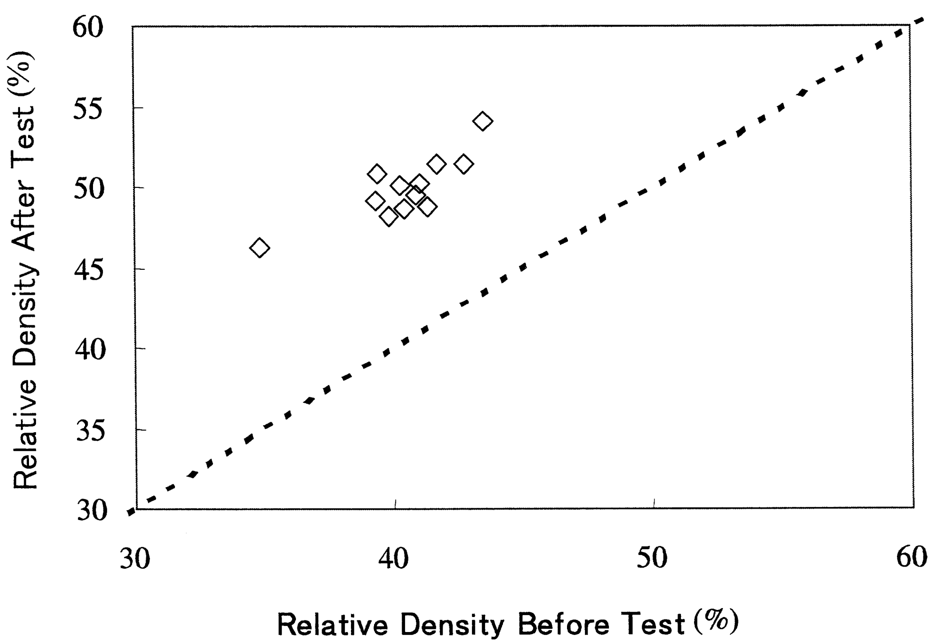

Figure 3 Relative Density of Model Ground before and after Test

When it is assumed that the flow of the model ground at the center of the soil box, which has about ten times length of the depth of the liquefied ground in the direction of the flow, is one-dimensional viscous flow as shown in Figure 4, the non-steady state velocity at the ground surface can be expressed by Equation (1),

$$Vs(t) = \sum_{i=1,2,3}^{\infty} 16 \frac{H^2}{(i\pi)^3} \frac{\rho g}{\mu} \theta \left[1 - \exp\left\{ -\left(\frac{i\pi}{2H}\right)^2 \frac{\mu}{\rho} t \right\} \right] \cdot \sin\frac{i\pi}{2} \qquad (1)$$

,where μ, ρ, H, θ are the coefficient of viscosity, density of liquefied soil, the thickness of the model ground and the gradient of the ground surface. The coefficient of viscosity μ can be estimated from the observed velocity V_A and the time T_A at point A in Figure 2 under an assumption that the relative density of the model ground does not change before point A and that the viscosity of the liquefied soil keeps constant. The steady state velocity at the surface V_{AS} can be obtained as follows ;

$$V_{AS} = \frac{1}{2} \frac{H^2}{\mu} \rho g \theta \tag{2}$$

This velocity can be considered as a steady state velocity when the viscosity of the liquefied soil had maintained constant without any increase of the relative density of the model ground. One example of thus-obtained steady state surface velocity is shown with the velocity obtained from the model test in Figure 2.

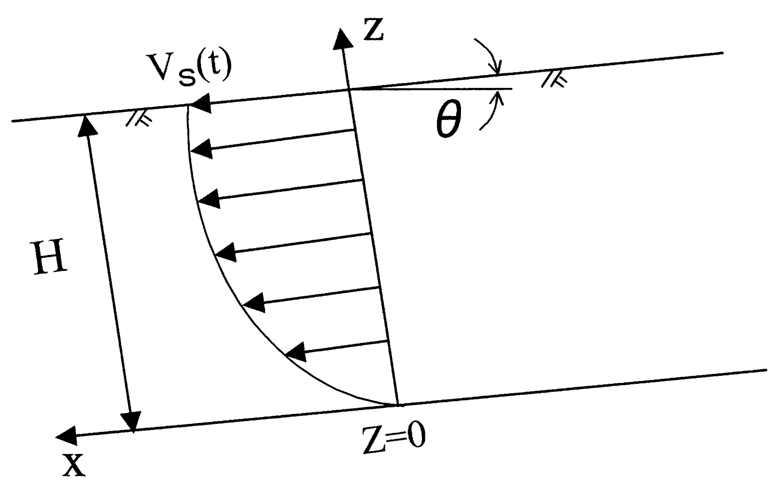

Figure 4 One-Dimensional Viscous Flow

Figure 5 shows a relationship between the steady state surface velocity and the thickness of the liquefied soil of the model ground. Equation (2) says that the steady state velocity is proportional to a square of the thickness of the liquefied soil H. However, The relationship shown in Figure 5 seems to contradict to Equation (2). The dotted line in Figure 5 which was drawn by the least mean square method, suggests that the steady state velocity is mostly proportional to a square root of the thickness of the liquefied soil. This experimental fact can be explained by considering the following similitude law for the flow of the liquefied soil ;

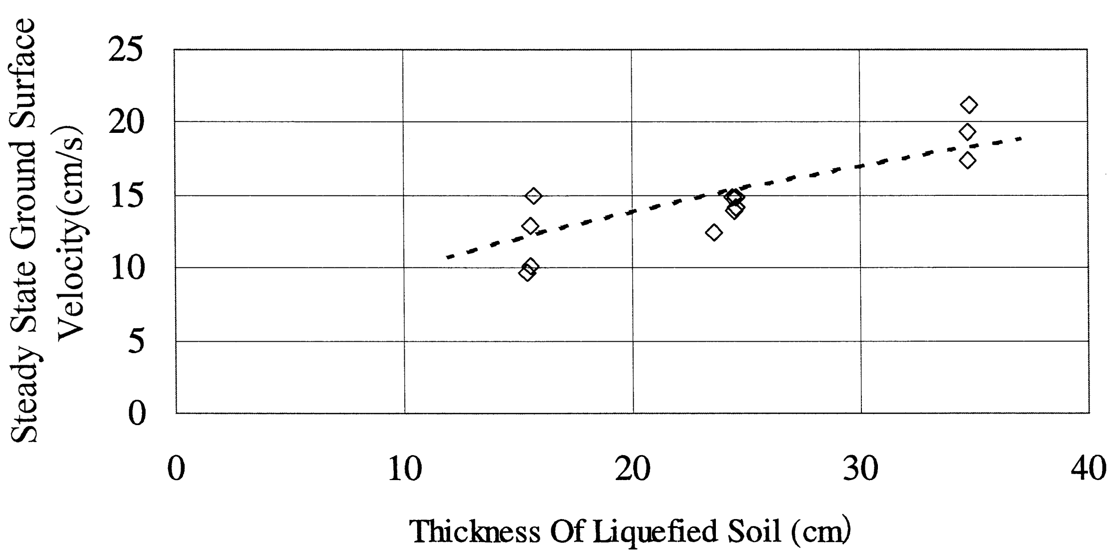

Figure 5 Relationship between Steady State Ground Surface Velocity and Thickness of Liquefied Soil

When two liquefied grounds with thickness H_1 and H_2 are flowing in a steady state condition due to of the gravity as shown in Figure 6, the relationship between the shear stresses τ_1 , τ_2 and the shear strain velocities $\dot{\gamma}_1$, $\dot{\gamma}_2$ is expressed by Equations (3) and (4) .

$$\tau_1 = \mu_1 \dot{\gamma}_1 \tag{3}$$

$$\tau_2 = \mu_2 \dot{\gamma}_2 \tag{4}$$

where, μ_1 and μ_2 are the coefficients of viscosity of two liquefied soil with the thickness H_1 and H_2 , respectively, The ratio of the shear stress τ_2/τ_1 is equal to the ratio of the thickness H_2/H_1 ($=\lambda$) . Therefore,

$$\frac{\mu_2 \dot{\gamma}_2}{\mu_1 \dot{\gamma}_1} = \lambda \tag{5}$$

is obtained. Since non-dimensional shear strains γ_1 and γ_2 are equal to each other, the following relationship is obtained.

$$\frac{\mu_2}{\mu_1} \cdot \frac{T_2}{T_1} = \lambda \tag{6}$$

, where T is a symbol for time.

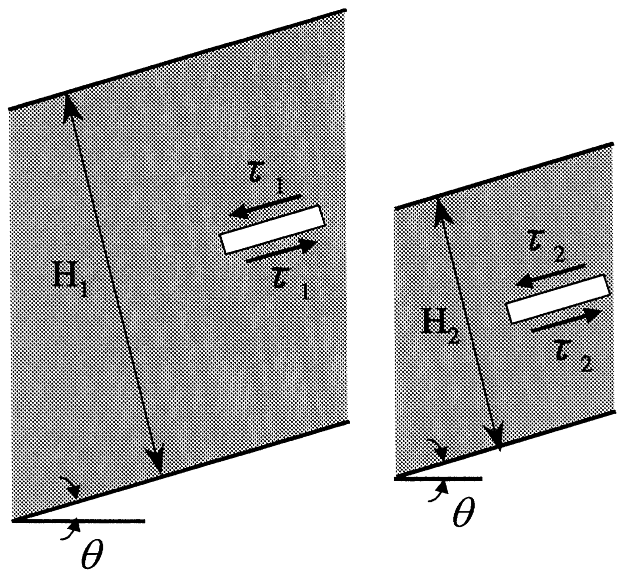

Figure 6 Flow of Liquefied Soil with Two Kinds of Thickness

On the other hand, If it is assumed that the Reynolds' number Re is constant in the flows of liquefied grounds with the thickness H_1 and H_2,

$$\mathrm{Re} = \frac{\rho_1 V_1 L_1}{\mu_1} = \frac{\rho_2 V_2 L_2}{\mu_2} \tag{7}$$

is obtained, where ρ , V are density of the liquefied soil and the velocity of the flow. L is a symbol for length. The suffixes 1, 2 show the respective cases of the flow with two different thickness. The symbol for length L is replaced with H, the thickness of the liquefied soil and ρ_1 is equal to ρ_2. Therefore,

$$\frac{\mu_2}{\mu_1} = \lambda \cdot \frac{V_2}{V_1} \tag{8}$$

is obtained. From Equations (6) and (8) the following conclusions can be introduced ;

$$\frac{V_2}{V_1} = \sqrt{\lambda} \tag{9}$$

$$\frac{\mu_2}{\mu_1} = \lambda^{3/2} \tag{10}$$

Equation (9) shows that the velocity of the flow is in proportion to a square root of to the thickness. The model test results shown in Figure 5 well supports the relationship introduced from Equation (9).

Furthermore, Equation (10) suggests that the coefficient of viscosity is proportional to a square root of the thickness of the liquefied soil cubed. Figure 7 is a relationship between the coefficient of viscosity and the thickness of the liquefied soil, which was obtained by the model tests. This experimental results also coincides with the relationship of Equation (10).

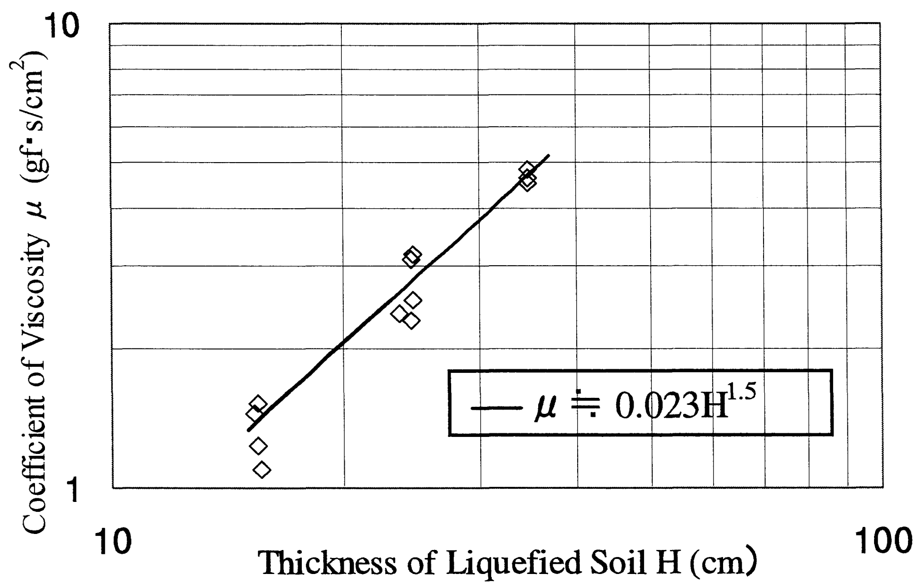

Figure 7 Relationship between Coefficient of Viscosity and Thickness of Liquefied Soil

Effects of Relative Density And Input Acceleration on Surface Velocity of Model Ground

The flow tests of the model grounds were conducted by using three kinds of the sands as shown in Figure 8. The methods of the model tests was previously mentioned. Figures 9 and 10 show relationships of the ground surface velocity in the steady state with the amplitude of the sinusoidal input acceleration of the shaking table and the relative density of the model ground in the case of sand A. These results suggests that flow velocity of model grounds is influenced by these two factors. In particular, the relative density strongly affects the flow velocity of the liquefied soil.

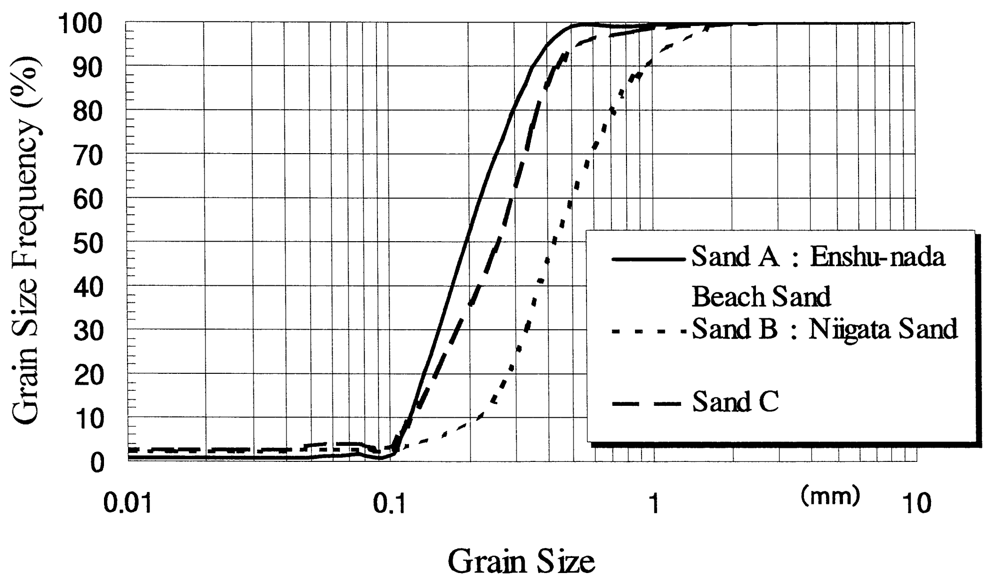

Figure 8 Grain Size Characteristics of Model Ground Materials

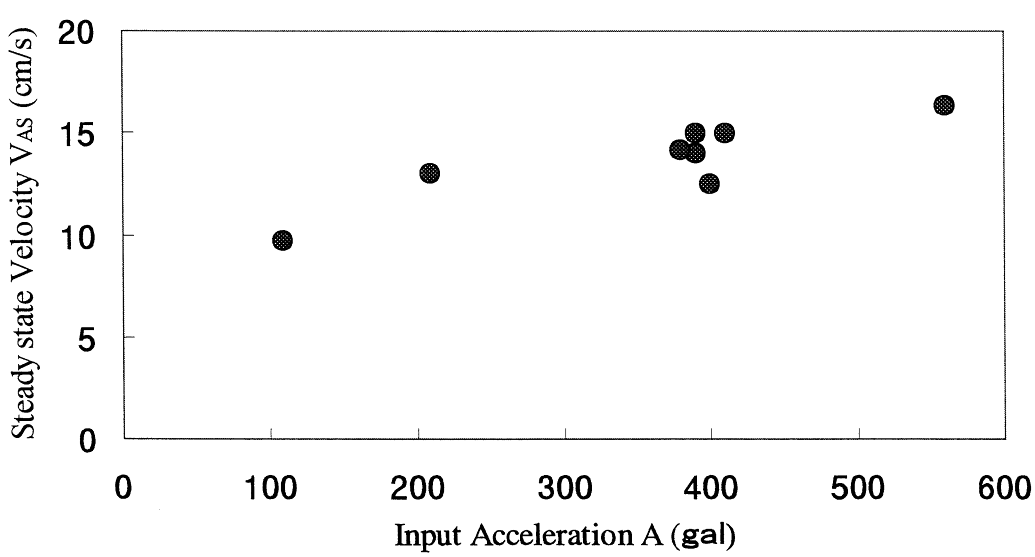

Figure 9 Effect of Magnitude of Input Acceleration on Steady State Velocity of Model Ground

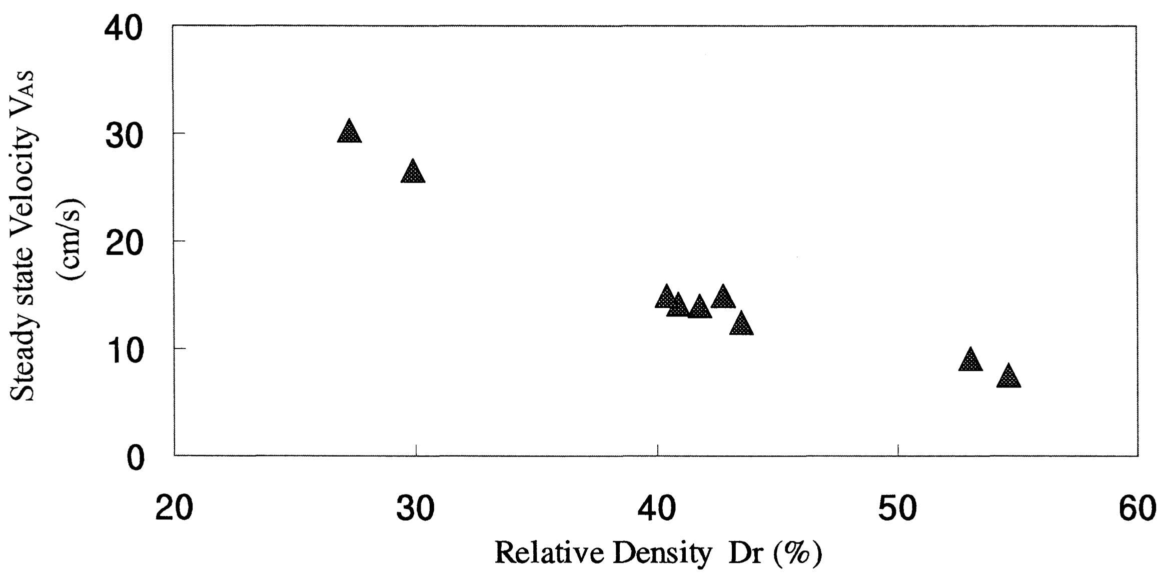

Figure 10 Effect of Relative Density of Model Ground on Steady State Velocity

The following regression formula for the relationship of ground surface velocity with the input acceleration and the relative density was obtained from the test results using three kinds of the sands ;

$$V_{AS} = 480\, D_r^{-1.75} A^{0.48} \tag{11}$$

where, V_{AS} is the steady state ground surface velocity (cm / s), where D_r and A are the relative density of model ground (%) and the input acceleration (cm / s^2), respectively. Figure 11 shows the steady state ground surface velocities predicted by the regression formula in comparison with the experimental data.

Prediction of Ground Surface Displacements by the Similitude Law

As mentioned previously, the Reynolds' similitude law holds for the flow of the liquefied soil, in which the ground velocity increases in proportion to a square root of the thickness of the liquefied soil. This fact was confirmed by the shaking table tests. Therefore, the surface displacements of actual grounds can be predicted based on the model tests by applying this similitude law.

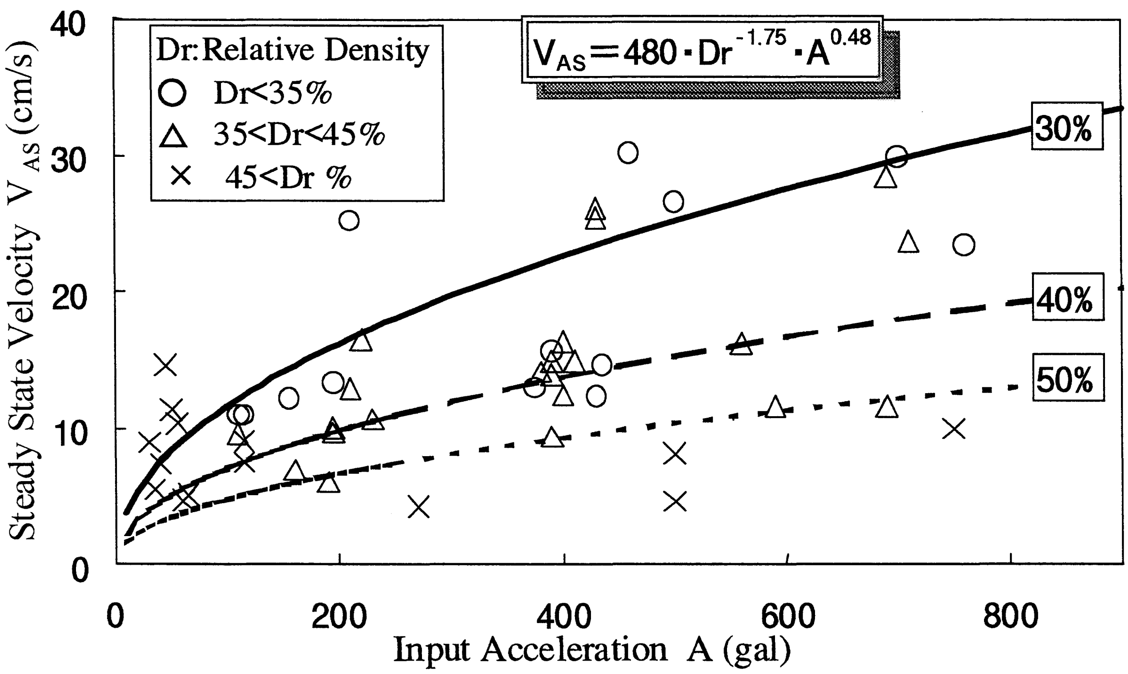

Figure 11 Relationship of Steady State Ground Surface Velocity with Input Acceleration and Relative Density

Equation (11) shows the surface velocity of the model ground in the steady state which has 25 cm thickness and 6% surface gradient. The ground surface velocity V_R (cm / s) of the actual ground with a thickness H (m) and surface gradient θ (%) can be written according to the similitude law as follows ;

$$V_R = 480 \cdot \frac{\sqrt{H}}{\sqrt{0.25}} \cdot \frac{\theta}{6} D_r^{-1.75} A^{0.48} \tag{12}$$

The ground surface displacement D (m) can be obtained by multiplying the surface velocity by the duration of the time of the ground flow T_f.

$$D = 1.6\sqrt{H} \cdot \theta \cdot D_r^{-1.75} A^{0.48} T_f \tag{13}$$

The relative density D_r can be replaced with the SPT-N value as follows ;

$$D_r = 21\sqrt{\frac{N}{\sigma'_V + 0.7}} \tag{14}$$

where, σ'_V is the effective overburden pressure (kgf / cm^2). The SPT-N values $\overline{N}$ corrected by the effective overburden pressure is written by ;

$$\overline{N} = \frac{1.7\,N}{\sigma'_V + 0.7} \tag{15}$$

Therefore, Equation (16) is obtained.

$$D = 0.0125\sqrt{H} \cdot \theta \cdot A^{0.48} \frac{T_f}{\overline{N}^{0.88}} \tag{16}$$

In the case studies on the liquefaction-induced ground displacement in the past earthquakes, the ground surface displacement D has been measured by the aerial survey, while the thickness of the liquefied soil H, the surface gradient θ and the modified SPT-N values $\overline{N}$ have been estimated by geological and topographical surveys as shown in Table 1[1), 2)] . However, The duration of the time of the ground flow T_f and the acceleration A should be estimated in order to predict the ground surface displacements by using Equation (16) . These two quantities were estimated as follows ;

Table 1 Results from The Case Studies

Earthquake	Surface Displacement D(cm)	Thickness Of Liquefied Soil H(cm)	Gradient Of Ground Surface θ (%)	Modified N-Value $\overline{N}$
1983 Nihonkai-Chub	150	430	0.8	14
	190	290	0.9	8
	210	250	2.0	17
	220	200	2.3	12
	170	260	0.8	15
	110	100	1.0	13
1995 Kobe	59	1280	0.2	11
	80	930	0.6	20
1964 Niigata	380	1190	0.8	14
	260	1240	0.9	12

Figure 12 shows the time histories of accelerations recorded during the three earthquakes of the case studies (in Kawagishi-cho in the 1964 Niigata, Akita Harbor in the 1983 Nihonkai-Chubu and in the past Island in the 1995 Kobe) . These time histories were divided into several parts where the acceleration maintained mostly constant as shown in Figure 12.

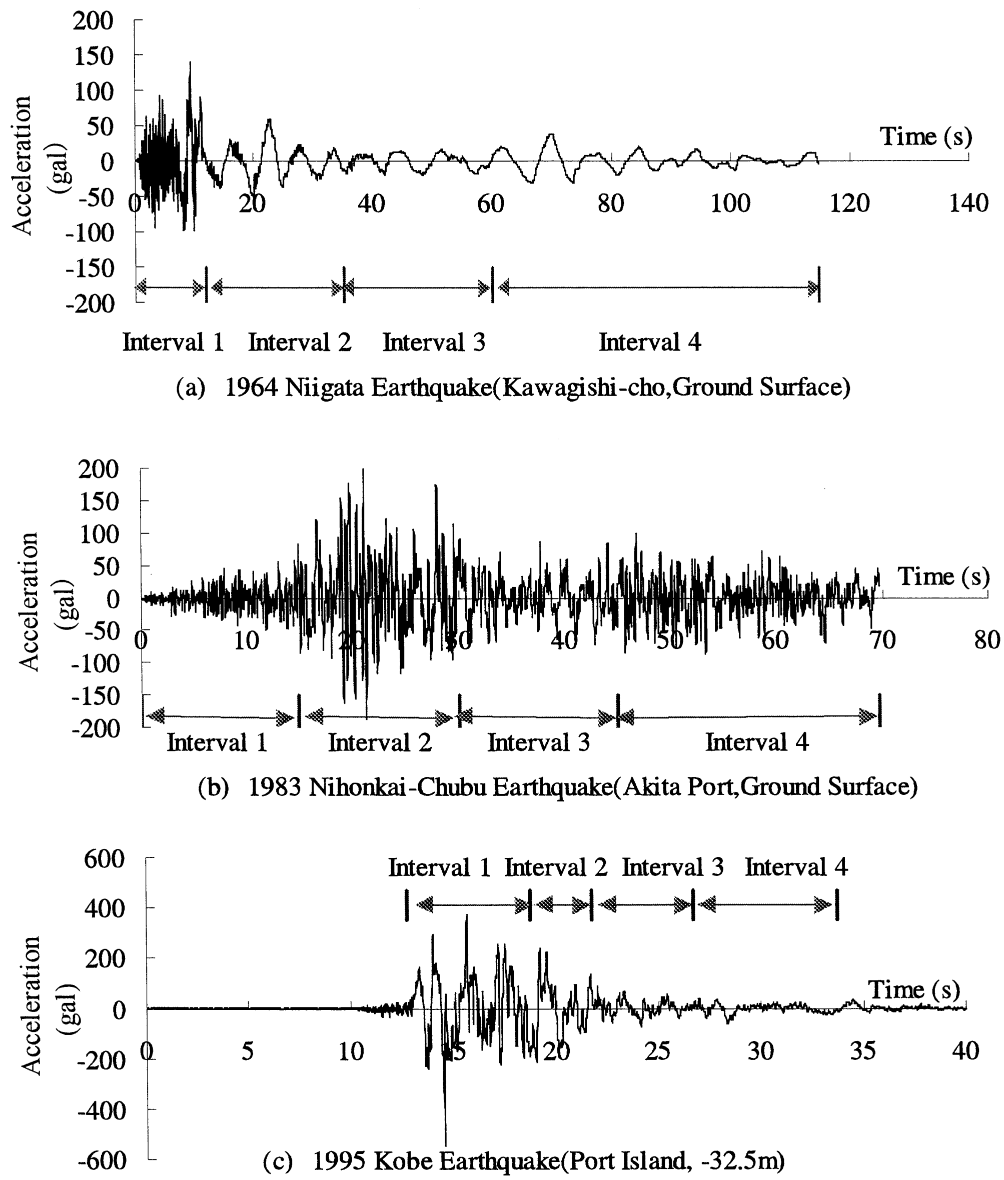

Figure 12 Time Histories of Ground Acceleration of Earthquakes for The Case Studies

T_i and A_i are the duration of the time in the i segment and the mean magnitude of the acceleration, respectively. The total value of ground surface displacement can be calculated as a summation of the displacements in each segments.

$$D = \frac{0.0125 \cdot \sqrt{H} \cdot \theta}{\overline{N}^{0.88}} \sum_{i}^{n} A_i^{0.48} T_i \tag{17}$$

The ground surface displacements estimated by Equation (17) is shown in Figure 13 in comparison with the displacements measured by the aerial survey in the past case studies. *A* good coincidence between the ground displacements predicted from the model test results and the observed ones suggests that the ground displacement of actual grounds can be quantitatively predicted based on model test by applying the similitude law.

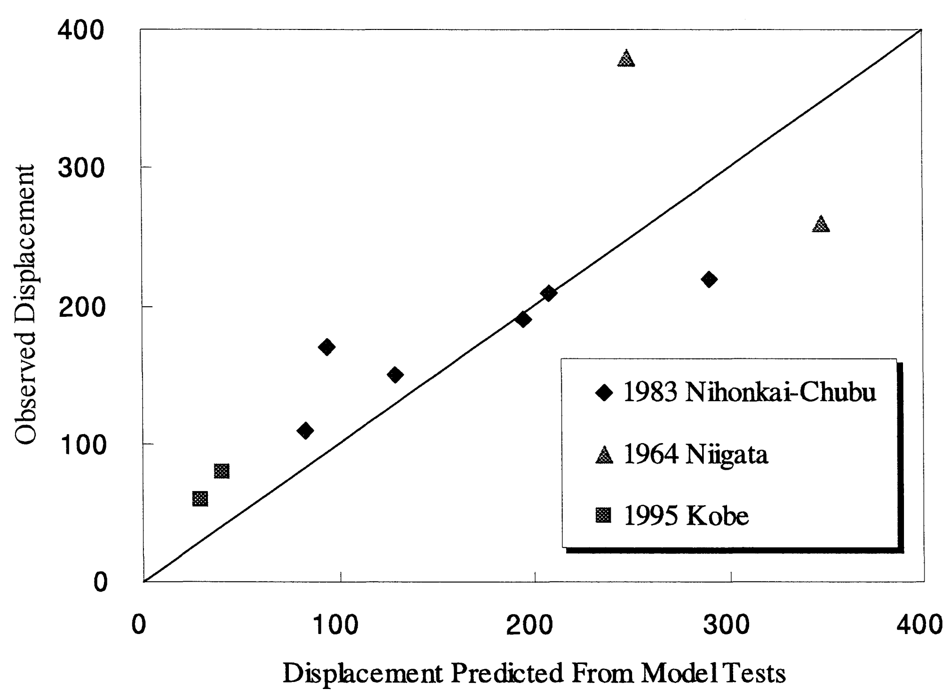

Figure 13 Comparison between Ground Surface Displacement Predicted from Model Test and Measured Values in Case Studies

Conclusion

The shaking table test of the flow of the liquefied ground clarified that the surface velocity of the flow is in proportion to a square root of the thickness of the liquefied soil and that the coefficient of viscosity is proportional to a square root of the thickness cubed. This experimental results showed that Reynolds' similitude held for the flow of the liquefied soil.

The ground surface displacements of actual grounds, which were predicted from model test results by applying the similitude law have a good coincidence with the displacements measured in the past case studies.

Reference

1) M. Hamada and T. D. O'Rourke, " Case Studies of Liquefaction and Lifeline Performance during Past Earthquakes ", Vol.I, Japanese Case Studies, Technical Report NCEER-92-0001, 1992
2) M. Hamada and K. Wakamatsu, " A Study on Ground Displacement Caused by Soil Liquefaction ", Journal of J.S.C.E. No.596 / III - 43, pp.189-208, 1998

SEISMIC ZONATION FOR LIQUEFACTION IN CALIFORNIA

Mark J. DeLisle and Charles R. Real

California Department of Conservation
Division of Mines and Geology
801 K Street, MS 12-31
Sacramento

ABSTRACT

Zones of required seismic investigation have been designated for portions of the San Francisco Bay area and over 100 jurisdictions in Los Angeles, Orange and Ventura counties, California. This activity is part of a two-step process to identify when new buildings for human occupancy must consider higher construction standards for seismic safety in California's high-risk areas. These zones bound areas likely to contain geologic conditions susceptible to liquefaction during earthquakes and serve to target areas where state law requires that site-specific geotechnical investigations be performed before a permit to build can be granted.

Liquefaction zones are based on the presence of cohesionless soils that are, or could become saturated. The geologic criteria for zone delineation are based on the geologic age of the deposits, grain-size distribution, depth to free water using historic-high water levels, and the 10% in 50 years peak ground acceleration expected in the area. Where sufficient geotechnical data are available, the Seed-Idriss simplified method is used to better define the areal extent of potentially hazardous deposits.

INTRODUCTION

Prompted by damaging earthquakes in northern and southern California, in 1990 the State Legislature passed the Seismic Hazards Mapping Act (the Act). The Governor signed the Act, codified in the Public Resources Code as Division 2, Chapter 7.8, which became operative on April 1, 1991. The Act directs the California Department of Conservation, Division of Mines and Geology (CDMG) to delineate seismic hazard zones. The purpose of the Act is to reduce the threat to public health and safety and to minimize the loss of life and property by identifying and mitigating seismic hazards. Cities, counties, and state agencies are directed to use the seismic hazard zone maps in their land-use planning and permitting processes. The Act requires that site-specific geotechnical investigations be performed prior to permitting most urban development projects within the hazard zones. Evaluation and mitigation of seismic hazards are to be conducted under guidelines established by the California State Mining and Geology Board (SMGB) (1997).

The Act also directs SMGB to appoint and consult with the Seismic Hazards Mapping Act Advisory Committee (SHMAAC) in developing criteria for the preparation of the seismic hazard zone maps. SHMAAC consists of geologists, seismologists, civil and structural engineers, representatives of city and county governments, the state insurance commissioner and the insurance industry. In 1993, the SMGB developed initial criteria for delineating seismic hazard zones to promote uniform and effective statewide implementation of the Act. These criteria include recommendations for mapping regional liquefaction hazards. They also direct CDMG to develop a set of probabilistic seismic maps for California and to research methods that might be appropriate for mapping earthquake-induced landslide hazards.

A pilot liquefaction study undertaken within the city of San Francisco evaluated methods used to assess liquefaction potential over a large geographic area, and produced the prototype maps. This area was selected because detailed geologic data, abundant geotechnical information, high seismicity and documented historical liquefaction occurrences are readily available.

In 1996, technical working groups established by SHMAAC reviewed the prototype maps and the techniques used to create them. The reviews resulted in recommendations that (1) the process for liquefaction zoning remain unchanged and (2) earthquake-induced landslide zones be delineated using a modified Newmark analysis. Criteria for delineating seismic hazard zones (SMGB, in press) were prepared from recommendations by SHMAAC and these technical working groups. CDMG investigations are conducted according to these specified guidelines. The resultant Official Seismic Hazard Zones are the products of a three-dimensional integration of geotechnical and geological data. An advanced geotechnically-oriented geographic information system (GIS) capable of subsurface stratigraphic correlation is used for data integration and spatial analysis.

In addition to the city of San Francisco, CDMG Seismic Hazard Mapping Program has designated zones of required seismic investigation for over 100 jurisdictions in Alameda, Los Angeles, Orange and Ventura counties, California. Additional work is ongoing throughout southern California and the San Francisco Bay area.

MAPPING LIQUEFACTION POTENTIAL

Liquefaction occurs in water saturated sediments that are strongly shaken by moderate to great earthquakes. Liquefied sediments are characterized by a loss of shear strength and resulting soil failure, which can cause permanent ground deformations and damage to man-made structures. A number of methods for mapping liquefaction hazard have been proposed; Youd (1991) highlights the principal developments and notes some of the widely used criteria. Youd and Perkins (1978) demonstrate the use of geologic criteria as a qualitative characterization of susceptibility units, and introduce the mapping technique of combining a liquefaction susceptibility map and a liquefaction opportunity map to evaluate liquefaction potential. Liquefaction susceptibility is a function of the capacity of sediments to resist liquefaction and liquefaction opportunity is a function of the seismic ground shaking severity. The application of the Seed Simplified Procedure (Seed and Idriss, 1971) for evaluating liquefaction potential allows a quantitative characterization of susceptibility of geologic units. Tinsley and others (1985) applied a combination of the techniques used by Seed and others (1983) and Youd and Perkins (1978) for mapping liquefaction hazards in the Los Angeles region. The method applied by CDMG's Seismic Hazard Mapping Program is similar to Tinsley and others (1985) combining geotechnical data analyses, and geologic and hydrologic mapping.

GEOLOGIC CONDITIONS

Surficial Geology

Geologic criteria such as age, depositional environment, relative density, grain-size distribution and the depth to free ground water affect the liquefaction susceptibility of a geologic unit. Understanding the depositional environment and the ages of the geologic units, combined with the penetration resistance and ground water data allows the assessment of liquefaction susceptibility.

Because of the seismic zonation program and in collaboration with the United States Geological Survey (USGS) a new generation of 7.5 minute (1:24,000 scale) geologic quadrangle maps is being produced in some of the project areas. These maps include a more detailed differentiation of Quaternary units for purposes of assessing earthquake hazards.

Subsurface Geology and Geotechnical Characteristics

Borehole information is used to determine general subsurface conditions. Water depths, local site stratigraphy, and standard penetration tests (SPT) or converted blow counts are used to characterize the geotechnical properties of each stratigraphic unit. Several geologic cross sections are constructed across the study area using areal geology and borehole lithology information to make subsurface stratigraphic correlations.

Recorded blow counts where the sampler diameter, hammer size or drop distance differ from those specified for a Standard Penetration Test are converted to SPT blow counts. The actual and converted SPT blow counts are normalized using a common effective overburden pressure and adjusted for equipment and operational procedures using a method described by Seed and Idriss (1982) and Seed and others (1985).

The assessment of regional liquefaction potential is partially based on the logs of exploratory boreholes and wells filed by numerous private and public agencies and organizations. This work has resulted in a digital data base, which at the present time contains over 10,000 borehole logs for southern California and approximately 1000 logs for the San Francisco Bay area. Figures 1 and 2 show the number of records for principal geotechnical parameters contained in the database for the two areas investigated. Figures 3 and 4 present the percentage of the actual and converted SPT blow counts entered into the database for the two areas. CDMG plans to make these data and other data in the database accessible in the future.

GROUNDWATER CONDITIONS

Soils below a permanent or perched groundwater table are usually saturated, whereas soils above the water table are usually not saturated, although such soils may become saturated temporarily during or after storms. For CDMG's evaluation, a groundwater surface map, showing the historically highest known ground water, is prepared. Soils above the mapped water surface are considered non-liquefiable. Data are plotted and tabulated, and depths to of ground water are contoured.

GEOTECHNICAL DATA ANALYSES

Liquefaction Opportunity

According to the criteria prepared by SMGB (1993), liquefaction opportunity is a measure, expressed in probabilistic terms, of the potential for ground shaking strong enough to generate liquefaction. Analyses of in-situ liquefaction resistance require assessment of liquefaction opportunity. The minimum level of seismic excitation to be used for such purposes is taken to be that level of peak ground acceleration (PGA) with a 10% probability of exceedance over a 50-year period.

In the analyses of in-situ liquefaction resistance the PGA and magnitude values are derived from maps for the entire state prepared by Petersen and others (1996) later modified to account for soil conditions (Petersen, personal communication). Figure 5 shows the PGA having a 10% probability of exceedance in a 50-year period for the San Francisco area for alluvium. It is assumed that soil conditions are alluvium over the entire map area. Similar maps for soft rock and rock conditions are also available. These maps are a byproduct of a CDMG partnership with the USGS to assess the ground shaking potential for California as part of the National Earthquake Hazard Reduction Program recommendations for the year 2000 building code.

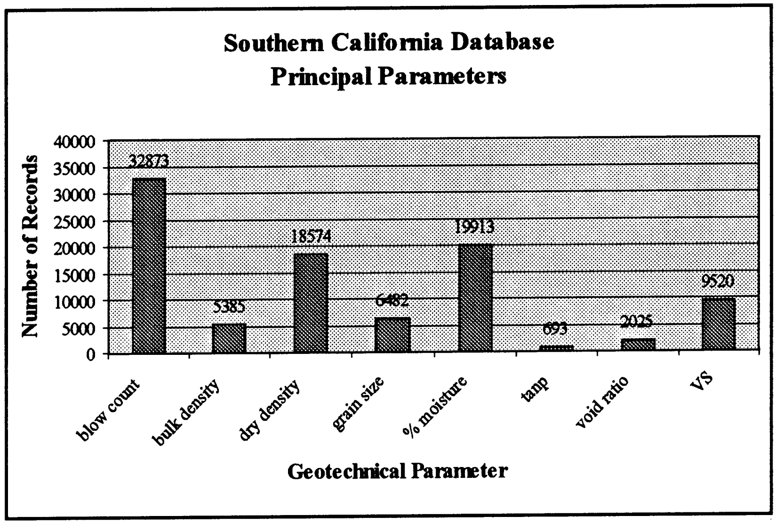

Figure 1. Principal geotechnical parameters in the southern California database.

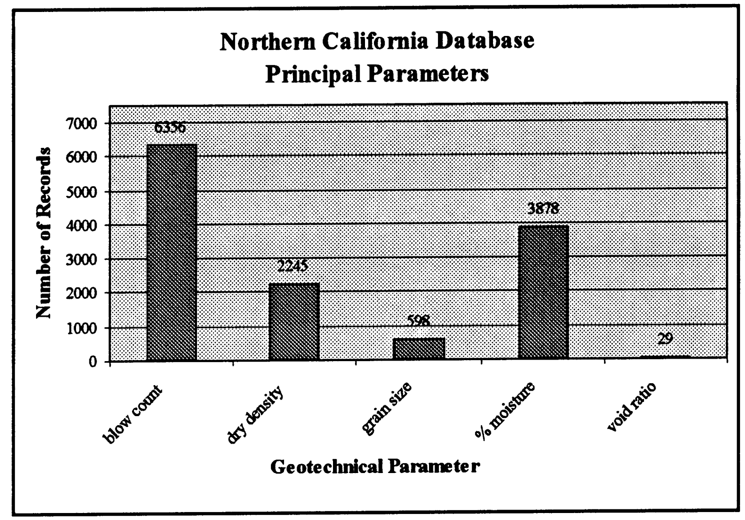

Figure 2. Principal geotechnical parameters in the northern California database.

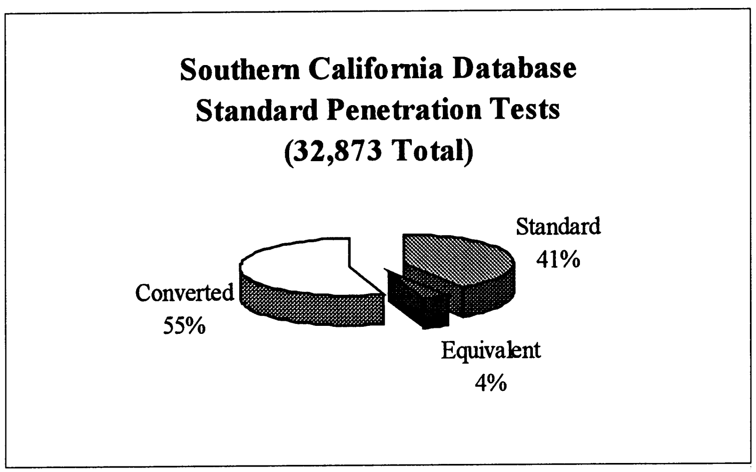

Figure 3. Standard penetration tests in southern California database.

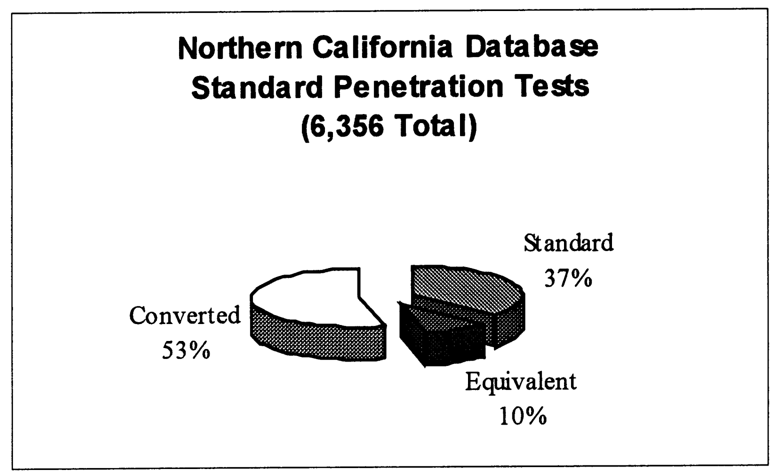

Figure 4. Standard penetration test in northern California Database.

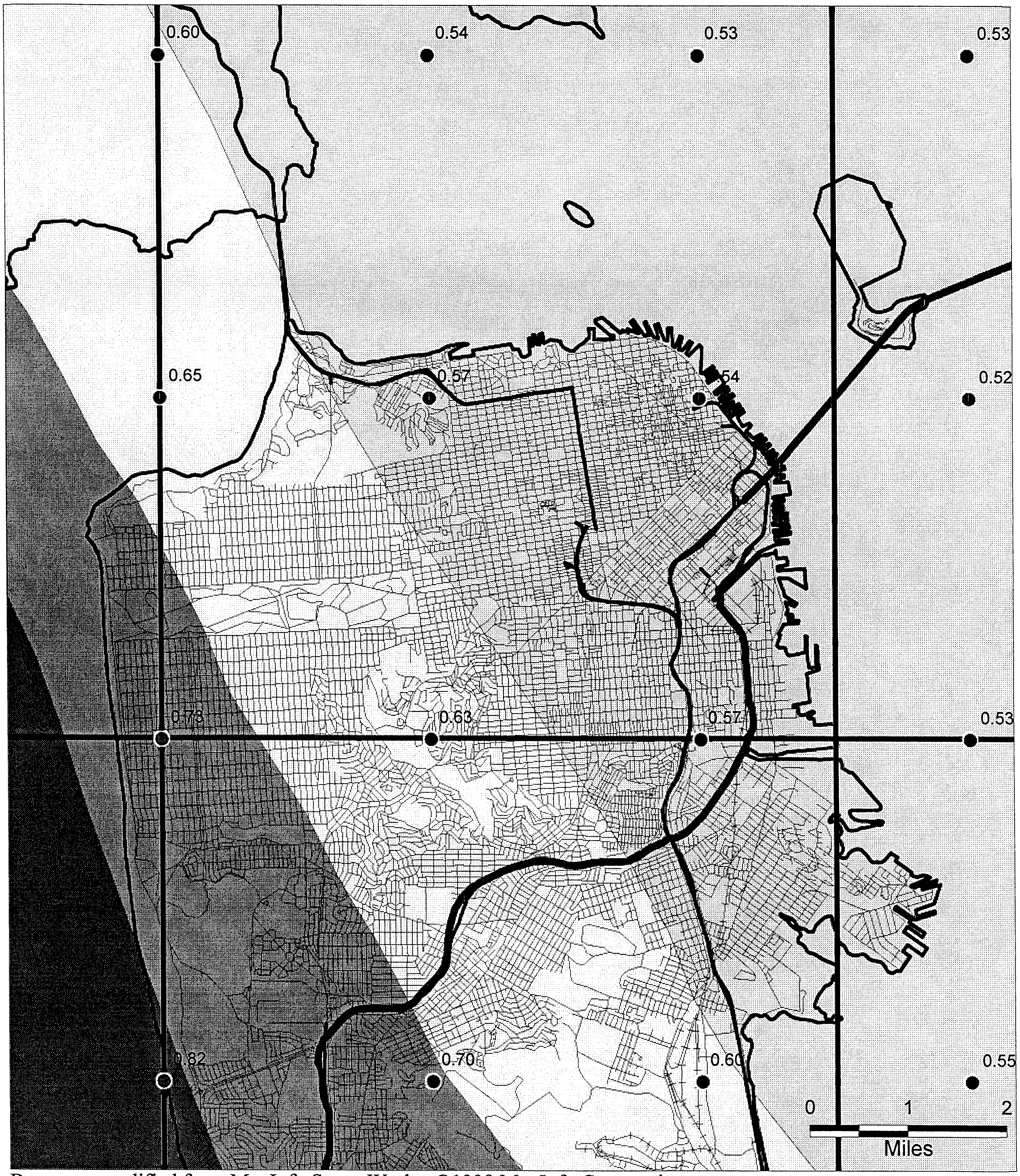

Base map modified from MapInfo Street Works ©1998 MapInfo Corporation

Figure 5. Portions of the San Francisco North and South 7.5 Minute Quadrangles and Adjacent Quadrangles (from Petersen and others, 1996).

10% EXCEEDANCE IN 50 YEARS PEAK GROUND ACCELERATION (g)

1998

ALLUVIUM CONDITIONS

Liquefaction Susceptibility

Liquefaction susceptibility reflects the relative resistance of soils to loss of strength when subjected to ground shaking. Primarily, physical properties and conditions of soil such as sediment grain-size distribution, compaction, cementation and depth govern the degree of resistance. These properties and conditions are correlated with geologic age and environment of deposition. With increasing age of a deposit, relative density may increase through cementation of the particles or by compaction due to the increase in thickness of the overburden sediments. Grain size characteristics of a soil also influence susceptibility to liquefaction. Sands are more susceptibility than silts or gravels. Cohesive soils are generally not considered susceptible to liquefaction. Soil characteristics and processes that result in lower liquefaction susceptibility generally result in higher penetration resistance to the soil sampler. Therefore, blow count or cone penetrometer values are useful indicators of liquefaction susceptibility.

Saturation is required for liquefaction, and the liquefaction susceptibility of a soil varies with the depth to ground water. Very shallow ground water increases the susceptibility to liquefaction (more likely to liquefy). Soils that lack resistance (susceptible soils) are typically saturated, loose sandy sediments. Soils resistant to liquefaction include all soil types that are dry or sufficiently dense.

CDMG's inventory of areas containing soils susceptible to liquefaction begins with evaluation of geologic maps, cross sections, geotechnical test data, geomorphology, and groundwater hydrology. Soil property and soil condition factors such as type, age, texture, color, and consistency, along with historical depths to ground water are used to identify, characterize, and correlate susceptible soils. Because Quaternary geologic mapping is based on similar soil observations, findings can be related in terms of the map units.

Quantitative Liquefaction Analysis

Liquefaction susceptibility maps show the areal distribution of sediments calculated to be liquefiable under given ground-motion parameters. The pattern of susceptibility may not reflect the surface geology in many locations because of subsurface sediments and hydrologic considerations.

CDMG performs quantitative analyses of geotechnical data to evaluate liquefaction potential using the Seed Simplified Procedure (Seed and Idriss, 1971; Seed and others, 1983; National Research Council, 1985; Seed and Harder, 1990; Youd and Idriss, 1997). This procedure calculates soil resistance to liquefaction, expressed in terms of cyclic resistance ratio (CRR) based on SPT results, groundwater level, soil density, moisture content, soil type, and sample depth. CRR values are then compared to calculated earthquake-generated shear stresses expressed in terms of cyclic stress ratio (CSR). When calculating CSR, the PGA taken from alluvial soil conditions is multiplied by a magnitude weighting factor in order to account for the number of cycles of strong shaking. Weights vary about the value of 1, being less if the magnitude is less than 7.5 and greater if the magnitude is larger than 7.5. The factor of safety (FS) relative to liquefaction is determined by the equation: FS=CRR/CSR. FS, therefore, is a quantitative measure of liquefaction potential. Generally, a factor of safety of 1.0 or less, where CSR equals or exceeds CRR, indicates the presence of potentially liquefiable soil. CDMG uses FS, as well as other considerations such as slope, free face conditions, and thickness and depth of potentially liquefiable soil, to construct liquefaction potential maps, which then directly translate to Zones of Required Investigation.

Non-SPT values, such as those resulting from the use of 2-inch or 2 1/2-inch inside diameter ring samplers, are translated to SPT-equivalent values if reasonable factors can be used in conversion calculations. Few borehole logs, however, include all of the information (soil density, moisture content, sieve analysis, etc.) required for an ideal Seed Simplified Analysis. For boreholes having acceptable penetration tests, liquefaction analysis is performed using logged density, moisture, and sieve test values, or using assigned average test values of similar materials.

LIQUEFACTION ZONES

Criteria for Zoning

Liquefaction mapping criteria developed by SHMAAC and adopted by the SMGB (in press) are:

Liquefaction Hazard Zones are geographic areas meeting one or more of the following criteria:

1. Areas known to have experienced liquefaction during historic earthquake;

2. All areas of uncompacted fills containing liquefaction susceptible material that are saturated, nearly saturated, or may be expected to become saturated;

3. Areas where sufficient existing geotechnical data and analyses indicate that the soils are potentially liquefiable; and,

4. In areas of limited or no geotechnical data, susceptibility zones may be identified by the following geologic criteria:

    (a) Areas containing soil deposits of late Holocene age (current river channels and their historic floodplains, marshes and estuaries), where the M7.5-weighted peak acceleration that has a 10% probability of being exceeded in 50 years is greater than or equal to 0.10 g and the historic-high water table is less than 40 feet below the ground surface; or

    (b) Areas containing soil deposits of Holocene age (less than 11,000 years), where the M7.5-weighted peak acceleration that has a 10% probability of being exceeded in 50 years is greater than or equal to 0.20 g and the historic-high water table is less than or equal to 30 feet below the ground surface; or

(c) Areas containing soil deposits of latest Pleistocene age (between 11,000 years and 15,000 years), where the M7.5-weighted peak acceleration that has a 10% probability of being exceeded in 50 years is greater than or equal to 0.30 g and the historic-high water table is less than or equal to 20 feet below the ground surface.

A flow chart summarizing the criteria for delineating zones of required investigation for liquefaction is shown in Figure 6.

CONCLUSIONS

California law requires that, in order to obtain a permit for construction, proposed projects located within seismic hazard zones have a geotechnical investigation at the project site that validates the level of hazard and recommends appropriate countermeasures. With support from the Federal Emergency Management Agency (FEMA), California's Seismic Hazard Mapping Program has completed a zonation project covering portions of Los Angeles, Orange and Ventura counties. Zones of required seismic investigation for areas having a potential for liquefaction were designated for 39 7.5 minute quadrangles covering approximately 6,200 square kilometers of land and over 100 jurisdictions in southern California (Figure 7). Currently the Seismic Hazard Mapping Program is continuing its work in the three county area with the support of FEMA.

In the San Francisco Bay area the Seismic Hazard Mapping Program has completed zonation projects covering the cities of San Francisco and Oakland (Figure 8) and is currently working in the south San Francisco Bay area.

Although the land is already urbanized in many of the areas zoned by CDMG, new construction activity is high due to infill and redevelopment. Program staff have met with the affected jurisdictions to discuss the purpose of the maps, their basis, and legal requirements for implementation. A liquefaction evaluation report accompanies the map discussing the basis for the zones and has figures in the report showing locations of boreholes, water depth contours and the Quaternary geology used.

"Guidelines for Evaluating and Mitigating of Seismic Hazards in California" were published by SMGB (1997). A three-day course, co-sponsored by U.C. Berkeley and the Southern California Earthquake Center (SCEC), on "Evaluation and Mitigation of Seismic Hazards" was presented to local regulators in southern California. U.C. Berkeley repeated the course for the geotechnical consulting industry in Los Angeles and again for the San Francisco Bay area. SCEC helped form an "Implementation Committee," representing the six county southern California region, to recommend detailed procedures that will assist local agencies with implementing the state guidelines.

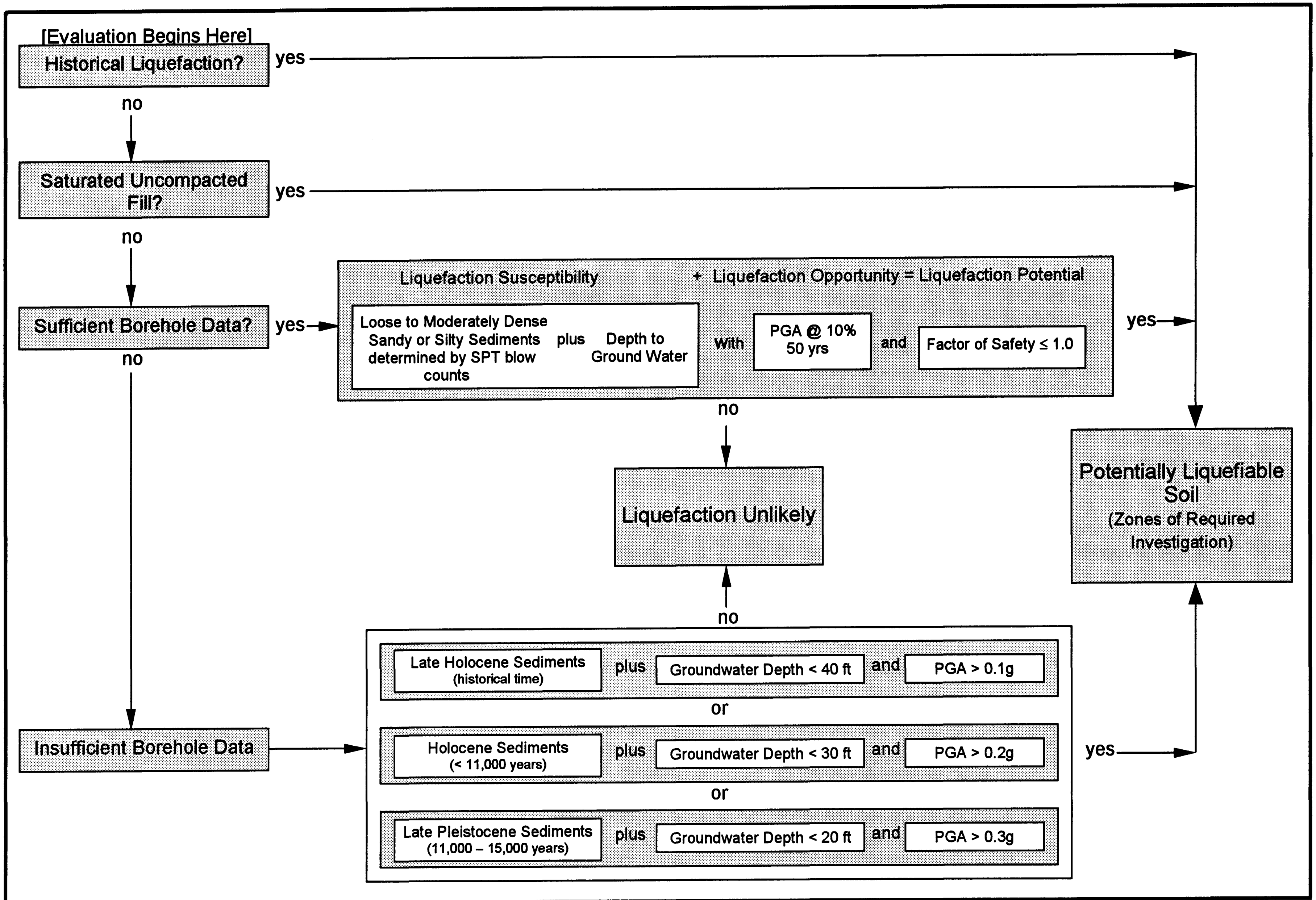

Figure 6. Flow chart summarizing SMGB criteria used to delineate zones of required investigation for liquefaction hazard in California.

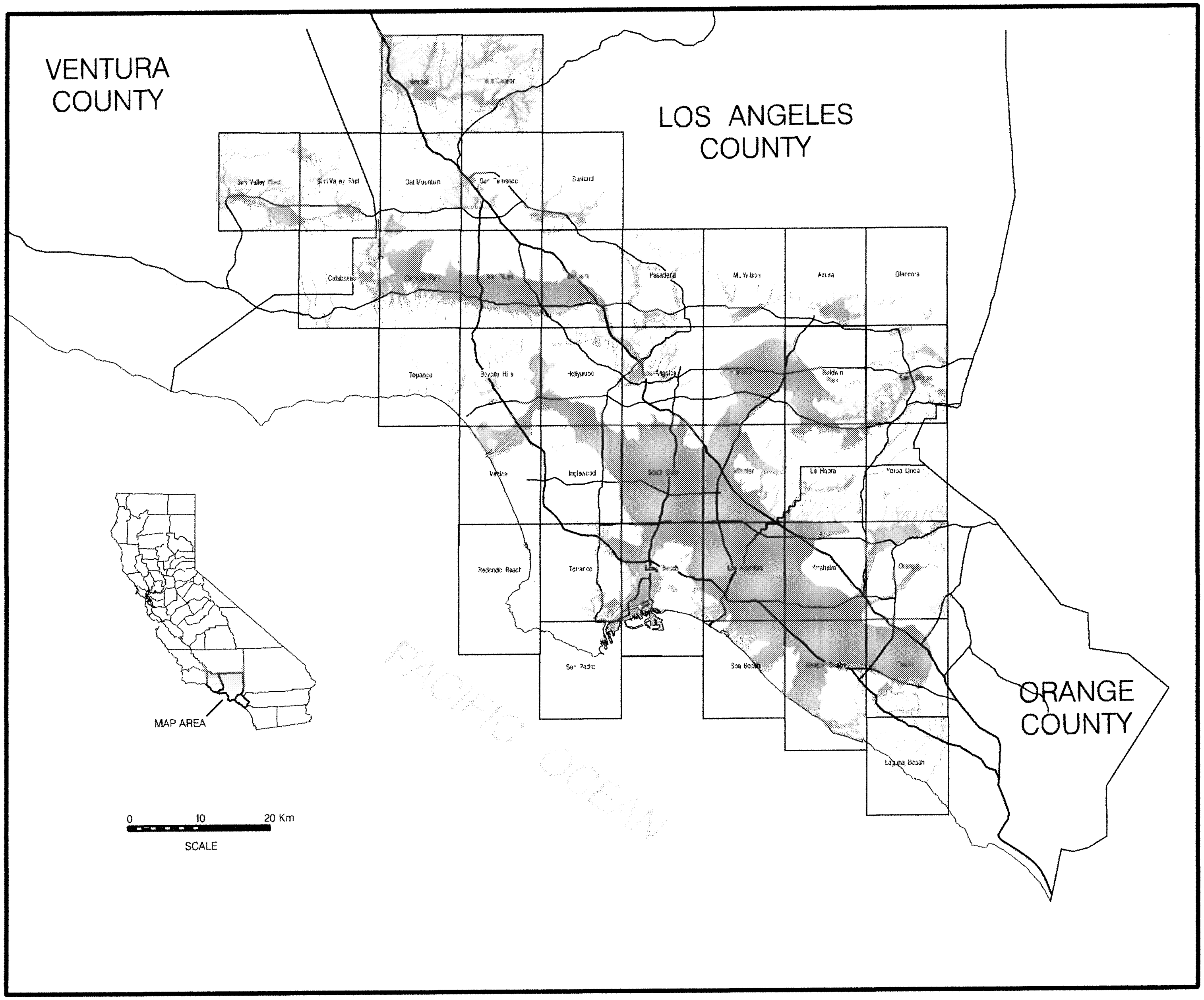

Figure 7. Mosaic of 7.5' quadrangles in southern California that have been released as Official Seismic Hazard Zone Maps. Zones of required investigation for liquefaction hazard are shown as shaded regions.

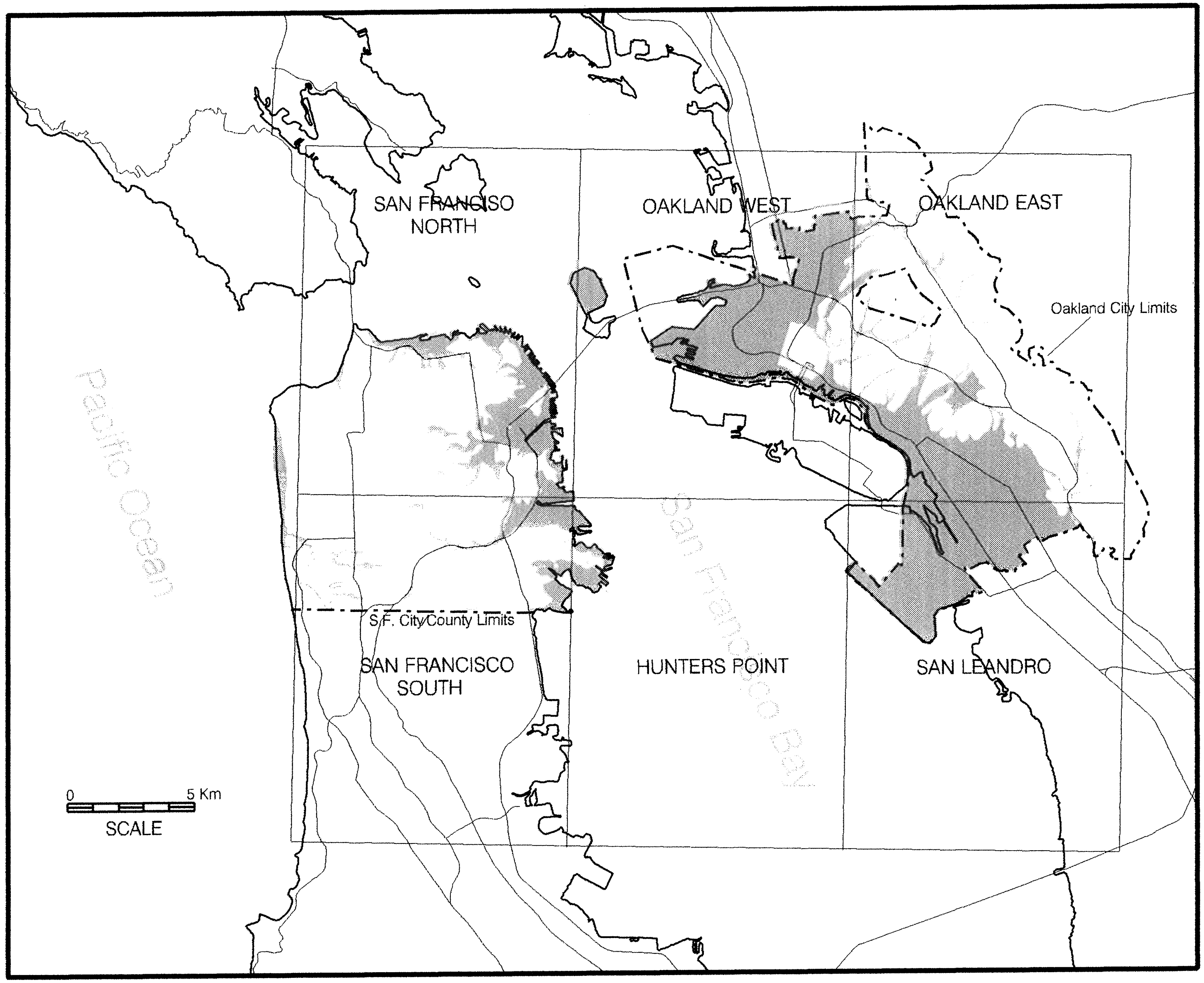

Figure 8. Mosaic of 7.5' quadrangles in the San Francisco Bay area. Zones of required investigation for liquefaction hazard are shown as shaded regions.

These efforts are expected to raise the quality of standard geotechnical practice with regard to earthquake hazards in California.

ACKNOWLEDGMENTS

Seismic zonation in the southern California region and in the City of Oakland are partially supported by Federal Emergency Management Agency grants administered through the California Office of Emergency Services.

REFERENCES

California State Mining and Geology Board, 1993, Criteria for delineating liquefaction hazard zones: Unpublished California State Mining and Geology Board document developed by the Seismic Hazards Mapping Act Advisory Committee.

California State Mining and Geology Board, 1997, Guidelines for evaluating and mitigating seismic hazards in California: California Department of Conservation, Division of Mines and Geology, Special Publication 117, 74 p.

California State Mining and Geology Board, in press, Criteria for delineating seismic hazard zones: California Department of Conservation, Division of Mines and Geology, Special Publication 118, 21 p.

National Research Council, 1985, Liquefaction of soils during earthquakes: National Research Council Special Publication, Committee on Earthquake Engineering, National Academy Press, Washington, D.C., 240 p.

Petersen, M.D., Bryant, W.A., Cramer, C.H., Cao, T., Reichle, M.S., Frankel, A.D., Lienkaemper, J.J., McCrory, P.A., and Schwartz, D.P., 1996, Probabilistic seismic hazard assessment for the State of California: California Department of Conservation, Division of Mines and Geology, Open File Report 96-08; U.S. Geological Survey Open File Report 96-706, 33p.

Seed, H.B. and Idriss, I.M., 1971, Simplified procedure for evaluating liquefaction potential: Journal of the Soil Mechanics and Foundations Div., ASCE, v. 97, no. SM9, p. 1,249-1,273.

Seed, H.B. and Idriss, I.M., 1982, Ground motions and soil liquefaction during earthquakes: Monograph Series, Earthquake Engineering Research Institute, Berkeley, California, 134 p.

Seed, H.B., Idriss, I.M., and Arango, Ignacio, 1983, Evaluation of liquefaction potential using field performance data: Journal of Geotechnical Engineering, v. 109, p. 458-482.

Seed, H.B., Tokimatsu, Kohji, Harder, L.F., and Chung, R.M., 1985, Influence of SPT procedures in soil liquefaction resistance evaluations: Journal of Geotechnical Engineering, ASCE, v. 111, no. 12, p. 1,425-1,445.

Seed, R.B. and Harder, L.F., 1990, SPT-based analysis of cyclic pore pressure generation and undrained residual strength: Proceedings of the H. Bolton Seed Memorial Symposium, v. 2, p. 351-376.

Tinsley, J.C., Youd, T.L., Perkins, D.M., and Chen, A.T.F., 1985, Evaluating liquefaction potential, *in* Ziony, J.I., editor, evaluating earthquake hazards in the Los Angeles region, an earth science perspective:, U.S. Geological Survey Professional Paper 1360, p. 263-316.

Youd, T.L. and Perkins, D.M., 1978, Mapping liquefaction-induced ground failure potential: Journal of the Geotechnical Engineering Division, ASCE, v. 104, no. GT4, p. 433-446.

Youd, T.L., 1991, Mapping of earthquake-induced liquefaction for seismic zonation, *in* Proceedings of the Fourth International Conference on Seismic Zonation, v. 1, p. 111-147.

Youd, T.L. and Idriss, I.M., 1997, Proceedings of the NCEER workshop on evaluation of liquefaction resistance of soils: Technical Report NCEER-97-0022, 277 p.

VERIFICATION OF THE SIMILITUDE LAW FOR FLOW OF LIQUEFIED GROUND

S. Hadush[1]
A. Yashima[2]
and
R. Uzuoka[3]

1 - Graduate Student, Department of Civil Engineering, Gifu University, Gifu, Japan
2 - Professor, Department of Civil Engineering, Gifu University, Gifu, Japan
3 - Research Engineer, Earthquake Disaster Mitigation Research Center, Hyogo, Japan

ABSTRACT

This paper discusses fluid dynamics analysis based numerical method for prediction of liquefaction induced ground flow. The pseudoplastic and the Bingham models are used to represent the behavior of liquefied soil. The numerical method is applied to verify the similitude law for liquefied ground flow, which states, flow velocity is proportional to the square root of the liquefied ground thickness. The numerical method reproduced the tendency of the experimental results as well as the proposed similitude law very well. Therefore, the similitude law holds.

INTRODUCTION

It has long been a customary practice in Geotechnical engineering to analyze the deformation and failure of geomaterials based on the framework of continuum mechanics, a branch of solid mechanics, employing the mathematical theories of elasticity and plasticity. These theories have been successfully implemented in different numerical approaches such as the famous FEM (Finite Element Method). Large deformation problems, however, give rise to numerical instabilities due to excessive distortion of the finite element mesh.

Large deformation problem includes several practical problems. Liquefaction induced lateral spreading is one of the phenomenon categorized as a large deformation problem. In 1964 many structures were found to be damaged due to liquefaction during the Niigata earthquake in Japan. Some were reported to be damaged due to lateral spreading[1]. During the 1971 San Fernando earthquake a flow slide on the upstream side of the Lower San Fernando dam was observed[2]. A large ground displacement occurred and the sewage pipes were damaged during the 1983 Nihonkai-Chubu earthquake[3]. The 1995 Hyogoken-Nambu earthquake caused serious damage of structures located along the coastal lines and rivers due to lateral spreading[4]. As a result, lateral spreading due to liquefaction began to be taken into consideration and a method to predict lateral spreading became necessary to make a rational seismic structural design.

In this study, we discuss a fluid dynamics analysis based numerical method to predict lateral spreading of a liquefied subsoil and using this method we verified the law of similitude for liquefied ground flow proposed by Hamada *et al*[5] based on experimental results. The numerical method reproduced the tendency of experimental results as well as the similitude law very well.

ANALYTICAL METHOD

Modeling of Liquefied Soil

There have been many debates in the last few years whether liquefied soil behaves like a solid or fluid. The point of view that the liquefied soil behaves like solid states that liquefaction reduces the stiffness of the soil significantly, and the ground deforms as a solid under the influence of gravitational force. In contrast, the point of view that the liquefied soil behaves like a fluid states that liquefaction reduces the stiffness of the soil to a negligible extent, and intrinsically the ground behaves as a fluid. Hamada*et al.*[5] investigated the behavior of liquefied soil during ground flow using several case studies and experiments and concluded that liquefied soil behaves as a fluid during ground flow, but after the earthquake motion ceases, the stiffness of the liquefied soil recovers and it returns to behaving as a solid body. Uzuoka *et al.*[6] treated the liquefied soil as a Bingham fluid and carried out several numerical analyses supported with experimental results. We do share the point of view that states liquefied soil behaves like a fluid during ground flow and we model liquefied soil as a fluid in this study.

Pseudoplastic Model

Hamada *et al.*[5] studied the mechanisms of liquefaction-induced ground displacements based on, among other techniques, experiments conducted on liquefied ground models. From the investigations they carried out they concluded that liquefied soil behaves as a pseudoplastic fluid during ground flow, but after the earthquake motion ceases, the stiffness of the liquefied soil recovers and it returns to behaving as a solid body.

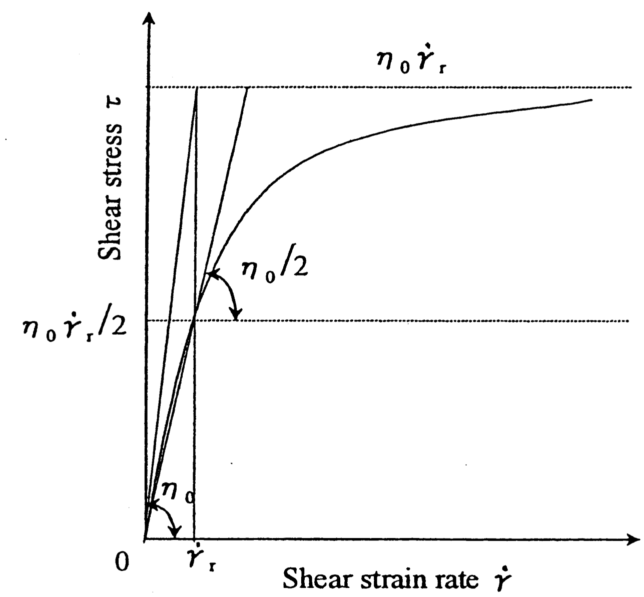

Figure 1: Shear stress-shear strain rate relation for a psuedoplastic fluid

The group of non-Newtonian fluids in which the viscosity coefficient decreases as the shear strain rate increases are generally called pseudoplastic fluids. The relationship between the shear stress, τ, and shear strain rate, $\dot{\gamma}$, for such fluids, can be expressed with the curve in Figure 1. Approximating the curve with a hyperbola gives the following equation.

$$\tau = \eta_0 \dot{\gamma}/(1 + \dot{\gamma}/\dot{\gamma}_r) \tag{1}$$

where η_0 is the initial viscosity coefficient; $\dot{\gamma}_r$ is the shear strain rate when the secant viscosity becomes equal to $\eta_0/2$, called the reference shear strain rate.

Bingham Model

In this case the liquefied soil is modeled as a Bingham fluid, which is one of the viscoplastic models in consideration of the residual strength. In a pure shear condition, the shear stress-shear strain rate relationship of the Bingham model can be expressed as follows:

$$\tau = \eta \dot{\gamma} + \tau_r \tag{2}$$

where τ is the shear stress, η is the viscosity after yield, $\dot{\gamma}$ is the shear strain rate and τ_r is the yield strength (= minimum undrained strength). Uzuoka *et al.* (1998) confirmed that the Bingham model is applicable to the behavior of liquefied soil and expressed the Bingham viscosity by equivalent Newtonian viscosity η'. They assumed the equivalent viscosity coefficient as follows:

$$\eta' = \eta + \frac{\tau_r}{2\dot{\gamma}} = \eta + \frac{R_r \cdot p}{2\dot{\gamma}} \quad ;if \;\; \dot{\gamma} \neq 0 \qquad \eta' = \infty; \quad if \;\; \dot{\gamma} = 0 \tag{3}$$

in which,

$$\dot{\gamma} = \sqrt{(1/2)\dot{e}_{ij}\dot{e}_{ij}} \tag{4}$$

where R_r is the residual strength ratio and $\dot{\gamma}$ is the second invariant of the deviatoric strain rate tensor.

Figure 2 summarizes the relation between the viscosity and the shear strain rate obtained by three different measurement methods[7,8], including measurements of the flow displacement from the lateral spreading experiment, from the load acting on a steel sphere pull-up test and from the experiment with a viscometer. Sand was used as a test sample material in the experiments. The relative density D_r of the samples ranged from 20% to 60%.

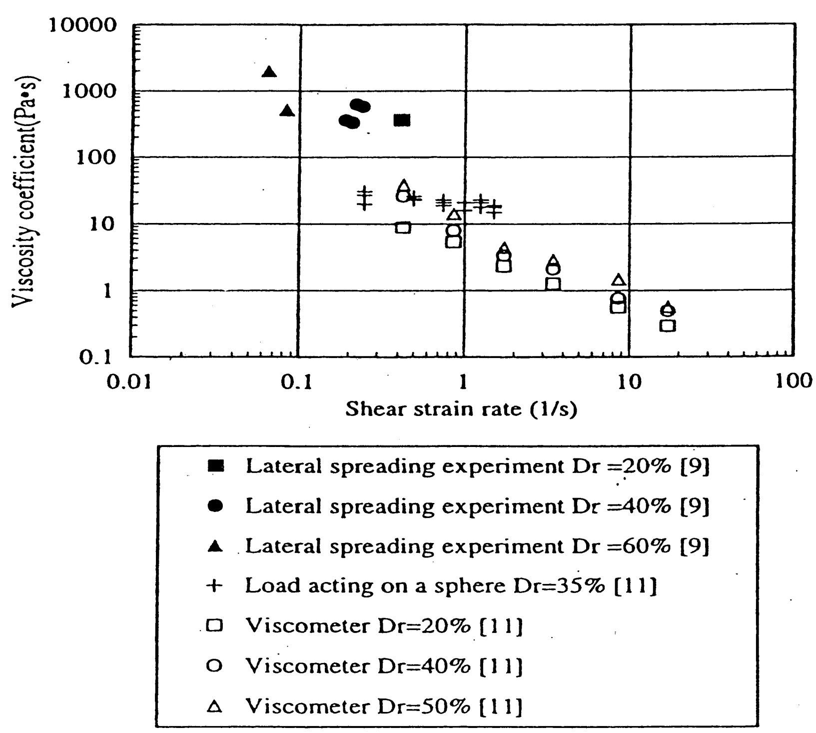

Figure 2: Viscosity coefficient of liquefied soil[7,8]

Governing Equations

Fluid dynamics analysis with Eulerian description is more advantageous for problems involving free boundaries. The motion of an incompressible, uniform density fluid is governed by the continuity and momentum equations. These are the mathematical expressions of the mass and momentum conservation principles, respectively. The Navier-Stokes equations in which Newtonian viscosity is incorporated have been widely used in fluid dynamics and are expressed as follows:

$$\frac{Dv_i}{Dt} = \frac{-1}{\rho}\frac{\partial P}{\partial x_i} + \nu\frac{\partial}{\partial xj}[\frac{\partial v_i}{\partial x_j}] + g_i \tag{5}$$

where D is the Lagrangian derivative, v_i is the velocity vector, ρ is the mass density, P is the hydraulic pressure, g_i is the gravity acceleration vector, and $\nu(\equiv \eta/\rho)$ is the kinematic viscosity.

Numerical Scheme

In order to solve the Navier-Stokes equations, different researchers have developed different numerical methods. The numerical code in our analysis uses the SIMPLE method[9]. The acronym, SIMPLE, stands for Semi-Implicit Method for Pressure Linked Equations and describes the iterative procedure by which the solution to the discretised Navier-Stokes equations is obtained. The SIMPLE formulation is based on a finite volume discretisation on a staggered grid of the governing equations. Computational solutions of the governing equations are often obtained on a staggered grid. This implies that different dependent variables are evaluated at different grid points. The finite volume method is to discretise the integral form of the governing equations, in contrast to the finite different method, which is usually applied to discretise the differential form of the governing equations.

Free Surface Treatment

We must pay attention to free surface treatment in fluid dynamics analysis with Eulerian description in order to predict the surface displacement during lateral spreading. Several methods have been previously used to approximate free boundaries in finite difference numerical simulations. The numerical code uses the Volume of Fluid (VOF) method[10] to express free surface. The VOF method is based on the concept of fractional volume of fluid. In the VOF method a state function F, whose value is unity at any point occupied by fluid and zero otherwise, is defined. The average value of F in a cell would then represent the fractional volume of the cell occupied by fluid. In particular, a unit value of F would correspond to a cell full of fluid, while a zero value would indicate that the cell contained no fluid. Cells with F value between zero and one must then contain a free surface. The state function F of a cell is defined as follows:

$$F^{n+1} = F^n + \frac{1}{V}\sum_{i=1}^{k} f_i \tag{6}$$

where F^{n+1} is F at the present step, F^n is F at the previous step, V is the volume of the cell surface and f_i is the fluid volume flux which moves through each cell surface.

SIMILITUDE LAW

It is important to apply the law of similitude in order to discuss model experimental results in conjunction with the results of case studies on actual ground. Hamada *et al.*[5] proposed a law of similitude for the flow of liquefied ground applying the Reynolds law of similitude encountered in fluid dynamics. The summary of their derivation is explained here. Assuming the Reynolds number of the actual ground to be equal to that of the model ground, the following equation holds:

$$Re = \rho_m V_m L_m / \eta_m = \rho_p V_p L_p / \eta_p \tag{7}$$

where ρ is fluid density; V is velocity of the flow; L is the characteristic dimension of length; η is fluid viscosity; and suffixes p and m are for actual and model ground, respectively. Putting liquefied ground thickness H as the characteristic linear dimension L, since $\rho_m = \rho_p$ if sand is used as the model ground material, Eqn (7) can be expressed as follows:

$$V_m H_m / \eta_m = V_p H_p / \eta_p \tag{8}$$

Let the geometrical scale of the model of the actual ground be $\lambda = H_m / H_p$, Eqn (8) can be rearranged as follows:

$$\lambda \cdot V_m / V_p = \eta_m / \eta_p \tag{9}$$

The apparent viscosity coefficient η depends on the shear strain rate. From Figure 1 and Eqn (1) the apparent viscosity coefficient can be given by the following equation:

$$\eta_m = \eta_{0,m} / (1 + \dot{\gamma} / \dot{\gamma}_{r,m}) \quad \text{and} \quad \eta_p = \eta_{0,p} / (1 + \dot{\gamma} / \dot{\gamma}_{r,p}) \tag{10}$$

In the above equations, η is the apparent viscosity coefficient, η_0 is the initial viscosity coefficient, $\dot{\gamma}_r$ is the reference shear strain rate. The following equation is derived from Eqn (10)

$$\frac{\eta_m}{\eta_p} = \frac{\eta_{0,m}\dot{\gamma}_{r,m}}{\eta_{0,p}\dot{\gamma}_{r,p}} \cdot \frac{\dot{\gamma}_{r,p} + \dot{\gamma}_p}{\dot{\gamma}_{r,m} + \dot{\gamma}_m} \tag{11}$$

Since the ground strain γ and the reference shear strain γ_r are non-dimensional numbers, those of the model and actual ground are equal. Representing the dimension of time with T the following equation is obtained;

$$\frac{\eta_m}{\eta_p} = \frac{\eta_{0,m}\dot{\gamma}_{r,m}}{\eta_{0,p}\dot{\gamma}_{r,p}} \cdot \frac{T_m}{T_p} \tag{12}$$

where T_m is time with respect to model ground; and T_p is time with respect to actual ground. In Eqn (12), $\eta_{0,m} \cdot \dot{\gamma}_{r,m}$ and $\eta_{0,p} \cdot \dot{\gamma}_{r,p}$ denote the shear strength of liquefied soil. The maximum shear strength of liquefied soil is in proportion to the vertically confined pressure, i.e. ground layer thickness, it follows:

$$\frac{\eta_{0,m}\dot{\gamma}_{r,m}}{\eta_{0,p}\dot{\gamma}_{r,p}} = \lambda \tag{13}$$

Eqn (12) can then be rearranged as follows:

$$\frac{\eta_m}{\eta_p} = \lambda \frac{T_m}{T_p} \tag{14}$$

Substituting Eqn (14) into Eqn (8) gives the following equation:

$$V_m = \sqrt{\lambda} V_p \quad , \quad T_m = \sqrt{\lambda} T_p \tag{15}$$

We can also obtain a law of similitude using the Bingham model. In the Bingham model, the equivalent viscosity cofficients for that of the model and actual grounds, respectively, can be expressed as follows:

$$\eta_m' = \eta_m + \frac{R_r \cdot P_m}{2\dot{\gamma}_m} \quad and \quad \eta_p' = \eta_p + \frac{R_r \cdot P_p}{2\dot{\gamma}_p} \tag{16}$$

The Bingham viscosity coefficients η_m and η_p are very small (η_m, $\eta_p \simeq 0$) and can be neglected. Therefore, from Eqn (16) we can get the following:

$$\begin{aligned} \frac{\eta_m'}{\eta_p'} &= \frac{R_r \cdot P_m}{R_r \cdot P_p} \cdot \frac{\dot{\gamma}_p}{\dot{\gamma}_m} \\ &= \frac{P_m}{P_p} \cdot \frac{\dot{\gamma}_p}{\dot{\gamma}_m} \end{aligned} \tag{17}$$

Since the ground strain γ is a non-dimensional number, $\gamma_p = \gamma_m$. Representing the dimension of time with T we obtain;

$$\frac{\eta_m'}{\eta_p'} = \frac{P_m}{P_p} \cdot \frac{T_m}{T_p} \tag{18}$$

Assuming that the vertically confining pressure P of liquefied soil is in proportion to the ground layer thickness, the following equation holds:

$$\frac{\eta_m'}{\eta_p'} = \lambda \cdot \frac{T_m}{T_p} \tag{19}$$

Substituting Eqn (19) into Eqn (8) gives the following equation:

$$V_m = \sqrt{\lambda} V_p \quad , \quad T_m = \sqrt{\lambda} T_p \tag{20}$$

Thus, the similitude law remains the same for both Pseudoplastic and Bingham models.

VERIFICATION OF SIMILITUDE LAW

Experiment

As described in the previous section Hamada *et al.*[5] investigated the mechanisms of liquefaction induced ground displacement using different techniques including experiments conducted on liquefied ground models. One of their main conclusions was that the Reynolds Similitude law encountered in fluid dynamics can be applied between models and actual grounds, and that the velocity of ground flow is proportional to the square root of the layer thickness.

In the experiment a sloped ground of 15 to 30 cm in thickness was prepared in a 3.0 m long by 1.0 m wide soil box, as shown in Figure 3. Liquefaction was caused by shaking the soil box in the horizontal direction perpendicular to the direction of ground displacement. The gradient of the ground surface was 1% to 5%, and the soil box was shaken with a sinusoidal wave having a maximum amplitude of 500 cm/s^2 at 2.9 to 5.0 Hz. The movement of targets placed in the ground was measured with a camcorder and converted in a numerical form to obtain a time history of the ground displacement.

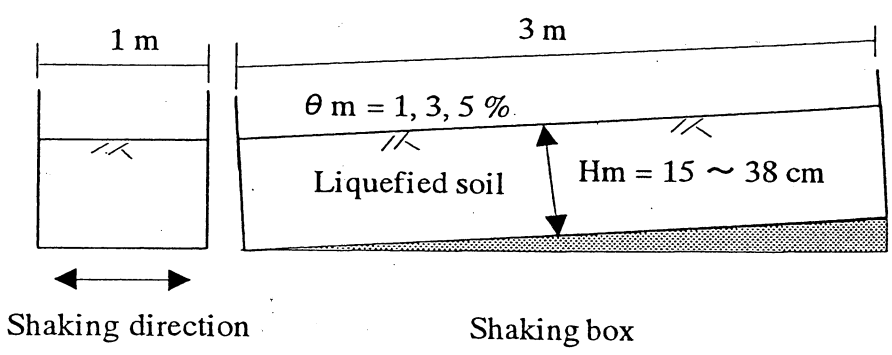

Figure 3: View of the soil box used in the experiment[5]

Figure 4 shows the relationship between flow velocity and liquefied soil layer thickness, obtained from the experiments. The velocity stands for the ground surface velocity when the flow comes to a steady state, i.e. when the velocity is almost constant. It was shown that this velocity is approximately proportional to the square root of liquefied soil layer thickness, indicating that the earlier mentioned law of similitude holds between ground models having different liquefied soil layer thickness. In this study we verified the law of similitude proposed by Hamada *et al.* [5] using a fluid dynamics based numerical analysis.

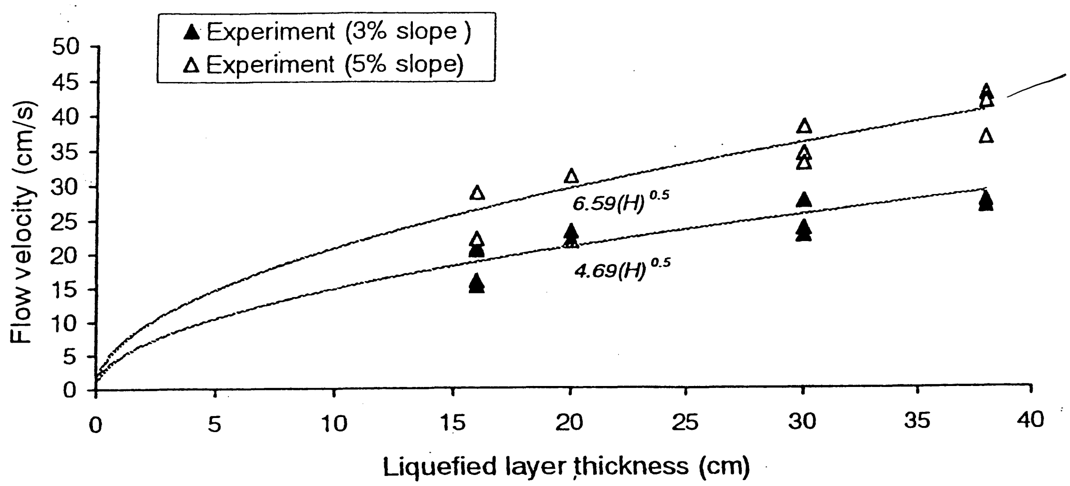

Figure 4: Flow velocity to layer thickness relations from experiment[5]

Numerical Model

Figure 5 shows a typical two-dimensional numerical model used for this analysis based on the experimental set up for the 5% ground slope. Four types of models with ground thicknesses of 15, 20, 25 and 30 cm are used in the analysis for verification of the law of similitude obtained from the experiments shown in Figure 4. The height of the initial surface indicated in Figure 5 is only for the 30 cm thick model. However, the initial surface is obviously different from model to model. The pitch sizes are 2 cm in the x and y directions and 1 cm in the z direction. The boundary conditions of the soil container wall on the right, left and bottom side are non-slip boundaries.

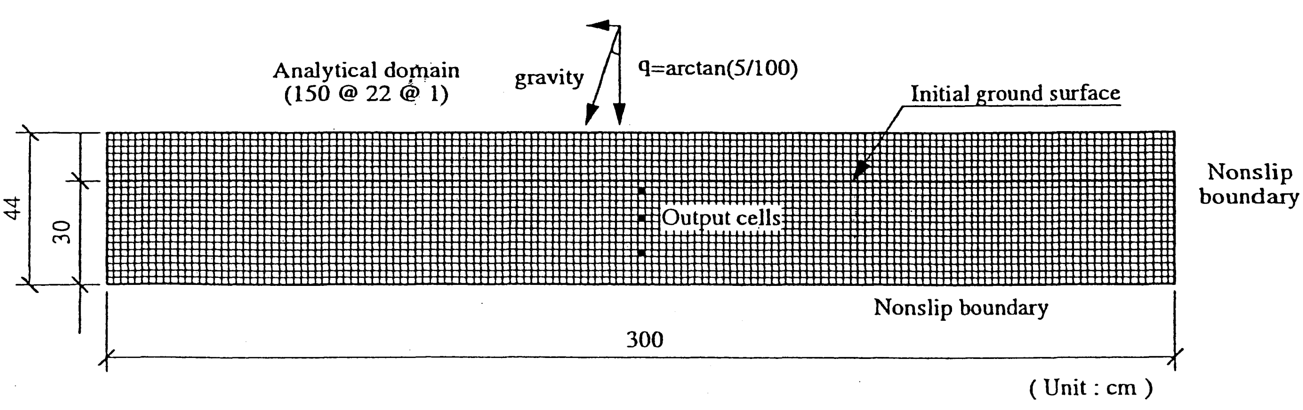

Figure 5: Two-dimensional numerical model used for the analysis

For the model shown in Figure 5, the total number of cells is 3300 ($= 150 \times 22$). The number of free degrees for pressures is 3300, that for velocities is 6772 ($= 151 \times 22 + 150 \times 23$), and the total degrees of freedom are 10,072. The simulation incorporated gravity as the only external force and did not consider the vibration force because its direction was perpendicular to the ground slope. We assumed that the whole ground was completely liquefied. A saturated unit weight of 17.93 kN/m^3 is used to calculate the body force in the model material. The calculation time increment is updated in each calculation step to satisfy the stability condition. The stability condition is judged in each cell and each direction by the equation CFL (Courant-Friedrichs-Lewy) $= v_i \Delta t / \Delta x \leq 0.1$, where v_i is the velocity, Δt is the calculation time increment, Δx is the finite difference grid pitch. For all cells, the minimum Δt is set as the time increment for next calculation step.

Model Parameters

In driving the law of similitude, Hamada *et al.*[5] treated liquefied subsoil as a pseudoplastic fluid. In our analysis for verification of the experimental results, the psuedoplastic model which was described earlier, is, therefore, used to represent the behavior of liquefied soil layer. Based on the pseudoplastic fluid theory, the following constitutive model was used to extend the existing non-Newtonian fluid analysis code.

$$\eta = \frac{A \cdot P}{(\dot{\gamma}_r + \dot{\gamma})} \tag{21}$$

in which the maximum stress ratio A is given by

$$A = \frac{\eta_0 \cdot \dot{\gamma}_r}{\rho g h} \tag{22}$$

where P is the overburden pressure, ρ $(= 17.93 \mathrm{kN/m}^{3})$ is liquefied soil unit weight and h is the liquefied layer thickness. We used the experimental results shown in Figure 2 for setting material parameters. In order to reproduce the flow velocities obtained in the experiments, we have adopted the mean viscosity value from the three types of viscosity measurments shown in Figure 2. Table 1 summarizes the values of ground slope (θ), initial viscosity coefficient (η_0), reference shear strain rate ($\dot{\gamma}_r$) and maximum shear stress ratio (A) used in the simulation. We assumed that the viscosity measurments in the experiment were effective at the middle depth of the liquefied layer. Owing to the existing difficulties in exactly representing the experimental boundary and soil conditions in the numerical analysis, we could not use the same material parameters in both 3% and 5% ground slope cases.

Table 1: Analytical parameters used in the simulation

θ (%)	η_0 (Pa· s)	$\dot{\gamma}_r$(1 / s)	A
3	100.0	0.7	0.027
5	137.3	0.5	0.039

More attention was given to the main target, which is verifying the law of similitude obtained in the experiment. Therefore, the analytical parameters were set taking into consideration the flow velocities obtained in the experiments.

Simulation Result and Discussion for Experiment

The simulated flow velocity to liquefied layer thickness relations are shown in Figure 6 together with the results from the experiment.

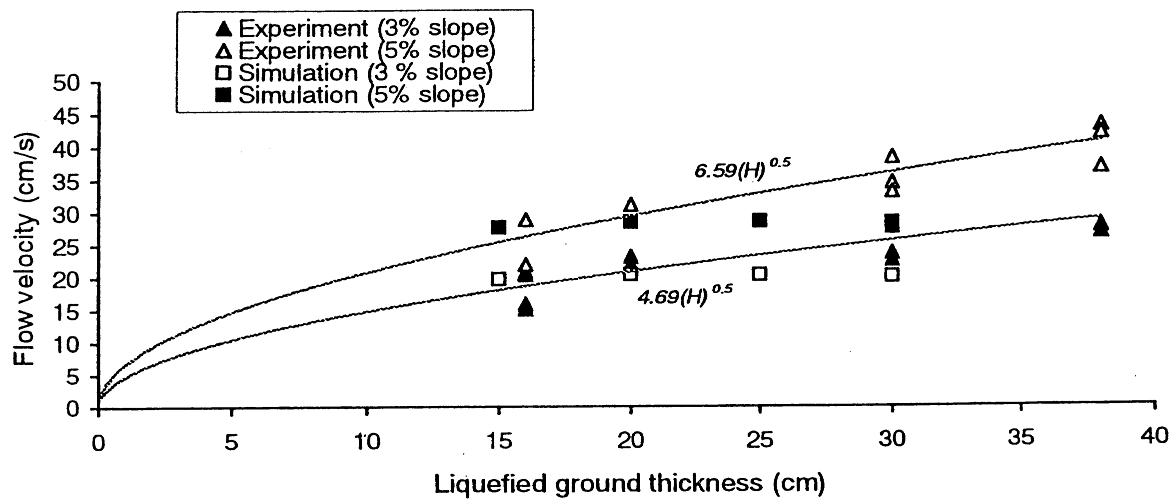

Figure 6: Simulated flow velocity to layer thickness relations

The simulated velocity results obtained in the 15, 20, 25 and 30 cm thick models for 3% and 5% ground slopes are plotted in this figure. In the experiment, different soil conditions such as relative density (D_r) were used to obtain the law of similitude. In the simulation, however, it is difficult to represent all the conditions of the experiment.

In order to analyze the numerical results, we have used those results from experiment obtained under similar soil conditions. Table 2 and Figure 7 show good example of experimental results obtained under similar soil conditions.

Table 2: Experimental result obtained under similar soil condition

H_m(cm)	D_r	θ(%)	T_m(s)	D_m(cm)	V_m(cm/s)
16	51	3	0.6	17.1	20.9
30	43	3	0.6	28.1	22.6
16	54	5	0.6	17.6	29.9
30	41	5	0.6	19.9	33.1

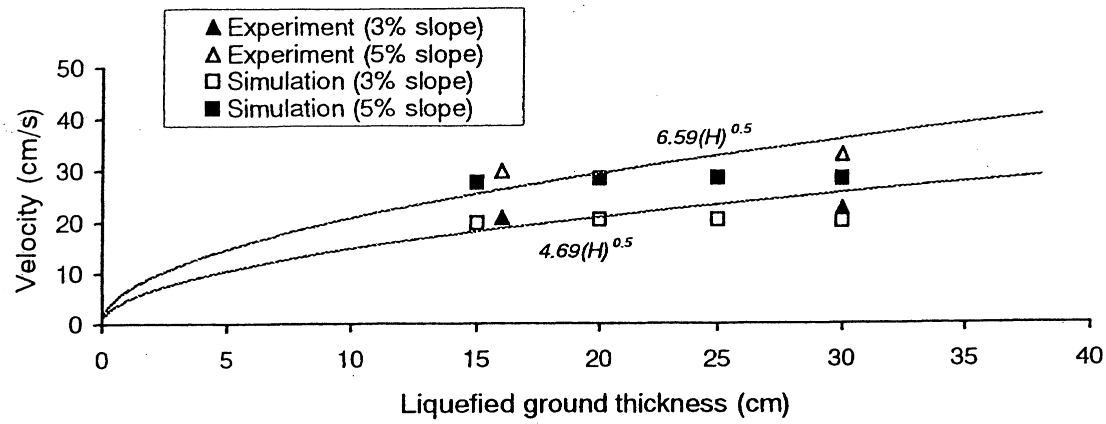

Figure 7: Experimental result under similar soil condition

From Figures 6 and 7, it can be seen that the simulation has reproduced the tendency of experimental results very well. In both experiment and simulation, a relatively lower velocity was observed for the models with larger thickness. For example, in the experiment, despite a lower D_r type soil was used in the 30 cm thick model than in the 16 cm thick one, the obtained flow velocity for the 30 cm thick model is slightly lower than anticipated as shown in Figure 7. One main reason for this problem is because the soil chamber length used in the experiment was fixed regardless of liquefied soil depth. The effect of box length on the velocity results can also be seen in the simulated velocity time history curves shown in Figure 8 and Figure 9, for the 3% and 5% ground slope cases, respectively. It can be seen that negative velocity was generated in the models with larger thicknesses due to the effect of small chamber length.

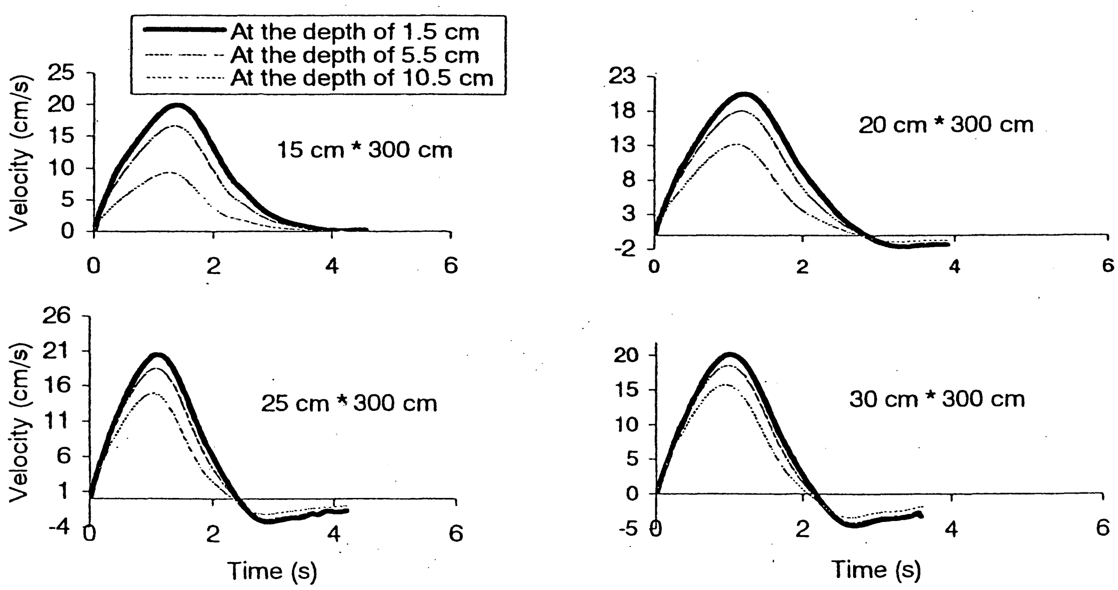

Figure 8: Simulated velocity time history curves for the 3% ground slope.

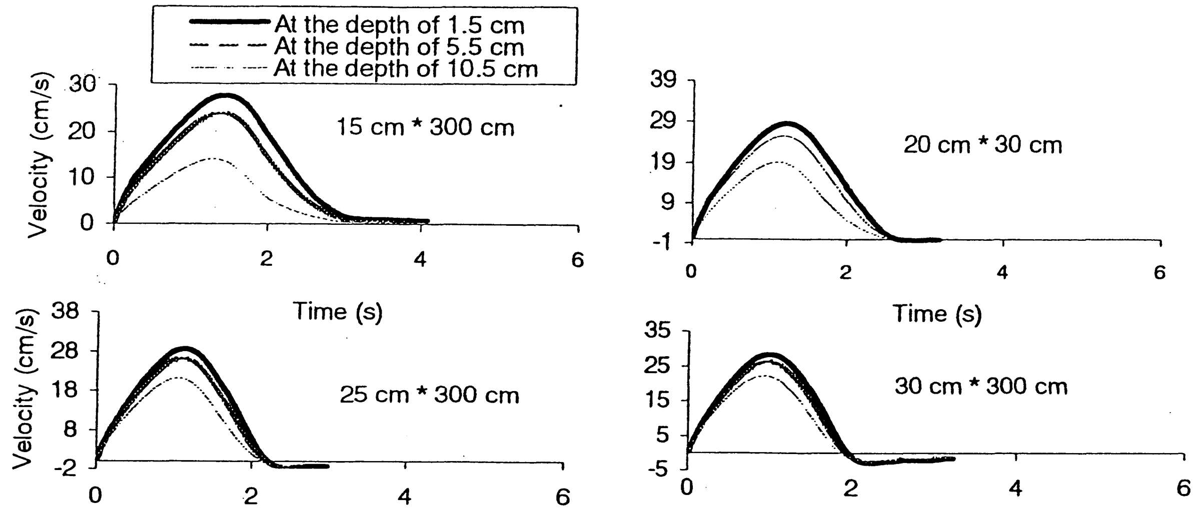

Figure 9: Simulated velocity time history curves for the 5% ground slope.

Verification of Similitude Law

We have also carried out simulations to analyze the proposed law of similitude using layer thicknesses larger than those used in the experiment. To avoid the effect of model length (= chamber length in the experiment case) on the results, we used models with proportional length and depth dimensions. Taking the experimental result obtained for the 20 cm thick model as a reference result, we set the length to depth ratio of the ground models with larger thicknesses to be 15 (= 300cm/20cm). Based on this approach, simulations were carried out for 30, 40, 50 and 60 cm thick models. Figure 10 shows the simulated velocity to liquefied layer thickness relations obtained using the above mentioned approach. It can be clearly seen that the simulated results reproduced the tendency of proposed similitude law very well. Figure 11 shows the simulated velocity time history curves for the 30 cm thick model based on the proportional dimension approach.

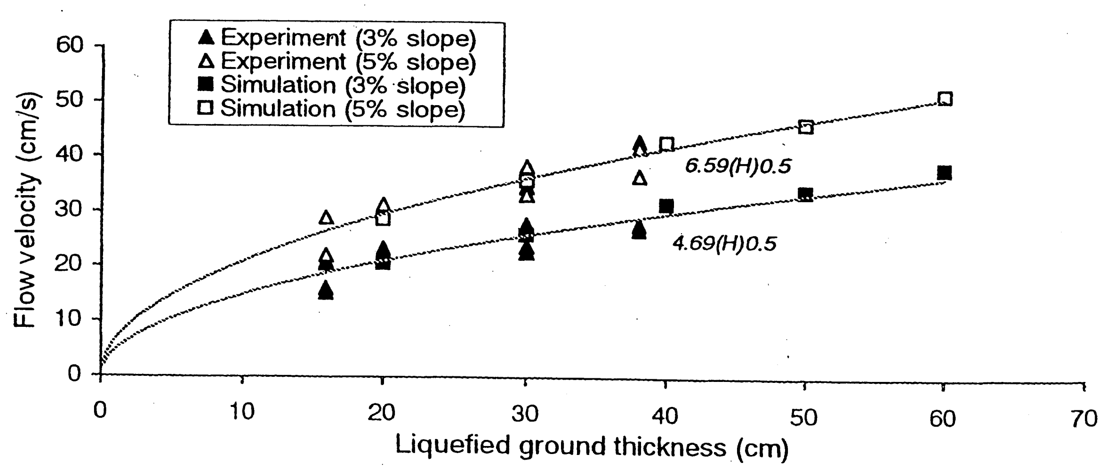

Figure 10: Simulated velocity to layer thickness relations for proportional models

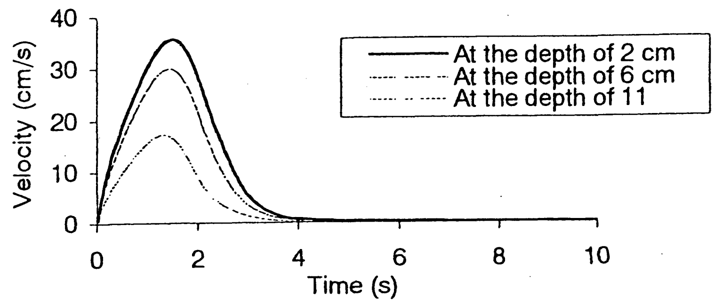

Figure 11: Velocity time history curve for 30 cm thick model

Simulation Based on Bingham Model

We have also carried out simulations based on the Bingham model described earlier. In this case, the liquefied ground is treated as a Bingham fluid. The following constitutive equation[6] was used in the analysis:

$$\eta' = \eta + \frac{\tau_r}{2\dot{\gamma}} \tag{23}$$

where η' is the equivalent viscosity, η is the Bingham viscosity, R_r is the residual strength ratio and $\dot{\gamma}$ is the second invariant of the deviatoric strain rate tensor. Table 3 summarizes the analystical parameters used in this simulation.

Table 3: Analytical parameters used in the analysis

θ (%)	η_0 (Pa· s)	R_r(1 / s)
3	1.0	0.018

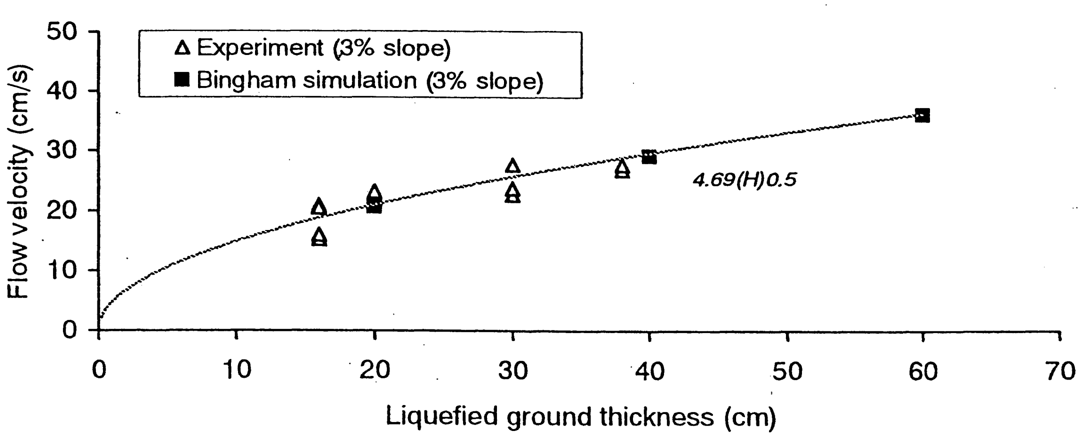

Figure 12: Simulated velocity layer thickness relations using the Bingham model

In a similar way to the previous simulation, 3 models with proportional length to depth dimensions are used in this analysis. The length to depth ratio of each model is kept to be 15, the same as in the previous simulation. Figure 12 shows the simulated velocity to layer thickness relations for 20, 40 and 60 cm thick models together with the experimental results for the 3% ground slope case. It can be clearly seen that the simulation results reporoduced the tendency of the similitude law very well.

CONCLUSIONS

This paper discussed fluid dynamics analysis based numerical method for prediction of liquefaction induced ground flow. We used the pseudoplastic and the Bingham models to represent the behavior of liquefied layer during ground flow in the numerical analysis. We applied the numerical method to verify the similitude law for liquefied ground flow using several liquefied ground models. The simulation results reproduced the tendency of the experimental results as well as the proposed similitude law very well. Therefore, the similitude law, which states liquefied ground flow velocity is proportional to the square root of the liquefied ground thickness, holds.

ACKNOWLEDGMENTS

The authors wish to thank Professor Masanori Hamada of Waseda University, Japan for numerous useful discussions on the similitude law.

REFERENCES

[1] Hamada, M., Yasuda, S., Isoyama, R. and Emoto, K., Observation of permanent ground displacements induced by soil liquefaction. Proceedings of Japan Society of Civil Engineering, 1986, no. 376, Vol. **III**-6, pp. 211-220 (in Japanese).

[2] Seed, H. B., Lee, K.L., Idriss, I. M. and Makdisi, F. I., The slides in the San Fernando Dams during the Earthquake of February 9, 1971. *Journal of the Geotechnical Engineering Division,* ASCE, 1975, **101**(GT7), 651-688.

[3] Hamada, M., Saito, K., Yasuda, S. and Isoyama, R., Earthquake damge by liquefaction-induced permanent ground displacement, Proceedings of Ninth World Conference on Earthquake Engineering, Tokyo, Japan, 1988, Vol. **VIII**, pp. 213-218.

[4] Hamada, M., Isoyama, R. and Wakamatsu, K., Liquefaction-induced ground displacement and its related damage to lifeline facilities. *Soils and Foundations*, Special Issue on Geotechnical Aspects of the January 17 1995 Hyogoken-Nmabu Earthquake, 1996, 81-97.

[5] Hamada, M. and Wakamatsu, K., ***A study on ground displacement caused by soil liquefaction.*** Journal of Geotechnical Engineering, JSCE, 1998, no. 596, Vol.**III**-43, pp. 189-208 (in Japanese).

[6] Uzuoka, R., Yashima, A., Kawakami, T. and Konrad (1998) : ***Fluid dynamics based prediction of liquefaction induced lateral spreading***, Computers and Geotechnics, 1998, no. 3/4, Vol. **22**, pp. 243-182.

[7] Hamada, M., Sato, H. and Kawakami, T., A consideration of the mechanism for liquefaction-related large ground displacement, Proceedings from the Fifth U.S.-Japan Workshop on Earthquake Resistant Design of Lifeline Facilities and Countermeasures Against Soil Liquefaction. Technical report NCEER-94-0026, Salt Lake City, USA, 1994, pp. 217-232.

[8] Kawakami, T., Suemasa, N., Hamada, M., Sato, H. and katada, T., Experimental study on mechanical properties of liquefied sand, Proceedings from the Fifth U.S.-Japan Workshop on Earthquake Resistant Design of Lifeline Facilities and Countermeasures Against Soil Liquefaction. Technical report NCEER-94-0026, Salt Lake City, USA, 1994, pp. 285-299.

[9] Patanker, S. V. and Spalding, D. B., ***A calculation procedure for heat, mass and momentum transfer in three-dimensional parabolic flows.*** International Journal of Heat Mass Transfer, 1972, **15**, 1787-1806.

[10] Hirt, C. W. and Nichols, B. D., ***Volume of fluid (VOF) method for the dynamics of free boundaries.*** J. Comput. Phys. 1981, **39**, 201-225.

LIMIT STATE MODEL FOR SOIL-PILE INTERACTION DURING LATERAL SPREAD

Siang-Huat, Goh and Thomas D. O'Rourke

Graduate Research Assistant and Professor, respectively
School of Civil and Environmental Engineering
Cornell University
Ithaca, NY 14853

ABSTRACT

This paper describes an analytical model and design procedure for foundation piles subjected to large lateral ground deformation triggered by liquefaction. The model involves the use of p-y curves, but avoids the empiricism associated with the selection of degradation coefficients or reduction factors. To obtain a proper p-y characterization of the reaction between laterally deformed liquefied soil and an embedded pile, triaxial extension is recognized as the most appropriate analogue for the loading conditions. A suite of undrained triaxial extension tests was carried out using Nevada sand to establish the relevant strength and deformation parameters. Using the material parameters obtained from these tests, 2-D FLAC analyses were performed to develop strain-softening p-y curves. Application of these p-y curves to the analyses of centrifuge experiments involving lateral spread effects on piles yields good agreement between the computed and measured responses. The strain-softening model provides excellent predictions of the measured peak and residual moments. Furthermore, the computed soil pressure diagrams agree well with the recommendations made by the Japan Road Association, which were calibrated using case histories from the 1995 Kobe earthquake.

INTRODUCTION

Liquefaction-induced permanent ground deformation has been the cause of extensive damage to pile foundations of buildings, bridges, and waterfront structures. During the 1964 Niigata earthquake, lateral spread of liquefied soils resulted in excessive deformation and failure of reinforced concrete piles supporting a number of buildings, including the NHK Building, Niigata Family Courthouse, and Niigata Hotel [Hamada et al., 1986; Hamada and O'Rourke, 1992]. Bartlett and Youd [1992, 1995] reported that lateral spread was the cause of damage to more than 250 bridge structures during the 1964 Alaska earthquake. In most instances, lateral displacements of liquefied deposits of fine silt, sand, and gravel towards river channels caused damage to bridge foundations, abutments, piers, and superstructures. More recently, extensive pile damage due to lateral spread was observed after the 1995 Kobe earthquake [Hamada and Wakamatsu, 1996; Matsui and Oda, 1996].

There are several methods for analyzing the response of a single pile or pile group to lateral load. One of the most commonly used methods involves p-y curves, which define the relationship between horizontal soil reaction p, and lateral pile displacement y. Application of the p-y approach for analyzing lateral spread effects requires that appropriate p-y relationships be developed for liquefied soil conditions. Currently, p-y characterization of liquefied soil relies heavily on empirical rules involving the application of degradation coefficients or reduction factors to the strength and stiffness of the unliquefied soil [e.g., Yoshida and Hamada, 1991; Meyersohn, 1994; Chaudhuri, 1998; Ishihara and Cubrinovski, 1998].

To account for the fundamental behavior of liquefied soil in a more rigorous manner, p-y relationships need to be assessed with respect to the undrained behavior of sand and its constitutive relationships. This paper provides a description of an analytical model that was developed to evaluate soil-pile interaction for conditions of liquefaction-induced lateral spread. The analytical model was developed at Cornell University in conjunction with centrifuge experiments performed at Renssalaer Polytechnic Institute (RPI). The centrifuge experiments [Abdoun, 1997] provided a means of calibrating and checking the model under controlled conditions of inertial similitude in which key soil layering, soil properties, and pile characteristics could be varied to assess the model's predictive capabilities under diverse conditions of practical interest for design. This paper focuses on the stress transfer from liquefying soil to vertical piles during lateral spread and the corresponding application of this characterization in the numerical simulation of soil-pile interaction.

MODEL ASSUMPTIONS AND IDEALIZATIONS

Figure 1 shows a condition of lateral spread in which the soil moves horizontally against the pile foundation. During the process, the development of shear strains in the soil is caused by a combination of (i) lateral soil displacement relative to the pile, and (ii) dynamic shaking. This results in a stress state involving complex three-dimensional

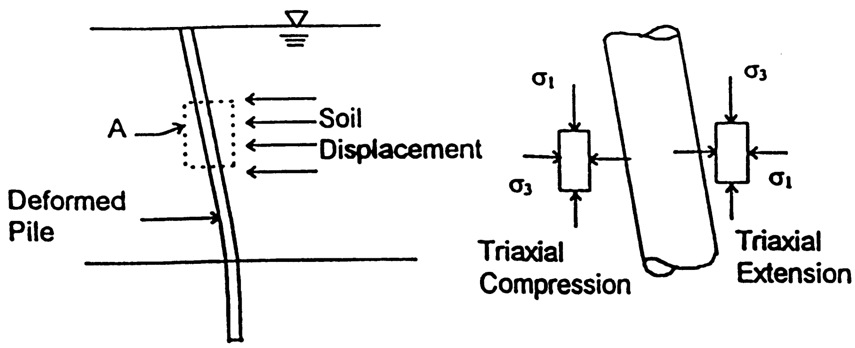

(a) Cross Section (b) Detail

Figure 1 Schematic of Relative Soil-Pile Movement and Analogous Triaxial Loading Conditions

stress relations and shear transfer. To reduce the complexity of the problem, the simplified interaction model proposed in this paper invokes the key assumption that stress transfer from soil to pile during lateral spread is controlled principally by static undrained loading in response to relative soil-pile movement, rather than dynamic load components governed by cyclic ground shaking. Large lateral movement induced by liquefaction is accompanied by large monotonically increasing shear strains in the soil surrounding the pile. These strains are likely to exceed their cyclic counterparts, with the static loading component becoming dominant as the magnitude of lateral spread increases. Based on the results of Ishihara et al. [1991], the static loading response during ground flow is also expected not to be influenced by the application of cyclic loads leading up to liquefaction. Hence, by uncoupling the static and dynamic components of undrained shear deformation, the problem is simplified significantly. The assumption that pile response during lateral spread is controlled by static loading conditions is fully testable; static loading can be evaluated by laboratory soil testing, and the results incorporated in an analytical model that is compared against centrifuge measurements and field observations.

In Figure 1b, the loading conditions on the upstream and downstream sides of the pile are shown as being analogous to undrained triaxial extension (TE) loading and compression (TC) unloading, respectively. Because load transfer occurs principally on the upstream side, triaxial extension, as opposed to compression, is a more appropriate analogue to characterize soil-pile interaction under lateral spread involving large horizontal displacements of the soil mass. This distinction is important, as it has been widely reported by Vaid et al. [1990] and Yoshimine and Ishihara [1998], among others, that soil specimens tested in triaxial extension exhibit lower strengths and more contractive behavior than identical specimens tested in compression. By incorporating relevant soil parameters that pertain to the triaxial extension mode of loading, the proposed interaction model strives to provide a simple but realistic representation of field loading conditions.

LABORATORY TEST PROGRAM AND RESULTS

The development of the proposed interaction model begins with the strength characterization of liquefiable soil in undrained triaxial extension. An experimental program was undertaken to determine the undrained strengths and moduli of Nevada test sand prepared at several relative densities and tested at different initial confining pressures. The properties of this sand are well documented by Abdoun [1997], who prepared the RPI centrifuge models using the same granular material.

The triaxial specimens had an initial diameter and height of 7.0 cm and 17.0 cm, respectively, and were prepared using the method of dry pluviation. This is the same method used to deposit the Nevada sand in the RPI centrifuge tests [Abdoun, 1997], and was adopted in the triaxial testing program to ensure that a consistent soil fabric was present in both the triaxial tests and the centrifuge experiments. The procedure for pluviating the specimens is similar to that described by Arulmori et al. [1992]. After pluviation, back pressure was applied and the specimens were saturated until "B" values of 0.97 or higher were obtained. This was followed by isotropic consolidation to different effective stress levels before the specimens were subjected to strain-controlled undrained extension unloading.

In this program, the Nevada sand specimens were prepared to three different initial void ratios : 0.737, 0.699 and 0.661, corresponding to relative densities (Dr_i) of 40%, 50% and 60% respectively. For each initial relative density, the specimens were isotropically consolidated under confining pressures ranging from 30 kPa to 500 kPa. They were then unloaded extensionally under undrained conditions to axial strains as high as 12%.

Selected results from a suite of triaxial extension tests are presented in Figure 2. In this study, the Dr = 40% specimens are of special interest because they correspond to the initial state of the sand prepared in the centrifuge models. The stress-strain measurements shown in Figure 2a strongly suggest that, under undrained extension, two distinct shear strengths are mobilized during the course of straining. The peak strength is mobilized at very small strains, corresponding to the maximum deviatoric stress. As shown in Figure 2b, this is also denoted as the collapse state, after the nomenclature adopted by Sladen et al. [1985]. On the other hand, the minimum strength is associated with

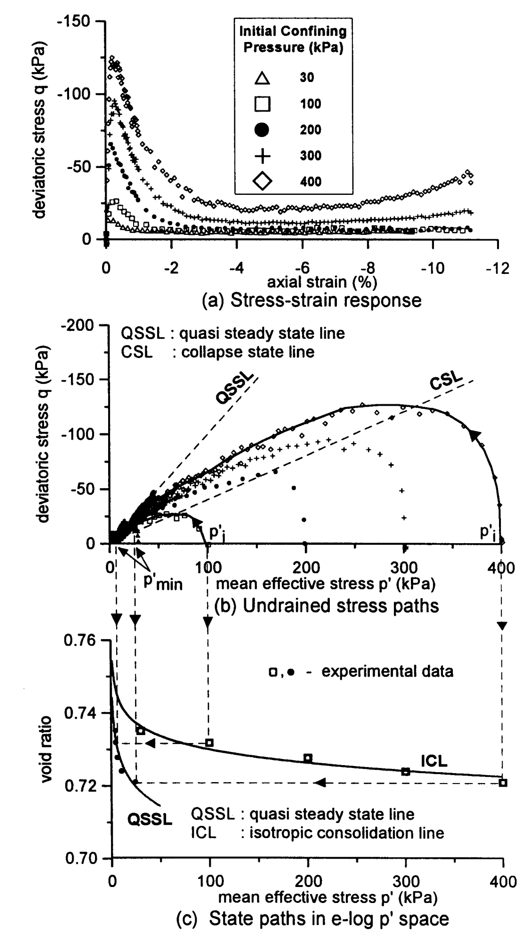

Figure 2 Results from Triaxial Extension Tests (Nevada Sand, Dr=40%)

what Ishihara [1993] has identified as the quasi-steady state (QSS) condition. In the literature, this condition has also been called phase transformation, critical state, or simply, steady state. The term 'minimum strength' is recommended for future use as a simple expedient for identifying the lowest strength condition without adopting a terminology that implies an underlying cause or mechanism. In this paper, the subscript 'min' is applied (eg. p'_{min}, q_{min} and s_{umin}) to the lowest strength condition. The mobilization of two distinct undrained strengths, and the transition from one to the other, are key features of the soil-pile interaction model proposed in this paper.

Undrained triaxial compression tests were carried out by Yamamuro and Lade [1997] on Nevada sand with similar relative density (Dr=42% compared with Dr=40% in this study) and grain size characteristics (% fines = 6% compared with zero fines content in this study). In contrast to the contractive behavior illustrated in Figure 2 for triaxial extension, their results showed fully dilatant behavior even at a very low confining pressure of 25 kPa. Such observations are consistent with the generally recognized fact that sand exhibits contractive behavior at much higher relative densities under triaxial extension than compression [Vaid et al., 1990; Yoshimine and Ishihara, 1998]. This aspect of soil behavior emphasizes the importance of applying the appropriate mode of loading in strength characterization tests.

Figures 2b and 2c show the stress and state paths for two specimens consolidated to p'_i = 100 kPa and 400 kPa. Also shown in Figure 2c are the initial and final states of the test specimens plotted in the form of the isotropic consolidation line (ICL) and quasi-steady state line (QSSL). However, in soil mechanics practice, these data are more commonly presented in the e-log p' space.

Figure 3 is a compilation of QSS data and their best-fit lines from extension tests carried out by (i) Vaid et al. [1990] using Ottawa sand, (ii) Yoshimine and Ishihara [1998] using Toyoura sand, and (iii) the present authors using Nevada sand. To accommodate the different stress quantities used by different groups of researchers, two separate plots are presented. In Figure 3a, a comparison is made between Vaid et al.'s data and the authors' data using σ'_3 (effective confining stress) as the stress quantity. Figure 3b shows the corresponding comparison with Yoshimine and Ishihara 's data, plotted using the mean effective stress p'. From the comparisons, it is clear that, despite the different types of sand and preparatory void ratios, the slopes of the QSS linear fits are very

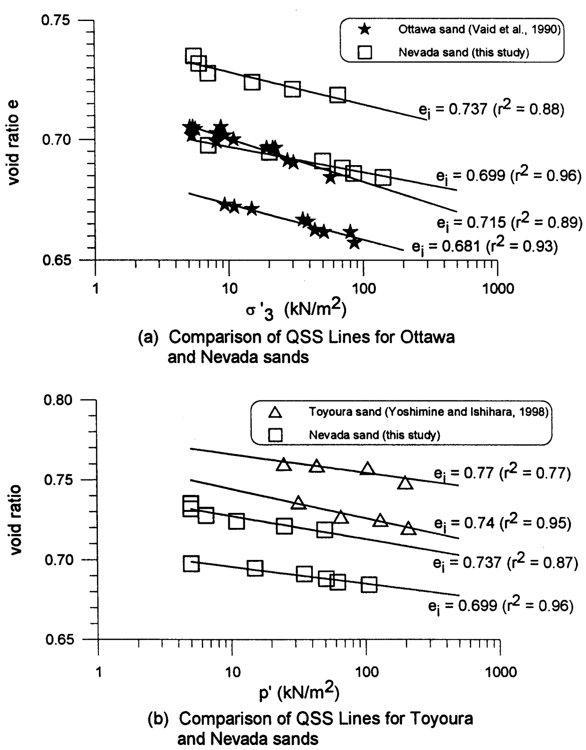

Figure 3 QSS Lines for Common Sands at Different Void Ratios

similar. These lines are characteristically very flat, implying that small variations in void ratios can result in large changes in minimum strengths. This has practical implications for the centrifuge experiments considered in this study. It suggests that, even for a very well prepared model, there may exist significant and often highly localized, variations in the undrained soil strengths due to small pockets of non-uniformities in the soil model. The practical implication with respect to laboratory testing is that considerable expertise and care are required to prepare triaxial specimens with such tight control over initial void ratio.

As pointed out by Vaid et al. [1990], the QSS lines in extension are not unique, but depend on the initial or depositional void ratio e_i. The issue of non-unique steady-state lines is of practical significance in that the initial void ratio may be viewed as an index of the soil structural fabric immediately upon deposition. This fabric, in turn, depends on the grain characteristics (shape, grain size distribution, etc) and the medium of transport (air, water, etc.). For a given geological deposit, it may be expected that, during formation, there is an almost constant depositional void ratio associated with the grain characteristics and mode of transport. As the soil deposit builds up over time, the increase in confining stresses causes the bottom layers to consolidate, resulting in insitu void ratios that are smaller than the depositional values.

The same consideration is applicable in the RPI centrifuge experiments, in which the liquefiable Nevada sand layer was prepared to an initial relative density of approximately 40% for model thicknesses of 12 and 16 cm. Under a centrifugal acceleration of 50g, the insitu stresses are equivalent to those generated by prototype thicknesses of 6 and 8 m respectively. As a result, the soil experiences void ratio reductions with depth that reflect the increased overburden stresses. This is analogous to the changes experienced by the triaxial specimens, which were prepared to the same initial void ratios (or relative densities) before being consolidated under different confining pressures prior to undrained extension unloading. Therefore, the QSS line shown in Figure 3 for Nevada sand with e_i = 0.737 (Dr=40%) may be considered an appropriate representation of the undrained minimum strength conditions that develop at different depths of the Nevada sand layer in the centrifuge model.

It is useful to relate the peak and minimum strengths, s_{up} and s_{umin} , to the initial mean effective stress p'_i. The linear e-log p' plots shown in Figure 3 suggest that critical state concepts [e.g., Schofield and Wroth, 1968] may be used to do so.

Minimum strength s_{umin}

For the Dr=40% triaxial specimens, Figure 4a re-plots the ICL and QSSL of Figure 2c so that the effective stresses are in the log scale. The resulting lines are approximately linear and parallel. Following the nomenclature used in critical state soil mechanics, the equations of these lines are given by :

$$\text{ICL}: \quad e = N + \lambda \ln p'_i \qquad (1)$$

$$\text{QSSL}: \quad e = \Gamma + \lambda \ln p'_{min} \tag{2}$$

where p'_i = initial mean effective stress,
p'_{min} = mean effective stress at minimum strength condition,
N = void ratio e on the ICL when the mean effective stress p'_i = 1 kPa
Γ = void ratio e on the QSSL when the mean effective stress p'_{min} = 1 kPa
λ = the slope of the ICL and QSSL lines in the e - ln p' space.

Since the void ratio remains unchanged during undrained loading, (1) and (2) can be equated to yield the relation:

$$\frac{p'_i}{p'_{min}} = e^{\frac{\Gamma - N}{\lambda}} \tag{3}$$

From Figure 4b, there is an approximately linear relationship between q_{ss} and p'_{ss} given by

$$q_{min} = M_{QSS}\, p'_{min} \tag{4}$$

where
$$M_{QSS} = \frac{6 \sin \phi_{QSS}}{3 - \sin \phi_{QSS}} \tag{5}$$

(3) and (4) can be combined to give

$$q_{min} = M_{QSS} e^{-\frac{\Gamma - N}{\lambda}} p'_i \tag{6}$$

Hence, a linear relationship exists between q_{min} and p'_i . For a given p'_i, q_{min} may be obtained if the parameters Γ, N, λ and M_{QSS} are known. Figures 4a and 4b present estimates of these parameters using the triaxial measurements from the Dr = 40% tests. Substituting these values into (6), the following relationship is obtained :

$$q_{min} = 0.071\, p'_i \tag{7}$$

The experimental correlation between these two quantities is shown in Figure 4e, and is mathematically described by :

$$q_{min} = 0.073\, p'_i \tag{8}$$

Although there is some nonlinearity of the data in Figure 4e at higher confining pressures, the overall regression is not significantly different from the results obtained using a low pressure subset, as shown in the inset on the same figure. For depths up to about 10m, such as in the centrifuge tests, the low pressure subset is a good representation of the stress conditions in the soil.

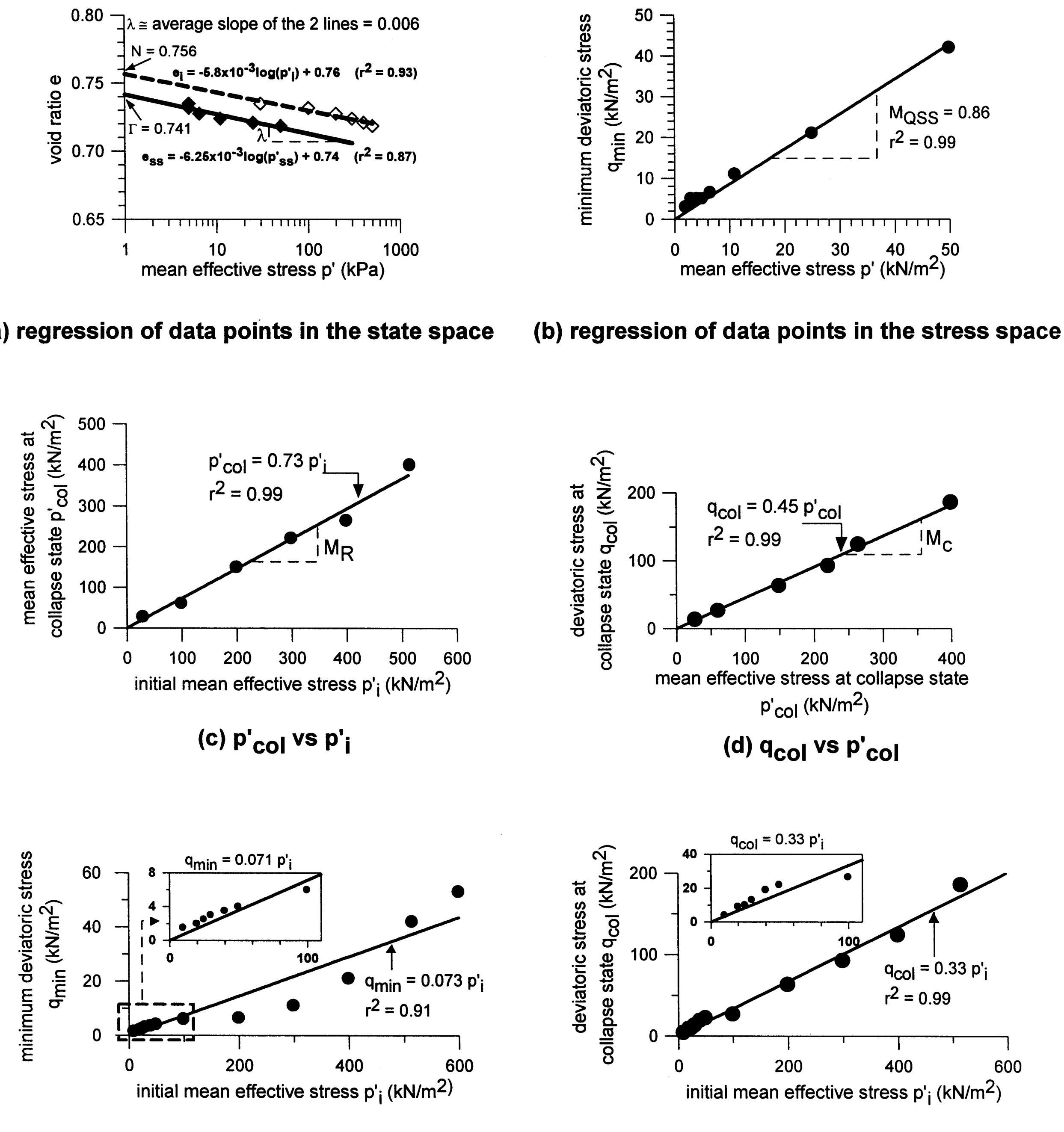

(a) regression of data points in the state space

(b) regression of data points in the stress space

(c) p'_{col} vs p'_i

(d) q_{col} vs p'_{col}

(e) Measured steady state deviatoric stresses vs initial confining pressures

(f) Measured peak deviatoric stresses vs initial confining pressures

Figure 4 Determination of model parameters and strength correlations from triaxial test results

The minimum undrained shear strength s_{umin} is related to the minimum deviatoric shear stress q_{min} as follows :

$$s_{umin} = (q_{min}/2) \cos \phi_{QSS} \tag{9}$$

By substituting for q_{min} using (6), (9) can be rewritten as

$$s_{u\,min} = M_{QSS} e^{-\frac{\Gamma - N}{\lambda}} p'_i \cos \phi_{QSS} / 2 \tag{10}$$

Substituting values of M_{QSS} , ϕ_{QSS} , Γ, N and λ (obtained from Figures 4a and 4b and equation (5)) into (10), the relationship between the minimum undrained strength s_{umin} and the initial mean effective stress p'_i is obtained as

$$s_{umin} = 0.034\, p'_i \tag{11}$$

Peak strengths s_{up}

A linear relationship between the peak deviatoric stress at collapse q_{col} and p'_i can be obtained if the stress paths shown in Figure 2b are geometrically similar. Visually, the shapes of the measured stress paths support this postulate. Mathematically, this requires that the ratios M_R ($= p'_{col} / p'_i$) and M_c ($= q_{col}/p'_{col}$) remain constant for all values of p'_i, where p'_{col} = the mean effective stress at collapse. These requirements are validated by the experimental data shown in Figures 4c and d, in which linear regression yields

$$p'_{col} = M_R\, p'_i = 0.73\, p'_i \tag{12}$$

and

$$q_{col} = M_c\, p'_{col} = 0.45\, p'_{col} \tag{13}$$

Equations (12) and (13) can be combined to give

$$q_{col} = M_c M_R\, p'_i = 0.33\, p'_i \tag{14}$$

Equation (14) agrees very well with the experimental correlation shown in Figure 4f.

The peak strength s_{up} is related to the deviatoric shear stress at collapse q_{col} as follows :

$$s_{up} = q_{col} / 2 \tag{15}$$

Combining (14) and (15), the following relationship between s_{up} and p'_i is obtained :

$$s_{up} = M_c M_R\, p'_i / 2 = 0.17\, p'_i \tag{16}$$

Estimation of peak and minimum strengths in the centrifuge tests

Since Nevada sand in the centrifuge tests was prepared to the same initial void ratio as the triaxial specimens, the correlations represented by eqns (11) and (16) can be used to estimate the minimum and peak undrained strengths, respectively, at different depths in the centrifuge model associated with the extensional loading imposed on the soil during lateral spread. Assuming $K_o = 0.5$, which is representative of most normally consolidated soils, the effective mean stress at selected depths are computed and tabulated in Table 1, together with values of s_{umin} and s_{up} computed using (11) and (16), respectively. In the next section, these strength estimates are used for developing p-y curves that take into account strain-softening effects.

Table 1 Effective confining stresses and undrained strengths at various depths

depth (m)	σ'_v (kPa)	σ'_h (kPa)	p'_i (kPa)	s_{up} (kPa)	s_{umin} (kPa)
1.0	9.4	4.7	6.3	1.1	0.21
2.0	18.8	9.4	12.5	2.1	0.43
3.0	28.2	14.1	18.8	3.2	0.64
4.0	37.6	18.8	25.1	4.3	0.85
5.0	47	23.5	31.3	5.3	1.06
6.0	56.4	28.2	37.6	6.4	1.28

NUMERICAL DERIVATION OF P-Y CURVES

Soil-pile interaction under lateral load is a complex three-dimensional problem. At intermediate to large depths, however, the displacements in the vertical direction are small compared to their horizontal counterparts. Under this condition, the load transfer mechanism may be modeled as a two-dimensional plane strain problem. Chen and Poulos [1993], for example, have used plane strain conditions to analyze the soil-pile interaction associated with pile groups. In this study, a similar approach is adopted, in which 2-D simulations are performed using FLAC [Itasca, 1995] to obtain the p-y response for a single pile laterally loaded in a strain-softening elasto-plastic medium.

Figure 5a is a 2-D cross-sectional view of a circular pile installed in a half-space. The corresponding finite difference grid is shown in Figure 5b. Because of symmetry, only half the pile is analyzed. To minimize the influence of boundary effects, the edges of the grid are set at a distance of 40 times the pile diameter D from the pile face. In addition, a very thin layer of interface elements is placed between the pile and the surrounding soil to model the effects of adhesion at the soil-pile interface.

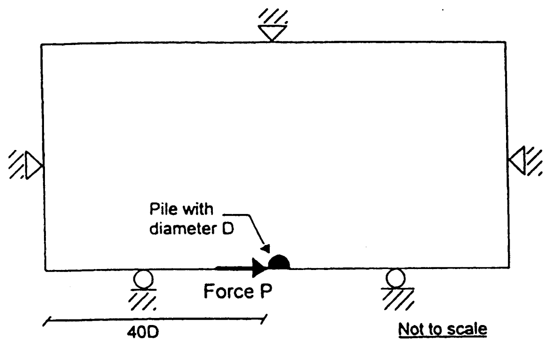

(a) 2-D Cross Section

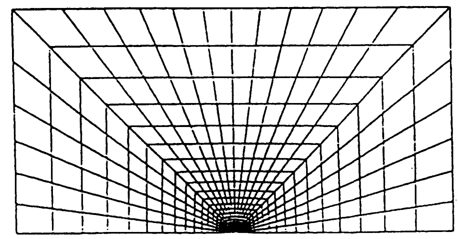

(b) Finite Difference Grid

Figure 5 2-D Model of Soil-Pile System for FLAC analyses

Estimation of the Undrained Modulus of Nevada sand

A good p-y characterization requires the specification of the appropriate soil deformation modulus surrounding the pile. For the Nevada sand used in the centrifuge experiments, estimates of the undrained modulus can be obtained from the stress-strain relationships measured in the triaxial extension tests. As shown in Figure 2a, these moduli are highly strain-dependent. To account for the nonlinear nature of these curves in a simple and reasonable manner, an equivalent secant modulus E_{sec} is often adopted for elastic-perfectly plastic analyses. In this study, a secant modulus, $E_{\varepsilon 50}$, corresponding to 50% of the peak axial strain was chosen as the representative modulus.

The estimated modulus, $E_{\varepsilon 50}$, was found to be dependent on the initial confining pressure. In Figure 6, these estimates are plotted against the corresponding initial effective stresses p'_i. The data points are regressed using both a linear and power function, the latter being similar to the one proposed by Hardin and Drnevich [1972] for initial soil modulus. For the range of confining pressures considered, the regression results suggest that both functions provide good and comparable fits to the experimental data. In view of this, it was decided to adopt the linear function, as it yields a direct and simple relationship between $E_{\varepsilon 50}$ and p'_i, given by :

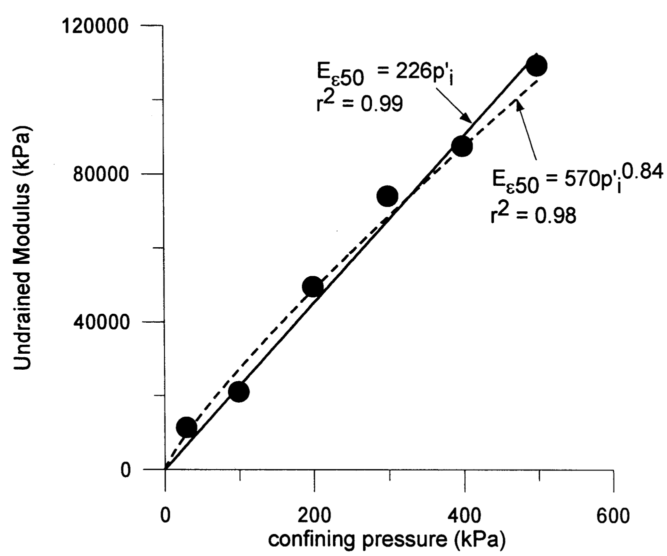

Figure 6 Variation of Secant Moduli with Confining Pressure

$$E_{\varepsilon 50} = 226\, p'_i \qquad (17)$$

Equation 17 can be combined with equation 16 to yield the following relationship between $E_{\varepsilon 50}$ and s_{up} :

$$E_{\varepsilon 50} = 1330\, s_{up} \tag{18}$$

Peak and minimum strength parameters

For undrained loading, the soil may be modeled as a frictionless Mohr-Coulomb material with a cohesion representing the undrained shear strength s_u. The experimental data presented earlier have shown that the mobilized strength of a loose, contractive sand varies substantially from a peak to a minimum as the specimen is strained under triaxial extension. These peak and minimum strengths may be estimated from the values shown in Table 1 for Dr=40% Nevada sand.

At any depth, the variation of the undrained strength from its peak to its minimum value is controlled by a softening parameter. Vermeer and DeBorst [1984] showed that the plastic deviatoric strain ε_{ps} may be used as an appropriate softening parameter. As the built-in softening model in FLAC also uses the same quantity, it is a logical and convenient choice for use in the present study. In undrained loading, the condition of zero volume change implies that the plastic deviatoric strain ε_{ps} is equal to the plastic axial strain ε_{pa} . The latter quantity, however, is not easily determined from the measured stress-strain curves shown in Figure 2a, because it is difficult to separate the plastic component from the total axial strain. To overcome this difficulty, it was assumed that the axial strain during the post-peak response is fully plastic. With this assumption, the measured stress-strain curves of Figure 2a can be used to estimate a softening model in which the undrained strength s_u varies approximately with plastic deviatoric strain in the manner depicted in Figure 7.

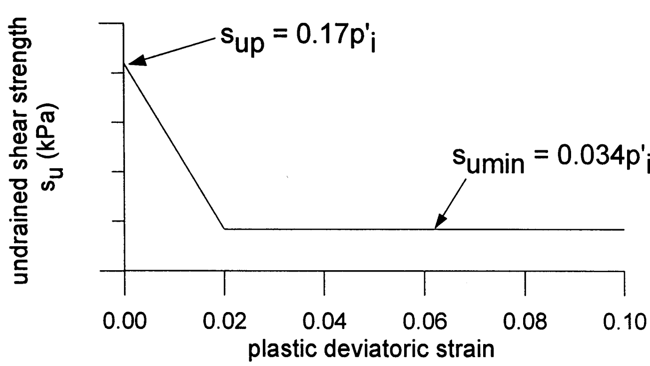

Figure 7 Variation of Undrained Shear Strength with Plastic Deviatoric Strain

FLAC Analyses and Results

To obtain the p-y response, the soil is laterally loaded by prescribing the rigid horizontal motion of the pile, in the direction shown in Figure 5a. Due to the highly nonlinear nature of the problem, the displacements are applied in small increments. At the end of each increment Δy, the soil reaction Δp acting on the pile is added to the load at the beginning of the increment to yield the total force p (per unit length of the pile) required to displace the pile by the cumulative distance y.

In Figure 8, computed normalized p-y responses are shown for the limiting conditions of perfect and no adhesion between the soil and pile. These conditions simulate a rough and smooth soil-pile interface, respectively. The results from FLAC analyses can be compared against the theoretical values reported by Randolph and Houlsby [1984], who used limit state theories to show that the ultimate normalized loads associated with a rigid circular pile moving through a perfectly plastic, cohesive material are 11.94 (rough) and 9.14 (smooth) respectively. The FLAC results show that, due to strain softening in the soil, the peak resistances are approximately 80~85% of their non-softening counterparts. More significantly, the residual resistances mobilized in the soil are drastically reduced to 20~25% of their peak values.

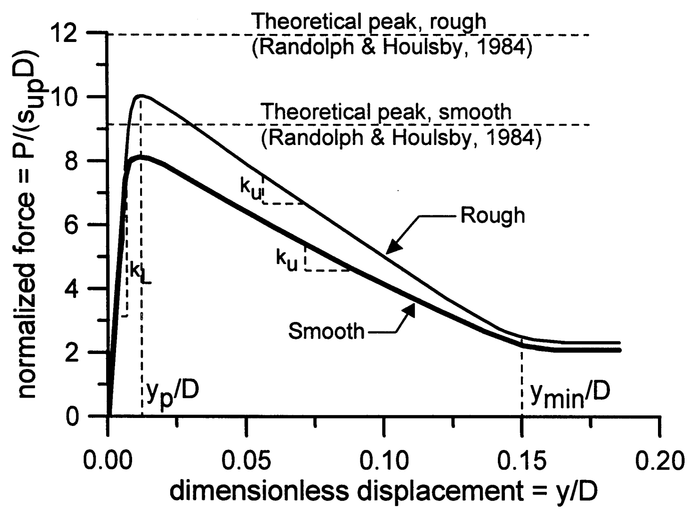

Figure 8 Strain-Softening Normalized p-y Curves

The p-y curves are also characterized by the slopes of the loading branch k_L and unloading branch k_u . For the p-y curves shown in Figure 8, the steep slopes associated with the loading branch are obtained directly from FLAC analyses. However, the unloading branches have been modified to achieve 3-D elastic stability of the pile during rebound. Although not shown, the negative slopes of the unloading branch derived from FLAC analyses are almost as steep as those of the loading branch. As explained in Appendix A, the use of such steep slopes during unload may result in a potentially unstable, instantaneous 'snapback' of the pile. This is analogous to the well-known rupture problem encountered in rock mechanics when the load frame is insufficiently stiff relative to the unloading stiffness of the rock specimen being tested. In the field, however, pile response during rebound involves the interaction of stored energy dissipation and viscous soil response that impedes rapid changes in loading and pile geometry. Such behavior is supported by the RPI centrifuge experiments, in which pile rebound was observed to be a stable and gradual process. Appendix A also shows how the reduced k_u that is required for 3-D stability may be estimated using the elastic pile properties and the peak/residual soil resistances of the p-y response. The p-y curves shown in Figure 8 reflect the use of these reduced slopes.

For the elastic pile used in the RPI centrifuge experiments, stability considerations require that the slope along the unloading branch be reduced so that the mobilized resistance gradually decreases from its peak value at 0.015D to its final residual value at approximately 0.3D. Although this establishes the maximum unloading stiffness required to achieve a stable response, it is not necessarily the k_u value that pertains to actual unloading conditions in the field. As described shortly, the appropriate k_u that applies in the field is calibrated through real loading conditions of piles tested in the centrifuge.

NUMERICAL ANALYSIS OF RPI CENTRIFUGE MODEL 3

Strain-softening p-y curves similar to those in Figure 8 were used in BSTRUCT to analyze the RPI centrifuge experiments [Abdoun, 1997]. BSTRUCT is a finite element (FE) code [e.g., Meyersohn, 1994] that can be used for the analyses of piles, frames, pipelines and other buried structures. The soil-pile configuration is modeled using a combination of beam elements, spring-slider elements and/or rotational springs. By accounting for both geometric and material non-linearities of the pile and soil, it is possible to study pile performance under large soil displacements that strain the pile material beyond its elastic limit.

Figure 9 shows the soil-pile arrangement and the FE model corresponding to RPI centrifuge model 3. The prototype being simulated involves a single pile of diameter 60 cm, length 8 m and EI = 8000 kN-m^2. The pile is free at the top, and is embedded in a two-layer soil system. In prototype units, this is equivalent to a 6.0 m layer of uniform Nevada sand, prepared at a relative density of about 40%, placed on top of a 2.0 m slightly cemented sand layer. Details pertaining to the centrifuge experiment, such as model preparation, instrumentation and test results, are found in Abdoun [1997].

(a) soil-pile system (b) finite element mesh (c) free-field lateral displacements

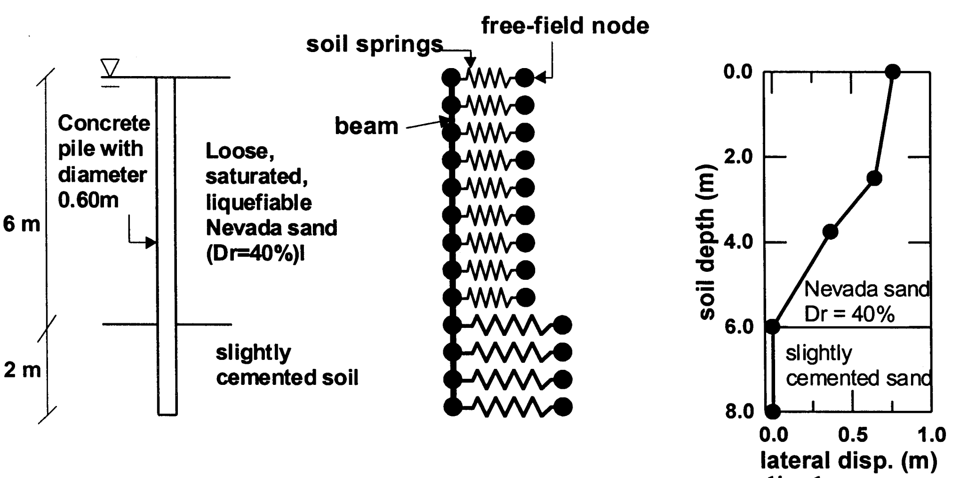

Figure 9 FE Model for Centrifuge Model 3

The soil springs that model the liquefiable soil are spaced 0.0625m apart, and are governed by the normalized strain-softening p-y curve shown in Figure 8 for the smooth soil-pile interface. As explained earlier, the slope of the unloading branch shown in this figure represents the maximum allowable that is required to achieve a stable rebound. The appropriate slope that pertains to field conditions is determined by successively increasing the value of y_{min}/D, until a good compliance between the measured and computed responses is obtained. At the base of the pile, the behavior of the non-liquefiable sand is modeled using the p-y curves back-figured by Abdoun [1997] from centrifuge lateral pile load tests carried out in this lightly cemented material.

Figure 9c shows the free-field lateral displacement profile measured in the centrifuge at the end of lateral spread. The discretized profile is applied in the form of incremental displacements to the free-field nodes of the corresponding soil springs.

Figure 10 compares the measured and computed moment histories at a pile depth of 5.75m. Due to its proximity to the boundary separating the liquefiable layer from the cemented sand, the moments measured at this location are the maximum moments induced in the pile. The effect of the sinusoidal base excitation is manifested in the cyclic component of the measured response, while the dominant effect of lateral spread is reflected in the mean trend of the measured moment history. This mean trend is characterized by a peak and a residual moment, both of which exceed by a substantial margin the cyclic moment amplitude induced by ground shaking. This provides strong evidence in support of the key assumption that the pile response during lateral spread is controlled principally by the static load component.

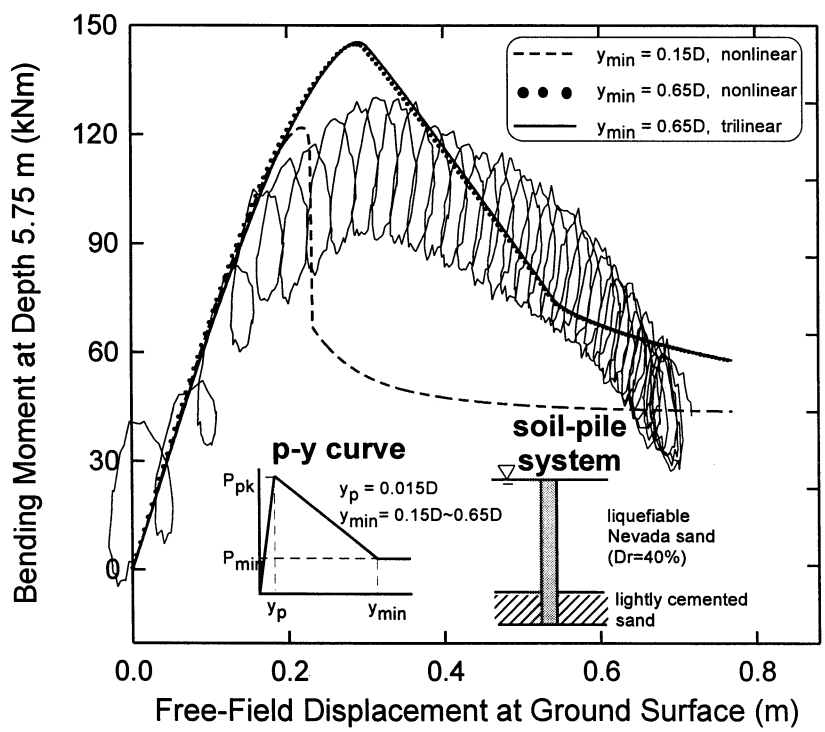

Figure 10 Centrifuge Measurements vs Model Predictions for Model 3

Three computed moment histories are shown in Figure 10. The 'nonlinear' responses are obtained by using the actual p-y curves derived from FLAC analyses (like those shown in Figure 8), as opposed to a trilinear p-y profile adopted for simplification. The use of y_{min} = 0.15D, which satisfies the minimum criterion for rebound stability, results in reasonable predictions of both the maximum and residual moments, but does not capture well the unloading phase of the moment history. Through a series of successive increments, it was found that, when y_{min} = 0.65D, the unloading moment history can be modeled accurately, together with favorable-predictions of both the peak and residual moments. Furthermore, there is little noticeable difference between the 'nonlinear' and 'trilinear' responses, which suggests that the latter may be used as a convenient approximation without much loss in accuracy. Henceforth, the trilinear p-y profile with y_{min} set to 0.65D, will be used in subsequent analyses presented in this paper.

Figure 11 shows the bending moment distributions along the pile at different stages during lateral spread. In stage 1, the moments in the pile have yet to attain their maximum values. Stage 2 corresponds to the instance when the maximum moments develop along the pile. There is good agreement between the computed and measured moments at this stage. On the other hand, stage 5 shows the computed and measured residual moment distributions at the end of lateral spread. Again, there is good agreement between the two.

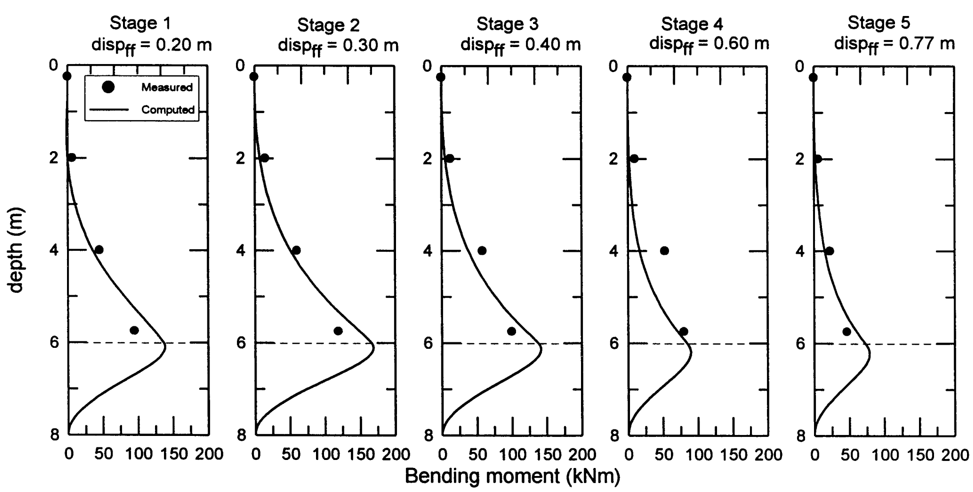

Figure 11 Measured vs Computed Bending Moment Histories for Model 3

The moment distributions along the pile during rebound are shown in stages 3 and 4. In stage 4, the FE analyses underpredict the measured moments quite substantially at depths between 2 and 5 m. This again illustrates the difficulty associated with modeling the unloading phase of the soil-pile interaction problem, and suggests that the simplified treatment of y_{min} in this paper may not have fully captured some of the complex mechanisms at work during the unloading process. However, this should not detract unduly from the ability of the proposed model to capture accurately the maximum and residual moment distributions along the pile, with the former distribution being especially important for design purposes.

NUMERICAL ANALYSIS OF RPI CENTRIFUGE MODEL 5a

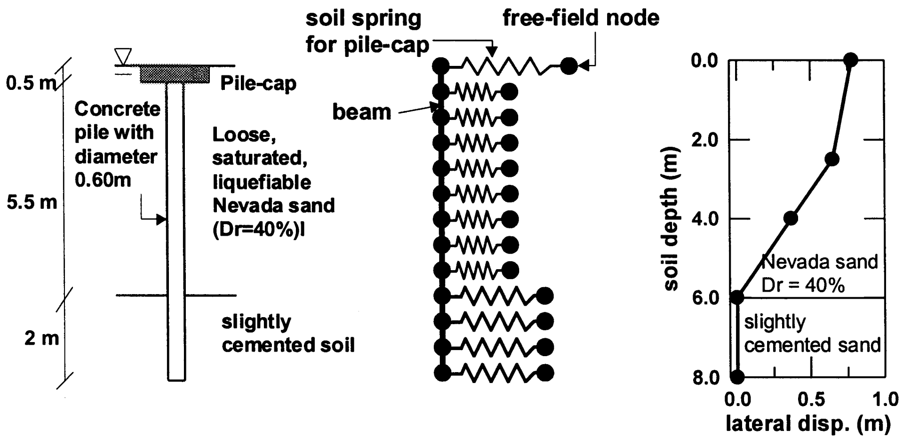

(a) soil-pile-cap system (b) finite element mesh (c) free field lateral displacements

Figure 12 FE Model for Centrifuge Model 5a

Figure 12 shows the soil-pile arrangement and the FE model corresponding to RPI centrifuge model 5a, which is identical to model 3 except for the presence of a pile-cap (2.5m x 2.0m x 0.5m). For the most part, the modeling considerations are the same as those described for model 3. The restraining effect of the pile cap, however, must be taken into account. This is achieved by specifying the appropriate pile-cap properties for the affected beam elements, and re-tuning the force-displacement response of the soil springs adjacent to the pile cap to reflect the passive pressures that may be mobilized over this depth.

For a pile cap embedded in the liquefiable Nevada sand layer, the passive earth pressures are functions of the undrained shear strengths and may be computed using a method similar to that for calculating earth pressures under undrained conditions in clay. The lateral passive pressure p_{hp} is

$$p_{hp} = \gamma z + 2s_u \tag{20}$$

in which γ is the total unit weight, z is the depth below ground surface, and s_u is the undrained soil strength. The appropriate values of s_{up} or s_{umin} are substituted in (20) to model peak and minimum condition of undrained strength. Figure 13 shows a schematic representation of the peak passive force acting on the pile-cap.

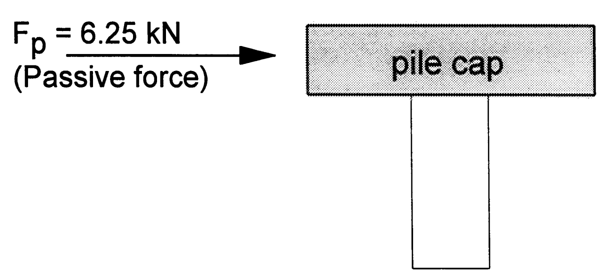

Figure 13 Peak Passive Force Acting on the Pile cap

The measured free-field lateral ground displacements at the end of the test are shown in Figure 12c. As was done for the earlier models, this piecewise linear profile is discretized and incrementally applied to the system of soil springs as prescribed nodal displacements.

Figures 14 and 15 compare the model predictions with the centrifuge measurements when the pile cap is present. In Figure 14, the computed bending moment history near the boundary between the liquefied soil and cemented sand agrees very favorably with the measured response. The comparisons also turn out well for the bending moment distributions plotted in Figure 15. Although the trends shown in these figures are similar to those recorded in model 3, it is noted that both the measured peak and residual moments are significantly increased when the pile-cap is present. This is largely due to the contribution of the passive earth pressures acting on the pile-cap, the effects of which are well replicated in the numerical response when the p-y curves of the affected soil springs are specified accordingly.

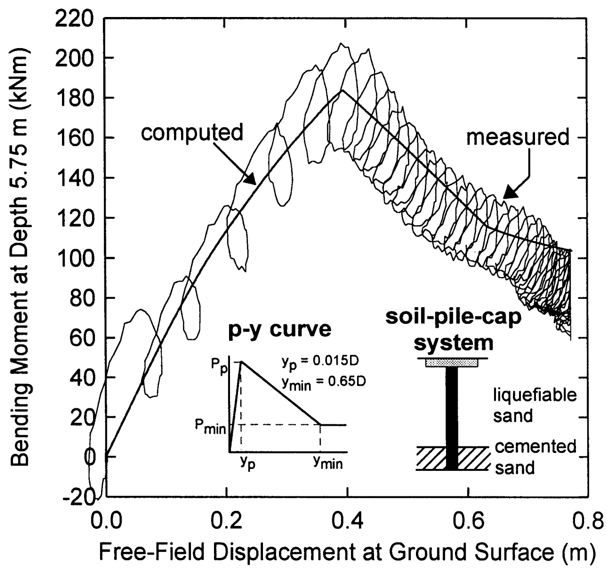

Figure 14 Measured vs Computed Bending Moment Histories for Model 5a

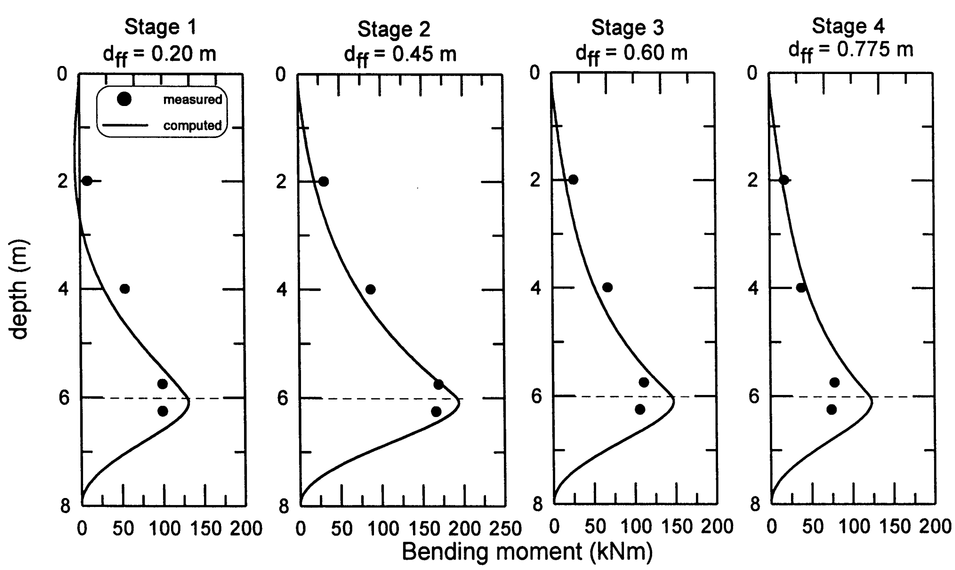

Figure 15 Computed vs Measured Bending Moment Distributions for Model 5a

COMPARISON OF MODEL PREDICTIONS WITH THE JAPANESE HIGHWAY CODE

Figure 16 shows the pressure diagrams for models 3 and 5a corresponding to the instants at which the maximum moments develop in the two piles. The distributions are approximately triangular, which reflect the assumed linear variation of the peak undrained soil strength s_{up} with depth. In both models, the pressure reversal near the 6 m boundary indicates that there is pile displacement relative to the soil at this level. This implies that the slightly cemented sand does not act as a perfect restraint. Neglecting this slight pressure reversal, the magnitude of the computed pressure exerted near the base is approximately 41 kN/m^2.

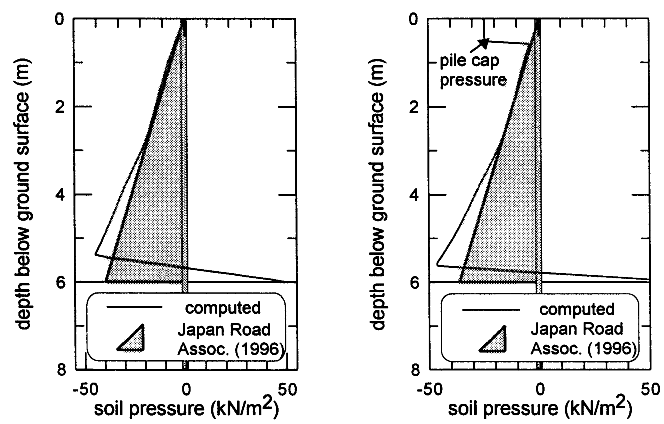

(a) Model 3 (b) Model 5a

Figure 16 Computed Pressure Diagrams for Models 3 and 5a

Based on case histories calibrated after the 1995 Kobe earthquake, the Japan Road Association (JRA) [1996] recommends that the pressure acting on piles due to ground flow be taken as 30% of the overburden pressure, as shown in Figure 17. This inherently gives rise to a triangular pressure distribution acting on the pile during lateral spread. For a soil which has a total saturated unit weight of 20 kN/m^3, the overburden pressure at a depth of 6 m is 20 x 6 = 120 kN/m^2. Using the JRA recommendation, the liquefied soil pressure acting at this level is estimated as 0.3 x 120 kN/m^2 = 36 kN/m^2. The resulting pressure diagrams, shown shaded in Figure 16, are in good agreement with the computed distributions.

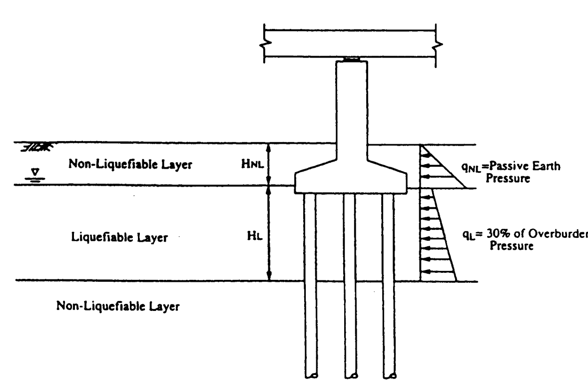

Figure 17 Idealization of Ground Flow Force for Seismic Design of Bridge Foundations (Japan Road Association, 1996)

CONCLUSIONS

Soil-pile interaction during lateral spread is a complex three-dimensional problem. In this paper, a simplified model is proposed in which triaxial extension is used as the most appropriate analogue for the development of undrained shear stress in soil during liquefaction and its transfer to piles during lateral spread. To establish the relevant soil strength and deformation parameters, a suite of triaxial extension tests was carried out using Nevada sand. The results suggest that the peak and minimum strengths can be linearly related to the initial mean effective stresses. By accounting for both peak and minimum strengths, strain-softening p-y curves were numerically generated using 2-D FLAC analyses. Application of these p-y curves to the analyses of centrifuge experiments involving lateral spread effects on piles show favorable agreement between the computed and measured responses. The strain-softening model provides excellent predictions of the measured peak and residual moments. Furthermore, the computed soil pressure diagrams agree well with the recommendations made by the Japan Road Association, which were calibrated using case histories from the 1995 Kobe earthquake.

ACKNOWLEDGEMENTS

The work reported in this paper was sponsored by the Multidisciplinary Center for Earthquake Engineering Research (MCEER). The authors gratefully acknowledge their collaboration with Professor R. Dobry and Dr. T. Abdoun of RPI.

REFERENCES:

Abdoun, T. (1997), "Modeling of Seismically Induced Lateral Spreading of Multi-Layered Soil and Its Effect on Pile Foundations", Ph.D. Thesis, Rensselaer Polytechnic Institute, Troy, NY.

Arulmoli, K., Muraleetharan, K. K., Hossain, M. M. and Fruth, L. S. (1992), "VELACS Laboratory Testing Program, Soil Data Report" The Earth Technology Corporation, Project No. 90-0562, Irvine, CA.

Bartlett, S. F. and Youd, T. L. (1992), "Case Histories of Lateral Spread Caused by the 1964 Alaska Earthquake", Case Studies of Liquefaction and Lifeline Performance During Past Earthquakes, Vol. 2, United States Case Studies, Technical Report NCEER-92-0002, NCEER, Buffalo, NY.

Bartlett, S. F. and Youd, T. L. (1995), "Empirical Prediction of Liquefaction-Induced Lateral Spread", Journal of Geotechnical Engineering, ASCE, Vol. 121, No. 4, pp. 316-329.

Chaudhuri, D. (1998), "Liquefaction and Lateral Soil Movement Effects on Piles", Ph.D. Thesis, Cornell University, Ithaca, New York.

Chen, L. and Poulos, H. G. (1993), "Analysis of Pile-soil Interaction Under Lateral Loading Using Infinite and Finite Elements", Computers and Geotechnics, Vol. 15, No. 4, pp. 189-219.

Hamada, M., Yasuda, S., Isoyama, R., and Emoto, K., (1986), "Study on Liquefaction-Induced Ground Displacements", A Report by Research Committee, Association for the Development of Earthquake Prediction, Tokyo.

Hamada, M and O'Rourke, T. D. (1992), "Case Studies of Liquefaction and Lifeline Performance During Past Earthquakes", Vol. 1, Japanese Case Studies, Technical Report NCEER-92-0001, NCEER, Buffalo, NY.

Hamada, M. and Wakamatsu, K. (1996), " Liquefaction, Ground Deformation and Their Caused Damage to Structures", The 1995 Hyogoken-Nanbu Earthquake, Japanese Society of Civil Engineers, Tokyo.

Hardin, B. O. and Drnevich, V. P. (1972), "Shear Modulus and Damping in Soils: Design Equations and Curves", Journal of the Soil Mechanics and Foundations Division, ASCE, Vol. 98, No. SM7, pp. 667-692.

Ishihara, K., Verdugo, and R. Acacio, A.A. (1991), "Characterization of Cyclic Behavior of Sand and Post-seismic Stability Analyses", Proceedings 9th Asian Regional Conference on Soil Mechanics and Foundation Engineering, Vol. 2, Bangkok, Thailand, pp. 45-70.

Ishihara, K. (1993), "Liquefaction and Flow Failure During Earthquakes", Geotechnique, Vol. 43, No. 3, pp. 351-415.

Ishihara, K. and Cubrinovski, M. (1998), "Soil-Pile Interaction in Liquefied Deposits Undergoing Lateral Spreading", Proceedings XI Danube-European Conference, Keynote Lecture, Croatia.

Itasca Consulting Group (1995), "FLAC : Fast Lagrangian Analysis of Continuum".

Japan Road Association (1996), Specifications for Highway Bridges, Part V Seismic Design, Japan (in Japanese).

Matsui, T. and Oda, K. (1996), "Foundation Damage of Structures", Special Issue on Geotechnical Aspects of the January 17, 1995 Hyogo-Ken Nambu Earthquake, Soils and Foundations, pp. 189-200.

Meyersohn, W. D. (1994), "Pile Response to Liquefaction-Induced Lateral Spread", Ph.D. Thesis , Cornell University, Ithaca, NY.

Randolph, M. F. and Houlsby, G. T. (1984), "The Limiting Pressure on a Circular Pile Loaded Laterally in Cohesive Soil", Geotechnique, Vol. 34, No. 4, pp. 613-623.

Schofield, A. N. and Wroth, C. P. (1968), "Critical State Soil Mechanics", McGraw-Hill Book Co., London.

Sladen, J. A., D'Hollander, R. D. and Krahn, J. (1985), "The Liquefaction of Sands, A Collapse Surface Approach", Canadian Geotechnical Journal, Vol. 22, No. 4, pp. 564-578.

Vaid, Y. P., Chung, E. K. F. and Kuerbis, R. H. (1990), "Stress Path and Steady State", Canadian Geotechnical Journal, Vol. 27, No. 1, pp. 1-7.

Vermeer, P.A. and de Borst, R. (1984), "Non-Associated Plasticity for Soils, Concrete and Rock", Heron, 29(3), pp 3-64.

Yamamuro, J.A. and Lade, P.V. (1997), " Static liquefaction of very loose sands", Canadian Geotechnical Journal, No. 34, pp 905-917.

Yoshida, N. and Hamada, M. (1991), "Damage to Foundation Piles and Deformation Pattern of Ground Due to Liquefaction Induced Permanent Ground Deformation", Technical Report NCEER-91-0001, NCEER, Buffalo, NY, pp. 147-160.

Yoshimine, M. and Ishihara, K. (1998), "Flow potential of sand during liquefaction", Soils and Foundations, Vol. 38, No. 3, pp 189-198.

APPENDIX A

For stable pile-soil response during soil strain softening, the unloading stiffness of the soil adjacent to each section of the pile should everywhere be less than the capacity of the pile at that section to release load in response to displacement. This condition requires that the unloading stiffness of the soil be less than the stiffness of the pile.

As illustrated in Figure A.1, the decrease in soil reaction, Δp_{si} , at any pile section i during strain softening is given by :

$$\Delta p_{si} = k_{ui}\, \delta_i \qquad \text{(A.1)}$$

in which k_{ui} is the unloading stiffness of the soil (see Figure 8) at section i and δ_i is the change in pile deflection caused by the reduction in pile load over the same section from its peak, P_p , to its minimum, P_{min} .

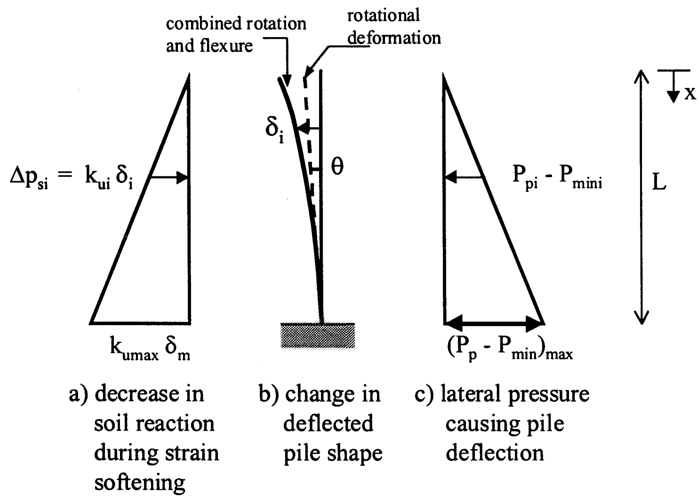

Figure A.1

For stable unloading, the following condition must be met :

$$\Delta p_{si} < P_{pi} - P_{mini} \tag{A.2}$$

Because of the triangular pressure and stiffness distributions with depth, it follows from (A.2) that

$$\sum_{i=1}^{n} k_{ui}\delta_i \Delta x_i < \frac{1}{2}(P_{pi} - P_{mini})_{max}\, L \tag{A.3}$$

where Δx_i is the thickness of the pile section i.

In addition :

$$k_{ui} = k_{umax}\frac{x_i}{L} \tag{A.4}$$

Combining (A.3) and (A.4) results in :

$$k_{umax} < \frac{(P_{pi} - P_{mini})_{max}\, L^2}{2\sum_{i=1}^{n} x_i \delta_i \Delta x_i} \tag{A.5}$$

Recognizing that

$$k_{umax} = \frac{(P_{pi} - P_{min\,i})_{max}}{\Delta y^* \, D} \quad (A.6)$$

in which Δy^* is the change in normalized displacement from the y^* at P_p , results in

$$y^* = \frac{2\sum_{i=1}^{n} x_i \delta_i \Delta x_i}{DL^2} \quad (A.7)$$

If the pile increments associated with i approach zero, then

$$y^* = \frac{2\int_0^L f(x)x\,dx}{DL^2} \quad (A.8)$$

in which f(x) is the equation for elastic deflection of the pile that accounts for flexure and basal rotation in the form of

$$f(x) = f_f(x) + f_r(x) \quad (A.9)$$

where

$f_f(x)$ = the displacement profile due to flexure

$$= \frac{w_o}{120EIL}\left[x^5 - 5L^4x + 4L^5\right] \quad (A.10)$$

$f_r(x)$ = the linear displacement profile due to rotation

$$= \theta\,(L-x) \quad (A.11)$$

w_o = the force per unit length at the base of the triangular distribution

and

θ = basal rotation of the pile.

Seismic Site Response and Liquefaction-Induced Shear Deformation

Zhaohui Yang
Columbia University, New York, NY-USA 10027

Ender Parra
INTEVEP, SA, Venezuela

and

Ahmed Elgamal
University of California, San Diego, La Jolla, CA-USA 92093

ABSTRACT

A constitutive model is developed to reproduce salient aspects associated with seismically-induced soil liquefaction (medium to dense clean cohesionless soils). Attention is mainly focused on the deviatoric (shear) stress-strain response mechanism. Soil cyclic shear behavior during liquefaction is modeled to display a significant regain in stiffness and strength with the increase in deformation during each cycle of applied load. Constitutive model parameters are selected to represent medium, medium-dense and dense clean cohesionless soils. The developed constitutive model is included in a fully coupled (solid-fluid) effective stress site amplification computational code (***CYCLIC 1D***). This code may be executed over the Internet using readily available web browsers such as Internet Explorer or Netscape Navigator (site address **http://casagrande.ucsd.edu**).

INTRODUCTION

During liquefaction, recent records of seismic site response (Holzer *et al.* [11], Elgamal and Zeghal [7], Zeghal and Elgamal [26], Youd and Holzer [25]) have manifested a possible strong influence of soil dilation during cyclic loading. Such phases of dilation may result in significant regain in shear stiffness and strength at large cyclic shear strain excursions, leading to: i) associated instances of pore-pressure reduction, ii) appearance of spikes in lateral acceleration records (as a direct consequence of the increased shear resistance), and most importantly, iii) a strong restraining effect on the magnitude of cyclic and accumulated permanent shear strains. This restraint on shear strain has been referred to as a form of cyclic-mobility in a large number of pioneering liquefaction studies (*e.g.,* Seed and Lee [19], Casagrande [2], Castro [3], Castro and Poulos [4], Seed [20]). For the important situations of biased strain accumulation due to an initial locked-in shear stress (e.g., lateral spreading), this pattern of behavior may play a dominant role in dictating the extent of shear deformations.

Currently, the above mentioned effects are thoroughly documented by a large body of experimental research (employing clean sands and clean non-plastic silts), including centrifuge experiments (*e.g.,* Dobry *et al.* [5], Taboada [22], Dobry *et al.* [6]), shake-table tests, and cyclic laboratory sample tests (Arulmoli [1]). A thorough summary has been compiled (Elgamal *et al.* [9]) of the relevant: i) seismic response case histories, ii) recorded experimental response (centrifuge, shake table and laboratory), and iii) available constitutive models to simulate this phenomenon.

In the following pages, the main characteristics of the above-described shear stress-strain mechanisms are presented. Thereafter, the constitutive model is discussed, and the salient model response characteristics are presented. Results from site response simulations using the Internet site (**casagrande.ucsd.edu**) are also included.

LATERAL SPREADING MECHANISM

As an illustration, one-dimensional shear stress-strain histories (Figure 1) calculated from recorded centrifuge experiment acceleration and LVDT records (Dobry *et al.* [5], Dobry *et al.* [6], Taboada [21], Elgamal *et al.* [8], Taboada and Dobry [22]) display the pattern of cycle-by-cycle accumulation of shear strain. This experiment simulated the dynamic behavior of a 10m thick, infinite slope (effective inclination angle 4.2°) layer of clean Nevada sand (relative density $D_r \simeq 40\%$). In Figure 1, the 5-12 second time window includes several cycles in which soil displays a significant regain in shear stiffness and strength, as the cyclic shear strain increment increases. This cyclic mobility mechanism can significantly reduces the total accumulated shear strain due to liquefaction. Accuracy in reproducing this mechanism is among the most important goals of the developed constitutive model.

CONSTITUTIVE MODEL

Currently available constitutive models that reproduce important aspects of the above shear mechanism include those by Iai [12], Iai *et al.* [13], Kramer and Arduino [15], and Tateishi *et al.* [23]. The model described herein follows the procedures developed by Prevost [18], based on the multiple yield surface plasticity concept (Iwan [14], and Mroz [16]). It was modified (Parra [17], Yang [24]) from its original form (Prevost [18]) to model the shear stress-strain features discussed above (Fig. 1). Special attention was given to the deviatoric – volumetric strain interaction under cyclic loading; in particular during loading – unloading – reloading near the yield envelope (Parra [17], Yang [24]).

Figures 2 and 3 illustrate the mechanism of model response. These figures depict a simulation of a biased cyclic triaxial stress - strain history. A static driving "locked-in" deviatoric stress was simulated by applying load cycles in the range of 0.0 kPa to 60 kPa (Figure 2). Under this loading history, gradual pore pressure buildup and liquefaction occurs (i.e., effective confinement approaches zero, Figure 3). During liquefaction the model reproduces a stable cycle-by-cycle accumulation of axial deformation. For engineering applications, three performance scenarios were selected (Elgamal *et al.* [10]) to represent

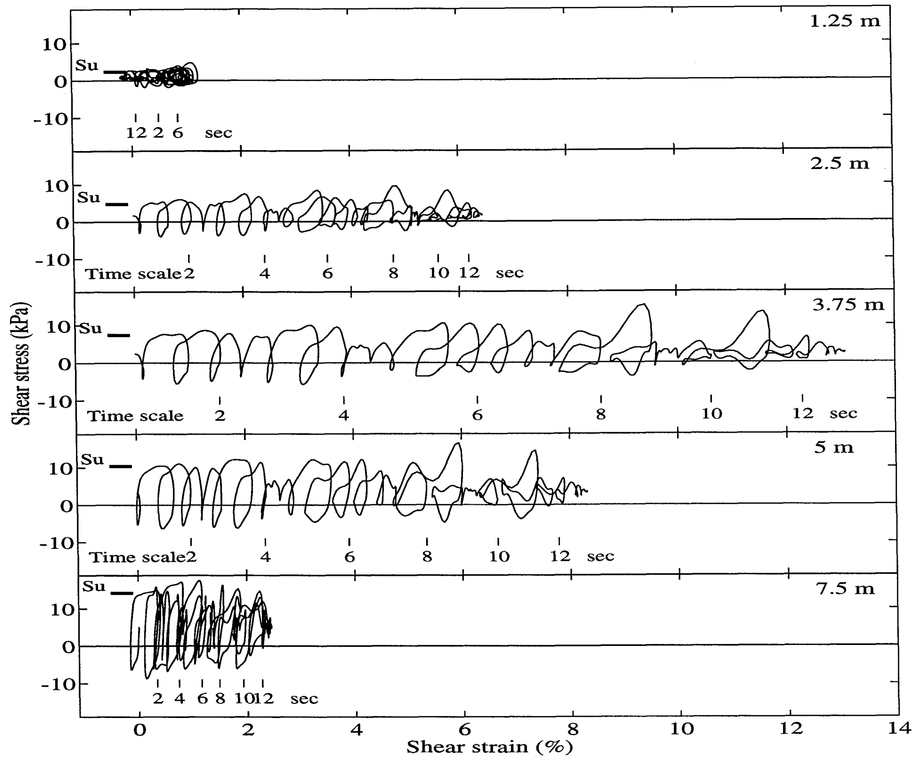

Figure 1: RPI Model 2 shear stress-strain histories with superposed static stress due to inclination (Taboada 1995, Dobry et al. 1995, Elgamal et al. 1996).

clean medium, medium-dense and dense sand (or silt) situations (relative density in the range of about 40% to 90%). In Figure 2, maximum accumulated cycle-by-cycle axial deformations are about 1.3% (medium), 0.5% (medium-dense) and 0.3% (dense).

The medium sand response was calibrated by extensive laboratory tests (Arulmoli *et al.* [1]) and centrifuge experiments (Parra [17], Yang [24]). At this point, the deformation characteristics for the medium-dense and dense sand situations are based on engineering judgement (motivated by the literature review in Elgamal *et al.* [9]). Further data is needed to refine the estimates of the proposed model (Figs. 2 and 3), particularly for the medium-dense and dense sand situations.

DISCUSSION

1. The soil classification into broad categories of medium, medium-dense and dense was motivated by:

   - Difficulties associated with accurate classification of soil relative density back-figured from Cone Testing or Standard Penetration Blow Counts.
   - Reduced emphasis on a residual soil strength during liquefaction to dictate magnitude of accumulated shear deformations, with possible large fluctuations (in accumulated shear strain) due to relatively small changes in this residual strength. In this regard, Figure 2 for instance suggests a small difference in maximum accumulated axial strain per cycle (during liquefaction) of 0.2% for a relative density ranging from medium-dense to dense situations.
   - Challenges related to correlations with laboratory testing results, including sample disturbance, test type, applied load path, and other factors.

2. A "damage" modeling parameter can be activated to allow the model to reproduce stiffness and strength degradation (as a function of total accumulated plastic shear strain).

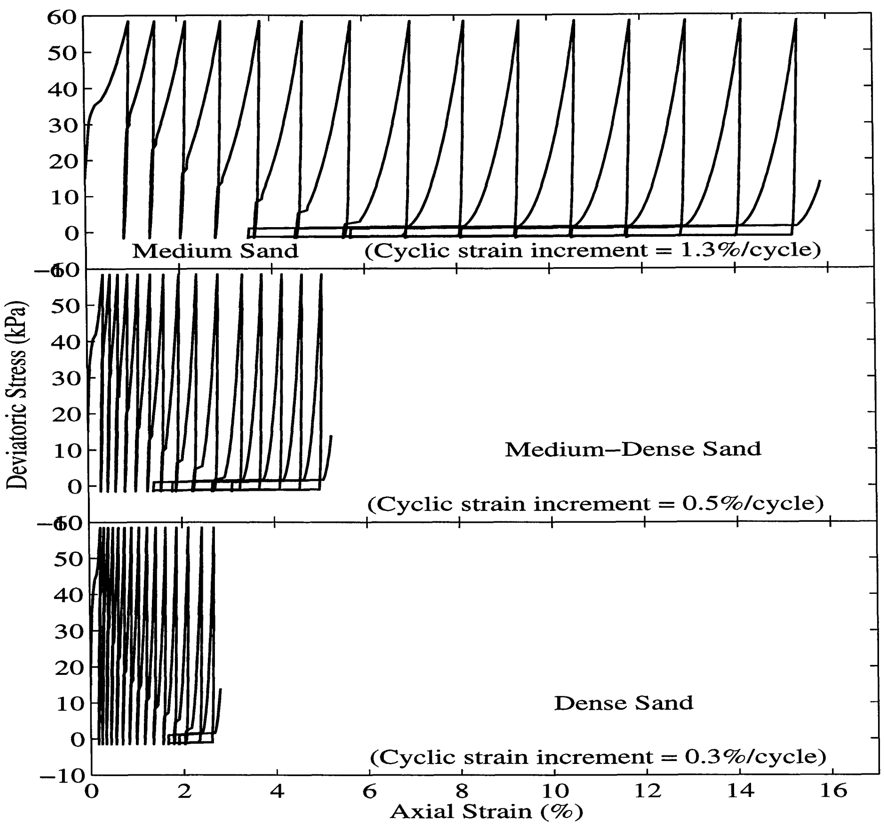

Figure 2: Simulation of undrained biased cyclic triaxial tests.

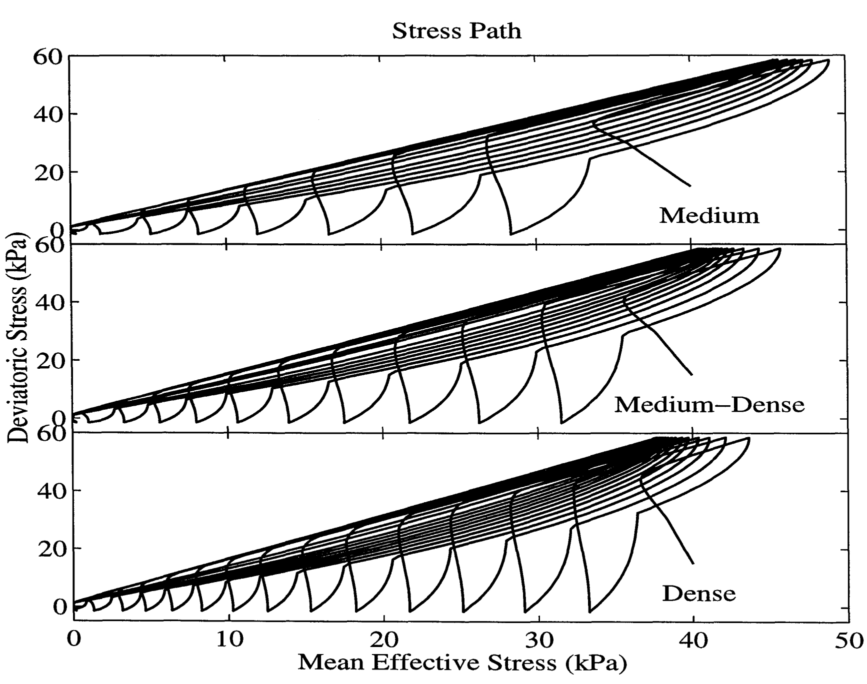

Figure 3: Computed stress path during undrained biased cyclic triaxial tests.

3. Loose cohesionless soils may possibly display a dominant contractive response with little dilative tendency and much increased level of accumulated shear deformations. Such deformations can be easily reproduced by the developed constitutive model (among many others). However, the emphasis placed on the deformation ranges of Figure 2 reflects the interest in: i) estimation of deformations that might be objectionable despite the absence of a flow-failure (performance-based design assessments), and ii) applicability to liquefaction countermeasure effectiveness (e.g., by densification). In this regard, the accurate estimation of very large flow-failure deformations is not a primary goal, since loose soils (that may be vulnerable to flow-failure) are unacceptable from a practical engineering point of view.

CYCLIC 1D

A site amplification computer code (*CYCLIC 1D*) that includes the above described constitutive model is currently available for execution using commonly available Internet browsers such as Internet Explorer or Netscape Navigator (**http://casagrande.ucsd.edu**). The *CYCLIC 1D* website is displayed in Figure 4. Currently, the user can (Figure 5): i) define element height (the soil stratum consists of 10 elements), ii) choose a stratum inclination angle, and iii) select/scale a base input earthquake motion.

Figures 6 and 7 show the results of a numerical simulation motivated by the centrifuge experiment VELACS model 2 (Taboada and Dobry [22]). This experiment simulated the dynamic behavior of a 10m medium dense ($Dr \simeq 40\%$) clean Nevada sand stratum in a mild-slope situation. The results of this experiment are among the main sources employed for calibrating our constitutive model. The numerical simulation employed an inclination angle of 4.0°, and the results (Figs. 6 and 7) show the involved cyclic-mobility lateral spreading response characteristics.

In Figure 6, acceleration near ground surface is seen to display asymmetric response with spikes that are directly related to the instances of excess pore-pressure drop during liquefaction. Associated lateral spreading is also seen to accumulate on a cycle-by-cycle basis. In Figure 7, the cyclic mobility characteristics are displayed in terms of: i) high stiffness and strength in the shear stress-strain response during liquefaction, and ii) phases of increase in shear strength (and increase in effective stress) as the stress path travels above the phase transformation line during cyclic loading.

SUMMARY AND CONCLUSIONS

A new constitutive model is developed to model the cyclic shear behavior of clean cohesionless soils during liquefaction (emphasis on medium to dense sand scenarios). The underlying mechanisms are based on observed soil response during earthquakes, centrifuge experiments and cyclic laboratory tests. A range of response characteristics (pore pressure buildup and accumulated deformations) is proposed as a first step towards a performance-based liquefaction design methodology. An Internet site (**http://casagrande.ucsd.edu**) is available for using the developed constitutive model to conduct seismic simulations of level and sloping site response.

ACKNOWLEDGMENTS

The research reported herein is supported by the Pacific Earthquake Engineering Research Center (PEER) and the United States Geological Survey (grant No. 99HQGR0020). This support is gratefully acknowledged.

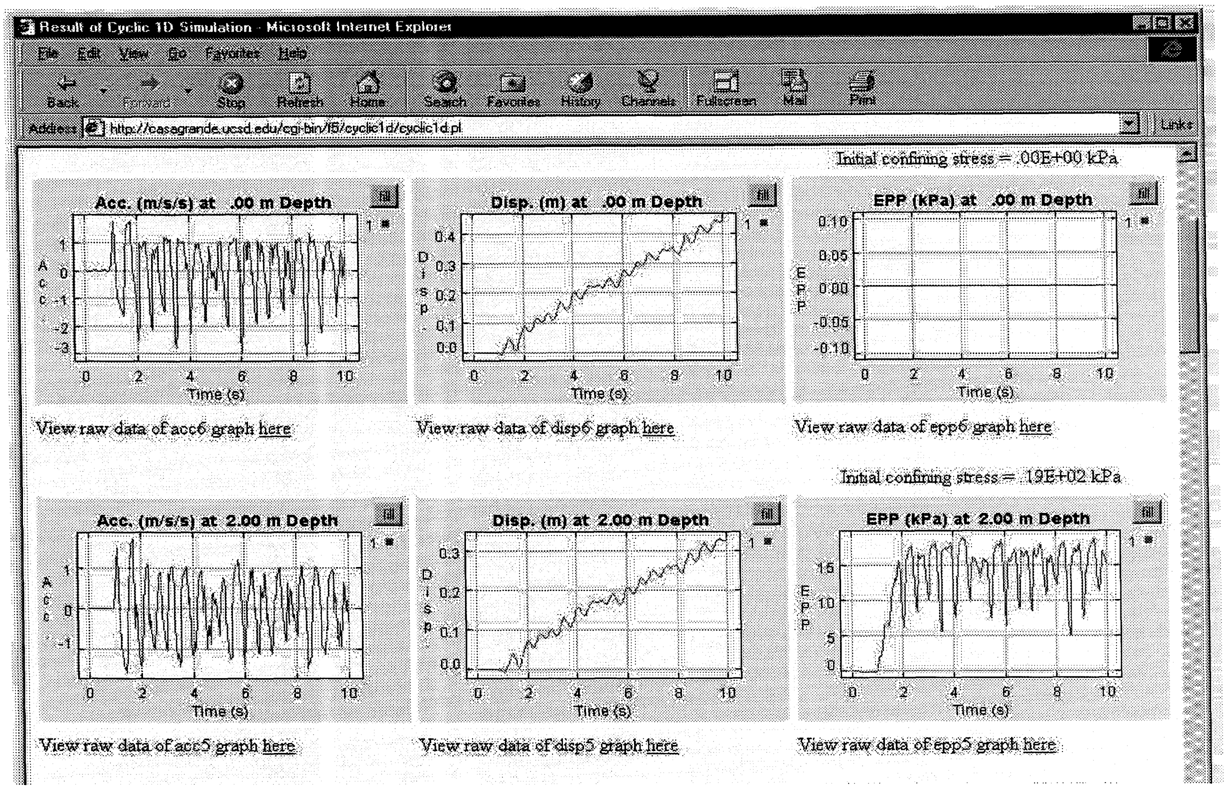

Figure 6: CYCLIC 1D simulation of inclined slope response - response time histories.

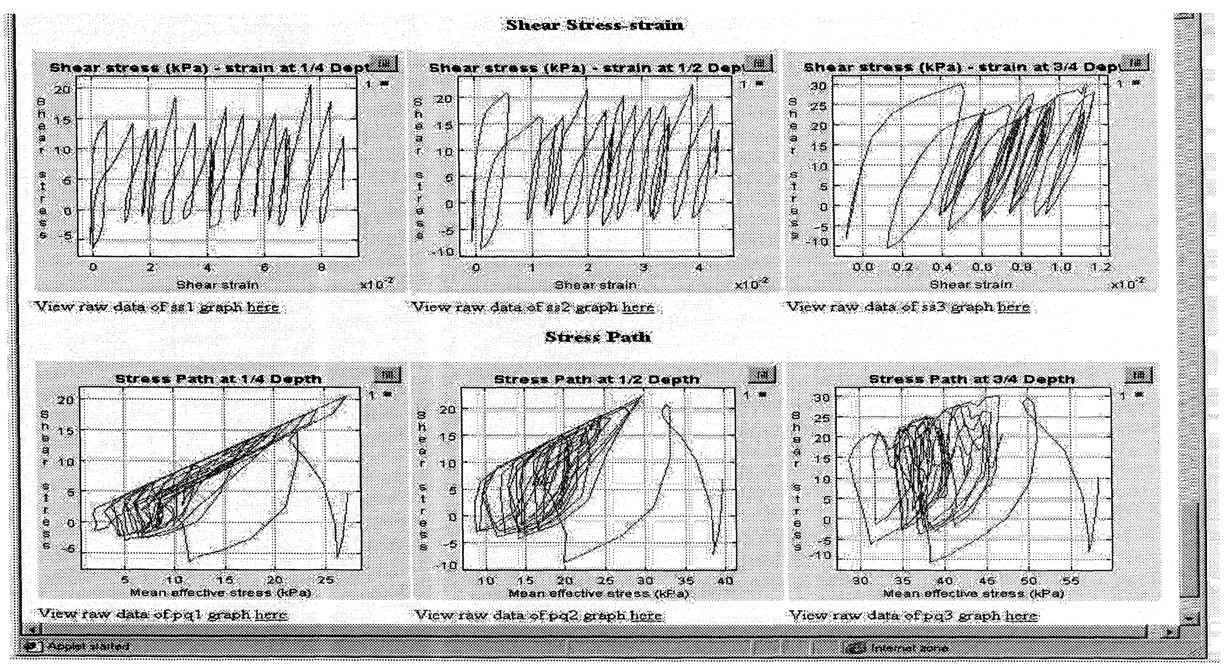

Figure 7: CYCLIC 1D simulation of inclined slope response - stress-strain histories and stress paths.

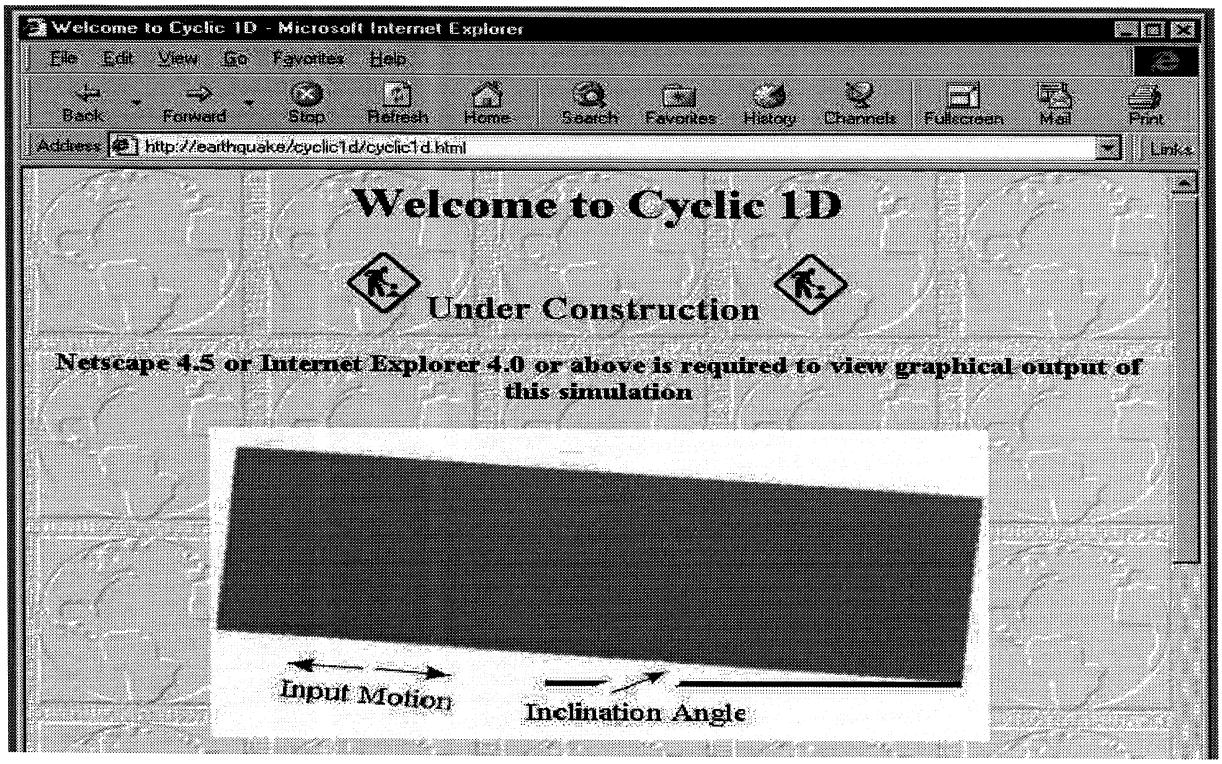

Figure 4: ***CYCLIC 1D*** **website (http://casagrande.ucsd.edu).**

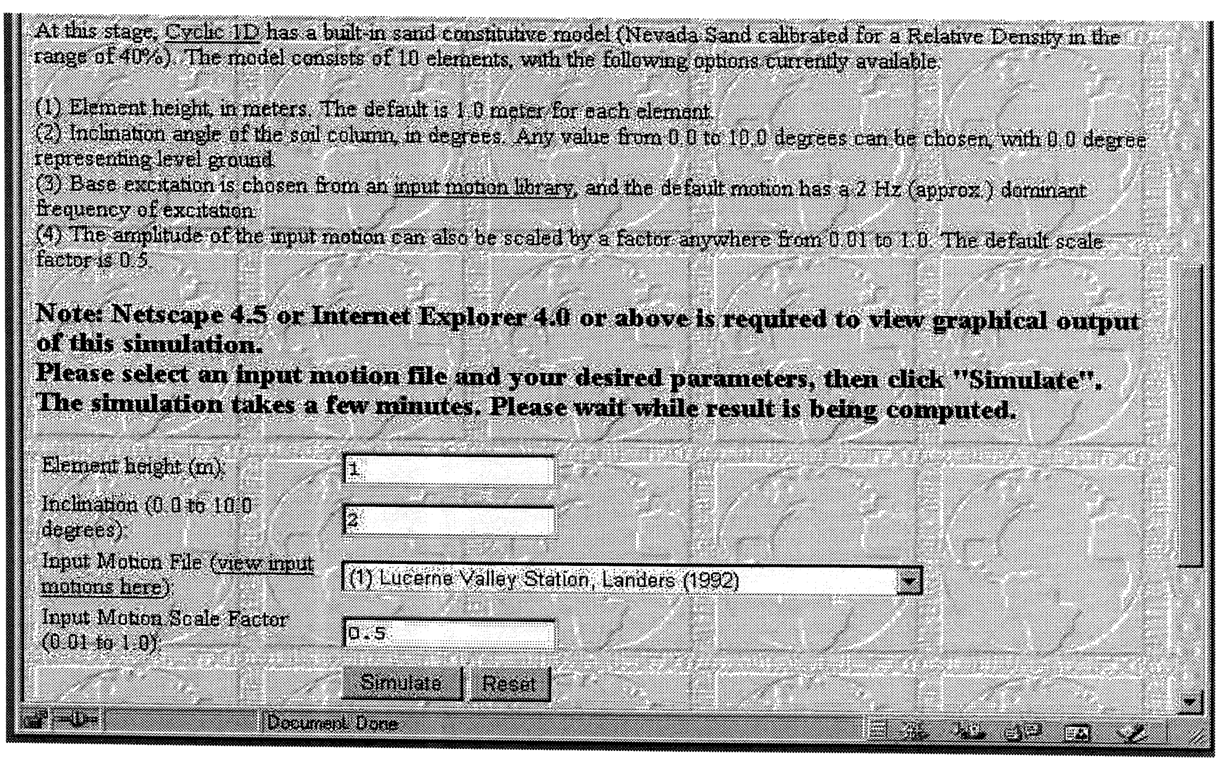

Figure 5: ***CYCLIC 1D*** **currently available user options.**

References

[1] Arulmoli, K., Muraleetharan, K. K., Hossain, M. M. and Fruth, L. S. (1992). "VELACS: VELACS: Verification of Liquefaction Analysis by Centrifuge Studies, Laboratory Testing Program, Soil Data Report", *The Earth Technology Corporation, Project No. 90-0562*, Irvine, California.

[2] Casagrande, A. (1975). "Liquefaction and Cyclic Deformation of Sands - A critical Review", Proceedings, 5th Pan-American Conference on Soil Mechanics and Foundation Engineering, Buenos Aires, Argentina; also published as Harvard Soil Mechanics Series No. 88, January 1976, Cambridge, Massachusetts.

[3] Castro, G. (1975). "Liquefaction and Cyclic Mobility of Saturated Sands", Journal of the Geotechnical Engineering Division, ASCE, 101, GT6, 551-569.

[4] Castro, G and Poulos, S. J. (1977). "Factors Affecting Liquefaction and Cyclic Mobility", Journal of the Geotechnical Engineering Division, ASCE, Vol. 103, No. GT6, June, pp. 501-516.

[5] Dobry, R., Taboada, V. and Liu, L. (1995). "Centrifuge Modeling of Liquefaction Effects During Earthquakes", Proc. 1st Intl. Conf. On Earthquake Geotechnical Engineering (IS-Tokyo), Keynote Lecture, Ishihara, K. Ed., 3, Balkema, Nov. 14-16, Tokyo, Japan, 1291-1324.

[6] Dobry, R. and Abdoun, T. (1998). "Post-Triggering Response of Liquefied Sand in the Free Field and Near Foundations", Proc. Geot. Eq. Engrg. and Soil Dynamics III, V1, Dakoulas, P., Yegian, M. and Holtz., R. D., Eds., Geot. Special Publication No. 75, ASCE, Seattle, Washington, Aug 3-6, keynote lecture, 270-300.

[7] Elgamal, A. -W. and Zeghal, M. (1992). "Analysis of Wildlife Site Liquefaction During the 1987 Superstition Hills Earthquake," 4th Japan - U.S. Workshop on Earthquake Resistant Design of Lifeline Facilities and Countermeasures Against Soil Liquefaction," Tokai Univ. Pacific Center, Hawaii, NCEER, SUNY-Buffalo Report No. NCEER-92-0019, Hamada M. And O'Rourke, T.D., eds., May.

[8] Elgamal, A. -W., Zeghal, M., Taboada, V. M. and Dobry, R. (1996). "Analysis of Site Liquefaction and Lateral Spreading using Centrifuge Model Tests", Soils and Foundations, 36, 2, June, 111-121.

[9] Elgamal, A. -W., Dobry, R., Parra, E. and Yang, Z. (1998). "Soil Dilation and Shear Deformations During Liquefaction", Proc. 4th Intl. Conf. on Case Histories in Geotechnical Engineering, S. Prakash, Ed., St. Louis, MO, March 8-15, 1238-1259.

[10] Elgamal, A., Yang, Z., Parra, E. and Dobry, R. (1999). "Modeling of Liquefaction-Induced Shear Deformation," Proc. 2nd Intl. Conf. on Earthquake Geotechnical Engineering, Lisboa, Portugal, 21-25 June, Seco & Pinto (Ed.), Vol.2, 895-900, Balkema.

[11] Holzer, T. L., Youd T. L. and Hanks T. C. (1989). "Dynamics Of Liquefaction During the 1987 Superstition Hills, California, Earthquake", Science, Vol. 244, 56-59.

[12] Iai, S. (1991). "A Strain Space Multiple Mechanism Model for Cyclic Behavior of Sand and its Application", Earthquake Engineering Research Note No. 43, Port and Harbor Research Institute, Ministry of Transport, Japan.

[13] Iai, S., Morita, T., Kameoka, T., Matsunaga, Y. and Abiko, K. (1995). "Response of a Dense Sand Deposit During 1993 Kushiro-Oki Earthquake", Soils and Foundations, 35, 1, March, 115-131.

[14] Iwan, W. D. (1967). "On a class of Models for the Yielding Behavior of Continuous and Composite Systems", *Journal of Applied Mechanics, ASME*, Vol. 34, pp. 612 – 617.

[15] Kramer, S. L. and Arduino, P. (1999). "Constitutive Modeling of Cyclic Mobility and Implications For Site Response," Proc. 2nd Intl. Conf. on Earthquake Geotechnical Engineering, Lisboa, Portugal, 21-25 June, Seco & Pinto (Ed.), Vol. 2, 895-900, Balkema.

[16] Mroz, Z. (1967). "On the Description of Anisotropic Work Hardening", *Journal of the Mechanics and Physics of Solids*, Vol. 15, pp. 163 – 175.

[17] Parra, E. (1996). "Numerical Modeling of Liquefaction and Lateral Ground Deformation including Cyclic Mobility and Dilative Behavior in Soil Systems", *Ph.D. dissertation*, Dept. of Civil Engineering, Rensselaer Polytechnic Institute.

[18] Prevost, J. H., (1985). "A Simple Plasticity Theory for Frictional Cohesionless Soils", *Soil Dynamics and Earthquake Engineering*, Vol. 4, No. 1, pp. 9 – 17.

[19] Seed, H. B. and Lee, K. L. (1966). "Liquefaction of Saturated Sands During Cyclic Loading", Journal of the Soil Mechanics and Foundations Division, ASCE, 92, SM6, Nov., 105–134.

[20] Seed, H. B. (1979). "Soil Liquefaction and Cyclic Mobility Evaluation for Level Ground During Earthquakes", Journal of the Geotech Engng Division, ASCE, 105, No. GT2, Feb., 201-255.

[21] Taboada, V. M. (1995). "Centrifuge Modeling of Earthquake-Induced Lateral Spreading in Sand using a Laminar Box", *Ph.D. Thesis*, Rensselaer Polytechnic Institute, Troy, NY.

[22] Taboada, V. M., and Dobry, R. (1998). "Centrifuge Modeling of Earthquake-Induced Lateral Spreading in Sand", Journal of Geotechnical and Geoenvironmental Engineering, ASCE, 124, No. 12, 1195-1206.

[23] Tateishi, A., Taguchi, Y, Oka, F. and Yashima, A. (1995). "A Cyclic Elasto-Plastic Model For Sand and Its Application Under various Stress Conditions", Proc. 1st Intl. Conf. On Earthquake Geotech Engng, 1, 399-404, Balkema, Rotterdam.

[24] Yang, Z. (1999). "Identification and Numerical Modeling of Earthquake Ground Motion and Liquefaction", *Ph.D. dissertation*, Dept. of Civil Engineering and Engineering Mechanics, Columbia University, New York, NY (in completion).

[25] Youd, T. L., and Holzer, T. L. (1994). "Piezometer Performance at the Wildlife Liquefaction Site", *J. Geotech. Engrg.*, ASCE, 120(6), 975-995.

[26] Zeghal, M. and Elgamal, A. -W. (1994). "Analysis of Site Liquefaction Using Earthquake Records", Journal of Geotechnical Engineering, ASCE, 120, No. 6, 996-1017.

APPLICATION OF 3-D DISTINCT ELEMENT METHOD TO LIQUEFACTION

Kimiro MEGURO* and Tsuneo KATAYAMA**

*: International Center for Disaster-Mitigation Engineering (INCEDE),
Institute of Industrial Science (IIS), The University of Tokyo
4-6-1 Komaba, Meguro-ku, Tokyo 153-8505, JAPAN
Tel: +81-3-5452-6436, Fax: +81-3-5452-6746
E-mail: meguro@incede.iis.u-tokyo.ac.jp

**: National Institute of Earthscience and Disaster Prevention,
Science and Technology Agency of Japan

ABSTRACT

Using a 3-Dimensional Distinct Element Model (3D-DEM), a new method is proposed to consider the effects of pore-water in DEM directly with a simple algorithm. In this method, the region of DE simulation model, which is composed of many particle elements, is considered as an assembly of cubic shaped blocks having virtual boundary. Behavior of pore-water is calculated using each block as a unit volume in order to make the algorithm of calculation simple. Numerical results obtained by the proposed method show that various phenomena related to liquefaction, which were difficult to be simulated by conventional methods like the finite element method and 2D-DEM, etc., can be simulated and this new idea has extended the field of the DEM application.

INTRODUCTION

This paper introduces a new method to consider the effects of pore-water in the distinct element method (DEM) directly with a simple algorithm using 3-dimensional DEM. Conventional researches on liquefaction by DEM were carried out using mainly 2-dimensional model and shear displacement was applied to the model composed of particles under constant volume condition which took into account the undrained condition indirectly [1]. Although there were models which considered the effects of pore-water in a simple way, these models were based on regular arrangement of particle elements and the effects of sudden change of volume and shapes of voids, which are essential to follow the behavior of pore-water pressure, could not be simulated [2]. The main reasons of the above problems were that there was no efficient method, by which the time history of change of void volume could be calculated, and this problem made it very difficult to simulate the movement of pore-water in between neighboring voids.

As a pioneer research in tackling this problem, Tarumi and Hakuno tried to analyze the mechanism of liquefaction using 2-dimensional model (2D-DEM) composed of randomly packed particles with different radii [3]. They calculated changes of voids at every time step and with the change of void volume, the excessive pore-water pressure acting on the element was calculated. However, they could not analyze the mechanism of liquefaction practically. It was difficult to make a model with large void ratio using 2D-DEM and complicated algorithm for calculation of changes of void volume required long CPU time.

Here, we propose an extended 3D-DEM which can simulate the changes of pore-water volume with a simple algorithm by considering the behavior of pore-water using blocks, made by dividing the region of calculation virtually, in order to take the effects of pore-water efficiently [4].

3-D DEM WITH THE EFFECTS OF PORE-WATER BEHAVIOR

In the proposed method, the region of the specimen is divided into appropriate blocks and the behavior of pore-water is considered and calculated using these blocks as a unit volume as shown in **Figs. 1(a)** and **1(b)**. With this method, changes of volume and shapes of voids due to the movement of particle elements can be easily taken into account.

The followings are the explanations of the method. Although the proposed method is based on 3-dimensional model, to make its concept easily understood, we explain the method by using the 2-dimensional figures as shown in **Figs. 1(b) - 1(e)**. First, we calculate the excessive pore-water pressure generated due to the change of volume of void in a block at every time step. Next, we compare the excessive pore-water pressure of the block with those of surrounding six blocks. When there is a difference in pore-water pressure among the adjacent blocks, pore-water flows following Darcy's law (**Fig. 1(c)**). The forces due to the excessive pore-water pressure act in the direction of the line connecting the center of the block and element centers

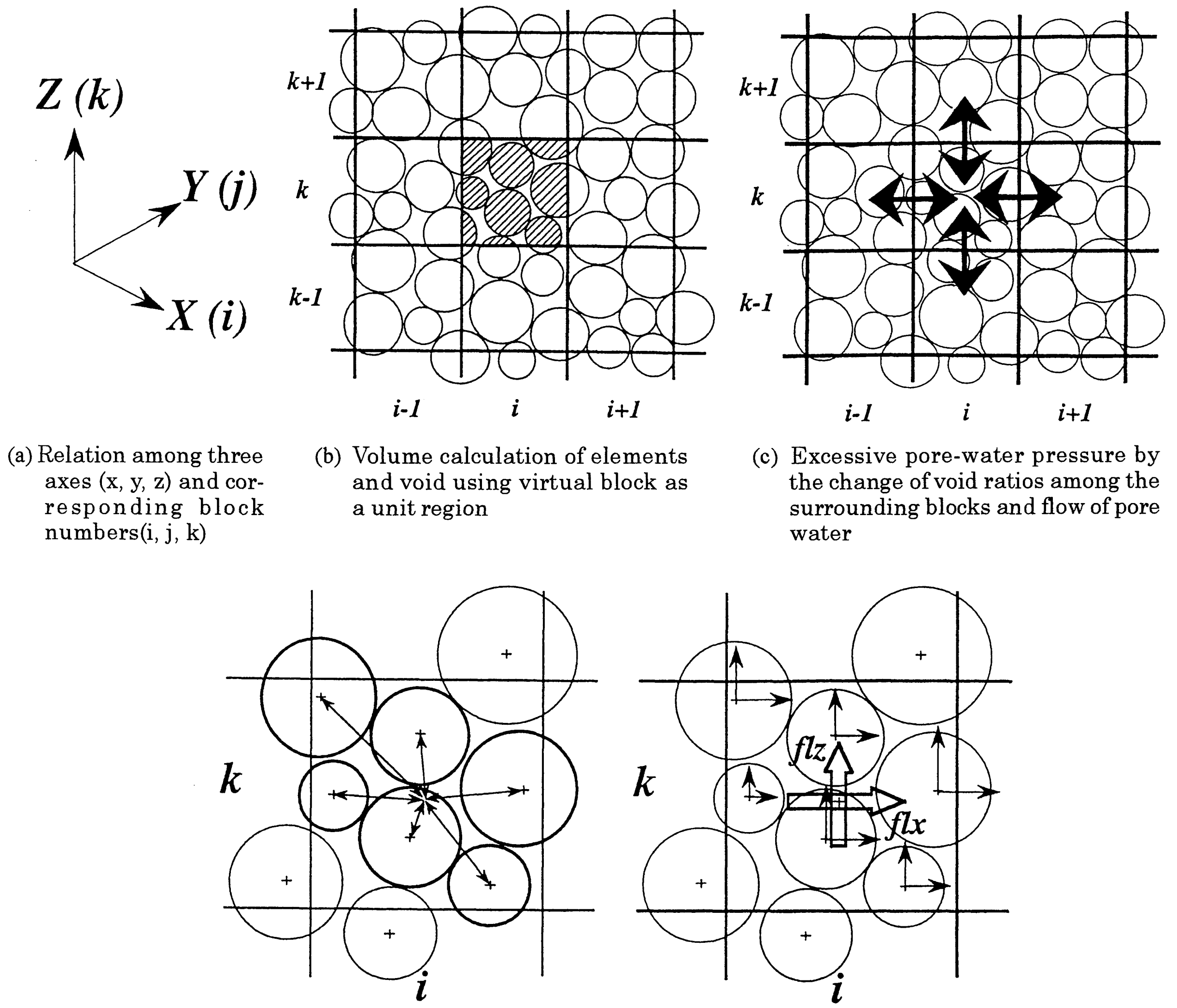

(a) Relation among three axes (x, y, z) and corresponding block numbers(i, j, k)

(b) Volume calculation of elements and void using virtual block as a unit region

(c) Excessive pore-water pressure by the change of void ratios among the surrounding blocks and flow of pore water

(d) Directions of the forces acting on the elements due to excessive pore-water pressure

(e) Forces acting on elements due to water flow in the block

Figure 1 DE modeling considering pore-water behavior

(Fig. 1(d)). When the excessive pore-water pressure is positive, the direction of the force becomes from inside to outside, and for in negative pressure, it is from outside to inside of the block. The forces acting on the elements due to the flow of pore-water caused by the difference of the excessive pore-water pressure between the adjusting blocks are calculated by the 3-D relative velocity between pore-water flow and behavior of the element, and the size of the element. **(Fig. 1(e))**

In this research, the total volume of the elements in a block is defined as summation of all the occupying parts of the elements. As a simpler way, there is a method to calculate the total volume of the elements in a block based on the assumption that the total volume of the elements can be simply calculated by summation of whole volume, not a part, of the elements in case whose centers belong to the block [5]. Namely, the element volume of a block is just calculated simply by summation of whole volume of all elements whose centers are located inside of the block. However, with this method, there are following problems and without solving these problems, it is difficult to adopt this idea.

With this idea, even when a part of the element volume is included in a block, if its center is located outside of the block, that part of the volume is ignored while the center is located inside of the block, even when a part of the element is not included in the block, that part of the element is considered as a part of element volume of the block. Therefore, to make this bad effect smaller, relatively larger size of block should be used so that many elements can belong to a block. However, still, there is a big problem when the center of an element goes across the boundary of the block during certain time increment, the volume of whole element is suddenly recognized as the other block's element volume. This gives unrealistic change of excessive pore-water pressure. In our method used in this research, no such problems arise as mentioned above.

MODELS AND NUMERICAL RESULTS

This section includes the introduction of the model used and the results of the simulation. The main purpose of this paper is to show the applicability of the proposed method to simulate liquefaction, therefore, detail explanation, especially, quantitative discussion will be introduced in further publications.

First, we explain the procedure to prepare the model used in this study, and then, introduce the numerical results of 3D-DEM liquefaction simulation and discuss its mechanism.

Within the hatched range of calculation region in **Fig. 2**, elements having random radii were generated. Their centers were set regularly at the grid corners with the size of maximum diameter of the given distribution of radius (**Fig. 3(a)**). By free fall method, gravity acceleration was applied to these elements and they fell into the box which was filled with water. To make loosely packed model, relatively larger friction coefficient was used.

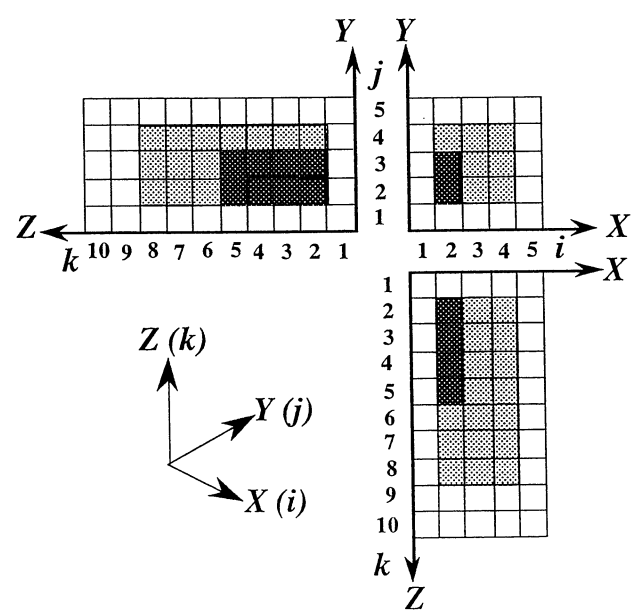

Figure 2 Block number used in the simulation (Hatched areas show the region of elements at initial state)

Figure 3(b) shows the model with the void ratio of about 93% made by the above mentioned procedure. At this stage, Z-coordinates of most of the elements became k $\leqq$ 6. Time history of excessive pore-water pressure while the elements are falling down into the box filled with

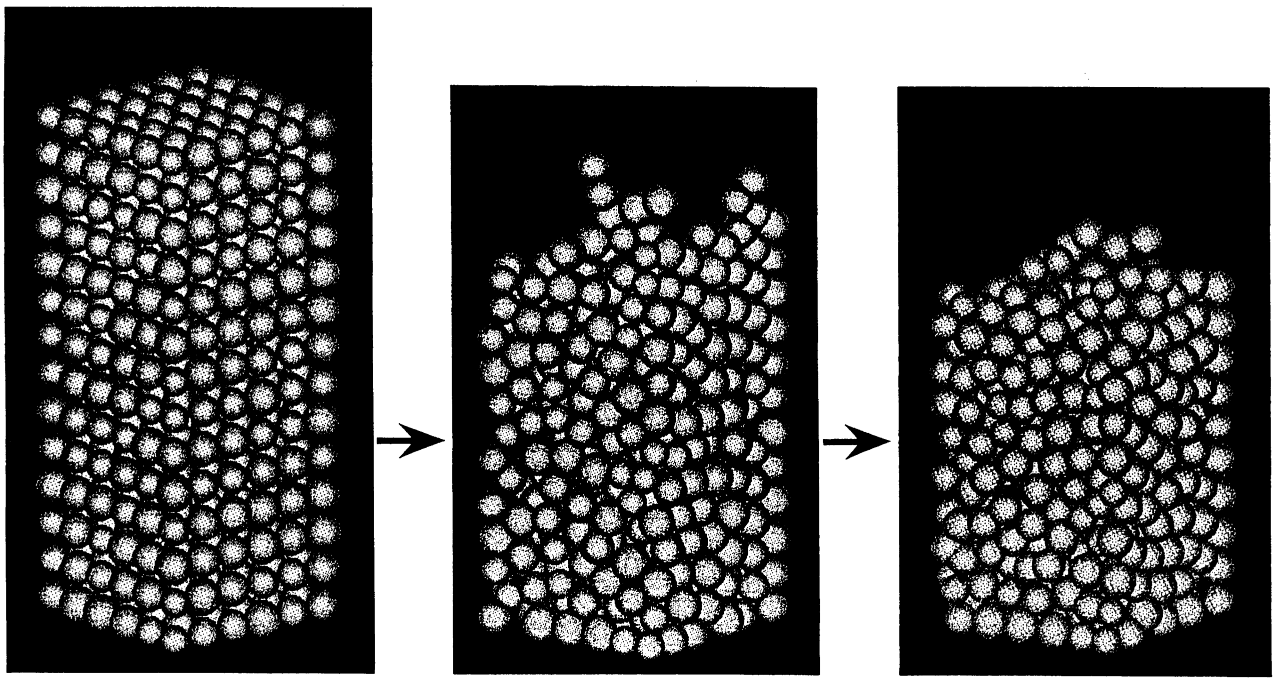

(a) Particle location at initial state

(b) Particle location of the model for liquefaction analysis

(c) Particle location of the model after liquefaction analysis

Figure 3 Changes of volume and particle location

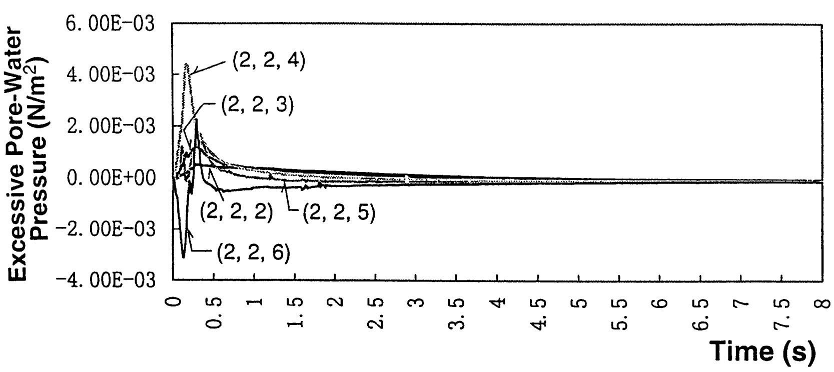

Figure 4 Time history of excessive pore-water pressure during preparation of the model in Fig. 3 (b)

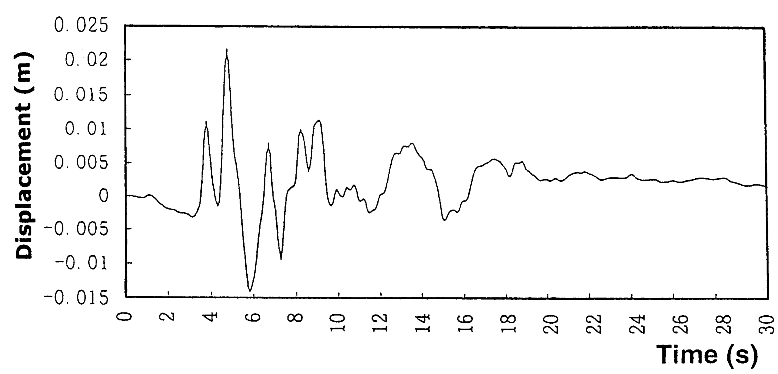

Figure 5 Time history of input motion (displacement)

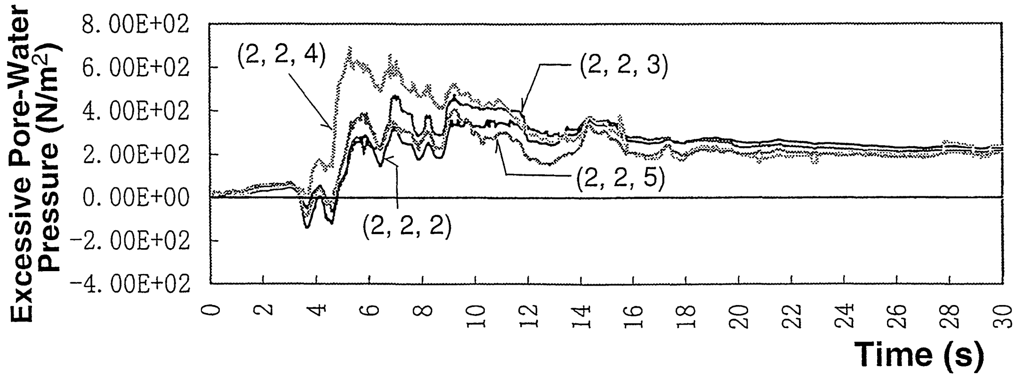

(a) Time history of excessive pore-water pressure of individual block

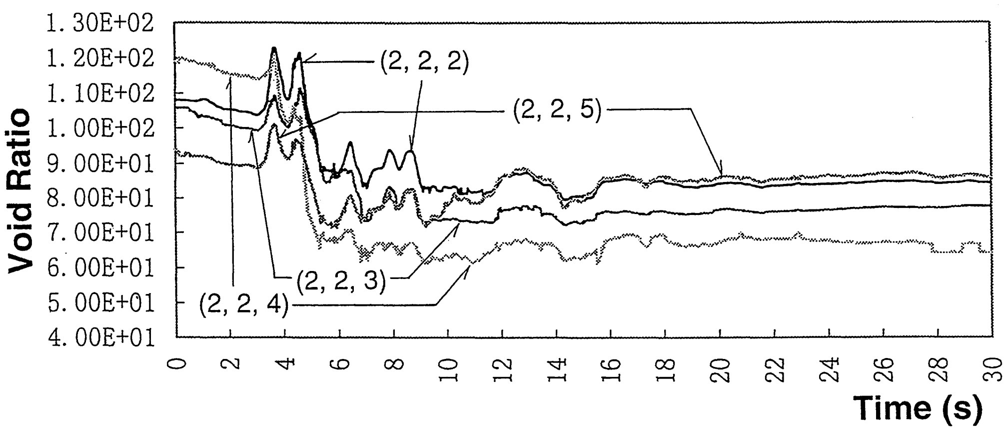

(b) Time history of void ratios of individual block

Figure 6 Time history of excessive pore-water pressure and void ratios at four blocks {(2, 2, k), k=2, 5}

liquid is shown in **Fig. 4**. Due to the movement of elements, excessive pore-water pressure became negative in the upper blocks, while in bottom blocks, positive pressure was generated. As time passed, changes of excessive pore-water pressure became stable and small due to movement of pore-water between adjacent blocks. In the simulation for preparing the model in **Fig. 3(b)**, we used relatively large coefficient of permeability in order to make the model stable in shorter time.

Using the model in **Fig. 3(b)**, we analyze the process of liquefaction by applying the displacement input motion as shown in **Fig. 5** to the base and two walls in X direction. As we applied the external force by displacement control of two walls in X direction, to avoid the rapid change in excessive pore-water pressure, the boundary of block, which is used as a unit volume for considering behavior of pore-water efficiently, is also moved with the same displacement as input motion. In this analysis, we assumed that the blocks (k=6 and 7) located around the surface of the model had free water surface.

The results of analysis are shown in **Figs. 6** and **7**. These figures show the time history of excessive pore-water pressure and the void ratio in 8 blocks that are located at hatched areas in dark color in **Fig. 2**. Four

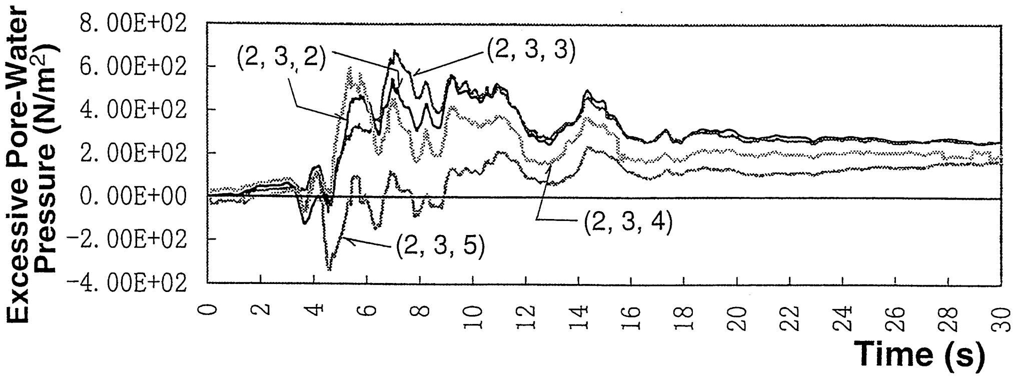

(a) Time history of excessive pore-water pressure of individual block

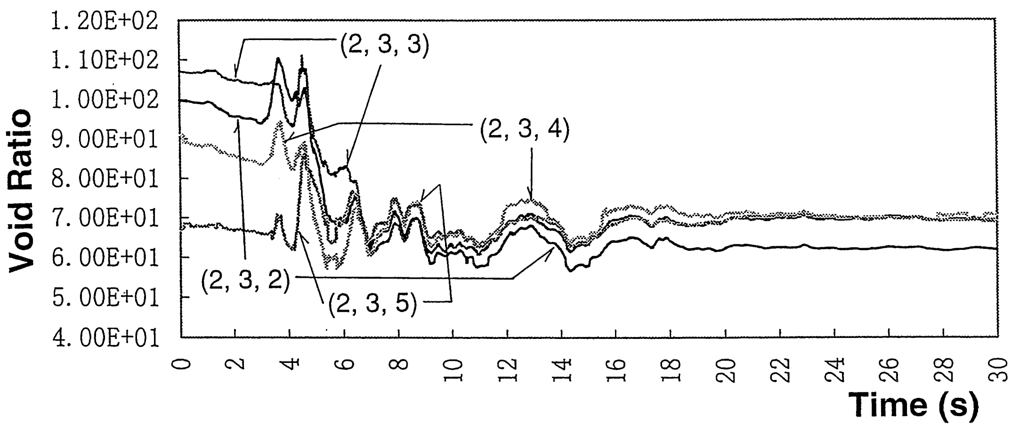

(b) Time history of void ratios of individual block

Figure 7 Time history of execessive pore-water pressure and void ratios at four blocks {(2, 3, k), k=2, 5}

blocks in **Fig. 6** are {(2, 2, k), k=2, 5} and those in **Fig. 7** are {(2, 3, k), k=2, 5}, respectively.

Liquefaction started at about four seconds when large displacement applied, and progressed by the large displacement input. When the amplitude of the input motion was getting smaller, the excessive pore-water pressure gradually decreased and became stable. When we compared the changes of excessive pore-water pressure and void ratio, it was clear that the excessive pore-water pressure occurred when the external vibration broke the structure of elements and stress skeleton. In the blocks whose initial void ratios were large, void ratios became small resulting in developing positive excessive pore-water. On the other hand, the negative excessive pore-water pressure was developed due to increase of void ratio in the blocks where the initial void ratio was small like the block (2,3,5) in **Fig. 7**. Liquefaction in the block (2,3,5) began when its void ratio became similar to those in the other blocks.

There is a trend that in general, the excessive pore-water pressure in the blocks close to surface is easily dissipated comparing to the blocks in the lower part of specimen because the pore-water easily moves from block to block in the surface layers. These phenomena of complex process of quick increase and dissipation of pore-water pressure could be simulated for the first time by introducing the pore-water directly to the DEM.

Figure 3(c) shows the particle location after the liquefaction analysis. We can clearly see that the void ratio of specimen becomes smaller than the initial value resulting in making the specimen compacted. This is because of the restructuring of particle arrangement and dissipation of pore-water due to the liquefaction.

By the way, it is not related to the liquefaction directly, with the scale of specimen used in this study (relation among the total number of elements, area of calculation and the size of blocks), when we compare the void ratios at initial state in **Figs. 6** and **7**, there is a large difference among void ratios in different blocks. It is not realistic to use constant coefficient of permeability if the number of elements in a block is small and/or local difference of void ratios in different blocks is very large. To solve this problem, it is necessary to adopt the model which has plenty of elements in a block or to treat the coefficient of permeability as the function of void ratio in the analysis.

CONCLUSIONS

With the new 3-D DEM proposed in this study, complicated liquefaction process such as generation and dissipation of excessive pore-water pressure and restructuring of particle arrangement can be simulated. These phenomena have not been analyzed well by the conventional methods. From the results, we can say that the method proposed has high potential to study the various phenomena related to liquefaction. Especially in this method, because the changes of pore-water pressure can be taken into account directly, there are many strong points that complicated phenomena like boiling sand behavior or changes of stiffness due to the level of liquefaction, etc. can also be simulated.

REFERENCES

1) S. Sawada, K. Toki and N. Yoshida: Sandy soil liquefaction simulation by distinct element method using elliptical shaped elements, Proc. 30th annual conf. of Japanese Geotechnical Society, pp. 773-776, 1995. (in Japanese)
2) H. Kiyama, T. Nishimura and H. Fujimura: An advanced distinct element model coupling with pore water, 499/III-28, Journal of Geotechnical Engineering, Japan Society of Civil Engineers, pp. 31-39, 1994. (in Japanese)
3) M. Hakuno and Y. Tarumi: A granular assembly simulation for liquefaction of sand, Proc. of Japan Society of Civil Engineers, No.398/I-10, pp.129-138, 1988.
4) K. Meguro and T. Katayama: Trial of 3-demensional distinct element simulation of sandy soil liquefaction, SEISAN KENKYU (Technical report of IIS, University of Tokyo), Vol. 48, No. 11, pp. 15-18, 1996. (in Japanese)
5) H. Nakase, H. Ishikawa and M. Fujitani: A simulation study on liquefaction using distinct element method, Proc. 6th Japan-US workshop on Earthquake Resistant Design of Lifeline Facilities and Countermeasures Against Soil Liquefaction, pp. 309-318, Sept., 1996.

CHARACTERISTICS OF GROUND MOTIONS AT A LIQUEFIABLE SITE

J. Yang
JSCE Principal Researcher, Disaster Prevention Research Institute,
Kyoto University, Kyoto 611-0011, Japan
Fax: +81-774-384070 E-mail: yang@catfish.dpri.kyoto-u.ac.jp

T. Sato
Professor, Disaster Prevention Research Institute,
Kyoto University, Kyoto 611-0011, Japan
Fax: +81-774-384070 E-mail: sato@catfish.dpri.kyoto-u.ac.jp

ABSTRACT

Local soil conditions play a key role in the amplification of earthquake waves. In particular, surface liquefiable layers may produce a significant influence on ground motion during strong earthquakes. In this paper, the response of a liquefiable site during the 1995 Kobe earthquake is studied using vertical array records, with particular attention on the effects of nonlinear soil behavior and liquefaction on the ground motions. The characteristics of the recorded ground motions are analyzed using a smoothed spectral ratio technique. The loss of soil stiffness occurring in surface liquefied layers is identified based on the spectral analyses. Furthermore, a fully coupled finite element analysis of the ground response is performed, and the effects of soil behavior and pore pressure buildup on the characteristics of the ground motions at different depths are addressed.

INTRODUCTION

It is well known that the amplification of earthquake waves comes from the strong contrast between the physical properties of the bedrock and sedimentary soils. There has been considerable interest in evaluating site amplification and ground response during earthquakes. In seismology the subsurface soils are conventionally treated as linear elastic materials. Such an assumption is generally acceptable if the motion is weak so that the induced shear strain in soils is low (e.g., the shear strain is less than 10^{-5}). However, if the earthquake motion is strong enough to result in a large level of shear strain, the elastic assumption becomes questionable. Laboratory findings by geotechnical engineers have shown that the stress-strain behavior of soils is nonlinear (e.g., Seed and Idriss, 1970). In particular, for saturated sandy soils subjected to strong cyclic loading under undrained conditions, the gradual buildup of excess pore water pressure will result in a significant degradation of soil stiffness and the soil may reach a liquefaction state. Many constitutive equations based on laboratory test results have been developed for modeling soil nonlinearity and liquefaction. There is a concern, however, that the laboratory samples may not be representative of field conditions because of sample disturbance. Thus, it would be of great value to study the nonlinearity in soil response for large strains through in-situ earthquake observations. The study would also be helpful in verifying and refining the available laboratory observations and analytical simulations on soil behavior and ground response.

A desirable way to investigate in-situ soil behavior is through field observations obtained from vertical arrays in strong earthquakes. These array records make it possible to separate the local soil effects from source and path effects. One can investigate the nonlinear soil response by examining the Fourier spectral ratio between ground surface and bedrock motions. In addition, using these records, it is also possible to investigate the behavior of soils between the stations at different depths and how much depth influences the ground motion. However, one problem encountered in doing so is the lack of motion records in strong earthquakes which may bear the character of nonlinear soil effects. Recently, some researchers have been trying to find observational evidence of the nonlinear site effects from earthquake motion data (e.g., Beresnev et al., 1995).

In this paper, the vertical array records obtained at Port Island, Kobe, during the 1995 Kobe earthquake are used to study nonlinear soil amplification. The unique features of the Port Island records are that (1) the site consisted of a reclaimed loose surface layer which liquefied during shaking events, it is believed that the nonlinear soil behavior must have been documented by the acceleration records; (2) the records included detailed acceleration data at reasonably spaced depth intervals, the maximum recorded acceleration reached approximately 0.6 g and the deepest accelerometer was located at the depth of 83 m. In this study, the characteristics of the recorded ground motions are analyzed using the spectral ratio technique, and the nonlinearity occurring in the shallow liquefied layer during earthquake is identified. A fully coupled, inelastic finite element analysis is performed to analyze the ground response at the array site. The simulated stress-strain histories of soils and excess pore water pressures at different depths are presented, and their effects on the characteristics of the ground motions are addressed.

SITE CONDITIONS AND STRONG MOTION RECORDS

The site is at Port island which is an artificial island located on the west-south side of Kobe, Japan. A downhole array was installed at the north-west corner of Port Island in August 1991. The array consisted of three-component accelerometers located at the surface, the depths of 16 m, 32 m and 83 m, respectively. The soil profile at the array site is shown in Fig. 1. From the surface to the depth of 19 m there was a reclaimed layer which consisted of decomposed granite. The site investigation indicated that the SPT values of the surface reclaimed layer were very low. Hence, there existed a high liquefaction susceptibility in that layer.

The recorded strong earthquake motions in horizontal components are shown in Fig. 2 for the surface and the depth of 83 m (G.L.-83 m). It should be mentioned that the orientation error in the accelerometer at G.L.-83 m has been corrected according to the displacement orbits for each station in horizontal plane (Sugito et al., 1996). The corrected displacement orbits at four stations along the depth are shown in Fig. 3. Figure 4 depicts the distribution of peak horizontal accelerations with the depth. Clearly, it can be seen that a significant reduction of the amplitudes of horizontal motions occurred when the seismic waves travelling from the bottom to the surface. The de-amplification is believed to be caused by the liquefaction of shallow soils. Field investigations after the Kobe earthquake indicated that extensive liquefaction occurred in the reclaimed soil layer (Shibata et al., 1996).

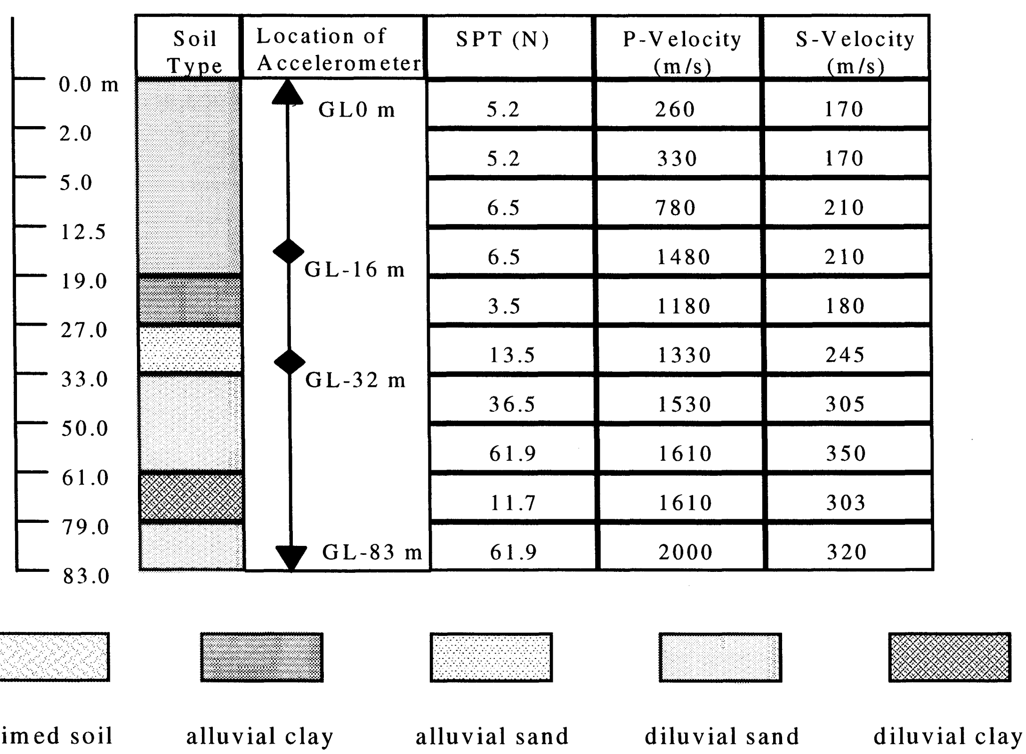

Figure 1. Soil profile at the array site, Port Island, Kobe

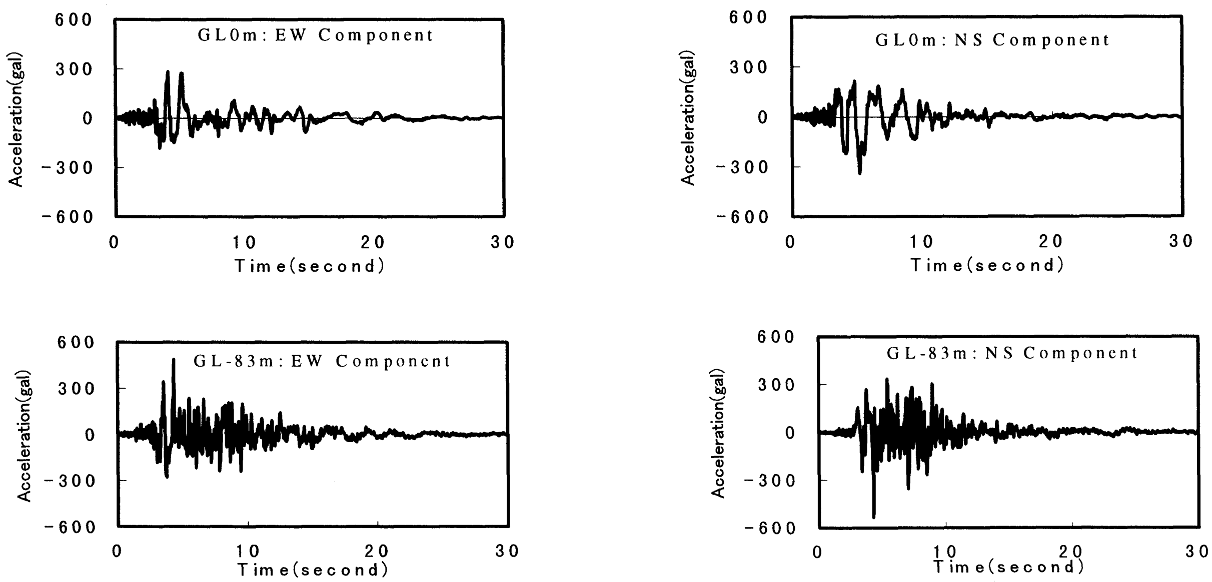

Figure 2. Vertical array acceleration records

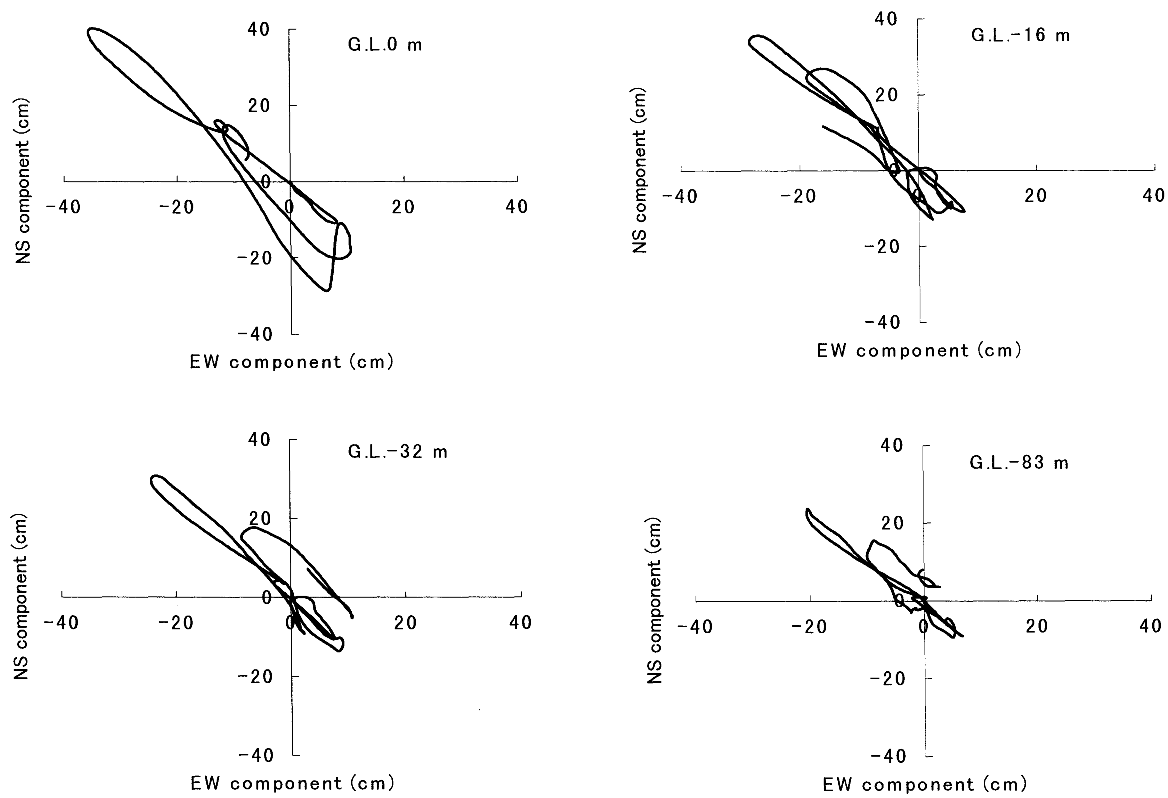

Figure 3. Displacement orbits at four stations along the depth

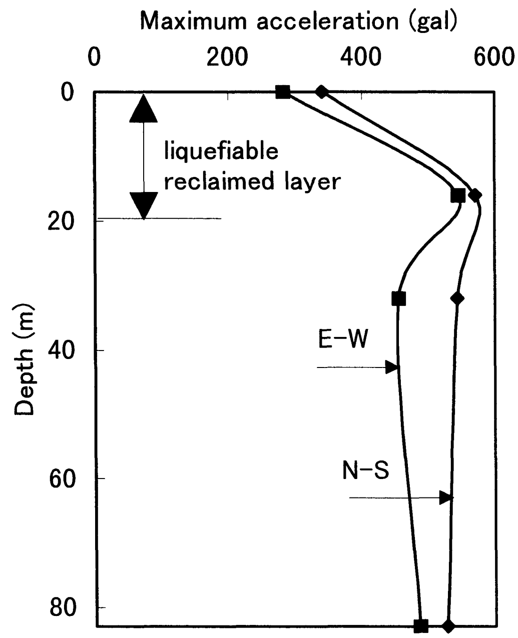

Figure 4. Distribution of maximum horizontal accelerations with the depth

SPECTRAL ANALYSIS OF GROUND MOTION

Subsurface soils subjected to a strong shaking may respond in a nonlinear manner. As a result, the amplitude of recorded surface motions may be reduced and the predominant period of the motions be lengthened. In general, this nonlinear behavior can be investigated by examining the Fourier or response spectral ratio between the surface motion and the motion recorded at other depths. However, because of the long duration of the acceleration records and uncustomary variation of the frequency content, it is recognized that to reach a reliable conclusion from the spectral analysis of the complete records would be difficult. An approach to deal with this problem is to divide the long records into several phases so as to capture the variation of frequency content during the shaking. In this study, the acceleration records are separated to three time phases according to the observed features of seismograms: Phase 1, from 0 to 3 seconds, contains weak earthquake motions with maximum acceleration was less than 100 gal; Phase 2: from 3 to 12 seconds, corresponds to strongest motions with maximum acceleration around of 560 gal; Phase 3, from 12 to 30 seconds, contains weak motions after the strong motions.

First, the Fourier spectra for the surface motions in two horizontal directions are investigated. In the calculation of the Fourier spectra, a smoothing of the spectra is performed by Parzen's spectral window. Figure 5 shows the spectral amplitudes for the surface motions in three phases in N-S and E-W directions, respectively. As expected, the predominant frequencies for both horizontal motions were decreased when the strong motion occurred. For N-S direction, the predominant frequencies dropped from about 4.5 and 10.8 Hz in Phase 1 to 0.6 Hz in Phase 2 The decrease in predominant frequency was associated with the strong earthquake shaking, which caused soil softening in shallow layers. Moreover, it is seen that the frequency content of the surface motion in Phase 2 is similar to those in Phase 3, indicating that the softened state of the soils persisted.

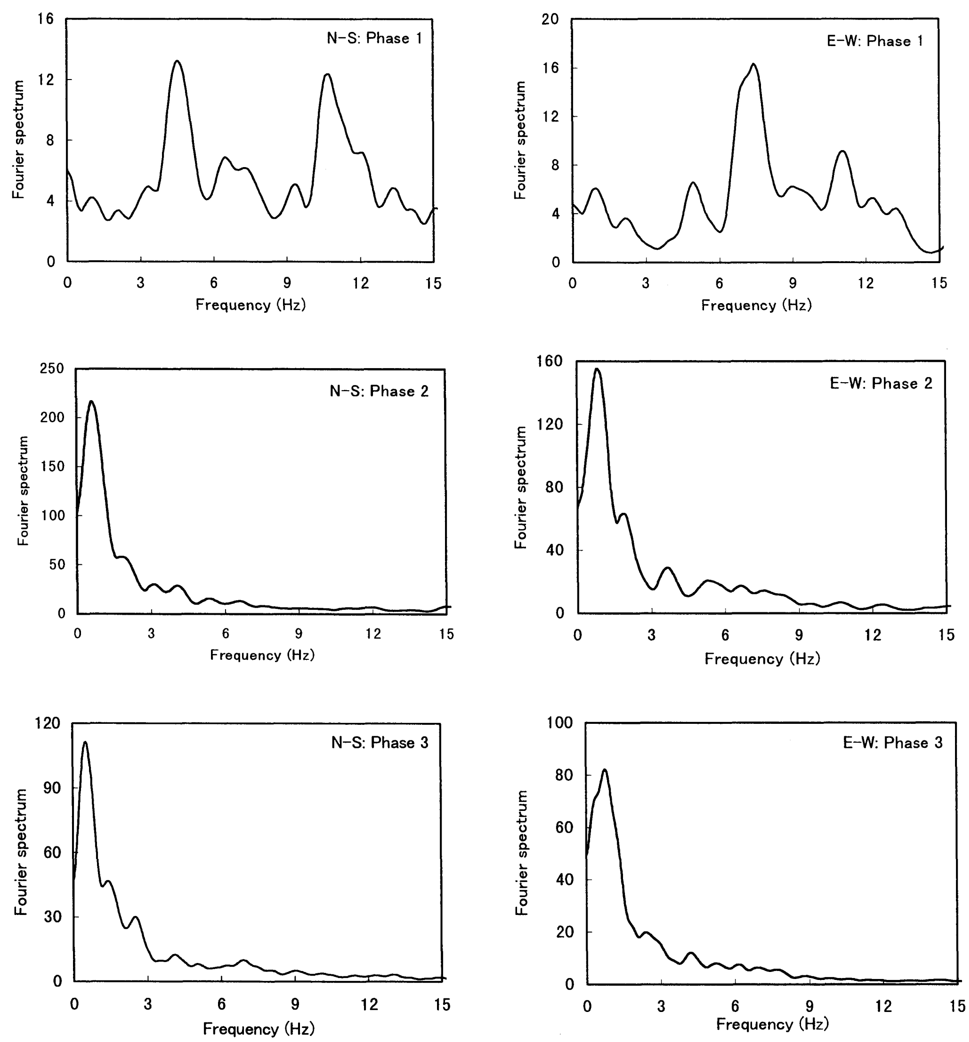

Figure 5. Fourier spectra of horizontal surface motions in three time phases

Next, the spectral ratios between the motions recorded at the surface and other stations are analyzed. These spectral ratios can be regarded as the transfer functions for the different locations. Figure 6 shows the spectral ratios between the surface motion and the motions at the depths of 16 m, 32 m and 83 m (denoted as SP0/SP16, SP0/SP32 and SP0/SP83, respectively) in three time phases, respectively, for N-S direction. In general, the features of the spectral ratios for E-W component are very similar to those for N-S component (Yang et al. 1999), therefore, the discussion is focused here on N-S component only.

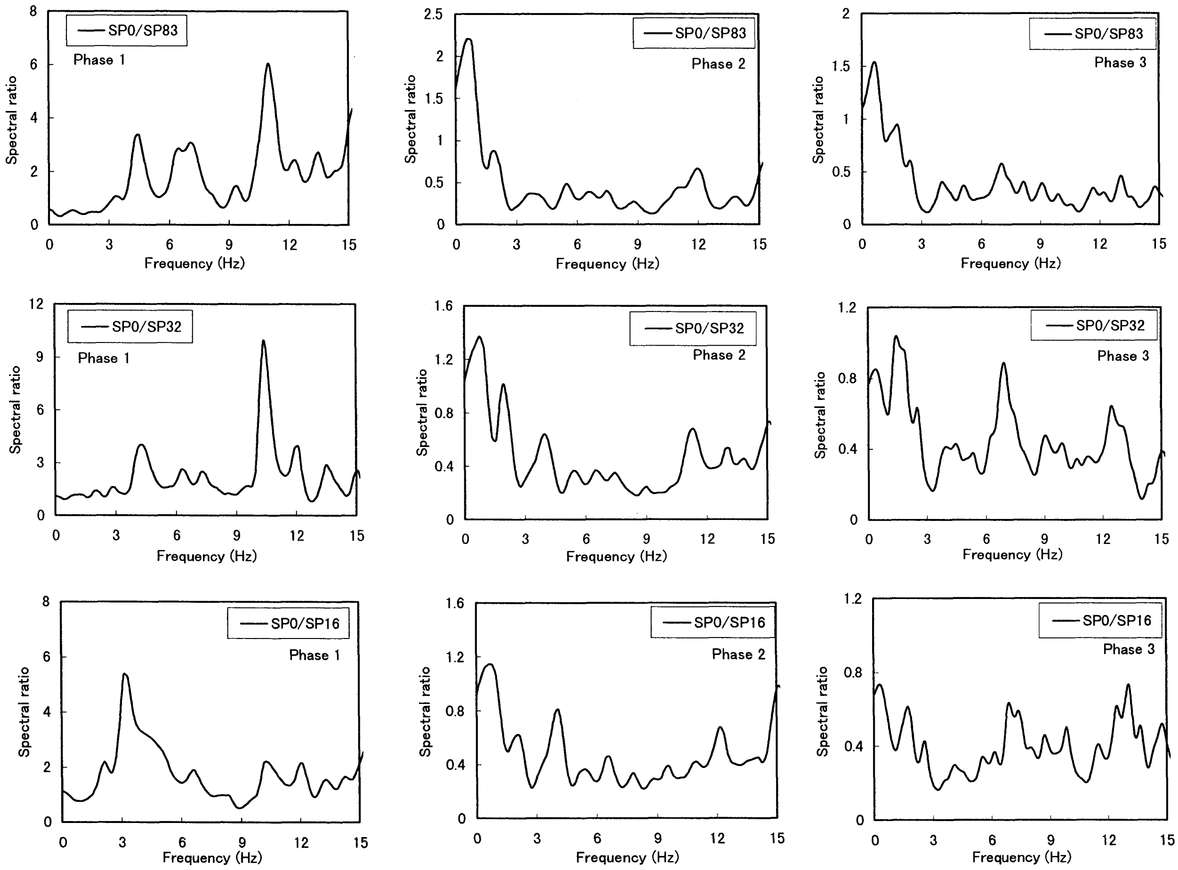

Figure 6. Spectral ratios for three time phases for N-S component ground motion

It can be seen from Fig. 6 that, in Phase 1, the spectral ratios SP0/SP83 and SP/SP32 are similar, with peak frequencies of around 4.5, 7, and 11 Hz, and 4.2, 6, 10.5 Hz, respectively. The dominant seismic waves were those with high frequencies in this phase. The spectral ratio SP0/SP16, however, exhibited a little different feature: the peak frequencies were around 3.2 and 6.6 Hz. This indicates that, even though the shaking during this stage was not strong enough, seismic motions with relatively longer periods became dominant, when the waves traveled through the surface reclaimed layer. The influence of the different soil layers on the ground motions was also well manifested in the surface motion records, as shown in Fig. 5: two predominant frequencies, around 4.5 Hz and 11 Hz, were observed in the spectra of surface motion in Phase 1. On the other hand, by comparing the spectral ratios in Phase 1 and 2, the influence of nonlinear soil behavior, which was attributed to a strong shaking, was clearly observed: the frequency content was obviously shifted to low frequency end, in other words, the predominant periods were lengthened when the strong motion occurred. Especially, it is noticed that, in phase 2 the amplitudes for the waves with frequency higher than 5 Hz were dramatically reduced, with amplification ratios below 1, while in phase 1 these waves were amplified notably. The difference for the two phases indicates that the increase in the predominant period was caused primarily by a strong decrease in the amplitude of low-period waves, rather than by amplification of long-period motion. Similarly, it is also noticed that the spectral ratios for the Phase 3 are in general similar to those in Phase 2.

As have been shown above, the surface reclaimed layer produced a significant influence in ground motion. This layer had a high liquefaction susceptibility. The spectral analysis of the recorded motions has shown that a large soil softening occurred in this layer during the strong shaking. It is possible to back-calculate the variation of soil stiffness during the earthquake from the field records. Here the shear modulus of the surface reclaimed layer before and after the strongest shaking was evaluated using the theory of wave propagation in a single layered system (Yang et al. 1999). With the identified fundamental frequency, the shear wave velocity and shear modulus for the liquefied surface layer (from the surface to the depth of 16 m) are calculated for the two time phases for N-S and E-W components, respectively, as shown in Table 1. These values correspond respectively to the average soil stiffness before and after the strongest earthquake shaking. It is seen that the reduction of shear modulus during the shaking event is remarkable: it is about 94% for N-S component and 86% for E-W component.

Table 1. Identified shear wave velocity and shear modulus for reclaimed layer

Component	V_{s1} time phase 1	V_{s2} time phase 2	G_1 time phase 1	G_2 time phase 2	Reduction of G $(G_1\text{-}G_2)/G_1$ (%)
N-S	205 m/s	51 m/s	79.8 MPa	4.9 MPa	94%
E-W	154 m/s	57 m/s	45.1 MPa	6.2 MPa	86%

PS logging : Vs=198 m/s G_0=74.5 MPa (average values for the surface layer, G.L. 0 m to G.L. -16 m)

COUPLED ANALYSIS OF THE RESPONSE OF ARRAY SITE

In this section, a fully coupled nonlinear finite element analysis of the site response to the recorded motions is performed. The purpose here is to simulate the acceleration time histories, pore water pressure responses and stress-strain histories of soils at different depths, and then to discuss their relations to the observed characteristics of ground motions.

The analytical procedure applied is a fully coupled effective-stress procedure for site response under multi-directional earthquake shaking (Li et al., 1992). The procedure is formulated within the framework of two phase theory by Biot (1941) and Zienkiewicz and Shiomi (1984). The basic assumptions made in the formulation are as follows: (1) the site is horizontally layered and it extends infinitely in horizontal directions, (2) the ground surface is free of stresses and the bottom boundary is impermeable, (3) soil below the water table is saturated and the water flow obeys Darcy's law, and (4) seismic waves travel along vertical direction only. These assumptions, in practice, conform to free-field soil deposits that are water saturated, essentially leveled, and subjected to earthquake shaking originating primarily from the underlying rock formulation.

The inelastic soil model incorporated in the procedure is a hypo-plasticity bounding surface model (Wang et al., 1990) which was developed within the framework of bounding surface theory (Dafalias, 1986). This model is capable of realistically simulating the soil behavior under a wide range of loading conditions. Some essential effects are captured, such as the compression and dilation induced effective stress change, the lateral stress change due to shaking and the significant reduction of stiffness upon liquefaction, etc. For level ground earthquake response problems, the model takes a reduced-order form and there are 10 model parameters to be determined for a particular soil (Li et al., 1992). The parameters are described as follows

- G_0 a coefficient defining elastic shear modulus using the following equation

$$G_{\max} = G_0 \frac{(2.973 - e_0)^2}{1 + e_0} \sqrt{pp_{atm}}$$

where e_0 is initial void ratio, p is effective mean normal stress and p_{atm} is atmospheric pressure.

- λ, κ the slopes of the virgin compression line and rebounded line
- R_f the slope of failure line
- R_p the slope of phase transformation line
- h_r characterizes the relationship between shear modulus and shear strain magnitude
- d characterizes the rate of the effective mean normal stress change caused by shear unloading
- k_r characterizes the amount of the effective mean normal stress change caused by shear loading
- b a parameter affecting the shape of the stress paths of the virgin shear loading. The analyzed results are not sensitive to this parameter.
- h_p a parameter controlling the amount of the shear strain increment due to the change of the maximum effective mean normal stress

Among these parameters λ and h_p are active only when the mean normal stress exceeds its maximum value in the loading history. Since during earthquakes the mean normal stress in soil is almost always less than its initial value, the two parameters are inactive for ground response analyses. The remained parameters should be calibrated specifically for a given soil either by laboratory tests or field data. In Fig. 7 the response of soil model to cyclic loading calibrated on the basis of the liquefaction resistance data for surface reclaimed soils is presented. The calibrated model parameters are given in Yang et al. (1999). A further detailed discussion on the constitutive model and the parameter calibration is beyond the scope of this paper. Readers are referred to

Wang et al. (1990) for more information.

The bottom boundary of soil deposits can be treated as a rigid base if the input motions are directly taken from downhole records. When the input motions are specified at outcropping rock, the underlying base can be approximately treated as an uniform elastic half-space characterized by its mass density and wave velocities and the boundary conditions can be established based on the theory of elastic wave propagation. In the present analyses, the acceleration records at G.L.-83 m serve as input motions.

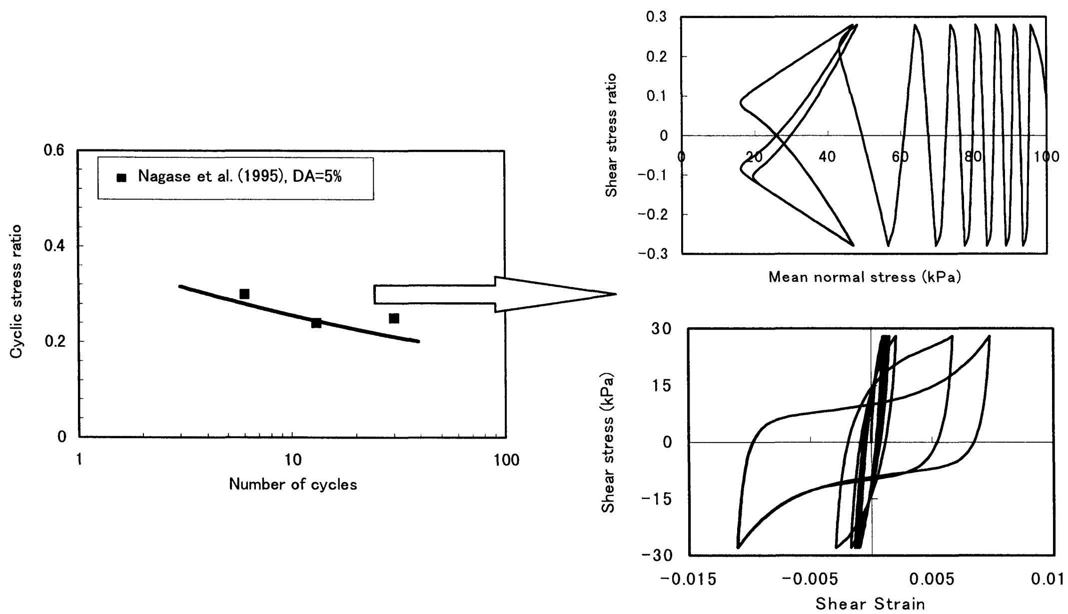

Figure 7. Undrained response of the model calibrating from cyclic strength data

The calculated and recorded acceleration time histories at the surface and the depths of 16 m, 32 m in N-S and E-W directions are shown in Fig. 8. In general , it can be seen that the calculated acceleration histories are similar to the field records. Considering the uncertainties involved in the analyses, the discrepancy between the calculations and records is considered acceptable. The computed stress-strain histories at depths of 7.7 m, 24 m and 51.3 m during the shaking are shown in Fig. 9 for N-S and E-W directions, respectively. Here, the shear stress is correspondingly normalized to the initial effective vertical stress. Obviously, it is seen that the soils at different depths exhibited quite different behavior during earthquake in either direction. The soils at the shallow depth (7.7 m) showed a dramatic reduction of soil stiffness during the shaking. Especially, it is noted that the shear modulus of soils was almost reduced to zero while the shear strain remained at a large level at the final stage of strong shaking, this indicates that the soils liquefied fully. The soils at deeper layer (51.3 m), on the other hand, responded generally in a very small nonlinear manner, with no appreciable reduction of stiffness and with a low level of strain. The stress-strain history for the soils at the depth of 24 m exhibited a moderate reduction of shear modulus, but the soils did not fully lose strength throughout the earthquake. The calculated strain levels for the soils at the three different depths are in good agreement with the evaluations by Kazama *et al.* (1996), in which the stress strain relationships were directly calculated from downhole records using integration technique. According to their study the maximum strain for reclaimed soils between the surface and the depth of 16 m is around 1% to 2%, for the soils between the depths of 16 m and 28 m is around 0.6% and for the soils between the depths of 32 m and 83 m is 0.1% to 0.2%. Figure 10 depicts the excess pore water pressure responses at the depths of 7.7 m and 51.3 m during the shaking. It is seen that an abrupt rise in excess pore water pressure occurred during the phase of strongest excitation (Phase 2, 5 to 8 s). For the soils at the depth of 7.7 m, the excess pore pressure reached the value of initial effective vertical stress around at 9 s, which resulted in a full soil liquefaction. Corresponding to this stage, the soil stiffness was reduced significantly, and consequently, the frequency content of surface motion was decreased notably, as shown in Fig. 5.

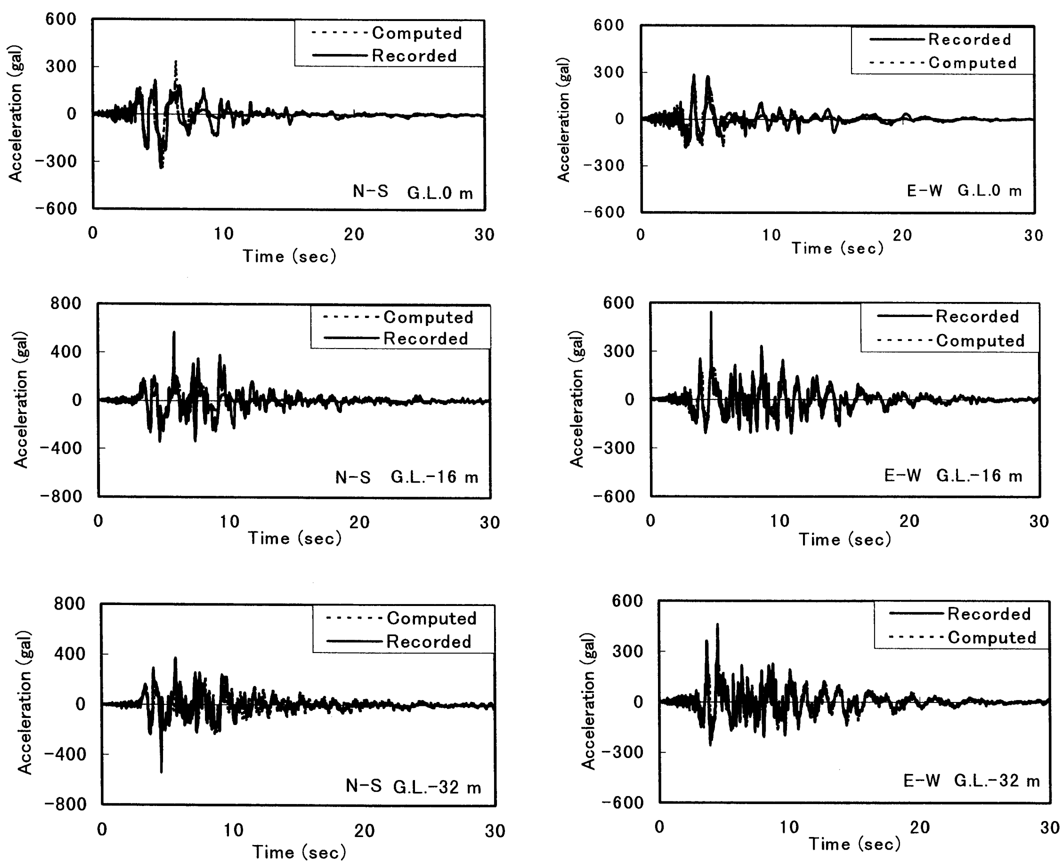

Figure 8. Simulated and recorded acceleration time histories at different depths

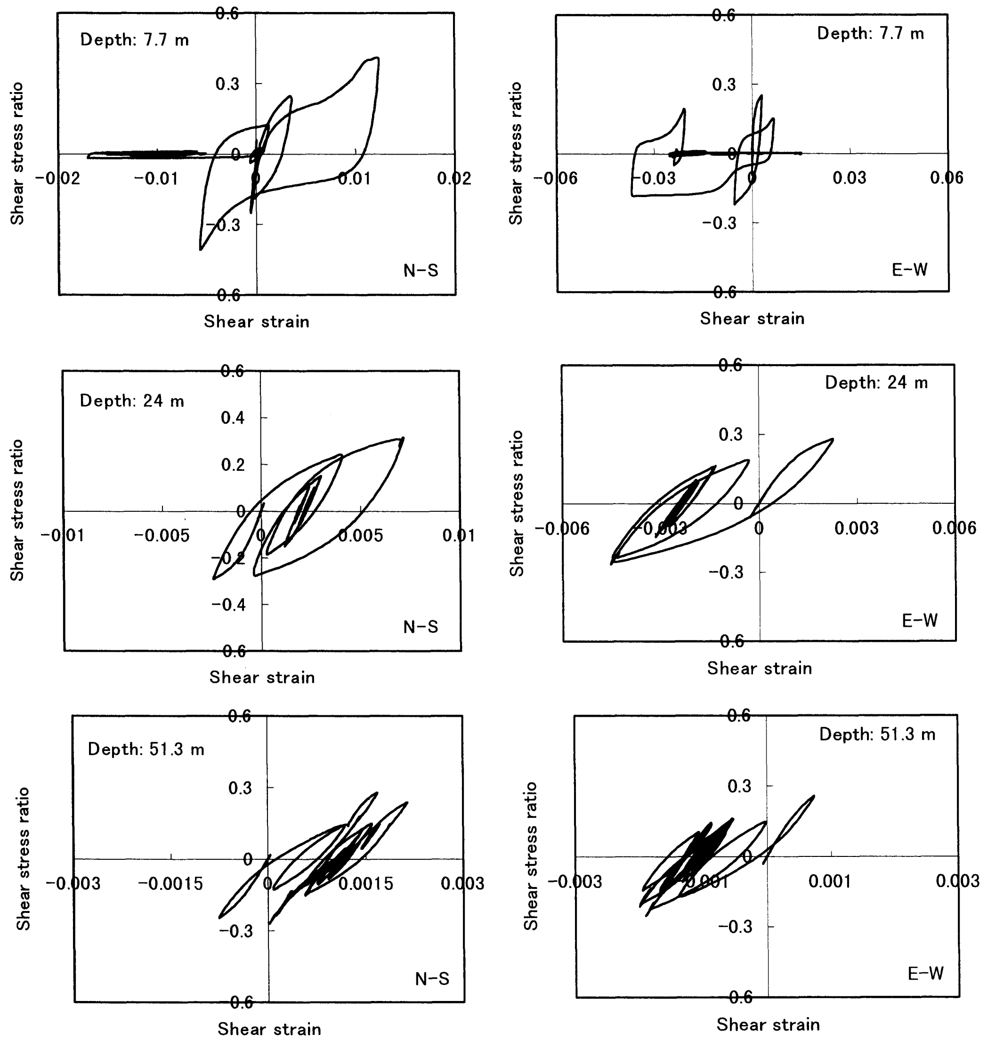

Figure 9. Calculated stress-strain histories of soils at different depths

To clearly show the relation of ground motion and the soil behavior during earthquake, in Fig. 11 the recorded surface motion in N-S component, and its Fourier spectra in the three time phases, as well as the stress-strain histories of soils at the depth of 7.7 m at different stages are given. It is obvious that, at the first time stage which corresponds to weak shaking, the soil responded linearly with the strain level less than 0.01%, meanwhile the generated excess pore water pressure at this stage was very small, as shown in Fig. 10. Corresponding to this stage, the spectra of surface motion were dominated by high frequency components. During the time stage of 3 to 6 s, which corresponds to strong shaking, the soil exhibited an obvious nonlinearity with the peak strain of the order of 1%. The generated excess pore pressure reached 75% of initial effective vertical stress at 6 s. During the period from 6 to 12 s, the abrupt loss of soil stiffness upon liquefaction was clearly observed. The amplitude of shear strain approximately reached the value of 2%. Correspondingly, the long-period waves were dominant in surface motion.

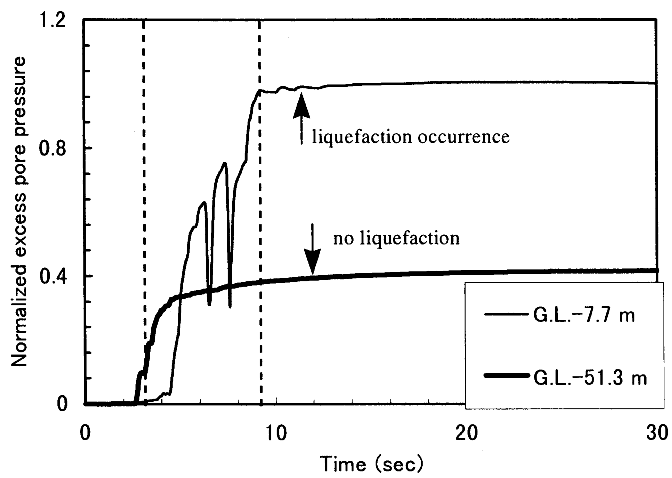

Figure 10. Calculated excess pore water pressure responses at different depths

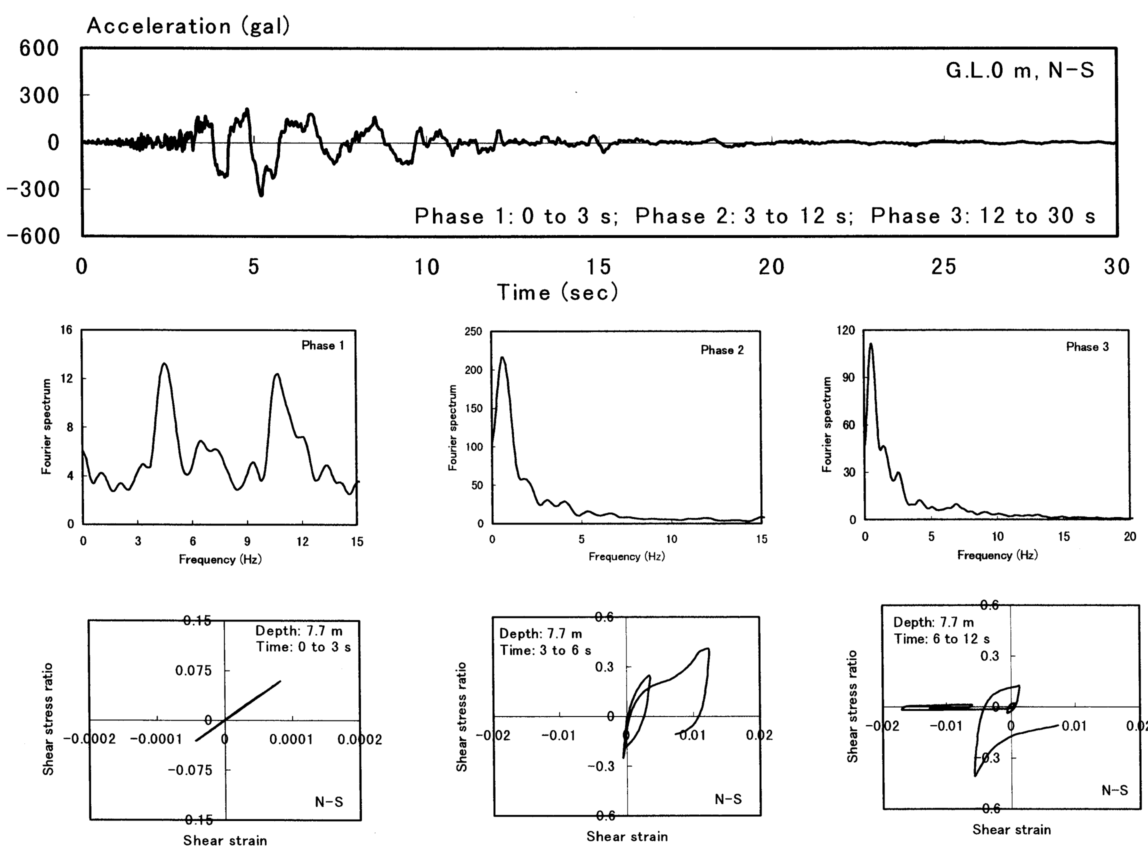

Figure 11. Relation of soil behavior and ground motion during shaking history

CONCLUSIONS

In this paper, the effects of nonlinear soil response and liquefaction on ground motion are studied for the case history of a liquefiable site subjected to the 1995 Kobe earthquake. The present study indicates that:

(1) There are large differences in the characteristics of ground motions before and after the strongest earthquake shaking. The peak frequencies in spectral ratios were shifted to lower frequencies when the strongest motions occurred.

(2) The increase in the predominant period of surface motion was caused primarily by a strong decrease in the amplitude of low-period waves, rather than by amplification of long-period motion.

(3) The surface reclaimed soils played a key role in the variation of the characteristics of ground motion. A significant reduction in the stiffness of surface soils was caused by the strongest shaking which resulted in liquefaction.

(4) The numerical simulations indicated that a large soil softening due to high excess pore water pressure occurred in shallow layer, while the deep soils exhibited a very small nonlinear response with a low level of excess pore pressure.

(5) The simulated stress-strain histories and excess pore water pressure response are closely related to variations of the characteristics of ground motions during shaking. Corresponding to the initial weak motion stage, the surface soil responded linearly and the ground motion was dominated by high frequency waves. When the strongest shaking occurred, the soil performed nonlinearly and an abrupt loss of stiffness took place upon liquefaction, correspondingly, the surface motion was dominated by long-period waves.

ACKNOWLEDGMENTS

The first author wishes to thank Dr. X.S. Li, Hong Kong University of Science and Technology, for helpful discussions on the constitutive model and numerical procedure employed in this study. The downhole acceleration data and soil profile for the array site were provided by Kobe City Development Bureau, Japan. The authors would also like to acknowledge the financial support provided by the Ministry of Education, Japan, during the course of the study.

REFERENCES

Beresnev, I.A., Wen, K.L. & Yeh, Y.T. (1995). “Seismological evidence for nonlinear elastic ground behavior during large earthquakes,” *Soil Dyna. Earthquake Engrg.*, 14, 103-114.

Biot, M.A. (1941). “General theory of three-dimensional consolidation,” *J. Appl. Physics*, 12, 155-164.

Dafalias, Y.F. (1986). “Bounding surface plasticity, I. Mathematical foundation and the concept of hypoplasticity,” *J. Engrg. Mech.*, ASCE, 112, 966-987.

Kazama, M., Yanagisawa, E., Inatomi, T, Sugano, T. and Inagaki, H. (1996). "Stress strain relationship in the ground at Kobe Port Island during 1995 Hyogo-ken nambu earthquake inferred from strong motion array records," *Proc. of JSCE*, No.547/III-36, 171-182.

Li, X.S., Wang, Z.L. and Shen, C.K. (1992). "SUMDES, a nonlinear procedure for response analysis of horizontally-layered sites subjected to multi-directional earthquake loading," *Report,* Dept. of Civil Engrg., Univ. of Calif., Davis, Calif.

Nagase, H., Shinji, R., Kimura, K. and Tsujino, S. (1995). "Liquefaction strength of undisturbed sand subjected to overconsolidation (in Japanese)," *Proc. of the Thirtieth Japan National Conf. on Geotech. Engrg.*

Seed, H.B. and Idriss, I.M. (1970). "Soil moduli and damping factors for dynamic response analysis," *Report EERC 70-10*, Earthquake Engrg. Res. Cent., Univ. of Calif., Berkeley, Calif.

Shibata, T., Oka, F. and Ozawa, Y. (1996). "Characteristics of ground deformation due to liquefaction," *Soils Found.*, Special Issue, pp. 65-79.

Sugito, M., Sekiguchi, K., Yashima, A., Oka, F., Taguchi, Y. and Kato, Y. (1995). "Correction of orientation error of borehole strong motion array records during the South Hyogo Earthquake of Jan. 17, 1995," *Proc. of JSCE,* No.531/I-34, 51-63.

Wang, Z.L., Dafalias, Y.F. and Shen, C.K. (1990). "Bounding surface hypoplasticity model for sand," *J. Engrg. Mech.*, ASCE, 116, 983-1001.

Yang, J., Sato, T. and Li, X.S. (1999). "Seismic amplification at a soft soil site with liquefiable layer," *J. Earthquake Engrg.* (accepted for publication).

Zienkiewicz, O.C. and Shiomi, T (1984). "Dynamic behavior of saturated porous media: the generalized Biot formulation and its numerical solution," *Int. J. Nume. Anal. Methods in Geomech.*, 8, 71-96.

De-Liquefaction Shock Waves

Bruce L. Kutter[1]
and
Daniel W. Wilson[2]

1 – Professor, Department of Civil and Environmental Engineering
University of California, Davis, CA, USA

2 – Facility Manager, Center for Geotechnical Modeling
University of California, Davis, CA, USA

Abstract

It is well known that during undrained cyclic loading, medium density sands exhibit cyclic mobility and a strain stiffening tangent shear modulus. (The shear modulus actually increases as shear strain increases.) The strain-stiffening response, associated with a drop in pore pressures caused by dilatancy, causes the classical banana-shaped stress-strain curves. During cyclic mobility, there is a range of shear strain that can occur at very low effective stress with little shear resistance. At some particular shear strain, however, the dilatant tendency causes negative pore pressure increments and an increase in effective confining pressure that leads to strain-stiffening behavior. "De-liquefaction" is proposed as a term to describe the solidification due to dilatancy.

In centrifuge model tests and in field case histories, de-liquefaction has been observed to be accompanied by large magnitude, short duration spikes in acceleration time histories. By studying data from dense vertical accelerometer arrays in recent model tests, slow travelling (about 5 to 30 m/s) but spatially sharp (0.1 m wavelength or less) de-liquefaction wave fronts have been observed. This paper shows that these fronts bear resemblance to shock waves expected from classical nonlinear wave propagation theory for strain-stiffening media. A shock front can be thought of as a propagating singular surface across which deformation is continuous, but velocity and strain are discontinuous. A new procedure for interpolating acceleration time histories at points between accelerometers is developed to enhance resolution of the experimentally observed wave fronts. The new procedure uses the wave equation to map time histories into the space between accelerometers.

It is not possible to predict the formation of a shock front using linear or equivalent-linear procedures because the phenomenon is inherently nonlinear. Nonlinear calculations may be used to predict the formation of a shock front. Once a discontinuous shock front forms, however, the use of continuum finite elements is theoretically incorrect.

Introduction

After a medium to medium-dense sand undergoes initial liquefaction due to cyclic loading, the application of a shear strain can trigger a temporary decrease in pore water pressure associated with dilatancy (Seed and Lee 1966). The cyclic strain amplitude in dilatant soils is restricted by the strain at which dilatancy is triggered because the dilation is accompanied by a stiffening of the soil. The limited straining associated with cyclic loading of dilatant soils was recognized by Casagrande (1971) when he proposed the term "cyclic mobility" to describe this phenomena.

The reduction in pore pressure can develop quite suddenly, resulting in a highly nonlinear transition from a "liquefied" to a "solid" state. Recent field recordings (Holzer et al. 1989) have shown evidence of the importance of soil dilatancy on seismic site response; spikes in acceleration records have been attributed to dilatancy (Zeghal and Elgamal 1994). In centrifuge model tests, many researchers have reported dramatic spikes in acceleration records associated with the onset of dilation (Dobry et al. 1995, and Fiegel and Kutter 1992).

Balakrishnan and Kutter (1999), using data from a centrifuge model depicted in Figure 1, showed that acceleration spikes are closely associated with pulses of reduced pore pressure. They superimposed a set of acceleration time histories with nearby pore pressure time histories and showed clearly that the acceleration spikes are closely associated with the pulses of reduced pore pressure as shown in Figure 2.

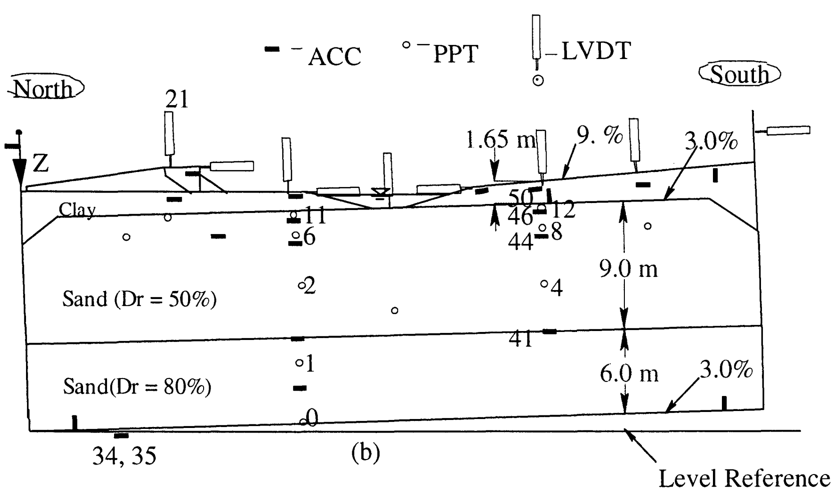

Figure 1. Configuration and instrumentation of Model U50 (Balakrishnan and Kutter 1999)

In this paper, liquefaction is defined as a state for which the mean effective stress (p′) is approximately zero. If there is no effective stress, there can be no friction between particles and no shear resistance. From laboratory testing of saturated soil specimens, it is well known that, on average, pore pressure increases and p′ decreases as the number of cycles of shear stress increases. But it is also well known that large strain cycles can cause a temporary reduction in pore pressure, temporarily increasing p′, due to the dilative tendency of soils that are denser than critical. After a strain pulse triggers dilation, unloading of the shear stress relieves the reduction in pore pressures and p′ may again decrease. In this paper, we use a new term, "de-liquefaction" to describe the temporary solidification of soil caused by dilatancy at large shear strains, and "re-liquefaction" to describe the return to a state with $p' \approx 0$ due to the unloading of the shear stress.

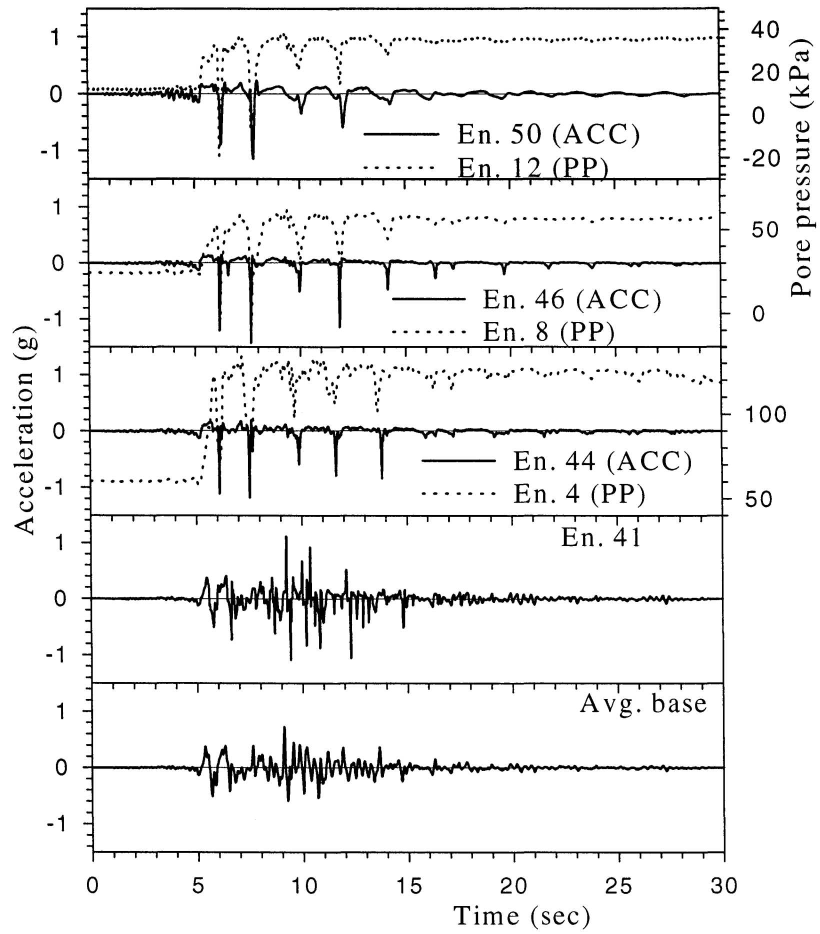

Figure 2. Results from the vertical array of accelerometers and pore pressure transducers in model U50. Instrument entry numbers correspond to locations noted in Figure 1.

It should be noted that de-liquefaction is associated with shear-induced dilatancy; and it is different than sedimentation. Sedimentation involves the solidification due to settlement of a suspension of particles through the pore fluid, as described by Scott (1986). In contrast, shear-induced de-liquefaction may occur in the absence of densification. Of course, it is likely that solidification of liquefied soil may also be triggered by a combination of sedimentation and dilatancy.

Many researchers have obtained element test data showing the phenomena of cyclic de-liquefaction and re-liquefaction. One example of a laboratory test showing repeated de-liquefaction and re-liquefaction of 70% relative density Nevada Sand is shown in Figure 3 (Chen 1995). Figure 3 was obtained from an undrained torsional hollow test with constant total normal stresses ($\sigma_z = \sigma_r = \sigma_\theta = 200$ kPa) during stress controlled cycles of $\tau_{z\theta}$. Examination of this data clearly shows that during undrained loading, the shear modulus is very small while the effective stress is small. But after dilatancy is triggered, the tangent shear modulus increases with strain.

Because the shear modulus (G) increases with strain amplitude, the shear wave velocity (V_s) will increase as strain amplitude increases (V_s = v, where ρ is the soil mass density). In other strain-stiffening materials, for example gasses in compression, it is well known that a shock wave can be developed due to a large disturbance. Kutter and Balakrishnan (1999) suggested that the large acceleration spikes observed in model tests could be attributed to "de-liquefaction shock waves." This paper explains the possible

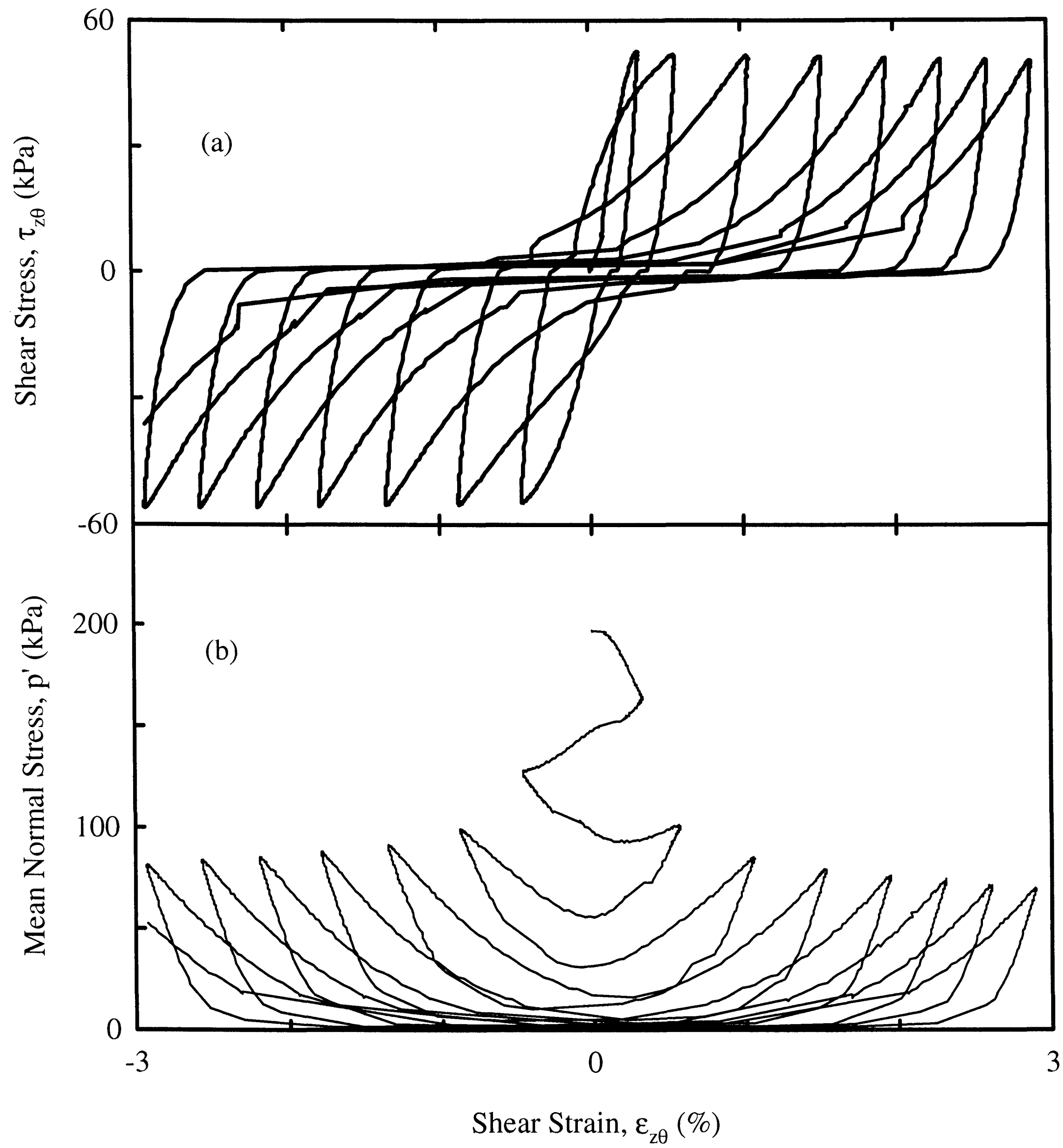

Figure 3. Torsional hollow cylinder test of a medium-dense Nevada Sand (Chen 1995)

mechanism of the formation of shear shock waves as soil de-liquefies. The following sections of this paper include a review of some basic concepts of nonlinear wave propagation and theoretical criteria for the formation of shear shock waves. Expressions for the shock wave velocity are also presented. Finally, evidence is presented that show that the acceleration spike waves observed in centrifuge model tests are consistent with shock waves.

Non-Linear Shear Wave Propagation Concepts

Figure 4 shows a non-linear strain-stiffening stress-strain curve that is typical for a pulse causing dilation and de-liquefaction. We select the zero strain reference at a point O where the shear stress is zero. Suppose that the tangent modulus at point O is G_o, and the tangent modulus at the peak of the stress cycle

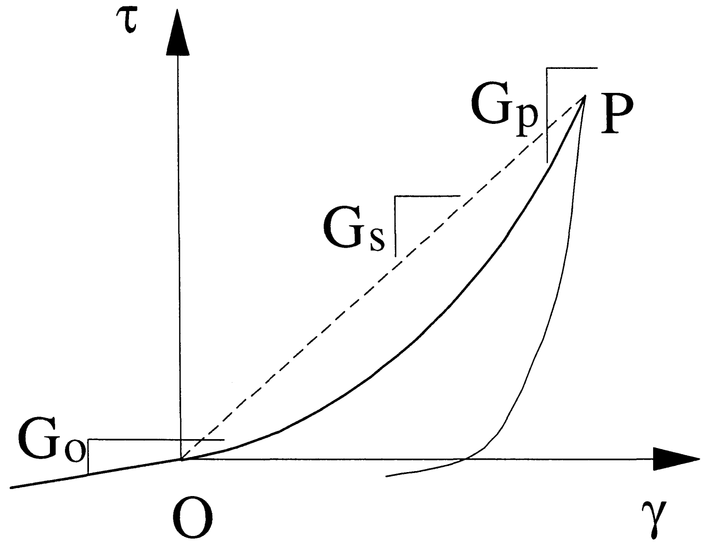

Figure 4 Typical stress-strain relationship for a pulse of shear stress in a dilatant soil that de-liquefies.

(point P) is G_p. The initial increment of a shear stress wave will travel at a speed V_{so} (equation 1) and the peak stress increment will travel at a speed V_{sp} (equation 2):

$$V_{so} = \sqrt{G_o/\rho} \tag{1}$$

$$V_{sp} = \sqrt{G_p/\rho} \tag{2}$$

If the shear modulus was constant, then the peak velocity would equal the initial velocity, and the stress wave would travel through a uniform soil without changing shape. This is the assumption of linear and equivalent linear wave propagation calculations such as SHAKE.

If the shear modulus decreases with strain, then the peak velocity will be less than the initial velocity and the wave will disperse (i.e. the wave front will lengthen).

If, as indicated in Figure 4, the peak shear wave velocity is greater than the initial shear wave velocity, the peak of the stress wave will propagate faster than the beginning of the stress wave and the wave front will become sharper. If the peak of the stress wave catches up with the beginning of the stress wave, a shock wave forms.

Figure 5 illustrates these concepts with three superimposed isochrones of horizontal particle velocity, v, horizontal acceleration, a, and shear stress, τ, for an idealized de-liquefaction wave travelling upward through a soil deposit. It is assumed that initially (prior to $t = t_o$), the entire soil deposit is liquefied and is moving with a constant uniform velocity v_i to the left. While the velocity is uniform and constant, the shear strain rates will be zero, and there will be zero dynamic shear stresses.

Figure 5 supposes that at $t = t_o$, the base motion decelerates to zero velocity. This causes shear strains in the adjacent overlying soil. If the soil dilates and de-liquefies, a wave of shear stress will propagate up through the soil. Suppose at some time $t_A > t_o$ the wave front has progressed to point A_o and the peak of

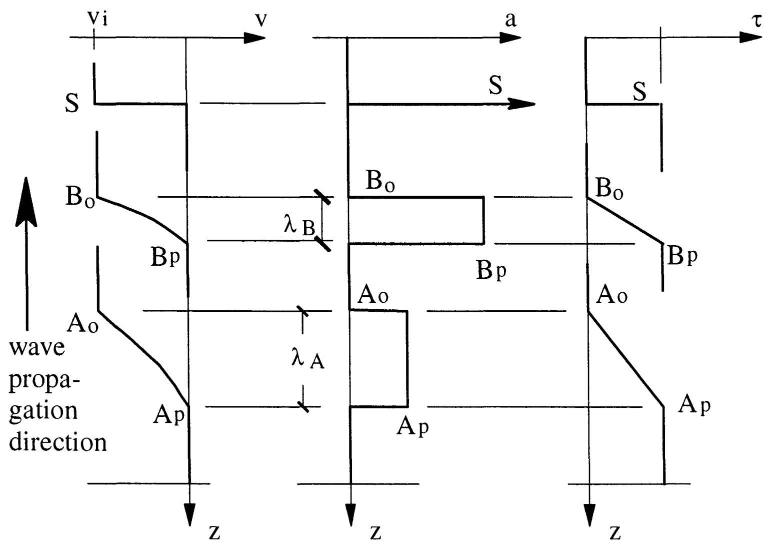

Figure 5. Isochrones of horizontal velocity, horizontal acceleration, and shear stress as a function of depth illustrating the formation of a shear shock wave.

the stress wave has progressed to point A_p. Below point A_p the horizontal velocity is zero and above A_o the velocity is still v_i. Suppose that the horizontal acceleration pulse is uniform at time t_A and has amplitude a_A. The amplitude will be determined by the velocity change across the wave and the duration the wave pulse, T_A, and the change in velocity: $a_A = \Delta v/ \Delta t = v_i/T_A$. The duration of the wave pulse is proportional to the length of the pulse, λ, and inversely proportional to the average wave propagation speed, V_{sAvg} ($T = \lambda/ V_{sAvg}$), providing:

$$a_A = \frac{\Delta v \cdot V_{sAvg}}{\lambda} \tag{3}$$

The shear stress at any depth can be determined by integration of the mass times acceleration of the soil above that depth:

$$\tau = \int_0^z \rho \cdot a \cdot dz \tag{4}$$

For the supposed uniform acceleration pulse, this results in a linear increase in shear stress with depth over the length of the pulse, and uniform shear stresses above and below the pulse as indicated in Figure 5c. Note that point A_o and A_p are associated with points O and P in Figure 4.

Because the soil stiffens as the shear stress increases, the peak of the shear stress wave will be propagating upward at velocity V_{sp} which is greater than V_{so}. So, at some later time $t_B = t_A+\Delta t$, the peak of the wave will have traveled a distance $V_{sp}\ \Delta t$, which is greater than the distance traveled by the front of the wave ($V_{so}\ \Delta t$). Therefore, the length of the wave pulse $\lambda_B < \lambda_A$. To produce the same change in velocity over a shorter wavelength, a greater pulse of acceleration is required; $a_B > a_A$.

As the peak continues to travel faster than the front of the wave, it is only a matter of time (and available space) before the peak catches up with the front. At time $t = t_S$ the shear stress and velocity become discontinuous at the front, and the acceleration theoretically approaches infinity. The location in space

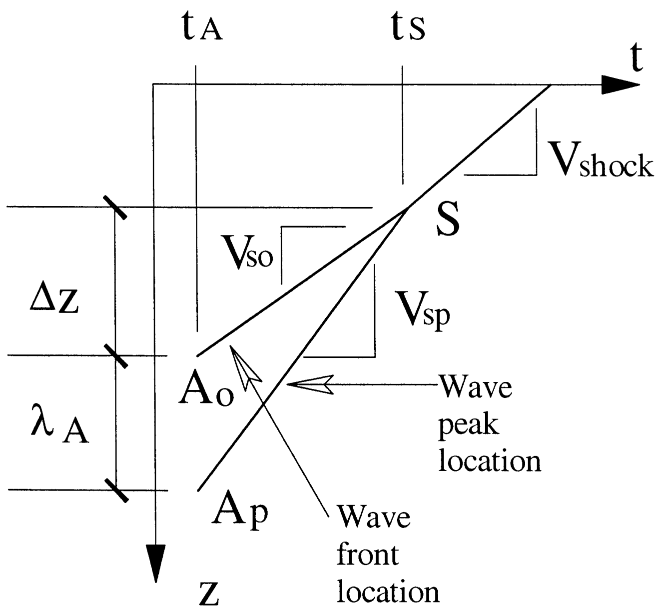

Figure 6. Characteristics of the wave front, the wave peak, and the shock wave for the example presented in Figure 5.

and time at the point of formation of the shock front is determined by the intersection of the velocity characteristics of the front of the wave and the peak of the wave, as shown in Figure 6. If the wave front travels a distance Δz between times t_A and t_S then the peak of the stress wave travels a distance $\Delta z + \lambda_A$. Setting the travel time (t_S - t_A) equal:

$$\frac{\Delta z}{V_{so}} = \frac{\Delta z + \lambda_A}{V_{sp}} \tag{5}$$

provides an expression for the distance required for the shock to form:

$$\Delta z = \frac{\lambda_A V_{so}}{V_{sp} - V_{so}} \tag{6}$$

and this corresponds to a time required for the formation of the shock

$$t_S - t_A = \frac{\lambda_A}{V_{sp} - V_{so}} \tag{7}$$

From these expressions, it is clear that the greater is the difference between V_{sp} and V_{so}, the smaller is the distance required for the shock to form.

After the shock wave forms, it is no longer possible for the peak to travel faster than the front. Based upon established theories of nonlinear wave propagation (e.g., Bedford and Drumheller 1994, the shock wave will travel at an intermediate speed corresponding to the secant modulus, G_s.

$$G_s = \frac{[\tau]}{[\gamma]} \tag{8}$$

The square brackets in the expression for the secant modulus represent the jump in enclosed quantity across the shock front; e.g., $[\tau]$ is the difference between the shear stress in front and behind the shock. The shock wave velocity is then:

$$V_{shock} = \sqrt{G_s / \rho} \tag{9}$$

For the idealized example depicted in Figures 4 and 5, this corresponds to the secant modulus from O to P.

Experimental Evidence of De-Liquefaction Shock Waves

Kutter and Balakrishnan (1999) describe animations of acceleration data in centrifuge model tests and observed very short wavelength spikes of acceleration travelling upward at low speed. One particular spike was determined to travel at a speed of only 6 m/s. This speed can be determined by scaling the distance between accelerometers in Figure 1 and dividing by the time lag between spikes of acceleration apparent in Figure 2. Study of the animations led to the idea that the spikes of acceleration are associated with shock waves in de-liquefying soil.

Centrifuge test description

In another centrifuge experiment conducted at UC Davis (Wilson 1998), a profile of liquefying sand was instrumented with a denser vertical array of accelerometers, as indicated in Figure 7. The soil profile in this test consisted of two horizontal layers of fine, uniformly graded Nevada sand ($C_u = 1.5$, $D_{50} = 0.15$ mm). The lower layer was at a relative density (D_r) of about 80%, while the upper layer was at $D_r \approx 35\%$. Models were tested in a Flexible Shear Beam (FSB) container at a centrifugal acceleration of 30 g. The sand layers were air pluviated, subjected to a vacuum (typically achieving ≈ 90 kPa vacuum), flushed with carbon dioxide, and then saturated under vacuum. The pore fluid was a viscous mixture of water and hydroxy-propyl methyl-cellulose (HPMC) (Stewart et al. 1998). The viscosity of the pore fluid was increased to improve the simultaneous scaling of consolidation and dynamic processes. The results presented are in prototype units. See Kutter (1992) for a discussion of the applicable scaling laws.

The profile was shaken with scaled versions of the strong motion accelerogram from Port Island (83 m

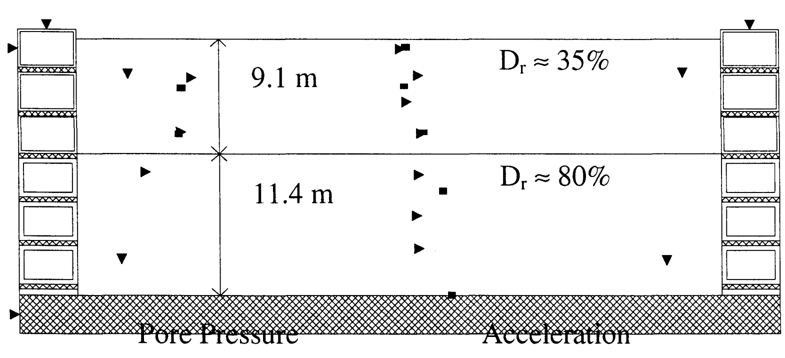

Figure 7. Model layout in Csp2

depth, NS direction) in the Kobe Earthquake. A partial set of time histories from the central vertical array of accelerometers and pore pressure transducers during one shaking event is presented in Figure 8. The recorded pore pressures indicate the excess pore pressure ratios ($r_u = \Delta u/\sigma_{vo}'$) approached 100% throughout the loose sand layer early in shaking. Accelerations near the bottom, middle, and top of the loose sand layer show progressive and dramatic overall de-amplification of the earthquake motion. The formation of shock waves due to de-liquefaction can be observed approximately 3, 4, 6.5, and 8 seconds into shaking. The large (but short duration) spikes of acceleration coincide with sharp decreases in pore pressure as the soil transitions from contractant to dilatant behavior.

The acceleration records can be integrated in time to obtain displacement and velocity time histories, and the acceleration distributions can be integrated over depth at each time step to obtain dynamic shear-stress time histories. Zeghal and Elgamal (1995) describe these procedures. The procedure of Zeghal and Elgamal, however, assumes that the accelerometer spacing is small in comparison to the wavelength, and this is not likely to be accurate if the waves tend to shock.

New Procedure to Interpolate Acceleration Data Between Measurement Points

A new procedure was developed to interpolate acceleration values at positions between the accelerometers. The procedure leverages the high sampling frequency in the time domain to augment the relatively sparse sampling frequency in the space domain using the wave equation to map time domain data into the space domain. In this procedure:

1. The soil profile is divided into two-node, one-dimensional elements with nodes at each accelerometer. Consider an element of length L bounded by nodes numbered i and i + 1with acceleration time histories denoted by $a_i(t)$, and $a_{i+1}(t)$, respectively.
2. The wave propagation velocity, V_s, is assumed to be constant in each element for a given time increment. This velocity is measured manually as the length of the element divided by the travel time for an obvious peak of an acceleration pulse.
3. Waves are assumed to travel upward, with no downward reflected wave.
4. One approximation of the acceleration time history at a point Δz above node i can be calculated using the wave equation:

$$\hat{a}_i(\Delta z, t) = a_i\left(t - \frac{\Delta z}{V_s}\right) \tag{10}$$

5. The same point is also a distance L-Δz below node i + 1 and thus another approximation of the acceleration time history can be calculated using the wave equation:

$$\hat{a}_{i+1}(\Delta z, t) = a_{i+1}\left(t + \frac{(L - \Delta z)}{V_s}\right) \tag{11}$$

6. If the wave was linear and there was no damping, the two approximations for the acceleration should theoretically be identical. But since the system is nonlinear and there is damping, the two approximations will give different results. A weighted average of the two approximations was used to improve either individual approximation:

$$\hat{a}(\Delta z, t) = \left(\frac{L - \Delta z}{L}\right)\hat{a}_i(\Delta z, t) + \left(\frac{\Delta z}{L}\right)\hat{a}_{i+1}(\Delta z, t) \tag{12}$$

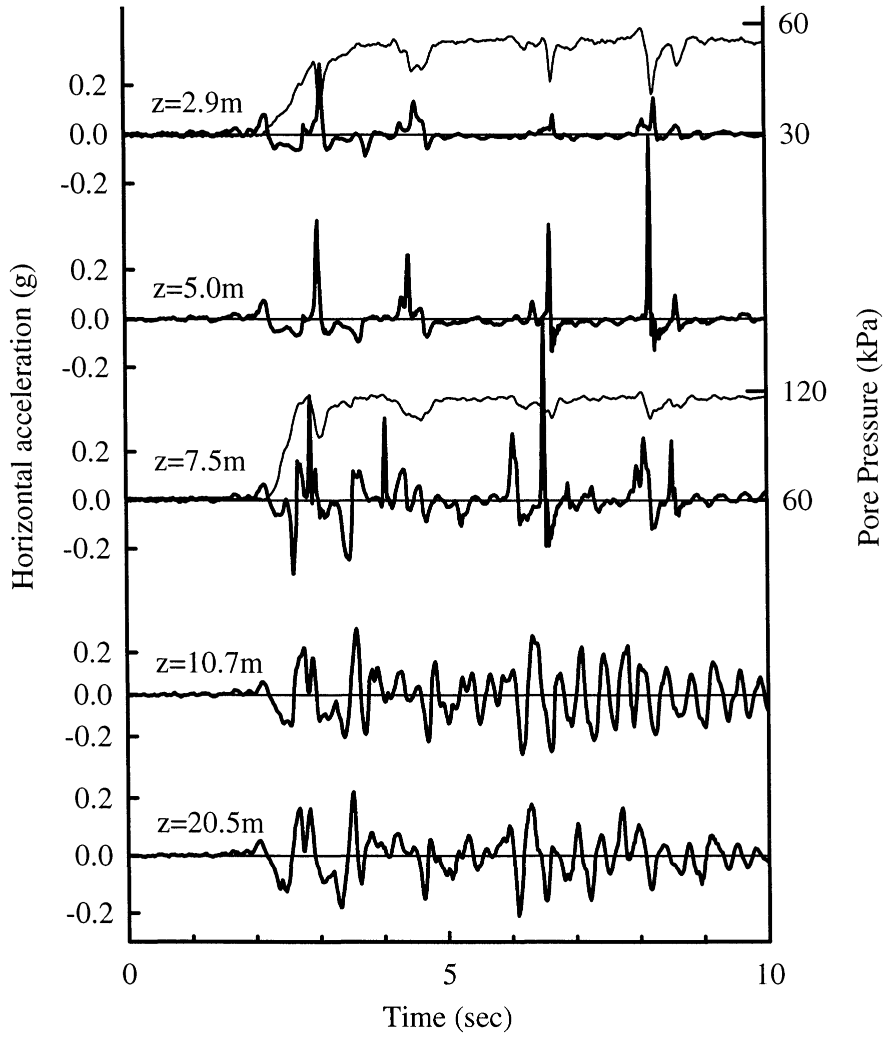

Figure 8. Soil profile response for model layout shown in Figure 7 for one simulated event. Pore pressure transducers are approximately at the same level as accelerometer depths.

Provided that the assumptions stated in steps 2 and 3 above are accurate, this new procedure allows for a reasonable interpolation of the acceleration wave shape between instruments when the wave shape is small compared to the instrument spacing. In comparison, the Zeghal and Elgamal (1995) procedure assumes a linear variation of acceleration between accelerometers, which should yield a reasonable interpolation when the wave shape is large compared to the instrument spacing.

The spatial distribution of displacements and velocities can be approximated using the same procedures using the displacement and velocity time histories calculated from the acceleration time histories. Snapshots of displacement, velocity, acceleration, and shear stress as a function of depth are shown in Figure 9. From these plots a sharp change in strain, velocity, and shear stress across the wave front is apparent.

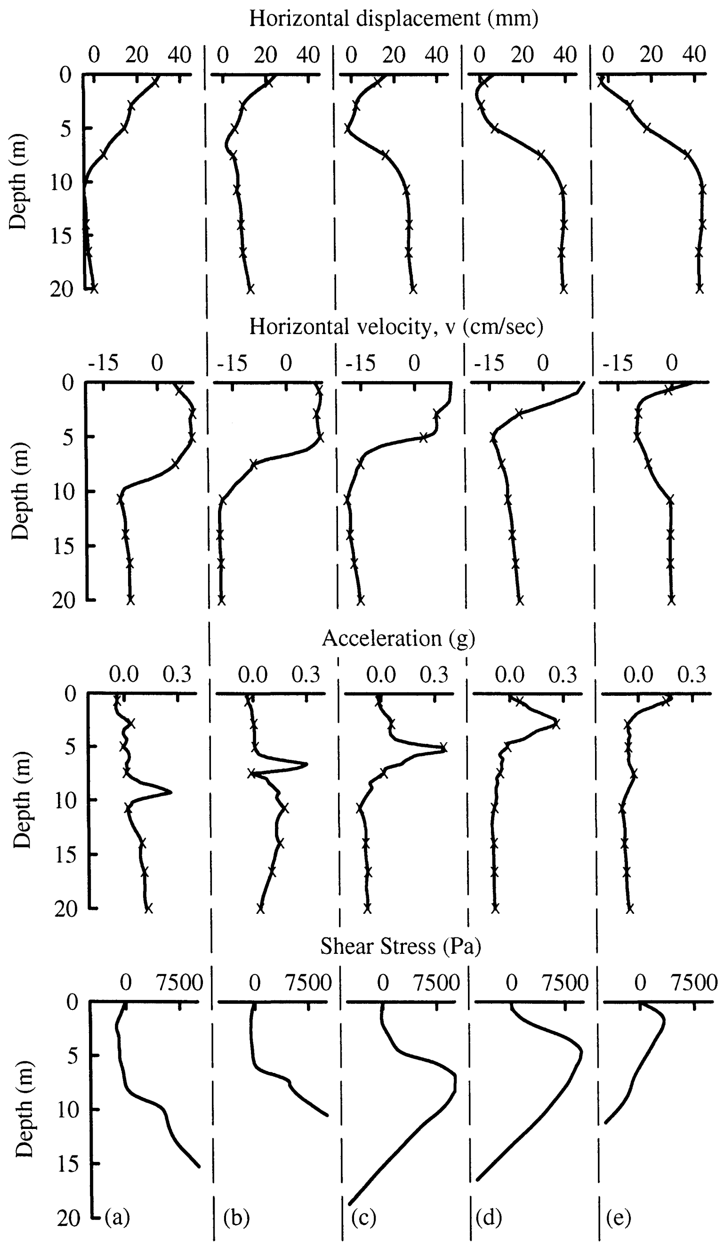

Figure 9. Displacement, velocity, acceleration, and stress distributions interpolated at: (a) t=2.81, (b) t=2.90, (c) t=2.99, (d) t=3.08, and (e) t=3.17 seconds. Depths of accelerometers are marked with an X. Solid lines represent interpolated values using procedure outlined herein.

Limitations of New Interpolation Procedure

The interpolation procedure requires knowledge of the wave propagation direction and velocity. For the present study the velocity was obtained by measurement of the propagation velocity for a particular acceleration pulse within the time interval of interest. Fortunately, the waves in liquefying soil did not appear to reflect downward from the ground surface; the waves in de-liquefying soil appeared to die out at the surface. Accounting separately for upward and downward propagating waves would require more sophisticated interpolation procedures.

Since wave propagation in de-liquefying soil is highly nonlinear, the wave propagation velocity is not truly constant as assumed. While this is clearly not exact, it is considered to be a significant improvement over assuming the acceleration varies linearly in space between measurement points. The wave propagation velocity of the shock wave appeared to be reasonably constant over a particular element as the shock wave passed through the element. The interpolations presented are thus most accurate near the wave front.

The third snapshot of acceleration seems to show the sharpest peak in acceleration. The interpolated width of the shock wave appears to be about 1 m. The acceleration pulse also has a very steep front, apparently increasing from 0.1 to 0.34 g in the space of about half a meter. In the centrifuge model tests, the accelerometers used were about 1 cm in diameter, which (at 30 g centrifugal acceleration) represents 0.3 m in the prototype. The size of the accelerometers may be a factor limiting the resolution of the minimum size of the shock front. The accelerometers will likely smooth the acceleration data over the size of the instrument. To more accurately resolve the shape of the shock wave, smaller instruments may be required.

Another factor that will limit the resolution of the wave front is the filtering and data sampling frequency. Dynamic acceleration data passed through 800 Hz low-pass anti-aliasing filters before being digitized at 2000 samples per second per channel on the centrifuge. No useful data thus exists for frequencies greater than 800 Hz in the model, which corresponds to 800/30 = 27 Hz in the prototype for the event presented. The observed acceleration spike pulses presented are as short as 0.05 seconds, which is near the limit of resolution introduced by the 27 Hz corner frequency of the filters. It appears that the thickness of the measured wave front is thus near the resolution limit of the instrumentation and data acquisition system as employed.

Interpretation of Data From Interpolation Procedure

From the data files, the time for the peak of the acceleration pulse to travel across each element was determined in order to estimate the average wave propagation velocity across each element. Element number 1 corresponded to the top two accelerometers and element two corresponded to the 2nd and 3rd accelerometer from the top, etc. For elements 1 to 4, propagation velocities of 26, 36, 18, 32 m/s were measured, respectively.

If the experimental wave front depicted in Figure 9 is a shock wave, it should be possible to compare the theoretical shock wave velocity (from equations 8 and 9) with the measured velocity of the wave front. To do this, lines were passed through the plots of displacement versus depth in Figure 9 to find the jump in shear strain. Next, the slope of the shear stress above and below the pulse were linearly projected to the location of the center of the pulse; the difference between these linear projections of shear stress at the center of the pulse was taken as the jump in shear stress. The data from these measurements is summarized in Table 1.

Table 1. Jump in strain, stress, and corresponding shock wave velocity

Snapshot Number (from Fig. 9)	$[\gamma]$	$[\tau]$ (kPa)	V_{shock} (eq. 8 & 9) (m/s)
1	0.0039	5.0	25.3
2	0.0029	5.0	29.4
3	0.0102	10.0	22.1
4	0.0071	10.0	26.5

These computed velocities are in very good agreement with the range in measured values for elements 1 to 4 listed above. These calculations suggest that equations 8 and 9 may be useful to calculate the velocity of the acceleration spikes (assuming that the jump in stress and strain are known).

Discussion and Conclusions

In centrifuge model tests and in field case histories, de-liquefaction has been observed to be accompanied by a spike in acceleration time histories. By studying data from dense vertical accelerometer arrays in recent model tests, slow travelling (about 10 m/s) but spatially sharp (about 0.1 m wavelength) de-liquefaction wave fronts have been observed. This paper explains the formation and propagation of these fronts using classical nonlinear wave propagation theory.

In linear undamped uniform media, a wave will propagate without changing shape or frequency content. In strain-stiffening media, waves will tend to steepen; in strain-softening media, waves will tend to broaden. When a wave steepens to the point that the velocity becomes discontinuous a shock wave is formed. A shock can be thought of as a propagating singular surface across which the deformation is continuous, but velocity and strain are discontinuous.

It is well known that during undrained cyclic loading, medium density sands exhibit cyclic mobility and a strain-stiffening tangent shear modulus during undrained loading. The tangent shear modulus actually increases as shear-strain increases. The strain-stiffening response, associated with a temporary reduction in pore pressures caused by dilatancy, causes the classical banana-shaped stress-strain curve. "De-liquefaction" is proposed as a term to describe the solidification due to dilatancy. Strain-stiffening is contrary to the monotonically decreasing modulus reduction curves that are commonly used by geotechnical earthquake engineers.

A significant effort has been made to process centrifuge model test data to enable better visualization of nonlinear wave propagation in soil. This was accomplished by producing animations of centrifuge data including velocity, acceleration, and shear stress distributions as a function of time and space. The application of shock wave theory to nonlinear wave propagation in soil was inspired by repeatedly studying animations of data recorded in centrifuge model tests.

A new procedure for interpolating acceleration values between discrete measurement locations is presented. The procedure uses the wave equation to map time domain data into space and requires knowledge of the wave propagation velocity and direction. Thus, it can be used to back-analyze data but not as a prediction tool. The new interpolation procedure allowed us to improve the resolution of images of the wave front derived from centrifuge model tests. These images indicate a clear acceleration spike, a sharp change in velocity across the wave front, and a jump in the shear stress indicative of a shock wave front.

Shock waves can give rise to very large, high-frequency acceleration pulses. The small wavelength associated with these spikes along with their short duration may or may not make their damage potential low. It is hoped that the data presented in this paper will help engineers to assess the importance of the de-liquefaction acceleration pulses.

In centrifuge models, we tend to experiment with relatively uniform layers of soil. In field situations, the soil profile is likely to be much more variable. The uniform conditions obtained in centrifuge tests may favor the development and stability of a de-liquefaction shock wave. A heterogeneous soil deposit might tend to disperse a shock wave. The size and frequency response characteristics of centrifuge and field instruments may affect recordings of shock waves.

Because de-liquefying soil is strain-stiffening, the speed of a shear wave or shock wave increases with the magnitude of the shear stress; it should be clear that there is no such thing as a unique shear wave velocity in liquefied soil. De-liquefaction waves observed on the centrifuge have been found to travel in the 5 to 30 m/s velocity range, but speeds approaching zero seem possible.

It is not possible to predict the formation of the shock front using linear or equivalent linear procedures because the phenomena is inherently nonlinear. Nonlinear calculations may be used to predict the formation of a shock front, but once a discontinuous shock front forms, the use of continuum finite elements would be theoretically inappropriate.

Acknowledgements

This paper presents experimental data from centrifuge model tests supported by the Pacific Earthquake Engineering Research Center (Award #6761) and the California Department of Transportation (Contracts 65V495 and 95A155). A. Balakrishnan conducted the centrifuge test depicted in Figure 1. Ross Boulanger and Ahmed Elgamal provided valuable comments in recent weeks as we formulated some of the concepts presented in this paper. Tom Kohnke and Dennis O'Brien helped conduct the model tests.

References

Balakrishnan, A. and Kutter, B.L. (1999). "Settlement, sliding and liquefaction remediation of layered soil," *Journal of the Geotechnical and Geoenvironmental Engineering Division*, ASCE, In Press, Vol. 125, No. 11, November.

Bedford, A. and Drumheller, D.S. (1994). *Introduction to elastic wave propagation*, Wiley, Chichester.

Casagrande, A. (1971). "On liquefaction phenomena," Report of Lecture to British Geotechnical Society, P.A. Green and P.A.S. Ferguson, reporters, *Geotechnique*, pp. 197-202.

Chen, Y.R. (1995). *Behavior of a fine sand in triaxial, torsional, and rotational shear tests*, Ph.D. dissertation, Department of Civil and Environmental Engineering, University of California, Davis.

Dobry, R., Taboada, V. and Liu, L. (1995). "Centrifuge modeling of liquefaction effects during earthquakes," *Proc. 1st Int. Conf. On Earthquake Geotechnical Engineering* (IS-Tokyo), Ishihara Ed. Balkema Rotterdam, Vol. 3, 1291-1324.

Elgamal, A. , Yang, Z., Parra, E., and Dobry, R. (1999). "Modeling of liquefaction-induced shear deformation," *Earthquake Geotechnical Engineering*, Proc. Second Int. Conf. On Earthquake Geotechnical Engr., Seco e Pinto (ed.), Balkema, Rotterdam, Vol. 3, 895-900.

Fiegel, G.L., and Kutter, B.L. (1992). "Liquefaction mechanism for layered soil," *Journal of Geotechnical Engineering*, ASCE, Vol. 120, No. 4, 737-755.

Holzer, T.L., Youd, T.L. and Hanks, T.C. (1989). "Dynamics of liquefaction during 1987 Superstition Hills, California Earthquake," *Science*, Vol. 244, 56-59.

Kutter, B.L. (1992). "Dynamic centrifuge modeling of geotechnical structures." *Transportation Research Record* 1336, TRB, National Research Council, National Academy Press, Washington, D.C., pp. 24-

30.

Kutter, B.L. and Balakrishnan, A. (1999). "Visualization of soil behavior from dynamic centrifuge model tests," *Earthquake Geotechnical Engineering*, Proc. Second Int. Conf. On Earthquake Geotechnical Engr., Seco e Pinto (ed.), Balkema, Rotterdam, Vol. 3, 857-862.

Scott, R.F. (1986). "Solidification and consolidation of a liquefied sand column," *Soils and Foundations*, Vol. 26, No. 4, 23-31.

Seed, H.B., and Lee, K.L. (1966). "Liquefaction of saturated sands during cyclic loading," *Journal of the Soil Mechnaics and Foundations Division*, ASCE, Vol. 92, SM6, Nov., 105-134

Stewart, D.P, Chen, Y.R., and Kutter, B.L. (1998). "Experience with the use of methylcellulose as a viscous pore fluid in centrifuge models," *Geotechnical Testing Journal*, GTJODJ, Vol. 21, No. 4, December, 365-369.

Wilson, D.W. (1998). *Soil-pile-superstructure interaction in liquefying sand and soft clay,* Ph.D. dissertation, UCD/CGM-98/04, Center for Geotechnical Modeling, Department of Civil and Environmental Engineering, University of California, Davis. http://cgm.engr.ucdavis.edu/reports.html.

Zeghal, M., and Elgamal, A.-W. (1994). "Analysis of site liquefaction using earthquake records," *Journal of Geotechnical Engineering*, New York :ASCE, Vol. 120, No. 6, pp.996-1017.

Zeghal, M., A.W. Elgamal, H.T. Tang, & J.C. Step 1995. Lotung Downhole Array. II: Evaluation of soil nonlinear properties. *Journal of Geotechnical Engineering*, New York: ASCE, Vol. 121, No. 4, pp. 363-378.

A SIMPLIFIED PRACTICAL METHOD FOR EVALUATING LIQUEFACTION-INDUCED FLOW

Susumu YASUDA
Proffessor
Tokyo Denki University, Japan

Nozomu YOSHIDA
Head of Devision
Sato Kogyo Co., Ltd., Japan

Hiroyoshi KIKU
Research Engineer
Sato Kogyo Co., Ltd., Japan

Kenji ADACHI
President
Jiban-Soft Factory Co., Ltd., Japan

ABSTRACT

A simplified method is proposed to evaluate the ground deformation due to liquefaction-induced flow. Under the assumption that liquefaction-induced flow occurs slowly after the main shaking, stress-strain relationship after liquefaction is obtained through the laboratory test in which sand sample is subjected to monotonic load after subjected to cyclic load causing liquefaction or more. The authors applied this method to the grounds behind quaywalls, a gentle slope and a river dike in Kobe, Noshiro and Hokkaido, respectively, where very severe damages occurred during past earthquakes, to demonstrate the adaptability of this procedure. The proposed method predict liquefaction-induced ground deformation well.

INTRODUCTION

Liquefaction brings very large residual deformation of grounds and earth structures such as ground flow behind quaywalls and settlement of embankments. Evaluation of the liquefaction-induced deformation is necessary for precise seismic design. However, it is hard to evaluate large deformation by almost all seismic response analytical codes because large strain cannot be considered in these codes.
The authors developed a simplified method to evaluate the liquefaction-induced large deformation. The code of the developed method is named "ALID" (Analysis for Liquefaction-induced Deformation). In the method, the authors assumed that residual deformation would occur in liquefied ground due to the reduction of shear modulus. In this paper, the reduction of shear modulus studied by laboratory tests are showed at first. Then principal of the method and some applications are presented.

TORSIONAL SHEAR TESTS TO STUDY POST LIQEFIEFACTION BEHAVIOR

Test apparatus and procedures

Torsional shear test apparatuses were used to study the post liquefaction behavior. Toyoura sand which is a clean sand was used at first to study the effects of density, confining pressure and severity of liquefaction. Then several sands were tested to study the effect of fines content. (Yasuda et al., 1998) Specimens were saturated, applied back pressure and consolidated. Then a prescribed number or prescribed amplitude of cyclic loadings was applied in undrained condition. Safety factor against liquefaction, FL, which implies severity of liquefaction was controlled by the number of cycles or amplitude of the cyclic loadings. After that a monotonic loading was applied under undrained condition with a relatively high speed of γ=10% in a minute, as shown in Figure 1. Relationships among shear stress, τ, excess pore pressure, Δu, and shear strain, γ in the monotonic loading were measured.

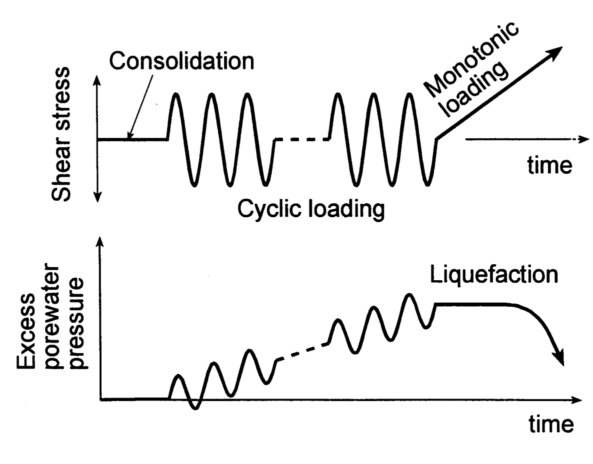

Fig.1 Procedure of cyclic and monotonic loading by torsional test device

Typical test results and definition of G_{0i}, G_N, G_1 and γ_L

Figure 2 shows stress-strain curves and excess porewater pressure-strain curves in the case of Toyoura sand with different relative densities, Dr. Scales of axes in Figure 2(c) are enlarged one of Figure 2(a). Shear strain increased with very low shear stress up to very large strain. Then, after a resistance transformation point, the shear stress increased comparatively rapidly with shear strain, following the decrease of pore water pressure. As shown in Figure 2(c), shear strain up to the resistance transformation point increased with the decrease of Dr. And, shear modulus up to the resistance transformation point decreased with the decrease of Dr. As shown in Figures 2, shear stress increased comparatively rapidly after a resistance transformation point.

The amount of strain up to the resistance transformation point is called the "reference strain at resistance transformation, γ_L" as shown in Figure 3. Stress-strain curves before and after the reference transformation point can be presented approximately by a bilinear model with G_1, G_2 and γ_L :

$$\tau = G_1\gamma \qquad \text{for } \gamma < \gamma_L \qquad (1)$$

$$\tau = G_1\gamma_L + G_2(\gamma-\gamma_L) \qquad \text{for } \gamma \geqq \gamma_L \qquad (2)$$

where G_1 and G_2 are the shear moduli before and after the reference transformation point, respectively.

To know the reduction rate of shear mudulus due to liquefaction, the rate of shear modulus G_1/G_0, which is the ratio of shear modulus after and before liquefaction, was calculated. Two types of G_0 were selected : ① $G_{0,i}$: secant modulus of stress-strain curves at γ=0.1 % in the case of without cyclic loading ($\Delta u/\sigma_v'$ =0) and ②G_N : estimated from SPT N-value by the formula of G_N=28N. In the first shear modulus, 0.1 % of shear strain was selected because the strain of soils which occurs in the ground due to overburden pressure is estimates as around γ=0.1 % in usual case. The second one is widely used for the design of foundation in Japan.

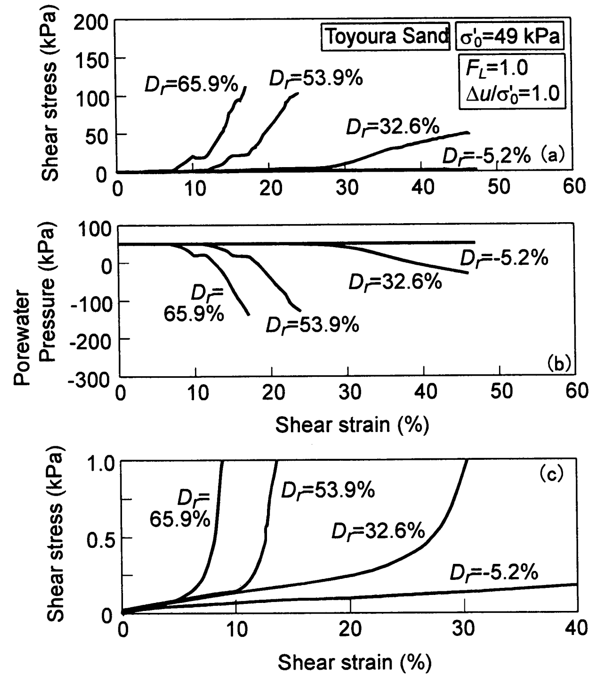

Fig.2 Stress-strain and strain-pore water pressure curves for Toyoura sand

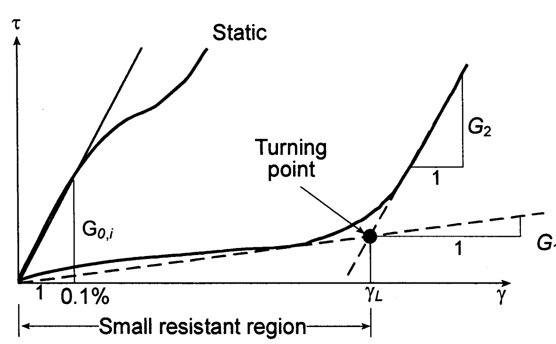

Fig.3 Definition of G_{0i}, G_1 , G_2 and γ_L

Relationships among shear modulus ratio, F_L and fines contents

Relationships between the shear modulus ratio, $G_1/G_{0,i}$ and fines content less than 75 μ m, Fc, in the range of FL =0.9 to 1.0 were plotted in Fig 4. The ratio $G_1/G_{0,i}$ increased with Fc. Though figures are not shown here, $G_1/G_{0,i}$ decreased with FL. Based on the test results, relationships among shear modulus ratio, FL and Fc are summarized as shown in Fig.5.

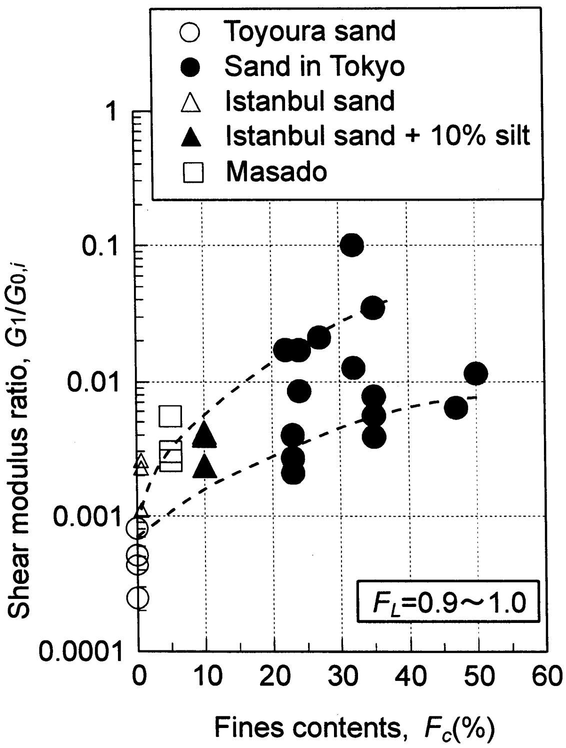

Fig.4 Relationships between shear modulus ratio and fines contents

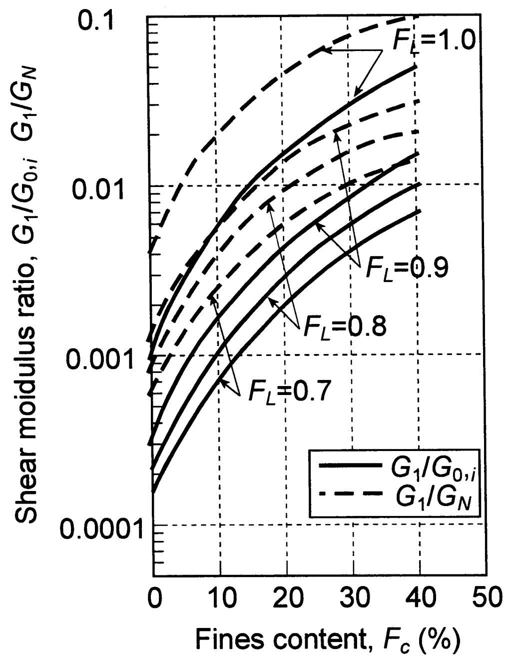

Fig.5 Summary of relationships among shear modulus ratio, FL and fines contents

OUTLINE OF THE PROPOSED METHOD

Concept of the proposed method

Figure 6 shows the concept of the stress-strain curves which are used in the proposed method for liquefaction-induced deformation. Line l denotes a backbone curve at the beginning of the earthquake. Point A in Fig.6 is supposed to be initial state of a soil element in the ground. When excess porewater pressure generates, material properties such as shear strength and elastic moduli change. Suppose that the backbone curve moves from l to m due to liquefaction, then strain should increases in order to hold the driving stress. Since driving stress, however, decreases according to the change of geometry, actual strain increment from state l to m is from A to C. Namely, strain increment caused by the change of material property is $\gamma_C - \gamma_A$' Ground flow stops when new material property comes to balance with a new driving stress, which is shown as point C in the figure. In the proposed method here, two paths : ①A to C through B and ② O to C through B are assumed though the actual path is A to C because of simplification. If the two paths are assumed, two procedures to analyze the liquefaction-induced deformation are available:

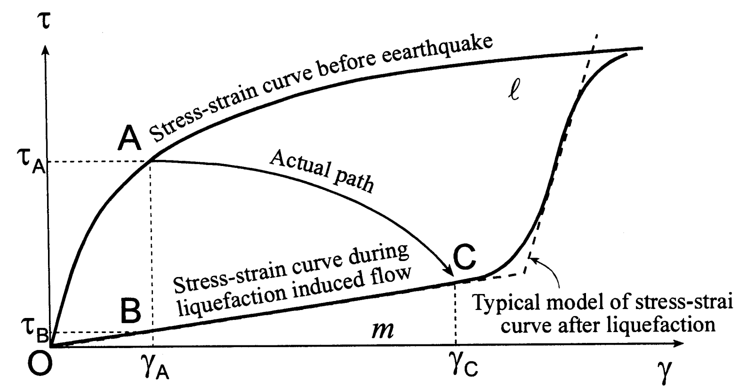

Fig.6 Schematic of stress-stain curves

a)Stress relaxation method

In the first stage, state before the earthquake is calculated by the FEM using stress-strain curve ℓ. Then by holding the strain, stress-strain curve is changed to m. In this stage, external stress and internal stress are not balanced because the strain is fixed. Therefore it is necessary to relax the unbalanced stress. During the process of the relaxation , increment of shear strain due to liquefaction, γ_c-γ_A and liquefaction-induced deformation of the ground can be calculated.

b)Self weight method

In the first stage, deformation of the ground is calculated by the FEM using stress-strain curve ℓ same as the stress relaxation method. Then the same gravity force is applied to the same model again by using the stress-strain curve m. Deformation due to liquefaction-induced flow can be evaluated by deducing the deformation form the second one to the first one.

Both methods have merits and demerits. Stress relaxation method is reliable and any stress-strain curve can be applied. However, special modification is necessary from the conventional FEM codes. Self weight method can not take into account the change of the driving force, but arbitary FEM program can be used. In the following analyses, the self weight method are employed with linear stress-strain relationships.

Modeling of the ground

In the modeling of the liquefied soil layers, FL of liquefiable layer is evaluated at first by some method. Then the rate of reduction of shear modulus due to liquefaction is estimated by laboratory tests or Fig.5. Shear modulus of the upper unliquefiable layers had better to be reduced because frequently cracks are induced in the unliquefiable layers during the liquefaction-induced flow. Shear modulus ten times larger than that in the liquefiable layer was applied in the following analyses based on several back analyses during past earthquakes.

If the boundary between ground and caisson or sheet pile walls is connected directly, the ground just behind the walls cannot settle. Therefore, it is recommended to use joint elements or double nodes which move together in the horizontal direction but move independently in the vertical direction.

Subsidence of the ground surface occurs by two mechanism : geometrical change due to the flow and densification due to dissipation of excess porewater pressure. The subsidence by the first mechanism is evaluated automatically in this analysis. Some additional analyses are necessary to evaluate the subsidence due to the second mechanism. Though an analytical procedure in FEM is available to evaluate the subsidence, simple estimation, for example estimation by the Ishihara and Yoshimine's method (1992), is recommended because modification of standard programs is not so easy.

Note for locking of element

Because undrained behavior is assumed in the analysis of liquefaction-induced flow, apparent bulk modulus or total bulk modulus of the liquefied sand can become very large, resulting in Poisson's ratio to be close to 0.5, In such a situation, it is known that deformation of the element is constrained as Poisson's ratio reaches to 0.5 if two point Gauss-Legendre integral that is commonly used in the finite analysis is employed in computing the element stiffness matrix. This phenomena is known to be locking of element. Reduced integral technique is known to be effective to avoid locking effect, but it creates another problems, i.e., hourglass instability. This problem can be avoided by employing the anti-hourglass stiffness. In this section, we examined various methods to compute element stiffness matrix in order to make the effect clear. Element stiffness matrix was computed by the following four methods:

1) Two point Gausse-Legendre integral
2) Reduced integral (one point Gausse-Legendre integral)
3) Reduced integral with anti-hourglass stiffness (Yoshida, 1989)
4) Condense from four triangular element

Two point Gauss-Legendre integral is the most common method in the finite element analysis. The quadrilateral element is divided into four elements by making a new node at the center of the element in the condense method. Element stiffness matrix of the quadrilateral element is made by eliminating the internal node internally. This condense dose not affect the result, therefore, if a computer code does not have this function, one can divid the quadrilateral element into four triangular element by hand. It is not recommended to divide a quadrilateral element into two triangular elements because stiffness has direction dependent characteristic.

The Uozakihama site shown later was used. The results are show in Fig.7, and can be summarized as follows:

a) A conventional method, i.e., two point Gauss-Legendre integration underestimate displacement very much. Therefore this method is not recommended.

b) Distinct hourglass mode deformation is observed if only reduced integration is employed. Therefore, deformation pattern of each element sometimes seems extraordinary. The average deformation, however, nearly the same with following two cases.

c) Both reduced integral with anti-hourglass stiffness and condense from triangular element show nearly the same displacements. Therefore reduced integral with anti-hourglass stiffness is the best

method because amount of calculation is smaller. If the computer code does not have anti-hourglass stiffness, one can use triangular elements by dividing a quadrilateral element into four triangular elements.
If one does not mind the deformation of each element but want only global feature, one can use reduced integral, too.

TYPICAL ANALYSED RESULTS

The proposed method "ALID" was applied to several structures which were damaged during past earthquakes, to demonstrate the adaptability of the method. Among them three cases are shown in this paper. In the analyses, shear modulus before the earthquake were estimated by SPT N-values, and FL was evaluated by the method introduced in the Specification for Highway Bridges (1996).

A caisson type quay wall at Uozakihama

A caisson type quay wall moved toward the sea and the ground behind the wall flowed at Uozakihama in Kobe during the 1995 Hyogoken-nambu earthquake. Horizontal displacement of the wall was 2.0 m and the flow extended to more than 100 m from the wall. Fig.8 shows the analyzed result. Horizontal displacement of the wall was 1.2 m and the flow extended more than 100 m. It can be said that analyzed results agree well with the actual damage.

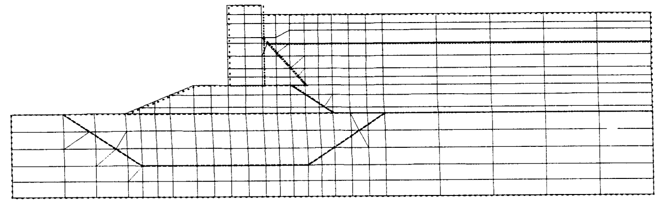

1) Two point Gausse-Legendre integral

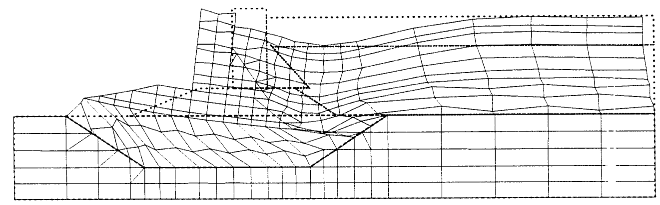

2) Reduced integral (one point Gausse-Legendre integral)

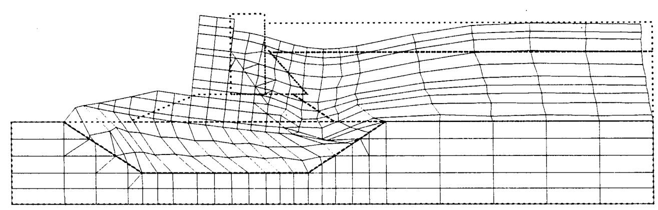

3) Reduced integral with anti-hourglass stiffness

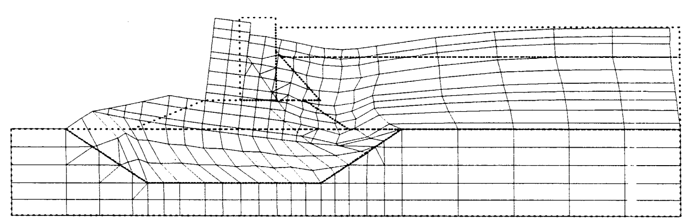

4) Condense from four triangular elemrnt

Fig.7 Comparison of deformation computed by four methods

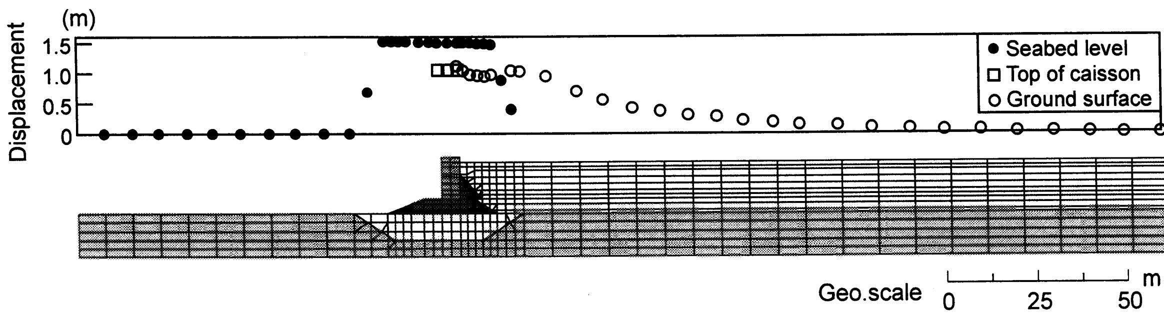

(a) Meshes for FEM and distribution of displacement

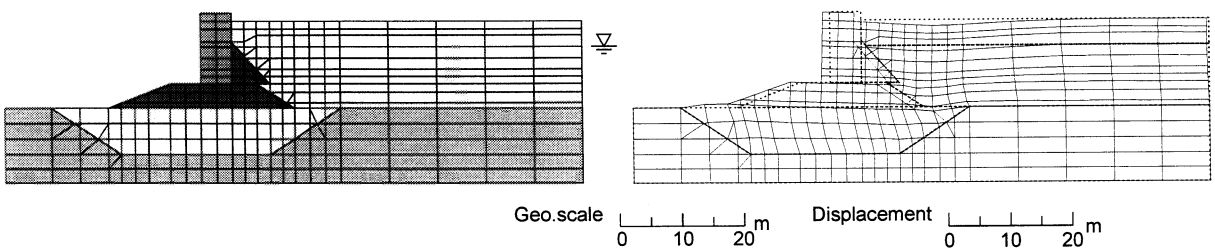

(b) Meshes for FEM and Deformation around caisson

Fig.8 Deformation of the ground behind a quay wall

A gentle slope at Aoba-cho

A very gentle slope with the gradient of about 1% flowed due to liquefaction at Aoba-cho in Noshiro City during the 1983 Nihonkai-chubu earthquake. Analyzed deformation is shown in Fig.9. Figure 10 compares the distribution of horizontal displacement. As shown in this figure, average displacement is fairly coinceded with the actual displacement. Exactly speaking, however, displacement is underestimated in the left side in the cross section. Two reasons may exist : ①a steep slope which is located at left outside from this figure pushed the soil layer to right direction and ②nodal points at left boundary cannot move in the horizontal direction in the analysis.

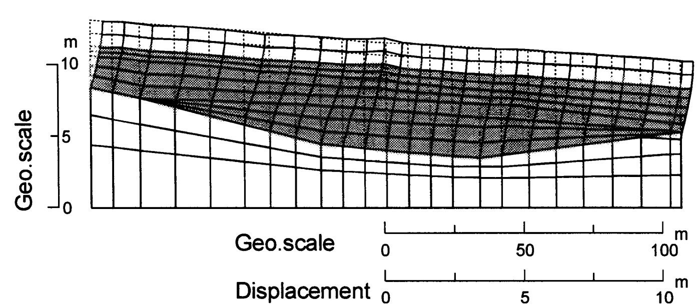

Fig.9 Deformation of a gentle slope

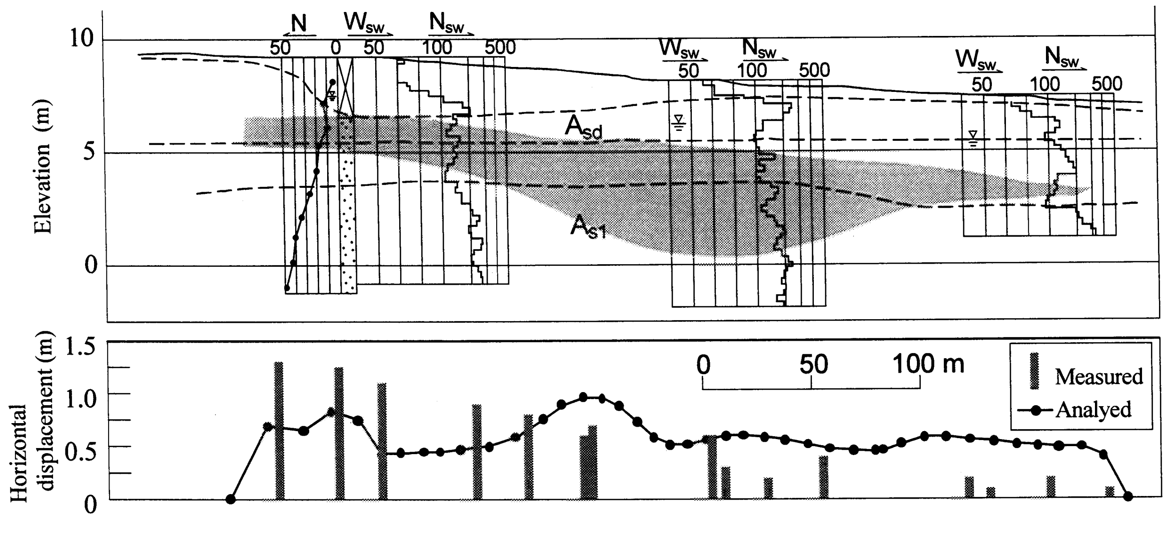

Fig.10 Distribution of displacements on the ground surface

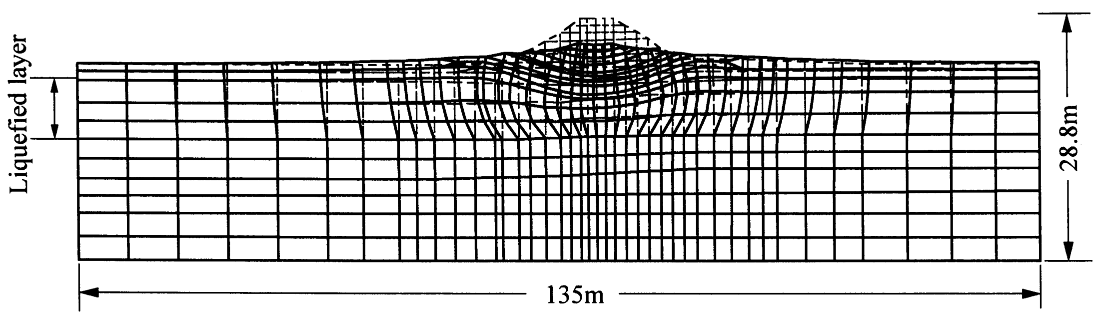

Fig.11 Deformation of a river dike

A river dike in Hokkaido

River dikes of the Siribeshi-toshibetsu river were damaged due to liquefaction during the 1993 Hokkaido-nansei-oki earthquake. Settlement of the dike at near Shin-ei Bridge was 2.6 m. Two shear moduli were assumed for the embankment in the analyses: ①shear modulus does not decrease②shear modulus decrease as same as the unliquefiable layer. Figure 11 shows the deformation analyzed under the second assumption. Analyzed settlement on the top of the embankment was 0.9 m and 3.2 m, respectively. Therefore, some reduction of shear modulus of embankment may be necessary.

CONCLUSIONS

A simplified method to evaluate liquefaction-induced deformation was proposed. Then adaptability of the method was confirmed by several case studies. As the proposed method is very sensitive for reduction of shear modulus, it is recommended to conduct laboratory tests. Moreover, special attention is necessary for locking effect. Reduced integral with anti-hourglass stiffness is the best method to avoid the locking effect. However, if the code does not have anti-hourglass stiffness, triangular elements by dividing a quadrilateral element into four triangular elements are also available.

AKNOWREDGEMENTS

Cyclic torsional shear tests were conducted by Mr. T. Terauchi and Mr. H. Morimoto. Soil data at the dike was provided by a technical committee organized by Japan Institute of Construction Engineering. The authors would like to express their thanks to them.

REFERENCES

1) Ishihara,K. and M. Yoshimine (1992): Evaluation of settlements in sand deposits following liquefaction during earthquakes, Soils and Foundations, 32: 173-188.

2) The Japan Road Association (1996): Specifications for Highway Bridges.

3) Yasuda, S., T. Terauchi, H. Morimoto, A. Erken & N. Yoshida (1998): Post liquefaction behavior of several sands, Proc. of the 11th European Conference on Earthquake Engineering.

4) Yoshida, N. (1989): Finite displacement analysis on liquefaction-induced large ground displacements, Proc., 2nd Japan-US Workshop on Liquefaction, Large Ground Deformation and Their Effects on Lifeline Facilities, : 207-217.

NUMERICAL EVALUATION OF LIQUEFACTION INDUCED GROUND OSCILLATION AND LURCH

by

Geoffrey R. Martin(1) and Ping Qiu(2)

(1) University of Southern California, Los Angeles, California
(2) Woodward Clyde Consultants, Santa Ana, California

ABSTRACT

The occurrence of liquefaction in soil layers at depth during earthquake ground shaking, can lead to large ground oscillations and permanent ground displacement (ground lurch) of overlying surficial soil layers. Past earthquakes have demonstrated that such ground displacements and associated shear deformations in the liquefied soil layer, can lead to significant damage to piles and buried pipelines. In the case of buried pipelines, relative displacements or ground oscillations in surface layers generated by non-uniform site conditions can result in ground cracking and compression leading to pipeline damage.

In this paper, a modified version of the one dimensional non-linear effective stress site response program DESRA (DESRA-MUSC) is used to illustrate the sensitivity of ground oscillation and lurch amplitudes to site stratigraphy and input ground motion characteristics. The features of the new program DESRA-MUSC are also described and are shown to be compatible with the practical application of numerical evaluations of ground oscillation and lurch potential for design purposes.

INTRODUCTION

As described by Youd (National Research Council, 1985), earthquake induced liquefaction of soil strata at some depth in level ground sites, "commonly decouples overlying soil blocks, allowing them to jostle back and forth on the liquefied layer during an earthquake." This is illustrated schematically in Figure 1. Pease and O'Rourke (1997) note a number of case studies providing field evidence of ground oscillation damage, and investigated this mechanism as the cause of pipeline damage in the Marina District during the 1989 Loma Prieta earthquake. The role of liquefaction induced ground oscillations in causing pipeline breakage in the Northridge earthquake is described by Holzer et al. (1999). In the case of pipelines, Pease and O'Rourke (1997) attribute damage to ground strains arising from differential ground oscillations associated with varying depths of liquefied soil, as shown in Figure 2. In the case of pile foundations, large ground oscillations or permanent ground lurch generated by a large velocity pulse, may place excessive displacement ductility demand on the piles, resulting in damage. For bridge viaduct structures, differential transverse or longitudinal displacements between adjacent bents, may lead to deck collapse.

The magnitude of ground oscillations or permanent ground lurch will depend on a number of variables including the amplitude and frequency characteristics of the firm ground post liquefaction ground motions underlying the liquefied soil layer, and the stress-strain characteristics and thickness of the liquefied ground layer. For large magnitude near field earthquakes in particular, where post liquefaction damage potential to pipelines and structures arising from ground deformations could be significant, an analytical approach to evaluating site specific ground oscillation lurch magnitudes is desirable. Such an analysis requires a non-linear effective stress approach to evaluate both earthquake excess pore pressure response and post liquefaction ground deformations. In this paper, a modified version of the non-linear effective stress site response program DESRA (DESRA-MUSC) is used to illustrate the sensitivity of ground oscillation and lurch amplitudes to site stratigraphy and input ground motion characteristics.

THE DESRA-MUSC COMPUTER PROGRAM

Background to the DESRA program

They computer programs DESRA and DESRA -2 are described and published by Finn et al. (1978) and Lee and Finn (1978) respectively. The constitutive model for excess pore pressure generation during earthquake induced ground response is based on the model described by Martin el. al. (1975), where shear strain amplitude dependent volume changes during drained loading cycles are coupled to pore pressure increases under undrained loading cycles through elastic rebound parameters. Non-linear ground response is characterized by a hyperbolic shear stress-shear strain curve initially defined by drained maximum shear modulus G_m and shear strength τ_m parameters. These parameters are subsequently degraded (Figure 3) as a function of pore pressures increases to selected low limiting values when excess pore pressures approach the initial vertical effective stress. Hysteresis loops are defined during load and unload cycles using the Masing criterion. The degradation rules used in DESRA for G_m and τ_m are:

$$G_{mt} = G_{mo}(1\text{-}u/\sigma'_{vo})^{1/2} \qquad (1)$$

and

$$\tau_{mt} = \tau_{mo}\ (1\text{-}\ u/\sigma'_{vo}) \qquad (2)$$

where G_{mt} and τ_{mo} are initial low strain modulus and shear strength respectively and G_{mt} and τ_{mt} are degraded values at time *t*.

A value of the excess pore pressure u approximately 90-95% of the initial vertical effective stress σ'_{vo} is often used to set values of the minimum limiting residual values approaching liquefaction.

Based on experimental data such as that shown in Figure 4, Matasovic and Vucetic (1993) noted equation (2) overestimates the stress degradation that occurs as pore pressures increase, and modified the degradation rule as:

$$\tau_m = \tau_m\ [(1\text{-}\ u/\sigma'_{vo})^{\nu}] \qquad (3)$$

Values of ν depend on soil type and were typically about 3.5. Comparisons between equations (2) and (3) are shown in Figure 5, together with a square root degradation rule used in analyses described in this paper.

Note that the degradation model does not take into account the post liquefaction undrained dilative behavior that can occur at large cyclic shear strains in the case of dense sands, such as illustrated in Figure 6, and the corresponding cyclic reductions in pore pressure. Such behavior has also been observed in the field (Zeghal and Elgemal, 1994) and in centrifuge tests. However, the post liquefaction low residual shear resistance (prior to dilation) will in most cases control ground oscillation amplitudes, particularly for looser sands and higher frequency input motions where cyclic shearing strains are less than those required to cause significant dilation. Note that values of residual resistance τ_m of about 0.1 σ'_{vo} seem representative of experimental data irrespective relative density.

As with all non-linear dynamic response programs, the key to practical application is the simplicity of the constitutive model and the ease of parameter selection to match insitu soil conditions. In this respect, two studies are noteworthy in promoting the practical application. Martin et. al. (1981) describe parametric studies using DESRA-2 to establish an approach to backfit the 4 volume change and 3 rebound constants in the model to match a given field liquefaction strength curves, established from say SPT data. Byrne (1991) describes a procedure to reduce volume change constants from 4 to 2, and relates parameters to relative density to match liquefaction strength curves, assuming reasonable and constant values of the rebound parameters. Values of G_m and τ_m may also be related to SPT blowcount, and Byrne (1991) notes good agreement with the simplified constitutive model and laboratory test data.

THE DESRA-MUSC PROGRAM

Over recent years the DESRA-2 program has been modified by research programs conducted at USC to form the program DESRA-MUSC. The modifications are described in detail by Qiu (1998), and are summarized below.

In relation to the previous discussion, the DESRA-MUSC program incorporates the option of using the 2 parameter Byrne (1991) volume change model used to match liquefaction strength curves, and the Matasovic and Vucetic (1993) residual resistance degradation model. Another key modification is the replacement of the hyperbolic backbone curve by the more versatile Iwan (1967) kinematic strain hardening model, which in a one-dimensional form, can be simulated numerically by a mechanistic array of elastic (k_i) and coulomb sliding resistance (R_i) elements as shown in Figure 7. Using this model, an initial loading or backbone curve may be built up as a piecewise linear approximation as shown in Figure 8. Usually 10-20 elements are sufficient to produce reasonable results. The model automatically simulates the Masing criteria resulting in hysteresis loop generation during cyclic loading. An additional bi-linear element has been added to simulate observed low strain damping.

From a practical standpoint, an initial backbone curve can be constructed using established relationships between G/G_m versus shear strain γ as shown in Figure 9, and knowledge of site shear wave velocities or G_{max} versus SPT blowout relationships. Unfortunately, G/G_m versus $\dot{\gamma}$ data is generally restricted to values of γ less than about 0.5%. Consequently, judgement is required to construct the balance of the backbone curve at larger strains to meet the assumed τ_m value, defined as residual lower strain resistance (approximately the drained strength for sands) as opposed to the large strain undrained strength for dilatant soils as shown in Figure 10. Clearly more research and test data is needed in the larger strain range, to better define the non-linear backbone curve shapes for response analyses.

As for the original DESRA-2 program, analyses may be performed in a totally undrained mode, or alternatively, allow dissipation and/or re-distribution of excess pore pressures incrementally in analysis time steps, by solving the one dimensional consolidation equation. The elastic rebound parameters define the coefficient of compressibility and permeability is used as an additional input parameter.

With the above program modifications, Qiu (1998) describes a number of earthquake site response analyses using the schematic approach shown in Figure 11. The DESRA-MUSC program includes a transmitting base boundary as illustrated. The following examples illustrate applications of the program to study liquefaction induced ground oscillation.

SINGLE LAYER SENSITIVITY STUDY

To illustrate the influence of input motion frequency and values of residual resistance on ground oscillation amplitudes, an idealized simple model was considered. The model comprises a 10 foot thick loose saturated sand layer (SPT blowcount N_{160} = 9) overlying soft rock and subjected to sinusoidal 0.8g amplitude ground (rock outcrop) input accelerations. Soil parameters used in the DESRA-MUSC analyses are listed in Table 1 below. And are consistent with a liquefaction strength curve for a sand with N_{160} = 9. Analyses were performed in an undrained mode simulating an impervious cap on top of the sand layer, with an assumed constant post residual resistance.

Table 1. Basic Material Properties in the Case Studies

Soil Properties	
SAND	
Unit Weight (pcf)	122
Friction Angle	33
Shear Wave Velocity (ft/s)	560
Residual Shear Resistance (psf)	200
BEDROCK	
Unit Weight (pcf)	130
Shear Wave Velocity (ft/s)	1800

Parameters for Pore Pressure Model	
k	0.0025
m	0.38
n	0.6
C_1	0.415
C_2	1.157
C_3	0.434
C_4	0.888

Effect of Input Frequency on Ground Oscillation

Figure 12 shows analysis results for 1, 2 and 5 hz input motions at a depth of 5 ft. Liquefaction is seen to occur after about 2 cycles when steady state accelerations drop to about 0.3g corresponding to an assumed post liquefaction residual resistance of 200 psf. For a 1 hz input motion, ground oscillation amplitudes are about ± 1 ft. (10% shear strain in 10 ft.) and show about a 1 ft. permanent ground lurch. As input frequencies increase to 2 and 5 hz, ground oscillation and permanent lurch amplitudes are seen to reduce significantly.

Effect of Assumed Residual Resistance

Figure 13 shows analysis results at a depth of 5 ft. for a 1 hz input frequency and for assumed residual resistance values of 80, 200 and 400 psf. Post liquefaction acceleration levels are reduced with reductions in residual resistance is would be expected. However, amplitudes of oscillation increase only slightly with decreased residual resistance although significant increases in permanent ground lurch occur.

CASE STUDY – MULTILAYER SITE PROFILE

The soil profile and physical soil properties used in the case study analyses are shown in Figure 14, and are representative of an actual site in Southern California. Field liquefaction strength curves for the three sand layers are shown in Figure 15 together with the matched analytical curves using the DESRA-MUSC parameters. The elastic rebound curves for the sands are also shown in Figure 15 together with the normalized shear strength-shear strain non-linear backbone curves. The latter curves were based on the ERPI (1993) G/G_{max} versus shear strain amplitude curves up to strains of about 1% and then extrapolated to estimated failure strains. Post liquefaction residual resistance values for the three sand layers were arbitrarily assumed equal to 0.15 times the average initial vertical effective stress in each layer namely: layer 3, 180 psf, layer 6, 360 psf, and layer 8 , 450 psf.

Total stress behaviour with no pore pressure increases was assumed for the clayey silts. For the clayey silts, the static undrained shear strengths were assumed for analyses with backbone shear stress-shear strain curves developed using the G/G_{max} versus shear strain amplitude curves given by Vucetic and Dobry (1991) for a PI = 50, with extrapolation to failure strains beyond 1%.

Two earthquake records were used as rock outcrop motions, namely the 1992 Landers earthquake Amboy record (M_w = 6.7 @ 74 km) scaled to 0.2g and the 1992 Cape Mendocino earthquake Petrolia record (M_w = 6.5 @ 9 km), scaled to 0.7g.

For the Amboy record, liquefaction occurred in the very loose sand layer 3 after about 29 seconds of shaking leading to ground oscillations of about 0.25 ft amplitudes as shown in Figure 16 and 17. No permanent ground lurch and only small pore pressure increases occurred in the denser sands of layers 6 and 8. The maximum shear strengths were not reached in the clayey silt layers. Note ground surface accelerations (Figure 16) were similar in amplitude and frequency to input accelerations, until liquefaction occurred in layer 3, at which time longer period acceleration pulses commenced.

For the Petrolia record, the shear strength of the layer 4 soft clayey silt was exceeded prior to liquefaction of the layer 3 sand. The soft clayey silt was hence the seat of the maximum ground oscillation amplitudes of about 0.5 ft as shown in Figures 18 and 19, with an associated permanent ground lurch also of about 0.5 ft. It is important to note (and often overlooked) that the strength of soft cohesive soils is often similar to the post liquefaction residual resistance of sands. Figure 20 show pore pressures increasing significantly in the denser sands of layers 6 and 8, but not contributing to ground displacements.

CONCLUSIONS

The occurrence of large ground oscillations and potential associated ground lurch resulting from underlying earthquake induced liquefaction at level ground sites, is clearly of design concern to both buried pipelines and bridges. Past earthquakes have graphically illustrated the damage potential of such ground displacements.

As the magnitude of ground oscillations or ground lurch depends strongly on the amplitude and frequency characteristics of earthquake ground motions, the depth of liquefied soil, and the relative density and residual resistance of liquefiable soils, a site specific approach to evaluate potential ground displacements is desirable.

In this paper, the practical application of the computer program DESRA-MUSC to evaluate ground oscillation and lurch displacements is described. Example illustrates the importance of input amplitude and frequency characteristics and the nature of site stratigraphy in controlling ground oscillations. The concept of post liquefaction small strain residual shear resistance as a major controlling factor in determining displacements in introduced. The need for research to better define and understand residual shear resistance as opposed to residual strength (of primary concern to flow slide potential) is strongly recommended.

ACKNOWLEDGEMENTS

The research described in this paper was funded jointly by an NSF grant to the National Center for Earthquake Engineering, Buffalo, and a Federal Highway Administration grant (FHWA Contract DTFH61-92-6-00106) to the National Center for Earthquake Engineering. This support is gratefully acknowledged.

REFERENCES

Byrne, Peter M., (1991). "A Cyclic Shear-volume Coupling and Pore Pressure Model for Sand", Proceedings: Second International Conference on Recent Advances in Geotechnical Engineering and Soil Dynamics, March 11-15, 1991, St. Louis, Missouri, Paper No. 1.24, pp. 47-55.

EPRI (1993). Guidelines for Determining Design Basis Ground Motions, Electric Power Research Institute, Palo Alto, California, Vol. 1, pp. 8-1 through 8-69.

Finn, W.D. Liam, Martin, Geoffrey R. and Lee, Michael K. W., (1978). "Comparison of Dynamic Analysis of Saturated Sands", Proceedings of the 1978 ASCE Conference on Earthquake Engineering and Soil Dynamics, Pasadena, California.

Holzer, Thomas L., Bennett, Michael J., Ponti, Daniel J., and Tinsley III, John C. (1999), "Liquefaction and Soil Failure During 1994 Northridge Earthquake," Journal of Geotehcnical and Geoenvironemtnal Engineering, Vol. 125, No. 6, pp. 438-452.

Ishihara, K., (1985). "Stability of Natural Deposit During Earthquake," Theme Lecture, Proceedings, 11th International Conference on soil Mechanics and Foundation Engineering, San Francisco, Vol. 2, pp. 321-376.

Iwan, W.D., (1967). "On a Class of Models for the Yielding Behaviors of Continuous and Composite System", Transactions of the ASME, Sept. 1967.

Matasovic, Neven and Vucetic, Mladen, (1993). "Cyclic Characterization of Liquefiable Sands," Journal of Geotechnical Engineering, ASCE, Vol. 119, No. 11, pp. 1805-1822.

Lee, M.K.W. and Finn, W.D.L. (1978). "DESRA-2, Dynamic Effective Stress Response Analysis of Soil Deposits with Energy Transmitting Boundary Including Assessment of Liquefaction Potential," Soil Mechanics Series No. 38, University of British Columbia, Vancouver.

Martin, G.R. Finn, W.D.L. and Seed, H.B. (1975). "Fundamentals of Liquefaction Under Cyclic Loading," Journal of the Geotechnical Engineering Division, ASCE, Vol. 101, No. GT5, pp. 423-438.

Martin, G.R., Lam, I.P., McCaskie, S.L., and Tsai, C.-F. (1981). "A Parametric Study of an Effective Stress Liquefaction Model," Proceedings, International Conference on Geotechnical Earthquake Engineering and Soil Dynamics, St. Louis, Missouri, Vol. 2, pp. 699-705.

Pease, J.W., and O'Rourke, T.D., (1997). "Seismic Response of Liquefaction Sites," Journal of Geotechnical and Geoenvironmental Engineering, Vol. 123, No. 1, pp. 37-45.

Qiu, Ping, Earthquake Induced Non-Linear Ground Deformation Analyses, (1998), Ph.D. Dissertation submitted to the Graduate School, University of Southern California.

Vucetic, M. and Dobry, R. (1991). "Effect of Soil Plasticity on Cyclic Response," Journal of Geotechnical Engineering, ASCE, Vol. 117, No. 1, pp. 89-107.

Youd, T.L. (1984). "Geologic Effects – Liquefaction and Associated Ground Failure," Proceedings, Geologic and Hydrologic Hazards Training Program, Open File Report 84-760, U.S. Geological Survey, Menlo Park, California, pp. 210-232.

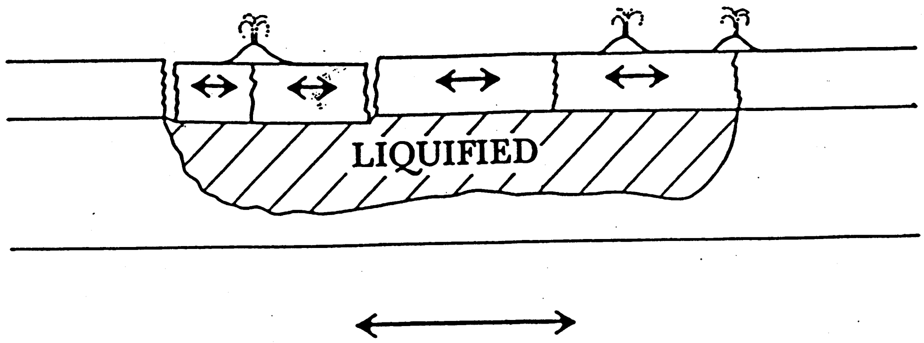

Figure 1 Mechanism of Ground Oscillation (after Youd, 1984)

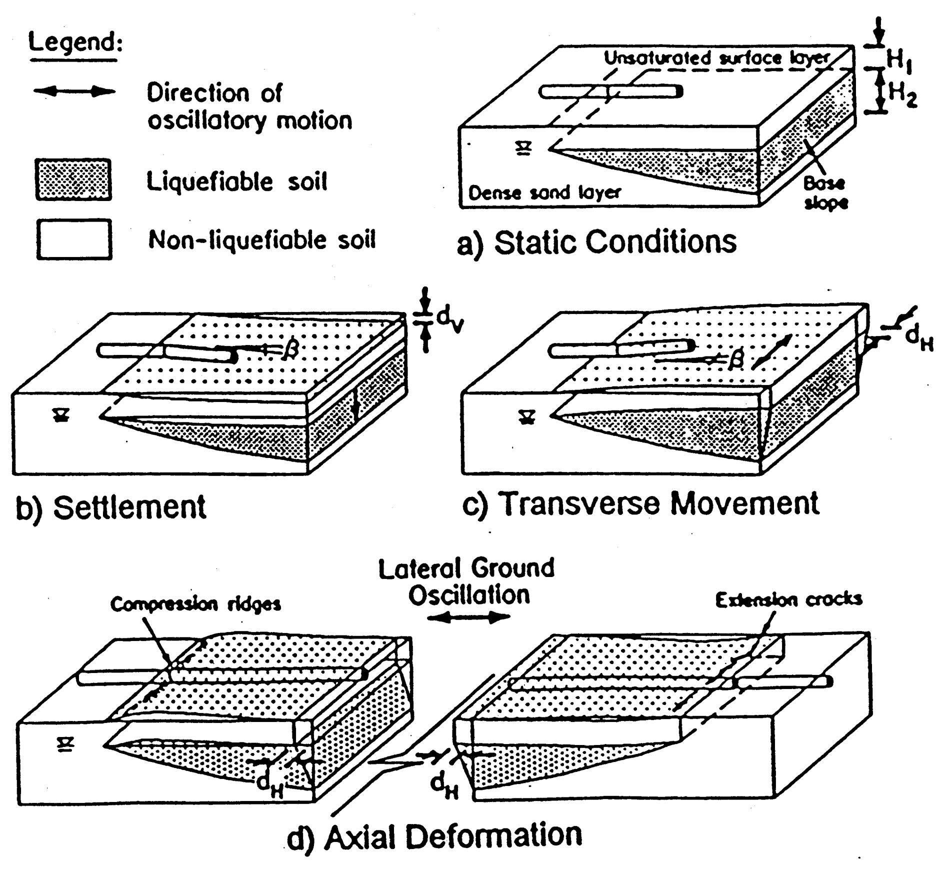

Figure 2 Schematic of Buried Pipeline Response to Transient Displacements at Liquefaction Sites (after Pease and O'Rourke, 1997)

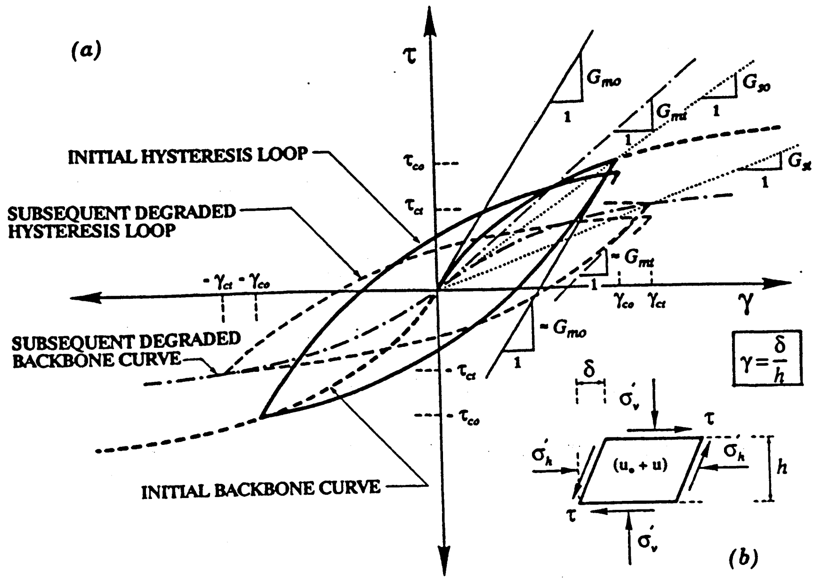

Figure 3 Degradation of Backbone Curves (after Matasovic and Vucetic; 1993)

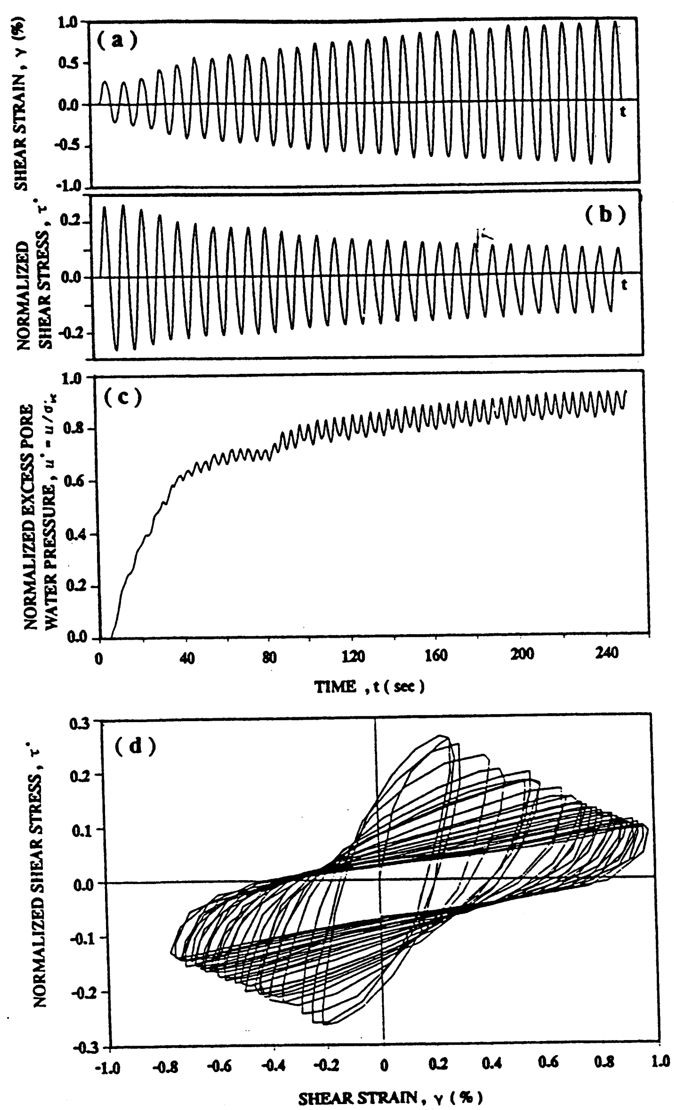

Figure 4 Results of Representative Cyclic Simple Shear Tests (after Matasovic and Vucetic, 1993)

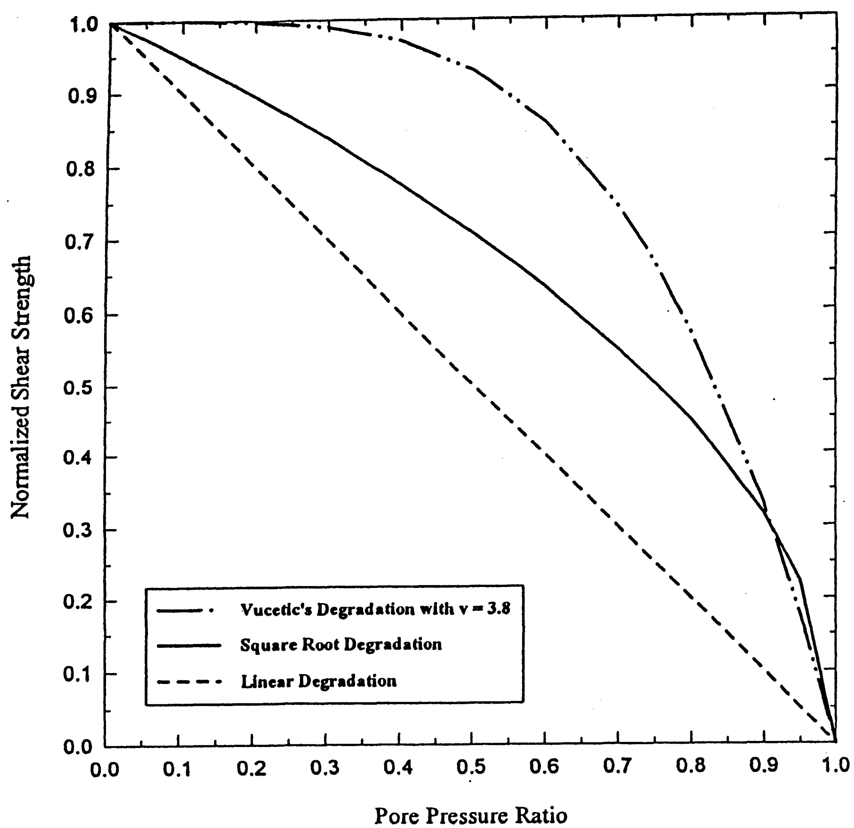

Linear Degradation Law:

$$\tau_{mt} = \tau_{m0}\left(1-\frac{u}{\sigma'_{v0}}\right)$$

Square Root Degradation Law:

$$\tau_{mt}' = \tau_{m0}\sqrt{1-\frac{u}{\sigma'_{v0}}}$$

The Vucetic's Degradation Law:

$$\tau_{mt} = \tau_{m0}\left(1-\left[\frac{u}{\sigma'_{v0}}\right]^{v}\right)$$

Figure 5 Comparison of Stress Degration Laws (after Qiu, 1998)

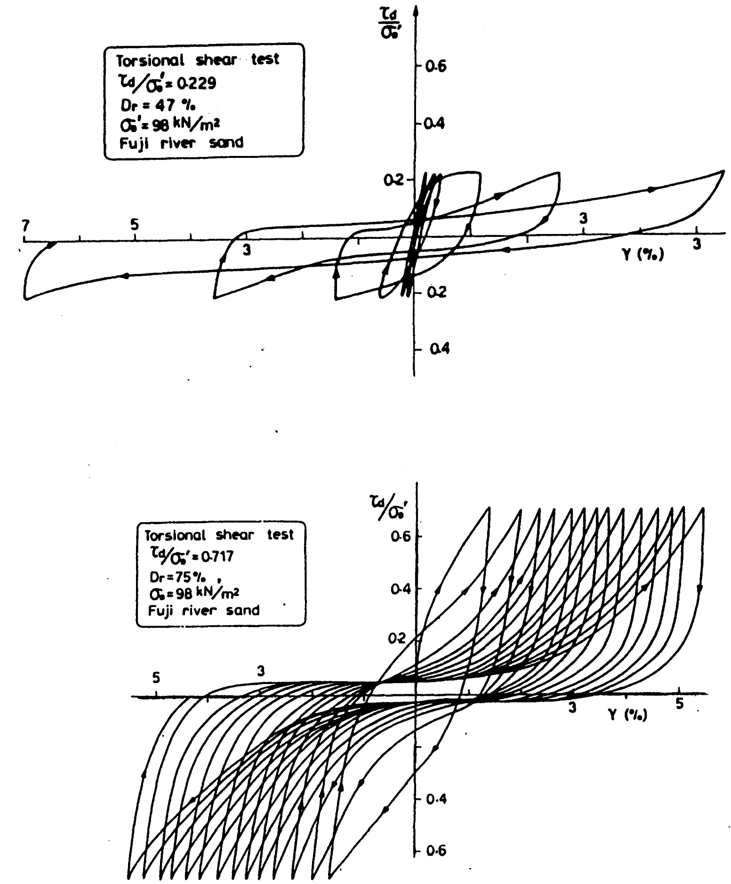

Figure 6 Cyclic Torsional Tests on Saturated Sands (after Ishihara, 1985)

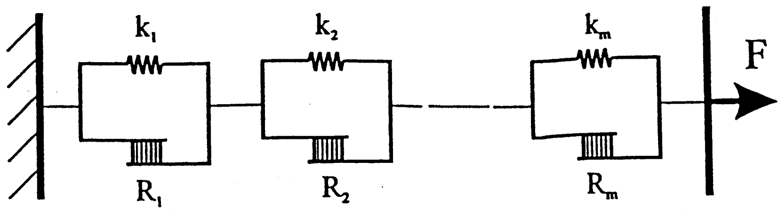

Figure 7 Mechanistic Iwan Model

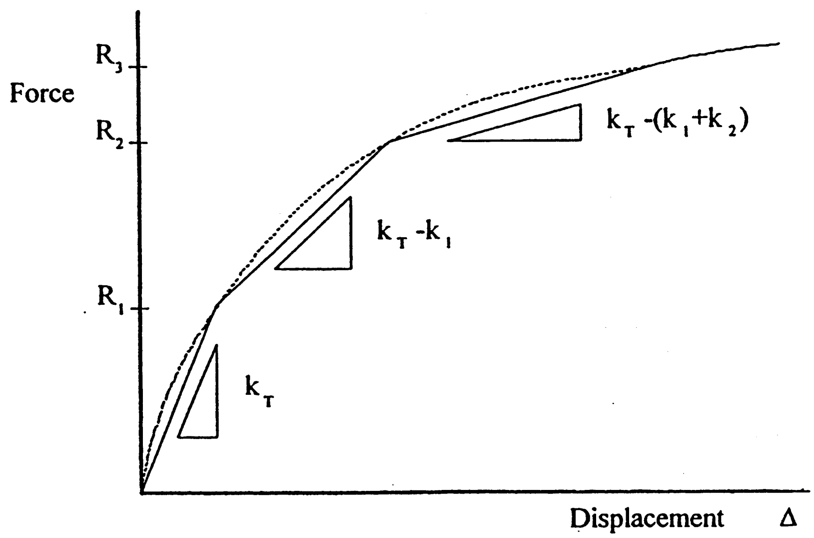

Figure 8 Piecewise Linear Approximation to Backbone Curve

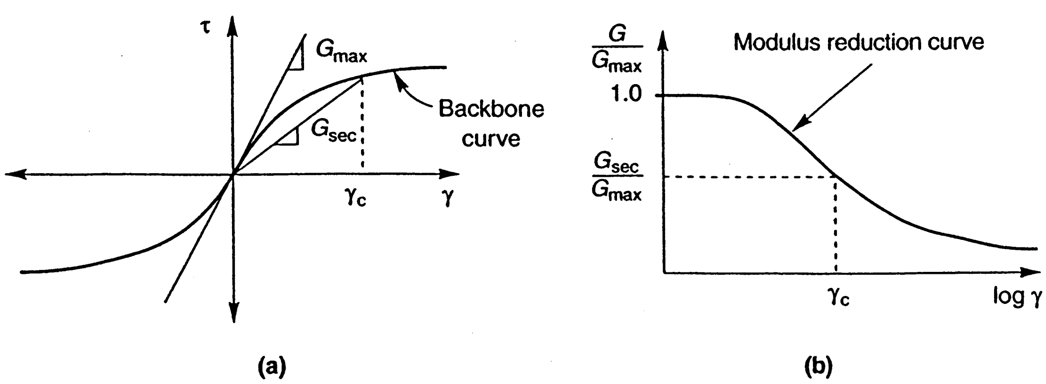

Figure 9 Backbone Curve Showing Variation of G_{sec} with Shear Strain

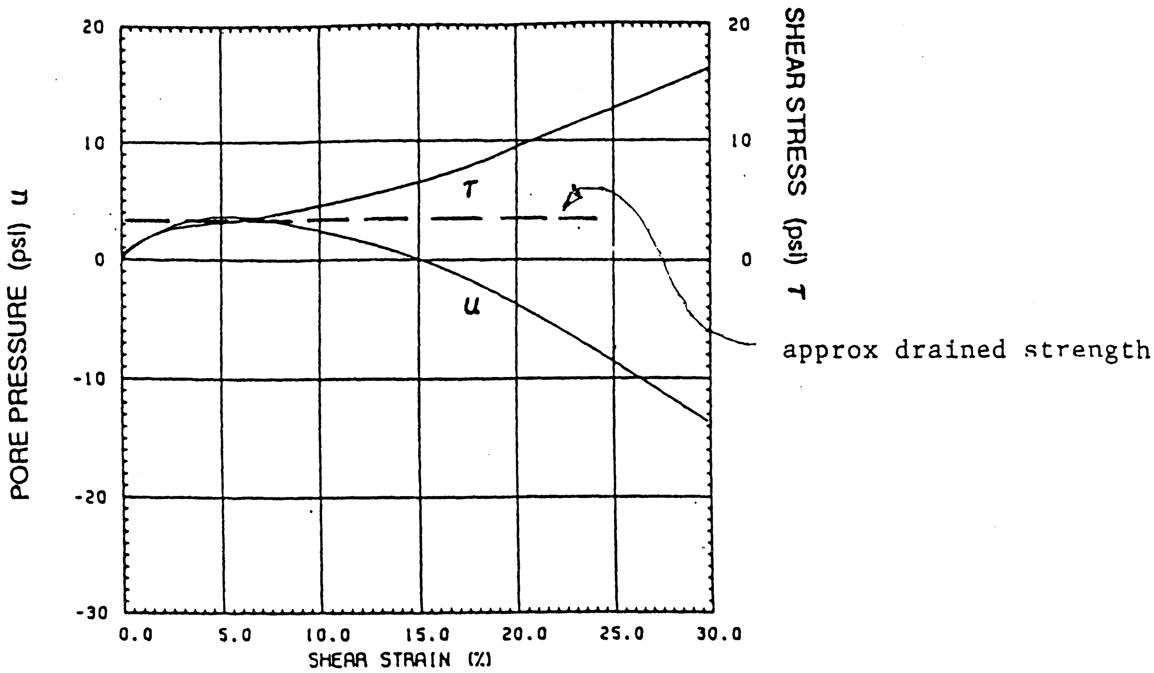

Figure 10 Rapid Monotonic Undrained Simple Shear Test on a Medium Dense Silty Sand

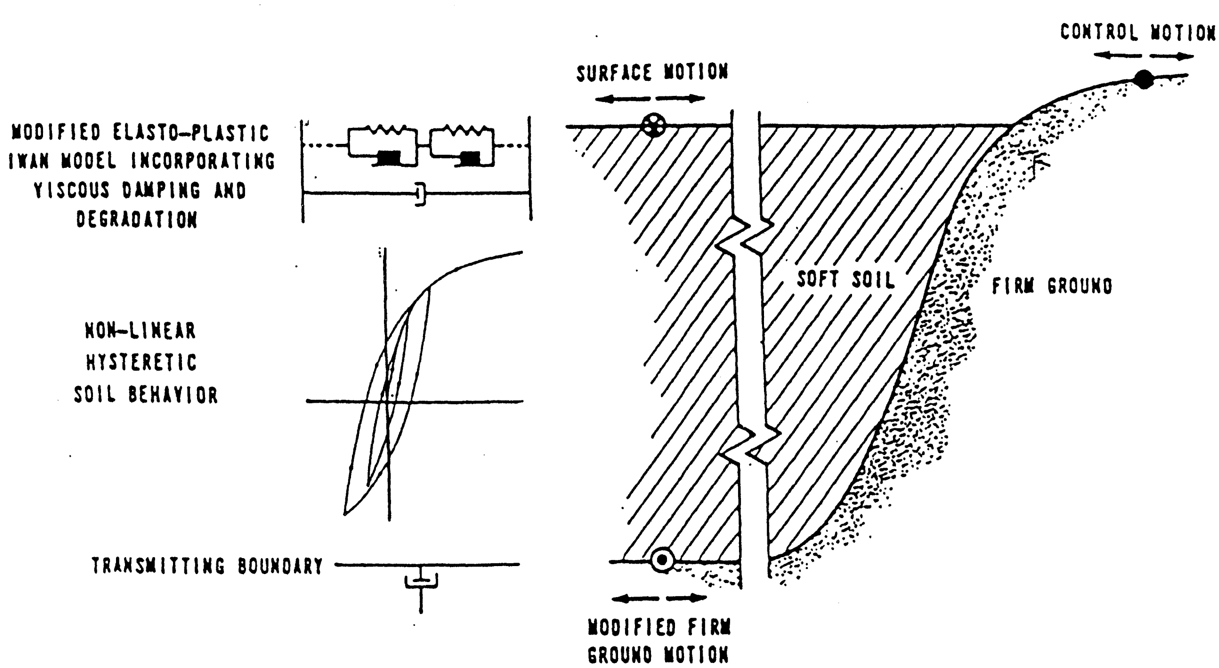

Figure 11 General Features of the DESRA-MUSC Program

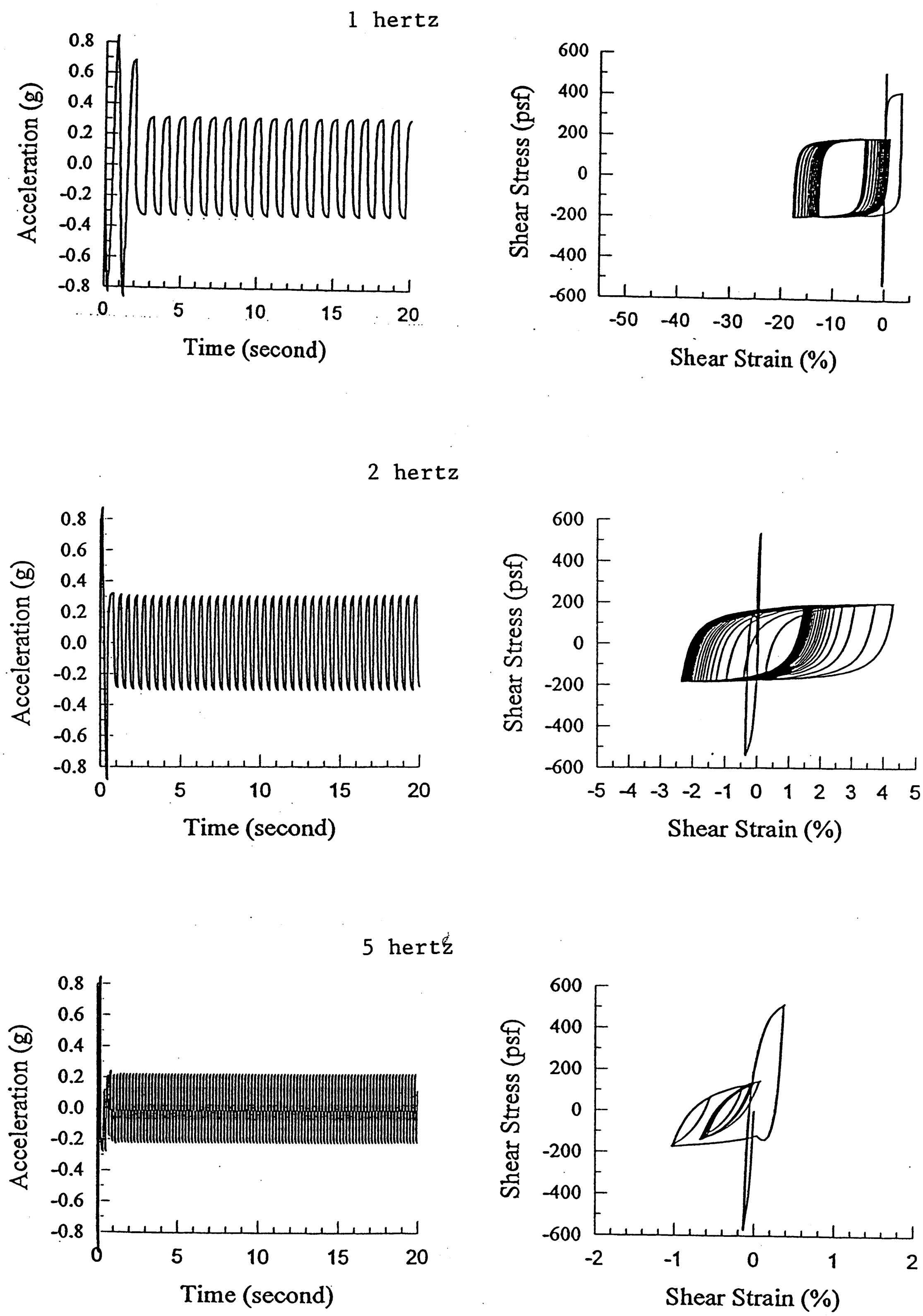

Figure 12 Effect of Input Frequency on Ground Oscillation

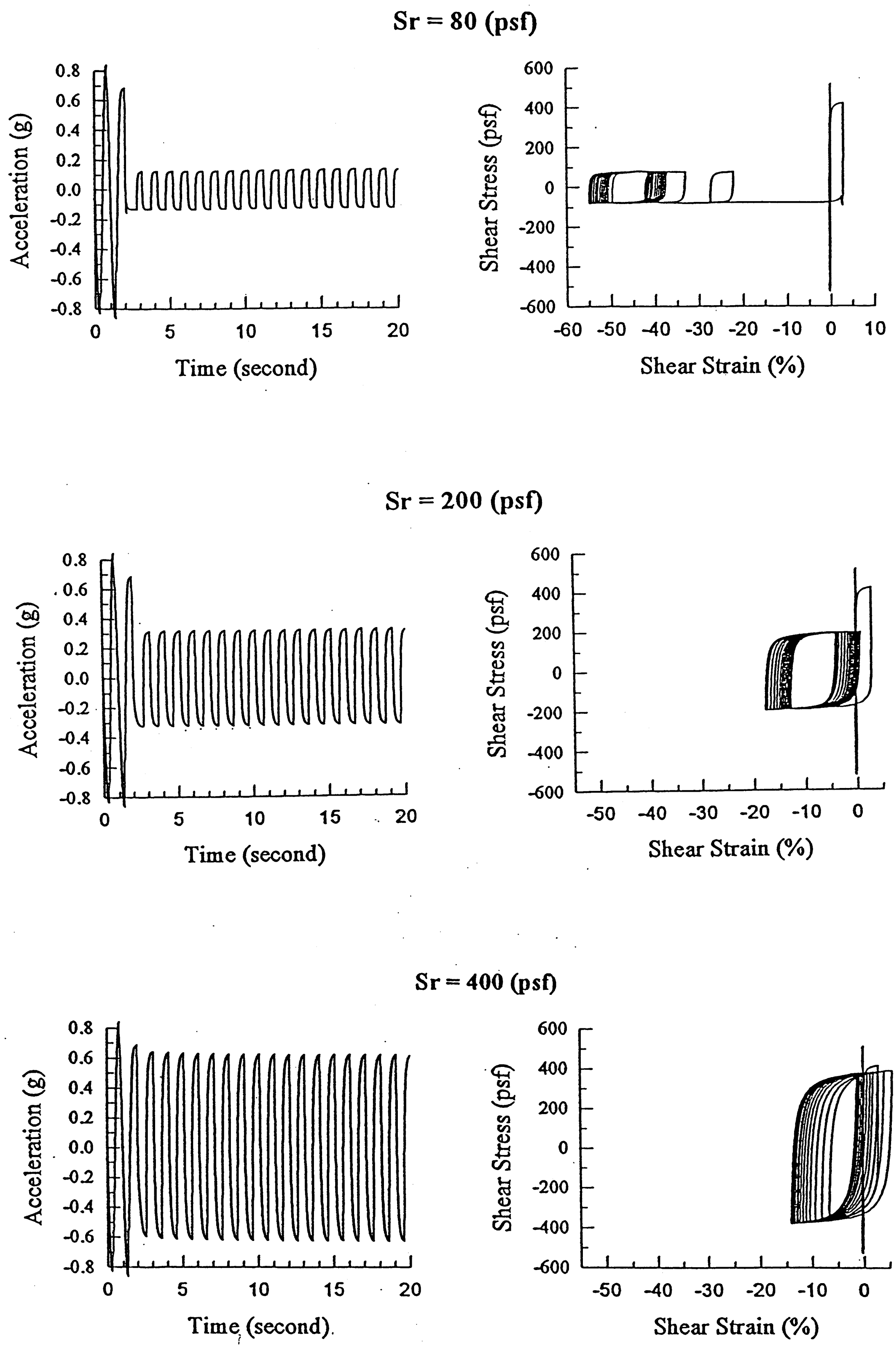

Figure 13 Effect of Residual Resistance on Ground Oscillation (after Qiu, 1998)

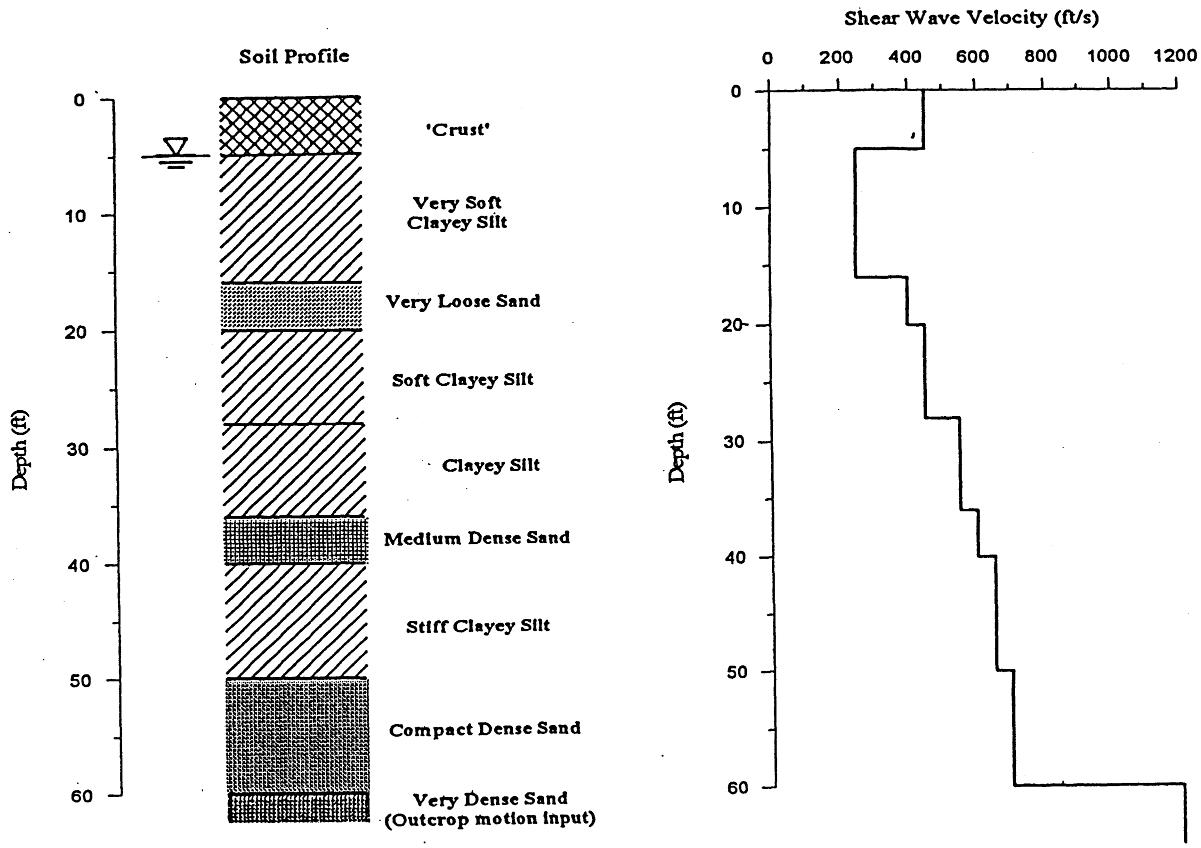

Soil Materials Used in the Case Studies

Layer No	Unit Weight (pcf)	Cohesion (psf)	Friction Angle	Shear Wave Velocity (ft/s)	SPT Blowcount
1	110	1200	N.A.	450	N.A.
2	110	400	N.A.	250	N.A.
3	110	N.A.	30	400	15
4	110	450	N.A.	450	N.A.
5	110	1500	N.A.	550	N.A.
6	110	N.A.	30	600	20
7	110	1800	N.A.	650	N.A.
8	110	N.A.	35	700	25
Bedrock	125	N.A.	N.A.	1200	N.A.

Figure 14 Soil Profile Used in Case Study Analyses (after Qiu, 1998)

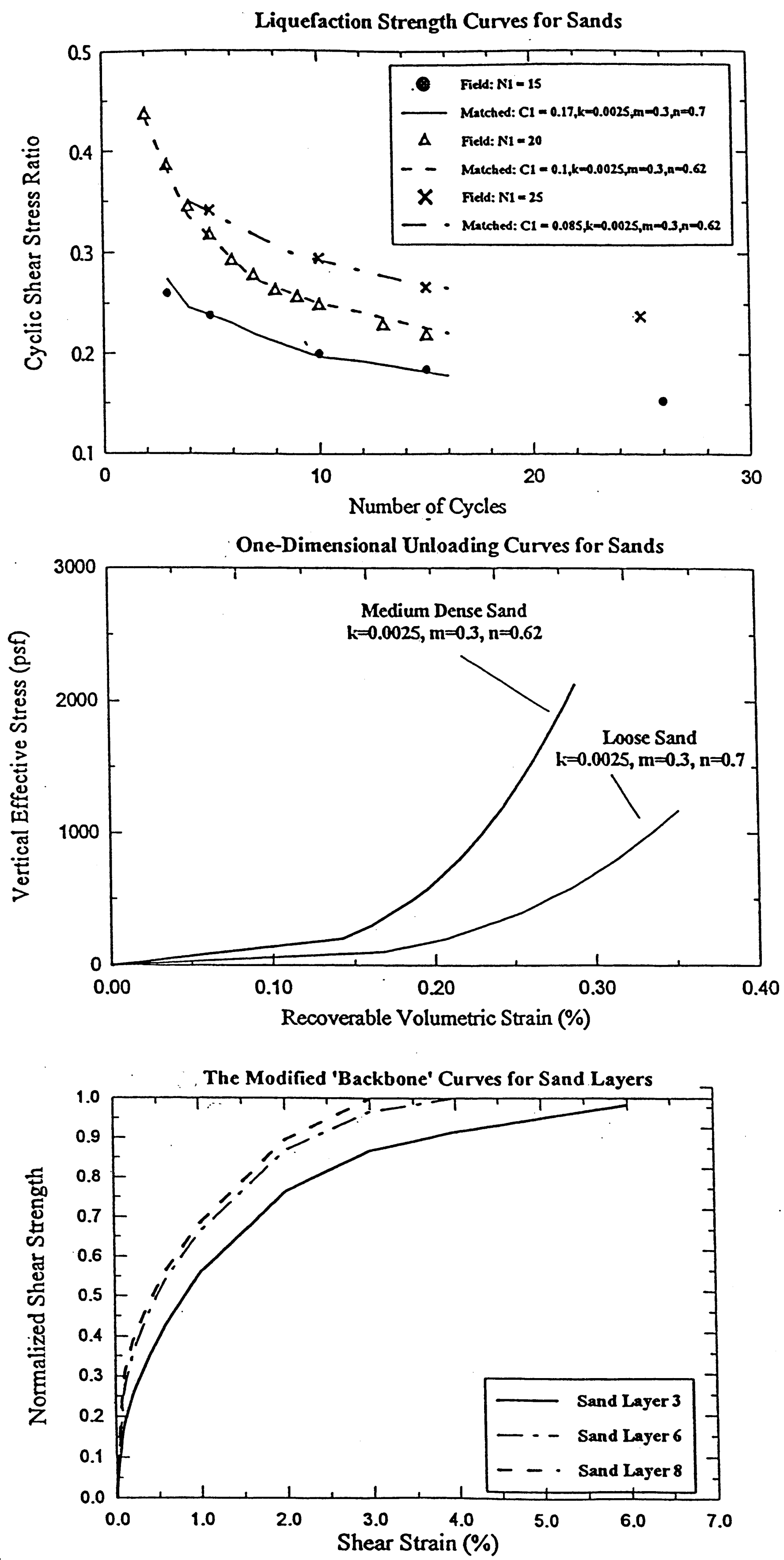

Figure 15 Liquefaction Strength, Elastic Rebound and Backbone Curves for Sand Strata Used in Case Study Analyses (after Qiu, 1998)

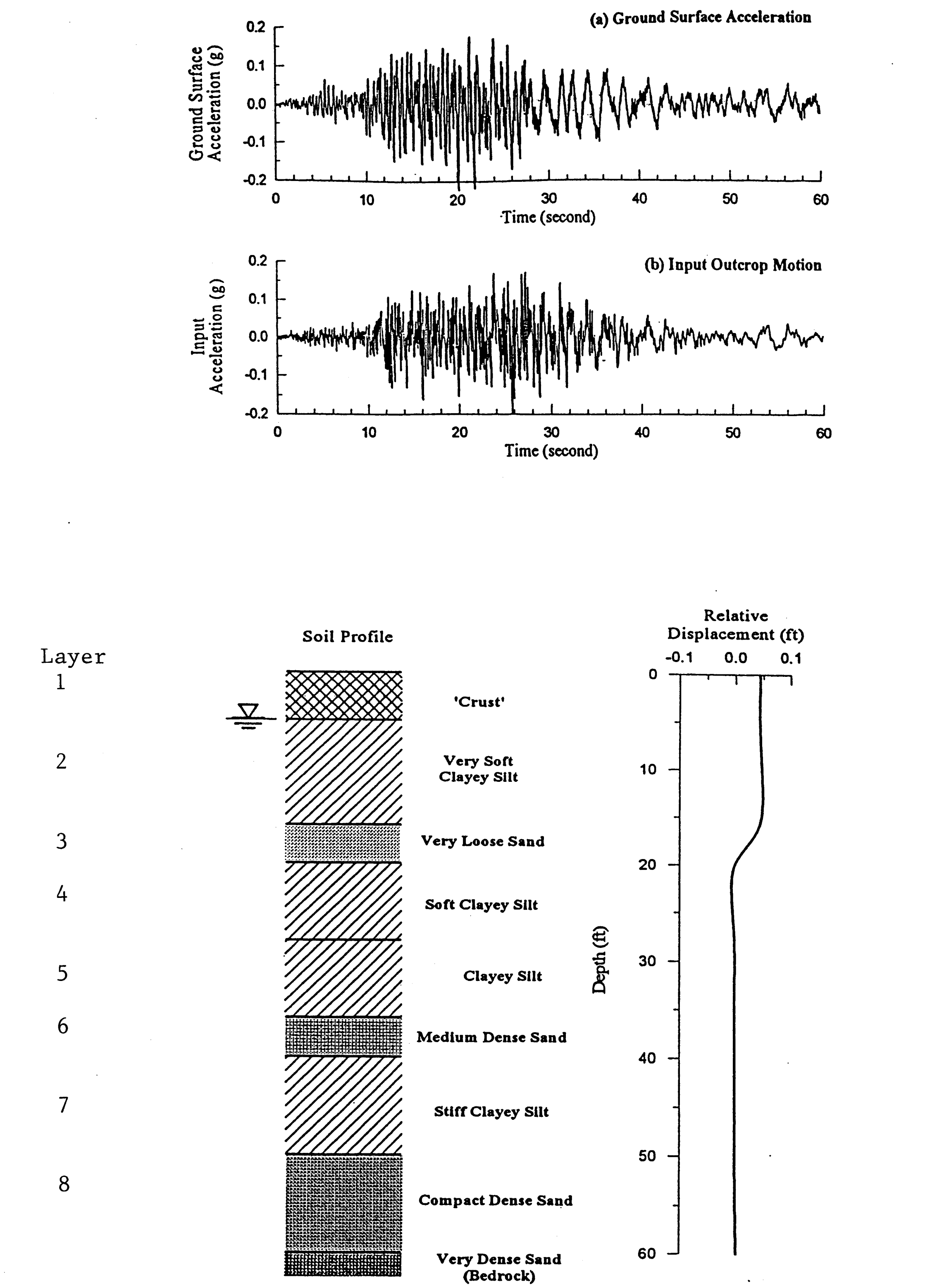

Figure 16 Acceleration and Ground Displacement Response: Amboy Record (after Qiu, 1998)

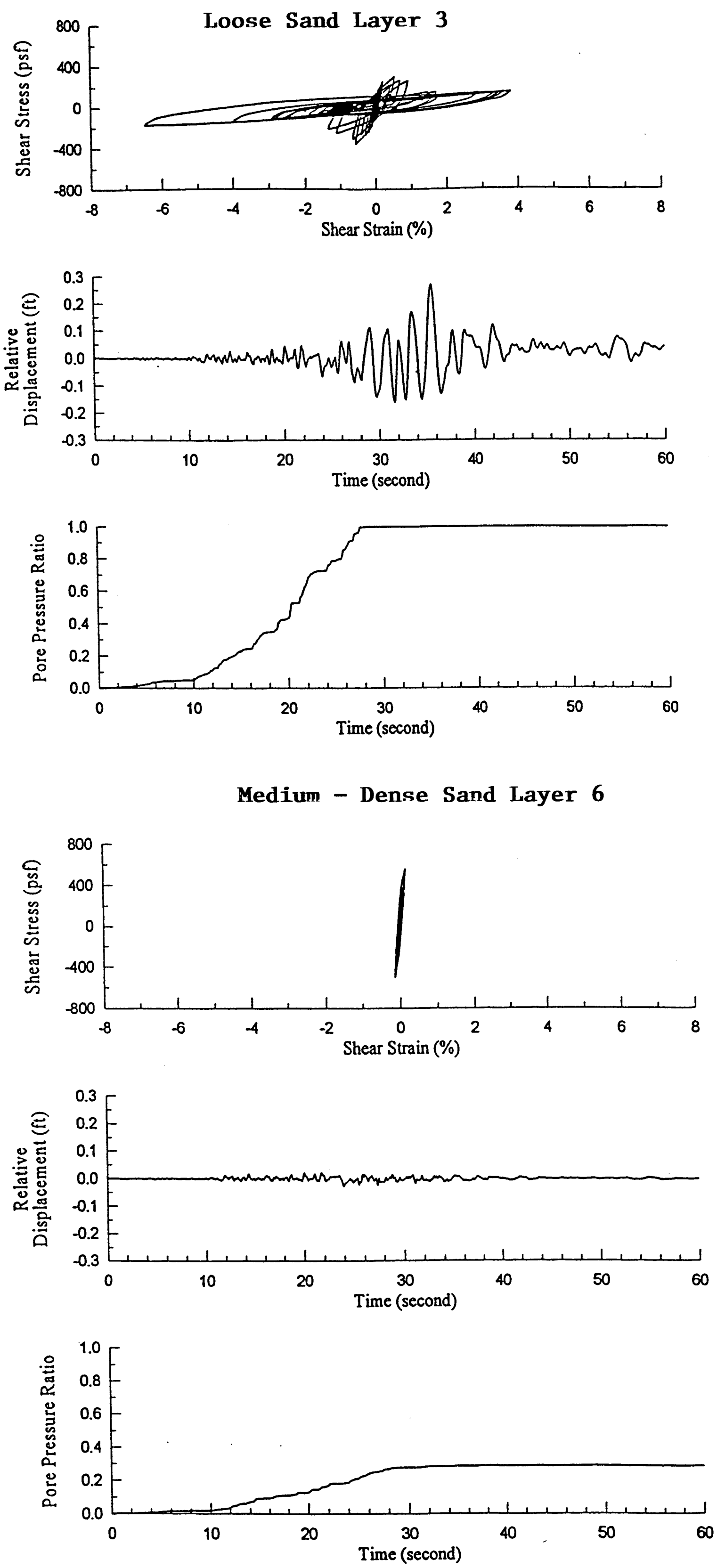

Figure 17 Pore Pressure, Dispalcement and Stress-Strain Response: Amboy Record (after Qiu, 1998)

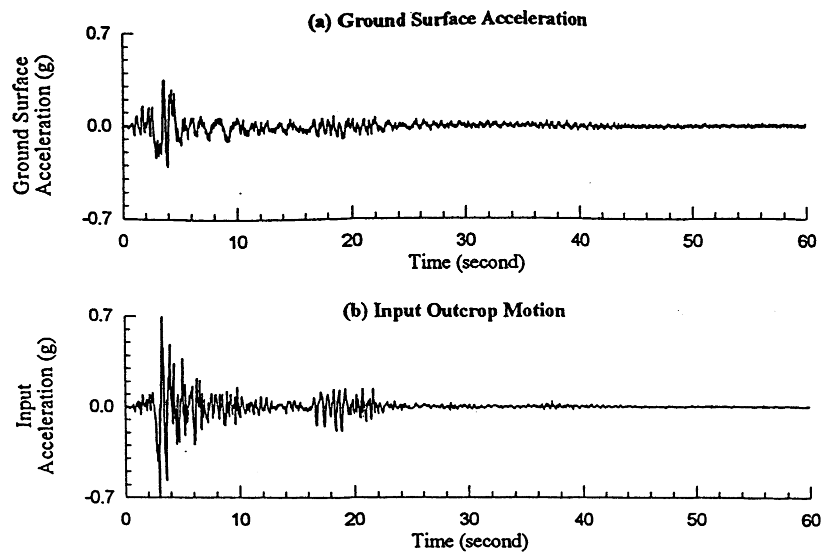

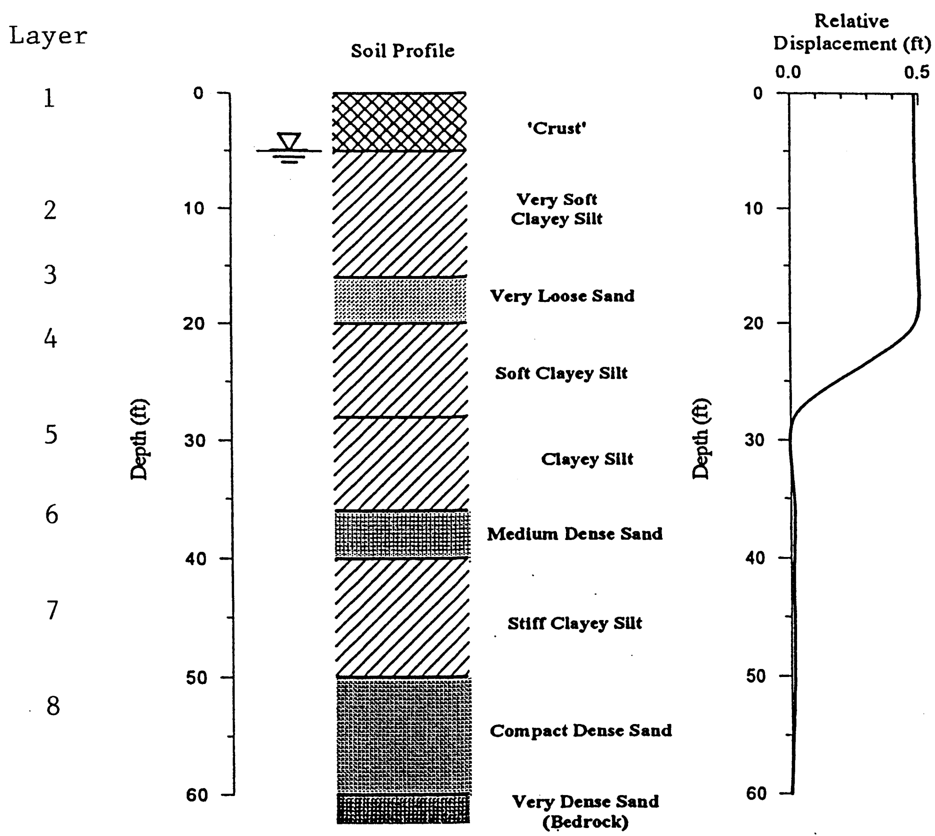

Figure 18 Acceleration and Ground Displacement Response: (after Qiu, 1998)

Loose Sand Layer 3

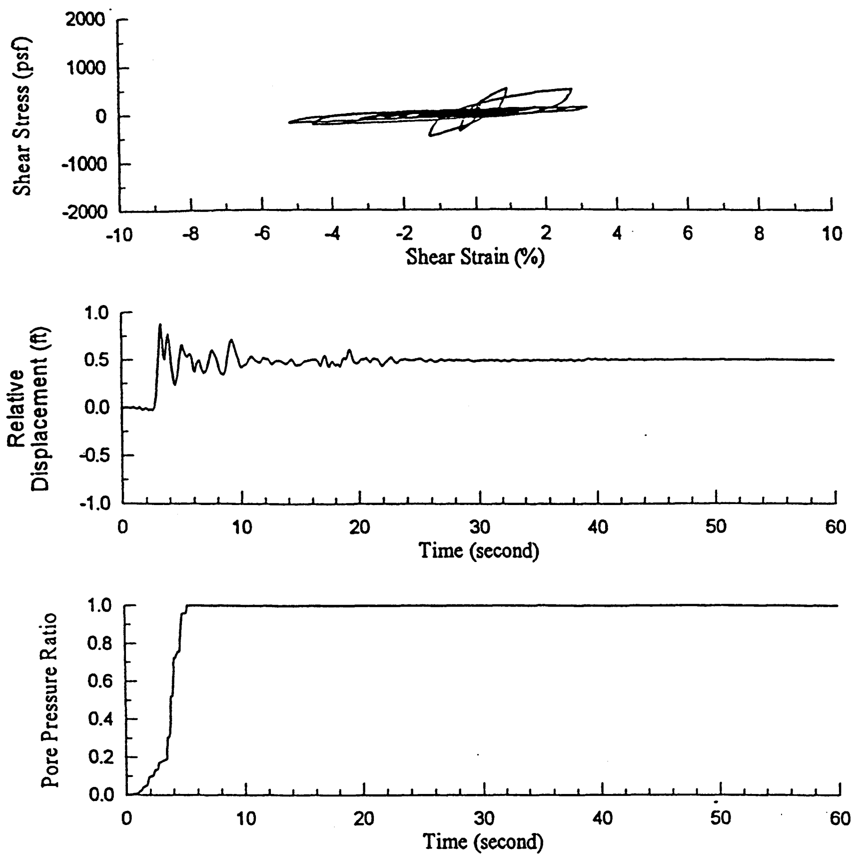

Soft Clayey Silt Layer 4

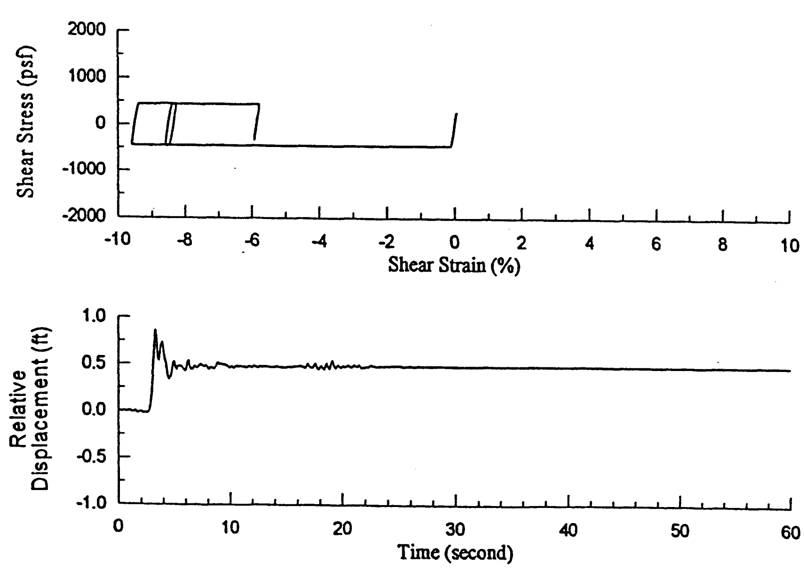

Figure 19 Pore Pressure, Displacement and Stress-Strain Response: Petrolia Record (after Qiu, 1998)

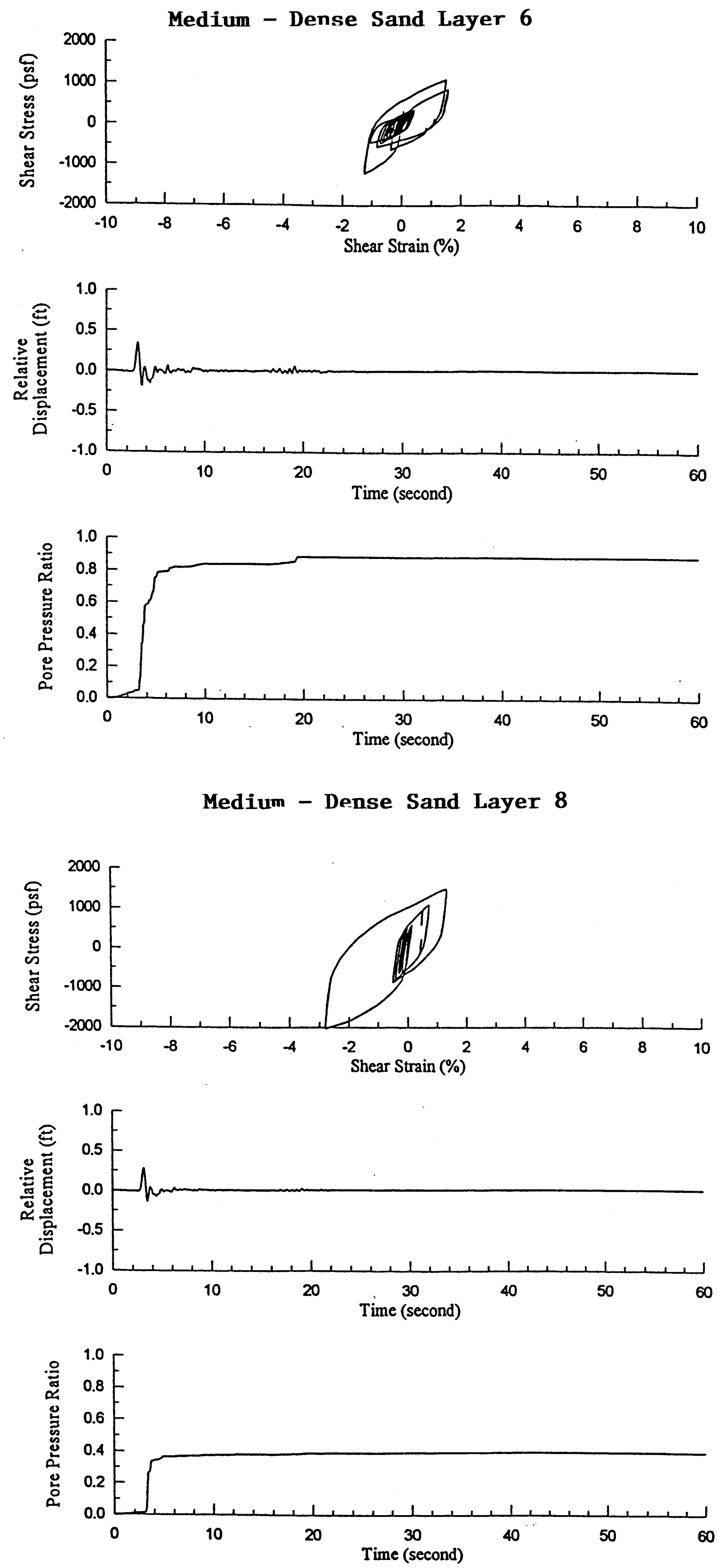

Figure 20 Pore Pressure, Displacement and Stress-Strain Response: Petrolia Record (after Qiu, 1998)

TIME DEPENDENT GROUND MOTION AMPLIFICATION DUE TO LIQUEFACTION ON MAN-MADE ISLAND

Y. Furumoto[1], F. Oka[2], M. Sugito[1] ,A. Yashima[1] and Y. Fukagawa[3]

[1]Department of Civil Engineering, Gifu University,
Yanagido, 1-1, Gifu, 501-1193, Japan
[2]Department of Civil Engineering, Kyoto University,
Sakyo-ku, Kyoto, 606-8501, Japan
[3]Development Bureau, Kobe City Government
Kano-cho 6-5-1, Kobe, 650, Japan

ABSTRACT

Two sets of borehole array records obtained from the Great Hanshin Earthquake as well as its fore and after shocks, are investigated. One of the station is located in Port Island in Kobe City where the severe liquefaction occurred and the records from the main event includes the typical phenomena of liquefaction. The other station is located in Rokko Island in Kobe City where the liquefaction phenomena was not predominant as it was in Port Island.

The nonlinear ground motion amplification, depending on the level of input ground motion as well as their spectral characteristic, are carefully investigated. Two numerical techniques for seismic response analysis of ground are applied for these stations; one is the frequency-dependent equivalent linearization technique for frequency domain analysis, and the other is the effective stress-based liquefaction analysis. The discussion is focused on the amplification characteristic of these two reclaimed lands depending on their reclamation history. Time-dependent amplification ratio for peak ground motion and spectral contents are demonstrated, which is caused by the recovery of soil rigidity due to the decrease of excess pore water pressure after the main event.

INTRODUCTION

The nonlinear ground motion amplification due to the level of input motion at bedrock is one of the significant topics in the field of earthquake engineering. The extremely valuable borehole records at Port Island in Kobe City were obtained during the 1995 Hyogoken-Nambu Earthquake. At this station, a great number of array records were obtained after June 1994 until December 1996. The other borehole records except the ones from the 1995 Eartqhuake have been obtained at Rokko Island which is also the reclaimed land in Kobe City. Based on these records, the authors discuss the nonlinear ground motion amplification at the soft reclaimed ground, focusing on its time-dependent characteristic due to the decrease of excess pore water pressure after the large event.

BOREHOLE ARRAY OBSERVATION SYSTEMS

Figure 1 shows the locations and layout of array systems of two borehole stations as well as their soil profiles and velocity structures. In Figs.1(b) and (c), the area where the liquefied sand spouted out is represented. It is clear that the liquefaction was much severe at Port Island than at Rokko Island. Each observation system consists of 4 acceleration sensors as shown in Fig.1(d). At PI station, the acceleration sensors are installed at the depth of GL.-0.0m, -16.0m, -32.0m, and –83.0m. At RI station, the sensors are installed at the depth of GL.-0.0m, -35.0m, -98.0m, and –154.5m.

The reclamation work was finished in 1969 at PI station site and in 1979 at RI station site. A decomposed granite soil known as "Masado" was used in the reclamation area of Port Island, and sedimentary rock debris of the Kobe Group, which includes sandstone, mudstone and tuff, was used for Rokko Island. The shear wave velocity in the alluvial layer in the depth of 25 ∼ 34 meters at RI station is smaller than that in the depth of 19 ∼ 27 meters at PI station, which mainly depends on the term of consolidation. At PI station, the velocity structure has been investigated after the earthquake by using the suspension-type investigator. Figure 1(d) shows the distribution of shear wave velocity at both stations. As shown in Fig.1(d), the shear wave velocity of the alluvial clay at PI station is 180 m/sec, and that at RI station is 115 m/sec.

The records from 39 earthquakes, including the 1995 Hyogoken-Nambu Earthquake, have been compiled. Table 1 gives the list of these earthquakes with the classification of dataset depending on their recording time. In Table 1, the group A includes the records obtained before the main event occurred on Jan.17, 1995. In the group B and C, only the records at PI station were obtained. On the other hand, the records were not obtained at PI station during the term for group D.

CORRECTION OF ORIENTATION ERRORS OF BOREHOLE RECORDS

The correction of orientation error of borehole records is an indispensable task for use of engineering analyses (Kamata, et. al., 1987). The orientation error of buried seismograph sensors regarding the records used in this study has been investigated (Sugito, et. al., 1996). Figure 2 shows the horizontal displacement orbits for each depth of seismograph at PI station. An error of 22 degrees in the horizontal plane has been detected for the sensor installed at the depth of G.L.-83 m. The peak acceleration of each time history is significantly affected by the correction of the error in the order of 60 % larger or smaller than the original peak value. For example, the peak acceleration in NS and EW components of the corrected time histories were –526.7 and 486.2 cm/sec^2, respectively, while those for uncorrected were –670.5 and –304.6 cm/sec^2, respectively.

All the records obtained at G.L.-83m have been corrected by the rotation of the coordinate in the horizontal plane. Since the records at RI station have not been obtained from the 1995 Earthquake, and the records from other earthquakes are not large enough to detect the orientation error, the original data have been used in the present study.

GROUND MOTION AMPLIFICATION IN CASE OF WEAK INPUT MOTION

Amplification Characteristic of Peak Ground Motion

The amplification characteristics of peak acceleration at both two stations are compared. The amplification ratio of peak acceleration normalized by the value at G.L.-83m (PI station) and at G.L.-154.5m (RI station) for the records classified in the group A and group E, as well as amplification ratio for the main event at PI station and that for group D at RI station, are represented in Figs.3 and 4. The upper part in Fig.3 shows the result for the group A which is in the term before the 1995 Earthquake. As for the horizontal ground motion, it is observed that the peak acceleration at the PI station is amplified significantly in the surface layers more shallow than 16 meters. In the case of RI station, the peak horizontal acceleration is not amplified in surface layers. In the middle part (c) of Fig.3, the distribution of the peak acceleration during the Hyogoken Nambu Earthquake at PI station is shown. It is clear that the effect of soil liquefaction or reduction of rigidity of soil on amplification of peak ground motion is predominant near the ground surface. In the lower part of Fig.3, 9 days or more after the 1995 Earthquake, the amplification ratio in horizontal components is nearly the same as it was before the 1995 Earthquake both at PI and RI stations. These results in Fig.3 demonstrate that the soil properties, specially the dynamic soil properties recovered in a weak or 10 days after the large event.

Figure 4 shows the result for the case of peak velocity. Its amplification characteristic is almost the same as the one of peak acceleration. It may be concluded that the very soft alluvial layer existing between GL.-24 m and GL.-34 m at RI station could reduce the ground motion intensity in the upper surface layers, and the peak ground motions were not amplified as much as those at PI station.

Amplification Characteristic of Spectral Contents

The amplification characteristics of acceleration response spectra at both the stations are compared. Figure 5 shows the amplification ratio of acceleration response spectra obtained from typical records in each group of recording term. Figure 5(a) shows the results obtained at PI station. It is clear that the amplification ratio for high frequency range such as f>2.0 Hz are very low in the case of the main event (Fig.5(b)) and the case of group B (Fig.5(c)) which is in the term right after the main event. The amplification ratio in the range f>2.0 Hz recovered approximately after 10 days after the main event, as shown in group E in Fig.5(d).

RESPONSE ANALYSIS OF BOREHOLE ARRAY STATIONS

Frequency-Dependent Equivalent Linearization Technique (FDEL)

The amplification characteristic of ground motion has been examined for these two stations by using the modified equivalent linearization technique, FDEL, in which a frequency -dependent equivalent strain is incorporated in the numerical analyses (Sugito, 1993). The equivalent linearization technique, in which nonlinear characteristics of shear modulus and damping of soils that depend on the levels of shear strain are modeled as an equivalent linear relation, has been applied frequently for earthquake response analysis of ground, especially in the case of practical fields. The advantage of the technique compared with the nonlinear time domain analysis is that the algorithm is quite simple and the inversion, such as the estimation of input bed rock motion from surface motion, is possible. The computer program, 'SHAKE' (Schnabel et al., 1972), is based on the equivalent linearization technique and has contributed very much to the field of earthquake engineering. It was, however, pointed out that the numerical results do not agree with the observed ground motion in the case of very soft ground and strong ground motion levels.

The technique FDEL(Sugito, 1993) employs as concept of equivalent strain $\gamma_f(\omega)$ that determines the shear modulus and damping in such a way as,

$$\gamma_f(\omega) = C\gamma_{\max} \frac{F_\gamma(\omega)}{F_{\gamma_{\max}}} \tag{1}$$

where C= constant, $\gamma_{\max}$ = maximum shear strain, $F_\gamma(\omega)$= Fourier spectrum of shear strain time history, and $F_{\gamma\max}$ represents the maximum of $F_\gamma(\omega)$. The equivalent strain $\gamma_f(\omega)$ controls the equivalent shear modulus and damping as they are defined to be proportional to the Fourier amplitude of strain time history. The constant C controls the level of equivalent strain uniformly along the frequency axis, and it has been fixed as C=0.65 on the basis of the numerical calculations compared with the strong motion records (Sugito, 1993).

Figure 6 shows the amplification ratio for PI and RI stations with three input motion levels of the peak acceleration as 26.3, 105.3, and 526.7 cm/sec^2. These input motions are scaled from the record obtained at G.L.-83m of PI station in N-S component during the 1995 Earthquake(Fig.8). As shown in Fig.6, the amplification factor at ground surface level at PI station is relatively high in the case of weak input motion, and depends on the input motion level. On the other hand, the amplification factor at ground surface at RI station is not so large even in the case of weak input motion. These results are consistent with the observed ones. It can be concluded that the soft alluvial layer at RI station (G.L.-24 m～ -34 m) reduces the ground motion amplification even in the weak input motion level, which is so called as the base isolation effect.

The liquefaction potential index, P_L(Japan Road Association,1996), is evaluated based on the comparison between the shear stress analysed and liquefaction strength for saturated sandy layer from the ground water level down to G.L.-20m. Figure 7 shows the variation of P_L width respect to input motions scaled from the record obtained at G.L.-83m of PI station in N-S component during the 1995 Earthquake(Fig.8). It is noted that P_L is reduced by base isolation effect at RI station.

Effective Stress-based Liquefaction Analysis

Three-dimensional effective stress-based liquefaction analyses have been carried out in order to understand the basic behavior of the liquefied reclaimed islands. The soil profiles at two observation stations in Port Island and Rokko Island were modeled with three-dimensional finite element mesh.

The constitutive model adapted in the numerical analyses is based on the concept of the nonlinear kinematic hardening rule which had originally been used in the field of metal plasticity. Oka et al. (1992) derived a cyclic elasto-plastic constitutive model for sand. Tateishi et al. (1995) incorporated a new stress dilatancy relationship and an accumulative-plastic-strain-dependent shear modulus to modify the original model. The constitutive model is formulated under the three dimensional stress condition and its validity of the constitutive model has been verified by the experimental evidences from a hollow cylindrical torsional shear tests under various stress conditions (Tateishi et al., 1995).

The constitutive model has been incorporated into a coupled finite element-finite difference (FEM-FDM) numerical method for the liquefaction analysis of a fluid-saturated ground. The applicability of the proposed numerical method had been verified by past studies (Yashima et al., 1995; Taguchi et al, 1996; Oka et al., 1996, 1997).

Port Island and Rokko Island are modeled by the rectangular solid element mesh. 39 elements and 160 nodes are used to model the reclaimed ground and natural deposit from the ground surface down to GL –83 m for Port Island. On the other hand, 45 elements and 184 nodes are used to model the ground profile from the ground surface down to GL –93.5 m for Rokko Island. Most numerical parameters for the analysis are determined based on the results of the past field investigations and laboratory tests for the simulation of Port Island. On the other hand, the liquefaction strengths of the reclaimed ground and alluvial (diluvial) sand layer for Rokko Island are assumed to be equal to those of the corresponding layers for Port Island due to the lack of the experimental results. The elastic shear modulus derived from the shear wave velocity of alluvial layers at Rokko Island is, however, smaller than that at Port Island, as aforementioned in chapter 2. Basic numerical parameters are summarized in Table 2. Three components of acceleration records with the correction of orientation error are applied at GL –83 m as the base input accelerations for Port Island simulation. The same input accelerations are used at GL –93.5 m for Rokko Island simulation because the main event was not obtained at RI station.

Figure 9 shows the time histories of the excess pore water pressure ratios in the reclaimed ground (GL –16 m) and alluvial (diluvial) sandy soil layer (GL –32 m for PI station and GL –40 m for RI station). Note that in the initial state, the excess pore water pressure is zero. On the other hand, once the ground is liquefied, the excess pore water pressure ratio is 1.0. It can be readily seen that the reclaimed ground at Port Island starts to liquefy at around 8 sec on the time axis. The maximum values of the built up excess pore water pressure at alluvial (diluvial) sandy layer at Port Island is found to be 80 % of the initial effective overburden pressure. On the other hand, the excess pore water pressure at both reclaimed ground and alluvial (diluvial) sandy layer for Rokko Island are about 70 % of the initial effective overburden pressure in spite of the same liquefaction strength for both soil layers. The difference of the excess pore water pressure at PI and RI stations is considered partly due to the de-amplification of the horizontal earthquake motion through the alluvial clay layer (from GL –24 m to GL –34 m) for RI station in which the shear wave velocity is much smaller than that for PI station.

The distributions of the excess pore water pressure ratio along the numerical columns for both PI and RI stations are plotted in Fig.10. It is found that the whole reclaimed layer below sea level for PI station was liquefied by the strong motion during the earthquake. On the other hand, the reclaimed layer at RI station did not liquefied.

TIME-DEPENDENT AMPLIFICATION RATIO DUE TO DICREASE OF EXCESS PORE WATER PRESSURE

The time-dependent amplification ratio due to the decrease of excess pore water pressure is investigated. It could be caused by the recovery of the rigidity of sandy soils that once liquefied. Figure 11 shows the variation of the acceleration amplification ratio from G.L.-83m level to the ground surface at PI station as well as that from GL.-154.5 m to the ground surface at RI station. It is observed in Fig.11(a) that the amplification ratio decreases in horizontal ground motion just after the main event, and then gradually recovered in about a weak. On the other hand, the amplification factor of up-down component, which mainly consists of P-wave does not change so such as that of horizontal components. In the case of RI station in Fig.11(b), the recovery of the amplification ratio is not evident, since the records were not obtained until 90 hours after the main event. Figure 12 shows the variation of the velocity amplification ratio. In the case of PI station the recovery in the horizontal components is recognized as the case of peak acceleration.

The recoveries of the frequency contents are shown in Fig.13. Figure 13(a) shows the variation of the amplification ratio of acceleration response spectrum for f=7.14 Hz and 1.54 Hz at PI station. The decrease and the recovery of the amplification ratio is predominant for the high frequency content (f=7.14 Hz), and they are not clear for the middle frequency content (f =1.54 Hz). The recovery of the amplification ratio for f=7.14 Hz is quite similar to that of peak acceleration and velocity.

At both the artificial islands the excess pore water pressure were observed. Though the observation sites of the two artificial islands where the excess pore-water pressure were measured, are not close to the array observation stations, the soil profiles are similar to those of array observation stations, respectively. Figure 14 shows the variation of the excess pore water pressure at both the islands after the main event. Though there are not enough data points, it is observed in Fig.14(a) that the excess pore water pressure decreased in some hundreds hours to the level before the main event. This is quite consistent with the recovery of the amplification ratio of the peak acceleration, velocity, and high frequency content.

SUMMARY

The amplification characteristics of strong ground motion at two reclaimed lands were investigated based on the borehole records obtained from 39 earthquakes including the 1995 Hyogoken Nambu Earthquake. The major conclusions can be summarized as follows.

(1) The amplification characteristic of peak ground motion and spectral contents at Port Island and Rokko Island in Kobe City were discussed. The borehole array records at the two islands are classified regarding their recording term such as before and after the 1995 Hyogoken Nambu Earthquake.

(2) It was found that the amplification characteristic depended on the softness of the alluvial layer under the reclaimed sand. The consolidation term of the alluvial layer at PI station is about 26 years and that of RI station is 16 years. It was pointed out that the ground motion was not amplified at RI station where the shear wave velocity of alluvial layer was less than that at PI station. This is considered as one of the reasons for the difference of the level of liquefaction at these islands during the main event.

(3) Two techniques for response analysis of ground were applied to the two borehole stations. One is the modified equivalent linearization technique in frequency domain, and the other is the effective stress-based liquefaction analysis. In the former analysis, response analysis for several levels of input motion were performed and the results were consistent with the borehole records; namely, the very soft alluvial layer at RI station could reduce the ground motion propagated to upper reclaimed layer, which is so-called base isolation effect. The effective stress-based liquefaction analysis at those two stations with the same input motion shows that the liquefaction is much severe at PI station, which is quite consistent with the observed data.

(4) The time-dependent amplification ratio resulted from the recovery of the soil rigidity after the main event was specially demonstrated. It was found that the amplification ratio of peak acceleration, peak velocity as well as the higher frequency contents decreased considerably just after the main event, and then gradually recovered in about a week. The result was compared with the record of the excess pore water pressure at two islands.

ACKNOWLEDGEMENT

Mr.Hiro Amano of Ichikawa Komuten Co., a former student of Gifu University, is acknowledged for his help in data compilation and graphical outputs.

REFERENCES

Japan Road Association (1996). Design Code for Road Bridges, —Earthquake Registant Design —, Vol.V (in Japanese)

Kamata,A., Oishi,H., and Sekiguchi,K. (1987). Three dimensional earthquake observation of buried pipelines. *Suido Kyokai Zasshi*, 56:5, 39-53.

Oka,F., Yashima,A., Kato,M. and Sekiguchi,K.(1992). A constitutive model for sand based on the non-linear kinematic hardening rule and its application. Proc. 10th WCEE, Madrid, pp.2529-2534.

Oka,F., Sugito,M., Yashima,A., Taguchi,Y. and Sekiguchi,K.(1996). Analysis of strong motion records from the South Hyogo Earthquake of January 17, 1995. Engineering Geology, Vol.43, pp.85-106.

Oka,F., Yashima,A., Sugito,M. and Taguchi,Y.(1997). Three dimensional liquefaction analysis of reclaimed island. Proc. 7th Int. Offshore and Polar Eng. Conf., Honolulu, Vol.1, pp.665-670.

Sugito,M. (1993). Frequency- dependent equivalent strain for earthquake response analysis of soft ground, *Proc. of Third Republic of China and Japan Joint Seminar on Natural Hazards Mitigation, Taiwan*, 409-422.

Sugito,M., Sekiguchi,K., Yashima,A., Oka,F., Taguchi,Y., and Kato,Y. (1996). Correction of orientation error of borehole strong motion array records obtained during the South Hyogo Earthquake of Jan.17, 1995. *Journal of Japan Society of Civil Engineers*, 531:I-34, 51-63.

Taguchi,Y., Tateishi,A., Oka,F. and Yashima,A.(1996). Three-dimensional liquefaction analysis method and array record simulation in Great Hanshin Earthquake. Proc. 11th WCEE, Acaplco, No.1042.

Tateishi,A., Taguchi,Y., Oka,F. and Yashima,A.(1995). A cyclic elasto-plastic model for sand and its application under various stress conditions. Proc. 1st Int. Conf. On Earthquake Geotechnical Eng., Tokyo, pp.399-404.

Yashima,A., Oka,F., Taguchi,Y. and Tateishi,A.(1995). Three dimensional liquefaction analysis considering the compressibility of fluid phase. Proc. 40th JGS Symposium, pp.257-264 (in Japanese).

Table 1 List of earthquakes.

category	EQ. NO.	occ. Time	M	depth (km)	epicenter	latitude (deg.)	longitude (deg.)	GL0.0m peak acceleration(cm/sec^2) PI NS	PI EW	PI UD	RI NS	RI EW	RI UD	ref.
A Group	01	94.06.28 13:09	4.6	13	Kyoto,Center	35.08.	135.39.	5.395	6.047	2.664	2.019	2.275	3.665	
	02	94.07.28 10:02	4.1	9	Osaka,South	34.19.	135.19.	3.878	4.831	7.944	2.474	2.815	7.095	
	03	94.10.24 11:51	4.3	15	Kyoto,Center	35.00.	135.31.	8.852	12.098	3.045	3.276	2.686	2.968	
	04	94.11.09 20:27	4.0	14	Hyogo,East	34.55.	135.23.	3.765	8.758	1.942	2.507	2.712	2.526	
	05	94.11.10 00:38	3.9	14	Hyogo,East	34.55.	135.23.	4.504	6.985	2.118	3.874	3.263	3.288	
main event	06	95.01.17 05:46	7.2	13	Awaji Island	34.64.1	135.17.9	340.900	282.600	567.100	-	-	-	*1
B Group	07	95.01.17 05:53	4.9	8	Hyogo,Southeast	34.40.7	135.08.9	28.521	35.183	119.216	-	-	-	*1
	08	95.01.17 08:58	4.7	19	Awaji Island	34.35.2	135.00.4	45.601	32.880	18.563	-	-	-	*1
	09	95.01.18 05:25	4.5	15	Hyogo,Southeast	34.41.8	135.10.9	79.558	52.833	38.592	-	-	-	*1
	10	95.01.18 13:34	4.0	15	Hyogo,Southeast	34.41.3	135.10.5	43.818	25.557	27.250	-	-	-	*1
C Group	11	95.01.19 01:00	4.0	14	Hyogo,Southeast	34.47.8	135.19.7	7.253	12.927	7.804	-	-	-	*1
	12	95.01.19 01:52	3.3	10	Osaka Bay	34.38.7	135.07.5	5.868	6.854	12.519	-	-	-	*1
	13	95.01.19 02:23	3.4	14	Hyogo,Southeast	34.41.7	135.02.1	13.131	5.109	7.994	-	-	-	*1
	14	95.01.19 05:10	3.2	18	Hyogo,Southeast	34.39.8	135.09.6	19.320	21.603	21.861	-	-	-	*1
D Group	15	95.01.20 15:38	3.7	14	Hyogo,Southeast	34.41.9	135.12.3	-	-	-	6.238	10.415	17.981	*2
	16	95.01.23 21:44	4.3	16	Hyogo,Southeast	34.37.6	135.19.1	-	-	-	23.06	25.893	63.029	*2
	17	95.01.25 23:16	4.7	17	Hyogo,Southeast	34.47.4	135.18.8	-	-	-	27.441	17.154	30.801	*2
E Group	18	95.01.26 01:01	3.5	13	Hyogo,Southeast	34.46.0	135.16.0	10.863	10.719	5.273	2.731	3.239	5.247	
	19	95.01.26 23:08	3.5	15	Hyogo,Southeast	34.47.4	135.18.6	6.036	2.702	11.390	6.212	2.66	6.407	
	20	95.01.28 08:06	3.0	5	Hyogo,Southeast	34.41.0	135.10.7	18.801	23.559	17.654	-	-	-	*1
	21	95.01.29 09:41	3.3	14	Hyogo,Southeast	34.39.4	135.08.6	13.067	5.048	10.664	2.43	1.989	5.064	
	22	95.01.29 16:02	3.6	13	Hyogo,Southeast	34.41.1	135.10.8	16.721	19.770	8.329	4.991	5.328	15.341	
	23	95.02.02 16:19	4.2	18	Hyogo,East Coas	34.41.7	135.09.0	64.699	65.489	34.238	21.741	20.692	46.29	
	24	95.02.03 04:36	3.7	15	Hyogo,East Coas	34.41.8	135.11.2	21.046	7.273	7.854	2.089	2.111	5.707	
	25	95.02.03 20:37	3.4	12	Hyogo,East Coas	34.43.8	135.16.0	9.385	7.210	8.103	22.291	16.69	21.238	
	26	95.02.06 13:00	3.5	12	Hyogo,East	34.47.6	135.19.5	3.250	5.783	3.627	4.23	4.183	6.744	
	27	95.02.18 21:37	4.9	13	Awaji Island	34.26.7	134.48.4	17.800	13.373	9.068	10.684	8.559	7.823	
	28	95.02.24 08:03	3.3	15	Hyogo,East Coas	34.42.9	135.12.5	14.230	12.438	12.253	2.001	3.089	2.778	
F Group	29	95.03.05 10:04	3.2	15	Hyogo,East Coas	34.43.7	135.14.8	4.037	6.147	5.764	5.846	6.318	8.821	
	30	95.04.06 10:50	4.0	12	Hyogo,Southeast	34.47.4	135.19.2	4.940	7.692	4.632	6.303	6.828	11.925	
	31	95.05.04 05:53	3.6	15	Hyogo,Southeast	34.41.7	135.11.1	27.715	10.012	8.866	7.253	10.662	23.629	
	32	95.05.04 17:42	4.1	18	Osaka Bay	34.32.2	134.54.3	8.623	8.298	5.258	3.806	3.314	2.5	
	33	95.05.08 02:36	3.3	14	Hyogo,East Coas	34.42.6	135.12.8	29.402	24.465	16.438	4.113	4.443	6.992	
	34	95.05.15 07:33	3.4	13	Osaka Bay	34.38.8	135.07.9	14.469	10.118	14.048	5.603	3.223	8.152	
	35	95.05.19 20:35	4.4	19	Osaka Bay	34.36.4	135.02.1	7.684	6.539	4.002	2.652	4.395	3.48	
	36	95.05.28 10:34	4.0	14	Hyogo,Southeast	34.40.4	135.10.1	22.180	29.056	17.369	-	-	-	*1
	37	95.06.19 08:38	3.4	13	Hyogo,Southeast	34.45.8	135.16.2	17.754	10.071	17.127	-	-	-	*1
	38	95.09.12 06:30	3.6	16	Hyogo,Southeast	34.41.5	135.11.8	84.620	35.063	22.541	8.579	11.208	23.683	
	39	95.10.14 02:04	4.8	17	Osaka Bay	34.37.0	135.06.4	60.261	47.480	71.438	19.599	21.758	26.943	

*1: no recond at Rokko Island station
*2: no recond at Port Island station

Table 2 Parameters for effective stress-based liquefaction analysis.

(Port Island Borehole Array Station)

depth (GL, m)	soil layer	void ratio e	V_s (m/s)	Liquefaction strength N=10	N=30
0.0	sandy gravel (reclaimed)	0.60	140	(non-liquefiable)	
(sea level) -2.4	sandy gravel (reclaimed)	0.60	180	0.22	0.17
-5.0	sandy gravel (reclaimed)	0.60	195	0.22	0.17
-12.6	sand with gravel (reclaimed)	0.60	220	0.22	0.17
-19.0	alluvial clay	1.50	180	(non-liquefiable)	
-27.0	alluvial sand	0.60	245	0.40	0.30
-33.0	diluvial sand with gravel	0.50	305	0.45	0.35
-50.0	diluvial sand	0.50	350	0.60	0.40
-61.0	diluvial clay	1.20	303	(non-liquefiable)	
-79.0	diluvial sand with gravel	0.50	320	0.60	0.40
-83.0	base				

(Rokko Island Borehole Array Station)

depth (GL, m)	soil layer	void ratio e	V_s (m/s)	Liquefaction strength N=10	N=30
0.0	sandy gravel (reclaimed)	0.60	220	(non-liquefiable)	
(sea level) -2.8	sandy gravel (reclaimed)	0.60	220	0.22	0.17
-4.0	clayey gravel (reclaimed)	0.60	260	0.22	0.17
-10.0	sandy gravel (reclaimed)	0.60	260	0.22	0.17
-24.0	alluvial clay	1.50	115	(non-liquefiable)	
-34.0	alluvial sand	0.60	250	0.40	0.30
-44.0	diluvial sand with gravel	0.50	380	0.60	0.40
-75.0	diluvial clay	1.20	260	(non-liquefiable)	
-93.5	base				

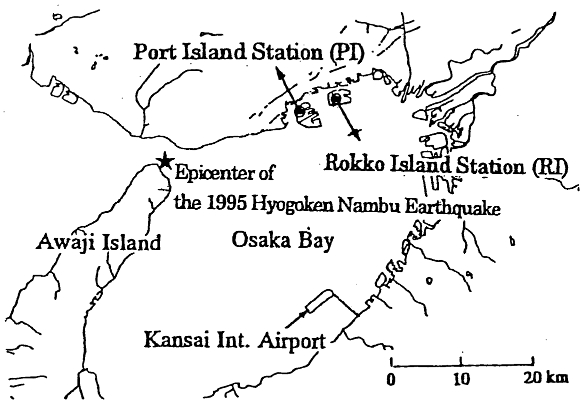

(a) Location of array observation stations.

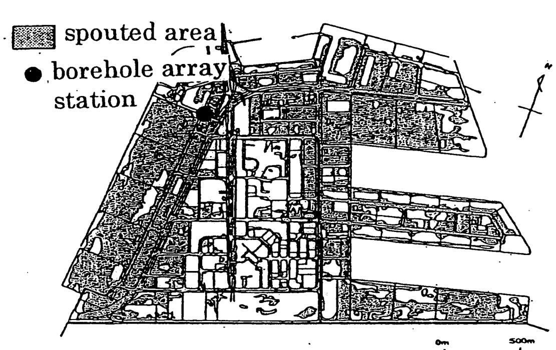

(b) Spouted area of liquefaction sand in in Port Island

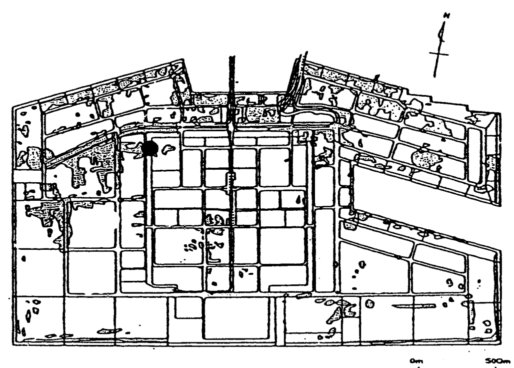

(c) Spouted area of liquefaction sand in Rokko Island

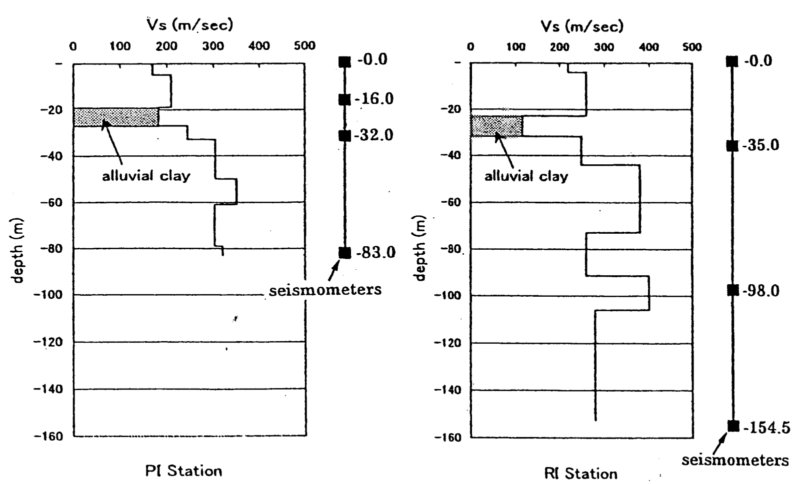

(d) Velocity structure and layout of seismometers

Fig.1 Location and velocity structure models for borehole array observation stations.

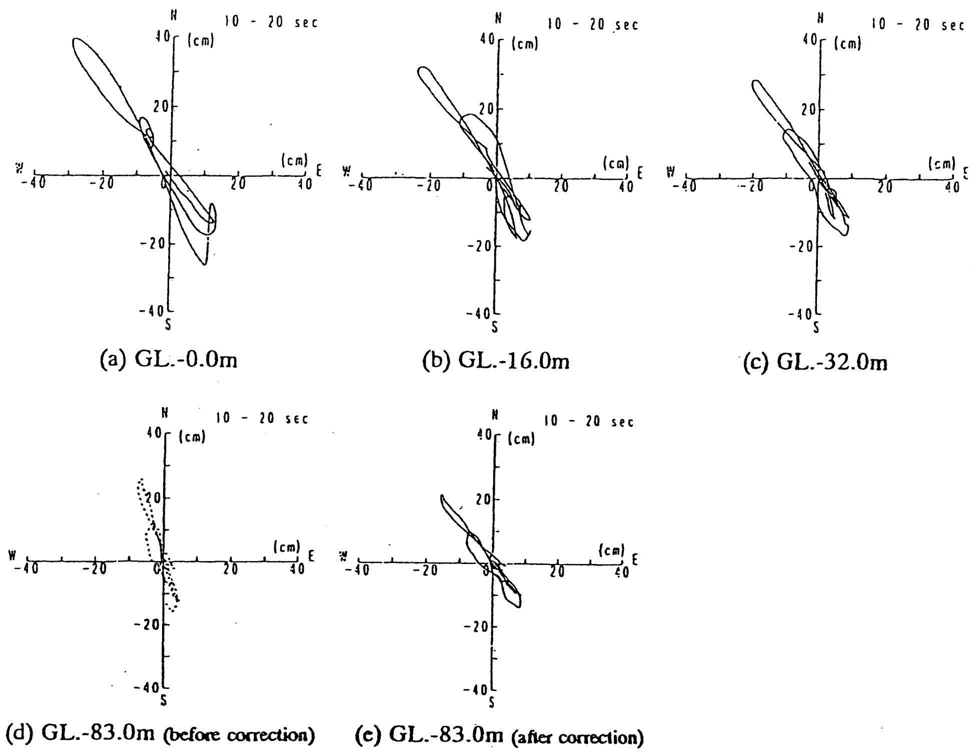

Fig.2 Displacement orbits at various depth (Port Island, Kobe City).

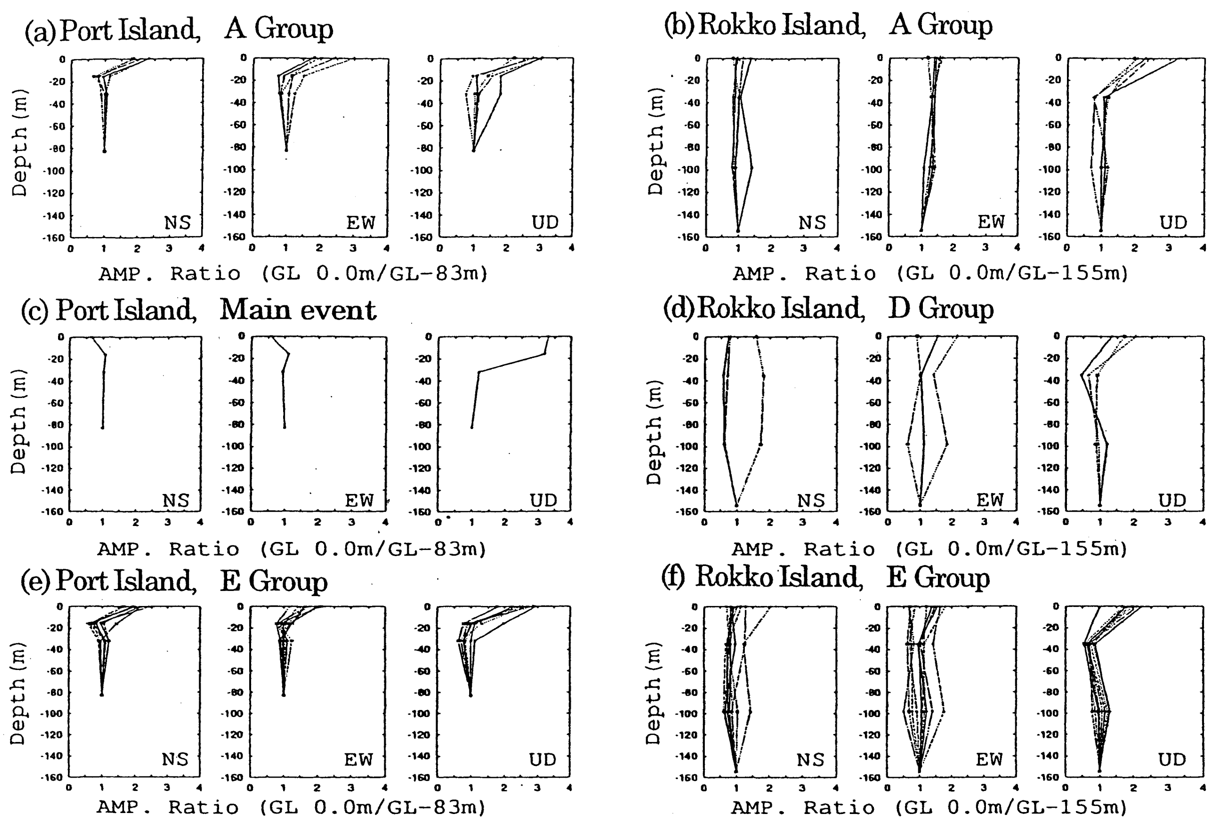

Fig.3 Amplification characteristic of peak acceleration.

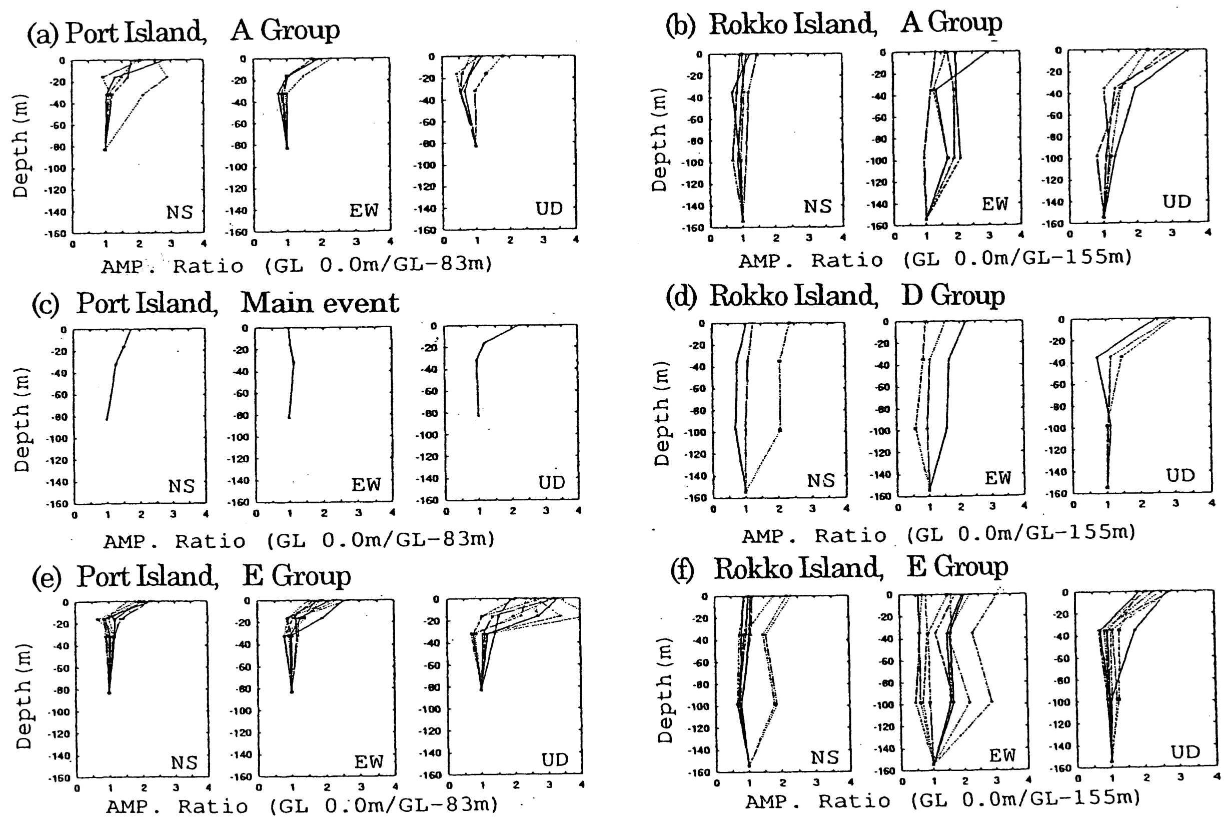

Fig.4 Amplification characteristic of peak velocity.

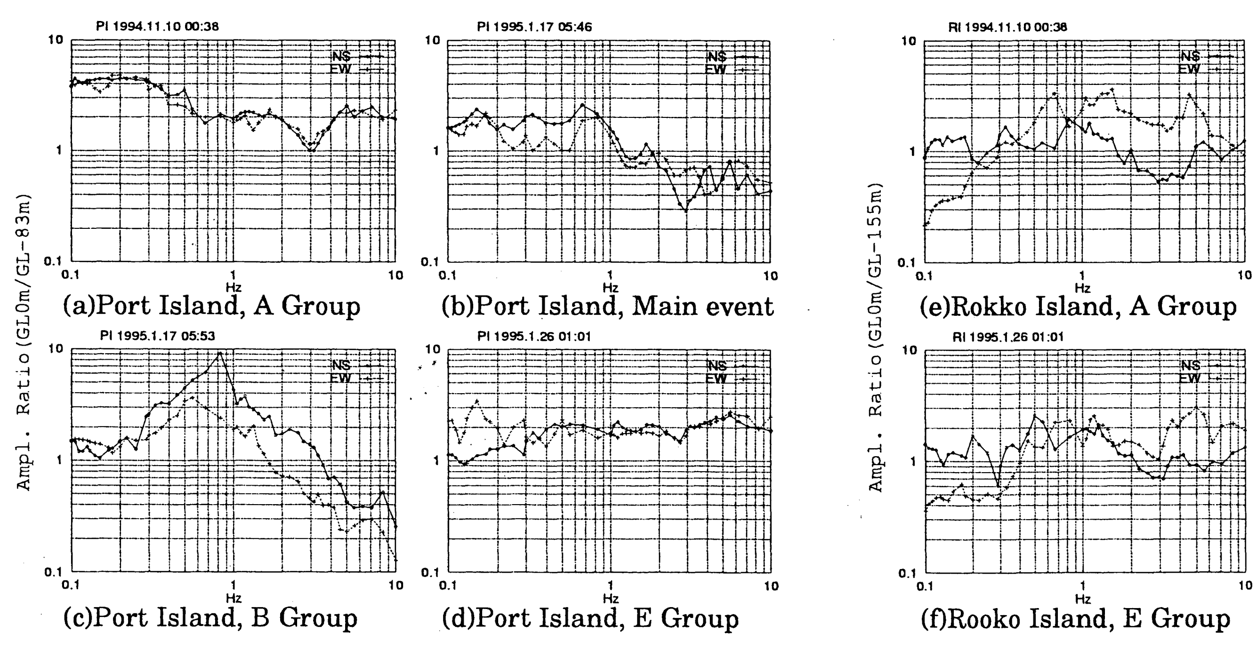

Fig.5 Amplification of acceleration response spectra.

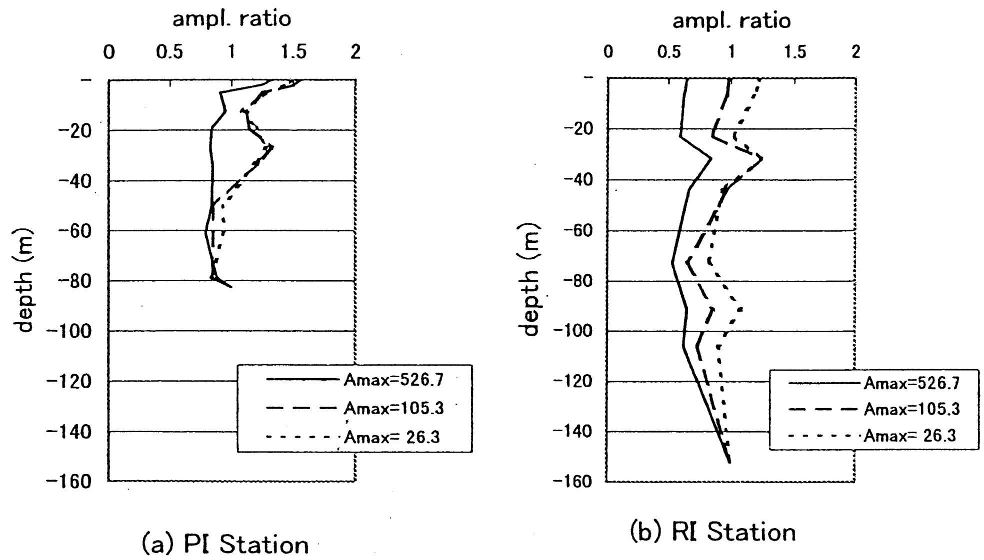

Fig.6 Amplification characteristic of peak acceleration depending on input ground motion levels.

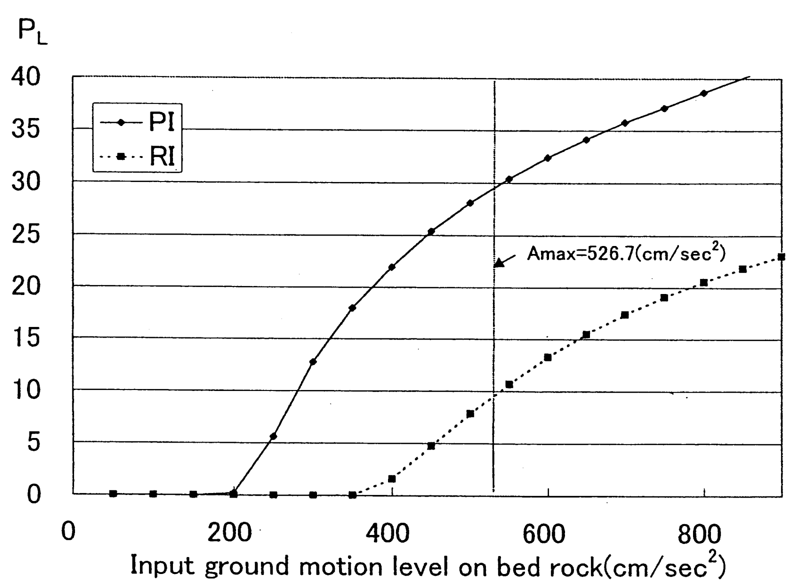

Fig.7 Variation of liquefaction potential index (P_L) depending on input ground motion levels.

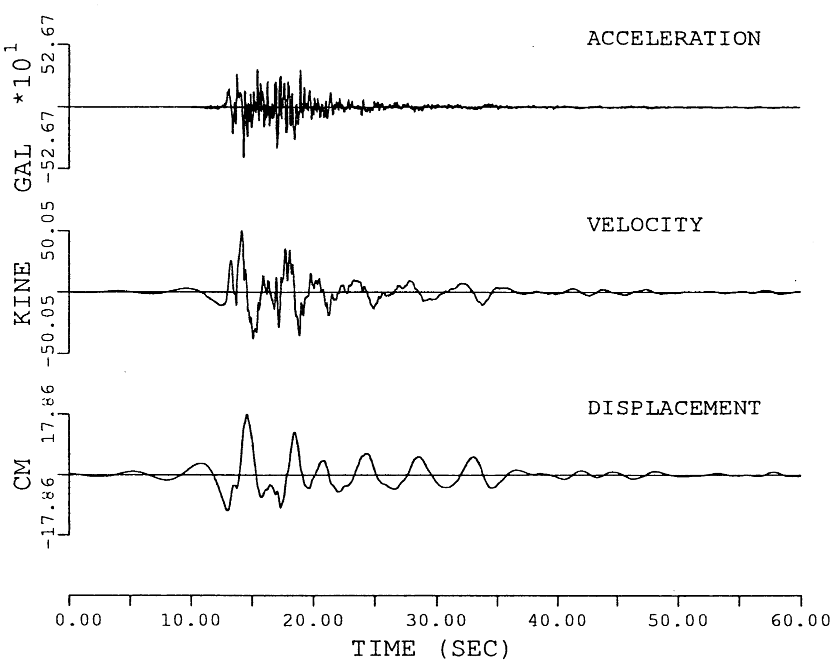

Amax= -526.7	gal	Vmax= 50.1	kine	Dmax= 17.9	cm
Atau= 249.0	gal	Kshindo= 5.5			

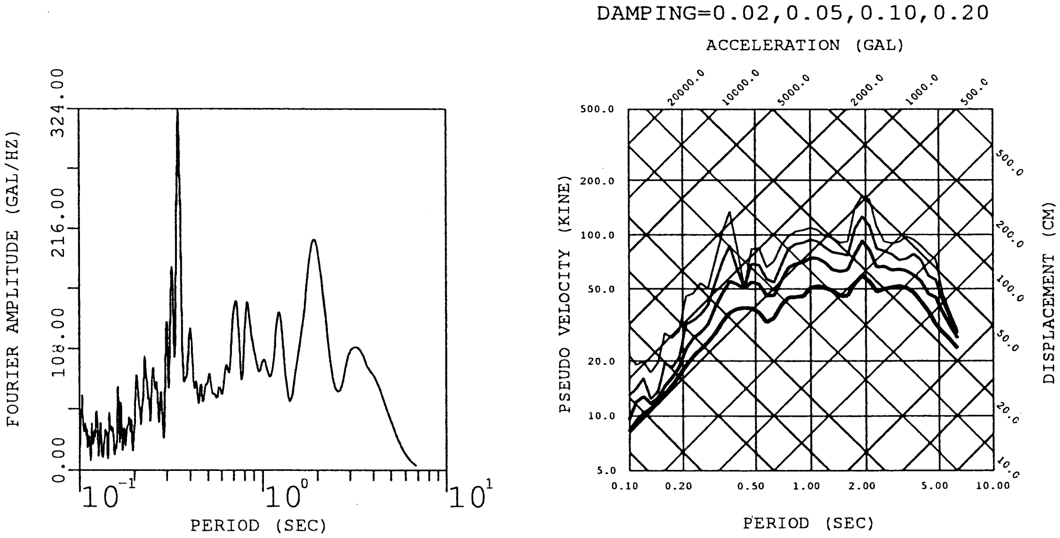

Fig.8 Strong motion record obtained at GL-83m of PI in NS component during the 1995 Hyogoken Nambu eqrthquake. (Acceleration,velocity,displacement,acceleration fourier Spectrum and response spectra)

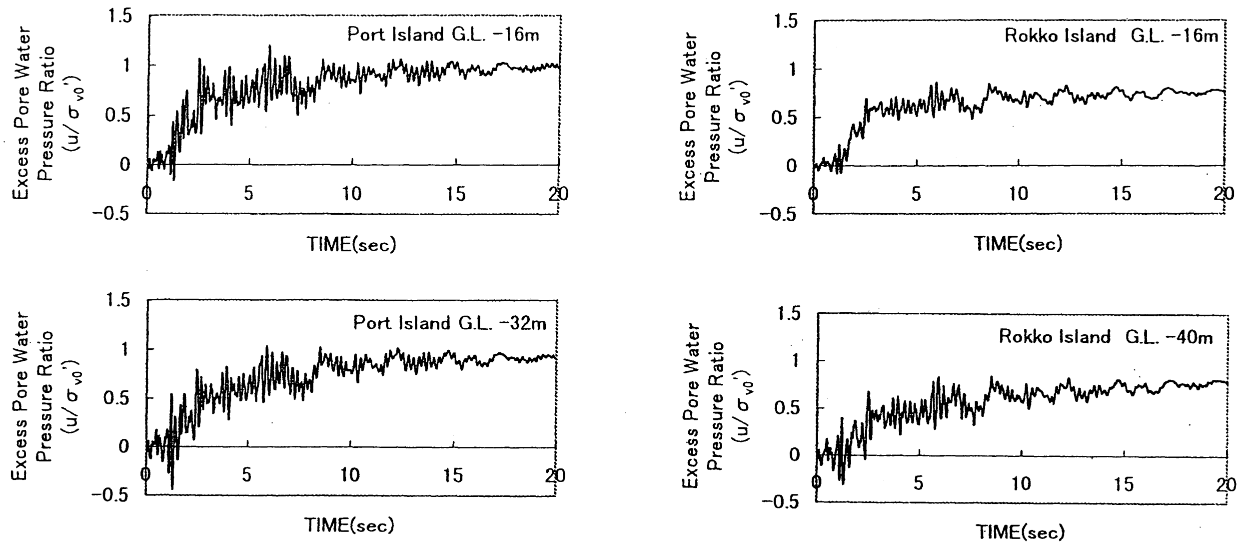

(a) Port Island

(b) Rokko Island

Fig.9 Time history of excess pore water pressure ratio.

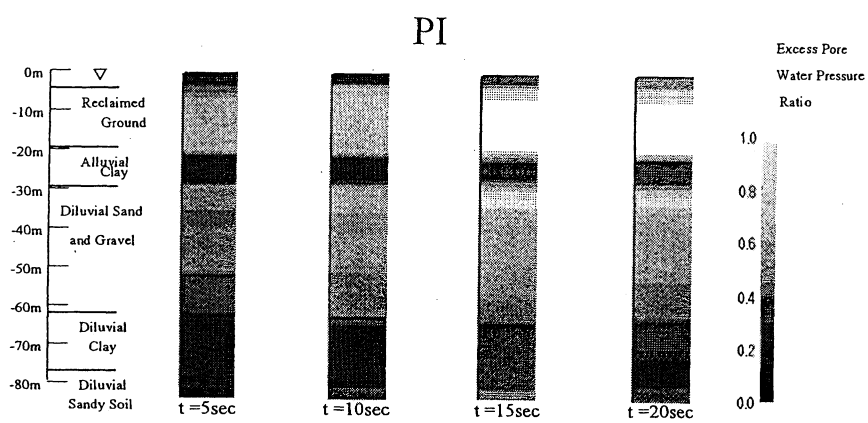

(a) Port Island

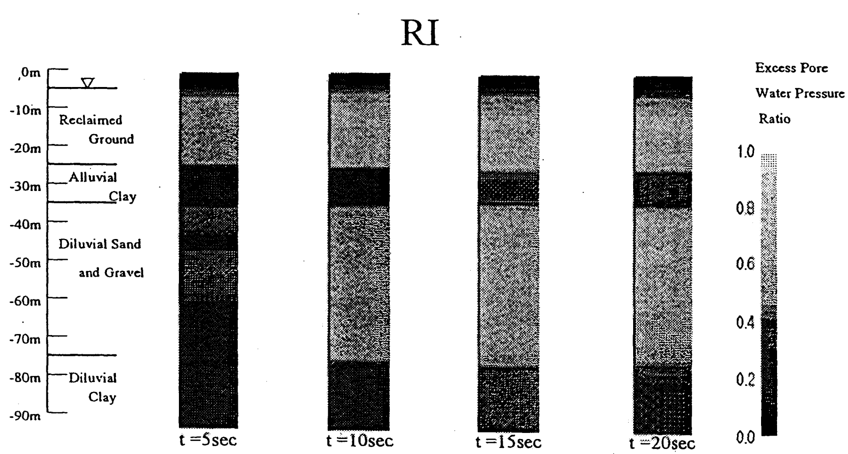

(b) Rokko Island

Fig.10 Distribution of excess pore water pressure ratio.

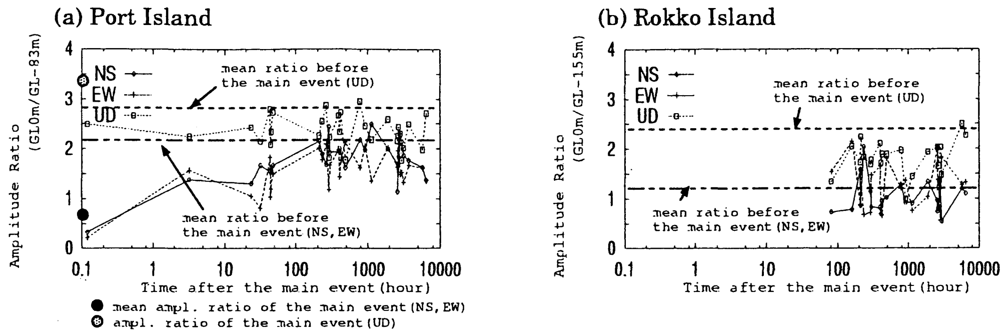

Fig.11 Time dependent amplification characteristic of peak acceleration

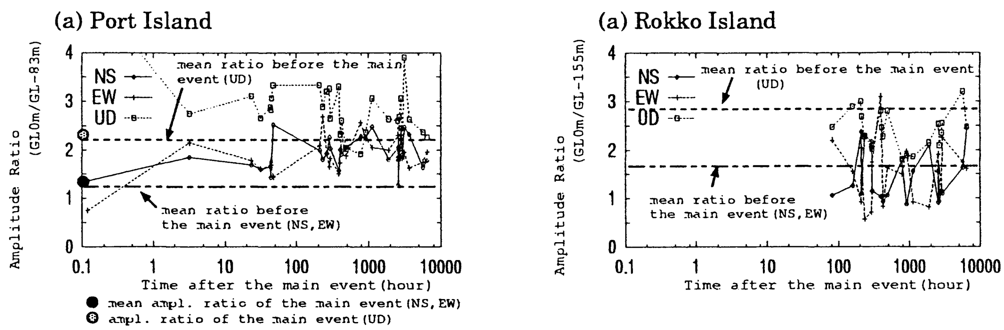

Fig.12 Time dependent amplification characteristic of peak velocity

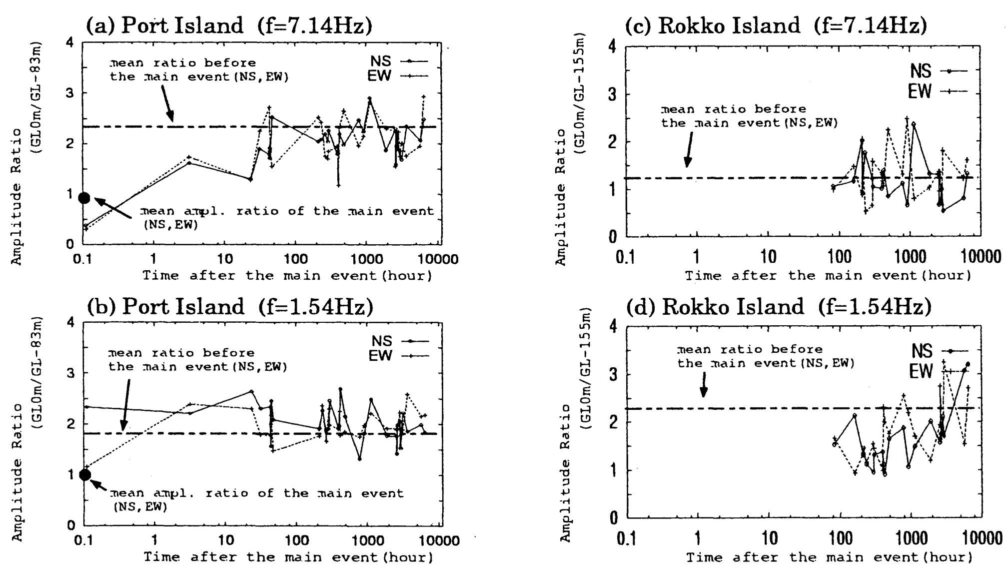

Fig.13 Time dependent amplification characteristic of response spectra

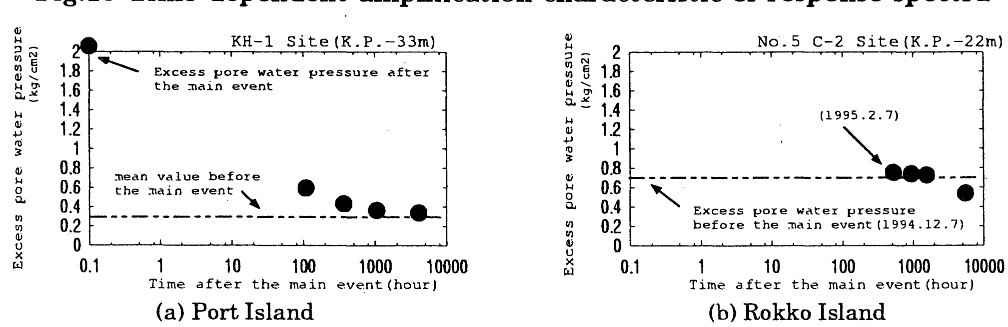

Fig.14 Variation of excess pore water pressure ratio

Lifelines and Earthquake Effects

Quantifying Earthquake and Geologic Hazards for the Portland, Oregon Water System Vulnerability Assessment
By D. Ballantyne, C. Scawthorn, and A. Vessely

The 1995 Kobe Earthquake and the New JWWA Seismic Design Guideline for Waterworks Facilities
By M. Matsushita

Estimation of Post Earthquake Water System Serviceability
By M. J. O'Rourke

Development of New Aseismic Joints for Casing Pipes of Underground Transmission Lines
By E. Miura, T. Tanaka, Y. Oda, and N. Ito

Case Study of Granada Trunk Line During Two Near-Field Earthquakes
By C. A. Davis

Success in Lifeline Seismic Mitigation Programs
By L. V. Lund

Effects of Material Property on Inelastic Shell Buckling Strength of Line Pipe
By N. Suzuki, A. Katoh, E. Matsuyama, and M. Yoshikawa

Large Deformation Behavior of Low-Angle Pipeline Elbows
By K. Yoshizaki, M. Hamada, and T. D. O'Rourke

Summary of the Earthquake Resistant Design Standards for Railway Structures
By A. Nishimura

Visual Interpretation of Site Dynamic Response
By M. Zeghal, C. Oskay, M. K. Sharp, and R. Dobry

Formulation of Level 2 Earthquake Motions for Civil Engineering Structures
By T. Ohmachi

Quantifying Earthquake and Geologic Hazards for the Portland, Oregon Water System Vulnerability Assessment

Donald Ballantyne, PE, Vice President, and Charles Scawthorn, SE, Senior Vice President, EQE International
Andrew Vessely, PE, CEG, Associate Engineer, Cornforth Consultants, Inc.

ABSTRACT

This paper describes geologic hazard quantification for the multi-hazard system vulnerability assessment of the Portland, Oregon's water system. The two hazards that pose the greatest risk are earthquake (including ground motion, landslide, and liquefaction), and intense rain (including landslide, turbidity, and flood).

The primary supply (surface water) is transported to the city through three, 40 km-long conduits. The corridor is subject to earthquake and rain-induced landslides. The secondary supply (groundwater) is pumped from the Columbia River south shore well field which is founded on moderately liquefiable, silty sand. The final transmission segment crosses liquefiable material along the Willamette River. The supply system schematic is shown in Figure 1.

Earthquake ground motions are quantified considering crustal sources and an interface subduction source. Liquefaction vulnerability is based on recent site specific and regional studies. The landslide risk assessment relies on geologic mapping developed for the project, and landslide history along the corridor.

INTRODUCTION

Thirty-eight hazards were considered in the Multi-hazard System Vulnerability Assessment (SVA) of the Portland, Oregon, Bureau of Waterworks water system. The SVA project is summarized in *Multi-Hazard Risk Assessment For Lifelines Part 2 - Case Study For The Portland, Oregon Water Supply System* (Ballantyne,et al, 1999). This paper describes quantification of the geologic hazards for the SVA.

The 38 hazards were subdivided into four major hazard categories: natural, human/technological, transportation, and lifeline service. Table 1 presents a summary of the natural hazards analyzed and their risk-based ranking. Geologic hazards addressed in this paper are identified.

PROJECT APPROACH ISSUES

The intent of the project was to use hazard information developed for other projects when ever possible, and only to assess hazards in detail when no other resources were available. Such information had been developed for different purposes, and was often available, but in different formats. The project team included consultants addressing a range of hazards. Many of these consultants were selected because of their expertise with specific hazards in the region, but were not necessarily familiar with quantification of hazards in the form to be used in this risk assessment. Therefore, one of the significant project tasks was to put information into a useful common format. Hazards were ranked by supply and distribution systems, respectively, as described in the following subsections.

Table 1
Summary Of Natural Hazards And Rankings

Hazard	Discussed in this Paper	Very High	High	Moderate	Low
Intense Rain on Snow					
Landslide (rain induced)	X	X			
Turbidity		X			
Fire in Watershed (Turbidity)		X			
Flood–Bull Run, Sandy rivers		X			
Flood–Columbia, Willamette rivers		X			
Wind/Ice Storm (Power)			X		
Winter Snow/Ice Storms (Structural)					X
Wind/Tree Fall (Structure Impact, Slope Destabilization)					X
Earthquake					
Ground Motion	X	X			
Liquefaction	X	X			
Landslide	X	X			
Surface Faulting	X				X
Seiche					X
Volcanic Activity					
Sandy River Lahar/Debris Flow	X		X		
Ash Fall (Turbidity, Electrical)	X				X
Land/Rock Slides/Debris Flow (non-rain induced)			X		
Microbial Contamination				X	
Prolonged Freezing					X
Urban Firestorms, Forest Park Fires					X

Supply Facilities

Hazard rankings for the supply facilities were categorized as follows: (1) preliminary categories were identified in the interview process and during SVA project meetings where the hazard matrix was reviewed; and (2) the potential effect of each hazard was evaluated as to whether it would affect one or multiple components at any time. Hazards with a recurrence interval of 1,000 years or less were considered in the project. A preliminary ranking was conducted for each hazard, estimating the level of risk considering the possible extent and consequences of damage, as follows:

- Very High – hazard events that could result in loss of overall system service because of damage to multiple facilities. In general, this group includes hazards that have the potential for making both the Bull Run surface water and groundwater system inoperable at the same time. Frequency-severity (also termed recurrence-intensity) relationships have been developed for these hazards, and they are included in the system model to assess the probability of damage to multiple facilities.

- High – hazard events that could result in loss of service from either the Bull Run or groundwater supply; i.e., one or the other, not both. These hazards are examined but not modeled as they would impact only one supply at a time, allowing for continued service through redundancy in the system.

- Moderate – hazard events that could result in loss of service to limited supply areas, and/or cause significant damage to Bureau facilities, but without loss of the Bull Run or groundwater supplies.

- Low/Very Low – hazard events with expected recurrence intervals significantly longer than 1,000 years and/or would result in limited damage and no loss of service.

Distribution (Backbone) Facilities

On review of the distribution facilities, it was concluded that the only hazard that could have an impact on multiple system components is an earthquake. (Note: although a power outage could impact multiple pump stations, in general pump stations have emergency power supplies.) Therefore, SAFENET, a proprietary post-earthquake network serviceability evaluation tool was used to model post-earthquake distribution system functions.

INTENSE RAIN-ON-SNOW EVENT

An intense rain-on-snow event is thought to produce the highest "water application rate" to the ground. This hazard category includes both rain-on-snow and intense rain. There are a number of sub-hazards that result from the intense rain-on-snow storms that are highly correlated, including (1) landslides, (2) turbidity events, and (3) floods on the Bull Run and Sandy Rivers, as shown in Figure 2. Other types of storm events including wind storms and ice storms, and longer periods or wider areas of rainfall that result in flooding on the Columbia River are not correlated to an intense rain-on-snow event. A fire in the watershed during the season before an intense rain-on-snow storm increases the probability of occurrence, and duration, of a turbidity event. We will focus on rain induced landslides, the geologic hazard in this group, with a brief discussion of related hazards. Some of the intense rain on snow hazards are correlated.

Rain-Induced Landslide

Landslides can be initiated by reduction in the strength of the soil as a result of being saturated, by rain, or from increased loading due to earthquakes. This section discusses landslides induced by rain. Landslides can occur in the watershed, along the conduit corridors, and to a lesser degree, at other locations within the system. Landslides can damage facilities as a result of impacting the facility with sliding debris, burying the facility, or the facility moving as part of the slide. Dam #2, the lower dam in the Bull Run watershed, is constructed on an ancient landslide. Washington Park Reservoir Nos. 3 and 4, the reservoirs serving the Portland central business district, are located at the toe of a large moving landslide. Landslides will occur in the watershed, exposing soils that can easily erode during heavy rains, increasing turbidity in the reservoirs. There is a very low probability that landslides will occur into the reservoirs that could result in a seiche and/or wave that could overtop a dam.

The project geotechnical consultant developed landslide probabilities based on historic data from landslides along the Bull Run corridor (Cornforth, 1998a). There was inadequate information on dates of occurrence to relate landslides directly with intense rain on snow, or rain events. It appears there is a correlation between intense rain and landslides, based on recent historical events. Therefore, the supply side hazard risk model assumes that landslides will occur during the 4-month rainy season, from November through February (the return period assumes 4 wet months and 8 dry months). The model also considers the sensitivity of the assumption that the landslides are directly correlated with intense rains, similar to turbidity events, and flooding on the Bull Run and Sandy Rivers.

The majority of landslide risk for the water supply system is associated with ancient landslide terrain located in the Bull Run corridor from the headworks to approximately 3 miles northwest of the Sandy River crossing. Within this area are three types of geologic terrain:

- Ancient Landslide Terrain. The majority of the Bull Run corridor is comprised of ancient landslide terrain that developed as the Bull Run River eroded through more resistant geologic units (Troutdale Formation) into softer geologic units (Sandy River Mudstone). This led to undercutting of the overlying more resistant layer, which eventually resulted in massive landsliding along both sides of the valley.

- Historically Active Slide Terrain. The historically active slide terrain includes 17 landslides that have occurred within the ancient slide terrain since the original construction of the conduits in the 1890s. Six of these slides have resulted in damage to the conduits, and seven others have come close to damaging the conduits. Nearly all of the slides have been remediated.

- Stable Terrain. Stable terrain consists of geologic units that show no evidence of landsliding and includes the majority of the conduit alignments west of the Sandy River crossing. In general, this material represents a very low risk for slide hazards.

Two types of landslides are considered for the Bull Run corridor:

- Flow slides occur during high intensity winter storms and are typically 20 to 200 feet in width. Downslope movement of a surficial layer occurs rapidly and can move tens to hundreds of feet.

- Translational slides are much larger in size and deeper, and move at a much slower rate (inches per year or less). They typically exhibit creep-like movement during winter, and zero or very slow movement in the summer.

Landslide hazard curves were developed for each geological terrain by estimating the probability of a significant landslide anywhere along the conduit run for recurrence intervals of 10, 50, 100, 500, and 1,000 years. In this context, significant landslides include only those landslides judged large enough to result in failure of one or more conduits. The probabilities reflect the geologic conditions as they currently exist, and can be affected by man-made activities such as excavations, logging, and surface water management.

The landslide probabilities for stable terrain and ancient landslide terrain were developed based on historical data over the past 100 years and extrapolated based on experience and judgment. The probabilities for flow slide failures took into consideration that the more susceptible flow slide areas have probably failed already, and that creeping slide terrain could be slowly stressing the conduits in undetermined locations. Table 2 lists the probability of conduit slides for the three geologic terrains and two slide types. The probabilities refer to the likelihood of a landslide occurring anywhere along the length of the slide terrain. Note that the slide probabilities do not include the probability of earthquake-induced landslide, which is addressed in the earthquake hazard section.

Table 2
Estimated Probabilities Of Conduit Landslide Damage During 4-Month Rainy Period (Rain Induced)

Item	Probability of Conduit Landslide Damage for Given Return Period (years)				
	10	50	100	500	1,000
Remediated Flow	0.00	0.00	0.01	0.05	0.10
Remediated Translational	0.01	0.07	0.15	0.75	1.00
Ancient Flow	0.60	0.99	1.00	1.00	1.00
Ancient Translational	0.01	0.07	0.15	0.75	1.00
Inactive	0.01	0.05	0.10	0.50	1.00

Based on these results, we have used a 10-year recurrence interval for a landslide that damages one or more conduits occurring somewhere in the Bull Run corridor. The majority of the alignment is in ancient landslide terrain. Flow slides, the most likely to move, occur rapidly, with widths that would be damaging to the conduits. In subsequent analyses, the probability of failure is distributed by length of corridor, where the corridor may contain Conduits 2 and 4, Conduit 3, or Conduits 2, 3, and 4.

Related Hazards

The water quality from Bull Run unfiltered water supply must be maintained at an acceptable level for drinking. To continue use, the turbidity must be kept below 5 turbidity units. Intense rains result in localized erosion in the watershed which increase turbidity. If a significant fire were to occur in the watershed, the turbidity would be worse during subsequent rains.

Intense rains may cause flooding in local rivers, including the Bull Run and Sandy. Flooding may cause scour/bank erosion along the river damaging the conduits adjacent to the river and/or foundations of the conduit bridges crossing the river. Extreme flooding could result in hydraulic loading on the conduit bridge decks. Flooding could result on the Columbia River from of a number of occurrences: (1) the dikes could fail, (2) the dikes could overtop, and (3) stormwater pumps could lose power for an extended period. The Willamette River submarine crossings could be damaged due to scour. This risk would be increased during periods of high flow.

Wind or ice may be associated with intense storms. These hazards may result in damage to power lines, disrupting electrical power supply to system facilities. Disruption of power to the groundwater system is of particular concern because it has no emergency power supply, and portable generators would be too small to drive the large pumps.

Correlation of Intense Rain Sub-Hazards

It is important to consider the correlation of hazard events, including geologic hazards, with other hazards. Some hazard events, such as earthquakes, will impact multiple facilities during the same event, potentially rendering the entire system inoperable. There may be correlated hazards that impact different facilities during the same period, resulting in loss of system service.

By definition, correlated events have a higher probability of occurring during the same period compared to uncorrelated events. For example, high turbidity in the Bull Run and rainfall-induced landslides are closely correlated.

Uncorrelated events are, in general, not a concern. For example, an intense rain-on-snow event and an earthquake event are uncorrelated. That is, probabilistically, there is no relationship between occurrence of an earthquake and occurrence of an intense rain-on-snow event. The probability of concurrently having a significant earthquake and a significant rain-on-snow event is very low. The probability is the product of the probabilities of the two independent events

We concluded that there are strong correlations between sub-hazards affecting different components of the Bull Run supply, but there are no correlations between pairs of hazards that would affect the Bull Run and groundwater supplies at the same time.

The most significant question becomes whether these sub-hazards are correlated events that impact the Bull Run supply and the groundwater supply; i.e., is there a pair of any of the intense rain-on-snow sub-hazards that affect both the Bull Run supply and the groundwater supply? Table 3 shows a summary of this correlation.

Table 3
Correlation Of Intense Rain-On-Snow Sub-Hazards

Hazard Event	Turbidity	Land-slide	Flood on Bull Run and Sandy Rivers	Flood on Columbia River	Flood on Willamette River	Ice and Wind Storms
Turbidity						
Landslide	Yes					
Flood on Bull Run and Sandy Rivers	Yes	Yes				
Flood on Columbia River	No	No	No			
Flood on Willamette River	No	No	No	Yes		
Ice and Wind Storms	No	No	No	No	No	

There are some intense rain-on-snow sub-hazards that are correlated, and some that are not correlated. Intuitively, turbidity and landslide have a high degree of correlation. It is believed that when a 500-year intense rain-on-snow event (0.002 annualized) occurs, there is a high probability of having a flood event on the Bull Run and Sandy Rivers, a turbidity event, and a landslide along the conduits. From a system modeling perspective, it has only limited significance because the three sub-hazards events impact the same system, the Bull Run supply. The turbidity event is significant at a 5-year recurrence interval, the landslide event at a 10-year recurrence interval, and the flood event at a 100-year recurrence interval. For a 500-year event, they are all significant.

The hydraulic characteristics of the Columbia River drainage basin, and the Bull Run and Sandy river drainage basins are significantly different; therefore, flooding in these basins should not be correlated. The Columbia basin covers all of eastern Washington, and extends into southern British Columbia, Idaho, and eastern Oregon. Further, stream flow is controlled by a series of dams. The Bull Run drainage basin is much smaller. While there are two dams, during the periods when peak stream flows are expected, the reservoirs behind the dams would likely be full, and would have little impact on stream flow.

Flooding on the Willamette River may be related to flooding on the Columbia River because of the hydraulic backwater effects at the mouth of the Willamette River. In addition, the Willamette River drainage basin is considerably smaller than the Columbia River drainage basin, and is more likely to receive rain from the same storms that impact the Bull Run basin. However, flooding on the Willamette River does not affect either the Bull Run or the groundwater supplies. Therefore, the correlation of the Willamette River flooding with other intense rain-on-snow sub-hazards is not a concern.

Intense rain-on-snow events, and ice and wind storms, have different characteristics, and are not correlated. While every ice storm was accompanied by moderate to high wind speeds, none had excessive precipitation. Only one of the storms produced more than 2 inches of precipitation. Thus, the likelihood of significant flooding at Bull Run is quite low during such storms, and the probability of power outage from an ice storm coinciding with a problematic flood at Bull Run appears to be quite low.

EARTHQUAKE

The earthquake hazard is subdivided into the following categories: fault rupture, strong ground motion (or shaking), landslide, and liquefaction hazards. The initiating event for this hazard is a fault rupture, which releases accumulated strain energy. The release and transmission of energy causes ground shaking. Shaking can then cause liquefaction or landslides to occur.

Regional Seismicity

Seismic hazards in the Portland area are dominated by two sources: deep earthquakes along the Cascadia subduction zone occurring at the interface between the subducting Juan de Fuca Plate and the North American Plate, and shallow crustal events within the North American Plate. There is geologic evidence that subduction earthquakes occur approximately every 500 years, the most recent being in 1700. The USGS has included a third earthquake source zone in the Seattle area but not in the Portland area, even through the two areas arguably have a similar tectonic structure.

The USGS currently believes that the Pacific Northwest is under north-south compression, possibly relating to the geometry associated with the northwest movement of the Pacific Plate relative to the North American Plate. This north-south compression is occurring within the North American Plate. Earthquakes that occur within this plate are called crustal earthquakes. Crustal faults resulting from compressive forces are often thrust (reverse) faults, similar to that which caused the Northridge Earthquake.

The 1993 magnitude 5.6 Scotts Mills Earthquake, and the 1962 magnitude 5.2 Portland earthquakes were crustal events. The USGS and other researchers have identified shallow (crustal) faults and lineaments in the Portland area, the most pronounced of which is the Portland

Hills Fault paralleling the Willamette River through downtown Portland. The Portland Hills Fault is modeled with a slip rate of 0.1 mm/yr, with a characteristic earthquake of magnitude 7.0 with a return period on the order of 10,000 years. With this low slip rate/long return period, the fault has little effect on 500-year return probabilistic ground motions.

Strong Ground Motion

Strong ground motion is a significant hazard to Bureau facilities, whose vulnerability varies depending primarily on the type of construction and the earthquake criteria to which the facility was designed.

Strong ground motion can be characterized in two ways:

- Probabilistically, where a hazard curve is developed for a site, expressing the probability of various levels of PGA due to all sources,

- Scenario, where peak ground acceleration (PGA) is determined at a site or sites given a specified earthquake occurrence; i.e., magnitude and epicentral location are uniquely defined.

The USGS provides probabilistic seismic hazard curves for virtually any location in the United States (Frankel, 1996). For a distributed system such as the Bureau's water system, however, the use of probabilistic curves may generate overly conservative results. Therefore, PGA hazard curves were developed for this assessment based on scenario events in such a manner as to be generally consistent with the 1996 USGS National Seismic Hazard Maps.

Earthquake-Induced Landslide

In earthquakes, the soil resistance to sliding remains constant but the loading increases. If an earthquake occurs during the rainy season when the ground is saturated, there is a higher probability of a landslide than if the earthquake occurs during the dry season.

Cornforth Consultants developed probabilities for damaging slide movement for earthquakes with return periods of 100 and 500 years, summarized in Table 4 (Cornforth, 1998b).

The vulnerability of a slope to earthquake-induced ground motions depends on several factors including slope angle, slope material type, groundwater conditions, and level of ground shaking. Materials most susceptible to landsliding include rockfalls and soil debris slides. Slides are more susceptible to earthquake-induced movement during the wet season when groundwater tables are elevated.

In the Bull Run corridor, the material most at risk to earthquake-induced slope failures is colluvium on steeper portions of the ancient landslide terrain. This material can be predominantly rocky or can have significant portions of silt, clay, and sand mixed with rocky material, and is identified below as Ancient Landslide Terrain. Flow slides (or debris slides in drier material) have the highest hazard ratings. Translational landslides consist of a larger reactivation within ancient landslide terrain than flow/debris slides. Translational slides in the corridor typically have base shear zones in clay. These slides may be marginally stable and can be creeping small amounts without detection or noticeable distress to the conduits. These slides are less susceptible to earthquake ground motions.

Table 4
Seismic Landslide Hazard Ratings, Conduits 2, 3, and 4 - Bull Run Corridor

Geologic Terrain Traversed by Conduits	Probability of Conduit Slide Damage for Given Ground Motion			
	100-Year Return (10% g)		500-Year Return (20% g)	
	Dry Season	Wet Season	Dry Season	Wet Season
Historically Active Terrain				
Remediated Flow Slides	5	10	15	20
Remediated Translational Slides	10	20	20	35
Ancient Slide Terrain				
Flow or Debris Slides	20	50	60	80
Translational Slides	10	25	30	50
Terrain Not Previously Impacted by Slides				
	5	10	15	25

Hazard ratings for historically active slide terrain that have been remediated are generally moderate. Most have been remediated using rock fill buttresses. During an earthquake, the outer layer of the rockfill may ravel down the slope, but should not damage pipelines embedded in native ground below the rockfill. Remediated translational slides have been assigned a higher hazard rating than remediated flow slides die to their larger size and lower factors of safety.

Geologic terrain not previously impacted by landslides includes areas of locally steep topography where conduits traverse small creeks and streams. These areas have been assigned a moderate hazard rating for seismically-induced landslides.

Individual facilities are also vulnerable to landslides, where were quantified in a similar manner.

Liquefaction

The Groundwater Pump Station (GWPS) and the Willamette River pipeline crossings are vulnerable to liquefaction.

- Groundwater Facilities. There has been no liquefaction study focusing on the dikes along the Columbia River. The Groundwater Pump Station/Interstate Facility Seismic Vulnerability Study (Dames & Moore, 1996) made a conservative estimate that permanent ground deformations of up to 2 feet may occur during a maximum credible earthquake (MCE). The ground motion used for an MCE was 50 percent greater than for a 500 year return event. The Army Corp of Engineers (COE) indicated that because of the large dike cross-section, that even if liquefaction were to occur, the dikes would remain competent.

  Further, there is a low probability that an earthquake and flooding will occur at the same time. The COE indicated that the Columbia River only reaches flood stage once every 5 years. In the most extreme years, it has remained at flood stage for approximately 2 months. A more likely duration is estimated to be 15 days every 5 years, or 3 days per year. That is, the river is expected to be at flood stage approximately 1% of the time (0.01). To be conservative, that percentage might be doubled, allowing time for dike repair should they be damaged, so that the probability of the Columbia River being at flood stage is 0.02 *pa*. Multiplying 0.02 times the probability of a 100-year earthquake, 0.01, is 0.0002, or a 5,000-year return event, which is beyond the planning horizon for this study. In *Sewer*

Collection Facilities Seismic Vulnerability Assessment, a study for Portland Bureau of Environmental Services (BES) (Dames & Moore, 1997), Fujitani Hilts estimated that permanent ground deformations (PGD) in a 100-year event might only be 15% of that in a 500-year event (approaching an MCE). That would result in expected PGDs of 4 inches, which should have minimal impact on the function of the dikes.

- Willamette Crossings. Liquefaction/lateral spread PGDs for the Portland Quadrangle were obtained from the Oregon Department of Geology and Mineral Industries (DOGAMI) maps, Earthquake Hazard Maps of the Portland Quadrangle, Multnomah and Washington Counties, Oregon and Clark County, Washington (GMS-79). These PGDs were developed for a magnitude 8.5 subduction earthquake, representing a 500-year return earthquake. In the same BES study cited above, Fujitani Hilts used procedures similar to DOGAMI to estimate PGDs outside the Portland Quadrangle. They also recommended multiplying displacements for an M8.5 event by 0.15 for an estimate of PGDs for a magnitude 6.0 crustal event, representing a 100-year return earthquake. Additionally, Fujitani Hilts estimated the percent of area that would liquefy within each liquefaction zone. The results, modified for this study, are shown in Table 5.

Table 5
Expected Liquefaction Percentage And PGD

Lique-faction Region	PGD (inches) for an M8.5 Earthquake	Percent of Area to Liquefy in an M8.5 Earthquake	PGD (inches) for an M6.0 Earthquake	Percent of Area to Liquefy in an M6.0 Earthquake
0	0	0	0	0
4	12-24	2	2-4	1
3	24-36	5	4-6	2
2	36-48	10	5-7	3
1	>48	40	>7	8

None of the river crossings are located in the most liquefiable material. The Clay St., Mill Street (abandoned), and Ross Island crossings each have some portion in Region 2, highly liquefiable material, and the most likely to fail. The other three crossings all have some portion in Region 4, moderately liquefiable material. It is estimated that three crossings will fail in an earthquake with a 500-year return period. For a 100-year return event, it is estimated that there is about a 50% chance that one crossing may fail.

Surface Fault Rupture

Surface faulting is not a concern in the Portland area. Fault rupture associated with a subduction earthquake would be located off the Oregon coast, and should be of no consequence to Bureau facilities. Thrust or reverse faults that may result from north-south crustal compression typically do not reach the surface. By comparison, the San Andreas and Hayward strike slip faults in California have a very significant surface expression, and are considered when design facilities cross them. There is no evidence of surface faulting in the Portland area over the last 10,000 years.

VOLCANIC ACTIVITY

The Bull Run watershed is immediately west of Mount Hood, and active volcano in the Cascade Mountain range. Debris flow and ash fall hazards were both considered.

Sandy River Debris Flow

A debris flow along the Sandy River valley would result in the destruction of the conduit bridges crossing the river, and, thus, all three conduits. Debris flows generated by volcanic activity produce a phenomenon referred to as a lahar, a rapidly moving mud flow. The lahar could also damage Bonneville's Troutdale substation, which is one source of electrical power for the GWPS.

The evaluation of volcano hazards is based primarily on information contained in Open-File Report 97-89 published by the USGS "Volcano Hazards in the Mount Hood Region, Oregon." This report concludes that the probability of Mount Hood generated lahars affecting the Sandy River is between 1-in-15 and 1-in-30 during the next 30 years. This translates to an event with a mean recurrence interval of between 435 and 886 years. Such an event would probably not be the result of a volcanic eruption with associated magma and ash. Lahar flows from Mt. Hood would more likely result from sudden failure of a glacier.

A lahar flow could occur as the result of a volcanic eruption, which could produce ash. The USGS believes that such an event has a recurrence interval longer than this project's planning horizon.

It is expected that a debris flow would not be correlated to a regional earthquake event that would impact the other power supplies. Similarly, it is not expected that a debris flow is correlated to other hazard events that would impact other Bureau facilities within the project planning horizon. Therefore, this is considered to be an independent event, and is not included in the model.

A flood on the Sandy River could have the same impact on the system; i.e., loss of the Sandy River bridges. The probability of occurrence of the debris flow and flood on the Sandy River are combined when considering the priority of replacement of the Sandy River bridges with tunnels.

Ash Fall

The Bull Run watershed is susceptible to volcanic activity, and associated ash fall (tephra) from either Mt. Hood or Mt. St. Helens. Tephra is fragmented, solidified lava that rises into the air, is carried by winds, and falls back to the ground. Tephra falls can result in water supply turbidity, arcing on high voltage electrical insulators, and damage to rotating equipment if the ash is allowed to get inside bearings and cylinders. While Mount Hood has historically produced only moderate tephra falls, other volcanoes in the Cascade range, most notably Mount St. Helens, have produced large amounts of tephra. The USGS report indicates 30-year probabilities of tephra fall from all Cascade sources for two levels of accumulation. For the Bureau's area, 1 cm or more of tephra accumulation can be expected about once every 4,500 years, and 10 cm can be expected about every 9,000 years.

The Bonneville Power Administration has expressed concern about arcing. This could result if there was a light rain at the time ash fall occurred, resulting in a buildup of ash on insulators. As discussed elsewhere, the BPA system has a high level of redundancy.

Since the probability of occurrence of tephra fall is relatively small, and the consequence of damage is also likely to be small, tephra fall can be considered to have negligible effect on the reliability of the system. In general, tephra fall is beyond the 1,000-year planning horizon.

CONCLUSION

Of the 38 hazards evaluated, the Portland water system is most vulnerable to intense rain on snow events, and earthquakes. Volcanic activity which can produce debris flows and ash falls are high and low risk hazards, respectively.

One of the most significant consequences of rain on snow is landslides along the Bull run conduit system. The vulnerability of this hazard was quantified by mapping geologic formations, and relating results of detailed evaluations of similar materials to formations along the conduit corridor. Other intense rain-on-snow event hazards are correlated, including turbidity events, and flooding on the Bull Run and Sandy rivers. These could disrupt service to the Bull run supply, but should not impact the groundwater system operation.

Both the Bull Run surface water and groundwater systems are vulnerable to earthquake ground motion, liquefaction, and landslides. Ground motion information was developed using earthquake source zone information from the USGS, and modeled for selected epicenter locations. Liquefaction probability information was used from previous studies of Portland Water Bureau, and Environmental Services Bureau facilities. Landslide probabilities were developed for the Bull Run conduit corridor, considering information developed for rain-induced landslides, and relating the sites to similar formations that had been evaluated in detail in the Portland area.

Mount Hood volcanic activity can result in debris flows on the Sandy River, which can destroy pipeline bridge crossings. The USGS has estimated a recurrence interval for such an event in the order of 500 years. Ash fall from Mount Hood or other volcanoes in the region can disrupt the power system due to arcing across insulators, and causing turbidity in the surface water supply. Ash fall event recurrence intervals are longer than the 1000 years considered in this project.

ACKNOWLEDGEMENTS

The authors would like to acknowledge the Portland Bureau of Water Works, and in particular. William Elliott, Dennis Kessler, and James Doane, who were closely involved with the project. We would also like to acknowledge the USGS and the useful hazard information provided for both earthquake and volcanic hazards.

REFERENCES

Ballantyne, D.B., Kessler, D., Elliott, W. and Scawthorn, C., 1999. *Multi-Hazard Risk Assessment For Lifelines – Case Study for the Portland OR Water Supply System*, Proceedings, Fifth U.S. National Conference on Lifeline Earthquake Engineering, Seattle WA.

Cornforth Consultants, 1998a, Memorandum from Andy Vessely to Mark Pierepiekarz, EQE International, "Landslide Hazard Rating, Conduits 2, 3 and 4 - Bull Run Headworks to Mt. Tabor, Portland Water System Vulnerability Assessment," May 12.

Cornforth Consultants, 1998b, Memorandum from Andy Vessely to Mark Pierepiekarz, EQE International, "Seismic Landslide Hazard Ratings, Conduits in Bull Run Corridor and Selected Distribution Facilities, Portland Water System Vulnerability Assessment," July 7.

Dames & Moore, "Groundwater Pump Station/Interstate Facility Seismic Vulnerability Study," prepared for City of Portland, Bureau of Water Works, September 13, 1996.

Dames & Moore, "Sewer Collection Facilities Seismic Vulnerability Assessment," prepared for Brown & Caldwell, January 2, 1997.

Frankel, A., Mueller, C., Barnhard, T., Perkins, D., Leyendecker, E., Dickman, N., Hanson, S., and Hopper, M., 1996. National Seismic Hazard Maps, June 1996: Documentation, U.S. Geological Survey, Open-file Report 96-532, 110 p.

USGS Report 97-98, 1997, "Volcano Hazards in the Mount Hood Region,".

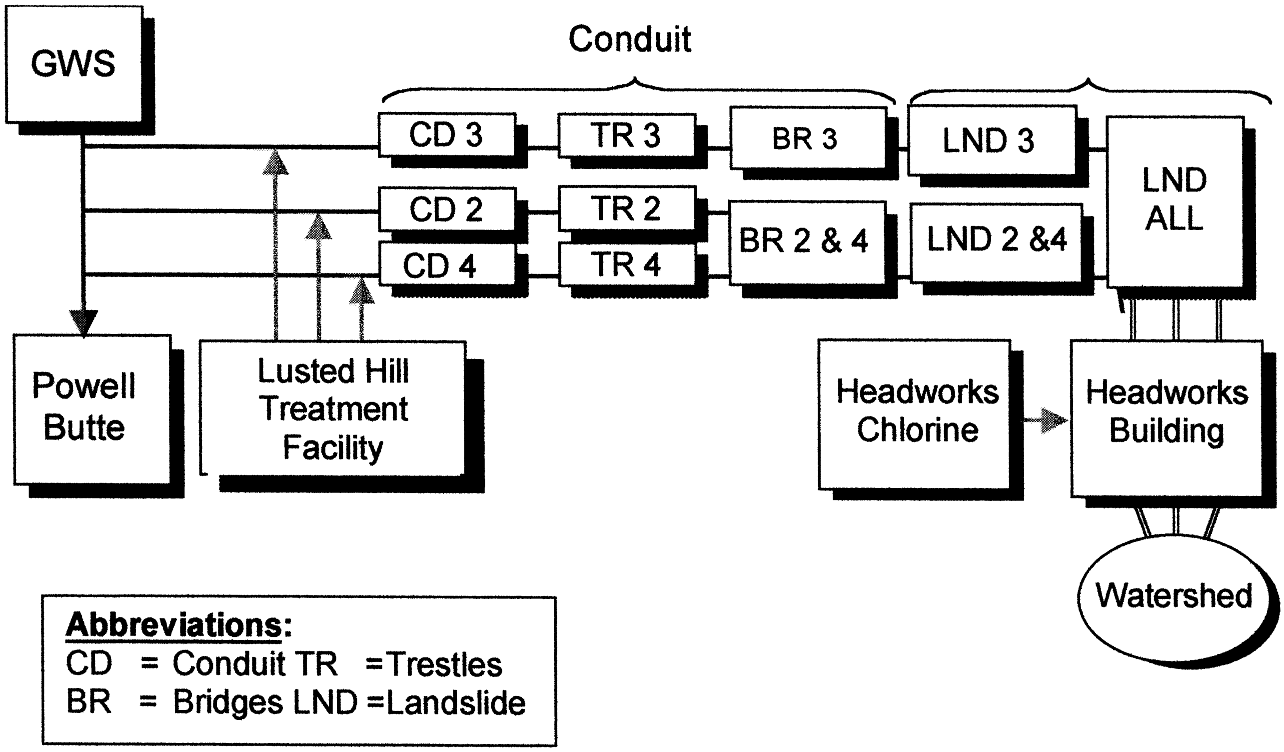

Figure 1
Supply System Schematic

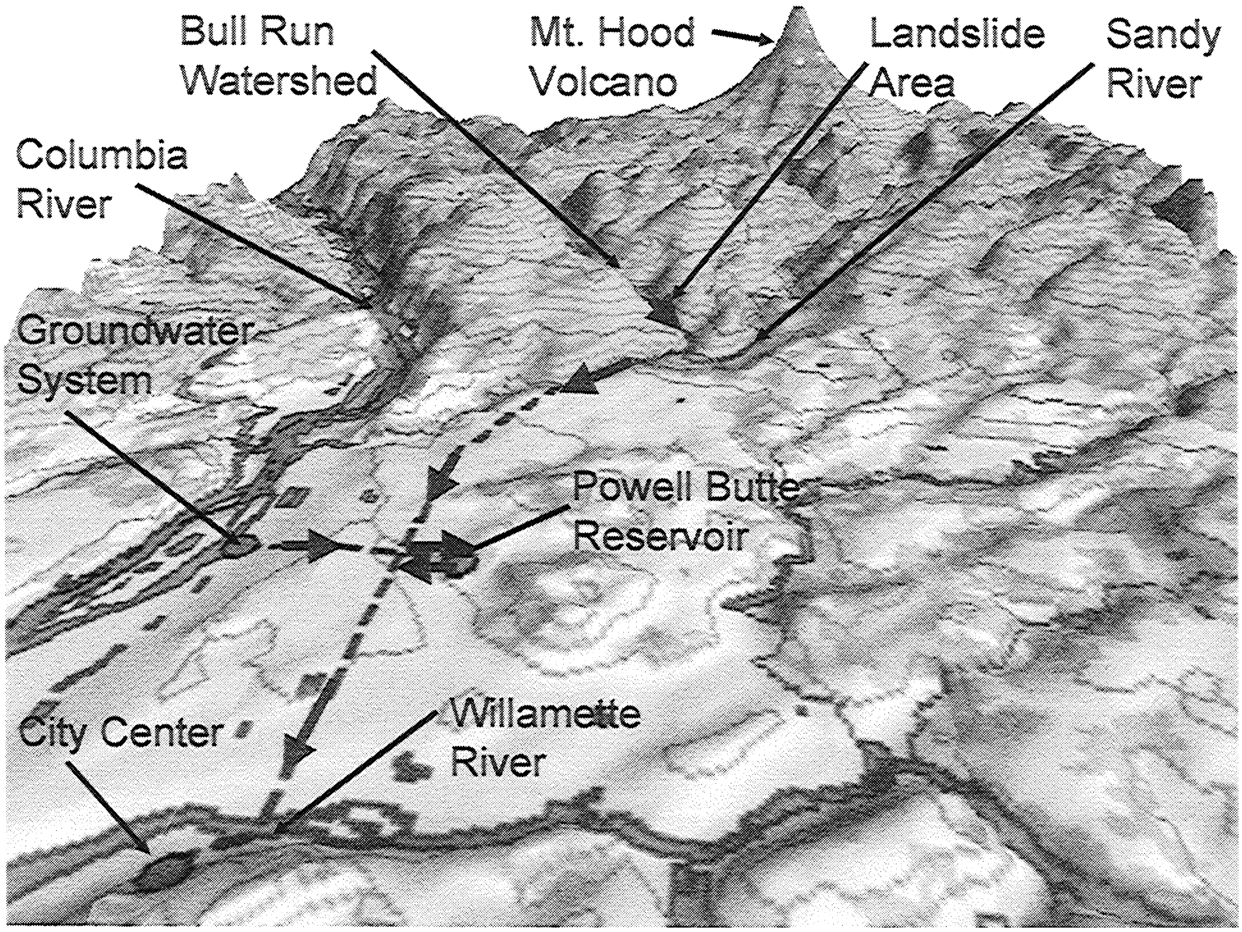

Figure 2
Bull Run and Sandy Rivers, with Mt. Hood in the distance, looking east from Portland (4X vertical exaggeration).

The 1995 Kobe Earthquake
And
The New JWWA Seismic Design Guideline
For Waterworks Facilities

Makoto MATSUSHITA
Kobe Municipal Waterworks Bureau
6-5-1, Kano-cho, Chuo-ku, Kobe, 650-8570, Japan
e-mail : makoto_matsushita@wb.city.kobe.jp

Abstract

The 1995 Hanshin-Awaji (Kobe) Great Earthquake destroyed waterworks facilities and water service had interrupted for almost three months. Japan Water Works Association (JWWA) gathered damage information and analyzed it in order to revise the existing seismic design guideline of 1979. After two years JWWA published new seismic design guideline for waterworks facilities in 1997. In this paper the author would like to introduce the basic idea of new JWWA design guideline, which includes the idea of two levels of earthquake motion and two ranks of facility importance, and the idea of systematic approach to service recovery. At the same time we should turn the eyes to the efforts of water utilities in Japan after the 1995 Kobe Earthquake. The author also introduces Kobe Water's reconstruction strategy and renovated Mutual Aid Agreement among water utilities.

Introduction

The first JWWA (Japan Water Works Association) seismic design guideline for waterworks facility was published in 1953. It contributed greatly to strengthen the water supply system. Later this guideline was revised in 1966 and in 1979. Particularly the 1979 Design Guideline is revised thoroughly based on the experience of many large earthquakes, mainly Miyagi Earthquake. After this revision the Design Guideline was left as it is for 17 years because this 1979 version was very much advanced at that time.

The Hanshin-Awaji Earthquake occurred on January 17th, 1995 and gave great shock on civil engineers in various fields. After this earthquake the seismic improvement of water system is highly concerned matter, and so many water utilities were longing that the existing design guideline for water facilities would be revised by JWWA in a short time.

In this paper the author briefly described the damage to water system, and evaluated the seismic design and preparedness that we provided for Kobe Water. Based on the new findings, JWWA revised existing "Design Guideline for Waterworks Facilities" and published the new one in 1997. The basic concepts of this guideline are newly introduced. In this paper the author describes the lessons that are drawn from the experience of the 1995 Hanshin-Awaji Earthquake, and the new JWWA design guideline based on these lessons. And finally, the author goes back to current situation of Kobe Water and discussed re-construction strategies.

What we have experienced and learned?

The 1995 Kobe Earthquake is the largest one, which attacked modern urbanized city in recent years in Japan. The water utilities have experienced long service interruption, hard repair work and emergency water supply in a large scale. We could share a mutual experience with them by joining assistant works. We Kobe Water, as a representative of all damaged water utilities would like to describe what we have experienced. And we should draw the lessons from this experience.

a. Water facilities - damage and performance

Water structures such as dams, purification plants and distribution reservoirs, all performed well. One reasons is thought to be a result of site selection and the other reason is JWWA seismic design guideline. Facilities were designed in accordance with this guideline.

Pipe networks were significantly damaged. Main reason is that pipe networks spread widely in the service area and have many joints, most of which could not follow the large ground motion. Service connections were also heavily damaged in a road and individual property.

b. Pipe damage analysis

1. Seismic joint should be used where the ground deformation is so large.
2. Ductile Iron Pipe (DIP) is enough strong in good ground condition. On the other hand Cast Iron Pipe (CIP) has problem in joint and pipe body itself. The weak pipe such as CIP, PVC and ACP, should be replaced to seismically strong pipe.

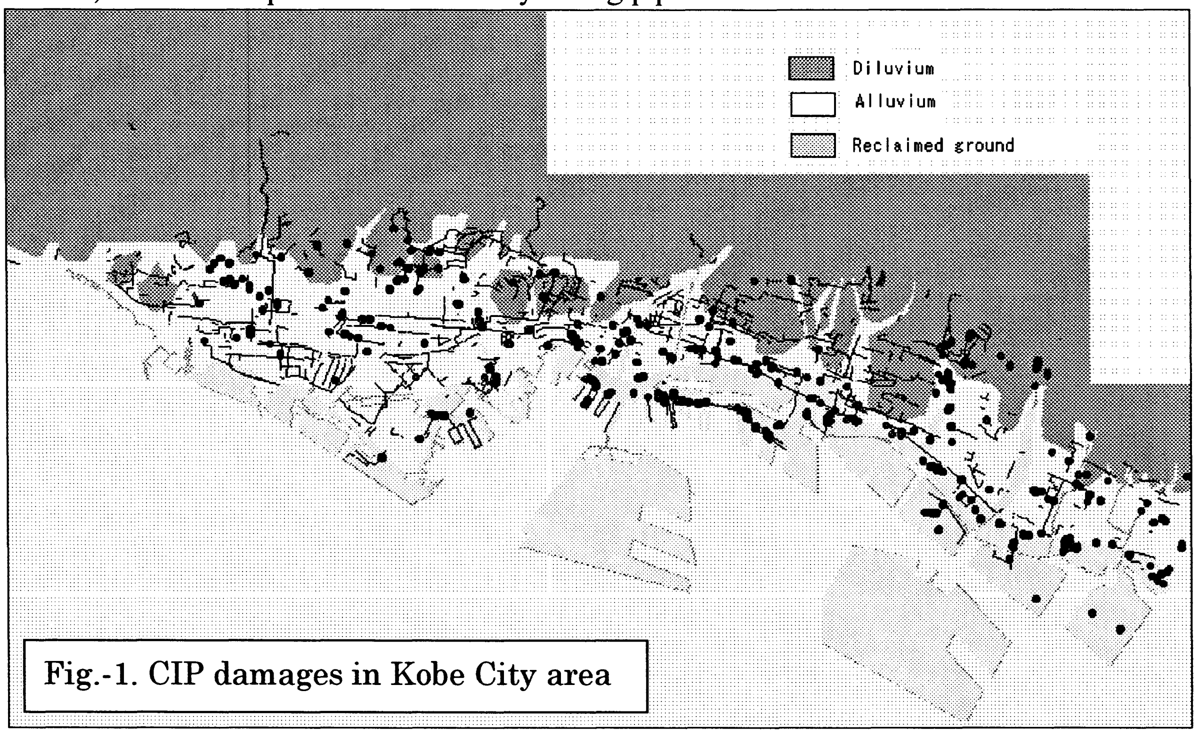

Fig.-1. CIP damages in Kobe City area

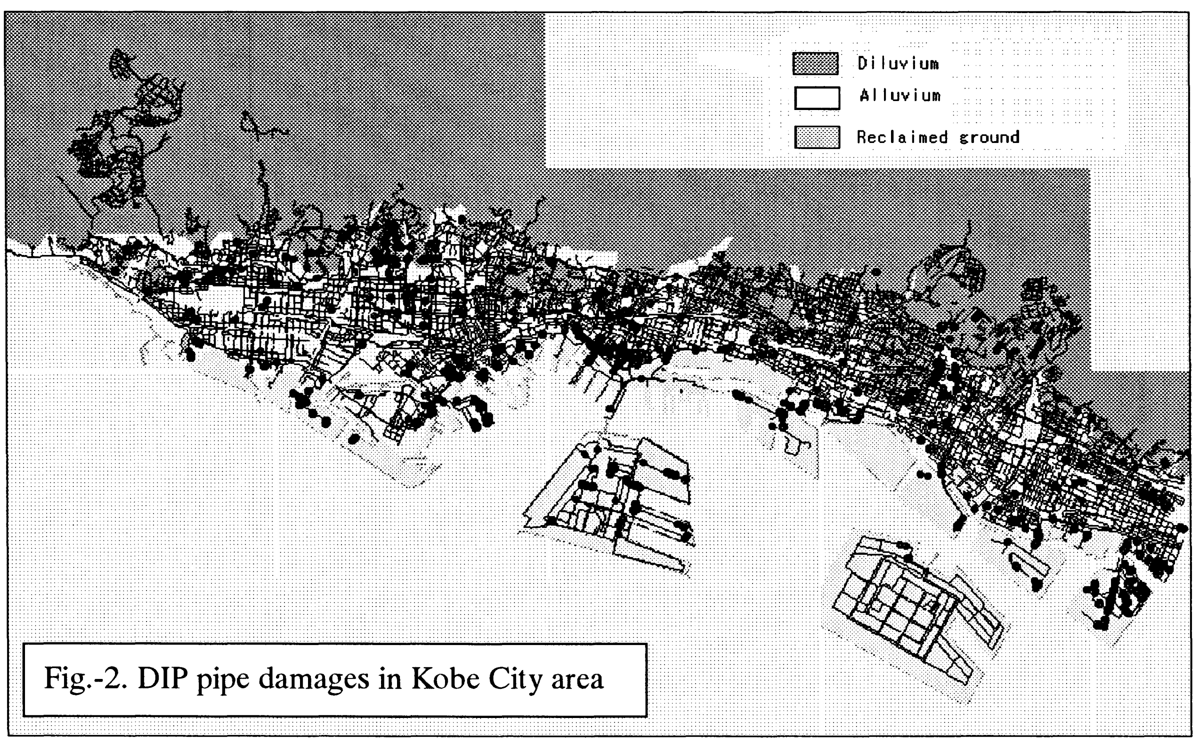

Fig.-2. DIP pipe damages in Kobe City area

The performance of service pipe has large impact on leaks and pressure decrease. The strong materials, for instance polyethylene (PE) pipe, should be used to meet the large ground motion.
3. Pipe system should be designed to renovate entire system in replacing old pipes.

c. Water system failure

Many distribution reservoirs had lost their water in a few hours just after the earthquake because water supply to tanks stopped and many pipe breaks occurred in a network. Water supply service had interrupted in the service area. To avoid the long term service interruption water system should have back up system in an emergency. Water system should be divided into two groups, one is designed so as not to be damaged even in any earthquake, the other is allowed to have some damages but it can be restored easily. Dams and purification plant are belonging to former group. In case of pipe system, the system itself should be designed to be able to continue water service by looped network or other backup route, even if some pipes are damaged.

d. Evaluation of former preparedness and Lessons learned

Former preparedness proved to be effective is as follows;

- pipe replacement
- capacity increase of service reservoir
- telemeter/telecontrol system
- back up for power supply
- conversion of disinfection system
- emergency shut-off system
- block distribution system
- water quality monitoring system

e. Emergency shut-off valve

Emergency shut-off valve worked practically in a real emergency. They enabled the reservoirs to store emergency water of 42,000m3, and this was used for drinking and repairing pipes.

f. Emergency water supply and repair works

Emergency water supply had started just after the earthquake. However, Kobe Water did not have sufficient number of water tank trucks. Neighboring Sanda City dispatched tank trucks on the same day and a few days later Osaka City and other cities also dispatched a large number of tank trucks to Hanshin Area. Kobe Water had to be confronted with the difficulty in the management of many assistant cities. The definite rules and the agreement for the assistance in an emergency are strongly required.

g. Customers' voice

Customer's voice was collected through telephone inquiries during the recovery works. They said the importance of water is stressed and is indispensable to maintain daily life. Usage of water is changing from for only drinking to for daily living, bathing and toilet.

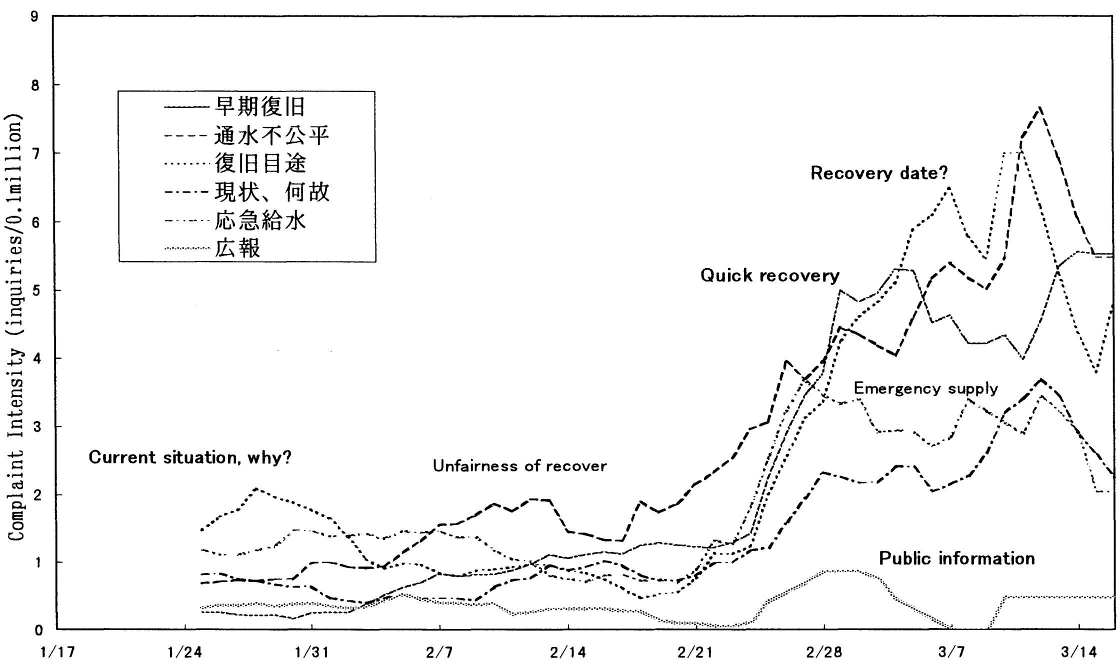

Fig.-3. Customer's voice and its intensity

h. Lack of water supply

Kobe Water' water resource depends mainly upon Yodo River through Hanshin Water Authority (HWA). This time HWA also damaged by the same earthquake. Kobe Water could not have sufficient volume of water to supply and to repair the water system. The total water volume stored in distribution tanks at 7:00 is an indicator for understanding the current situation of repair works. This indicator was gradually decreasing with the expansion of recovered area as the time progressed because of lack of water supply from HWA.

i. Traffic congestion

Hanshin Area situated between Osaka Bay and Rokko Mountains and there existed very long and narrow land area. Three railways, two highways and two national roads run east and west. Because railways and highways were closed after the earthquake, other roads were so clouded that repair team and water tank trucks did not run about within the city.

j. Collapse of Head Quarter Building and other buildings

Nobody expected that collapses of head quarter and other branch offices, which brought the information isolated situation without various maps and documents.

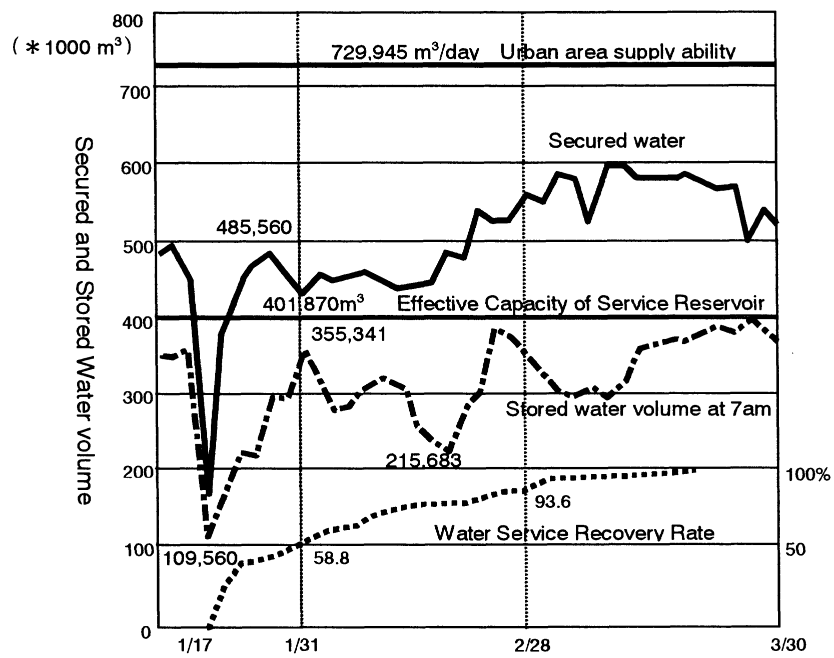

Fig.-4. Secured Water, Stored water and Recovery Rate

What should we do?

Viewing the severe damage of Kobe and surrounding area, JWWA announced the practical recommendations to all the water utilities in Japan. In this recommendations the practical method of diagnosis and retrofit of water facilities against the earthquake disaster, which should be launched rightly by water utilities, are stated. Following this, JWWA organized two special expert committees and started actual revising works written below;

1. To revise former design guideline based on the findings from the 1995 Kobe earthquake.
2. To revise the existing mutual aid scheme and to establish the new scheme in an emergency

Next we will explain how the lessons are taken into account in above two items.

The new JWWA seismic design guideline

Japan Water Works Association (JWWA) dispatched reconnaissance team to Kobe just after the Kobe earthquake in order to investigate the damage to water system facilities. After that JWWA set up a committee in April 1995, of which mission is to revise the design guideline by taking the new findings into account. The chair is Dr. Tsuneo Katayama of National Research Institute for Earth Science and Disaster Prevention Science, and the principal members are Dr. Kameda of Kyoto University, Dr. Hamada of Waseda University and Dr. Takada of Kobe University. The new guideline consists of four chapters and appendices with a total of over 300 pages. However, it is introduced here only a basic principles and concepts behind the new guideline.

a. General

The new guideline emphasizes that water utilities should consider a well balanced, comprehensive plan during the three distinct periods:

1. before earthquake (hazard forecast, preparedness and mitigation)
2. post-earthquake (emergency response plan)
3. re-construction (long-term system improvement plan)

b. Facility's importance

Principally facilities are divided into two ranks according to their importance. "Rank A" facilities have high importance, and "Rank B" facilities have ordinary importance. "Rank A" facilities are determined by taking into account the following items:

1. potentially to generate serious secondary disasters,
2. located in up-stream within the water system,
3. major facilities which do not have substitute or back up,
4. major distribution pipelines supplying to socially important institutions,
5. major facilities which are difficult to repair, and
6. information centers during a disaster.

What facilities belong to "Rank A" is determined by water utility itself, based on the experience, local disaster prevention plan and so on. "Rank B" facilities are all remaining facilities, which do not be included in "Rank A" facilities.

Ranking A or B is the most unique feature of the 1997 Design Guideline. Each water utility has a responsibility in evaluating and determining facilities' importance. This responsibility is quite important because each facility is a part of entire system and its damage will affect the total system performance.

c. Earthquake motion

In designing water facility its performance when an earthquake occurs should be examined by using two types of earthquake motions, “Level 1” and “Level 2”.

The Level 1 (L1) earthquake motion is equivalent to the conventional level of earthquake motion used for many structures prior to the 1995 Kobe earthquake. Structures are considered to subject to L1 earthquake motion once or twice during their service life.

The Level 2 (L2) earthquake motion has been introduced by assuming the occurrence of an inter-plate earthquake near the land area or intra-plate earthquake right below a site. Although the probability that waterworks facility will experience L2 motion is very low, its influence on structure is considered enormously great.

d. Target level of performance

The new guideline says that waterworks facility should have certain performance level in accordance with different earthquake motions (L1, L2) and facility importance (Rank A, Rank B). For L1 motion, “Rank A” facilities should not be damaged, while “Rank B” facilities may be allowed to suffer from light damage as far as their functions are maintained. For L2 motion, “Rank A” facilities should be designed that they do not give severe influence on human lives, and in case of light damage it can maintain their primary function.

When a water system experience L2 earthquake motion, some damages cannot be avoided, because waterworks facilities located every area where people live, in particular water pipe network spread widely in the service area. We should develop the quick repair and service recovery method by considering systematic approach, for example, dual supply main, loop system, block distribution system and so on.

Table –1. Facility importance and Earthquake motion

Facility Importance	Earthquake Motion	
	Level 1	Level 2
Rank A	No damage	No severe impact on human life. Individual facility may receive light damage, but will still function.
Rank B	Individual facility may receive light damage and may not be able to function. Early restoration possible.	Individual facility may receive some damage. The waterworks system retains its total ability will function.

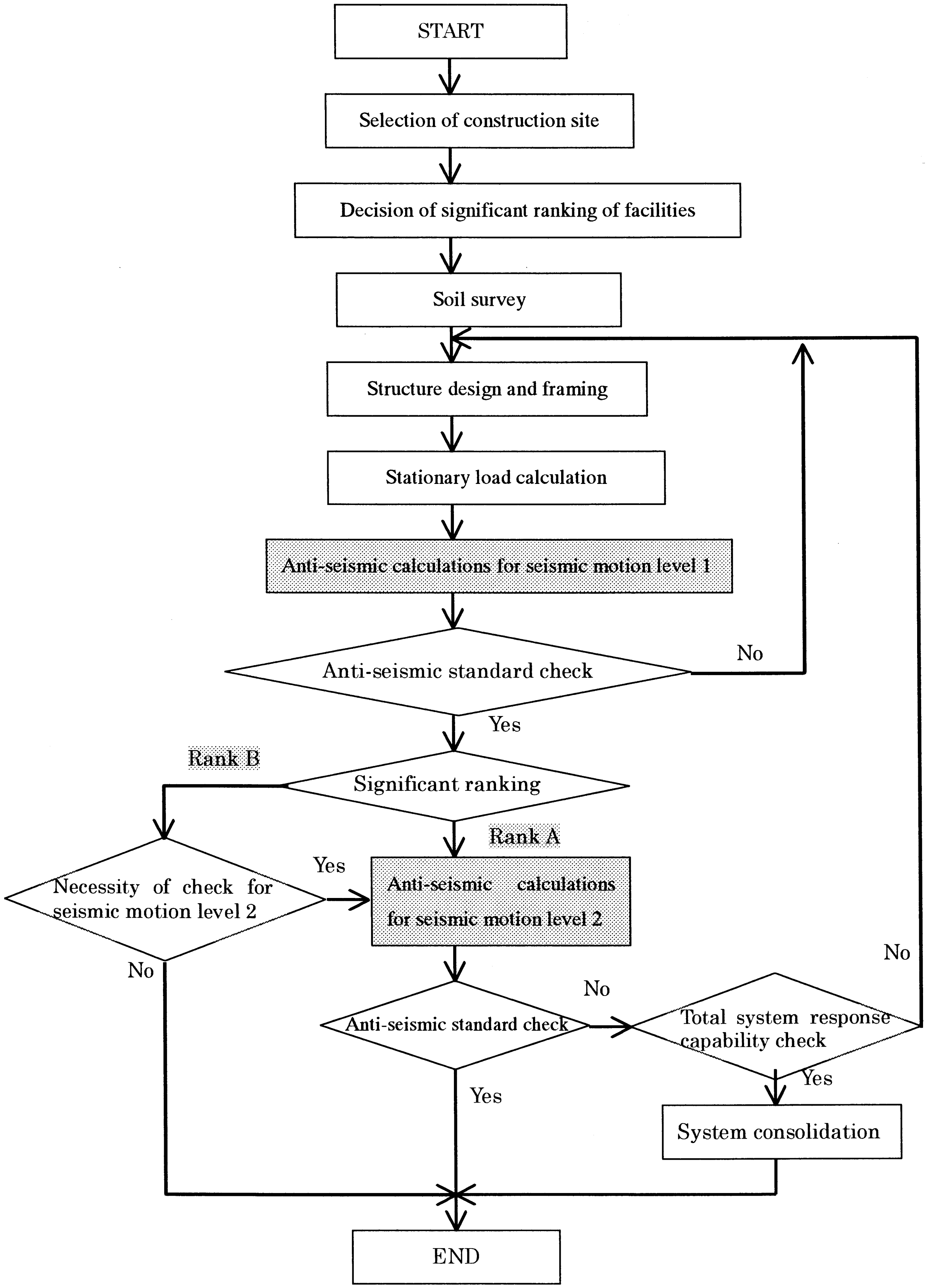

Fig.-5. Earthquake-Resistant design procedure

e. Earthquake-Resistant Design Procedure

Using these concepts the individual facility should be designed according to the procedure shown on flow chart of fig.-5. It is notable that two ranks of facility importance and two levels of earthquake motion are taken into account in this procedure.

f. Performance based design

The new guideline stressed that water facility is a part of entire system and a system is finally evaluated by its total system performance. The practical procedure of system design is not defined and not mentioned in this new guideline at present. We can say that an approach to "performance based design" has just started. From now water engineers will make effort to develop the practical method, and it is supposed that various new idea will be considered and abandoned on the way. So the 1997 guideline is said to be a "provisional version" in the preface (Dr. Katayama), therefore it will be revised and modified in future.

Mutual Aid Scheme

Many agencies include water utilities, various organization, self-defense force and private companies as well as volunteers came to assist Kobe Water in the 1995 Kobe earthquake. Both sides of Kobe and assistant agencies pointed out that a lot of problems still remained in assistant works. Some of them are written below:

1. Before Hanshin-Awaji, assistance works were performed according to the request bases. But attacked water utility could not afford to make request, particularly in an early confused days. No body knows to whom and how to make request. Definite rule was not provided.
2. There was also no definite rule for providing meals and accommodation for assistant team. Many assistant teams wanted to go to the most damaged area. It was difficult to allocate works. Some teams complaint with their works.
3. The unification of equipment including valves and other fittings is a key issue in practical assistant works. A necessity to unify the specification is strongly recognized by assistant agencies. This unification enables us to make "dispersed stock" of equipment among many utilities.

JWWA started a discussion about "assistant works by other agencies in an emergency" and to cope with this issue the new committee was set up in 1995. The committee presented "Report on Emergency Response against an earthquake and other disaster" to JWWA member utilities in February 1996. In this report the rule of assistance request, expenses and commanding system. The preparedness in ordinary time was also discussed and it is evaluated by identifying the

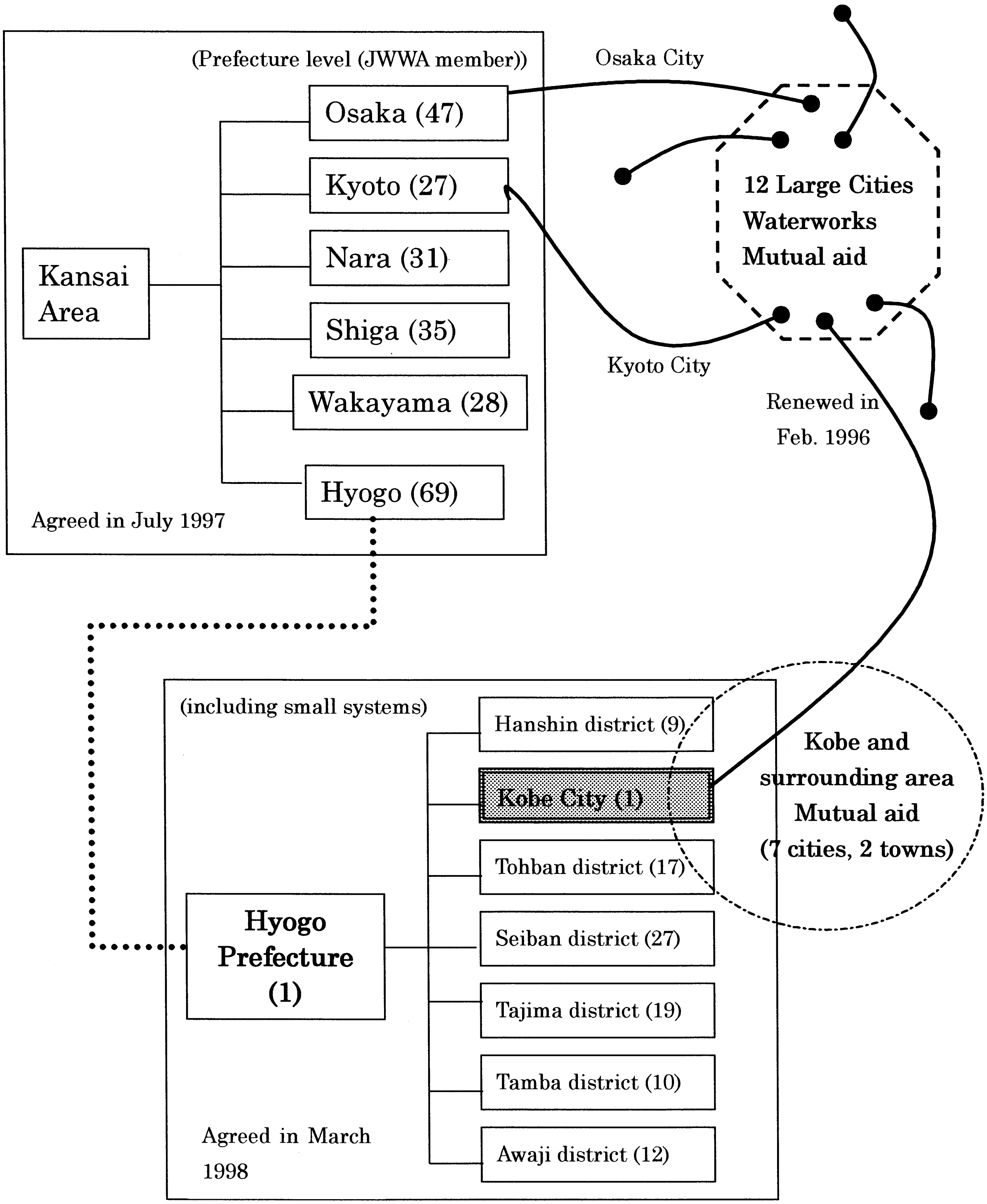

Fig.-6. Mutual aid scheme around Kobe Water resources and quantifying what kind and amount of resources.

In June 1996 twelve large cities in Japan renewed the mutual aid agreement based on the discussion at JWWA. And in Kansai area six prefectures, including Osaka, Kyoto, Nara, Shiga, Wakayama and Hyogo, signed a new agreement on mutual aid scheme in July 1997. Following this agreement Hyogo Prefecture conducted mutual aid in Hyogo and agreed by 69 water utilities in March 1998. These schemes are shown on fig.-6 in the next page.

The current status of Kobe Water

a. Seismic improvement of water system

Kobe Water enacted "Basic Plan of seismic improvement for waterworks facilities" in July 1995, six months later the earthquake. It has passed over four years. During these years tremendous effort were devoted to the re-construction works. The results are written below:

Table-2. The current status of Kobe Water

	1995 (Kobe Earthquake)	1999 (as of March)
Seismic pipe length (km (%))	253km(6.4%)	597km(14%)
Emergency shut-off valves	21	27
Emergency water cisterns	0	5
Large Capacity Water Main	---------	Under construction

b. Mutual aid agreement

As I already mentioned the mutual aid agreement among the twelve large cities was revised and renewed. All the large cities came to Kobe according to this agreement but we can not say that the aid activities were not performed efficiently. The new agreement proposed that two managing cities were appointed in an emergency, as for Kobe these two cities are Osaka and Hiroshima. These cities will manage all the assistant works instead of Kobe, keeping close communication. The other revised point is that the assistance will be made automatically, even if the suffering city can not afford making a request to ask assistance. Recently Kobe Water dispatched assistant team to Osaka City and Hiroshima City as an exercise to understand other water system and to find out problems in assistant works.

Kobe Water agreed Kansai area level mutual aid in 1997 and Hyogo prefecture level mutual aid in 1998. Kobe also agreed mutual aid with surrounding cities and some specified cities, Gifu and Shizuoka.

Conclusions

The 1997 JWWA design guideline and the mutual aid scheme are the new tools against a next big earthquake. These are all constructed and revised based on the experience of the 1995 Kobe earthquake. In this field Kobe Water accumulated enormous know-how in solving various problems. We Kobe Water will keep continuing to send information about reconstruction because it is our duty that we will be concerned on Lifeline Earthquake Engineering and Disaster Science as an actually experienced agency.

Acknowledgments

The author would like to thank Dr. M. Hamada of Waseda University, Dr. H. Kameda of Kyoto University, JWWA and Kobe Water, who gave me an opportunity to present this paper to the 7th US-Japan Workshop.

<Reference>

1. Tsuneo Katayama, "Principles of the new 1997 Earthquake-Resistant Design Guideline for Water Works Facilities in Japan", IWSA workshop on water and earthquake, November 17-18, 1998, Tokyo, Japan
2. JWWA, "Seismic Design and Construction Guidelines for Water Supply Facilities 1997 (Briefly English - translated Edition", November 1998
3. Makoto Matsushita, "Restoration Process of Kobe Water System from the 1995 Hanshin-Awaji Earthquake", 5th USCLEE, August 12-14, Seattle, USA

Estimation of Post-Earthquake Water System Serviceability

by

Michael O'Rourke
Professor of Civil Engineering
Rensselaer
Troy, NY 12180-3590

ABSTRACT

Current procedures for estimating post-earthquake serviceability of a water distribution system using the HAZUS methodology are reviewed, and illustrated through the use of an example. The parameters used to characterize both the wave propagation (WP) and permanent ground deformation (PGD) hazards are discussed, as well as fragility and other key relations currently embedded within the methodology. The sensitivity of serviceability results to alternate fragility relations and other parameters are determined. As one might expect system serviceability is significantly influenced by choices among existing and newly developed fragility relations as well as by expected variation in ground motion parameters (attenuation relations). Somewhat suprisingly, variations in the distribution of pipe damage between leaks and breaks, and the percentage of mapped liquefaction susceptible zones which actually liquefy during the event, have similar influence on serviceability results. Unfortunately, relatively little information on these later two parameters are available in the technical literature

INTRODUCTION

When utility system operators are planning a seismic retrofit or upgrade program for an existing system, an evaluation of the potential losses (e.g., direct repair costs and temporary system outages) due to future earthquakes is often the first task in the project. This initial loss estimation task provides a benchmark of the current, unimproved, status of the system in question. The probably benefits (e.g., reduced repair costs and shortened outage intervals) of various retrofit or upgrade strategies are then estimated in order to provide a rational basis for selecting which specific proposed improvements are actually implemented. Both of these tasks require loss estimation tools.

This paper focuses on one such loss estimation tool, namely HAZUS, the NIBS/FEMA Earthquake Loss Estimation Methodology. The HAZUS project was organized and directed by the National Institute of Building Sciences (NIBS) for the Federal Emergency Management Agency (FEMA). Technical supervision and review was provided by a seven person Project Working Group (PWG) chaired by Prof. Robert Whitman of MIT. The author served on the PWG. The GIS based HAZUS software was developed by Risk Management Solutions (RMS), and tested in two pilot studies. The first pilot study was conducted in Portland, OR, by Danes and Moore while the second was done by EQE for Boston, MA.

HAZUS is designed to produce loss estimates for use by state, regional and local governments in planning for earthquake loss mitigation, emergency preparedness, as well as response and recovery. The methodology deals with nearly all aspects of the built environment and with a wide range of different types of losses. Elements of the built environment considered by HAZUS include the general building stock, essential facilities (e.g., fire, police and emergency operations centers), transportation lifelines (e.g., highway, rail, bus and airports), and utility lifelines (e.g., potable water, wastewater, oil, natural gas, electric power and communications systems). The types of losses considered by HAZUS include: damage to structural and non-structural components for the general building stock; potential exposure to inundation, hazardous material release and fire following earthquake; estimates of debris, casualties, displaced households and short-term shelter needs; direct economic losses (e.g., business inventory, relocation expenses and rental income losses); and indirect economic losses (e.g., post-earthquake changes in general business activity).

Herein, HAZUS procedures for estimating post-earthquake serviceability of a potable water distribution system are reviewed. Future versions of HAZUS will have water system hydraulic analysis capability based on EPANET, KYPIPE or CYBERNET input data files. However in the current version, water system serviceability is taken to be a function of the damage rate (breaks per kilometer) for water system pipe. The parameters used to characterize the seismic hazard are identified, along with fragility relations and other key parameters. Finally the sensitivity of serviceability results to alternative fragility relations and potential variability in other key parameters is investigated.

SEISMIC HAZARDS

In general, the seismic environment is initially characterized by a user selected earthquake magnitude at a user selected epicenter. For buried pipe, the seismic hazards of interest are wave propagation (seismic shaking) and permanent ground deformation (liquefaction, etc.).

Wave Propagation Hazard

Seismic wave propagation (WP) refers to the transient strains and curvatures induced in the ground due to the passage of traveling seismic waves. For most pipe diameters, ground strain ε_g given by Eq.(1) is the more important effect.

$$\varepsilon_g = V_{max} / C \tag{1}$$

where V_{max} = the peak horizontal particle velocity, and C = the apparent propagation velocity of the waves with respect to the ground surface. Because of this, V_{max} is the ground motion parameter used in HAZUS to characterize the WP hazard. Based upon an attenuation relation (either default or a user selected relation), and local soil conditions, the HAZUS software claculates V_{max}. Although one can argue the relative merit of any given attenuation relation, when one plots observed values from a given event against predicted values, there is always a fair amount of scatter. For example, Figure 1 compares V_{max} at rock sites in the 1989 Loma Prieta event against values predicted by the Kamiyama et at. (1992) relation. The scatter in this figure is fairly typical in that, even with the "best" attenuation relation, observed values are only within a factor of two of predicted values.

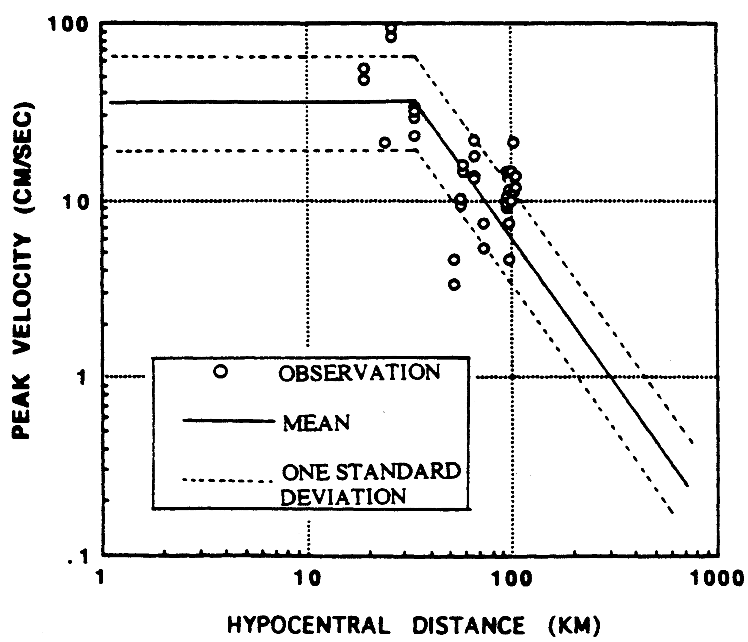

Fig. 1 Comparison of Peak Ground Velocity at Rock Sites in 1989 Loma Prieta Event with Kamiyama et al. Relation (after Kamiyama et al. 1992)

PGD Hazard

Permanent ground deformation (PGD) refers to non-transient ground movements such as surface faulting and liquefaction induced lateral spreading. Herein we will only consider lateral spreading. Due in part to the form of currently available fragility relations for buried pipe damage due to PGD, this hazard is characterized in HAZUS by the amount of ground movement.

Currently there are a number of relations for estimating the amount of PGD movement due to liquefaction induced lateral spreading. Arguably one of the most accurate was developed by Bartlett and Youd (1995). The displacement is a function of earthquake magnitude, source to site distance, site geometry, as well as three goetechnical parameters. In terms of scatter, most observed values are within a factor of two of the predicted. Although the Bartlett and Youd relation is reasonably accurate, it requires geotechnical parameters, specifically, particle size, fines content and liquefiable layer thickness, which typically are not available in the form of maps. As a result HAZUS uses the somewhat cruder Liquefaction Severity Index (LSI) developed by Youd and Perkins (1987).

$$\mathrm{Log}\,(\mathrm{LSI}) = -\,3.49 - 1.86 \log R + 0.98 M_w \qquad (2)$$

Note that LSI (in inches) is a function only of the horizontal distance to the energy source, R, (in kilometers) and the moment magnitude M_w, and hence is relatively easy to apply in system evaluation studies. On average, observed values of PGD displacement for events in Alaska and California are roughly half of LSI. That is, as noted by Youd and Perkins, LSI is an upper bound with observed values again for Alaska and California events rarely exceeding the LSI given by Equation (2).

Based upon user supplied information on liquefaction susceptibility within the study region, HAZUS evaluates the expected amount of PGD for various geological units. That is, the expected PGD movement for a area with modern (<500 years) flood plain deposits (High susceptibility) would be much larger than that for holocene glacial fill (Low susceptibility). However since not all of a given mapped geological unit (i.e., relative susceptibility area) is actually expected to move during the postulated event, a probability factor P_{ml} is used. The current P_{ml} factors in HAZUS are listed in Table 1

Relative Susceptibility	V. High	High	Mod.	Low	V. Low	None
P_{ml}	.25	.20	.10	.05	.02	0.0

Table 1 Proportion of Mapped Geological Unit Considered Susceptible to Liquefaction

COMPONENT VULNERABILITY

For buried pipelines, empirical correlations between observed seismic damage typically in repairs per kilometer of pipe, and some measure of ground motion are used in HAZUS to quantify component vulnerability.

Wave Propagation Fragility

Component fragility relations for wave propagation effects use peak ground velocity to characterize the hazard. Figure 2 shows the relation currently used in HAZUS, developed by O'Rourke and Ayala (1993) using observed behavior of 4 U.S. events and 2 Mexican events. In terms of scatter, the observed values are typically within a factor of roughly 2.5 of predicted values. The unexpectedly large observed damage rations were attributed to corrosion and variable subsurface conditions (e.g., at the edge of a valley). Based on Figure 2, the repair rate (RR in repairs per kilometer) in HAZUS for brittle pipe materials is given by

$$RR = 0.0001\ (V_{max})^{2.25} \tag{3}$$

where V_{max} is in cm/sec. The repair rate for ductile pipe is taken as 30% of the value from Eq. (3)..

Various authors have suggested modifications to wave propagation fragility relations to account for diameter, pipe material, joint type and corrosions effects. For example both Eidinger et al. (1995) and Honegger (1995) note reductions in damage ratio with increases in diameter. Specifically damage rates in the 1989 Loma Prieta event for welded steel pipe with diameters less than 12 inches were four times higher than those for larger diameters. Similarly, Honegger suggests that historic damage ratios for 1220 mm (48 in) diameter prestressed concrete pipe are about a third of those with 400 mm (16in).

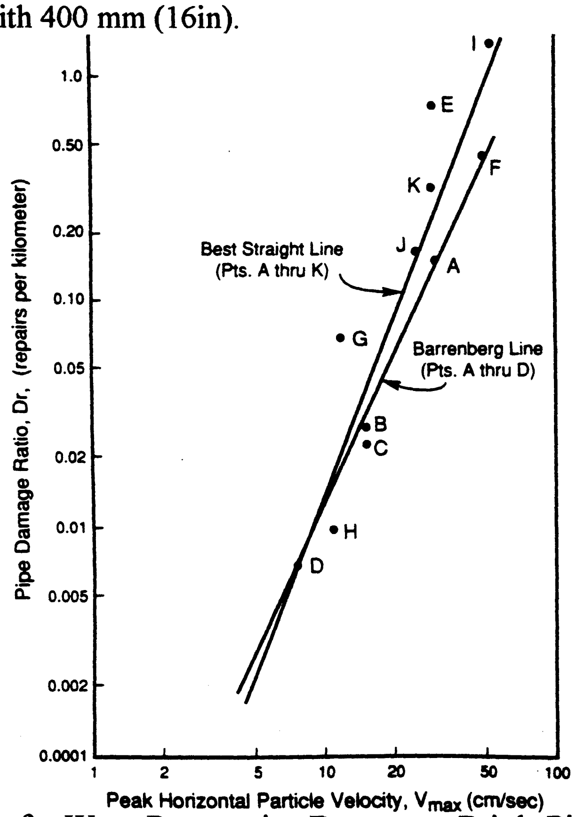

Fig 2 Fragility Relation for Wave Propagation Damage to Brittle Pipe Materials (after O'Rourke and Ayala, 1993)

PGD Fragility

Although PGD damage to buried pipe components is theoretically related to the amount of movement as well as the spatial extent of the PGD zone, the fragility relations in HAZUS simply use the amount of PGD movement to characterize the hazard. For brittle pipe, HAZUS uses a fragility relation based upon work by Honegger and Equchi (1992) and shown in Figure 3. The repair rate RR (again in repair per kilometers) is approximated in HAZUS by

$$RR = (PGD)^{0.56} \tag{4}$$

where PGD is the amount of ground movement in inches. In HAZUS, ductile pipe is assumed to sustain 30% of the corresponding brittle pipe damage for both WP and PGD hazards.

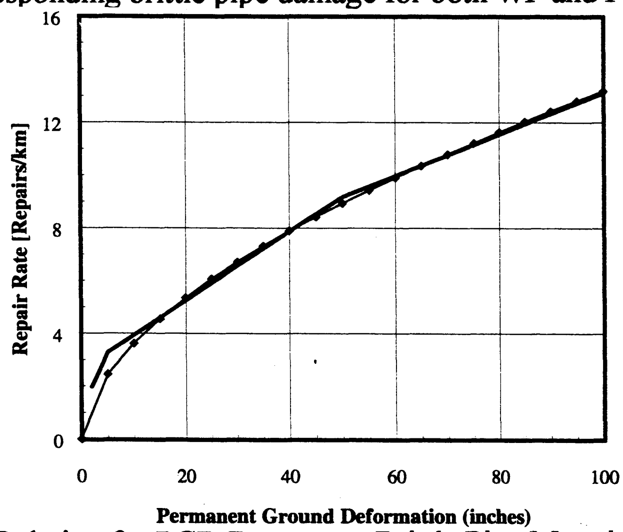

Figure 3 Fragility Relation for PGD Damage to Brittle Pipe Material (after Honeggar and Equchi, 1982)

SYSTEM PERFORMANCE

Having quantified the expected damage to the pipeline network, the direct losses (i.e., expected repair costs) can be calculated. However, in terms of impact upon the population served by the system, an equally important measure of damage is expected system functionality. By this we mean the percentage of customers with service immediately after the event . As noted previously, in the next version of HAZUS, an estimate of system functionality will be determined from a hydraulic model of the damaged system. However in the current version the relation in Figure 4 is used to estimate system serviceability. As one would expect, serviceability is a decreasing function of pipe damage, specifically pipe breaks per kilometer. For example, a serviceability index of 50% (half the service connections having adequate flow and pressure after the event) is expected for an average pipe break rate of 0.1. breaks/km. As explained by Bendimerad and Bouabid (1995) it is a synthesis of a number of existing serviceability relations.

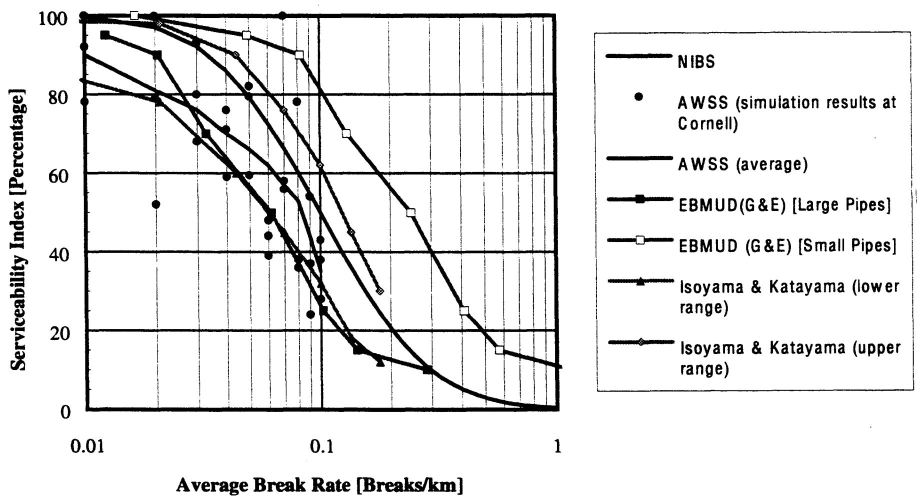

Fig. 4 System Performance Relationship (after Bendimerad and Bouabid, 1995)

In order to use the serviceability model shown in Fig, 4, one must distinguish between leaks and breaks. That is, a pipeline break has a much larger impact on functionality than a pipeline leak. Unfortunately, the information typically available after an event is the number and location of pipeline repairs (i.e., no discrimination between leaks and breaks). The author is aware of only one detailed study of earthquake damage which clearly separates leaks from breaks. In their study of pipeline damage in the 1949 and 1965 events in the Puget Sound area, Ballantyne et al. (1990) indicate that 85% of the repairs were leaks while the remaining 15% were breaks.

In HAZUS WP damage is assumed to result in 80% leaks and 20% breaks, while for PGD damage we assume 20% leaks and 80% breaks.

EXAMPLE PROBLEM

In this section an evaluation of system serviceability for a water distribution system is presented as an example. The scenario earthquake event results in the following variation of V_{max} across the pipe network; 50% of the pipe inventory is subject to comparatively low seismic shaking of V_{max} = 15 cm/sec, 35% of the pipe inventory is subject to V_{max} = 30 cm/sec while the remaining 15% is subject to comparatively high shaking with V_{max} = 50 cm/sec. The PGD hazard of interest is liquefaction induced lateral spreading. Ninety percent of the pipe inventory is located in areas with no liquefaction susceptibility, 7.5% is in a geological unit with moderate susceptibility area and expected PGD of 5 inches, while the remaining 2.5% is within a high susceptibility area with expected PGD of 20 inches.

Table 2 presents the expected WP repair rate calculation for the system with 75% of the pipe inventory being brittle (e.g., cast iron). For example from equation (3) the expected WP repair rate for brittle pipe with V_{max} = 30 cm/sec (moderate shaking) is

$$RR = 0.0001\ (30)^{2.25} = 0.21 \text{ repairs/km}$$

while the expected repair rate for ductile pipe again for moderate shaking is 0.3 x .21 or 0.063 repairs/km. Since ductile pipe is 25% of the inventory, the composite repair rate for moderate shaking is

$$0.75\ (.21) + 0.25\ (0.63) = 0.173 \text{ repairs/km}$$

Similar calculations for low and high shaking result in 0.036 and 0.548 repair/km respectively. Because of the distribution of pipe inventory between the three shaking intensity areas, the net repair rate for WP damage becomes

$$0.50\ (.036) + 0.35\ (.173) + 0.15\ (.548) = 0.161 \text{ repairs/km}$$

while the corresponding break rate (20% of WP damage assumed to be breaks) is 0.2 (.161) = 0.032 breaks/km.

Relative Hazard (shaking)	% Inventory	V_{max} (cm/sec)	Repair Rate (repair/km)	RR x %Inv.
Low	50%	15	0.036	0.018
Moderate	35%	30	0.173	0.061
High	15%	50	0.548	0.082
	100%			0.161 repair/km

Table 2 Wave Propagation Repair Rate Evaluation

Table 3 presents the expected PGD repair rate calculation for our sample system. For example from equation (4) the expected PGD repair rate for brittle pipe with PGD of 5 inches (moderate susceptibility) is $(5)^{0.56} = 2.46$ repairs/km.

However from Table 1 since only 10% of this geological unit is expected to actually experience PGD during the event, the effective rate for brittle pipe is 0.1 (2.46) = 0.246 repair/km. Also since the repair rate for the ductile pipe (25%) is 0.3 that for brittle, the composite repair rate for moderate susceptibility

$$RR = 0.246[0.75 + 0.25(0.3)] = 0.2 \text{ repair/km}$$

Similar calculations for the high susceptibility area results in 0.88 repairs/km. Considering the percent of pipe inventory exposed to these two PGD hazard levels, the net repair rate for PGD becomes

$$0.075\ (.20) + 0.025\ (.88) = 0.037 \text{ repairs/km}$$

while the corresponding break rate (80% of PGD damage assumed to be breaks) is 0.8 (.037) = 0.030 breaks/km

Relative Susceptibility	% Inventory	P_{ml}	PGD (in)	Repair rate (repair/km)	RR x % Inv.
None	90%	-	-	-	-
Moderate	7.5%	10%	5	0.20	0.015
High	2.5%	20%	20	0.82	0.022
	100%				0.037 repairs/km

Table 3 Permanent Ground Deformation Repair Rate Evaluation

Considering both WP and PGD break rates, the total break rate is 0.062 breaks/km and from Figure 4, the expected system serviceability is 72%.

SENSATIVITY ANALYSIS

In this section the relative sensitivity of water distribution system serviceability to variation in key parameters is determined. For simplicity a Base Case (Scenario 1) is established which corresponds to the sample problem in the previous section with the exception that all the pipes are brittle. As shown in Table 4 we have somewhat larger break rates (0.039 and 0.036 versus 0.0032 and 0.030) and somewhat lower serviceability (63% versus 72%)

Seismic Hazards

As one expects, pipe break rates and system serviceability results will change if the underlying seismic hazards are varied. Scenario 2 and 3 quantify expected changes. In Scenario 2 both V_{max} and the PGD displacement are increased by 50%. (e.g., 35% of the pipe inventory now subject to a V_{max} of 45 cm/sec) with respect to the Base Case while all other parameters remain unchanged. In Scenario 3, V_{max} and the PGD displacement are taken as 75% of the Base Case values. These variations in seismic hazards are considered realistic in relation to observed scatter in attenuation relations, as shown for example in Figure 1.

As show in Table 4 the WP break rate for Scenario 2 is about 2.5 times larger , and the PGD break rate is about 25 percent larger than the Base Case values. These break rates result in a significant decrease in system serviceability (34% compared to 63%). On the other hand the WP and PGD break rates for Scenario 3 are both lower than the Base Case values and the serviceability increases to 80%.

Alternate Fragility Relations

Figure 5 presents a WP fragility relation developed by O'Rourke et at. (1997) using observed damage to cast iron pipe in the 1994 Northridge earthquake. Also shown in Figure 5 is the current HAZUS WP relation from Figure 2 and Equation (3). Note that the two relations provide similar damage estimates for V_{max} of about 15 cm/sec, however, for larger values of V_{max} (e.g., about 50 cm/sec) the Northridge based relation predicts significantly less damage than the current HAZUS relation. The author believes that this difference is due, in part, to the somewhat

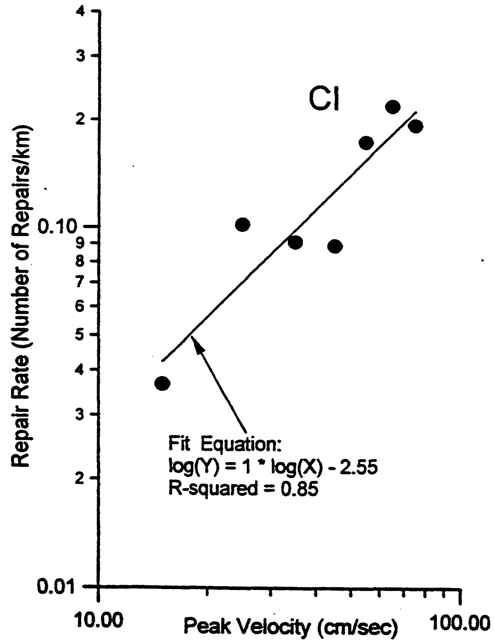

Figure 5 Wave Propagation Fragility Relation for Cast Iron in Northridge (after O'Rourke et al. 1997)

unique character of the Northridge ground motions in comparison to those used in developing Figure 2. The relation in Figure 2 is based on the 1985 Michoacon and the 1971 San Fernando events, among others. For these two events, ground strains and presumably WP damage was related to slower moving surface waves. However for Northridge, in areas with high V_{max} the peak ground velocity occurred early in the ground velocity time history and hence were in all likelihood due to faster moving direct body waves. That is, in terms of Equation (1), although the range of V_{max} values are similar, differences in the apparent propagation velocity with respect to the ground surface (high for Figure 5, low for Figure 2) could explain the observed differences in resulting damage rates.

Scenario 4 quantifies the sensitivity of system serviceability to alternate WP fragility relations. Specifically Scenario 4 corresponds to the Base Case with the exception that the relation in Figure 5 is used to determine WP damage. As shown in Table 4, we have the same PGD break rate, a smaller WP break rate and higher system serviceability for Scenario 4.

Figure 6 presents PGD fragility relation developed by O'Rourke et al. (1999) using observed fault crossing damage to asbestos cement pipe in the 1992 Landers event. Also shown in Figure 6 is the current HAZUS PGD relation from Figure 3 and Equation (4). Note that there is about a half an order of magnitude difference between these relations with the current HAZUS relation predicting higher damage rates.

Scenario 5 quantifies the sensitivity of serviceability results to alternate PGD damage relations. In comparison to the Base Case, we have the same WP break rate, a significant reduction in the PGD break rate, and a higher system serviceability.

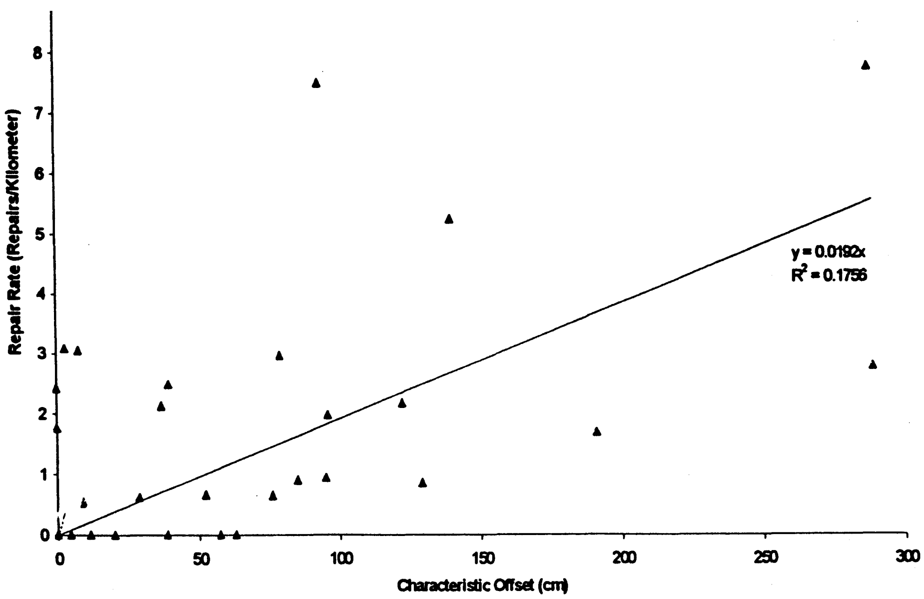

Figure 6 PGD Fragility Relation for Asbestos Cement Pipe in Landers (after O'Rourke et al. 1999)

P_{ml} Factor

The P_{ml} factors currently used by HAZUS and shown in Table 1 were based upon values suggested by a geotechnical subcontractor. Another subcontractor suggested significantly larger values. Scenario 6 is intended to quantify the impact of possible variation in the P_{ml} factor. Specifically a P_{ml} value of 50% is used for high susceptibility while a value of 30% is used for moderate susceptibility (compared to 20% and 10% respectively for the Base Case). That is Scenario 6 corresponds to an average of P_{ml} values suggested by the two subcontractors. As shown in Table 4, the WP break rate is unchanged (as expected) while the PGD break rate increases by a factor of about 2.7. As a result the system serviceability decreases to 36% (as compared to 63% for the Base Case).

Distribution of Leaks and Breaks

The distribution of pipe repairs into leaks or breaks (i.e., 20% of WP and 80% of PDG repairs assumed to be breaks) is based on engineering judgement and data from two events in the Pacific Northwest. Scenario 7 is intended to quantify the impact of possible variations in the repair to break conversion. Specifically in Scenario 7, 50% of all repairs (i.e., both WP and PGD) are assumed to be breaks. As shown in Table 4, the WP break rate increases by a factor of about 2.5 (i.e., 50% / 20%) while the PGD break rate decreases by about a third (i.e., 50% /

80%). As a result the system serviceability decreases to 42% (compared to 63% for the Base Case).

Scenario	Description	WP Rate (breaks/km)	PGD Rate (breaks/km)	Serviceability (%)
1	Base Case (all brittle)	0.039	0.036	63%
2	V_{max} and PGD displacement 50% larger	0.097	0.045	34%
3	V_{max} and PGD displacement 75% of Base Case	0.020	0.031	80%
4	T. D. O'Rourke et al. (1997) WP Fragility rel.	0.014	0.036	80%
5	M. O'Rourke et al. (1999) PGD Fragility rel.	0.039	0.005	83%
6	P_{ml} = 50% for high and 30% for moderate susceptibility	0.039	0.097	36%
7	# Breaks = 0.5 x # repair	0.097	0.023	42%

Table 4 Break Rate and System Serviceability for Variations in Key Parameters

CONCLUSIONS

Current procedures in the HAZUS Earthquake Loss Estimation Methodology for evaluation water system serviceability are reviewed. The impact of reasonable variation in key parameters is determined. It was found that all the parameters considered (V_{max}, PGD displacement, fragility relations for WP and PGD, the P_{ml} factor relating mapped susceptibility areas to areas actually expected to experience liquefaction, and the percentage of pipe repairs representing breaks) have similar influence upon system serviceability. That is, the P_{ml} factor and the percentage of repairs which are breaks, parameters infrequently addressed in the technical literature, are as important as the others which often are the subject of evaluation and study.

REFERENCES

Ballantyne, D., E. Berg, J. Kennedy, R. Reneau and D. Wu (1990). Earthquake loss estimation modeling of Seattle water system. Kennedy/Jenks, Inc., Seattle, WA. *Rept. to US Geol. Survey, Grant No. 14-08-0001-G1526.*

Bartlett, S. and T. L. Youd (1995). Empirical prediction of liquefaction-induced lateral spread. *J. of Geotechnical Eng.*, ASCE, Vol. 121, 316-329.

Bendimerad, F. and J. Bouabid (1995). Seismic reliability assessment of water systems. *Proc. 4th US Lifeline Earthquake Engr. Conf.*, San Francisco, CA, ASCE, pp. 280-287.

Eidinger, J., B. Maison, D. Lee, and B. Lau (1995). East Bay municipal utility district water distribution pipe damage in 1989 Loma Prieta earthquake. *Proc. 4th US Lifeline Earthquake Engr. Conf.*, San Francisco, CA ASCE, pp. 240-247.

Honegger D. and Eguchi, R., (1992), "Determination of relative vulnerability to seismic damage for San Diego County Water Authority (SDCWA) water transmission pipeline," EQE International, San Francisco, CA.

Honegger, D. (1995). An approach to extend seismic vulnerability relationships for large diameter pipelines. *Proc. 4th US Lifeline Earthquake Engrg. Conf.*, San Francisco, CA, ASCE, pp. 320-327.

Kamiyama, M., M. J. O'Rourke, and R. Flores-Berrones (1992). A semi-empirical analysis of strong motion peaks in terms of seismic sources, propagation path and local site conditions. *Tech. Rept. NCEER-92-0023*, Natl. Center for Earthquake Engrg. Res., Buffalo, NY.

O'Rourke, M. and Ayala, G., (1993), "Pipeline damage due to wave propagation," J. Geotechnical Engineering, ASCE Vol. 119, No. 9, Sept.

O'Rourke, M., Mitton, P., and Schiff, A., (1999) "Pipeline damage due to fault offsets in the Landers earthquake" Proc. 5th U.S. Nat'l Conf. Lifeline Earthquake Engineering, ASCE, Seattle, WA, August 1999

O'Rourke, T., Toprak, S., and Sano, Y., (1997) "Factors affecting water supply damage caused by the Northridge earthquake", Proc. 7th US-Japan Workshop on Earthquake Disaster Prevention for Lifeline Systems, Seattle, WA, Nov. 1997, pp. 57-69.

Youd, T. L. and D. M. Perkins (1987). Mapping of liquefaction severity index. J. of Geotechnical Eng., ASCE. Vol. 113, 1374-1392

DEVELOPMENT OF NEW ASEISMIC JOINTS FOR CASING PIPES OF UNDERGROUND TRANSMISSION LINES

Fusanori Miura[1], Toshiyuki Tanaka[2], Yasuhiro Oda[3], and Nobuzo Ito[3]

ABSTRACT

The purpose of this study is to develop new aseismic joints used to connect casing pipes of underground transmission lines that can sustain liquefaction-induced large permanent ground displacements. To achieve this purpose, we investigated the capability of currently used three kinds of aseismic joints. Bending, tension and compression tests were conducted in order to obtain the mechanical characteristics of the aseismic joints. In addition, characteristics of the pipe-soil interaction spring were obtained. Both characteristics showed strong nonlinearities and they were used in numerical parametric study. Prior to the parametric study, the validity of the numerical method was examined by comparing the results from experiments in which aseismic jointed pipes were subjected to vertical large ground displacements in sandy soil and the simulated results of the experiments. After the verification of the numerical method, we performed parametric study to investigate responses of aseismic jointed pipes subjected to large ground horizontal and vertical displacements caused by liquefaction and discussed whether the present aseismic joints had enough flexibility or not. Based on the results, we developed several new aseismic joints that had more flexibility in bending, tensile and compressive deformations.

---

[1] Professor, Faculty of Engineering, Yamaguchi University, 2-16-1 Tokiwadai, Ube, Yamaguchi Pref. 755-8611, Japan.
[2] Manager of Engineering Department, Uchida Tanko Co., Ltd., 58 Kogane-machi, Yokkaichi, Mie Pref., 512-8062, Japan.
[3] Chief Engineer, ditto..

INTRODUCTION

In past earthquakes, pipeline systems were severely damaged by liquefaction-induced lateral ground displacements. Liquefaction also caused floating of manholes and handholes and this resulted in the damage to pipes at the connection to them. To reduce such damage of pipeline systems, many kinds of aseismic joints have been developed and currently used. However, the 1995 Hyogoken-nanbu earthquake (the Kobe earthquake) caused severe damage to pipelines even though such aseismic joints were used. This requires reconsidering the capability of currently used aseismic joints during such extremely strong ground motions and resulting liquefaction-induced large ground displacements.

From this point of view, we investigated bending, tensile and compressive capabilities of three kinds of existing aseismic joints which were commonly used to connect casing pipes or to connect casing pipes and a handhole of underground transmission lines. In addition, we obtained characteristics of soil-pipe interaction springs. All these characteristics showed strong non-linearity and to take into account them in numerical analysis, we modified the analysis program for nonlinear soil-buried structure interaction problem, "B-STRUCT", which was originally developed in Cornell University. After verification of the modified program by comparing experimental results and simulation results, we performed a parametric study to investigate responses of aseismic jointed pipes subjected to large ground displacements of several patterns[1].

The results showed that the currently used aseismic joints could not afford the large ground displacement patterns, and based on the results we developed some new aseismic joints which have more capabilities of bending, tensile and compressive deformations than existing ones.

PARAMETRIC STUDTY ON RESPONSES OF PILELINES

Analyzed models

Hamada et al.[2, 3] measured lateral and vertical ground displacements due to liquefaction using aerial photographs for the 1964 Niigata earthquake, the 1983 Nihonkai-chubu earthquake, and the 1995 Hyogoken-nanbu earthquake and so forth. Based on the statistical analysis of the study, we analyzed five cases as shown in Fig.1.

Figure 1 (a) shows Case-1, in which a non-liquefied surface layer containing a handhole (H.H.) and pipeline with currently used aseismic joints above a liquefied sublayer was assumed to move in the axial direction of the pipeline. As shown in the left figure, the length of the analyzed pipeline with a handhole at the left end was 100m and the distribution of the ground displacement was a quarter-sine curve with the maximum displacement of 1.5m at the connection of the pipe and handhole. The handhole was assumed that it would not move. Aseismic joints were used every 4.0m in the pipeline corresponding the length of a pipe. The solid and open triangles in the figure represent the positions where the compression load and the pulling-out displacement were maximums, respectively.

Figure 1(b) shows Case-2, in which the pipeline with aseismic joints was subjected to ground displacements in axial direction again but no handhole. The distribution of the displacement was a half-sine curve with the maximum displacement of 1.5m. Aseismic joints were used every 4.0m. The open and solid triangles in the left figure represent the positions where the pulling-out displacement and the compression load were maximums, respectively.

Figure 1 (c) shows Case-3, in which a seawall was assumed to move 3.5m at maximum in the axial direction of the pipe and the ground displacement immediately reduced from the seawall. The shape of the curve was an inverse quarter-sine curve. The handhole, however, was fixed irrespective of the movement of the seawall. The solid and open squares in the left figure represent the positions where the compression load and pulling-out displacement were maximums, respectively. When the handhole was displaced corresponding to the displacement of the seawall, pulling-out occurred at the early stage of the application of the ground displacement.

Figure 1 (d) shows Case-4, in which the liquefied layer was assumed to move in the horizontal transverse direction of the pipe with the maximum displacement of 3.5m. The rhombuses represent the positions where the maximum pulling-out displacement occurred.

Figure 1 (e) shows Case-5, where the pipe was subjected to subsidence of the ground due to liquefaction. The maximum value of the subsidence was assumed to be 68 cm based on the past damage. The solid circle in the left figure represents the position where the maximum rotational angle was observed.

In these models, we assumed that the handhole and pipeline existed in a non-liquefied surface layer above a liquefied layer, and we also assumed that the non-liquefied surface layer was dragged by the flow of the liquefied layer. Therefore, the soil spring coefficients in the analyses were not reduced.

Simulation Results

The results from the parametric study are summarized in Table 1. The schematic drawing of the three currently used joints are shown in Fig.2. Type-A and Type-B joints are used to connect pipes and Type-C joint is used to connect a pipe and a handhole. The capacities of rotational angle, compressive load and pulling-out displacement for the three joints are listed in Table 2.

The result from Case-1 means that Type-C joint will be damaged because the magnitude of the maximum compressive load from the simulation was 235 KN while the capacity was 52.6 KN. The result also implies the possibility of pulling-out of Type-C joint at the handhole when the handhole was located at the end of right side of the pipeline, because the magnitude of pulling-out from the simulation was 9.4 cm while the tensile capacity of the joint was 3.87 cm.

The simulation result from Case-2 implies the possibility of pulling-out when Type-B joints were used, because the magnitude of pulling-out from the simulation result was 18.7 cm while the capacity was 16.7 cm. If Type-A joints were used, there would be no damage to the pipeline.

In Case-3, the simulation result implies that the Type-C joint would be damaged because the resultant maximum compressive load was 168 KN while the capacity was 52.6KN. If the handhole moved corresponding to the seawall with the same magnitude, there were many pulling-out in the pipeline.

In Case-4, no damage would occur. This means that the ground displacement in the axial direction of pipeline is more severe than that in the transverse direction.

In Case-5, if Type-A or Type-B joints were used at the end of the pipe, they would be damaged because the obtained rotational angle was 9.0 degrees while their capacities were 4.1 and 8.7 degrees, respectively. If Type-C joint were used, it would be also damaged because of the pulling-out capacity.

From the above numerical study, generally speaking, the present aseismic joints can not afford the ground displacement due to liquefaction. This means the necessity of development of new aseismic joints that have more capacities of tensile load, compressive load and pulling-out displacement.

DEVELOPMENT OF NEW ASEIMIC JOINTS

Type of new aseismic joints

Based on the above simulation results, we developed several new aseismic joints. They are classified into four categories, i.e., modified Type-As, modified Type-B, modified Type-C and others with mechanical stopper and they are shown in Fig. 3. Figures 3(a) and (b) are the modified Type-AL (long) and Type-AS (short) joints, (c) the modified Type-B and (d) the modified Type-C joints. Figures 3(e), (f) and (g) are joints with mechanical stoppers for tensile displacement and are called Type-D, Type-E and Type-F joints, respectively in this paper. The capacities of them are listed in Table 3.

Economical and workability evaluation of the new joints

The modified Type-B joint can be used to connect a pipe to a handhole as well as to connect pipes. But other joints, such as modified Type-A joints, Type-D, Type-E and Type-F joints must be used in combination with the modified Type-C joint when a pipe is connected to a handhole. We estimated the relative cost if these new aseismic joints were used and the results are summarized in Table 4. In Table 4, the workability of the new joints was also shown. Judging from both the cost and workability, the combination of modified Type-C joint and modified Type-A joints are recommended.

CONCLUSION

The results obtained from this study can be summarized as follows;

(1) From the parametric study on responses of a pipeline with a handhole subjected to large ground displacements caused by liquefaction, it was found that the currently used aseismic joints could not afford such large ground displacements.

(2) Based on the parametric study, we developed several new aseismic joints. They have more capacities of bending, tensile and compressive deformations.
(3) We also evaluated the cost and workability of the new aseismic joints. Based on the estimation, we proposed combinations of new aseismic joints for the connection between a pipe and a handhole, and for that between pipes with reasonable cost.

REFERENCES

1) F. Miura, T. Tanaka, Y. Oda, and N. Ito; Behavior of Aseismic Jointed Pipe Subjected to Large Ground Displacements, Optimizing Post-earthquake Lifeline System Reliability, Edited by W. M. Elliot and P. McDonough, TCLEE No.16, pp.711-720, Seattle Aug. 1999.
2) M. Hamada, S. Yasuda, R. Isoyama and K. Emoto; Study on Liquefaction Induced Permanent Ground Displacements, Association for The Development of Earthquake Prediction, Nov., 1986.
3) M. Hamada, R. Isoyama and K. Wakamatsu; The 1995 Hyogoken-Nanbu (Kobe) Earthquake, liquefaction, ground Displacement and Soil Condition in Hanshin Area, Association for Development of Earthquake Prediction, The School of Science and Engineering, Waseda University and Japan Engineering Consultants, Aug.1995.

Table 1 Maximum responses from the parametric study

Case	Max. Comp. Load (KN)	Max. Pulling-out (mm)
1	235	94
2	180	187
3	168	170
4	----	24
	Max. Rot. Angle (degree)	
5	9.0	58

Table 2 Capacities of the joints

	Type-A	Type-B	Type-C
Allowable Comp. Load (KN)	309.6	309.6	52.6
Allowable Pulling-out Displacement (m)	22.4	16.7	3.87
Allowable Rotational Angle (degree)	4.1	8.7	25.6

Table 3 Capacities of the new aseismic joints

Type	Offset (mm)		Load (KN)		Rotational angle(degree)
	Tension	Compression	Tension	Compression	
Modified Type-AL	187	171	2.7	2.7	0.5
Modified Type-AS	187	0	2.7	235.0	0.5
Modified Type-B	187	171	2.7	2.7	8.8
Modified Type-C	187	171	2.7	2.7	8.8
Type-D	100	0	33.6	172.0	0.5
Type-E	100	0	33.6	172.0	0.5
Type-F	100	0	33.6	172.0	0.5

Table 4 Cost and workability of new aseismic joints

Connection		Relative cost (Current=1)		Workability
Pipe and Handhole	Pipe and Pipe	Distance between handholes (m)		
		25m	50m	
Modified Type-B	Modified Type-B	3.1	3.2	Good
Modified Type-C	Modified Type-AL	1.5	1.3	Good
Modified Type-C	Modified Type-AS	1.5	1.3	Good
Modified Type-C	Type-D	1.8	1.6	Moderate
Modified Type-C	Type-E	2.3	2.1	Moderate
Modified Type-C	Type-F	2.0	1.8	Moderate

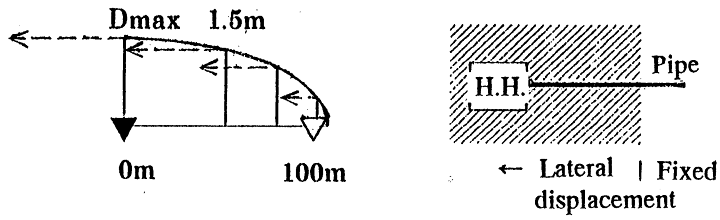

(a) Case-1

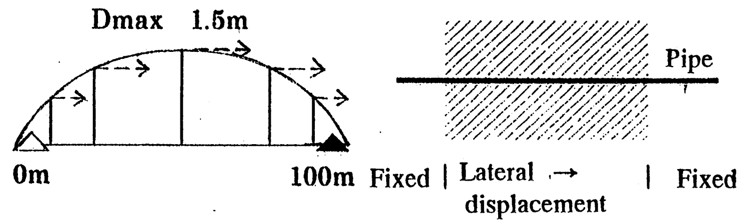

(b) Case-2

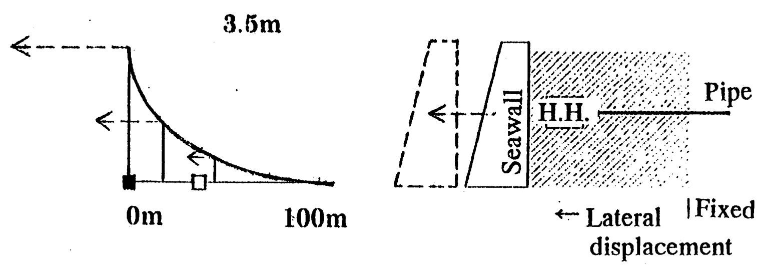

(c) Case-3

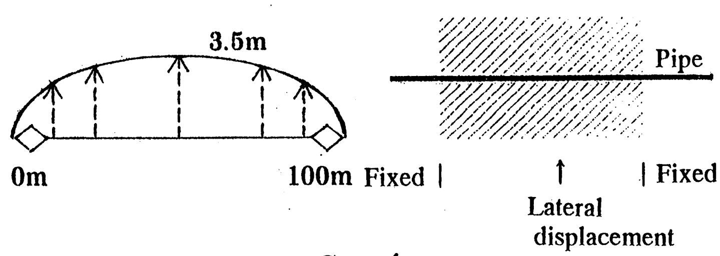

(d) Case-4

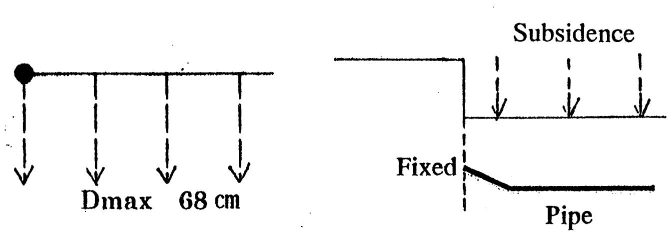

(e) Case-5

Figure 1 Models for parametric study

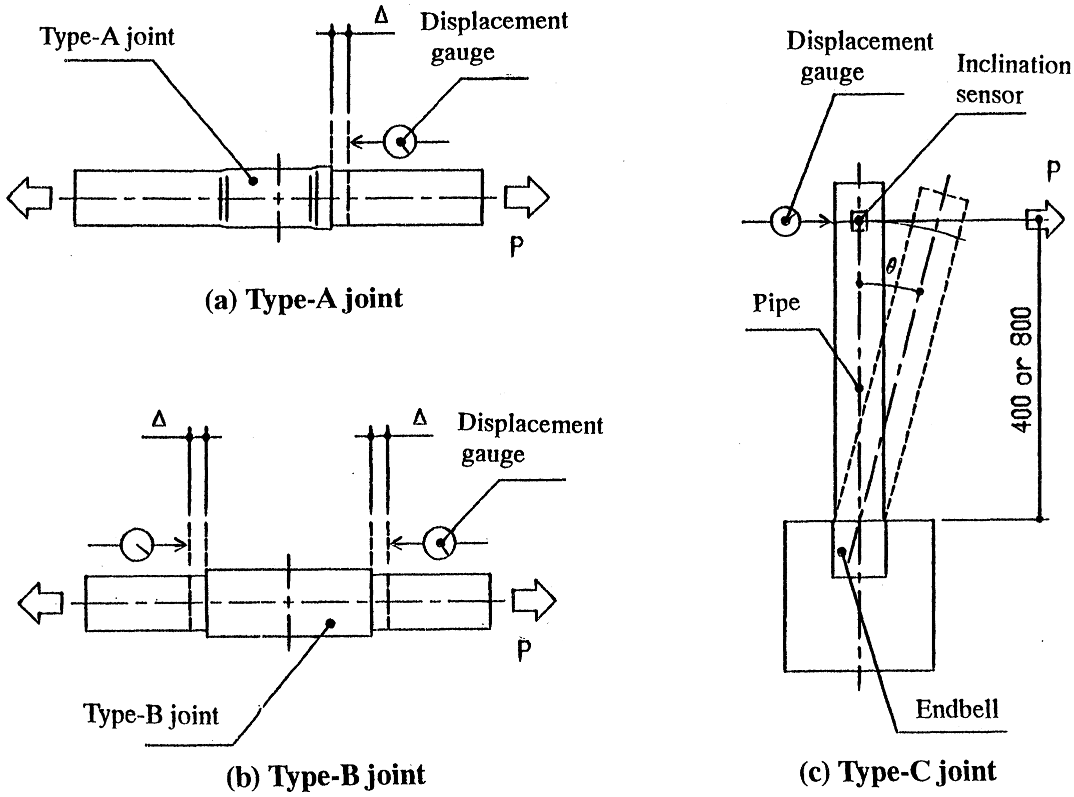

Figure 2 Currently used aseismic joints

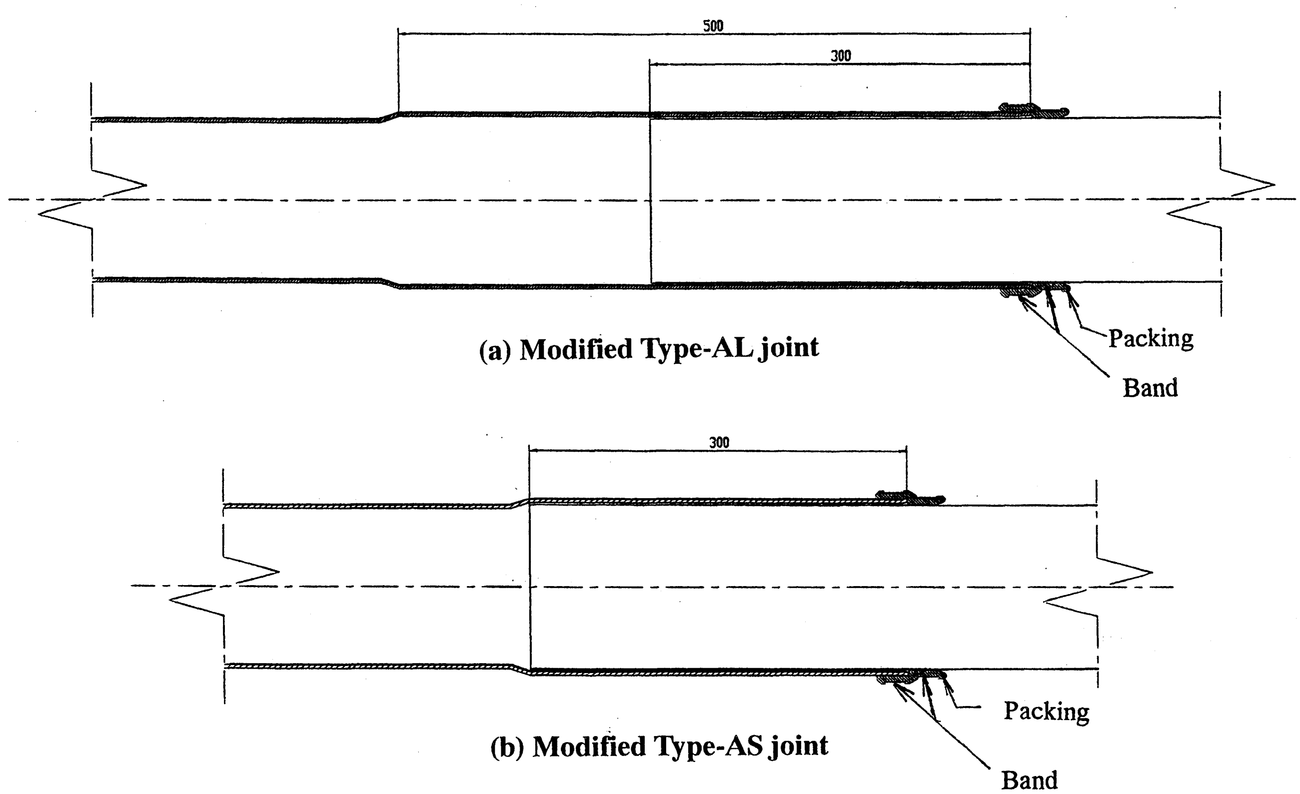

Figure 3 Proposed new aseismic joints

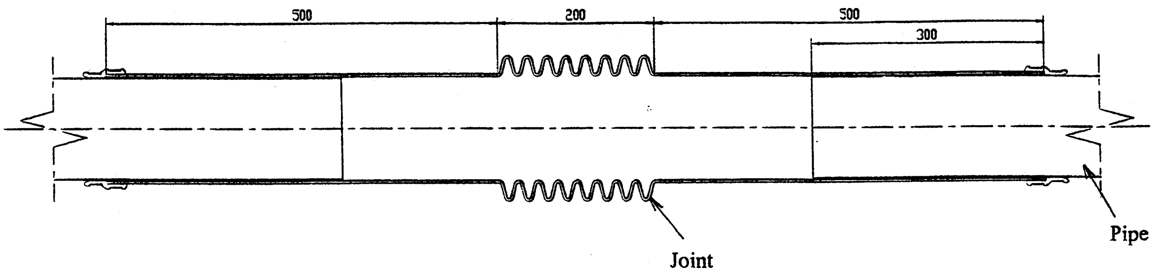

(c) Modified Type-B joint

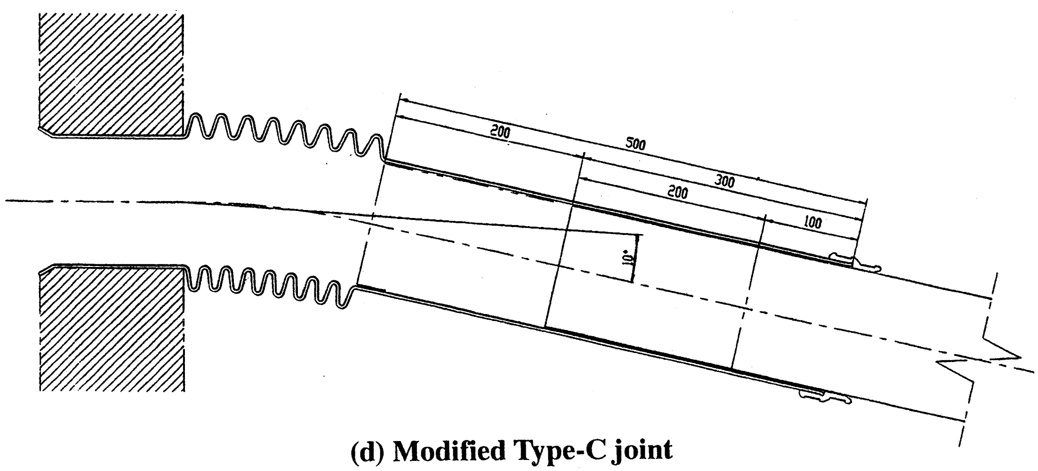

(d) Modified Type-C joint

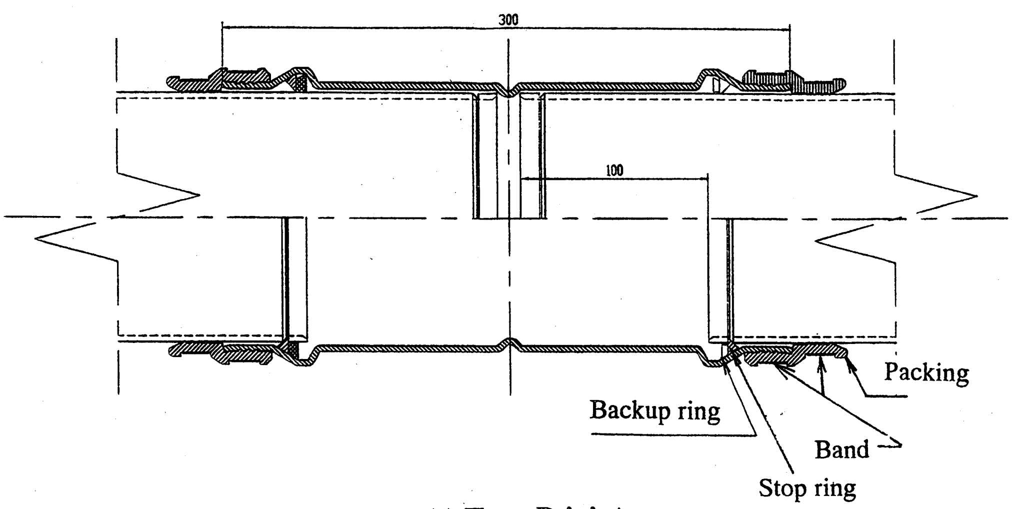

(e) Type-D joint

Figure 3 Proposed new aseismic joints

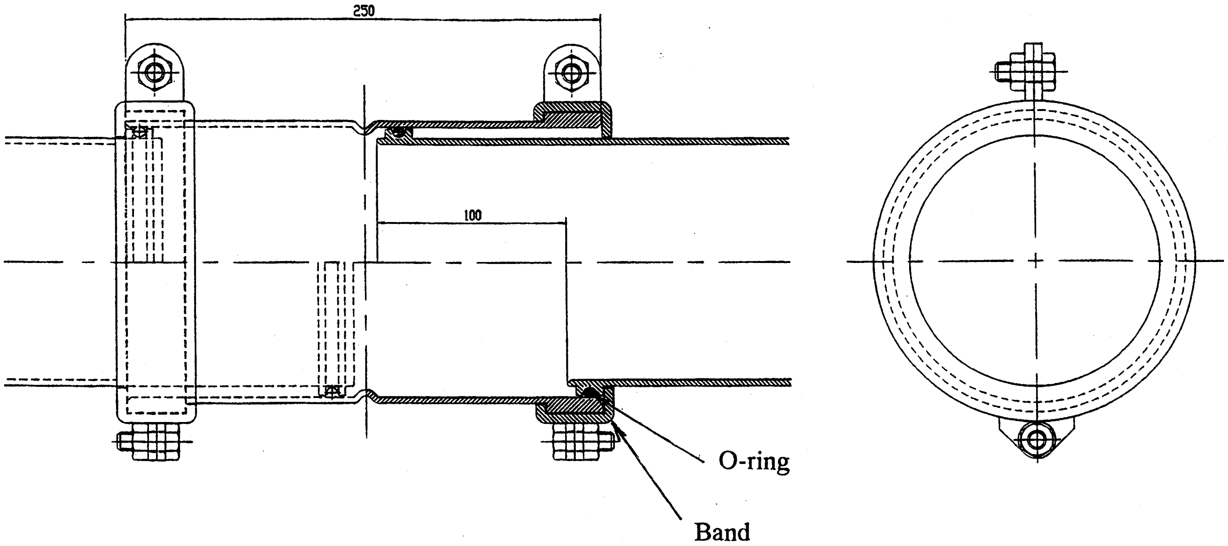

(f) Type-E joint

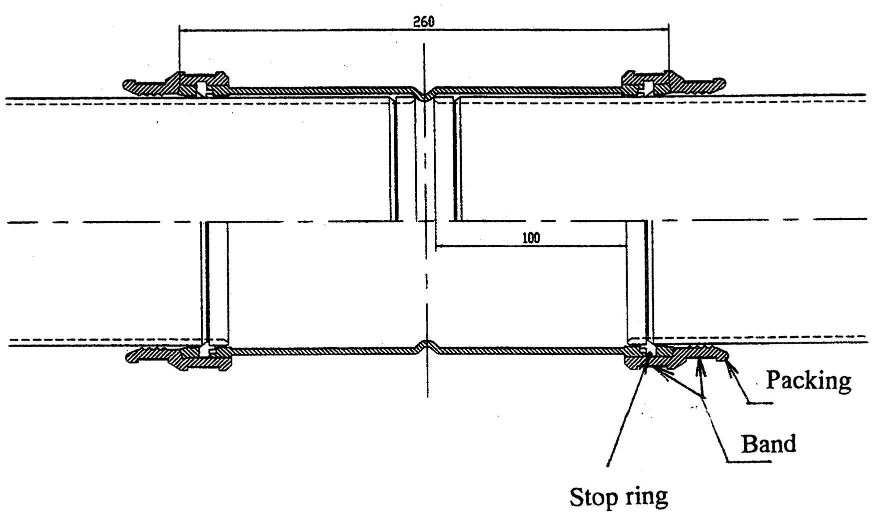

(g) Type-F joint

Figure 3 Proposed new aseismic joints

CASE STUDY OF THE GRANADA TRUNK LINE DURING TWO NEAR-FIELD EARTHQUAKES

C. A. Davis[1]

ABSTRACT

A case study of the Granada Trunk Line (GTL) is presented. The GTL is a large buried steel water pipe that was subjected to strong near-field ground motions (up to 1.0g pga and 110 cm/s pgv) and large permanent ground deformations during the 1971 San Fernando and 1994 Northridge earthquakes. Field survey measurements following the 1971 earthquake showed ground deformations of up to 8.65 feet, which caused extensive damage to the GTL in the form of tension cracks and compression wrinkling at the welded joints. Following the 1971 event, flexible couplings were installed along potions of the pipe to help reduce future damage. Investigations performed after the 1994 earthquake showed that deformations were significantly less than in 1971 and that the couplings helped reduce, but did not eliminate, damage. Comparison of the GTL seismic response during the two earthquakes indicates that damage resulted from permanent ground deformations and strong near-source transient ground strains. A portion of the pipe that passes through a soft saturated soil basin was not equipped with flexible joints and showed signs of oscillatory motion. Performance of the GTL in two similar sized earthquakes provides valuable information for understanding seismically induced ground deformations and pipe damage.

[1] Geotechnical Engineer, Department of Water and Power, Los Angeles, CA.

INTRODUCTION

The Granada Trunk Line (GTL) is a 125.7 cm (49 ½ inch) outside diameter, high pressure, major supply pipeline that serves portions of the San Fernando Valley in Los Angeles, California and is owned and operated by the Los Angeles Department of Water and Power (LADWP). The GTL originates on the Van Norman Complex (VNC), passes along the Jensen Filtration Plant (JFP), and extends down Balboa Boulevard; three sites important for the understanding of seismic induced permanent ground deformations and damage to lifelines (Youd, 1973; Dixon and Burke, 1973; Subcommittee on Water and Sewerage Systems, 1973; O'Rourke et al., 1992, O'Rourke and O'Rourke, 1995; Davis and Bardet, 1995).

The February 9, 1971 San Fernando and January 17, 1994 Northridge earthquakes caused severe damage to the GTL. A series of movements and breaks resulted along portions of the GTL located on the VNC and the JFP in 1971. In 1994, similar movements occurred on the VNC and JFP in addition to large deformations on Balboa Boulevard. Others (Holzer et al., 1999; O'Rourke and O'Rourke, 1995) have reported the 1994 Balboa Boulevard movements and damage. Davis (1999) reported the 1971 and 1994 movements and damage that resulted on the VNC and JFP. This report provides additional descriptions of site conditions and a more detailed comparison and simplified analyses of the reported damage from the two earthquakes.

BACKGROUND

The GTL was constructed in 1956 to provide domestic water and fire protection to higher elevations on the western side of the San Fernando Valley. Figure 1 shows a potion of the VNC, where the GTL originates (Davis and Bardet, 1995; Davis, et al., 1996), and extends westerly through the Upper Debris Basin and over to Balboa Blvd. The portion of GTL between the debris basin and Balboa Boulevard was relocated in 1967 for expansion of the Metropolitan Water Districts' JFP. As shown in Figure 1, the GTL now runs around the perimeter of the JFP within a dedicated utility corridor.

The utility corridor consists of an embankment fill of approximately 3 m in depth. The corridor is located at the toe of a constructed compacted embankment fill slope that extends to the west (Davis, et al, 1996). The embankments were constructed on saturated alluvium and debris deposits that consist of mixtures of sands, silts, and clays.

Both the 1956 and 1967 pipes were constructed with 125.7 cm outside diameter, 0.635 cm (1/4 inch) thick, ASTM A-283 grade C welded steel pipe. The connections were made with bell and spigot slip joints and fillet welds around the outside perimeter. The design hoop stress is 81 MPa (11,760 psi). The portion extending through the Upper Debris Basin was strengthened with ring stiffeners around the outside of the pipe. On the east side of the debris basin the pipe is encased in concrete under an earth fill dike. The inside of the pipe is lined with concrete mortar. The outside of the pipe is covered with a coal tar enamel undercoat overlain with a 2.54 cm cement mortar coating.

1971 SAN FERNANDO EARTHQUAKE

The February 9, 1971 San Fernando Earthquake occurred on the San Fernando Fault with a moment magnitude M_w of 6.7 and an epicentral distance of approximately 11 km north-east of the VNC. The VNC overlies the westerly boundary of the fault that ruptured toward the south and subjected the GTL to strong near-source pulses (Wald and Heaton, 1994). There were no seismic recordings in the immediate vicinity of the GTL, however, Scott (1973) interpreted time histories from a seismoscope located at the Lower San Fernando Dam, at the southern end of the VNC, approximately 3 km south of the GTL. Scott (1973) reported peak ground accelerations (pga) in the range of 0.6 g to 0.8 g and peak ground velocities (pgv) up to 110 cm/s.

Table 1. Breaks on the Granada Trunk Line from 1971 San Fernando Earthquake.

	Joint connection	Break/ displacement	1971 repair	Notes	Average strain (%)[2]
1	Mechanical coupling	Damaged coupling	Replaced coupling		
2	Welded bell and spigot	Lateral offset; compression?	Spliced 1.2 m pipe with 0.5 cm butt straps (3/16")	Few cm to 0.3 m of lateral offset	
3	Mechanical coupling	Compression and lateral displacement	Spliced 1.2 m pipe with 0.5 cm butt straps (3/16")	Coupling severely battered and compressed	
4	Mechanical coupling	Tension	Spliced in 1.5 m of pipe with butt straps[1]		+0.21
5	Welded bell and spigot	Tension?	butt strap	Joint located at vertical bend	-0.04
6	Welded bell and spigot	Compression	butt strap[1]	Joint located at vertical bend	
7	Welded bell and spigot	Compression	butt strap	Joint located at vertical bend	-0.11
8	Welded bell and spigot	Compression	Spliced in 1.2 m of pipe with butt straps		
9	Welded bell and spigot	Compression	Spliced in 1.2 m of pipe with butt straps		
10	Mechanical coupling	Compression	Spliced in 1.2 m of pipe with butt straps	Severe damage removed coupling	
11	Mechanical coupling	Tension	butt strap	Removed coupling	+0.11
12	Mechanical coupling		butt strap	Removed coupling	

[1] repair replaced with a mechanical coupling in 1973
[2] (+) tension, (-) compression

Pipe Breaks

Figure 1 and Table 1 summarize the GTL breaks that occurred during the 1971 earthquake. Damage to the GTL has previously been summarized by the Subcommittee on Water and Sewage Systems (1973) and O'Rourke et al. (1992). This paper provides more accurate information based on a detailed review of LADWP records. Davis et al. (1996) describes the discrepancies in earlier damage reports.

Damage to joints varied in size and type along the alignment. O'Rourke et al. (1992) reports that the greatest damage occurred at location 3, where compression severely damaged the mechanical coupling and bending occurred from lateral displacements of 0.5 m (1.5 ft). Many of the bell and spigot joints failed from compression yielding leaving permanent wrinkles in the pipe. The Subcommittee on Water and Sewage Systems (1973) also reported that some joints failed in tension. The exact location of the tension breaks were not reported, however, Table 1 notes tension or compression breaks and displacements, which were estimated by comparison with the average axial strain values. The average strains were determined from the survey measurements described in the next section.

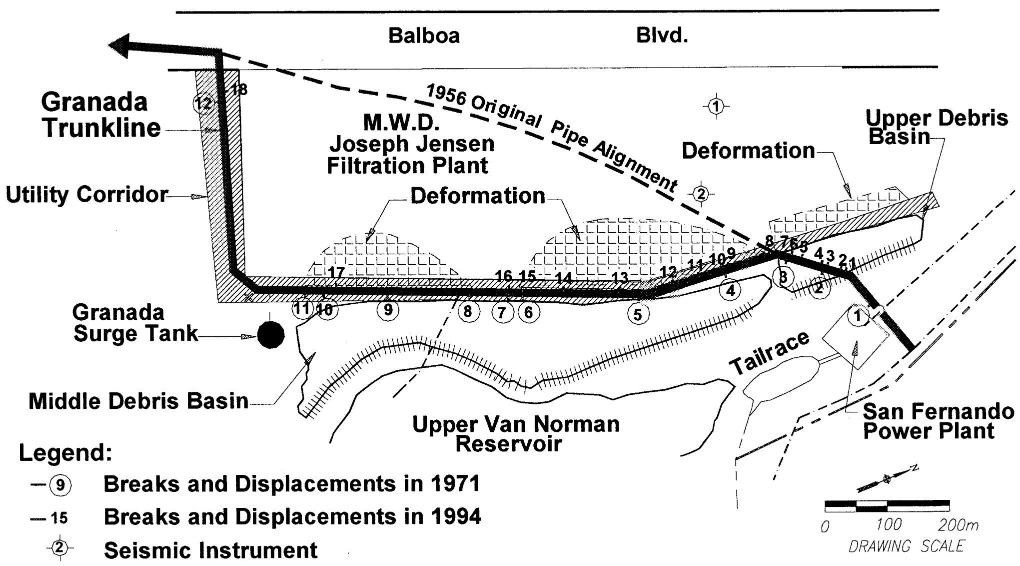

Figure 1. Plan view of the Granada Trunk Line on the Van Norman Complex showing the location of pipe breaks and displacements from the 1971 and 1994 earthquakes, original and relocated alignments, three regions of most significant ground cracking, and seismic instruments.

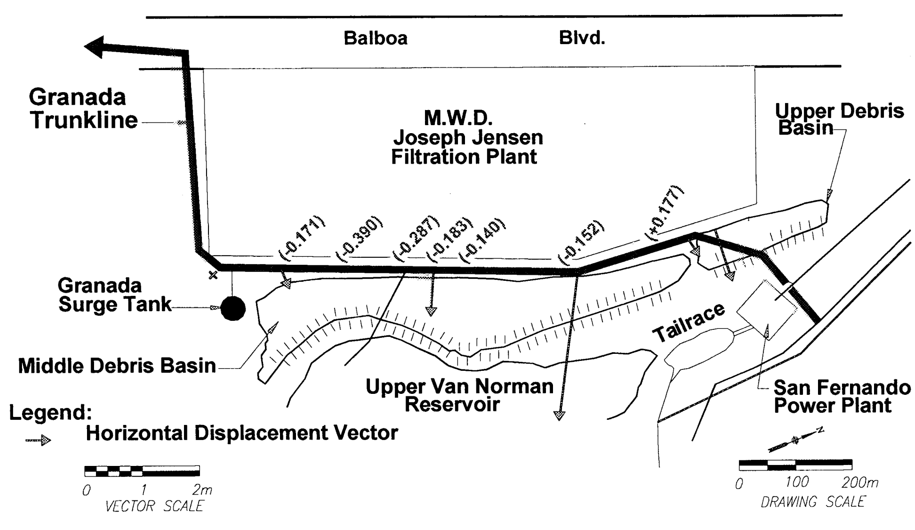

Figure 2. 1971 San Fernando Earthquake horizontal displacement vectors and settlement (in parenthesis) in meters measured along the utility corridor.

Permanent Ground Deformation

Figure 2 shows vectors of 1971 post earthquake deformation measured at monuments along the utility corridor. These displacements were calculated by comparing surveys of January 26, 1967, and February 17, 1971, to locate the GTL alignment. The traverse survey had an accuracy of 1/10,000. Each of these surveys measured angles and distances between monuments. The surveys showed no deformation at the location marked "x" in Figure 2. Holding this point constant, lateral displacements were calculated from the survey data. Longitudinal displacements were determined by summing the measured differences between consecutive monuments from location "x". Figure 2 shows settlements in parentheses, which were measured at selected locations on the top of the GTL pipe. The lateral movement vectors of Figure 2 were not corrected for differential tectonic movements. However, Yerkes et al. (1974) indicates a significant variation in bedrock movements below the GTL. Accounting for tectonic movements, the lateral vectors in Figure 2 would increase with a variation from zero at location "x" to 0.15 m (0.5 ft) on the north end.

Segregating vectors of Figure 2 into orthogonal components, the greatest lateral and longitudinal movement at the measured monuments was 2.6 m (8.65 ft) and 0.32 m (1.05 ft), respectively, near the center of the GTL. Settlements were as large as 0.39 m (1.28 ft) near the southern end of the utility corridor portion along the Middle Debris Basin. Uplift was measured near the north end of the GTL within the utility corridor along the same area where pressure ridges were noted following the earthquake (Converse, Davis and Associates, 1971). The horizontal displacements are on the same order of magnitude as that measured by O'Rourke et al. (1992) and greater than that estimated by other means following the 1971 earthquake (Converse, Davis and Associates, 1971; Woodward-Clyde Consultants, 1988). Settlements measured here are approximately half that presented by O'Rourke et al. (1992). The movements measured along the utility corridor in 1971 were a result of sliding of the compacted fill slope that extends west of the utility corridor.

Post Earthquake Repairs

Table 1 summarizes emergency repairs made immediately following the 1971 earthquake. At the welded joints, repairs were made by cutting out the damaged section of pipe and welding butt straps around the cut section. At places of severe damage and large lateral offsets, pipe segments were cut out and spliced with new segments using welded butt straps. Damaged mechanical couplings were removed and replaced with butt straps.

Additional repairs were made to the pipe in 1973. First, the entire length of pipe adjacent to the Middle Debris Basin was excavated to relieve any residual strain and to ensure that all damaged portions were repaired. Then nine long barrel mechanical couplings, which allow for 30.5 cm (12 inches) of movement in either direction along the pipe axis, were installed at approximately 91 m intervals within this same region. Other long barrel mechanical couplings were placed in the utility corridor south of the Middle Debris Basin. The long barrel couplings were installed mainly to improve the GTL seismic performance. The standard mechanical coupling at location 1 was also replaced. Prior to cutting the pipe for mechanical coupling installation, five strain gauges were installed on the GTL at various places along the portion adjacent to the Middle Debris Basin. The first cut for coupling installation was made near the south end of the JFP slope, (i.e. just north of 1971 location 9 in Fig. 1). A gauge located next to the cut location measured a tensile strain of 0.027 indicating the GTL retained a residual tensile stress of 54 MPa, even though the surface measurements along this portion of pipe showed compressional deformations. However, the cut next to damage location 8 measured compression strains, consistent with the surface deformations. In addition, all but two of the cuts made adjacent to the Middle Debris Basin pulled apart several millimeters, indicating a residual tensile strain persisted through most to the utility corridor. Strain measurements made by the gas company on a 56 cm diameter steel pipe in the utility corridor, reported in LADWP records, indicated a residual compressive strain south of location 8 in Fig. 1 and tensile strain north of that location.

1994 NORTHRIDGE EARTHQUAKE

The January 17, 1994 Northridge Earthquake occurred on an unmapped blind thrust fault with a M_w of 6.7 (Wald and Heaton, 1994) and an epicentral distance of approximately 11 km south of the VNC. The VNC overlies the north-easterly boundary of the fault that ruptured toward the north and subjected the GTL to strong near source pulses (Bardet and Davis, 1996). Figure 1 shows the location of 2 seismic instruments at the JFP that recorded the ground motion. Station 1 is located in a generator building that is founded on bedrock and shallow fill and recorded a 1.1g pga and 87 cm/s pgv. Station 2 is located in the administration building that is founded on deep compacted fill over soft saturated alluvium and recorded a 0.6g pga and 109 cm/s pgv (USGS, 1994).

Table 2. Breaks on the Granada Trunk Line from the 1994 Northridge Earthquake.

	Joint connection	Break/ displacement	Notes	Average strain (%)[1]
1	Welded bell and spigot	Crack at joint	Crack approx. 35 cm long	
2	Welded bell and spigot	Crack at joint	Crack approx. 35 cm long	
3	Welded butt strap	Jagged tears; folded inward 7.6 cm; separated to 10 cm	Lateral offset to 0.3 m; broke at 1971 repair	
4	Welded butt strap	Jagged tears; folded inward 7.6 cm; separated to 10 cm	Lateral offset to 0.3 m; broke at 1971 repair	
5	Welded bell and spigot	Spigot flared inward 1.3 cm; separated 5 cm		
6	Welded butt strap	Folded inward and separated 5 cm	broke at 1971 repair	
7	Welded butt strap	Jagged tears; folded inward 7.6 cm; separated to 5 cm	broke at 1971 repair	
8	Long mech. Coupling	29.2 cm residual compression displacement	Compressed 30.5 cm, closed then separated	
9	Welded bell and spigot	5 to 7.6 cm inside bulge	Wrinkling at joint	
10	Long mech. Coupling	5 cm compression displacement	Gasket OK	
11	Welded bell and spigot	Cement mortar failure	No observed joint displacement	+0.035
12	Long mech. Coupling	7.6 cm extensional displacement	Gasket OK	+0.064
13	Long mech. Coupling	7.6 cm extensional displacement	Gasket OK	-0.15
14	Long mech. Coupling	10 cm extensional displacement	Gasket OK	+0.10
15	Long mech. Coupling	5 cm extensional displacement	Gasket OK	-0.014
16	Welded butt strap	Cement mortar failure	No joint displacement; at 1971 repair	-0.004
17	Long mech. Coupling	7.6 cm extensional displacement	Gasket OK	-0.073
18	Long mech. Coupling	2.5+ cm extensional displacement		

[1] (+) tension, (-) compression

Pipe Breaks

Figure 1 and Table 2 summarize the breaks and displacements that occurred on the GTL in 1994 from the earthquake. As noted in Table 2, all breaks and displacements occurred at joint connections and were located with the aid of engineers, field supervisors, and welders who repaired the GTL. There were a total of seven pipe breaks of various sizes (locations 1 through 7), all occurring within the Upper Debris Basin. Table 2 presents three other locations where distress was noted during interior inspections (locations 9, 11, and 16). Measurements of pipe axial displacements were made at eight mechanical couplings (locations 8, 10, 12-15, 17, and 18) which were initially set with a 30.5 cm gap when installed in 1973.

The GTL suffered seven breaks within the Upper Debris Basin, the only region where long barrel mechanical couplings were not installed after the 1971 earthquake. At locations 1 and 2, two cracks occurred in the steel pipe within the concrete encased portion that underlies an embankment making up the eastern boundary of the basin. At locations 3, 4, 6, and 7 ruptures occurred where repairs had been previously made in 1971. These four breaks were major having jagged tears that were folded inward up to 7.6 cm with several centimeters of separation. The pipe was also deformed out-of-round in the vicinity of the ruptures. The break at location 5 occurred at the first joint east of location 6. Breaks at welded joints occurred within the heat affected area adjacent to the welds.

There were no breaks of welded joint connections through the utility corridor. However, there were locations of joint distress such as at location 9, where a welded slip joint wrinkled and deformed inward up to 7.6 cm. At locations 11 and 16 cement mortar failures at joints were noted, indicating significant axial stress. Location 16 was at a 1971 break repair. The axial pipe displacements at mechanical couplings and the strain measurements noted in Table 2 provide additional indications of the amount of movement and distress the GTL was subjected to. Average strains were determined from the survey measurements described in the next section.

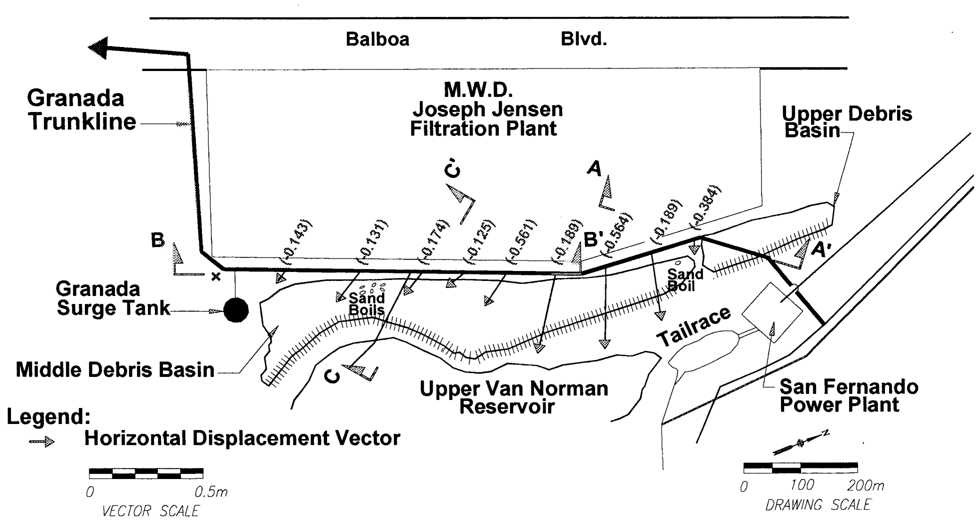

Figure 3. 1994 Northridge earthquake horizontal displacement vectors and settlement (in parenthesis) in meters measured along the utility corridor.

Permanent Ground Deformation

Figure 3 shows vectors of movement as measured along a line of monuments with horizontal and vertical control established after the 1971 earthquake. The monuments are made of iron pipes located in the utility corridor that are connected to the top of the GTL near each long mechanical coupling. The 1994 movement was estimated by comparing surveys of January 30, 1995 and September 22, 1976. The measurements are accurate to within ±3 mm (0.01 ft). Measurements of other monuments set in bedrock around the area indicate there was no significant differential horizontal tectonic movement along the

GTL alignment. Segregating vectors of Figure 3 into orthogonal components, the greatest lateral movements of 0.35 m (1.14 ft) were measured near the center of the pipe, while movements along the pipe axis were smaller and did not exceed 0.11 m (0.37 ft). Settlements ranged from 0.12 m (0.41 ft) to 0.56 m (1.85 ft), the largest occurring at points near the center of the pipe. The movements along the utility corridor are a result of sliding of the compacted fill slope, similar to that described for the 1971 earthquake.

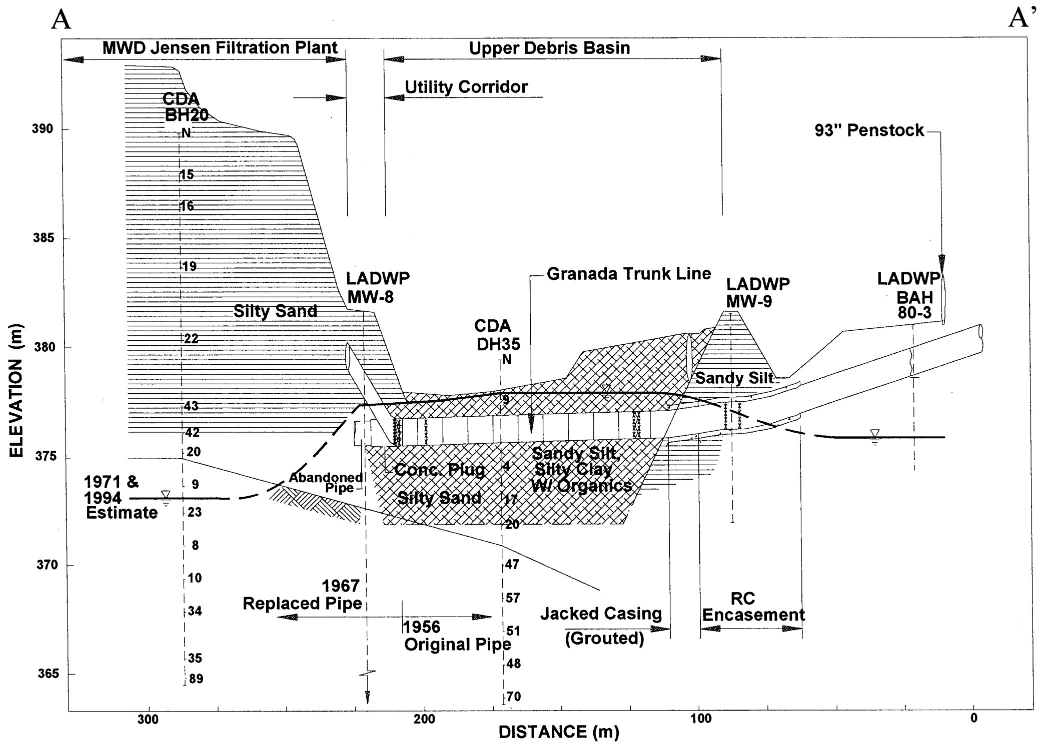

Figure 4. Section A-A' showing profile of Granada Trunk Line through the Upper Debris Basin as located in Figure 3. Vertical scale exaggerated for clarity. See Fig. 5 for legend.

GEOTECHNICAL CONDITIONS

Figures 4 and 5 show soil profiles along the GTL through the Upper Debris Basin and along the utility corridor adjacent to the Middle Debris Basin. The profile in Fig. 5 begins 213 m south of the point where the GTL enters the utility corridor. Figure 6 shows a generalized soil profile running east-west through the JFP. The soil profile along the GTL was determined from boring logs drilled prior to 1994 provided by the Metropolitan Water District of Southern California (Donald R. Warren Co., 1964 [DRW]; Converse Foundation Engineers, 1965, 1966 [CFE]; Converse, Davis and Associates, 1971 [CDA]), and three bucket auger holes drilled by the LADWP (LADWP, 1981). In addition, the LADWP drilled four hollow stem auger holes following the earthquake (LADWP, 1998) and installed groundwater monitoring wells. The boring logs were supplemented with profiles locating the ground surface as it presently exists, as it existed in 1966 at the time of utility corridor construction, in 1940 after constructing the debris basins, and 1913 before any development.

Subsurface Conditions

Soil conditions vary along the GTL alignment. East of the Upper Debris Basin, soils consist of alluvium underlain by Saugus Formation bedrock. Figure 4 shows soils through the Upper Debris Basin consisting of debris basin sediments underlain by alluvium and bedrock. The Upper Debris Basin is bound by a dike fill on the east and the utility corridor on the west. Figures 4 to 6 show soil layers below the utility corridor along with boring logs and uncorrected Standard Penetration Test (SPT) blow count data. Corrected SPT data for these logs are presented by O'Rourke et al. (1992). As shown in Figs. 4 and 5, deposits placed in the Middle Debris Basin underlie the utility corridor fill, which in turn overlay alluvium and bedrock. At a greater distance south, the utility corridor was constructed on excavated bedrock and upon compacted fill over bedrock.

The Upper and Middle Debris Basins were constructed in 1940 to collect debris sediments and divert storm water around the Upper and Lower Van Norman Reservoirs within the VNC. The two basins originally extended west of their present boundaries. Construction of the utility corridor through the basins created their present westerly boundaries. Sediments were deposited in pools of water detained behind spillways at each of the basins. Debris sediments consist mainly of loose sandy silt, silty sand, and silty clay, with organic material and occasional gravel and cobbles. The deposits are relatively weak as evidenced by the low SPT blow counts. Locations and extent of deposits were estimated by comparing the 1913, 1940, and 1966 ground surface elevations. The 1940 construction drawings were used to determine dike fills. Boring logs verify the accuracy of debris sediments shown in Figures 4 to 6.

On the north end, the GTL was placed within a 6 m deep deposit of debris basin sediments through the Upper Debris Basin. Near the south end, below the utility corridor, sediments deposited in the Middle Debris Basin reach a thickness of 6 m at the historic Bee Creek channel. Converse Foundation Engineers (1966) recognized fill for the utility corridor and JFP was to be located over these sediments. They recommended the soils be removed to a maximum depth of 1.8 m and a 0.9 m gravel and cobble layer be constructed at the base of the utility corridor embankment fill. They also recommended 0.6 m to 1.3 m of excavation west of the corridor and that less excavation could be performed if measures were taken for dewatering. Woodward-Clyde Consultants (1988) indicated that it is not known how much excavation was performed prior to placing fill. Boring DH16 (Converse, Davis and Associates) logged gravel and cobbles just below the elevation of embankment fill, indicating that some coarse base material may have been constructed. However, LADWP (1998) did not detect any overexcavation or coarse material when drilling through the utility corridor.

The fill, alluvium, and bedrock are composed mainly of silty sands and silts with some clays. Woodward-Clyde Consultants (1988) describes the fill as dense and well compacted. Fill along the JFP eastern side was constructed directly on debris basin sediments or alluvium. The alluvium is relatively loose, as evidenced by the low SPT blow counts, and reaches a thickness of about 12 m as shown in Figure 6. The Saugus Formation bedrock is of sandstone and siltstone and has an upper weathered zone that is commonly up to 6 m thick below which competent bedrock exists. The weathered zone of the Saugus Formation behaves very much like the weak alluvial soils.

Groundwater

Groundwater elevations along the GTL are presented in Figures 4 to 7. Two groundwater tables are presented representing elevations estimated at the time of the 1971 and 1994 earthquakes. Water elevations for 1971 were obtained from boring logs made in early 1971, following the earthquake (Converse, Davis and Associates, 1971) and extrapolated from borings from the mid to late 1960's located in the Middle Debris Basin (Converse Foundation Engineers, 1966).

Following the 1994 Northridge Earthquake groundwater information was obtained by Woodward-Clyde Consultants (1996) and from readings made in observation wells constructed by the LADWP in the utility corridor (LADWP, 1998). Woodward-Clyde Consultants (1996) provide information on groundwater to the west, within the main part of the JFP. Moriwaki and Gibson (1998) and Woodward-Clyde Consultants (1996) note that within the main part of the plant and throughout the north end of the plant (at the Main Control Building and north), groundwater elevations were relatively high and found to be at about the same level as in 1971. However, construction dewatering around the two finish water reservoirs, located near the south end of the site, locally lowered the water levels by approximately 3 m (Woodward Clyde Consultants, 1996). Post-earthquake readings by the LADWP indicates the groundwater under the utility corridor, adjacent to the Upper Debris Basin, remains relatively constant and is similar to that reported following the 1971 earthquake. However, groundwater adjacent to the Middle Debris Basin can change significantly throughout the year.

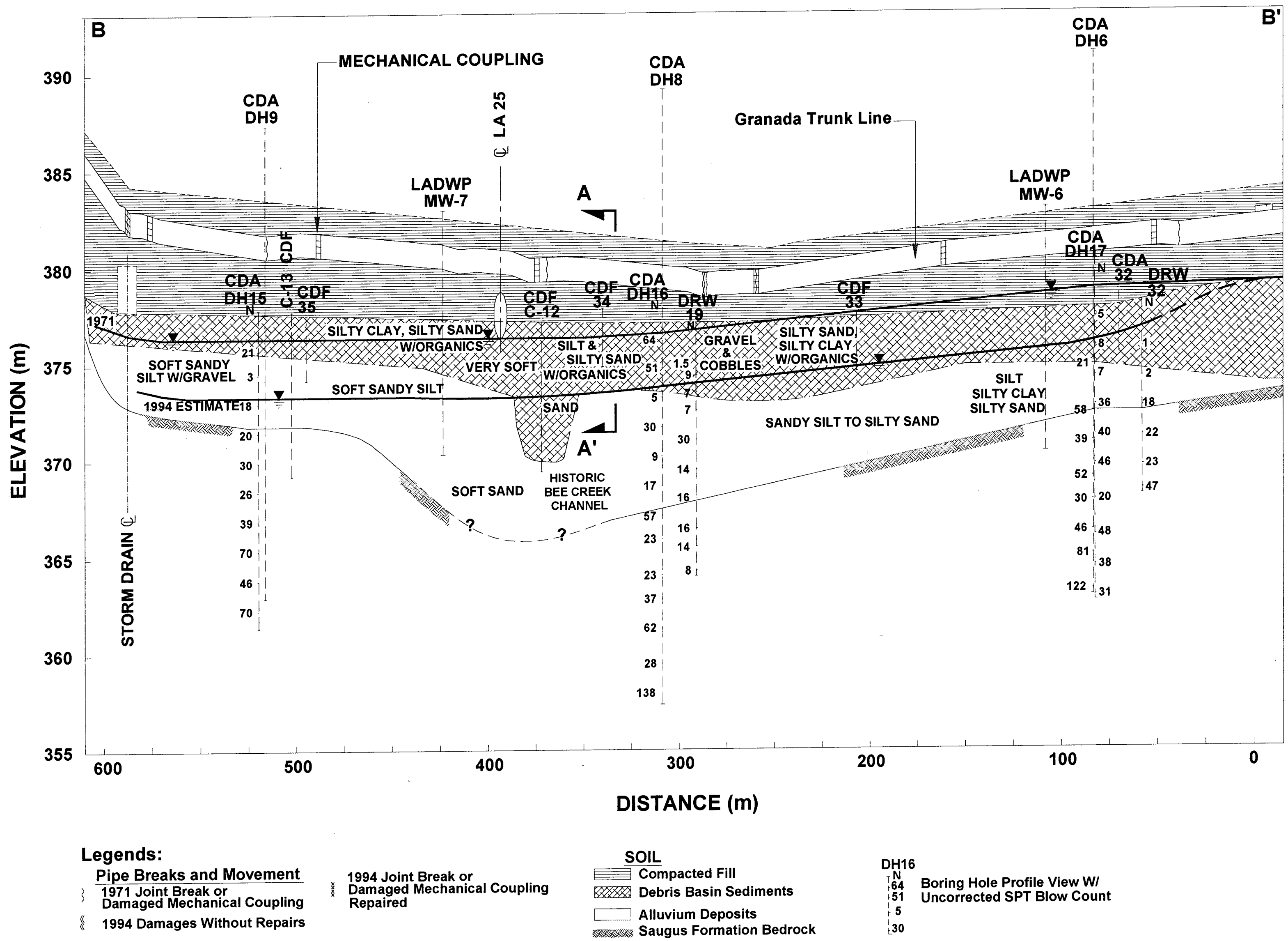

Figure 5. Section B-B' showing Granada Trunk Line profile through utility corridor as located in Figure 3. Profile begins 213 m south of location where the pipe enters the corridor. Vertical scale exaggerated for clarity.

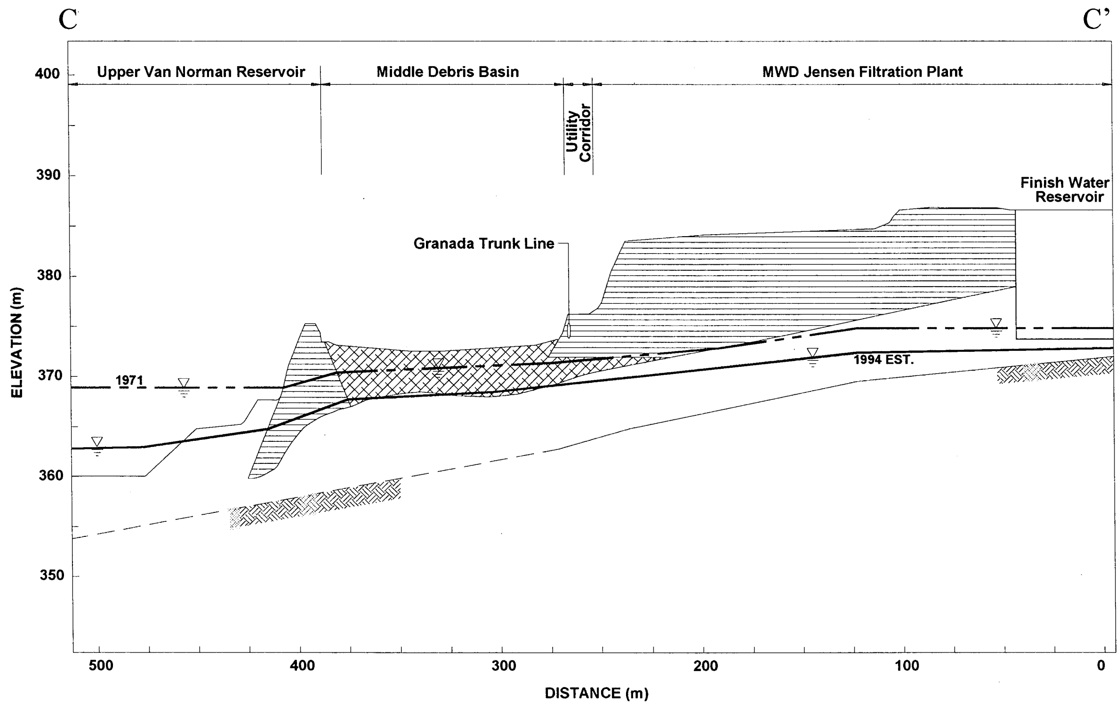

Figure 6. Section C-C' showing soil profiles and groundwater elevations as located in Figure 3. Vertical scale exaggerated for clarity. See Fig. 5 for legend.

There is a slight groundwater gradient from the northwest to the southeast across the JFP site (Converse Foundation Engineers, 1965; Woodward Clyde Consultants, 1996). Prior to placing fill for the plant, the south end of the Middle Debris Basin, where the utility corridor is now located, was a swampy wetland dammed by the embankment along the west side of the Upper Van Norman Reservoir (Reservoir). Figure 6 shows how the Middle Debris Basin had a groundwater gradient sloping slightly down to the east (Converse Foundation Engineers, 1966). Groundwater elevations on the JFP west side are mainly influenced by surface and subsurface flow from the west. Groundwater on the east side of the plant is affected by water elevations in the Middle Debris Basin. However, groundwater in the Middle Debris Basin is governed by water elevations in the Reservoir basin and annual storm flows. In 1971 the Reservoir was full, at the elevation indicated in Fig. 6. Immediately following the 1971 earthquake the Reservoir was lowered; it was permanently drained in 1979. Thus, following the 1971 earthquake the groundwater elevation in the Middle Debris Basin was also lowered. A groundwater observation well constructed in 1984 in the dike along the east side of the Middle Debris Basin (immediately adjacent to the Reservoir) has consistently shown groundwater at the top of the alluvium, 3 m to 4 m lower than in 1971. Although the groundwater levels throughout most the JFP may have been approximately at the 1971 levels, those along the toe of the slope adjacent to the Middle Debris Basin seem to have been lower as a result of draining the Reservoir. In addition, the construction dewatering may have also somewhat lowered groundwater levels southeast of the JFP finish water reservoirs (i.e. southern half of the Middle Debris Basin).

Readings taken below the utility corridor since 1997 (i.e. LADWP MW-6 and MW-7) show that the water levels adjacent to the Middle Debris Basin can fluctuate more than 4 m each year, with most all measurements falling below the 1971 levels. The highest groundwater levels occur during the height of the rainy season and the lowest at the end of or shortly after the dry season. After the rainy season, the groundwater levels adjacent to the Middle Debris Basin drop by approximately 15 cm to 30 cm per month. Whereas groundwater records presented by Scott (1987) indicate that the levels throughout the northern and western areas of the plant drop by approximately 2.5 cm to 5 cm per month during dry years. Thus, there is a transition in groundwater flow across the JFP site. It is difficult to project how the lower water levels near the toe of slope project toward the west in Fig. 6, since most of the historical groundwater measurements have been taken near the center and western side of the JFP (Scott, 1987; Woodward-Clyde Consultants, 1996).

Liquefaction and Ground Cracking

Figure 3 shows the location of sand boils observed in the MDB, adjacent to the utility corridor, following the 1994 earthquake. Thick brush, which existed all through the Upper and Middle Debris Basins, inhibited detailed inspections for additional evidence of sand boils and ground cracks in the area. Sand boils are direct evidence that soil liquefaction occurred. The northern sand boil was located by Woodward-Clyde Consultants (1996) and noted to be of a fine to medium clean sand, which is different from the sandy silts and silty sands encountered across most of the JFP site to the west. Soil logs shown in Fig. 5 indicate the saturated alluvium below the northern sand boil consisted of clean sandy layers. Saturated alluvial soils below the sand boils to the south were of sandy silts. Thus, the sand boils and soil logs provide sufficient evidence that soft saturated alluvial soils adjacent to the utility corridor did liquefy during the Northridge Earthquake. Evaluation of the low SPT blow counts using the method presented by Seed et al. (1985) indicates that liquefaction of these soft saturated soils was expected during the strong seismic shaking recorded in 1994. Intensive investigations following the 1971 San Fernando Earthquake (Converse, Davis and Associates, 1971; Dixon and Burke, 1973; Marachi, 1973) stated that soil liquefaction was the cause of large ground movements along the eastern slope of the JFP. However, Scott (1987) pointed out that the high overburden pressure provided from the deep fills and the large fines content in the alluvium reduce the potential for liquefaction. In addition, Scott (1987) noted that the weak alluvial foundation could allow the compacted slope to deform when subjected to large accelerations as in 1971 and 1994, with little to no pore pressure increase within the alluvium.

Woodward-Clyde Consultants (1996) and Moriwaki and Gibson (1998) described the ground cracking along the eastern slope of the JFP in 1994 as similar to that in 1971, but generally of less magnitude. Figure 1 outlines the three main areas of slope movement which were defined by the patterns of most significant cracking as mapped in 1971 and 1996 (Converse, Davis and Associates, 1971; Woodward-Lundgren and Associates, 1971; Woodward-Clyde Consultants, 1996). Figure 1 also shows that the pipe breaks within the utility corridor generally occurred within the boundaries of the ground cracks. Measurements by O'Rourke et al. (1992) using aerial photographs of the JFP substantiate the three deformation regions (Davis et al., 1996).

COMPARISON OF DAMAGE

In 1971 and 1994, damage resulted to the GTL along two main segments: through the Upper Debris Basin and through the utility corridor at the toe of the JFP slope. However, the 1971 and 1994 earthquakes did not affect the GTL in the same manner. An understanding of this variation provides valuable insight into the seismic behavior of soils and large diameter pipes.

JFP Slope

Moriwaki and Gibson (1998) provide a summary of the geotechnical seismic performance at the JFP during the 1994 earthquake and a brief comparison with the 1971 earthquake. The northern slope deformations were noted to be similar in both earthquakes, while all other areas deformed less in 1994. Following the 1971 earthquake vertical gravel drains were constructed in a portion of the center deformation region shown in Fig. 1. The purpose of the drains was to relieve any excess pore pressure buildup and reduce the effects of liquefaction. Moriwaki and Gibson (1998) indicate that these drains may have aided in reducing a portion of the slope deformations. In addition, they point out two other potential factors which may have reduced the 1994 deformations: (1) the level of ground shaking was less in 1994 than 1971, and (2) the condition of the alluvium improved since 1971 due to the surcharge of compacted fill completed in 1969. The present study found a reduced groundwater elevation under the eastern slope adjacent to the Middle Debris Basin in 1994. The lower water elevations reduce the degree of saturation of the debris deposits and alluvium under a portion of the slope and may have also been a factor in reducing the slope movements. Further evaluations are necessary to better determine the most important parameters effecting the JFP slope deformations, but are beyond the scope of this work.

Upper Debris Basin

In 1994, Table 2 notes compression and separations on either side of the Upper Debris Basin. Such detailed descriptions are not available for the 1971 earthquake. Also, after the 1971 earthquake the mechanical coupling located on the west side of the basin was removed, thus changing the boundary conditions for seismic response. In 1994, pipe joints on each side of the basin suffered compressional failure. The two joint cracks within the concrete encased pipe east of the basin and separations of the compressed joints on each side of the basin indicates that tension forces existed on each side of the pipe sometime during the shaking. The existence of compressive and tensile forces within the pipe on each side of the basin indicates strong oscillatory forces were present in the sediments. These forces may have resulted from transient ground motions from the propagating seismic waves coupled with weakening of the soft, saturated alluvial soils and debris sediments.

Figure 1 shows that pipe breaks occurred near the boundaries of the basin. It is postulated that the strong ground motions weakened the saturated alluvium and debris basin sediments near the beginning of the shaking and increased pore pressures leading to liquefaction. The softened soil within the basin responded with oscillatory displacements for the remainder of the shaking. The mass of soil near the center of the basin seems to have moved relatively uniformly, as there was not sufficient differential movement to cause damage. The ring stiffeners through the basin anchored the GTL to the surrounding soil, causing the pipe to move with the oscillating ground without slip across the interface. The oscillatory motion caused compressive joint failure and separations and tension cracks near the basin boundaries.

Forces associated with oscillatory motion are not easily analyzed. However, this case study provides a lower bound estimate. LADWP records provided 21 mill test results and 52 reports on steel weld tests for approximately 4 km of GTL pipe construction extending from the VNC to Rinaldi Street. The mill tests gave an average yield strength of 275 MPa, average ultimate tensile strength of 424 MPa, and average elongation at fracture of 30.5%. The weld tests showed that the metal fractured within the heat effected area adjacent to the weld, which is consistent with the observations following the 1994 earthquake. An average ultimate tensile strength of 460 MPa was determined from the weld test results. The pipe has a cross-sectional area of 0.025 m^2 giving a minimum force of 10 MN to 11.5 MN to cause the tensile fractures observed on the east side of the Upper Debris Basin.

Utility Corridor

Figure 1 and Table 1 indicate extensive damage along the utility corridor in 1971, while Table 2 shows little damage requiring repair in 1994. Following the 1971 earthquake, mechanical couplings that allow up to 30.5 cm of movement were installed to mitigate potential damage during earthquakes. This effort, combined with the smaller slope movements along most of the corridor, reduced the level of pipe damage.

Woodward-Clyde Consultants (1996) noted that the northern portion of the slope, adjacent to the Upper Debris Basin, moved about the same order of magnitude in 1994 as it did in 1971. Movements shown in Figures 2 and 3 indicate this to be generally true. However, the GTL extends only partly into this deformation region and therefore surveys for the GTL do not adequately define the northern movement. 1994 displacements evaluated using aerial photographs for the Northridge Earthquake, similar to that presented by O'Rourke et al. (1992) for the 1971 earthquake, confirm the observations of similar movements (O'Rourke, personal communication). Figure 2 and Table 2 show that just south of the Upper Debris Basin there were large displacements at the mechanical couplings and plastic wrinkling at one welded joint. This damage may be related to the northern most slope movements indicating that where the slope moved the same in both earthquakes there was similar pipe damage.

Tawfik and O'Rourke (1985) showed that the limiting compressive strength of the welded slip joints on the GTL is approximately 20 percent of the yield strength. Based on the mill test results, the GTL had an average yield strain of 0.00375, giving a average limiting compressive failure strain of 0.00075. The average permanent ground strains presented in Table 1 exceed the limiting compressive strain, indicating that axial strains associated with the 1971 permanent ground deformations were sufficient to damage the pipe joints. However, measurements taken during the 1973 repairs showed that some pipe regions that suffered compressive joint damage retained a residual tensile strain. The reason for this is unclear but may be a result of: (1) the lateral ground deformations and settlement were sufficient to place the pipe in a net tensile stress and occurred following the axial permanent deformations, or (2) some of the compressive joint failures resulted from strong transient ground motions.

The 1971 tensile failures indicate that the pipe was subjected to large localized tensile strain. The average tensile strains from ground movement parallel to the pipe axis presented in Table 1 are significantly less than that required to cause failure. Therefore the tensile fractures occurred from: (1) large localized tensile strains resulting from the combination of axial and transverse movements, (2) the tensile fractured joints contained flaws within the welds and/or, (3) transient ground motions developed large tensile stress.

Tables 1 and 2 show that the 1994 average axial strains were of the same order of magnitude as in 1971, even though the transverse strains were much smaller. It is therefore apparent that the flexible couplings served their purpose in reducing damage from permanent ground movements. The measurements made at the mechanical couplings from inside the pipe show compressional deformation on the north end of the utility corridor (i.e. locations 8 and 10) while the remaining couplings to the south show extension or no movement. Whereas, strain measurements made on the utility corridor surface show extensional deformation on the north end and compression on the south end. This apparent discrepancy indicates that the large transient ground motions caused the pipe to slip through the embedding soil leaving a permanent axial deformation. Interestingly, the total measured extensional deformation on the mechanical couplings adjacent to the Middle Debris Basin (37.8 cm) is approximately the same as the total coupling compressional movement (34.2 cm). The difference in movement is made up in the compressional deformation at location 9. The 1994 joint damage at locations 9, 11, and 16 suggests that the flexibility and spacing provided by the mechanical couplings was insufficient to eliminate damage.

The cause of damages at locations 9, 11, and 16 are not evident, they may have resulted from oscillatory motion as observed in the Upper Debris Basin or directly from the strong transient seismic waves. However, the lack of damage to the paved surface indicates that oscillatory forces along the deformation regions were negligible. The wrinkling at location 9 is very close to a mechanical coupling, which acts as a free moving joint. Thus, the axial stress at location 9, which normally would be assumed negligible, was very large. Two possible reasons for the increased stress are: (1) the coupling did not allow movement, and (2) the coupling closed, banging the two ends of pipe together and causing enough stress to damage the joint. The first possibility is not a likely scenario since the coupling at location 10, near the wrinkled joint, sustained a permanent movement of 5 cm. Therefore, the large transient motions must have closed the mechanical couplings. The coupling at location 8 (first coupling north of location 9) sustained 29.2 cm of permanent compressional displacement. The post-earthquake inspections noted that the two pipe ends had impacted each other during the earthquake before coming to rest with a 1.2 cm separation. Thus, it is possible that other couplings had also closed together sometime during the shaking.

More detailed analyses (e.g. O'Rourke and O'Rourke, 1995; O'Rourke and Castro, 1980) are necessary to understand the individual effects of transient ground motions and permanent ground deformations on the GTL during the 1971 San Fernando and 1994 Northridge earthquakes.

CONCLUSION

The 1971 San Fernando and 1994 Northridge earthquakes caused severe damage and extensive displacements to the Granada Trunk Line (GTL) on the Van Norman Complex. Damage was a result of oscillations of the soft soils in the Upper Debris Basin, movements of the Jensen Filtration Plant eastern slope, and large near-source transient ground strains. Ground oscillations resulted from weakening and liquefaction of soft saturated debris basin sediments and alluvial soils. The Jensen Filtration Plant slope movements resulted from the weak saturated underlying alluvial soils and debris basin deposits. Through the Upper Debris Basin damage to the GTL in 1994 was about as great as in 1971. However, the 1994 damage was less than in 1971 through the utility corridor, which is attributable to the installation of long mechanical couplings following the 1971 earthquake and a result of smaller slope movements at the Jensen Filtration Plant. The detailed measurements and observations described in this report are useful for understanding seismically induced ground deformations and damage to large diameter pipes.

ACKNOWLEDGEMENTS

Contributions from J. Chen who prepared drawings, the numerous employees at the Los Angeles Department of Water and Power who aided in collecting information, C. Anderson of the Metropolitan Water District, and T. D. O'Rourke from Cornell University, are gratefully acknowledged.

REFERENCES

Bardet, J.P. and C.A. Davis, 1996, "Engineering Observations on Ground Motion at the Van Norman Complex after the Northridge Earthquake," *Bull. Seism. Soc. Am.* - Special Northridge Issue 86, No. 1B, pp. S333-S349.

Converse, Davis and Associates, 1971, "Soil and Geologic Investigation, San Fernando Earthquake, Joseph Jensen Filtration Plant near Sylmar, California," Interim Report for the Metropolitan Water District of Southern California, Vol. 1 and 2, *Project No. 71-074-E.*

Converse Foundation Engineers, 1965, "Subsurface Investigation Proposed Water Filtration Plant Balboa Boulevard and San Fernando Road, Los Angeles, California," Conducted for McIntire and Quiros, Inc. in cooperation with The Metropolitan Water District of Southern California, *Project No. 64-677-A.*

Converse Foundation Engineers, 1966, "Subsurface Investigation Enlargement and Cleanout of Middle and Lower Debris Basins Balboa Filtration Plant Metropolitan Water District of Southern California," for McIntire and Quiros, Inc., *Project No. 66-343-A.*

Davis, C.A., 1999, "Performance of a Large Diameter Trunk Line During Two Near-Field Earthquakes," *Proc. Fifth U.S. Conf. Lifeline Eq. Eng.,* ASCE, Seattle, in press.

Davis, C.A., D.S. Kuo, P.S. Scantlin, J.C. Chen, and J.N. Wu, 1996, "Geotechnical Report on Earthquake Damage to the Granada Trunk line at the Van Norman Complex," Los Angeles Department of Water and Power, AX-500, Water Services Organization.

Davis, C.A., and J.P. Bardet, 1995, "Seismic Performance of Van Norman Water Lifelines," *Proc. Fourth U.S. Conf. Lifeline Eq. Eng.,* ASCE, San Francisco, 652-659.

Dixon, S.J., and J.W. Burke, 1973, "Liquefaction Case History," *Journal of Soil Mechanics and Foundation Engineering*, ASCE, Vol. 99, No. SM11, pp. 921-938.

Donald R. Warren Co., 1964, "Metropolitan Water District Filtration Plant Balboa Boulevard and San Fernando Road Second Supplement to Foundation Investigation," *Project No. F63-1267.*

Holzer, T.L., M. J. Bennett, D. J. Ponti, J. C. Tinsley, 1999, "Liqufaction and Soil Failure During the 1994 Northridge Earthquake," J. Geotech. and Geoenv. Eng., ASCE, 125, 6, pp.438-452.

LADWP, 1981, "Van Norman Pumping Station #2 Discharge Lines, Granada and Olden Street Connections - Geologic Exploration," *Water Engineering Design Division*, Memorandum by N.L. Buehring to A.V. La Monte, March 4.

LADWP, 1998, "Van Norman Complex, Geologic Characterization of the Middle and Upper Debris Basins," *Water Supply Division*, Memorandum by C. C. Plumb, Feb. 19.

Marachi, N.D., 1973, "Dynamic Soil Problems at the Joseph Jensen Filtration Plant," Vol. I, Part A, *N.O.A.A. Spec. Rpt.*, Washington D.C.,pp. 815-820.

Moriwaki, Y., and A. Gibson, 1998, "The Joseph Jensen Filtration Plant: A case History of Seismic Performance," *Proc. of the NEHRP Conf. And Workshop on Research on the Northridge, California Earthquake of January 17, 1994, CUREe*, Vol-IIIB, pp. 773-780.

O'Rourke, M. J., G. Castro, and N. Centola, 1980, "Effects of Seismic Wave Propagation upon Buried Pipelines," *Earthquake Engr. and Structural Dynamics*, Vol. 8, pp. 455-467.

O'Rourke, T.D., B.L. Roth, and M. Hamada, 1992, "Large Ground Deformations and Their Effects on Lifeline Facilities: 1971 San Fernando Earthquake", Vol. 2, Technical. Report NCEER-92-0002, *National Center For Earthquake Engineering Research.*

O'Rourke, T. D. and M. J. O'Rourke, 1995, "Pipeline Response to Permanent Ground Deformation: A Benchmark Case," *Proc. 4th U.S. Conf. on Lifeline Earthquake Engineering,* ASCE, San Francisco, Aug., pp. 288-295.

Scott, R. F., 1973, "The Calculation of horizontal Accelerations from Seismoscope Records," *Bull. Seism. Soc. Am.* 63, No. 5, pp. 1637-1661.

Scott, R. F., 1987, "Proposed Jensen Plant Expansion," report prepared for the Metropolitan Water District of Southern California, Agreement No. 1796.

Subcommittee on Water and Sewage Systems, 1973, "Earthquake Damage to Water and Sewerage Facilities," Vol. II, , *N.O.A.A. Spec. Rpt.*, Washington D.C., pp. 75-193.

Wald, D.J., and T.H. Heaton, 1994, "A Dislocation Model of the 1994 Northridge, California, Earthquake Determined from Strong Ground Motions," *United States Department of the Interior, U.S. Geological Survey,* Open-File Report 94-278.

Woodward-Clyde Consultants, 1988, "Geotechnical Investigation Joseph Jensen Filtration Plant Granada Hills, California," Draft Report Prepared for the Metropolitan Water District of Southern California, Vol. 1: *Proj. No. 8840172A.*

Woodward-Clyde Consultants, 1996, "Geotechnical Investigation Oxidation Retrofit Program Jensen Filtration Plant Granada Hills, California," Final Report Prepared for the Metropolitan Water District of Southern California, *Proj. No. 934E285A.*

Woodward-Lundgren and Associates, 1971, "Evaluation of the Effects of the February 9, 1971 San Fernando Earthquake on the Balboa Water Treatment Plant," *unpublished report,* prepared for Gibson, Dunn, and Crutcher, Oakland, CA.

U. S. Geological Survey, 1994, "Accelerograms Recorded at USGS National Strong-Motion Network Stations During the Ms=6.6 Northridge California Earthquake of January 17, 1994," Open File Report 94-141.

Yerkes, R.F., M.G. Bonilla, T.L. Youd, and J.D. Sims, 1974, "The Van Norman Reservoirs Area, Northern San Fernando Valley, California. Geologic Environment of the Van Norman Reservoirs Area," U.S. Dept. of the Interior, *Geological Survey Circular 691-A.*

Youd (1973) "Ground Movements in Van Norman Lake Vicinity During San Fernando Earthquake," *NOAA Spec. Rpt.*, Vol. III, pp. 197-206.

SUCCESSES IN LIFELINE SEISMIC MITIGATION PROGRAMS

Le Val Lund, P. E., M. ASCE

ABSTRACT

Some large lifeline organizations (water, power, and gas and transportation management) have undertaken significant seismic improvement programs. The seven organizations evaluated in this report have initiated and sustained these programs in a variety of ways. They have been educated by past earthquakes damaging their system or similar systems, research and educational programs. Top-level managers and their seismic advocates in economically and politically strong organizations have developed an overall view of their system earthquake vulnerabilities and developed adaptable, incremental seismic implementation programs. Multiple oversight organizations have contributed little to the process. The report will further discuss the broad cultural, economic, and political changes, which has shifted seismic mitigation from engineering to professional management orientation.

Le Val Lund, P. E., M. ASCE, Civil Engineer, Los Angeles, CA

LL 7-9-99

INTRODUCTION

Since the 1952 Kern County earthquake and many earthquakes since (1964 Alaska, 1971 San Fernando, I987 Whittier Narrows, 1989 Loma Prieta and 1994 Northridge earthquakes) have caused lifeline damage that has had both serious primary and secondary consequences and caused large federal outlays as a result of the United States Federal relief policy. Lifelines include water, wastewater, transportation, natural gas, liquid fuel, electric power and communications network systems.

While scientific and engineering knowledge has grown substantially as the result of these earthquakes and federal funding for research, there have been concerns in how to implement this knowledge. At the federal level, policies have been developed in others areas, namely, (a) assisting in the transfer of new scientific and engineering findings into seismic codes, (b) devising a policy to address seismic deficiencies in federally owned buildings, (c) rapid and efficient post-disaster response, and (d) the development of regional loss models. At the research level, policy analysis efforts have focus on federal and state policy, government insurance programs, seismic retrofit programs and land use planning. However, there is no overall programs or policy to develop seismic standards for lifelines, much less to adopt and implement them.

In the review of the case studies of lifeline organizations investigated in this study there appears to be some barriers to the implementation of seismic mitigation policies. Some of these are as follows:

a. High initial costs of some seismic mitigation measures.
b. Low cost effectiveness of seismic reduction measures.
c. A gap exists between the technical community and available technical solutions and the policy makers.
d. The few damaging earthquakes and denial of low-probability events.
e. The financial disincentives from the federal disaster relief policy, insurance, loans, and bond underwriting that fails to differentiate poor and good seismic risks.
f. Implementation of a strong emergency response and recovery programs.

Even though, seismic safety policies have been implemented, and this fact forms the basis for emphasizing successful examples of seismic mitigation in this report. By comparison, these successful examples are less common, but they nonetheless exist.

SUCCESSFUL SEISMIC IMPROVEMENT PROGRAMS

The following criteria have been used to determine successful lifeline earthquake risk reduction programs. These criteria are consistent with the definition of risk reduction as used in the United States Congress Robert T. Stafford Disaster Relief and Emergency Assistance (Congressional) Act (Public Law 93-288 as amended by P. L. 100-707)

a. Tangible risk reduction efforts undertaken within the lifeline system, such as, pipe replacement, building replacement or retrofit, equipment anchorage and enhancing system redundancy.
b. Non structural mitigation as the development and implementation of post earthquake emergency response and recovery programs.
c. As judged by many potential competing projects, economic, administrative, political, social, regulatory and environmental issues, the seismic risk reduction efforts undertaken in this study would on balance be regarded as being successful.

CASE STUDY APPROACH

Only successful cases of lifeline seismic reduction programs have been studied by a history of these cases. The case study approach is not designed to be statistical. Only seven successful cases have been included, which is a small sample and there maybe more successful cases. Unsuccessful cases have not been included and biases have no doubt entered into the cases evaluated. The initial case study was began with a specific set of questions sent to each lifeline agency prior to their interview. These questions arose from the initial thesis that top level decision making on seismic issues was fragmentary. The questions also presumed that the major influences on seismic improvement programs were the character of the organization itself and the persuasiveness of the inside advocates.

As important as these factors may be, it was found in the course of the study, factors external to the organization were extremely influential in the providing a setting to facilitate or inhibit seismic improvement activities. These other factors include federal and state legislation and regulations that can impede as well as encourage seismic improvement programs. These other factors include cultural trends, such as management decisions to down size organizations. Thus in the first year of the study it was discovered the original questions were no longer as useful as initial imagined.

Seismic improvement programs are not among the top level management ongoing worries. Seismic improvement programs typically arise because the system itself needs to be protected, and the ability to comprehend the systems perspective is often found in top level managers.

CASES SELECTED

Studies were limited to seven case studies west of the Rocky Mountains, and the cooperation from the organizations was outstanding. There was no initial success in getting cooperation with a communication organization. Five of the organizations were public and two were private. Three of the systems were domestic retail water systems, the Seattle (Washington) Water Department (SWD); Los Angeles (California) Department of Water and Power (LADWP), Water System and East Bay (Oakland, California) Municipal Utility District (EBMUD). The only example of real time earthquake response as a seismic reduction activity was the California Department of Transportation (Caltrans) Traffic Operations Center after the 1994 Northridge (California) earthquake. Questar Gas Company (Salt Lake City, Utah), (QGC), covered a retail natural gas distribution company. The Southern California Edison Company (SCE) and Los Angeles (California) Department of Water and Power (LADWP), Power System covered electric power supply.

POLITICAL AND REGULATORY ENVIRONMENTS

Engineers

The establishment of successful lifeline seismic risk reduction programs has not been primarily due to statutory or regulatory programs. What unites programs in this study, which implemented seismic risk reduction programs, was the desire of engineers to insure system and individual component performance. Incorporating technological advances in seismic engineering did this. Thereafter, organizational policy makers to support the continuing development of reliable lifeline systems which would limit monetary losses due to earthquake and which could be brought back on line quickly after earthquakes to ensure resumption of profitable service.

Legislation and Regulations

When government requirements, through legislation or regulations, have forced changes in how lifelines operated, they have often have not targeted more conspicuous public concerns such as water quality and environmental protection, solutions for which the organizations were able to voluntary incorporate into seismic elements.

Utility Restructuring

In the United States, the electric power industry is undergoing restructuring, some times referred to as "deregulation", in which the customers are being permitted to select their generation supplier which may be different than their organization which distributes the electric energy.

This has already happened in the telecommunication and natural gas industry. Electric power organizations are be broken up into generation, transmission and distribution organizations. This suggests the future regulatory environment of utilities will undergo fundamental changes. After almost a century of relative stability, where utilities operated as virtual monopolies, competition at the retail level will force new regulatory arrangements to forged and new mechanisms to be devised to ensure earthquake risk reduction programs will be undertaken in the next century. Seismic risk programs, as known today, maybe in jeopardy. How these will be accomplished is unknown.

Utility Governance

Virtually all lifeline organizations in the United States began as local private enterprises supplying products and services to small urban areas. In metropolitan areas, the lifeline companies were consolidated and due to monetary needs expanded, often of the financially weak private companies by municipal or regional bodies, who could take advantages of general obligation or revenue bonds and the minimizing of the payment of taxes. Government utilities are managed by local elected public bodies and do not come under the purview of the state public utility commissions.

National Standards

One area the federal government has avoided is the setting of national standards for the design, construction, equipment, and natural hazard lifeline risk reduction. States and local governments generally set minimum standards utilities must meet, typically in accordance with standards generated by nationally recognized private standard setting organizations. Utilities follow at least the minimum standards set by these, usually volunteer, private organizations. Only a few of these standards are seismically oriented. Federal agencies, most notably the Federal Emergency Management Agency (FEMA), National Institute of Building Sciences (NIST), National Science Foundation (NSF), Untied States Geological Survey (USGS) and National Institute for Standards and Technology (NIST) have supported research and other efforts to standardized codes and have encouraged private funding standard setting organizations to incorporate more stringent seismic standards. An example of this activity is the plan being developed between FEMA and American Society of Civil Engineers (ASCE) to form the American Lifeline Alliance (ALA). The ALA in cooperation with other lifeline standard setting organizations would establish lifeline seismic standards in areas where standards are missing using the current United States standard setting procedures.

In recent years, the frequency of devastating natural hazards, especially earthquakes, hurricanes and floods have increased the human and monetary losses caused by these events, in an expanding urbanized environment. To mitigate future losses, the federal government has instituted aggressive recovery and mitigation programs following these natural disasters. Public utilities (not private) utilities have benefited because they qualify for matching funds to construct new or retrofit or replace old ones. Private utilities are eligible for low interest loans.

Dynamic Nature of Lifelines

Large metropolitan lifelines in this study have experienced expansive growth and change since their beginning. The organizations studied all began as small entities and have expanded to serve large metropolitan cities or regions. Their successful transition has been a result of several factors some internal and some external to the organization. The following factors will be discussed with special consideration given to the establishment of seismic risk reduction programs.

a. **Size** - The organizations studied have become extremely large, growing from small engineering oriented companies into large professionally managed organizations. When they began, there were charismatic individuals like William Mulholland at LADWP and R. H. Thompson at SWD who combined engineering and management skills to design the water delivery systems for Seattle and Los Angeles. Over time after their retirement and as systems grew, management ranks expanded, authority disbursed, fewer people had the knowledge to understand the full complexities of their organizations. Therefore, executives and other personnel became specialized.

Size has changed the relationship between modern utilities and their oversight bodies, such as the public utilities commission. Today utilities are much larger than their oversight bodies and more knowledgeable about their operations, more technically competent, more able to influence public policy decisions.

Size implies an increase in complexity and the need for large preparatory studies or sophisticated models to understand the agency production and delivery systems, so proper risk analysis can be performed. The SWD, LADWP-Water and EBMUD, for instance, seismic improvement activities were begun by studies to establish the vulnerability of components to seismic risk. At SCE seismic improvement activities were significant enhanced by their System Earthquake Risk Assessment (SERA), a computer program which was able to prioritize what components of their system should be seismically retrofit or replaced and accomplished within budgetary limits. Later EBMUD used the SERA to evaluate their system and establish priorities for its seismic improvement program.

b. **Management** - In the organizations investigated in this study, engineers made the critical management decisions or worked closely with non-engineering executives who looked favorably on their recommendations. Simplifying the planning and implementation process, the organizational structure was relatively flat, with relatively few layers separating executive decisions from engineers. Now, more non-engineers have moved into executive positions and they have began to stress customer rates, profits and return on investments. While some might have thought seismic risk reduction programs would not be compatible with the goals as more non-engineers moved into executive ranks the organizations evaluated in this study, this has not been true. Management in these organizations approved seismic risk programs because they placed high values on the expected results and believed that human injury, death, loss of service, good will and revenue was an unacceptable option.

c. **Inside Advocates** - A common characteristic of the utilities in this study was the existence of knowledgeable engineers who purposely integrated seismic risk considerations into engineering operations. Since the 1930's, civil and geotechnical engineering departments in universities had begun incorporating seismic topics in their courses. After graduation, some civil engineers and geoscientist began integrating seismic considerations into every day decisions for location and design of new facilities, purchase of equipment or retrofit of these facilities. Because their suggestions did not markedly increase overall costs, they were accepted and integrated into line item budgets. Later in their careers, several of these individuals were able to build on their experience and advance comprehensive company wide seismic reduction programs. A key point is the development of seismic reduction programs is not always the result of single decisions as an aftermath of an earthquake, but was based on a series of small steps over a longer period of time.

d. **Sharing Information** - After the 1971 San Fernando earthquake executives at the LADWP made a deliberate decision to share information concerning damages it suffered and potential solutions with local, regional, state, national and international organizations. As a results many organizations including most of those in this study, sent teams of engineers to Los Angeles to study and learn from the LADWP experience. This type of activity has continued following subsequent earthquakes.

In 1974, C. Martin Duke, Professor of Civil Engineering, University of California at Los Angeles, formed the Technical Council on Lifeline Earthquake Engineering (TCLEE) of the American Society of Civil Engineers (ASCE) to permit academic and professional lifeline engineers to meet regularly to discuss and share lifeline seismic issues and research. Research included earthquake investigations and reconnaissance reports by TCLEE members, some of which were in cooperation with the Earthquake Engineering Research Institute (EERI).

Also in 1974, the California Water and Power Earthquake Engineering Forum (CWPEEF) was established by the California Department of Water Resources (DWR) which met three times during the year. Meetings alternated between northern and southern California locations to exchange seismic lifeline information and to hear from outside seismic academic and professional engineers. Member agencies who participated in the Forum including DWR, were LADWP, SCE, EBMUD, Metropolitan Water District of Southern California, Pacific Gas and Electric

Company, Southern California Gas Company, San Diego Gas and Electric Company, Los Angeles County Flood Control District, San Francisco Water Department, U. S. Bureau of Reclamation, and U. S. Army Corps of Engineers.

e. **Research Initiatives** - The primary role of the Federal government in promoting seismic risk mitigation has not been to mandate direct changes, but to provide information and resources to stimulate changes. The U.S. Congress has allocated funds for fundamental research since the 1964 Alaska earthquake. In 1977 the National Earthquake Hazards Reduction Program Act (NEHRP) and subsequent reauthorization, has authorized funds and formally specifying the roles and responsibilities of the federal government in earthquake mitigation. A major thrust of the federal government has been seismic risk in the areas of the country subject to earthquakes. The United States Geological Survey (USGS) has created along with state agencies detailed seismic hazard maps of Los Angeles, San Francisco, Salt Lake City and Seattle areas. Most utilities in these areas have benefited from these maps to more accurately determine seismic risk. QGC and SWD were also able to participate in USGS studies directly, which ultimately permitted them to establish their fundamental seismic mitigation practices.

f. **Disaster Assistance** - The principle the federal government should take an active role in repair of damaged public facilities following major disasters came into being when U. S. President Harry Truman proposed the Federal Disaster Act of 1950. It was an aftermath of the Midwestern U. S. floods where it was recognized communities could not rebuild unless federal funds were available. Although the law funds could be used to restore public facilities to their predisaster conditions, local authorities objected, eventually convincing the federal government to rebuild damaged structures rather than repairing them. Mitigation became mandatory with the passage of the Disaster Relief Act of 1974. The new law stated, as a condition of receiving disaster assistance, applicant must take actions to mitigate against future hazards and the rebuilding be done in conformance with applicable codes, specifications and standards. The 1988 Robert T. Stafford Federal Disaster Relief and Emergency Assistance Act provided the federal government would repair, restore, replace damaged public facilities assuming the costs be shared 75%-25% federal-state and cost effective mitigation measures be shared 50%-50% with states. Later amendments to the Stafford Act have changed the cost sharing to 90%-10% and 75%-25% federal-state respectively. And also permitted states to approve request from public bodies located in areas covered by disaster declarations to retrofit facilities not damaged, if those actions will significantly reduce potential damage from future events.

g. **Mandates** - Except in the statutes to regulate critical facilities, such as, nuclear power plants which generate electricity, the federal government has typically not enacted regulations mandating specific seismic risk reduction measures. The 1972 National Dam Inspection Act and 1986 Dam Safety Act were concerned with the performance of dams where failure could cause loss of life and property. Although these dam safety laws did not specify any mandatory seismic reductions to be taken by utilities, they did cause the utilities, to incorporate seismic elements if they choose. States are generally required to implement federal directives. Caltrans is a state agency and its budget is approved annually by the state legislature. Since 1971, the citizens have approved several propositions to issue general obligation bonds for seismic strengthening of highway and freeway structures. As a result of both government and public support for seismic risk reduction programs, Caltrans has become the national leader in transportation system seismic risk reduction. Local or regional agencies are generally independent business enterprises, administered by local board of directors, and oversight for specific programs, such as, seismic reduction have been left to internal managers to both design and implementation.

SEISMIC EVALUATION APPROACHES

The agencies studied used a variety of ways in which seismic evaluation studies have aided decision making in their seismic improvement programs. All seismic evaluation approaches involve combining estimates of earthquake hazards and vulnerabilities of systems and their components to assess expected losses and prospective reduced losses through seismic risk reduction measures. Site specific component approaches were developed in the 1970's at Southern California Edison Company (SCE) and Los Angeles Department of Water and Power (water and power systems) (LADWP). Early system seismic risk evaluation studies were made in the mid 1980's by SCE and Questar Gas Company (QGC). In the late 1980's site Seattle Water Department (SWD) and QGC used specific evaluations. In the early 1990's, a very thorough seismic risk evaluation was performed for the East Bay Municipal Utility District (EBMUD). As an aftermath of the 1994 Northridge earthquake, Caltrans Traffic Operations Center used its system evaluation capabilities to develop a bonus incentive system for bridge reconstruction to restore traffic patterns rapidly. Also after the 1994 Northridge earthquake LADWP (power system) began to develop seismic risk evaluation approach to address complex issues of the cost effectiveness of its seismic improvement program and the acceptability of its power system performance. Details of the programs are included ASCE-TCLEE Monograph No. 13.

CONCLUSIONS

a. The process of reducing the seismic risk of lifeline systems will be a gradual one, with technological innovations, developments and information sharing required as a basis for providing tools and credibility to seismic improvement programs.

b. Lifeline seismic mitigation programs will vary depending on the organization.

c. Outreach programs, including the development of university criteria, are desirable to communicate to professional managers and public policy makers the importance of earthquake and other natural hazard risk reduction measures.

d. The federal government has a clear, but limited interest in encouraging lifeline seismic risk reduction goals. The joint effort between FEMA and ASCE creating the American Lifelines Alliance will provide considerable assistance in achieving this goal.

e. With advent of utility lifeline restructuring (deregulation) and the partitioning of utility functions and the future accountability of reliability of service is unknown.

f. The issue of smaller utilities who due not have the personnel and financial resources to implement a seismic reduction program is unresolved.

ACKNOWLEDGMENTS

The author acknowledges Craig Taylor, Torrance, CA and Elliott Mettler, Woodland Hills, CA, the principal investigators of ASCE - TCLEE Monograph No. 13 and the National Science Foundation who funded the study.

REFERENCES

Data for this report was be taken from American Society of Civil Engineers, Technical Council on Lifeline Earthquake Engineering, Monograph No. 13, "Overcoming Barriers: Lifeline Seismic Improvement Programs" by Craig Taylor, Elliott Mettler and Le Val Lund, 1999, which lists significant number of references,

Prepared for 7th US-Japan Workshop on Earthquake Resistant Design of Lifeline Facilities and Countermeasures for Soil Liquefaction, August 15-17, 1999, Seattle, WA

LL 7-9-99

EFFECTS OF MATERIAL PROPERTY ON INELASTIC SHELL BUCKLING STRENGTH OF LINE PIPE

Nobuhisa SUZUKI, Akihiko KATOH,

Eiji MATSUYAMA and Masaki YOSHIKAWA

Engineering Research Center, NKK corporation,
1-1Minamiwatarida-cho, Kawasaki-ku, Kawasaki, 210-0855, Japan

Abstract

In order to improve the reliability of buried pipeline, many kinds of measures have been proposed. One of the most economical measure is improvement of steel pipe material. Especially, inelastic shell buckling strength of a pipe material is expected to directly improve the resistance of pipeline subjected to ground motion due to an earthquake.

From this point of view, the effects of material properties upon the inelastic shell buckling strength of a line pipe has been studied. As a material property which dominate the buckling strength of a material, the effects of strain hardening exponent n-value on the inelastic buckling is both experimentally and analytically studied.

On the basis of the study, the new type of a pipe is proposed which improves the reliability of pipeline subjected to ground motion. Furthermore, the degree of improvement of reliability against earthquake when the new type of a pipe is applied to the pipeline is discussed by the numerical analysis on buried pipeline subjected to ground motion.

Introduction

In 1995, a great earthquake occurred in western part of Japan. Not only many structure were destroyed but a lot of precious lives were lost. Since the earthquake, it has been more concerned to improve the seismic resistance of lifelines such as gas transportation pipe lines, water supply lines, telecommunication lines and so on.

In order to improve the reliability of pipeline, improvements of inelastic shell buckling strength of a pipe was discussed. In previous studies[1,2], it has been known that the buckling strength is a function of strain hardening performance of a material and geometrical shape of a pipe such as thickness-diameter ratio t/D. However effects of strain hardening exponent n-value on the inelastic shell buckling strength of a pipe has not been studied systematically.

In this study, several types of pipes with various strain hardening performance were manufactured and the effects of strain hardening performance is investigated by both experimental and analytical approach. Then, the deformability of a pipeline of different types of pipe materials were compared with respect to reliability against an earthquake.

Relations between pipe material and inelastic shell buckling strength

It was previously examined that inelastic axial shell buckling strain of a pipe is a function of both of strain hardening exponent n of a material and thickness diameter ratio t/D[1,2]. The equation of this relationship can be expressed as equation (1).

$$\varepsilon_b = 4/3 \cdot \sqrt{n} \cdot t/D \tag{1}$$

Where ε_b : *Axial Compression Strain,* n : *Strain Hardening Exponent,*

t : *Wall Thickness,* D : *Diameter*

n is defined as following equation (2).

$$S = A \cdot e^n \tag{2}$$

Where S : *True Stress,* e : *Logarithtic Strain,* A : *Constant,*
n : *Strain Hardening Exponent*

And also it has been studied that the existence of Luders' elongation of a material reduces inelastic buckling strain in comparison with those of round house yielding material which have no Luders' elongation[2]. Namely, it is expected that the pipe with round- house yielding behavior has a larger buckling strain compared with a Luders' elongation type pipe.

Consequently, increase of strain hardening exponent n-value and extinguishment of Luders' elongation of a material are very effective to improve the buckling strength of a material.

Evaluated Pipe Material

On the basis of above idea, several types of pipe materials have been manufactured. Table 1 and Table 2 shows the mechanical properties and geometrical dimensions of those pipes respectively. Type LE1 is Luders' elongation type with relatively low n- value. LN1 and LN2 are round house yielding type with relatively low n-value. HN1,HN2 and HN3 are round house yielding type with relatively high n-value.

Figure 1 shows the comparison of stress-strain curves of manufactured pipes.

Table 1 Mechanical properties of tested pipes

Pipe*1	YS MPa	TS MPa	YR*2 %	n-value*3
LE1	519	582	89	0.02
LN1	442	518	85	0.07
LN2	451	607	74	0.08
HN1	452	573	79	0.11
HN2	523	752	70	0.14
HN3	557	772	72	0.19

*1) LE : Luders' elongation type,
LN : Low n-value type
HN : High n-value type
*2) YR : Yield to tensile strength ratio (= YS/TS)
*3) The n-value estimated in strain range of 1～4%

Table 2 Geometry of tested pipes

Pipe	Pipe size			
	Outside diameter mm	Wall thickness mm	Length mm	Diameter to thickness ratio %
LE1	917	19.0	1830	48
LN1	610	15.4	1830	40
LN2	610	15.1	1830	40
HN1	711	16.0	1830	44
HN2	711	16.0	1830	44
HN3	610	15.1	1830	40

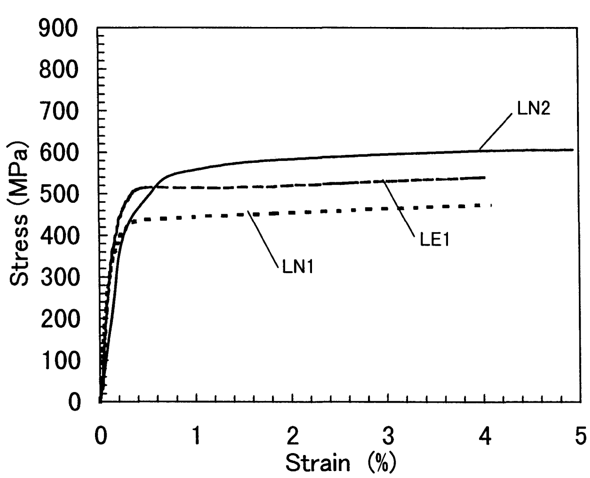

(a) Luders' elongation type and low n-value type

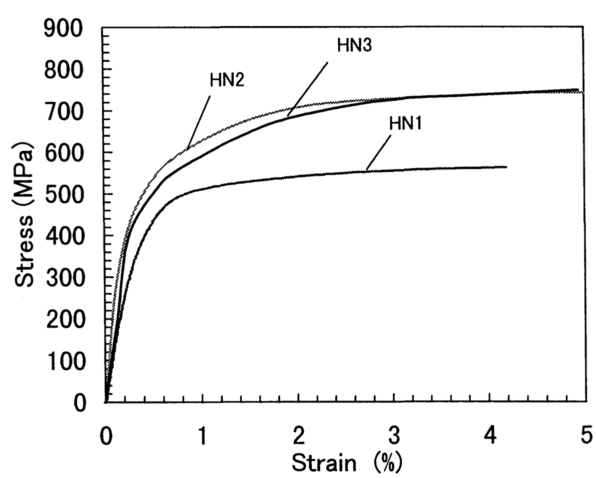

(b) High n-value type

Fig. 1 Stress strain relationships of tested pipes

Evaluation Test and Analysis

In order to evaluate the buckling strength of manufactured pipe materials which has different mechanical properties as shown in Fig.1, axial compression tests, bending tests and low cycle fatigue tests have been carried out. Furthermore, deformation behavior of those pipes have been numerically simulated by using elasto-palatic finite elements technique.

Axial compression buckling properties

Axial compression tests were carried out as shown in Photo 1. Strain distribution change in axial direction was monitored during a test. In all test cases, axially symmetric inelastic buckling, so called elephant foot type buckling was observed.

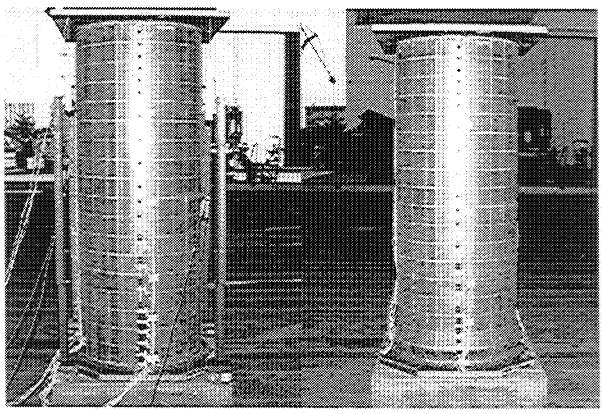

(a) before test (b) after buckling

Photo 1 Photograph of tested pipe

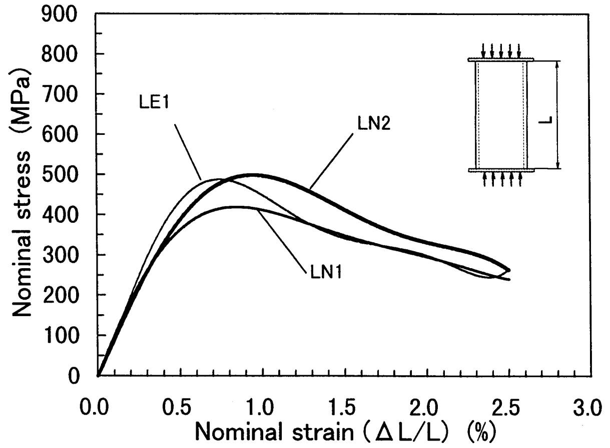

(a) Luders' elongation type and low n-value type

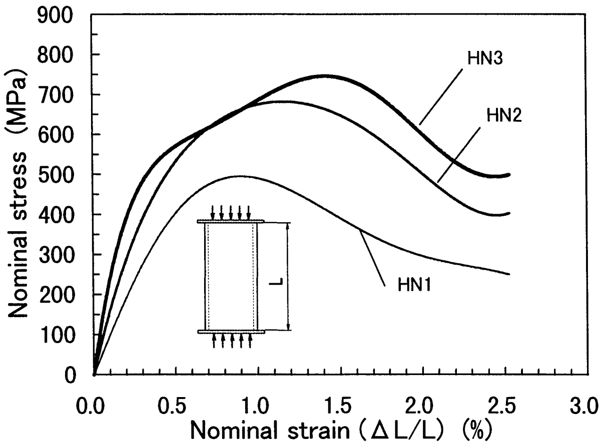

(b) High n-value type

Fig.2 Nominal stress - nominal strain curves in axial compression tests

Buckling point is defined as the maximum nominal stress point in nominal stress-strain curve. Figure 2 shows the relationship between nominal stresses and nominal strains. As shown in Fig.3, local axial strain distribution drastically changes just after the occurrence of buckling, because axial deformation is localized at the wrinkled area.

Figure 4 and 5 show the buckling strains obtained by axial compression test. It is confirmed that the material which has higher n-value shows higher buckling strain.

In order to verify the difference of buckling behavior due to the difference of strain hardening exponent n-value observed in experiments, numerical simulation by using finite element technique code of ADINA[4] were also performed. Stress and strain properties shown in Fig. 6 was adopted to the simulation. Three types of materials which are Luders' elongation type, round house type with low n-value and round house type with high n-value were chosen as reference material for comparison.

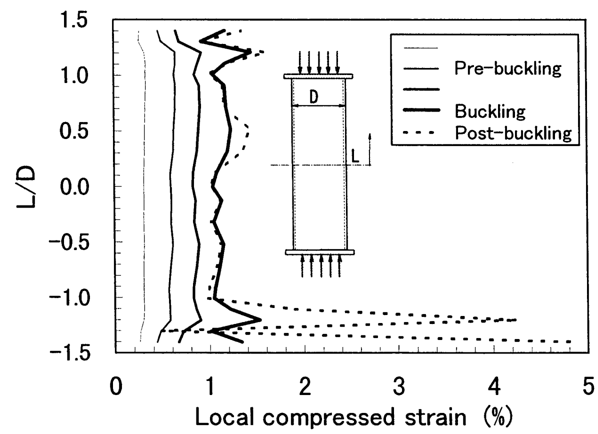

Fig.3 Strain distributions along longitudinal direction (HN1)

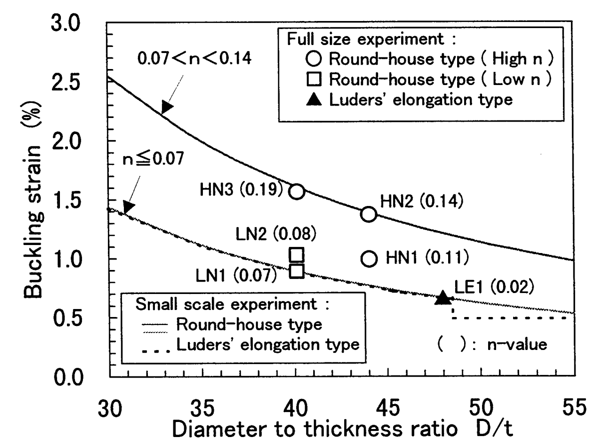

Fig.4 Buckling strains obtained by full scale axial compression tests

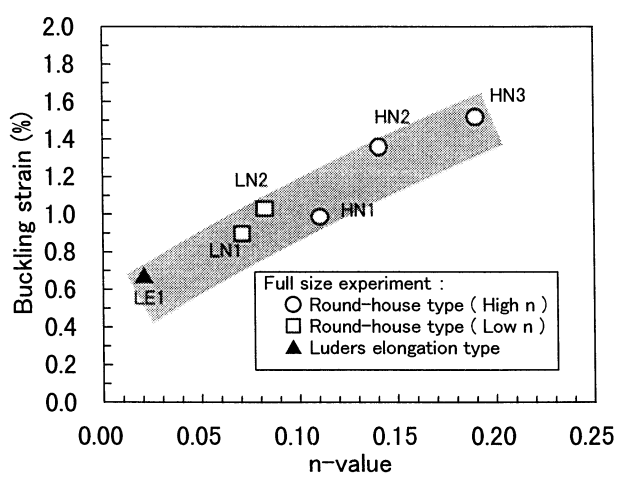

Fig.5 The dependency of buckling strain on n-value in axial compression tests

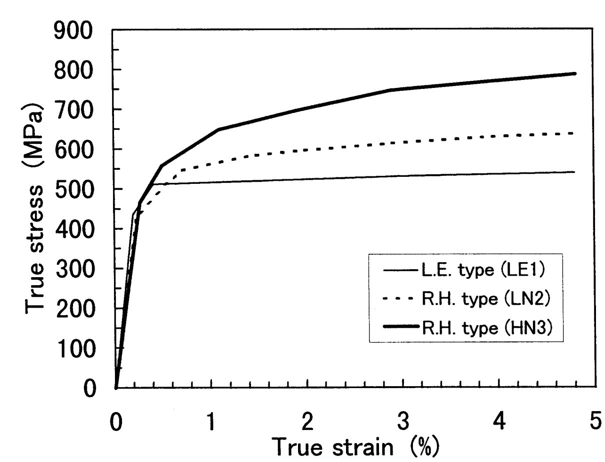

Fig.6 Mechanical properties of analytical model

Figure 7 shows the analytical results of nominal stress and nominal strain. Figure 8 shows the comparison of dependency of buckling strain on n-value obtained by experiments and analysis. Although buckling strains obtained by analysis are little bit higher than those by experiments and eq.(1), the tendency of the relationship between buckling strain and n-value corresponds well among analysis, experiments and eq.(1). It is also confirmed by the analysis that the material which has higher n-value has higher buckling strain.

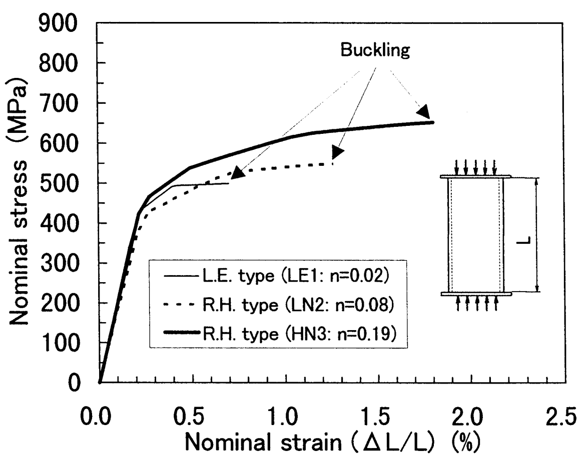

Fig.7 Nominal stress - nominal strain curve obtained by numerical analysis

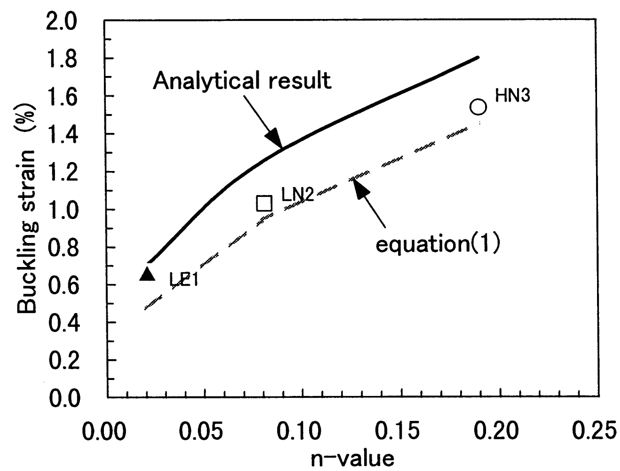

Fig.8 Comparison of the dependency of buckling strain on n-value between experiments and analytical results

Bending Buckling Properties

The bending tests for manufactured pipes were carried out in order to study the effect of n-value upon the bending buckling strength. Tested pipes were two typical types of materials, LN2 and HN3. LN2 was low n-value type and HN3 was high n-value type. Testing apparatus shown in Fig.9 was used. The appearance of bending test is shown in Photo 2.

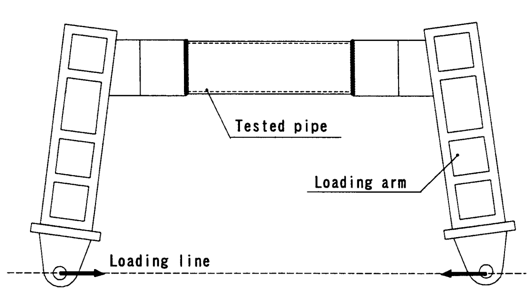

Fig.9 Geometry of tested pipe for bending

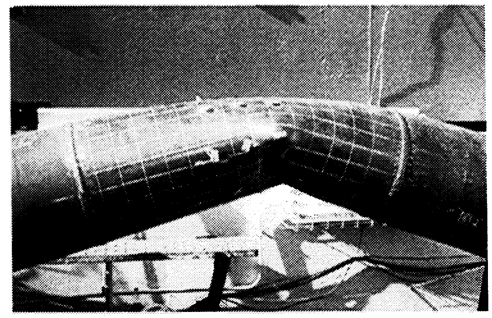

Photo 2 Photograph of tested pipe (LN2)

Strains were monitored by strain gauges mounted on the outer surface of the specimen during tests. Figure 10 shows the relation between bending moment and bending angle. Bending moment was defined as the applied moment at central section of a specimen and the bending angle was as the rotation angle of loading arm during test. As shown in Fig. 10, the pipe with higher n-value shows higher maximum bending moment under the condition of same pipe geometrical shape.

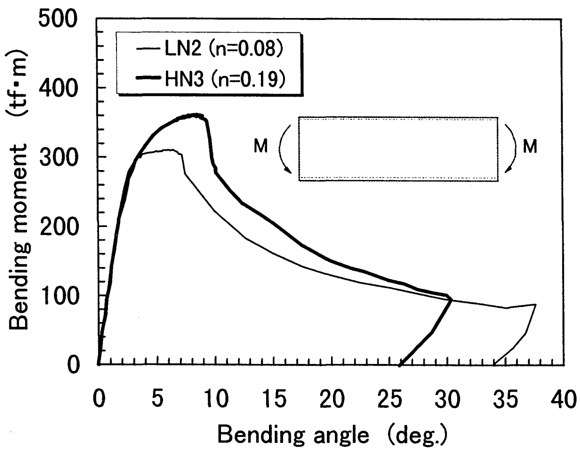

Fig.10 Bending moment - bending angle curve in bending tests

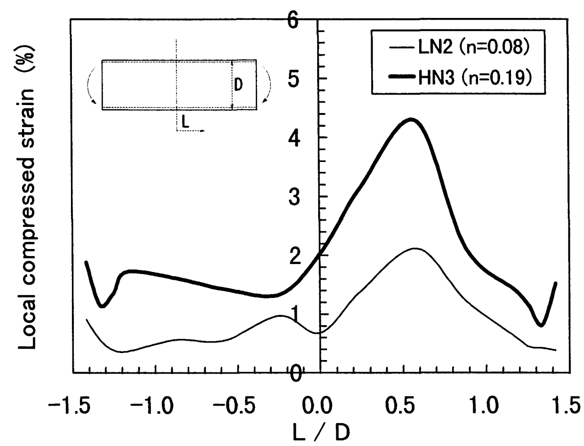

Fig.11 Longitudinal distributions of strain along intrados line in bending buckling

The buckling point is defined as maximum bending moment point in the relationship between bending moment and bending angle. Figure 11 shows the axial strain distribution in longitudinal direction at the maximum bending moment point which is in accordance with the buckling point. The bending buckling strain is defined as maximum strain value at the maximum bending moment point. As shown in Fig. 11, higher buckling strain is observed in higher n-value material as same in axial compression tests.

Not only experimental approach but numerical analysis is also carried out to study the effect of n-value upon the bending buckling strain of a material. Figure 12 shows the comparison of the relation between bending moment and bending angle obtained by experiment and numerical analysis. Both data agrees well.

Figure 13 shows the relationship between bending buckling strain and strain hardening exponent n-value of a material. As same in axial compression case, buckling strain increases with increase of n-value in bending mode.

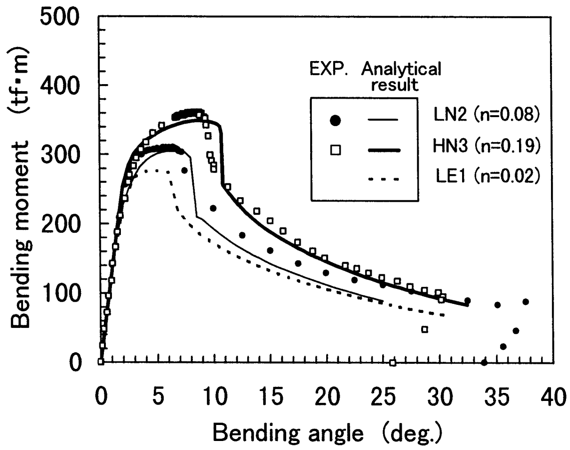

Fig.12 Comparison of bending moment - bending angle relation between experiments and analytical results

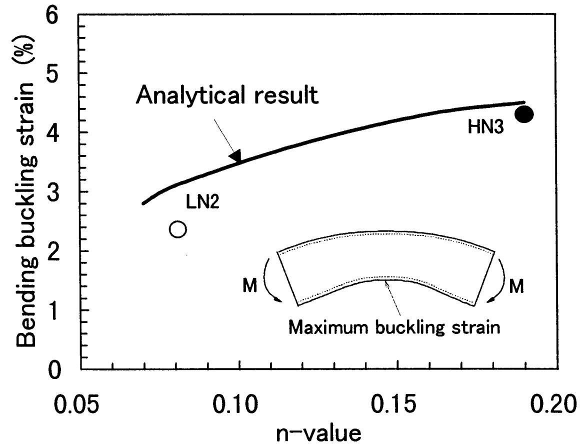

Fig.13 Comparison of dependency of buckling strain on n-value between experiments and analytical results

Low cycle fatigue strength

Former discussions in this paper are focused on the buckling strength, on the other hand, another important performance affects the resistance of a pipe material against earthquake is low cycle fatigue strength. Therefore, low cycle fatigue tests were carried out for the purpose of the effect of n-value upon the fatigue strength.

Hour glass type specimens fabricated from a pipe shown in Fig. 14 is used for low cycle fatigue tests. Electro-hydraulic fatigue testing machine is used. Test results are shown in Fig. 15 as S-N curve together with ASME fatigue design curve[5]. It is recognized that higher n-value material shows higher fatigue strength.

It is confirmed high n-value materials shows not only higher buckling strength but also higher low cycle strength in comparison with lower n-value materials.

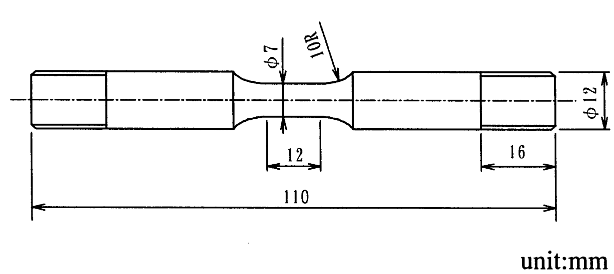

Fig.14 Geometry of specimen for low cycle fatigue test

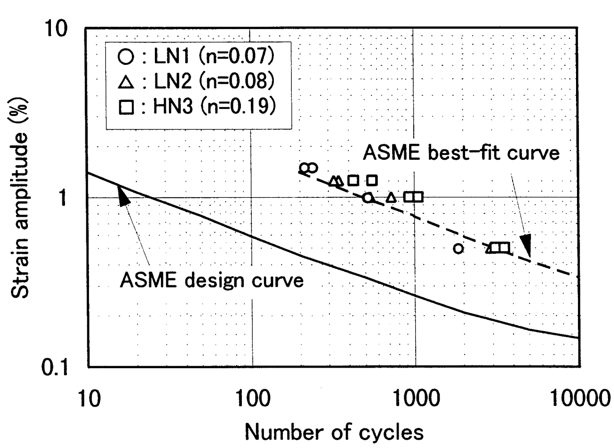

Fig.15 Comparison of low cycle fatigue strength

The effects of pipe material property on deformability of pipeline

In order to compare the deformability of pipeline subjected to ground motion, numerical simulation for two types of pipe materials was carried out.

Table 3 shows the two types of materials those stress- strain relationships were shown in Fig.1. Figure 16 shows the model of analysis which simulated buried pipeline subjected to fault displacement. And constants concerning to soil used in analysis was set as shown in Table 4. Numerical simulations were made by using finite element technique. Pipe parts are modeled as beam elements and soil parts are modeled as truss elements.

Analytical results are shown in Fig.17 as the relationship between the maximum strain of a pipe subjected to soil displacement normalized by its buckling strain and soil displacement for various D/t ratios ranged from 50 to 65. The D/t of 50 to 65 are common values for buried gas transportation pipeline.

Table 3 Pipe materials

	diameter (cm)	yield strength (MPa)	tensile strength (MPa)	yield to tensile strength ratio (%)	n-value	material type in Fig.1
1	61	451	607	74	0.08	LN2
2	61	523	752	70	0.14	HN2

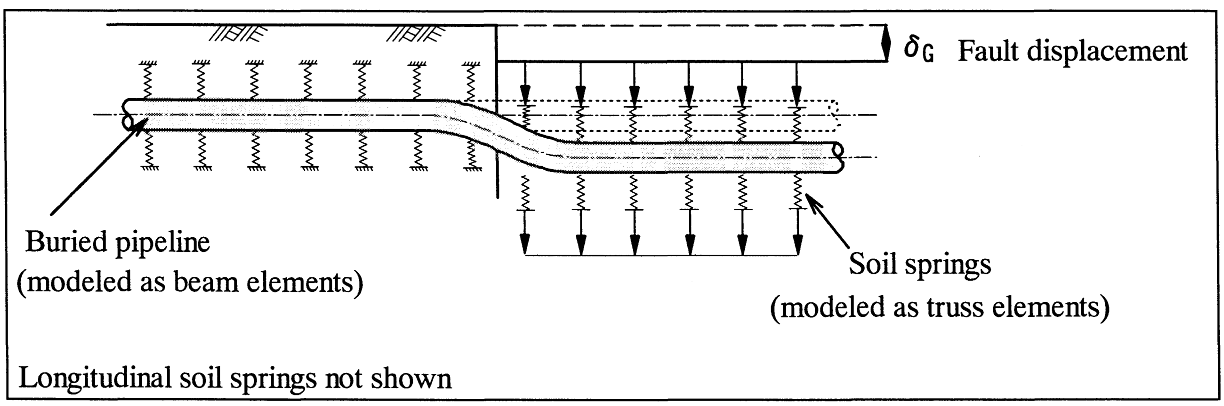

Fig.16 Analytical model of buried pipeline and fault movement

Table 4 Soil properties

Items		constants
Specific weight	(N/m^3)	1.77×10^4
Buried depth of pipeline	(m)	2.0
Angle of internal friction	(degree)	40°
Cohesion	(MPa)	2.9×10^{-2}
Yield strength of soil		obtained from Rankine's equation

In Fig.17, when the normalized strain reaches to unity, the possibility of the buckling would be very high. The value of $\varepsilon / \varepsilon_b$ for low n-value always located in unconservative side in comparison with those for high n-value in every simulated case. Especially for higher D/t values, the value of $\varepsilon / \varepsilon_b$ for low n-value reaches to unity at less than the fault displacement of 1.5m, while the $\varepsilon / \varepsilon_b$ for high n-value does not reach unity. The peak of the $\varepsilon / \varepsilon_b$ value appears in Fig.17 due to the effect of axial tensile strain component induced by large bending deformation. The deformability of a material with high n-value is more excellent than that with low n-value for various D/t ratios. It is confirmed that the improvement of material properties is very effective for improving the resistance of a pipeline to earthquake.

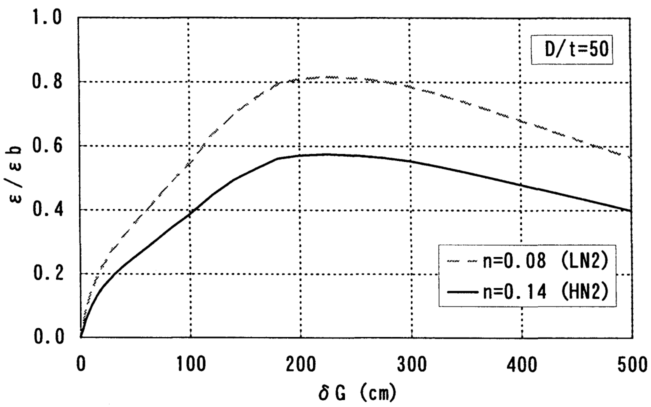

(a) D=610mm,t=12.2mm,D/t=50

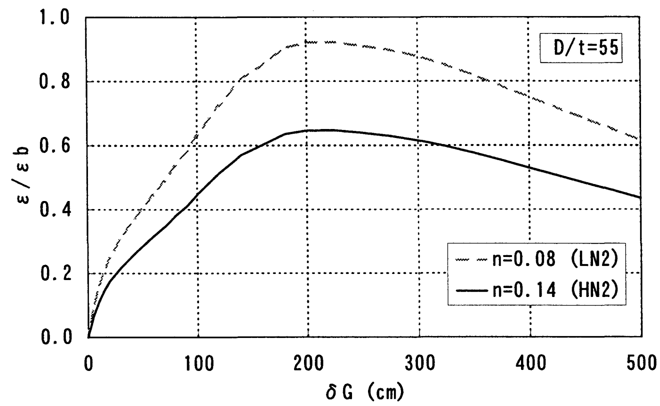

(b) D=610mm,t=11.1mm,D/t=55

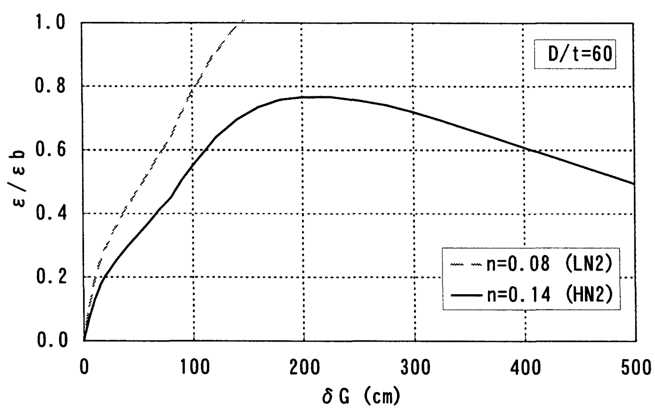

(c) D=610mm,t=10.2mm,D/t=60

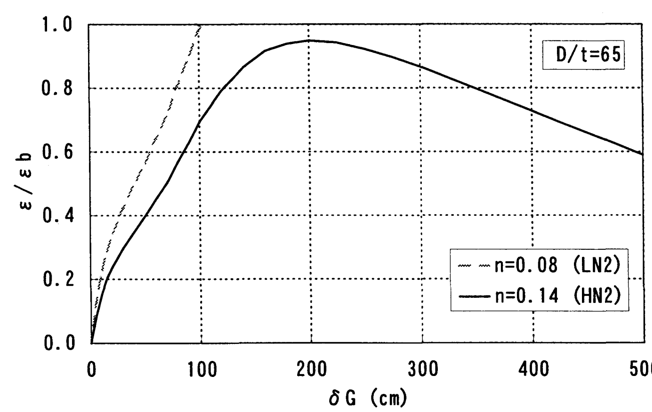

(d) D=610mm,t=9.4mm,D/t=65

Fig.17 Comparison of the deformability between low n-value pipe and high n-value pipe

Concluding Remarks

The effects of material properties on inelastic shell buckling strength of a steel pipe were studied by not only experiments and but numerical analysis.

Following conclusions were obtained.

1. Increase of strain hardening exponent of a material and extinguishment of Luders' elongation of a material are most effective to increase inelastic buckling strain of a pipe in both axial compression and bending mode.

2. The improvement of buckling strain of a pipe material largely contributed to improve the deformability of pipeline subjected to ground motion due to an earthquake.

3. It is confirmed that the improvement of a pipe material as increase of strain hardening performance is a very effective measure.

Reference

1) N. Suzuki, " The seismic design of buried pipeline taking account of permanent ground displacement", Doctor Thesis at Tohoku University, 1995 (in Japanese)

2) T. Katoh, H. Akiyama and H. Suzuki, " Local inelastic buckling resistance of a steel pipe subjected to axial compression load", J. of Architectural Institute of Japan", Vol.204, 1973 (in Japanese)

3) N. Ishikawa, S. Endo, M. Kurihara, N. Suzuki, A. Katoh and M. Yoshikawa, " Effects of the tensile properties and microstructural factore on the buckling property of the steel pipelines." Iron and Steel, 1999 (in Japanese)

4) K.J.Bathe, "F.E.Procedures", Prentice-Hall, 1996.

5) ASME, "Boiler & Pressure Vessel Code ,Sec.Ⅲ", 1997.

LARGE DEFORMATION BEHAVIOR OF LOW-ANGLE PIPELINE ELBOWS

Koji Yoshizaki[1]
Masanori Hamada[2]
and
Thomas D. O'Rourke[3]

1 – Visiting Scientist, School of Civil and Environmental Engineering, Cornell University, Ithaca, NY, and
Research Engineer, Tokyo Gas Co., Ltd., Tokyo, Japan

2-Professor, Department of Civil Engineering, Waseda University

3- Professor, School of Civil and Environmental Engineering, Cornell University, Ithaca, NY

ABSTRACT

Substantial permanent ground deformation (PGD) can be generated during earthquakes, causing deformation and strain that concentrates at pipeline elbows. This paper describes in-plane bending experiments that were conducted in the closing and opening mode to evaluate the response of various kinds of low-angle pipeline elbows to earthquake-induced PGD. The paper also describes Finite Element (FE) modeling that was performed to simulate the deformation behavior of low-angle pipeline elbows using linear shell elements. There is very good agreement between the analytical and experimental results for plastic deformation exceeding 30% strain.

INTRODUCTION

During earthquakes, permanent ground deformation (PGD) can damage buried pipelines. There is substantial evidence from previous earthquakes, such as the 1983 Nihonkai-Chubu (Japan Gas Association, 1984), the 1994 Northridge (O'Rourke et al., 1996), and the 1995 Hyogoken-Nanbu (Oka, 1996) earthquakes, of gas pipeline damage caused by earthquake-induced PGD in the form of liquefaction and landslides. Because elbows represent locations of local restraint with respect to flexural and axial deformation of buried pipelines, strains can easily accumulate in elbows in response to PGD.

Yoshizaki et al. (1998, 1999) have shown a favorable comparison between the results of in-plane bending experiments with 90° elbows and the analytical results of Finite Element (FE) modeling for strains as high as 25%. In the field, however, many elbows are installed with angles less than 90°, and damage to these facilities has been observed during past earthquakes.

The purpose of this paper is to present experimental results and an analytical method for assessing the behavior of buried pipelines with low-angle elbows subjected to very high levels of strain. In-plane bending experiments were conducted in the closing and opening mode for various kinds of elbows until the measured strain exceeded 30%. Finite Element (FE) modeling was also performed to represent the deformation behavior of the elbows.

BENDING EXPERIMENTS OF LOW-ANGLE PIPELINE ELBOWS

Experimental Method

In-plane bending experiments were carried out in the closing and opening mode for pipeline elbows with different geometric characteristics. The experiments involved pipe specimens with 100, 200 and 300-mm diameters and initial bend angles of 45°, 22.5° and 11.25°. The radius of curvature was 1.5 times the diameter. The elbows were composed of STPT 370 steel (Japanese Industrial Standard, JIS-G3456), with a specified minimum yield stress of 215 MPa and a minimum ultimate tensile strength of 370 MPa. The straight pipe was composed of SGP steel (JIS-G3452), with a minimum ultimate tensile strength of 294 MPa. The dimensions of the test pipes are presented in Table 1.

Table 1. Summary of Experimental Pipe Dimensions

Nominal diameter (mm)		100	200	300
Elbow	Outside diameter, Do (mm)	116.5	218.4	319.9
	Pipe thickness, t (mm)	5.4	6.8	7.4
	Do/t	21	32	43
Straight pipe	Wall thickness, t (mm)	4.1	5.2	6.5

Figure 1 illustrates the experimental setup. Straight pipes with lengths of about 2.5 times the diameter for 200-mm and 300-mm-diameter pipes and 5 times the diameter for 100-mm-diameter pipes were welded to each end of the test elbows. Displacement was applied with a hydraulic jack in one direction for both the closing and opening mode. Because it has already been confirmed by Minami et al. (1997) and Yoshizaki et al. (1998) that strain rate due to seismic motion has little influence on the stress-strain relationship of gas pipeline steel, the displacement was applied in a quasi-static state. Internal pressure of 0.1 MPa was added with nitrogen. The test was stopped if the both ends of the specimen came into contact with each other in the closing mode, a maximum load of 490 kN was attained, or leakage occurred.

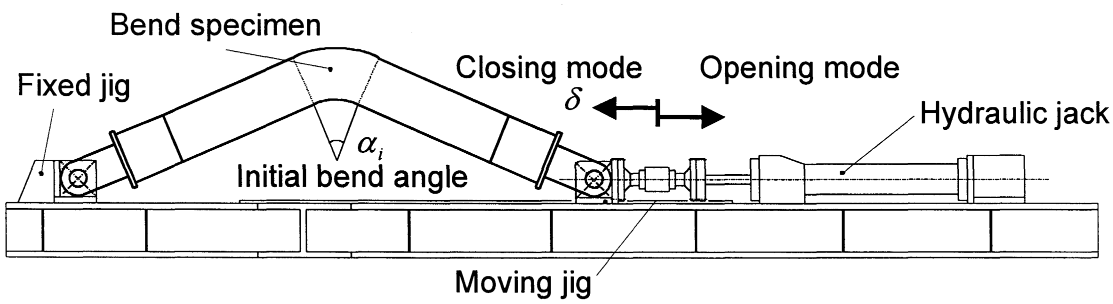

Figure 1 Experimental Setup

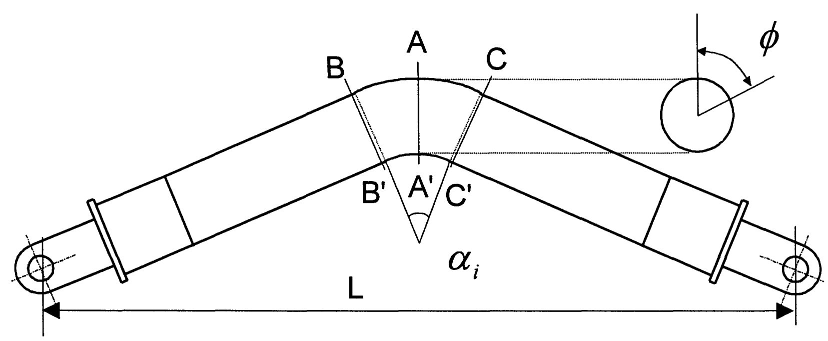

Figure 2 Strain Gauge Locations

Test data were obtained with a load cell, displacement meter, pressure gauge, and strain gauges that were bonded in the circumferential and longitudinal directions on the external pipe surface at the three cross-sections illustrated in Figure 2. As many as 150 strain gauges were used in each test set-up. During each experiment, the gauges, which reached their strain limit of 10%, had to be replaced to continue the acquisition of strain measurements at a given location. In addition, changes in the deformed shape of the A-A' section illustrated in Figure 2 (hereafter, "the central cross-section") were measured intermittently with a 3-dimentional displacement measuring device, employing five arms with five encoders.

Experimental Results and Discussions

Table 2 summarizes the experimental maximum strain, direction of maximum strain, maximum change in bend angle, and observations pertaining to leakage in combination with the results of the previous experiments on 90° elbows (Yoshizaki et al, 1999). In this table, maximum strain means the maximum value of all circumferential and longitudinal strains measured with strain gauges, and is expressed as positive if it is tensile and negative if compressive. For the 100-mm elbow with 22.5° of initial bend angle and the 200-mm elbow with 45° of initial bend angle, maximum strain could not be measured because cracking occurred at a location somewhat distant from the nearest gages. The change in bend angle $\Delta\alpha$ in this table was calculated with the following formula on the assumption that the specimen is a triangle:

$$\Delta\alpha = 2 \cdot \cos^{-1}\left(\frac{L-\delta}{L} \cos\frac{\alpha_i}{2} \right) - \alpha_i \qquad (1)$$

In this formula, L, δ and α_i are the initial distance between the ends of the specimen (illustrated in Figure 2), displacement of the jack, and initial bend angle, respectively. Figure 3 summarizes the maximum change in bend angle that could be carried out without exceeding the load limit of the hydraulic jack.

Figure 4 is divided into three principal plots showing (a) bending moment, (b) maximum strain, (c) % diameter change vs. change in bend angle. Here, the maximum strain represents the maximum of the absolute values of all measured strains. Bending moment, M, and % diameter change, β, are calculated with the following formulas:

$$M = F \cdot \frac{L-\delta}{2} \sqrt{\frac{L^2}{(L-\delta)^2 \cos\frac{\alpha_i}{2}} - 1} \qquad (2)$$

$$\beta = \frac{D_{\max} - D_{\min}}{\overline{D}_0} \times 100 \qquad (3)$$

In these formulas, F, $D_{\max}$, $D_{\min}$, and $\overline{D}_0$ are, respectively, reaction force measured by a load cell between the jack and the specimen, longest diameter (major axis) of the deformed central cross-section, its shortest diameter (minor axis), and the average of the initial diameter of the undeformed central cross-section.

The deformation behavior was different in the closing and opening mode. In the closing mode, no leakage occurred even when both straight pipes connected to the elbow came into contact with each other and the measured maximum strain exceeded 70%. Elbows with smaller initial bend angles experienced larger changes of bend angle, as indicated in Figure 3.

Table 2 Summary of Test Results

Nominal Diameter			100-mm	200-mm	300-mm
Closing mode	$\alpha_i =$ 90°	Maximum strain	25%, Circum.	30%, Circum.	25%, Circum.
		Max bend angle change, $\Delta\alpha$	78°	86°	81°
		Presence of leakage	No	No	No
	$\alpha_i =$ 45°	Maximum strain	32%, Long.	53%, Long.	43%, Long.
		Max bend angle change, $\Delta\alpha$	119°	118°	113°
		Presence of leakage	No	No	No
	$\alpha_i =$ 22.5°	Maximum strain	57%, Long.	41%, Circum.	72%, Long.
		Max bend angle change, $\Delta\alpha$	133°	134°	134°
		Presence of leakage	No	No	No
	$\alpha_i =$ 11.25°	Maximum strain	58%, Long.	53%, Long.	0.1%, Circum.
		Max bend angle change, $\Delta\alpha$	150°	145°	6°
		Presence of leakage	No	No	(Load limit)
Opening mode	$\alpha_i =$ 90°	Maximum strain	40%, Long.	42%, Long.	33%, Circum.
		Max bend angle change, $\Delta\alpha$	-44°	-33°	-44°
		Presence of leakage	Yes	Yes	(Load limit)
	$\alpha_i =$ 45°	Maximum strain	31%, Long.	22%†, Long.	3%, Circum.
		Max bend angle change, $\Delta\alpha$	-45°‡	-23°	-8°
		Presence of leakage	Yes	Yes	(Load limit)
	$\alpha_i =$ 22.5°	Maximum strain	13%†, Long.	9%, Long.	0.7%, Circum.
		Max bend angle change, $\Delta\alpha$	-22°‡	-10°	-4°
		Presence of leakage	Yes	(Load limit)	(Load limit)
	$\alpha_i =$ 11.25°	Maximum strain	9%, Long.	3%, Long.	—
		Max bend angle change, $\Delta\alpha$	-11°‡	-11°‡	—
		Presence of leakage	(Load limit)	(Load limit)	—

Circum.: Circumferential, Long.: Longitudinal †: Maximum strain could not be measured.
‡: Maximum bend angle change at full extension of elbow (see Figure 2)

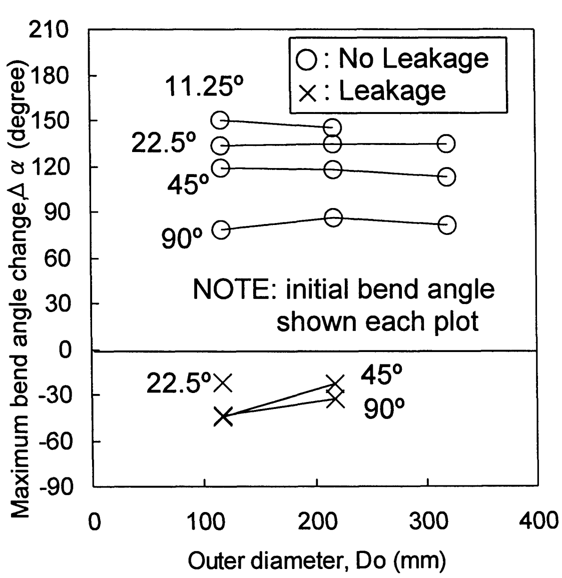

Figure 3 Maximum Changes in Bend Angle during Tests

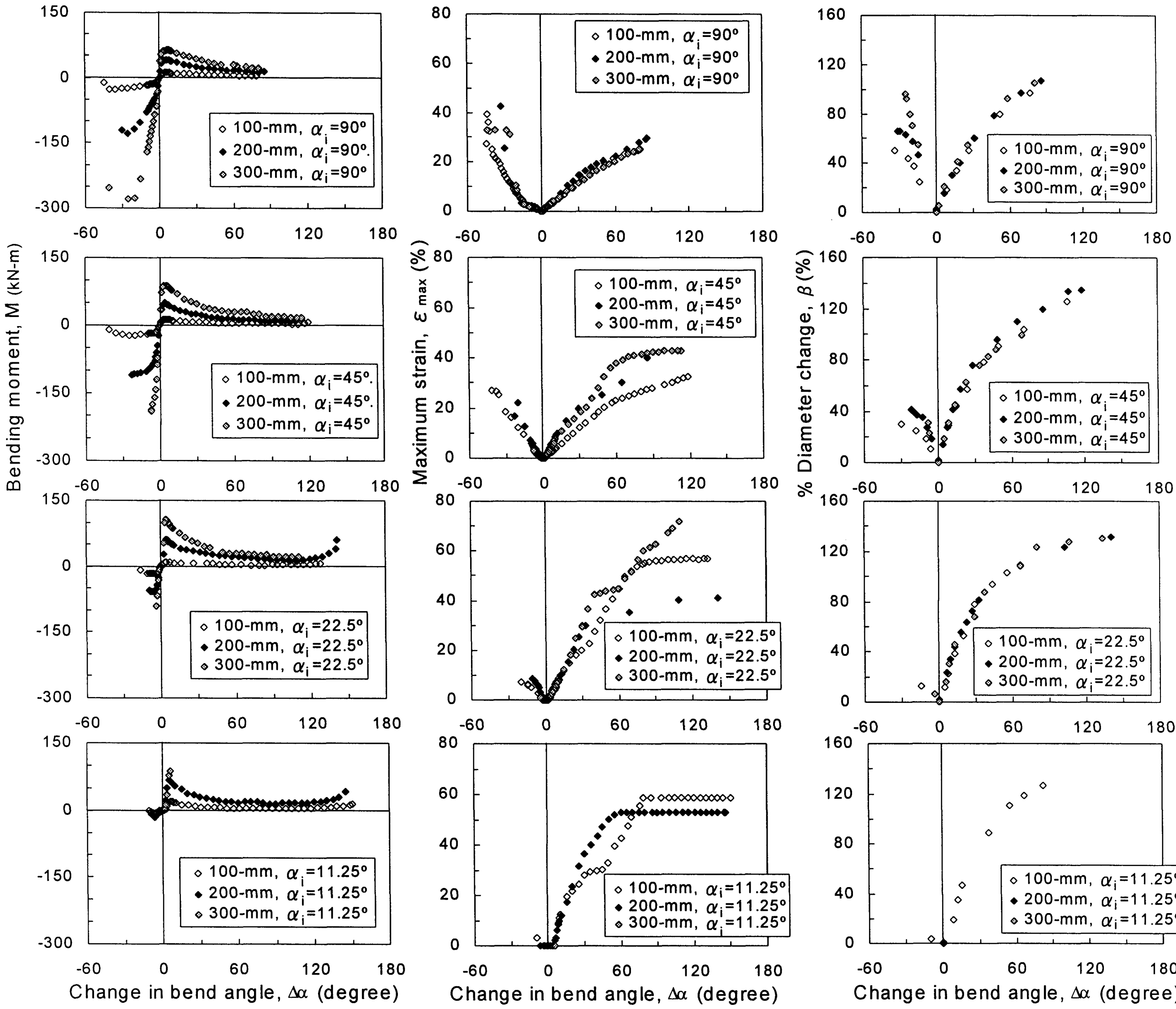

Figure 4 Results of Bending Experiments

Figure 5 shows the deformation behavior and the deformed shape of the central cross-section of a 300-mm elbow with 22.5° of initial bend angle. The deformation involved ovalization of the elbow. A maximum circumferential tensile strain of 10% was measured when the change in bend angle, $\Delta\alpha$, was 12° (see Figure 5 (a)). Further increases in $\Delta\alpha$ resulted in a shift of maximum strain from circumferential tension to longitudinal compression. A maximum longitudinal compressive strain of 74% was measured at ϕ = 120° (see Figure 2) when $\Delta\alpha$=134° (see Figure 5 (b)). Because of difficulties in locating and replacing strain gauges at the precise locations of high deformation and curvature, it is likely that the actual maximum strains were larger than those measured with strain gauges and plotted in the figure.

For the pipes, which had same initial bend angle, elbows with larger diameters had larger bending moments for a given change in bend angle, as shown in Figure 4 (a) in the closing mode. Pipe diameter, however, had little effect on the relationships between both maximum strain and % diameter change and changes in the bend angle, as shown in Figure 4 (b) and (c), respectively. For the same diameter pipes, elbows with smaller initial bend angles had larger peak values of moment with larger maximum strains for the same change in bend angle. The main reason for this behavior is that elbows with smaller initial bend angles experience greater localized deformation, which is similar to the buckling behavior of a straight pipe subjected to combined compression and bending.

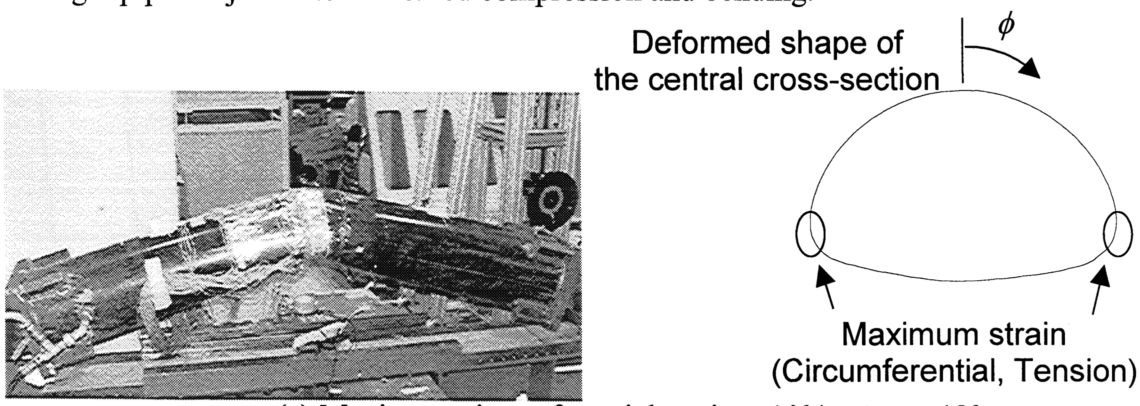

(a) Maximum circumferential strain = 10%, $\Delta\alpha$ = 12°

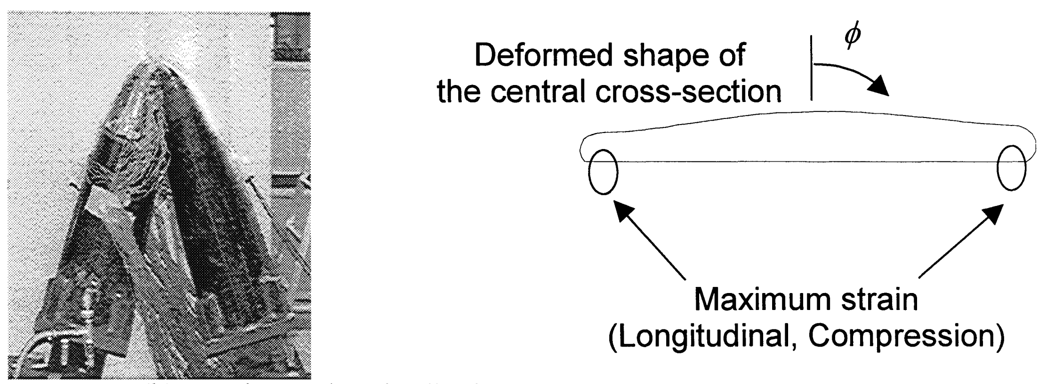

(b) Maximum longitudinal strain = -72%, $\Delta\alpha$ = 134°

Figure 5 Longitudinal and Transverse Deformation of a 300-mm-diameter Elbow with 22.5° of Initial Bend Angle in the Closing Mode

In contrast, leakage was observed in the opening mode for all cases except the ones at the load limit of the hydraulic jack. Figure 6 shows the deformation behavior and the deformed shape of the central cross-section of a 100-mm elbow with 45° of initial bend angle. In contrast with the closing mode, ovalization during the opening mode was accompanied by increases in vertical diameter at the central cross-section (see Figure 6 (a) and (b)). In response to this change in the central cross-section shape, the stiffness of the elbow became larger than that of the straight pipe. Bending was then concentrated at the location where one of the straight pipes was connected to the elbow. In all cases, leakage occurred near a straight pipe girth weld at ϕ = 180°.

The deformed shapes of the central cross-section are illustrated in Figure 6 (a) and (b). The maximum strains, however, were located near the welds connecting the straight pipes to the elbow. These maximum longitudinal strains are indicated with photos of the deformed test specimen in Figure 6 (a) and (b). The maximum strain measured near the crack was 31% in the longitudinal direction. Necking was observed in the pipe metal outside the heat-affected zone, but close to the crack. Figure 6(c) is a SEM (Scanning Electron Microscope) photograph of the fracture surface of the 100-mm-diameter elbow that indicates a ductile fracture.

Compared with the closing mode, the maximum changes in bend angle were much smaller, as shown in Figure 3. For the pipes that had the same initial bend angle, elbows with larger diameters sustained larger bending moments, larger maximum strains, and larger % diameter changes for the same change in bend angle, as shown in Figure 4 (a), (b) and (c), respectively.

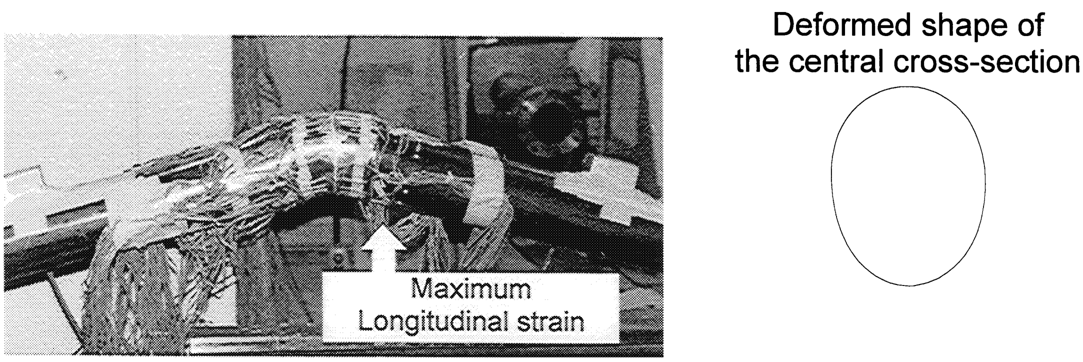

(a) Maximum longitudinal strain = 10%, $\Delta\alpha$ = -24°

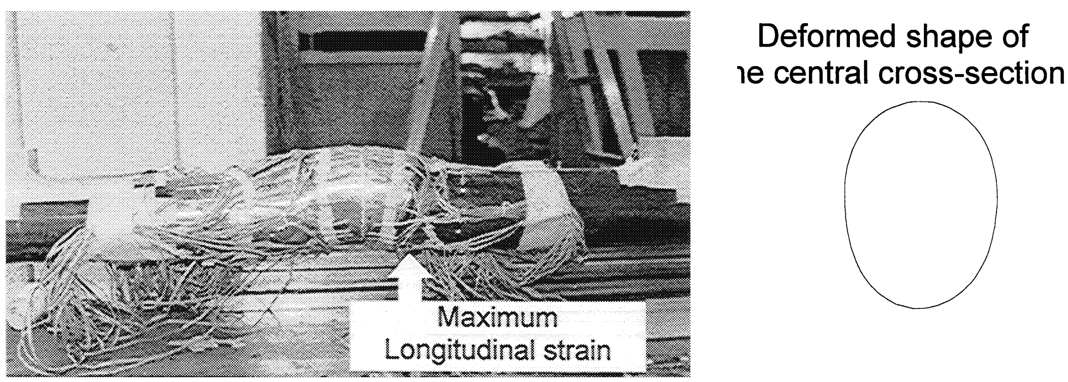

(b) Maximum longitudinal strain = 31%, $\Delta\alpha$ = -42°

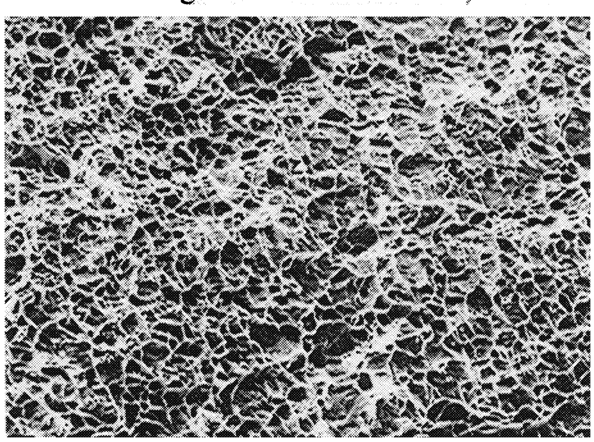

(c) SEM (Scanning Electron Microscope) photograph of the fractured surface

Figure 6 Longitudinal and Transverse Deformation and SEM Photograph of the Fractured Surface of a 100-mm-diameter Elbow with 45° of Initial Bend Angle in the Opening Mode

FINITE ELEMENT ANALYSES FOR LOW-ANGLE PIPELINE ELBOWS

Analytical Model

Finite element analyses were performed to represent the deformation behavior of the low angle elbows. Figure 7 shows the FE model for the 300-mm diameter pipe with 45° of initial bend angle. Because of symmetry, only a quarter of the specimen was modeled, for which half the pipe circumference was analyzed. The elements used in the model are isotropic linear shell elements. Seventy-two elements were employed around half the pipe circumference. As shown in the figure, the density of elements increased near the center of the elbow. The total number of elements was about 7500, of which 4500 were concentrated near the center of the elbow.

The average value of the actual thickness measured with an ultrasonic thickness meter was used in the analytical model. The stress-strain relationship from direct tension test data was approximated by a multi-linear trend as plotted in Figure 8. ABAQUS version 5.7 was used as a solver for the analyses with geometric nonlinearity and large strain formulation.

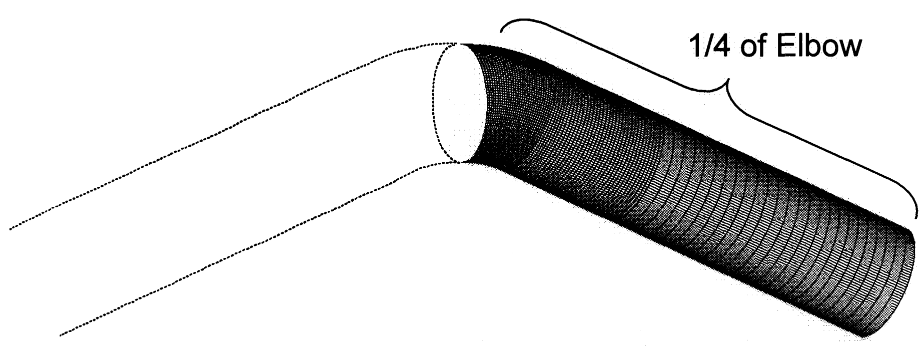

Figure 7 Finite Element Model for 300-mm-diameter Elbow with 45° of Initial Bend Angle

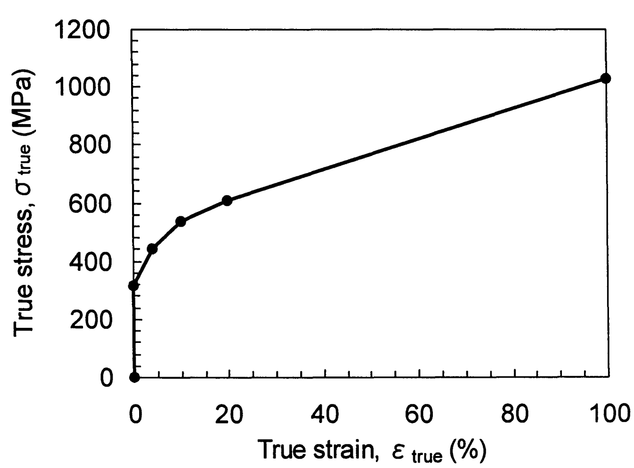

Figure 8 Stress-strain Curve of the Elbow Used in FE Modeling

Analytical Results and Discussions

Figure 9 compares the experimental and FE analytical results for the 300-mm elbows with 45° of initial bend angle. Good agreement was observed between the experimental and analytical results with respect to the bending moments and maximum strains plotted in Figure 6. The validity of the numerical modeling technique was confirmed for plastic deformation exceeding 30% strain, as shown in Figure 9 (c). The reason for the difference in maximum compressive strain between the experimental and FE analytical results for changes in bend angle above 60° (see Figure 9 (c)) is related to difficulties in locating and replacing strain gauges at high deformation and curvature.

Figures 10 (a) and (b) compare the analytical and experimental results for a 300-mm elbows with 45° of initial bend angle, α_i, when the change of bend angle, $\Delta\alpha$, was 110° in the closing mode. Good agreement between experimental and analytical results was also observed for the strain distribution of the central cross-section in the circumferential and longitudinal direction, as shown in Figures 10 (c) and (d), respectively.

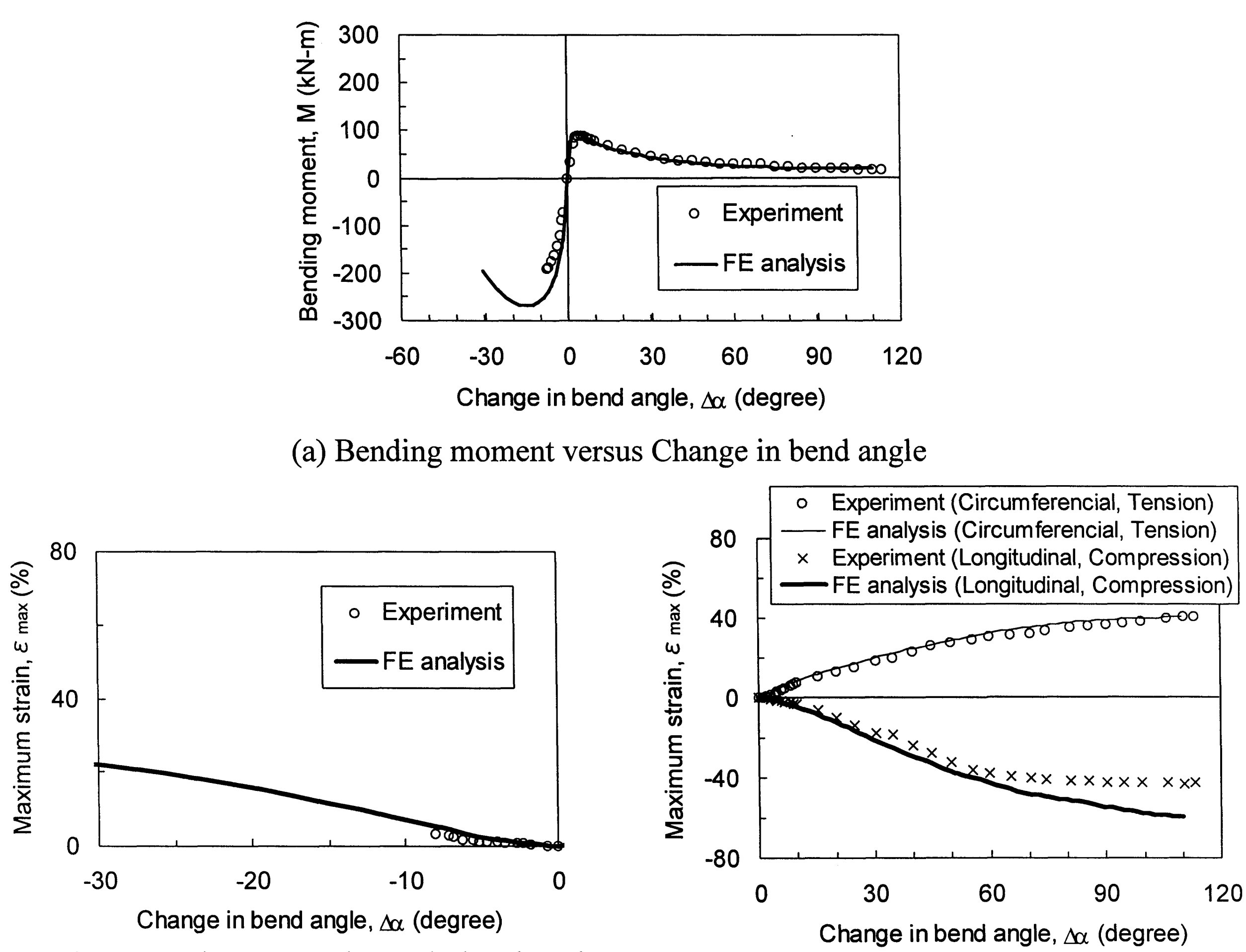

(a) Bending moment versus Change in bend angle

(b) Maximum strain versus Change in bend angle (Opening mode)

(c) Maximum strain versus Change in bend angle (Closing mode)

Figure 9 Comparison between Experiment and FE analyses for a 300-mm-diameter Elbow with 45° of Initial Bend Angle

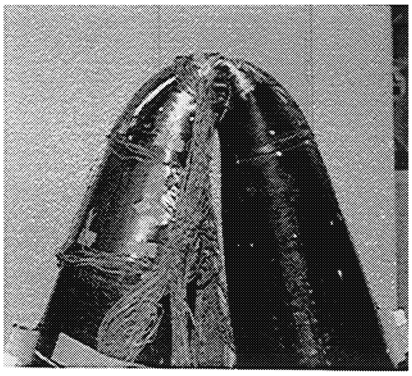

(a) Deformed shape (Experiment)

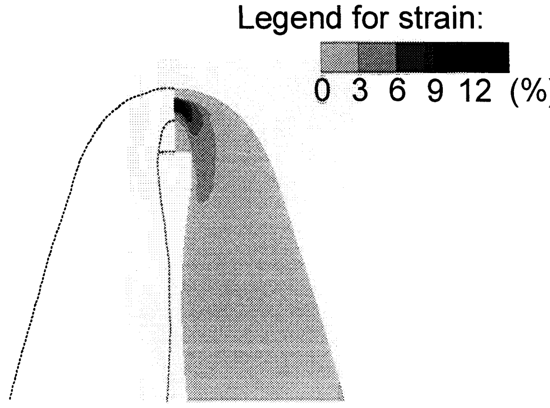

(b) Deformed shape and strain distribution (FE analysis)

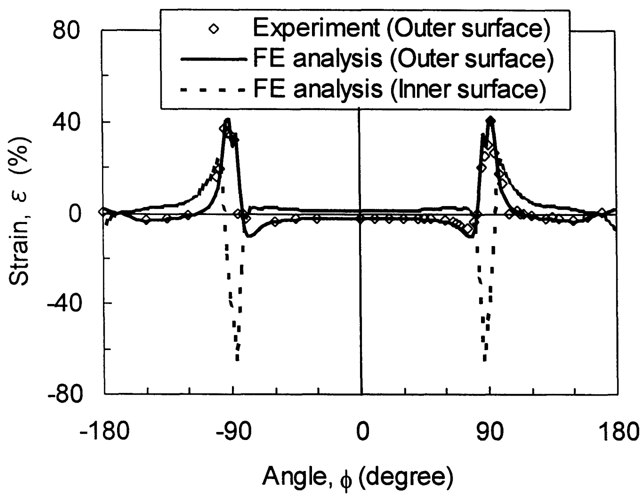

(c) Strain distribution in the circumferential direction

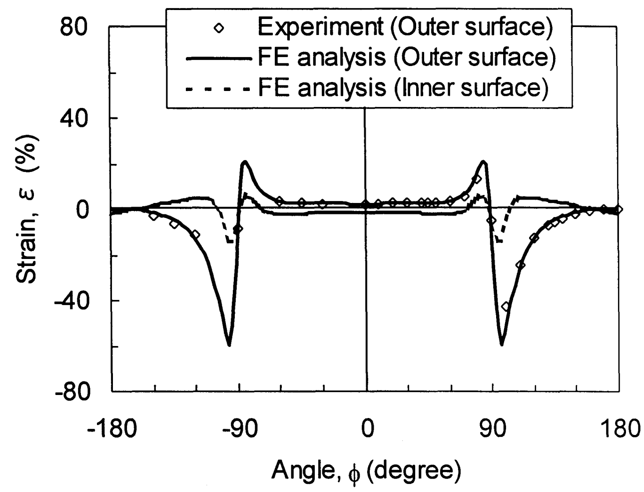

(d) Strain distribution in the longitudinal direction

Figure 10 Deformed Shape and Strain Distribution at the Central Cross-section of a 300-mm-diameter Elbow with 45° of Initial Bend Angle in the Closing Mode ($\Delta\alpha$ = 110°)

Figures 11 (a) and (b) compare the analytical and experimental results for a 100-mm elbow with 45° of initial bend angle when the change in bend angle was -45° in the opening mode. In the experiment, leakage occurred around one of the girth welds between the elbow and the straight pipes. The FE analytical model assumes symmetry, but it is not possible to make the specimen perfectly symmetric in the welding process. As a consequence, leakage occurs at locations of concentrated stress near the welds, but is not represented in the FE analysis. As shown in Figure 12, the validity of the model was confirmed for plastic deformation exceeding 30% strain.

A modeling technique named HYBRID MODEL (Yoshizaki et al., 1999) was developed for simulating the permanent ground displacement response of large-scale pipeline elbows with 90° of initial bend angle. The model uses shell elements in zones around the elbows that are likely to be subjected to large localized strain. The validity of the FE analytical model using shell elements presented in this paper implies that the HYBRID MODEL can be applied for pipelines with low-angle elbows.

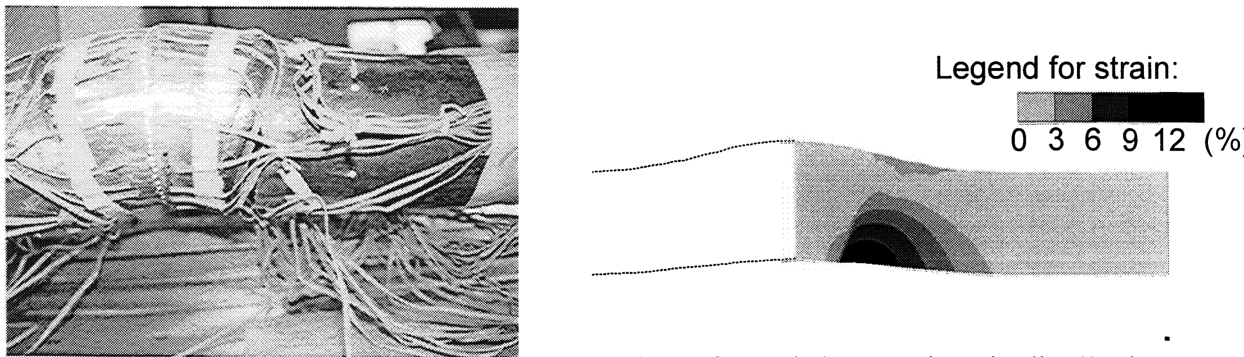

(a) Deformed shape (Experiment)

(b) Deformed shape and strain distribution (FE analysis)

Figure 11 Deformed Shape of a 100-mm-diameter Elbow with 45° of Initial Bend Angle in the Opening Mode ($\Delta\alpha$ = -45°)

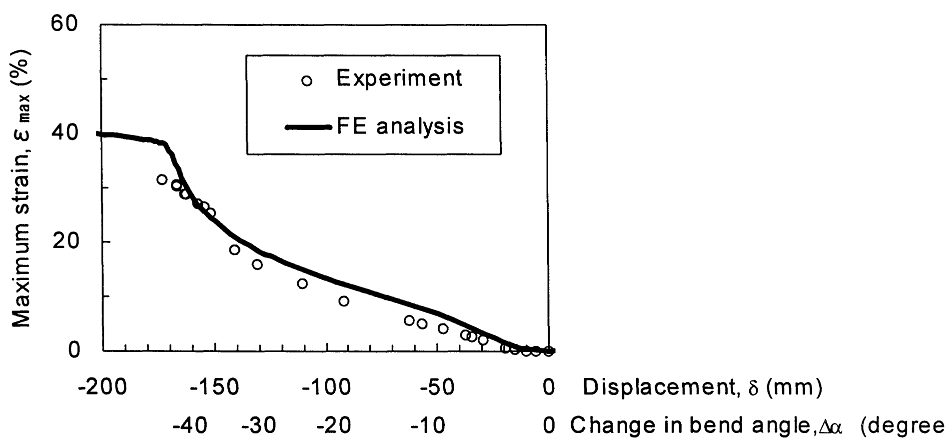

Figure 12 Comparison between Experiment and FE analysis for a 100-mm-diameter Elbow with 45° of Initial Bend Angle in the Opening Mode

CONCLUSIONS

This paper describes in-plane bending experiments that were conducted in the closing and opening mode to evaluate the response of various kinds of low-angle pipeline elbows to earthquake-induced PGD. In the closing mode, no leakage occurred even when both straight pipes connected to the elbows came into contact and measured maximum strain exceeded 70%. The deformation involved ovalization of the elbows. Pipe diameter had little effect on the relationship between maximum strain and bending angle. For the same diameter pipes, elbows with smaller initial bend angles had larger peak values of strain and % diameter change. In contrast, leakage was observed in the opening mode for all cases except the ones that reached the load limit of the hydraulic jack. The strain measured near the crack was 30% in the longitudinal direction. Compared with the closing mode, the maximum changes in bend angle were much smaller in the opening mode. For the same diameter pipes, elbows with smaller initial bend angle had smaller maximum changes in bend angle. For the pipes, which had the same initial bend angle, elbows with larger diameters had larger bending moments, larger maximum strains, and larger % diameter changes for same change in bend angle.

The paper also describes the Finite Element (FE) modeling that was performed to simulate the deformation behavior of the elbows using linear shell elements. There is very good agreement between the analytical and experimental results for plastic deformation exceeding 30% strain.

ACKNOWLEDGEMENTS

The authors wish to thank Mr. Noritake Oguchi, Mr. Hirokazu Ando, Mr. Hiroshi Sugawara, Mr. Naoto Hagiwara, Mr. Hiroshi Yatabe and Mr. Naoyuki Hosokawa of Tokyo Gas for their assistance.

REFERENCES

Ando, H., and Kobayashi, M. (1996), "Nonlinear Characteristics of Ground Constraint on Buried Pipes Caused by Lateral Displacement during Earthquakes", *Proceedings*, 11th World Conference on Earthquake Engineering, Acapulco, Mexico, Paper No. 1596, Elsevier Science.

ASME, "Boiler & Pressure Vessel Code", Section III, Division 1, Subsection NB, 3653.2, SI-13.

Hamada, M., Yasuda, S., Isoyama, R. and Emoto, K. (1986), "Observations of Permanent Ground Displacements Induced by Soil Liquefaction", *Journal of JSCE*, Tokyo, Japan, No.376, III-6, pp.211-220, (in Japanese).

Kobayashi, M., Ando, and H., Oguchi, N. (1995), "Dependence of Longitudinal Subgrade Reaction to the Buried Pipe on Displacement Velocities and Cycles of the Ground", *Proceedings*, 6th U.S.-Japan Workshop on Earthquake Disaster Prevention for Lifeline Systems, Technical Memorandum No. 3415, Public Works Research Institute, Tsukuba City, Japan, pp.91-106.

Kussmaul, K., Diem, H.K., Uhlmann, D., and Kobes, E. (1995), "Pipe Bend Behavior at Load Levels beyond Design", *Transactions*, 13th International Conference on Structural Mechanics in Reactor Technology, Vol. 13, No. 2, pp187-198.

Japan Gas Association (1982), "Recommended Practice for Earthquake Resistant Design of Gas Pipeline", Japan Gas Association, Tokyo, Japan (in Japanese).

Japan Gas Association (1984), "Nihonkai-Chubu earthquake and the City Gas", Japan Gas Association, Tokyo Japan (in Japanese).

Minami, F., Morikawa, J., Ohmasa, M., Toyoda, M., Konda, N., Arimochi, K., Ishikawa, N., Kubo, T. and Shimanuki, H. (1997), "Strength and Fracture Properties of Structural Steels under Dynamic Loading", *Proceedings*, 16th International Conference on Offshore Mechanics and Arctic Engineering, Yokohama, Japan, Vol.3, pp.283-292.

Ohuchi, H., and Sato, H. (1986), "An Experimental Study on the Large Deformation Behavior of the Pipe-Bend of Buried Pipeline", *Journal of Structural Engineering*, Tokyo, Japan, Vol.32A, pp.865-878, (in Japanese).

Oka, S (1996), "Damage of Gas Facilities by Great Hanshin Earthquake and Restoration Process",

Proceedings, 6th Japan-U.S. Workshop on Earthquake Resistant Design of Lifeline Facilities and Countermeasures Against Soil Liquefaction, NCEER-96-0012, Buffalo, NY, pp.111-124.
O'Rourke, T. D. and Palmer, M. C (1996), "Earthquake Performance of Gas Transmission Pipelines", *Earthquake Spectra*, Vol. 20, No. 3, pp.493-527.
Suzuki, N., Nasu, M., and Yano, T. (1993), "Very Low-cycle Fatigue Strength of Elbows having Initial In-plane Bending Deformation", *Journal of Structural Engineering*, Vol. 39A, pp1457-1464, (in Japanese).
Trautmann, C.H. and O'Rourke, T.D (1985), "Lateral Force-Displacement Response of Buried Pipe", *Journal of Geotechnical Engineering*, ASCE, Reston, VA, vol.111 No.9, pp.1077-1092.
Yoshizaki, K., and Oguchi, N. (1996), "Estimation of the Deformation Behavior of Elbows for an Earthquake-resistant Design", *Proceedings*, 11th World Conference on Earthquake Engineering, Acapulco, Mexico, Paper No. 1783, Elsevier Science.
Yoshizaki, K. and Oguchi, N. (1998), "Effect of Strain Rate on Stress/Strain Properties of Gas Pipeline Steel", *Proceedings*, 10th Japan Earthquake Engineering Symposium, Yokohama, Japan, pp. 3171-3174, (in Japanese).
Yoshizaki, K., Hamada, M. and O'Rourke, T. D. (1999), "Large Deformation Behavior of Pipelines with Elbows", *Proceedings*, 5th U.S. Conference on Lifeline Earthquake Engineering, ASCE, Reston, VA (in press).

Summary of the Earthquake Resistant Design Standards for Railway Structures

by

Akihiko NISHIMURA

ABSTRACT

The devastating damage including the large-scale cave-in of many railway structures occurred in the Hyogoken-Nambu Earthquake of January 17, 1995. By drawing a lesson from this earthquake, a new seismic design code for railway structure has been drawn up. The main procedure of this new code can briefly be described, which is to (1) decide the earthquake resistance performance of structures based on their importance, (2) calculate the responses on the surface of deposit layer by inputting the design earthquake motion in the base layer, and (3) calculate the responses of the structures by inputting the ground responses calculated in the step (2) and check the earthquake resistance performance. For the design earthquake motions, the type of earthquake motion caused by an inland earthquake is added in addition to the normal types. The earthquake resistance performance is defined by the damage of members and stability of foundations, which includes three ranks depending on the retrofitting degree after earthquakes. Moreover, dynamic analysis methods are decided in this new code as main tools for the response calculation and safety check of structures.

1. INTRODUCTION

The Hyogoken-Nambu Earthquake occurred on January 17, 1995, and devastated railroads, roads and many other important structures. This earthquake lead to re-examination of the existing seismic design standard at that time. Eventually, the Proposals on Seismic Standards for Civil Engineering Structures was prepared by the Japan Society of Civil Engineers and made public in two releases, in May 1995 and January 1996.

For the railroad-related industry, the Committee for Railroad Facility Seismic Structure Review set up by the Ministry of Transport immediately after the devastating earthquake, headed by Prof. Yoshiji Matsumoto, Science University of Tokyo, discussed the validity of the current seismic standard for railroad facilities and published the results in the Basic Concept on New Seismic Design Standard, in July

---

1 Structure Technology Division, Railway Technical Research Institute, Tokyo, Japan

1996. Based on this understanding, the Subcommittee for Seismic Standard Review, headed by Prof. Masanori Hamada, Waseda University, proposed the Design Standard for Railroad Structures and Its Explanatory of Earthquake-Resistant Design (herein Earthquake Resistant Design Standard) after two years of study and discussion. This standard is intended for bridges, overpasses, foundation structures, earth pressure resisting structures, open cut tunnels, and fills. Its application to fills, however, is only valid when the fill requires seismic design due to strategic importance, susceptible location to earthquake damage, or recovery difficulty. This paper introduces this standard as mainly applied to bridges.

2. BASIC PRINCIPLE OF THE NEW EARTHQUAKE RESISTANT DESIGN STANDARD

A lesson must be learned from the Hyogoken-Nambu Earthquake in developing a new earthquake resistant design standards code. Damages of this disastrous earthquake to structures are omitted here because they are described many literatures. The following causes were inferred from the survey and analysis of such damages[1]:

(1) Many of the structures were known to satisfy the bearing capacity level required by the design standard at that time to be resistant to a design lateral seismic coefficient of 0.2. In reality, actual acceleration of the earthquake far surpassed such a design level, which is why those structures were damaged.

(2) Viaducts of the Shinkansen that suffered serious damage, including the fall of a bridge, were originally designed to be more resistant to bending force than shear force. This imbalance aggravated the level of damage done to these structures. This was partly due to the fact that allowable stress against shear was set larger in the then existing standard than in that of today's standard.

(3) There was a great gap in the magnitude of damage done to adjoining viaducts, with some totally collapsed and others only cracking in columns. This was mainly due to the difference in strength of the ground geology.

These facts helped identify necessary factors to consider in development of new seismic standards: specifically, inland type tremors for seismic design, failure mode for evaluation of safety of members and dynamic characteristics of subsurface geology.

Based on the findings above, one can easily assume that seismic motions to be allowed for in earthquake design will considerably increase once inland type earthquakes are taken into consideration. Also, considering that such earthquakes have a long recurrence period of over a few centuries, one can easily realize that in the seismic design of a structure, deformation performance (earthquake resistance performance) should be evaluated for members of the structure and its foundation so that the structure will allow damage but never collapse.

Earthquake design of a railroad structure should therefore be carried out according to the following procedure. First, from the viewpoint of damage control, the degree of damage to a structure (earthquake resistance performance) should be identified. The responses on the subsurface layer of the ground should be calculated by using earthquake motions set for the foundation bed. The responses of a structure should be calculated by inputting the design earthquake motions into the structure. And finally, the earthquake resistance performance of the structure should be checked.

Two types of earthquake motion were considered in the development of our seismic design. One is L1 earthquake motion, which has a recurrence probability of a few times during the service life of the structure. The other is L2, which is a large earthquake motion such as from a large-scale plate border earthquake or an inland type earthquake that may occur during the life of the structure, even though the probability is low.

A structure should then be checked to see if it is resistant to such motions. During the process of developing this part of the standard, three kinds of performance were established based on the presumed level of repair or reinforcement that may be required following a major earthquake, considering the damage of members and stability of the foundation. Every structure built should satisfy these performances. Which performance the structure should be endowed with basically depends on the importance of the structure.

It is then decided that responses of a structure necessary to check these earthquake resistance performances be calculated by dynamic analysis. Static analysis may also be used, depending on the type of the structure.

The procedure of seismic design for a bridge and a viaduct based on the approach above is shown in Figure 1.

As indicated in the figure, there are two types of design methods. One is the non-linear spectrum method that easily calculates responses of a structure by selecting the type of ground based on geological survey and using the strength demand spectrum calculated by the proper earthquake motion determined for the ground selected. The other is the time history dynamic analysis that dynamically analyzes the detailed time history of the ground and the structure standing on it.

As a general rule, the non-linear spectrum method may be used. The other detailed analysis method may work better if a structure, as described later, is unable to describe its behavior in a system with only a single degree of freedom.

Major elements of earthquake resistant design, or setting of design earthquake motions, displacement of the structures, calculation methods for stress and other parameters, and safety checking methods for structures, are explained in the following pages.

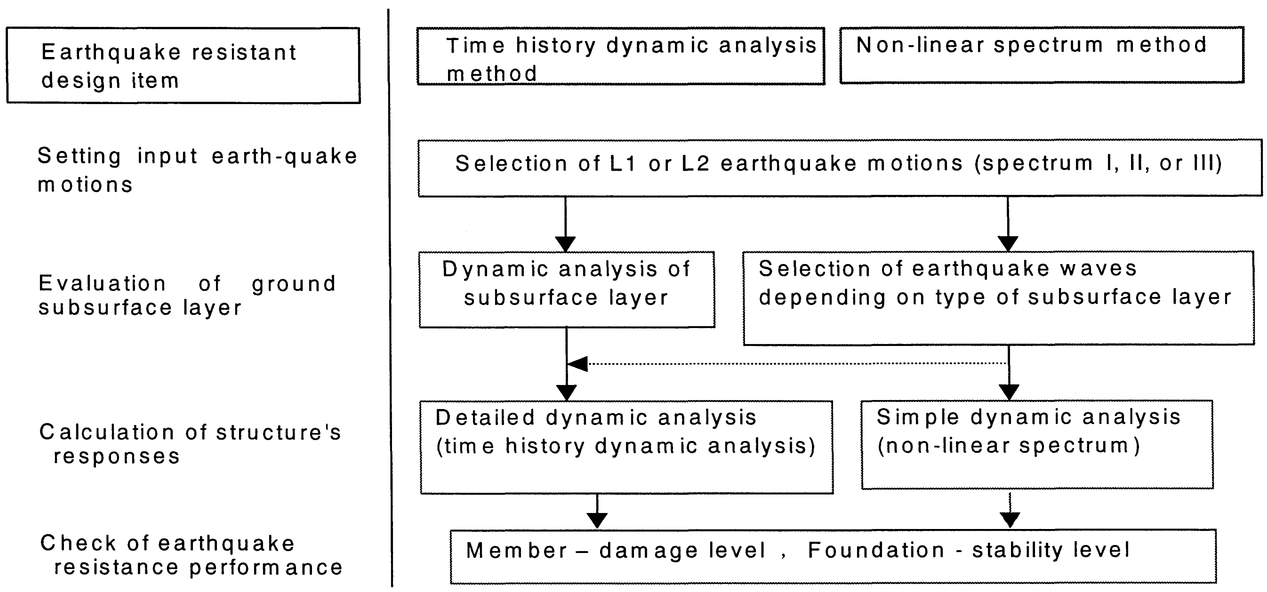

Fig. 1 Procedure of earthquake resistant design

3. SETTING OF DESIGN EARTHQUAKE MOTION

3.1 Setting of earthquake motions for the foundation bed

As earlier discussed, either L1 or L2 earthquake motion is selected in calculation of our proposed earthquake resistant design method.

L1 earthquake motion is conventionally used in combination with elastic design techniques and set either as static load (seismic coefficient method) or earthquake motion for dynamic analysis. Earthquake resistant design method using L1 has been developed based on vast experience. Thus, the current system can be used as is.

For L2 earthquake motion, the level of design earthquake motion typically considered was maximum 1G in elastic response acceleration for a structure standing on the typical type of ground. It is now important, after we experienced the large Hyogoken-Nambu Earthquake, to use values based on near field earthquake motions.

In this respect, the desired approach is to comprehensively consider geological information on active faults, geodetic information on crustal movement, and seismic information on earthquake activities, identify the positions of potentially dangerous active faults by area and predict the magnitude of each possible earthquake before determining earthquake motions. Prediction of recurrence period, scale, or characteristics of seismic motion of earthquakes caused by inland active faults is yet to ensure precision sufficient to provide a basis for earthquake resistant design. Therefore, for the time being we decided to establish standard earthquake motions in the area close to the active fault based on the record of strong motions and their analytical results of the past regional earthquakes, measured at the vicinity of their epicenters, including the devastating Hyogoken-Nambu Earthquake.

L1 and L2 earthquake motions will be set for the foundation bed for reasons described in Section 2. Their characteristics should then be determined in acceleration response spectra.
In doing this, the importance is put on setting of the foundation bed layer. It is ideal to assume a ground with the greatest possible shear elastic wave velocity. However, the subsurface layer of any good quality ground in which the foundation is typically placed may be used so that one can avoid extra problems in daily design work.
L1 earthquake motion in our proposed design method was then determined based on acceleration response spectra of good ground conventionally used in the allowable stress design method and the analysis of earthquake danger level with a recurrence period of 50 years. The maximum value of L1 is 250 gal (damping constant of 5%).

To determine acceleration response spectra of L2 earthquake motion, the following considerations were taken:
1) Acceleration response spectra (Spectra I) associated with marine earthquakes (magnitude class 8 with an epicenter distance of 30 - 40 km) considered in conventional design .
2) Acceleration response spectra (Spectra II), which are set for inland active fault earthquakes by statistical analysis based on past earthquake observation records. If the destruction mechanism of a fault can be identified, Spectra II may be substituted by acceleration response spectra calculated by analysis based on it (Spectra III).

Spectra II is usually obtained from the response spectra of waveforms generated by past earthquake motions and observed at good ground. In this case, it should not be an envelope of each response spectrum, but 90% probability of not being exceeded should be considered in setting of Spectra II. It should be noted that these spectra should be given as waveforms just on the fault. If there is an active fault near the construction site and the location of the fault is identified, its value may be used as one corrected by the distance from the fault to the structure.

The maximum value of Spectra II developed by this approach is 1700 gal (damping constant of 5%). Design earthquake motions are generally set based on the result of the fault survey. In practice, fault survey will be reviewed by checking available literature such as the Active Faults in Japan and other related literature.

3.2 Setting of Design Earthquake Motions on the Ground Surface

When calculating responses of a structure to earthquake motions, it may be done by dynamic analysis by modeling the subsurface layer and the structure altogether using the earlier-mentioned earthquake motions of the foundation bed. As a general rule, however, the foundation structure will be replaced by supporting springs to form a multiple mass point model for the superstructure, and earthquake motions on the ground surface will be used as input earthquake motions. In this case, one needs to know the earthquake motions on the surface ground, which can be calculated from dynamic analysis of the ground. In reality, there are difficulties in this calculation process such as setting of relationships between strain of the ground and shear elastic coefficient or damping constant. Considering such difficulties in actual calculation, design ground surface earthquake motions were determined by the ground type for simplification of calculation. As earlier mentioned, the nature of the subsurface layer needs to be identified with the best possible precision, which requires more divisions than just the three which are typically used in conventional designs. Thus, design surface ground earthquake motions have been determined for each of those ground types, in our case eight. The characteristic of each surface ground earthquake motion is also given in the form of acceleration response spectra. The types of ground used in this approach will be divided depending on natural frequency calculated based on initial shear elastic wave velocity of the subsurface layer.

In summary, our standard uses eight types of ground, while design ground surface earthquake motion has been set for each Spectra I and Spectra II of both L1 and L2 earthquake motions.

4. Earthquake Resistance Performance of Structures

4.1 Earthquake resistance performance of structures

In our proposed standard, when earthquake resistant design is developed, earthquake resistance performance of a structure should first be set and then the structure should be checked for that performance. Although there is no clearly explained definition of performance design in general, our definition is to clarify the ideal condition of a structure and attempt to provide a design that can achieve that ideal.

For seismic design, the definition of performance design may be interpreted this way as follows. The conditions of damage a structure may suffer from design earthquake motions is clearly determined, and if it is right or not, it should be checked. In other words, it is a damage control design method. This concept is already assimilated in the Concrete Design Standard Specification issued by the Japan Society of Civil Engineers, which occurred in the context of diversification of standards, advancement of analysis techniques, or growing demand. The major advantage of this method is ease of understanding because it clearly explains damage conditions. In practice, any method will do if it can prove it fully serves the purpose, so any design method that fits the situation may be used, which helps improve further development of technology. For the purpose of seismic design of railroad structures, the above mentioned method of determining performance with respect to possible damage to the structure and checking the structure for performance has been chosen.

In seismic design of a railroad structure, the following three performances are established for consideration:

1) Earthquake resistance performance I (PI): capability of maintaining the original functions without any repair and no major displacement occurring after being hit by an earthquake
2) Earthquake resistance performance II (PII): capability of making quick recovery of the original functions with repairs after being hit by an earthquake
3) Earthquake resistance performance III (PIII): capability of keeping the entire structure system in place without collapse after being hit by an earthquake

These performances are about ease of recovery of the structure after being hit by an earthquake. Therefore, the relationship between earthquake motions and earthquake resistance performance has been established as follows: PI should be satisfied by a structure against L1 earthquake motions, PII by a structure of greater importance against L2 and P III by other structures against L2.

Earthquake resistance performance describes the seismic resistance of a structure in terms of the level of damage to its building members and the level of stability of its foundation structure. This means compliance of a structure with the intended earthquake resistance performance requires appropriate setting of the level of damage of component members and the level of stability of its foundation. For the damage level to members, the damage level to each member should be set considering the seismic resistant role of each such member in the context of the entire structure composed of various members. For the stability level of the foundation structure, as it has a big impact on deformation of the structure, it should be determined considering supporting force or deformation involved.

Fig. 2 shows the relationships among earthquake resistance performance required for bridges and viaducts, the damage level of members, and the stability level of the foundation structure.

Earthquake resistance performance of a structure

PI: capability of maintaining the original functions without any repair and with no major displacement after being hit by an earthquake

PII: capability of making quick recovery of the original functions with repairs after being hit by an earthquake

PIII: capability of keeping the entire structure system in place without collapse after being hit by an earthquake

Damage of members

Damage level 1: No damage

Damage level 2: damage that may require repair depending on the situation

Damage level 3: damage requiring repair

Damage level 4: damage requiring repair and, depending on the situation, replacement of members

Stability of foundation

Stability level 1: no damage

Stability level 2: damage requiring repair depending on the situation

Stability level 3: damage requiring repair and, depending on situation, correction of the structure

Fig. 2 Relationships among earthquake resistance performance for bridges and viaducts, the damage level of members, and the stability level of the foundation

4.2 Principle of the damage level of members and stability level of the foundation and their limited values

It is considered appropriate to determine the damage level of members by considering the characteristics of the members, damage, and repair methods and in terms of a relationship with displacement on an envelope of the load-displacement curve. Take reinforced concrete member for example. It maybe set as follows:

In case failure mode precedes bending under action of general axial compressive force, the envelope of the load-displacement curve of a member in question is drawn as in Fig. 3. Certain physical phenomena, as shown in the figure, occur at changing points of the envelope. Considering this, each damage level may be determined as follows: displacement up to Point B for damage level 1, up to Point C for damage level 2, up to Point D for damage level 3, and after Point D for damage level 4. Once the relationship between damage level and displacement is established, displacement may be a good check item if displacement of a member is directly calculated by analysis. Examples of repair methods corresponding to these damage levels are shown in Table 1.

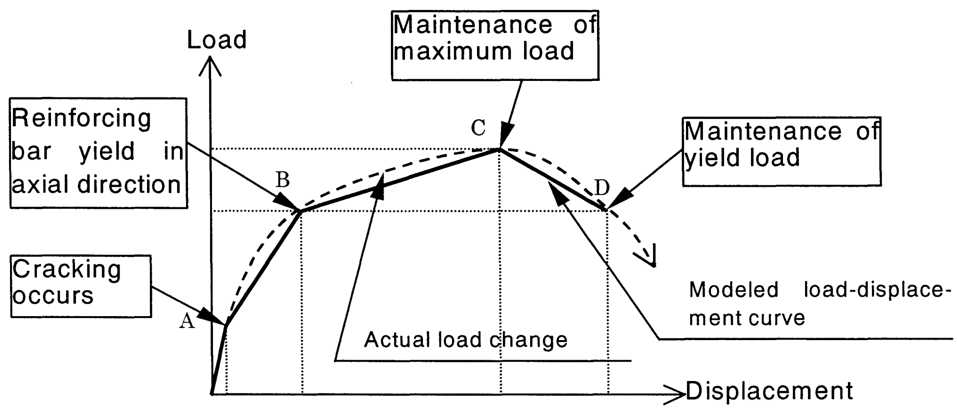

Fig. 3 Envelope of load-displacement curve for reinforced concrete members (under low axial force)

Table 1 Examples of repair methods by damage level for reinforced concrete and steel reinforced concrete members

	Damage level	Example of repair method
Damage level 1	No damage	No repair (may need to consider durability where necessary)
Damage level 2	Damage that may require repair depending on the situation	Filling of cracks and repair of sections wherever necessary
Damage level 3	Damage requiring repair	Filling of cracks and repair of sections. Hoops may require adjustment if necessary.
Damage level 4	Damage requiring repair and, depending on situation, change of members	• Filling of cracks, repair of sections, or correction of hoops • If rebar in the axial direction or steel is badly buckled, replacement of the damaged members may be necessary.

Determination of the stability level of the foundation requires identification of damage to the foundation in terms of bearing power and damage of its members. Damage to members should be determined as earlier mentioned. Damage level concerning stability should be determined by considering the effect of displacement of the foundation on usage of the structure and the level of bearing power of the foundation after the earthquake.

As indexes for that purpose, residual displacement and response plasticity rate of the foundation should be used. The latter is defined as the ratio of the foundation's response displacement at the time of the quake to yield displacement as calculated by the load-displacement curve of the foundation. Fig. 4 illustrates a simplified model of the load-displacement curve of the foundation.

Since the yield point in the calculation of displacement occurs by yield of the bearing ground or yield of members, these two, therefore, were put together to determine stability levels. Using those indexes, stability levels may be set as follows:

1) Stability level: In principle, load acting on the foundation should be less than its yield bearing capacity and no major displacement occur. Sectional force of members composing the foundation should exceed yield bearing capacity.

2) Stability level 2: Either bearing ground, members or both should have plasticity but yet maintain sufficient bearing power. No displacement detrimental to the maintenance of the structure's functions nor residual displacement should occur after the earthquake.

3) Stability level 3: Sufficient bearing power should be maintained to protect the structure from collapse by damage of the bearing ground or members.

Repair methods that may be applied to these stability levels are shown in Table 2. Damaged parts of a rigid frame viaduct, assumed based on the concept explained above, are illustrated in Fig. 5. Relationships between earthquake resistance performance of those damaged parts and damage levels of members or stability levels of the foundation are shown in Table 3 for limiting value guidelines.

Table2 Examples of repair methods by stability level

	Damage level	Suggested repair method
Stability level 1	• No damage • Action load less than yield bearing power	No repair
Stability level 2	Damage requiring repair depending on situation	Filling may be necessary at voids at the footing and around the foundation depending on situation.
Stability level 3	Damage requiring repair or correction of structure depending on the situation	• Ground improvement • Reinforcement of the foundation by expanding the footing diameter or driving more piles

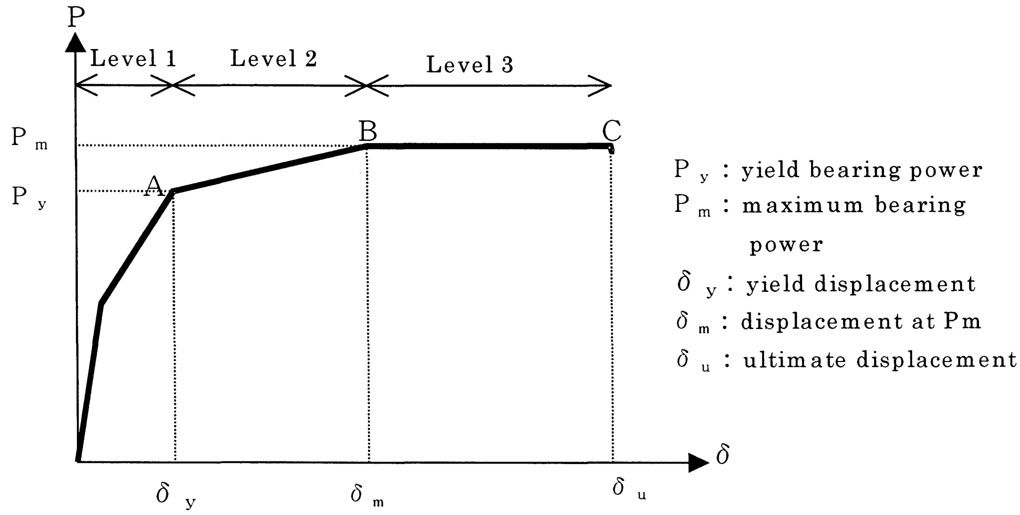

Fig. 4 Load-displacement curve of the foundation structure

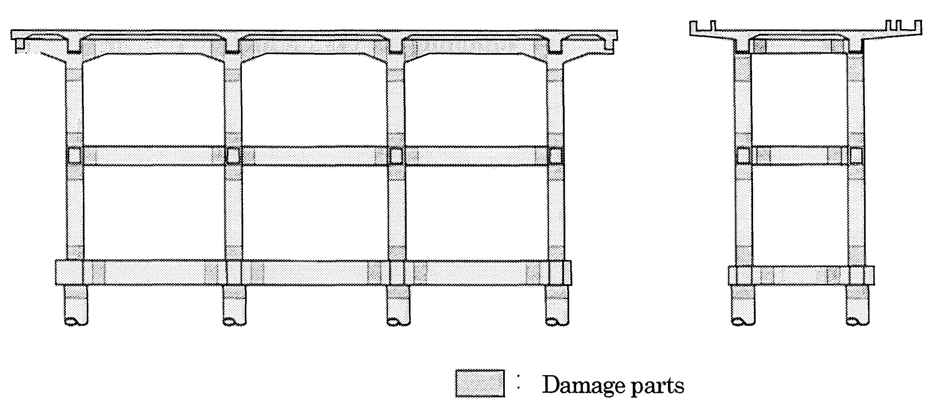

Fig. 5 damaged parts of a rigid frame viaduct

Table 3 Limiting value guidelines for earthquake resistance performance of a rigid frame viaduct, damage level of its members, and stability level of its foundation

Structure		PI	PII	PIII
Damage level of members	Superstructure girder and underground beam	1	2	3
	Other beams	1	3	4
	Columns	1	3	3
Stability level of foundation		1	2	3

4.3 Concept of degree of importance

Determination of the degree of importance of a railroad structure requires consideration of various factors, including possible influences of the damage level of the structure on human life, neighborhood, society, operation speed of trains and frequency of service, and the degree of difficulty of recovery in case of damage. Based on this concept, greater importance has been given to the following structures:

1) Structures of the Shinkansen bullet lines and those of passenger railroad lines in major big cities
2) Structures whose recovery is considered very difficult if the damage was done to cut tunnels, etc.

5. Evaluation of Surface Layer and Calculation of Displacement and Stress of Structures

L2 earthquake motions are given on the design foundation bed as earlier explained. Then, seismic design of a bridge should require response calculation of the subsurface layer using the earthquake motions of the foundation bed and evaluation of its earthquake resistance performance by inputting the said earthquake motions into the structure. In this case, since the earthquake motions are so large, both the ground layer and the structure are expected to show non-linear behavior. Therefore, evaluation of non-linearity of the ground layer and the structure is essential in seismic design.

5.1 Evaluation of subsurface layer

Characteristics of the subsurface layer must be carefully studied because the impact on earthquake resistance of the structure to be built is very great. Major methods to review the layer that requires sufficient care in earthquake resistant design of a structure are as follows:

(1) Irregular-shaped ground layer

According to past record, irregular shaped layers are known to cause serious earthquake damage due to resultant expansion of earthquake motions. An ideal method to evaluate such layers would be the finite element method. But

considering it is not a general design level, the incremental ratio of earthquake motions was calculated by ground response analysis and the results were already tabulated so that anybody can carry out appropriate calculation without difficulty.

(2) Liquefied ground layer

Liquefaction is a very serious factor to consider in seismic design. If any financially feasible measure is available, such as ground improvement that can stop liquefaction, it should be implemented. If not, the entire structure, including the superstructure, should be taken care of by comprehensive measures to prevent collapse or other disastrous damage against excessive response the structure may incur due to liquefaction or excessive displacement that the foundation may suffer due to ground subsidence or lateral flow.

In our method, judgment on whether the ground causes liquefaction or not when a major earthquake occurs is made using a conventional method that uses liquefaction resistivity. For the ratio of reinforcement against liquefaction required for that method, accumulated damage theory should be applied to adjust for the irregularity of the earthquake motions. The relationship between the ratio of reinforcement against liquefaction and the repetition time was corrected by the size of relative density, thereby totally improving calculation precision.

The Hyogoken-Nambu Earthquake caused lateral flow of the ground due to liquefaction that brought about serious damage. Learning from this lesson, it was decided to consider possible impacts of lateral flow into our design method. To evaluate such impacts, displacement of the ground that may cause lateral flow is assumed, and the assumed displacement is caused to act on the structure via coefficient of subgrade reaction, which follows the procedure same as that of the conventional response displacement methods.

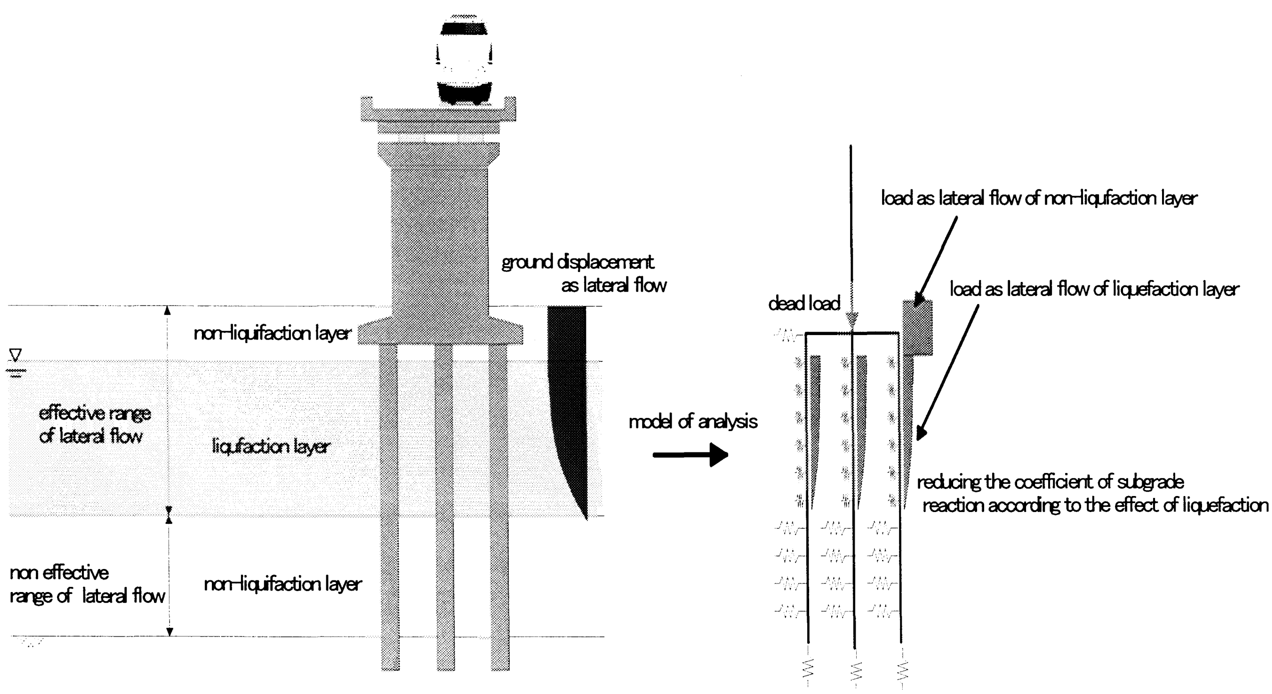

Fig.6 Calculation model of response of structures for lateral flow

(3) Soft ground layer

Soft ground amplifies earthquake motions in its fragile subsurface, causes great displacement and consequently may damage the pile foundation. This must therefore be considered for foundations in ground that is likely to cause large displacements. Displacement in this case may be calculated from earthquake response analysis of the subsurface layer. However, to simplify actual design procedure, natural frequencies of the ground were tabulated by the type of earthquake motion so that displacement can be easily and quickly calculated.

5.2 Calculation of responses of structures

Dynamic analysis should be the main method for seismic design of bridges. For a general structure, hysteresis properties of the structure may be determined in advance and responses can be calculated by using non-linear response spectra (strength demand spectra) obtained by dynamic analysis. In our standard, this method is referred to as the non-linear spectrum method. Strength demand spectra are the relationships between the yield seismic coefficient of a structure and the natural frequency of that structure expressed per response ductility factor. If yield seismic coefficient of a structure and its natural frequency (frequency for which the gradient of a line linking the origin and the yield point on the load-displacement curve of the structure is obtained as rigidity of the structure) are known, response plasticity rate of the structure when it is hit by an earthquake (response displacement) will easily be calculated.

For such structures as multiple-spanned bridges, structures with long frequencies, or new types of bridges whose behavior cannot be expressed in a system of only a single degree of freedom, dynamic analysis using a model of a system with multiple degrees of freedom should be used.

Foundation structures should also be designed using responses (mainly effects of inertial force of the superstructure). In case the foundation rests in soft ground layer which causes post-earthquake displacement beyond negligible levels, such effect should be considered. This method was already employed as the response displacement method in conventional design approaches. In our standard, the combinations of effects of inertial force of the superstructure and the degree of effect of ground displacement should be caused to change according to the relationship between the natural frequency of the structure and that of the ground in order to design structures in a cost-effective way.

6. Safety Checking (Earthquake Resistance Performance) of Structures

In checking earthquake resistance performance of a structure, our proposed procedure specifies that responses calculated as in Section 5 satisfy limiting values of the damage level of members and those of the stability level of the foundation, both mentioned in Section 4. This process is based on advance understanding of the relationship between displacement of the structure and the damage levels, which can be known by static non-linear analysis (push-over analysis). This means earthquake resistance performance of a structure should be checked by comparing deformation of the structure calculated by this static non-linear analysis with that by dynamic analysis. This analysis, however, generally requires treatment of the superstructure and the foundation as a single body. Since the accuracy of soil properties is usually lower than that of structures and smaller of soil is proposed in the standard ,the safety of the structures may be overestimated under seismic load. To avoid this, the verification is also carried out when the strength of soil doubled.

6.1 Check of damage levels of members

In checking damage levels of reinforced concrete and steel reinforced concrete members, the first step is judging the type of failure. In other words, bending failure mode should be used when shear force as members reach bending bearing capacity, is smaller than design shear bearing capacity and shear failure mode be used when it is larger.

For cases where bending failure mode is used, it should be confirmed that deformation of members does not exceed the limiting value of the damage level that corresponds with the earthquake resistance performance. For the use of shear failure mode, exceeding of shear bearing capacity beyond response is a required prerequisite.

6.2 Limiting value of stability level of the foundation

For stability level of the foundation, the following must be checked:

1) Response plasticity rate of the foundation
2) Damage level of foundation members

The method specified in 6.1 should be used for (2) above. For (1), the prerequisite is that responses of the structure do not exceed limiting values of plasticity rate that correspond with earthquake resistance performance calculated by static non-linear analysis.

7. Conclusion

This paper outlines our proposed earthquake resistance design standard. A good seismic design requires techniques to calculate deformation or stress and to check that the calculations can explain past earthquake damage with good precision. Development of our method discussed here was also partly based on damage analysis of the Hyogoken-Nambu Earthquake. Since damage of this disastrous earthquake are still being vigorously analyzed by various research institutes, more new findings are expected to come. It is therefore our responsibility to assimilate any such new findings for improvement of our design approach.

As non-linearity of structures and grounds need to be considered, our design method has become very complicated. Although complexity is not always justified, those complexities explained herein are all assimilated into our method as necessary steps to express the degrees of damage to the structure. This, we believe, enables us to show that a structure will suffer the degree of damage corresponding to its earthquake resistance performance when a major earthquake hits, rather than simply saying that a structure should remain unscathed.

Calculation, however, is generally done by computers, to which all design parameters and values on the ground, structural members, etc., are manually input. Care must therefore be taken in this manual work. Effort must also be made on further improvement of precision. It is a good that design calculation precision and quality is enhanced by computer, but one should note that no good design comes out of input of incorrect data.

REFERENCE

1. Akihiko Nishimura: "Earthquake resistant design for Railway Structures" , Quarterly Report of R.T.R.I , Vol.37, No.3 , pp.128-138, 1996

VISUAL INTERPRETATION OF SITE DYNAMIC RESPONSE

Mourad Zeghal, Caglar Oskay, Michael Keith Sharp, and Ricardo Dobry

Department of Civil Engineering
Rensselaer Polytechnic Institute
Troy, New York 12180

ABSTRACT

The dynamic response of site and infinite slope models tested in laminated centrifuge containers are commonly monitored at selected locations along the model height. These records provide valuable information but do not reflect the full soil system dynamic response.

In this paper, the recorded acceleration and displacement time histories are employed to reconstitute the motion and strain fields, and to develop a visual animation of the shaking. The response animation of a dense-sand infinite slope saturated with a viscous fluid showed: (1) a motion lag between soil columns adjacent to the laminar box and at the central zone of the box following liquifaction, and (2) a shear strain concentration within the lowermost layer of the liquefied soil strata.

INTRODUCTION

Most major pipeline failures in the city of San Fransisco during the 1906 earthquake occurred in the area affected by lateral spreading (Youd 1978). Recent earthquakes such as the 1989 Loma Prieta and 1995 Hyogoken-Nanbu events showed extensive damage to roads, canals, buried pipelines and building foundations associated with lateral spreading. In fact, liquefaction induced spreading caused billions of dollars damage in 1995 Kobe earthquake (Bardet *et al.* 1995). Nevertheless, the mechanisms of liquefaction induced lateral spreading, and associated subsurface deformation and strains are still not fully understood.

Lateral spreading is commonly documented in terms of ground surface permanent displacements at the end of shaking. In situ recordings of permanent displacement time histories as a function of depth are scarce, if not nonexistant. Centrifuge model testing provide an important alternative to assess lateral spreading mechanisms. This is especially true when tests are conducted in a laminar box, and lateral motions are monitored with LVDT's (Linear Variable Differential Transducers) in addition to accelerometers. A comprehensive suite of well instrumented infinite slope centrifuge models were tested at Rensselaer Polytechnic Institute (RPI). These tests provided a wealth of information on the associated mechanisms of liquefaction triggering and lateral spreading (Sharp 1999).

Zeghal *et al.* 1999, Elgamal *et al.* 1996 used acceleration and displacement recordings of centrifuge tests to evaluate point-wise local estimates of shear strains. These estimates emphasize local details and there is a possibility of missing some global response mechanisms. This paper is aimed at reconstituting the time history of soil system displacement and shear strain fields (as a function of depth). Visual animation of the identified lateral motion fields are then employed in interpretation and analysis of the observed response. The proposed approach represents a logical and simple extension of the point-wise shear strain estimates mentioned above.

Analyses of the dynamic response of a mildly sloping saturated sandy site showed shear concentration at the interface between the liquefied top soil strata and the underlying layer. A visual animation of the deformation time history revealed a slight phase lag between soil columns adjacent to the laminar box and those in the central zone of the box following liquefaction, and showed a progressive isolation of thickening top soil strata. In the following sections, a brief description of the analyzed centrifuge model test is given. Thereafter, the employed identification procedure is described. Finally, results of the conducted analysis are discussed.

SOIL PROPERTIES AND CENTRIFUGE MODEL DESCRIPTION

A suite of centrifuge tests were conducted at RPI using a laminar box and a Nevada sand at a 75% relative density. The laminar box was inclined 2^0 to the horizontal to simulate an infinite slope in free field conditions. Allowing for corrections to address

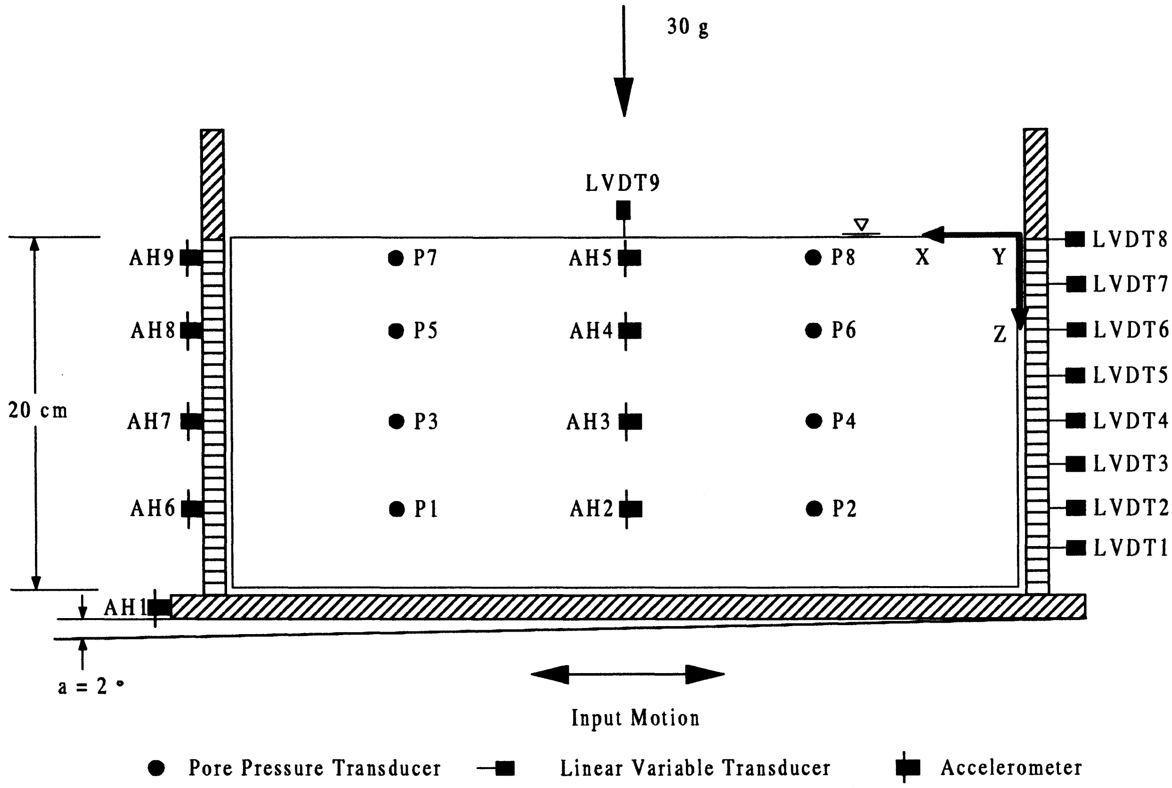

Figure 1: Setup and Instrumentation for the centrifuge test.

the effects of lateral inertia and weight of the rings as well as water level (Taboada 1995), this model inclination becomes a 4.8^0 prototype angle (Sharp 1999). A viscous fluid (Methocel) was employed to mimic real life permeability. Fig. 1 displays a sketch of the test setup. The soil system response was monitored with a series of accelerometers (within the soil and on the laminar box), LVDT's and pore pressure transducers. The model was excited parallel to the base of the laminar box with 2 Hz input signal (prototype frequency). The recorded horizontal accelerations in the soil layer and on the laminar box, excess pore pressures in the soil layer, and lateral displacement of the rings at various elevations are shown in Figs. 2-4.

EVALUATION OF SHEAR STRAIN AND DISPLACEMENT FIELDS

Using a simple shear beam model to represent the dynamic response of an infinite slope, Zeghal *et al.* (1999) and Elgamal *et al.* (1996) proposed a simple identification procedure to evaluate shear strains. Point-wise, second order accurate strain estimates at the locations of the accelerometers (level z_i) and halfway in between (level $(z_{i-1} + z_i)/2$) were evaluated using:

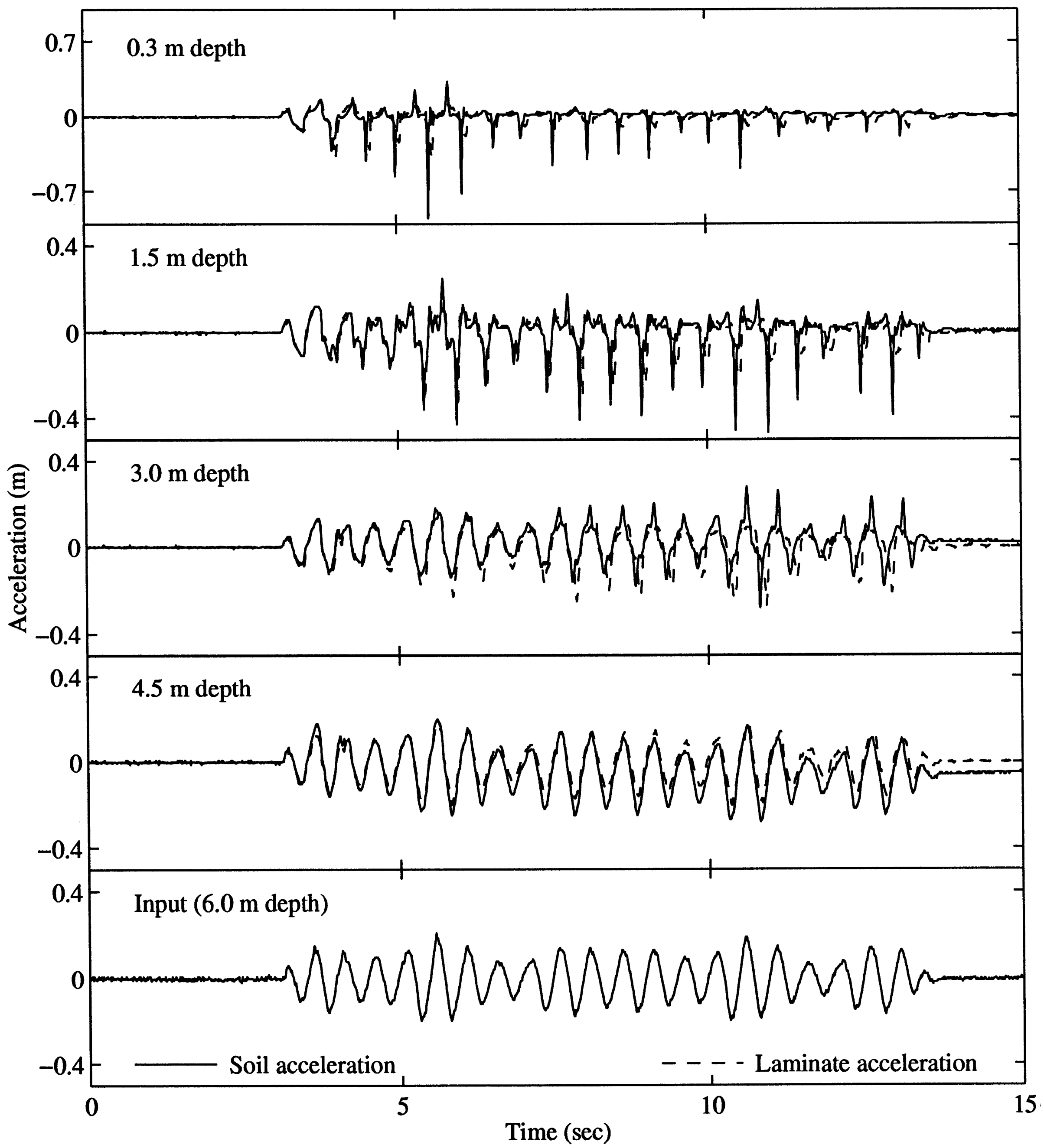

Figure 2: Acceleration time histories.

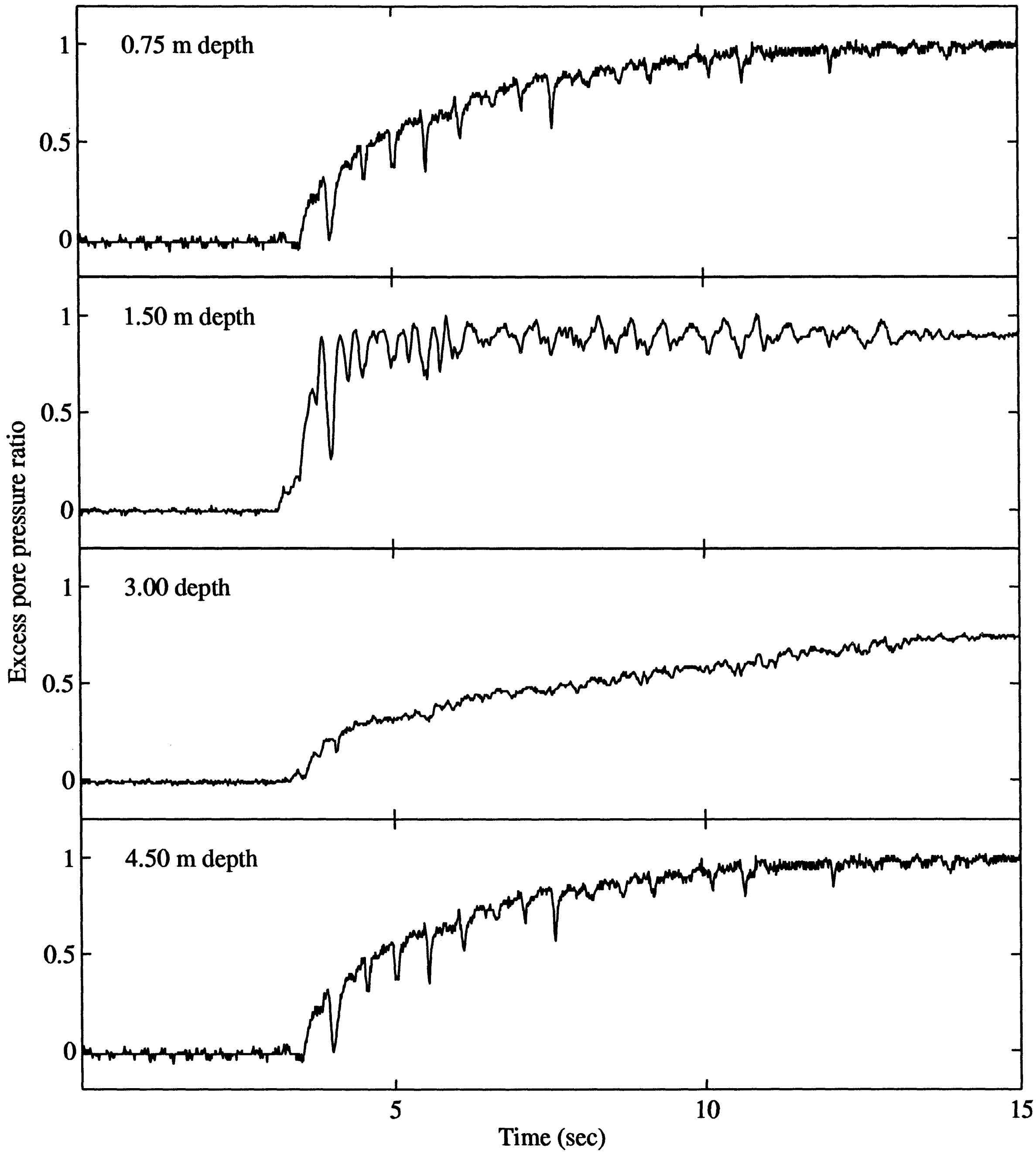

Figure 3: Excess pore pressure ratio time histories.

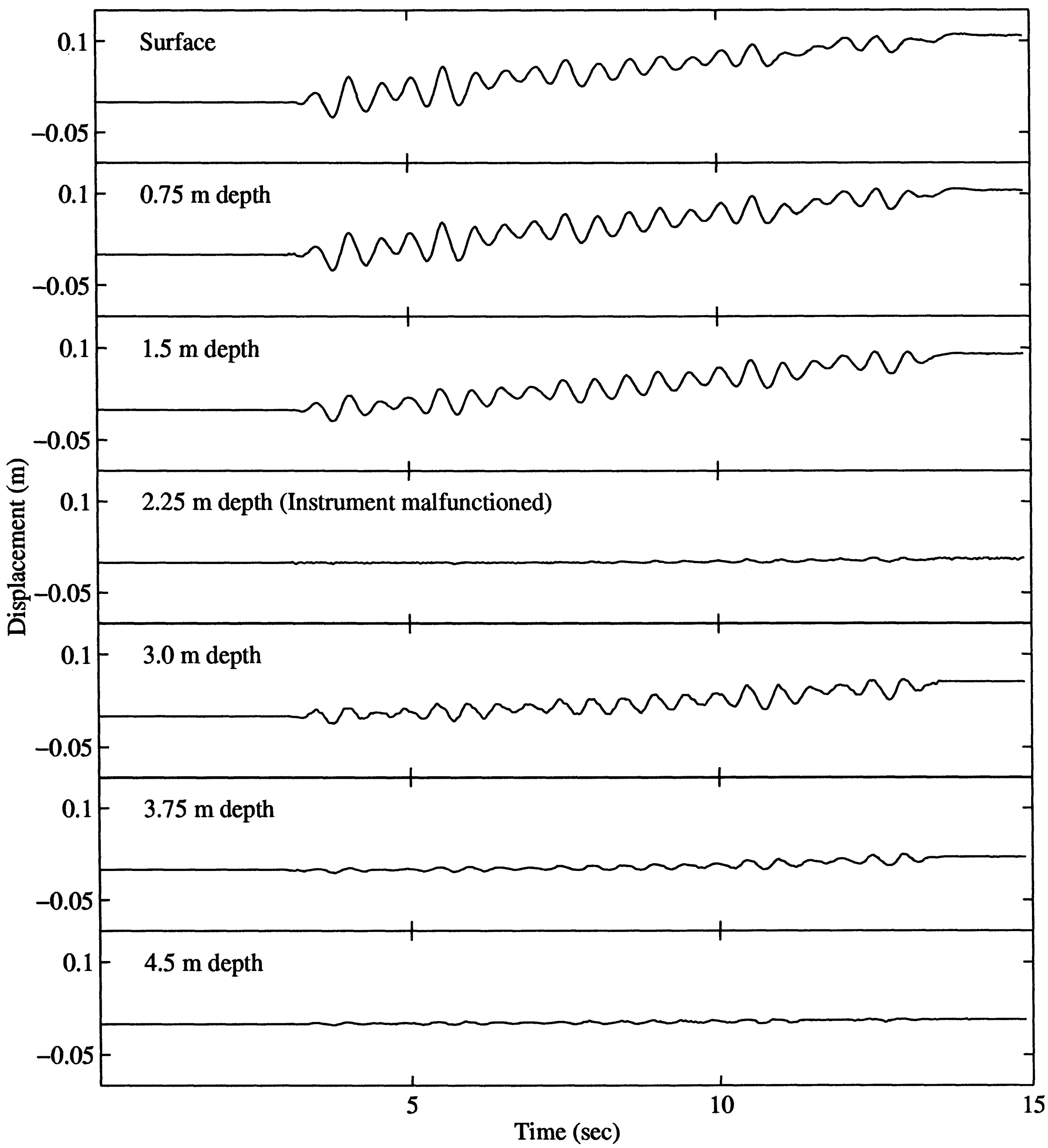

Figure 4: Displacement time histories.

$$\gamma_i(t) = \frac{1}{\Delta z_{i-1} + \Delta z_i}\left((u_{i+1} - u_i)\frac{\Delta z_{i-1}}{\Delta z_i} + (u_i - u_{i-1})\frac{\Delta z_i}{\Delta z_{i-1}}\right), \quad i = 2, 3, .. \tag{1}$$

$$\gamma_{i-1/2}(t) = \frac{u_i - u_{i-1}}{\Delta z_{i-1}}, \quad i = 2, 3, \ldots \tag{2}$$

in which $u_i = u(z_i, t)$ are either displacements furnished by LVDT recordings, or absolute displacements evaluated through double integration of the corresponding acceleration histories, and Δz_i are spacing interval between accelerometers. This approach provides valuable information, but fails to capture the dynamic nature of the vertical seismic propagation.

This paper proposes an alternative technique to evaluate the lateral motion profile of a soil system in a laminar box on the basis of a global spectral decomposition. The time history of the displacement field is expressed as :

$$u(z, t) = \sum_{i=1}^{n} \alpha_i(t)\phi_i(z) \tag{3}$$

in which ϕ_i are a complete set of shape functions that satisfy the soil system kinematic boundary conditions, α_i are generalized coordinates in the space of shape functions, and n is the number of functions used. Commonly, the soil system linear mode shapes are well suited to such decomposition as they introduce the least kinematic constraints. Furthermore, the seismic response of soil systems is often narrow banded, and only few shape functions are needed to accurately represent the displacement field. Note that the use of linear shape functions does not imply a linear behavior, as these functions are used only in a spectral decomposition. In this decomposition, nonlinearities in system response are reflected in the generalized coordinates, α_i. These coordinates are to be evaluated using the recorded motion, and thus only a limited number of shape functions may be used (to avoid aliasing errors, Oppenheim 1989). In this study, these coordinates were evaluated using a simple least squares optimization (Bard 1974) to minimize errors between the recorded motion and the spectral decomposition prediction (Eq. 3).

ANALYSIS OF AN INFINITE SLOPE DYNAMIC RESPONSE

Cross-correlation analysis of the recorded accelerations, along with results of miniature in-flight cone penetration tests of the infinite slope soil system (as shown in Fig. 5), suggested a shear wave velocity profile proportional to z^p (with $p = 0.33$ and z being the depth coordinate). The spectral decomposition of the displacement field of the soil system using a shear beam model and the corresponding mode shapes (Dobry *et al.* 1971) is then given by:

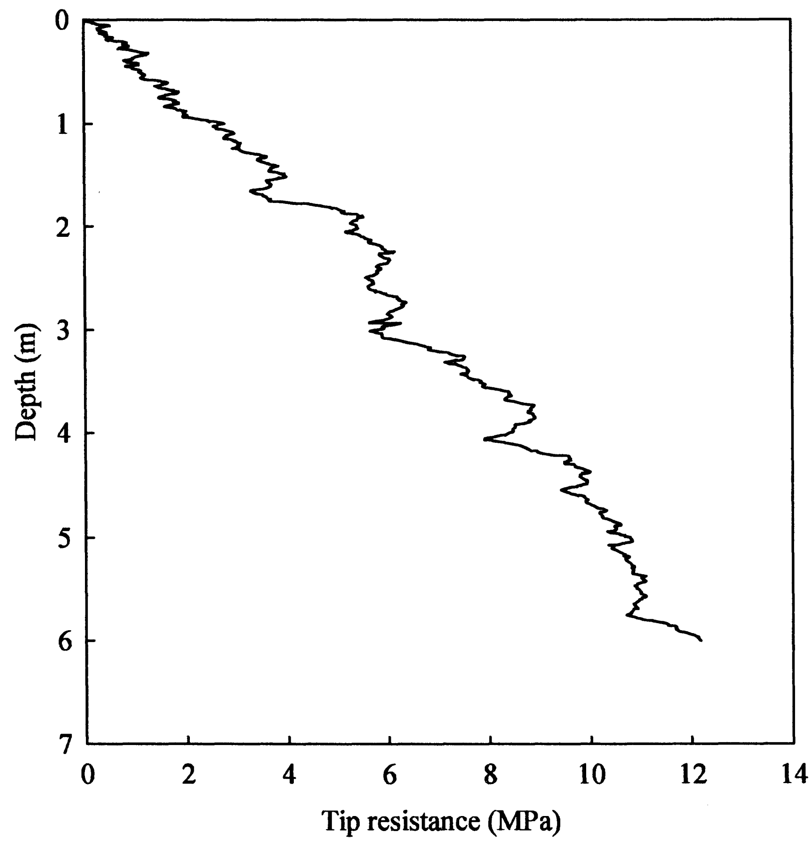

Figure 5: Representative in-flight cone penetration test results (Sharp 1999).

$$u(z,t) = \sum_{i=1}^{n} \alpha_i(t) \left(\frac{z}{H}\right)^{\frac{1}{2}-p} J_{-\frac{1-2p}{2(1-p)}} \left(r_i \left(\frac{z}{H}\right)^{1-p}\right) \tag{4}$$

The corresponding strain field reduces to:

$$\gamma(z,t) = -\sum_{i=1}^{n} \alpha_i(t)(1-p) \left(\frac{r_i}{H}\right) \left(\frac{z}{H}\right)^{\frac{1}{2}-p} J_{\frac{1}{2(1-p)}} \left(r_i \left(\frac{z}{H}\right)^{1-p}\right) \tag{5}$$

where J_q refers to the first kind Bessel function of the q^{th} order. The roots of the frequency equation, $J_{-\frac{1-2n}{2(1-n)}}(r) = 0$, define r_i.

Figs. 6 and 7 display the cyclic and plastic (permanent) components of the displacement field for selected instants as evaluated using the spectral decomposition, along with the measured motions. These displacements were evaluated using 4 shape functions and closely matched the motion recorded by the installed accelerometers and LVDT's. The associated strain field profile was found to be in a reasonable agreement with the point estimates (Zeghal and Elgamal 1993), as shown in Fig. 8. This profile showed that the largest strains occurred at the interface between the liquefied top strata and the underlying soil layer.

The identified displacement field was employed to develop a visual animation of the soil-laminar box system. Separate animations were developed for soil columns adjacent to the laminar box and at the central zone of the box. Fig. 8 exhibits a suite of snapshots of the identified motions (the lateral motion was exaggerated for visual clarity). A slight phase lag is seen to appear after liquefaction of the uppermost layers, along with strain concentration at the interface between the liquefied strata and the underlying soil.

CONCLUSIONS

The recorded acceleration and displacements of an infinite slope centrifuge test were analyzed using a spectral decomposition. The evaluated soil displacement field indicated a progressive liquefaction mechanism during shaking and strain concentration at the interface between the liquefied soil strata and the underlying soil. The soil displacement field was also found to be slightly out of phase with that of the laminar box after the onset of liquefaction.

REFERENCES

Bard, Y. (1974). *Nonlinear Parameter Estimation,* Academic Press, New York.

Bardet, J. P., Oka, F., Sugito, M., and Yashima, A. (1995). "The Great Hanshin Earthquake Disaster," *Preliminary Investigation Report,* University of Southern California, Los Angeles, California.

Dobry, R., Whitman, R. V., and Roesset J. M. (1971). "Soil Properties and One-Dimensional Theory of Earthquake Amplification," *Research Report R71-18,* School of Engineering, Massachusetts Institute of Technology.

Elgamal, A.-W., Zeghal, M., Dobry, R., and Taboada, V. M. (1996). "Analysis of Site Liquefaction and Lateral Spreading Using Centrifuge Testing Records," *Soils and Foundations.* Vol. 36, June.

Oppeinheim, A. V. and Shafer, R. W. (1989). *Discrete-Time Signal Processing,* Prentice Hall, New Jersey.

Sharp, M. (1999). "Development of Prediction Charts for Liquefaction Induced Lateral Spreading from Cone Penetration Testing," *Ph.D. thesis,* Rensselaer Polytechnic Institute, Troy, New York.

Taboada, V. (1995). "Centrifuge Modeling of Earthquake Induced Lateral Spreading in Sand Using a Laminar Box," *Ph.D. thesis,* Rensselaer Polytechnic Institute, Troy, New York.

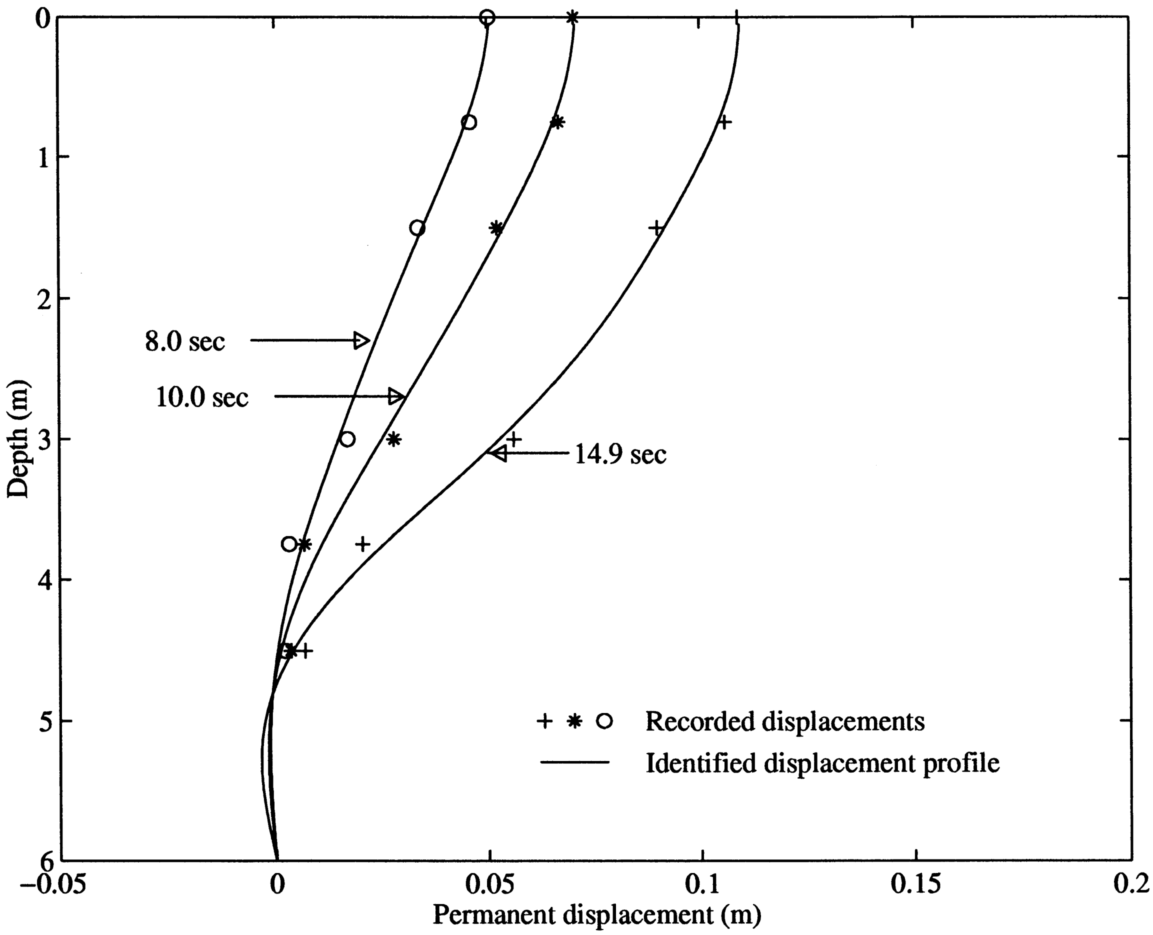

Figure 6: Profile of permanent lateral displacement for selected time instants.

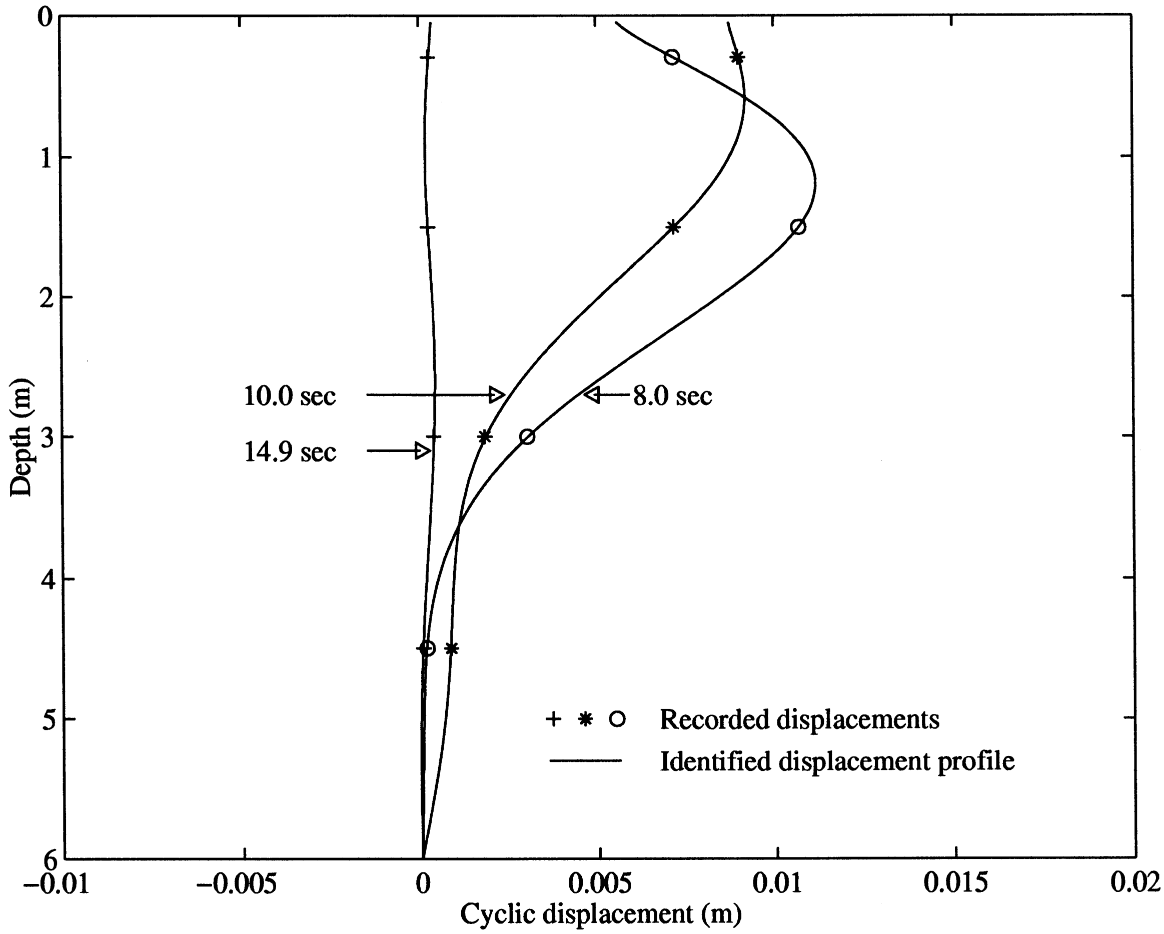

Figure 7: Profile of cyclic displacement for selected time instants.

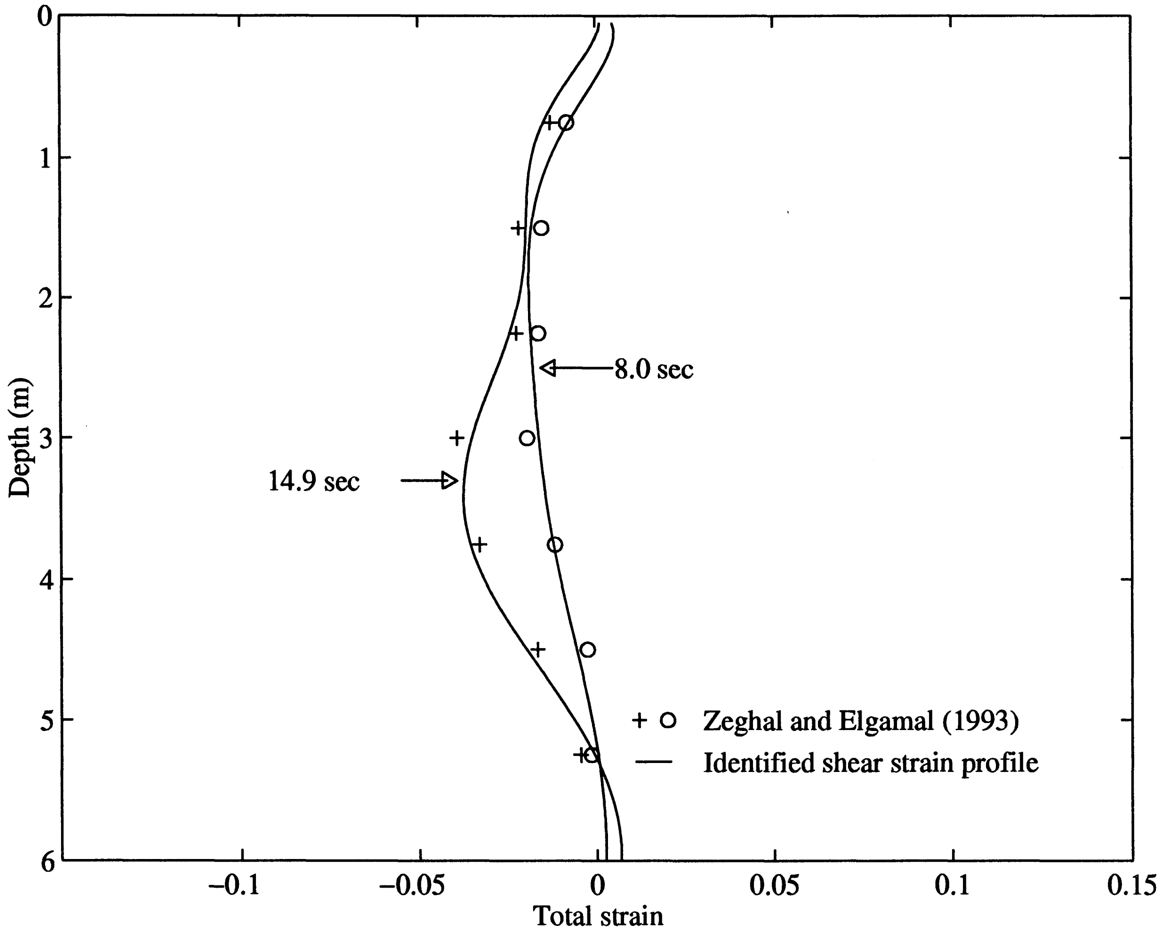

Figure 8: Profile of total strain (permanent and cyclic) for selected time instants.

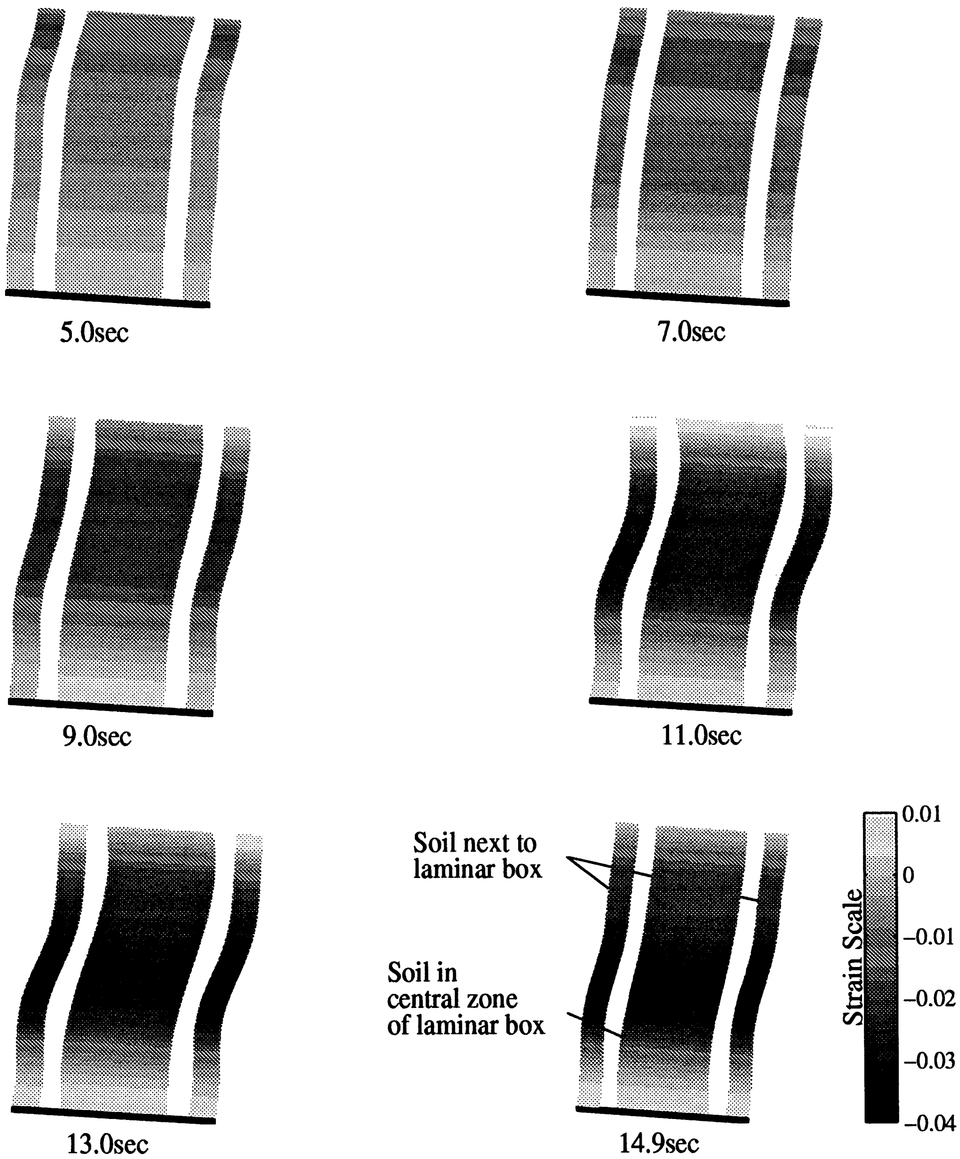

Figure 9: Snapshots of lateral motion animation.

Zeghal, M. and Elgamal, A.-W. (1993). "Lotung Site: Downhole Seismic Data Analysis", *a report submitted to the Electric Power Research Institute,* Department of Civil Engineering, Rensselaer Polytechnic Institute, Troy, NY.

Zeghal, M., Elgamal, A.-W., Tang, H. T., and Stepp J. C. (1995). "Lotung Downhole Array: Evaluation of Soil Nonlinear Properties," *Journal of Geotechnical Engineering* ASCE, Vol 121, No. 4, April.

Zeghal, M., Elgamal, A.-W. Zeng, X., and Arulmoli, K. (1999a). "Mechanisms of Liquefaction Response in Sand-Silt Dynamic Centrifuge Tests," *Soil Dynamics and Earthquake Engineering*, Vol. 18, No. 1, 71-85.

FORMULATION OF LEVEL 2 EARTHQUAKE MOTIONS FOR CIVIL ENGINEERING STRUCTURES

Tatsuo OHMACHI

Professor

Interdisciplinary Graduate School of Science and Engineering

Tokyo Institute of Technology

4259 Nagatsuta, Midori-ku, Yokohama, 226-8502 JAPAN

ABSTRACT

The Proposal issued by the Japan Society for Civil Engineers (JSCE) following the 1995 Hyogoken-nanbu earthquake requires to consider Level 2 (L2) motion in seismic design of civil engineering structures. The L2 motion addresses input motions of extremely high intensity like that experienced in Kobe city during the 1995 earthquake. Based on discussions in a task committee of JSCE, this paper describes about definitions and features of the motion, procedures to select scenario earthquakes followed by evaluation of the motion, and its lower bound.

INTRODUCTION

Following the 1995 Hogoken-nanbu earthquake, the Japan Society of Civil Engineers (JSCE) issued twice the "Proposal on Earthquake Resistance for Civil Engineering Structures[1)]"; the first in May, 1995, and the second in January, 1996. One of the requirements of the proposals is to consider two levels of input earthquake motion for seismic design of structures. Level 1 (L1) motion covers motions of moderately high intensity while Level 2 (L2) addresses motions of extremely high intensity of the nature of the strong motion experienced in Kobe city during the Hogoken-nanbu earthquake. The selection of the L1 and L2 motions is implicitly based on the expectation that the L1 motion will be experienced once or twice during the lifetime of the structure while the L2 motion has a very low probability of being experienced by the structure. The underlying design assumption is that the intensity of the L1 motion is comparable to the seismic loadings traditionally used in Japanese seismic codes for which structures are to remain within their elastic limits; for the L2 motion, structures are allowed to undergo plastic deformations as long as collapse and loss of life are prevented. For most Japanese seismic codes for civil engineering structures, the L2 motion is a new type of input earthquake motion to be considered in design. For this reason, in the above mentioned proposals, a main focus was placed on the L2 motion.

In Japan, L2 motion can most likely be caused by two types of earthquakes: interplate earthquakes occurring under the ocean and intraplate earthquakes associated with inland active faults. Regardless of the earthquake type and the difficulties associated with implementation, the proposal requires the L2 motion to be determined from the rupture process of the relevant faults affecting the structure considered.

As a whole, the concept of L2 motion as described in the proposals appears to be too general to be applied directly in design. For practical applications, more detailed guidelines are required for the estimation of the L2 motion, such as how to select scenario earthquakes and how to deal with the uncertainty inherent in the fault rupturing mechanism of future events. To respond to this need, a task committee formed by the JSCE two years ago clarified a number of these points. The committee's recommendations have been summarized in a recent report[2)].

This paper is based on work done by the JSCE committee on Level 2 Earthquake Motion. Any opinions, findings and conclusions or recommendations expressed in this paper are those of the author and do not necessarily reflect the views of the JSCE and the committee.

DEFINITIONS AND FEATURES OF THE L2 MOTION

In general, the concepts of intensity and probability of occurrence are not differentiated from one another when one refers to "level" in Level 2 Earthquake Motion. This tends to create some confusion considering the two types of earthquakes contributing to the L2 motion, i.e. interplate and intraplate events. These events have different return periods and different potential intensities. Intuitively one would expect long return period events to have higher intensities than shorter return period events. This is not necessarily the case for Japanese interplate and intraplate events. The interplate or subduction earthquakes of large magnitude have relatively short return periods (of the order of a few hundred years) while the intraplate earthquakes of moderate to large magnitude caused by active faults have very long return periods (of the order of thousand years). However, the more frequent interplate events are capable of more intense shaking than the longer return period intraplate events.

To eliminate this potential source of confusion, this paper refers to "level" as a measure of the intensity only and defines Level 2 Earthquake Motion as follows:

The Level 2 Earthquake Motion to be used as an input motion for the seismic design of a specific civil engineering structure is the maximum intensity earthquake motion to be reasonably possible at the site for the structure considered.

This definition for the L2 motion implies the following:

- L2 motion is dependent of the seismic environment and geology of the site, but is independent of social factors such as importance of the structure
- The L2 motion is a "so-called" source specific, site specific and structure specific motion.
- A preferred procedure to determine the L2 motion consists of selecting a set of scenario earthquakes based on the tectonic setting of the region, to evaluate the respective ground motions at the site taking into account the site soil characteristics and finally to select the most critical of these inputs based on the response of the structure considered.
- It is desirable to formulate the L2 motion from observed earthquake motions compatible with the points presented above by using a semi-empirical method
- A lower bound of L2 motion is given by moderate local earthquakes (about M_J 6.5) caused by blind faults, which are assumed to occur uniformly throughout Japan.

SELECTION OF SCENARIO EARTHQUAKES

A standard procedure to estimate L2 motion is shown in Fig. 1. The first step consists of selecting a set of realistic earthquakes that provide the greatest seismic threat to the structure. Taking into account all information available, one or more scenario earthquakes are selected by comparing intensity of ground motion resulting from every seismic source affecting the site under investigation. In this comparison process, empirical attenuation relationships are often used to estimate ground motion intensity in terms of peak acceleration, peak velocity, JMA seismic intensity or response spectrum.

In general, candidates for the scenario events are repeats of devastating historical earthquakes and potential large earthquakes on active faults. Hence, a large database containing in-depth information about active faults and historical earthquakes facilitates the selection of the scenarios to be considered. It should be noted that scenario earthquakes for a given structure may not be applicable to nearby structures if the structures have significantly different response characteristics. Accordingly, the structure's natural period is one key factor entering into the selection of the scenario earthquakes.

EVALUATION OF L2 MOTION FROM SCENARIO EARTHQUAKES

Once a set of scenario earthquakes has been selected, the L2 motion can be estimated by various methods. As shown in Fig. 1, these methods can roughly be classified into three groups: empirical, semi-empirical and theoretical. Since each of these methods have their own advantages and limitations, it is necessary to adapt them adequately. For example, at the present state, the empirical methods are applicable to a period range shorter than 1 or 2 sec, while the theoretical methods are applicable to the range longer than 1 or 2 sec. The semi-empirical methods [3], which use observed ground motion of small or medium size earthquakes are the most appropriate for the present purpose of L2 motion estimation. The main advantage of the semi-empirical methods is twofold: if properly applied, they appropriately reflect, without much effort, the wave propagation path and the local site effects of the L2 motion and they are adaptable to both the short and long period ranges. These methods however require observed earthquake motion at the site. Hence, the availability of a recorded earthquake motion at the site prior to the planning and design process greatly facilitates the L2 motion estimation.

In the absence of recorded time histories at the site, empirical or theoretical approaches can be used.
As long as a seismic source and the subsurface soil condition are given, the associated ground

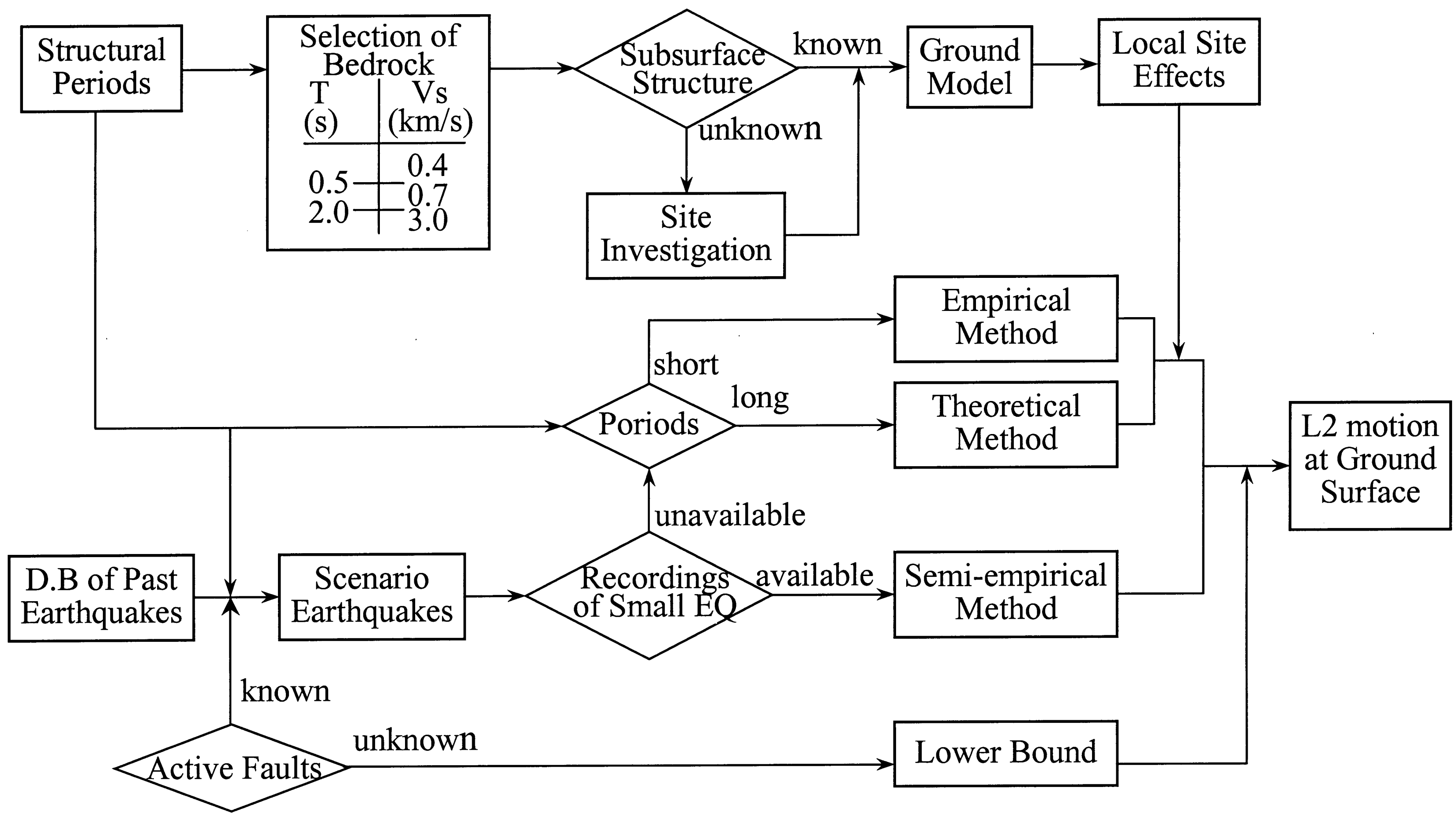

Fig.1 Flowchart to Formulate L2 Motion

motion for different periods can be evaluated to a satisfactory level of accuracy by numerical simulation. As an example of a numerical simulation[4] of the 1995 Hyogoken-nanbe earthquake using a 3-D boundary element method is shown in Figs. 2 and 3. In Fig. 2, a two-layered ground model used for the simulation is shown. The simulated area extends from the epicenter to Amagasaki and Takarazuka cities in the EW direction and from Rokko mountains to Osaka Bay in the NS direction. The source model presented by Ide et al.[5] was simplified and used in the simulation together with a source time function simplified as a ramp function having a rise time of 1.0 sec. The ground motion of periods longer than one second was simulated for comparison with the strong motion records. Comparisons of velocity time histories and their spectra at Kobe University for the NS, EW and vertical components are presented in Fig. 3. Some differences can be seen in the time histories, but inspection of the spectra indicates that they are mainly due to the shorter period components that were not considered in the simulation.

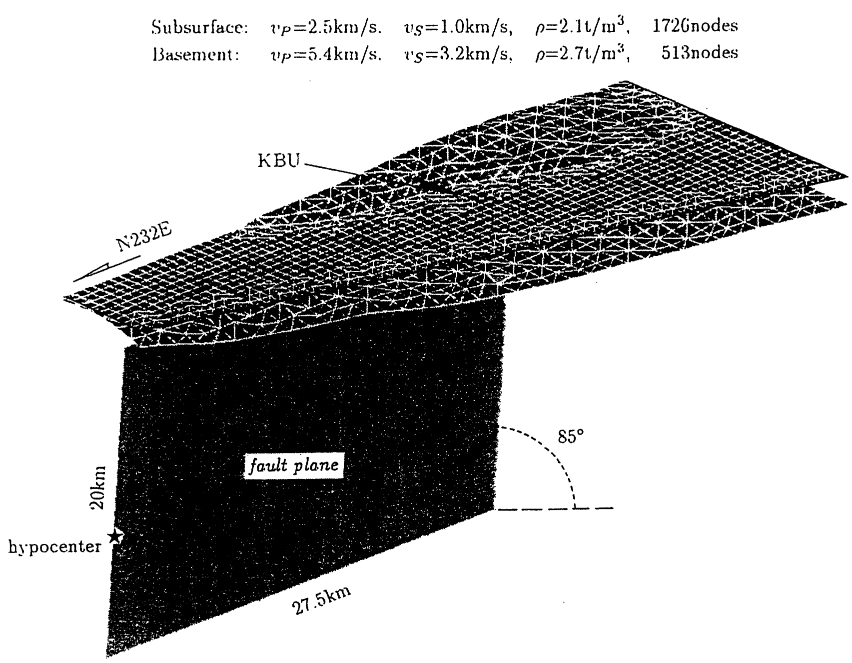

Fig.2 3-D numerical model to simulate the 1995 Hyogoken-nanbu earthquake[4]

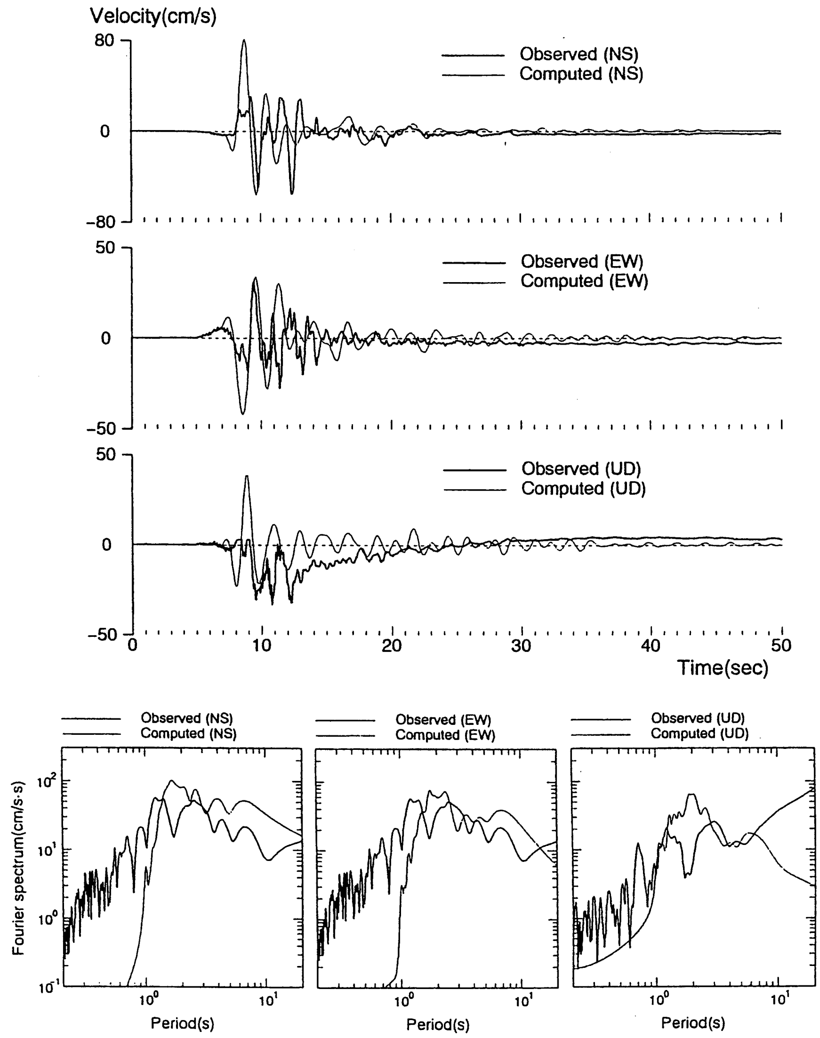

Fig. 3 Comparison of simulated and bserved strong motions at Kobe university [4)]

LOWER BOUND OF L2 MOTION

Uncertainty is inherent in the formulation of L2 motion. The uncertainty lies not only in the rupture process of future seismic faulting, but also in the location of active faults. As a matter of fact, present maps of active faults do not contain blind faults. However, inland earthquakes caused by blind faults have often affected various civil engineering structures.

In Fig .4 the solid short lines indicates the locations of the large active faults[6)] known as of today. As shown in Fig. 4, active faults are mapped mostly in the middle part of Japan, while shallow crustal events have occurred in many instances outside known fault zones. It seems safe to say that inland earthquakes are likely to occur anywhere in Japan, no matter whether they are caused by known active faults or blind faults.

Fig. 4 Distribution of active faults in Japan [6)]

In addition, according to recent studies [7)], inland earthquakes of magnitude M_J smaller than or equal to 6.5 are not likely to reveal their fault traces on the ground surface, even if the surface is not covered with sedimentary layers. On this basis an inland earthquakes of M_J 6.5 is thought to be a scenario earthquake that gives a lower bound for L2 motion. Trial calculations have shown that ground motion intensity produced by M_J 6.5 earthquakes is 6- on the JMA instrumental intensity scale for most part of Japan except for exposed hard rock sites. Similar calculation results are shown in Fig. 5 in terms of acceleration response spectra, for which a subsurface ground structure for Hanshin area shown in Table 1 was used with a vertical 10km × 10km seismic fault of either a strike-slip or a dip-slip type located variously. Judging from Fig. 5, the lower bound of the L2 motion is related to acceleration response of 1G at the ground surface in the period range of 0.1 ～1.0 sec, in which G denotes acceleration of gravity.

Table 1. Subsurface ground structure

Layer	S-wave velocity Vs(km/s)	P-wave velocity Vp(km/s)	Density ρ (t/m^3)	Q	Thickness (km)
1	0.35	1.6	1.7	15	0.20
2	0.55	1.8	1.8	25	0.30
3	1.00	2.5	2.1	35	0.50
4	3.20	5.40	2.6	37	----

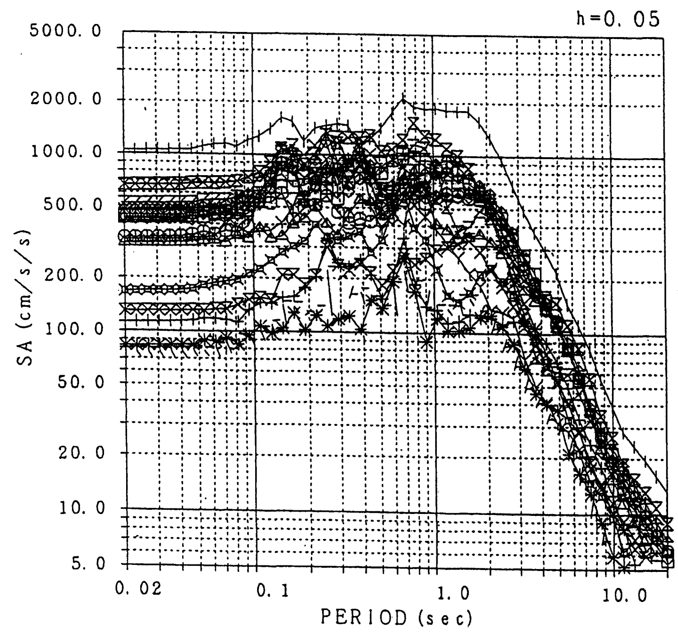

Fig. 5 Acceleration response spectra in near-field of M_J 6.5 earthquakes [2)]

CONCLUSIVE REMARKS

Since the JSCE Proposal was issued, various efforts have been made to facilitate practical application of the L2 motion. The efforts include detailed description about definitions and features of the motion, and a trial evaluation of its lower bound. In a word, the L2 motion is evaluated as a source-specific and site-specific motion. However, in designing a structure of less importance, a simplified procedure may be needed for practical application. In such a case, the lower bound of the L2 motion evaluated on a site-specific basis can be a substitute. This is because the L2 motion is much associated with the so-called performance-based design where the importance is taken into account in the structural performance under input earthquake motions, but not in evaluation of the motions.

There still remains much room for full implementation of the Proposal as regards:

1) The L2 motion should be described in terms of probability of occurrence in order to be widely used in the performance-based design.
2) Similarly, the L1 motion should be defined in a similar context as the L2 motion.
3) A subsurface ground structure extending to seismic bedrock should be explored throughout Japan as soon as possible.
4) Causes and effects of active faults should be studied from civil engineering points of view.
5) Rupture process of seismic faults should be characterized in detail to reduce uncertainty in evaluation of the L2 motion.

REFERENCES

1) Japan Society of Civil Engineers: Proposal on Earthquake Resistance for Civil Engineering Structures, 1996.
2) JSCE Working Group on L2 Motion: Level 2 Earthquake Motions, 1999. (in Japanese)
3) Irikura, K.: Prediction of Strong Acceleration Motion Using Empiricaol Green's Function, Proc. 7^{th} Jpn Earthq. Eng. Symp., pp.151-156, 1986.
4) Kataoka, S.: Simulation of the 1995 Hyogo-ken Nanbu Earthquake by a 3-D BEM, Technical Report No.54, Dept. of Civ. Eng., Tokyo Inst. Tech., pp.11-20, 1996.
5) Ide, S., Takeo, M. and Yoshida, Y.: Source Process of the 1995 Kobe Earthquake: Determination of spatio-Temporal Slip Distribution by Bayesian Modeling, Bull. Seism. Soc. Am., Vol.86, pp.547-566, 1996.
6) The research Group on Active Faults of Japan: Active Faults in Japan, rev. ed., University of Tokyo Press, 1991.
7) Takemura M.: Scaling Law for Japanese Intraplate Earthquakes in Special Relations to the Surface Faults and the Damages, Zisin (Jour. Seism. Soc. Jpn.) Vol. 51, No.2, pp.211-228, 1998.

Waterfront Structures, Pile Foundations and Buildings

Reliability and Redundancy of Engineering Systems by Information Entropy
By M. Hoshiya, K. Yamamoto, and H. Ohno

New Remedial Technique for Bridge Foundations Against Lateral Flow due to Liquefaction
By S. Mori and M. Terazawa

Centrifuge Modeling of Lateral Spreading Behind a Caisson Type Quay Wall During an Earthquake
By C-J. Lee, R. Dobry, T. Abdoun, and B-R. Wu

Residual Displacement of Gravity Quaywalls - Parameter Study Through Effective Stress Analysis
By S. Iai, K. Ichii, H. Sato, and H. Liu

Analysis on Liquefaction-Induced Subsidence of Shallow Foundation
By Y. Kobayashi, I. Towhata, and A. Acacio

Seismic Response Analysis of Pile Foundations at Liquefiable Sites
By W. D. L. Finn, T. Thavaraj, D. W. Wilson, R. W. Boulanger, and B. L. Kutter

Displacement Field of Granular Backfill Due to Earthquake Induced Quaywall Movement
By H. Akagi, K. Komiya, and H. Saitoh

Centrifuge Modeling of Effect of Superstructure Stiffness on Pile Bending Moments Due to Lateral Spreading
By R. Ramos, T. Abdoun, and R. Dobry

Applied Element Method: A New Efficient Tool for Design of Structure Considering its Failure Behavior
By K. Meguro and H. Tagel-Din

Reliability and Redundancy of Engineering Systems by Information Entropy

Masaru Hoshiya
Dept. of Civil Engineering, Musashi Institute of Technology
Kinya Yamamoto
and
Haruo Ohno
Dept. of Civil Engineering, Kogyokusha College of Technology

Abstract

Potential usefulness of information entropy is investigated for evaluating engineering systems' safety in terms of reliability, uncertainty and redundancy. The Shannon's information entropy(Khinchin(1957) and Kullback(1959)) can explain of not only a degree of uncertainties involved in systems, but also it can indicate a degree of inherent redundancy of systems. The entropy can gain comprehensively the insight into more than reliability.
First, a parallel system of consisting of four components subjected to a pullout loading is considered, where failure of a component does not necessarily mean the overall system failure and redistribution of the external force must be resisted by the remaining components. Sometimes, the redistribution may be repeated and as the result, a chain failure may occur. How to define the reliability and the reserve capacity or the redundancy after partial damages of such a system must be manifold and should be clearly stated to discuss the safety. Based on this example, a definition of a redundancy factor is proposed by the normalized entropy of a subsystem of various damage levels. It is made clear that this redundancy factor can quantitatively indicate the nature of reserve capacity. Another redundancy factor is also available, which is proposed by De, Karamchandani and Cornell(1989) and is the ratio of probability of system failure over the probability of any first component failure and the two redundancy factors are compared physically and numerically.
Second, a system of m components of ductile or brittle material is taken up to show how useful the proposed redundancy factor of this study is to evaluate system safety. The system reliability and the redundancy are discussed related with the system configuration, load redistribution after partial damages, material properties and uncertainty in the resistance and loading.
It is clear that the example models are simple prototypes of such systems as highly indeterminate structures and complicated networks of lifelines.

Introduction

Resurgence of and interest in system reliability have been highlighted after the Kobe earthquake, since not only building structures but also many lifeline facilities were damaged or destroyed.

Such systems are generally composed of many components and partial failure of some components does not necessarily lead to the overall system failure. Thus, rational evaluation of the safety is not easy, and the reliability and the reserve capacity of the system must be investigated after defining the physical interpretation. Actually, the issue on reliability and redundancy is not new and we must go back to the late sixties. To mention a few among many others, early time studies were carried out by Freudenthal and Shinozuka, et al(1966),Yao and Yeh(1969),Moses and Kinser(1967), Cornell (1967) and Hoshiya(1971) ,where they dealt with static problems and a system of consisting of many components were taken up as a basic model to discuss the reliability and redundancy. Recently, Wen et al(1999) proposed a framework for quantifying redundancy for a parallel system under dynamic loading.

This study focuses again on the classical parallel system in the sixties, but with the Shannon's information entropy as a tool to gain the insight and read more into the reliability and redundancy.

First, a parallel system of four components of stochastic resistances subjected to a stochastic pullout loading is studied, where failure of a component does not necessarily mean the overall system failure, and redistribution of the loading may be resisted by the remaining components. The repetitive redistribution may bring about a chain failure to the final collapse. The paths to the multiple component failures are various, and the reserve capacity from the first component failure to the final overall system failure where all components fail may be interpreted physically as a redundancy measure. Based on this example, a definition of a redundancy factor is proposed by the entropy of a subsystem of various damage levels reflecting the failure paths. It will be shown that the entropy which indicates a degree of uncertainty can be also a quantitative measure of redundancy. It is found that this redundancy factor is more meaningful than the redundancy factor defined by De, Karamchandani and Cornell(1989).

Second, a system of m components of ductile or brittle material is taken up to justify the definition. With the redundancy factor, the system reliability and the redundancy are discussed related with the system configuration, load redistribution after partial damages, material properties and uncertainty in the resistance and loading.

It is needless to say that the example models in this study are simple prototypes of such systems as highly indeterminate structures and complicated networks of lifelines.

Definition of Redundancy

Consider a parallel system of four components having stochastic resistances, which is subject to a stochastic pullout loading in Figure 1. If a component fails, the external load will be redistributed to the remaining components. Then ,should one of the components fail again, redistribution continues and may sometimes reach the failure of all components. This redistribution may stop at various intermediate stages. Therefore, the counting of all possible failure paths may remain a complicated procedure in order to find the probability of survival of some components, if the total number of components is large.

In order to discuss the redundancy, temporal results of probabilities of failure at different stages for five different systems of four components are shown in Table 1.

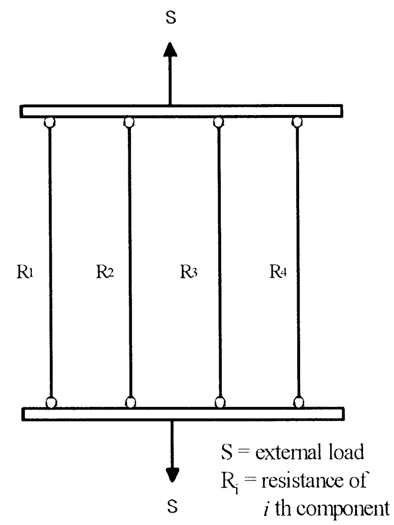

Figure 1 Redundant System

Table 1 Reliability and Redundancy Factor

System	A	B	C	D	E
$P(D_0)$	0.900	0.900	0.900	0.900	0.900
$P(D_1)$	0.090	0.050	0.020	0.025	0
$P(D_2)$	0	0.020	0.020	0.025	0
$P(D_3)$	0	0.020	0.050	0.025	0
$P(D_4)$	0.010	0.010	0.010	0.025	0.100
Reliability based on at least one component success $1-P(D_4)$	0.990	0.990	0.990	0.975	0.900
Probability of any first component failure $P_D = \sum_{i=1}^{4} P(D_i)$	0.100	0.100	0.100	0.100	0.100
Redundancy factor $R_R = \frac{P(D_4)}{P_D}$	0.1	0.1	0.1	0.25	1.0
Redundancy factor R_E	0.234	0.880	0.880	1.000	0

System A is found with the following probabilities. Probability of non component failure, $P(D_0)$ is 0.9, probability of only one component failure, $P(D_1)$ is 0.09, probabilities of two or three component failure, $P(D_2)$ and $P(D_3)$ are zero respectively, and probability of all four component failure, $P(D_4)$ is 0.01. The fact that the probability of two or three component failure is zero, but probability of all component failure is not zero means a chain failure occurrence. Here, it should be noted that D_i , i = 0 to 4 are mutually exclusive and collectively exhaustive. The probabilities shown for other systems may be read in the same way.

First, compare systems A and B. According to Wen, Wang and Song(1999) and De, Karamchandani and Cornell(1989), the redundancy of system is measured by the following redundancy factor.

$$R_R = \frac{P(\text{system failure})}{P(\text{any first component failure})} \tag{1}$$

$$= \frac{P(D_4)}{\{P(D_1) + P(D_2) + P(D_3) + P(D_4)\}} \tag{2}$$

where R_R is bounded between 0 and 1, and higher redundancy factor is indicated by a smaller system redundancy.

According to eq(2), both systems A and B have the same redundancy $R_R = 0.1$. However, if we take a careful look at probabilities of each path, we may find that the reserve capacity of system B is superior to that of system A, since the failure of more than one component in system A leads to a chain failure and thus to the overall collapse, whereas system B still remains safe even if two or three components fail.

In order to distinguish this difference, the following definition of redundancy factor is proposed. For a general system of consisting of m components, define the event D of system damage, or any first component failure, or say, one or more than one component failure, and the probability is like the denominator of eq(2) as

$$P_D = P(D) = P(D_1 \cup D_2 \cup \cdots \cup D_m)$$

$$= \sum_{i=1}^{m} P(D_i) \tag{3}$$

and the probability of failure of i components conditioned on the system damage is

$$P_{Di/D} = \frac{P(D_i)}{P_D} \tag{4}$$

Then the redundancy factor is defined by

$$R_E = \frac{-\sum_{i=1}^{m} P_{Di/D} \log_2(P_{Di/D})}{\log_2(m)} \tag{5}$$

In fact, this R_E is nothing but the normalized entropy of the subsystem of damage which shows the degree of uncertainty that the possible damage stages of the system involve, and the greater the value R_E is, the greater the uncertainty becomes. R_E takes zero to unity. It will be understood that this degree of uncertainty is equivalent to the degree of reserve capacity as shown in the next discussions.

Now, let us go back to the comparison between systems A and B. The two systems have the same reliability of 0.90 based on non component failure or the reliability of 0.99 based on at least one component success and the same redundancy factor $R_R = 0.1$. Are they equal in the light of safety ? The answer is no, if the redundancy factor R_E is compared with R_R. The system A is more inclined to a chain failure, and as the result, R_E of system A is 0.234 which is far smaller than 0,880 of system B.

Second, compare systems B and C. Since both R_R and R_E take the same values in this case, they have the same redundancy. This means that even R_E can not distinguish probabilities of different paths of damage, which is , however, less important as long as the reserve capacity is concerned.

Third, system D has a different reliability of 0.975 from those of systems A,B and C. Although simple comparison between them is not meaningful, system D has the same $P(D_i)$, i = 1 to 4 and takes the maximum redundancy factor of 1.0 which a system of four components can attain. It is noted that R_R of system D is 0.25 which means insufficient redundancy compared to those of systems A, B and C. This is a contradiction, since system D has obviously maximum redundancy at this reliability level , that is, R_R does not properly take into account the reserve capacity of the system.

Fourth, system E is the other extreme case and this system has zero of the redundancy factor R_E which is intuitively understood if we consider the probabilities of one to three components is zero and consequently the first component failure means immediately a chain failure and thus this system has no reserve capacity , that is $R_E = 0$. In system E, $R_R = 1.0$ and this value corresponds rightly to $R_E = 0$.

As a conclusion, the redundancy factor R_E defined by eq(5) can be an index to indicate reserve capacity of more general network systems or these sorts of structures. On the other hand, R_R has some limitation as demonstrated.

Redundancy of Systems of Brittle and Ductile Materials

Systems of different numbers of components, which are ductile or brittle, are analyzed by the Monte Carlo simulation. It is assumed that failed components of ductile systems still carry at least the maximum yielding capacities, whereas they are removed from the brittle systems, when failed. The external load S is lognormally distributed with the mean of 240 and the standard deviation of 60 commonly for every system. The component resistances are also lognormally distributed as indicated in Tables 2 and 3. The detailed procedure of the Monte Carlo simulation is described in the paper by Hoshiya(1971).

The following observations are obtained from the results in Tables 2 and 3, and in Figure 2.

(1) Material Properties(Ductile or Brittle)

The redundancy factor R_E of the ductile systems is always greater than R_E of the brittle systems irrespective of the number of components m. This is because the ductile material has greater reserve capacity than the brittle material.

(2) Number of Components(m)

When the number m of components increases, the redundancy factor R_E of the ductile systems decreases to almost a constant value. This may indicate the increase of m does not necessarily help strengthening the reserve capacity. On the other hand, the redundancy factor R_E of the brittle systems is lower and almost independent of the number of components, since chain failure is more frequent in the brittle systems and the redundancy is not affected by the number of components.

The fact that both the systems can not expect greater redundancy by simply increasing the number of components is already pointed out by many researchers in the late sixties and early seventies, and because of this main cause due to the effect of chain failure, Shinozuka called interestingly the systems " statically indeterminate, but statistically determinate systems in the past(from personal communication)".

Two faulty cases are pointed out below.

(1) Look at the ductile systems of fewer components. For example, in a case of m = 2, $P(D_1) = 0.03$ and $P(D_2) = 0.01$. Thus, the system having two damage events has $R_E = 0.8113$. If we should have reversibly $P(D_1) = 0.01$ and $P(D_2) = 0.03$, we still have the same R_E value of 0.8113. Obviously the reliability of 0.97 of the latter case is lower than the reliability of 0.99 of the former case.

(2) The redundancy factor R_R tends to decrease as the number of components m increases, both in the ductile and brittle systems. This means the redundancy will increase as m increases. Check, for example, the value of 0.0112 of R_R in the ductile system of sixteen components, which inconsistently indicates a very high redundancy.

Conclusively, R_R may be employed for a simple system of fewer components, but not a system of many components, whereas R_E may be employed for a system of many components having a chain failure potential except for a system of a few components.

Table 2 Failure Paths of Ductile System (2000 Trial)

	External Load LN(240,60)							
	Original system, m=							
	2	4	6	8	10	12	14	16
	Component resistance LN(,)*							
Probability of failure of components	(240,60)	(120,30)	(80,20)	(60,15)	(48,12)	(40,10)	(34.3,8.6)	(30,7.5)
0	0.9600	0.9290	0.9125	0.8945	0.8670	0.8590	0.8375	0.8220
1	0.0300	0.0490	0.0580	0.0705	0.0790	0.0805	0.0805	0.0915
2	0.0100	0.0130	0.0130	0.0240	0.0255	0.0330	0.0360	0.0375
3		0.0040	0.0080	0.0050	0.0125	0.0125	0.0170	0.0165
4		0.0050	0.0040	0.0025	0.0060	0.0055	0.0115	0.0095
5			0.0025	0.0010	0.0050	0.0045	0.0030	0.0095
6			0.0020	0.0010	0.0010	0.0015	0.0030	0.0030
7				0.0000	0.0010	0.0010	0.0025	0.0020
8				0.0015	0.0005	0.0005	0.0025	0.0030
9					0.0005	0	0	0.0010
10					0.0020	0.0005	0.0025	0.0005
11						0	0.0005	0.0010
12						0.0015	0	0
13							0.0010	0.0010
14							0.0025	0
15								0
16								0.0020
$P(D_0)$	0.9600	0.9290	0.9125	0.8945	0.8670	0.8590	0.8375	0.8220
$1-P(D_m)$	0.9900	0.9950	0.9980	0.9985	0.9980	0.9985	0.9975	0.9980
P_D	0.0400	0.0710	0.0875	0.1055	0.1330	0.1410	0.1625	0.1780
Redundancy factor R_R	0.2500	0.0704	0.0229	0.0142	0.0150	0.0106	0.0154	0.0112
Redundancy factor R_E	0.8113	0.6605	0.6159	0.4752	0.5603	0.5163	0.5907	0.5575

*coeficient of variation = 0.25

Table 3 Failure Paths of Brittle System (2000 Trial)

	External Load LN(240,60)							
	Original system, m=							
	2	4	6	8	10	12	14	16
	Component resistance LN(,)*							
Probability of failure of components	(240,60)	(120,30)	(80,20)	(60,15)	(48,12)	(40,10)	(34.3,8.6)	(30,7.5)
0	0.9600	0.9290	0.9125	0.8945	0.8670	0.8590	0.8375	0.8220
1	0.0030	0.0135	0.0240	0.0405	0.0490	0.0455	0.0515	0.0625
2	0.0370	0.0010	0.0035	0.0055	0.0075	0.0125	0.0150	0.0165
3		0	0.0005	0.0005	0.0015	0.0020	0.0015	0.0085
4		0.0565	0	0	0.0005	0.0015	0.0020	0.0030
5			0	0	0	0	0.0005	0.0010
6			0.0595	0	0	0.0005	0	0
7				0	0	0	0	0
8				0.0590	0	0	0	0
9					0	0	0	0
10					0.0745	0	0	0
11						0	0	0
12						0.0790	0	0
13							0	0
14							0.0920	0
15								0
16								0.0865
$P(D_0)$	0.9600	0.9290	0.9125	0.8945	0.8670	0.8590	0.8375	0.8220
$1-P(D_m)$	0.9630	0.9435	0.9405	0.9410	0.9255	0.9210	0.9080	0.9135
P_D	0.0400	0.0710	0.0875	0.1055	0.1330	0.1410	0.1625	0.1780
Redundancy factor R_R	0.9250	0.7958	0.6800	0.5592	0.5602	0.5603	0.5662	0.4860
Redundancy factor R_E	0.3843	0.4021	0.4327	0.4193	0.4023	0.4157	0.3870	0.4263

*coeficient of variation = 0.25

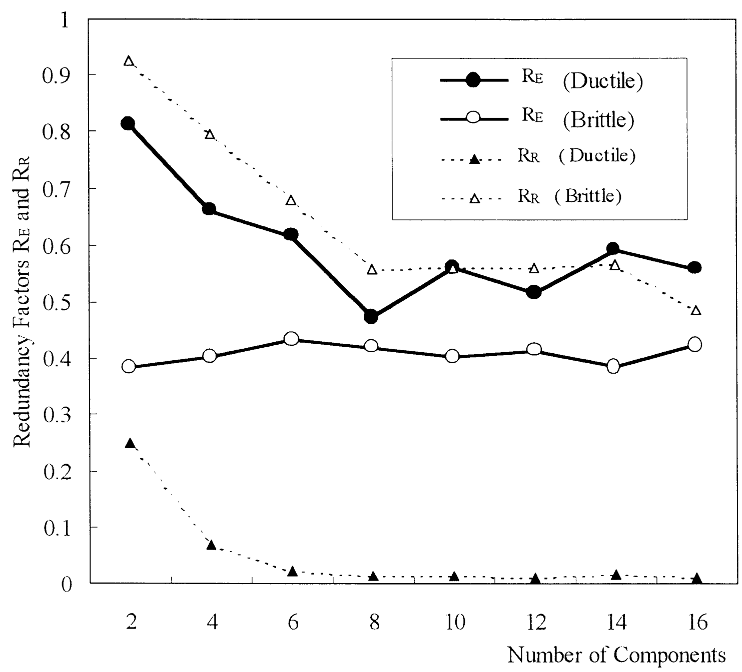

Figure 2 Redundancy Factors R_E and R_R

Concluding Remarks

(1) A redundancy factor R_E is proposed to gain the insight into and to evaluate the reliability and redundancy of systems of many components. R_E is defined by a normalized entropy of the damage subsystem D, and is expressed by equation(5).

(2) The redundancy factor R_E can be a good indicator to evaluate redundancy of systems which may be subject to a chain failure. Although the example model used is a simple parallel system, it is a simple prototype of statically indeterminate structures or lifeline networks.

(3) The redundancy factor R_E may play a major role in the following topics.

(a) evaluation of an optimal alternative of a lifeline network for earthquake damage mitigation.

(b) evaluation of the safety level requirements of current seismic design codes of structures.

(c) evaluation of repairing construction methods of damaged structures.

Finally, we should note that there are a series of study on usage of entropy to discuss system uncertainty by Ziha(1998,1999), where redundancy is analyzed by the relative uncertainty measures.

References

Cornell,C.A. 1967. Bounds of the Reliability of Structural Systems, Journal of Structural Division, ASCE, Feb.

De,R.S., Karamchandani,A. and Cornell,C.A. 1989. Study of Redundancy in Near-Ideal Parallel Structural Systems, 5th International Conference on Structual Safety and Reliability, 975-982

Freudenthal,A.M., Garrelts,J.M. and Shinozuka,M. 1966. The Analysis of Structural Safety, Journal of Structural Division, ASCE, Feb.

Hoshiya,M. 1971. Reliability of Redundant Cable System, Journal of Structural Division, ASCE, Nov.

Khinchin,A.I. 1957. Mathematical Foundations of Information Theory, Dover Publications, New York

Kullback,S. 1959. Information Theory and Statistics, Dover Publications, New York

Moses,F. and Kinser,D. E. 1967. Analysis of Structural Reliability, Journal of Structural Division, ASCE

Wen,Y.K., Wang,C.-H.and Song,S.H. 1999. Structural Redundancy Under Stochastic Loads, Stochastic Structural Dynamics, 213-220

Yao,J.T.P. and Yeh,H.Y. 1969. Formulation of Structural Reliability, Journal of Structural Division, ASCE, Dec.

Ziha,k. 1998. Entropy of a Subsystem of Events, 20th International Conference Information Technology Interfaces ITI'98, 451-454

Ziha,k. 1999. Usage of Relative Uncertainty Measures, 21st International Conference Information Technology Interfaces ITI'99, 269-274

New Remedial Technique for Bridge Foundations against Lateral Flow due to Liquefaction

Shin'ichiro MORI
Associate professor
Department of Civil and Environmental Engineering
Ehime University
3 Bunkyo, Matsuyama, Ehime 790-8577 JAPAN
Fax +81-89-927-9845 , Phone +81-89-927-9818
mori@coe.ehime-u.ac.jp

and

Masato TERAZAWA
Chief Structural Engineer
Technology Department, Civil Engineering Division
Tobishima Corporation
2 Sanbancho, Chiyoda-ku, Tokyo 102-8332 JAPAN
Fax +81-3-3288-5285 , Phone +81-3-3288-6507
Masato_Terazawa@tobishima.co.jp

ABSTRACT

During the 1995 Hyogoken-Nanbu (Kobe) earthquake, a large number of bridge foundations suffered severe damage not only due to strong motions but also due to liquefaction-induced lateral ground flows, particularly in the waterfront area of Hanshin region. After the earthquake, as remedial measures against the lateral flow, many projects simply adopted some geotechnical methods like sand compaction pile, gravel drain, etc. In this paper, a new structural technique is proposed as realistic remedial measure for the bridge foundations against the liquefaction lateral flow. In this technique, the resistance of the foundation far from a waterfront line is effectively redistributed to the foundation near the line by tying the consecutively neighboring foundations with rigid PC cables. An application of the technique in design and installation has also been described in this paper.

INTRODUCTION

During the1995 Hyogoken-Nanbu (Kobe) earthquake, significant soil liquefaction occurred in an extensive area of reclaimed land of Kobe and its neighboring cities in Japan. As a result, liquefaction-induced lateral ground movements caused serious damage to the foundations of road-bridges and buildings (Hamada, et al., 1995). Before this disaster, many researches on the liquefaction-induced lateral ground movement were energetically carried out, however very few remedial measures against it had been applied to the real structures (Editorial Committee on "Planning, Design and Installation of Liquefaction Remediation", 1993). Even during the post-earthquake rehabilitation and application of remedial measures, conventional method like soil improvement in surrounding ground or supplementary piles with spread footing has mainly been applied to overcome the problems due to lateral movement of pile foundations of road-bridges (Hamada, 1999). Therefore, as a number of cities in Japan are settled in alluvial plain or along its waterfront, and many pile-foundationed structures exist in here, some effective remedial measures for existing as well as to be constructed structures are required to be developed.

Focusing on the characteristics of the foundation of a bridge passing over a waterway and the peculiarity of the lateral spread displacement due to liquefaction at waterfront area, the basic concept of a new remedial technique for the bridge pile-foundation was developed (Mori, 1998). In this technique, other foundations are made to share the load that acts on the foundation adjacent to revetment, and to constrain the relative displacement of every two foundations, which consequently restricts the girder collapse and foundation deformations.

Not only the basic concept of the developed method has been described in this paper, but also the application of the technique to a real road-bridge has been presented in terms of effectiveness, installation economy and construction term to demonstrated the technique as a new realistic remedial measure.

BASIC CONCEPT OF PROPOSED TECHNIQUE

Liquefaction-induced lateral spread and associated structural damage

In remediation against liquefaction-induced lateral spread of ground displacement, it is important to consider the mechanism of the phenomenon as well as the causes and modes of damages to the structures. A typical illustration of the liquefaction-induced lateral spread and the associated structural damages at an adjacent area to waterway is made in Figure 1. It can be said from the figure that the lateral ground displacement may have been triggered by revetment moving towards the waterway. As a general tendency, the amount of horizontal

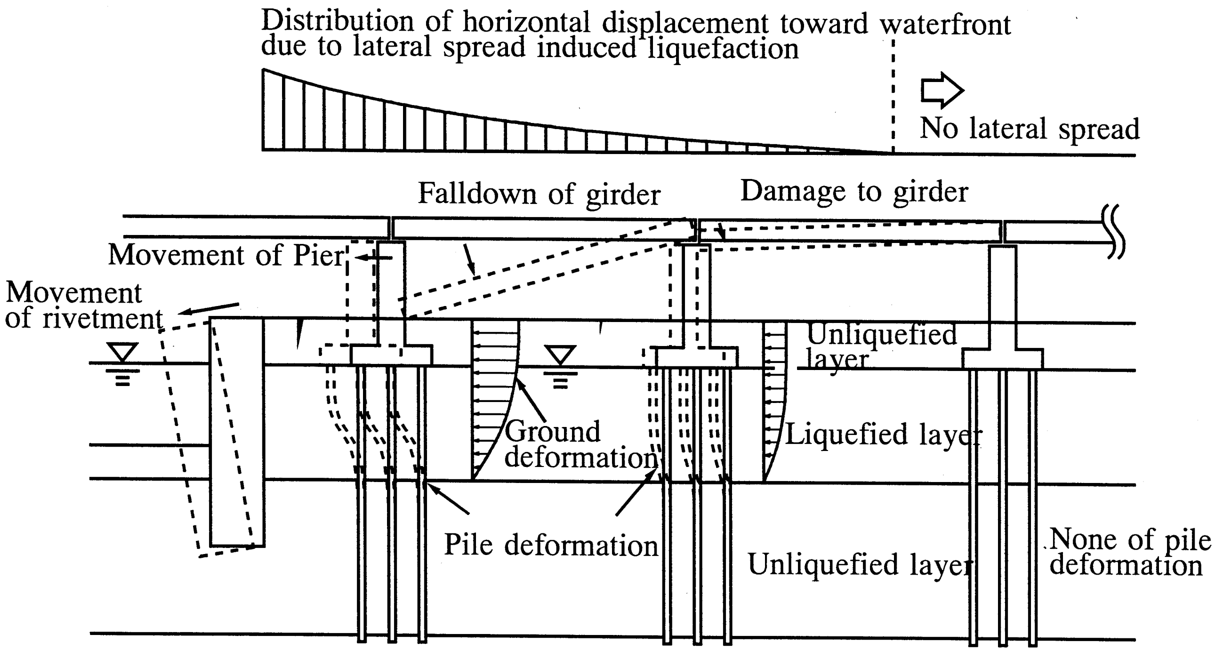

Figure 1. typical illustration of the liquefaction-induced lateral spread and the associated structural damages at an adjacent area to waterway

movement of ground towards the waterway due to the lateral spread is the largest in an area adjacent to the revetment, whereas it decreases towards the inland area. According to the investigation results in the 1995 Hyogoken-Nanbu earthquake, the influenced area of lateral spread in most of the cases was reported to have extended approximately up to 100 m inland from the revetment line (Ishihara and Yasuda, 1995).

The degree of influence of the lateral spread on the bridge foundation is intuitively expected to be proportional to the amount of horizontal displacement of its surrounding ground. In fact, the expectation was already proved appropriately in the case of pile foundation by their displacement relationship investigated by the Investigation Committee on the Damage to Highway Bridges by the 1995 Hyogoken-Nanbu earthquake (1995), as shown in Figure 2. For this reason, the influence is high at the bridge foundation adjacent to the revetment and low towards inland, finally diminishing at the place far from the revetment. Similarly, the horizontal displacement of the foundation and the opening of the span of neighboring foundations increase with the closeness to the revetment. The horizontal displacement of the piles just after their breakage or deformation then results in the reduction of residual supporting capacity of foundation, ultimately leading to the damage of shoes and the girder fall-down.

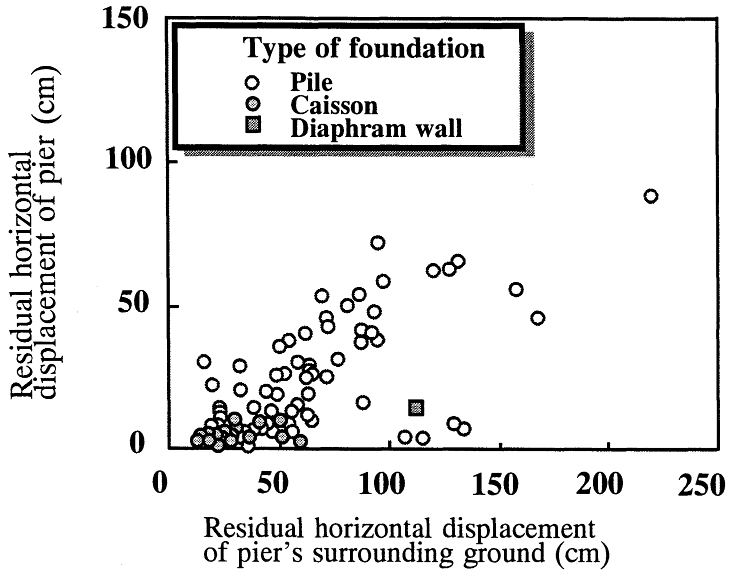

Figure 2. Relationship of residual horizontal displacement of bridge pier and its surrounding ground **(Data: Investigation Committee on the Damage to Highway Bridges by the 1995 Hyogoken-Nanbu earthquake, 1995.12)**

Peculiarity of damage

The fact that the foundations adjacent to the revetment not the foundation far from revetment are influenced the most by large lateral spread loading implies that the whole bridge does not yet resist the lateral spread loading with its maximum ability. This is the emphasized peculiarity of damage to bridge foundations due to the lateral ground flow.

Basic concept of proposed technique

Foundations adjacent to the revetment move excessively because of the large lateral spread, whereas the foundations far from the revetment are expected to remain resistant to large horizontal displacement due to little influence of the lateral spread. Moreover, the neighboring bridge foundations are often arranged linearly and oriented perpendicularly to the waterfront line. Based on these features, a new structural remedial measure has been proposed. The proposed remedial technique enables the other foundations that have sufficient residual resistance in sharing the huge amount of loads due to the lateral spread that act on the foundations adjacent to revetment. This is simply done by tying up the consecutive neighboring foundations with highly rigid ties (e.g., large-section PC cables). This technique is called the Tying Foundations method, as a structural remedial technique against the lateral ground flow. As the strategy of earthquake resistant design of the bridges recommends that the structures should disperse the horizontal inertia forces, as in the case of a multi-span

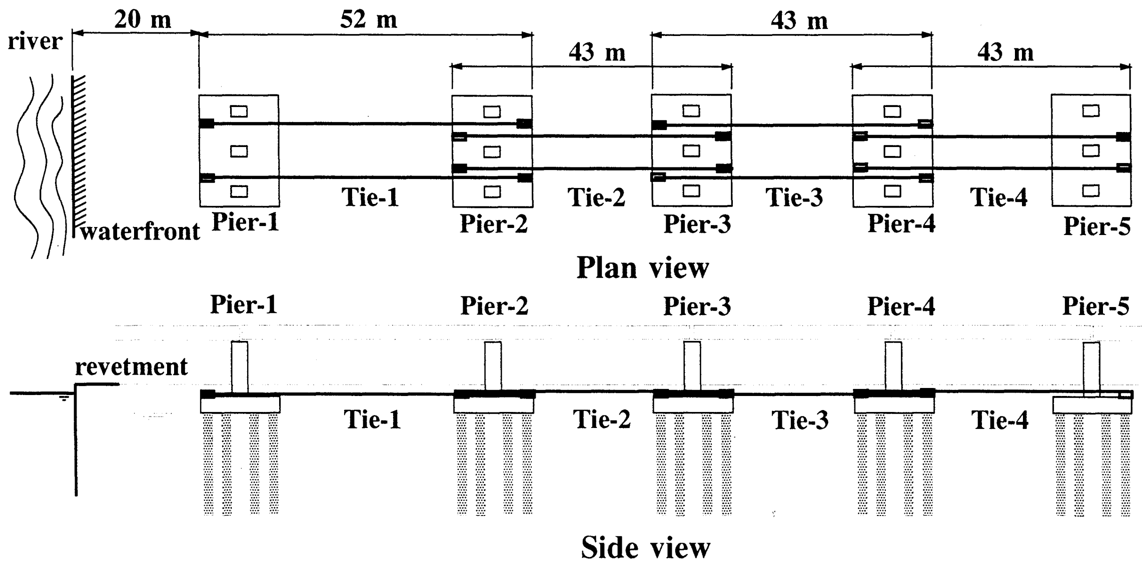

Figure 3. Schematic diagram of an existing highway bridge selected for the trial design application of the proposed technique

continuous structure, the basic concept of it is applied to the proposed technique.

Applicability

The proposed remedial technique is effective for all the structures like bridges, tanks, buildings, etc. that are perpendicularly oriented to the waterfront line. It, however, is not applicable to the bridges parallel to the revetment line.

TRIAL APPLICATION OF THE PROPOSED TECHNIQUE

Description of existing bridge

The whole structure of an existing highway bridge selected for the trial design application is shown in Figure 3. This bridge passes over a waterway and its axis is exactly perpendicular to the revetment line. The bridge piers starting from the waterway line have been named Pier 1, Pier 2, ... and Pier 5. The distance between the revetment line and the outer edge of the footing of Pier 1 is 20 m; the center-to-center distance between the Piers 1 and 2 is nearly 40 m, and that between the Piers 2 and 3, 3 and 4, and 4 and 5 is 31 m, assumed to be the same. The structural features of all the piers and their foundations including the ground conditions are same. The foundation detail is shown in Figure 4. It consists of a reinforced concrete footing, 12.25 m wide, 17.4 m deep, 2.5m thick supported by 18 cast-in-place concrete piles of 1.5 m diameter and 56 m length.

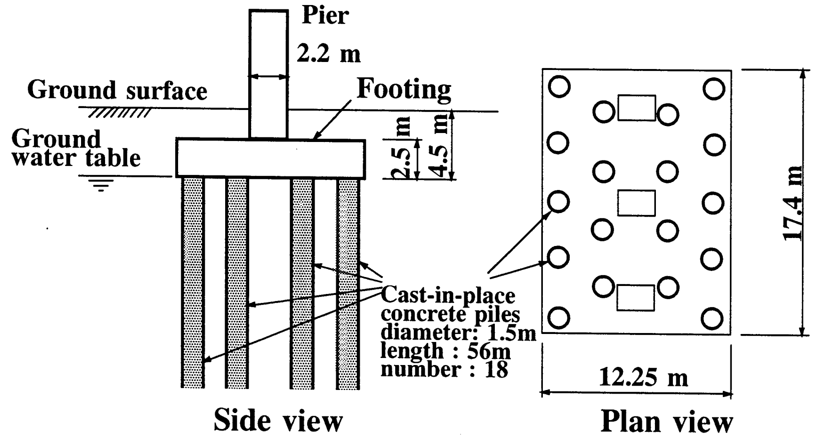

Figure 4. Foundation detail

Ground conditions

The soil profile of the bridge site, as shown in Figure 5, consists of a diluvial sandy soil deposit at the bottom below 60m from the ground surface, a 25m thick alluvial sandy soil layer with SPT N-value increasing with the depth, a 21m thick soft alluvial silty soil layer, a 10m thick alluvial loose sand layer, and a 4.5m thick embankment. SPT N-value of the 10m thick alluvial sand layer is very small in a range of 2 to 5; so the liquefaction potential for this layer calculated as per the Specifications for Highway Bridges shows a high possibility of liquefaction of this layer. Design soil constants are shown in Table 1. The ground water table is at 4.5 m below the surface, which is exactly the bottom of the pier footing.

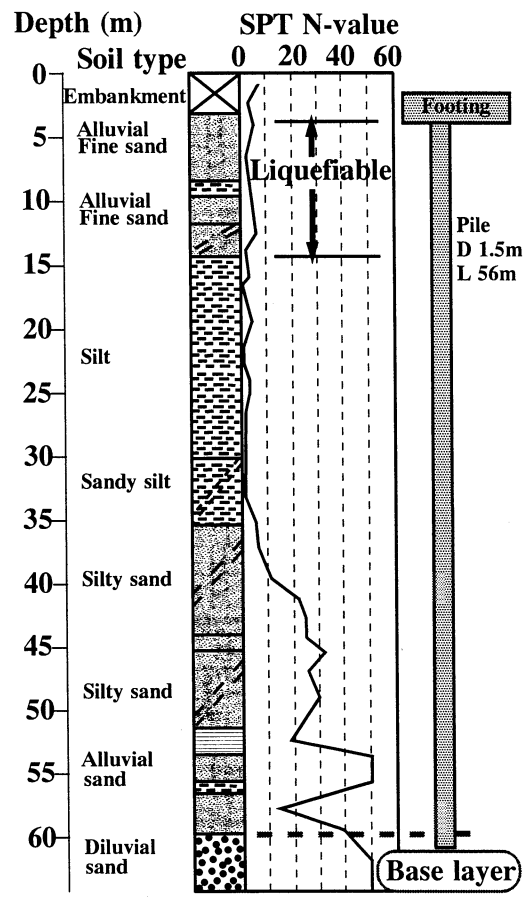

Figure 5. Soil profile of the bridge site

Lateral resistance of pile foundation

For the analysis model of the whole bridge system to which is applied the technique, it is required to model the lateral resistance of pile foundation into a single spring with nonlinear deformation behavior. Then, the nonlinear relationship was obtained by push-over analysis of

Table 1. Design soil constants

Soil type	Thickness (m)	Depth (m)	SPT-N	Unit weight (g/cm^3)	Cohesion (kPa)	Internal angle (degree)	Young's modulous (kPa)	Note
Fill	4.5	4.5	3	1.6	0	30	8232	Unsaturated
Sandy soil	10	14.5	3	1.8	0	27	0	Liquefiable
Cleyey soil	21	35.5	2	1.6	20	0	5488	Unpermitable
Sandy soil	25	60.5	26	1.9	0	35	71344	
Sandy soil	— —	— —	50	2	0	35	137200	Bearing stratum

Water table : G.L.-4.5 m

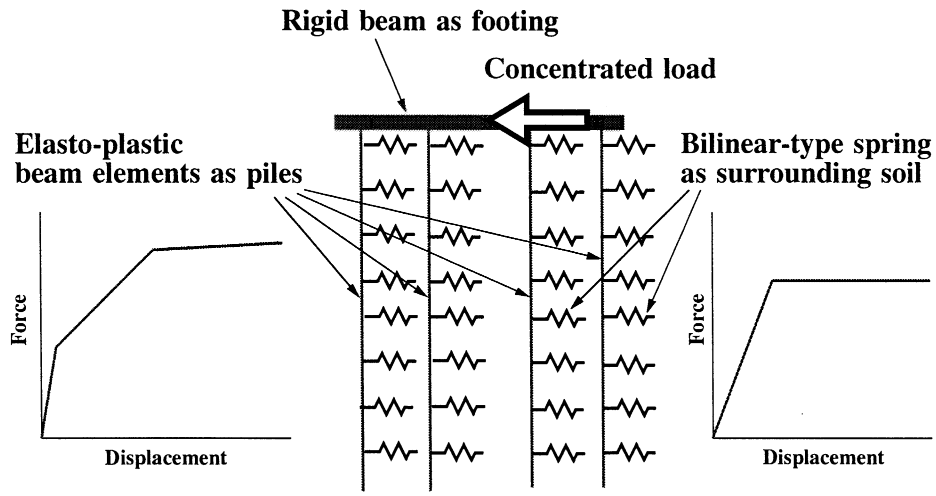

Figure 6. Model of push-over analysis for load-displacement relationship of foundation

a 2-D beam-spring model, as shown in Figure 6, that consisted of four beam elements as piles with nonlinear deformation behavior fixed to a rigid beam as footing with a concentrated load at its center, and springs as surrounding ground with bilinear deformation behavior. The obtained relationship between horizontal load and displacement of the bottom of footing is shown in Figure 7. The yield values of load and displacement defined as the state of re-bar's yielding in all the piles are Py = 626 ton (6.13 MN) and δy = 7.6 cm, and ultimate values defined as the state of compression failure in all the piles are Pu = 892 ton (8.74 MN) and δu = 22.3 cm respectively. The allowable ductility factor for the residual bearing capacity of pile foundation as prescribed by the Design Specifications of Highway Bridges (1996) is 2, which gives 15.2 cm as allowable value of horizontal displacement, δa of the foundation. So the bridge collapses when the lateral flow load exceeds 783 ton (7.67 MN), which is the resistant value corresponding to the allowable displacement obtained from Figure 7. Therefore, a load of 783 ton is considered the maximum allowable load for the foundation.

Lateral flow load

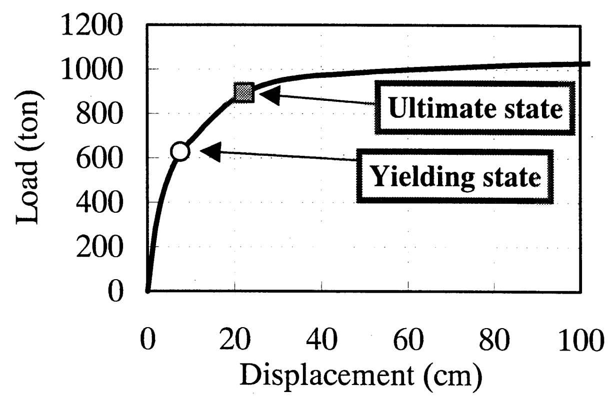

Figure 7. Relationship between horizontal load and displacement of the bottom of footing

The specification revised in 1996 prescribes the necessity of assessing the influence of the lateral ground flow on the bridge foundations that are located in a range up to 100 m from the revetment. As per the specification, the influence of the lateral flow as a horizontal distributed load in 50 to 100 m area from the revetment is half of that inside 50 m range. Distributed load along the depth of liquefiable soil layer should be calculated by using a coefficient of 0.2 in earth pressure, whereas that along the depth of unliquefiable subsoil above the ground water table should be calculated as passive earth pressure. The distributed load calculated as per the specification, as shown in Figure 8, is then converted into an equivalent concentrated load that acts at the center of the bottom of footing as modeling of lateral load in this study. The value of the concentrated load thus comes to be 1396 ton (13.68 MN). As the distance of Pier 1 from the revetment is 26 m, and that for Pier 2 is 66 m, Pier 3 is 97 m, and Piers 4 and 5 is over 100 m, a load half of 1396 ton must act on the Pier 3 as per the specification, but no load is supposed to act on it for the simplicity. So the equivalent concentrated loads acting are 1396 ton (13.68 MN) on the Pier 1 and 698 ton (6.84 MN) on the Pier 2; these loads on Piers 1 and 2 are named P1 and P2 respectively.

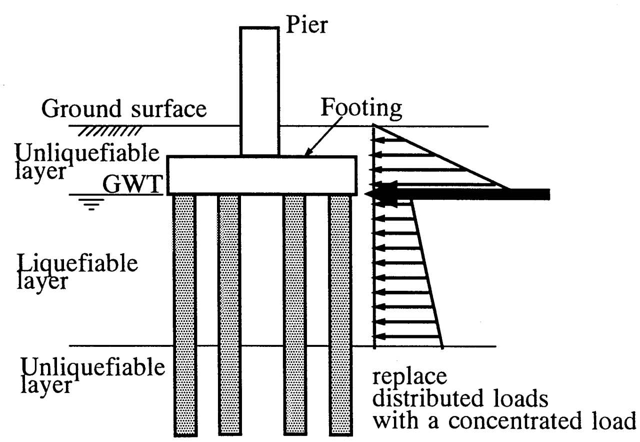

Figure 8. Modeling of lateral load acting on pile foundation

Another load condition in which the equivalent concentrated loads acting are 919 ton (9.01 MN) on Pier 1 and 460 ton (4.51 MN) on Pier 2 is also considered with different water table i.e. 3.4 m below the ground surface. But, as the load on Pier 2 does not exceed the allowable load, i.e., 783 ton, remediation is required only at Pier 1, not at Pier 2. Let us consider then the case of ground water table below 4.5 m as Case 1 and the case of that below 3.4 m as Case 2.

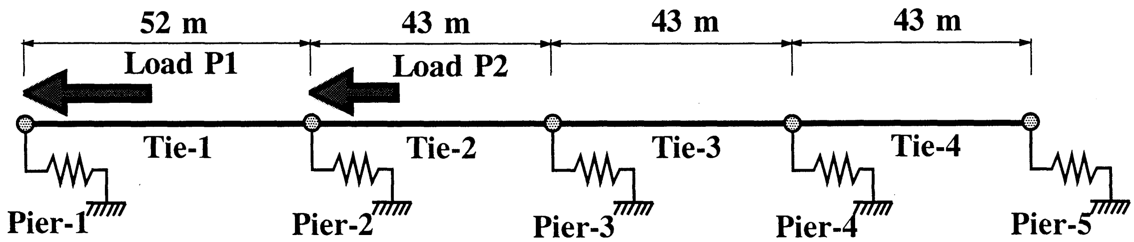

Figure 9. An example of the analysis model in a case of tying 5 foundations

Tie cable

For this technique, high rigidity is required in the cables used in tying the neighboring footings of foundations. So, PC cables with a large diameter are recommended for this reason and for ease in the installation. In this study, corrosion-proof PC cables with 360 ton (3.53 MN) breaking strength, 2.0×10^6 kg/cm^2 (196 GPa) Young's modulus and 18.75 cm^2 section area are used. A basic number of cables by which the cables should be increased is 10 and nominal number of cables is 20. When design result does not satisfy the design criteria, the number of cables must be increased by the basic number. Besides this, the allowable displacement of foundation as per the criteria is 15.2 cm, the allowable opening of span as per original criteria is 10 cm. Similarly, the allowable tension load on the cables is 135 ton (1.32 MN) as per the other code that prescribes the safety factor for PC cables to yield due to tensile force as 2.5. The cables are anchored at the far ends of every two tied footings.

Initial planning

It is very important in practical design to estimate the initial scale of construction, i.e., the numbers of tied foundations and PC cables in this technique. In the initial estimation of the number of tied foundations, at least the sum of their lateral resistances should be more than that of the lateral spread loads on foundations. And for the number of PC cables, simple calculations or preparation of chart is required. If the whole system of bridge with this technique has a linear deformation behavior, the estimation can easily be made by solving the equilibrium equations with equivalent linear spring constants of foundations considering the reduction of soil constants due to liquefaction. The calculation details have been avoided in this paper.

Analysis model

An example of the analysis model in a case of tying 5 foundations is shown in Figure 9. The

Table 2. Design result for pier foundations

Pier	Horizontal displacement in cm		Foundation reaction in ton	
	Case 1	Case 2	Case 1	Case 2
Pier 1	14.2	11.3	763.6	705.1
Pier 2	11.2	9.7	704.3	673.4
Pier 3	7.6	---	626.2	---
Allowable	15.2	15.2	783	783

Table 3. Design result for ties and spans

Tie (Span)	Tension in ton per piece		Opening of span		Cable Number	
	Case 1	Case 2	Case 1	Case 2	Case 1	Case 2
Tie 1 (Pier 1&2)	21.1	10.7	3.0	1.6	30	20
Tie 2 (Pier 2&3)	31.3	---	3.6	9.7	20	---
Tie 2 (Pier 2&3)	---	---	7.6	0.0	---	---
Allowable	135	135	10	10	---	---

Cable strength: 360 ton

model consists of linear elastic cable members as PC cables and nonlinear springs with multi-linear skeleton reflecting the feature shown Figure 7 as pile foundations. Concentrated loads mentioned above are applied onto the nodes as Piers 1 and 2. The length of elastic member is adopted as the distance of corresponding anchorage. In design, the required number of foundation is tied.

Design result

According to the results of the design, remediation was successfully achieved in Case 1 by tying three foundations with 30 cables (Piers 1 and 2) and 20 cables (Piers 2 and 3), and in Case 2 by tying two foundations with 20 cables (Piers 1 and 2). The results are shown in Tables 2 and 3. The results satisfy the both allowable displacement of foundation and the allowable opening of span. Moreover, the resulted safety factors are 4.3 times higher in Case 1 and 12.6 times higher in Case 2 than the required ones. This implies that cables are sufficiently safe even against unexpected continuous breakage, since the required property of the cables is the rigidity, not the strength.

Study on number of tying foundations

In order to understand the peculiarity of the proposed technique, a comparison of the results is made by increasing the number of tied foundations. Number of PC cables is 20, the same in

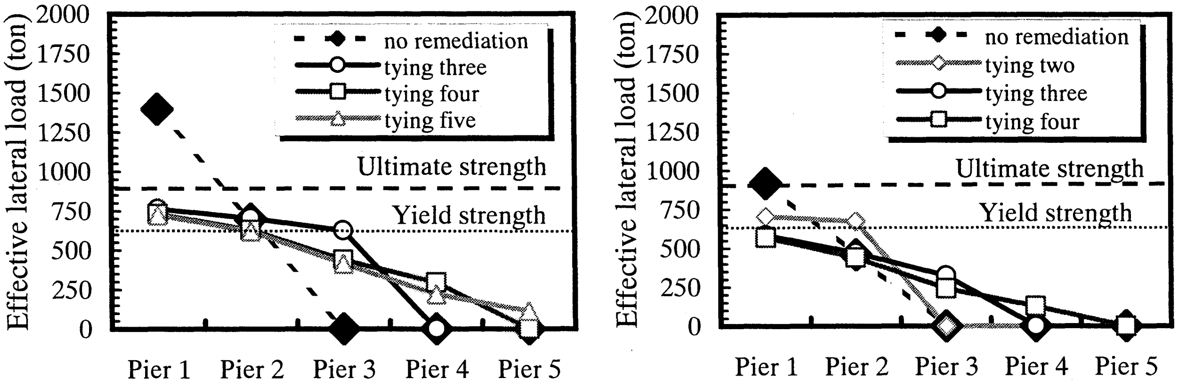

(a) Case 1 (W.T.=-4.5 m) (b) Case 2 (W.T.=-3.5 m)

Figure 10. Variations of foundation effective loads with the number of foundations

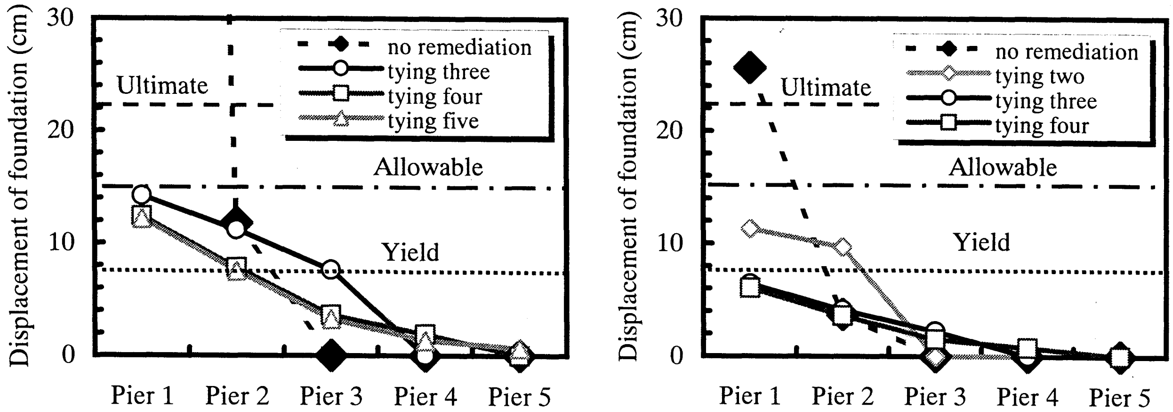

(a) Case 1 (W.T.=-4.5 m) (b) Case 2 (W.T.=-3.5 m)

Figure 11. Variations of foundation displacements with the number of foundations

every span of all the cases. Load case 1 for 4 or 5 foundations and load case 2 for 3 or 4 foundations are considered for the comparison.

Figure 10 shows the variations of foundation reaction/effective load with the number of foundations. This figure suggests that the proposed technique is a method of load-dispersion. In Case 1, the effectiveness in the reduction of load acting on Pier 2 is almost negligible, but the reduced load in Pier 1 is distributed through Pier 2 to Pier 3 or Piers 3 and 4 or Piers 3, 4 , and 5, whereas in Case 2 for 3 or 4 foundations, the results show the same tendency as in Case 1, but Piers 1 and 2 share nearly the equal load. Figure 11 shows the variations of foundation displacements with the number of foundations. For gradual opening of spans and unexpected larger load, one more foundation tying than the design result is recommended.

Applicability for inclined bridge

The proposed technique is effective only for the bridges whose axes are nearly perpendicular to the revetment line, on the contrary, it is not effective to the bridge whose axes are inclined to the revetment line. However, without mentioning any details, the applicability of the technique is assured by another case study in which the inclination of bridge axis is less than 15 degrees.

STUDY ON INSTALLATION

Installation and procedure

Application of the technique in tying the foundations does not need any special machine and new technology as well. The procedure of application of the technique to the above mentioned

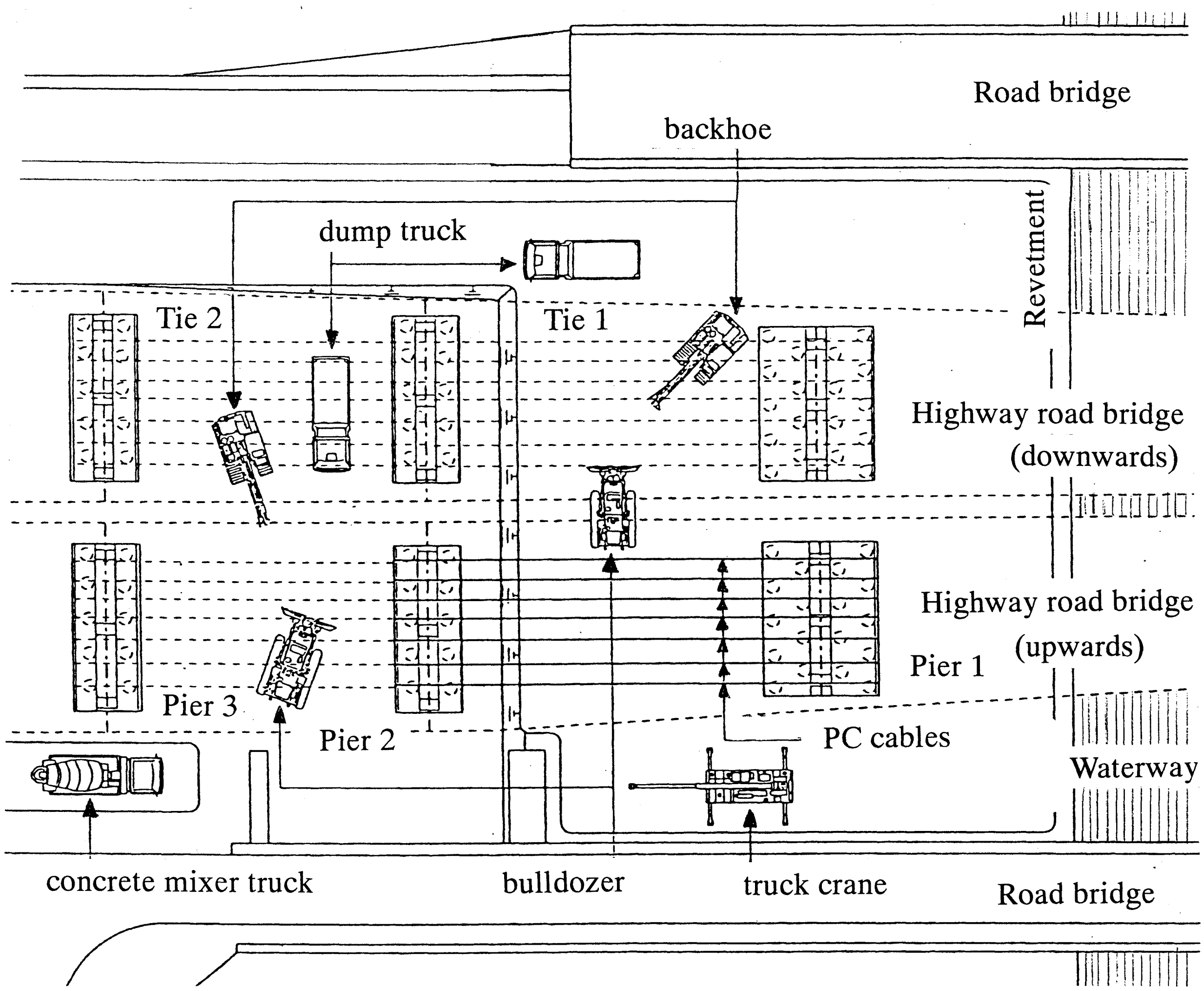

Figure 12. Installations outline in Case 1

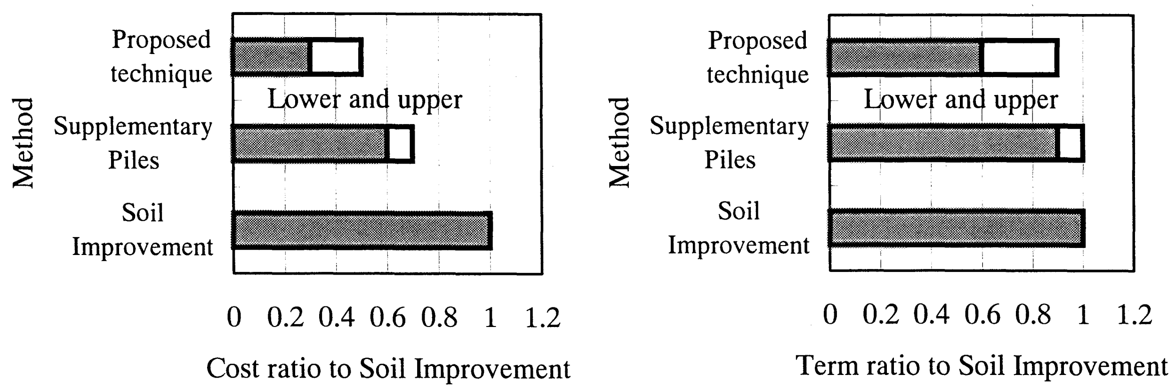

(a) Cost ratio to Soil Improvement **(b) Term ratio to Soil Improvement**

Figure 13. Comparison of construction costs and terms between the proposed technique and other conventional remedial methods

existing bridge is as : (1) downward excavation of soil up to the level of footing and a little deeper excavation for anchorage work space, (2) setting hollow steel angles for cable anchorage, (3) placement of PC cables, (4) placement of anchorage concrete, (5) initial tensioning of PC cables, and (6) backfilling the excavated area. Furthermore, this procedure can even be carried out in a narrow space; the only demerit is that the application is difficult when the excavation between specified foundations for placing PC cables restricted.

The installations outline in Case 1 described in the previous section is illustrated in Figure 12. Required heavy equipment are backhoe, bulldozer, dump truck, truck crane (for placement of PC cables), and concrete mixer truck. In order to make the technique effectively, an initial tensioning of PC cables is required to diminish the slack as far as possible. But, the initial tension should be very small for the integrity of foundations. For this reason, small initial tensioning may require temporary staging for momentarily supporting PC cables.

Economy and period of installation

According to the design result and the application procedure mentioned above, a construction plan involving the required period and cost estimation was made. In two parallel road-bridges with real conditions of the existing bridge site were considered. It costs 760 million yens and takes 5.5 months in Case 1 for tying three foundations, and 160 million yens and 4.5 months in Case 2 for tying two foundations. The cost in Case 1 is much more expensive than that in Case 2 because of the difference in excavation volume which is too large due to reflection of the real conditions of the construction site conditions. If excavation volume is proportional to the area of construction, the cost in Case 1 probably becomes 1.5 times higher at the most than that in Case 2.

In order to grasp the economy of the proposed technique, a comparison of construction costs and terms between the proposed technique and other conventional remedial methods was made under the same conditions in design and construction. As a result, the cost and construction term advantages of the technique are clarified in Figures 12 and 13.

CONCLUDING REMARKS

The Tying Foundations method, as a structural remedial technique for the bridge foundations against the liquefaction-induced lateral ground flow is proposed, in which the resistance of the foundation far from a waterfront line is effectively transferred to the foundation near the line by tying the consecutively neighboring foundations with highly rigid ties, e.g., large-section PC cables.

The application results of the design and the analysis of an existing highway bridge with simple analytical models clarified the effectiveness of the proposed technique. The technique was comprehended as a method of load-dispersion. The effectiveness in the reduction of load acting on the piers adjacent to a waterfront line was interpreted by the redistribution of the reduced load to the piers far from the waterfront line.

The comparison of construction costs and terms between the proposed technique and other conventional remedial methods justified the advantages of the technique over others.

ACKNOWLEDGEMENTS

The applicability of the proposed technique was reviewed by the Investigation Committee on Remedial Measures for Highway Bridge Foundation against Liquefaction-Induced Lateral Flow chaired by Dr. Toshio Iwasaki. Authors would like to express their appreciation to Prof. M. Hamada, Prof. S. Yasuda, and Prof. M. Huyuki for their critical reviews. Authors would also like to thank many committee members from Public Work Research Institute, Metropolitan Expressway Public Corporation, Hanshin Expressway Public Corporation, and some 12 construction companies for their constructive discussions.

REFERENCES

Editorial Committee on "Planning, Design and Installation of Liquefaction Remediation": Planning, Design and Installation of Liquefaction Remediation, Japanese Society of Soil Mechanics and Foundation Engineering, 1993.2 (in Japanese).

Hamada,M., Isoyama,R., and Wakamatsu,K. : The 1995 Hyogoken-Nanbu (Kobe) Earthquake

Liquefaction, Ground Displacement and Soil Condition in Hanshin Area, ADEP, Waseda Univ. and JEC, 194pp., 1995.8.

Hamada, M.: Present circumstance and issues for future research on and development of aseismic reinforcement, *The Foundation Engineering and Equipment, Sougou Doboku Kenkyusho. Co.,Ltd., Vol.27, No.4*, pp.2-6, 1999.4 (in Japanese)

Investigation Committee on the Damage to Highway Bridges by the 1995 Hyogoken-Nanbu earthquake: *Report on the damage to highway bridges by the 1995 Hyogoken-Nanbu earthquake*, pp.46-55, 1995.12 (in Japanese).

Ishihara, K. and Yasuda, S. : Geotechnical damages in coastal regions, *Reports in Urgent Meeting on Investigation of Hanshin Earthquake Disaster*, Japan Society of Civil Engineers, pp.13-18, 1995.2 (in Japanese).

Japan Road Association: Design Specifications of Highway Bridges – Part V Seismic Design, 227p., 1996.12 (in Japanese)

Mori, S.: New Remediation of bridge foundations against liquefaction-induced lateral ground flow; Consecutive footings tying method, *Construction Machinery and Equipment, Japan Industrial Publishing Co. Ltd.*, Vol. 34, No. 5, pp. 42-46, 1998.5 (in Japanese).

Mori, S. and Terazawa, M.: Applicability of new remedial technique for bridge foundations against liquefaction-induced lateral ground flow, *Proceedings of the 53rd National Conference of Japan Society of Civil Engineers, Vol.1-B*, pp.616-617, 1998.10 (in Japanese)

Centrifuge Modeling of Lateral spreading behind a caisson type quay wall during an earthquake

Chung-Jung LEE[1], Ricardo DOBRY[2], Tarek ABDOUN[2]. and Bing-Ru WU[1]

ABSTRACT

Lateral spreading of a saturated cohesionless soil near a quay wall is a costly type of liquefaction–induced ground failure. It may destroy buildings, bridges, and waterfront structures. A series of three centrifuge model tests were carried out to study both the deformation characteristics of the backfill and the response of a caisson type quay wall during liquefaction induced by a strong earthquake. The 120:1 model was first spun at an acceleration of 120 g, and then was subjected to base shaking with the help of an in-flight shaker. Changes of pore water pressure at different locations within the soil, earth pressure profiles along the quay wall and bearing pressure distributions beneath the wall footing were monitored during the shaking. Accelerations of the quay wall and of the soils at different depths were also measured. This rather complete instrumentation was used for studying both the dynamic soil-structure-water interactions involving the quay wall and the effect of liquefaction on the earth pressures acting on the wall. The measured lateral movements and vertical deformations of the backfill behind the quay wall were compared with those observed in waterfront areas at Port Island in the 1995 Hyogoken-Nambu earthquake in Japan.

---

[1] National Central University, Chungli, TAIWAN, ROC
[2] Rensselaer Polytechnic Institute, Troy, NY, USA

Correspondent: Tarek ABDOUN
Dept. of Civil Engineering, Room 4018, JEC
Rensselaer Polytechnic Institute, Troy, NY, 12180
e-mail: abdout@rpi.edu

INTRODUCTION

Liquefaction and related phenomena occurred extensively in Port Island during the 1995 Hyogoken-Nambu earthquake (Max. peak horizontal acceleration 0.54g, max. vertical acceleration 0.45 g). The field investigation showed the characteristic damage pattern of a caisson type quay wall to be in the form of large deformation of the quay wall (including lateral movement, rotation, and settlement) and substantial ground movements (lateral and vertical) of the backfill. Seaward displacements of the caisson type quay walls were about 5m maximum and 3m average. The vertical settlements were about 2.2 m maximum and 1.5m average. The maximum tilt toward the sea was around 4 degrees. Permanent lateral ground displacements behind the quay walls extended 100-150m inland (Ishihara, et al. 1996).

Lateral spreading of soil near a quay wall is a costly type of liquefaction–induced ground failure. It destroys buildings, bridges, and waterfront structures (Inaqaki, et al.1996, Towhata, et al. 1996). In this paper, a series of 2-D centrifuge modeling with in-flight shaking were carried out to study both deformation characteristics of the backfill and the response of a caisson type quay wall during liquefaction induced by an earthquake. The extent of backfill in the model was wider enough to cover the length of most significant observed spatial variation of the deformation behind the model quay wall. Therefore, the deformation patterns of backfill can be investigated in detail. A complete instrumentation was used for studying the development of dynamic earth pressures and pore water pressures during liquefaction as well.

TEST EQUIPMENT

This research employs physical prototype modeling using the centrifuge facilities at RPI. The 100 g-ton centrifuge machine installed at RPI has an in-flight platform radius of 3.0 m and can test a payload of 1 ton at 100 g or 0.5 ton at 200 g. A large in-flight computer-controlled centrifuge shaker with a 13.6 metric ton maximum actuation force capacity was used to impart base dynamic excitation (Van Laak 1996). A large rigid model container with internal dimensions of 87.5 cm (L) x 37 cm (W) x 35.8 cm (H) was employed (Fig. 1). The model dimensions shown in Fig. 1 are in centimeters, and the prototype dimensions in parentheses are in meters.

The dimensions of the model quay wall 10 cm in height and 8.33 cm in width tested at a 120g gravitation field, therefore, the model (Fig. 1) represents a prototype quay wall 12 m in height and 10 m in width sitting on a loose sand foundation 6m in depth. The lateral extent of backfill is 74.6 m also in prototype. The water table is 1.0 m above the ground surface.

Horizontal (AH#) and vertical (AV#) accelerometers were installed both in the quay wall and underneath its base and embedded in the backfill as shown in Fig. 1. Therefore, the response of the model wall and of the backfill in the free field could be studied. The horizontal displacement of the quay wall was monitored with a horizontal LVDT (LHT). The vertical displacements of the quay wall and the backfill were recorded by a row of

LVDTs (LV#) along the surface. The model wall, having a specific gravity of 1.92, was developed especially for this project. Six earth pressure cells (EP#), three on the back face of the wall and the others on the base, were used to measure the total contact pressures of the wall and base, respectively. Three pore water pressure transducers (P#) were located at the same positions as the earth pressure cells, so as to be able to monitor the corresponding effective stresses. Two pore water pressure transducers were also embedded in the backfill soil to investigate the pore water pressure buildup in the free field during shaking. A total of 25 transducers and a sampling rate of 3968 samples/second were used.

MODEL CONSTRUCTION AND TEST PROCEDURE

Soil Properties

Nevada No. 120 fine sand was used as foundation soil and backfill. This soil has a D_{50} of 0.15mm; and a permeability of 6.6×10^{-5} m/s at 1g. Extensive data about the cyclic characteristics of this soil was reported by Arulmoli et al. (1992).

Test Procedure

The loose foundation soil layer (40% relative density) was built first by raining oven dried sand from a V-shaped hopper at a height of 4 ± 1 cm. Thereafter, the model quay wall was placed on the loose layer and the same process of deposition was used to build the backfill behind the wall until the desired elevation. The raining process was interrupted as needed to place transducers or to rain a layer of colored sand at specified elevations. A row of marked spaghetti was vertically implanted along the center of the model at regular intervals and at predetermined positions (Fig. 1). As spaghetti absorbs water it softens and deforms together with the surrounding soil. The colored sand layers (2 mm in thickness) used together with the vertical spaghetti are good indicators of the deformations.

In an effort to accurately model the time scaling for pore fluid dissipation within the sand, a pore fluid having a viscosity higher than water was used. A mixture of water and Methocel cellulose ether was used for this purpose. Two solutions of 2.0% and 2.5% were used in two of the tests to achieve a viscosity 60 times and 120 times, respectively, that of water alone. The sand bed was vacuumed and saturated with the fluid having the viscosity of either 60 or 120 times the viscosity of water, depending on the test. It took 12-24 hours to saturate a sample. After saturation, the model was spun at 120 g centrifugal acceleration and finally was subjected to 20 cycles of sinusoidal base acceleration having about 0.18 g prototype peak amplitude, and a frequency of 1 Hz, also in prototype units. After shaking, the soil bed was excavated to expose the colored sand layers and spaghetti. The deformation patterns behind and in front of the wall were plotted. Three centrifuge tests were conducted and listed in Table 1.

Table 1 Test conditions

Model No	Peak Acceleration(g)	Test g-level	Viscosity of pore fluid
QWTEST2	0.20	120 g	60 x μ_{water}
QWTEST3	0.13	120 g	μ_{water}
QWTEST4	0.15	120g	120 x μ_{water}

TEST RESULTS AND DISCUSSION

As shown in Fig. 1, the model quay wall was equipped with six earth pressure cells (EP1-EP6) and three pore water pressure transducers (P1-P3) along the center of model. Table 2 lists the positions of the earth pressure cells (EPC) and pore water pressure transducers (PPT), in prototype units.

Table 2 Positions of EPCs and PPTs in the quay wall (prototype units)

Instrument No	Elevation[1] (m)	Distance (m)
EP1	2.4	
EP2	6.0	
EP3	9.6	
EP4	12.0	1.8[2]
EP5	12.0	5.0[2]
EP6	12.0	8.2[2]
P1	2.4	
P2	9.6	
P3	12	5.0[2]
P4	6.0	21.0[3]
P7	6.0	47.0[3]

[1] depth below top of quay wall
[2] measured from the Point B in Fig.1 toward the seaside
[3] measured from the line AB in Fig.1 toward the sand side

Excess pore water pressures during shaking

The measured time histories of excess pore water pressure on the back face of wall (line AB in Fig. 1) during shaking are shown in Fig.2. The ratio of excess pore water pressure shown in Fig. 2 is defined as:

$$\mathbf{r_u} = \frac{\Delta \mathbf{u}}{\sigma_v'} \qquad (1)$$

where $\Delta\mathbf{u}$ = excess pore water pressure; σ_v' = initial effective overburden pressure. The value of $\mathbf{r_u}$ reaches 1.0 if the soil liquefies. The value of $\mathbf{r_u}$ measured at P1 (2.4 m below the top of the quay wall) rose rapidly and oscillated between positive and negative values with a maximum positive value of about 0.9 and a minimum negative value of about –0.2 (Fig.2). The value of $\mathbf{r_u}$ measured at P2 (9.6 m below the top of quay wall) oscillated between positive and negative values with a maximum positive value of about 0.5 for the model saturated with water. The more viscous fluid is used in the test, the lower are the maximum positive values and minimum negative values of $\mathbf{r_u}$. At larger depths, the lower maximum positive values and minimum negative values of $\mathbf{r_u}$ were measured. No liquefaction occurred behind the quay wall in any of these measured points. However, the value of r_u at P4 (located 21 m away from the quay wall and 6 m in depth) and at P7 (located 47 m away from the quay wall and 6 m in depth), as shown in Fig. 3, rose to about 1.0. This indicates that liquefaction did occur there.

Elements located near the quay wall were subjected to lateral extension (LE) and lateral compression (LC) during shaking. It is expected that due to these increase (LC) and decreased (LE) lateral pressures, the soil should develop alternatively positive and negative $\mathbf{\Delta u}$. On the other hand, soil elements far away from the soil-wall interaction zone developed positive $\mathbf{\Delta u}$ during shaking. Therefore, a complicated flow pattern with pore fluid flowing from the far field to the field near the wall is expected. The lower viscosity of the fluid is used the more quick dissipation or equalization of the excess pore water pressures in the soil occurred because of the higher permeability. Figure 4 displays the profiles of pore water pressure along the face of the wall at different elapsed times for QWTEST3. For comparison the horizontal displacement of the quay wall (D) in Fig.4 at each elapsed time are also shown to indicate each profile. The figure shows the pore water pressures changed rapidly during any given cycle. Shaking started at t = 0.38sec. From t = 0.38 to 0.74sec in Fig. 4, the wall started moving outward because of the increase of the pore water pressure and the inertia of the wall. As a result, elements located near the wall were subjected to LE and developed negative $\mathbf{\Delta u}$ during outward wall movement. This negative excess pore water pressure tended to compensate the positive $\mathbf{\Delta u}$ induced in the soil during shaking. Therefore, the pore water pressures in the soil elements near the wall didn't build up as much as those in the free field. From t = 0.74 to 1.18sec, the wall started moving inward and the pore water pressures continuously increased due to LC. From t=1.18 to 1.81sec, the wall moved outward again and the pore water pressure decreased.

Distribution of earth pressures on the wall during shaking

The earth pressure cells were attached on the back face of wall to measure the total earth pressures and on the base to measure the contact pressures. The pore water pressure transducers were installed at the same elevations and positions to measure the pore water pressures (Table 2), so as to calculate the corresponding effective earth pressures or effective contact pressures. The distributions of measured maximum total earth pressures before (solid symbols) and during shaking (hollow symbols) are shown in Fig.5. This figure shows that the values of increment of total earth pressure during shaking at the various depths were nearly constant of about 15 to 20 kPa.

Recorded accelerations

Figure 6 shows the time histories of acceleration at AH7, which was embedded at 6 m depth and 47 m from the quay wall. The acceleration records show a drop in the acceleration amplitude for Model QWTEST4 ($\mu=120\mu_{water}$) and Model QWTEST2 ($\mu=60\mu_{water}$) after about 3 cycles. When a more viscous fluid was used the pore pressure dissipated less (Fig. 3) and the acceleration amplitude dropped more. Figures 7 and 8 present the time histories of the acceleration at AH3, which was also embedded at 6 m depth and 9.6 m from the quay wall, and at AH9, which was embedded at 3 m beneath the wall base, respectively. These recorded accelerations were very similar to the input acceleration. This figure together with Fig. 2 confirms that no liquefaction occurred within about 12 m from the wall because of lateral seaward displacement of the wall. In principle, factors affecting the wall movement should include the inertial force of the wall itself, the dynamic earth pressures as well as the pore water pressures generated in the backfill, and any reduction in the shear strength of the base soil. Figure 9 shows the change of the inertia force together with the increment of the measured total earth pressure with the time due to earthquake loading for QWTEST4. In this figure, seaward inertial forces are taken to be positive. The total earth pressure (including effective earth pressure and pore water pressure) is calculated using the measured earth pressure at EP2 times the height of wall. From the comparison of the increment of total earth pressure and the values of inertial force, it is concluded that the inertia force (about twice the increment of the total earth pressure) may play a major role in contributing significant movements of quay walls during earthquakes.

Displacement of quay wall and settlement of backfill

The displacements of wall were obtained from the measurements taken by three LVDTs installed on the top and face of the quay wall. LHT measured the horizontal displacement of the top of wall. LV1 and LV2 measured the vertical settlements of the top at two sides of the wall, and thus calculation of tilt angles was possible. Figure 10 shows that both a tilt angle and a horizontal displacement toward seaside gradually developed for Model QWTEST4. After the tests, the soil bed was excavated to expose the marked spaghetti and colored sand layers. The deformation pattern behind the quay wall was plotted. Figure 11 is the deformation pattern near the quay wall for Model QWTEST3. The failure plane can be clearly observed in the photograph.

The measured lateral displacements of the ground surface at any distance inland are normalized by the displacement at the quay wall line and shown in Fig. 12. As expected, the measured lateral displacement decreases with increasing distance from the quay wall. The distribution of ground surface settlement with distance to the quay wall is shown in Fig. 13. The ground subsidence tends to decrease with increasing the distance from the quay wall. The test results show considerable agreement with the field data (solid line in Figs. 12 and 13) observed in waterfront areas at Port Island in the 1995 Hyogoken-Nambu earthquake (Ishihara et al.1996).

CONCLUSIONS

A series of three centrifuge model tests was conducted to assess the seismic behavior of the quay wall embedded in liquefiable soil of various permeabilities. A complete instrumentation on the back face of the quay wall provided the profiles of both the total earth pressures and pore water pressures for analysis. The excess pore water pressure ratio measured at the backfill near the quay wall reached about 0.5. The fact that no liquefaction occurred within 12m behind the quay wall even the loose sand used in the tests may result from lateral extension induced in the soil by the large seaward movements of the wall.

The magnitudes of the increment of total earth pressure during shaking at various depths were nearly constant and were about 15 to 20 kPa. From the comparison of the increment of the total earth pressure and the magnitude of the inertial force associated with the wall accelerations, it is concluded that the inertial force may be very significant in determining the movements of quay walls during earthquakes. Reduction of shear resistance between the wall and the base soils due to the pore water pressure buildup (r_u=0.5) may also contribute to wall movements. The ground surface lateral displacements and settlements at any distance inland decrease with increasing the distance from the quay wall. The test results show reasonable agreement with observed field data.

ACKNOWLEDGEMENT

The first author would like to acknowledge the financial support provided from the National Science Council of the Republic of China to perform this research. Additional support was provided by the National Science Foundation under the U.S.-Japan Earthquake Resistant Design & Remediation of Lifelines and Deep foundations Subjected to Liquefaction: Centrifuge Modeling and Engineering Interpretations , Grant No. CMS-9812581.

REFERENCES

Arulmoli, K., Muraleetharan, K. K., Hossain, M. M., and Fruth, L. S. (1992). Verification of Liquefaction Analysis by Centrifuge Studies Laboratory Program Soil Data. Report: The Earth Technology Corporation.

Inagaki, H., Iai, S., Sugano, T., Yamazaki, H, and Inatomi, T. (1996). Performance of Caisson Type Quay Wall at Kobe Port. Special Issues of soils and Foundations, Japanese Geotechnical Society, pp.119-136.

Ishihara, K., Yasuda, S., and Nagase, H. (1996). Soil Characteristic and Ground Damage. Special Issues of soils and Foundations, Japanese Geotechnical Society, pp.109-118.

Towhata, I., Ghalandarzadeh, A., Sundarraj, K.P., and Vargas-Monge, W. (1996). Dynamic Failures of Subsoils Observed in Water front Areas. Special Issues of soils and Foundations, Japanese Geotechnical Society, pp.149-160.

Van Laak, P. (1996). Development of Dynamic Modelling Capability for a Geotechnical Centrifuge. Ph.D. Thesis, Rensselaer Polytechnic Institute, Dept. of Civil Engineering.

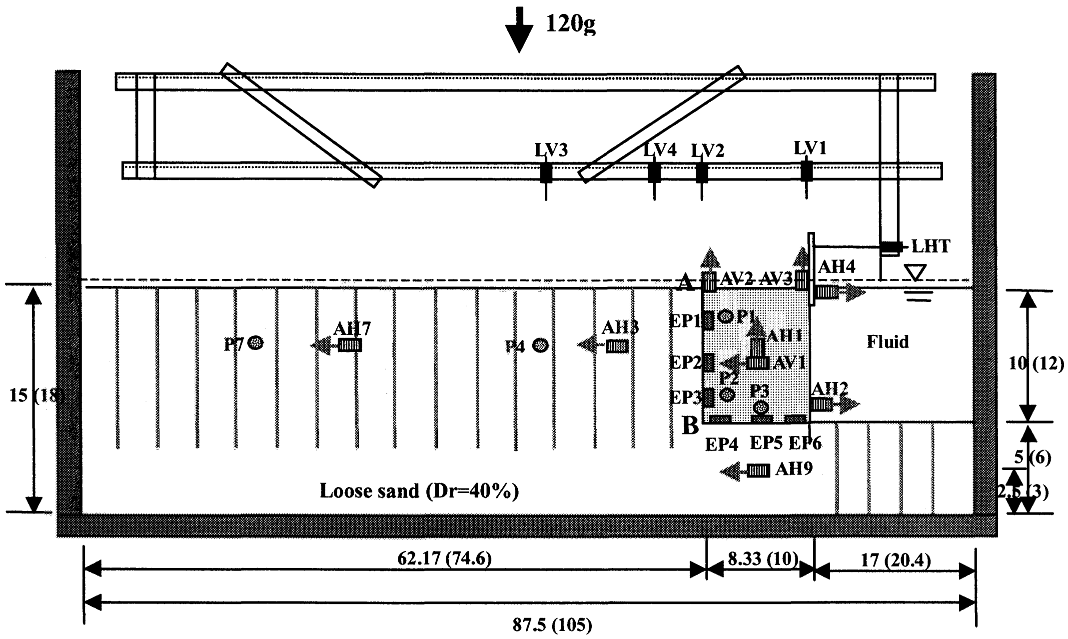

Fig. 1 Setup of model quay wall : Model dimensions are in centimeters and prototype Dimensions (in parentheses) are in meters

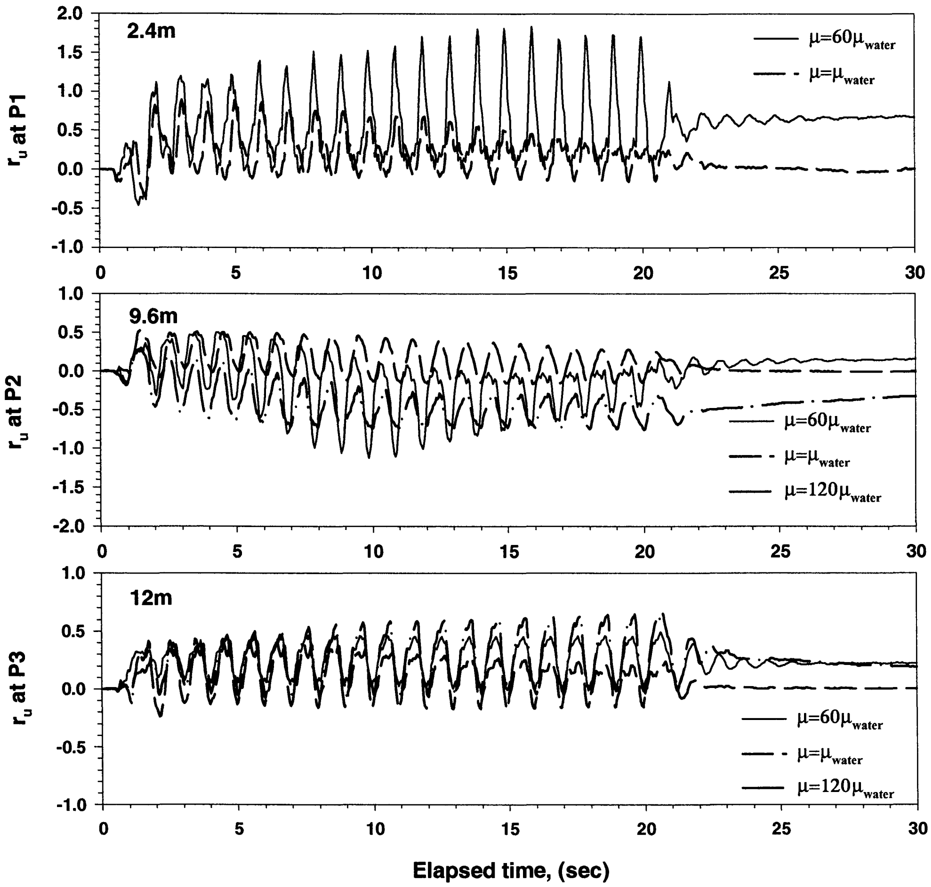

Fig. 2 Time histories of excess pore water pressure ratio (r_u)

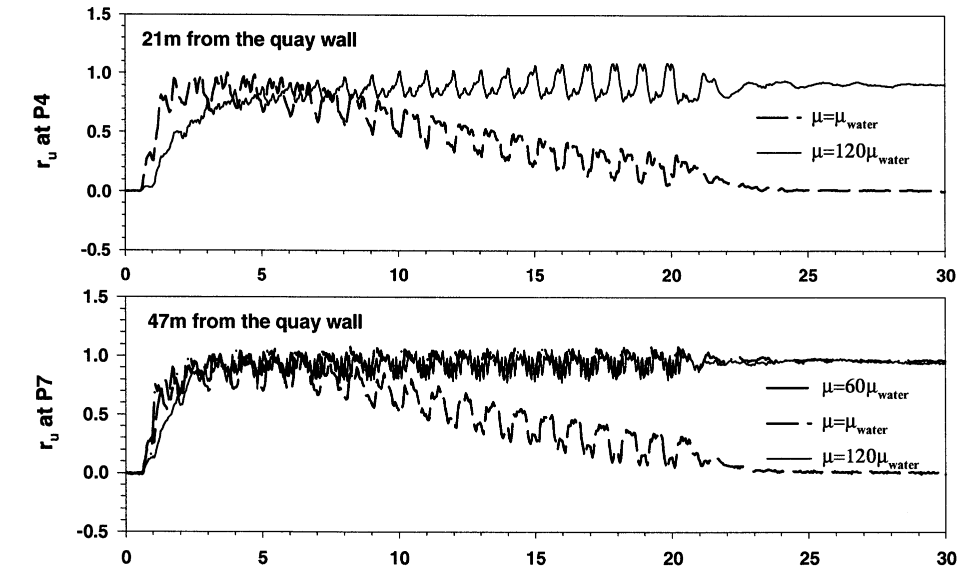

Fig. 3 Time histories of excess pore water pressure ratio at free field

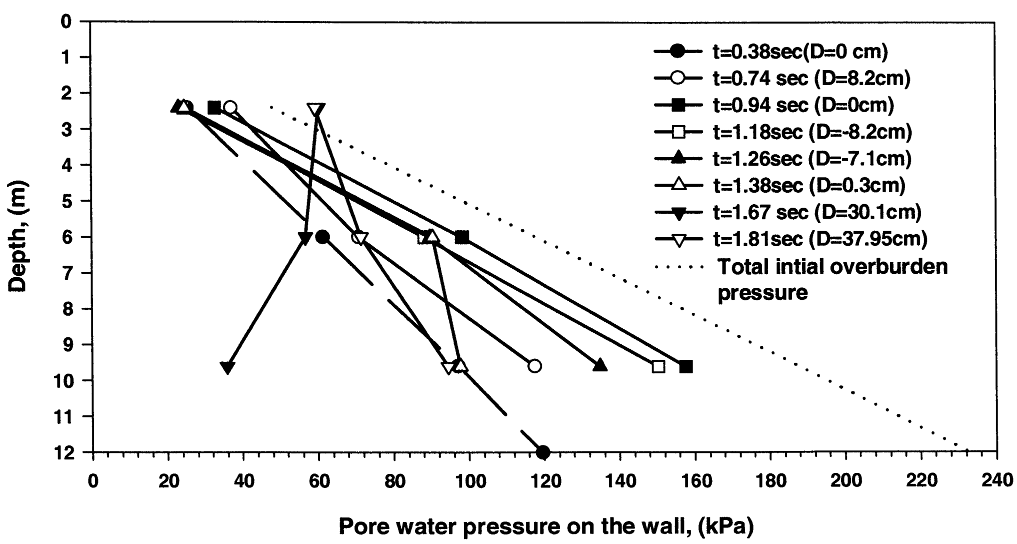

Fig. 4 Profiles of pore water pressure vs. time

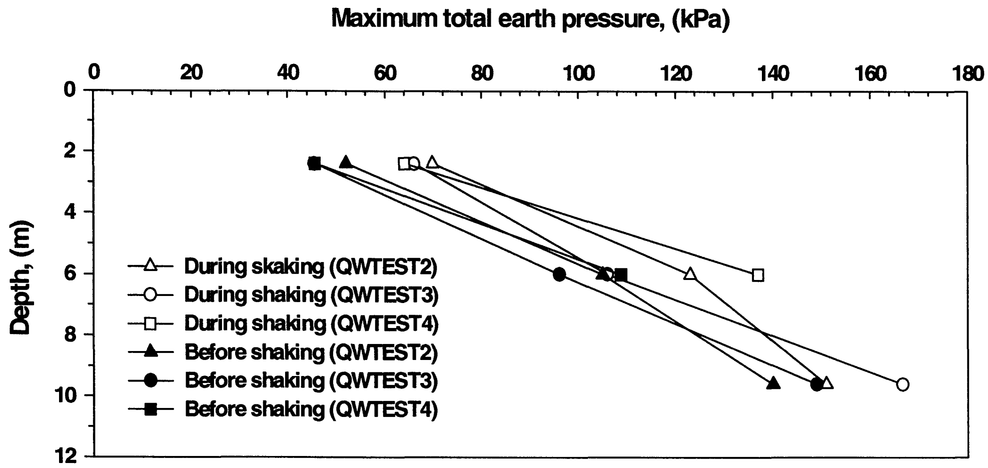

Fig. 5 Profiles of total earth pressure

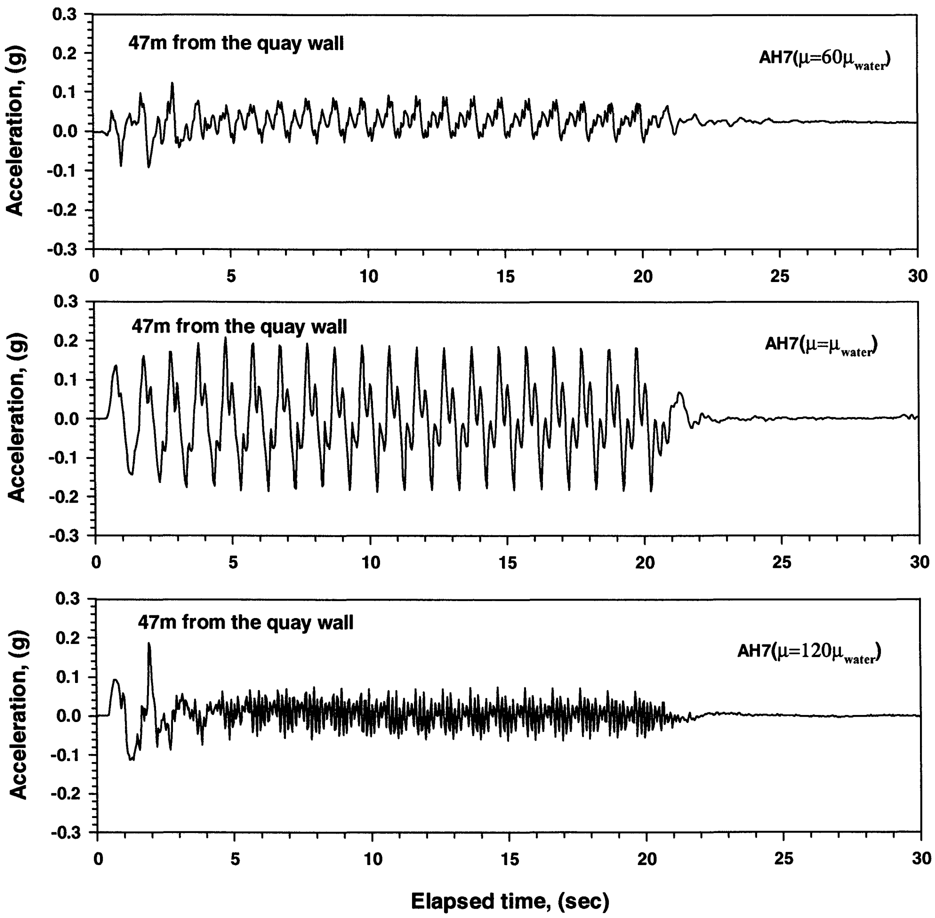

Fig. 6 Time histories of acceleration at AH7

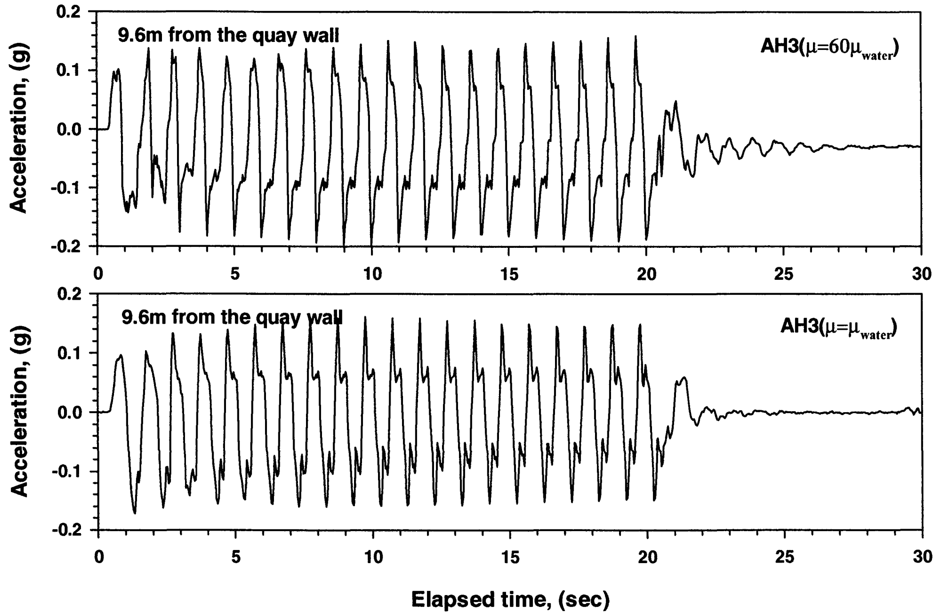

Fig. 7 Time histories of acceleration at AH3

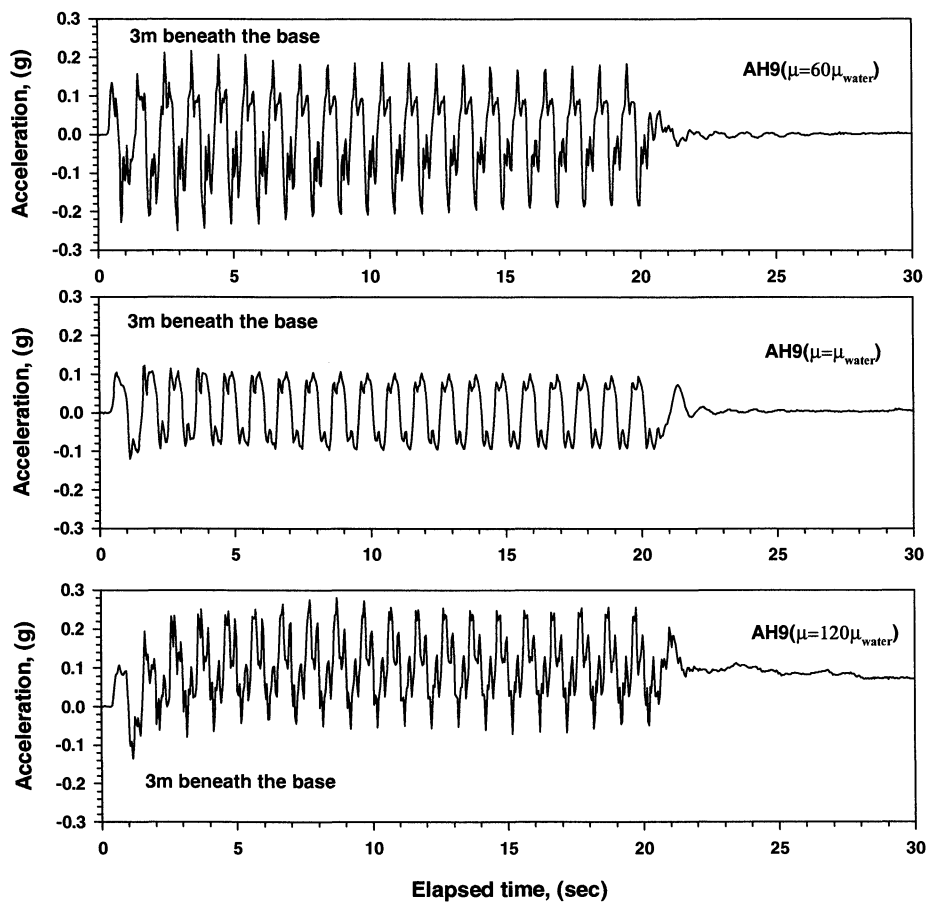

Fig. 8 Time histories of acceleration at AH9

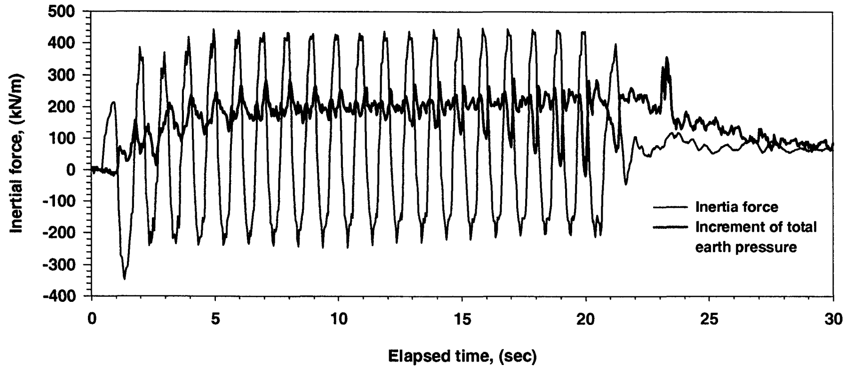

Fig. 9 Comparison of inertial force and total earth pressure increment

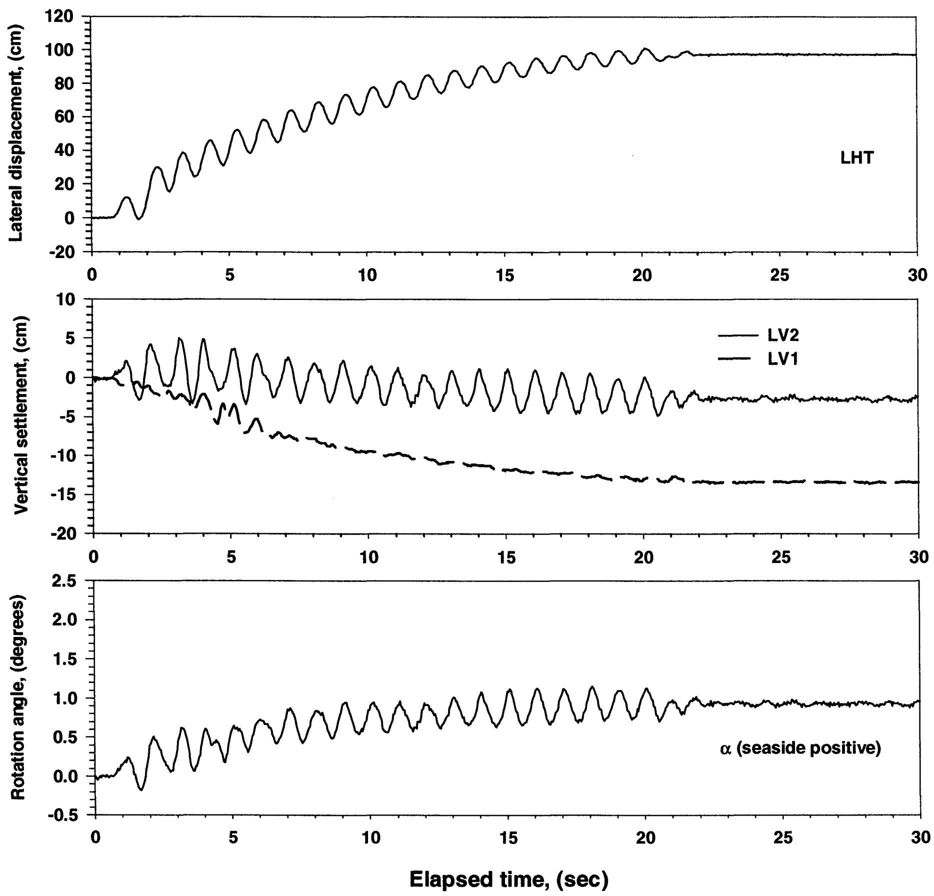

Fig. 10 Time histories of quay wall deformation

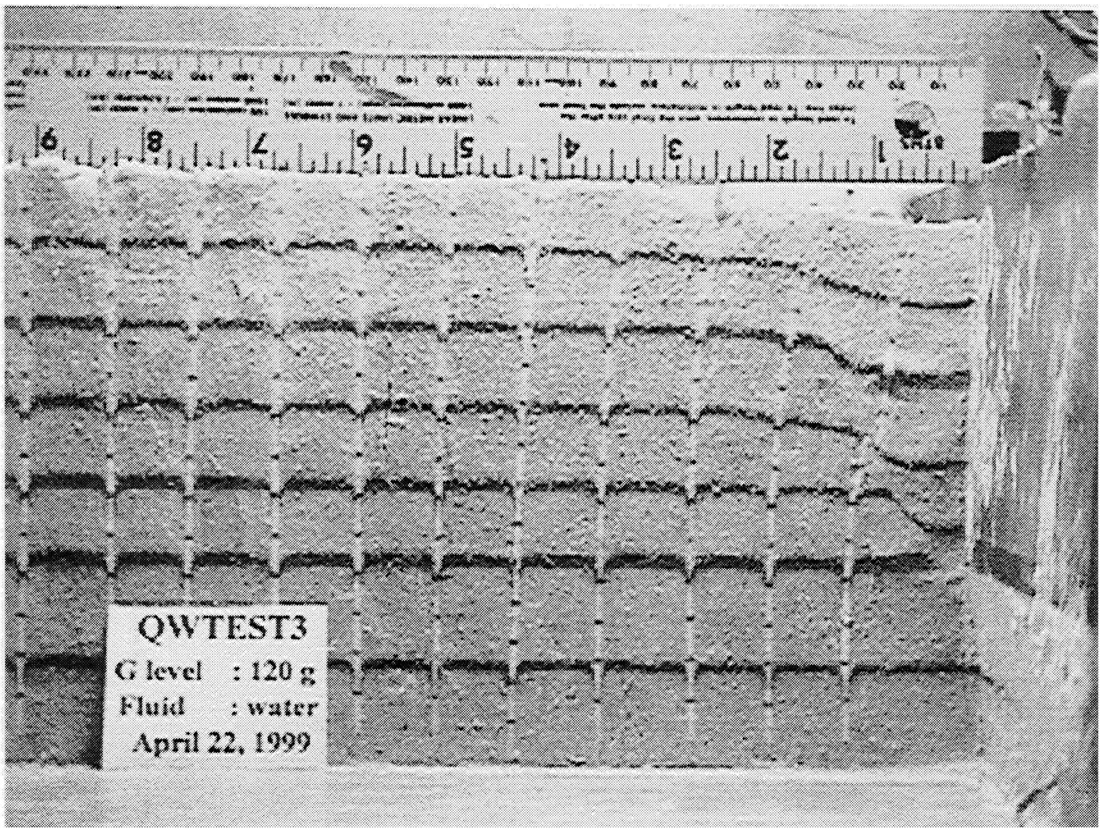

Fig. 11 Failure plane behind the quay wall

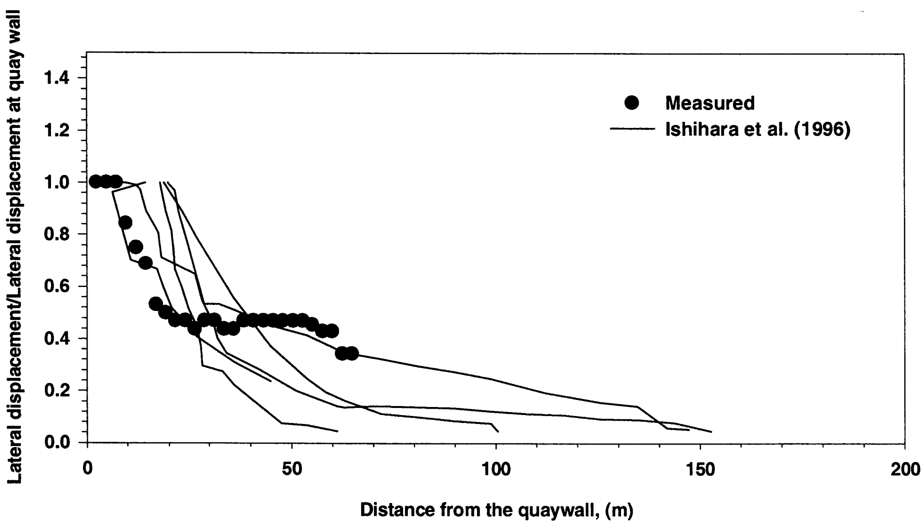

Fig. 12 Normalized distributuin of lateral displacement behind the quaywall

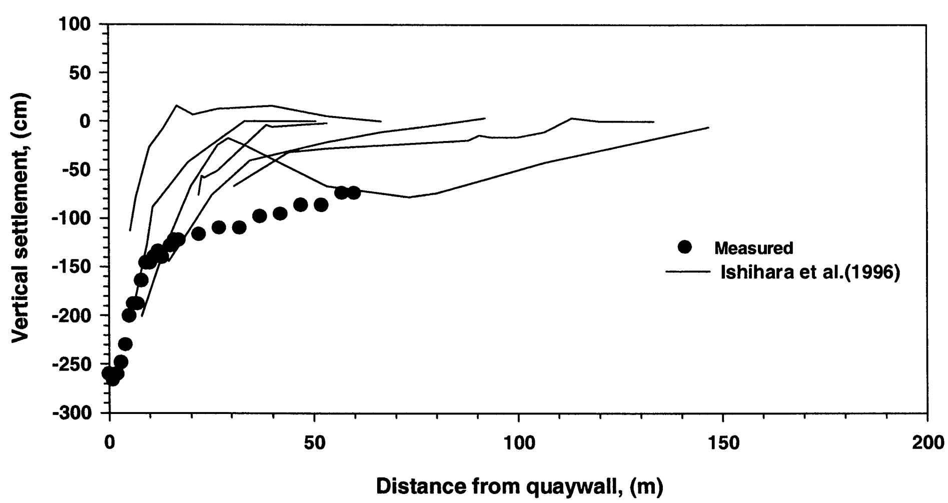

Fig. 13 Settlement of the ground surface behind the quay wall

Residual Displacement of Gravity Quaywalls
- Parameter Study through Effective Stress Analysis -

Susumu IAI, Port and Harbour Research Institute, Japan
Koji ICHII, Port and Harbour Research Institute, Japan
Hiroyuki SATO, Port and Harbour Research Institute, Japan
Hanlong LIU, Hohai University, China

ABSTRACT

Seismic performance of gravity quaywalls is studied through effective stress analysis by varying structural and geotechnical parameters of quaywalls under various levels of shaking. Major parameters studied are width to height ratio of a gravity wall, thickness of soil deposit below the wall, and geotechnical conditions represented by SPT N-values of subsoil below and behind the wall. The effective stress analysis is based on the multiple shear mechanism (FLIP), which demonstrated the applicability to the seismic analysis of gravity quaywalls at the Hyogoken-Nambu (Kobe) earthquake of 1995.

The results of the parameter study are summarized in terms of residual horizontal displacement of the wall. Among the parameters considered in this study, the most sensitive parameter is the SPT N-values of subsoil below and behind the wall. The second is the thickness of the soil deposit below the wall. Although the width to height ratio of a gravity wall is a sensitive parameter for a quaywall with firm foundation, the effect of this parameter becomes less obvious when the soil deposit below the wall becomes thick.

Based on the results of the parameter study, a simplified procedure is developed for evaluating residual horizontal displacement of a gravity quaywall under seismic excitations. In this procedure, residual horizontal displacement is evaluated based on the three parameters mentioned earlier for 0.1 to 0.6g excitations. Order-of-magnitude displacements evaluated through the simplified procedure are consistent with those measured in the past earthquakes, suggesting reasonable applicability of the simplified procedure for evaluating order-of-magnitude displacement of a gravity quaywall.

INTRODUCTION

Effective stress analysis is a powerful tool for studying seismic performance of quaywalls and bulkheads (Iai et al. 1996; Iai, 1998b; Iai et al. 1998). It is particularly useful for identifying deformation/failure mode and evaluating limit-state performance in terms of displacements, stresses and ductility factors. An example is the effective stress analysis on the seismic performance of caisson type quaywalls during the 1995 Hyogoken-Nambu earthquake. The quaywalls in Kobe Port moved 5 m maximum, about 3 m on average, toward the sea. The walls also settled about 1 to 2 m and tilted about 4 degrees toward the sea. Figure 1 shows a typical cross section and deformation of the caisson walls. The model parameters for the effective stress analysis were calibrated based on in-situ and laboratory investigations, including in-situ freeze sampling. The results of the effective stress analysis, shown in Figs. 2 and 3, were consistent with those measured, including the mode and extent of deformation/failure. In particular, the analysis was successful in capturing the mode of deformation/failure associated with significant deformation in the loose soil deposit below the wall.

The scope of work in those previous studies was limited to particular case studies in order to study in detail the applicability of the effective stress analysis. A limited parameter study was performed in those studies in order to identify the major cause of damage with respect to the relevant case histories. A general seismic performance of gravity quaywalls, however, has not yet been discussed in the previous studies. In this study, a more comprehensive parameter study is performed through the effective stress analyses, varying geotechnical and structural parameters for a gravity quaywall under various levels of seismic excitation. This parameter study aims to

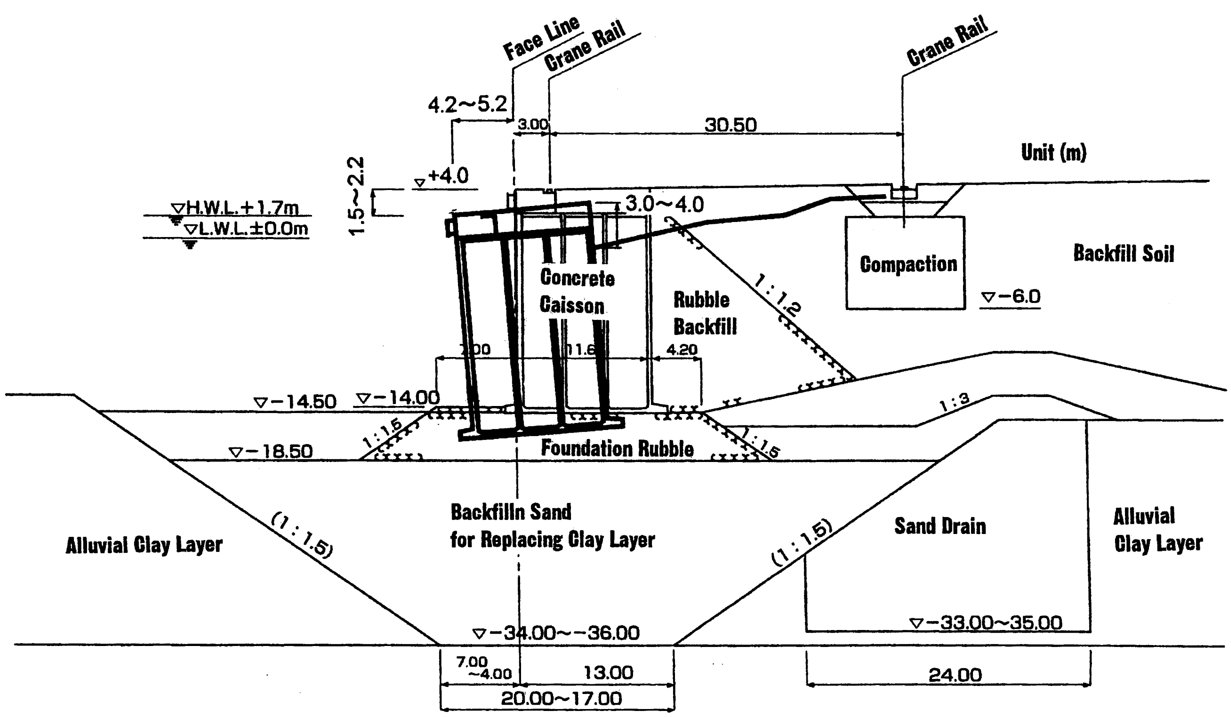

Fig. 1 Cross section and deformation of a quaywall at Kobe Port (RC-5, Rokko Island)

achieve two objectives. One is to identify major parameters governing the seismic performance of a gravity quaywall. The other is to develop a simplified procedure for evaluating order-of-magnitude displacement of a gravity quaywall. The computer code FLIP (Iai et al, 1992) is used, which is the same computer code as used in the previous studies.

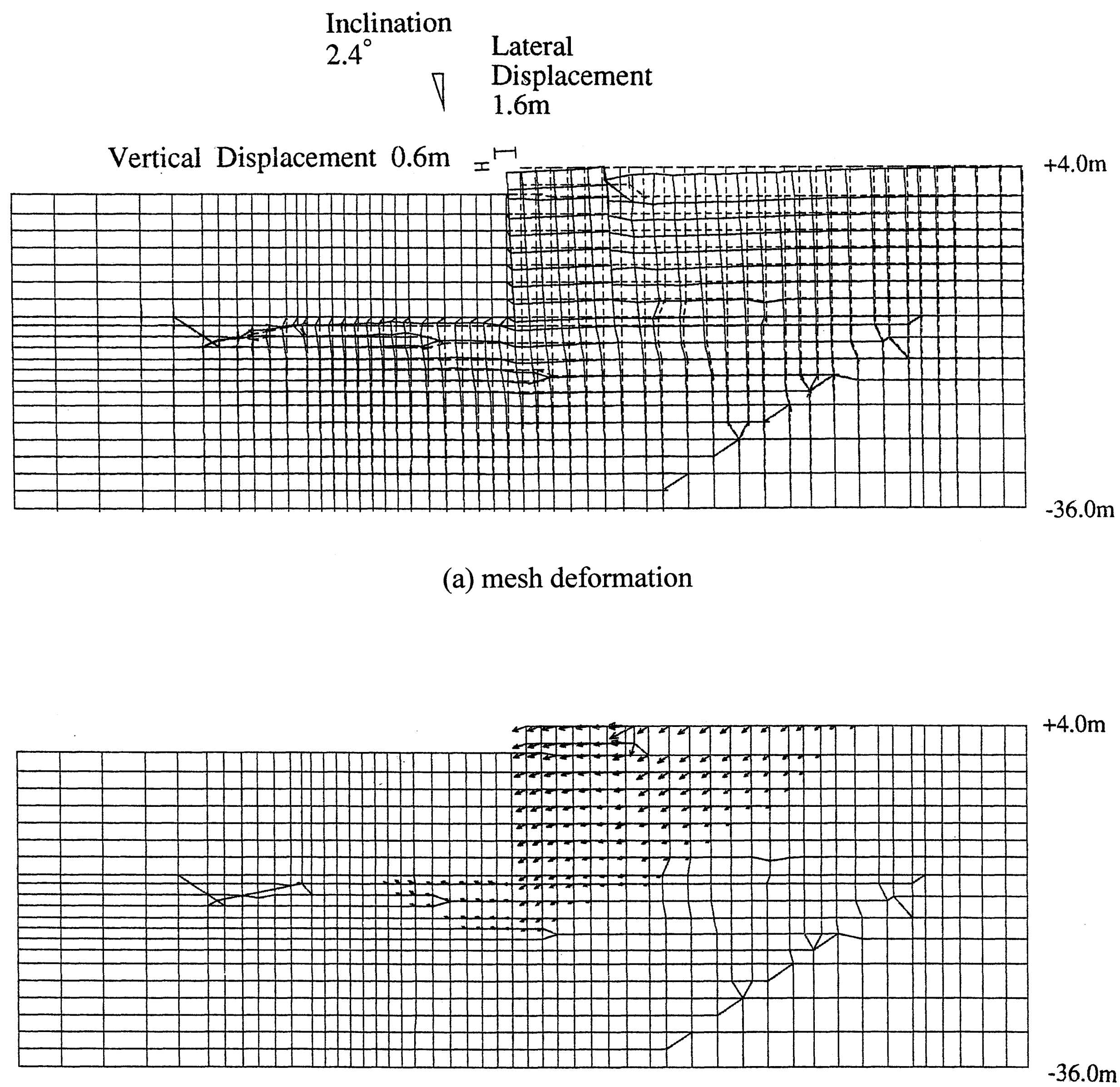

(a) mesh deformation

(b) displacement vectors (after Iai et al, 1998)

Fig. 2 Computed deformation of a quaywall at the end of shaking

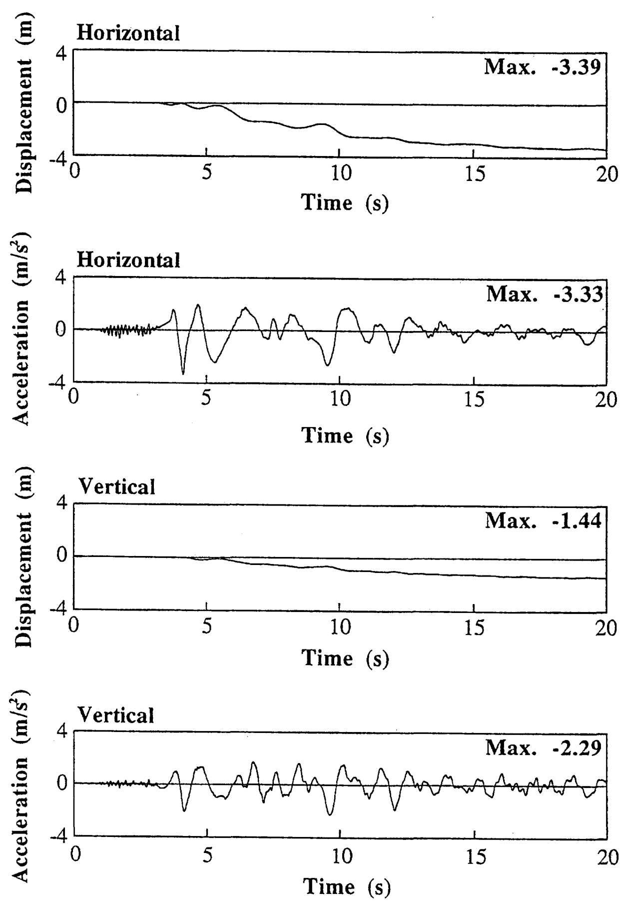

Fig. 3 Computed accelerations and displacements at the upper seaside corner of the caisson for a quaywall (after Iai et al, 1998)

PARAMETERS CHARACTERIZING GRAVITY QUAYWALL

The factors governing seismic performance of a gravity quaywall include wall dimensions, thickness of soil deposit below the wall, liquefaction resistance of subsoil below and behind the wall, as well as levels of seismic shaking at the base layer. In this study, the soil deposit below the wall was represented by a sand backfill used for replacing the original soft clay deposit in order to attain the required bearing capacity. The effects of this soil deposit on the deformation of a gravity quaywall may be approximately the same as those of a natural sand deposit below the wall and, thus, the results of the parameter study may be applicable not only for a quaywall with sand replacement studied here but also for a quaywall constructed on a natural sand deposit.

The standard cross section used for the parameter study is shown in Fig. 4. Major cross sectional dimensions were specified by a width (W) and height (H) of a gravity wall, and a thickness of subsoil (D1). For simplicity, the thickness of backfill (D2) was assumed the same as the wall height (H). A width to height ratio of a gravity wall (W/H) is one of the most important parameters in the conventional seismic design and correlated with the seismic coefficient used in the pseudo-static method as shown in Fig. 5. The width to height ratio (W/H) was thus considered a major parameter in this study. The parameters used in this study were W/H=0.65, 0.90, 1.05, which correspond to the seismic coefficients of K_h=0.1, 0.2, 0.25, respectively.

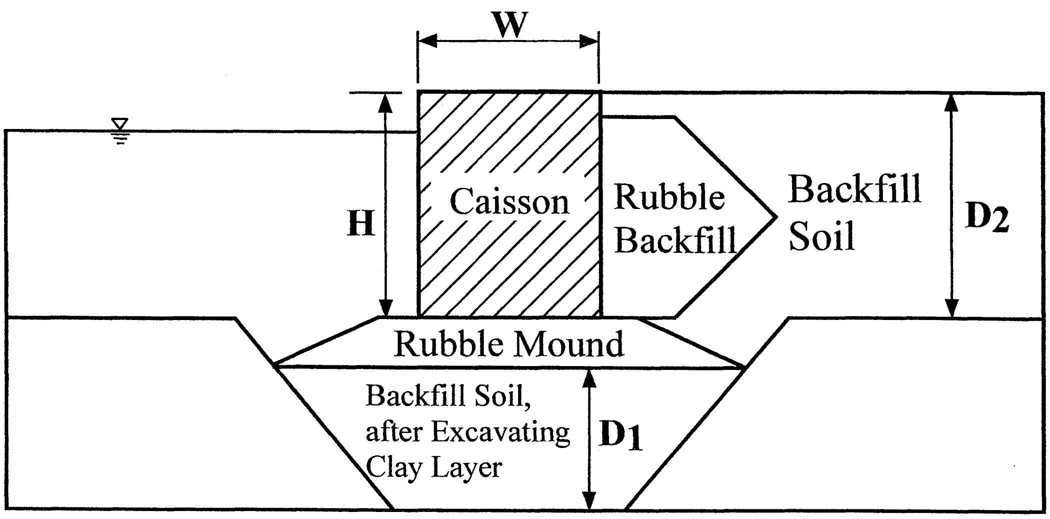

Fig. 4 Typical cross section of a gravity quaywall for parameter study

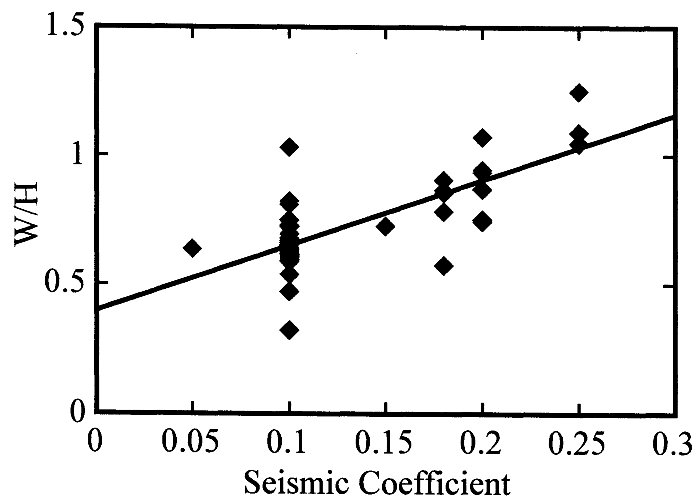

Fig. 5 Correlation between the width to height ratio (W/H) and seismic coefficient of a gravity quaywall

The peak accelerations of the input seismic excitation assigned at the base layer as incident wave (as of 2E) ranged from 0.1 to 0.6 g. The time history of the earthquake excitation was that of the incident wave (2E) at the Port Island (Kobe) vertical seismic array site at a depth of –79m.. This time history, shown in Fig. 6, is often used in Japan for evaluating seismic performance of high earthquake resistant quaywalls under Level 2 earthquake motions (Ministry of Transport, 1997).

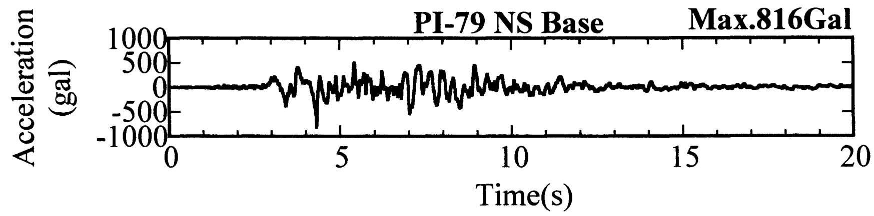

Fig. 6 Time history used as input excitation (2E)

Thickness of the soil deposit below the wall (D1) was specified by a ratio with respect to the wall height (H), ranging from D1/H=0.0 (i.e. a rigid base layer located immediately below the wall) to D1/H=1.0 (i.e. thick soil deposit below the wall). For simplicity, the geotechnical conditions of the soil deposits below and behind the wall were assumed to be the same with each other, represented by equivalent SPT N-value (SPT N-value corrected for the effective vertical stress of 65 kPa). The equivalent SPT N-value has been widely used for assessment of liquefaction potential in Japanese port areas (Iai et al, 1989). Model parameters for the effective stress analysis were determined from the equivalent SPT N-values based on a simplified procedure (Morita et al., 1997). Other conditions assumed for the effective stress analysis include: wall height H=13m, water level=2m lower than the top of the wall, thickness of the rubble mound=4m, and unit weight of caisson=2.3tf/m^3.

All the analyses were performed for the plane strain condition based on finite element method. Before the earthquake response analysis, a static analysis was performed with gravity under drained conditions to simulate the stress conditions before the earthquake. The results of the static analyses were used for the initial conditions in the earthquake response analyses. The seismic analyses were performed under undrained conditions (Zienkiewicz and Bettess, 1982) to approximate the behavior of saturated soils under transient and cyclic loads during earthquakes. The input earthquake motion mentioned earlier was specified at the bottom boundary through equivalent viscous dampers to simulate a incident transmitting wave (i.e. 2E). In order to simulate the incoming and outgoing waves through the side boundaries of the analysis domain, equivalent viscous dampers were also used at the boundaries. The effect of the free field motions was also taken into account by performing one dimensional response analysis at the outside fields and assigning the free field motion through the viscous dampers.

The structures made of concrete caissons were modeled using linear elastic solid elements. The soil-structure interfaces were modeled by the joint elements. The sea water was modeled as incompressible fluid and was formulated as an added mass matrix based on the equilibrium and continuity of the fluid at the solid-fluid interface (Zienkiewicz, 1977). For more details, refer to Iai et al. (1998).

PARAMETER SENSITIVITY ON QUAYWALL DISPLACEMENT

Results of the parameter study were summarized in terms of residual horizontal displacement (d) at the top of the wall. The residual horizontal displacement was normalized with respect to the wall height (H). Effects of the major parameters on the normalized residual horizontal displacement (d/H) will be discussed below.

Width to Height Ratio (W/H)

Effects of width to height ratio (W/H) on the displacement are shown in Fig. 7 for equivalent SPT N-value of 15. When the foundation below the wall is rigid (i.e. D1/H=0), increasing W/H reduces the wall displacement. When the foundation soil is medium to dense (i.e. with equivalent SPT N-values of 15) and thick (i.e. D1/H=1.0), however, the effects of W/H become less obvious.

Input Excitation Level

Effects of input excitation level are shown in Fig. 8 for W/H=0.9, which corresponds to the seismic coefficient of k_h=0.2 (see Fig. 5). Except for the equivalent SPT N-values of 5 and 8, at which extensive liquefaction significantly increases the displacement, the normalized displacement for the excitation of 0.2 g at the base layer are within d/H<0.03. The horizontal displacement of a wall for d/H=0.03 is, for example, 0.3 m for a gravity quaywall with H=10 m, suggesting that the quaywall designed with the seismic coefficient of 0.2 based on the conventional pseudo-static method withstands the excitation of 0.2 g at the base layer if a margin of displacement in the order of 0.3 m is allowed.

Equivalent SPT N-value

Effects of equivalent SPT N-value are shown in Fig. 9 for W/H=0.9. Obviously the thickness of soil deposit below the wall significantly affects the displacement. For a wall put on a rigid foundation (D1/H=0), effects of the equivalent SPT N-value of soil behind the wall are relatively small. For a wall put on a thick soil deposit (D1/H=1.0), effects of the equivalent SPT N-values of soil below and behind the wall are significant.

Thickness of Soil Deposit below Wall

Effects of thickness of soil deposit below the wall are shown in Fig. 10 for W/H=0.9. When the level of excitation is high, significant increase in the displacement is recognized for D1/H<0.5 and for smaller SPT N-values, suggesting that the existence of soil deposit below the wall and its SPT N-values are two important factors to affect the displacement.

Overall Parameter Sensitivity

Among the parameters considered in this study, the most sensitive parameter affecting the quaywall displacement under a prescribed level of shaking is the SPT N-values of subsoil below and behind the wall. The second is the thickness of the soil deposit below the wall. Although the width to height ratio of a gravity wall is a sensitive parameter for a quaywall with firm foundation, the effects of this parameter become less obvious when the soil deposit below the wall is thick.

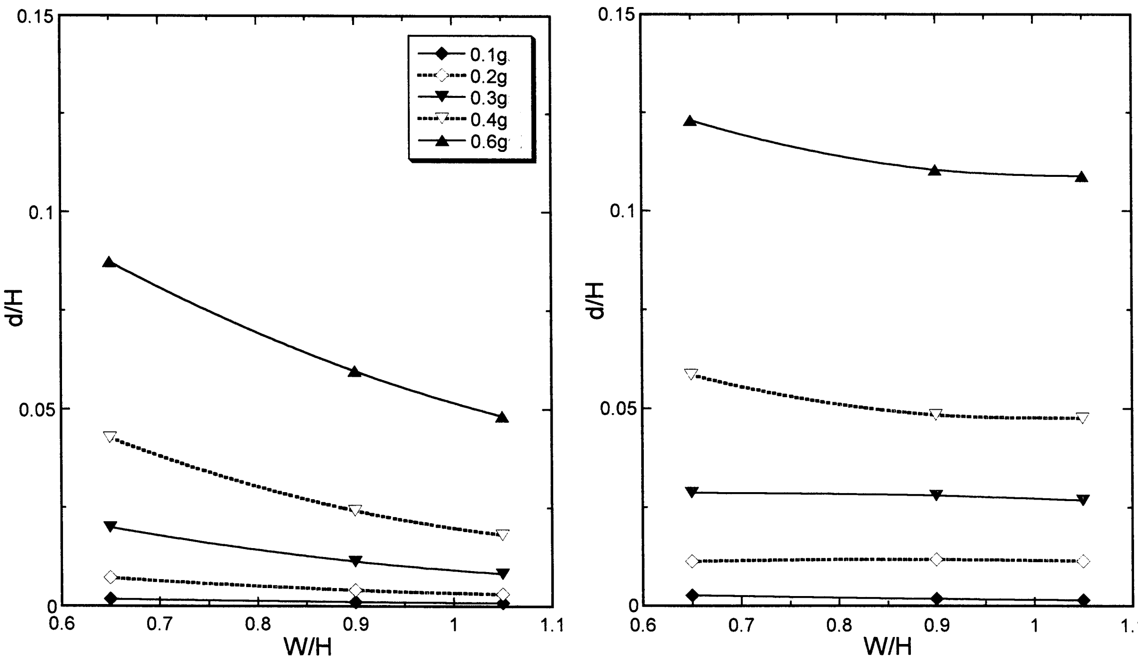

(a) D1/H=0.0

(b) D1/H=1.0

Fig.7 Effects of width to height ratio W/H (for equivalent SPT N-value of 15)

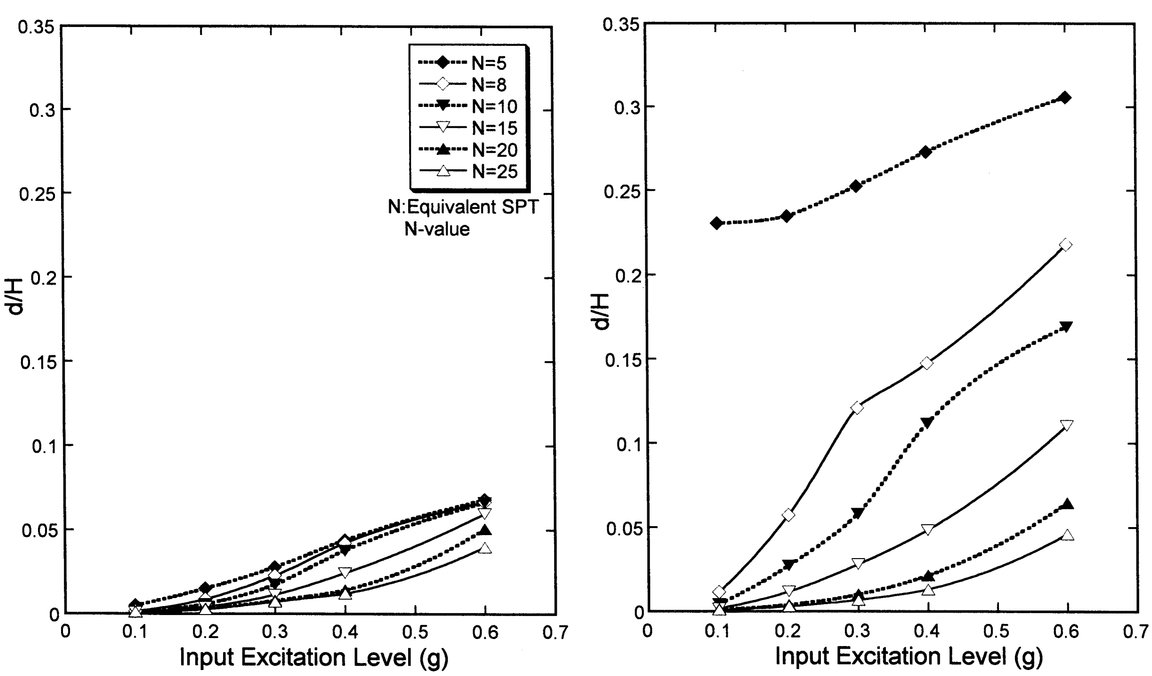

(a) D1/H=0.0

(b) D1/H=1.0

Fig.8 Effects of input excitation level (for W/H=0.9)

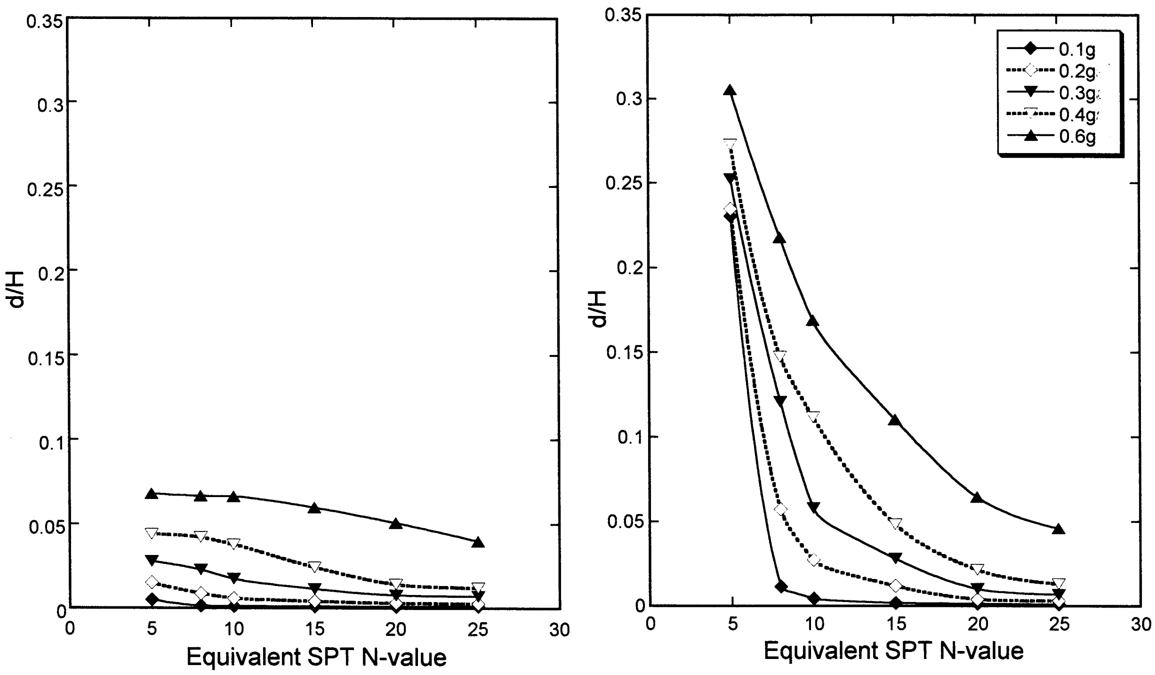

(a) D1/H=0.0

(b) D1/H=1.0

Fig.9 Effects of equivalent SPT N-value (for W/H=0.9)

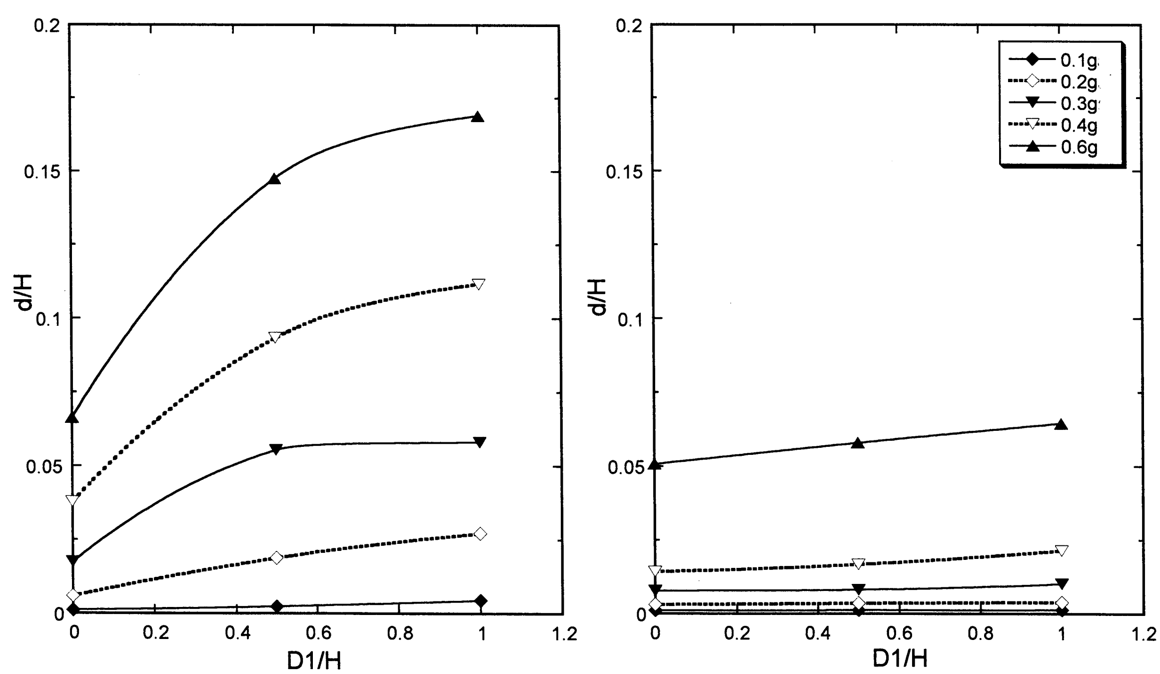

(a) Equivalent SPT N-value (10)

(b) Equivalent SPT N-value (20)

Fig.10 Effects of thichness of soil deposit below the wall (for W/H=0.9)

SIMPLIFIED PROCEDURE FOR EVALUATING WALL DISPLACEMENT

As mentioned earlier, the effective stress analysis is particularly useful for identifying deformation/failure modes and evaluating limit-state performance of quaywalls and bulkheads. The effective stress analysis, however, requires high level of engineering and reasonable amount of resources and, hence, it is not always easy to apply for routine design practice. A simplified procedure is needed for evaluating order-of-magnitude displacement in routine design practice.

Although Newmark type analysis is often adopted as a simplified procedure to evaluate earthquake induced displacement, the Newmark type analysis often underestimates displacement of those retaining structures with submerged backfill (Iai et al., 1998a). A new procedure is needed to include the cyclic behavior of saturated soil below and behind the wall in evaluating the quaywall displacement. The results of the parameter study obtained in the previous chapter offer a basis to meet this need.

Based on the results of the parameter study shown in the previous chapter, a simplified procedure is easily developed for evaluating gravity quaywall displacement. The flow chart for the simplified procedure is shown in Fig. 11. In this procedure, the displacement is evaluated with respect to the parameters in the order of its sensitivity to the displacement.

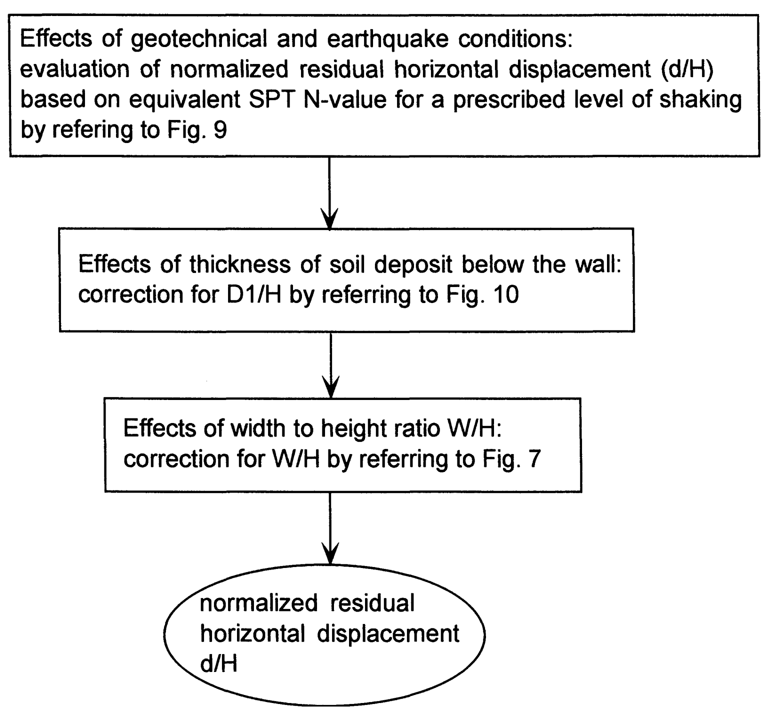

Fig. 11 Flow chart for simplified evaluation of residual displacement of a gravity quaywall

Applicability of the proposed procedure was studied in two aspects. One was based on additional parameter study to confirm that the figures shown in Figs. 9 and 10 are applicable to the conditions other than the particular values of W/H and D1/H used for the parameter study. The results shown in Figs. 12 and 13 may confirm the general applicability of Figs. 9 and 10.

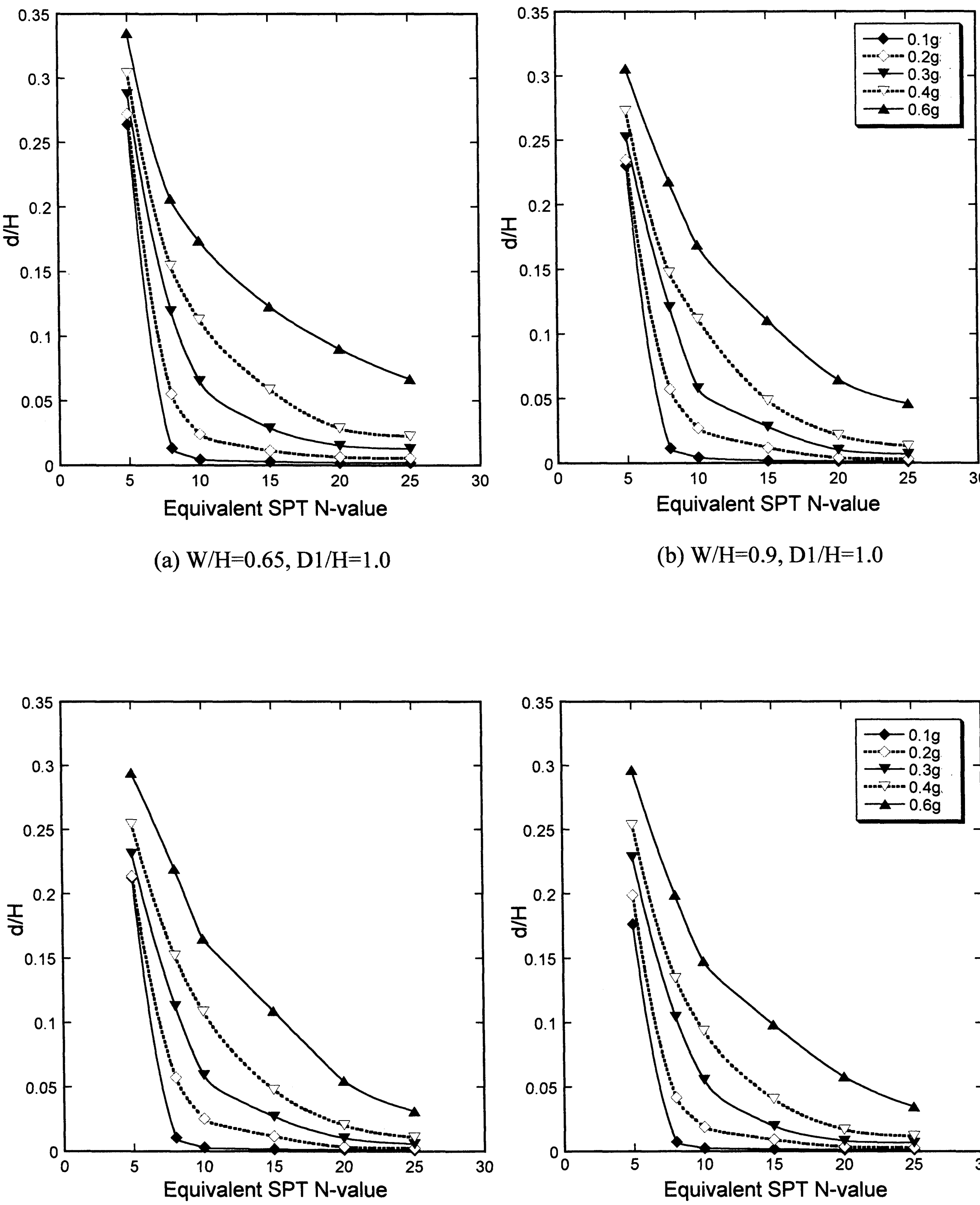

(a) W/H=0.65, D1/H=1.0

(b) W/H=0.9, D1/H=1.0

(c) W/H=1.05, D1/H=1.0

(d) W/H=0.9, D1/H=0.5

Fig. 12 Effects of input excitation level (for various W/H and D1/H)

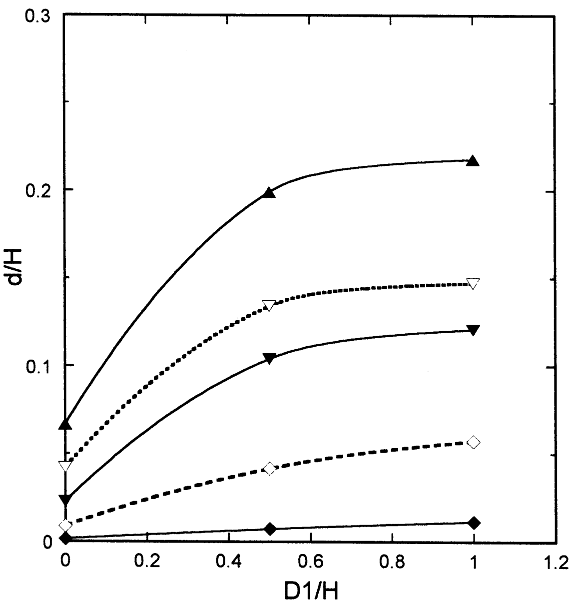

(a) W/H=0.9 (8)

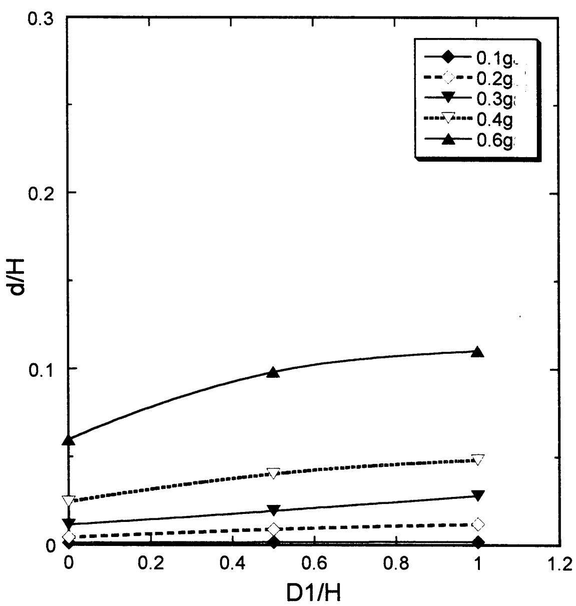

(b) W/H=0.9(15)

Fig. 13 Effects of thickness of soil deposit below the wall
(for W/H=0.9 with equivalent SPT N-values of 8 and 15)

Overall applicability of the proposed procedure was evaluated based on the case history data. Two case histories were used. One was the quaywall performance at Kushiro Port during the 1993 Kushiro-oki earthquake. A typical cross section of gravity quaywalls at Kushiro Port is shown in Fig. 14. As shown in this figure, a caisson wall was put on a firm foundation with SPT N-values ranging from 30 to 50, with a loose backfill having equivalent SPT N-values of about 5 to 10. Shaken with a peak bedrock acceleration of 0.28g, residual displacement of the caisson walls in the Kushiro port ranged from d/H=0.0 to 0.06, on the average d/H=0.02 (Iai and Mizuno, 1994).

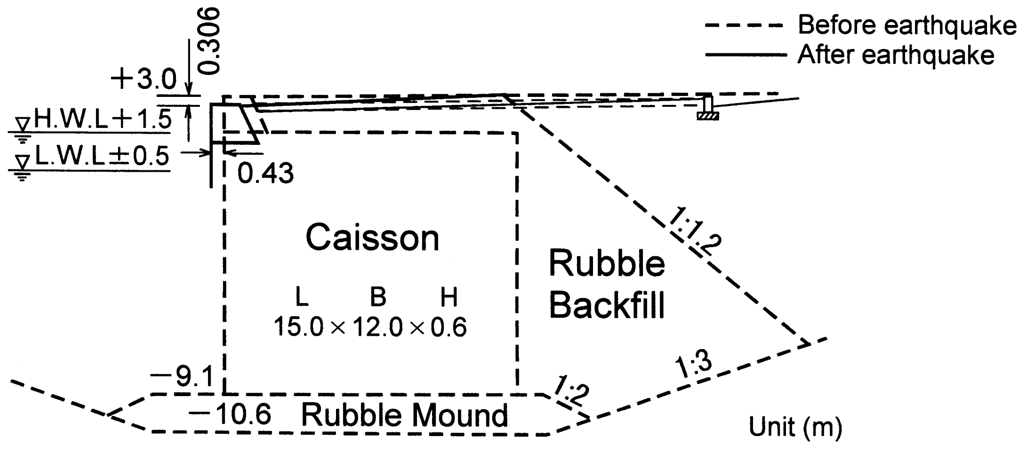

Fig. 14 Cross section and deformation of a quaywall at Kushiro Port
(West Port District No.2 West quaywall –9m)

The other was the quaywall performance at Kobe Port during the 1995 Hyogoken-Nambu earthquake. A typical cross section of gravity quaywalls at Kobe Port was shown in Fig. 1. As shown in this figure, a caisson wall was put on a loosely deposited decomposed granite. The equivalent SPT N-values for subsoil below and behind the wall were 10 on the average. Shaken with a peak acceleration of 0.55g at a depth of GL-32m, as recorded at the Port Island vertical seismic array site, residual displacement of the caisson walls having sand deposit D1/H=1.0 (for D1 ranging from 15 to 20m) ranged from d/H=0.10 to 0.30, on the average d/H=0.20 (Inagaki et al, 1996).

The order-of-magnitude displacements of a gravity quaywall were evaluated based on the major parameters relevant to these two case histories. The results are shown in Table 1. They are basically consistent with those measured, suggesting reasonable applicability of the simplified procedure. In particular, the simplified procedure demonstrated the capability to evaluate wide range of displacements, ranging from the displacement in the order of one-tenths of meters to those with one order higher.

Table 1 Simplified evaluation of residual horizontal displacements

Case Histories		
Case History	Kushiro Port, West Port District 1993 Kushiro-oki earthquake	Kobe Port, Rokko Island 1995 Hyogoken-Nambu earthquake
measured horizontal displacement at the earthquake (d/H)	d/H=0 to 0.06 on the average d/H=0.02	d/H=0.1 to 0.3 on the average d/H=0.2
Simplified Evaluation		
input excitation level	0.28 g recorded at -79m at the vertical seismic array site To be rounded to 0.3 g for simplified evaluation	0.55 g at –32m at the vertical seismic array site To be rounded to 0.6 g in simplified evaluation
equivalent SPT N-value	equivalent SPT N-values about 5 to 10 d/H=0.018 to 0.028 based on Fig. 9(a)	equivalent SPT N-value about 10 d/H=0.17 based on Fig. 9(b)
D1/H	D1/H=0 no correction needed for D1/H based on Fig. 10	D1/H=1.0 no correction needed for D1/H based on Fig. 10
W/H	W/H=1.04 to 1.09 correction factor of 0.7 to 0.8 is needed for W/H=0.9 based Fig. 7(a)	W/H=0.64 to 0.74 correction factor of 1.1 is needed for W/H=0.9 based on Fig. 7(b)
normalized horizontal displacement based on simplified procedure (d/H)	d/H=0.013 to 0.022 To be rounded to d/H=0.02	d/H=0.19 To be rounded to d/H=0.2

CONCLUSIONS

Seismic performance of a gravity quaywall was studied through effective stress analysis by varying structural and geotechnical parameters under various level of shaking. Major conclusions obtained from this parameter study are as follows.

(1) Among the parameters considered in this study, the most sensitive parameter affecting the quaywall displacement under a prescribed level of shaking is the SPT N-values of subsoil below and behind the wall. The second is the thickness of the soil deposit below the wall. Although the width to height ratio of a gravity wall is a sensitive parameter for a quaywall with firm foundation, the effect of this parameter becomes less obvious when the soil deposit below the wall is thick.

(2) A simplified procedure is proposed to evaluate the order-of-magnitude displacement of a gravity quaywall. In this procedure, residual horizontal wall displacement under a prescribed level of shaking is evaluated based on the three parameters mentioned above.

(3) Applicability of the proposed simplified procedure was confirmed by case history data. The procedure demonstrated the capability to evaluate a wide range of displacements, ranging from the displacement in the order of one-tenths of meters to those with one order higher.

REFERENCES

Iai, S., Tsuchida, H., and Koizumi, K. (1989) : A liquefaction criterion based on field performances around seismograph stations, Soils and Foundations, Vol., 29, No.2, pp.52-68

Iai, S., Matsunaga, Y. and Kameoka, T. (1992) : Strain space plasticity model for cyclic mobility, Soils and Foundations, Vol.32, No.2, pp.1-15

Iai, S. and Mizuno Y. (1994) : Damage to ports and airport, Report on 1993 Kushiro-oki & Noto-peninsula-oki earthquakes, Japanese Geotechnical Society, pp.159-185 (in Japanese)

Iai, S., Ichii, K. and Morita, T. (1996) : Evaluating ground displacement behind bulkheads, Proc. the 6th Japan-U.S. Workshop on Earthquake Resistant Design of Lifeline Facilities and Countermeasures against Soil Liquefaction, Technical Report NCEER-96-0012, pp.629-638

Iai, S. (1998a) : Rigid and flexible retaining walls during Kobe earthquake, Proc. 4th International Conference on Case Histories in Geotechnical Engineering, St. Louis, pp.108-127

Iai, S. (1998b) : Seismic analysis and performance of retaining structures, Geotechnical Earthquake Engineering and Soil Dynamics III, ASCE Geotechnical Special Publication No.75, Vo..2, pp.1020-1044

Iai, S., Ichii, K., Liu, H., and Morita, T. (1998) : Effective stress analyses of port structures, Soils and Foundations, Special Issue on Geotechnical Aspects of the January 17 1995 Hyogoken-Nambu earthquake, pp.97-114

Inagaki, H., Iai, S., Sugano, T., Yamazaki, H. and Inatomi, T. (1996) : Performance of caisson type quay walls at Kobe Port, Soils and Foundations, Special Issue on Geotechnical Aspects of the January 17 1995 Hyogoken-Nambu earthquake, Japanese Geotechnical Society, pp.119-136

Morita, T., Iai, S., Liu, H., Ichii, K., and Sato, Y. (1997) : Simplified method to determine

parameters of FLIP, Technical Note of the Port and Harbour Research Institute, No.869, p.36 (in Japanese)
Zienkiewicz, O.C. (1977) : The Finite Element Method, 3rd edition, Mc Craw-Hill Book Co.
Zienkiewicz, O.C. and Bettess, P. (1982) : Soils and other saturated media under transient, dynamic conditions, Soil Mechanics-Transient and Cyclic Loads, Pande and Zienkiewicz (eds.), Johne Wiley & Sons, pp.1-16

ANALYSIS ON LIQUEFACTION-INDUCED SUBSIDENCE OF SHALLOW FOUNDATION

Yoshikazu Kobayashi Visiting Researcher, Technical University of Delft
Ikuo Towhata University of Tokyo
and
Alexis A.Acacio University of the Philippines

ABSTRACT

Analytical procedure was developed to predict the subsidence of buildings resting on shallow foundation into liquefied subsoil. The method is characterized by the reduced amount of input data as well as short time of computation. Those goals were achieved by the use of deformation modes which were observed in shaking table model tests. The proposed method was then applied to building subsidence in Dagupan city in the Philippines where liquefaction affected buildings significantly. The comparison of observed and calculated subsidences shows that the proposed method well predicts the subsidence when the extent of damage is substantial. On the contrary, minor extent of subsidence is overestimated by the proposed method. This is probably because the proposed method considers the liquefied sand as a complete liquid without rigidity, while the sand may have maintained some rigidity when the extent of subsidence was less.

INTRODUCTION

Among a variety of effects caused by subsurface liquefaction is the subsidence of shallow foundations. Fig.1 illustrates a typical damage of subsidence during the 1964 Niigata earthquake. The damaged building lost its function due to intolerable subsidence and tilting, despite that no structural damage occurred. Fig.2 indicates the damaged shape of the Niigata Airport Building during the same earthquake. This building subsided ultimately 1.2m. An eyewitness report states that this subsidence occurred after the end of strong shaking (Japan. Geotech. Society, 1999). Fig.3 further demonstrates subsidence of an oil storage tank in Kobe, 1995. The flexible connection between the tank and pipes made it possible for the tank to avoid fatal leakage of oil.

It is important that there is so far no good means to predict the subsidence of shallow foundations in spite of the importance of the phenomenon. One of the reasons for this seems to be the difficulty associating the calculation. Fig.3 suggests that the body of the tank penetrated into subsoil, which means that sliding occurred between the tank and the soil. Hence, in a numerical analysis, there has to be a sliding element or its equivalence at the soil-structure interface. Another difficulty is the large deformation/displacement. Most of the conventional approach of analysis cannot take into account the fact that the increased buoyancy force after subsidence mitigates further subsidence. This fact means that the subsidence ultimately stops at the moment when the buoyancy is in equilibrium with gravity. In other words, the small-displacement analysis overestimates the subsidence. This point is important in prediction of subsidence, although it may not be so in lateral deformation of, for example, revetment walls. Although prediction of subsidence by means of centrifuge tests (Liu and Dobry, 1997) is attractive, the required time and availability of facilities might be a problem.

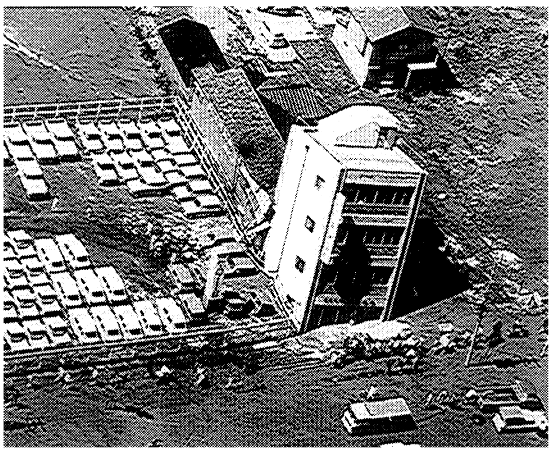

Fig.1 Subsidence and tilting of building resting on liquefied soil in Niigata (Japanese Geotechnical Society, 1999).

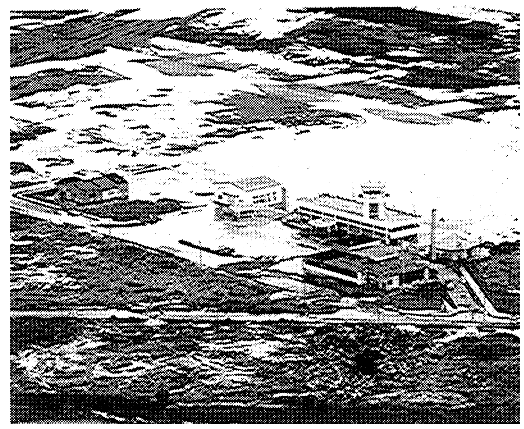

Fig.2 Subsidence of Niigata Airport Building (Japanese Geotechnical Society, 1999).

The authors have been developing an analytical procedure for prediction of liquefaction-induced ground displacement (Towhata et al., 1999a). This method is characterized by its simplicity despite that such issues as loss of rigidity of liquefied sand, large-displacement formulation, and development of displacement with time are taken into account. It is attempted in this text to apply this method to the problem of subsidence of shallow foundation into liquefied subsoil.

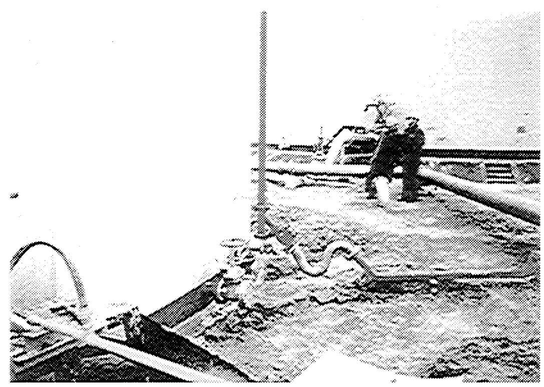

Fig.3 Subsidence of oil storage tank and bending of flexible joint during the 1995 earthquake in Kobe.

SUBSIDENCE OF BUILDING RESTING ON LIQUEFIED SUBSOIL

The present study is concerned with subsidence of building which rests upon a shallow foundation. When liquefaction occurs beneath the building, the surface structure without pile subsides downwards. When the extent of subsidence is minor, restoration is possible by, for example, jacking up. In some cases, even no restoration is practiced. On the contrary, a significant subsidence affects the serviceability of the building. Hence, it is desired to, firstly, determine the maximum tolerable magnitude of subsidence, and thereafter to calculate the possible magnitude of subsidence. In case the calculated subsidence exceeds the limit of tolerance, some mitigation measure is necessary.

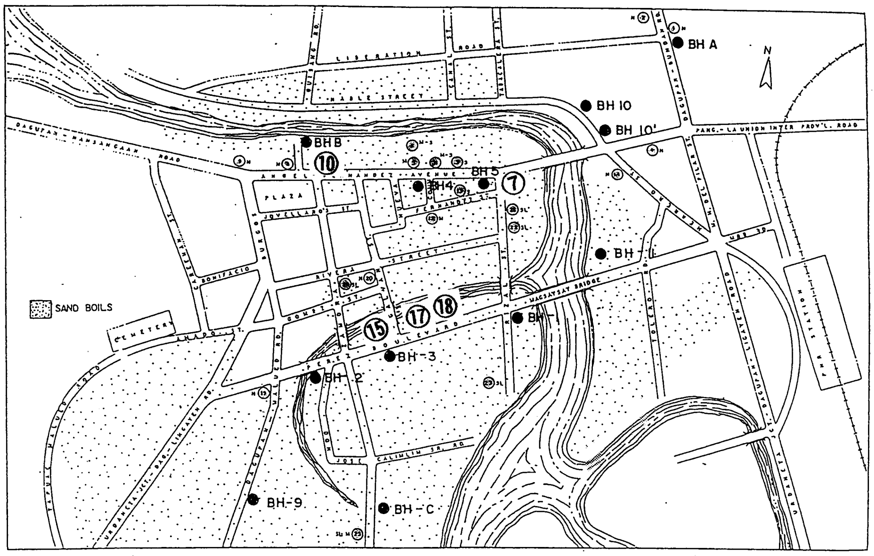

Fig.4 Map of Dagupan city with location of studied buildings (Acacio, 1997).

Prior to discussing the method of prediction of subsidence, it is important to review past experiences of building subsidence so that the developed method of prediction may avoid unnecessary complexity. One of the most detailed case studies of building subsidence caused by liquefaction is found in the city of Dagupan which experienced liquefaction during the 1990 Luzon earthquake in the Philippines.

Fig.5 Damaged situation of building No.7.

Ishihara et al. (1993) reported the extent of building damage in Dagupan. Tokimatsu et al. (1994) revealed that the thicker layer of liquefied sandy deposits made more serious the extent of building damage. Acacio (1997) conducted a detailed study on the shape of damaged buildings and their foundations which are useful for the present study. Fig.4 illustrates the map of the Dagupan City in which the locations of studied buildings are indicated. Fig.5 manifests the damaged shape of building No.7 for which the magnitude of subsidence was 0.45 m. Fig.6 shows the subsidence of building No.15. Sinking 0.55 m, this building was abandoned after the quake. Moreover, Fig.7 demonstrates the substantial inclination of building No.18. Although the inclination is another interesting topic of study, the present study cannot yet predict it. In addition to the buildings shown in figures, many ones were affected by subsidence. When the extent of damage was light, building are still in service without restoration.

Fig.6 Damaged shape of building No.15.

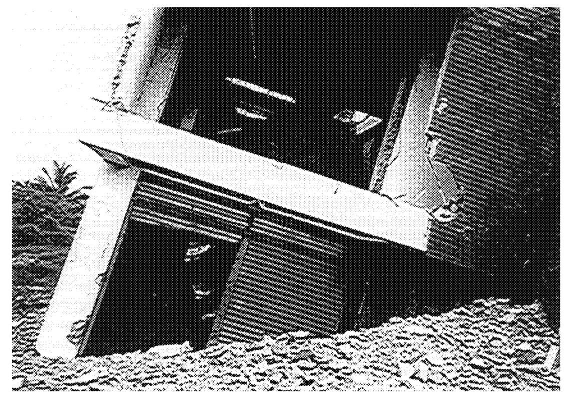

Fig.7 Inclined building No.18.

Acacio (1997) conducted Swedish penetration tests at many places in Dagupan city and assessed the thickness of liquefied layer. The present study makes use of this assessed thickness in the calculation of building subsidence. It should be borne in mind that the assessment of liquefaction layer by the conventional approach of factor of safety against liquefaction was not possible or was of limited reliability. This is because the magnitude of surface acceleration, which is one of the keys of the calculation of factor of safety, was not measured at any station in the country.

METHOD OF PREDICTION OF SUBSIDENCE

The proposed method (Towhata et al., 1999a) has been developed based on the following ideas;

1) the distribution of horizontal displacement induced by liquefaction is expressed by a sinusoidal function of depth,
2) liquefied sand behaves similar to viscous liquid with limited shear strength (Bingham liquid) or without strength (Newtonean liquid),
3) the flow and large deformation of liquefied subsoil occurs under the condition of constant volume which stands for undrained condition; when subsidence caused by consolidation is important, a few percent of the thickness of liquefied layer is added to the calculated subsidence.
4) the displacement of subsoil makes the overall potential energy as small as possible (principle of minimum potential energy); the displacement ultimately stops at the maximum possible value when the minimum potential energy is attained,
5) the time history of displacement towards the maximum possible value can be calculated by considering the liquefied sand as viscous liquid with/without residual shear strength,
6) the calculation of time history of displacement is developed by using the theory of Lagrangean equation of motion.

These ideas are going to be applied to the problem of subsidence of shallow foundation. Be noted that the present method is concerned with the overall behavior of subsoil and such details of deformation as finite element analysis is concerned with is out of scope.

Figure 8 illustrates the method of analysis. A symmetry is assumed around the central axis of a building. Since the building rests upon a shallow foundation, the liquefaction in the subsoil immediately causes subsidence of the building. Fig.8 also shows the idea that the subsidence of building induces lateral displacement of liquefied subsoil. In a crowded downtown area, the adjacent buildings along the same street prevents soil displacement normal to the plane of Fig.8. Hence, it is reasonable to apply the illustrated two-dimensional plane-strain analysis to a cross section which includes the building and the street. The center of the street is made the zero-displacement boundary where the lateral motions of liquefied subsoil from two sides of a street meet and cancel each other.

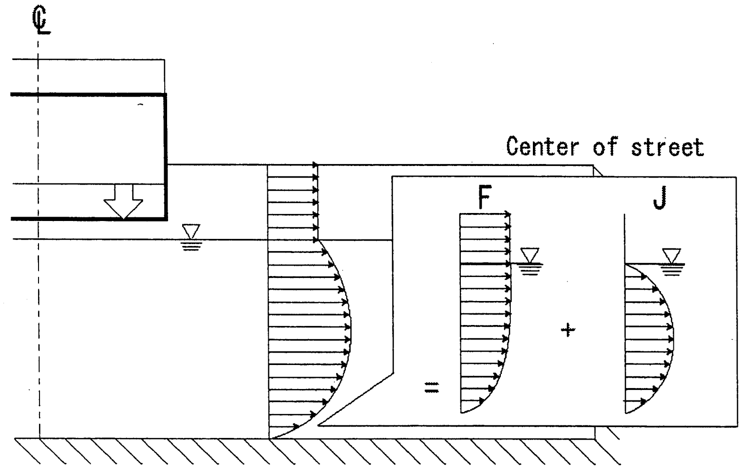

Fig.8 Two-dimensional model of liquefied ground with subsidence of building at surface.

Figure 9 indicates the shape of lateral displacement of liquefied slope which was observed in a large-scale shaking table test in 1-g field. The lateral displacement as shown by grids of colored sand indicates the maximal at the surface, while null displacement at the bottom. This mode of displacement has been approximated by a sine function such as

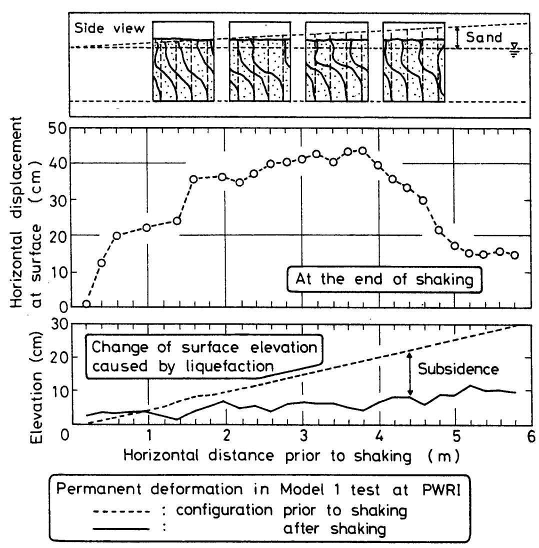

Fig.9 Observed shape of subsoil deformation of slope model during liquefaction (Sasaki et al., 1992).

$$U(x,z) = F(x)\sin\frac{\pi z}{2H} \qquad (1)$$

where U stands for the lateral displacement, which is a function of horizontal (x) and vertical (z; positive upward) coordinates. Moreover, H is the thickness of liquefied layer, and $F(x)$ is the surface displacement. The mode of displacement expressed by Eq.1 is going to be called "F" mode in this text. Be noted that the thickness of liquefied layer can be determined separately by using SPT, Swedish penetration, or CPT among others.

Shaking table tests on subsidence of shallow foundations revealed that the F mode is not the only one choice. Fig.10 shows the observed displacement in tests with a surface building. It is noteworthy that the lateral displacement is null at both top and bottom of a liquefied layer, while taking the maximal at the middle. Being called J mode hereinafter, this mode of deformation is expressed by

$$U(x,z) = J(x)\sin\frac{\pi z}{H}. \quad (2)$$

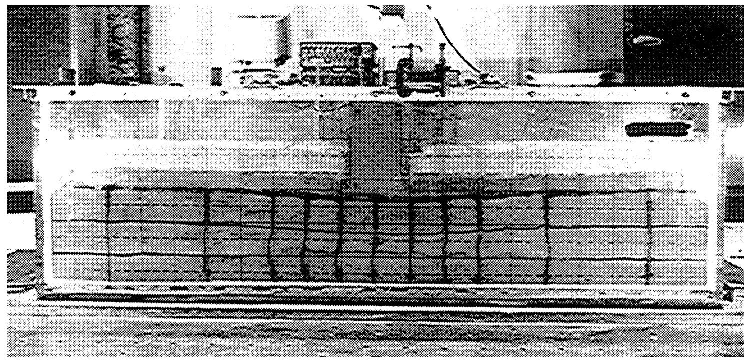

Fig.10 Observed shape of subsoil deformation under shallow foundation (Acacio, 1997).

It seems, therefore, that the real distribution of lateral displacement is, in general, a combination F and J modes. Fig.11 shows that a variety of displacement distribution can be expressed by changing the ratio of F and J;

$$U(x,z) = F(x)\sin\frac{\pi z}{2H} + J(x)\sin\frac{\pi z}{H} \quad (3)$$

Accordingly, the volume flux of flow of liquefied soil is derived by

$$\text{Volume flux} = \int_0^H U(x,z)dz = \frac{2H}{\pi}\{F(x) + J(x)\} \quad (4)$$

The vertical displacement, $W(x,z)$, of liquefied subsoil is expressed by F and J by integrating the constant-volume (undrained) equation;

$$\frac{\partial U}{\partial x} + \frac{\partial W}{\partial z} = 0 \quad (5)$$

Particularly, the uplift of the ground surface, δH, is given by the x-derivative of the volume flux due to the constant-volume condition;

$$\delta H = \frac{d(\text{volume flux})}{dx} = \frac{2}{\pi}\frac{d(HF + HJ)}{dx} \quad (6)$$

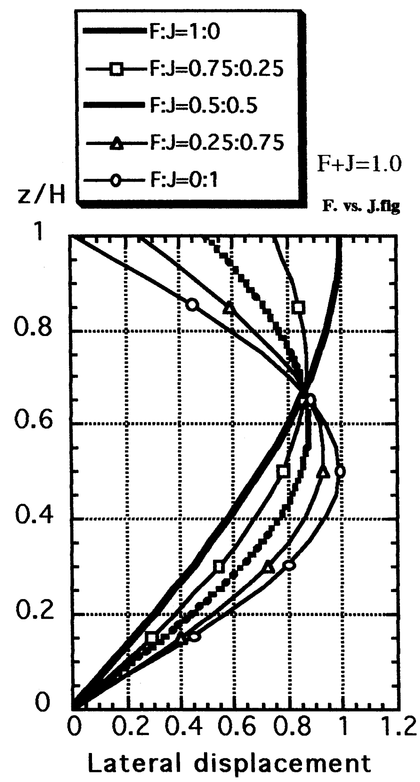

Fig.11 Variety of distribution of lateral deformation expressed by combination of F and J modes.

When the consolidation settlement is important, the solution of one-dimensional consolidation can be added to solutions of Eqs 5 and 6. Since both horizontal and vertical displacements are expressed by means of F and J, it is now possible to calculate the increment of potential energy during flow of liquefied soil, Q, which consists of the following components of gravity and strain energies in the subsoil;

1) gravity energy of liquefied deposit,
2) gravity energy of surface unliquefied layer together with building, and
3) strain energy in surface unliquefied layer due to horizontal compression ($\partial U/\partial x$).

Since the liquefied subsoil is supposed to be liquid without volume change, no strain energy occurs in it. The principle of minimum potential energy can give the values of F and J at the state of force equilibrium. The details of the method is similar to Towhata et al. (1999a) which employed only F component.

One of the problems that occur in the new F-J theory described above is that the solutions of F and J are often indeterminate. Many sets of solution are possible for the same soil conditions. To overcome this problem, the present analysis develops the equation of motion and derive the solutions of time history of F and J which are designated by f(x,z,t) and j(x,z,t), respectively.

By using the technique of discretization in x direction and linear interpolation, it is possible to describe the kinetic energy, K, and the potential energy, Q, of the whole subsoil by using f , j , $(\partial f/\partial t)$ and $(\partial j/\partial t)$ at nodal points. Moreover, the liquefied sand is considered to be a viscous liquid with certain magnitude of undrained shear strength. For experimental studies on the viscous nature of liquefied sand, refer to Towhata et al. (1999b). It is, hence, possible to express the dissipation of energy due to apparent viscosity of liquefied sand;

$$D = \iint_{\substack{liquefied\\subsoil}} \eta\left\{\left(\dot{\varepsilon}_x - \dot{\varepsilon}_z\right)^2 + \dot{\gamma}_{xz}^{\ 2}\right\} dxdz \tag{7}$$

in which η stands for the viscosity coefficient of liquefied subsoil and dots ($\dot{}$) indicate time derivatives.

Since the potential (Q), kinetic (K), and dissipation (D) energies are expressed by nodal values of f_i and j_i (*i* designates the *ID* number of nodal points) as well as their time derivatives, the theory of Lagrangean equation of motion gives a set of equation of motion in terms of f's and j's;

$$\begin{cases} \dfrac{d}{dt}\left\{\dfrac{\partial K}{\partial(\partial f_i/\partial t)}\right\} + \dfrac{\partial Q}{\partial f_i} = -\dfrac{1}{2}\dfrac{\partial D}{\partial(\partial f_i/\partial t)} \\ \dfrac{d}{dt}\left\{\dfrac{\partial K}{\partial(\partial j_i/\partial t)}\right\} + \dfrac{\partial Q}{\partial j_i} = -\dfrac{1}{2}\dfrac{\partial D}{\partial(\partial j_i/\partial t)} \end{cases} \tag{8}$$

ANALYSIS ON SUBSIDENCE OF BUILDINGS IN DAGUPAN CITY

General Scope

Acacio (1997) assembled information about subsidence of many buildings in the city of Dagupan. Depth of foundation, size of footing, contact pressure at the bottom of footing, depth of ground water table, magnitude of subsidence, and thickness of liquefied sandy deposit are available, although some of the data are less certain than others.

The rate of subsidence is significantly affected by the data of viscosity coefficient of liquefied sand, while the ultimate subsidence is not. To avoid errors caused by uncertainty of viscosity of liquefied sand, the present analysis focuses on the ultimate value of subsidence which would be an overestimation. This idea means that the subsidence continues for a long time even after the end of strong shaking as occurred in Niigata Airport building in 1964 (Japanese Geotechnical Society, 1999).

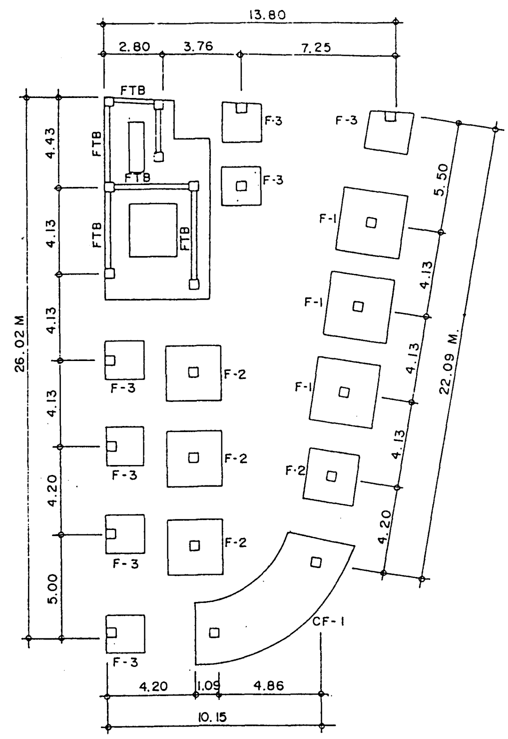

Fig.12 Foundation plan of Building No.7 (Acacio, 1997).

As illustrated in Fig.8, the axis of symmetry at which no lateral displacement occurs was placed at the center of a building. Another boundary with zero lateral displacement was located at the center of the street as mentioned before. Inclination is out of scope. The distance from the edge of a building to this fixed end is set equal to 5m which is typical of the half of the width of streets in the city.

The input data which are needed for the present analysis is as follows; surface topography, thickness of liquefied deposit, thickness of surface unliquefied layer, size and weight of building, unit weight of soils, and deformation modulus of surface unliquefied soil. Among those data, the deformation modulus is set equal to zero automatically when tensile deformation occurs in the surface layer.

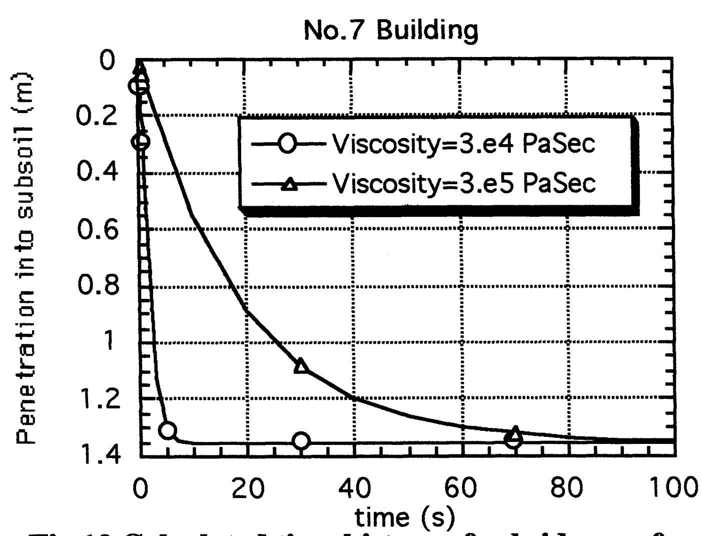

Fig.13 Calculated time history of subsidence of Building No.7.

Analysis on Building No.7

Building No.7 is the one in Fig.5 and was situated at the corner of Andel Fernandez Avenue and

Rizal Street. Fig.12 shows the foundation plan of this building where isolated footings are connected in one direction by tie beams. Acacio (1997) reported that this building had the bottom of the foundation at 1.5m below the surface and the contact pressure was 84kPa with three storeys. The subsidence was reported to be 0.45m, while inclination was 2 degrees. It should be noted that the reported "subsidence" is actually the differential subsidence between the building and the surrounding ground surface. To be more precise, it will be called "penetration" into subsoil in the present text;

$$\text{Penetration} = \text{Subsidence of building} - \text{subsidence of ground surface} \tag{9}$$

The analysis was made of one half of the shorter length, approximately 6m, of this building. Thus, the analysis supposed that the lateral flow of soil underneath occurred towards the right of Fig.12. Elastic modulus in the surface unliquefied layer was set equal to 10780 kPa as has been commonly employed in past analyses (Towhata et al., 1999a). On the contrary, the foundation of the building was considered to be rigid as compared with soil; hence no lateral elongation/contraction occurred in the analysis.

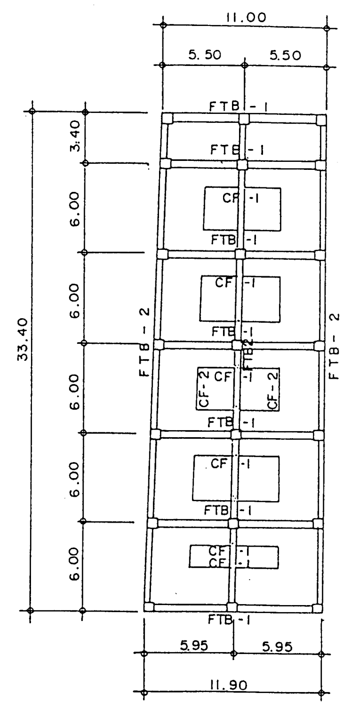

Fig.14 Foundation plan of building No.10 (unit: meter).

Two kinds of viscosity was assumed to the liquefied subsoil; $3\times10^4 Pa \bullet \text{sec.}$ and $3\times10^5 Pa \bullet \text{sec.}$, both of which were significantly greater than the viscosity of water ($0.001 Pa \bullet \text{sec}$) without vortex. The calculated time history of subsidence (penetration into subsoil) is illustrated in Fig.13. Although the greater viscosity delayed the development of subsidence, the ultimate value of subsidence was independent of the choice of viscosity. The ultimate subsidence of was much greater than the observed penetration of 0.45m.

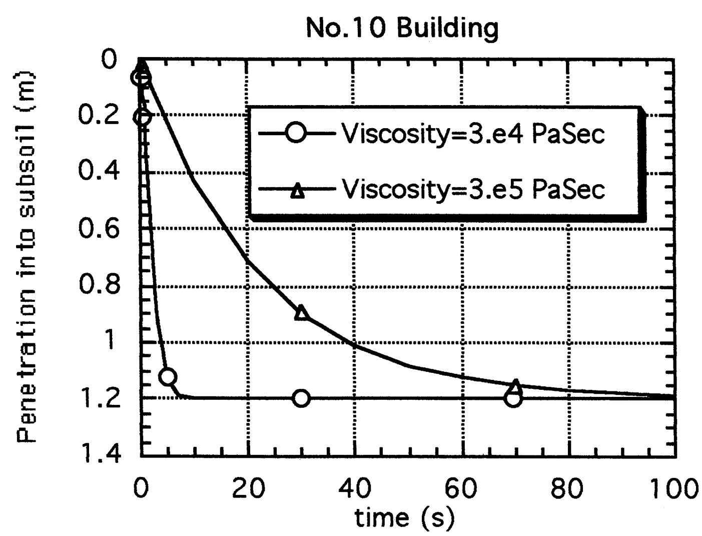

Fig.15 Calculated time history of penetration of building No.10.

Analysis on Building No.10

The building No.10 faced the A.Fernandez Avenue. With four storeys, the contact pressure at the base of the footing was 70 kPa on average. Its foundation consisted of continuous footing in two directions as manifested in Fig.14 and appears to be rigid. This building penetrated into subsoil by 0.8m while tilting was two degrees. No structural damage occurred in spite of sand boiling around the foundation. Since this building was sandwiched by adjacent buildings, the idea of two-dimensional flow appears to be reasonable. The analysis was conducted on one half of the length of the building, namely 16.7m, normal to the direction of the street.

The calculated time history of penetration into subsoil is manifested in Fig.15 where the choice of viscosity did not affect the ultimate penetration. The calculated value of the ultimate penetration was 1.2m which was greater than the observed 0.8m.

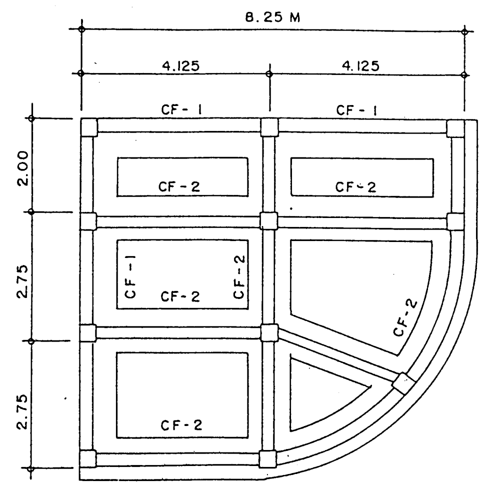

Fig.16 Foundation plan of Building No.15 (Acacio, 1997).

Analysis on Building No.15

Portrayed in Fig.6, the building No.15 was situated at the corner of Perez Boulevard and Galvan Street. Hence, it should be borne in mind that the two-dimensional analysis (Fig.8) in the present study is not very relevant. The plan view of its foundation, in which footings are continuous in two directions, is indicated in Fig.16. Being two-storeyed, the contact pressure at the base of the foundation was, on average, 55 kPa. This building penetrated into subsoil by 0.55m while significantly tilting by 11 degrees. The analysis was conducted on one half of the width of the building; 4.3m.

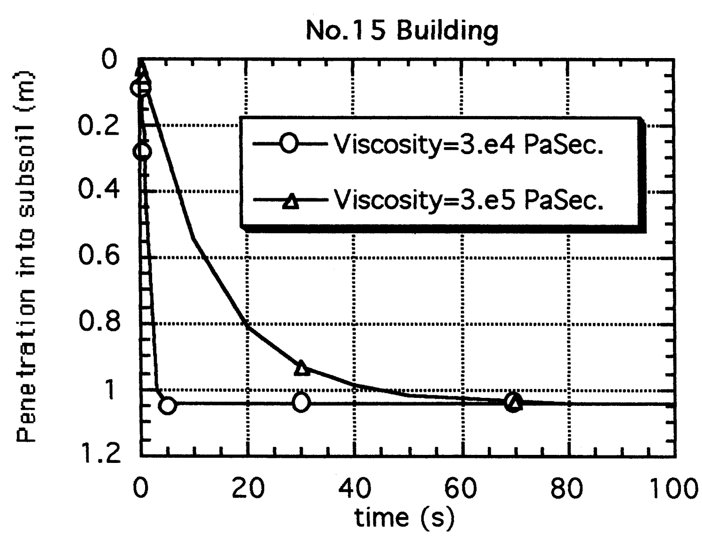

Fig.17 Calculated time history of subsidence of Building No.15.

The calculated time history of penetration is manifested in Fig.17 where the choice of viscosity did not affect the ultimate penetration. The calculated value of the ultimate penetration was

1.04m which was greater than the observed 0.55m.

Analysis on Building No.17

The building No.17 was located on Perez Boulevard. It penetrated into subsoil by 1.0m while tilting slightly by one degree. Its foundation had continuous footings in one direction while tie beams were installed in two directions, as indicated in Fig.18. The contact pressure at the base of the footings were 68 kPa on average. Being sandwiched by adjacent buildings, this building suits the idea of two-dimensional analysis. Hence, the idea of two-dimensional analysis appears reasonable. The analysis was conducted on one half of the length of the building, the size in the direction parallel to the direction of flow; 18.1m.

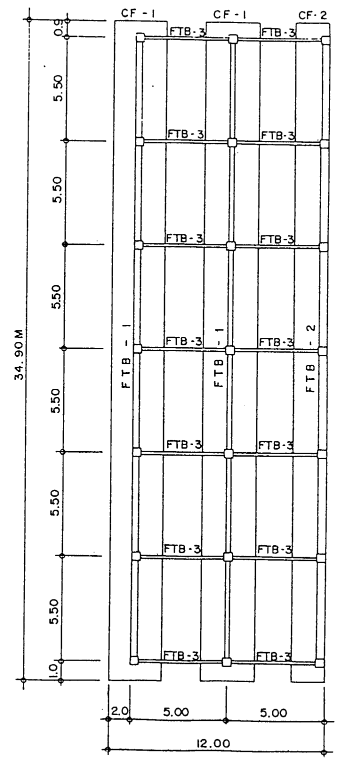

Fig.18 Foundation plan of Building No.17 (Acacio, 1997).

The calculated time history of penetration into subsoil is manifested in Fig.19 where the choice of viscosity did not affect the ultimate penetration. The calculated value of the ultimate penetration was 0.82m which was smaller than the observed 1.0m.

Summary of Analyses

Four analyses as described above show that the calculation of penetration tends to overestimate the real penetration. The overall summary of analyses on 14 buildings, however, suggests something different. Fig.20 compares the calculated and observed penetration; see ○ in the figure. Generally, the calculation overestimates the observed subsidence. This is particularly true when the observed subsidence was less than 0.5m. It is noteworthy that a better agreement occurs when the observed subsidence was greater than 0.5m. Thus, it seems that the proposed method of calculation satisfactorily reproduces the behavior of completely liquefied subsoil that induced larger subsidence. When the observed

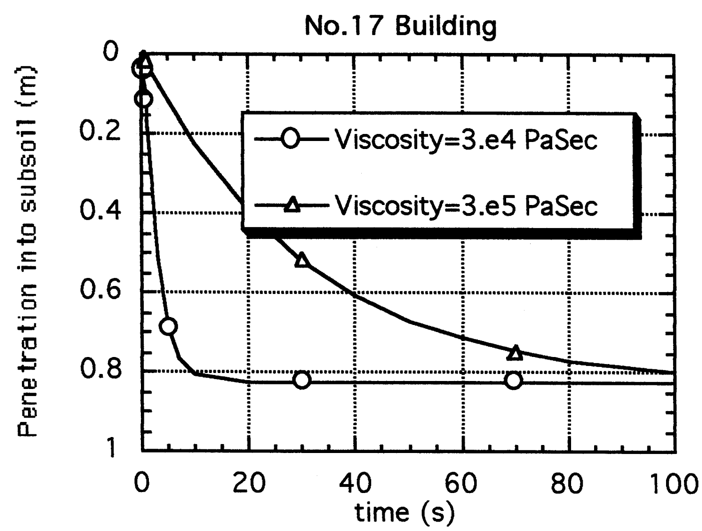

Fig.19 Calculated time history of subsidence of Building No.17.

subsidence was smaller, conversely, the extent of liquefaction of subsoil was probably not so significant, and sand probably maintained a certain extent of shear strength, contrary to the assumption of viscous liquid in the analysis. In such a situation, the calculation overestimated the magnitude of subsidence.

The solid circles (●) in Fig.20 stands for 70% of the calculated ultimate subsidence. The agreement between this 70% of prediction and the observation is good for this type of complicated problem. Thus, tentatively, the authors recommends the use of this 70% empirical reduction for a better prediction. It is interesting that a similar percentage worked well in a three-dimensional prediction of liquefaction-induced flow failure of gentle slopes (Orense and Towhata, 1998).

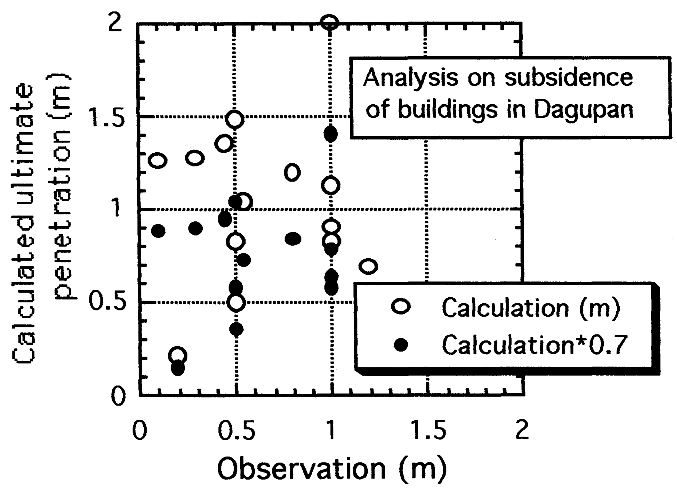

Fig.20 Comparison of observed and calculated subsidence.

CONCLUSION

An analytical method of calculation of subsidence of shallow foundation, such as tanks and buildings without piles, was developed. The summary of this paper is as shown below.

1) With reference to shaking table test results, two modes of lateral displacement in liquefied subsoil were taken into consideration.
2) With reference to the experience, the subsidence of building is supposed to continue after strong earthquake motion until the ultimate force equilibrium is achieved.
3) Although the analysis requires input data of viscosity of liquefied sand, the ultimate subsidence is not affected by this parameter.
4) The calculated ultimate subsidence overestimates the observed subsidence when the extent of liquefaction is not significant. Roughly, 70% of the calculated ultimate subsidence is a good approximation of the observation.

REFERENCES

Acacio,A,A, (1997): "Risk assessment of structures with shallow foundations resting on liquefiable deposits, Ph.D. Thesis, Univ. Tokyo.

Ishihara,K., Acacio,A.A. and Towhata,I. (1993): "Liquefaction-induced ground damage in Dagupan

in the July 16, 1990 Luzon earthquake," Soils and Foundations, Vol.33, No.1, pp.133-154.
Japanese Geotechnical Society (1999): "Air photographs of the Niigata city immediately after the earthquake in 1964," Ed. I.Towhata, ISBN4-88644-054-1.
Liu,L. and Dobry,R. (1997): "Seismic response of shallow foundation on liquefiable sand," Journal of Geotechnical and Geoenvironmental Engineering, ASCE, Vol.123, No.6, pp.557-567.
Orense,R.P. and Towhata,I. (1998): "Three dimensional analysis on lateral displacement of liquefied subsoil," Soils and Foundations, Vol.38, No.4, pp.1-15.
Sasaki,Y., Towhata,I., Tokida,K., Yamada,K., Matsumoto,H., Tamari,Y., and Saya,S. (1992): "Mechanism of permanent displacement of ground caused by seismic liquefaction", Soils and Foundations, Vol.32, No.3, pp.79-96.
Tokimatsu,K., Kojima,H., Kuwayama,S., Abe,A., and Midorikawa,S. (1994): "Liquefaction-induced damage to buildings in 1990 Luzon earthquake," Journal of Geotechnical Engineering, ASCE, Vol.120, No.2, pp.290-307.
Towhata,I., Orense,R.P. and Toyota,H. (1999a): "Mathematical principles in prediction of lateral ground displacement induced by seismic liquefaction," Soils and Foundations, Vol.39, No.2, pp.1-19.
Towhata,I., Vargas-Monge,W., Orense,R.P. and Yao,M. (1999b): "Shaking table tests on subgrade reaction of pipe embedded in sandy liquefied subsoil," to be published by Soil Dynamics and Earthquake Engineering Journal.

SEISMIC RESPONSE ANALYSIS OF PILE FOUNDATIONS AT LIQUEFIABLE SITES

W.D. Liam FINN[1], T. THAVARAJ[2], D.W. WILSON[3], R.W. BOULANGER[3], and B.L. KUTTER[3]

SUMMARY

Seismic response analyses were conducted on pile groups in liquefiable soils which were subjected to earthquake excitation on the large centrifuge at the University of California at Davis. The analyses were done using a simplified 3-D effective stress finite element program. Tests and analyses of a single pile and a 2×2 pile group subjected to an input acceleration record with a peak acceleration of 0.49 g are presented. There is good agreement between computed and measured free field porewater pressures, pile cap accelerations, time histories of moments and the distributions of maximum moments with depth.

1. INTRODUCTION

In engineering practice, comprehensive methods for seismic response analysis of pile foundations are based primarily on linear elastic behaviour and use either boundary elements or finite element methods. Published graphs of the results are limited to relatively small pile groups because of the substantial computing time required. These methods do not take into account the nonlinear behaviour of soil under strong shaking. The reduction in soil stiffness and the increase in damping associated with strong shaking are sometimes modelled crudely in these analyses by making arbitrary reductions in shear moduli and arbitrary increases in viscous damping.

A new approach to 3-D nonlinear seismic response analysis of pile groups which removes some of the limitations of current methods has been developed at the University of British Columbia (Wu and Finn, 1994; Wu and Finn, 1997a,b). It is based on a simplified 3-D representation of the foundation soils. By relaxing some of the boundary conditions associated with a full 3-D analysis, the computing time can be substantially reduced. The method is incorporated in the program PILE3D.

PILE3D analyzes the soil in terms of total stresses. The program has been modified to allow effective stress analysis by including a porewater pressure model to allow the generation of seismic porewater pressures due to shaking. The porewater pressure model is that developed by Martin, Finn and Seed (1975) but modified by adopting the two parameter model for volume change suggested by Byrne (1991). During seismic response analysis, the soil properties are changed continuously to reflect the effects of the seismic porewater pressures on moduli and strength.

This paper describes validation of the modified program PILE3D-F (Wu, Finn and Thavaraj, 1998) using data from centrifuge tests on single piles and pile groups in liquefiable soils. These tests were run at the University of California at Davis and have been reported by Wilson (1995) and Wilson et al. (1997).

2. SIMPLIFIED 3D SEISMIC ANALYSIS OF PILE FOUNDATIONS

The basic assumptions of the simplified 3D analysis are illustrated in Figure 1. Under vertically propagating shear waves the soil undergoes primarily shearing deformations in xOy plane except in the area near the pile where extensive compressional deformations develop in the direction of shaking. These compressional deformations generate shearing deformations in yOz plane. Therefore, the assumptions are made that dynamic response is dominated by the shear waves in the xOy and yOz planes and the compressional waves in the direction of shaking, Y. Deformations in the vertical direction and normal to the direction of shaking are neglected. Comparisons with full 3D elastic solutions confirm that these deformations are relatively unimportant for horizontal shaking (Wu and Finn,

[1] Anabuki Chair of Foundation Geodynamics, Dept. of Safety Systems Construction Engineering, Kagawa University, Takamatsu, Kagawa, Japan, and Dept. of Civil Engineering, University of British Columbia, Vancouver, B.C. (finn@civil.ubc.ca)
[2] Civil Engineering, University of British Columbia, Vancouver, B.C. (thava@civil.ubc.ca)
[3] Civil & Environmental Engineering, University of California at Davis, Davis, California

1997a). Applying dynamic equilibrium in Y-direction, the dynamic governing equation of the soil continuum in free vibration is written as

$$\rho_s \frac{\partial^2 v}{\partial t^2} = G^* \frac{\partial^2 v}{\partial x^2} + \theta G^* \frac{\partial^2 v}{\partial y^2} + G^* \frac{\partial^2 v}{\partial z^2} \tag{1}$$

where G^* is the complex modulus, v is the displacement in the direction of shaking, ρ_s is the mass density of soil, and θ is related to Poisson's ratio, μ of the soil. In this case, $\theta = (2-\mu)/(1-\mu)$.

Piles are modelled using ordinary Eulerian elastic beam theory. Bending of the piles occurs only in the yOz plane. Dynamic soil-pile-structure interaction is maintained by enforcing displacement compatibility between the pile and the soil.

The finite element code PILE3D-F (Wu, Finn and Thavaraj, 1998) incorporates these concepts of dynamic soil-pile-structure interaction. An 8-node brick element is used to represent the soil and a 2-node beam element is used to simulate the piles, as shown in Figure 1. The loss of energy due to radiation damping is modelled following the procedure proposed by Gazetas et al. (1993) in which a velocity proportional damping force per unit length is applied along the pile. The global dynamic equilibrium equation for the pile soil system is written in matrix form as

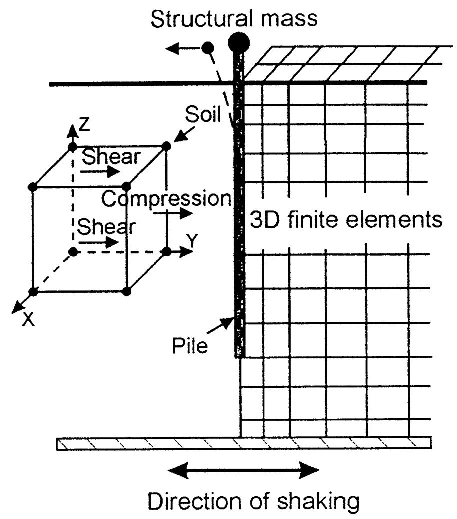

Figure 1. Quasi-3D model of pile-soil response.

$$[M]\{\ddot{v}\}+[C]\{\dot{v}\}+[K]\{v\}=-[M]\{I\}\cdot \ddot{v}_0(t) \tag{2}$$

in which $\ddot{v}_0(t)$ is the base acceleration, $\{I\}$ is a unit column vector, and $\{\ddot{v}\},\{\dot{v}\}$ and $\{v\}$ are the relative nodal acceleration, velocity and displacement, respectively.

Direct step-by-step integration using the Wilson-θ method is employed in PILE3D-F to solve the equations of motion in Equation (2). The non-linear hysteretic behaviour of soil is modelled by using an equivalent linear method in which properties were varied continuously as a function of soil strain. The seismic porewater pressures are generated continuously and their effects on soil properties taken into account. Additional features such as a tension cut-off and shearing failure are incorporated in the program to simulate the possible gapping between soil and pile near the soil surface and yielding in the near field.

Centrifuge Tests

Dynamic centrifuge tests of pile supported structures in liquefiable sand were performed on the large centrifuge at University of California at Davis, California. The models consisted of two structures supported by single piles, one structure supported by a 2x2 pile group and one structure supported by a 3x3 pile group. The typical arrangement of structures and instrumentation is shown in Figure 2. Full details of the centrifuge tests can be found in Wilson et al. (1997). Only the single pile system (SP1) and the (2x2) pile group (GP1) are studied here.

The model dimensions and the arrangement of bending strain gauges in systems SP1 and GP1 are shown in Figs. 3 and 4, respectively. In the (2x2) group pile system GP1, the mass and the length of the column that carries the superstructures mass are 233 Mg and 10.9 m respectively. Model tests were performed at a centrifugal acceleration of 30g.

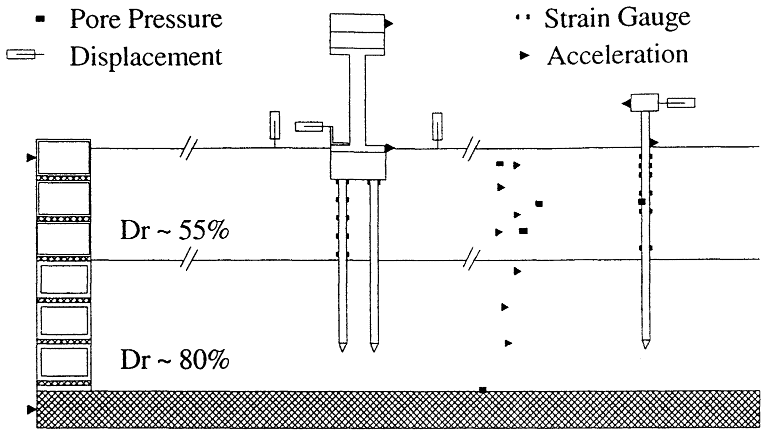

Figure 2. Schematic of model layout and instrumentation for centrifuge tests

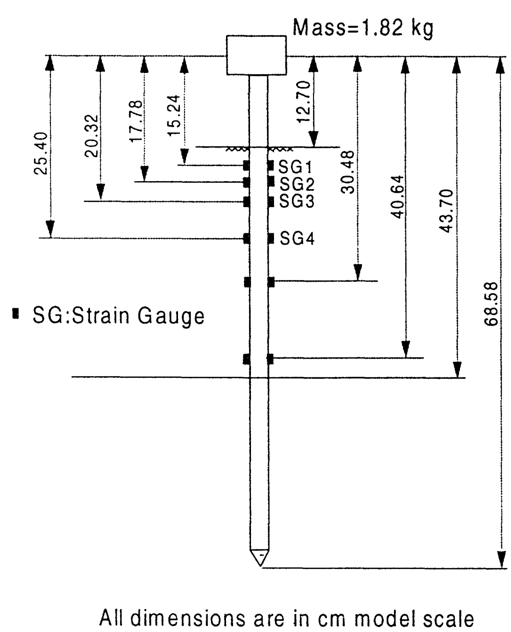

Figure 3. Instrumented pile for single pile test.

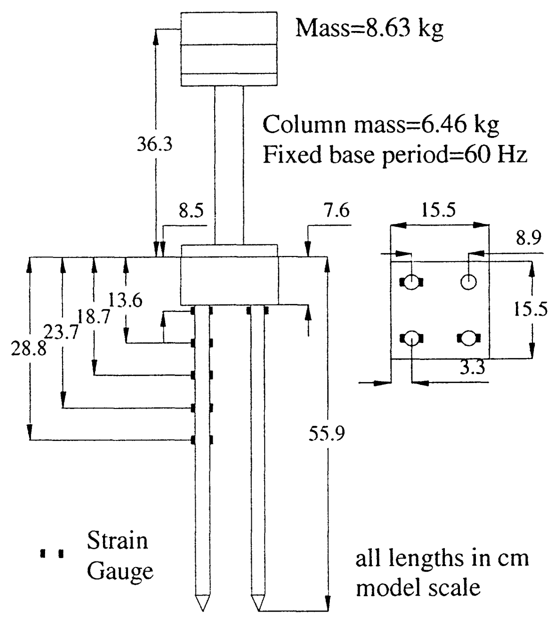

Figure 4. Instrumented test piles and details of superstructure for 2×2 pile group.

The soil profile consists of two level layers of Nevada sand, each approximately 10m thick at prototype scale. Nevada sand is a uniformly graded fine sand with a coefficient of uniformity of 1.5 and mean grain size of 0.15 mm. Sand was air pluviated to relative densities (D_r) of 75%-80% in the lower layer and 55% in the upper layer. Prior to saturation, any entrapped air was carefully removed. The container was then filled with a hydroxy-propyl methyl-cellulose and water mixture under vacuum. The viscosity of this pore fluid is about ten times greater than pure water to ensure proper scaling. Saturation was confirmed by measuring the compressive wave velocity from the top to the bottom of the soil profile.

The responses of the single pile and the 2x2 pile group to the Santa Cruz acceleration record obtained during the 1989 Loma Prieta earthquake, scaled to 0.49 g is described and analyzed here.

3. EFFECTIVE STRESS DYNAMIC ANALYSIS OF SINGLE PILE

Finite Element Model of the Single Pile-Superstructure System

The finite element mesh used in the analysis is shown in Figure 5. The finite element model consists of 1649 nodes and 1200 soil elements. The upper sand layer which is 9.1 m thick was divided into 11 layers and the lower sand layer which is 11.4 m thick was divided into 9 layers. The single pile was modeled with 28 beam elements. 17 beam elements were within the soil strata and 11 elements were used to model the free standing length of the pile above the soil. The superstructure mass was treated as a rigid body and its motion is represented by a concentrated mass at the center of gravity. A rigid beam element was used to connect the superstructure to the pile head.

Soil and Pile Properties

The small strain shear moduli G_{max}, were estimated using the formula proposed by Seed and Idriss (1970).

$$G_{max} = 21.7\, k_{max}\, P_a \left(\frac{\sigma'_m}{P_a} \right) \tag{3}$$

in which k_{max} is a constant which depends on the relative density of the soil, σ'_m is the initial mean effective stress and P_a is the atmospheric pressure. The constant k_{max} was estimated using the approximation suggested by Byrne (1991). The program PILE3D-F accounts for the changes in shear moduli and damping ratios due to dynamic shear strains at the end of each time increment. The shear strain dependencies of the shear modulus and damping ratio of the soil were defined by the curves suggested by Seed and Idriss (1970) for sand, shown in Figure 6. The friction angles of the upper and the lower layers were taken as 35° and 40°, respectively.

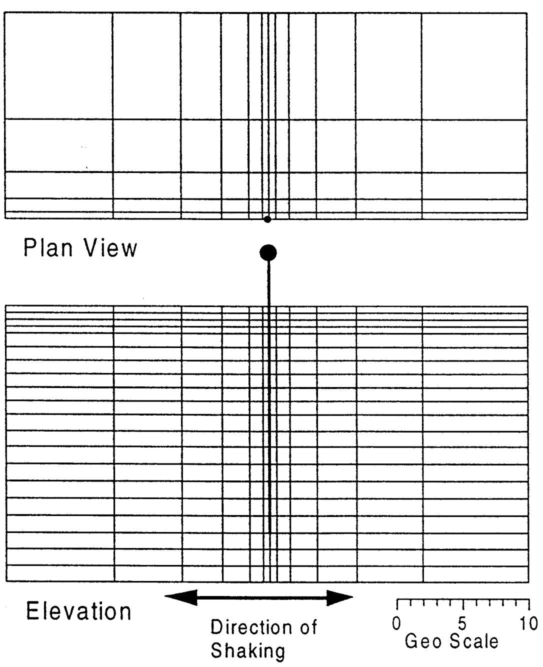

Figure 5. Finite element mesh for single pile.

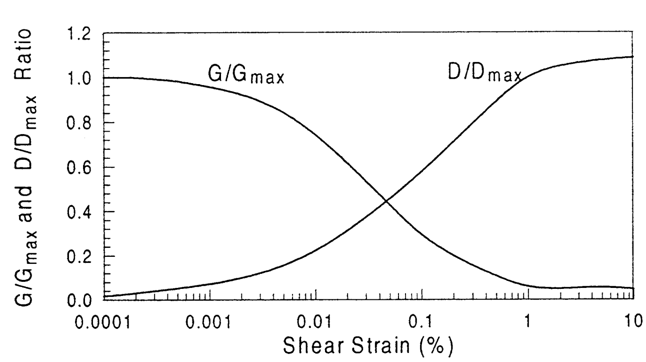

Figure 6. Variation of shear modulus and damping ratio with shear strain used in the analysis.

Porewater Pressure Effects

The seismic porewater pressures were generated in each individual element depending on the current volumetric strain prevailing in that element. The soil properties, the moduli and the strength were modified continuously to account for the effects of the changing seismic porewater pressures. A residual strength of 5% of the initial effective overburden stress was used as a lower limit for the shear strength as the porewater pressure ratios approached 100%.

Earthquake Input Motion

The Santa Cruz acceleration record was scaled to 0.49 g and used as input to the shake table. The base accelerations of the model were measured at the east and west ends of the base of the model container. Wilson et al.(1995) showed that both accelerations agreed very well.

The base input acceleration is shown in Figure 7.

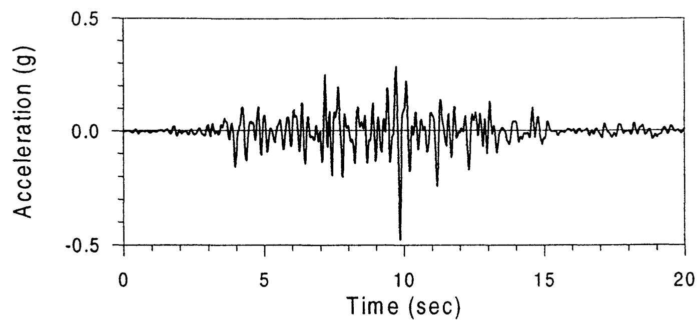

Figure 7. Input acceleration time history.

Results of Single Pile Analysis

Porewater Pressure Response: Figure 8 shows comparisons between measured and computed porewater pressures at three different depths; 1.14 m, 4.56 m, and 6.78 m in the free field. There is generally good agreement between the measured and computed porewater pressure responses.

Bending Moment Response: Figure 9 shows the measured and computed bending moment time histories at two different depths; 0.76 m and 1.52 m. Generally there is a very good agreement between the measured and computed time histories. Figure 10 shows the profiles of measured and computed maximum bending moments with depth. The comparison between measured and computed moments is fairly good, although the maximum moment is overestimated by 10% to 20% between 1 m and 4 m depths.

4. ANALYSIS OF 2×2 PILE GROUP

Effective stress analyses were also carried out to simulate the response of the (2x2) pile group- superstructure system. The finite element mesh is similar in type to that in Figure 5 except for the presence of the pile cap.

The pile cap was modeled with 16 brick elements and treated as rigid body. The superstructure mass was treated as a rigid body and its motion was represented by a concentrated mass at the center of gravity. The column carrying the superstructure mass was modeled using beam elements and is treated as a linear elastic structure. As the stiffness of this column element was not reported, it was calculated based on the fixed base frequency of the superstructure reported by Wilson et al. (1997) as 2 Hz.

Results of (2×2) Group Pile Analysis

Acceleration Response: Figure 12 shows computed and measured pile cap acceleration time histories. There is a good agreement between the measured and computed values.

Bending Moment Response: Figure 13 shows time histories of measured and computed moments at a depth of 2.55 m. The measured and computed time histories compare quite well. Residual moments were removed from the time history of measured moments before the comparison was made. Figure 14 shows the measured and computed bending moment profiles with depth. They also compare very well.

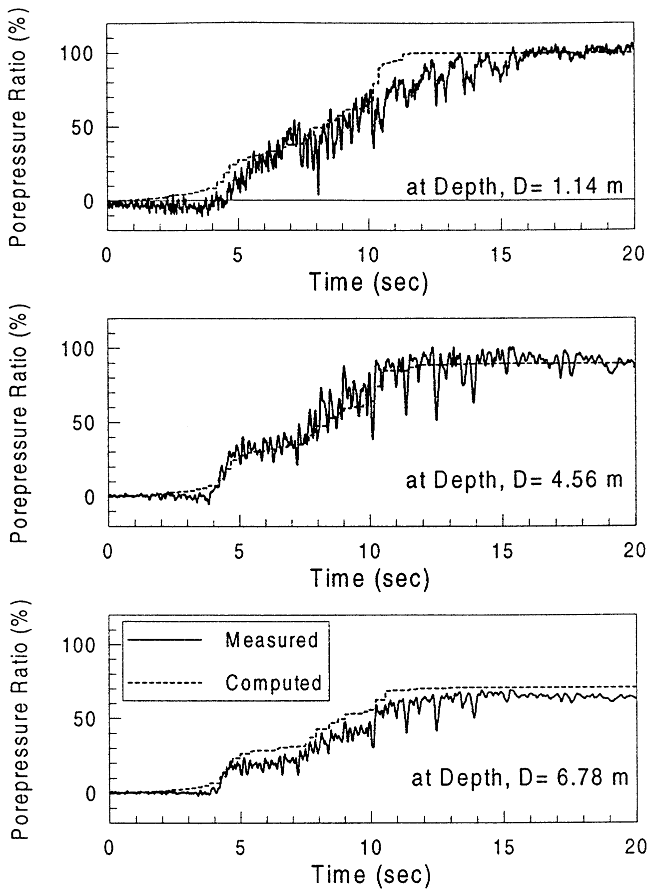

Figure 8. Comparison of measured and computed porewater pressure time histories at three depths.

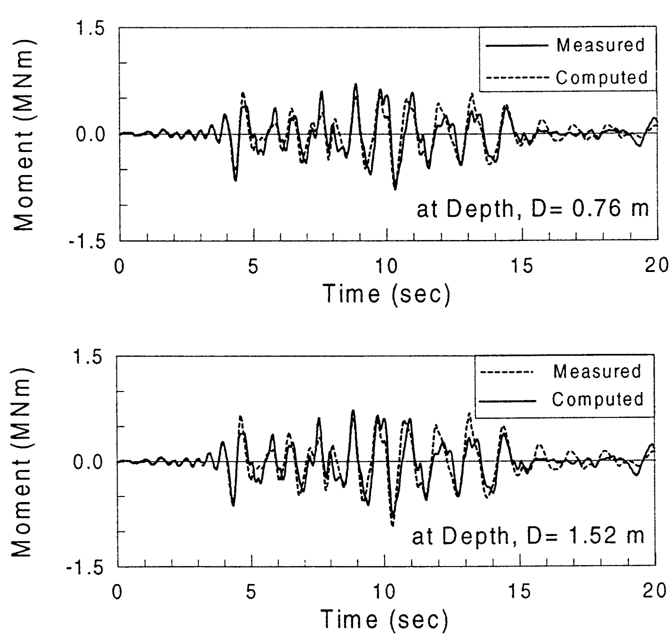

Figure 9. Comparison of measured and computed bending moment time histories at two depths for the single-pile supported system.

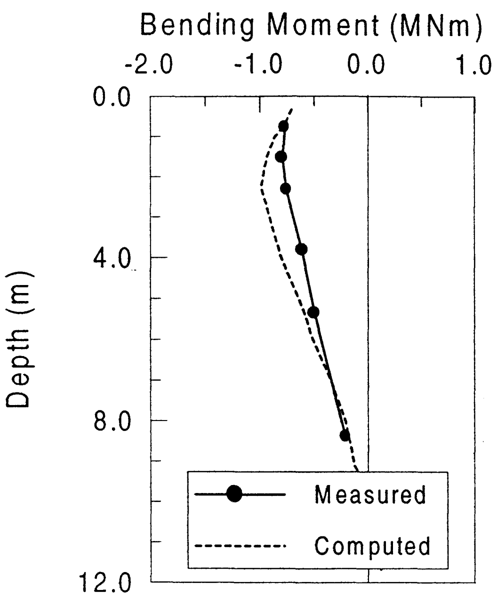

Figure 10. Comparison of measured and computed maximum bending moments profiles along the single pile.

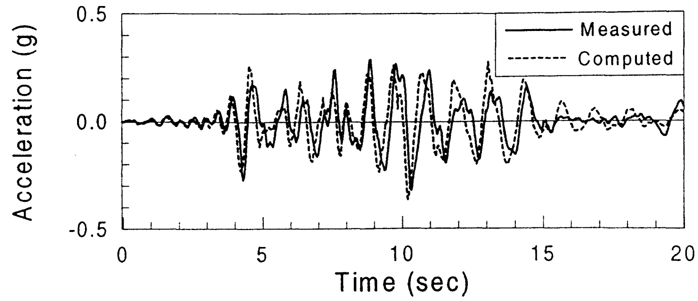

Figure 11. Comparison of measured and computed superstructure acceleration time histories for the single-pile supported system.

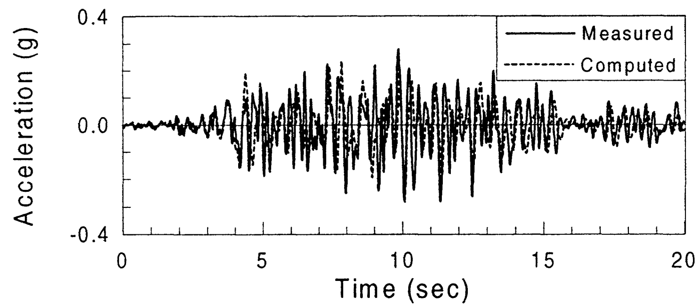

Figure 12. Comparison of measured and computed pile ca acceleration time histories for 2x2 pile group.

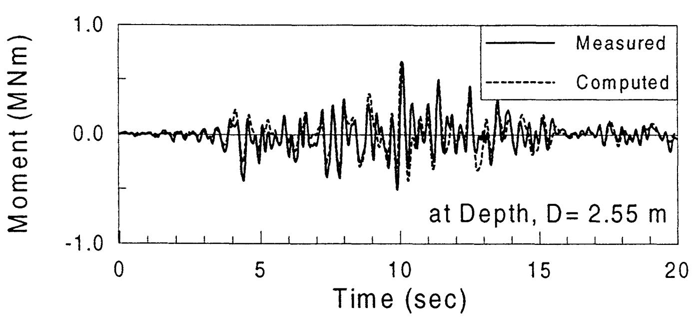

Figure 13. Comparison of measured and computed bending moment time histories for the 2x2 pile group.

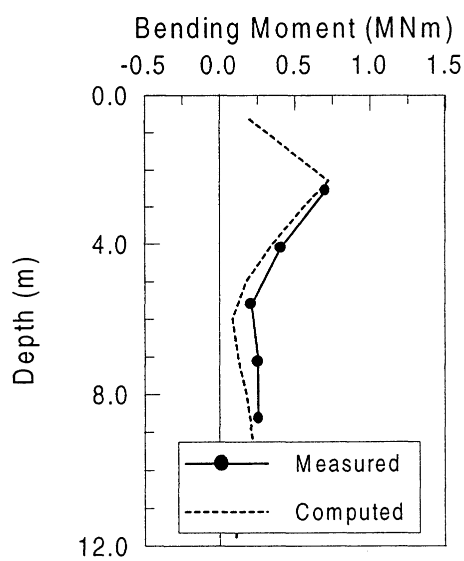

Figure 14. Comparison of measured and computed maximum bending moments along a pile in the 2x2 pile group.

5. CONCLUSION

The preliminary simulation studies conducted on the University of California centrifuge tests so far, including the two representative tests reported here, suggest that the program PILE3D-F has the capability to analyze pile foundations in potentially liquefiable soils with sufficient accuracy for engineering purposes.

6. ACKNOWLEDGEMENTS

The development of PILE3D-F was funded by a grant from the National Science and Engineering Research Council of Canada to the first author. The centrifuge tests were funded by the California Department of Transportation.

7. REFERENCES

Byrne, P.M. (1991). "A cyclic shear-volume coupling and pore pressure model for sand." *Proc. 2nd Int. Conf. on Recent Advances in Geotechnical Earthquake Engineering and Soil Dynamics*, St. Louis, Report 1.24, 1:47-56.

Gazetas, G., K. Fan and A. Kaynia (1993). "Dynamic response of pile groups with different configurations." *Soil Dynamics and Earthquake Engineering*,12:239-257.

Martin, G.R., W.D. Liam Finn and H.B. Seed (1975). Fundamentals of liquefaction under cyclic loading. Journal of Geotechnical Engineering Division, ASCE, Vol. 101, GT5:423- 438.

Seed, H.B. and I.M. Idriss (1970). "Soil moduli and damping factors for dynamic response analysis." *Report #EERC70-10*, Earthquake Engineering Research Center, Berkeley, CA.

Wilson, D.W., R.W. Boulanger and B.L. Kutter (1997). "Soil-pile-superstructure interaction at soft or liquefiable sites - Centrifuge data report for CSP1-5." *Report No. UCD/CGMDR- 97/01-05*, Center for Geotechnical Modeling, Dept. of Civil and Environmental Engineering, University of California at Davis, CA.

Wilson, D.W., R.W. Boulanger, B.L. Kutter and A. Abghari (1995). "Dynamic centrifuge tests of pile supported structures in liquefiable sand." *Proc., National Seismic Conf. on Bridges and Highways*. Sponsored by Federal Highways Admin. and Caltrans, San Diego, CA.

Wu, G. and W.D. Liam Finn (1994). "PILE3D - prototype program for nonlinear dynamic analysis of pile groups." Dept. of Civil Engineering, University of B.C., Vancouver.

Wu., G and W.D. Liam Finn (1997a). "Dynamic elastic analysis of pile foundations using finite element method in the frequency domain." *Canadian Geotechnical J.*, Vol. 34, 1:34-43.

Wu., G and W.D. Liam Finn (1997b). "Dynamic nonlinear analysis of pile foundations using finite element method in the time domain." *Canadian Geotechnical J.*, Vol. 34, 1:44-52.

Wu, G., W.D. Liam Finn and T. Thavaraj (1998). "PILE3D-F: Program for dynamic nonlinear effective stress analysis of pile groups." Civil Engineering, University of B.C., Vancouver.

Displacement field of granular backfill due to earthquake induced quaywall movement

Hirokazu Akagi[1], Kazuhito Komiya[2] and Hironobu Saitoh[1]

1) Department of Civil Engineering, Waseda University
3-4-1, Ohkubo, Shinjuku, Tokyo 169-8555, Japan
2) Department of Civil Engineering, Chiba Institute of Technology
2-17-1, Tsudanuma, Narashino, Chiba 275-8588, Japan

Abstract

An experimental investigation of the displacement field of the granular backfill due to earthquake-induced quaywall movement was carried out. A pile of aluminum rods was used to simulate a granular backfill in the experiment. The pile of aluminum rods was repeatedly vibrated on a shaking table. The sidewall, i.e. the model quaywall was moved away from the aluminum rod pile during the vibration period. The displacement field of the backfill was observed and recorded on videotape. The magnitude of the acceleration used did not appear to control the displacement field of the backfill. The magnitude of the input wave number during the quaywall movement determined the backfill displacement field. Similar results were obtained by numerical simulation using a distinct element method. This research on the displacement of the granular material backfill indicates that it originates from momentum transfer from the quaywall in the earthquake.

Introduction

The Hyogo-ken Nanbu Earthquake of 1995 caused serious damage to many port facilities in the Kobe harbor, especially to the numerous caisson-method quaywalls, which protected reclaimed land. These collapsed by sliding, tipping over or subsidence. Ground fissure and ground subsidence was generated in the backside of the quaywall. Since the superstructures of the caisson-method quaywall were designed to be quake-resistant, they were not completely destroyed. Nevertheless, serious damage was done to the quaywall, because the seismic forces displaced the ground around the quaywall. The collapse of the quaywall by displacement of the ground could not have been predicted since the conventional earthquake-resistant design method predicts that the strength of the structure increases because:

(1) the ground deformation which arises from the seismic force, and the ground flow which occurs with liquefaction are not considered in the conventional technique.

(2) the interaction between the ground and structures cannot be taken into account.

Therefore, it is necessary to consider both the displacement of the ground and the mutual dynamic response of the ground and structures accurately in order to rationally evaluate the earthquake performance of the structure and to assess the safety of the structure.

In this study, indoor vibration testing was performed using a quaywall model and granular ground material in order to determine the effects of the seismic collapse mechanisms of the quaywall on the backfilled ground response. Granular materials made by piling up aluminum rods were used to model the backfilled ground of the quaywall in the experimental studies. Two kinds of collapse mode of the quaywall were investigated, horizontal movement and tipping over of the quaywall by an earthquake. A distinct element method(DEM) program was used to predict the ground movement of the back of the quaywall and when it decays during an earthquake. The numerical results are compared with the experimental measurements.

Experimental studies

Figure 1 shows the outview of the indoor vibration test apparatus. The test apparatus consisted of the quaywall model and the backfilled aluminum rods which represented the ground. The quaywall model was assembled on an indoor vibrating table. The quaywall model is made of rigid boards and can move horizontally or rotate about the axis A, with an angular velocity of ten degrees per minute around the air cylinder as shown in Figure 1.

The model ground material in the back of the quaywall model was made by piling 10 cm aluminum rods.1.6 mm and 3.0 mm diameter rods were mixed in a weight ratio of 3:2. After piling up, the density of the aluminum rods ground was 2.27 g/cm^3. A 20 mm square lattice was superimposed upon the pile of aluminum rods in order to enable observ ation of the displacement. The table was vibrated sinusoidally for 20 seconds.

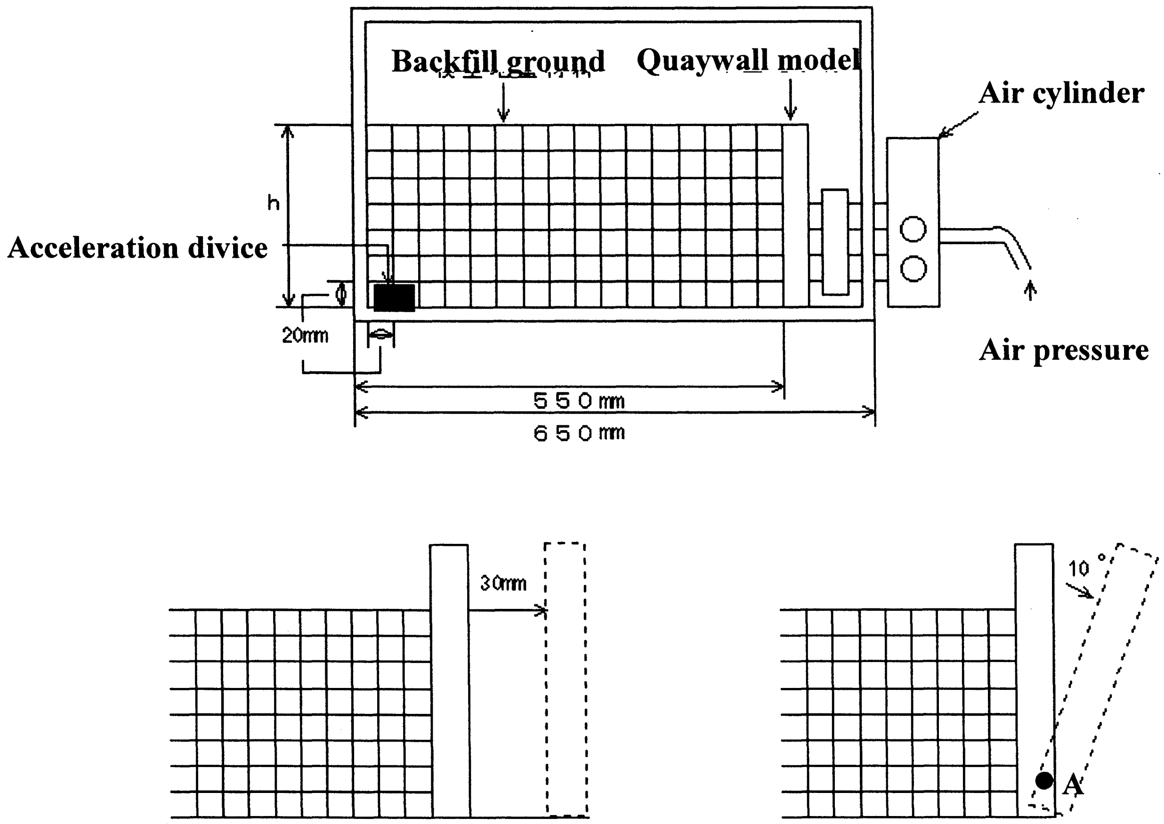

Sliding of the quaywall

Rotating of the quaywall

Figure 1 Indoor test apparatus

In this case, the experiment was carried out under the assumption of two modes of quaywall decay with the action of the seismic force. The first is the mode in which the quaywall moves horizontally through slippage between the quaywall and the ground. Ten seconds after the movement of the vibrating table was started, the quaywall model was moved evenly using an air cylinder to simulate the sliding of the quaywall. The quaywall model had two horizontal displacement speeds 1.12cm/s and 0.52cm/s. The second quaywall-decay mode is that in which the quaywall rotates due to unequal ground settlement or ground flow. In this simulation the quaywall model was rotated at an angle of 10 degrees per minute. The maximum acceleration and the quaywall decay modes adopted in this experiment are listed in Table 1. During these experiments, the movement of the rods and the quaywall model were photographed using a digital video camera every 1/30 second. The lens curvature strain error of the video camera was corrected using image analysis after the experiment.

Table 1 Series of experimental condition

Frequency	1.0 Hz, 2.0 Hz, 3.0 Hz
Maximum acceleration	100 gal, 200 gal, 300 gal
Quaywall-decay mode	Sliding, Rotating
Moving time of quaywall	2.53 sec., 5.73 sec.

Experimental results

Figures 2 show the displacement vector at the cross point of the lattice which was superimposed upon the pile of aluminum rods. From these figures, it is clear that the region which produced a large displacement expanded as the input frequency increased. The slip line did not appear clearly when a 1 Hz frequency was applied. On the other hand, sharp ground slip occurred behind the quaywall model with a vibration of 3 Hz.

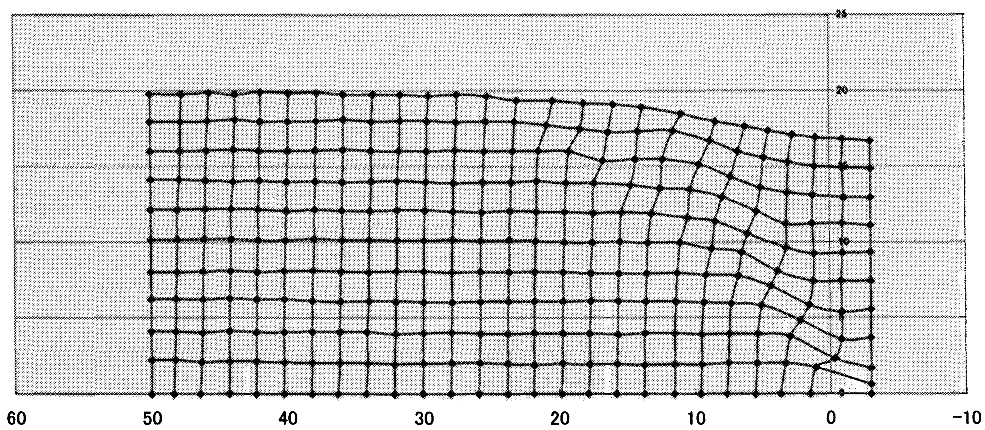

1Hz 300gal Sliding quaywall v=0.52(cm/s)

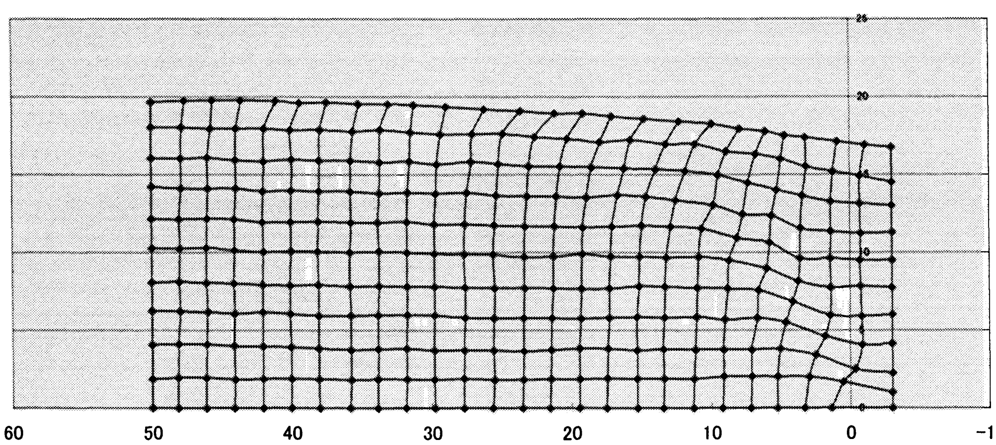

3Hz 300gal Sliding quaywall v=0.52(cm/s)s

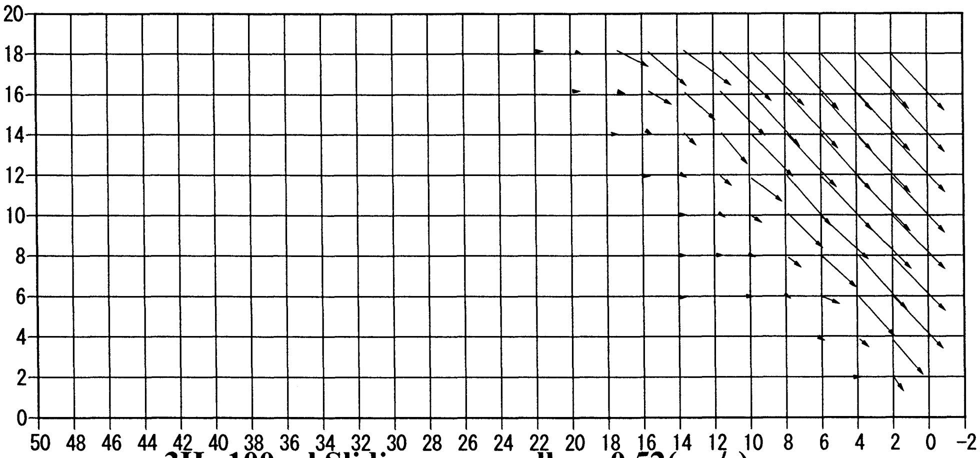

3Hz 100gal Sliding quaywall v=0.52(cm/s)

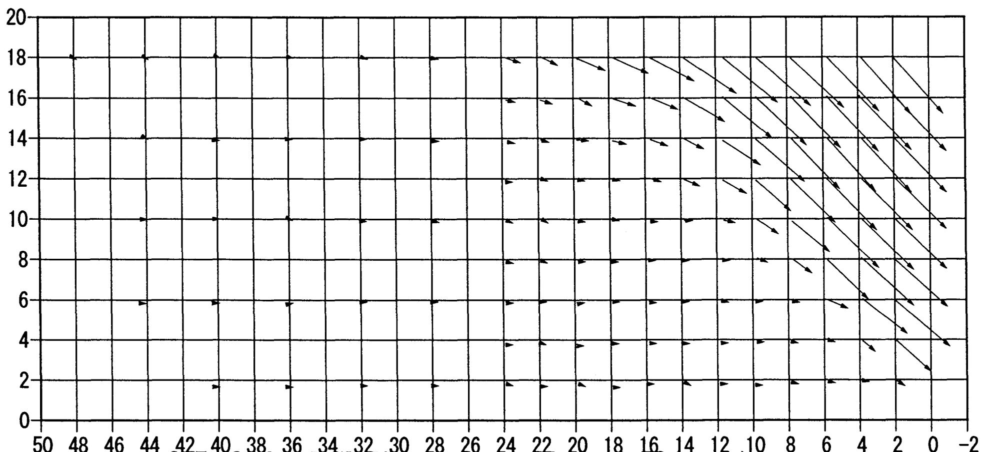

3Hz 200gal Sliding quaywall v=0.52(cm/s)

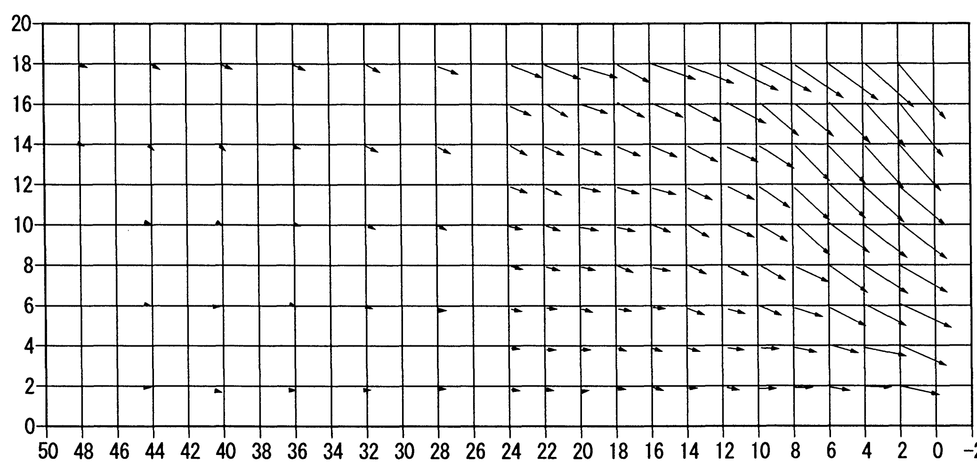

3Hz 300gal Sliding quaywall v=0.52(cm/s)

Figures 3 Displacement vectors due to 20 sec. Vibration

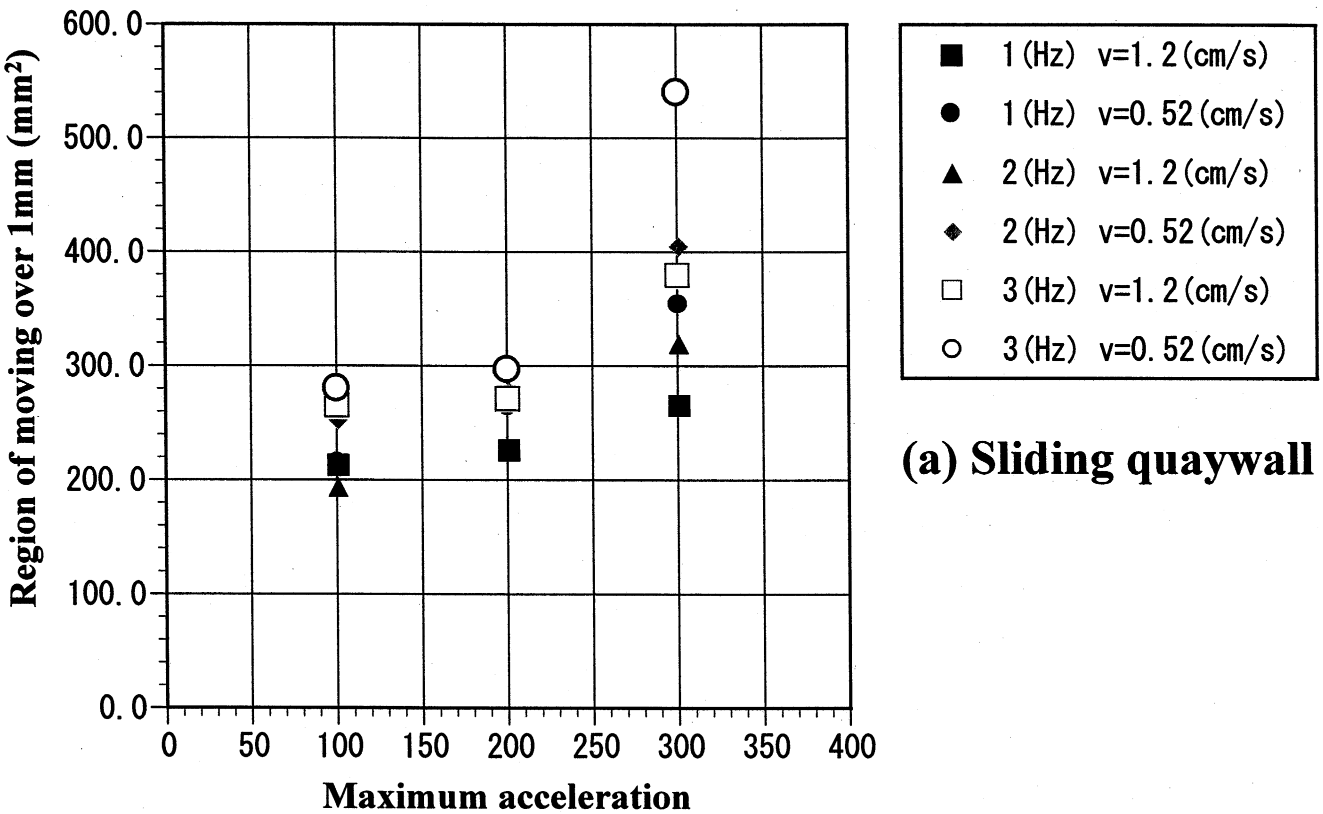

(a) Sliding quaywall

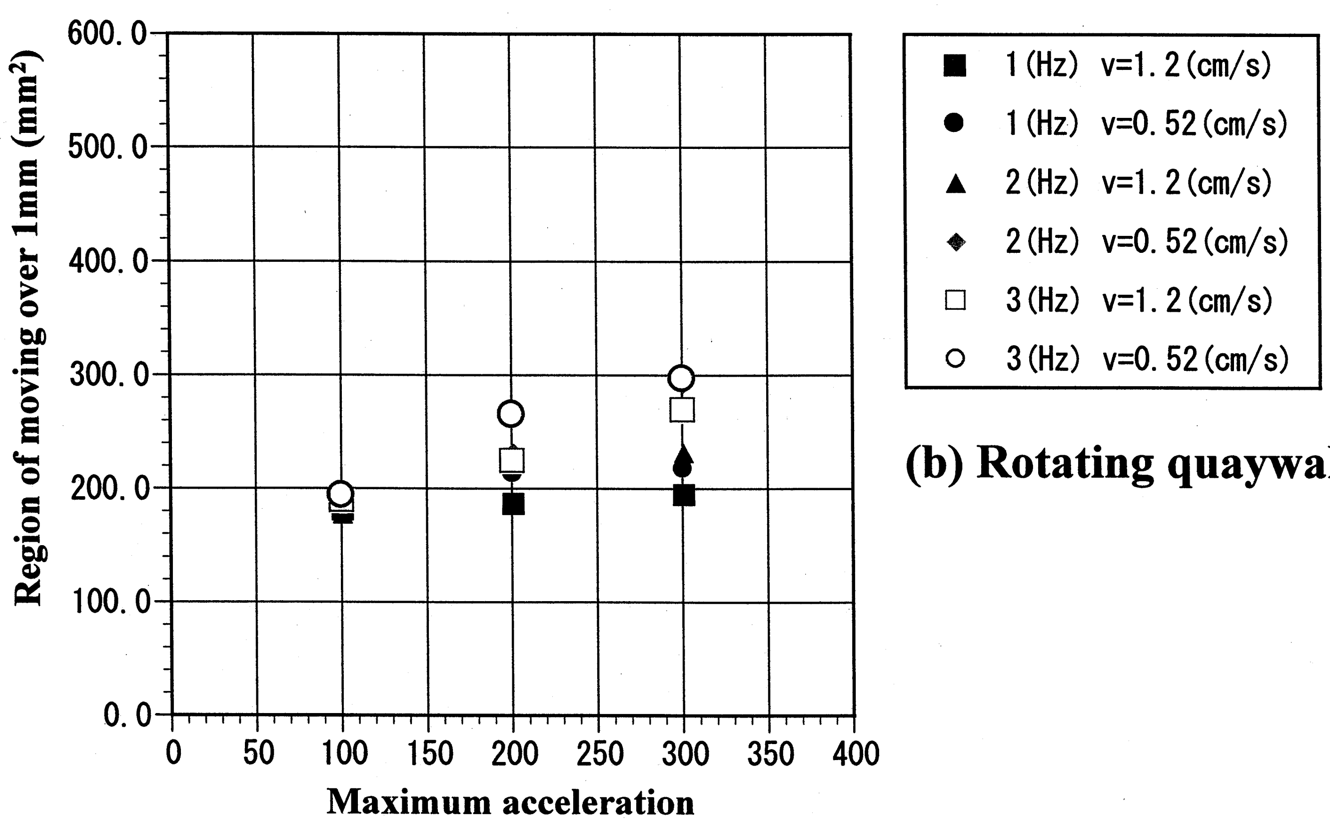

(b) Rotating quaywall

Figures 4 Relationships between Maximum input acceleration and Region of the ground with large displacement

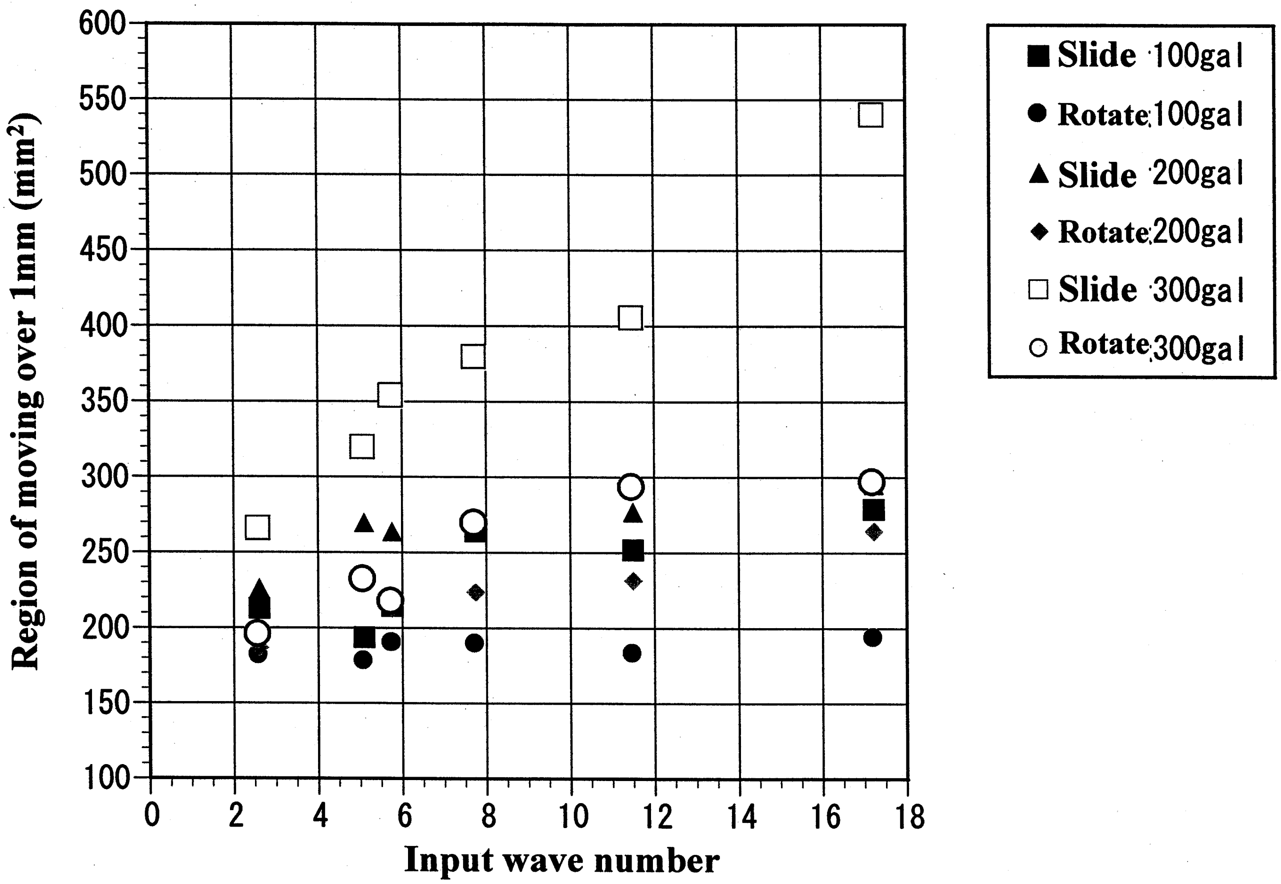

Figure 5 Relationships between Input wave number and Region of the ground with large displacement

Figures 3 show the moving locus of the cross point of the lattice during vibration. Large displacements occurred in the ground when the input acceleration became large. The region of the ground with a large displacement expanded when the velocity of the ground displacements were small.

Figures 4(a) and 4(b) show the relationship between the largest input acceleration and the region in which the ground has moved over 1 mm due to the excitation of the vibrating table. This region grows with increases in the amount of the largest input acceleration in both the case of a sideways move and a rotation.

Figure 5 shows the relationship between the input wave number and the region in which the displacement was more than 1 mm. The input wave was defined as the number by which the total moving time of the wall was multiplied at a given input frequency. The area of over 1 mm displacement was proportional to the increasing input wave number when the largest input acceleration became large.

Numerical investigations

The numerical simulation was carried out using a distinct element method[1]. In this analysis, elements of 2.10 cm and 1.12 cm diameter were randomly placed in weight ratios of 2:3. The initial ground was specified after a free fall analysis to a rigid bottom surface until it attenuated unwanted vibrations. Figure 6 shows the view of elements after a free fall analysis. The ratio of the diameters and weights of the elements were equal to those used in the experiments.

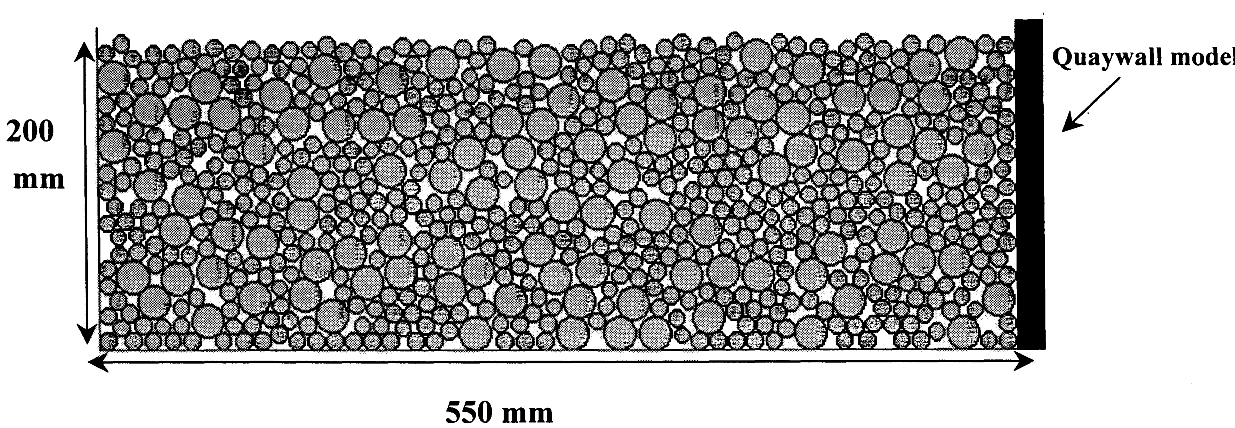

Figure 6 Initial location of quaywall model and elements

The density of the ground after the free fall analysis was 2.27g/cm3. The material properties used in this analysis are shown in table 2. A horizontal vibrational force was applied from the rest condition to all elements for 20 seconds. Quaywall models were moved 30 mm after 10 second of time had elapsed.

Table 2 Input parameters

	Element interaction	Wall interaction
Normal spring coefficient Kn	9.00×10^9 N/m/m	1.80×10^{10} N/m/m
Tangential spring coefficient Ks	3.00×10^8 N/m/m	6.00×10^8 N/m/m
Normal coefficient of cohesion η n	1.41×10^5 Ns/m/m	2.81×10^5 Ns/m/m
Tangential coefficient of cohesin η s	2.57×10^4 Ns/m/m	5.14×10^4 Ns/m/m
Coefficient of friction μ	0.29	0.29

Numerical results

Figure 7 shows the ground displacements which were obtained by DEM calculations. The ground displacements which were measured in the indoor laboratory tests were also plotted in this figure. For the ground settlement, the numerical results were in exact agreement with the experimental observations. The relationship between the largest input acceleration and the total displacement of the elements is shown in Figure 8. The total displacement is defined as the sum of the displacement vectors of all of the elements. It is clear from this figure that the amount of total displacement increased as the largest input acceleration increased. Figure 9 shows the relationship between the input wave number and the total displacement vector of the elements. The total displacement vector increased as the input wave number increased when the wave acceleration was large.

Mesh=indoor vibration test results

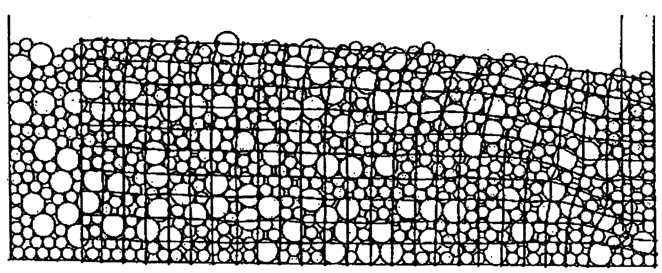

3 Hz 300gal Sliding quaywall

Figure 7 Ground deformation obtained by DEM analysis

Conclusions

In this study, the deformation and the collapse of the backfill ground in the quaywalls caused by the earthquake were investigated by indoor laboratory vibration tests and distinct element analyses. The

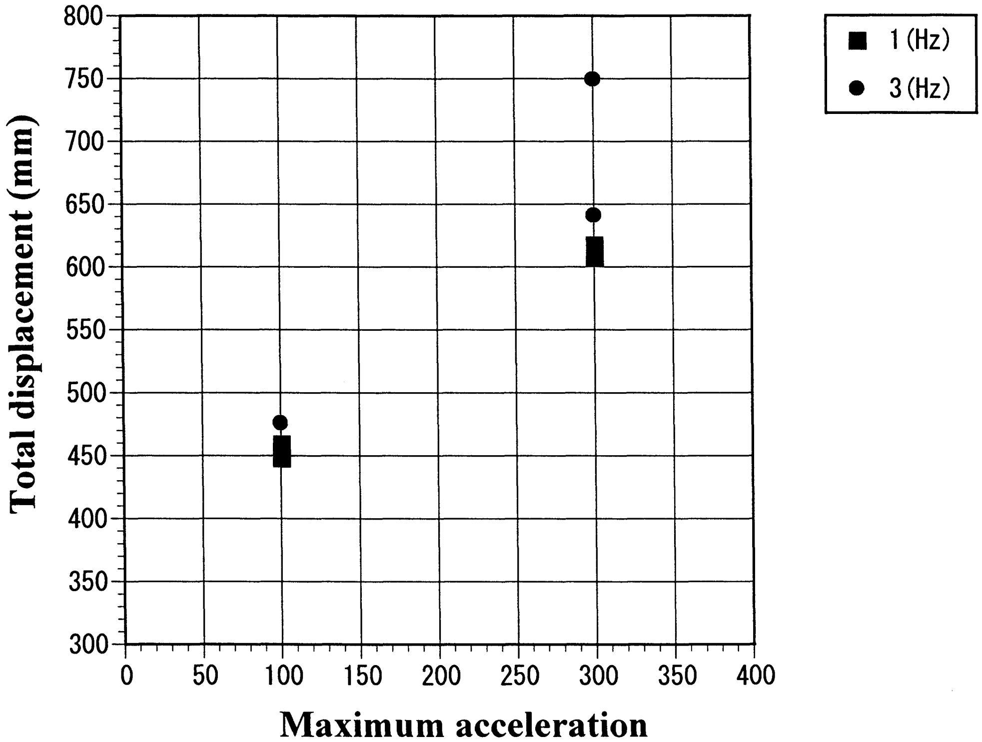

Figure 8 Relationships between Maximum input acceleration and Total displacement

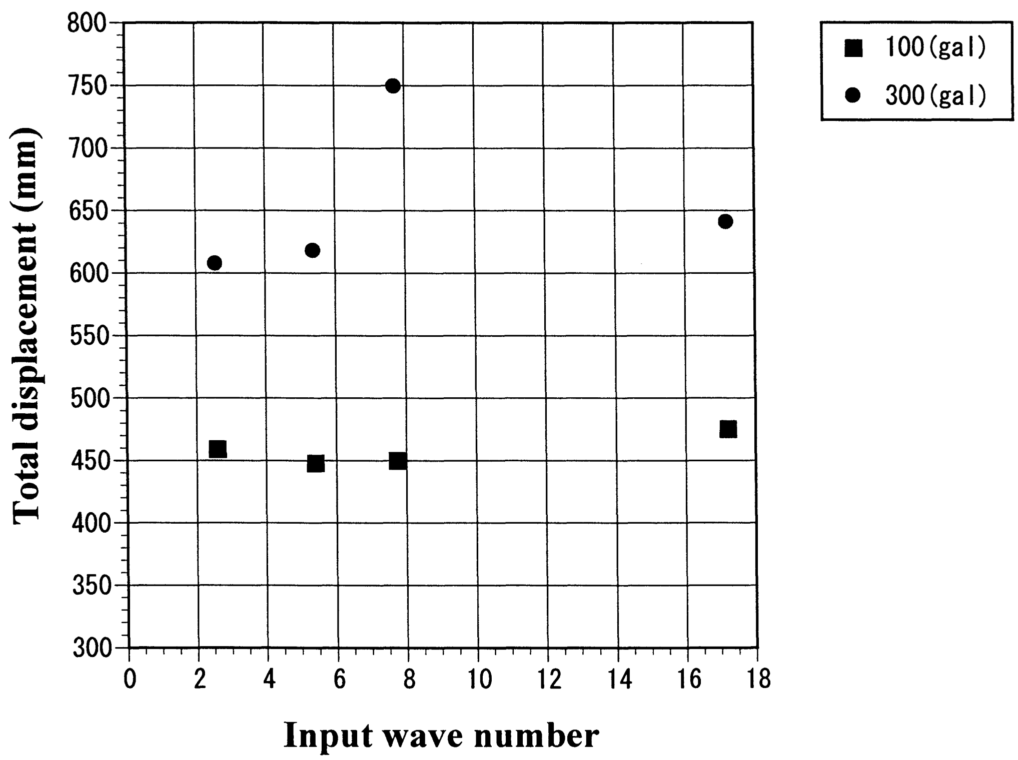

Figure 9 Relationships between Input wave number and Total displacement

ground displacement due to the earthquake was affected by the acceleration, the frequency and the velocity of displacement, i.e, the region which produced a large displacement expanded as the input frequency increased. The ground behind the quaywall did not collapse in the case of a frequency of 1 Hz, while a ground slip occurred behind the quaywall with a 3 Hz frequency. The region of the ground with a large displacement expanded when the velocity of the ground displacements was small. This region increased with an increasing amount of the largest input acceleration in both the cases of sideways moves and rotations. The ground behavior obtained using DEM calculations were in exact agreement with the observations of the indoor vibration tests. This region increases with increasing input acceleration.

References

(1) Cundall & Strack：A Discrete Numerical Model for Granular Assemblies, Geotecnique, vol.29, pp.47～65, 1979

CENTRIFUGE MODELING OF EFFECT OF SUPERSTRUCTURE STIFFNESS ON PILE BENDING MOMENTS DUE TO LATERAL SPREADING

Ramos R.[1], Abdoun T.[1], and Dobry R.[1]
Department of Civil Engineering,
Rensselaer Polytechnic Institute,
Troy, NY 12180, USA

ABSTRACT:

Lateral spreading of sloping ground or of soil near a waterfront is a common occurrence of liquefaction-induced ground failure in earthquakes. Particularly damaging is the effect of the permanent ground displacements on deep foundations of buildings and bridges, as shown in the last 20 years by a number of earthquakes. Examination of case histories indicate that this is essentially a pseudo-static, soil-structure interaction phenomenon caused by the pressure of the laterally moving liquefied and nonliquefied soil layers on the piles and pile cap constituting the deep foundation. Which ones and how much of these effects are present in any situation depend in a complicated way on a number of factors, including the free-field permanent displacement and the restraining stiffness of the superstructure. This last factor is especially important for pile-supported bridge piers, where the lateral stiffness of the bridge can play a significant role on the foundation response.

The effect of the superstructure lateral on the lateral displacement of the foundation and the induced maximum bending moments in the piles is studied by means of four centrifuge model tests. The bridge stiffness is modeled as a horizontal spring, k, connected above ground to the top of the pile; in the four models, the stiffness of this spring is different, varying from $k = 0$ to very stiff. The test with the unrestrained foundation ($k = 0$) indicated that the lateral pressure exerted by the liquefied soil per unit area of the pile has an approximately inverted triangular shape with depth, with a maximum pressure of about 17.7 kN/m^2 occurring at the top of the pile. The maximum bending moments along the pile in the models with $k \neq 0$ are predicted using the same triangular load and a simple structural model. A simpler, constant, rectangular liquefied soil pressure is also used in conjunction with the same structural model. Both triangular and rectangular pressure distributions predict well the measured trends: smaller positive pile bending moments at depth and smaller pile head displacements and increasing negative bending moments at shallow elevations, as k increases.

[1] Rensselaer Polytechnic Institute, Troy, NY

Introduction

Lateral spreading of sloping ground or of soil near a waterfront is a common occurrence of liquefaction-induced ground failure in earthquakes. Particularly damaging is the effect of the permanent ground displacements on deep foundations of buildings and bridges, as shown in the last 20 years by a number of earthquakes. Examination of case histories indicate that this is essentially a pseudo-static, soil-structure interaction phenomenon caused by the pressure of the laterally moving liquefied and nonliquefied soil layers on the piles and pile cap constituting the deep foundation. Which ones and how much of these effects are present in any situation depend in a complicated way on a number of factors, including the free-field permanent displacement and the restraining stiffness of the superstructure. This last factor is especially important for pile-supported bridge piers, where the lateral (typically longitudinal) stiffness of the superstructure can play a significant role on the foundation response.

The effect of the superstructure stiffness on the lateral displacement of the foundation and on the induced maximum bending moments in the piles is studied by means of four model centrifuge tests, labeled Models 3Abdoun, 2free-24, 2free-49, and 2free-168. The bridge stiffness is modeled as a horizontal spring connected above ground to the top of the pile; in the four models, the stiffness of this spring, k, is different, varying from k = 0 to very stiff. The Model 3Abdoun of an unrestrained foundation (k = 0), had already been reported (Abdoun, 1997). The results indicated that the maximum pressure exerted by the liquefied soil per unit area of the pile has an approximately inverted triangular shape with depth, with a maximum pressure of about 17.7 kN/m^2 occurring at the top of the pile (Dobry and Abdoun, 1998).

Model Description

The basic setup of the four centrifuge experiments is presented in Fig. 1. These tests study the effect of superstructure stiffness on a pile subjected to lateral spreading. The RPI flexible laminar box container is used. The model consists of an individual end-bearing pile going through a uniform liquefiable sand layer. The prototype single pile being simulated is 60 cm in diameter, is embedded 8 m in ground, has a bending stiffness, EI = 8000 kN-m^2, and is embedded in the two-layer soil system. The displacement at the top of the pile is restrained by a horizontal spring connected at z = -0.85 m simulating the stiffness of the superstructure. The corresponding horizontal spring constants for Models 3Abdoun, 2free-24, 2free-49, and 2free-168, are k = 0, 24, 49, and 168 kN/m, respectively. The bending moments are measured at six positions along the pile using strain gauges SG1 to SG6. The displacement at the restraint is measured using LVDT6. The soil deformations in the free field are measured by connecting LVDTs to the laminar box rings (LVDT1 to LVDT5). The prototype soil profile consists of 6 m layer of Nevada sand saturated with water, having a relative density of about 40%, and placed on top of a 2 m slightly cemented, nonliquefiable sand layer. The soil is instrumented with piezometers PPT1 and PPT2. Two accelerometers are connected to the rings (A5 and A6), while two accelerometers measure accelerations in the liquefied soil (A2 and A3). The acceleration of the slightly cemented sand layer is also measured

(A4). The whole model is slightly inclined to the horizontal to induce lateral spreading. Figure 2e presents the prototype input acceleration that consisted of 40 cycles of amplitude of 0.3 g and a frequency of 2 Hz applied parallel to the base.

Test Results

Figure 2 shows typical results obtained from a centrifuge test using the setup presented in Fig. 1. These particular results are from Model 3-Abdoun reported by Abdoun (1997). The pore pressure (Fig. 2d) first increased rapidly and then more slowly. After the shaking stopped, the excess pore pressure slowly dissipated. The lateral displacements in the free field increased monotonically or stayed constant during the shaking (Fig. 2a). The maximum permanent lateral displacement occurred at the ground surface. The maximum ground surface displacement for Models 3-Abdoun, 2free-24, 2free-49, and 2free-168 at the end of shaking was 80, 90, 72, and 68 cm, respectively. In all four tests, the pile head displacement (Fig. 2b) and bending moments (Fig. 2c) first increased reaching a maximum and then decreased to a final permanent value. These maximum and permanent values of pile head displacement and bending moments decrease as the stiffness of the horizontal spring of the test, k, increases, presumably because of the additional force exerted by the spring to the head of the pile. Figure 3 shows the free field displacement profile at the end of the test measured in Model 3-Abdoun.

Figure 4 presents the profile of maximum recorded pile bending moments for the four centrifuge models. As the magnitude of the spring constant, k, increases, the maximum recorded moment at $z = 5.75$ m decreases and the moments recorded in the pile at shallow depths increase in the negative direction. Also, the depth at which the moment diagram crosses the zero axis, increases as k increases.

Limit Equilibrium Analyses

Abdoun (1997) suggested a limit equilibrium analysis to evaluate maximum bending moments measured in lateral spreading centrifuge tests involving instrumented piles. Abdoun concluded that the maximum moments at 5.75 or 6 m depth for a number of centrifuge experiments of individual piles and pile groups, could be predicted with a rectangular liquefied soil pressure distribution on the pile foundation of 9.25 kN/m^2. Dobry and Abdoun (1998) concluded that the maximum bending moments at all depths for a test such as Model 3-Abdoun are better predicted assuming an inverted triangular pressure distribution with a pressure of 17.7 kN/m^2 at the ground surface, and zero at 6 m depth (Fig. 6).

Using the same concept recommended by Abdoun (1997), the authors found that the maximum moment at $z = 5.75$ m for Model 3-Abdoun can be predicted exactly using a rectangular pressure distribution of 11 kN/m^2.

Abdoun (1997) modeled the pile as a cantilever beam fixed at the bottom of the pile, Fig. 5a. This structural model assumes that the pile does not rotate at the interface between the bottom slightly cemented layer and the liquefiable layer. The predicted lateral displacement of the pile using this structural model and the inverted triangular pressure distribution is 15.7 cm, which is much less than 30 cm measured in Model 3-Abdoun. The discrepancy between the predicted and measured moment is attributed to rotation at the bottom of the pile.

To improve the structural model of Fig. 5a, a rotational spring, k_r, was added at a depth of 6 m to incorporate the finite stiffness of the bottom nonliquefiable layer, Fig. 5b. The maximum pile head displacement obtained in Model 3-Abdoun was used to calculate the value of k_r. This measured maximum pile head displacement is 30 cm, which is the sum of two displacements: one related to the deformation of the pile due to the pressure exerted by the liquefied soil on the pile, Δ_{def}, and the other related to the rotation at the rotational spring, Δ_{rot} (occurring at the interface between liquefied soil and the bottom slightly cemented layer). That is, $\Delta_{def} + \Delta_{rot} = 30$ cm. Using the triangular pressure distribution of 17.7 kN/m^2, Fig. 6, suggested by Dobry and Abdoun (1998) and modeling the pile as a cantilever beam, the displacement at the pile head due to the pressure of the liquefied soil, gives $\Delta_{def} = 15.7$ cm. Then, the displacement at the pile head associated with the rotation of the rotational spring, k_r, can be calculated as $\Delta_{rot} = 30 - 15.7 = 14.3$ cm. Assuming small rotation, the rotation of spring k_r can be calculated as $\theta = 14.3$ cm/600 cm = 0.023833 radians, where 600 cm is the length of the pile. Finally, the rotational spring constant is calculated as the moment at the rotational spring assuming a triangular pressure distribution divided by the rotation of the rotational spring. That is, $k_r = M/\theta$ = 127.44kN-m/0.02833 rad = 5347 kN-m/rad. In a similar manner, if the pile is loaded with the rectangular pressure distribution of 11 kN/m^2, the rotational spring constant, k_r, is found to be 4280 kN-m/rad .

Figure 6 presents the analytical model used to evaluate the results of Models 3-Abdoun, 2free-24, 2free-49, and 2free-168. It represents the pile as a beam 6.85 m in length, supported at the base by rotational spring k_r and at the top by horizontal spring k. The values of this spring are k = 0, 24, 49 and 168 kN/m depending on the test. Two different pressure distributions are used to predict the maximum bending moments (Fig. 6): the inverted triangular load of maximum pressure 17.7 kN/m^2 suggested by Dobry and Abdoun (1998) and the rectangular pressure distribution of 11 kN/m^2 obtained by the authors. The magnitude of the rotational spring used in the analysis depends on the pressure distribution. The values are k_r = 5347 kN-m/rad for the inverted triangular distribution, and k_r = 4280 kN-m/rad for the rectangular pressure distribution. In Fig. 6, F_s is the force taken by the spring, which is calculated as part of the solution.

Comparisons between the computed pile bending moments using the analytical model of Fig. 6 in conjunction with either rectangular or triangular pressure distribution, and those measured in Models 3-Abdoun, 2free-24, 2free-49, and 2free-168, are shown in Fig. 7. It can be observed that the calculated moment distributions using triangular pressure agree well with the measurements from Models 3-Abdoun and 2free-24, while for Models 2free-49 and 2free-168, having a stiffer spring at the top, the measured moments are somewhat overpredicted. This overprediction is less when the rectangular pressure distribution is used. Both triangular and rectangular pressure distributions predict well the trends of decreasing positive moments at depth and increasing negative moments in the pile near the ground surface, as k increases.

Conclusions

The effect of superstructure horizontal stiffness on the bending moments induced on a pile by lateral spreading was studied using centrifuge models. Results of four centrifuge tests, Models 3-Abdoun, 2free-24, 2free-49, and 2free-168, with a superstructural horizontal stiffness k = 24, 49, and 168 kN/m, respectively, were presented and discussed.

In all tests, the recorded pile head displacement and bending moments increased reaching a maximum, and then decreased to a final permanent value. The final permanent values of pile head displacement and of bending moments at depth decreased as the value of the horizontal stiffness increased.

The maximum measured bending moments always occurred at the interface between the liquefied soil and the cemented layer and they decreased as the horizontal stiffness k increased. Similarly, the maximum pile head displacement decreased as k was increased. Negative bending moments appeared at shallow depths when the horizontal spring was introduced, and they increased with the value of k.

The recorded maximum bending moments along the pile were predicted using both the inverted triangular distribution of 17.7 kN/m^2 recommended by Dobry and Abdoun (1998), and a rectangular pressure distribution of 11 kN/m^2 obtained by the authors. Both distributions predicted well the observed trends. At higher values of k a better prediction of the bending moment values was obtained with the rectangular pressure distribution, while for low values of k a better prediction was obtained with the triangular pressure distribution.

Acknowledgements

This study is partially supported by the Multidisciplinary Center for Earthquake Engineering Research (MCEER), and specially the MCEER-FHWA Project. Tarek Abdoun's work was partially supported by the National Science Foundation (NSF). Ricardo Ramos was partially supported by the University of Puerto Rico at Mayaguez. All this support is very gratefully acknowledged.

References

Abdoun, T. (1997). "Modeling of Seismically Induced Lateral Spreading of Multi-Layer Soil Deposit and Its Effect on Pile Foundations," Ph.D. Thesis, Dept. of Civil Engineering, Rensselaer Polytechnic Institute, Troy, NY

Dobry, R. and Abdoun, T. (1998). "Post-Triggering Response of Liquefied Sand in the Fee Field and Near Foundations," Proceedings, Third ASCE Specialty Conference on

Geotechnical Engineering and Soil Dynamics, Seattle, WA, August 3-8, 1998, pp. 270-300.

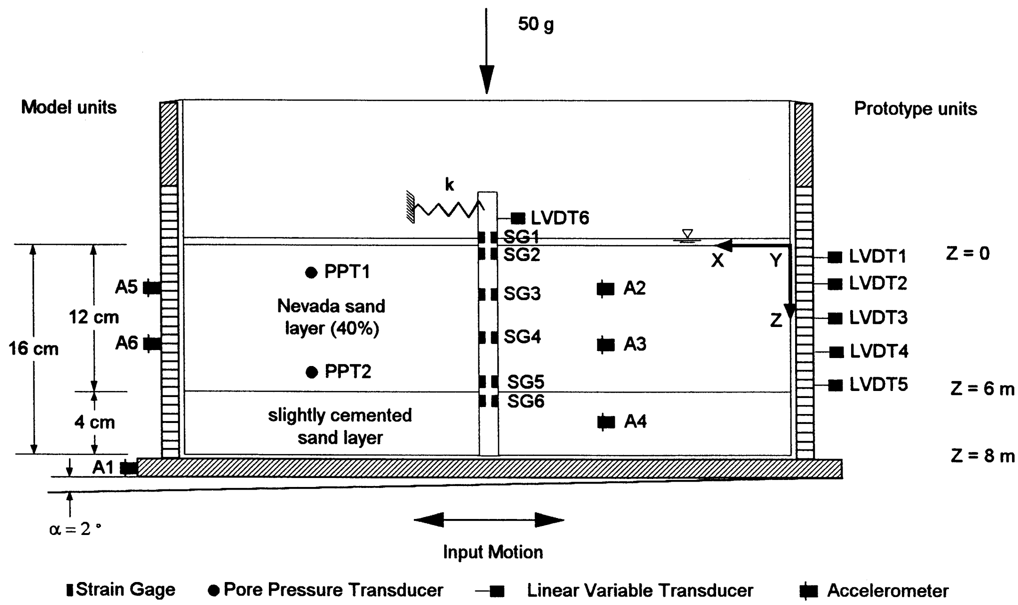

Figure 1: Test setup of centrifuge models

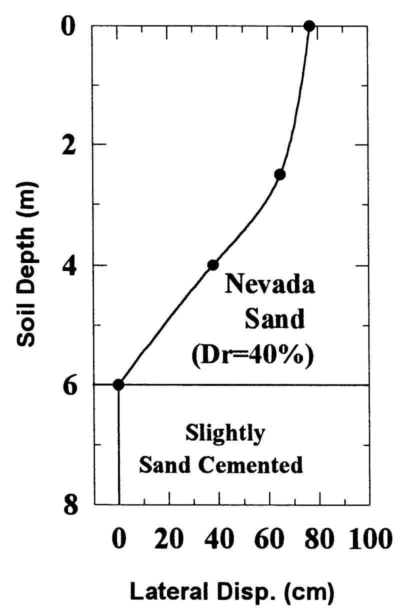

Figure 3: Free field displacement profile at the end of shaking, Model 3-Abdoun

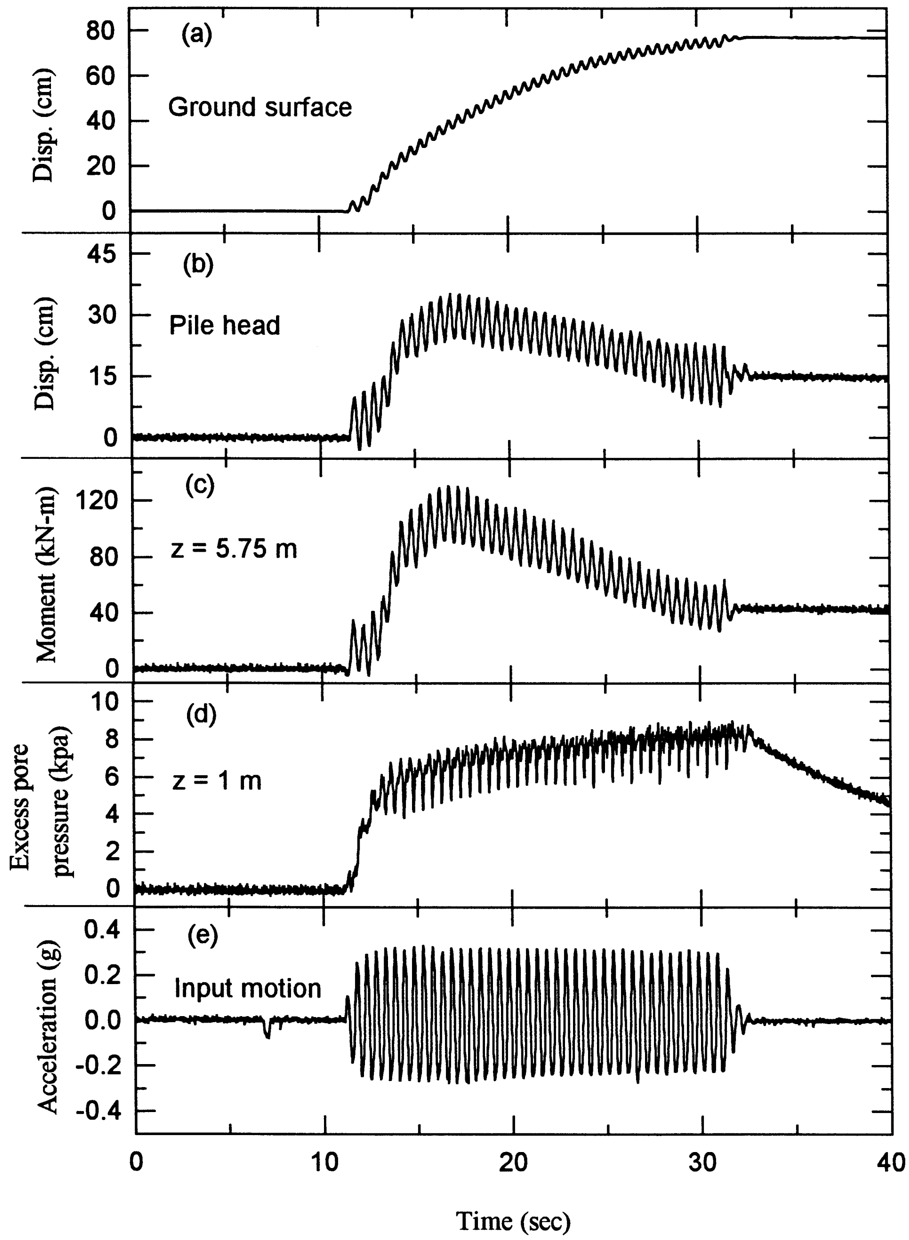

Figure 2: Typical results, Model 3-Abdoun

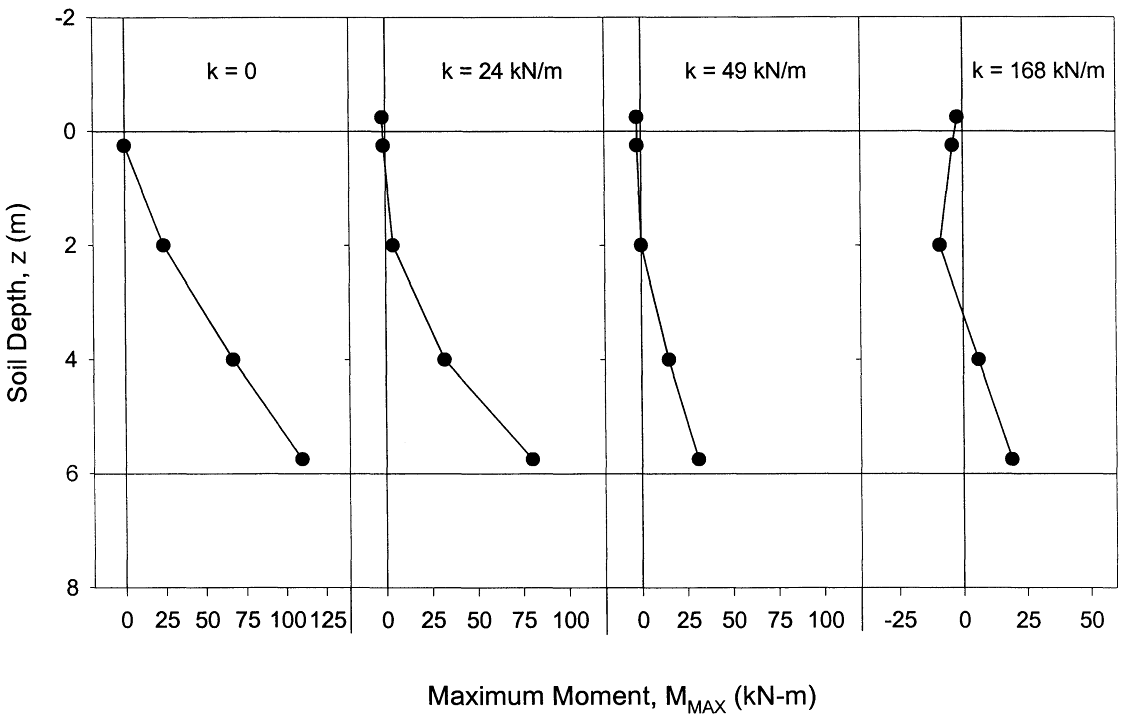

Figure 4: Recorded maximum bending moment profiles in four centrifuge tests

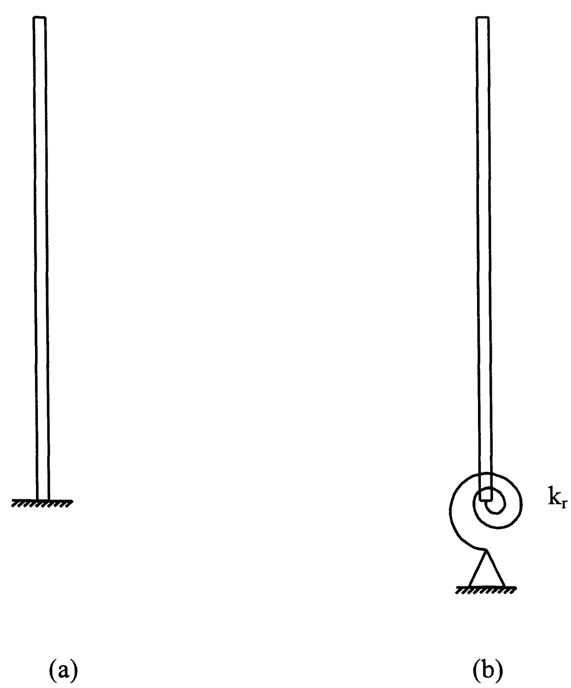

Figure 5: Structural models used to analyze the pile in Model 3-Abdoun

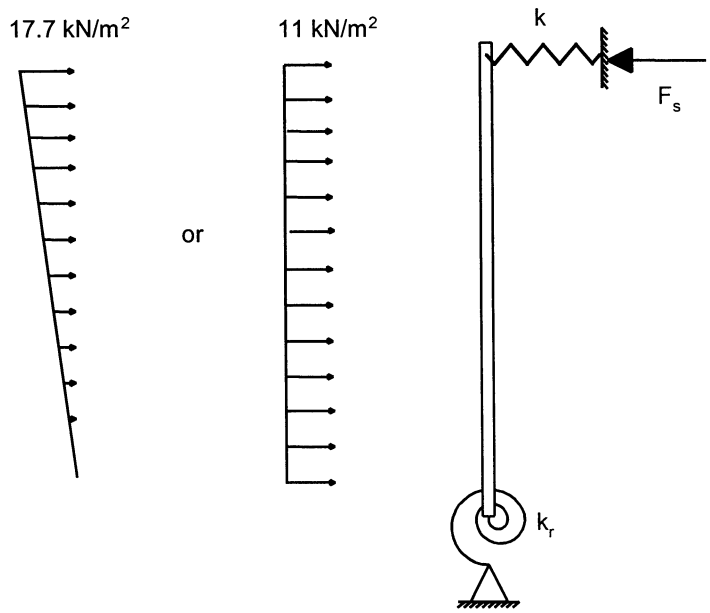

Figure 6: Structural model used in limit equilibrium analyses

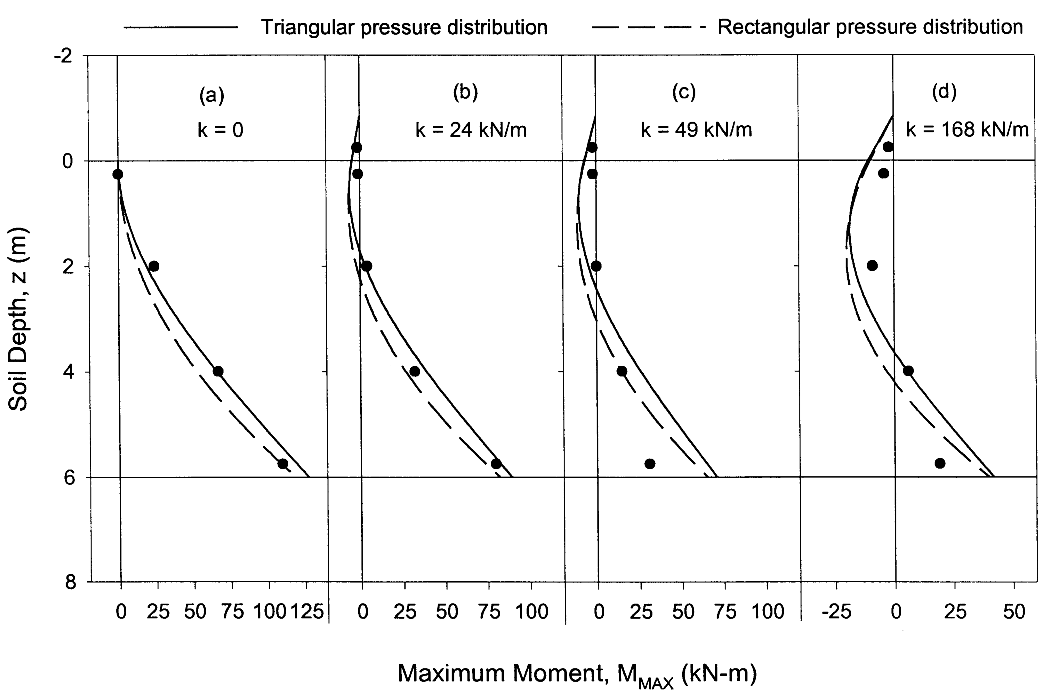

Figure 7: Comparison between recorded and predicted maximum moments using limit equilibrium analyses

APPLIED ELEMENT METHOD: A NEW EFFICIENT TOOL FOR DESIGN OF STRUCTURE CONSIDERING ITS FAILURE BEHAVIOR

Kimiro MEGURO* and Hatem Tagel-Din**

*: International Center for Disaster-Mitigation Engineering (INCEDE),
Institute of Industrial Science (IIS), The University of Tokyo
4-6-1 Komaba, Meguro-ku, Tokyo 153-8505, JAPAN
Tel: +81-3-5452-6436, Fax: +81-3-5452-6746
E-mail: meguro@incede.iis.u-tokyo.ac.jp

**: Visiting Researcher, INCEDE, IIS, The University of Tokyo

ABSTRACT

A new efficient numerical model named Applied Element Method (AEM) is proposed for discussing a new philosophy of design of structure. Although formulation and material model adopted in the method are simple, highly nonlinear behavior of structures in both static and dynamic conditions can be simulated accurately in reasonable CPU time. Conventionally, structures were designed based on the assumption that a well designed structure would survive till its life time and never collapse, however, this was wrong and it miss-guided people in some sense not to think seriously about the chaotic situation. To show the accuracy and applicability of the method, numerical results of nonlinear behavior of reinforced concrete structures obtained by the AEM are compared with experimental and/or theoretical results.

INTRODUCTION

During earthquakes, buildings suffer from the different types of damage. Structure damage is classified into seven groups, as shown in **Table 1**, according to the Architecture Institute of Japan (AIJ)[1]. In the first five groups, partial damage occurs to the structural and non-structural elements without collapse of the structure. Partial and complete collapse of structures is important topic under research because it causes extensive causalities inside and outside of the structures. In addition, collapse of a structure may lead to failure or collapse of neighbor structures. Recent earthquakes, like Hyogo-Ken Nanbu Earthquake (Kobe Earthquake), show that structural failure was major cause of death toll[2].

Many important questions can not be answered unless the numerical technique can follow detailed collapse behavior. For example, "What is the effect of collision between falling structural elements and neighbor structures", "What happens if structures having different dynamic characteristics collide during earthquakes?", "If a structure collapse, where and how do they undergo collapse?" and "What is the duration of collapse?". From the experience of Kobe Earthquake, Science and Technology Agency of Japan decided to build huge capacity (1,200 tf, over 0.9 G, ± 200 kine, ± 100 cm) three dimensional shaking table facility up to 2005. Using the facility, we can construct real-scale building and/or structure on the table and simulate complete collapse behavior of them. However, it is still impossible to carry out many experiments of every different type of structures. To fulfill this, an accurate but simple numerical technique is important. This numerical technique should satisfy the conditions of "*accuracy*", "*simplicity*" and "*applicability*". The term, "accuracy", means that realistic results should be obtained. "Simplicity" indicates that the method should not be complicated. Finally, "applicability" means that the method can be applied for a wide range of applications in reasonable CPU time. Studying the existing numerical techniques, we can find easily that these three conditions can not be fulfilled by one specified numerical technique.

To clarify the problems, a brief overview about the advantages and disadvantages of existing numerical technique are introduced. Numerical methods for structural analysis can be classified into two categories. In the first category, model is based on continuum material equations. The Finite Element Method (FEM) is typical example of this category. Smeared Crack approach[3] can not be adopted in zones where separation occurs between structural elements. While, Discrete Crack Methods[3] assume that the location and direction of crack propagation are predefined before the analysis. With this group of the methods, analysis of structures, especially concrete structures, can be performed at most before collapse. The FEM can fulfill only the conditions of "accuracy". On the other hand, it is difficult to accept that the FEM fulfills the second requirement, which is "*simplicity*". Many complications arise if the behavior is highly nonlinear from either material or geometrical point of view. For example, it is very difficult or impossible to use the FEM to study behavior of materials or structures that change their status from continuum state to perfectly discrete state, like behavior of structures before and during collapse. In brief, the FEM can answer only the following question which is "Will the structure fail or not?" Unfortunately, it is very difficult to use the FEM for the second important question, which is "How does the structure collapse?" Although displacement of structural elements at failure may become tens of meters, analysis using the FEM could be performed till the start of failure, which means tens of centimeters at most.

The second group of methods uses the discrete element techniques, like the Rigid Body and Spring Model (RBSM)[4] and the Modified (or Extended) Distinct Element Method (MDEM[5], EDEM[6]). The main advantage of these methods is that they can simulate the cracking process with relatively "simple" techniques compared to the FEM, while the main disadvantage is that crack propagation depends mainly on the element shape, size and arrangement[7, 8]. Analysis using the RBSM could not be performed up to complete collapse of the structure. On the other hand, the EDEM can follow the structural behavior from zero loading and up to complete collapse of the structure. However, the accuracy of EDEM in small

Table 1 Damage level of structures as defined by the AIJ[1)]

Damage level	***Damage of members***
1- No damage	No damage is found.
2- Slight damage	Columns, shear walls or non-structural walls are slightly damaged.
3- Light damage	Columns or shear walls are slightly damaged. Some shear cracks in non-structural walls are found.
4-Moderate damage	Typical shear and flexural cracks in columns, shear cracks in shear walls, or severe damage in non-structural walls are found.
5- Heavy damage	Spalling of concrete, buckling of reinforcement, and crushing or shear failure in columns are found. Lateral resistance of shear walls is reduced due to heavy shear cracks.
6- Partial collapse	The building is partially collapsed due to severely damaged columns and/or shear walls.
7- Total collapse	The building is totally collapsed due to severely damaged columns and/or shear walls.

Table 2 Organization of research results

<table>
<tr><td></td><td></td><td colspan="2">Static</td><td colspan="2">Dynamic</td></tr>
<tr><td>Geometry</td><td>Material</td><td>Monotonic</td><td>Cyclic</td><td>Monotonic</td><td>Cyclic</td></tr>
<tr><td rowspan="2">Small deformation (linear)</td><td>Elastic</td><td>I</td><td rowspan="2">III</td><td rowspan="5">V</td><td rowspan="5">VI</td></tr>
<tr><td>Nonlinear</td><td>II</td></tr>
<tr><td rowspan="2">Large deformation (nonlinear)</td><td>Elastic</td><td colspan="2">IV</td></tr>
<tr><td>Nonlinear</td><td colspan="2">Covered in dynamics</td></tr>
<tr><td colspan="2">Collapse process</td><td colspan="2">No meaning</td></tr>
</table>

deformation range is less than that of the FEM. Hence, the failure behavior obtained by repeated many calculations is affected due to cumulative errors and it can not be predicted accurately using the EDEM. This means that the EDEM can answer qualitatively only the second question, "How does the structure collapse?" The EDEM fulfill totally the conditions of "simplicity" and partially fulfills the "applicability", however, the "accuracy" requirements are still questionable.

From the fact discussed above, we can say that there is no proper method among current available techniques by which total behavior of structures from zero loading to collapse can be followed with reliable accuracy, reasonable CPU time and with relatively simple material models.

The major advantages of the Applied Element Method (AEM) are simple modeling and programming, and high accuracy of the results with relatively short CPU time. Using the AEM, highly nonlinear behavior, i.e. crack initiation, crack propagation, separation of structural elements, rigid body motion of failed elements and collapse process of the structure can be followed with high accuracy[9)].

To cover a wide range of applications, analyses should be performed for different fields of application and the results should be verified by comparing with theoretical and/or experimental results whenever possible. The main factors affecting structural analysis can be categorized as:

1. Effects of inertia forces: The loading types are divided into two categories, static and dynamic loading conditions. In dynamic loading case, the inertia and damping forces should be taken into account and hence, loading is a function of time.
2. Effects of the direction of loading: The analyses are divided into two categories, monotonic and cyclic loading conditions. In monotonic loading condition, the load direction is constant while its value increases, and in case of cyclic loading, the load direction and values are changing.
3. Effects of geometrical changes: In some analyses, the deformations are considered small with respect to the structural dimensions. It can be assumed that the structure geometry is constant and effects of geometrical changes on the stiffness matrix or internal forces are negligible. In other cases, like buckling cases, deformations are large and geometrical nonlinear behavior should be discussed.

4. Effects of material properties: The material behavior can be assumed as linear or nonlinear behavior. In linear behavior, all stress-strain relations are constant while in nonlinear case, cracking, yield of the material and nonlinear stress-strain relations should be considered.

The organization of the research done is shown in **Table 2**. This table shows all meaningful application ranges, which should be covered by the proposed numerical model. The dark area indicates that there is no meaning to perform simulation, like simulation of collision effects in static loading condition. In the lightly hatched area, application in static loading conditions is not reasonable sometimes because in case of nonlinear material, structural elements, like concrete elements in large deformation range, tend to separate and become unstable. This indicates that the effects of inertia forces and rigid body motions become dominant. Therefore, this range is covered in dynamics. The main purposes of this paper are to explain the background and outline of newly proposed model, AEM, and to introduce some of the results of AEM in order to show the applicability of the method.

OVERVIEW OF THE AEM

With the AEM, structure is modelled as an assembly of small elements, which are made by dividing the structure virtually, as shown in **Fig. 1 (a)**. The two elements shown in **Fig. 1** are assumed to be connected by pairs of normal and shear springs located at contact points, which are distributed around the element

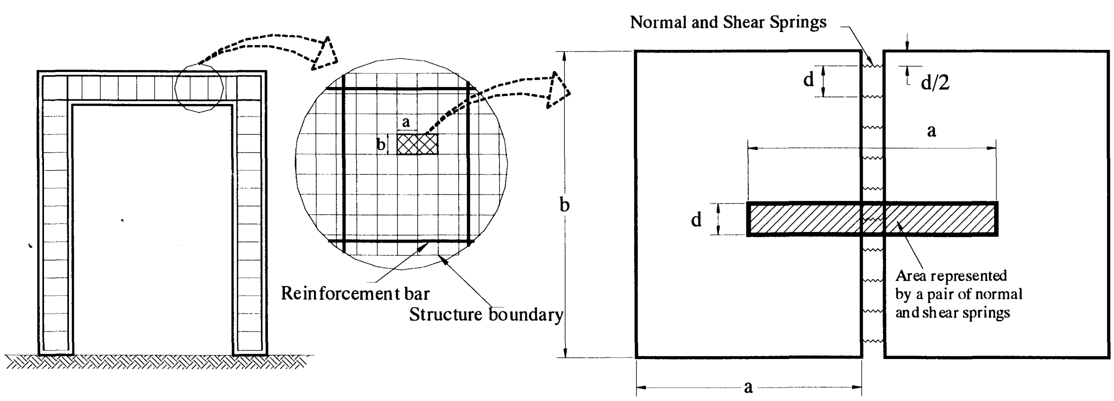

(a) Element generation for AEM

(b) Spring distribution and area of influence of each pair of springs

Fig. 1 Modelling of structure to AEM

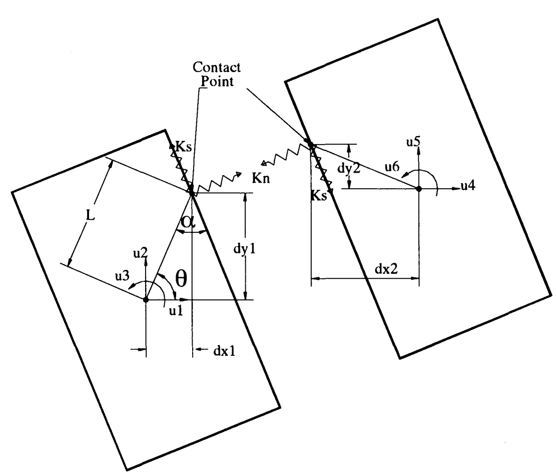

Fig. 2 Element shape, contact point and degrees of freedom

edges. Each pair of springs totally represent stresses and deformations of a certain area (hatched area in **Fig. 1 (b)**) of the studied elements. In case of reinforcement, two pairs of springs are used, for concrete and for reinforcement bar. This means that the reinforcement spring and concrete spring have the same strain and the effects of separation between reinforcement bars and surrounding concrete can not be easily considered within an element. However, when we look at the behavior of element collection as a unit, due to the stress conditions, separation between elements occurs because of failure of concrete-springs before the failure of reinforcement-springs and hence, relative displacement between reinforcement bars and surrounding concrete can be taken into account automatically. This is a unique point which continuum equation based models, like FEM, do not have. In the proposed method, reinforcement springs can be set at the exact location of the reinforcement bars in the model. It should be emphasized that effects of stirrups, hoops and concrete cover can be easily considered. Each of the elements has three degrees of freedom in two-dimensional model. These degrees of freedom represent the rigid body motion of the element. Although the element motion is as a rigid body, its internal deformations are represented by the spring deformation around each element. This means that although the element shape doesn't change during analysis, the behavior of assembly of elements is deformable.

The global stiffness matrix is determined by summing up the stiffness matrices of individual pair of springs around each element. The developed stiffness matrix has total effects from all of the pairs of springs according to the stress situation around the element. This technique can be used both in load and displacement control cases.

STATIC SMALL DEFORMATION ANALYSIS

In this section, the applicability of the AEM for RC structures in small deformation range is discussed. Simulation results of elastic materials and nonlinear behavior of RC structures under monotonic and cyclic loading conditions are introduced and compared with theoretical or experimental results.

Effect of Element Size (Elastic Material Condition)

Adjustment of element size in the analysis is very important. Simulation of structures using elements of large size leads to increasing the structure stiffness and failure load. This means that the calculated displacements become smaller and the failure load gets to be larger than the actual one. To make this effect clear, we carried out a series of simulations using the laterally loaded cantilever models as shown in **Fig. 3**. The dimensions of the models are also shown in the figure. The Young's modulus is assumed as $2.1\text{x}10^7$ tf/m^2 and elastic analysis was performed using the proposed method. The results were compared with the theoretical results of elastic structure. The percentage of error in maximum displacement and the CPU time (CPU: DEC ALPHA 300 MHz) are shown in **Fig. 4**.

To discuss the effect of the number of connecting springs, the analyses were performed using two models with 20 and 10 springs connecting each pair of adjacent element faces for each case of different element size. From **Fig. 4**, it is evident that increasing the number of base elements leads to decreasing the error but increasing the CPU time. Use of only one element at the base leads to about 30% error of theoretically calculated displacement. This error reduces to less than 1% when the number of elements at the base increases to 5 or more. However, the CPU time increases rapidly. When we compare the results using 20 and 10 springs, although the CPU time in case of 10 springs is almost half of that in case of 20 springs, the accuracy of the results of 10 springs model is same as that in case of 20 springs. From this figure, it can be concluded that usage of large number of elements together with relatively few number of connecting springs leads to high accuracy in reasonable CPU time.

Figures 5 and **6** show the normal and shear stresses distribution at the base of the studied columns for different number of base elements. From these figures, the followings should be noticed:

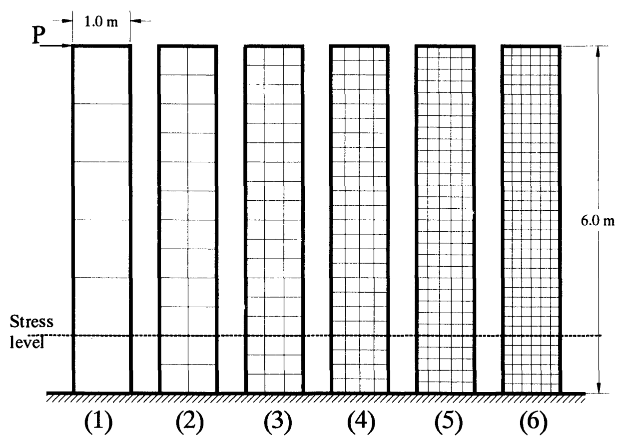

Fig. 3 Dimensions and element arrangements of laterally loaded cantilever models

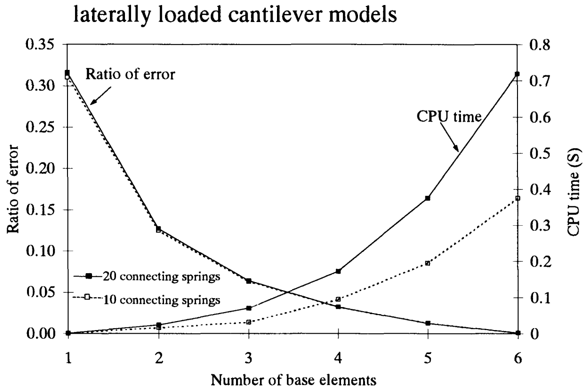

Fig. 4 Relations between the number of base elements, ratio of error and CPU time

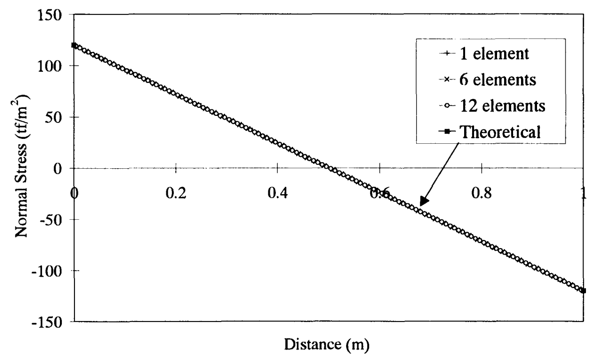

Fig. 5 Normal stress distribution at the column base

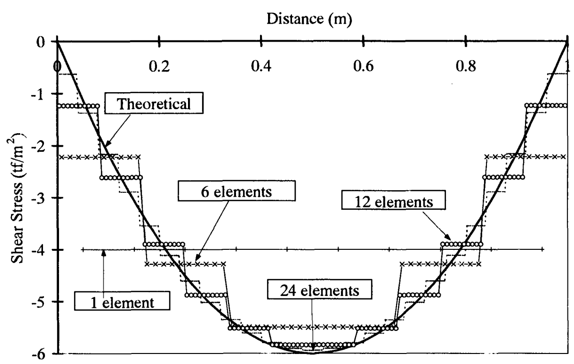

Fig. 6 Shear stress distribution at the column base

- Calculated normal stresses are very close to the theoretical values even in case of the smaller number of elements at the base.
- Shear stresses are constant for the same element.
- Shear stresses are far from the theoretical values in case of the smaller number of elements at the base and become close to the theoretical results as the number of elements increases.

This means that behavior in which the effect of shear stresses is minor, like the case of slender frames, can be simulated accurately by elements of relatively large size. To improve the accuracy of analysis using elements of large size, attention should be paid for the unsupported length of the structure. On the other hand, in case of walls and deep beams, elements of small size should be used to follow the fracture behavior in the shear dominant zones.

Effect of Element Arrangement

To verify the accuracy of the proposed method in comparison with other numerical techniques using rigid elements, such as RBSM and DEM, Brazilian test simulation is performed using square shaped concrete specimens subjected to concentrated loads. Three different mesh configurations are used. In Case (1), the elements are set parallel to the specimen edges, while in the second case, the elements are 45 degrees inclined to the specimen edges. In the third case, the load is applied to the diagonal of the square and the elements are parallel to the specimen edges. The distance between loading points is 20 cm in all cases and 10 springs were set between each two adjacent faces. The results are summarized in **Table 3**. Theoretical failure load is 12.5 tf in Cases (1) and (2). In this simulation, compression failure under the applied load is not permitted. Only tension cracks are permitted.

Table 3 Brazilian test results of specimens

Fracture Criterion	**Case (1)**	**Case (2)**	**Case (3)**
Number of elements	2500	3280	3280
AEM *(Principal Stress)*	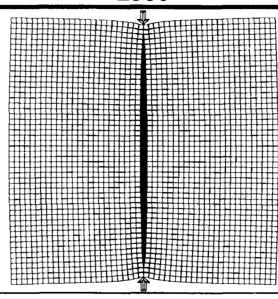	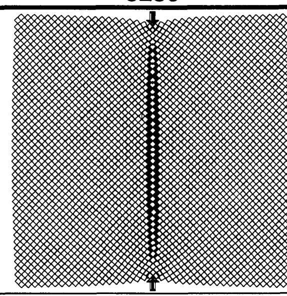	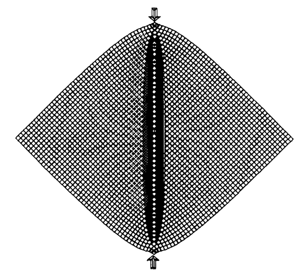
Failure Load	12.5 tf	12.5 tf	11.7 tf
RBSM or DEM type *(Normal and Shear Stresses)*	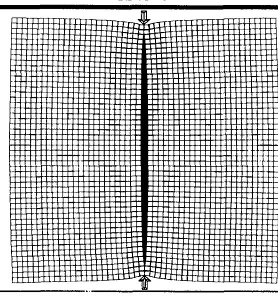	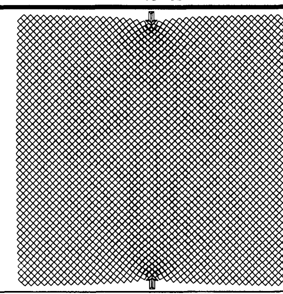	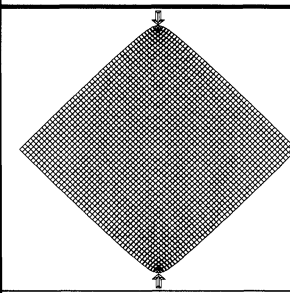
Failure Load	12.5 tf	*Not failed*	*Not failed*

From the results, it can be noticed easily that the obtained failure load by the proposed model does not change even when different mesh arrangement is adopted, while by RBSM or DEM, failure load can not be calculated in case of 45° discretization mesh in Case (2). Although the normal and shear stress applying to element edges are different in Cases (1) and (2), the principal stresses, which dominate the occurrence of cracking, do not change. This means that results obtained by RBSM or DEM depend on the element shape and arrangement because of the use of Mohr-Coloumb's failure criterion based on two components of stresses (not based on principal stresses). This makes the application of Mohr-Coloumb's failure criterion suitable only for brick masonry type of structures but not suitable for continuum materials where the cracking behavior is dominant by the principal stresses.

Verification under Cyclic Loading

This section introduces application of the AEM to cyclic loading conditions. The simulation results are compared with a double cantilever beam subjected to cyclic loading. The dimensions of the beam, reinforcement details and loading points are shown in **Fig. 7**. For more details about the experiment, refer to Ref. (10). The material properties are: σ_y=4,600 kgf/cm^2, σ_c=380 kgf/cm^2, σ_t=22.0 kgf/cm^2 and E_c=250 tf/cm^2, following the Ref. (10). In this case, diagonal tension cracks, nonlinear stress-strain relations of concrete[3)], nonlinear behavior of reinforcement bars[11)] before and after yield are considered.

Half of the structure is modeled using 330 square elements. The number of distributed springs set between each two adjacent faces is 10. Four and half load cycles are applied to the beam in 400 load increments for each. The reinforcement bars are modeled as continuous springs connected elements together at each reinforcement bar location. The total elapsed time of the analysis is about 30 minutes (CPU: DEC ALPHA 300 MHz). It should be noticed also that the loading points and the support locations change during analysis when the load direction is reversed. The applied load cycles are shown in **Fig. 8**. The numbers inside the figure correspond to the deformed shape and crack patterns shown **Fig. 12**.

Figure 9 shows the relation between the total applied load and displacement under the loading plates. A good agreement between the calculated and experimental load-deformation relations can be seen. From the figure, it is noticed that the prediction of failure load is very close to the experimental result. However, accuracy of the calculated unloading stiffness, especially before yield of reinforcement, is a little less than that of experiment. This is because of the improper crack closure mechanism.

Using the proposed model, stresses and strains at any point in concrete or steel of the specimen can be calculated easily. **Figures 10** and **11** show the stress-strain relations for main reinforcement at point "A" and concrete at point "B", respectively. The location of these points is shown in **Fig. 12**. It can be noticed from these figures that compression failure of concrete occurs at the connection between the beam and the column together with yield of main reinforcement, which agrees well with the experiment. After yield of reinforcement, stiffness is drastically reduced and relatively large displacement occurs, as shown in **Fig. 9**.

Figure 12 shows the deformed shapes and crack patterns at different loading stages. Different illustration scale factors are adopted to follow the cracking behavior. Two groups of cracks can be identified easily. During loading cycles, one group opens while the other group tends to close. The crack width increases when the applied load increases. In addition, tension cracks parallel to centerline of the column appear. Compression failure of elements at the connection between the beam and the column can be seen by following element overlaps. Dislocations of some elements before failure and after repetition of cycles are also obvious.

The above mentioned discussions show that the proposed model can be applied for fracture behavior of RC structures, such as, failure load, deformations, crack generation and propagation, etc. It should be emphasized that although the shape of elements used in the simulations is square, it does not have big effect to the crack generation or propagation in the material. Diagonal cracks, as shown in **Fig. 12**, coincide well with those obtained

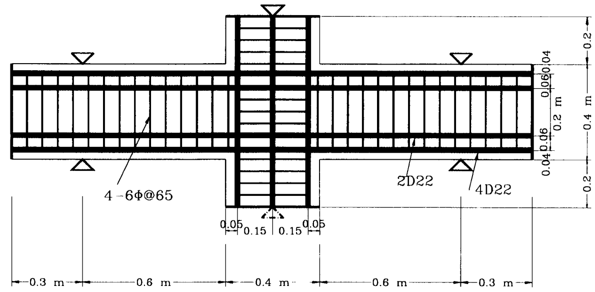

Fig. 7 Dimensions and reinforcement of a double cantilever

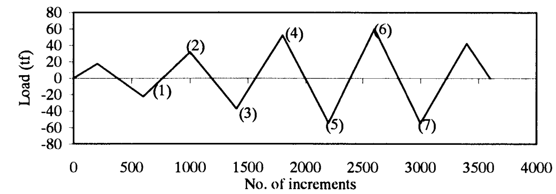

Fig. 8 Load cycles applied to a double cantilever

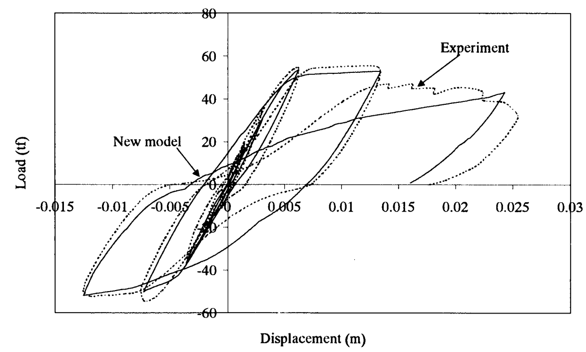

Fig. 9 Load-displacement relation of a double cantilever

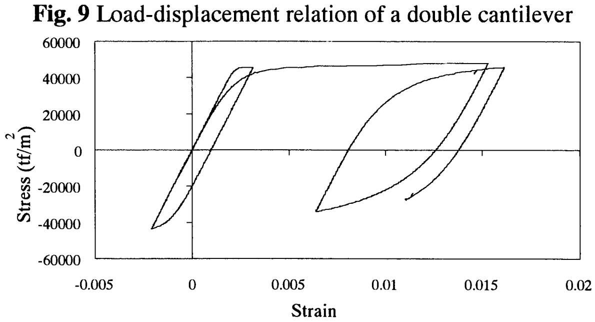

Fig. 10 Stress-strain relation for steel at point "A"

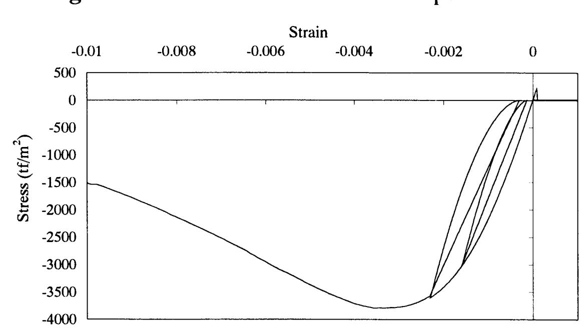

Fig. 11 Stress-strain relation for concrete at point "B"

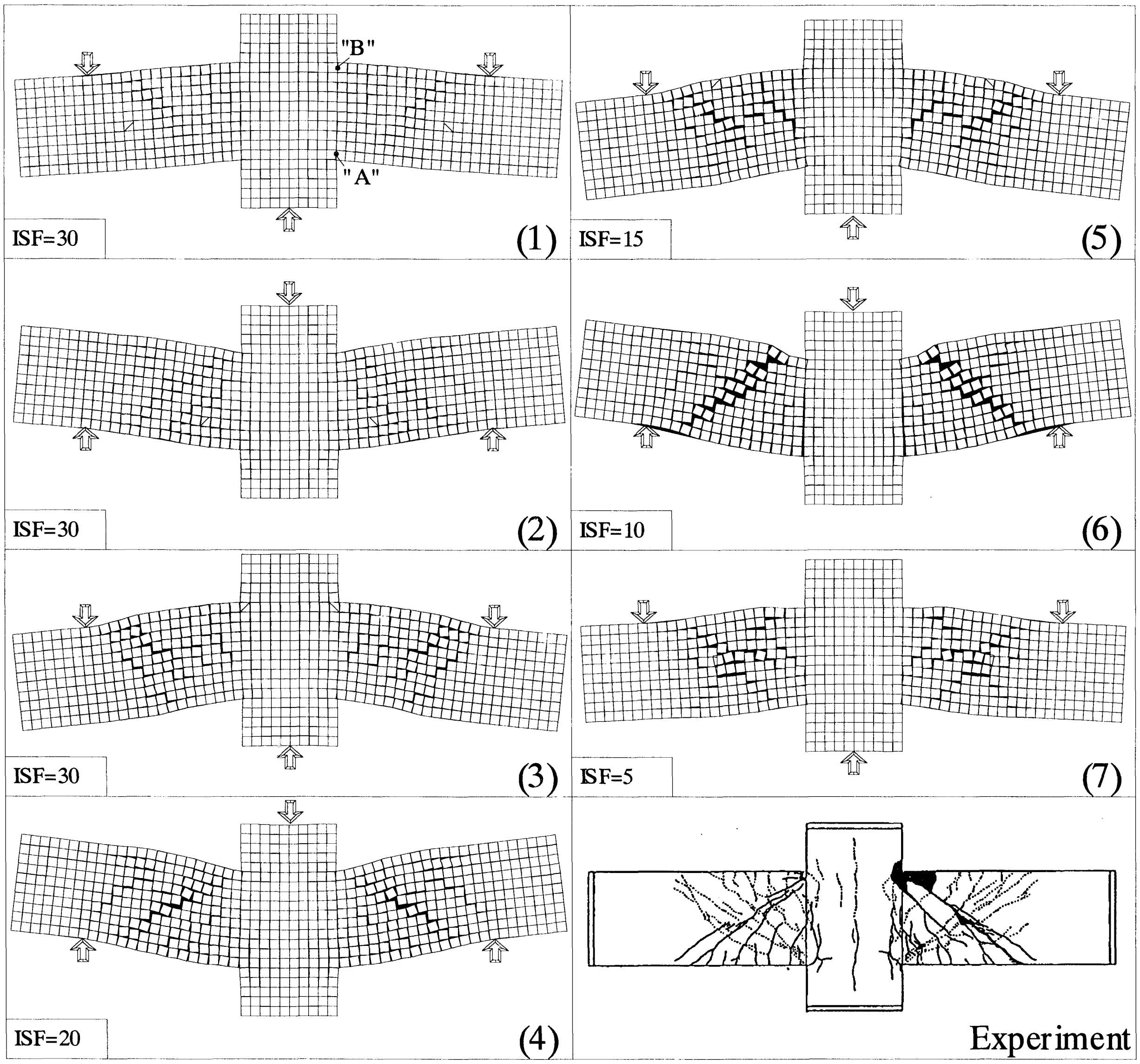

Fig. 12 Deformed shape and crack patterns of a double cantilever (ISF: Illustration Scale Factor)

from the experiment. In the simulation using rigid elements, like RBSM[4], shapes and distributions of elements should be decided before the simulation based on the assumption that crack locations and direction of propagation are known.

LARGE DEFORMATION ANALYSIS

In this section, the applicability of the AEM for RC structures in large deformation range is discussed. The applicability of the method for buckling analysis, rigid body motion and collision of structural elements during collapse is addressed. The effects of the geometrical changes of the structure during simulations are considered by adopting the geometrical residuals technique[12), 13)]. The advantage of this technique is that there is no need to determine the geometrical stiffness matrix, resulting in making the simulation easier without affecting the accuracy of the results. This technique can be applied either for static[12)] or dynamic loading cases[13)].

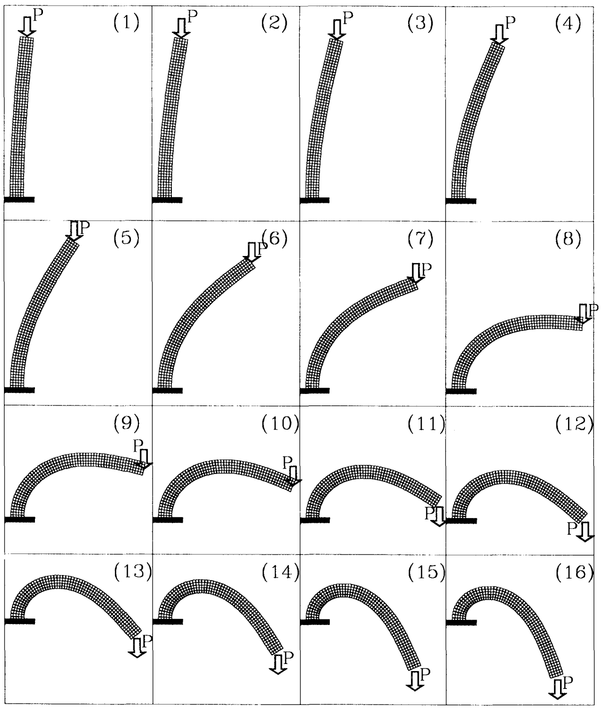

Fig. 13 Post buckling behavior of a cantilever

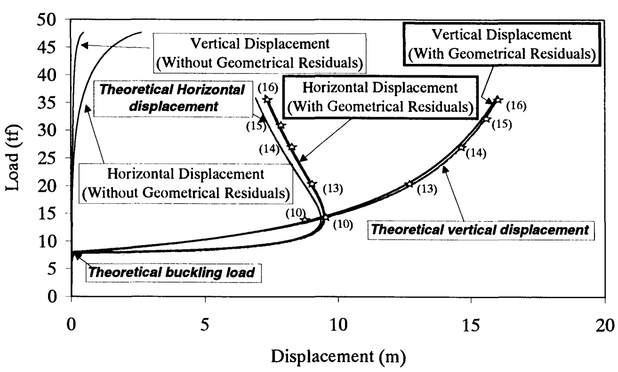

Fig. 14 Load-displacement relation of an elastic cantilever under vertical load

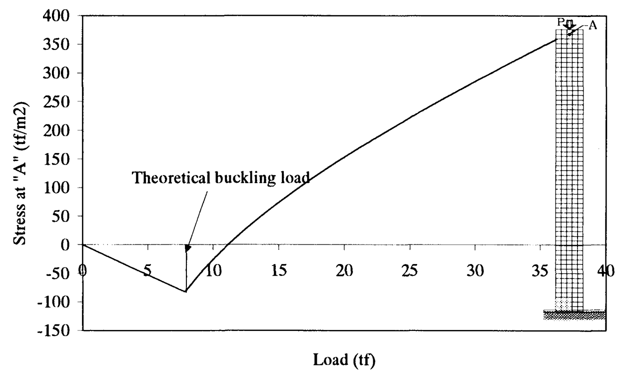

Fig. 15 Load-stress relation at point "A"

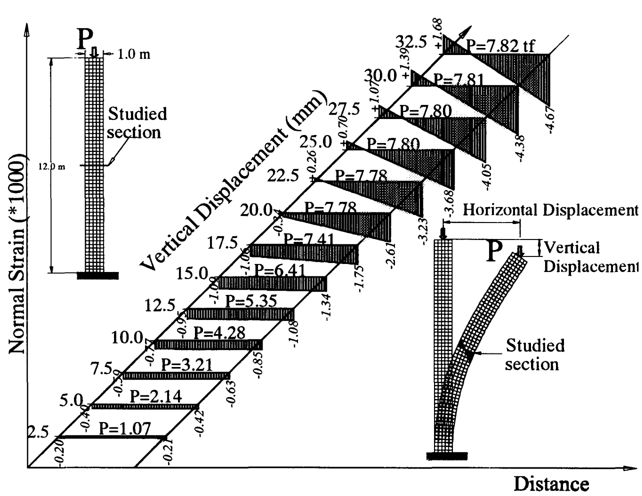

Fig. 16 Variation of internal stress distribution during buckling

Buckling and Post-Buckling Behavior of Structures

In this case study, a fixed base elastic cantilever under axial load is used. The load direction is assumed constant and applied in static way during analysis. The height of the cantilever is 12.0 m and the cross section is (1.0 m x 1.0 m). The Young's modulus assumed is 8.4 x 10^4 tf/m^2. The analysis is performed using 300 elements. The load is applied at the top of the column with the constant-rate vertical displacement. To break symmetry of the system, the stiffness of one of edge elements was increased by just 1% relative to the other elements (initial imperfection). The theoretical results of vertical and horizontal displacements can be obtained by following Ref. (14). **Figure 13** illustrates the deformed shapes of the cantilever during and after buckling. It is obvious that highly nonlinear geometrical changes can be followed. **Figure 14** shows the horizontal and vertical displacements at the loading point in three different cases with and without consideration of the geometrical residuals together with the theoretical load-displacement relations.

In theoretical results, the effects of axial and shear deformations are not considered. Although these effects are relatively small, they are taken into account in our analysis. From **Figs. 13** and **14** the following can be noticed:

1. The load-displacement relation obtained when the geometrical residuals are considered is close to the theoretical values till very large displacements. This gives evidence that the proposed method is accurate and numerically stable.
2. The calculated buckling load without consideration of geometrical residuals, only with modification of geometry, was about 47 tf which is quite larger than the theoretical one (7.8 tf). This means that modification of the geometry only during the analysis is not sufficient.
3. The calculated load-displacement relation is tangent to the horizontal line at the buckling load value which agrees well with the theory.
4. Slight increase in the load after buckling results in very large displacements. This indicates that applying load control technique after buckling leads to very large deformations during small number of increments.
5. When the vertical displacement is about 9 m, horizontal displacement begins to decrease.
6. The cantilever shape changes after buckling to an arch, which makes the stiffness of the specimen increase after buckling.

Figure 15 shows the load-stress relation at the point "A" under the applied load. Before buckling, stress is uniform compression and increases in a linear way. When reaching the buckling load, compression stresses are released till reaching zero when the direction of load becomes parallel to the cantilever end edge, stage (8) in **Fig. 13**. Finally, tension stresses are developed.

Changes in internal stresses of an intermediate section during analysis are shown in **Fig. 16**. Before buckling, stresses are almost uniform compression and only axial deformations are observed. After reaching the buckling load, although the applied load is constant ($P \approx 7.8$ tf), bending moments generates and large deformation occurs because of the buckling bending moments. This shows one of the strong points in our analysis that mechanical behavior of any point in the structure can be followed accurately even if large deformations occur.

Analysis of an RC Building Model Subjected to Series of Base Excitations

Recently, the size of scaled model specimens for structural tests tends to become larger and larger. A large scaled model test enables us to obtain data similar to real structures. However, since it requires large size testing facilities and large amount of research funds, it makes difficult to execute parametric tests. This section introduces the simulation results of a scaled RC building model (1/15) subjected to magnified base excitation. The test structure was an eleven-storied building model. A general view of the model and sections are shown in **Fig. 17**. For more details about the structure shape or applied load, refer to Refs. (15) and (16). A series of base excitations were applied to the structure in order from small to large amplitudes. The shape of these excitations is same, namely, their frequency characteristics are same while amplitudes are different, from 40 Gal to 800 Gal, as shown in **Fig. 18**. The excitation G800 was applied twice to the structure, with normal (G800-1) and doubled (G800-2) time scale, respectively. This makes the numerical analysis more complicated because cumulative damage to the structural elements affects the response.

The structure is modelled using 1,232 square-shaped elements. The comparison between the measured and simulated response of different floors is shown in detail in Ref. (9). The following factors are considered in the simulation using the AEM:

1. Stress-strain relation of concrete under cyclic loading[3].
2. Stress-strain relation of reinforcement under cyclic loading[11].
3. Additional bending moments because of load eccentricities at columns during tests.
4. Large deformation, separation and rigid body motion of structural members during failure[13].
5. Collision of structural members with each other and with the ground[17].

The natural periods and modes, shown in **Fig. 19**, could be calculated using eigen value analysis. Different mode shapes and natural periods could be obtained easily. This indicates that the analysis can be performed in frequency domain as well as in time domain.

Because of limitations of space, selected samples of the results are introduced in this paper. The calculated and measured responses of the roof in case of G600 and G800 are shown in **Figs. 20** and **21**, respectively. Although the structural behavior is highly nonlinear, with cracking, yield of reinforcement and crushing of concrete, excellent agreement between calculated and measured displacement responses could be obtained. Moreover, it is clear that the effects of cumulative damage during the applications of G40, G200 and G400 are considered automatically.

Most of experiments of RC structures have been performed till failure but before complete collapse, where geometrical changes are generally small. It is very difficult to extend the experiments to follow the collapse process of structures. Difficulty arises from the fact that capacities of shaking tables have been limited and even when the capacity is enough, it is not safe to perform such kind of experiments, especially for full-scaled structures. It may also result in damage of shaking table or surrounding area due to large collision forces.

The experiment was performed up to the G800-2 with doubled time scale, where the structure failed from the structural viewpoint, but it did not collapse. Therefore, numerical results of the same building subjected to a destructive excitation are

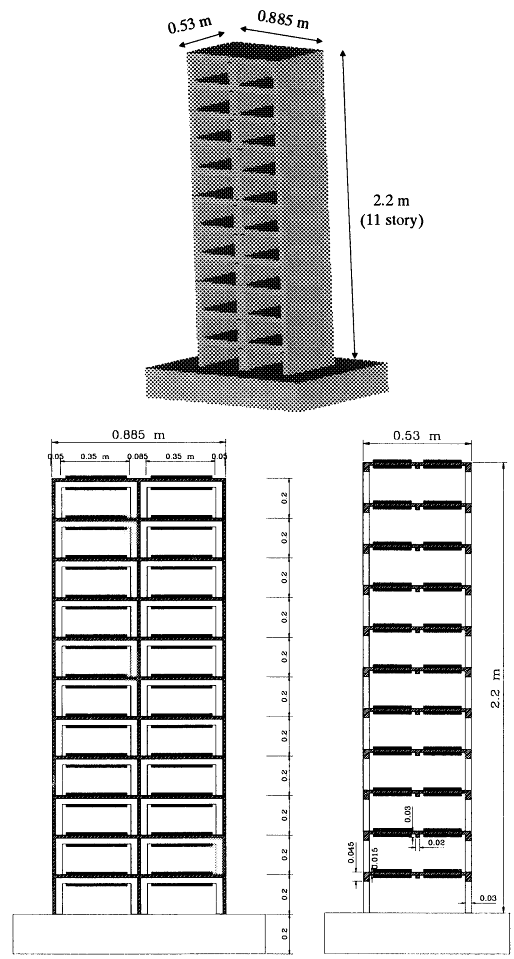

Fig. 17 Shape, dimensions and loading of a small-scaled RC building model under lateral excitation

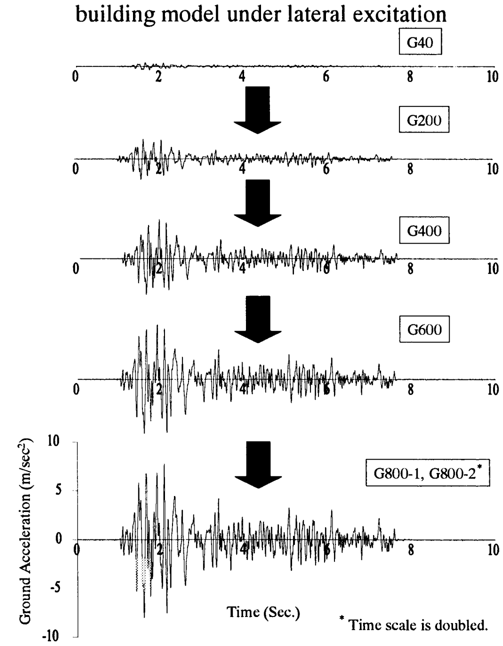

Fig. 18 Input base accelerations, G40, G200, G400, G600, G800-1 and G800-2 used for shaking table experiments.

also introduced. The amplitude of the base excitation of G800 is multiplied by 1.5 and its time scale is doubled. This destructive acceleration is applied to the same structure and the structural response during the process of failure including complete collapse is studied. As the collapse process is very complicated and it may not be represented accurately using two-dimensional model, relatively simple models for concrete crushing and reinforcement cut are adopted[17]. The analysis is performed using time increment of 0.0025 and 0.0005 seconds before and after recontact between elements occurs, respectively. The collapse history, shown in **Fig. 22**, can be summarized as follows:

1. Failure starts by excessive cracking, yield and cut of reinforcement at base floors.
2. Columns and beams of lower floors suffered complete damage while the upper floors suffered slight damage but it moves together in rigid body motion and rotates around the failed structural elements till they collide with the ground.

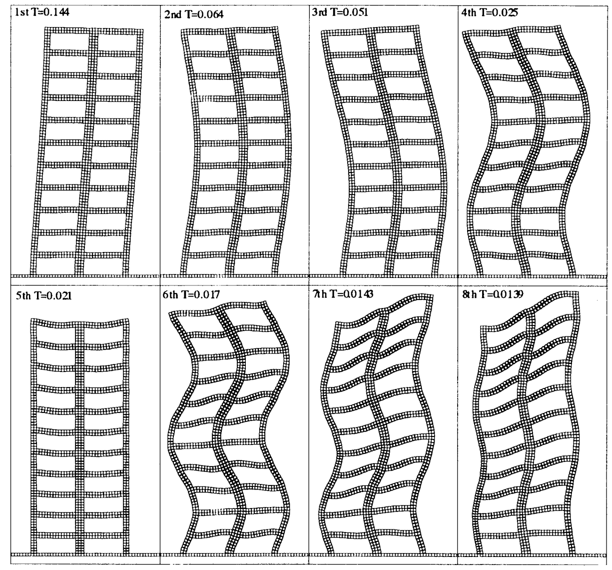

Fig. 19 Eigen values and modes of the building model.

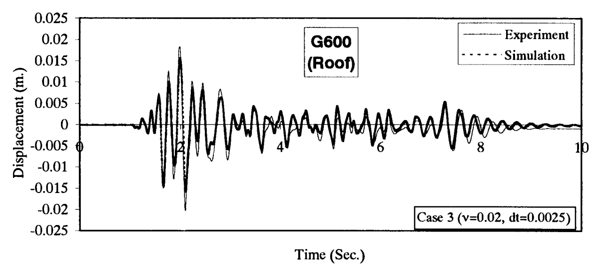

Fig. 20 Displacement response at the roof for G600 (damping ratio=0.02, simulation time increment=0.0025)

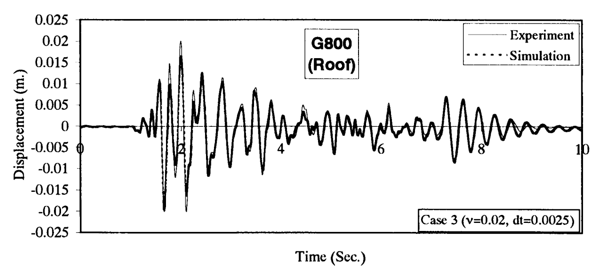

Fig. 21 Displacement response at the roof for G800-1 (damping ratio=0.02, simulation time increment=0.0025)

CONCLUSIONS

In the paper, the Applied Element Method for structural analysis is introduced. The main advantage of this method is that it is simple, accurate and applicable to wide range of problems. For the accuracy, it can be said that it has the same accuracy as the FEM where it can be used and better accuracy compared with the RBSM or EDEM. The formulations used are simpler than that of the FEM. The main advantages of the AEM are:

1. The formulation used are simple compared to the FEM.
2. All reinforcement details, like reinforcement bar location and concrete cover, can be considered easily and without any additional complications in the element shape or arrangement.
3. In case of RC structures, material models used are for plain concrete and reinforcement bars separately. This means that the adopted material models are not affected by the reinforcement ratio. While in the Smeard Crack approach, material models are different and based on to the reinforcement ratio[3].
4. Internal stresses and strains of any point in the material, either reinforcement bars or concrete, can be followed easily.
5. The AEM has wide range of application. It can be applied to static and dynamic cases, monotonic and cyclic loading conditions. It can be applied for small and large deformation ranges.

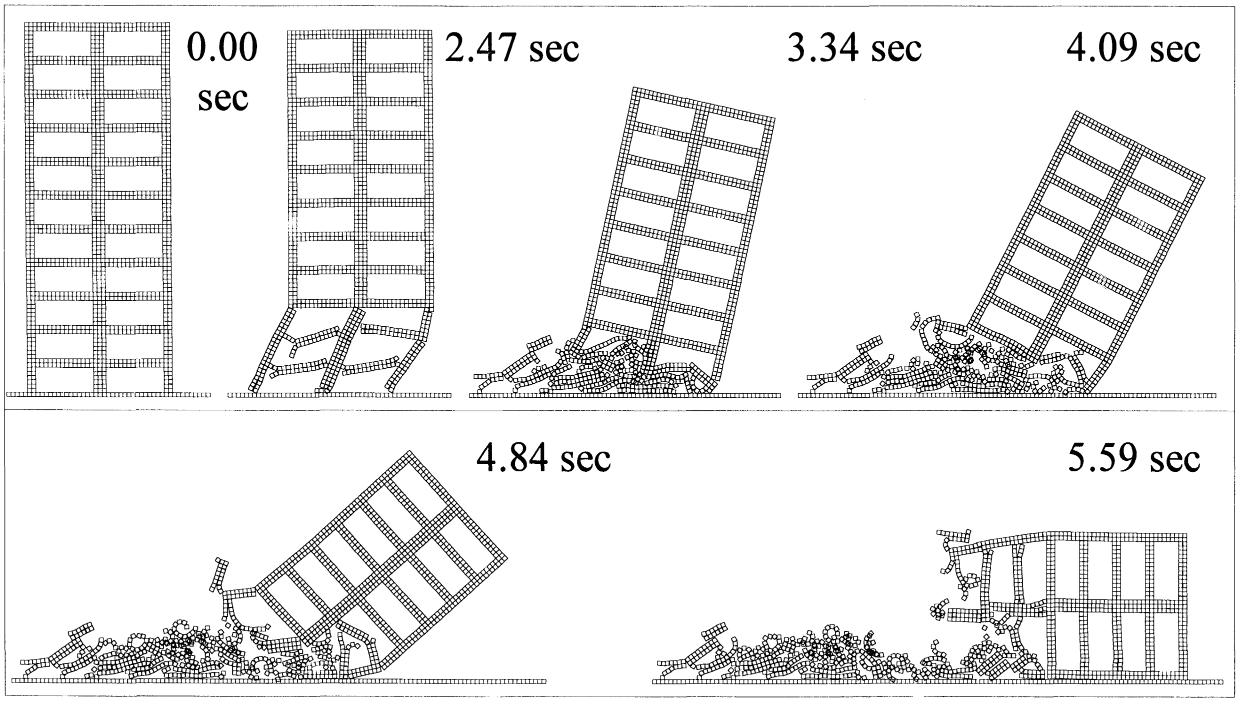

Fig. 22 Simulation of collapse process (Amplitude: 1200 Gal, Time scale: double)
(In the experiment, this case could not be performed because of limitation of shaking table capacity.)

6. Although the shape of adopted elements is square, it has almost no effect on the crack propagation direction, especially in monotonic loading condition. While in the RBSM and EDEM methods, the crack propagation is strongly affected by the element shapes and arrangement.
7. The AEM can be applied for studying the nonlinear dynamic behavior of structures. Effects of cracking, concrete crushing, yield of reinforcement can be considered.
8. The rigid body motion and collision of structural elements during collapse can be followed with reliable accuracy.
9. No previous knowledge about the collapse process is needed before the analysis.
10. For future study of detailed collapse mechanism of structures, additional effects like buckling of reinforcement bars and spalling of concrete cover, etc. are needed to be modeled which are not taken into account yet.
11. It is very difficult, or impossible, to follow complete collapse behavior using methods that assumes continuum material, like FEM and BEM, where failure analysis is still restricted to cases where crack locations are known before the analysis.
12. The EDEM is one of the few models that can simulate such collapse behavior. The main advantages of the AEM compared to the EDEM are high accuracy and short CPU time. With the AEM, the time increment can be enlarged before collision starts while with the EDEM, the time increment is restricted to a certain small value, which is function of the material type and element size. It can not be enlarged even before collision starts. In the AEM, longer time increment can be used before collision and it makes the CPU time required shorter.

REFERENCES

1. Architectural Institute of Japan: A report on damage during Miyagiken-Oki Earthquake of 1978, 1979 (in Japanese).
2. Nishimura A. et. al.: Statistical report on casualty of the Great Hanshin Earthquake, Advances in Legal Medicine 3, July 1997.
3. Okamura H. and Maekawa K.: Nonlinear analysis and constitutive models of reinforced concrete, Gihodo Co. Ltd., Tokyo, 1991.
4. Kawai T.: Recent developments of the Rigid Body and Spring Model (RBSM) in structural analysis, Seiken Seminar Text Book, Institute of Industrial Science, The University of Tokyo, pp. 226-237, 1986.
5. Meguro K. and Hakuno M.: Fracture analyses of structures by the modified distinct element method, Structural Eng./Earthquake Eng., Vol. 6. No. 2, 283s-294s., Japan Society of Civil Engineers, 1989.
6. Meguro K. and Hakuno M.: Application of the extended distinct element method for collapse simulation of a double-deck bridge, Structural Eng./Earthquake Eng., Vol. 10. No. 4, 175s-185s., Japan Society of Civil Engineers, 1994.
7. Kikuchi A., Kawai T. and Suzuki N.: The rigid bodies-spring models and their applications to three dimensional crack problems, Computers & Structures, Vol. 44, No. 1/2, pp. 469-480, 1992.
8. Ueda M. and Kambayashi A.: Size effect analysis using RBSM with Vornori elements, JCI (Japan Concrete Institute) International Workshop on Size Effect in Concrete Structures, pp. 199-210, 1993.
9. Tagel-Din H.: A new efficient method for nonlinear, large deformation and collapse analysis of structures, Ph.D. thesis, Civil Eng. Dept., The University of Tokyo, Sept. 1998.
10. Oscar A. and Lopes Batiz: Earthquake Resistance of Precast Reinforced Concrete Structures, Doctor thesis, The University of Tokyo, 1992.
11. Ristic D., Yamada Y., and Iemura H.: Stress-strain based modeling of hystertic structures under earthquake induced bending and varying axial loads, Research report, No. 86-ST-01, School of Civil Engineering, Kyoto University, March, 1986.
12. Meguro K. and Tagel-Din H.: Simulation of buckling and post-buckling behavior of structures using applied element method, Bulletin of Earthquake Resistant Structure Research Center, IIS, University of Tokyo, No. 32, pp. 125-135, 1999.
13. Meguro K. and Tagel-Din H.: A new simple and accurate technique for failure analysis of structures, , Bulletin of Earthquake Resistant Structure Research Center, IIS, University of Tokyo, No. 31, pp. 51-61, 1998.
14. Timoshinko S. and Gere J.: Theory of Elastic Stability, McGraw-Hill Inc., 1961.
15. Okada T., Kumazawa F., Horiuchi S., Yamamoto M., Fujioka A., Shinozaki K. and Nakano Y.: Shaking table tests of reinforced concrete small scale model structure, Bulletin of Earthquake Resistant Structure Research Center, IIS, University of Tokyo, No. 22, pp. 13-40, 1989.
16. Kumazawa F. and Okada T.: Shaking table tests of reinforced concrete small scale model structure (Part 2), Bulletin of Earthquake Resistant Structure, IIS, University of Tokyo, No. 25, pp. 25-37, 1992.
17. Tagel-Din H. and Meguro K.: Applied element simulation for collapse analysis of structures, Bulletin of Earthquake Resistant Structure Research Center, IIS, University of Tokyo, No. 32, pp. 113-123, 1999.

Appendix

Working Group Sessions

Report from Working Group No. I

Report from Working Group No. 2

Report from Working Group No. 3

Agenda

Participants Roster

REPORT FROM WORKING GROUP 1
LIQUEFACTION AND GROUND DEFORMATION

Reporters :
Ross Boulanger, Masanori Hamada, Masakatsu Miyajima and Leslie Youd

The topic of liquefaction and ground deformation was covered in 20 presentations over four sessions. These presentations and accompanying papers covered a range of important issues and generated valuable discussions among the participants. Closing discussions were necessarily focussed on only a few key points. This summary will only briefly identify some of the key issues identified in the four sessions and closing discussions.

Probabilistic liquefaction evaluation and mapping methods are increasingly needed for loss estimation models. Some participants urged additional research in the development of probabilistic liquefaction evaluations and areal mapping methods, noting that the loss estimation models can be sensitive to these inputs. Probabilistic forms of SPT- or CPT-based liquefaction relationships (e.g., CRR – $N_{1\text{-}60}$ charts) were noted to be affected by the sparse case history data at the higher range of penetration resistances. The resulting relationships depend significantly on whether they are derived solely from the empirical field data or incorporate the additional information provided by experimental data that correlates to the full range of penetration resistances.

Several diverse empirical, similitude and analytical models were presented for estimating lateral ground displacements due to liquefaction. Several participants expressed views that the information from these different approaches should be fully integrated with each other. For example, the basic physics or mechanisms of liquefaction-induced deformations as may be identified by laboratory testing, physical modeling, or numerical analyses, should be used to guide the functional form of parameters in semi-empirical or empirical models.

The basic mechanisms involved in lateral spreading or liquefaction-induced deformations were also the subject of debate, including the representation of liquefied soil behavior as a viscous liquid, solid, or a combination of behaviors. The influence of impeded drainage, permeability, fines and other factors on field behavior were noted to still be poorly understood. Additional experimental studies are needed to understand the role of such factors and to distinguish what are the dominant basic mechanisms affecting liquefaction-induced deformations.

Transient as well as permanent ground deformations were noted as being important to different types of field design problems. Design approaches for estimating the transient deformation (e.g., ground lurching) due to liquefaction were discussed. It was noted that the approaches that have been developed for permanent deformations do not generally give guidelines on the magnitude of transient deformations, and hence further work in this area is needed.

The capabilities and limitations of current constitutive models and analysis methods for liquefaction were discussed. The view was expressed that the complex field behavior, which includes the effects of bifurcation, impeded drainage, three-dimensional geometry, heterogeneity, and numerous other factors, make it unlikely that accurate predictions can ever be reliably made in practice. The alternative viewpoint was that these numerical methods can be calibrated against physical model tests and case histories and then be more comfortably used in design of comparable structures, with caution advised when the problem falls outside the range of conditions covered by the calibrations.

Geologic conditions are always the essential beginning point for evaluating liquefaction and liquefaction-induced deformations. Knowledge of geologic structures and settings can provide important guidance or limits on expected behavior that may not be captured by direct application of certain liquefaction evaluation methods. The need was stressed for a logical review of any analysis method against the basic geologic information available to make sure that unreasonable results were not being produced. While this has long been an essential part of geotechnical engineering, its importance requires that it continue to be stressed.

REPORT FROM WORKING GROUP 2
LIFELINES AND EARTHQUAKE EFFECTS

Reporters :
Donald Ballantyne, Le Val Lund, Makoto Matsushita and Kimiro Meguro

SUMMARY

1. Phases - Mitigation, Emergency, and Reconstruction. One approach to categorizing earthquake engineering is to group activities into three phases: mitigation, emergency, and reconstruction. The three phases clarify research and development activities in the earthquake preparedness throught process. All of the papers presented in the lifeline sessions addressed issues in the mitigation phase. Mr. Matsushita's paper also addressed mutual aid and interties between adjacent utility systems, that would be considered part of the emergency phase, and the proposed rebuilding plan for the Kobe water system, a reconstruction phase activity. Professor Michael O'Rourke's discussion regarding loss modeling could be applicable to both the emergency phase (real time loss modeling), and the reconstruction phase where projects should be prioritized. Dr. Craig Davis's presentation on the Granada Trunk line damage was also applicable to reconstruction.

2. Ground Motion Input - Level 2. The Japanese have implemented the Level 2 design load provision in their national design code applicable to all civil structures. It is the intent that all structures remain functional following a Level 1 earthquake, an event that they will likely see during their life. Special, or important facilities must remain functional following a Level 2 earthquake, an event that is highly unlikey during it's useful life. Two issues were discussed: 1) is a level 2 event comparable to a Maximum Credible Earthquake, a definition that is used in the US, and 2) what facilities are designated as special or important. In the United States, dams and nuclear power plants would be built to remain operable (or to safely shut down with out damage), but few other facilities are designed to meet such rigorous critreria. The Japanese comments indicated the two questions were still under discussion.

3. Liquefaction Hazard Mapping. During the workshop, Mr. Delisle from the California Division of Mines and Geology, made a presentation on California's liquefaction hazard mapping program. They have specified criteria and a procedure for mapping the entire state. The maps only indicate whether the soil is liquefiable, or not liquefiable. The maps are being developed in response to state regulation. The group discussed mapping efforts underway in Japan, and in other locations in the US. Some mapping programs incorporate several levels on susceptibility. Several mapping projects have produced maps showing expected PGD for given earthquake ground motions. There was no clear direction for future mapping. During the workshop, Professor Mike O'Rourke had raised the issue about the need for a "percent of liquefied area" estimating procedure to be developed. Don Ballantyne had raised the same issue in a paper presented at the 5th US-Japan conference in 1995, but there has still been no significant advancement. The percent of liquefiable area is directly propostional to the estimated pipeline failure rate. If the estimate of percent of the area that will liquefy is increased from 5% to 10%, the resulting number of pipeline failures will double. The USGS is working with PG&E to develop an approach for PG&E to use in prioritizing gas pipeline replacement in California.

4. JWWA Pipe Design for 1.2 to 2.0% PGD. The most recent version of the JWWA seismic design guidelines "recommends" that pipe to be installed in liquefiable soils be designed to accommodate 1.2% to 2% strain. Steel, ductile iron, PVC, and polyethylene pipe manufacturers are developing products and/or supporting documentation to show that their respective products meet the JWWA requirements. There was a discussion regarding whether this new provision was a design "standard" or a "recommendation". The consensus was that it is a recommendation. In the US, there is currently no standard or guideline requiring that pipe accommodate a specified strain if it is to be installed in liquefiable soil. Several provisions are in place requiring the designer to consider a special design in liquefiable areas.

In summary, the new Japanese design standards for civil facilities have made significant strides in advancing the state of design. At the time of the workshop, some of the details required to implement the new standards had yet to be resolved.

REPORT FROM WORKING GROUP 3
WATERFRONT STRUCTURES, PILE FOUNDATIONS AND BUILDINGS

Reporters:
Susumu Iai, Bruce Kutter, Geoffrey Martin and Fusanori Miura

SUMMARY

1. Variety of Approaches. The workshop proceedings include a wide variety of approaches to describe the seismic behavior of Waterfront Structures, Pile Foundations and Buildings. These approaches include numerical modeling, constitutive modeling, simplified procedures, new practical design concepts, and physical modeling in centrifuges and shaking tables. Each of these approaches has advantages and disadvantages. By using a combination of these methods, significant progress may be made, particularly in relation to developing a mechanistic understanding of soil-foundation or soil-wall interaction and for validating numerical models.

2. Numerical And Constitutive Modeling. In the numerical modeling arena, Finite Element Methods (FEM), Discrete Element Methods (DEM), Finite Difference Methods, and Applied Element Method (AEM) methods have been used in different papers presented in this workshop. In the DEM, particles are individually modeled. The number of particles that may be analyzed using DEM is limited by the memory and computing power; this limitation is becoming less severe as computing power increases.

In FEM and Finite Difference procedures, soil is modeled as a continuum. The key to continuum modeling is to implement appropriate constitutive and structural interface models into the numerical models. The constitutive models used for research presented in this workshop included models based upon equivalent linear elasticity, plasticity and viscosity models. The goal here is in developing a constitutive model that enables prediction of the deformation of liquefying or liquefied soil. If it is truly "liquefied" then use of viscosity models has some attraction. Even if the soil is not exactly representative of a viscous fluid, viscosity models can be calibrated by a large range of field case histories and then used as a framework for prediction of the magnitude and patterns of deformation caused by liquefaction. However, in a fundamental sense, effective stress models have the advantage of including effects of pore pressure re-distribution or drainage during the earthquake and prediction of liquefaction triggering times.

The constitutive relationships that define the lateral force on a pile as a function of the relative movement between the soil and pile remains a major challenge. The lateral force is important to enable prediction of the loads and deformations imposed on the pile and superstructure during both cyclic loading and during monotonic lateral spreading. Approaches presented in this workshop included 3-D and quasi-3-D dynamic finite element modeling, cyclic p-y curves for analysis of dynamic soil-pile interaction, and monotonic p-y curves to assess the loads transmitted to a pile during monotonic lateral spreading.

3. **1-g and Centrifuge Shaking Table Tests.** Centrifuge and 1-g model test data was presented that elucidated the performance of seawall structures during earthquakes and the dynamic behavior of soil-pile-systems. A significant number of papers presented in the conference included reference to model test data. A healthy trend that seems to be increasing is the use of centrifuge data produced at one university by researchers at different universities. The expanding volume of instruments used in modern model tests has produced large data sets that can be used to study a variety of phenomena. Data from one model test can be used to evaluate site response issues, soil-structure interaction issues, and the mechanisms of development of permanent deformation.

4. **New Practical Design Ideas for Mitigation.** One interesting paper in the conference presented a cable restraining system to prevent large relative deformations of foundations for bridges. Bridge piers located near the waterfront often move more than those far from the waterfront and the relative movement may lead to sections of bridge deck falling off of their supports. Additional work may be needed to assess the dynamic loading that may be imposed on these restraining cables.

5. **Probability, Redundancy, and Variability.** While many of the above approaches are based upon deterministic concepts, the uncertainty associated with their application to practice is accepted. Many engineers feel that they cannot understand the stochastic system until they understand a deterministic system, and therefore the geotechnical engineering profession is still focusing on deterministic approaches. There are at least two key questions that could be addressed:

1) What is the probability that a given behavior will occur at a point?
2) What is the scale of the spatial variability of the performance?

Of the limited number of studies that address uncertainty, many focus on questions similar to question (1). Few papers attempt address question (2). Spatial variability will cause differential movements, and as geotechnical engineers know, differential movements are often more damaging than uniform movements.

FUTURE TRENDS OF EARTHQUAKE ENGINEERING RESEARCH

1. **Experimental Data Bases.** It is clear that future research will continue to place emphasis on comparisons between data obtained from laboratory shaking table or centrifuge tests and numerical models. It is important that laboratory tests be carefully conceived to provide a database that meets the needs of analysis approaches.

Many papers in the conference present one theory and compare it to one set of data from a model test or a series of field measurements. Papers often imply that if one data set agrees with the theory, then the theory must be right. We should keep in mind that the data may also support competing theories, and that theories need to be adaptable to a wide range of boundary conditions and site characteristics. It is clear that soil-foundation-structure interaction in the presence of liquefied soil results in complex cyclic and permanent deformation behavior. Hence much care is needed in establishing the best possible database for analytical interpretation. To further our understanding of soil-foundation-structure interaction, we need to be more objective:

1) In analysis of experimental data, we should also objectively examine theories that appear consistent with the data and attempt to optimize theoretical approaches with respect to practicality for design and adaptability to varying conditions.

2) We should attempt to devise experiments (such as centrifuge model tests) that do not lead to potential ambiguous interpretation. Inclusion of additional instruments at key locations may enable less ambiguous interpretation. For example, a complete set of pore pressure data, both free field and near structures, is desirable to provide a full mechanistic understanding of observed behavior.

3) Similitude laws are an integral part of both 1-g shaking table tests and centrifuge tests. To understand the results from these tests for analytical interpretation and for general application to field conditions, the documentation of similitude assumptions and approximations should accompany test results. For example, data on the coefficient of permeability and the non-linear coefficient of compressibility of soils used are important characteristics in the assessment of potential effects of pore pressure re-distribution or drainage in the vicinity of model foundations or walls.

2. Effect of Lateral Spread on Pile Foundations. Lateral spread interaction involves an understanding of the input ground motion characteristics, the initiation of liquefaction, the stress-strain behavior of liquefied soils, and the magnitude of induced ground deformation. Subsequent force or displacement demands on a piled foundation structure depend on the type of structure, ground stratigraphy including the thickness of a possible non-liquefied surface layer, and the physical characteristics and thickness of the liquefied layer or layers. To obtain a complete understanding of the many variables affecting this problem and to develop practical design methodologies, systematic experimental and analytical studies of all aspects will be required in the future.

Program of the 7th U.S.-Japan Workshop

August 14 (Saturday)

Informal Gathering/Registration	18:00 - 19:00

Day 1 – August 15 (Sunday)

Registration	11:00 - 13:00
Opening Ceremony *Chaired by Prof. T. D. O'Rourke*	13:00 - 13:20
Opening Remarks: Prof. M. Hamada and Prof. J. P. Bardet	
♦ Technical Session I *Chaired by Prof. M. Hamada and Prof. I. M. Idriss*	13:20 – 15:00
♦ Coffee Break	15:00 – 15:30
♦ Technical Session II *Chaired by Prof. T. D. O'Rourke and Prof. F. Miura*	15:30 – 17:30
♦ Reception	17:00 – 20:30

Day 2 – August 16 (Monday)

♦ Technical Session III *Chaired by Prof. S. Yasuda and Prof. J. P. Bardet*	8:10 – 10:10
♦ Coffee Break	10:10 – 10:30
♦ Technical Session IV *Chaired by Prof. L. Finn and Dr. S. Iai*	10:30 – 12:10
♦ Lunch	12:10 – 13:30
♦ Technical Session V *Chaired by M. O'Rourke and Prof. K. Wakamatsu*	13:30 – 15:30
♦ Coffee Break	15:30 – 15:50
♦ Technical Session VI *Chaired by Prof. T. Ohmachi and M. L. Lund*	15:50 – 18:10
♦ Banquet	19:30 –

Program of the 7th U.S.-Japan Workshop (Cont'd)

- Banquet Presentation: Utilization of Earthquake Ground Motions Recorded in Down Hole Arrays. *Prof. I. M. Idriss, University of California, Davis, CA*

Day 3 August 17 (Tuesday)

♦ Technical Session VII *Chaired by Dr. F. Yamazaki and Dr. T. Holzer*	8:30 – 10:30
♦ Coffee Break	10:30 – 10:50
♦ Technical Session VIII *Chaired by Prof. Y. L. Youd and Prof. M. Hoshiya*	10:50 – 12:50
♦ Lunch	12:50 – 2:00
♦ Group Discussion Led by Workshop Reporters	2:00 – 3:00
♦ Workshop Closure	3:00 – 3:10

U.S./Canada Workshop Reporters:

L. Finn and T. Y. Youd: Liquefaction and Ground Deformation

L. Lund and M. O'Rourke: Lifelines

B. Kutter and G. Martin: Waterfront Structures, Pile Foundations and Buildings

Note: Reporters (both U.S. and Japanese) will provide a 10-15 minute synopsis of important issues raised associated with each of the three workshop topics. The presentations will be from 2-3 p.m. on August 17. (Japanese reporters will be identified by the time of the workshop.)

U.S. Participants

Tarek ABDOUN
Department of Civil Engineering
Rensselaer Polytechnic Institute

Donald BALLANTYNE
EQE International

Pedro ARDUINO
Department of Civil Engineering
University of Washington

Jean Pierre BARDET
Department of Civil Engineering
University of Southern California

Ross BOULANGER
Department of Civil and Environmental Engineering
University of California at Davis

Craig DAVIS
Department of Water and Power, Los Angeles, CA

Mark DELISLE
Division of Mines and Geology
California Department of Conservation

Ahmed ELGAMAL
Department of Civil Engineering
University of California at San Diego

Siang-Huat GOH
School of Civil and Environmental Engineering
Cornell University

Thomas HOLZER
U.S. Geological Survey

Jian-Ping HU
Department of Civil Engineering
University of Southern California

I. M. IDRISS
Department of Civil and Environmental Engineering
University of California at Davis

Sang-Soo JEON
School of Civil and Environmental Engineering
Cornell University

Steven KRAMER
Department of Civil Engineering
University of Washington at Seattle

Bruce KUTTER
Department of Civil and Environmental Engineering
University of California at Davis

Le Val LUND
Los Angeles, CA

Geoffrey MARTIN
Department of Civil Engineering
University of Southern California

Michael O'ROURKE
Department of Civil Engineering
Rensselaer Polytechnic Institute

Thomas O'ROURKE
School of Civil and Environmental Engineering
Cornell University

William "Woody" SAVAGE
Geosciences Department
Pacific Gas and Electric Company

Kenneth STOKOE, II
University of Texas at Austin

John TINSLEY, III
U.S. Geological Survey

T. TOBITA
Department of Civil Engineering
University of Southern California

Selcuk TOPRAK
U.S. Geological Survey

Zhaohui YANG
Columbia University

T. Leslie YOUD
Department of Civil Engineering
Brigham Young University

Japan Participants

Hirokazu AKAGI
Department of Civil Engineering
Waseda University

Y. FURUMOTO
Department of Civil Engineering
Gifu University

Masanori HAMADA
Department of Civil Engineering
Waseda University

Masaru HOSHIYA
Department of Civil Engineering
Musashi Institute of Technology

Susumu IAI
Port and Harbour Research Institute

T. KATADA
Musashi Institute of Technology

T. KAWAKAMI
Department of Marine Civil Engineering
Tokai University

Hiroyoshi KIKU
Sato Kogyo Company

Makoto MATSUSHITA
Kobe Municipal Waterworks Bureau

Eiji MATSUYAMA
Engineering Research Center
NKK Corporation

Kimiro MEGURO
Institute of Industrial Science
University of Tokyo

Fusanori MIURA
Faculty of Engineering
Yamaguchi University

Masakatsu MIYAJIMA
Department of Civil Engineering
Kanazawa University

Shin'ichiro MORI
Department of Civil and Environmental Engineering
Ehime University

Akihiko NISHIMURA
Structure Technology Division
Railway Technical Research Institute

Tatsuo OHMACHI
Interdisciplinary Graduate School
of Science and Technology
Tokyo Institute of Technology

Yuichi SANO
Konoike Construction Co.

H. SEGED
Department of Civil Engineering
Gifu University

T. SATO
Disaster Prevention Research Institute
Kyoto University

Sumio SAWADA
Disaster Prevention Research Institute
Kyoto University

Kazue WAKAMATSU
Institute of Industrial Science
University of Tokyo

Fumio YAMAZAKI
Institute of Industrial Science
University of Tokyo

Jun YANG
Disaster Prevention Research Institute
Kyoto University

A. YASHIMA
Department of Civil Engineering
Gifu University

Koji YOSHIZAKI
Tokyo Gas Company

MULTIDISCIPLINARY CENTER FOR EARTHQUAKE ENGINEERING RESEARCH
A National Center of Excellence in Advanced Technology Applications

University at Buffalo, State University of New York
Red Jacket Quadrangle ■ Buffalo, New York 14261-0025
Phone: 716/645-3391 ■ Fax: 716/645-3399
E-mail: mceer@acsu.buffalo.edu ■ WWW Site: http://mceer.buffalo.edu